# *Proceedings*
# 33rd International Conference on Ground Control in Mining

## *Edited by*


**Thomas Barczak**[4]
**Matt Ingold**[2]
**Syd S. Peng**[10]
**Donna Schmidt**[3]
**Steve Tadolini**[7]
**Melanie Thompson**[2]


## *Primary Technical Reviewers*

**Joe Cybulski**[3]
**Dennis Dolinar**[9]
**Essie Esterhuizen**[9]
**John Ellenberger**[9]
**Gerry Finfinger**[9]
**Keith Heasley**[10]
**Tristan Jones**[9]
**Ted Klemetti**[9]
**Michael McCarter**[12]
**Brijes Mishra**[10]
**Michael Murphy**[9]
**Kyle Perry**[11]
**Vince Scovazzo**[6]
**Steve Tadolini**[7]
**Ihsan Tulu**[9]
**Erik Westman**[13]
**Joe Zelanko**[8]
**Peter Zhang**[1]

1. Alpha Natural Resources
2. Consultant (Freelance Editor)
3. DOL, Mine Safety and Health Administration
4. Editorial consultant and Coal Age Field Editor
5. ICGCM Inc.
6. John T. Boyd Company
7. Orica
8. Rosebud Mining Company
9. NIOSH, Office of Mine Safety and Health Research
10. West Virginia University
11. University of Kentucky
12. University of Utah
13. Virginia Tech


July 29 - 31, 2014

## 33rd International Conference on Ground Control in Mining

# ORGANIZING COMMITTEE

**Tom Barczak,** ICGCM**,** Venetia, PA
**Michael Bayerl,** Hilti Entwicklungsgesellschaft GmbH, Kaufering, Germany
**Jonathan Bowler,** Golder Associates (UK) Ltd., Burton on Trent, United Kingdom
**Al Campoli,** Jennmar Corporation, Pittsburgh, PA
**Jinsheng Chen,** DSI Underground Systems, Inc., Martinsburg, WV
**Ismet Canbulat,** Anglo American, Brisbane, Australia
**Mark Colwell,** Colwell Geotechnical Services, Caloundra, Australia
**Joe Cybulski,** USDOL - MSHA, Pittsburgh, PA
**Gerry Finfinger,** NIOSH (retired), Office of Mine Safety and Health Research, Pittsburgh, PA
**Richard Gray,** DiGioia, Gray & Associates, LLC, Greensburg, PA
**Gregory Hasenfus,** Consol Energy Inc., Canonsburg, PA
**Keith Heasley,** West Virginia University, Morgantown, WV
**Bruce Hebblewhite,** University of New South Wales, Sydney, Australia
**Greg Hinshaw,** J. H. Fletcher & Co., Huntington, WV
**Anthony Iannacchione,** University of Pittsburgh, Pittsburgh, PA
**Ted Klemetti,** NIOSH, Office of Mine Safety and Health Research, Pittsburgh, PA
**Raj Kallu,** University of Nevada, Reno, Reno, NV
**Yi Luo,** West Virginia University, Morgantown, WV
**Christopher Mark,** Mine Safety and Health Administration, Pittsburgh, PA
**Michael McCarter,** University of Utah, Salt Lake City, UT
**Brijes Mishra,** West Virginia University, Morgantown, WV
**David Newman,** Appalachian Mining and Engineering, Inc., Lexington, KY
**Dan Payne,** BHP Billiton Mitsubishi Alliance, Emerald, Australia
**Syd S. Peng,** West Virginia University, Morgantown, WV
**Kyle Perry,** University of Kentucky, Lexington, KY
**Tim Ross,** Agapito Associates, Inc., Grand Junction, CO
**Jamal Rostami,** Penn State University, University Park, PA
**John Rusnak,** Peabody Energy Inc., St. Louis, MO
**Vincent Scovazzo,** John T. Boyd Company, Richland, WA
**Sam Spearing,** Southern Illinois University, Carbondale, IL
**Daniel Su,** Consol Energy Inc., Canonsburg, PA
**Stephen Tadolini,** Orica, St. Clairsville, OH
**Michael Trevits,** NIOSH (retired), Office of Mine Safety and Health Research, Pittsburgh, PA
**Erik Westman,** Virginia Tech, Blacksburg, VA
**Joe Zelanko,** Rosebud Mining Company, Kittanning, PA
**Peter Zhang,** Alpha Natural Resources, Inc., Waynesburg, PA

# Sponsors

**Agapito Associates, Inc.,** Grand Junction, CO
**BASF, The Chemical Co.,** Cleveland, OH
**CONSOL Energy, Inc.,** Canonsburg , PA
**DSI Mining Americas (Fasloc, Inc.),** Salt Lake City, UT
**J. H. Fletcher & Co.,** Huntington, WV
**Golder Associates Inc,** Burton-on-Trent, U.K.
**Heintzmann Inc.,** Cedar Bluff, VA
**Hilti North America,** Tulsa, OK
**Jennmar Corp.,** Pittsburgh, PA
**Orica,** Georgetown, KY
**Rosebud Mining Company**, Kittanning, PA
**Strata Products Worldwide**, Sandy Springs, GA
**West Virginia Coal Association,** Charleston, WV
**West Virginia University**, Morgantown, WV



# Syd S. Peng Ground Control in Mining Award

The Society for Mining, Metallurgy, and Exploration (SME) is pleased to announce that Dr. Ismet Canbulat has been selected as the 2013 recipient of the SME Syd S. Peng Ground Control in Mining Award. Established in 2005, the Syd S. Peng Award recognizes individuals that have demonstrated technical and scientific excellence in advancing the understanding of ground control technologies or approaches by either publication or direct applications in the mining industry.

When notified about this award, Ismet responded, "I am extremely thrilled and honoured to receive this prestigious award; this is one of the most memorable events of my professional career. I sincerely thank the SME and the selection committee for recognizing my contributions with this award. Many of my current and past colleagues have contributed to my professional growth I therefore accept the award on behalf of all of us. Thank you."



Ismet received his BSc Mining Engineering degree from Istanbul Technical University. He moved to South Africa in 1993 and worked for the Council for Scientific and Industrial Research (CSIR). While working at the CSIR he obtained his MSc Mining Engineering degree from the University of the Witwatersrand and his PhD from University of Pretoria.

After 10 years in research, Ismet moved to consultancy and worked for Groundwork Consulting and later at Strata Engineering in Australia. In 2006, Ismet joined Anglo American Metallurgical Coal in Brisbane, where he is currently the Principal Geotechnical Engineer for underground operations. He is also an Adjunct Associate Professor at the Mining Engineering Department of the University of New South Wales, where he lectures Strata Control Graduate Diploma Courses.

Ismet is a member of Engineers Australia, Australasian Institute of Mining and Metallurgy, Southern African Institute of Mining and Metallurgy, Australian Geomechanics Society, International Society for Rock Mechanics, Bowen Basin Underground Geotechnical Society. He is also a registered Professional Engineer through Board of Professional Engineers Queensland. Ismet has been author and co-author of over 40 technical papers published in refereed journals and conference proceedings.

Ismet and his lovely wife Semsa have been married happily for 20 years and have a son, Tolga. They all live in Brisbane Australia.

## *About The Syd S Peng Ground Control in Mining Award:*

The purpose of the award is to provide recognition to individuals that have demonstrated technical and scientific excellence in advancing the understanding of ground control technologies or approaches by either publication or direct applications in the mining industry.

Dr. Keith Heasley, Award Committee Chair

# Syd S. Peng Ground Control Scholarships

As a part of the Syd S. Peng Ground Control in Mining Award - an undergraduate and/or graduate scholarship, or scholarships, will be awarded annually to encourage the development of ground control engineers. The scholarship will be a minimum of $5,000 (U.S.) and provided in a single payment to the recipient by January 1 (so the funds are available for the Spring Semester).

The 2013 scholarships were awarded and the recipients were recognized during the banquet at the Annual SME Meeting held in Salt Lake City, Utah. The 2013 recipients were:

- Behrooz Abbasi – Southern Illinois University at Carbondale
- Kevin Harris – University of Kentucky
- Evan Keffeler – University of Nevada, Reno
- Christopher Newman, West Virginia University
- Peng Zhang, West Virginia University




**Pictured from left to right is Evan Keffeler, Kevin Harris, Behrooz Abbasi.**

**Not pictured are Christopher Newman and Peng Zhang.**

# Kazem Oraee Scholarship for Mining

The **Kazem Oraee Scholarship for Mining** award is to promote underground mining engineering and more specifically, the ground control discipline. Recent trends indicate that a shortage of competent ground control engineers may exist if this trend is allowed to continue. To help remedy the situation and promote the ground control engineering discipline, an undergraduate OR graduate scholarship, will be awarded annually at the International Conference on Ground Control in Mining (ICGCM) to encourage the development of ground control engineers. The scholarship recipient will receive $5,000 (US) provided in a single payment and a commemorative certificate/statue.

The 2013 winner was Nan Zhou. He was selected from 30 well qualified candidates. Nan is a second year Ph.D. student at China University and Mining Technology (CUMT). He has been conducting on innovative backfill longwall coal mining while continuing his studies at the university. In this effort, he has worked tireless to perform in-mine surveys and monitoring of several coal mines. He received two coveted Chinese national awards for his dedication and efforts in completing 11 coal industrial projects. His Ph.D. research project is entitled "Mechanism of Preventing and Controlling Mining-Induced Dynamic Hazards Under Hard Roofs in Waste Rock Backfilling Coal Mining".




**Jingyi Cheng accepting the award for Mr. Zhou at the 32nd ICGCM conference.**

# 32nd ICGCM – The Best of Ground Control in Mining



(From left to right) James Pile (BHP Billiton), Bruce Hebblewhite (University of New South Wales), Kevin Harris (University of Kentucky), Sam Spearing (Southern Illinois University), Heather Lawson (NIOSH), Steve Tadolini (Orica), Syd Peng (WVU)

The Best of Ground Control was held at the 2014 SME Annual Meeting & Exhibit on February 24, 2014, Salt Lake City, Utah. This is a standing SME session at the Annual Meetings in the Coal & Energy Division. The six technical papers were selected from the 32nd International Conference of Ground Control in Mining (ICGCM 2013). This was an exceptional line-up and very well attended at the conference. The papers are selected during the conference based on technical originality and merit and the quality of the presentation. In keeping with the original vision of Dr. Syd S. Peng for the conference, a diverse group of selections are sought from industry, academia, manufacturers, consultants, and government.

# Mine Visit Courtesy of Consol Energy

A visit to one of Consol Energy's longwall mines gave attendees a chance to see a modern American longwall operation.



# TABLE OF CONTENTS

## Fundamental Research Studies

1. **A Case Study of Topography–related Stress Rotation Effects on Multi–seam Stability**, *I. Tulu, T. Klemetti, E. Esterhuizen, NIOSH, Office of Mine Safety and Health Research, Pittsburgh, PA, J. Sumner, Lone Mountain Processing Inc., ST. Charles, VA* ..... 1
2. **To What Extent the Mechanical Properties of Coal Play Role in Coal Mine Bumps? A Comparison Between Bump and Non–bump Prone Coal**, *G. Rashed, S. Peng, West Virginia University, Morgantown, WV* ..... 8
3. **Experimental Observations and Interpretations on Fracture Networks, Strength and Deformability of Coal Masses under Three-Dimensional Loading Conditions**, *P. He, P. Kulatilake, University of Arizona, Tucson, AZ, M. He, D. Liu, China University of Mining and Technology (Beijing), Beijing, China* ..... 13
4. **Analyses of De-Confinement Mechanisms of Unstable Failures in Underground Mining Conditions**, *R. Gu, U. Ozbay, Colorado School of Mines, Golden, CO* ..... 22

## Operator Case Histories and Experiences

5. **Learning Our Geotechnical Limits and Pushing Our Longwalls Through Them**, *R. Campbell, Blackrock Mining Solutions Pty Ltd, Mackay, Australia* ..... 27
6. **Mitigation of a Massive Sandstone Channel's Impact on Longwall Face Evaluation and Enhancement of Hydraulic Fracturing Technique**, *J. Lu, D. Su, G. Hasenfus, M. Van Dyke, L. Stull, Consol Energy Inc., Canonsburg, PA* ..... 35
7. **The Implementation of Rock Mechanics Into a Multiple Level Limestone Mine**, *D. Newman, Appalachian Mining and Engineering, Inc., Lexington, KY* ..... 41
8. **Multi–seam Mining Over Old Workings with Small Pillars - A Case Study**, *P. Zhang, S. Peterson, Alpha Natural Resources, Inc., Waynesburg, PA, J. Pugh, Alpha Natural Resources, Inc., Charleston, WV, P. Bucks, C. Vass, Alpha Natural Resources, Inc., Sutton, WV* ..... 47
9. **Ground Control Design Considerations for Reducing Longwall-Induced Stress and Seismicity Associated with Massive Sandstone under Deep Cover**, *D. Su, G. Hasenfus, L. Stull, Consol Energy Inc., Canonsburg, PA* ..... 54
10. **A Case Study of a Low Overburden Longwall Recovery with Pre-Developed Recovery Entries**, *J. Stankus, X. Li, Keystone Mining Services, LLC, an affiliate of Jennmar, Pittsburgh, PA, B. Hanson, R. Ochsner, Signal Peak Energy, LLC, Roundup, MT, L. Ma, D. Faulkner, Keystone Mining Services, LLC, Pittsburgh, PA* ..... 63
11. **Sandy Creek Waterfall—case Study of Successful Management of the Potential Impacts of Longwall Mining on a Sensitive Natural Surface Feature**, *R. Walsh, BHPBilliton Illawarra Coal, Wollongong, Australia, B. Hebblewhite, University of New South Wales, Sydney, Australia, G. Li, NSW Dept of Industry and Investment, Maitland, Australia, K. Mills, Strata Control Technology, Wollongong, Australia, M. Nicholson, Michael Nicholson Consulting Pty Ltd (formerly BHPB Illawarra Coal), Wollongong, Australia, J. Barbato, Mine Subsidence Engineering Consultants, Sydney, Australia, P. Brannon, BHPBilliton Illawarra Coal, Wollongong, Australia* ..... 71

12. **Challenges of Room and Pillar Mining at 900 M Depths in the Czech Republic**, *W. Schloemer, New World Resources, Karvina, Czech Republic, J. Golasowski, OKD, a. s., Karvina, Czech Republic, R. Vochta, OKD, a.s., Karvina, Czech Republic, M. Mikoláš , V. Hudeček, VŠB –TU Ostrava, Ostrava, Czech Republic*.....80
13. **Ground Response As a Longwall Advances Into a Backfilled Recovery Room under Low Cover**, *D. Gearhart, T. Jones, C. Compton, T. Minoski, NIOSH, Office of Mine Safety and Health Research, Pittsburgh, PA, R. Ochsner, Signal Peak Energy, Roundup, MT*.....87

## Local Stability (Roof, Rib, and Floor) Control Strategies

14. **Suspension Designs Required in the Logical Framework**, *R. Seedsman, Seedsman Geotechnics Pty Ltd, Mittagong, Australia*.....97
15. **Understanding and Optimizing the Performance of Passive Primary Support on Coal Mines**, *A. Spearing, A. Mishra, Southern Illinois University Carbondale, Carbondale, IL, R. Taushanoff, Minova North America, Georgetown, KY, J. Sell, Minova International, Bowerston, OH, T. Kostecki, Southern Illinois University Carbondale, Carbondale, IL*.....105
16. **Investigating the Contributing Factors to Rib Fatalities Through Historical Analysis**, *T. Jones, K. Mohamed, T. Klemetti, NIOSH, Office of Mine Safety and Health Research, Pittsburgh, PA*.....113
17. **Update: Analysis and Case Study of Impact-Resistant Steel Sets for Underground Roof Fall Rehabilitation**, *D. Faulkner, J. Ma, J. Stankus, Jennmar Corporation, Inc, Pittsburgh, PA*....124
18. **Meeting the Challenges of Floor and Sidewall Strata Control in UK Deep Coal Mines**, *L. Kent, Golder Associates (UK) Ltd., Burton on Trent, United Kingdom, J. Bowler, Golder Associates (UK) Ltd, Burton on Trent, United Kingdom, D. Moore, UK Coal Production Ltd, Doncaster, United Kingdom, S. Walker, Thoresby Colliery Ltd, Mansfield, United Kingdom*.....134

## Ground Control Design Tools and Mine Design Practices

19. **The Caterpillar HW300 Quickscan**, *P. Kleiterp, Caterpillar Highwall Mining Systems, Sliedrecht, Netherlands*.....144
20. **Ground Control in the Underground Coal Mines of Colombia**, *C. Mark, USDOL - MSHA, Pittsburgh, PA*.....150
21. **Strata Control Investigations During Fully Mechanized Coal Pillar Extraction in Indian Coalfields**, *R. Singh, S. Ramani, A. Singh, R. Kumar, A. Singh, CSIR-CIMFR, Dhanbad, India*.....158
22. **A Case Study for Multiple Seam Calibration of LaModel in Bump Prone Ground**, *K. Harris, M. Raffaldi, K. Perry, University of Kentucky, Lexington, KY*.....165
23. **A Comparison Between ARMPS and the New ARMPS-LAM Programs**, *P. Zhang, Carlson Software, Watertown, MA, K. Heasley, West Virginia University, Morgantown, WV, Z. Agioutantis, Technical University of Crete, Greece*.....170

## Equipment and Support Product Developments

24. **FlexKnot: An Innovation in Roof and Rib Surface Control**, *A. Bhagwat, Orica, Bowerston, OH, D. King, Bekaert Corporation, Van Buren, AR*.....175
25. **Development of Road Header Roof Bolting Module**, *S. Farrell, J.H. Fletcher & Co., Huntington, WV*.....182

26. **Development of Mechanized Ground Support Installation Equipment for Improved Safety in Narrow Vein Mine Conditions**, *W. Kendall, J.H. Fletcher & Co., Huntington, WV, M. Ferster, Stillwater Mining Co., Nye, MT*.....185
27. **Introduction of a New Superior Coating on Ground Support Products**, *R. Oler, DSI Underground Systems Inc, West Jordan, UT, J. Chen, DSI Underground Systems Inc, Martinsburg, WV*.....189
28. **Fiber Reinforced Polymer Rockbolts for Ground Control in a Strong Jointed Rock Mass**, *S. Mohanty, T. Vandergrift, Agapito Associates, Inc., Golden, CO, G. Chin Hwi, Parsons Brinckerhoff Pte., Ltd., Singapore, T. Ross, Agapito Associates, Inc., Golden, CO, M. Lee, Parsons Brinckerhoff Pte., Ltd., Singapore, Germany*.....193
29. **A Novel and Effective Method to Develop Tension in a Roof Bolt**, *P. Gramlich, J. Clingan, DSI Underground Systems, Martinsburg, WV*.....199
30. **Development and Application of the TT Anti-Friction Washer for Use with Tensioned Roof Bolt Systems**, *T. Cook, T. Sub, J. Stankus, Jennmar Corporation, Inc, Pittsburgh, PA*.....204

## Ground Control Instrumentation and Ground Monitoring Systems

31. **Time Dependent Mining Induced Subsidence Measured By Differential Interferometric Synthetic Aperture Radar**, *J. Wempen, M. McCarter, University of Utah, Salt Lake City, UT*.....209
32. **Tracking and Tracing in Terms of Transportation Logistics of Hard Coal Mines**, *M. Mondring, RAG Mining Solutions, Herne, Germany, L. Berger, ecom instruments inc., Katy, TX*...216
33. **Photogrammetric Monitoring of Rock Mass Behavior in Deep Vein Mining**, *D. Benton, S. Iverson, J. Johnson, L. Martin, NIOSH, Office of Mine Safety and Health Research, Spokane, WA*.....221
34. **Introduction of a Measurement Based Ground Control Management System to a Deep Level Potash Mine**, *A. Garcia, J. Bowler, A. Preddy, Golder RMT (Golder Associates (UK) Ltd., Burton-on-Trent, United Kingdom, H. Duffty, Cleveland Potash Ltd,, Boulby Mine, Redcar and Cleveland, United Kingdom*.....228
35. **A Liquid Settlement System for Measuring Roof Sag During Development Mining - A Comparison Between Place Change Mining and a Miner–bolter**, *A. Shaffer, Agapito Associates Inc., Grand Junction, CO, J. Pile, BHP Billiton, Waterflow, NM*.....232

## Numerical Modeling Developments and Applications

36. **Rock Slope Stability Comparison Between Deterministic and Probabilistic Block Theory Analyses for An Open Pit Mine**, *P. Kulatilake, J. Zheng, B. Shu, T. Sherizadeh, University of Arizona, Tucson, AZ, J. Deng, Sichuan University, Chengdu, China*.....236
37. **Combined Effects of Rock Bedding Orientation and Topography on Stresses Around Mine Openings**, *A. Molavi Tabrizi, University of Akron, Akron, OH, W. Griffith, University of Texas at Arlington, Arlington, TX, E. Pan, Y. Zhao, University of Akron, Akron, OH*.....243
38. **Stability of a Gateroad Used Simultaneously for Two Retreating Longwall Faces**, *S. Prusek, A. Walentek, Central Mining Institute, Katowice, Poland, L. Kloc, Kompania Weglowa S.A., Katowice, Poland, L. Klabis, A. Malesza, Kompania Weglowa S.A., Bytom, Poland*.....248

39. **Three Dimensional Analysis of Strain and Ground Surface Displacement Caused By Underground Mining in the Vicinity of Geotechnical Barriers**, *R. Misa, K. Tajduś, Strata Mechanic Research Institute Polish Academy of Science, AGH University of Science and Technology, Crakow, Poland, A. Sroka, Technische Universität Bergakademie Freiberg, Strata Mechanic Research Institute Polish Academy of Science, Freiberg, Germany*.....255

## Material Studies and Rockmass Characterization

40. **Multi-stage Testing Procedures, Verification, and Results for Strong, Brittle Sandstone**, *M. Murphy, G. Esterhuizen, G. Morrow, NIOSH, Office of Mine Safety and Health Research, Pittsburgh, PA*.....261
41. **Use of a Plate Loading Device to Quantitatively Evaluate Weak Rock Mass Classifications in the Underground Gold Mines of Nevada, USA**, *R. Kallu, E. Keffeler, S. Warren, R. Watters, University of Nevada, Reno, Reno, NV*.....272
42. **Roof Geotechnical Properties for Roof Control Purposes in Illinois Coal Field**, *A. Osouli, Southern Illinois University Edwardsville, Edwradsville, IL, I. Shafii, B. Moradi Bajestani, Southern Illinois University Edwardsville, Edwardsville, IL*.....278
43. **Application of Various Probing Methods for Rock Characterization in Boreholes Drilled for Roof Bolting**, *A. Naeimipour, Penn State University, University Park, PA, J. Rostami, Penn State University, State College, PA*.....284
44. **Rock Characterization Using Time - Series Classification Algorithms**, *S. Bahrampour, J. Rostami, A. Naeimipour, Pennsylvania State University, State College, PA, C. Collins, J.H. Fletcher, huntington, WV*.....293
45. **Estimating Coal Strength Based on Historical Laboratory Tests and Geomechanics Classification**, *A. Zingano, University Federal of Rio Grande do Sul, Porto Alegre, Brazil, R. Cabral, Departamento Nacional da Produção Mineral, Brasilia, Brazil, S. Oliveira, Departamento Nacional da Produção Mineral, Florianopolis, Brazil, S. Guazelli, J. Koppe, Univ Fed Rio Grande do Sul, porto alegre, Brazil*.....298

## Subsidence, Slope Stability, and Environmental Issues

46. **Mechanics of Horizontal Movements Associated with Coal Mine Subsidence in Sloping Terrain Deduced From Field Measurements**, *K. Mills, SCT Operations Pty Ltd, Wollongong, Australia*.....304
47. **Development of An Enhanced Methodology for Ground Movement Predictions Due to Longwall Mining in the Illinois Basin**, *Z. Agioutantis, VCCER, Virginia Tech, Blacksburg, VA, D. Barkley, Illinois Dept of Natural Resources Office of Mines and Minerals, Springfield, IL, M. Karmis, Virginia Tech, Blacksburg, VA, S. Elrick, University of Illinois, Champaign, IL*.....312

## Regulatory, Safety Management, and Risk Assessment Issues

48. **Mine Water vs. Drinking Water—technical Execution and Legal Relationship in Germany**, *T. Papst, A. Preusse, RWTH Aachen University, Aachen, Germany*.....320
49. **Risk Analysis and Risk Ranking in Tunneling: A Case Study**, *B. Oraee, Imperial College London, London, United Kingdom, N. Hosseini, H. Eskandar, Azad University of Iran, Tehran, Iran, K. Oraee, University of Stirling, Stirling, United Kingdom*.....324

## Chinese Mining Practices and Solutions


50. **Strata Movement Around Large Mining Height Face Area with Fully Mechanized Method in Steeply Dipping Thick Seam**, *Y. Wu, Xi'an University of Science and Technology, Xi'an, China, P. Xie, H. Wang, J. Dou, X. Gao, Y. Zeng, Xi'an University of Science and Technology, Xi'an, China, D. Yun, Xi'an University of Science and Technology, Xi'an, China* ..... 331
51. **Study on the Modified Model of Probability Integral Method**, *Z. Hongzhen, D. Kazhong, F. Hongdong, China University of Mining and Technology, Xuzhou, China* ..... 338
52. **Overburden Strata Movement for the Longwall Mining of Shallow Seam under the Gobs of Room and Pillar Mining**, *F. Wang, S. Tu, A. Liu, China University of Mining and Technology, Xuzhou, China, Z. Zhang, X. Ma, Ordos Wulan Coal Group Corporation Limited, Ordos, China* ..... 344
53. **Development of the 3D Numerical Modeling of Roof Bolts for Studying the Bolt/Rock Interaction**, *W. Li, China University of Mining and Technology, Xuzhou, China, J. Bai, China University of Mining and Technology, Xuzhou, Jiangsu, China, V. Dao, Hanoi university of mining and geology, TuLiem* ..... 352
54. **The Impact Factors of Overburden Movement in Longwall Mining of Shallow Coal Seams**, *Y. Li, J. Wang, China University Of Mining and Technology Beijing, Beijing, China, S. Peng, West Virginia University, Morgantown, WV* ..... 360
55. **Underground Mining Technology in Chinese Coal Mines**, *j. Wang, L. Wang, Y. Li, B. Yang, China University of Mining and Technology (Beijing), Beijing, China* ..... 367
56. **Overburden Failure Characteristics of Extra-Thick Seam Using Top Coal Caving Mining Method at Tongxin Coal Mine**, *Z. Zhu, H. Zhang, Liaoning Technical University, Fuxin, China, B. Yu, Datong Coal Mine Group Company, Datong, China, Y. Chen, Liaoning Technical University, Fuxin, China, L. Huo, Datong Coal Guodian Tongxin Coal Mine Co. Ltd., Datong, China* ..... 373
57. **Validation of Overburden Failure Zone in Complex Extra Thick Coal Seam by EH–4 Magnetotelluric Method**, *H. Rong, H. Zhang, J. Han, Liaoning Technical University, Fuxin, China, G. Li, F. Yang, Fushun Mining Group Co. Ltd., Fushun, China* ..... 379

AUTHOR'S INDEX ..... 386

# A Case Study of Topography–Related Stress Rotation Effects on Multi–seam Stability

**Ihsan Berk Tulu**, Engineer
**Ted Klemetti**, Acting Team Leader
**Essie Esterhuizen**, Senior Scientist
Ground Control
NIOSH, Office of Mine Safety and Health Research
Pittsburgh, PA

**James Sumner**, Mining Engineer
Lone Mountain Processing Inc.
ST. Charles, VA

## ABSTRACT

The complex interaction between multiple seam pillar extraction panels and variable topography can generate unexpected ground control problems. This case study describes stress-related damage in multiple seam workings that resulted in difficult operating conditions and compromised the safety of the support crews. The damage appeared to be caused by horizontal stress but the unexpected location of the damage baffled the authors. A 2D Finite element analysis was conducted of the mine layout and surface topography in an attempt to explain the observed failure. It was discovered that the topography resulted in the rotation of the major stress at the location of the current workings. The stress rotation caused asymmetrical interactions between the workings on the different coal beds, which can explain the unexpected response observed in the mine. Consequently the layout of the next panel was changed by locating the vulnerable entry 30 ft away from its originally planned position. The new location was selected to locate the entry in favorable stress conditions. The change in layout resulted in a significant improvement in conditions when the next panel was mined. At the time of writing this paper, a full panel has been developed using the modified layout without undue ground control problems. The case study demonstrates that numerical models can help engineers to interpret and solve complex multi-seam interaction problems.

## INTRODUCTION

Multi-seam interactions in coal mines can cause large variations in the coal bed stress when mining above or below previously mined workings. The elevated or reduced stresses can result in adverse ground conditions. When combined with variable topography the interaction can cause stress rotations and complex rock response. This paper presents a case study in which baffling interactions occurred during development mining below previously mined workings. The interactions caused unexpected stress-related damage in the rock surrounding the development, which required substantial additional support to maintain safe working conditions. It was only after conducting a detailed stress analysis of the situation that the cause of the unexpected interactions was identified and a solution to the problem became apparent. At the time of writing this paper, a full panel has been developed using the proposed solution with significantly improved ground conditions and operator safety.

## MINING AND GEOTECHNICAL PARAMETERS AT THE CASE STUDY MINE

The Darby Fork No. 1 Mine is operated by Lone Mountain Processing Inc. and is located in Harlan County, KY. The mine produces bituminous coal from the Darby and Kellioka coal beds by the retreat room and pillar mining method. The operator has been mining the Owl, Darby, and Kellioka coal beds for last 20 years. This paper is concerned with mining in the Kellioka seam, located below the workings in the Owl and Darby coal beds.

### Mining Layout

The workings on the Kellioka coal bed are accessed from the Darby by a set of three slopes which connect to the L-7 Right panel (Figure 1). The Kellioka, Darby, and previously mined Owl panels have been stacked vertically so that the panel edges and barrier pillars between panels are superimposed. The depth of cover varies between 300 and 2,000 ft, and the thickness of interburden between the Kellioka and the Darby coal beds varies between 30 ft and 50 ft. In the Kellioka the L-7 panel was developed first to provide access from the Darby coal bed. The operator developed and retreat-mined the L-8 and L-9 panels to the east followed by the L-6 panel to the west. The L-7 panel was mined due north and the L-8, L-9, and L-6 panels were mined due south. Pillars in the L-7 panel were not extracted to provide access to the remainder of the Kellioka workings and to provide intake ventilation.

The production pillars are designed to 80’ x 80’ centers with 70° crosscuts. Panel width is 320 ft, barrier pillar is 170 ft (before slab cut), with slab cuts of approximately 30 ft taken during retreat mining. Entries and crosscuts are mined at 16–18 ft wide. The mining height varies between 6 ft and 7 ft, while the coal bed thickness varies around 3–4 ft. Analysis of the layout using the Analysis of Multiple Seam Stability (AMSS) design software indicates that the pillar dimensions exceed the National Institute for Occupational Safety and Health (NIOSH) recommendations for global stability (Table 1).

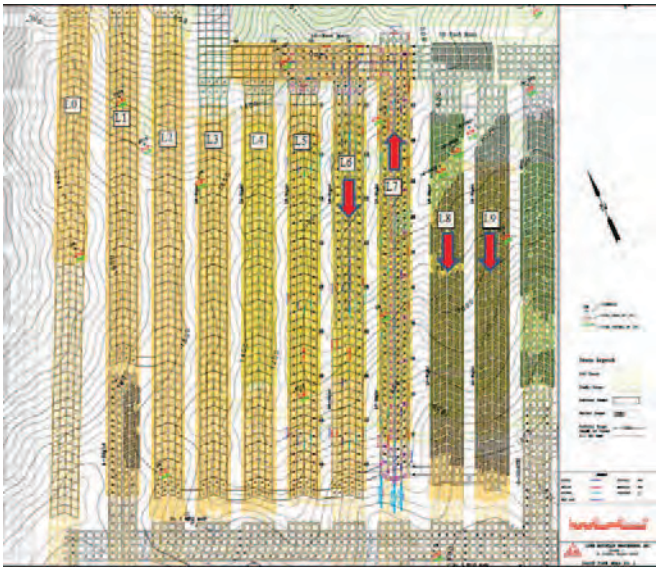


**Figure 1. General layout of panels in area of interest, showing cover depth contours and direction of plane development in the Kellioka coal bed.**

**Table 1. AMSS input parameters and results.**

| Input Parameters | |
|---|---|
| Coal Mine Roof Rating (CMRR) | 45 |
| Interburden thickness (ft) | 40 |
| Previous seam thickness (ft) | 5 |
| Gob width (ft) | 400 |
| Age of older workings | 2 |
| Active mine entry height (ft) | 6 |
| Depth of cover (ft) | 1350 |
| Entry width (ft) | 18 |
| Crosscut spacing (ft) | 100 |
| Number of entry | 5 |
| Pillar width (ft) | 80 |
| AMSS Results | |
| Development stability factor | 2.17 |
| Retreat section stability factor | 1.73 |
| NIOSH 2010 recommended stability factor | 1.30 |

### Geotechnical Parameters

The immediate roof of the Kellioka workings is described as dark gray shale that has uniaxial compressive strength varying between 7,589 and 15,180 psi and average Brazilian tensile strength of 1,100 psi. The Coal Mine Roof Rating (CMRR) of the roof rocks is estimated to be 45. This is similar to Kellioka shale roof ratings in the NIOSH CMRR database (Molinda and Mark, 1994). The roof shale is of a medium strength (dents when struck by ball peen hammer), and is relatively massive but can delaminate into thin slabs in the roof of an entry. The interburden between the Kellioka and the overlying Darby coal beds consists of dark shale that may contain a sandstone bed. The thickness of the sandstone is variable over the panels, varying between 10 and 20 ft near the center of panel L-7 to less than 2 ft over the L-1 and L-0 panels. The thicker sandstone is reported to result in improved roof stability in the Kellioka. The sandstone is not thought to be within reach of the rock bolts installed in the Kellioka.

Roof and rib support varies considerably, depending on local ground conditions. During entry development, the cuts are about 20–25 ft and cuts of 35–40 ft are taken in the crosscuts because conditions are generally good. The basic support in the panels consists of 6-ft-long No. 6 torque-tension bolts, fully grouted on 4-ft spacing. Supplementary support is two 12-ft-long super-bolts (75 grade 7/8 in) installed every other row. Where cutters develop, bolts are installed in the corner of the entry, angled at 45 deg. over the rib. Rib bolts 6 ft long are installed every 8 ft. Additional super-bolts are installed in the intersections. Screen and straps are widely used. A walk-through bolter is used that has the capability to install vertical and angled bolts, including rib bolts. In some of the poor roof areas it became necessary to install rows of timber cribs.

It was observed that the horizontal stress is able to initiate roof cutters in the shale roof of the Kellioka coal bed. The stronger roof above the Darby did not experience noticeable horizontal stress-related issues. Stress mapping (Mark and Mucho, 1998) was conducted in the L-6 and L-7 panels to establish the direction of the major horizontal stress. Measurements of cutter orientation at intersections indicate that the major horizontal stress is aligned at approximately N70E, which agrees with the regional stress orientation that one would expect in the Southern Appalachian coal field (Mark and Gadde, 2008). It is also observed that the direction of development of the production panels is favorably oriented at 45 deg to the major horizontal stress.

## GROUND CONDITIONS OBSERVED

### Initial Panel Mining

During development of the L-7 panel, which was advanced due north, the ground conditions were relatively good. Some roof cutter formation was observed in the western entry (No. 1) which was not entirely unexpected because of the orientation of the major horizontal stress. Figure 2 shows that the N70E orientation of the major horizontal stress can be expected to produce stress related damage along the western entry. The entry has deteriorated over time and has collapsed at several locations. The conditions in the other entries are reasonable, with no collapses or significant cutter roof observed. The cross cuts in panel L-7 are generally in a good condition. The pillars within the L-7 panel do not show any sign of excessive vertical loading, in spite of the depth of cover of up to 1800 ft. This is evidence of the success of the strategy of stacking the Kellioka panels below the extracted Darby and Owl panels.

Development of the L-8 and L-9 panels was conducted to the south without undue stability issues, considering the relatively weak shale roof and cover depths approaching 1,800 ft. Both panels were successfully retreat mined before moving over to the L-6 panel.

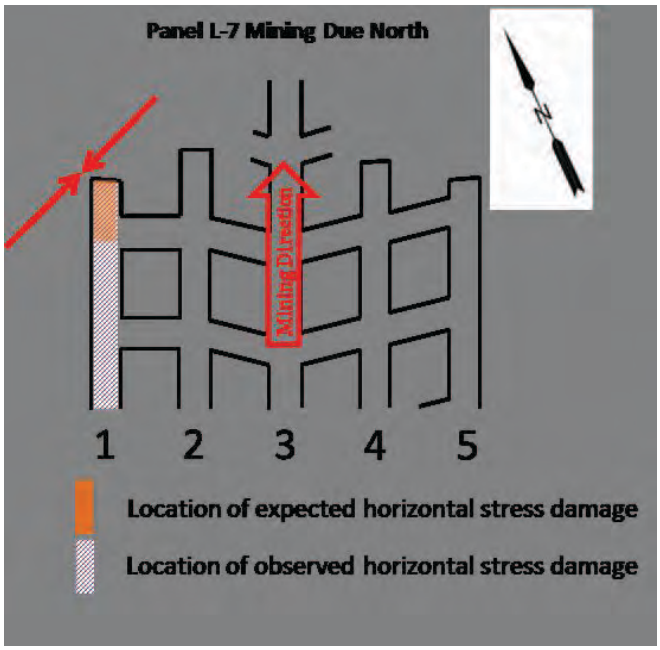



**Figure 2. Sketch showing expected and observed location of horizontal stress damage in the L-7 panel.**

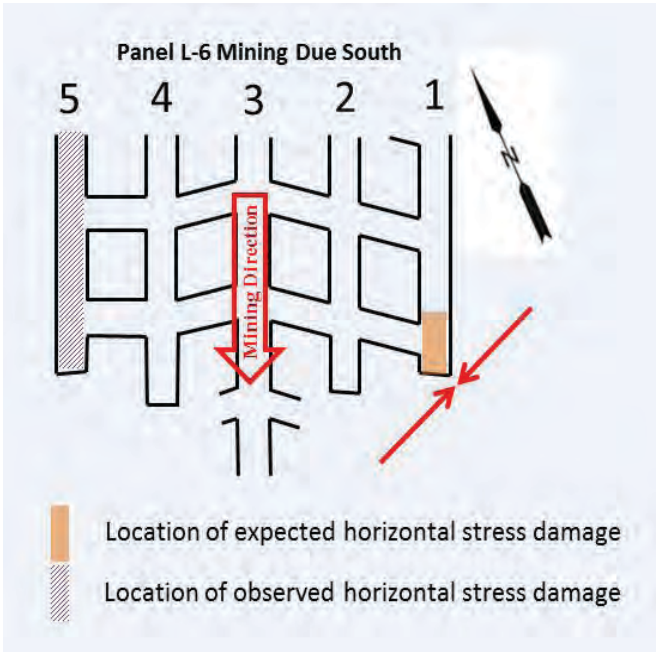



**Figure 3. Sketch showing expected and observed location of horizontal stress damage in the L-6 panel.**

### Unexpected Stress Related Damage in the L-6 Panel

When the L-6 panel was developed, also advancing to the south, conditions changed dramatically. Unexpectedly the No 5 entry (western) experienced symptoms of stress related damage, while the other four entries and the cross cuts were unaffected (Figure 3). The roof damage in the No. 5 entry appeared to be classic horizontal stress related damage with the formation of roof cutters along the length of the entry (Figure 4). The cutters formed outby the face and developed towards the face, resulting in uneven roof which is difficult to support using the walk-through bolter. The cutters were mostly located along the eastern corner or along the center of the No. 5 entry. Some floor heave occurred near the center of the entry. The conditions in the No. 5 entry deteriorated to such an extent that it became necessary to install timber cribs to support the roof. Figure 5 shows the timber cribs installed near crosscut 9, while figure 6 shows excellent conditions observed in the No. 4 entry, near crosscut 7. Roof cutters and poor conditions continued to be experienced as the L-6 panel development advanced towards the south, with an improvement in roof conditions towards the end of the panel, after crosscut 41.

### Attempt to Improve Conditions by Increasing the Pillar Size

In an attempt to alleviate the cutter formation in entry No. 5, the pillar between entries 4 and 5 was enlarged by about 30 ft by locating entry No. 5 further to the west. As a result, the outer (western) rib of entry No. 5 was located vertically underneath the edge of the overlying barrier pillar in the Darby coal bed. The enlarged pillar was implemented between crosscuts 10 and 19 but did not result in improved conditions. This idea was abandoned for the remainder of the panel by reverting back to the normal pillar size. Figures 7 and 8 show conditions observed in entry No. 5 in the wide pillar area.



**Figure 4. Roof cutter indicating classic horizontal stress related damage in entry No. 5 of panel L-6.**

### Baffling Aspect of Damage Observed in the L-6 Panel

The stress related damage observed in the No. 5 entry of the L-6 panel was unexpected because the No. 1 entry was expected to be subject to horizontal stress related damage (Mark and Mucho, 1994), as shown in Figure 3. The No. 5 entry was actually expected to be in a favorable situation because it was supposed to be in a zone of relieved horizontal stress. The fact that the exact opposite occurred baffled the authors and indicated that something was lacking in the understanding of the problem.

A possible explanation proposed for the poor condition in the L-6 panel was that thinning of the sandstone in the interburden may have contributed to the poorer conditions. However, this does not explain why the L-9 panel had good ground conditions in spite of



**Figure 5. Cribbing installed in No. 5 entry near crosscut 9, panel L-6 to control poor roof conditions.**



**Figure 6. Good conditions in entry 4 near crosscut 7 in panel L-6. Note absence of rib spalling owing to de-stressing by overmining in the Darby about 37 ft overhead. Cover depth is about 1,000ft.**

the sandstone being less than 5 ft thick over a large portion of the panel. Nor does it explain why the western entry of panel L-7 was failing where the sandstone is 16 ft thick.

The adverse ground conditions in the No. 5 entry was a concern because of the safety hazard associated with support installation in damaged roof, production delays and the potential loss of reserves. There was also concern for the feasibility of safely mining the L-1 to L-5 panels where the interburden was thinner and contained less sandstone. It was necessary to understand the cause of the adverse conditions so that an appropriate solution could be developed.

## NUMERICAL STRESS ANALYSIS

Numerical stress analysis was conducted in an attempt to explain the unexpected stress re-distribution that was occurring at the location of the L-6 panel. The Phase2 finite element software (Hammah and Curran, 2009) was selected to conduct the analyses.



**Figure 7. Looking inby (due south) showing support and conditions in the No. 5 entry between crosscuts 18 and 19, panel L-6. Heavey loading of the rib on the right (western side) is seen which is directly underneath the edge of the overlying barrier pillar in the Darby coal bed about 30 ft above.**



**Figure 8. Looking inby (due south) showing floor heave near center of No. 5 entry, near crosscut 13, panel L-6. A single row of cribs was installed to control the roof.**

The software allows horizontal and vertical stress redistribution around mine openings to be investigated.

The use of finite element methods for coal mine panel design is not customary in day-to-day planning and design of coal mine workings because of the time and effort required to create a model and evaluate the results. Multi-seam mining layouts in the US are usually evaluated using empirically based software such as AMSS (Mark et al., 2007) and the boundary element program LaModel (Heasley, 1998). Both AMSS and LaModel use the frictionless laminated model (Salamon, 1991) to estimate stress distributions around coal mine workings in bedded strata. AMSS analyzes a two-dimensional cross section through the various multiple seams while LaModel allows a plan view of the multiple seams to be discretized

and stresses and convergence distribution on the seam horizons to be calculated. LaModel can analyze large areas of single or multiple-seam coal mines very efficiently and it can analyze the effect of topography on vertical stress distribution (Heasley et al., 2007).

AMSS and Lamodel can only be used for vertical stress analysis because of the base assumption that the overburden consists of a frictionless laminated material. Since vertical stress is usually the main concern in multi-seam mine design these two software packages are well suited for the analysis of the majority of multi-seam interaction problems. However, horizontal stress impacts were a concern at the case study mine and it was unlikely that the laminated models would provide insight into the stress re-distribution by evaluating the vertical stress only. Consequently, the finite element analysis was conducted to provide full stress tensor results, allowing the combined effect of the multiple seam interactions, the mountainous topography and the initial horizontal stress to be evaluated.

**Finite Element Model Design**

The analysis was conducted by modeling different sections across the panels, capturing the topographic effect of the mountains and a stream valley. In this paper only the results from the one cross section is presented. The model simulated vertical stress due to gravity and the horizontal stress was assumed to be twice the vertical stress. Since the aim of this analysis is to understand the mechanisms, the rock and coal were modelled as elastic materials. Full extraction of the panels in the Darby and the Owl coal beds was modeled with entry development on the Kellioka. The gob in the Owl and Darby panels was modeled as a soft material that attracted loads similar to what would be predicted by an abutment angle of 21°. Figure 10 show the overall model layout and surface topography modeled.



**Figure 9. Looking outby (due north) showing typical support and roof damage along eastern side of the roof of entry 5 in panel L-6. Note rib bolts and 45 degree bolts installed in the corner. Screen and straps were installed on-cycle.**

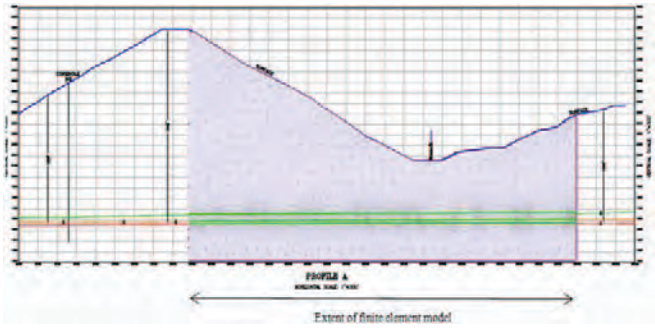



**Figure 10. Cross section AA and the Phase2 model geometry.**

**Effect of the topography**

The model results in Figure 11 show that asymmetric displacements are induced in the overburden and at the location of the coal seams being mined. The asymmetry is related to the mountain on the left side of the plot. Non-symmetrical displacements are clearly seen passing through the barrier pillars. Note that although panel L-7 is underneath the valley bed in this section, it is subject to asymmetrical displacements because the mountain on the left (west) is higher than on the right (east). This asymmetrical effect from the mountain can help to explain the asymmetrical response of the entries in the Kellioka.

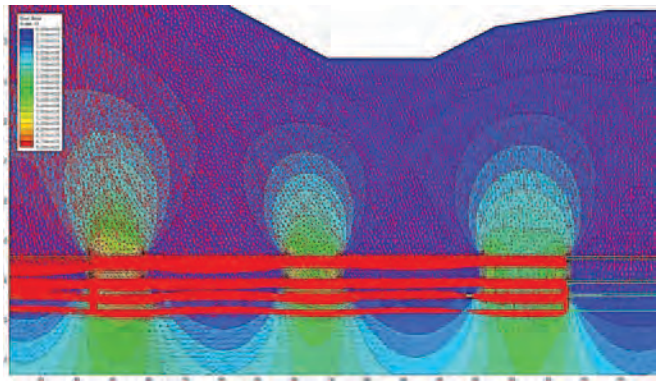


**Figure 11. Numerical model results showing total displacements (red arrows) and vertical stress contours after mining on the Owl and Darby panels.**

**Asymmetrical Stress Redistribution at Panel L-6**

The potential impact of the asymmetrical loading of the coal beds on entry stability was evaluated by modeling entry development on the Kellioka and considering the potential for rock failure. The rock mass in the model was assigned typical moderate shale strength and the 'strength factor (SF)' (similar to a safety factor) was calculated at the center of each model element. Figure 12 shows the strength factor results for the L-6 panel on profile AA'. The results clearly show that:

- The rock surrounding the western entry (No. 5 entry) in panel L-6 has lower SF values than elsewhere, as observed in the underground workings.

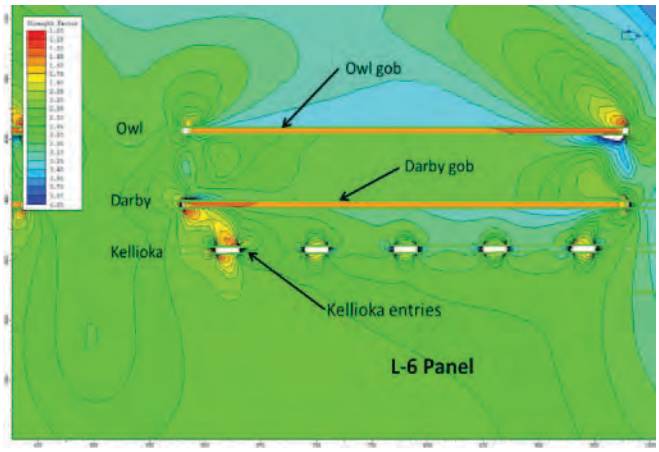



**Figure 12. Numerical model results showing strength factor contours around L-6 panel looking due north.**

- The roof at the eastern corner of the No. 5 entry is shown to be less stable, confirmed by underground observations that the eastern corner displayed more cutter activity.
- The rock surrounding the No. 1 to No. 4 entries has relatively higher SF values, also confirmed by underground observations.
- The proximity of the Kellioka entries to the Darby extracted panel results in unfavorable interaction between these two excavations, contributing to poor conditions in the western-most Kellioka entries.
- Because of the asymmetric loading, the No. 1 entry is relatively protected from adverse stress interaction.

## DISCUSSION

The 2D FE numerical model results provide an explanation for the unusual failure observed in the western-most entries of panel L-6 and L-7. The damage appears to have been caused by asymmetrical loading of the rock by the mountain slope to the west of these panels. The asymmetrical loading appears to have caused damage to entry 1 of panel L-7 and again to entry 5 of panel L-6.

The relatively good conditions experienced at Panels L-8 and L-9 were due to the slope of the mountain being nearly parallel to the long axis of the panels, and therefore did not cause asymmetrical loading. The mountain-slope effect also explains why widening the pillar between entry 5 and entry 4 in panel L-6 did not result in improved conditions, because the entry was moved into a less favorable stress condition directly under the highly stressed abutment of the overlying Owl panel.

### Implementing a proposed solution

Once the stress interaction impact was revealed in the model, it was a simple matter to suggest that the No. 5 entry should be located further to the east, to remove it from the adverse edge effect. The model was adjusted by shifting the Kellioka entries shifted 30 ft to the east as shown in Figure 13. The results indicate that the adverse stress interaction no longer exists and the rock damage can be expected to be significantly reduced.

The proposed solution was implemented in the L-5 panel by shifting both the No. 5 and No. 4 entry by 15 ft for a total shift of 30 ft to the east. This resulted in a smaller pillar dimension between

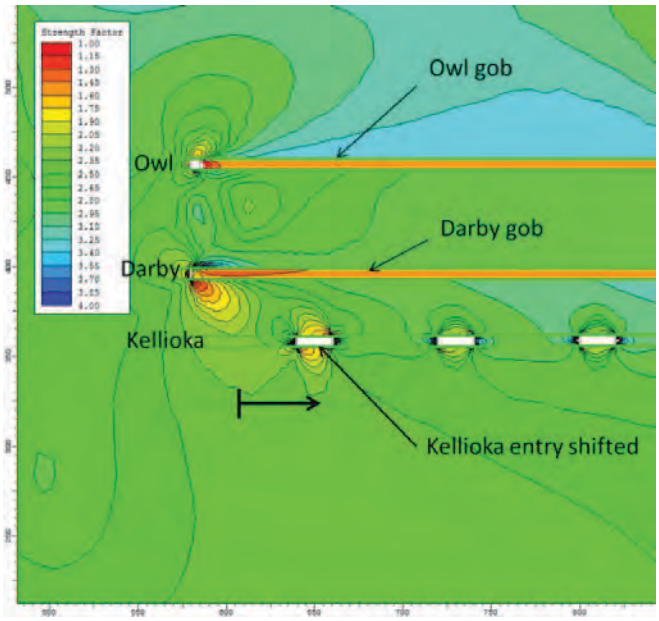



**Figure 13. Numerical model result showing strength factor contours around panel L-6 if the western entry on the Kellioka is shifted towards the east by 30 ft. View looking north.**

the No. 4 - No. 5 and No. 3 – No. 4 entries. However, the presence of the overlying Darby working provided sufficient vertical stress relief to result in stable pillars. At the time of writing this paper the L-5 panel had been fully developed and the conditions in the No. 5 entry were noticeably improved compared to the situation in panel L-6. Figure 14 shows the location of the worst conditions and Figure 15 shows the typically good conditions observed in the No. 5 entry of the L-5 panel. At worst, there were small cutters and floor cracks along the entry, but they were insignificant compared to difficult ground conditions encountered during mining of the L-6 panel.



**Figure 14. Worst conditions observed in entry No. 5 of the L-5 panel.**

## CONCLUSION

Adverse stress impacts on the rock surrounding entries at a multiple seam coal mine were investigated. At first the conditions were completely baffling to the authors because stress-related damage was occurring in an unexpected location.

In an attempt to explain the occurrence of the failure, two-dimensional finite element stress analyses were conducted. The stress analysis models included the effects of the initial horizontal stress, the effect of thevariable topography on vertical stress, and the details of the mined panels and entry development.



**Figure 15. Typical good conditions observed in entry No. 5 of the L-5 panel.**

The results indicated that the unusual stress damage was most likely related to the effect of the mountainous topography, which produced a rotated stress field at the location of the current workings. The rotated stress resulted in asymmetrical interactions between the upper and lower workings, explaining the baffling damage observations.

Once the cause of the stress-related damage was identified, it was clear that the affected entry should be located further away from the edge of the overlying mined panel. This solution was implemented at the mine and the next panel was successfully developed with minimal stress-related damage.

Reviewing the extent of damage in the Kellioka entries and orientation of the mountain slope, it appears that the impact of the mountain slope may be affected by factors such as the depth of cover, lateral extent of the mountain slope, steepness of slope, and relative height of mountain peaks. Further work is required to investigate the relative importance of each of these parameters.

## REFERENCES

Hammah, R. E., and J. H. Curran. (2009). It is Better to be Approximately Right than Precisely Wrong: Why Simple Models Work in Mining Geomechanics. In *43 rd US Rock Mechanics Symposium and*, vol. 4. 2009.

Heasley, K. A. "Numerical modeling of coal mines with a laminated displacement-discontinuity code." PhD diss., advisor: Miklos D. G. Salamon, Dept. of Mining Engineering. Colorado School of Mines, 1998.

Heasley, K.A. and Zacharias, G.A. (2007). LaModel: A Boundary-Element Program for Coal Mine Design. In *Proceedings of the New Technology for Ground Control in Multiple-seam Mining*. Pittsburgh, Pennsylvania 2007: NIOSH Open Industry Briefing. NIOSH IC 9495. 29–33.

Mark, C., F.E. Chase, and D.M. Pappas. (2008). Analysis of multiple seam stability. In *Proceedings of the 26th International Conference on Ground Control in Mining. Morgantown, WV: West Virginia University, pp. 5B18*. 2007.

Mark, C., and M. Gadde. (2008). Global Trends in Coal Mine Horizontal Stress Measurements. In Proceedings of the 27th International Conference on Ground Control in Mining, Morgantown, West Virginia: West Virginia University. (2008). 319-331.

Mark, C., and T. P. Mucho. "Longwall mine design for control of horizontal stress." *US Bureau of Mines Special Publication* (1994): 01-94.

Molinda, G.M., and Mark C. (1994). *Coal mine roof rating (CMRR): A practical rock mass classification for coal mines*. Vol. 9387. US Dept. of Interior, Bureau of Mines, 1994.

Salamon M.D.G. (1991). Deformation of stratified rock masses: A laminated model. In J. S. Afr. Inst. Min. Metall., V 91, No. 1. pp. 9-25.

# To What Extent the Mechanical Properties of Coal Play Role in Coal Mine Bumps? A Comparison Between Bump and Non–Bump Prone Coal

**Gamal Rashed**, Graduate Research Assistant
**Syd S. Peng**, Professor
Mining Engineering Department
West Virginia University
Morgantown, WV

## ABSTRACT

Coal bump is a sudden manifestation of the release of strain energy stored in a coal pillar (Peng, 2008). It is a very serious mining hazard that adversely affects the safety and productivity of the mines. Several case histories in mining have described coal pillars or faces of coal failing violently with an accompanying ejection of debris and broken material into the working areas of the mine (Campoli, 1987; Osterwald, 1962; Peperakis, 1958; Garvey and Ozbay, 2013). These failures resulted in large losses of life and total collapses of entire mine panels (Chase, Zipf, and Mark, 1994; Zingano, Koppe, and Costa, 2004). There are questions in the literature about whether or not the coal itself plays a significant role in bump. Rice (1935) mentioned that structurally strong coal is one of the key factors for bump; however, the strength of the Pocahontas #3 coal seam is low, and it bumped. Moreover, it is not obvious in the literature whether the strength of the tested coal samples is the inherent strength or if it is influenced by the shape or the size of the specimen.

The main objective of this paper is to answer the following question: To what extent does the mechanical properties of the coal have an impact on the potential for violent failure? The best approach to answer this question is to compare the mechanical properties of two kinds of coals from bump-prone (Utah coal-Sunnyside seam) and non-bump-prone (WV coal-Sewickley seam). This comparison includes uniaxial compressive strength, modulus of elasticity, shear strength (cohesion and friction angle), and the burst index.

## INTRODUCTION

Coal mine bumps are sudden, violent bursts of coal from a pillar or pillars or a block of coal, resulting in a section, the whole pillar, or the solid block of coal being thrown into an open entry, with shattered coals piling up to the roof line; these bursts are accompanied by audible noises (Peng, 2008). Because of the catastrophic nature of these sudden failures, understanding the causes of a coal mine bump is essential to create a safe underground working environment. This phenomenon has motivated many ground control researchers to conduct extensive field investigations throughout the past century. Most investigators (Holland, 1958; Iannacchione and Zelanko, 1994; Campoli, 1987) agreed that the geological conditions that lead to coal bumps include great overburden depth and strong and stiff overlying stratum. However, there are questions about whether the coal itself plays a significant role in bumps or not. On one hand, Rice (1935) mentioned how the natural condition is one of the key factors associated with coal mine bumps, and how a structurally strong coal is among those natural conditions. Braeuner (1994) observed that bursts occurred in almost all types of hard coals. On the other hand, Mine 3 operating in the Pocahontas #3 coalbed near Keen Mountain, Buchannan County, VA, experienced bumps (Campoli, 1987), but the UCS of Pocahontas #3 coal seam is 1,798 psi, which is low.

The influence of the mechanical properties of coal on the potential for violent failure does not receive much attention in the literature. Moreover, the effect of coal strength on bumps is not clear, which might be due to the fact that the shape and size of the tested coal samples are not mentioned explicitly in the literature. It is well known that the size and the shape of the coal sample affect its ultimate strength. In the literature, very often, the coal strength is mentioned without mentioning the shape or the size of the coal samples. Hence, it is not fair to compare the strength of different kinds of coal where the shape and the size of the samples are different or unknown. This ambiguity about the strength of coal prompted us to investigate whether or not the mechanical properties of coal play a substantial role in coal mine bumps. In order to answer this question, the mechanical properties of bump-prone coal (Utah coal-Sunnyside seam) have been compared with non-bump-prone coal (WV coal- Sewickley seam).

## MECHANICAL PROPERTY TESTS

The following mechanical properties have been examined for both the bump-prone and non-bump-prone coals: unconfined compressive strength, modulus of elasticity, shear strength (cohesion and friction angle), and the burst index. All the results and conclusions drawn from this research are based on an experimental work on coal specimens from both the Utah and WV coals.

**Unconfined compressive strength**

To avoid erroneous variations in strength, the uniaxial compressive strength tests were conducted on coal samples of the same shape and size. The coal samples have a width to height ratio of 3, and the size of the samples is 3 inches x 3 inches x 1inch. The coal samples have been tested under a load control of 314 lb/sec.

Figure 1 shows the unconfined compressive strength (UCS) for 52 coal samples from both Utah and WV coals which represent both Sunnyside and Sewickley coal seams respectively. The two solid lines in Figure 1 represent the average UCS for both Utah and WV coals. The average UCSs for Utah and WV coals are 7,652 psi and 6,360 psi, respectively. Hence, the average UCS for Utah coal is approximately 1.2 times the average UCS for WV coal.

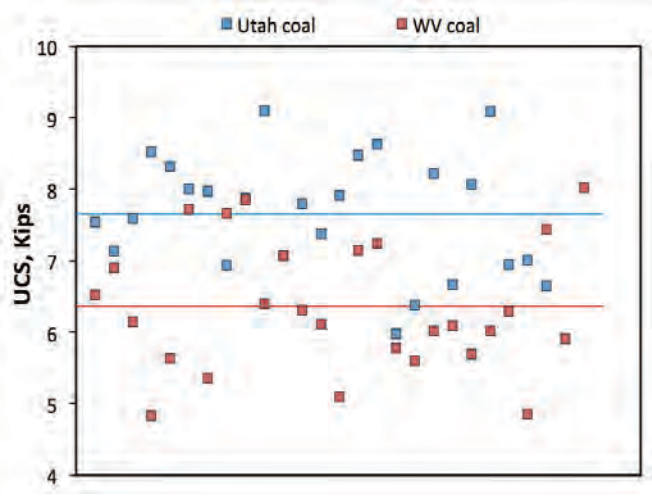



**Figure 1. The UCS for bump prone coal (Utah coal) and non-bump prone coal (WV coal).**

As shown in Figure 1, the average UCS for Utah coal is very close to maximum UCS of WV coal samples, and the average UCS for WV coal is very close to the minimum UCS of the Utah coal samples. The standard deviation for WV coal is higher than that for Utah coal, which is why the degree of scattering for WV coal is higher than that for Utah coal. In other words, the degree of confidence is higher in Utah coal samples.

According to Obert and Duvall (1967), the higher the strain energy that can be stored in coal pillar, the more likely the coal will bump. The strain energy per unit volume in a uniaxially loaded coal sample is $\sigma^2/2E$, where $\sigma$ is the uniaxial compressive strength of coal. Hence, with all mechanical properties identical except the UCS, the coal with the highest UCS would be more likely to burst. Consequently, the potential for bump is higher for Utah coal compared to WV coal because the average UCS for Utah coal is approximately 1.2 times more than the average UCS for WV coal. Does the 20% difference in UCS between Utah coal and WV coal cause bump? First, the 20% difference in strength might not cause bump because the bias in picking the samples might have an effect. Second, since the stress state in an underground mine is tri-axial, it could be necessary to consider the tri-axial strength of the coal specimens, rather than just the UCS. Therefore, the shear strength should be taken into consideration, in addition to the UCS.

It is worth mentioning that the failure of the Utah coal specimens is accompanied by a high-pitch noise or acoustic emission. In contrast, the failure of WV coal is accompanied by a low noise. Unfortunately, no acoustic emission equipment was used during testing of the coal samples.

**The modulus of elasticity**

"Tangent Young's modulus, $E_t$, is the slope of the axial stress-axial strain curve at some fixed percentage, generally 50%, of the peak strength" (Brady and Brown, 1993). Figure 2 shows the tangent Young's modulus for Utah and WV coals. The two solid lines in Figure 2 represent the average Young's modulus for Utah and WV coals. The average Young's moduli for Utah and WV coals are 305,000 psi and 302,000 psi, respectively. As shown in Figure 2, for WV coal, the coal sample with the minimum Young's modulus is far from the average value. Therefore, if this value is omitted from the test results, the average Young's modulus for WV coal becomes 307,000 psi, which is slightly higher than Utah coal. Hence, the difference between Young's modulus for Utah and WV coal is insignificant.

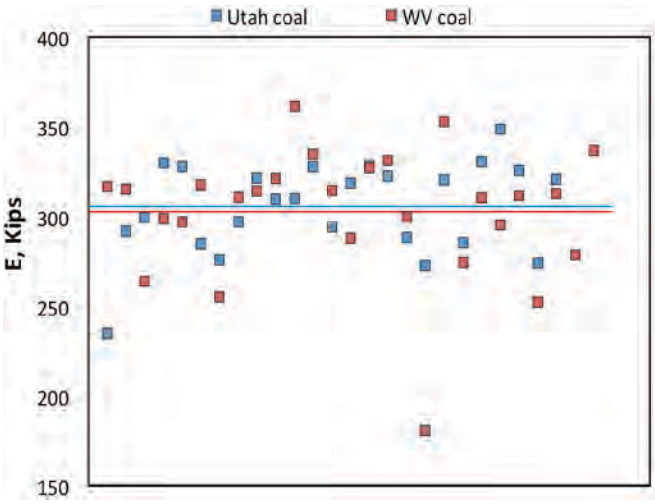



**Figure 2. Comparing Young's modulus for Utah and WV coals.**

Maleki (1995) stated that most coal bumps have occurred in mines where the Young's modulus ratio (roof- or floor-to-coal) was greater than 8, and the strength ratio (roof- or floor-to-coal) was greater than 4. However, severe bumps occurred at two room and pillar operations where Young's modulus and the strength ratio were as low as 5 and 3, respectively.

Since the difference in the Young's modulus between Utah coal and WV coal is insignificant, it is likely that Young's modulus of coal does not play a significant role in bump.

**Shear strength**

To the authors' knowledge, there is no data or results in the literature about the influence of shear strength parameters for coal on the potential for violent failure. The strength of coal or rock is not constant. Rather, it depends on three parameters: UCS, shear strength parameter (friction angle), and confining pressure. The variation of strength resulting from stress conditions can be

represented by the Mohr failure envelope. The maximum principal stress at failure can be calculated from Equation (1).

$$\sigma_1 = \sigma_c + k\sigma_3 \quad (1)$$

where $\sigma_1$= maximum principal stress,

$\sigma_c$= UCS,

$\sigma_3$= minimum principal stress,

*K*= tri-axial constant = (1 + sin φ)/(1 – sin φ)

ϕ = internal friction angle of coal

The GCTS Direct Shear Testing System RDS-200 was used to determine the frictional shear strength for 25 coal samples from both Utah and WV coals. As shown in Figure 3, the shear strength for Utah coal is higher than that for WV coal. The cohesion and friction angle for Utah and WV coals are 436 psi and 39°, and 328 psi and 32°, respectively. These shear strength parameters affect the tri-axial strength of coal pillar. The higher the shear strength of coal, the higher the tri-axial strength.

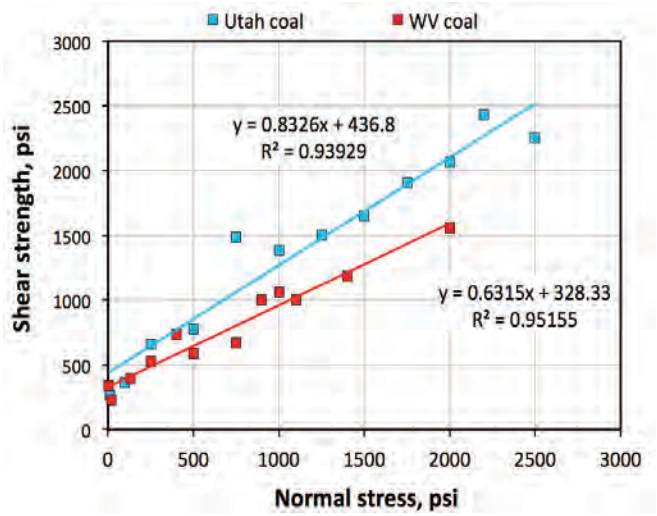



**Figure 3. Direct shear strength for Utah and WV coals.**

As mentioned previously, the UCS of Utah coal is 1.2 times the UCS for WV coal. However, in underground mines, the state of stress is tri-axial not uniaxial. Therefore, it is better to investigate the tri-axial strength using Equation (1). Since the friction angles of Utah and WV coals are 39° and 32°, respectively, the tri-axial constant, *K*, would be approximately 4.4 for Utah coal and 3.3 for WV coal. For the sake of explanation, assume that $\sigma_3$ equals 2,000 psi. The tri-axial strength of Utah coal will be 1.26 times more than the tri-axial strength of WV coal.

It is obvious that the tri-axial strength of Utah coal exceeds the tri-axial strength of WV coal by 26 %. However, this is not significant enough to confidently say that the strength of coal plays a significant role in the bump. Campoli (1987) documented that a friable coal experienced bump in both Mine 1, which is operating in the Pocahontas No. 4 Coalbed of the Pocahontas Formation and in Mine 5, which is operating in the No. 2 Gas Coalbed of the Kanawha Formation.

**Bump index**

The total energy imparted to the coal specimen during loading is divided into two components: the first component is the elastic strain energy that is released immediately upon release of the applied load. The second component is the permanent strain energy that is irrecoverable upon release of the applied load.

The bump index is determined by the elastic strain energy in the uniaxial compression loading and unloading tests on rock specimens up to approximately 80% of the compressive strength. The ratio of the strain energy retained, the elastic energy (Ee), to the strain energy dissipated, the plastic energy (Ep), provides the bump index (Peng, 2008). The tendency of coal to burst depends on its ability to accumulate elastic strain energy. As the elastic strain energy decreases, the permanent strain energy increases. Table 1 shows the classification for bump susceptibility according to the bump index (Peng, 2008).

**Table 1. Bump susceptibility depending on the bump index.**

| Degree of bump susceptibility | Bump index |
|---|---|
| Severely susceptible | > 5 |
| slightly susceptible | 2-5 |
| Not susceptible | < 2 |

Figure 4 shows an example of the loading-unloading stress-strain curve for both Utah and WV coals. The coal specimens were loaded up to 80% of their average uniaxial compressive strength, shown in Figure 1, which is approximately 55,000 lb for Utah coal and 46,000 lb for WV coal. The unloading stage starts as soon as the coal specimens reach the specified values. As shown in Figure 4, for Utah coal, the Ep is very small compared to the Ee stored in the coal specimens. That is why the bump index is high for Utah coal. For WV coal, the Ep is slightly bigger. That is why the bump index is low.

Table 2 shows the bump index results for both Utah coal and WV coal. The bump index for all specimens from Utah coal is more than 5, which is the threshold limit between slightly and severely susceptible to bump. It is highly recommended to classify Utah coal as very severely susceptible to bump because its bump index is significantly higher than the threshold limit recommended for severely susceptible to bump, as shown in Table 2. All specimens from WV coal are classified as slightly susceptible to bump because the bump index for these samples is between 2 and 5. The average bump index for Utah coal is more than three times that. The bump index for sample 4 from Utah coal is 5.2 times the bump index for sample 3 from WV coal.

Generally, Utah coal has higher Ee and less Ep than WV coal. The mechanical characteristic that seems to distinguish between bump-prone and non-bump-prone coal is that the non-bump-prone coal tends to plastically deform under stress so that, when failure occurs, it takes place slowly.

**Table 2. Bump susceptibility index for Utah and WV coals.**

| | Sample # | Bump index | Classification | Avg. bump index |
|---|---|---|---|---|
| **Utah coal** | 1 | 9.85 | Very severely susceptible | 10.71 |
| | 2 | 12.24 | Very Severely susceptible | |
| | 3 | 7.59 | Severely susceptible | |
| | 4 | 13.16 | Very severely susceptible | |
| **WV coal** | 1 | 3.69 | Slightly susceptible | 3.25 |
| | 2 | 2.79 | Slightly susceptible | |
| | 3 | 2.52 | Slightly susceptible | |
| | 4 | 4.03 | Slightly susceptible | |

The calculated bump index is further validated by field observations. Utah coal, classified as very severely susceptible to bump, experienced bump several times. WV coal, classified as slightly susceptible to bump, does not experience any bump. Therefore, the bump index is very reliable method for distinguishing between bump-prone and non-bump-prone coal. This conclusion agrees with Braeuner (1994), who states that the bump index is a more reliable indicator than the UCS to predict whether a coal is liable to bump because coal of low to medium strength, 1,523 psi to 2,147 psi, exhibited severe bursts.

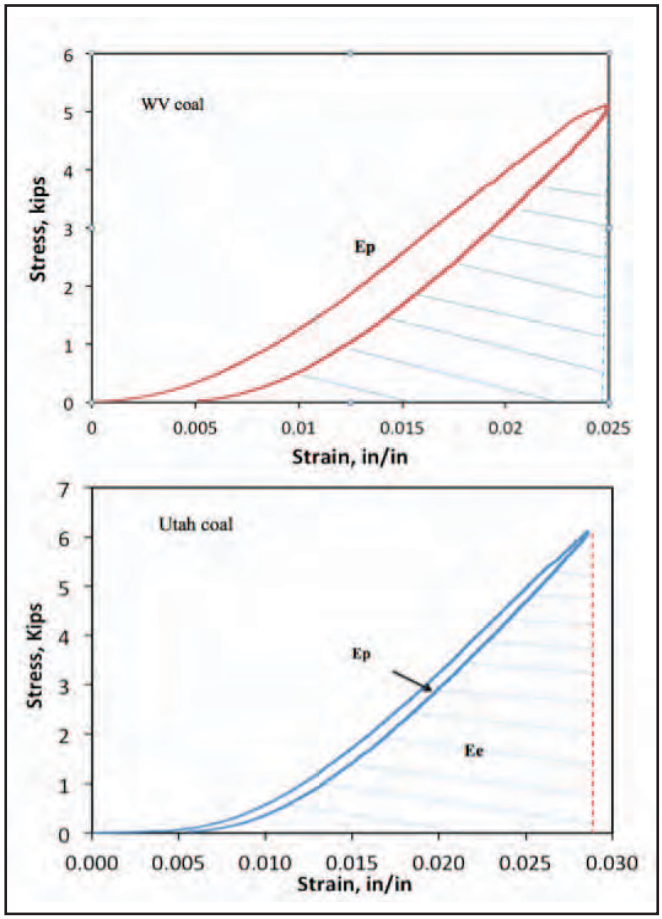



**Figure 4. The typical loading-unloading stress-strain curve used to calculate the bump index for (a) Utah coal and (b) WV coal.**

## CONCLUSION

The test results performed in this research showed that the bump index is a reliable method to distinguish between bump-prone and non-bump-prone coal (Utah and WV coals). According to the bump index, Utah coal (Sunnyside seam) is classified as very severely susceptible to bump because it has the ability to store more energy, while dissipating little energy. The UCS of Utah coal is 1.2 times greater than the UCS for WV coal. The 20% difference in UCS is not sufficient to determine bump-prone or non-bump-prone. When the frictional shear strength is added to the UCS, the tri-axial strength for Utah coal becomes 1.26 times the tri-axial strength of WV coal. This is still not significantly high enough to be confident that the strength of coal plays a significant role in bump. Since the Young's modulus is almost the same for both Utah and WV coals, it is unlikely to play a significant role in the coal bumps.

Therefore, the mechanical properties of the coal (UCS, Young's modulus and shear strength) do not play a significant role in bump. That means the local variation of the geological conditions is the controlling factor in bump, hence future research in bump should focus more on these geological conditions surrounding the pillars. Moreover, the general conclusion drawn from this research might not be extrapolated to all kinds of coal seams, because only two kinds of coals have been compared in this research.

## REFERENCES

Braeuner, G. (1994). *Rockburst in Coal Mines and Their Prevention*. London: Taylor & Francis, pp. 152.

Brady, G. H. B and Brown, T. W. (1993). *Rock Mechanics for Underground Mining*. 2nd ed. London: Chapman and Hall, pp. 571.

Campoli, A. A. (1987). *Coal Mine Bumps: Five Case Studies in the Eastern United States*. Ann Arbor: University of Michigan, pp. 48.

Chase, F. E., Zipf, R. K., and Mark, C. (1994). "The massive collapse of coal pillars - case histories from the United States." In: *Proceedings of the 13th International Conference on Ground Control in Mining*. Morgantown, WV: West Virginia University, 69–80.

Garvey, R. and Ozbay, U. (2013). “Assessing coal bumps from excess energy in finite difference models.” In: *Proceedings of the 32nd International Conference on Ground Control in Mining*. Morgantown, WV: West Virginia University, 164–168.

Holland, C. T. (1958). “Cause and occurrence of coal mining bumps.” *Mining Engineering, SME-AIME Transactions*, pp. 994–1004.

Iannacchione, A. T. and Zelanko, J. C. (1994). “Pillar mechanics of coal mine bursts: a control strategy.” In: *Proceedings of the 16th World Mining Congress*. Sofia, Bulgaria: Canadian Institute of Mining, Metallurgy and Petroleum, 15–23.

Maleki, H. N. (1995). “An analysis of violent failure in U.S. coal mines, case studies.” In: *Proceedings of Mechanics and Mitigation of Violent Failure in Coal and Hard-Rock Mines. SP 01-95*. Washington, DC: U. S. Bureau of Mines, pp. 5–26.

Obert, L. and Duvall, W. (1967). *Rock Mechanics and the Design of Structure in Rock*. Ann Arbor: University of Michigan, pp. 650.

Osterwald, F. W. (1962). “USGS relates geologic structures to bumps and deformation in coal mine workings.” *Mining Engineering April 1962*: 63–68.

Peng, S. S. (2008). *Coal Mine Ground Control*. 3rd ed. Morgantown, WV: S. S. Peng.

Peperakis, J. (1958). “Mountain bumps at the Sunnyside mines.” *SME-AIME Transactions*, 982–986.

Rice, G. S. (1935). “Bumps in coal mines of the Cumberland Field, Kentucky and Virginia: causes and remedy.” *U. S. Bureau of Mines Report of Investigations 3267*, pp. 36.

Zingano, A., Koppe, J., and Costa, J. (2004). “Violent coal pillar collapse - A case study.” In: Proceedings of the 23rd International Conference on Ground Control in Mining. Morgantown, WV: West Virginia University, pp. 190–196.

# Experimental Observations and Interpretations on Fracture Networks, Strength and Deformability of Coal Masses under Three–Dimensional Loading Conditions

**Peng-Fei He**, Ph.D. Student
Rock Mass Modeling and Computational Rock Mechanics Laboratories
University of Arizona
Tucson, AZ

**Pinnaduwa H.S.W. Kulatilake**, Professor and Director
University of Arizona
Tucson, AZ

**Man-Chao He**, Professor, Head Department
**Dong-Qiao Liu**, Ph.D. Student
China University of Mining and Technology (Beijing)
Beijing, China

## ABSTRACT

CT scanning tests were used to detect the pre-existing fracture systems of 36 cubical coal blocks. Systematic procedures were developed to construct the pre-existing fracture geometry of the cubical coal blocks from the CT images. Based on the constructed fracture systems, the fracture tensor components were calculated to capture the directional effects of the fracture system of the cubical coal blocks. The effect of the pre-existing fracture system and different combinations of confining stresses on the strength and deformability of coal masses was investigated at a preliminary level using some true triaxial test results and the computed fracture tensor components. The strength of the cubical coal blocks in the loading direction was found to be closely related to the summation of the fracture tensor components in the two perpendicular directions to the loading direction and the level of the confining stress system. The deformability of cubic coal blocks in the loading direction was found to be correlated to the fracture tensor component in the same direction.

**Key words:** Coal; CT scanning; true triaxial test; fracture tensor components; strength and deformability

## INTRODUCTION

Accidents associated with underground mining result in very significant fatalities and economic loss among US industries. The report as of 02/21/2014 by the Mine Safety and Health Administration shows that, from 2003 to present, the total number of fatalities of coalmines has reached 321 in the US (Mine Safety and Health Administration, 2014). Many coal deposits are found in significantly fractured host rock, classified as weak rock under available rock mass classification systems. Coal mass itself is also a typically weak sedimentary rock, composed of intact coal interspaced with usually three sets of approximately orthogonal discontinuities: bedding planes, face cleats, and butt cleats. Consequently, underground coal mines experience all kinds of difficulties to control the ground deformations and failures under complicated geology, discontinuity systems, geo-mechanical properties, and in-situ stress systems, resulting in many injuries, fatalities, and economic losses. The most common ground control problems experienced in the underground coalmines are roof falling, sidewall convergence, pillar cracking, and floor heaving. To arrive at a safe, economical design of coal pillars and to control the hazardous deformations of excavations in underground coalmines, it is very important to estimate the strength and deformability of the coal masses and host rocks in an accurate manner. Due to the pre-existing fracture system, the geo-mechanical behavior of coal masses under three-dimensional (3-D) stress systems can be very complicated.

Based on the rock fracture data available from a dam site in China, Wu and Kulatilake (2012) performed a series of strength and deformability numerical analyses to obtain rock mass mechanical parameter values in every 45° direction in 3-D. Their numerical results clearly indicated that the strength and deformability modulus of rock masses are highly influenced by the pre-existing fracture system of the rock masses. Anisotropic mechanical properties of coal masses can result from both the anisotropy of the fracture system, as well as the anisotropy of the in-situ stress system. However, the existing rock mass classification systems (Rock Mass Rating, Q system, and Geological Strength Index) evaluate the rock masses without adequate considerations of joint orientations and fracture size. Due to the assumption of isotropic rock mass behavior (Hoek, 2007), the Hoek-Brown strength criterion lacks the ability of capturing the anisotropic behaviors of the coal masses or host rocks.

Kulatilake, Park, and Malama (2006) used a mixture of Glastone, sand, and water to simulate brittle rocks and to prepare jointed model material blocks for laboratory strength and deformability testing. They performed uniaxial and biaxial compressive tests on the jointed model material blocks having different joint geometry configurations. In their paper, they proposed a 3-D rock mass failure criterion and validated a 2-D failure criterion using the biaxial compressive test results. They also showed that the intermediate principal stress plays an important role on the jointed block strength. Therefore, it is necessary to investigate the strength and deformability of coal masses under 3-D loading systems, incorporating methodologies to detect and quantify the pre-existing fracture systems. Such research results can also be applied to the host rocks having anisotropic pre-existing fracture systems.

## OBJECTIVES AND SCOPE OF THE RESEARCH

This study is the first phase of developing a 3-D anisotropic rock mass strength criterion applicable for rock masses with anisotropic pre-existing fracture systems. One of the aims of the research was to examine the feasibility of detecting the pre-existing fracture geometry of the cubic coal blocks by CT scanning tests and quantifying it by fracture tensor-based methodologies (Oda, 1982; Kulatilake, Wang, and Stephansson, 1993) to capture the anisotropic behaviors of rock masses. Another objective was to study the effect of the pre-existing natural fracture systems and different combinations of confining stresses on the strength and deformability of coal masses using CT scans and true triaxial tests.

## RESEARCH PROCEDURES

The study covered in the paper is a collaborative research effort between the University of Arizona and China University of Mining and Technology, Beijing (CUMTB). The main steps of the research approach are given below:

(1) Geomechanical laboratory tests were conducted on 21 cylindrical samples of diameter/length ratio of 0.5 to estimate the geo-mechanical properties of intact coal and saw-cut coal joints. The coal samples are from Yongli colliery, Dongsheng coal field, Inner Mongolia. The coal seam belongs to Yan'an formation, Lower Jurassic-Middle Jurassic (200 Ma-160 Ma). Table 1 lists the geomechanical properties obtained for the coal. With respect to the joint properties, joint shear stiffness (JKS) was found to vary from 0.1 to 0.8 GPa/m when the joint normal stress ($\boldsymbol{\sigma}_n$) level changed from 0.25 MPa to 1 MPa. The following relation was obtained between joint normal stiffness (JKN) and joint normal stress for saw-cut joints: JKN= (20.15±0.61) $\sigma_n$.

**Table 1. Summary of the geomechanical properties of the coal.**

| | Uniaxial compressive strength, UCS (MPa) | Young's modulus, E (GPa) | Poisson's ratio, υ | Tensile strength, $\sigma_t$ (MPa) | Cohesion, $C_0$ (MPa) | Internal friction angle, φ (°) | Basic friction angle, $\varphi_b$ (°) |
|---|---|---|---|---|---|---|---|
| Mean | 20.9 | 2.57 | 0.35 | 1.2 | 8.4 | 25.9 | 31.8 |
| Std. Dev. | 5.0 | 1.31 | 0.10 | 0.2 | - | - | 1.3 |

(2) Thirty-six cubical coal blocks of side length 110mm were subjected to body CT scanning by a powerful industrial CT scanning machine available at CUMTB.

(3) Systematic procedures were developed to construct the fracture network that exists in each cubical coal block and to quantify the geometric information of each fracture. Some face cleats and butt cleats that are approximately perpendicular to the bedding planes were constructed, based on the CT slice information obtained parallel to the bedding planes. Bedding planes and other cleats were constructed from the CT slice information obtained perpendicular to the bedding planes.

(4) Based on the construction results obtained in step (3), the fracture tensor for each sample was calculated. Oda (1982) proposed the concept of fracture tensor. Fracture tensor is a comprehensive index of the joint geometry parameters: joint density, orientation, joint size, and the number of joint sets. By modeling joints as equivalent thin circular discs, the general form of the fracture tensor at the 3-D level for the *k*th joint set can be expressed as

$$F_{ij}^{(k)} = 2\pi\rho \int_0^{\infty} \iint_{\Omega/2} r^3 n_i n_j f(n, r) d\Omega dr \quad (1)$$

where ρ is the joint density (which means the average number of joints per unit volume), r is the radius of the circular joint, n is the unit normal vector of the joint plane, f(n, r) is the joint probability density function of n and r, and Ω/2 is a solid angle corresponding to the surface of a unit hemisphere, and $n_i$ and $n_j$ (i,j = x, y, z) are the components of vector n in the rectangular coordinate system considered in the paper. If the joint orientation, n, and joint radius, r, are mutually independent, the following equation can be written for the fracture tensor for *k*th joint set:

$$F_{ij}^{(k)} = 2\pi\rho \int_0^{\infty} r^3 f(r) dr \iint_{\Omega/2} n_i n_j f(n) d\Omega \quad (2)$$

where f(n) and f(r) are the probability density functions for unit normal vector n and size r, respectively. If a rock mass have N sets of joints, the fracture tensor for the rock mass can be expressed as

$$F_{ij} = \sum_{k=1}^{N} F_{ij}^{(k)} \quad (3)$$

Kulatilake, Wang, and Stephansson (1993) proposed the concept of directional fracture tensor component and related this parameter to the directional deformability and strength of jointed rock masses.

The directional fracture tensor component in direction *l* for a rock mass can be expressed as

$$F_{ll} = \sum_{k=1}^{N} F_{ll}^{(k)} \quad (4)$$

In the conducted study, the geometry of each and every fracture plane was constructed using the discretized form of the fracture tensor expression given below:

$$F_{ij} = 2\pi\rho \frac{1}{M} \sum_{m=1}^{M} r_m^3 n_i^m n_j^m \quad (5)$$

where M is the number of fracture planes in the rock mass.

(5) The samples that were subjected to CT scanning were also subjected to true triaxial tests under different combinations of confining stresses. The stress-strain diagrams obtained from the tests were used to obtain coal block strengths under different confining pressures; also, the tangential deformability modulus was estimated at the 50% failure stress level.

(6) The results obtained for strength and deformability parameters were compared with fracture tensor parameter values to obtain possible relations between strength/deformability and fracture tensor parameters under different confining stress conditions**.**

## DETECTION AND QUANTIFICATION OF THE PRE-EXISTING FRACTURE NETWORKS

### CT Scanning of Cubical Coal Blocks

The photograph of each face of the CB15 sample is given in Figure 1 as an example of the cubical coal blocks. The faces of the cubical coal blocks were marked as A, B, C, D, E, and F. The bedding planes can be seen from A, B, C, and D faces; whereas, E and F faces are sub-parallel to the bedding planes. To detect the fractures inside the cubical coal blocks, the blocks were subjected to CT body scanning by a powerful industrial CT scanning machine (see the panorama in Figure 2). The schematic of CT body scanning is shown in Figure 3. The parameters used for CT scanning are listed in Table 2. A cluster of X-rays from the resources is shot at the specimen. After penetrating the specimen, the residual X-rays continue to transmit and arrive at the detector. After the raw data are processed by the Matlab software package, hundreds of matrices of gray values of each point belonging to the same section of cubical coal blocks can be obtained. The gray values range from 0 (pure black: void) to 255 (pure white: solid). Through image processing, these matrices can be converted to gray level images for each section. According to the specific configuration of the cubical coal blocks, the sections obtained are parallel to the bedding plane at a spacing of 0.125mm. These parallel sections are only capable of capturing the fracture geometric information of face cleats and butt cleats that are usually approximately perpendicular to the bedding planes. To detect the bedding planes, the sections perpendicular to the bedding planes are required. The same column of the matrices for the parallel sections can be extracted and rearranged into a new vertical matrix (Figure 4). These new vertical matrices are used to construct the vertical CT images, which are capable of capturing the geometric information of bedding planes. A construction example of CT images perpendicular to the bedding plane is given in Figure 5. To validate the effectiveness of these CT images, the CT images close to A, C, E, and F faces were compared with the corresponding photographs of these faces. To make the comparison, face A should be rotated clockwise by 180 degrees, face E should be flipped upside down, and face F should be rotated clockwise by 180 degrees. Figure 6 shows that the CT images are in good agreement with the face photographs. These findings indicate that the used CT scanning methodology is a feasible and effective method to detect the fracture networks inside the cubical coal samples.

**Table 2. Parameter values used for CT scanning.**

| | | | |
|---|---|---|---|
| **Voltage** | 200KV | **Resolution** | 1229×1229 |
| **Current** | 2mA | **Offset** | 12.9 |
| **Amplification** | 1.471 | **Layer** | 800 |




**Figure 1. Photographs of faces of CB15 sample.**

### Fracture Network Constructions for the Cubical Coal Blocks

A procedure was developed to construct fracture planes that exist in coal blocks using CT images parallel and perpendicular to the bedding planes. First, the traces belonging to the same fracture plane were marked starting from the first CT image to the subsequent CT scans until no trace was seen on the next CT image. Then, on each trace, some key points were marked and their 3-D coordinates were recorded. Even though CT images were available at an extremely close spacing, to reduce the construction time, the CT images available at a spacing of 10mm were used. As the next step, the 3-D coordinates were subjected to multiple linear regression analysis to find the equation of the fracture plane. The reasonably high multiple R values that were obtained indicate successful fracture plane fits. For the fracture planes with only one trace available from the CT images, 2-D linear regression analysis was used instead of multiple linear regression analysis. The previously mentioned equations were then used to calculate the dip and dip direction of the fracture plane. The irregular fracture plane was then simplified to a polygon. The polygon was then split into a number of triangles. The area and 3-D coordinates of the center point of the polygon were calculated based on these discretized triangles. The equivalent diameter for each fracture plane was also calculated to perform fracture tensor calculations.

For a fracture plane, when more than one trace is available from CT scans, it is possible to calculate the equation of theplane and its true dip and its dip direction. In addition, procedures were developed to calculate the coordinates of the center of the area (GX, GY, and GZ) and area of the fracture plane. Some of these fracture planes may be represented as equivalent squares, depending on the shape of the fractures in the 3DEC software.

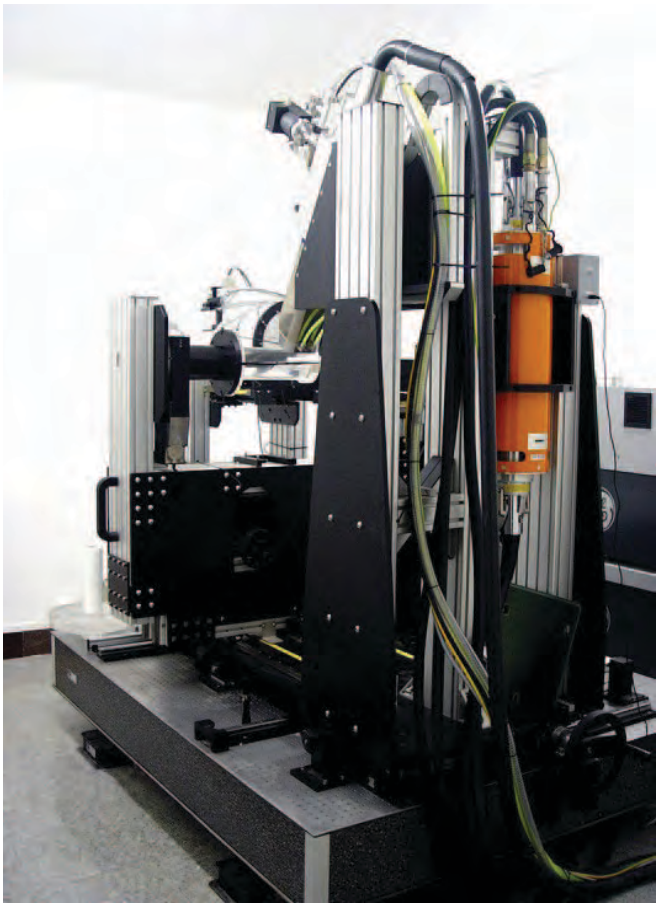


**Figure 2. Panorama of CT scanning machine.**

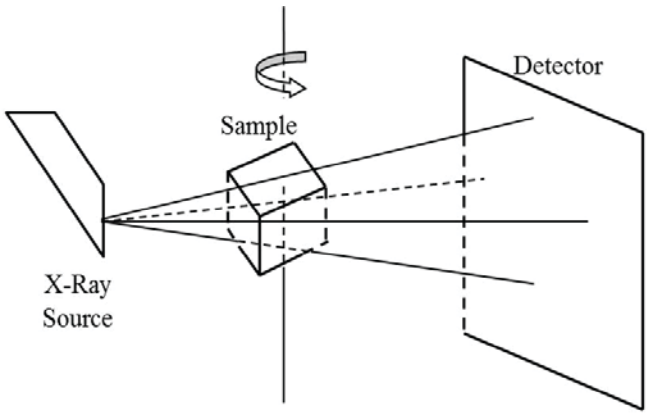



**Figure 3. Schematic of CT body scanning.**

To keep this option open, the equivalent side length of a square (ES) was also calculated for each fracture plane. Table 3 shows typical calculated results. For fracture planes 1–6, the equation of the plane is X = AY+BZ+C; for fracture planes 7–10, the equation of the plane is Z = AX+BY+C.

For a cleat, when only one trace is available from a CT image parallel to the bedding plane, only the strike of the cleat can be estimated. Therefore, for such cleats, the dip angle was assumed to be 90°. The equation for such cleats is given by X = AY+C. Table 4 provides results of 5 cleats out of 160 available for the CB6 sample

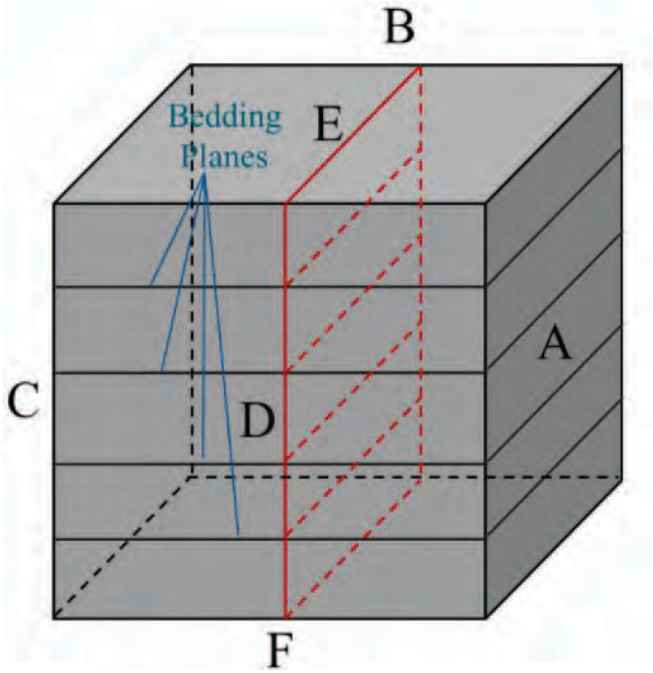



**Figure 4. Schematic of constructing CT image perpendicular to the bedding planes.**

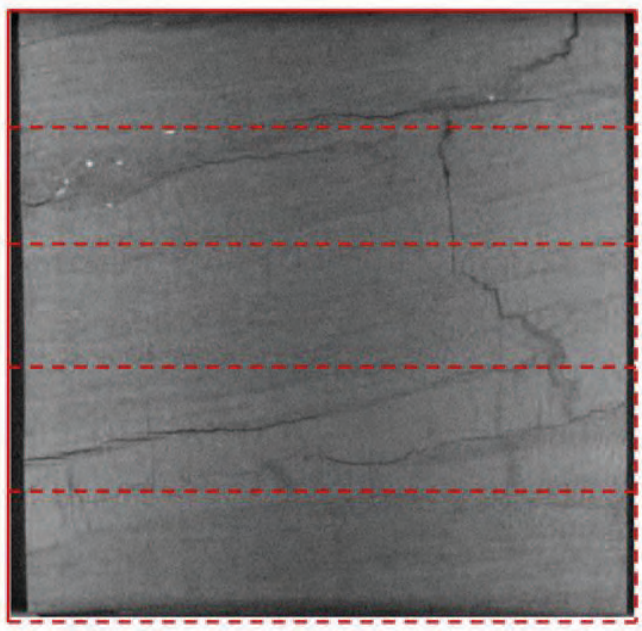


**Figure 5. Construction example of CT image perpendicular to the bedding planes.**

as an example. Note that these fracture planes will be modeled as rectangular fractures in numerical modeling which will beconducted in the future. Therefore, the lengths and heights for the equivalent rectangles were also calculated.




**Figure 6. Comparison between CT images and photographs of corresponding faces of CB15 sample.**

The equation for such fracture planes is given by Z = BY+C. Note that these fracture planes also will be modeled as rectangular fractures in numerical modeling in the future. Therefore, the lengths and heights for the equivalent rectangles were also calculated.

**Fracture Tensor Calculations**

Based on the aforementioned equation (5) and fracture network construction procedures, fracture tensors for the cubical coal blocks were calculated. Table 6 shows the calculation results of the fracture tensor for 10 blocks (9 components, principal values, principal direction vectors, the first invariant of the fracture tensor, $I_1$ and the second invariant of the deviatory fracture tensor, $J_2$). $I_1$ is a measure of the porosity of the rock mass resulting from the fractures. $J_2$ is a measure of the degree of anisotropy of the fracture system. The values given in Table 6 show that, in most of the samples, the fracture system is dominated by the bedding planes. The photographs also depicted this finding.

**Table 3. Estimated 3-D fracture geometry parameters for Sample CB6 from CT scans.**

| Fract. # | R | C | A | B | Dip (°) | Dip dir. (°) | GX mm | GY mm | GZ mm | Area (mm$^2$) | ED (mm) | ES (mm) |
|---|---|---|---|---|---|---|---|---|---|---|---|---|
| 1 | 0.97 | 72.16 | 0.68 | -0.02 | 89.01 | 124.29 | 80.57 | 12.50 | 5.55 | 284.39 | 19.03 | 16.86 |
| 2 | 0.95 | 46.69 | -2.93 | -0.33 | 83.92 | 18.83 | 22.29 | 2.81 | 49.02 | 564.36 | 26.81 | 23.76 |
| 3 | 0.98 | 41.54 | 0.76 | -0.02 | 88.92 | 127.09 | 48.69 | 11.00 | 49.46 | 478.33 | 24.68 | 21.87 |
| 4 | 0.98 | 52.59 | 0.15 | 0.02 | 88.99 | 278.67 | 62.54 | 53.08 | 104.53 | 438.26 | 23.62 | 20.93 |
| 5 | 0.96 | 46.61 | 0.22 | 0.14 | 82.31 | 282.45 | 63.97 | 13.20 | 104.48 | 234.76 | 17.29 | 15.32 |
| 6 | 1.00 | 122.64 | -5.95 | 0.43 | 85.91 | 189.53 | 103.15 | 10.85 | 104.37 | 81.93 | 10.21 | 9.05 |
| 7 | 0.99 | 38.88 | -0.07 | -0.06 | 5.46 | 48.62 | 26.43 | 75.50 | 32.22 | 172.40 | 14.82 | 13.13 |
| 8 | 0.98 | 26.97 | 0.05 | -0.06 | 4.50 | 318.34 | 29.20 | 18.27 | 27.43 | 426.76 | 23.31 | 20.66 |
| 9 | 0.82 | 21.14 | -0.03 | -0.02 | 2.00 | 58.68 | 27.05 | 11.51 | 20.13 | 415.58 | 23.00 | 20.39 |
| 10 | 0.79 | 86.59 | 0.00 | -0.04 | 2.39 | 356.76 | 75.21 | 55.41 | 84.46 | 6598.28 | 91.66 | 81.23 |

Fract. #: Fracture number; R: Regression coefficient; A, B, C: Coefficients of the regression equation; Dip and Dip dir.: Dip angle and Dip direction of the fracture plane; GX, GY, GZ: X, Y, Z coordinates of the center of area of the fracture plane; Area: Area of the fracture plane; ED: Diameter of an equivalent circular shaped fracture; ES: Side length of an equivalent square shaped fracture

**Table 4. Estimated fracture geometry parameters for 5 cleats (as an example) of sample CB6 from single traces coming from CT scans parallel to the bedding planes.**

| Fract. # | R | C | A | B | Dip (°) | Dip Dir. (°) | GX mm | GY mm | GZ mm | Area (mm$^2$) | ED (mm) | EL (mm) | EH (mm) |
|---|---|---|---|---|---|---|---|---|---|---|---|---|---|
| 1 | 1.00 | -6 | 0.25 | 0.00 | 90.00 | 104.26 | 9.64 | 62.88 | 2.50 | 182.90 | 15.26 | 36.58 | 5.00 |
| 2 | 0.91 | -5002 | 77.8 | 0.00 | 90.00 | 179.26 | 27.59 | 64.63 | 2.50 | 78.80 | 10.02 | 15.76 | 5.00 |
| 3 | 0.99 | 371 | -4.93 | 0.00 | 90.00 | 191.46 | 19.98 | 71.16 | 2.50 | 173.63 | 14.87 | 34.73 | 5.00 |
| 4 | 0.90 | 246 | -3.13 | 0.00 | 90.00 | 197.69 | 44.51 | 64.13 | 2.50 | 49.37 | 7.93 | 9.87 | 5.00 |
| 5 | 0.96 | -231 | 2.85 | 0.00 | 90.00 | 160.64 | 41.20 | 95.76 | 2.50 | 68.52 | 9.34 | 13.70 | 5.00 |

EL: length of an equivalent rectangular fracture; EH: height of an equivalent rectangular fracture

For a fracture plane, when only one trace is available from either face B or D or a CT image plane perpendicular to the bedding plane, only the apparent dip angle and the apparent dip direction angle of the fracture plane can be estimated for the fracture. These fractures can belong to either the bedding planes or cleats. Table 5 provides estimated fracture parameter values for 5 bedding planes out of 115 fracture planes that exist in the CB6 sample as an example.

**Table 5. Estimated fracture geometry parameters for 5 bedding planes (as an example) of sample CB6 from single traces coming from CT scans perpendicular to the bedding plane.**

| Fract. # | R | C | A | B | Dip (°) | Dip Dir. (°) | GX mm | GY mm | GZ mm | Area ($mm^2$) | ED (mm) | EL (mm) | EH (mm) |
|---|---|---|---|---|---|---|---|---|---|---|---|---|---|
| 1 | 0.94 | 108.65 | 0.00 | -0.08 | 4.48 | 0.00 | 4.58 | 80.17 | 102.37 | 64.55 | 9.07 | 7.05 | 9.15 |
| 2 | 0.86 | 102.10 | 0.00 | -0.14 | 7.84 | 0.00 | 4.58 | 81.79 | 90.83 | 22.27 | 5.32 | 2.43 | 9.15 |
| 3 | 0.89 | 47.40 | 0.00 | -0.07 | 4.18 | 0.00 | 4.58 | 6.76 | 46.91 | 53.12 | 8.22 | 5.81 | 9.15 |
| 4 | 0.83 | 89.76 | 0.00 | -0.08 | 4.59 | 0.00 | 32.03 | 64.27 | 84.60 | 645.62 | 28.67 | 70.56 | 9.15 |
| 5 | 0.99 | 28.85 | 0.00 | -0.06 | 3.25 | 0.00 | 41.18 | 20.71 | 27.67 | 335.37 | 20.66 | 36.65 | 9.15 |

**Table 6. Calculation results of fracture tensors for 10 blocks.**

| Sample # | CB1 | CB2 | CB3 | CB4 | CB5 | CB6 | CB7 | CB8 | CB9 | CB10 |
|---|---|---|---|---|---|---|---|---|---|---|
| $F_{XX}$ | 0.156 | 0.142 | 0.219 | 0.023 | 0.253 | 0.507 | 0.305 | 0.101 | 0.060 | 0.419 |
| $F_{XY}$ | 0.008 | 0.003 | 0.003 | 0.001 | 0.029 | 0.017 | 0.027 | 0.005 | 0.010 | 0.020 |
| $F_{XZ}$ | 0.018 | 0.011 | 0.016 | 0.010 | 0.021 | 0.021 | 0.133 | 0.025 | 0.002 | 0.030 |
| $F_{YX}$ | 0.008 | 0.003 | 0.003 | 0.001 | 0.029 | 0.017 | 0.027 | 0.005 | 0.010 | 0.020 |
| $F_{YY}$ | 0.130 | 0.017 | 0.042 | 0.009 | 0.035 | 0.075 | 0.067 | 0.050 | 0.167 | 0.047 |
| $F_{YZ}$ | 0.021 | 0.013 | 0.025 | 0.028 | 0.009 | 0.026 | 0.307 | 0.024 | 0.030 | 0.022 |
| $F_{ZX}$ | 0.018 | 0.011 | 0.016 | 0.010 | 0.021 | 0.021 | 0.133 | 0.025 | 0.002 | 0.030 |
| $F_{ZY}$ | 0.021 | 0.013 | 0.025 | 0.028 | 0.009 | 0.026 | 0.307 | 0.024 | 0.030 | 0.022 |
| $F_{ZZ}$ | 0.039 | 0.032 | 0.061 | 0.151 | 0.026 | 0.045 | 1.586 | 0.055 | 0.015 | 0.066 |
| $F_1$ | 0.033 | 0.010 | 0.025 | 0.004 | 0.021 | 0.030 | 0.007 | 0.026 | 0.010 | 0.032 |
| $n_{1X}$ | -0.130 | 0.020 | 0.035 | 0.040 | -0.012 | -0.021 | -0.005 | 0.188 | -0.010 | -0.001 |
| $n_{1Y}$ | -0.196 | 0.860 | 0.815 | 0.981 | -0.511 | -0.495 | 0.982 | 0.671 | -0.184 | 0.839 |
| $n_{1Z}$ | 0.972 | -0.510 | -0.579 | -0.190 | 0.860 | 0.869 | -0.191 | -0.717 | 0.983 | -0.543 |
| $F_2$ | 0.130 | 0.038 | 0.076 | 0.023 | 0.034 | 0.089 | 0.291 | 0.064 | 0.059 | 0.076 |
| $n_{2X}$ | -0.372 | -0.105 | 0.104 | 0.996 | -0.160 | -0.061 | 0.995 | 0.465 | -0.996 | -0.104 |
| $n_{2Y}$ | 0.918 | 0.510 | -0.579 | -0.054 | 0.850 | 0.868 | -0.014 | -0.704 | 0.089 | 0.540 |
| $n_{2Z}$ | 0.136 | 0.854 | -0.809 | -0.069 | 0.503 | 0.493 | -0.099 | -0.537 | 0.006 | 0.835 |
| $F_3$ | 0.162 | 0.144 | 0.221 | 0.157 | 0.259 | 0.509 | 1.660 | 0.115 | 0.174 | 0.423 |
| $n_{3X}$ | -0.919 | -0.994 | -0.994 | 0.078 | -0.987 | -0.998 | 0.100 | -0.865 | -0.089 | -0.995 |
| $n_{3Y}$ | -0.344 | -0.036 | -0.032 | 0.187 | -0.132 | -0.043 | 0.190 | -0.232 | -0.979 | -0.057 |
| $n_{3Z}$ | -0.192 | -0.100 | -0.105 | 0.979 | -0.092 | -0.049 | 0.977 | -0.445 | -0.184 | -0.087 |
| $I_1$ | 0.325 | 0.191 | 0.322 | 0.183 | 0.314 | 0.627 | 1.958 | 0.206 | 0.243 | 0.532 |
| $J_2$ | 0.005 | 0.005 | 0.010 | 0.007 | 0.018 | 0.068 | 0.781 | 0.002 | 0.007 | 0.046 |
| FXX: Perpendicular to E-F faces; FYY: Perpendicular to B-D faces; FZZ: Perpendicular to A-C faces. | | | | | | | | | | |

## TRUE TRIAXIAL TESTS AND ANALYSIS OF RESULTS

### True Triaxial Tests

The cubical coal blocks that were subjected to CT scanning were then subjected to true triaxial loading test by a testing machine available at CUMTB (Figure 7). This equipment has an individually servo-controlled loading head in each of the three mutually perpendicular directions with a maximum capacity of 500KN. Cubical rock blocks of 160 mm and 110 mm side length can be tested on this machine. Figures 8 and 9 show two experimental stress-strain results obtained from true triaxial tests. Note that the confining stress applied to the CB3 cubical block sample is higher than that applied to the CB1 cubical block sample. This has resulted in more ductile behavior in the CB3 sample compared to that of the CB1 sample. These stress-strain diagrams were then used to obtain coal block strengths under different confining pressures. These diagrams were also used to estimate the tangential deformability modulus at 50% of the failure stress level.

### Analysis of Results

After observations and interpretations of the aforementioned test results, the findings, with respect to the effect of anisotropic fracture systems on the strength and deformability modulus of the cubic coal blocks, can be summarized as follows:



**Figure 7. True triaxial testing equipment.**

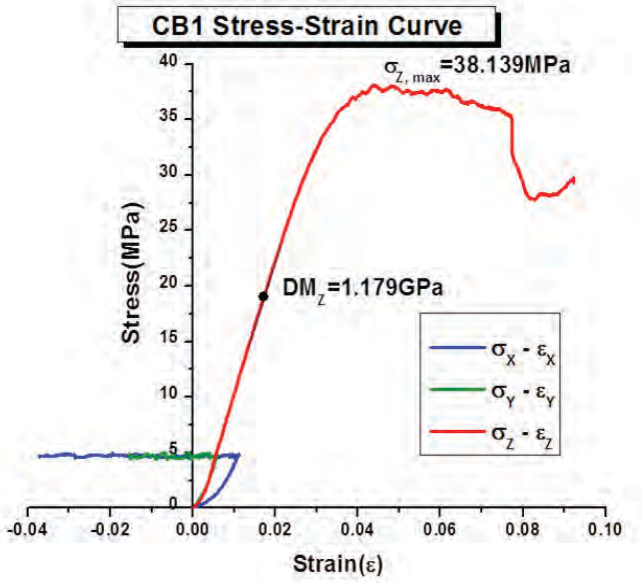



**Figure 8. Obtained stress-strain diagrams for CB1 sample.**

(1) The summation of the fracture tensor components in the two perpendicular directions to the loading direction is a favorable parameter to evaluate the effect of anisotropic fracture system on the coal mass strength in the loading direction. When the confining stress system is the same, the higher the summation of the fracture tensor components in the two perpendicular directions to the loading direction, the lower the cubic coal block strength (Figure 10).

(2) The fracture tensor component in the loading direction is a favorable parameter to evaluate the effect of the anisotropic fracture system on the rock mass deformability modulus in the same direction. When the confining stress system is the same, the higher the fracture tensor component in the loading direction, the lower the deformability modulus of the cubic coal blocks in the same direction (Figure 11).

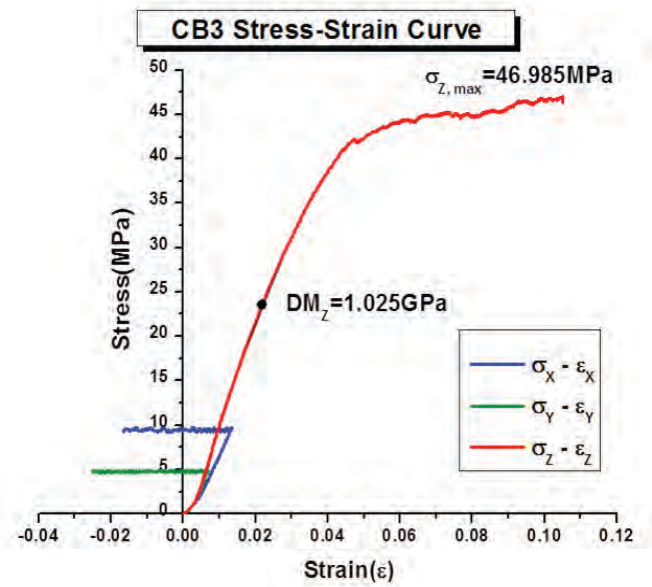



**Figure 9. Obtained stress-strain diagrams for CB3 sample.**

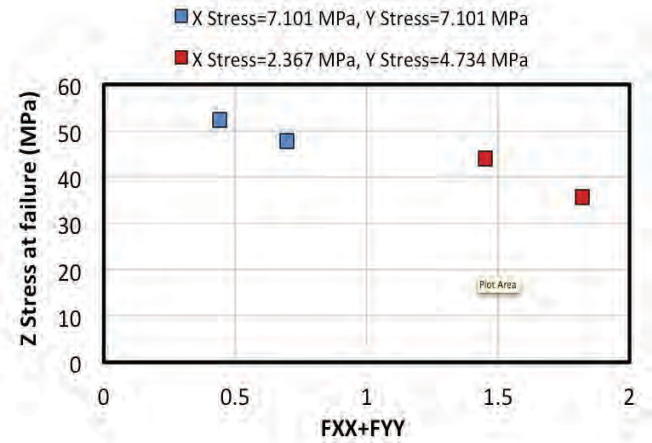



**Figure 10. Z stress at failure vs FXX+FYY.**

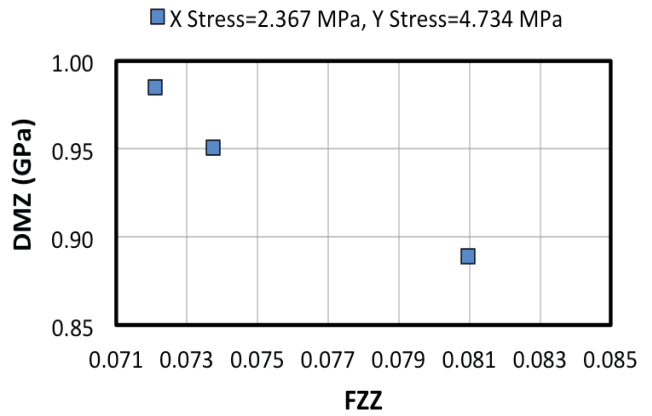



**Figure 11. Deformability modulus in Z direction (DMZ) vs FZZ.**

With respect to the effect of confining stresses on the strength and deformability modulus of the cubic coal blocks, the following statements can be made from the observations:

(1) When the summation of the fracture tensor components in the two perpendicular directions to the loading direction is within a small range, the higher the confining stress system, the higher the cubic coal block strength in the loading direction (Figure 12). For the samples shown in Figure 12, corresponding to $\sigma_y$ = 0, 4.73 and 9.47 MPa, the summation of the said fracture tensor components are within a difference of 0.25, 0.05 and 0.30, respectively. Figure 12 shows that the block strength has increased up to about 180% due to the changes in confining stresses shown in the figure. Note that the effect of the confining stresses on the strength is much higher than the 0.25 (25%) coefficient of variation obtained for the uniaxial compressive strength of the tested coal due to natural variability (Table 1).

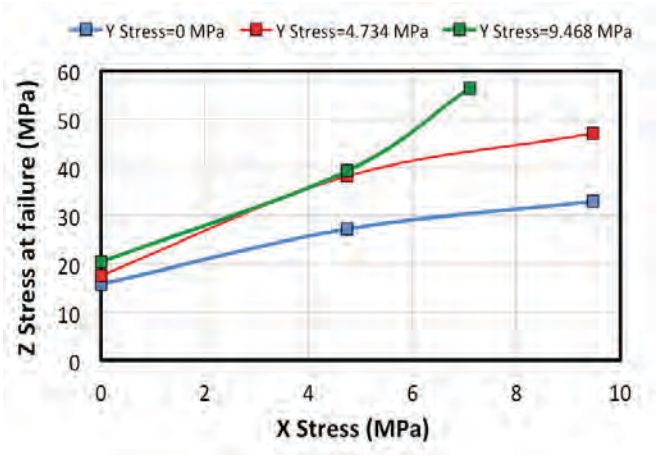



**Figure 12. Z stress at failure vs X stress for different Y stresses.**

(2) When the fracture tensor component in the loading direction is more or less the same (within a difference of 0.12), the confining stresses have little influence on the deformability modulus in the loading direction.

## DISCUSSIONS AND CONCLUSIONS

The CT scanning test is an effective way to obtain the pre-existing fracture geometry of the cubic coal blocks. To capture all the pre-existing bedding planes, face cleats, and butt cleats, it is necessary to obtain CT slices in the direction parallel to the bedding plane, as well as in the direction perpendicular to the bedding plane. Depending on different curvatures of the fracture plane, it is necessary to model the fractures either by single planes or by multiple piecewise planes. In representing fracture shape in a numerical model, rectangular shaped fractures may be used as approximations for the elongated shaped fractures; square or circular disc shaped fractures may serve as good approximations for the non-elongated polygonal shaped fractures. The developed construction procedure provides a systematic way to calculate the geometric parameters of each fracture. The calculated fracture tensor components in the selected three orthogonal directions were found to be in good agreement with the intuitive estimations obtained from the corresponding block photographs and CT slices.

This observation indicated that the fracture tensor component in a specific direction is an important parameter in evaluating the fracture influence in the corresponding direction in the geometric sense. Once the fracture tensor in a certain coordinate system is known, the fracture tensor component in any direction can be calculated in a convenient way by using the rules of tensor operations. From the fracture tensor calculation results, the fracture tensor component in the direction perpendicular to the bedding plane is found to be dominant for most of the cubical coal blocks. This finding is in good agreement with the fact that the bedding planes are the major discontinuities for sedimentary rocks. Fracture tensor based methodologies seem effective in summarizing the pre-existing fracture system to capture the fracture system scale effect and anisotropy.

CT scanning test results, in combination with true triaxial test results, provided very useful information in developing relations between strength/deformability parameters of coal blocks and fracture tensor parameters under different, confining stress conditions. The strength of cubic coal blocks in a particular direction is closely related to the summation of the fracture tensor components in the two perpendicular directions to the said specific direction and the confining stress system. The deformability of cubic coal blocks in a particular direction is correlated to the fracture tensor component in the same direction. Strength and deformability of rock masses should be treated as tensors rather than scalars to allow accommodation of anisotropic, scale-dependent properties for jointed rock masses in investigating deformation and stability of the interested rock masses. Fracture tensor components can be used as the characteristic parameters in combination with geo-mechanical properties and in-situ stress to perform numerical analysis to evaluate the loading capacity and deformability of the interested coal/rock masses. This technique can be used to arrive at safe and economical designs of coal pillars and to predict the potential hazardous deformations in underground coalmine excavations.

Because the available experimental data were limited, only a few points exist in Figures 10, 11, and 12. In the future, numerical models of coal blocks having different fracture networks will be subjected to the same confining stress systems numerically under true triaxial loading to investigate the influence of the fracture networks on the strength and deformability modulus of coal masses. In addition, numerical models of coal blocks with the same fracture networks will be subjected to numerical true triaxial tests under different confining stress combinations to study the effect of confining stress on the strength and deformability modulus of coal masses. Finally, both the experimental and numerical results will be used to develop a new 3-D strength criterion for the coal masses.

## REFERENCES

Hoek, E. (2007). "Rock mass properties." *Rocscience. Hoek's Corner: Practical Rock Engineering.* https://www.rocscience.com/education/hoeks_corner

Kulatilake, P. H. S. W., Park, J., and Malama, B. (2006). "A new rock mass failure criterion for biaxial loading conditions." *Geotechnical and Geological Engineering 24* (4): 871–888.

Kulatilake, P. H. S. W., Wang, S., and Stephansson, O. (1993). "Effect of finite size joints on the deformability of jointed rock

in three dimensions." *International Journal of Rock Mechanics and Mining Sciences & Geomechanics Abstracts 30* (5): 479–501.

Mine Safety and Health Administration. (2014). "Coal mining fatalities by state by calendar year as of 2/21/2014." *MSHA Fatality Statistics, United States Department of Labor.* http://www.msha.gov/stats/charts/coalbystates.pdf

Oda, M. (1982). "Fabric tensor for discontinuous geological materials." *Soils and Foundations 22* (4): 96–108.

Wu, Q. and Kulatilake, P. H. S. W. (2012). "REV and its properties on fracture system and mechanical properties, and an orthotropic constitutive model for a jointed rock mass in a dam site in China." *Computers and Geotechnics 43*: 124–142.

# Analyses of De-Confinement Mechanisms of Unstable Failures in Underground Mining Conditions

**Ruixiang Gu**, Ph.D., Research Associate
**Ugur Ozbay**, Professor
Mining Engineering Department
Colorado School of Mines
Golden, CO

## ABSTRACT

The de-confinement mechanisms of unstable failures as they occur in deep coal mining conditions are investigated using a distinct element numerical modeling code. The Mohr-Coulomb and continuously yielding joint constitutive models were used to study the compressive failures in coal and slip behavior of coal-rock interfaces, respectively. The effect of strength variations within interfaces on the failure mechanism of mining faces is also studied. The stability of interface slip failures was found to have a significant role in the failure mode of coal sidewalls. When the interfaces experience stable slip failures, the sidewalls are more likely to fail in a stable manner. With occurrence of unstable slips at interfaces, unstable compressive failures of sidewalls are triggered. The numerical modeling results support the proposed de-confinement mechanisms and emphasize the importance of including the coal-rock interface behavior in the analyses of unstable compressive failures. The significance of the proposed mechanisms in underground mining conditions is that rock discontinuities with large cohesion drop can become potential factors, inducing unstable compressive failures at ribs and mining faces. Therefore, the de-confinement mechanisms should be taken into consideration in mine design.

Keywords: coal bump, rock burst, de-confinement, stable failure, unstable failure, CY model

## INTRODUCTION

Compressive failures in rock are known to occur in deep underground mines and tunnels under the influence of changing stress fields because of mining excavations. (Kaiser, Yazici, and Maloney, 2001; Ellenberger, Heasley, Swanson, and Mercier, 2001; Gale, et al., 2001; Bajpayee and Schilling, 2009; Stiros and Kontogianni, 2009). Such failures can occur in a stable, gradual manner or an unstable, violent manner. Unstable failures can manifest themselves as coal bumps in underground coal mines. This paper presents numerical modeling methodologies developed with the objective of improving the understanding of mechanisms of such unstable failures as they occur in deep coal mines. The focus is on the unstable failures caused by sudden de-confinement of mining faces and sidewalls. The commercially available software Universal Distinct Element Code (UDEC) is used for the numerical modeling studies analyses. This model incorporates two softening constitutive laws that can be used for failure stability analysis. The continuously yielding (CY) joint model is suitable for simulating post-peak softening of coal-rock interfaces, and the Mohr-Coulomb strain softening (MCSS) model can be used for the studies of compressive failure behavior of rocks. The capability of UDEC, with its CY joint and MCSS models, in simulating stable and unstable failures was verified in previous studies (Gu and Ozbay, 2012; Gu and Ozbay, 2013; Kias, Ku, Garvey, and Ozbay, 2011). This study focuses on the possible mechanisms of unstable sidewall failures triggered by a sudden de-confinement resulting from unstably failing coal-rock interfaces.

## STIFFNESS CRITERIA

For failure stability analysis, the stiffness criterion proposed by Salamon (1974) and then later modified by Rice (1983), which is shown in Figure 1, was adopted. The block on the left column in Figure 1 (ai) is subjected to a horizontal pull force T applied on the spring, resulting in a movement of $\delta_o$. Depending on the magnitude of the normally applied stress $\sigma_n$, the block slides by an amount $\delta$ along the contact surface. The stiffness k determines the amount of elastic strain energy that can be stored in the spring. If the spring stiffness is greater than the post-peak stiffness of the interface, as in Figure 1 (aii), the block slides stably during sliding. The spring with a low stiffness, as in Figure 1 (aiii), results in an unstable shear failure. For the stability of rock compressive failures, the stiffness criterion proposed by Cook (1965) was used as shown in Figure 1 (b). According to this criterion, if the energy accumulated within the loading system, represented by the spring in Figure 1 (bi), is in excess of what can be consumed by the rock specimen, the failure occurs unstably. The shaded area in Figure 1(bii) is the excess energy available from the unstable failure.

## SOFTENING CONSTITUTIVE MODELS

The CY joint model accounts for non-linear hardening and softening during shear failure of rock interfaces. The interface shear stress-displacement curve is set to approach a target shear strength $\tau_m$ by changing the instantaneous gradient of the curve based on the difference between strength and stress, as shown in Figure 2. As normal stress increases, target shear strength increases. The increase in the target shear strength results in an

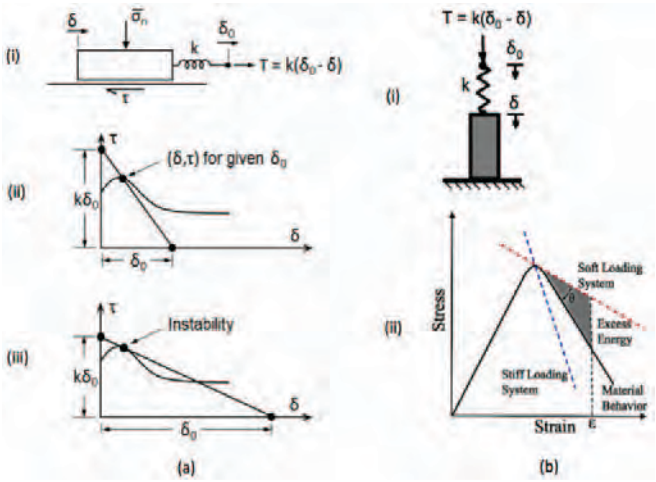



**Figure 1. Conditions for stable and unstable failures: (a) interface slip failure (Rice 1983), (b) compressive failure (Cook 1965).**

increase in shear strength of the modeled interface. The target shear strength continuously decreases with the increasing plastic shear displacement increment. This results in a softening behavior in the post-peak region of the interface.

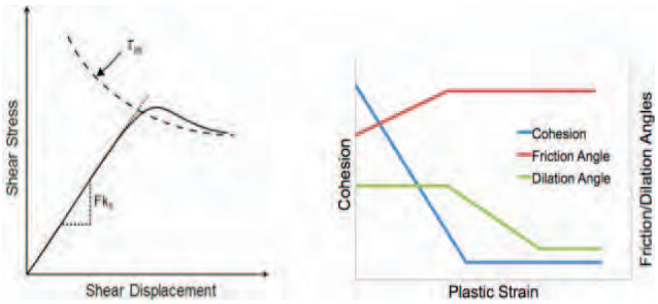



**Figure 2. (a) The shear stress–displacement curve and the target shear strength τm of the CY joint model (Itasca Consulting Group, 2010); and (b) a conceptual representation of variations of cohesion, friction angle and dilation angle in the MCSS model.**

MCSS model is used for simulating full load-deformation behaviors of rocks under compressive loading. In this model, cohesion, friction angle, and dilation angle can harden and soften at the onset of plastic yield, as shown in Figure 2 (b), as compared to perfectly plastic Mohr-Coulomb (MC) model, in which such properties are set to remain constant during failure.

## UNSTABLE FAILURE AND DE-CONFINEMENT MECHANISMS

Many researchers have shown that the resistance provided by the coal-rock interfaces could be an important factor that affects the strength of coal materials (Mark and Bieniawski, 1986; Gale, 1998; Su and Hasenfus, 1999; Lu, Ray, Morsy, and Peng, 2008). As such, the failure stability of mining faces and sidewalls is likely to be affected by the shear properties of the interfaces. Taking into consideration the mechanical response of interfaces, a de-confinement mechanism is forwarded for use for failure stability analysis of coal faces. The emphasis is on the de-confinement effects resulting from unstable slip failures at the interfaces (Figure 3). The variation of shear strength along interfaces is also considered for stability assessments of both interface and sidewall failures.

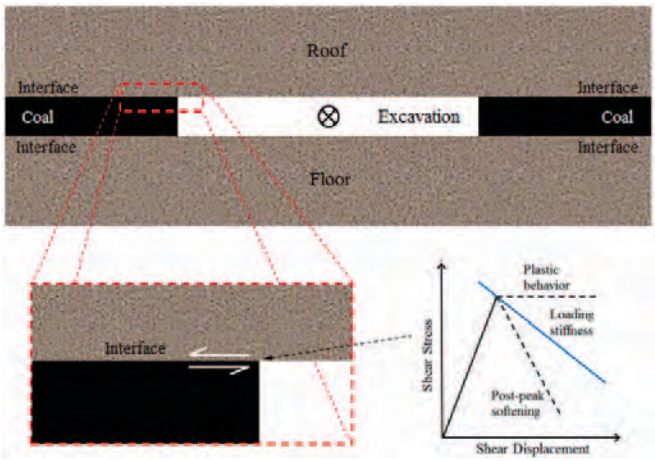



**Figure 3. Mining geometries used for modeling of de-confinement induced unstable compressive failures in sidewalls (mining advances perpendicular to the plane causing shear stress increase at the interfaces close to the sidewalls).**

## NUMERICAL MODELING

### Failure stability modeling using MC and CY joint models

When modeling coal-rock interfaces to exhibit elastic-perfectly plastic behavior, the possibility of unstable slip failure occurring along interfaces is inherently ignored. Potential compressive unstable failures in a coal seam would also be unaccounted for under perfectly plastic interface conditions. To signify the differences between perfectly plastic and softening post-behaviors, an idealized interface (Figure 4) was modeled first using the MC model and then using the CY softening model.

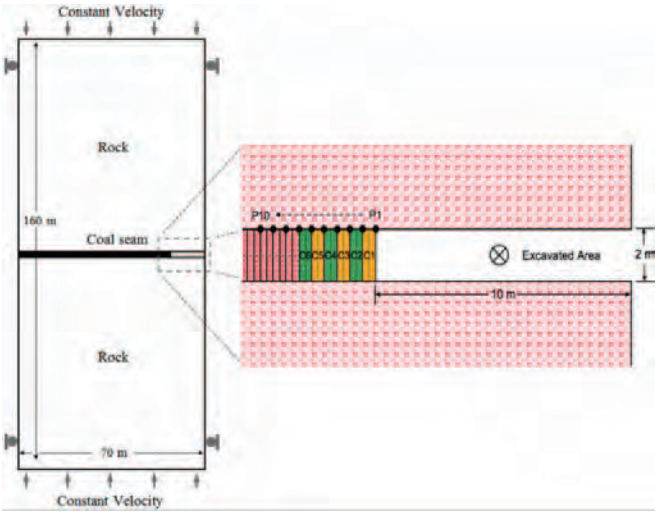



**Figure 4. Model for studies of de-confinement mechanisms for the stability of sidewalls.**

The input parameters for both MC and CY joint model are shown in Table 1. For both cases, the coal seam is modeled as a MCSS material using the input parameters that are listed in Table 2. The roof and floor are assigned the elastic model with a Young's modulus of 50 GPa and a Poisson's of 0.3. The model shown in Figure 4 was loaded by applying a constant velocity at the top and bottom to simulate mining advancing perpendicular to the plane. Six measurement points in the coal seam, labeled C1 to C6 in the figure, are used to record the vertical stresses carried by the coal during mining. Ten measurement points on the coal-roof interface (i.e., P1 to P10) are used to record the shear stress on the interface.

**Table 1. Input parameters of the MC and CY joint model.**

| | Parameter Symbols | Description | Value |
|---|---|---|---|
| **MC** | jkn | Joint normal stiffness | 50 GPa/m |
| | jks | Joint shear stiffness | 50 GPa/m |
| | jfric | Joint friction angle | 20° |
| | jcoh | Joint cohesion | 2.5 MPa |
| **CY** | jkn | Joint normal stiffness | 50 GPa/m |
| | jks | Joint shear stiffness | 50 GPa/m |
| | jen | Joint normal stiffness exponent | 0 |
| | jes | Joint shear stiffness exponent | 0 |
| | jfric | Joint intrinsic friction angle | 30° |
| | jif | Joint initial friction angle | 59° |
| | jr | Joint roughness parameter | 0.1 mm |

**Table 2. Input parameters of the MCSS model for the coal.**

| | |
|---|---|
| Cohesion (Plastic strain (in millistrain), cohesion (in MPa) | 0.00, 2.2<br>0.05, 2.2<br>36.00, 0.2 |
| Friction angle (Plastic strain (in millistrain), friction angle (in deg.) | 0.00, 23.0<br>0.02, 30.0<br>7.80, 30.0 |
| Dilation angle (Plastic strain (in millistrain), dilation (in deg.) | 0.0, 15.0<br>0.5, 15.0<br>1.0, 5.0<br>1.5, 5.0 |

Figure 5 and Figure 6 show the variation in shear stress and normal stress as loading increases over the coal face. With the MC model at the coal-rock interfaces, the interfaces exhibit stable slip failures, as indicated by the gradual and continuous changes in the shear stress in Figure 5 (a) (Gu and Ozbay, 2014). The coal seam at points C1, 2, 3, and 4 also experience stable compressive failures as shown in Figure 5 (b). With the CY joint model at the coal-rock interfaces, the softening behavior results in unstable slip failures of the interfaces, as indicated by the rapid and discontinuous decreases in the shear stress as shown in Figure 6 (a) (Gu and Ozbay, 2014). The unstable slip failures cause unstable compressive failures at the coal seam as indicated by the rapid and discontinuous changes in the vertical stress, as shown in Figure 6 (b).

**Role of interface strength properties in failure stability**

The interfaces between different rock materials can include strong regions with clean but rough surfaces or weathered weak surfaces. To study the role of interface surface properties in failure stability, an idealized model was developed in UDEC. Figure 7 shows the approach used for modeling interface strength variation by implementing strong rock bridges (barriers) and weak regions along the coal-rock interfaces.

Figure 8 shows the model geometry used for the analyses of the interface strength variations and their effects on the stability of coal face failures. The excavation advances for 10 m in the direction indicated by the white arrow. The white and red lines on the interfaces represent weak regions and barriers, respectively.

The results from UDEC simulations indicate that both the stability and intensity of the failures at mining faces are significantly affected by the presence of weak regions along the roof-coal and coal-floor interfaces. Figure 9 shows the vertical stress records from a simulation without weak regions and a simulation with a weak region length of 2.0 m and a barrier length of 0.5 m. Comparing the results given in these figures, it can be seen that, when there are weak regions present along the interface, as shown in Figure 9 (b), more unstable compressive coal failures can occur. The magnitude of these failures is larger than those with no weak regions on the interfaces, as shown in Figure 9 (a). Increased sections of coal material tend to fail over a short time period, and they fail earlier than those with no weak region do.

## CONCLUSIONS

Coal failure stability in underground coal mines is studied using the distinct element-based numerical model UDEC. The modeling approach makes use of the softening constitutive laws, namely the Mohr-Coulomb strain softening model for the compressive failures and the CY joint model for the slip failures along coal-rock interfaces. The main findings of the study include the following:

- During loading, unstable failures are signified by sudden losses of load, while stable failures follow a relatively smooth and gradual reduction in load.

- Unstable interface failures provide a sudden de-confinement to coal rib, thus triggering unstable compressive failures in sidewalls.
- Competent, rough interfaces are more likely to fail unstably compared to weaker, planar interfaces, which are likely to fail as perfectly plastic material.
- Strength variation of coal-rock interfaces can promote unstable compressive failures in mining faces.

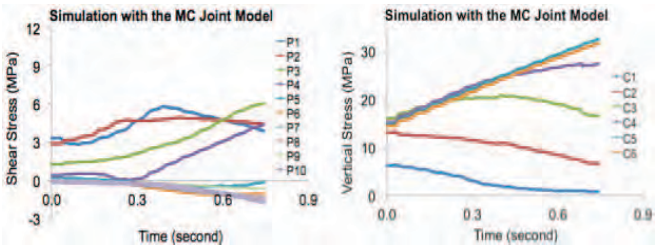



**Figure 5. Stress - time curve of in the simulation with the MC model on coal - rock interfaces: (a) shear stress - time curve of the interface measurement points, and (b) vertical stress - time curve of the coal measurement regions.**

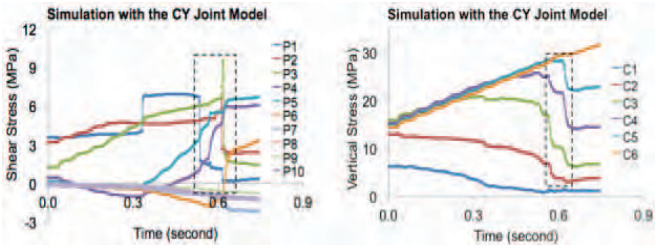



**Figure 6. Stress - time curve of in the simulation with the CY model on coal - rock interfaces: (a) shear stress - time curve of the interface measurement points, and (b) vertical stress - time curve of the coal measurement regions.**

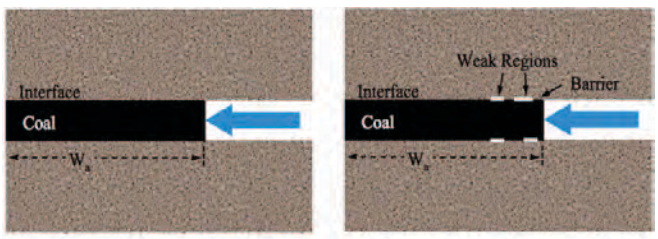



**Figure 7. Interface representation used for de-confinement mechanisms simulations.**

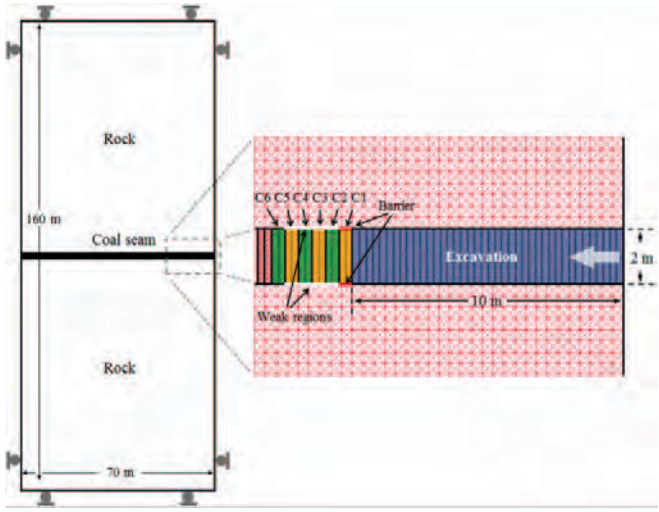



**Figure 8. Model for studies of de-confinement mechanisms involving weak regions for the stability of mining faces.**

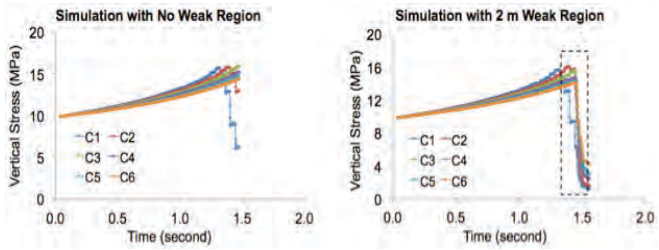



**Figure 9. Vertical stress - time curves of the measurement regions in the simulation: (a) without weak region, and (b) with a weak region of 2.0 m and a barrier of 0.5 m.**

## REFERENCES

Bajpayee, T. S. and Schilling, S. R. (2009). "Stability mapping to examine ground failure risk: a field study at a limestone mine." In: *Proceedings of the 28th International Conference on Ground Control in Mining*. Morgantown, WV: West Virginia University, pp. 135–142.

Cook, N. G. W. (1965). "A note on rockbursts considered as a problem of stability." *Journal of the South African Institute of Mining and Metallurgy 65*: 437–446.

Ellenberger, J. L., Heasley, K., A., Swanson, P. L., and Mercier J. (2001). "Three dimensional microseismic monitoring of a Utah longwall." In: *Proceedings of the 38th US Rock Mechanics Symposium*. Washington, DC. pp. 1321–1326.

Gu, R. and Ozbay, U. (2012). "Distinct element model analysis of unstable failure of rock discontinuities." In: *Proceedings of the 46th US Rock Mechanics/Geomechanics Symposium*. Chicago, IL: American Rock Mechanics Association, pp. 24–27.

Gu, R. and Ozbay, U. (2013). "Distinct element model analysis of stable and unstable shear failure." In: *Proceedings of the 47th US Rock Mechanics/Geomechanics Symposium*. San Francisco: American Rock Mechanics Association, pp. 23–26.

Gu, R. and Ozbay, U. (2014). "Distinct element analysis of unstable shear failure of rock discontinuities in underground mining conditions." *International Journal of Rock Mechanics and Mining Sciences 68*: 44–54.

Gale, W. J. (1998). "Coal pillar design issues in longwall mining." In: *Proceedings of Coal 1998: Coal Operators' Conference*. Wollongong, Australia: University of Wollongong and the Australasian Institute of Mining and Metallurgy, pp. 133–146.

Gale, W. J., Heasley, K. A., Iannacchione, A. T., Swanson, P. L., Hatherly, P., and King, A. (2001). "Rock damage characterization from microseismic monitoring." In: *Proceedings of the 38th US Rock Mechanics Symposium*. Washington, DC: American Rock Mechanics Association, pp. 1313–1320.

Kaiser, P. K., Yazici, S., and Maloney, S. (2001). "Mining-induced stress change and consequences of stress path on excavation stability – a case study." *International Journal of Rock Mechanics and Mining Sciences 38* (2):167–180.

Kias, E. M. C., Gu, R., Garvey, R., and Ozbay, U. (2011). "Modeling unstable rock failure during a uniaxial compressive strength test." In: *Proceedings of the 47th US Rock Mechanics Symposium*. San Francisco, CA: American Rock Mechanics Association, pp. 26–29.

Lu, J., Ray, A., Morsy, K., and Peng, S. (2008). "Effects of rock/coal interface property on coal pillar strength." In: *Proceedings of the 27th International Conference on Ground Control in Mining*. Morgantown, WV: West Virginia University, pp. 262–267.

Mark, C. and Bieniawski, Z. T. (1986). "Field measurements of chain pillar response to longwall abutment loads." In: *Proceedings of the 5th Conference on Ground Control in Mining*. Morgantown, WV: West Virginia University, pp. 114–122.

Rice, J. R. (1983). "Constitutive relations for fault slip and earthquake instabilities." *Pageoph 121* (3):443–475.

Salamon, M. D. G. (1974). "Rock mechanics of underground excavations." In: *Proceedings of the 3rd Congress of the International Society for Rock MechAnics, Vol.1B*. Denver, CO: International Society for Rock Mechanics, pp. 951–1099.

Stiros, S. C. and Kontogianni, V. A. (2009). "Coulomb stress changes: from earthquakes to underground excavation failures." *International Journal of Rock Mechanics and Mining Sciences 46* (1): 182–187.

Su, D. W. H. and Hasenfus, G. J. (1999). "Coal pillar strength and practical coal pillar design considerations." In: *Proceedings of the Second International Workshop on Coal Pillar Mechanics and Design*. Pittsburgh, PA: National Institute for Occupational Safety and Health, pp. 155–162.

# Learning Our Geotechnical Limits and Pushing Our Longwalls Through Them

**Richard N Campbell**, Managing Director
Geotechnical Engineering
Blackrock Mining Solutions Pty Ltd
Mackay, Australia

## ABSTRACT

The world's ever-expanding demand for energy and coking coals has resulted in the underground mining industry looking at taking on increasingly marginal and geotechnically challenging deposits. The drivers for this change include a reduced availability of open cut reserves and a lack of remaining "good coal leases". The lack of plum deposits is forcing some companies wanting to enter the coal supply market to purchase and operate in higher risk, lower margin areas.

As geotechnical professionals, we are expected to develop strategies to facilitate safe and productive mining in ground that once would have been avoided. To be successful in these reserves, we are required to use every tool available, from exploration data to longwall automation, and invent or reinvent some new tools along the way.

This paper presents geotechnical case studies of challenges in longwall mining and some of the methods developed and used to allow longwall mining to succeed where others said we would fail.

## INTRODUCTION

The recent boom times in the coal industry, pre- and post–Global Financial Crisis (GFC), have resulted in many companies rushing to grow their share of, or enter, the underground coal industry. In an effort to get the coal on the belt, the industry has seen cases of rapid and risky acquisitions, poorly managed or ill-defined exploration/characterisation programs and a lack of sound engineering diligence. A simple staged approach, such as that demonstrated in Figure 1, can minimise the geotechnical risk if applied correctly.

The economic tide has turned, operations have returned to a cost per tonne-driven situation, and as professional engineers we are being called on to minimise ground control-related delays and costs, to maximise returns, while at the same time ensuring no harm is done, development keeps in front of the longwall and the trains are filled as per the schedule.

This paper presents geotechnical case studies where efficient ground control has been the goal, where by using a sound engineering practice and maximising the use of available technology has provided effective situations, and where "normal" longwall mining has not be possible.

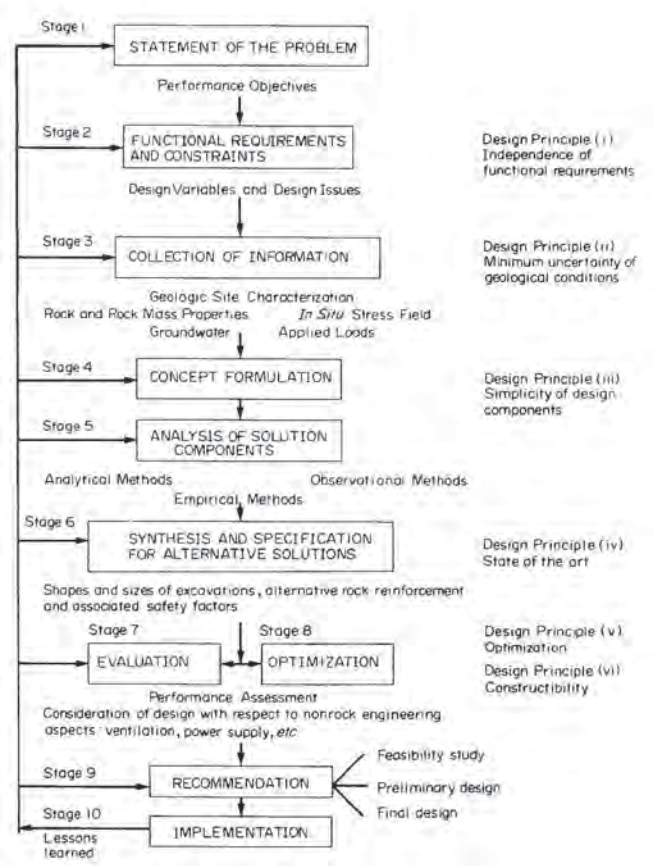



**Figure 1. Geotechnical assessment approach after Bieniawski 1993.**

## CASE STUDY 1: LONGWALL INSTALL FACE DESIGN OPTIMISATION

### Background

A greenfield longwall operation that had been celebrated as the fastest ever transition through the process from exploration project to operating board and pillar (B&P) mine to expansion into a longwall mine in recent history. After four years of successful B&P mining, a 300-meter-wide set of longwall face equipment and associated power and belt upgrades were procured and delivered. The shields are 2m wide and designed to cut a 4.0 to 5.2m height from a 5.5-6m thick seam.

The conversion from a 0.8Mt B&P operation to a longwall was based on geological and geotechnical data, as well as a mine plan and schedule that identified significant fault systems and intrusions. The geotechnical conditions resulted in the first longwall block having three install faces (LW1A, B & C) and, of course, three longwall salvages; the second block (LW2A & B) would have two of each. LW3 was separated from LW2by a major fault zone, resulting in the need for a new set of gate roads. Figure 2 depicts the mine plan and longwall blocks.

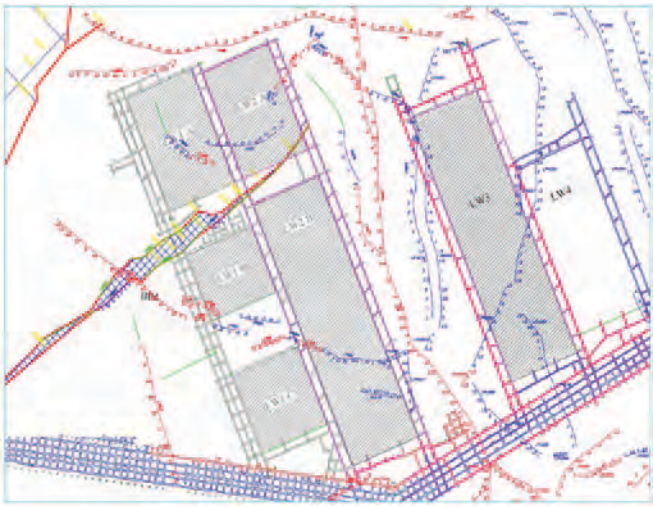


**Figure 2. Mine plan showing longwall blocks.**

Production forecasts in excess of 5.5 million run of mine (ROM) tonnes/year were used to justify the longwall upgrade capital investment. The pressure on development float and costs was significant, so all efforts to minimise any potential delays and costs were put into the longwall install faces.

The longwall equipment required installation roads with a run of face width of 9m and gate ends 11m wide. At the time, it was one of the largest install faces in the district.

### Geotechnical investigation

Due to the greenfields nature of the reserve, the initial install face (LW1 C) was developed and supported using what was considered a conservative pattern, taking significant time and cost (initial design reports highlighted a lack of data), and relied on empirical relationships. The support strategy for LW1 C is summarised in Table 1.

**Table 1. Summary of the original longwall install face support strategy.**

| | |
|---|---|
| **Run of Face - 9m wide** | |
| 10 x 1.8m X grade roof bolts - roof fully meshed | Per meter |
| 4 x 10m long point anchored tendons (420 kN UTS) | Per meter |
| 3 x 1.8m X-grade ribs bolts and rib mesh | Per meter |
| **MG and TG ends - 11m wide** | |
| 11 x 1.8m X grade roof bolts - roof fully meshed | Per meter |
| 6 x 10m long point anchored tendons (420 kN UTS) | Per meter |

The first install road was developed using the support strategy detailed in Table 1 and required a total of 1,250 x 10m long tendons to be installed. The result was a significant negative impact in longwall float, as the scheduled period to complete the install face was over-run by more than 28 days.

As a result, mine management decided to undertake a full geotechnical characterisation program by:

- Drilling an additional cored hole at the location of the LW1A install face;
- Running the full range of wireline tools, including acoustic scanner;
- Taking multiple samples for triaxial testing;
- Reviewing the site's existing sonic velocity-to-UCS relationship;
- Reviewing available in-situ stress magnitude and orientation data estimated from borehole breakout and hyrofrac measurements; and
- Reviewing and analysing monitoring data collected during the formation of LW1C install face (telltales and extensometers).

Bedding shear strength was the only remaining un-quantified parameter.

The data collected was aimed at developing a calibrated numerical (FLAC) model that would allow the mine to run a parametric study to optimise the support strategy, as illustrated in Figure 3.

Three basic runs were used, these being:

1. The "base case" using the data from the sonic UCS relationship and a moderate bedding shear strength;
2. A "strong case" using strong bedding planes and no structures; and
3. A "weak case", with a weak bedding plane strength with faults.

The results are summarised in Figure 4. At the time, the weaker model was considered as the most likely geotechnical setting due to structures and bedding shears seen in the core and acoustic scanner analysis.

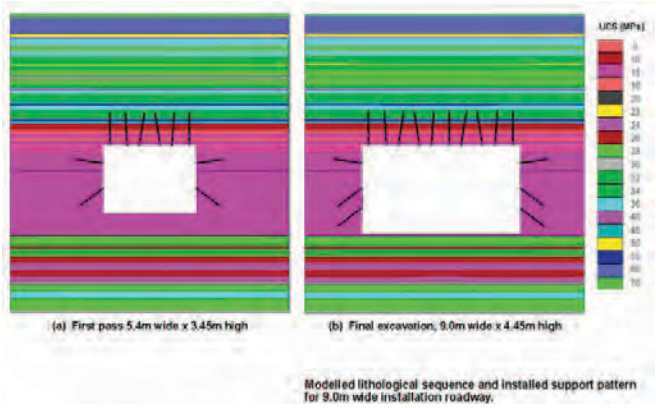



**Figure 3. FLAC geological model for the longwall install face (the actual model extended 50m below, 300m to left and right and 200m above the section illustrated).**

The range of results varied from no need for tendons of any sort in the strong case, to a mild cable pattern in the weak bedding shear strength model. The outcome was the acceptance of a revised support strategy, as detailed in Table 2.

**Summary**

The geotechnical investigation and analysis filled the design gaps in the original dataset, proving a full site characterisation, and allowed the operation to develop a refined geotechnical model for the strata, allowing the design to be tested against actual site deformation data.

The revised support plan required only 470 x 8m grouted cables, and once completed, provided a more stable (less creep monitored) installation face. It saved around 70% of the costs and time associated with the original support plan.

The development and support was completed significantly ahead of schedule, providing the mine with a solution for its longwall float issues. The revised support plan is still in use and, to date, has provided the mine with a fit-for-purpose solution.

## CASE STUDY 2: PRACTICAL USE OF LONGWALLAUTOMATION AND SHEARER PATH DATA TO MANAGE LONGWALL EQUIPMENT LIMITATIONS IN AN UNDULATING AND FAULTED THICK COAL SEAM

**Background**

A set of 2m-wide shields in a 145-shield face was designed and procured for mining a thick seam with a cutting height range of 3.0 to 5.2m. The geotechnical inputs for the longwall design called for 1350-toncapacity shields, 320 bar (80t/m$^2$) set pressure, 380 bar high set pressure and 420 bar(100t/m$^2$) yield pressure and a tip to face of 650mm while cutting a 1.0m web.

The longwall equipment was procured on the basis that longwalls have successfully operated in steep seams around the world, with maingate (MG) to tailgate (TG) cross-grades of 1:4, and potentially the same seam rise in direction of retreat. Issues occur where rapid changes in grade are required.

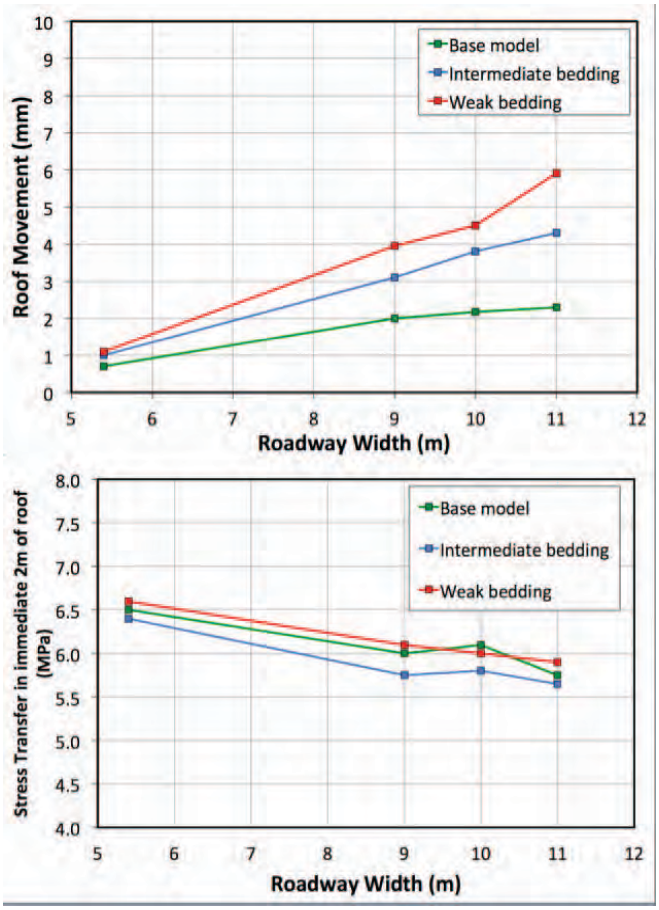



**Figure 4. Summary of the modelling results.**

The target reserve is covered by a 3D seismic survey, and had a significant number of exploration holes confirming structures and seam reduced levels (R.L.s) and changes in seam thickness, along with data from existing development panels. The seam geometry is characterised as extreme undulating with rapid gradient changes from essentially flat (1:20) to <1:5 across the block from MG to TG, as well as panel rise in the direction of retreat ranging from 1:20 to 1:6.

**Table 2. A summary of the revised longwall install face support strategy.**

| **Run of Face - 9m wide** | |
|---|---|
| 10 x 1.8m X grade roof bolts - roof fully meshed | Per meter |
| 3 x 8m long grouted cables tendons (580 kN UTS) | Every 2 meters |
| 3 x 1.8m X-grade ribs bolts and rib mesh | Per meter |
| **MG and TG ends - 11m wide** | |
| 11 x 1.8m X grade roof bolts - roof fully meshed | Per meter |
| 4 x 8m long grouted cables tendons (580 kN UTS) | Every 2 meters |
| 3 x 1.8m X-grade ribs bolts and rib mesh | Per meter |

In addition, there are significant faults of >10m within the longwall blocks, along with graben structures displacing the full seam thickness found in most blocks.

Figure 5 is a gradient change plan showing areas of the reserve having a change in grade of greater than 1:10 as colour scale, less than 1:10 is black.

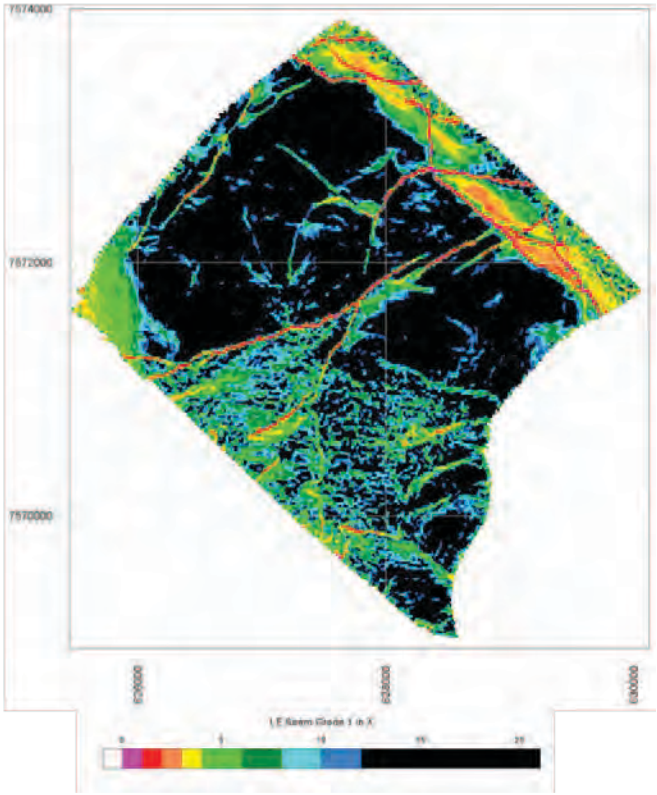



**Figure 5. Seam gradient change model, measured in terms of change in the surface gradient on a 15m x 7.5m grid size.**

Figure 6 is a seam roof elevation model for an area planned to have three longwall panels. The major issue here was rapid variation in the direction of gradient change, which is exaggerated around faults.

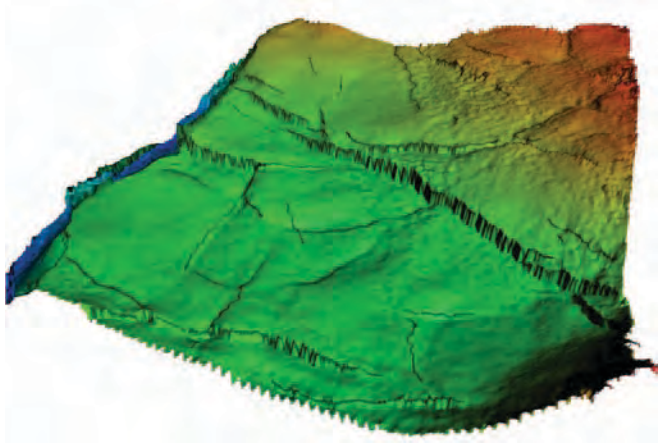


**Figure 6. Target seam elevation model, H:V exaggeration of 1:3 illustrating the seam "topography" and faulting.**

**The Problem**

During normal operations, the geometry of the armoured face conveyor, shearer and shields results in a maximum grade change of up to 3.7° (1:15) from horizontal, and even less if the shields are heading down. If changes greater than this are attempted, the shearer drum hits the canopy tips. Typical controls to manage this risk are taking one grading cut of 75mm, followed by two level cuts. These result in the pans and shields being on the same grade each time the grade change cut is made, as illustrated in Figure 7. With this limitation in ability to change grade, it was found the longwall face could not handle the required changes in geometry.

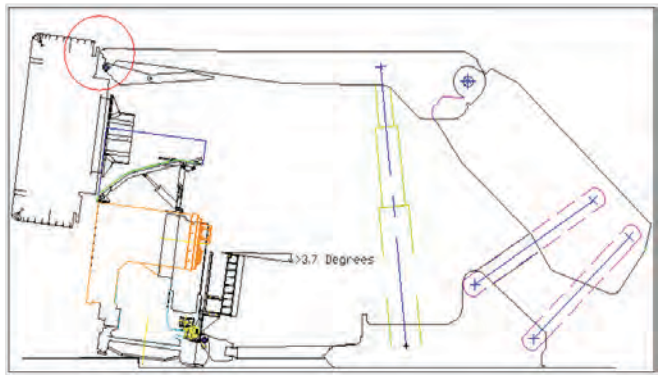



**Figure 7. Potential clash point between shearer drum and canopy tips if change in grade exceeds 3.7 degrees.**

Traditional face mapping and horizon control flight paths were used as an initial starting point, but suffered from a lack of realism from an operator's point of view. Such longwall face sections do not easily account for or accurately depict seam undulations, faults and/or cut profile and cut heights – in this sense, it can be difficult to utilise flight plans that do not represent the actual face geometry.

The result was a longwall that poorly executed flight plans, was often cutting out of seam, had poor roof and face control and was often experiencing significant cavities and delays. In addition, the shearer often collided with the canopy tips, the relay bars became

bridged out, and damage to dog bones and shear pins in the AFC pan line was commonplace.

**Geotechnical Considerations**

As is often the case in thick seam longwall mining, the key to maintaining geotechnical control of the roof is maintenance of a thick (>0.8m) coal roof beam. As such, a key driver for success was to predict the flight path required to maintain the roof beam, compare the actual flight path against the plan, and issue corrective actions in a rapid and easily understood manner.

Typical tools used by site geotechnical engineers are longwall face mapping, creep measurements, face straightening string lines and leg pressure surveys, which have been the mainstay for geotechnical engineers to assist in managing face conditions.

In this mine, the normal tools just were not working.

## LONGWALL AUTOMATION SOLUTIONS FOR GEOTECHNICAL ENGINEERS

In 2006, real-time leg pressure, system health monitoring and data analysis packages such as LVA became mainstream in Australia, providing a step change in the way geotechnical engineers receive and analyse strata conditions. These packages allowed for the provision of predictive tools for weighting and cavity formation, hydraulic performance, yielding and loading rates.

More recently, longwall automation systems have delivered shearer, AFC pan push and shield function automation to assist in avoiding collisions and standardising operations. The use of this data has mainly been the domain of the longwall manager and automation engineer, with the geotechnical engineer typically being left out of the loop. The details on the development and testing of much of this technology are available via ACARP project reportsC15002, C10100 and C9015.

The current generation of longwall equipment now incorporates technology that is able to record and transmit to the surface real-time:

- Three-dimensional, XYZ coordinate-based location data;
- AFC pan geometry data for roll and pitch;
- Face straightness;
- Shearer cut height; and
- Horizon control information (infrared cameras).

In addition, technology is currently being used for maingate creep monitoring and shield convergence monitoring (Kelly et .al, 2005; Kelly and Hainsworth, 2005, Reid et.al, 2001), all of which are vital to the geotechnical engineer for maintaining longwall face conditions, especially as mines take on increasingly difficult geology and complex fault systems, such as that illustrated in Figure 8.

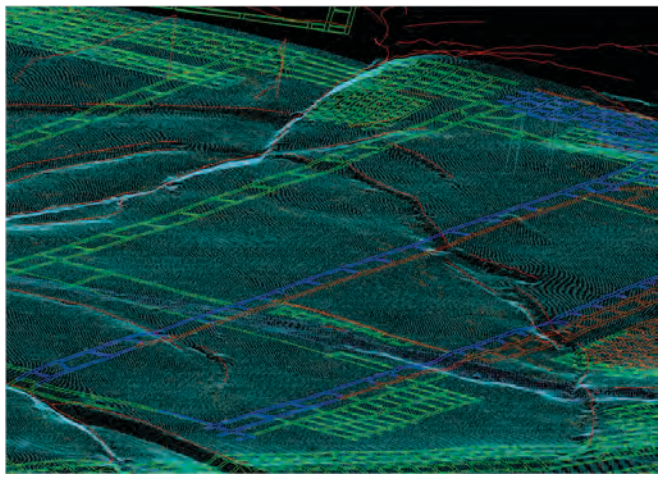


**Figure 8. Geological model of the seam floor showing complex fault geometries planned to be mined through.**

## GEOTECHNICAL USES OF AUTOMATION DATA

Shearer path data can be exported on a shear-by-shear basis and compared against the geological model and planned horizon, allowing for real time corrections to be made for pan pitch and roll, cut height and actual horizon, as illustrated in Figure 9. With data exported from the actual cut horizon in XYZ coordinates, for floor profile and cut height, it is now possible to import this data into the geological modelling packages and comparison on a daily, weekly or full panel length scale. Figure 10 demonstrates the ability to compare the geological model against the cut seam floor data over the length of a panel. Using this data, we can now confirm the correct horizon is being followed and see any unpredicted variations in the seam geometry that may indicate an unresolved structure ahead of mining.

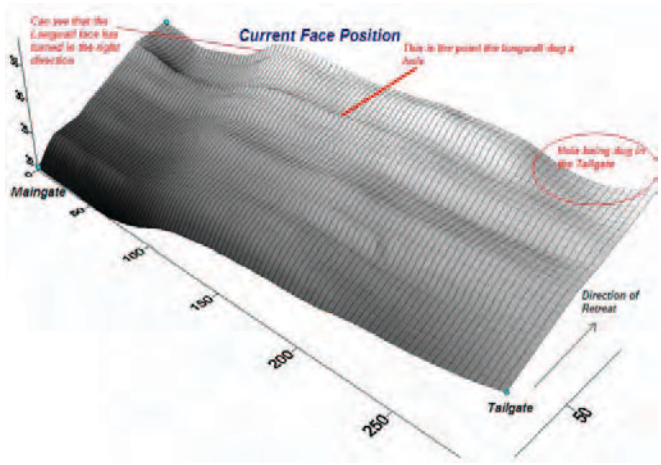



**Figure 9. Cut floor geometry data gathered from the shearer, showing 5 shears.**

With increasingly accurate seam input data for exploration tools, such as high-quality 3D seismic and geological modelling packages, fault systems can be resolved in true XYZ space, allowing flight plans to be anticipated well in advance in order to achieve accurate flight plans and horizon control. As the acceptance of automation increases and the technology becomes

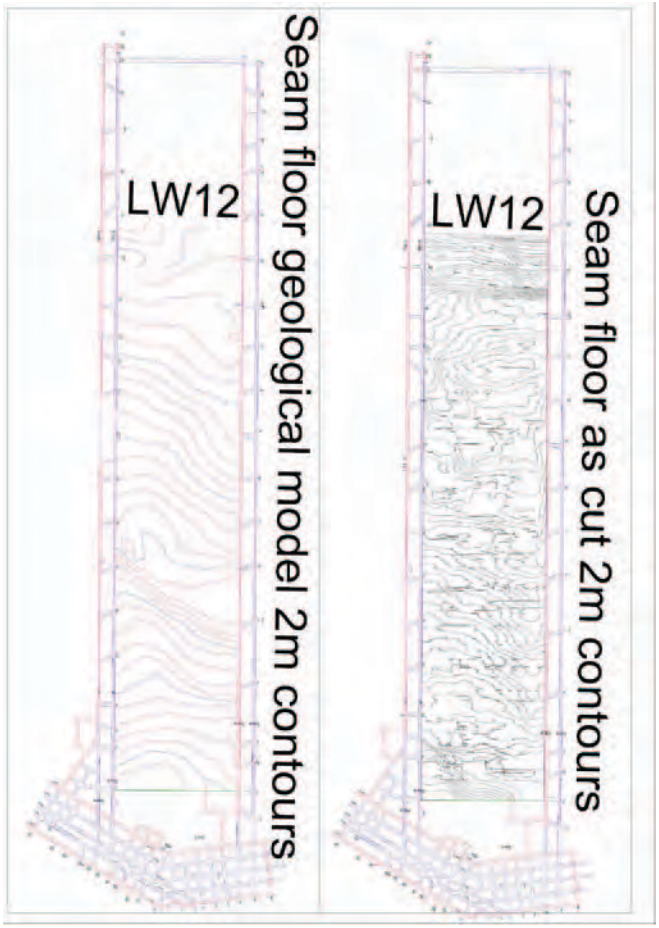



**Figure 10. Comparison between the geological model and as-cut seam floor.**

more robust, it is possible to pre-programme the cut height, pan angle changes and flight path into the shearer while enforcing controlled cut parameters to restrict equipment operations to within manufacturers' operational limits, protecting machinery while under automation. With the intent being the automation control will handle the typical conditions, and human intervention will be reduced to the exceptions to the rules, such as small seam rolls, washouts, poor roof conditions, and weighting events.

With the data from the longwall system being analysed on a shear-by-shear basis we are able to reconcile the seam model and make rapid corrections as required. Maximising the geotechnical performance of the longwall and minimising the risks associated with out-of-horizon cutting and incorrect flight paths.

Currently, the only limit to this technology is the resolution of the geological model, resources to run the reconciliation process in a rapid timeframe and operator acceptance, all of which have been overcome.

## LW GEOTECHNICAL CONDITION MONITORING

With live data being analysed from the automation systems Trigger Action Response Plan (TARP), triggers for geotechnical conditions can be set in a database and the data received from the automation system instantly tested against those triggers, as illustrated in Figure 11.This gives operators, supervisors and management access to easily-understood TARP levels on a 24/7basis,and a shear-by-shear basis without subjective measurements or opinions. The data can be presented and viewed on web pages from anywhere in the world. Figure 12 illustrates the face straightness page, showing the past five shears.

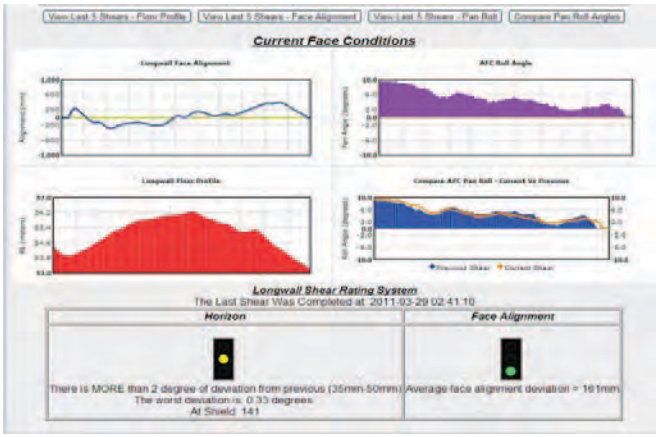



**Figure 11. Real time face condition monitoring data and TARP levels.**

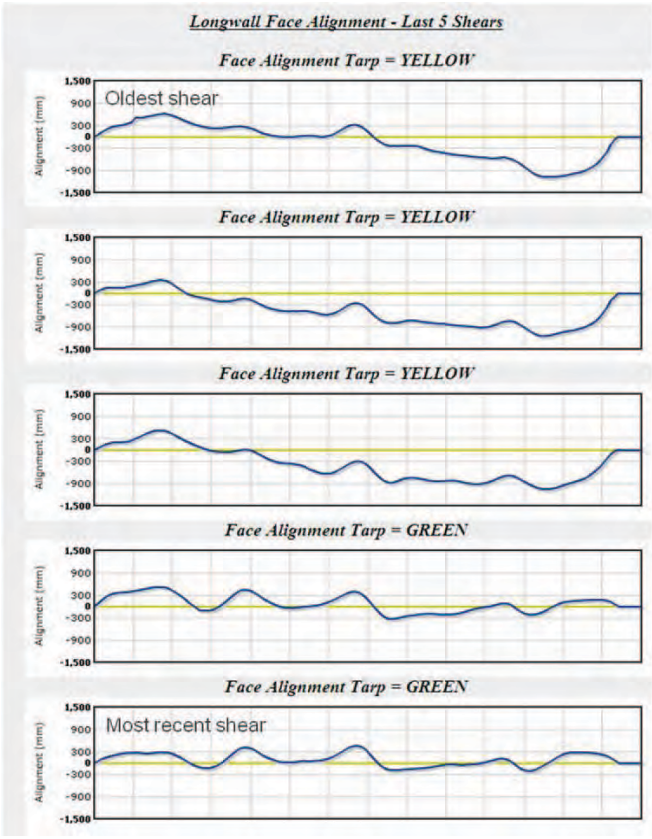



**Figure 12. Longwall face alignment data for previous five shears, upper graph oldest, lower graph most recent, showing increasing face straightness.**

If a flight plan has been issued in preparation for mining through a structure, the actual cut geometry can be tested against plan, as illustrated in Figure 13.

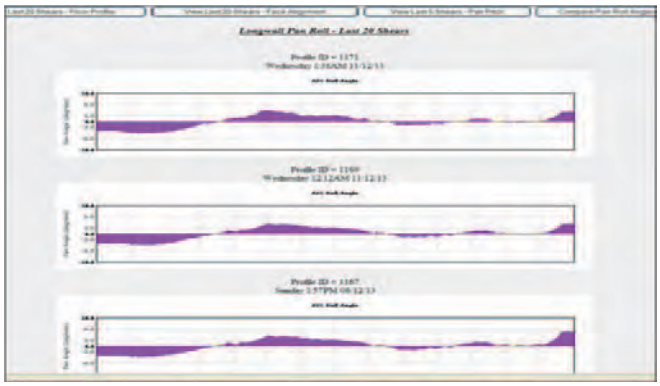


**Figure 13. AFC pan roll data from three successive shears, illustrating compliance to the flight plan.**

The data depicted in Figure 13 illustrates a flight plan with the expectation that:

1. From MG to 25shield,the face will dip at 3 to 4 degrees;
2. From 21 to 75 shield, the face will transition and rise at 2 to 3 degrees; and
3. From mid-face to the TG, the face will transition and run essentially flat to the normal grade into the TG.

If any significant deviations to the above plan were detected from either operators overriding the automation system or the geological model not being accurate, corrective actions can be issued immediately – such as, for example, automatic straightening cuts, changes in cut height and gradient changes to the shearer via state tables. Once issued, the result can then be monitored and checked.

## ACCURATE LONGWALL FACE GEOMETRY AND MAPPING

As part of the data that is generated from the shearer, the geotechnical engineer can use the cut floor profile (Z level in terms of RL) and the cut height (height of the MG drum) profile, as illustrated in Figure 14, to increase the accuracy of face mapping, tonnes per shear calculations and any dilution.

As part of this screen, it can be seen where the operators have had to duck under an area in the mid-face where cavities have been present and the face was double chocked.

The floor RLs and cut height can be simply exported from the database and imported into CAD-based drafting packages to automatically draw a true representation of the longwall face profile. The structures and faulting mapped can then be overlain to generate real face sections that the operators can review as they inspect the face. An example of a longwall face map drafted using the true cut profile is illustrated in Figure 15.

It was found that the longwall officials and operators could relate significantly better to the automation-generated profiles, as the

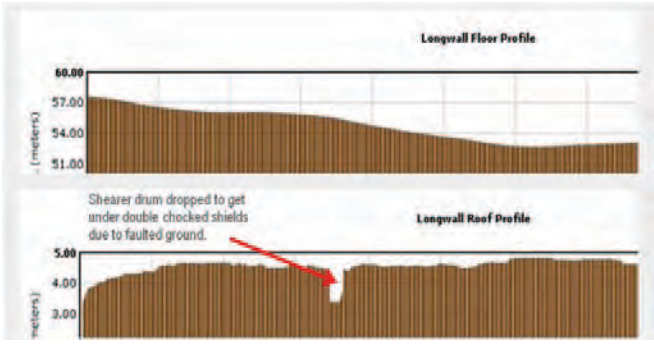



**Figure 14. Combination of data including cut floor profile (RL) and cut height.**

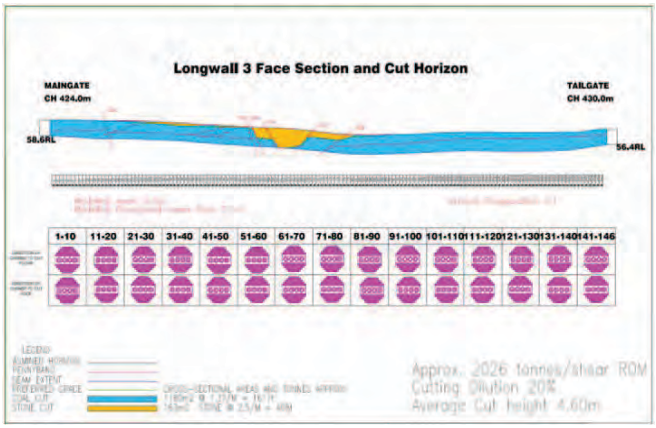



**Figure 15. Longwall face map using automation data for seam floor RL and cut height.**

drawing matched what they sawas they walked the length of the face, in terms of rolls and humps in the floor and the height of the cut. This greatly increases the ability to pass on accurate and meaningful information about the seam and the flight paths expectations in the coming shears.

## CONCLUSIONS

With the mounting demand to exploit increasingly marginal coal reserves, the onus is on geotechnical professionals to develop strategies to facilitate safe and productive mining in ground that once would have been avoided.

This paper has demonstrated how the use of sound engineering practices has delivered geotechnical solutions in less-than-optimal geological settings for longwall mining.

In addition, gaining and using the maximum data available for the current generation of longwall automation systems has been demonstrated as a valuable tool to assist in managing difficult geotechnical situations where “normal” longwall mining has not been possible.

**REFERENCES**

Bieniawski Z.T. 1993. "Classification of rock masses for engineering: the RMR system and future trends." In: Hudson J, ed. *Comprehensive rock engineering*. Vol. 3.Pergamon Press, 553–573.

Kelly, M.S., Hainsworth, D.W., Reid, D., Caris, C., et al. 2005. "ACARP Project C10100, Landmark Longwall Automation Project Final Report". *CSIRO Exploration & Mining Report*. No. *P2005/54,* January.

Kelly, M.S., Hainsworth, D.W. 2005."Outcomes of the Landmark Longwall Automation Project with Reference to Ground Control Issues."In *Proceedings, 24th International Conference on Ground Control in Mining*. Morgantown, West Virginia. Aug.2-4, 66-73.

Reid, D. C., Hainsworth, D. W., Ralston, J. C., McPhee, R. J. 2001."Longwall shearer guidance using inertial navigation (ACARP project C9015)."*CSIRO, Exploration and Mining Report 832F*, 2001.

# Mitigation of a Massive Sandstone Channel's Impact on Longwall Face Evaluation and Enhancement of Hydraulic Fracturing Technique

**Jun Lu**, Geomechanical Engineer
**Daniel W.H. Su**, Senior Geomechanical Engineer
**Greg J. Hasenfus**, Senior Geomechanical Engineer
**Mark Van Dyke**, Geologist
**Luke Stull**, Geologist
Consol Energy Inc.
Canonsburg, PA

## ABSTRACT

This paper presents the evaluation, enhancement and comparison of two hydraulic fracturing techniques which were employed to mitigate the impact of a massive sandstone channel on two successive longwall faces. The hydraulic fracturing technique and Longwall Visual Analysis (LVA) software were initially employed to mitigate the impact of thick, massive sandstoneroof during mining of longwall Panel 21. Improved longwall face conditions and productivity were observed as Panel 21 mined through the sandstone channel. However, moderate sandstone fractures and falls at the face were still present in areas where hydraulic fracture influence was not present. Such adverse conditions caused two to three weeks of production delays due to large face cavities, jammed face conveyor and subsequent face gluing.

Based on the mining experience in Panel 21, and site-specific roof geology in Panel 22, a modified and more effective hydraulic fracturing program was employed. Fewer well-placed holes were drilled, and larger volume of water was pumped into each hole in order to propagate the individual horizontal pancake fractures over a larger area, thereby enhancing caving and relieving face pressure caused by overhang of the massive sandstone. Longwall Visual Analysis (LVA) software was also employed at Panel 22 to predict the cavity risk index and guide the longwall face crew in double-pulling shields behind the shearer drum. This helped to reduce the tip-to-face distance at the critical spots along the longwall face, which helped mitigate the formation of the roof cavities and failure of massive sandstone onto the face conveyor.

Underground observations, face advance rate and face rock delay analysis confirmed that longwall face conditions and advance rate in Panel 22were significantly improved comparedto those of Panel 21. Consequently, safety and productivity were improved.

## INTRODUCTION AND BACKGROUND

Safety and production of coal mining operations can be greatly affected if hard-to-cave strata, such as thick sandstone, limestone and/or competent conglomerate, encroach close to the coal seam top and overhang for a considerable length before it caves (Peng, 2008).

A nearly 1,000-foot-wide sandstone channel was projected to run through the mid-panel area of three consecutive longwall panels (Panels 20, 21 and 22) (Figure 1) in a southwestern Pennsylvania Pittsburgh seam coal mine which has an approximate overburden depth of 600 ft. This same sandstone channel was known to cause significant longwall face roof control problems in the distant B-panel area in 1998 and 1999 (Su et al., 2001). More recently, it induced many large face cavities and caused substantial production delay in Panel 20. Subsequently, hydraulic fracturing of the sandstone and Longwall Visual Analysis (LVA) software were employed to help mitigate the sandstone impact in Panel 21(Su et al, 2012). LVA is a software package that continuously monitors, analyzes and displays shield pressures and shearer position in longwall mines.Based on the data collected, the LVA shield monitoring software calculates a Cavity Risk Index (CRI) from patterns of yielding and loading rates across a longwall face. The CRI in the LVA software provides real-time warnings of cavity risk to longwall operators. The LVA software has been used successfully in Panel 21 (Su et al, 2012) and Australian coal mines to predict roof weighting and longwall face cavity formation over the past few years (Hoyer, 2011).

Four holes were drilled and hydraulically fractured in Panel 21, each hole using an average water volume of 14,000 gallons and an average pumping rate of 25 barrels per minute. LVA software was employed to guide the longwall, e. g., to identify where and when to double-pull shields in order to reduce the tip-to-face distance at the critical spots along the longwall face. This resulted in improved longwall face conditions and productivity as Panel 21 mined through the sandstone channel.

Unfortunately, moderate sandstone fractures and falls at the face were still present, particularly in areas where hydraulic fracturing did not extend. These adverse face conditions caused two to three weeks of production delays, due in large part to jammed face conveyor and face gluing of roof cavities. Based on these results, it was determined that better hydraulic fracturing coverage of the sandstone, through additional water injection volume and improved hole placement, could be beneficial in helping to promote sandstone caving and relieve stress at the longwall face.

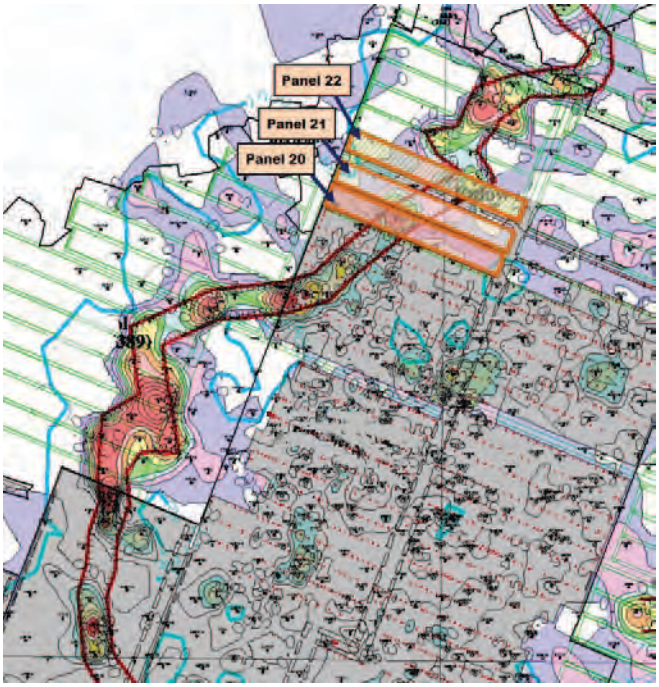



**Figure 1. Projection of massive sandstone channel.**

## GEOLOGIC RECONNAISSANCE AND CONSIDERATIONS

Since prior trending and regional roof geology indicated that the massive roof sandstone channel would continue beyond Panel 21 (Figure 1), exploration efforts were targeted to delineate and quantify the channel across Panel 22in order to determine whether additional fracing would be warranted. The program consisted of surface coreholes, as well as extensive exploration of gateroad sections including in-mine mapping of entries, fiberscope inspection of roof boreholes and in-mine roof coring.

To determine the general location of the sandstone channel, roof scope holes were examined along the track entry at intervals of one to two breaks (approximately 270 to 540 ft) with the use of a 20 ft (6.1 m) fiberscope. In-mine observations of sandstone encounters, as well as seam rolls and other transitional features such as slips and changes in roof coal thickness, were then recorded to refine the location and trends of the channel as it crossed the gate sections. To determine the total thickness and characteristics of the channel, the roof was then cored at strategic locations using an in-mine core rig. The rig is capable of drilling as deep as 60 ft into the roof.

Similar to Panel 21, gate entry observations and scoping results for Panel 22 indicated that the center of the sandstone channel would encroach to within 5 ft of the 5½-ft thick main bench. However, unlike Panel 21, the channel within Panel 22 would likely change directions, meandering in S-curve fashion from breaks 28 to 29 on the tailgate side to breaks 22 to 23 at the headgate (Figure 2). Furthermore, scoping results indicated that the sandstone at both the tailgate and headgate would likely be thick, which was subsequently confirmed by in-mine roof coring that proved the sandstone to be greater than 50 ft thick near channel center. In-mine coring also indicated that thechannel consisted of mostly medium-tocoarse-grained, medium-tomassively-bedded sandstone.

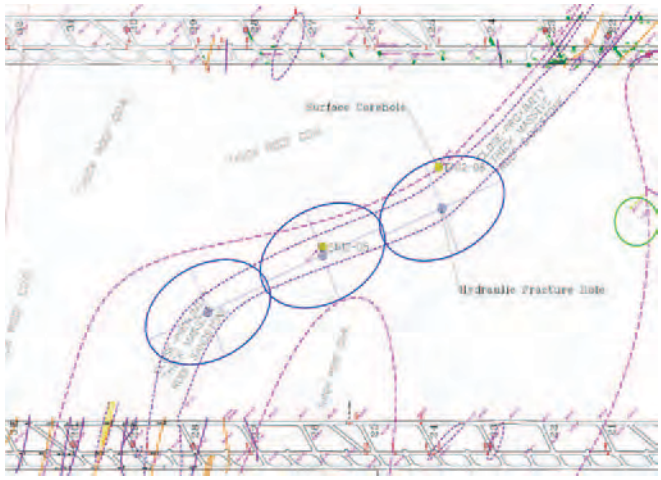



**Figure 2. Panel 22 sandstone channel and hydraulic fracture hole locations.**

To confirm the suspected path of the meandering channel, as well as its thickness and characteristics, two strategicallyplaced surface core holes were then drilled within Panel 22 (Figure 2). Results not only confirmed the path of the channel, but also showed that the sandstone near panel center was indeed massive, up to 63 ft thick and encroached to within 5 ft of the main bench near panel center(Figures 3 and 4).



**Figure 3. Example of Panel 22 channel sandstone.**

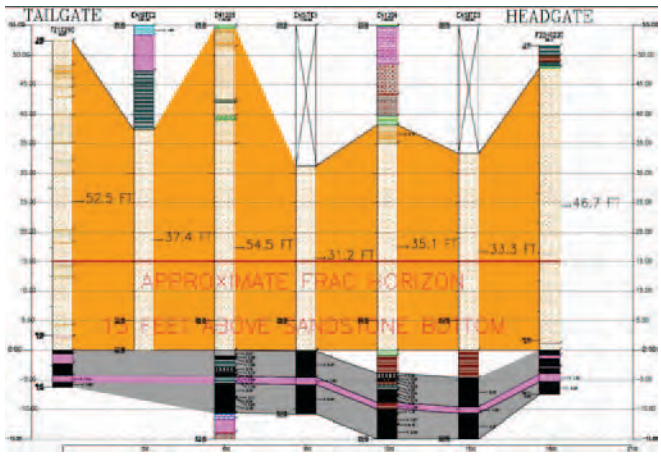



**Figure 4. Sandstone section across Panel 22.**

Based on these data, as well as prior analyses and experiences (Su et. al, 2001 and Su, et. al, 2012) and mining considerations (including shield design), it was concluded that the Panel 22 would benefit from hydraulic fracturing of the thick and

massive sandstone roof. Additionally, the easterly meandering, relative narrow Panel 22 channel was considered well suited for hydraulic fracturing. Past in-situ horizontal stress measurements (Su and Hasenfus, 1995) indicated that, within the Pittsburgh seam overburden, hydraulic fracturing would produce elliptical, horizontal (pancake) fractures. Additionally, based on Panel 21 experiences and fluid volumes, it was assumed that individual holes could induce hydraulic fractures extending 600 ft (183 m) in the E-W direction and 400 ft (122 m) in the N-S direction. With this information, three locations across Panel 22 were selected to hydraulically fracture the sandstone channel in order to promote sandstone caving and improve longwall face conditions through the channel (Figure 2 and ).

## HYDRAULIC FRACTURING OF THE PANEL 22 SANDSTONE CHANNEL

The primary purpose of fracturing the sandstone channel hydraulically is to break the thick sandstone into thinner layers to reduce the interval of periodic weighting at the longwall face. In other words, to prevent the sandstone from cantilevering over the shields and putting abundant pressure at the face that may cause sandstone failure at and ahead of the longwall face. Once the sandstone breaks and caves to form the gob, it would provide effective support to the main roof, which further mitigates the stress at the face.

Su, et al (2012) employed the Flac3D models to analyze the stress distributions at the longwall face. Figure 5 shows the shear stress contour around the longwall face without a frac and with one frac horizon, respectively. Apparently, if no frac horizon is present in the thick sandstone, the maximum shear stress in the sandstone is more than 4,000 psi, while the shear strength of the sandstone is only about 3,000 psi. Consequently, the sandstone above the longwall face isprone to break, resulting in mining heights of 8 ft or greater, which are above the shields' maximum reach of 7.5 ft. Consequently, these face areas effectively become unsupported, resulting in sandstone falling at the face and large roof cavities. On the other hand, with one frac horizon at 15ft above the bottom of the sandstone, the maximum shear stress in the sandstone is reduced to 1,500 - 2,000 psi. Consequently, the sandstone likely would remain stable. Therefore, fracing could theoretically reduce the shear stress at the face and eliminate sandstone failure at and ahead of the longwall face.

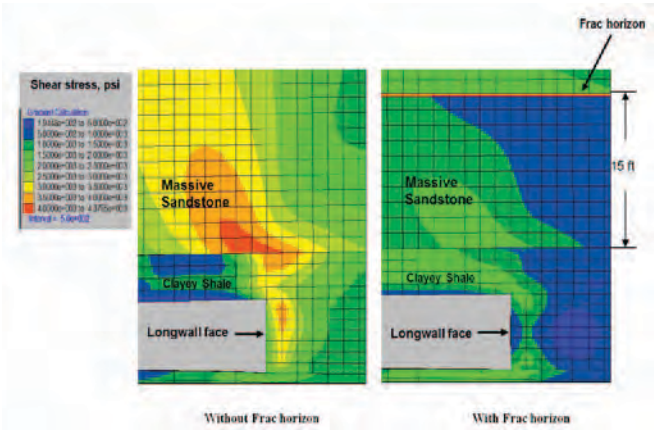



**Figure 5. Comparison of shear stress without/with frac horizon.**

From the experience and evaluation of the Panel 21 fracing program and from the roof geology delineated by underground scope holes, underground coreholes and surface coreholes, mine management decided to drill three frac boreholes 560 ft (171 m) apart along the center axis of the sandstone channel across the 1,500-ft (457-m) wide Panel 22 longwall. The three Panel 22 frac holes were drilled and successfully perforated on August 13, 2012 at an elevation of 601.2~603.2 ft for Hole #1 (located at Panel 22 mid-face area), 701.6~703.6 ft for Hole #2 (located near the Panel22 tailgate) and 601.2~603.2 ft for Hole #3 (located near the Panel 22 headgate) (Figure 2 and 4). For each hole, within the 2 ft perforation interval, there were nine shots along the spiral perforation tool. Each shot was estimated to penetrate about 40 inches into the sandstone formation.

On August 17 and 18, 2012, these three frac holes were successfully water-fraced by Nabors Well Services (formerly Superior Well Services). Water frac was chosen in lieu of the much more expensive nitrogen foam frac (about three times more expensive), although nitrogen foam could enhance fracture propagation. From the analysis and evaluation of the Panel 21 frac program, more water could have been pumped into each frac hole to propagate the individual horizontal pancake fractures to enable them to overlap one another to enhance caving and to relieve face pressure. Therefore, approximately 1,000 barrels, or 42,000 gallons of water, were used for each frac hole in Panel 22. Also, to ensure proper propagation of the horizontal pancake fracture, a pumping rate of 35 barrels per minute was maintained throughout the pumping process for each frac hole. For comparison, the four Panel 21 frac holes were fraced and pumped with an average water volume of 14,000 gallons and at an average pumping rate of 25 barrels per minute.

Figure 6 shows the pressure vs. time and pumping rate vs. time for one of the frac hole. The fracture initiation pressure in this frac hole was 5,930 psi, the Instantaneous ShutIn Pressure (ISIP) was 504 psi and the average pumping rate was 35 barrels per minute. Note that the low ISIP indicates creation and presence of horizontal pancake fracture, since the in situ minimum horizontal stress (horizontal stress in the north-south direction) is about 3,400 psi. Substantial flow back was observed in both Holes #1 and #3, while flow back was observed in Hole #2 immediately after fracing of Hole #1. On August 23, the lubricant used in the fracing operation was observed at 18 ft above the roof line in the underground core hole drilled at Crosscut 30 of the Panel 22 tailgate, which is about 800 feet southwest of the #2 Frac hole. No frac lubricant was observed in the underground core holes drilled along the Panel 22 headgate.

Based on the amount of water used and underground observation, the estimated horizontal pancake fracture ellipsoid in each hole in Panel 21 was about 250 ft (76.2 m) in the E-W direction and 150 ft (45.7 m) in the N-S direction. While, the estimated horizontal pancake fractures ellipsoid in each hole in Panel 22 was about 600 ft (183 m) in the E-W direction and 400 ft (122 m) in the N-S direction. The expanded horizontal pancake fracture ellipsoid was expected to improve the longwall face condition when mining through the sandstone channel.

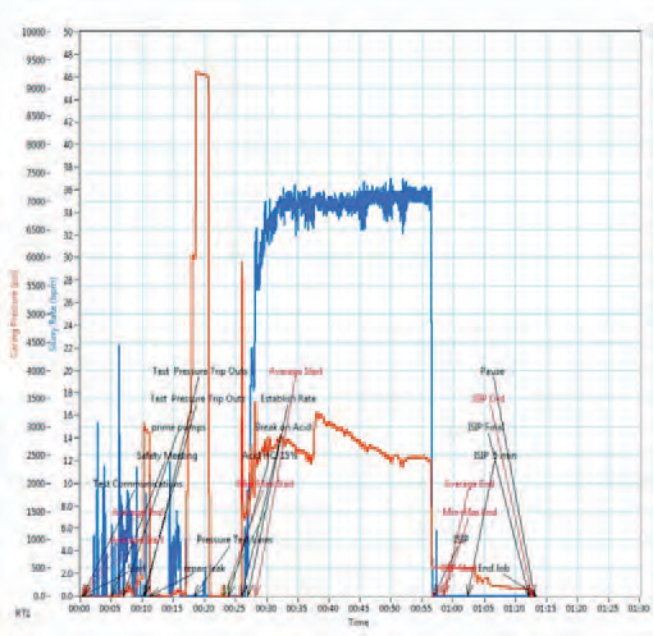


**Figure 6. Pressure and water injection rate vs. time for fracing hole #3.**

## FACE MONITORING AND EVALUATION

To evaluate the effect of enhanced sandstone fracturing program, which was achieved by pumping three times more water into each frac hole within Panel 22, underground face conditions were continuously monitored once the Panel 22 longwall face first encountered the inby edge of the sandstone channel in early January 2013. By the end of February 2013, the longwall face had successfully mined through the sandstone channel.

### Longwall Visual Analysis (LVA) Face Monitoring

As in Panel 21, LVA software was employed to guide mine management and to provide early cavity formation warning to mitigate the formation of roof cavity and sandstone falls.

During the entire monitoring period, LVA had recorded and sent out alerts prior to each occurrence of sandstone failures at the Panel 22 longwall face, which occurred primarily between crosscuts 28 to 6.5 and concentrated within a small area from shields 170 to 220 on the tailgate side. Information from the LVA software was used daily by mine management to successfully guide the longwall face crew to institute double-pull behind the shearer drum to reduce the tip-to-face distance at the critical spots along the longwall face, which helped to mitigate the formation of roof cavities and sandstone falls. Figure 7 shows a real-time monitoring interface for Panel 22.

Figures 8 and 9 are the load cycle maps that show the Time-Weighted Average Pressure (TWAP) at Panels 22 and 21. Weighting events are displayedas horizontal bands of “hot” or red colors. Areas of difficult roof conditions and roof cavities typically display “cool” or blue/green colors. These figures clearly indicate thatmore blue/green colors zones are presentin Panel 21 than in Panel 22, which indicated that more roof potout, or cavity, were present in Panel 21 when mining through the sandstone channel area. Underground observations, which monitored the sandstone

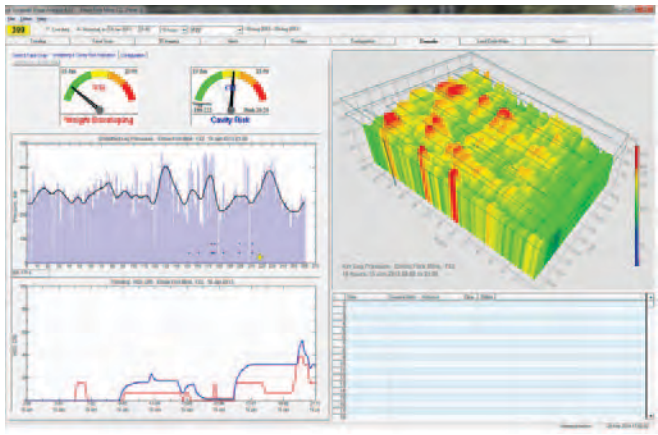


**Figure 7. LVA monitoring interface.**

failure and immediate roof potout, also confirmed the LVA load cycle maps. Note that the blue/green colors area near the headgate and tailgate doesn’t reflect difficult roof conditions or roof cavities. Rather, they reflect the effect of the gate road pillars.

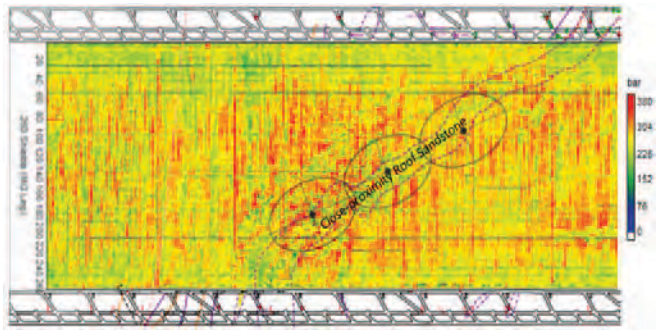



**Figure 8. Time-Weighted Average Pressure (TWAP) for Panel 22.**

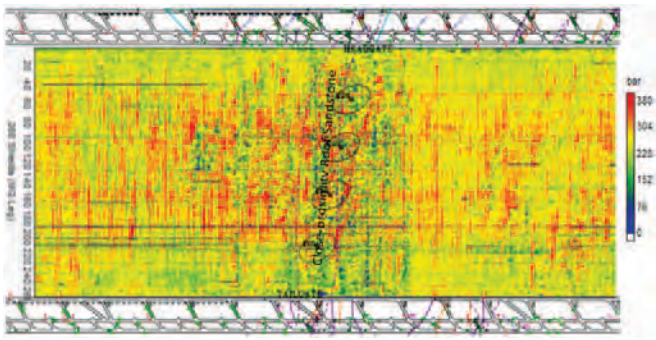



**Figure 9. Time-Weighted Average Pressures (TWAP) for Panel 21.**

### Underground Observations

Daily underground face condition monitoring was initiated at the Panel 22 longwall when it first encountered the inby edge of the sandstone channel in early January 2013. The correlations among the observed face conditions, hydraulic fracturing hole locations and the LVA cavity formation prediction were recorded daily and are shown in the Figure 10. Note that the red shaded areas show

the locations of the large chunk sandstone falls at the face, while the brown shaded areas show the locations of the roof coal potout without sandstone failure. During the underground face monitoring period, occasional minor sandstone failure was observed near the tailgate side between crosscuts 28 to 26. 5, which caused limited delay. After the longwall face passed crosscut 26. 5 on the tailgate side, no sandstone failure were observed at the face except for some minor roof coal and shale potout. Some delays were observed when the sandstone dipped down again near crosscut 23. Sincemore water was pumped into each frac hole during the Panel 22fracing operation to propagate the individual horizontal pancake fractures to enable them to overlap one another, more water was observed at the face when mining through the sandstone channel (Figure 10). Note that only slight water dripping was observed at the face when mining through the sandstone channel in Panel 21.

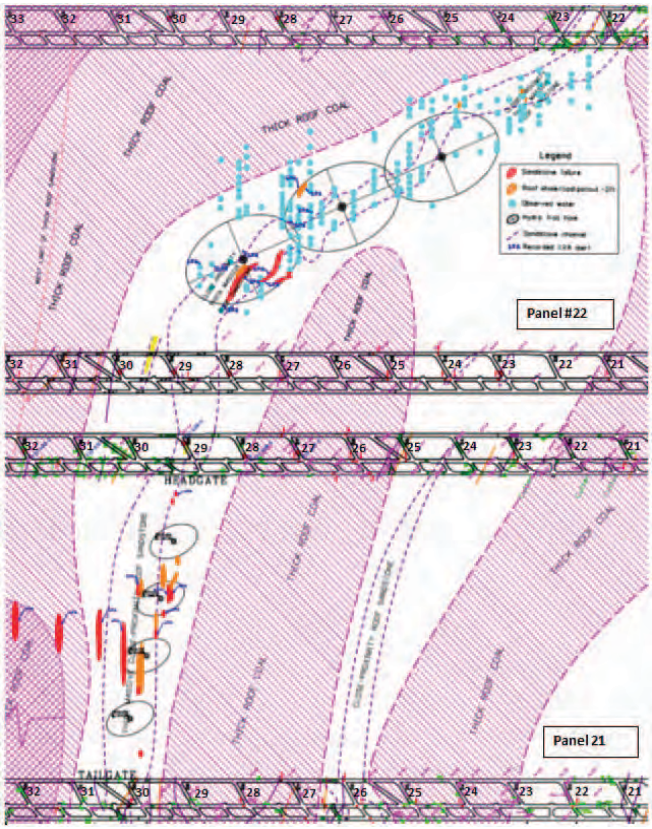



**Figure 10. Correlation among the observed face conditions, the hydraulic fracturing hole locations, and LVA cavity formation prediction in Panels 21 and 22.**

LVA recording and underground observation results reveal a very strong correlation between the LVA cavity index and the observed sandstone falls at the face. The Bucyrus PMCR shields employed in Panel 22 had a lower set load density (5.8 ton/ft$^2$ at 4,500 psi) and were not designed for sandstone geology. Note that several CRI warnings were present between crosscuts 28 to 27 where no sandstone failure was present. This might be a direct result of the shield double-pull activity. Since the LVA sent out a CRI warning message prior to each potential cavity formation, the longwall crew instituted shield double-pull behind the shearer drum and reduced the tip-to-face distance at the spotwhere potential sandstone failure might occur. This has prevented the sandstone failure from occurring and mitigated the potential formation of face cavity.

**Face Advance Rate and Rock Delay**

By the end of February 2013, the Panel 22 longwall face had successfully mined through the sandstone channel, which extended from crosscut 29.5 on the tailgate side to crosscut 22 on the headgate side. Compared to the Panel 21 longwall, the face condition has improved. Since the frac ellipsoids in Panel 21 are smaller than those of Panel 22, a few moderate face potouts and sandstone failures were present at the Panel 21 longwall face where horizontal pancake sandstone fractures were not present, which caused about two to three weeks of face delays between crosscuts 32 to 30. Figures 11 to 14 show the comparison of the longwall face advance rates and rock delays. In Panel 21, the weekly advance rate and the average rock delay were about 11.2 ft/shift and 110 minutes/shift, respectively. For comparison, the Panel 22 longwall kept a fairly good advance rate of about 15.6 ft/shift and an average rock delay of only 27.5 minutes/shift.

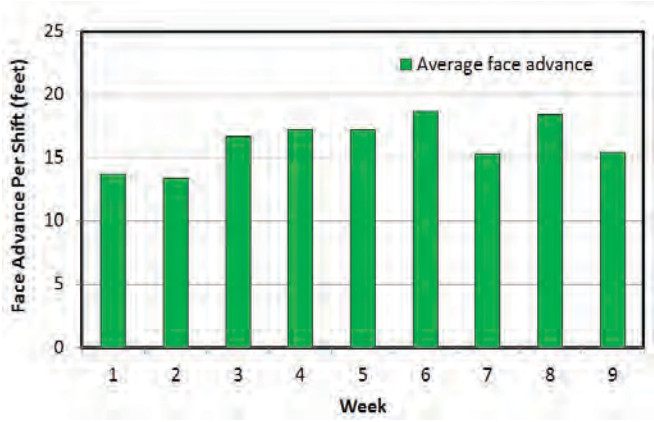



**Figure 11. Panel 22 weekly advance rate.**

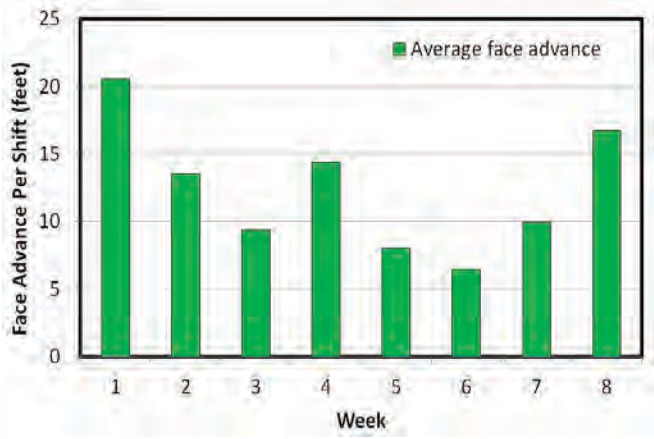



**Figure 12. Panel 21 weekly face advance rate.**

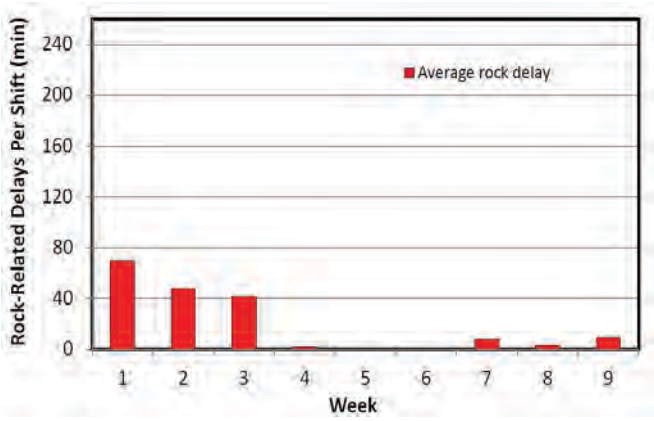



**Figure 13. Panel 22 average weekly rock delays.**

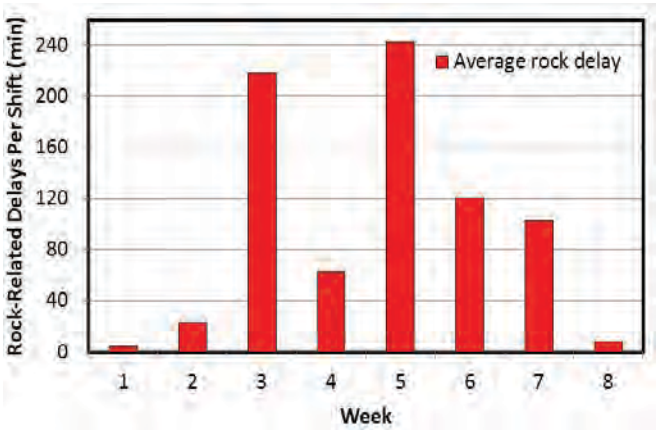



**Figure 14. Panel 21 average weekly rock delays.**

## CONCLUSIONS

Mining experience and roof geology in the current and previous panels indicate that when a thick, massive sandstone channel is present at 5 to 8 ft above the Pittsburgh seam main bench,undesired sandstone overhang is highly probable, unless the face shields employed possess high set load density, i.e., greater than 7.0 tons/ft$^2$. Without properly designed shields, the hydraulic fracturing technique is an effective tool for mitigating the impact of a massive sandstone channel onlongwall face operations. Based on the underground observations, longwall advance rate and rock delay, the hydraulic fracturing program and the LVA software have achieved their intended purposes of improving safety and increasing productivity at Panels21 and 22. Moreover, the modified hydraulic fracturing program used in Panel 22 has enhanced the horizontal pancake fractures, which further mitigate the impact of the sandstone channel. Comparing to Panel 21, less fracing holes were drilled and more water was pumped into the frac holes in Panel 22 during the fracing operation to propagate the individual horizontal pancake fractures to enable them to overlap one another. With the enhanced hydraulic fracturing program, longwall face conditions and advance rate in Panel 22 weresignificantly improved, while rock delaywas largely reduced comparing to those of Panel 21.

## REFERENCES

Hoyer, D. (2011). "Early warning of longwall weighting events and roof cavities using LVA software." In: *Proceedings of the 30th International Conference on Ground Control in Mining*. Morgantown, WV: West Virginia University, 207–213.

Peng, S. S. (2008). Coal Mine Ground Control (3rd edition). Morgantown, WV, 750.

Su, D., Hasenfus, G. (1995). "Regional horizontal stresses and its effect on longwall mining in the northern Appalachian coal field." In: *Proceedings of the 14th International Conference on Ground Control in Mining*. Morgantown, WV: West Virginia University, 39–45.

Su, D.,Hasenfus, G., Stull, L., Lu, J., Van Dyke M., Morgan, S., Kelley, P., Teter, D. (2012). "Impact of a Massive Sandstone Channel on a 1500-Foot (457-Meter) Wide Longwall Face – Mitigation and Evaluation." In: *Proceedings of the 31stInternational Conference on Ground Control in Mining*. Morgantown, WV: West Virginia University.

Su, D., McCaffrey, J., Barletta, L., Thomas, E., Toothman, R. (2001). "Hydraulic fracturing of sandstone and longwall roof control – implementation and evaluation." In: *Proceedings of the 20th International Conference on Ground Control in Mining*. Morgantown, WV: West Virginia University, 1-10.

# The Implementation of Rock Mechanics Into a Multiple Level Limestone Mine

**David A Newman**, President
Appalachian Mining and Engineering, Inc.
Lexington, KY

## ABSTRACT

In the 1950s, an underground limestone mine in the Camp Nelson Formation was developed from an outcrop exposure. The Camp Nelson Limestone met the requirements for DOT stone and aggregate. The mine ownership changed several times, which resulted in distinct mine designs in Level 1. Based upon the production requirements and an attempt to maximize limestone recovery from a single level, a variety of pillar dimensions and three mining heights (28 feet, 68 feet and 83 feet) were developed. This was sufficient prior to reaching the mineable extent of Level 1.

Level 2 introduced previously unknown ground control challenges. These included:

- Pillar spalling and a significant back fall on the Level 1 - Level 2 decline;
- Laminated immediate back and the need to bolt the back on Level 2;
- Delamination of the back adjacent to the Level 1 - Level 2 decline resulting in bolt shearing, and floor heave in isolated areas of Level 2;
- Multiple level interaction, the need to design pillars based upon numerical modeling as columnization between Levels is infeasible: and
- Water inflow as the mine approached a river.

To meet the challenges, a testing program to determine rock strength and physical properties was implemented along with numerical (LAMODEL and FEM) modeling, and borescope inspections of the immediate back.

The efforts to implement rock mechanics were re-focused as Level 2 approached its mineable limit and the initial attempt to drive a decline to Level 3 was unsuccessful. A second decline site was selected based on interburden stability, a consistent shale parting for the Level 3 back horizon, results from numerical models of the immediate back and multiple level interactions, and the projected low water inflow. The mine is operating on Levels 2 and 3 with long-term planning and ground monitoring for Level 3.

## BACKGROUND AND HISTORY

An underground limestone mine in the Camp Nelson Limestone was developed from the outcrop in the 1950s. The reserve is bounded on three sides by a river and a well-known fault system on the fourth side. The aggregate product is suitable for DOT use and found a ready market in a major city, several smaller cities and the network of interstate highways.

## LEVEL 1

The majority of Level 1 was developed on 100-ft centers with 50-ft-wide headers and crosscuts with a 28-ft mining height. The mine layout, as shown in Figure 1, consists of an east-west main and four north-south submains, from which rooms were developed. The east-west main was denoted as the W-1 header. Parallel headers to the north of the east-west main are denoted as W-2, W-3, etc., while those headers to the south are referred to as A, B, and C, etc. Similarly, the north headers to the west of the east-west main are denoted N-1 through N-41 and those to the south are S-1 through S-41. This nomenclature defines a series of headers and crosscuts that are common in all three levels. To the author's knowledge, there were no strength or physical property tests conducted on the Camp Nelson Limestone at this time. Mine design was based solely upon the mine superintendent's observation of ground conditions.

Pillar centers in the rooms and the layout of the rooms vary as a reflection of changes in mine ownership. There are a wide variety of square and rectangular pillar geometries that do not conform to the 50-ft x 50-ft pillars and 50-ft-wide opening. Back and pillar conditions are excellent; therefore, with the exception of spot bolting at the portal and in isolated areas, Level 1 was not roof bolted. Level 1 was naturally ventilated as multiple "punch outs" were driven for air.

### Level 1 - Ground Conditions

When the physical boundaries of Level 1 were reached, the mine management decided to take floor shots for additional stone. The initial round of 40-ft floor shots produced an area of 68-ft mining height (shown in brown) everywhere with the exception of the area adjacent to the portal (shown in black). This 28-ft area is used for

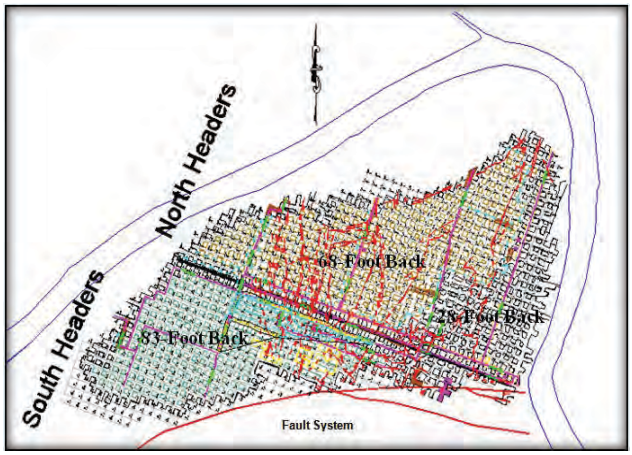



**Figure 1. Layout of Level.**

underground shops, equipment storage and, at one time, a concrete block plant. The plan was to develop a decline to Level 2 when an interstate expansion placed a demand for aggregate that could not be met while driving the decline to Level 2. Consequently, a second round of floor shots, this time 15-ft deep, were developed in the southwest area of the quarry, producing an 83-ft mining height (shown in cyan). The pillar dimensions range from +/- 40 ft to +/- 60 ft wide, leaving a width-to-height ratio ranging between 0.48 and 0.72. The slender pillars began to spall and the back conditions deteriorated, resulting in back falls. A contractor was brought in to install 7-ft fully grouted bolts from a man basket using a jackleg drill. This was revised to 11-ft-long torque-tension bolts based upon borescope inspections of the immediate and main back. The intent was to prolong recovery of floor shots in order to fulfill the stone orders while concurrently developing twin declines to Level 2.

## LEVEL 2

As the remainder of the Level 1 floor reserves were being recovered, twin open cut declines were developed from Level 1 to Level 2. The declines were driven from opposing sides of Level 1 (from N-14 on the east and N-32 on the west) to a common center at N-23. Empty haul trucks would enter from the west and loaded trucks would exit from the east side, which was closest to the primary crusher. The decision to drive an open cut as opposed to a slope was based on the premise that more saleable stone would be created in the open cut, and back support would not be required above the decline because of the historically excellent Level 1back. The Level 2 back horizon was selected primarily to provide a minimum interburden of 70-ft to 90-ft between the 68-ft mining height on Level 1, and secondarily to maintain a 10% grade for truck haulage. As the east and west declines approached the 10% grade, the focus intensified to find a suitable back horizon. The initial observation was that the Camp Nelson at the base of the decline was laminated and likely not to be self-supporting, as is Level 1. This marked the first application of rock mechanics to the mine design. Tensile strength and point load index tests were conducted on prospective ledges to determine which ledge would provide the best back conditions.

### Level 2 - Ground Conditions

A back horizon was identified based upon the tensile strength data and the stability of a composite beam created using 6-ft-long fully grouted resin bolts spaced on 6-ft centers. Although an attempt was made to columnize the pillars on Level 2 with those on Level 1, it is complicated by variable pillar centers on Level 1 and by the fact that mine surveying on Level 1 is incomplete. A standard of 100-ft centers with 50-ft mine headers and crosscuts was chosen to replicate the centers on Level 1.

Ground control problems on Level 2 began with floor heave in the W-2 through W-5 headers between crosscuts N-20 and N-7. The floor heave was concentrated in areas where the pillars on Level 1 (shown in black on Figure 2) do not overlie the Level 2 pillars (shown in red). In Figure 2, the east side of the Level 1-Level 2 decline is shown in brown, with the bottom area and access to Level 2 located at N-22 to N-24. The floor heave ranged between 2.8 ft and 4.0 ft near the W-2 to W-4 headers and the N-20 to N-11crosscuts. Uniaxial compressive strength tests were conducted on core samples obtained from three in-mine exploration drill holes. The holes were drilled from Level 1 through what would become Level 3. The intent was to enable planning of the eventual development of a third level.

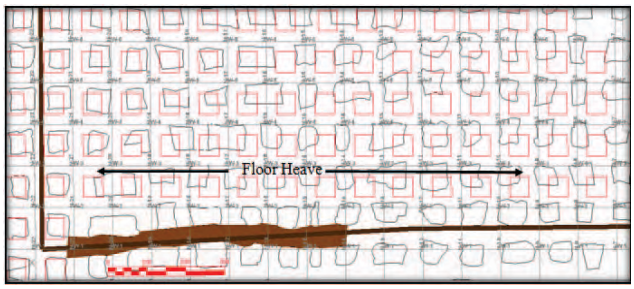



**Figure 2. Overlay of pillars from Level 1 (black) with those from Level 2 (red).**

An examination of the exploration holes clearly showed that the initial 20 ft of Level 2 floor consisted of a soft, weak limestone. The floor heave resulted from a combination of the soft limestone layer, increased overburden thickness on Level 2, and the pillars on Level 2 being offset and not columnized with the overlying Level 1 pillars. The extent of the floor heave was controlled by the area where the pillars were not columnized.

Water inflow developed on the outer perimeter of Level 2 where the mine workings were extended past the Camp Nelson outcrop of Level 1. At this point, Level 2 began encroaching on the river's flood plain. Once mining extended past the Level 1 perimeter, the upper portion of the overburden became a saturated unconsolidated material. Approximately 30,000 gallons/day entered the northern-most headers.

As the extent of mining on Level 2 was reached, mine management decided to develop a third level as opposed to taking floor shots on Level 2. Level 3 is the future of the quarry; the reserves on Level 2 were reaching the physical barriers, those being the river and the fault system. An initial set of three declines were driven from N-21, N-22, and N-23 beginning at W-10. A combination of water inflow and poor back conditions

terminated this access to Level 3. The only alternative was to drive twin declines from within core of the mine. Mine management recognized that there was limited time and opportunity to develop the twin declines between Level 2 and Level 3. Therefore, the mine was focused on defining the Camp Nelson geology, the design of the declines, and on Level 3, a clear understanding of rock mechanics constraints.

## LEVEL 3 GEOLOGY AND DESIGN

The Level 3 back horizon, a 2-in-thick shale parting, was identified in all four of the exploration boreholes. There are two advantages to using the shale parting for the Level 3 back. As can be seen in Figure 3, the shale parting is the only consistent discontinuity against which Level 3 header shots will easily separate from the immediate back. The location of the shale parting is 69 ft to 71ft below the floor of the 68-ft back on Level 2, which aids in reducing multiple level interaction.




**Figure 3. Shale parting identified as the most suitable back horizon for Level 3.**

The twin declines to Level 3 were developed in the center of the mine in W-6 and W-8 from N-19 to N-12, as shown in Figure 4. Similar to the Level 1-Level 2 decline, the twin Level 2-Level 3 declines were developed as open cuts. The Level 2 back was re-bolted and meshed in anticipation of a loss of access to the Level 2 back once the twin declines were shot. The highwall between Level 2 and Level 3 was meshed to allow "loose" material to be contained between the highwall and the mesh.

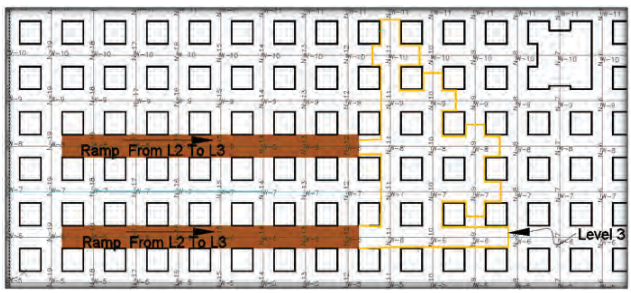



**Figure 4. Twin declines from Level 2 to Level 3 and extent of level development.**

Once the declines reached Level 3, an alternative back horizon, a stylolite located 29 in above the shale parting, was observed in the exposed highwall. The two alternative back horizons are illustrated in Figure 5. An investigation was conducted regarding the most favorable back horizon. A series of rock strength and physical property tests, summarized in Table 1 and Table 2, were conducted on rock samples from the immediate back horizons. The alternative back horizons were evaluated using finite element and assuming 6-ft-long fully grouted roof bolts spaced on 7-ft centers. In Figure 6, the fractures as observed in the drill core are shown in green. The finding of the FEM analysis, as shown in Figure 6 and Figure 7, is that the stylolite back horizon provides more stable back conditions. This conclusion regarding the stability of the stylolite back horizon has proven to be accurate in the area of Level 3 (see Figure 4) developed to date. The area is stable with a flat back.

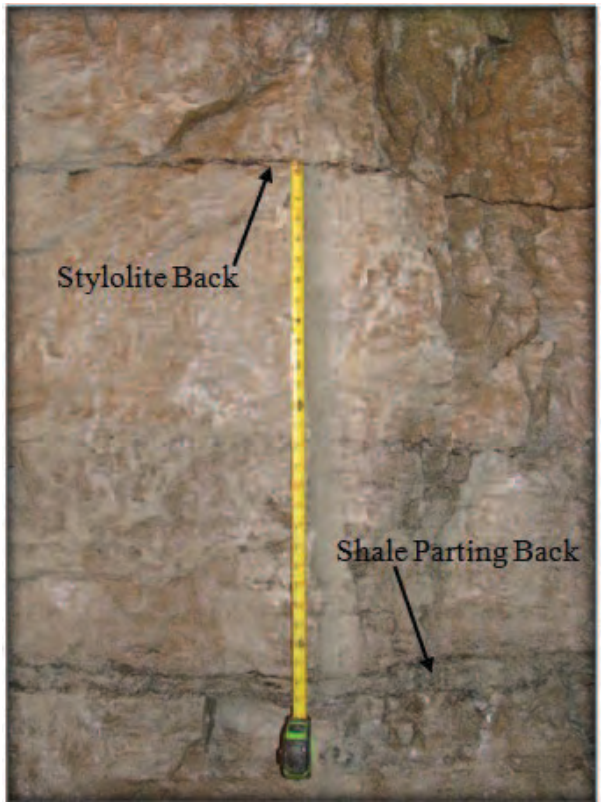



**Figure 5. Two alternative back horizons.**

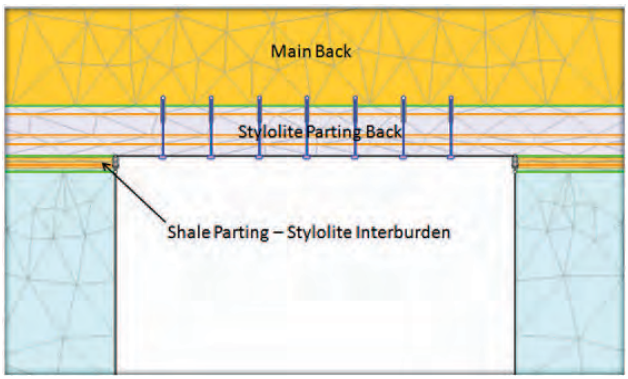



**Figure 6. FEM of the stylolite back.**

**Table 1. Uniaxial compressive strength results from Level 3.**

| Level 3 Back Alternatives – Camp Nelson Limestone<br>Uniaxial Compressive Strength Test Results | | | | | | | | | | |
|---|---|---|---|---|---|---|---|---|---|---|
| | | Test Interval | | | | | | | | |
| Bore-hole No. | Specimen No. | Top (feet) | Bottom (feet) | Specimen Length (in.) | Specimen Diameter (in.) | Length/ Diameter Ratio | Failure Load (lbs.) | Uniaxial Comp. Str ($lb/in^2$) | Tangent Modulus ($lb/in^2$) | Tangent Poisson Ratio (in/ in) |
| Main Back | | | | | | | | | | |
| Hole 1 | UC-5 | 61.84 | 62.31 | 4.691 | 1.874 | 2.50 | 44,200 | 16,025 | 8.27E+06 | 0.20 |
| Hole 2 | UC-8 | 61.57 | 62.04 | 4.679 | 1.879 | 2.49 | 38,054 | 13,723 | 9.10E+06 | 0.19 |
| Styolite Back | | | | | | | | | | |
| Hole 1 | UC-3 | 67.94 | 68.41 | 4.694 | 1.850 | 2.54 | 33,009 | 12,280 | 7.07E+-6 | 0.15 |
| Hole 1 | UC-4 | 64.03 | 64.50 | 4.652 | 1.874 | 2.48 | 47,681 | 17,287 | 7.77E+06 | 0.23 |
| Hole 2 | UC-7 | 66.02 | 66.46 | 4.353 | 1.871 | 2.33 | 15,970 | 5,809 | 5.87E+06 | 0.12 |
| Hole 2 | UC-10 | 66.96 | 67.40 | 4.391 | 1.873 | 2.34 | 39,438 | 14,314 | 9.27E+06 | 0.23 |
| Shale Parting Back | | | | | | | | | | |
| Hole 1 | UC-1 | 69.04 | 69.51 | 4.714 | 1.873 | 2.52 | 25,252 | 9,165 | 5.36E+06 | 0.07 |
| Hole 1 | UC-2 | 69.97 | 70.36 | 3.899 | 1.873 | 2.08 | 16,805 | 6,099 | 4.84E+06 | 0.15 |
| Hole 2 | UC-6 | 69.88 | 70.35 | 4.711 | 1.867 | 2.52 | 15,190 | 5,549 | 1.02E+07 | 0.45 |
| Hole 2 | UC-9 | 68.49 | 68.90 | 4.146 | 1.876 | 2.21 | 49,168 | 17,788 | 8.30E+06 | 0.19 |
| Statistical Analysis | | | | | | | | | | |
| | | | | | Main Back | Average | 14,874 | 8.69E+06 | 0.20 | |
| | | | | | | Std. Deviation | 1,627 | 5.91E+05 | 0.01 | |
| | | | | | Styolite Back | Average | 12,422 | 7.49E+06 | 0.18 | |
| | | | | | | Std. Deviation | 4,865 | 1.42E+06 | 0.06 | |
| | | | | | Shale Parting Back | Average | 9,650 | 7.17E+06 | 0.21 | |
| | | | | | | Std. Deviation | 5,654 | 2.53E+06 | 0.17 | |

A LAMODEL analysis was the next phase of integrating rock mechanics into the engineering design of Level 3. The intent of the LAMODEL analysis is to avoid high stress multiple level interaction where possible and to anticipate when columnization of pillars is not possible. A series of LAMODELs were developed that integrated the pillar geometries of all three levels with the three different mining heights (28 ft, 68 ft and 83 ft) on Level 2. Figure 8 depicts the mining geometry near the Level 2-Level 3 declines and within the mined perimeter of Level 3. The Level 1 pillars are depicted in gray, those on Level 2 are shown in green, and the Level 3 development is shown in blue.

Pillar stability on Level 3 was not the primary concern, because Level 3 was under relatively light overburden, 300 ft to 400 ft, and the safety factor of the 50-ft x 50-ft pillars exceeded 2.0. This is shown in the total stress contours in Figure 9. The boundaries in Figure 9 and 10 depict the interfaces between the different mining heights on Level 2. Multiple seam interaction is the most significant concern, as this can initiate floor heave when pillars are not columnized, in addition to affecting the immediate back stability. Although the pillars on Levels 2 and 3 are shown as columnized, this will be confirmed by future surveying.

The areas of concern in Figure 10 are the transitions between negative (tensile) and positive (compressive) stress. These areas may initiate bending in the immediate and main back. At present, Level 3 is driving into a transition zone in the north. Borescope inspection holes will be drilled in every intersection with the option of installing telltale monitors to indicate back movement and bed separation.

## FINDINGS AND CONCLUSIONS

During the past 60 years, the mine has transformed from a single level, naturally ventilated drift mine to a multiple level operation with internal shafts and fans for ventilation. The integration of routine mine surveying and rock mechanics was slow given the history of Level 1 and its long-term stability without the installation of supplementary support. Instability on Level 1 was limited to the slender pillars within the 83-ft back area. This changed with the development of Level 2. Laminated immediate back, the inability to columnize pillars between Levels 1 and 2, floor heave on Level 2, back falls and water inflow to Level 2 necessitated a focus on quantitative analysis of back, pillar and floor stability.

The success of remediating ground control problems on Level 2 reinforced the need to examine the ground conditions on Level 3 prior to reaching the bottom of the twin declines. Consequently, the stylolite back horizon was selected before the declines reached Level 3. The availability of site-specific rock mechanics data made the FEM analysis and ultimate selection of the Level 3 back part of the routine mine design. The success of the back selection prompted mine management to examine the magnitude and distribution of total (overburden + multiple level) and multiple level stresses using LAMODEL. This enabled the ground control concerns for the remainder of Level 3 to be managed by anticipation.

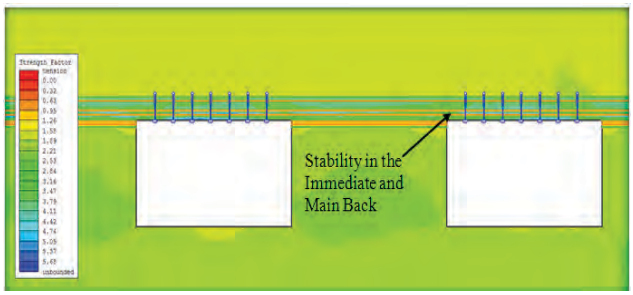



**Figure 7. FEM analysis of the stylolite back horizon.**

**Table 2. Tensile strength results from Level 3.**

| Level 3 Back Alternatives – Camp Nelson Limestone<br>Brazilian Indirect Tensile Strength Test Results | | | | | | | | |
|---|---|---|---|---|---|---|---|---|
| | | Test Interval | | | | | | |
| Borehole No. | Specimen No. | Top (feet) | Bottom (feet) | Specimen Length (in.) | Specimen Diameter (in.) | Length/ Diameter Ratio | Failure Load (lbs.) | Tensile Strength (lb/ in$^2$) |
| Main Back | | | | | | | | |
| Hole 2 | B-13 | 61.97 | 62.07 | 0.990 | 1.879 | 0.53 | 3,856 | 1,320 |
| Hole 2 | B-14 | 62.07 | 62.17 | 0.966 | 1.879 | 0.51 | 1,288 | 452 |
| Hole 1 | B-7 | 62.31 | 62.40 | 0.872 | 1.874 | 0.47 | 2,388 | 930 |
| Hole 1 | B-8 | 62.40 | 62.49 | 0.915 | 1.874 | 0.49 | 4,558 | 1,692 |
| Styolite Back | | | | | | | | |
| Hole 1 | B-5 | 64.50 | 64.59 | 0.931 | 1.874 | 0.50 | 2,687 | 980 |
| Hole 1 | B-6 | 64.59 | 64.69 | 0.950 | 1.874 | 0.51 | 3,577 | 1,279 |
| Hole 2 | B-12 | 65.82 | 65.92 | 0.998 | 1.871 | 0.53 | 4,907 | 1,673 |
| Hole 2 | B-11 | 65.92 | 66.02 | 0.975 | 1.871 | 0.52 | 2,504 | 874 |
| Hole 2 | B-15 | 67.34 | 67.43 | 0.865 | 1.873 | 0.46 | 769 | 302 |
| Hole 2 | B-16 | 67.43 | 67.54 | 1.059 | 1.873 | 0.57 | 1,407 | 452 |
| Hole 1 | B-4 | 67.74 | 67.84 | 1.003 | 1.875 | 0.53 | 4,954 | 1,677 |
| Hole 1 | B-3 | 67.84 | 67.93 | 0.921 | 1.875 | 0.49 | 3,720 | 1,371 |
| Shale Parting Back | | | | | | | | |
| Hole 2 | B-17 | 68.30 | 68.41 | 1.059 | 1.876 | 0.56 | 313 | 100 |
| Hole 2 | B-18 | 68.41 | 68.52 | 1.050 | 1.876 | 0.56 | 602 | 195 |
| Hole 1 | B-2 | 68.71 | 68.82 | 1.056 | 1.873 | 0.56 | 1,909 | 614 |
| Hole 1 | B-1 | 68.82 | 68.92 | 1.039 | 1.873 | 0.55 | 3,248 | 1,063 |
| Hole 2 | B-10 | 69.67 | 69.77 | 1.014 | 1.867 | 0.54 | 4,404 | 1,481 |
| Hole 2 | B-9 | 69.77 | 69.88 | 1.101 | 1.867 | 0.59 | 3,368 | 1,043 |
| Statistical Analysis | | | | | | | | |
| | | | | | Main Back | Average | 3,023 | 1,098 |
| | | | | | | Std. Deviation | 1,468 | 532 |
| | | | | | Styolite Back | Average | 3,066 | 1,076 |
| | | | | | | Std. Deviation | 1,518 | 519 |
| | | | | | Shale Parting Back | Average | 2,307 | 749 |
| | | | | | | Std. Deviation | 1,640 | 542 |

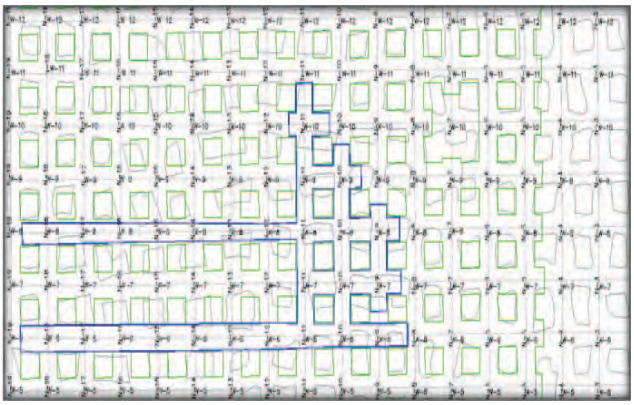


**Figure 8. Layout of multiple level LAMODEL.**

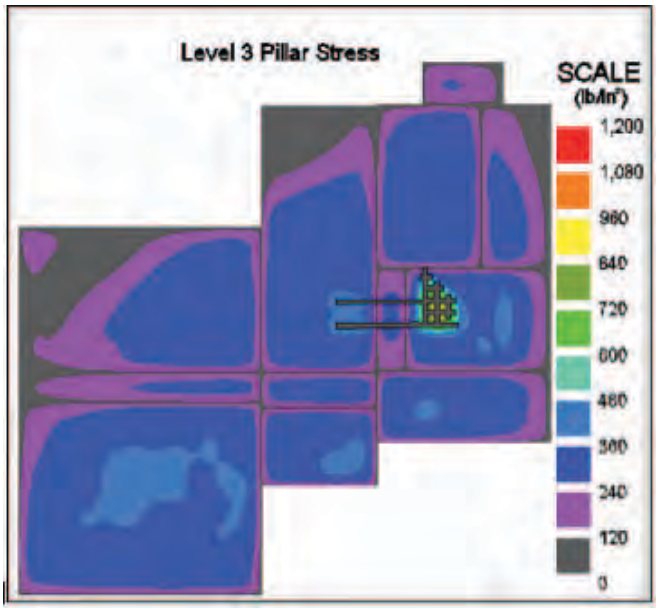



**Figure 9. LAMODEL output for Level 3 pillar stress.**

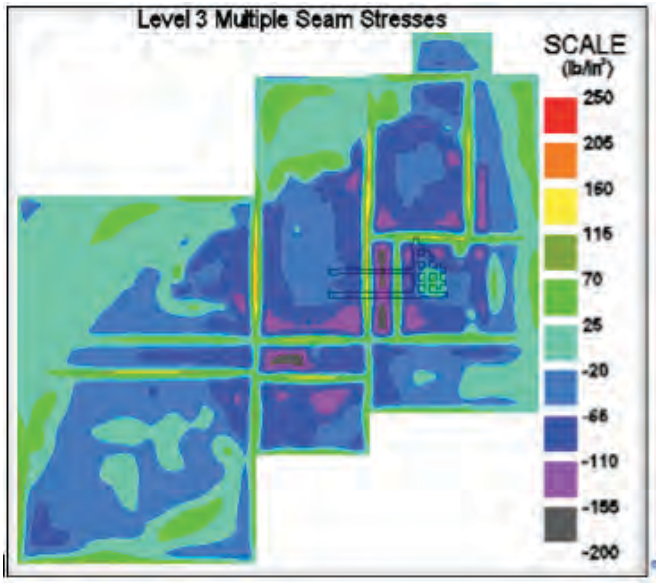



**Figure 10. Multiple level interaction projected on Level 3.**

# Multi–Seam Mining Over Old Workings with Small Pillars - A Case Study

**Peter Zhang**, Senior Geotechnical Engineer
**Scott Peterson**, Senior Director Geology
Operational Performance Group
Alpha Natural Resources, Inc.
Waynesburg, PA

**Joe Pugh**, VP Engineering, Methods and Standards
Operational Performance Group
Alpha Natural Resources, Inc.
Charleston, WV

**Patrick Bucks**, Mining Engineer
**Chris Vass**, Chief Engineer
Brooks Run North Region
Alpha Natural Resources, Inc.
Sutton, WV

## ABSTRACT

Room and pillar mining under shallow depth is usually conducted with a high extraction ratio, which leaves small pillars with a low safety factor in some old workings in abandoned mines. Pillar sloughage, squeezing or even collapse may have occurred in those old workings with small pillars, either at the time of mining or later. The conditions of the pillars in abandoned mines can affect mining above them. Subsidence fractures and abutment pressure are indications of multi-seam interaction caused by squeezing or collapse of small pillars. To mine over areas with potentially unstable small pillars, the panel layout in the upper seam should be such that multi-seam interaction can be minimized and proper roof and rib support should be installed in the influence zones. This case study presents an example of multi-seam mining above small pillars under a shallow depth of cover. Though the interburden is relatively thick and competent, interaction is still present over the influence zones. Pillar stability and multi-seam interaction analysis, numerical modeling and in-situ monitoring are presented to demonstrate how the upper seam can be mined safely over the small pillars.

## INTRODUCTION

Room and pillar mining under shallow depth is usually conducted with a high extraction ratio. Small pillars with low safety factors were left in some abandoned mines in the past. Pillar sloughage, squeezing or even collapse may have occurred in the area with small pillars, either at the time of mining or later. The conditions of those old small pillars have a significant impact on upper-seam mining. Subsidence fractures and abutment pressure are indications of multi-seam interaction caused by squeezing or collapse of small pillars. To mine over areas with potentially unstable small pillars, pillar sizes and panel layouts in the upper seam should be designed to minimize the influence of multi-seam interaction, and proper roof and rib support should be installed in the influence zone.

Smaller pillars can be referred to as those with a width-to-height ratio of less than 3. Stability of these small pillars is largely influenced by the safety factor, width-to-height ratio, panel size, and time elapsed after mining. When the safety factor is small, small pillars have a great possibility of failure, and this could be either by squeezing or collapse.

Pillars tend to deteriorate over time and fail when their bearing capacity is exceeded by overburden load. Though pillar failure can be progressive, it tends to occur quickly after mining (van der Merwe, 2003). In abandoned mines, pillar failures over time could be associated with time-dependent rib sloughage as a result of weathering or floor softening. Ribs are often susceptible to weathering when clay parting is present within the mining height. Rib sloughage would increase the stress in the pillars with the reduction of actual pillar dimensions, eventually reducing the safety factor of the pillars. Claystone floor could become soft from mine flooding, creating abutment pressure over the adjacent pillars with relatively competent floor. As the actual conditions of pillar and roof/floor in abandoned mines are often difficult to know, old maps and core holes are primarily the only information available to judge stability of small pillars. When mining above the failed pillars, additional precautions should be taken to prevent roof and rib failures.

This paper presents a case with overmining above small pillars in old workings. Figure 1 shows the layout in both seams (the shaded area shows the old workings in the lower seam). Current mining is in the Upper Freeport seam, with only development mining under a depth of cover of 200 feet maximum. The entry width is about 20ft and the entry height is about 7 ft. Panels are laid out with a 7-10 entry system and 30 × 40 ft pillars. The immediate roof is shale, supported by four 6 ft fully-grouted torque tension bolts on four-foot spacing as the primary support, and two 10 ft cable bolts on eight-foot spacing as supplementary support as needed.

The lower seam was mined by the room and pillarmethod in the Lower Kittanning seam in the 1980s. The interburden thickness between the two seams is about 130 ft. Figure 2 shows a typical geologic column of the interburden. The interburden consists of bedded shale and sandstone, which accounts for about 40%. The coal in the Lower Kittanning seam is relatively strong without partings. The immediate roof and floor is shale. The entry width in the lower seam is 20 ft, and the mining height 8 ft. Figure 3 shows part of the mining layout in the lower seam with various pillar sizes. Some pillars were as small as 20 ft × 20 ft, while some other

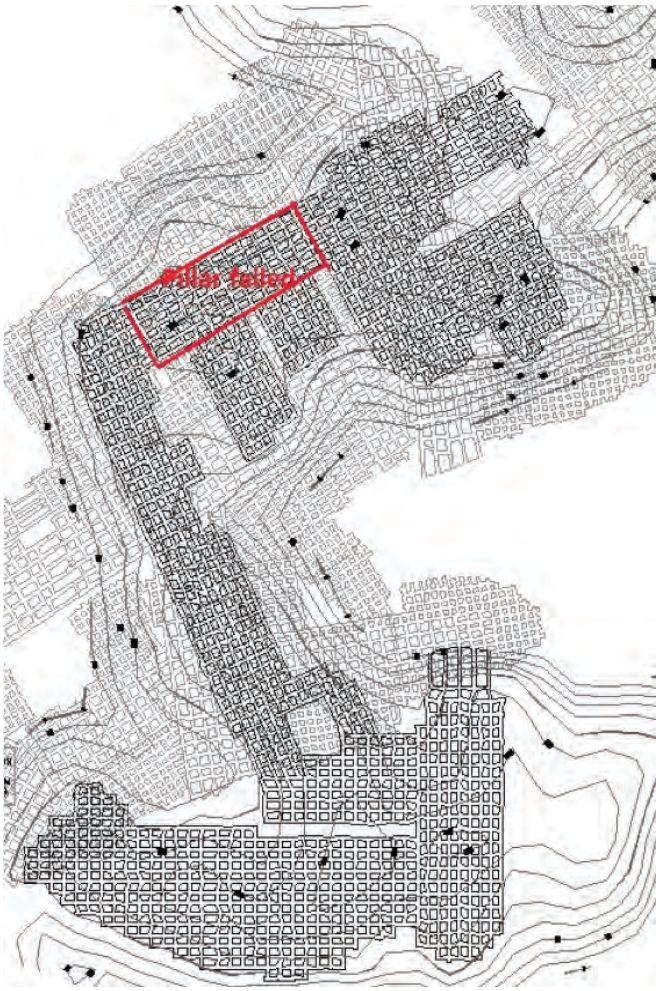



**Figure 1. Layout in the upper and lower seams.**

pillars were as large as 40 ft × 50 ft. Secondary mining with 16 ft pillar splitting was conducted on some of the 40 ft× 40 ft pillars. Different sizes of barrier pillars were left between the panels.

With 130 ft of interburden, it seems that multi-seam interaction is minor and the upper seam is mineable even if the small pillars had already failed. However, the focus of this study is not the mineability of the upper seam, but the stability of small pillars in the lower seam and its impact on overmining as well as proper roof/rib support in the influence zone.

## STABILITY ANALYSIS OF SMALL PILLARS

The overburden depth in the lower seam ranges from 150 ft to 330 ft. Typical small pillars are 20 ft × 20 ft and 40 ft × 40 ft with pillar splitting of 16 ft, cut at the center. Other large-sized pillars and different sized barrier pillars are also used in the abandoned mine. The ARMPS safety factors of the typical small pillars in the lower seam are calculated and shown in Figure 4. It can be seen that the 20 ft × 20 ft pillars have a safety factor of less than 1.0 when the overburden depth is greater than 300 ft, and the 40 ft× 40 ft pillars with splitting have the same safety factor as the 20 ft × 20 ft pillars. The safety factors of pillars with different sizes are also calculated and shown in Figure 3. It can be seen that all of the 20 ft × 20 ft pillars have a safety factor close to 1.0. According to

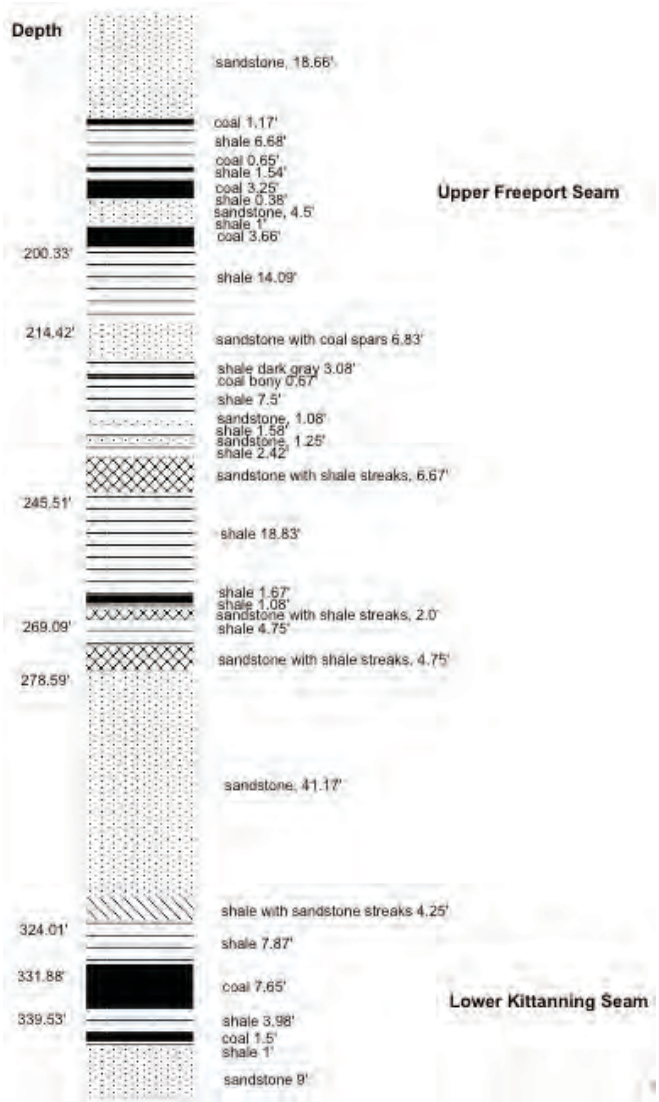



**Figure 2. Geological column of the interburden strata.**




**Figure 3. Pillar dimensions and layout in the Lower Kittanning seam.**

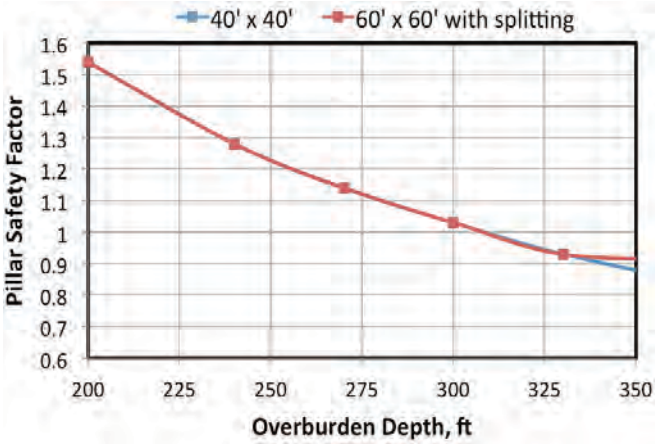



**Figure 4. Safety factors of small pillars udner different overburden depth in the Lower Kittanning seam.**

ARMPS, the pillars with a safety factor of 1.0 means that they have 50% of the possibility of either stability or instability, while the pillars with a safety factor of less than 1.0 are more likely to fail.

Actual occurrences of pillar failure are also associated with width-to-height ratio. Mark (1999) studied the failure cases from ARMPS database and concluded that most massive pillar collapses or squeezes occurred when the width-to-height ratio was less than 3 and the safety factor was less than 1.5 (Figure 5). In this case, the small and split pillars have a width-to-height ratio of 2.5 and 1.5, respectively. It seems that these pillars could already fail during or shortly after mining. However, pillar stability is also affected by strength of the coal and overburden, the roof/floor, and the existence of large pillars in the surrounding area. The strength of the Lower Kittanning seam is fairly strong, and the competent interburden strata could also contribute to the stability of small pillars surrounded by barriers or large pillars. Therefore, it is hard to say that all small pillars with safety factors less than 1.5 have failed. Three possibilities could exist for the condition of the small pillars in the lower seam. In the best case, all the pillars in the lower seam are still stable, while in the worst case, some small pillars with safety factor less than 1.5 could have squeezed or collapsed. Another possible scenario is that some pillars are stable in certain areas while other pillars have failed in those locations where small pillars with low safety factors were left over a large area. Although the upper seam is mineable, precautions for roof and rib support should be taken over the multi-seam influence zone where small pillars have either squeezed or collapsed.

## NUMERICAL MODELING OF STRESS TRANSFER IN THE INTERBURDEN

Mining in the upper seam can create stress concentration in the pillars, and transfer the stress through interburden to the pillars in the lower seam. Some small pillars in the lower seam may be close to a critical state of stability. This additional stress may cause pillar failure in the lower seam during active mining in the upper seam, which would have an impact on the roof stability of the upper seam. Therefore, the mining layout in the upper seam should be designed to minimize disturbance to the lower seam.

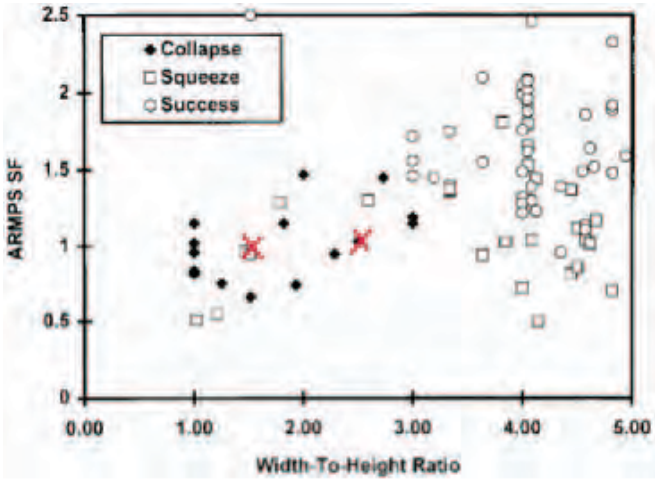



**Figure 5. Pillar failures vs safety factor for width-to-height ratio (Mark, 1999).**

To understand the stress transfer with upper seam mining, FLAC 3-D numerical software is used to model the stress distribution with the mining of both seams. The model is set up based on the geological information from Figure 1. Figure 6 shows the set-up of the 3-D model and Table 1 shows the rock properties used in the model. The lower seam is mined with 20 ft× 20 ft pillars, while the upper seam is mined by an eight-entry system with 30 ft× 40 ft pillars in the model. The model simulates two steps of mining; the lower seam is mined in the first step, and the upperseam mined in the second step. The distribution and transfer of vertical stresses are obtainedfrom the model.

Figure 7 shows the vertical stress distribution in the interburden. The vertical stress concentrates in the pillars and the barrier pillars, but the stress concentration zones are restricted within 30-40ft from the coal seams. With 130 ft of interburden, there is generally no significant interaction between two seams if no pillar failure occurs in the lower seam. Figure 8 shows the magnitude of the vertical stress on the pillars in the upper seam across the panel.

Figure 9 shows the magnitude of the vertical stress in the lower seam. The maximum vertical stress is about 1,400-1,580 psi. The peak vertical stress under the barrier pillars of the upper seam is about 50-80 psi higher than that under the panel of the upper seam, mainly due to the pressure arch effect. It can be inferred that upper seam mining using the pillar size in the model could cause a vertical stress change of 25-40 psi in the small pillars in the lower seam. As this change only accounts for about 3% of the vertical stress in the small pillars, their stability would notbe affected.

Based on modeling of stress transfer to the lower seam as a result of upper seam mining, it can be concluded that with a large interburden thickness, the impact of upper seam mining on the stability of pillars in the lower seam is minimal. However, considering the uncertain stability of the small pillars with low safety factors in the lower seam, the pillar sizes in the upper seam should be designed as though the small pillars have already failed. When the interburden thickness is large (> 3-5 times entry width), superimposition of pillars and panels is not necessary, and also impractical if the panel layout in the lower seam is irregular.

**Table 1. Rock properties used in the model.**

| Rock Type | Young's Modulus ($\times 10^6$ psi) | Poisson's Ratio | UCS (psi) | Tensile Strength (psi) | Cohesion (psi) | Internal Friction Angle (degree) |
|---|---|---|---|---|---|---|
| Sandstone | 2.50 | 0.10 | 3,600 | 360 | 998 | 32 |
| Shale | 2.00 | 0.20 | 1,600 | 160 | 462 | 30 |
| Coal | 0.30 | 0.30 | 900 | 40 | 270 | 28 |

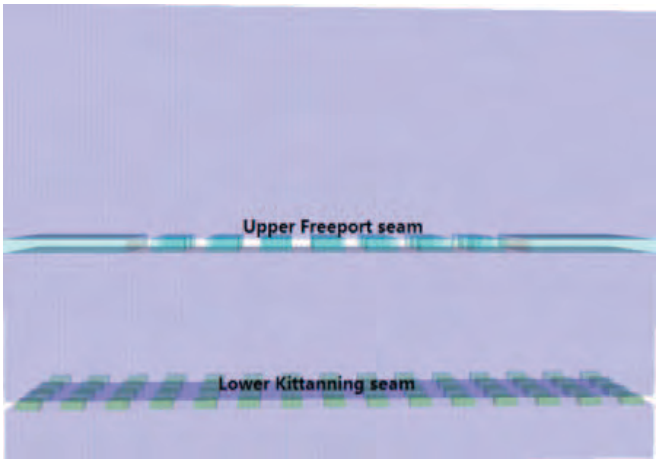



**Figure 6. Numerical model.**

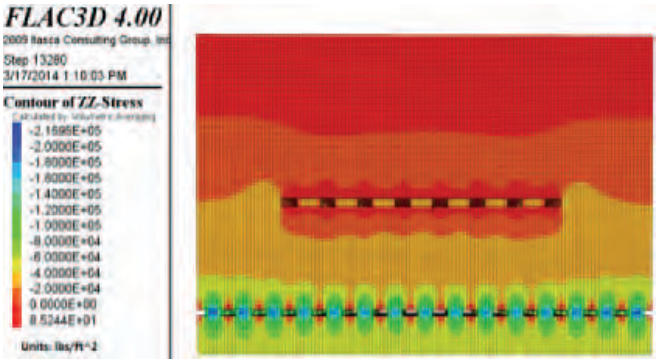



**Figure 7. Vertical stress distribution over the interburden.**

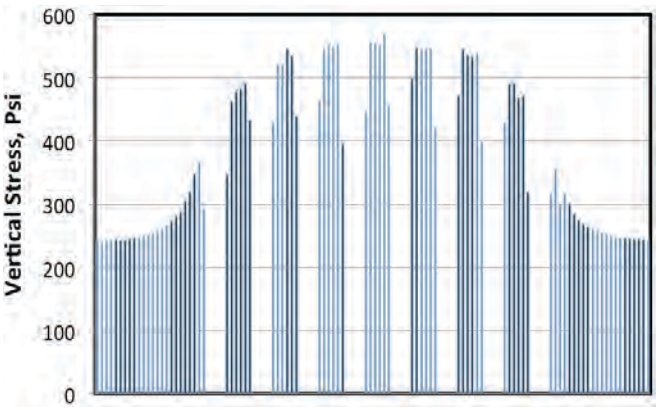



**Figure 8. Vertical stress distribution in the upper seam.**

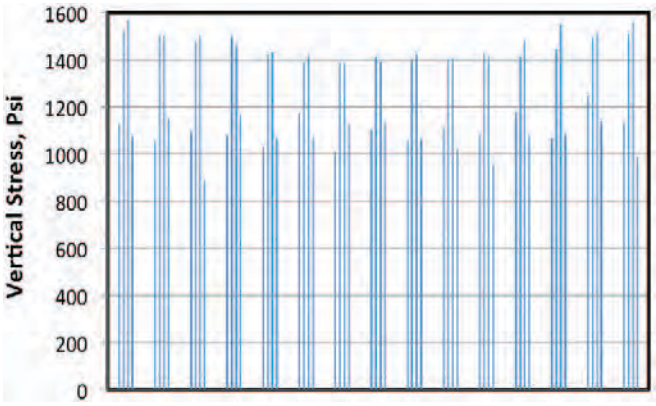



**Figure 9. Vertical stress distribution in the lower seam.**

## UNDERGROUND OBSERVATIONS OF MINING ABOVE SMALL PILLARS

The upper seam has been mined over a large area above small pillars, but observations suggest that pillar failure in the lower seam only occurred over a small area, as shown in Figure 1. The failed pillars in the lower seam were 20 ft × 20 ft and 40 ft× 40 ft with pillar splitting, as shown in Figure 3. The pillar safety factor is between 0.9 and 1.1 over the failure area. Based on the observed roof condition in the upper seam, the pillars over this area were either squeezed or collapsed. The timing of the pillar failure in the lower seam is unknown, but it was not during active mining in the upper seam. Based on the amount of subsurface subsidence, it can be inferred that the pillars were squeezed in the area outlined in yellow, but collapsed in the area outlined in red. It should be noted from Figure 3 that other 20 ft × 20 ft pillars with safety factors slightly larger than 1.0 are stable. Smaller panel size or shallower overburden depth may contribute to the stability of these small pillars.

Minor fractures with different orientations were observed in the roof over the squeezed area. The fractures were generally closed and tight, and no roof sagging or cutters were seen in the area. No floor drop was observed over the area except where fractures were present in the roof. Figure 10 shows the normal roof condition in the mine, while Figure 11 shows the roof with fractures. Pans or steel straps were used to provide skin control to the roof where fractures were present.

Both closed fractures and open cracks in the immediate roof were observed over the collapsed area. The area is zoomed in Figure 12,withroof fractures and cracks mapped along the third entry (travelway). A floor drop of about 1.5-2.0 ft was seen between crosscut #15 and crosscut #16, where several cracks across the section were observed in the roof. Figure 13 shows a crack in the



**Figure 10. Normal roof conditions.**



**Figure 11. Fractured roof.**

roof extended into the pillar, indicating that it was created by subsurface subsidence as a result of pillar collapse in the lower seam. The cracks and fractures in the roof stopped at the barrier pillar and larger pillars in the lower seam. The pillar failure in the lower seam created a gob-solid boundary at the edge of the barrier pillar. The cracks in roof were mostly within about 70 ft from the gob-solid boundary. The roof across the section was scoped. The holes were wet, but no separations were seen in all of the 10-ft scope holes. As a result of snow and rain, water has been dripping from the roof in the area outlined in red, but the area outlined in yellow was dry.

The mining height in the upper seam is about 7 ft, and a fireclay of 2-3 ft is present around the mid-height of the seam. Rib sloughage occurred at some places where the weak fireclay breaks at the pillar rib from weathering in the outby area. With an overburden depth of less than 200 ft, rib bolts are not needed in the mine – but around crosscut #16, significant rib sloughage occurred so that rib bolts with mesh had to be installed (Figure 14). The sloughage could be caused by abutment pressure around the gob-solid boundary.




**Figure 12. Mapped roof cracks and fractures in the travelway over the pillar collapsed area.**



**Figure 13. Cracks in the roof and pillar.**

## MULTI-SEAM INTERACTION

Multi-seam interaction occurs if the pillars in the lower seam fail. The pillar failure in the lower seam would create subsidence fractures and abutment pressure over the influence zone around gob-solid boundary. In this case, AMSS (NIOSH, 2013) is run by assuming that the area with small pillars had failed and become gob. The results show that multi-seam interaction is unlikely, but the safety factor of the 30 ft × 40 ft pillars in the upper seam is reduced from 3.80 under the development load to 2.30 under multi-seam pressure.

Though AMSS indicates that multi-seam interaction is unlikely, precautions still need to be taken to minimize roof and rib failures within the influence zone. The influence zone can be predicted by subsurface subsidence, and the influence zone can be defined as the distance from the edge of the barrier pillar in the lower seam



**Figure 14. Rib support at the abutment pressure zone.**

to the flat bottom of subsidence in the upper seam. The extent of the influence zone depends on interburden thickness, the collapsed height of pillars, and the strength of the interburden. A general subsidence program (Luo, 2013) was used to predict subsurface subsidence. The equivalent mining height was adjusted until the subsidence was about 1.5 ft, as observed underground. The predicted subsidence over the gob-solid area is shown in Figure 15. It can be seen that the ground becomes flat within about 70 ft from the gob edge, which agrees well with underground observations. The subsurface strain is also predicted and shown in Figure 16. The tensile strain occurs with about 50 ft from the gob edge, and compressive strain occurs from about 50 ft to 100 ft from the gob edge. Underground observations showed that major cracks occurred within about 70 ft from the edge of the barrier pillar. Tension cracks or fractures have a significant influence on roof stability, particularly when more than one parallel crack occurs in an entry or crosscut. Fractures could also occur in the area where subsided ground is flat, but the fractures tend to be closed and tight and the impact on roof stability is minimal, though pans may be installed for skin control.

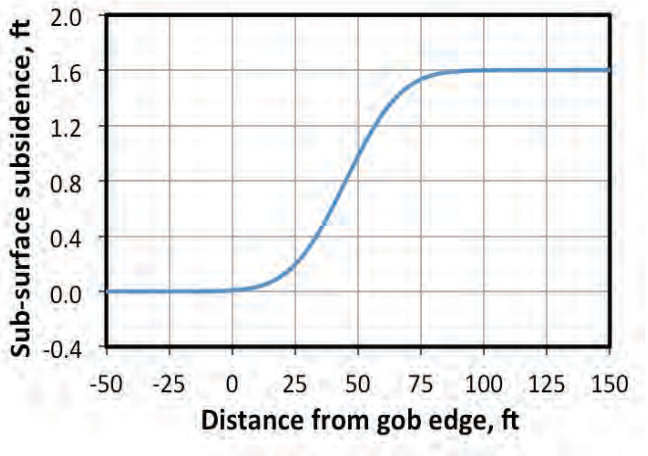



**Figure 15. Predicted sub-surface subsidence at the upper seam level over the gob-solid area.**

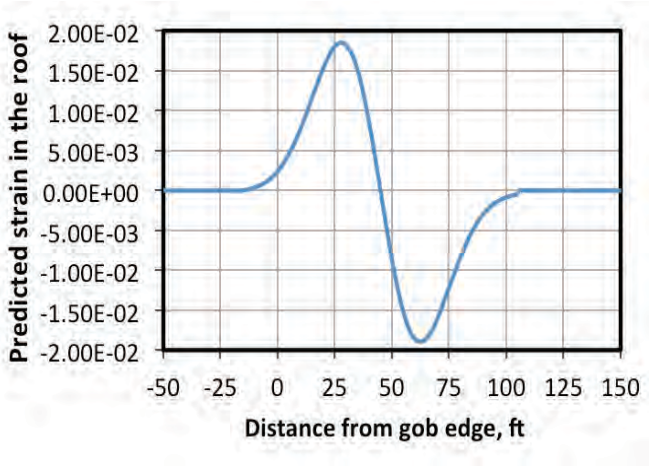



**Figure 16. Predicted sub-surface strain at the upper seam level over the gob-solid area.**

Particular attention should be paid to support the roof in the influence zone. In this case, steel straps or pans were used for skin control and 10 ft cable bolts were used for supplementary support. An abutment pressure zone is present over the barrier pillar, and rib support should be considered within one or two blocks from the gob edge, depending on the rib condition. As the mine is shallow in this case, rib support was only used around the crosscut right over the edge of the barrier pillar.

## CONCLUSIONS

Based on a case study of multi-seam mining over small pillars under a shallow depth, the following conclusions can be made.

Multi-seam interaction exists when mining over small pillars under shallow depth if the small pillars fail. The stability of small pillars has to do with the safety factor, width-to-height ratio, strength of interburden, and the existence of large pillars in the surrounding area. Small pillars over a large area are most likely to have failed when the ARMPS (NIOSH, 2010) safety factor is close to or less than 1.0.

Multi-seam interaction occurs mainly over the influence zone, as determined by the amount and extent of subsurface subsidence and abutment pressure. Proper roof and rib support should be installed in the influence zone to minimize the risk of roof and rib falls.

Superimposition of pillars or panels is not necessary when the interburden thickness is large, but the pillars in the upper seam should be designed as though the small pillars with a low safety factor in the lower seam have already failed.

**REFERENCES**

NIOSH (2010). Analysis of Retreat Mining Pillar Stability, ARMPS Software: http://www.cdc.gov/niosh/mining, National Institute for Occupational Safety and Health, Pittsburgh, PA.

NIOSH (2013). Analysis of Multi Seam Stability, AMSS Software, http://www.cdc.gov/niosh/mining.National Institute for Occupational Safety and Health, Pittsburgh, PA..

Y. Luo. (2013). CISPM-W Subsidence Prediction Program, Department of Mining Engineering, West Virginia University.

Itasca Consulting Group, FLAC 3D, Version 4.00.32, User's Guide, 2009.

Mark, C. (1999). "Empirical methods for coal pillar design." *Proceedings of the Second International Workshop on Coal Pillar Mechanics and Design*, pp. 145-154.

van der Merwe, J. N. (2013). "Predicting coal pillar life in South Africa." *The Journal of The South African Institute of Mining and Metallurgy*, Jun. pp. 293-301.

# Ground Control Design Considerations for Reducing Longwall–Induced Stress and Seismicity Associated with Massive Sandstone under Deep Cover

**Daniel W.H. Su**, Senior Geomechanical Engineer
**Gregory J Hasenfus**, Sr. Geomechanical Engineer
**Luke A Stull**, Geologist
Consol Energy Inc.
Canonsburg, PA

## ABSTRACT

Thick, massive sandstone present in close proximity of the mining horizon can create difficult longwall caving issues, which may lead to severe face loading and subsequent face roof control problems. Under deep cover, such delayed caving and overhang not only impose additional loading on the gateroad pillar system, but they also increase the potential for large seismic events. Such a combination of thick, massive sandstone geology and deep cover was present over a portion of a southwestern Virginia coal mine, which was confirmed via detailed in-mine roof scoping and mapping. Large seismic events were recorded over a district of 1,000-foot-wide longwall panels. This paper presents the ground control design changes implemented to reduce longwall-induced stresses in the sandstone, to reduce longwall abutment pressures in the gateroad pillars, and to reduce the magnitude of mining-induced seismic events. A series of two-dimensional finite element models were constructed and analyzed to evaluate the longwall-induced stresses in the sandstone above the gateroad pillars and the abutment pressures within the gateroad pillars. Results from the analyses indicated that reducing the panel width from 1,000 to 700 feet reduced the longwall-induced stresses in the sandstone by a factor of 2.0. Specifically, the probability of sandstone stability improved from 29% for the 1,000-foot-wide panel district to over 95% for the 700-foot-wide panel districts. Also, the subcritical 700-foot-wide panel, coupled with a change in pillar design, considerably reduced the longwall-induced abutment pressures in the gateroad pillars, which significantly increased the gateroad pillar stability factor. Surface subsidence measurements conducted over the 1,000-foot-wide panel district and two new 700-foot-wide panel districts were in very good agreement with those predicted by the finite element models. In addition, results from the models indicated that wider panels with a smaller district may produce the same probability of sandstone stability. One four-panel district and one five-panel district with the new ground control design changes have been mined successfully. The panel width was found to be the most influential factor in determining the longwall-induced stresses in the sandstone and in the gateroad pillars. The thickness and massive nature of the sandstone, the proximity of the sandstone, and the strength of the sandstone were also found to be important factors. Seismic monitoring over the two mining districts that employed 700-foot-wide panels confirmed the reduction of one order of seismic magnitude when compared with those measured over the 1,000-foot-wide panel district.

## INTRODUCTION

This paper presents the ground control challenges experienced by a southwestern Virginia longwall mine that extracts the Pocahontas No. 3 metallurgical coal seam. The depth of cover within the subject mine ranges from 1,350 to 2,300 feet, and the seam thickness ranges from 5 to 8 feet. The mine started its first longwall panel in 1987 under massive sandy shale roof with two noticeable seismic events in 1988 and 1989 beneath about 2,000 feet of cover. At that time, the gateroad pillars were somewhat under-designed, and the caving-induced shock wave was believed to have triggered a localized coal bump in both cases. When the longwall operation moved to the Northeast panel district, two seismic events were also recorded under about 2,200 feet of cover, although no coal bump was observed. All of these seismic events originated in previously mined-out gob areas, and their impact on the mining operation was minimal.

In 2001, the mine started its first 1,000-foot-wide longwall panel within a 10-panel district. For the outby portion of this district starting from Panel 4, massive sandstone in close proximity was mapped, based on existing corehole data and in-mine roof scope hole data On February 14, 2005, while mining Panel 6, a seismic event occurred in the gob of Panel 5, which interrupted ventilation and production and caused the evacuation of the mine. Subsequent to the seismic event, mine management decided to change the pillar design to increase the pillar safety factor and to change the primary bolting system from five-foot point-anchored Grade 90 bolts to six-foot fully grouted Grade 60 torque-tension bolts to prevent bolt failure in the tailgate behind the longwall face. On July 9, 2007, while mining Panel 9, another seismic event occurred in the gob of Panel 8, which also disrupted ventilation and production and again caused evacuation of the mine. Fortunately, no injury was associated with these occurrences. Nevertheless, as a result of the events in Panels 6 and 9, significant ground control design changes were implemented to improve safety and minimize the probability that these large seismic events could again disrupt ventilation and production. This paper presents the ground control design changes implemented to reduce longwall-induced stresses in the sandstone,

to reduce longwall abutment pressures in the gateroad pillars, and to reduce the magnitude of mining-induced seismic events.

## GEOGRAPHIC AND REGIONAL GEOLOGIC SETTING

The mine is located in the southwest corner of Virginia, and extracts coal from the Pennsylvanian Age Pocahontas No. 3 seam. Strike and dip for the seam are N38E and 0.5°, respectively. Although the No. 3 seam can have in-seam rock partings, no partings of significance were observed within the study area.

The mine also lies within the Appalachian Plateau physiographic province (Figure 1). Although the highly faulted Valley and Ridge province is only several miles to the south of the mine, there has been only one significant fault encountered by the mine. Bearing the name Keen Mountain after a nearby community, it is a right lateral strike-slip fault. Historically, the mine plan was modified to avoid the fault. Moreover, there are several small-scale structural features that run both parallel and transverse to the major faults and upheaval of the Valley and Ridge. These primarily consist of localized slickensides and slip-type features, and are typically abated with proper local ground control measures.




**Figure 1. Mine location.**

Common to this particular coalfield, like many others, is a sequence of cyclothems consisting of sandstones, coals and shales (Figure 2). Sandstones for the Central Appalachian region in particular are generally more developed than other regional coalfields. The sandstones found within the Pocahontas formation are generally massive, thick, well cemented and strong. Present-day overburden depth for the mine ranges between 1,350 and 2,300 feet, with an average overburden of about 1,750 feet (Figure 3).

## EXPLORATION AND MAPPING

In advance of mining, overburden and near-seam geology are evaluated through a combination of coreholes and coalbed methane (CBM) well E-logs. In addition, upon mining, 20-foot roof holes are systematically examined via fiberscope for roof geology and roof stability to aid in geologic interpretation and roof support recommendations. Where feasible, additional surface coreholes have been drilled to extract core for testing of rock properties. These rock properties are especially valuable when determining

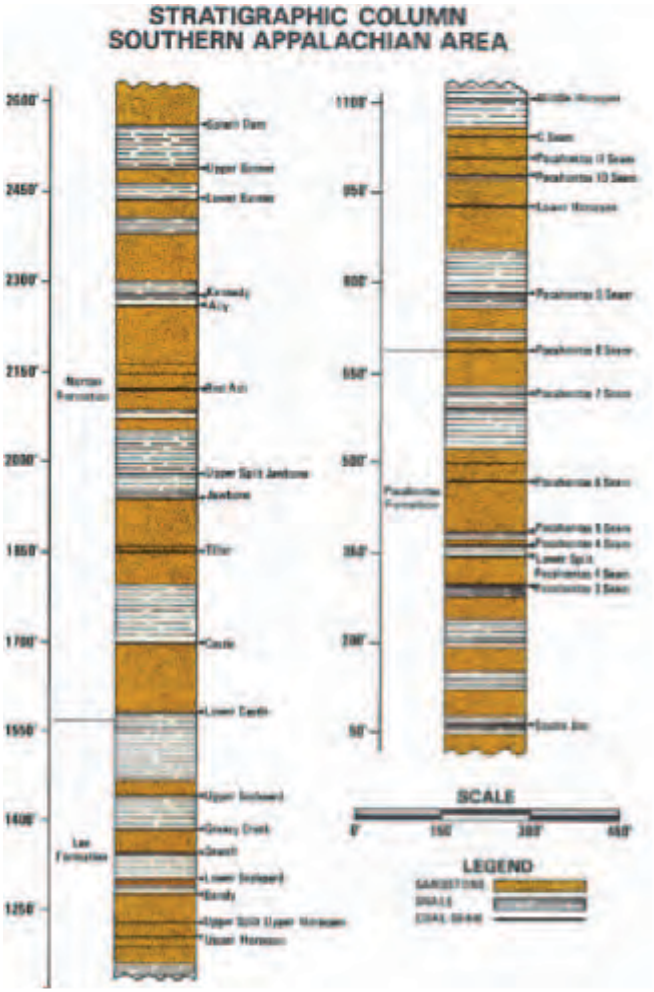



**Figure 2. General strata column.**

the strength and bedding characteristics of sandstone units found within close proximity to the mine roof. Table 1 lists the typical uniaxial compressive strength of the sandstone and shale units up to 72 feet above the Pocahontas No.3 seam.

As shown in Figure 4, the interval to the first roof sandstone ranges from 0 feet (i.e., within the immediate roof) to greater than 20 feet. Typically, where the interval to first sandstone is small (<5 feet), the sandstone also tends to become thicker. Generally, the first sandstone overlying the seam is between 0 and 30 feet thick and is sometimes found to be massive (Figure 5).

As a result of the Panel 6 and Panel 9 occurrences of 2005 and 2007, respectively, an extensive study was conducted to assess geologic variables and mine geometries that contributed to their causes. In addition to pillar and panel geometry, it was determined that four geologic factors likely contributed to the larger caving and seismic events; as a result, an overlay map was created of those four factors, including: 1) where the interval-to-sandstone is less than five feet, 2) where the overburden exceeds 2,000 feet, 3) where the first overlying sandstone thickness is greater than 20 feet, and 4) where the expected initial caving height is less than 15 feet (Figure 6).

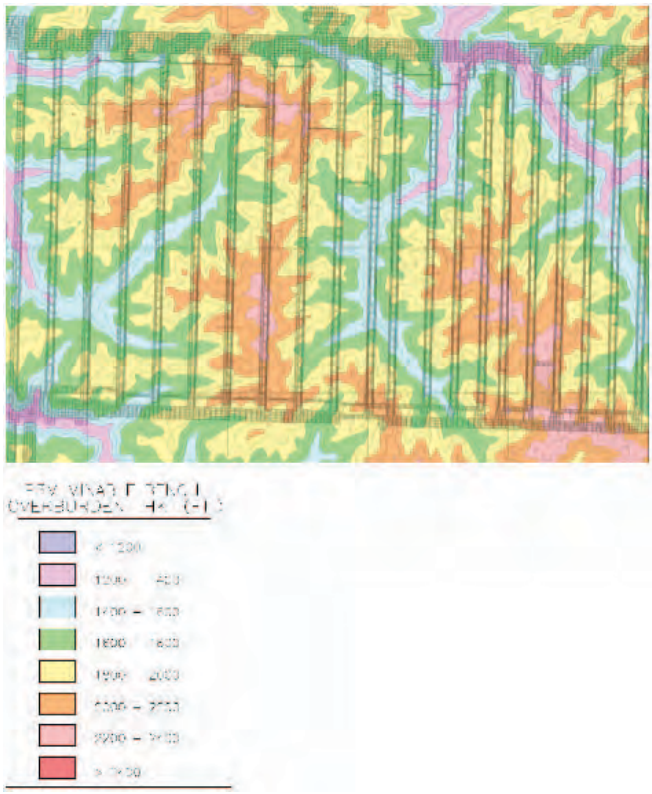


**Figure 3. P3 seam overburden.**

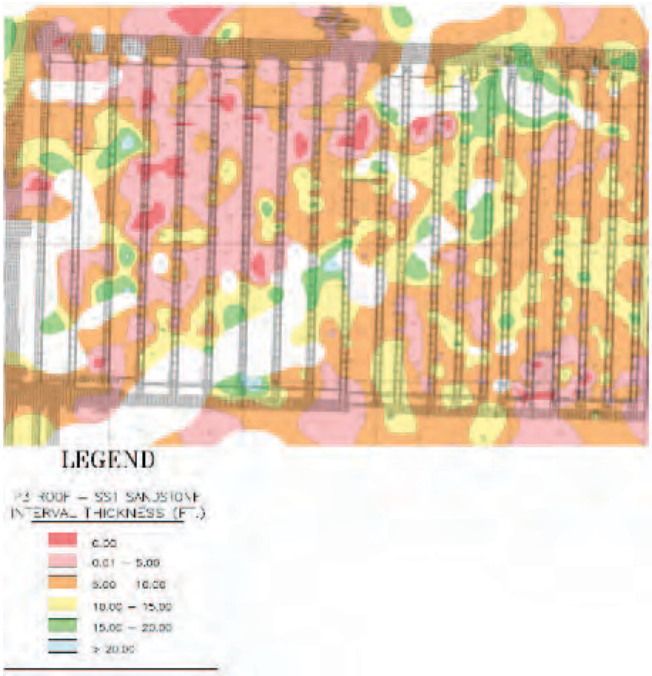



**Figure 4. Interval to sandstone.**

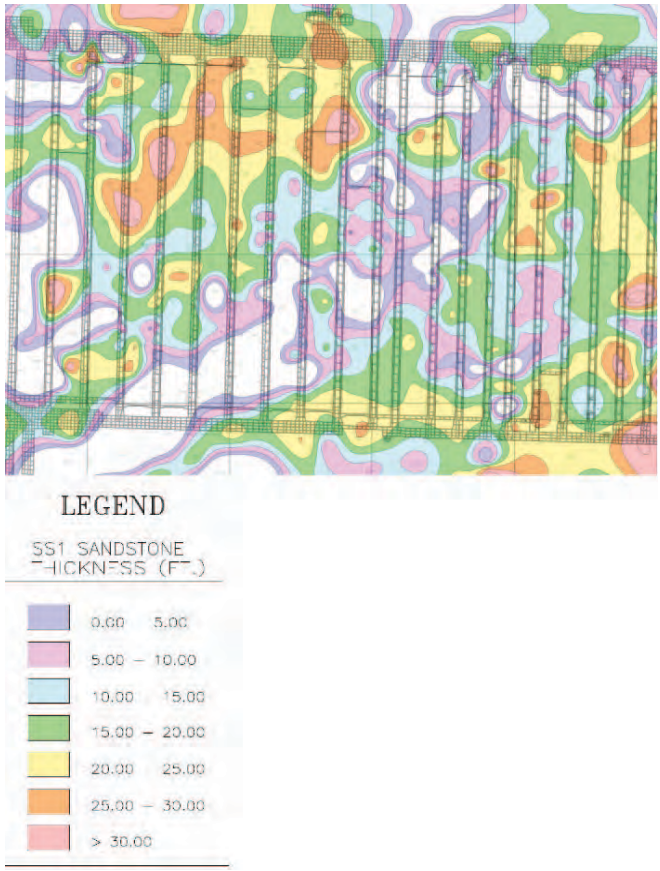



**Figure 5. First overlying sandstone thickness.**

## IMPORTANT PARAMETERS AFFECTING INDUCED STRESSES IN SANDSTONE AND ABUTMENT PRESSURES IN GATEROAD PILLARS

### Geologic Parameters

From the geologic history and recent extensive underground geologic mapping described above, five major parameters are identified as the primary controlling factors affecting the longwall-induced stresses in the sandstone and the longwall-induced abutment stresses in the gateroad pillars. These parameters, in descending order of importance, are 1) overburden depth, 2) caving height, 3) interval to sandstone, 4) sandstone thickness and 5) sandstone quality (or strength). Overburden depth defines the pre-mining stress level and, thus, the longwall-induced stress level, and is considered the most influential parameter. Caving height, on the other hand, defines the thickness of the rock layers above the Pocahontas No. 3(P3) seam that would cave readily behind the longwall face, and which could provide immediate support to the thick sandstone layers overhanging and cantilevering over the longwall face supports. Such immediate support to the overhanging and cantilevering sandstone layers serves two purposes: it reduces the stress in the sandstone, and it provides cushion to prevent air blast in the event of massive sandstone caving. The interval to sandstone is important, since a small interval to sandstone typically implies low caving height, unless the sandstone quality is poor. Sandstone thickness is important, since the ability of the sandstone to deflect and cave is inversely proportional to the cubic power of its thickness (conventional beam theory). For example, with

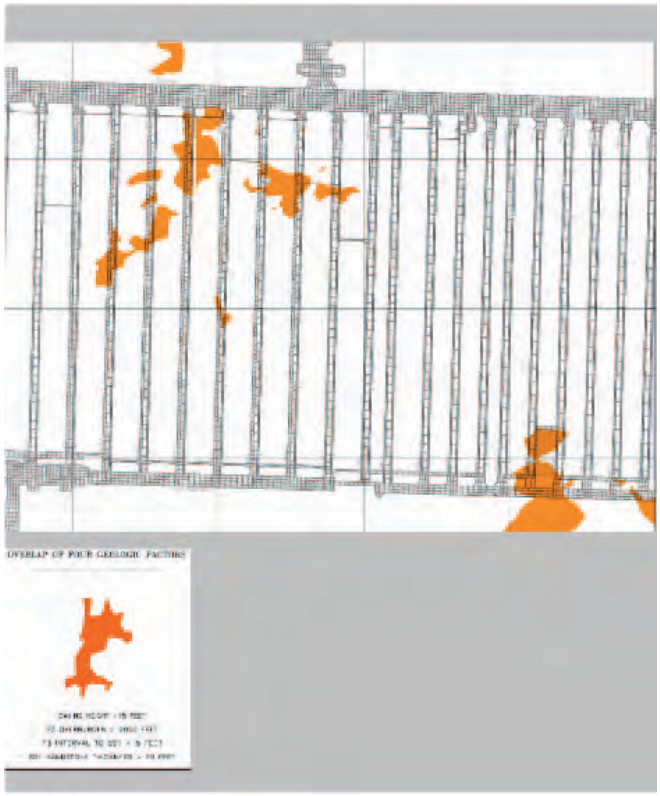


**Figure 6. Hazard map.**

everything being equal, a 50-foot-thick sandstone layer is eight times less likely to cave compared to a 25-foot-thick sandstone layer. Finally, the importance of sandstone quality, or strength, is readily obvious, as a laminated sandstone would cave and relieve stress much more readily than a massive sandstone.

### Operational Parameters

Among the operational parameters, panel width and gateroad pillar design are the most influential parameters affecting the longwall-induced stresses in the sandstone and the longwall abutment pressures in the gateroad pillars. The effect of panel width on the longwall-induced stresses in the sandstone can be evaluated using the following fixed-end beam equation:

$$\sigma = wL^2/2t^2 \quad (1)$$

Where, σ is the maximum tensile stress present at the top surface of a thick sandstone layer directly above the edge of the longwall gob, *w* is the distributed load on the sandstone beam, *L* is the width of the longwall gob or the longwall panel width, and *t* is the thickness of the sandstone layer. Clearly, doubling the panel width would increase the maximum tensile stress in the sandstone by a factor of 4. Conversely, reducing the panel width by a factor of 2 would reduce the maximum tensile stress in the sandstone by 75%.

The effect of gateroad pillar design on the longwall-induced stresses in the sandstone is not as straightforward. However, a properly designed gateroad pillar system serves to separate individual longwall gobs, thus preventing the neighboring gobs from joining together to increase the effective gob width. A properly designed gateroad pillar system also serves to protect the ventilation system, which will be discussed later.

## DESIGN CHANGES IMPLEMENTED TO REDUCE LONGWALL-INDUCED STRESSES IN THE SANDSTONE AND GATEROAD PILLARS

Since the depth of cover, potential caving height, sandstone interval and sandstone strength are all fixed geologic parameters present at a given site, changing the panel width and gateroad pillar design are the primary operational options for reducing the longwall-induced stresses in the sandstone and the longwall abutment pressures within the gateroad pillars.

### Panel Width Modification and Two-Dimensional Finite Element Analyses

A number of two-dimensional ABAQUS finite element models were constructed to evaluate the effect of panel width on the stress distributions within the thick, massive sandstone under a given overburden depth and interval to sandstone. A probabilistic analysis was then conducted from the stress distributions of a given model to calculate the corresponding probability of sandstone stability. A zero interval to sandstone and a cover depth of 2,000 feet were used for the first series of models to evaluate the relative sandstone stability among the models. Figures 7, 8 and 9 illustrate the Mises stress distribution (ABAQUS, 2013) under 2,000 feet of cover in the thick, massive sandstone with zero caving potential for panel widths of 1,400, 1,000 and 700 feet. Clearly, the Mises stress over the four-panel, 1,400-foot-wide model is much higher than those of the 1,000-foot-wide and 700-foot-wide models. The gray Mises stress contours represents areas of sandstone which would have fractured based on the average laboratory obtained uniaxial compressive strength of 21,000 psi (Table 1).

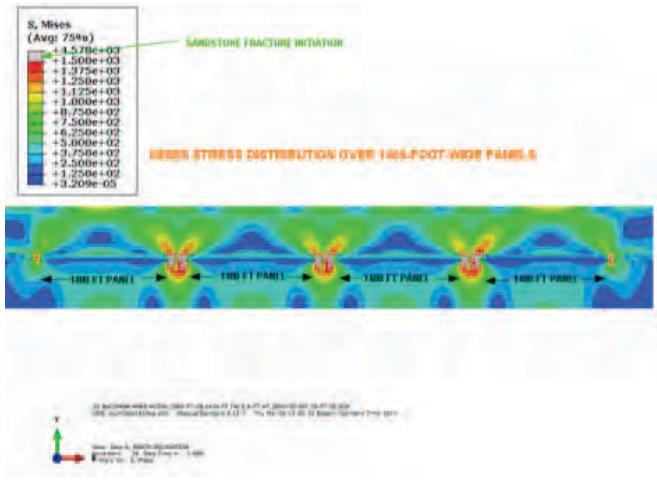



**Figure 7. Mises stress distribution over 1,400-foot-wide panels.**

Table 2 lists the comparison of probability of sandstone stability among District 1A (1,000-foot-wide panels under 2,300 feet of cover, 0-foot caving potential), District1B (1,000-foot-wide panels under 2,000 feet of cover, 0-foot caving potential), District 2 (combination of one 500-foot, one 1,000-foot and two 700-foot panels under 2,150 feet of cover, 0-foot caving potential), and

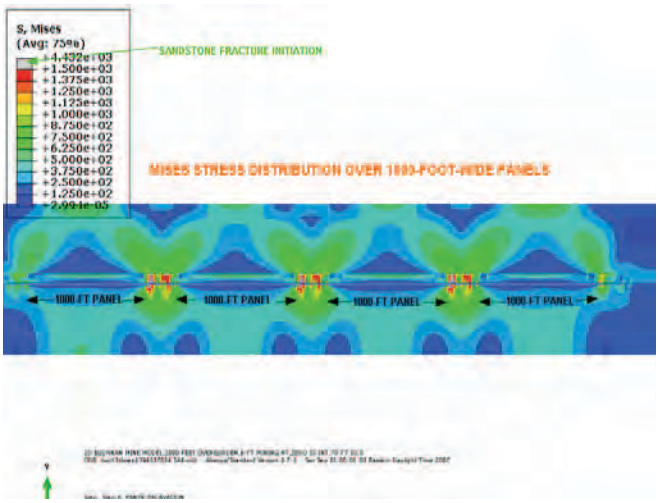



**Figure 8. Mises stress distribution over 1,000-foot-wide panels.**

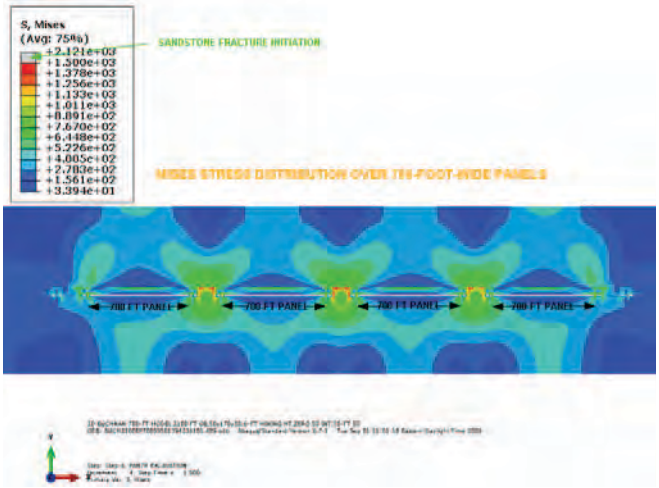



**Figure 9. Mises stress distribution over 700-foot-wide panels.**

District 3 (700-foot-wide panels under 2,200 feet cover, 0-foot caving potential). The probability of sandstone stability was calculated from the average Mises stress along the edge of the gob, where the Mises stress was the greatest, over the entire thickness of the sandstone layer. Standard deviations of the Mises stress distribution and the laboratory determined compressive strength was used to compute the probability of sandstone stability. Table 2 indicates that, for District 1A, the sandstone would fail about seven out of eight times. For District 1B, the sandstone would fail about three out of four times. On the other hand, the sandstone in District 2 is expected to remain stable about seven out of eight times, and the sandstone in District 3 is expected to remain stable about nine out of 10 times. Clearly, under such a multi-panel district scenario, the 700-foot-wide panels serve to reduce the longwall-induced stresses in the sandstone considerably, and thus significantly improve the probability of sandstone stability. Effectively, the 700-foot-wide panels are 700% more stable than the 1,000-foot-wide panels.

**Pillar Design Modification – ALPS Stability Factors**

Since the panel widths under consideration were all subcritical compared to the depth of cover present, changing the pillar design could significantly change the pillar stability factor, which in turn could affect the longwall-induced stresses in the sandstone. The pillar design employed in District 1A, due to an operational modification, was 90ft x 130ft x 50ft centers, which yielded an ALPS stability factor of 0.54 under 2,300 feet of cover.

**Table 1. Uniaxial compressive strength of sandstone estimated from point load tests.**

| Height Above Top Coal (ft) | Unit Thickness (ft) | Lithology | Uniaxial Compressive strength (psi) |
|---|---|---|---|
| | | | |
| 72.12 | 22.10 | Hard Sandstone, Crossbedded | 18,800 |
| 70.77 | 1.35 | Sandstone Spars | 19,400 |
| 67.47 | 3.30 | Hard Sandstone | 19,900 |
| 64.67 | 2.80 | Sandstone Spars | 19,700 |
| 61.52 | 3.15 | Hard Sandstone W/ Shale Streaks | 19,800 |
| 46.12 | 15.40 | Crystallized Sandstone | 18,800 |
| 35.33 | 10.79 | Hard Sandstone, Crossbedded | 22,500 |
| 34.17 | 1.16 | Shale, Dark Gray | 9,400 |
| 28.64 | 5.53 | Hard Sandstone W/ Shale Streaks | 22,900 |
| 24.57 | 4.07 | Hard Sandstone, Massive | 20,200 |
| 20.87 | 3.70 | Hard Sandstone W/ Shale Streaks | 21,300 |
| 11.77 | 9.10 | Sandstone, Gray, W/Shale Streaks | 21,700 |
| 8.01 | 3.76 | Intbd Sandstone & Shale, Gray | 29,500 |
| 4.04 | 3.97 | Sandstone, Gray, W/Shale Streaks | 28,500 |
| 0.00 | 4.04 | Shale, Dark Gray | 14,200 |
| | | | |
| Seam height = | 6.50 | COAL | |
| | | | |
| | | Roof Sandstone Strength | |
| | | Average | 21,769 |
| | | Weighted Average | 20,966 |
| | | | |
| | | Maximum | 29,500 |
| | | Minimum | 18,800 |

The pillar design employed in District 1B was also 90ft x 130ft x 50ft center, which yielded an ALPS stability factor of 0.64. However, the pillar design employed in Districts 2 and 3 was 50ft x 170ft x 50ft, which yielded an ALPS stability factor of 0.95 under the deepest covers present over the two districts. Such a significant improvement in the pillar stability factor serves two purposes: (1) with patterned standing support in the #1 and #2 entries, the #2 entry stays open behind the longwall face on the tailgate side, which enables the mine to keep the tailgate on intake from start to finish, and (2) with the pillars remaining stable between panels, overriding of stresses between panels is reduced and the gateroad pillars serve to separate the individual panels.

## SURFACE SUBSIDENCE MEASUREMENT

Surface subsidence measurement, conducted on various surface control points retroactive to the 2007 event, indicated that the 1,000-foot-wide longwall faces produced larger vertical movements than normally projected in deep, hard rock-dominated overburden. As shown in Figure 10, center-panel movements approached 3.0 feet for first panel mining and as much as 3.5 feet for second panel mining, which was 46% to 58% of total seam extraction (i.e., for extraction heights ranging from 6.0 to 6.5 feet). This is notable, given that the Pocahontas No.3 seam overburden consists of as much as 70 to 80% hard rock (e.g., sandstone and strong sandy shale), and that the panel widths were only 45 to 60% of the depth (i.e., the 1,000-foot-wide panels were subcritical from the standpoint of producing theoretical maximum subsidence). In part, this indicated that, for the 1,000-foot-wide panel design and corresponding gate design, there not only had to be substantial re-compaction of the gob, but also substantial gateroad deformation and panel-to-panel gob interaction.

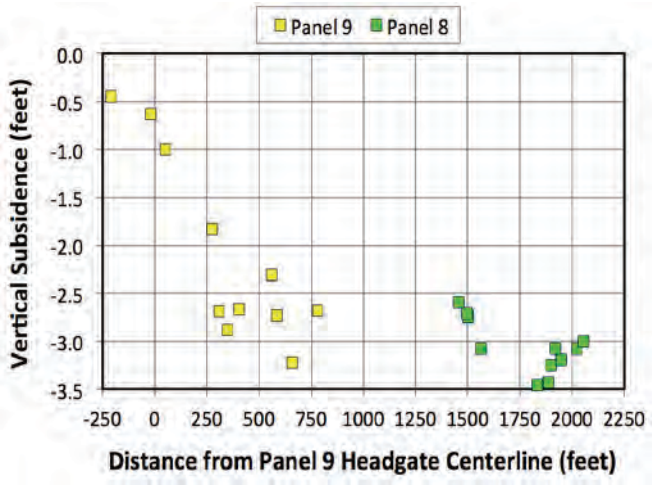



**Figure 10. Subsidence for 1,000-foot-wide panels.**

With the introduction of the 700-foot-wide face in 2008, center-panel subsidence has been systematically measured. An example is provided in Figure 11, which shows center panel subsidence measurements after first and second (i.e., subsequent) panel mining. In comparison with Figure 10, it is obvious that reduction of panel width from 1,000 feet to 700 feet significantly reduced center-panel subsidence. With the 700-foot-wide face, center-panel movements for first-panel mining range from about 0.8 to 1.7 feet (1.3 average), and increased to between 1.4 and 2.7 feet (2.0 average) after second-panel mining. It is also readily apparent from Figure 11 that, all other things being equal, center-panel subsidence for the 700-foot-wide panels increases with depth. Although this trend is counterintuitive from a traditional subsidence theory standpoint, it is likely indicative of both increased gob compaction and gate road deformation with increased depth, i.e., with increased vertical stress.

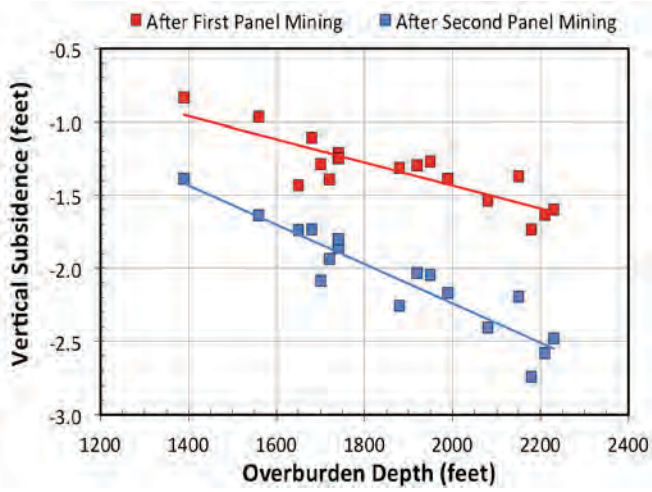



**Figure 11. Center-panel subsidence relationship with depth for 700-foot-wide panels.**

In addition to data shown in Figure 11, subsidence measurements have also indicated an approximate 10% increase in subsidence after third-panel mining and little to no increase after fourth-panel mining. Although such longer-term measurements may be influence by time, they strongly suggest that under the current 700-foot face scenario, active panel influence likely extends no more than two panels into the gob from the active tailgate.

## SURFACE SEISMIC MONITORING

In addition to surface subsidence, mining-induced seismicity has also been continuously monitored and triangulated since 2009 via an automated surface seismic network consisting of five to six surface stations situated at the periphery of the active mining area (see Figure 12). As configured, the network is capable of detecting mining-induced seismic events with Richter local magnitudes as small as magnitude -2.0 (i.e., -2.0 $M_L$). Based in part on observed precision and relative location with respect to mine works, event epicenter accuracy is estimated to be less than 200 feet for events larger than 0.5 $M_L$, although in many cases the accuracy is likely much better. Note that smaller events, assumed to be associated with immediate gob caving, have been observed to trail the face by less than a few hundred feet. Vertical control is not well constrained due to lack of sensors at depth (no down hole or seam level sensors).

Since startup of the system in January 2009, the network has monitored the retreat of nine panels within covers ranging from about 1,400 to 2,300 feet. During this time, a total of 77 events have occurred with magnitudes greater than or equal to 1.0 $M_L$. Of these, 10 had magnitudes greater than 2.0 $M_L$, nine ranged between 2.0 $M_L$ and 2.5 $M_L$, and one was at 3.2 $M_L$. As seen in Figure 13, with only a few exceptions, all of these +1.0 $M_L$ events have occurred in cover deeper than 1,800 feet, and the vast majority

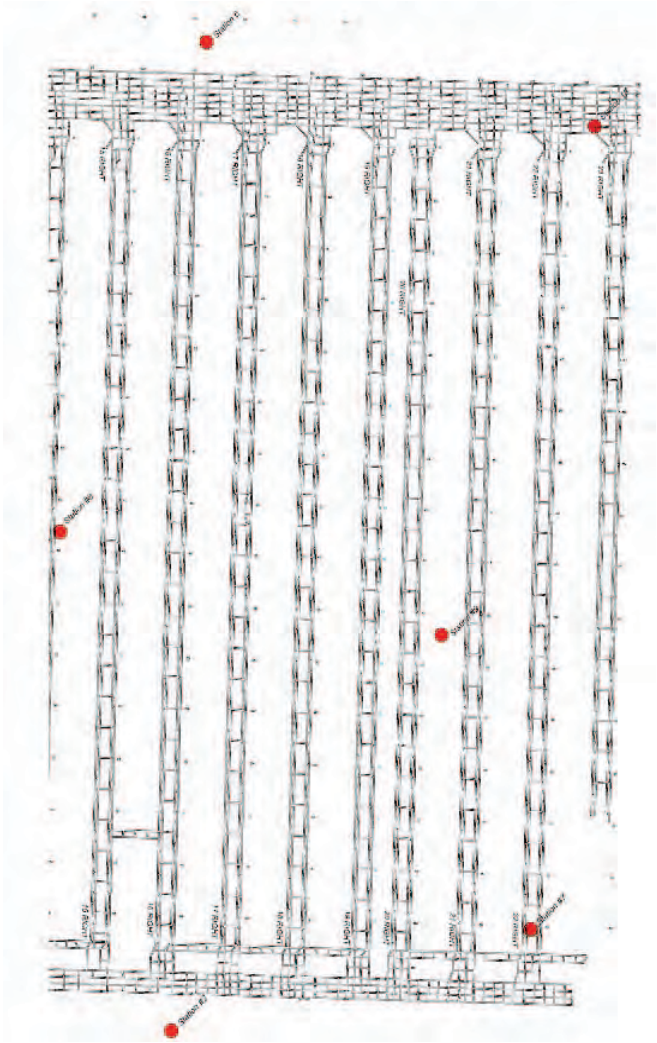


**Figure 12. Locations of surface microseismic monitoring stations.**

within cover greater than 2,000 feet. All of these larger events occurred under ridgeline topography.

Relative to mine geometry, all but eight of the +1.0 $M_L$ events trailed the active longwall face by more than 500 feet, or otherwise more than a full gob width away; also, over two-thirds of all +1.0 $M_L$ events occurred more than 1,000 feet behind the active face, with an average trailing distance of all events approaching 2,000 feet. In addition, except for one suspect event, all of the +1.0 $M_L$ events occurred either on the tailgate side of active panel or in the prior two panels. Additionally, none of these events were noticed by (felt by) longwall face crews. Furthermore, during first-panel mining in both new districts, seismic activity was minimal, confirming the ability of the intervening barrier to effectively separate the interaction of district gobs.

By comparison, during mining of the 1,000-foot-wide District 1A and District 1B panels, at least 12 mining-induced seismic events were significant enough to be recorded by outside regional monitoring networks. The magnitude of these 12 events ranged from 2.3 to 4.3 $M_L$, and averaged about 3.1 $M_L$, or approximately one order of magnitude greater than events observed within the

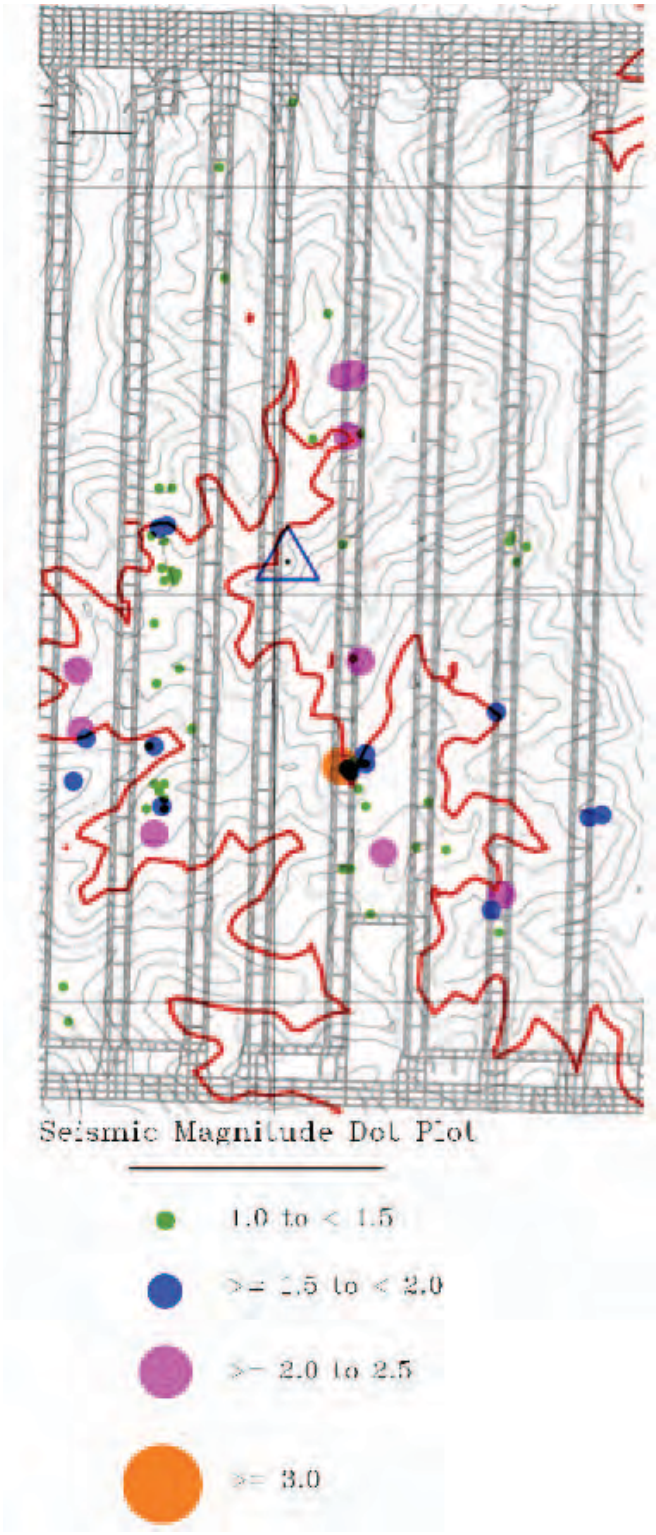



**Figure 13. Locations of microseismic events over a five 700-foot-wide panel district.**

700-foot-wide panels. In addition, many of those 12 events were readily felt by face crews, and two instances corresponded with the 2005 and 2007 occurrences that severely impacted ventilation and production. Note, however, that no event within the 700-foot-wide or 1,000-foot-wide panels has corresponded with observable pillar failures at or near the face.

## CONSIDERATION OF WIDER PANELS

In addition to reducing panel width for multiple-panel districts, another means of addressing deep-cover sandstone (high stress) concerns could be through the use of single-panel districts, or wider single panels separated by solid coal barriers. Such methods have been used in the western U.S. coalfields to mitigate longwall stress impacts within bump-prone deep cover environments (Gilbride and Hardy, 2004; Maleki, 2006; Pariseau et al, 2008). The concept would be to segregate each panel into a separate district, thereby achieving two primary goals: separate, or otherwise minimize, gob-stress interaction on a per-panel basis; and separate gob ventilation interaction on a per-panel basis. Separation of the gobs should not only enhance tailgate stability, but also bleeder ventilation since each tailgate would remain in a typical bleeder-loading condition, directly adjacent to only one gob, and with more open entries, rather than in an isolated loading condition between gobs.

In support of this concept, it should be noted that, regardless of panel width, throughout the subject mine history the first panel per district has never induced significant stress or seismic-related problems. As previously discussed, this is also evident in the recent subsidence and seismic data collected within the last three districts. In addition, since there would be little to no gob interaction, and significantly more "between-panel" pillar support, there should be little to no concern from prior panel stress or caving concerns. For example, even if a large caving event occurred in a prior panel, it would be isolated from the current panel as well as from the rest of the mine if panels were progressively sealed.

Towards this end, a 1,150-foot-wide panel was selected for further modeling and evaluation. Based in part on back calculation to achieve a conservative tailgate bleeder loading ALPS stability factor, total gate widths were selected to be 250 feet (50ft, 150ft, 50ft entry centers), with single-panel district barriers on 170-foot centers (approximately 150ft rib-to-rib dimension) (see Figure 14). The combination of these factors produces recoverable reserves and development requirements nearly equivalent to the current 700-foot-wide panel for a five-panel district configuration. Figure 15 illustrates the Mises stress distribution in the sandstone above a single 1,150-foot-wide longwall panel under 2,300 feet of overburden. Clearly, the longwall-induced Mises stress over the single 1,150-foot-wide panel is less that computed over the 700-foot-wide, five-panel district, which has been demonstrated to be stable and successful, and the calculated probability of sandstone stability over the single panel is more than 99%.

## DISCUSSION

Hasenfus and Su (1992) suggested that, in order to successfully model longwall overburden response, a practical and valid numerical model – whether it is a finite element, finite difference, boundary element or discrete element method – must be able to closely simulate both underground pillar pressure and surface subsidence. In other words, to demonstrate that a given numerical model is valid for simulating longwall mining and the associated stress redistribution and strata deformation, detailed site geology and pertinent rock properties as well as the mine geometry must be used as the primary model input, and ultimately the model output

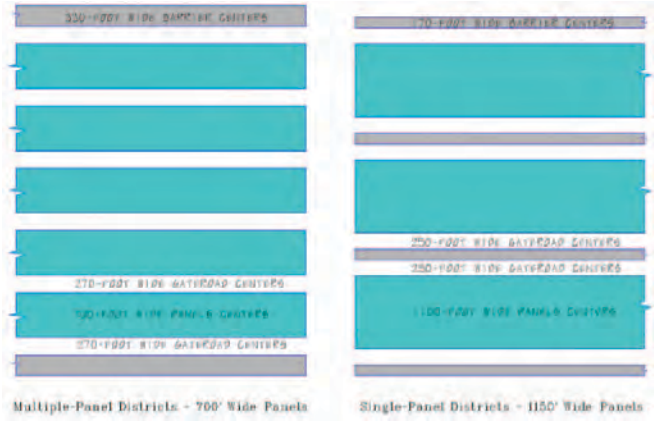



**Figure 14. Wider single-panel district concept.**

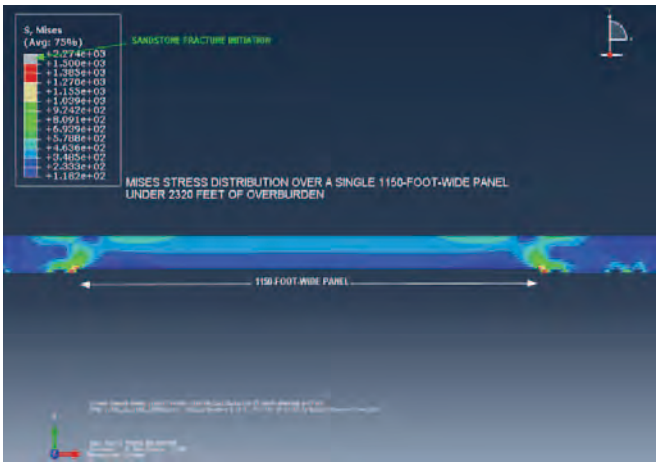



**Figure 15. Mises stress distribution over a single 1,150-foot-wide panel under 2,300 feet of overburden.**

should closely match anticipated and/or measured pillar pressure and surface subsidence.

The ABAQUS model used in this paper not only closely simulates the underground pillar pressure distributions (Su and Hasenfus, 1999), it also provides a fairly accurate prediction of longwall-induced surface subsidence. For the 1,000-foot-wide panels, the measured mid-panel maximum subsidence was 3.5 feet, while the ABAQUS model predicted a mid-panel maximum subsidence of 3.54 feet. Over the 700-foot-wide panel district, the measured maximum subsidence was 2.2 feet, while the ABAQUS computed subsidence was 2.34 feet. Such an accurate prediction of both underground pillar pressure and surface deformation serves to validate the ABAQUS model's accuracy and versatility. Thus, the ABAQUS model lends itself as a proven numerical model to accurately simulating longwall-induced stresses and deformations under different mining geometry and geologic conditions.

From Equation (1), a 1000-foot-wide panel is expected to store 6 times more strain energy, since the strain energy is proportional to the square of induced stress, and 4 times more potential energy than a 700-foot-wide panel. Thus, a 700-foot-wide panel stores approximately 10 times less energy, which is equivalent to one order of seismic magnitude and which has been confirmed from comparisons among surface seismic measurements over Districts 1A, 1B, 2 and 3.

## CONCLUSIONS

Significant ground control design changes were implemented in a southwestern Virginia coal mine after two recent large seismic events to reduce longwall-induced stresses in the sandstone, to reduce longwall abutment pressures in the gateroad pillars, and to reduce the magnitude of mining-induced seismic events. One four-panel district and one five-panel district with the new ground control design changes have been mined successfully.

A series of two-dimensional finite element models were constructed and analyzed to evaluate the longwall-induced stresses in the sandstone above the gateroad pillars and the abutment pressures within the gateroad pillars. Results from the analyses indicated that reducing the panel width from 1,000 to 700 feet would reduce the longwall induced stresses in the sandstone by a factor of 2.0. Specifically, the probability of sandstone stability improves from 29% for the 1,000-foot-wide panel district to over 95% for the 700-foot-wide panel districts. In addition, modeling results indicate that wider panels with a smaller district may produce the same probability of sandstone stability.

The subcritical 700-foot-wide panel, coupled with a change in pillar design, considerably reduced the longwall-induced abutment pressures in the gateroad pillars, which significantly increased the gateroad pillar stability factor. Panel width was found to be the most influential factor in determining the longwall-induced stresses in the sandstone and in the gateroad pillars. The thickness and massive nature of the sandstone, the proximity of the sandstone and the strength of the sandstone were also found to be important factors.

Surface subsidence measurements conducted over the two new districts that employed 700-foot-wide panels were in very good agreement with those predicted by the finite element models. Seismic monitoring over the two mining districts that employed 700-foot-wide panels confirmed the reduction of one order of seismic magnitude when compared with those measured over the 1,000-foot-wide panel district.

## REFERENCES

ABAQUS, (2013). Theory Manual, Version 6.13.

Gilbride, L. and Hardy M. (2004). "Interpanel Barriers for Deep Western U.S. Longwall Mining." *Proceedings of the_23rd International Conference on Ground Control In Mining*, Morgantown WV, 35-41.

Hasenfus, G.J. and Su, D.W.H. (1992). "A Comprehensive Integrated Approach for Longwall Development Design." *Proceedings of the Workshop on Coal Pillar Mechanics and Design*, Santa Fe, New Mexico, 225-237.

Maleki, H. (2006). "Caving, Seismicity, and Mine Design in Four Utah Coal Mines." *Proceedings of the 25th International Conference on Ground Control in Mining*, Morgantown WV, 268-276.

Pariseau, W.G., McCarter, M.K. and McKenzie, J. (2008). "Inter-panel Barrier Pillar Study in a Deep Utah Coal Mine." *Proceedings of the 42nd U.S. Rock Mechanics Symposium (USRMS)*, San Francisco CA, 9.

Su, D.W.H. and Hasenfus, G. J. (1999). "Coal Pillar strength and Practical Coal Pillar Design Considerations." *Proceedings of the Second International Workshop on Coal Pillar Mechanics and Design*, Vail, Colorado, 155-162.

# A Case Study of a Low Overburden Longwall Recovery with Pre–Developed Recovery Entries

**John C. Stankus**, President
**Xiaoting Li**, Senior Ground Control Engineer
**Lumin Ma**, Senior Ground Control Engineer/Geoscientist
**Dakota Faulkner**, R&D/Mechanical Engineer
Keystone Mining Services, LLC, An Affiliate of Jennmar
Pittsburgh, PA

**Brad Hanson**, President
**Robert Ochsner**, Chief Mine Engineer
Signal Peak Energy, LLC
Roundup, MT

## ABSTRACT

The 3 Right pre-developed longwall recovery entry at Signal Peak Energy's Bull Mountain No. 1 mine was designed to prevent the abnormal roof conditions encountered in its first two recovery entries. Unique geological conditions, such as the low overburden of approximately 200 feet and prevalence of roof joints in the sandstone overburden, contribute significantly to abnormal conditions during longwall recovery. The 3 Right recovery entry was 42 ft wide and developed in two stages, 21 ft wide in each stage. The entry roof was reinforced with steel wire mesh/non-metallic recovery mesh, high-capacity primary bolts and cables. After all the support was installed, the entry was completely backfilled with specially designed, cuttable, low-density cement. The roof bolting and backfill design were based on current practices in this mine and successful practices in other mines in the U.S. and Australia. Extensive instrumentation was installed in the recovery entry for continuous monitoring of load transfer as the face approached and cut into the recovery entries. The support design was completely successful with a smooth cut-through on January 29 and 30, 2014, significantly reducing the shield recovery time and meanwhile protecting the safety of miners. Based on actual observance and practices of the 3 Right recovery entry, recommendations on improvement and modifications of roof support for 4 Right recovery room are presented.

## GEOLOGICAL AND MINING CONDITIONS OF THE RECOVERY ENTRIES

Bull Mountain Mine No. 1 of Signal Peak Energy, LLC is located 30 miles north of Billings, Montana, and currently mines bituminous coal from the Mammoth coal seam. The mine employed a conventional recovery entry in Panel #1 and pre-developed recovery entries in Panels #2 and #3 (Figure 1). The typical mining and geological conditions are as follows:

### Overburden Depth

The overburden above the Mammoth coal seam in the #1-#4 Right recovery areas is approximately 200 ft. This low cover, in combination with specific roof geological features (especially the prevalent roof joints), constitute unique ground movement characteristics when the longwall face advances into the recovery entry if no sufficient roof support is installed.

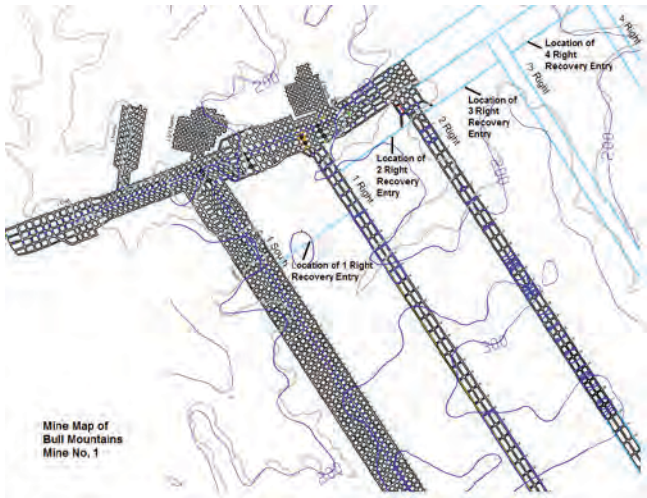



**Figure 1. Location of #1 - #4 Right recovery entries and overburden depth contour.**

### Typical Roof Lithology

The Mammoth seam has an average thickness of 10 ft, and its roof consists of shale, siltstone/sandstone and rider coal (Rehder seam). The shale thickness averages 2.6 ft, and sandstone/siltstone 25.8 ft. The immediate floor consists mainly of shale and sandstone/siltstone. The thickness of floor shale averages 0.7 ft, sandstone/siltstone 12.4 ft. Shown in Figure 2 is a typical stratigraphic column.

### Sandstone Jointing

The sandstone joint set striking at 060 deg parallels the most widespread MSHA (Mine Safety and Health Administration) photo-lineaments, and appears to be most persistent over the entire mine property (Agapito & Associates, Inc., 1988). Average joint spacing for the 060° striking set is approximately 20 ft. The longwall face orientation is parallel to the 060° strike joint set in

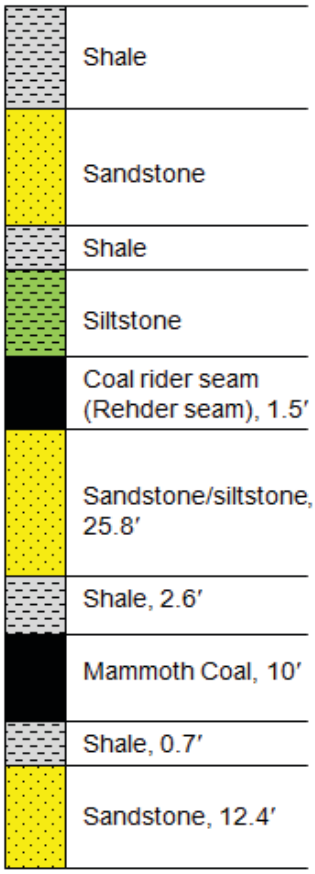



**Figure 2. Typical stratigraphic column (not to scale).**

order to minimize sandstone cantilever overhang distances and minimize frontal abutment stress during longwall retreat.

### Longwall Roof Cavability and Abutment Stresses

During longwall retreating from the set-up entry, roof conditions in the face were normal. As observed underground, the roof normally caves periodically after shields move outby approximately 70 ft. Also, the frontal and side abutment stresses normally are very low.

### Shield Capacity

Generally, the face width is 1,250 ft, and 181 line shields and 8 gate shields are used with respective ratings of 1,130 and 1,260 tons. The respective set densities are 6.9-7.2 tons/ft$^2$, and 7-7.5 tons/ft$^2$.

## ROOF CONDITIONS AND CAUSES OF ABNORMAL CONDITIONS IN 1 RIGHT AND 2 RIGHT RECOVERY ENTRIES

The mining height is approximately 10 ft. Overburden depth ranges from 200 ft–260 ft. In 1 Right, a 20 ft-wide conventional recovery was attempted, but ended up being 12 ft wide measuring from shield tips to the outby rib. Additional wood cribs were installed reducing the entry to 9 ft. The pre-developed 2 Right recovery entry was 30 ft wide, with three rows of Φ36 in/Φ24 in diameter, cuttable, pumpable cribs within the recovery entry and one row of Φ30 in diameter, non-cuttable, pumpable cribs on the outby pillar side. Based on underground examinations and principles of roof rock movement characteristics of longwall mining, the roof conditions are analyzed.

### 1 Right Recovery Roof Conditions

Shown in Figure 3a and Figure 3b are the roof conditions in the 1 Right recovery. The angled roof shear was 5 - 9 degrees from the vertical. The broken rock reached a height of approximately 20 ft above the roof line.



**Figure 3a. Roof conditions in 1 Right recovery area showing angled shear due to rock rotational movement.**



**Figure 3b. Roof conditions in 1 Right recovery area showing broken roof rock applying significant loads on shields.**

***Causes of Abnormal Roof Conditions***

*(1) Roof Rock Movement Characteristics of Longwall Mining*

Shown in Figure 4 are the roof rock movement characteristics behind and above the shields in the 1 Right recovery entry. Due to the fact that the orientation (N060E) of the major jointing set in the roof sandstone/siltstone parallels the face line, the roof caved easily after the shields moved outby, and a cantilever of rock was formed above the shields. The cantilever beam rotated with a pivot point at the outby rib line, and applied additional load on the shields. Over time, the rotational movement of the cantilever beam induced an angled shear face near the outby rib line, which eventually broke if sufficient supplemental and/or standing support was not installed.

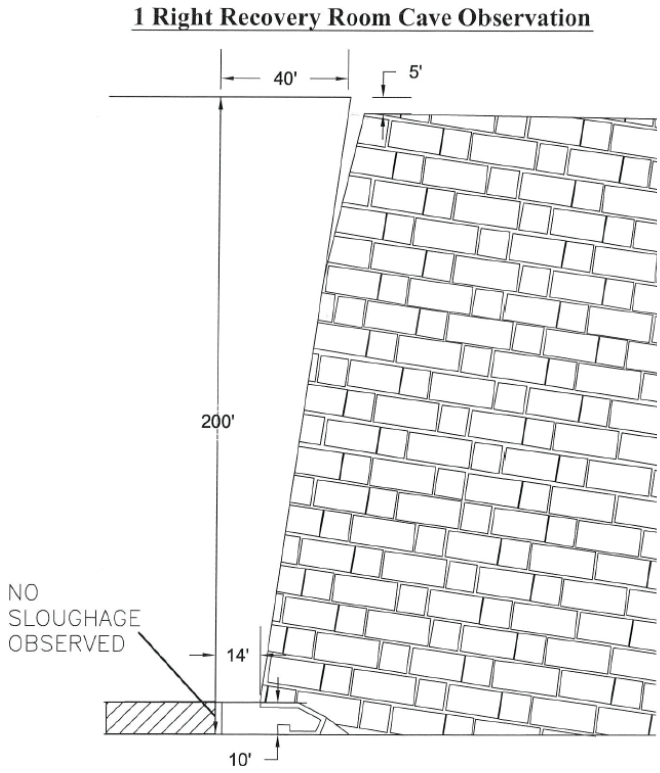



**Figure 4. Roof rock movement characteristics behind and above shields.**

*(2) Surface Subsidence Features*

Generally, there are three zones of movement in the overburden strata associated with subsidence: (1) fragmented (or caving) zone, (2) fractured zone, and (3) continuous deformation zone. The fractured zone can be as high as 30-50 times the seam thickness. The overburden depth in the 1 Right recovery face area was 200 ft–260 ft, and the mining height 10 ft. Therefore, the observed surface fractures (in the fractured zone) were induced by underground longwall mining.

**2 Right Recovery Entry Roof Conditions**

Shown in Figure 5a and Figure 5b are the roof conditions in the 2 Right recovery entry and face. Approximately 24in of roof convergence was measured in the recovery entry after the fender pillar yielded. The fender pillar refers to the coal between the longwall face and recovery entry. Prior to this convergence, large pieces of rock fell in front of and above the shield tips, which significantly slowed down the movement of the longwall face. After the initial convergence, the roof did not deteriorate any further.



**Figure 5a. Roof conditions in 2 Right recovery entry and face showing significant roof convergence after the fender pillar yielded.**

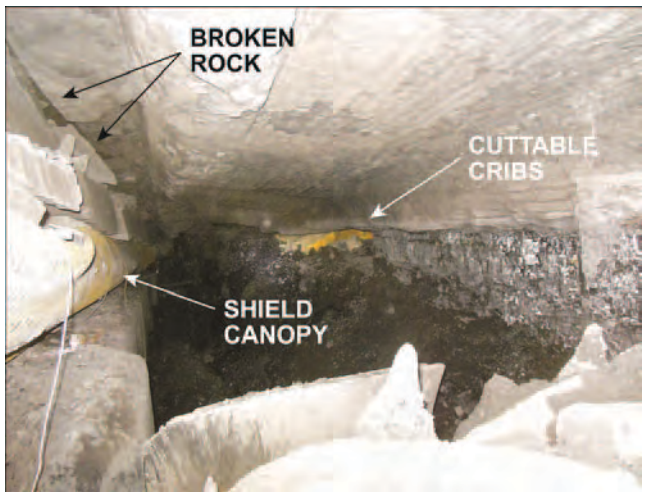



**Figure 5b. Roof conditions in 2 Right recovery entry and face showing broken roof rock applying significant loads on shields.**

***Abnormal Roof Conditions***

(1) Load Transfer to Outby Pillar and Shields a fter the Fender Pillar Yielded/Failed:

Shown in Figure 6 is the load transfer mechanism when the fender pillar yields. Load is transferred to the outby pillars through the pumpable cribs, and to the face shields. In 2 Right, on the tailgate side, the fender pillar began to yield when its width was approximately 15 ft, and completely yielded at 10 ft. In contrast, the fender pillar on the headgate side stayed stable when its width

was 15 ft, and only began to yield when it narrowed to 7 ft. This can be attributed to: (1) roof loading condition in the tailgate side (two gobs) is much worse than that in the headgate side (one gob), (2) a higher seam height of 11 ft on the tailgate side as compared to 9 ft on the headgate side, and (3) the overburden on the tailgate side was higher at 250 ft, versus 200 ft on the headgate side.

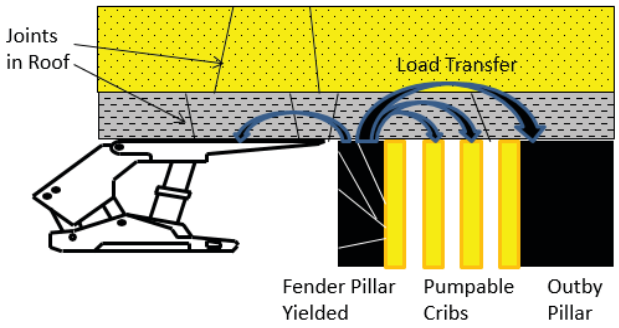



**Figure 6. Load transfer mechanism when the fender pillar yielded.**

(2) Prevalent Roof Joints:

The prevalent joints in the roof caused the sandstone to break in large pieces in front of and above the shield tips a fter load transfer occurred, inducing significant load on the shields.

(3) Face Advance Delay Due to Installation of Recovery Mesh:

Due to the MSHA requirements for recovery mesh over the shields, face advance was delayed for a period of time for installation of the recovery mesh, which allowed the roof to deteriorate and significant loading to occur.

***Shield Interaction with Abutment Load and Recovery Room Support***

The weight transfer initiated at the tailgate and progressed to the headgate. During the load transfer process, the abutment load distributed to the shields and the face. Installation of the roof mesh necessitated the face shutting down to unroll and reattach the mesh across the face. The slow advance rate, slowed caving behind the shields, and face roof conditions deteriorated. Subsequent to the weight transfer, many shields became "iron bound." The recovery work continued, but many of the shields had to be blasted under the toes to gain some "leg", i.e. hydraulic ram extension. Convergence continued as the shields were being advanced and the remaining yielded fender was mined. Roof conditions on the face and recovery chutes further deteriorated. Convergence on some of the standing support in the recovery entry measured in excess of 2 ft. In order to control the roof conditions, an 8-ft-thick pack wall, constructed of 1,000 psi concrete material, was installed along the outside rib of the recovery entry. After installation of the pack wall, roof convergence significantly decreased. As a result of the blasting, it was necessary to mine some floor to obtain a level surface. After establishing a level floor, shields were extracted. During shield recovery, no weight transfer was observed on the "walker" shields. Due to the excessive loads, many of the standing supports in the recovery room yielded and/or failed. However, the installed roof support (bolts, cables, trusses, roof channels, etc.) did not fail and provided effective support.

## ROOF SUPPORT DESIGN AND CELLULAR CONCRETE BACK-FILL OF 3 RIGHT RECOVERY ENTRY

The 3 Right recovery entry was 42 ft wide and was developed in two stages: (1) first the inby 21-ft-wide section, and (2) the outby 21-ft-wide section (Figure 7). The inby section was completely bolted along with steel wire mesh, and then the recovery mesh was installed. This section was then completely backfilled with the cuttable low-density concrete material. The outby 21-ft-wide section was then developed, bolted, wire meshed and completely backfilled. The function of each component of the support system is detailed as follows:

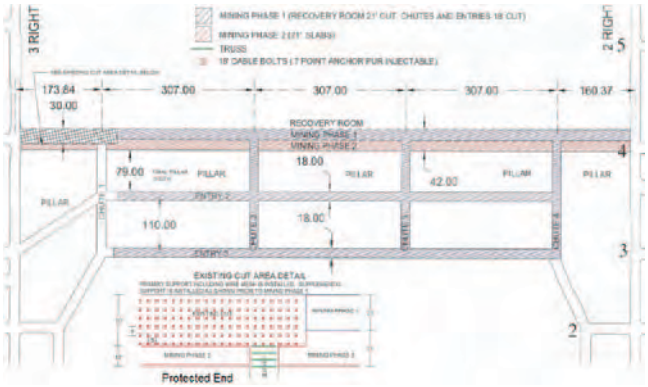



**Figure 7. Mining sequence and supplemental support in the protected end.**

### Primary and Supplemental Support

A 5 ft × 0.804 in J-Bar, grade 75, non-tensioned, fully-grouted bolt-on 4 ft × 4 ft centers is used as primary support, along with wire mesh in the recovery entry. The minimum yield and tensile strength of the grade 75 × 0.804 in J-Bar is 42,081 lbs and 50,700 lbs, respectively. As supplemental support, 25-ft and 16-ft-long, fully-grouted, 62-ton capacity, 1.10-in-diameter cable bolts along with a 20 ft, T3 roof channel were installed. To reinforce the outby rib, a roof/rib angled channel along with two, 5 ft × 0.80 in J-Bar, grade 75 bolts were installed on spacing every 4 ft. In the transition zone between Phase 1 and Phase 2, two cross-installed cables were installed to reinforce the roof beam (Figure 8). In addition, three rows of 5/-in-diameter wire ropes were installed on the roof to attach the recovery mesh.

In the chutes, two rows of 25-ft-long fully-grouted, 62-ton capacity cable bolts were installed along with a 30-ton cable truss system as supplemental support.

### Calculation of Roof Reinforcement Density Index (RDI)

The RDI includes all the intrinsic support elements, such as primary bolts and supplemental cables. The quantitative rating is obtained by determining the load capacity of each element per unit area of roof support and multiplying by the element length. Where multiple types of support are used, the ratings for individual supports are summed. The RDI units of psi× ft are converted to mega-pascals (MPa), so it can be compared against

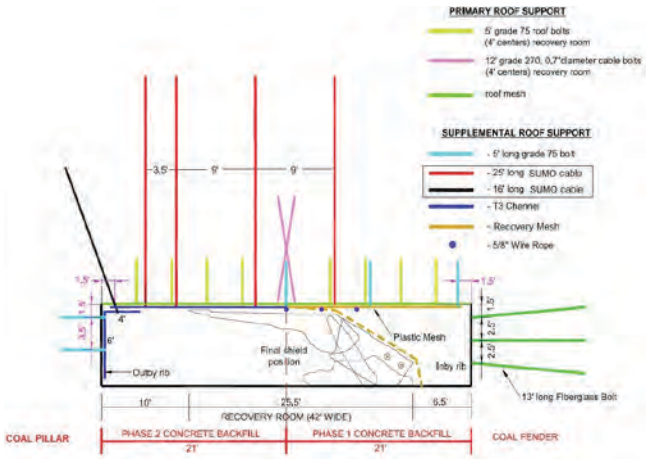



**Figure 8. Typical primary and supplemental roof support in 3 Right recovery entry.**

the NIOSH (National Institute for Occupational Safety and Health, 1998) database.

The rating for primary bolts ($RDI_p$) is:

$$RDI_p = \frac{42{,}081 \text{ lbs} \times 11 \times 5'}{42' \times 4' \times 144 \ psi/psf} \times \frac{0.3048 \ m/ft}{145 \ psi/MPa} = 0.20 \ MPa \cdot m$$

The rating for supplemental bolts ($RDI_s$) is:

$$RDI_s = \frac{[62 \ ton \times (4 \times 25' + 16') + 40 \ ton \times 2 \times 12'] \times 2{,}000 \ lbs/ton}{42' \times 4' \times 144 \ psi/psf} \times \frac{0.3048 \ m/ft}{145 \ psi/MPa} = 1.42 \ MPa \cdot m$$

Therefore, the RDI value for the proposed roof support plan for the recovery entry is 0.20 + 1.42 = 1.62 MPa·m. Note that the RDI index calculated for this case does not take into account the additional surface and rib control achieved by using wire mesh, recovery mesh, roof/corner channels and rib bolts.

**Calculation of Standing Support Density (SSD)**

By definition, the SSD value is calculated for per-unit area of the proposed 3 Right recovery room. The entire recovery room was filled with cuttable concrete with an ultimate strength of at least 800 psi, or 5.5 MPa; therefore, the SSD value is 5.5 Mpa. Listed in Table 1 are the parameters for the 3 Right recovery room, 2 Right recovery room and 11 failure cases from the 130 recovery room case study database (NIOSH) (Oyler et al., 1998). The parameters include overburden depth, CMRR, RDI, SSD and shield capacity. The 11 failure cases in the US, Australia and South Africa include six recovery rooms with weighting-type failure and five recovery rooms with roof fall failure. By comparing the data in Table 1, the designed roof support plan for the 3 Right recovery entry is very conservative in terms of RDI, SSD, CMRR, and shield capacity values.

**Low-Density Concrete Backfill and Ventilation**

Due to the fact that floor elevation dips from tailgate to headgate, bulkheads were built and low-density concrete was pumped from headgate to tailgate through surface boreholes (Figure 9). Backfill rates are 800 cubic yards or less, and no more than two feet fill depth per zone per 12 hours a day, then 12 hours of initial curing. Backfill cement density was continuously monitored. Test samples of the backfill cement were taken every hour of pumping, 20% of samples were submitted and tested by a certified laboratory after curing at least 28 days, and a minimum unconfined compressive strength (UCS) of 800 psi was required.

Inspections to confirm full contact of the cement to the roof was performed using boreholes and cameras along with witness pipes installed at the top of the forms and bulkheads. Observation of the Phase 1 backfill contact to the roof were made during Phase 2 mining. If voids were encountered, they were filled with polyurethane (PUR). Mining would not continue until the PUR was cured with a minimum UCS strength of 800 psi.

Ventilation was provided across the top of the entire backfill until the final lift was poured and the backfill was completed. A minimum air flow rate of 6,000 CFM was maintained.

## 3 RIGHT RECOVERY ENTRY CUT-THROUGH AND POST-ANALYSIS

The 3 Right recovery entry was successfully cut-through on January 29 and 30, 2014 without any sign of roof/rib cutter or significant loading. The panline and shields were completely recovered by February 12, and face roof conditions remained stable during the entire recovery process.

**Underground Examination**

The mining height in the face was approximately 11 ft, including 9 ft of coal seam and 2 ft of floor rock. The concrete was in complete contact with the roof, and appeared stronger than coal due to its lack of cleats and fractures. No roof/rib sloughage or loading was observed on the face. This condition would indicate that the stress was completely controlled by the pre-installed roof/rib support system (bolts, cables, steel channels, mesh, etc., see Figure 10). Fiberglass bolts were installed in the middle of the concrete with a row spacing of 6 ft for rib control and perpendicular to the face as a horizon indicator for the shearer. No floor heave was observed on the face. The roof strata caved easily behind the shields; also, the pre-installed non-metallic recovery mesh was observed lying down perfectly behind the shields (Figure 11).

Shown in Figure 12a and Figure 12b are the views of chutes #1 and #2 from the face when the concrete was completely cut out. A 1- to 2-ft-thick portion of concrete was left on the outby pillar rib. No indication of stress or roof/rib sloughage was observed on the face or in the chutes after the cut-through. The concrete/coal pillar corners remained sharp with absolutely no signs of pressure.

**Shield Leg Pressure Monitoring Results**

Shown in Figure 13 are the shield leg pressure output data within the last 63 passes inby the recovery entry versus the baseline shield leg pressure output data. A time interval of 27 hours existed

Table 1. Relevant parameters for recovery room.

| Failure type /parameter | Mine location, country/state | Overburden depth, m (ft) | CMRR | RDI, MPa·m | SSD, MPa | Shield capacity, metric ton |
|---|---|---|---|---|---|---|
| Major overburden weighting | US/PA | 220 (720) | 40 | 0.88 | 0.0 | 635 |
| | US/CO | 140 (460) | 35 | 0.62 | 0.3 | 590 |
| | AUS/NSW | 275 (900) | 45 | 0.0 | 0.0 | 617 |
| | AUS/QLD | 190 (620) | 50 | 0.76 | 0.1 | 726 |
| | S. Africa | 70 (230) | 35 | 0.55 | 0.0 | 327 |
| | US/AL | 610 (2,000) | 47 | 0.15 | 0.2 | 590 |
| Face break or fall | US/MD | 190 (620) | 40 | 0.33 | 1.2 | 599 |
| | US/AL | 610 (2,000) | 57.5 | 0.15 | 0.0 | 590 |
| | US/AL | 610 (2,000) | 57.5 | 0.15 | 0.1 | 590 |
| | US/AL | 610 (2,000) | 68 | 0.32 | 0.2 | 590 |
| | S. Africa | Not Available (N.A.) | N.A. | N.A. | N.A. | N.A. |
| Parameters of 2 Right recovery room | US/MT | 67 (220) | 59 | 0.99 | 0.34 | 1,025 (line shield) or 1,143 (gate shield) |
| Parameters of 3 Right recovery room | US/MT | 61 (200) | 59 | 1.62 | 5.5 | 1,025 (line shield) or 1,143 (gate shield) |

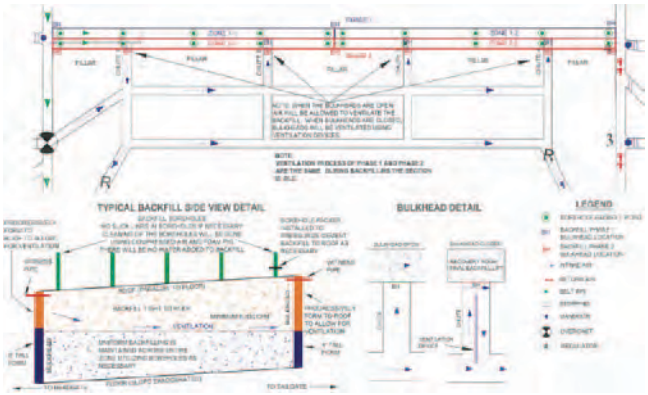



**Figure 9. Low-density concrete backfill and ventilation.**

between two loading events, which refer to the increases of shield leg pressures. When the coal fender narrowed down to 6 ft at 8:00 a.m. on January 29, 2014, some shield leg pressures increased to greater than 6,800 psi, and the shields yielded. These shield leg pressures returned back to normal when the roof rock caved behind the shields, indicating a pressure release.

Also, when only a 4 ft thickness of concrete remained at 11:00 a.m. on January 30, 2014, and the shields were in the final position, some shield leg pressures were larger than 6,800 psi, and the shields yielded. This indicated that most of the load on the concrete transferred to the outby pillars, and part of the load to the face shields. These shield leg pressures returned back to normal again when the roof rock caved behind the shields. This time period of shield yielding seemed relatively longer than the first time, probably due to the larger roof overhang between the canopy



**Figure 10. Exposed bolts, channel, and steel mesh.**

tip and outby concrete/coal pillar when the shields were in final position ready for retrieval.

Moreover, shield pressures indicated that the shields in the middle and tailgate side of the face incurred much higher leg pressures than those on the headgate side.

### Shield Convergence Measurements

Shown in Figure 14 is the shield convergence versus shield number and date. The chart indicated that (1) as the time passed when the shields sat at their final position, the shield convergence typically became larger, with a maximum value of 3.5in on shield #120 measured on February 9, and (2) the shields in the middle and



**Figure 11. Recovery mesh (yellow) laid down behind the shields.**



**Figure 12a. Views of Chutes #1 and #2 after cut-through of the recovery entry in chute #1.**

tailgate side of the face incurred larger convergences than those at headgate side of the face. This may be due to the fact that the loading condition, because of gobs on both sides, was higher than the headgate side (one side gob, other side solid panel).

### Surface Subsidence Measurements

Shown in Figure 15 are the measured surface subsidence contours. Five feet of surface subsidence was measured 210 ft inby the 3 Right recovery entry. The surface subsidence values decrease toward the recovery entry, with 1 ft of surface subsidence directly above the middle of the recovery entry.



**Figure 12b. Views of Chutes #1 and #2 after cut-through of the recovery entry showing chute #2.**

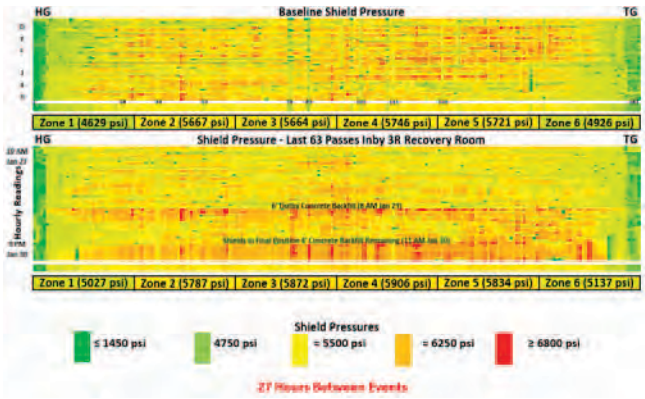



**Figure 13. Shield leg pressure graphs.**

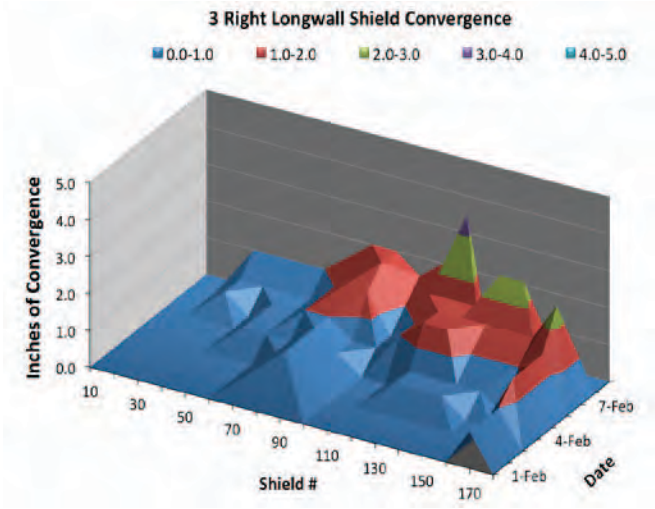



**Figure 14. Shield convergence measurements in a 3-D chart.**

### Load Transfer Mechanism

Shown in Figure 16 is the load transfer mechanism when the fender yields. Load is transferred to the solid back-filled concrete, and to the face shields. When the roof rocks caved behind the

shields, the load on the shields will then be significantly reduced. The concrete with a compressive strength of 800 psi appeared stronger than the coal as observed in the 3 Right recovery face, which is effective in controlling the transferred load due to the homogeneous nature of the concrete.

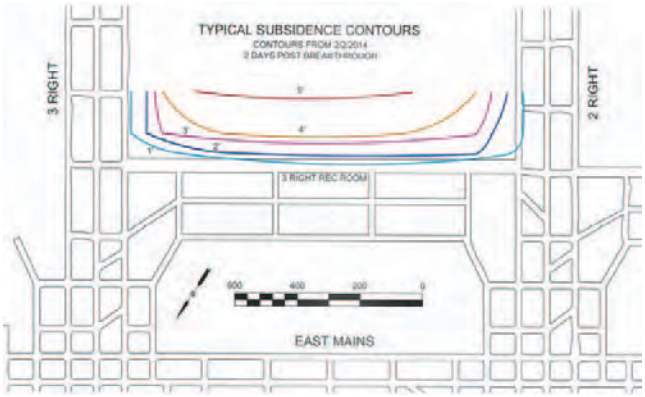



**Figure 15. Surface subsidence contours.**

### Final Shield Location

Shown in Figure 17 is the final shield location relative to the positions of supplemental cables, the T3 roof channel, the recovery mesh and the 1 ft– to 2 ft-thick concrete left on the outby pillar rib. The entire roof/rib support system sufficiently controlled the roof joints and established a competent beam structure to prevent roof/rib cutter and potential roof beam rotation.

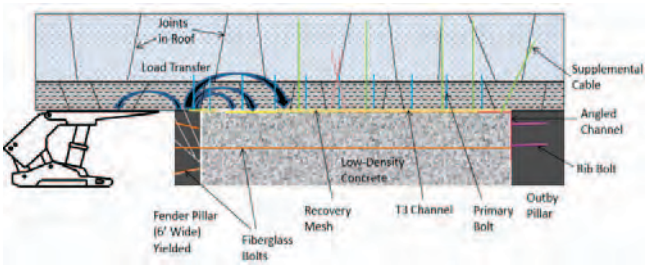



**Figure 16. Load transfer mechanism when the fender coal pillar yielded.**

## SUMMARY/RECOMMENDATION

The 3 Right pre-developed recovery entry was designed based on mining experience in 1 Right and 2 Right recovery entries and mine-specific geological and mining conditions, especially the low cover of 200 ft and joint-prevalent features. The successful cut-through of the 3 Right recovery entry on January 29 and 30 can be mainly attributed to: (1) completely backfilled low-density concrete, (2) pre-installed primary and supplemental bolts along with a T3 roof channel, steel and non-metallic recovery meshes, fiberglass bolts in the inby pillar (fender), steel rib bolts in the outby pillar, and angled roof/rib channel. This roof support system along with the pre-installed concrete fill controlled the prevalence of joints in the roof and loads induced by longwall retreating, effectively transferred the abutment stress, eliminated the time delay associated with installing recovery mesh and bolts on the face, and provided the underground miners a very safe environment for recovering the longwall equipment. The shield retrieval period of time was within 15 days.

Based on the analysis of the 1, 2, and 3 Right longwall recoveries, the support design for the 4 Right pre-developed recovery will basically be kept the same. Some possible minor changes include: (1) adjustment of the low-density concrete strength, (2) feasibility of adding an additional recovery chute, and (3) modifying the type and/or length of some bolts, especially in the transition zone of the Phase 1 and Phase 2 concrete backfill.

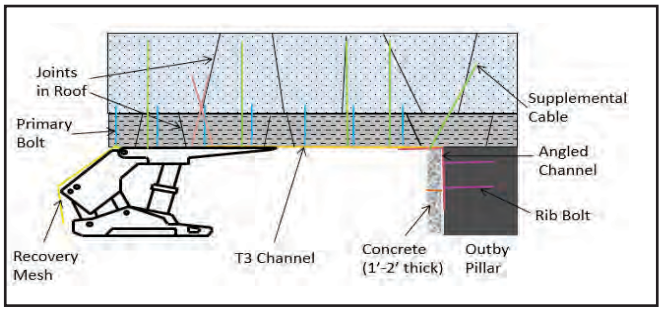



**Figure 17. Final shield position in the recovery entry.**

## REFERENCES

J.F.T. Agapito & Associates, Inc., (1988). *The 1988 Geotechnical.* Characterizations for Longwall Mining at the Mammoth Seam Bull Mountain, Montana.

Oyler, David, et.al., (1998). "International Experience with Longwall Mining into Pre-Driven Rooms." In: *Proceedings of the 17th International Conference Proceedings on Ground Control in Mining, Morgantown, WV.*

# Sandy Creek Waterfall—Case Study of Successful Management of the Potential Impacts of Longwall Mining on a Sensitive Natural Surface Feature

**Richard V Walsh**, Manager Subsidence Engineering
Bhpbilliton Illawarra Coal
Wollongong, Australia

**Bruce K Hebblewhite**, Professor of Mining Engineering
University of New South Wales
Sydney, Australia

**Gang Li**, Principal Subsidence Engineer
Nsw Dept of Industry and Investment
Maitland, Australia

**Ken W Mills**, Senior Geotechnical Engineer
Strata Control Technology
Wollongong, Australia

**Michael A Nicholson**, Principal
Michael Nicholson Consulting Pty Ltd
(Formerly BHP Billiton Illawarra Coal)
Wollongong, Australia

**James Barbato**, Subsidence Engineer
Mine Subsidence Engineering Consultants
Sydney, Australia

**Peter J Brannon**, Manager, Planning
BHP Billiton Illawarra Coal
Wollongong, Australia

## ABSTRACT

BHP Billiton Illawarra Coal operates Dendrobium Mine in an area 10-20km west-northwest of Wollongong in the Southern Coalfield of New South Wales, Australia. The mine recently completed longwall mining in Area 3A adjacent to an overhanging rock feature known as Sandy Creek Waterfall, which had been identified as a significant, and potentially sensitive natural surface feature of the environment. This waterfall lies within the Sydney drinking water catchment area, in a surface terrain of variable topography where non-conventional subsidence behaviour such as valley closure, and far-field horizontal movements are known to occur, over and above conventional subsidence responses to mining. As a part of the conditions of approval to mine, Illawarra Coal undertook to protect the waterfall and the section of Sandy Creek immediately upstream of the waterfall from the effects of longwall mining using an innovative management process and an array of very high resolution monitoring systems.

This paper outlines the type of non-conventional subsidence effects that can occur; the range of different monitoring regimes adopted in response to such effects in order to develop an understanding of the valley closure phenomenon in proximity to the waterfall and provide suitable early warning data. The paper also describes the management processes that were adopted, incorporating the use of these monitoring regimes in order to successfully protect the waterfall from the valley closure effects of mining four adjacent longwall panels in close proximity to the waterfall while continuing to maximise recovery of the coal resource in the area.

The management structure adopted involved a technical committee, a steering committee, and an external independent reviewer. The technical committee was responsible for design of the monitoring systems, interpretation of the results, and making timely recommendations to the company steering committee who were then able to make informed decisions on when to cease mining each adjacent panel. The steering committee comprised Illawarra Coal management and technical personnel. Although the steering committee took advice from the technical committee, all decisions relating to mining were made by the steering committee. An external reviewer was engaged by the steering committee at the end of each longwall panel to review the results, interpretation and management decisions. This management structure was effective in successfully protecting the very sensitive structure of Sandy Creek Waterfall from potential impacts of nearby mining in the midst of active ongoing natural erosion processes.

## INTRODUCTION

Sandy Creek Waterfall lies within the Sydney Metropolitan Special Catchment Area at the point where Sandy Creek flows into the Cordeaux Reservoir. The Waterfall is approximately 20 m high and has an overhang which is 75 m long, up to 21 m deep and has a minimum thickness of less than 1 m. The overhang consists of the basal 6 m of the Hawkesbury Sandstone. The overhang has formed by preferential erosion of the softer Bald Hill Claystone which lies under the Hawkesbury Sandstone (see Figure 1).

BHP Billiton Illawarra Coal's Dendrobium Mine extracts coal using longwall mining techniques from the Wongawilli Seam below the Catchment Area. Illawarra Coal recognised the significance of the Waterfall during the preparation of the 2007 Environmental Assessment for Dendrobium Area 3. The company offset Longwalls 6 to 8 away from the Waterfall to ensure that conventional subsidence movements did not adversely impact the Waterfall and committed to:

(i) the formation of a Technical Committee,
(ii) the development of a Management Plan, and
(iii) providing flexible longwall finish lines.

The Development Consent approved the maximum footprint for mining and set specific performance criteria for the Waterfall. The Dendrobium Development Consent (2008) conditions specified that:

a) no rock fall occurs at Sandy Creek Waterfall or from its overhang;

b) the structural integrity of the waterfall, its overhang and its pool are not impacted;
c) cracking in Sandy Creek within 30 m of the waterfall is of negligible environmental and hydrological consequence; and
d) negligible diversion of water occurs from the lip of the waterfall.

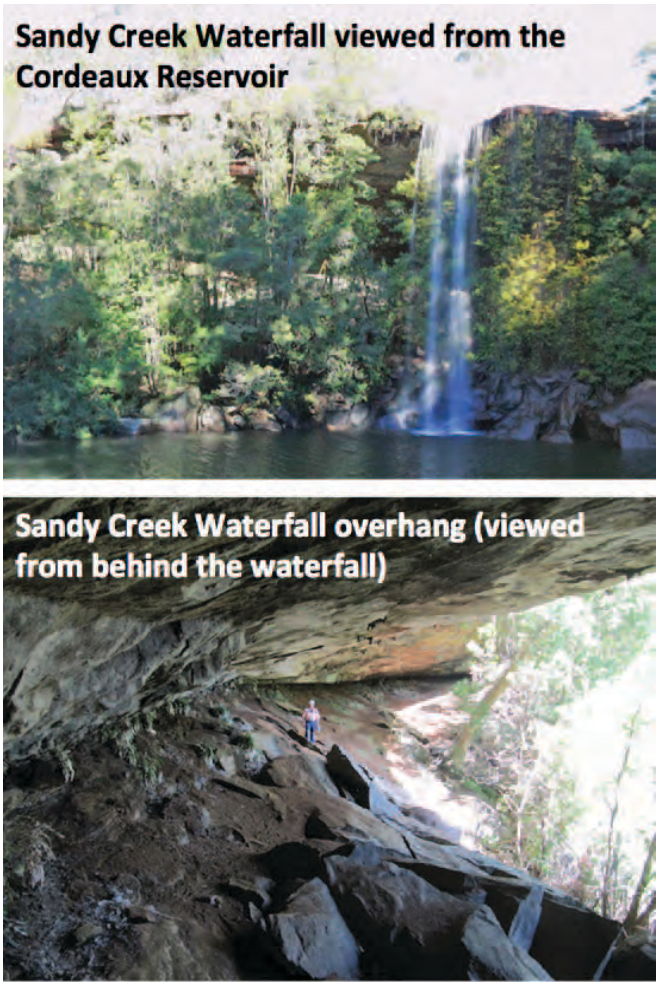



**Figure 1. Sandy Creek Waterfall viewed from the Cordeaux Reservoir (a) and Sandy Creek Waterfall overhang (viewed from behind the waterfall) (b).**

In order to effectively understand the subsidence behaviour generated by mining Longwalls 6 to 8, and the potential impact on the waterfall, and ensuring compliance with the above Consent conditions, the company installed a comprehensive array of monitoring instrumentation, both above the longwall panels and in the region of the waterfall. The site investigation and instrumentation regime consisted of: core drilling and testing; laser scanning of the cavity beneath the waterfall; in situ stress measurements plus monitoring of stress changes; conventional and far-field subsidence deformation ground surveying; high resolution valley closure surveying; micro-seismic activity; groundwater and rainfall; ground and surface temperatures; and sub-surface bedding plane shear movements using inclinometers.

Longwalls 6 to 8 were mined towards the waterfall. A planned finish line for each panel was indicated in the initial mine plans, but the actual finish line for each longwall was determined by the Management Plan, based on the regular review of monitoring results during mining. Figure 2 shows the location of the longwall panels with actual finish lines; and the various instrumentation sites relative to the location of the waterfall and the surface contours.

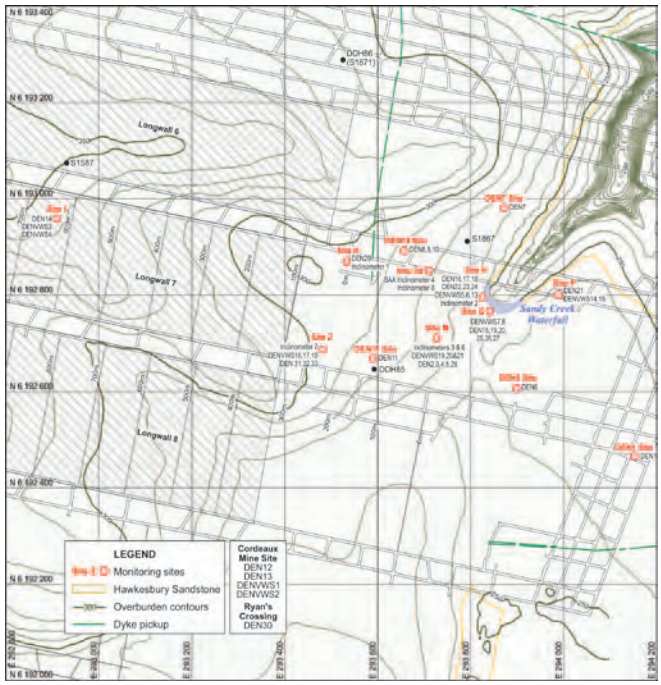



**Figure 2. Longwalls 6 to 8 relative to waterfall, surface contours and instrumentation sites.**

## SUBSIDENCE BEHAVIOUR

As a result of the irregular surface topography in the area where mining was taking place, it was necessary to take account of the expected non-conventional subsidence behaviour which occurs commonly in this region of the Southern Coalfield of NSW. NSW Department of Planning (2008) defined the conditions for both conventional and non-conventional subsidence behaviour as follows:

*The conventional or general model of surface subsidence, which finds worldwide acceptance, is based on assuming the following site conditions:*

- *the surface topography is relatively flat;*
- *the seam is level;*
- *the surrounding rock mass is relatively uniform and free of major geological disturbances or dissimilarities;*
- *the surrounding rock mass does not contain any extremely strong or extremely weak strata; and*
- *the mine workings are laid out on a regular pattern.*

*Where these conditions are not met, surface subsidence effects vary from those that would be predicted using the conventional model. Such subsidence effects are generally known as 'non-conventional'.*

Some of the commonly experienced consequences of non-conventional subsidence behaviour include: valley closure,

valley floor uplift (or upsidence), and some forms of far-field horizontal deformations – all of which can occur within the conventional "angle of draw" concept due to undermining or closely adjacent mining; but are also experienced at locations that fall well outside the typical angle of draw (25 – 35 degrees). These non-conventional phenomena are common in regions of irregular surface topography – ranging from steeply incised, near-vertical sided valleys and gorges, to gently sloping valleys and down-slopes. This type of behaviour has been widely observed and reported in Australia, but is also evident in the coalfields of Pennsylvania and West Virginia. Non-conventional subsidence behaviour is far more difficult to predict using the commonly used profile or influence function analytical and related numerical models. Experience in Australia, supported by an extensive database of subsidence behaviour, has led to a range of appropriate and reasonably high confidence level empirical prediction techniques, and improving levels of numerical modelling prediction capabilities.

Figure 3 shows data from the Southern Coalfield for valley closure magnitudes relative to the distance between longwall panel ends and valley centres.

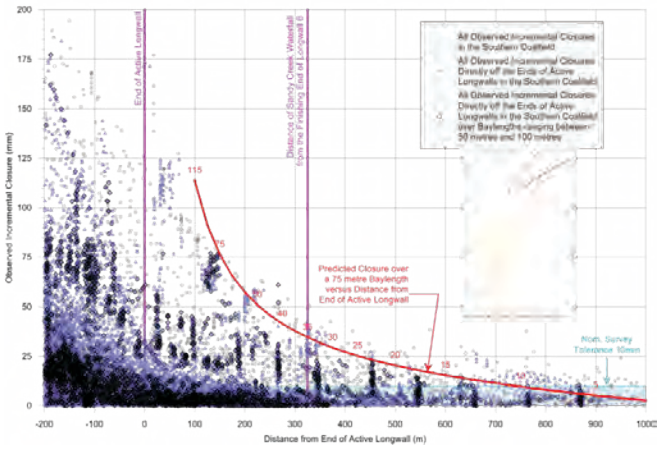



**Figure 3. Measured incremental valley closure relative to distance from longwall panels (source: MSEC, 2014).**

## MONITORING DATA

### Monitoring Instrumentation and Investigations

In 2009, a program of site investigation drilling was undertaken to determine the stratigraphy, rock

properties, and in situ stresses across the site. Overcore stress measurements and an initial batch of ANZI stress change monitoring instruments were also installed in the boreholes during this drilling program. Conventional 3D survey lines were installed to measure subsidence movements above the longwall panels and at several locations across Sandy Creek. Strain gauges were installed across a number of prominent cracks on the waterfall overhang. The temperature was also monitored at the strain gauge locations to try to compensate for surface thermal variations that were found to range from 0°C to 50°C.

In 2010, a second batch of stress change monitoring instruments was installed at two sites closer to the waterfall, named Sites G and H (see Figure 2). Vibrating wire stress change monitoring instruments were included as an independent measurement to correlate with stress changes interpreted from the ANZI strain cells and provide temperature monitoring below the ground. Two additional sites, remote from the waterfall location, were also established during this campaign to act as independent controls for the instrumentation systems. Overcoring stress measurements were made at several sites in the general vicinity of the waterfall to measure the in situ stresses in the Hawkesbury Sandstone.

During the lead up to the first precautionary stoppage in Longwall 6 it became clear that the conventional three dimensional (3D) survey lines previously installed and surveyed at the site were not sensitive enough to detect the very low level of deformation that the stress cells were indicating may be initiated. In response to this realisation and the need to instigate an alternate high resolution monitoring technique to complement the stress cell data, a network of eight high resolution one dimensional survey monitoring points was established across Sandy Creek Waterfall and the valley immediately downstream. Figure 4 shows the location of these lines overlain on an aerial photograph of the site.

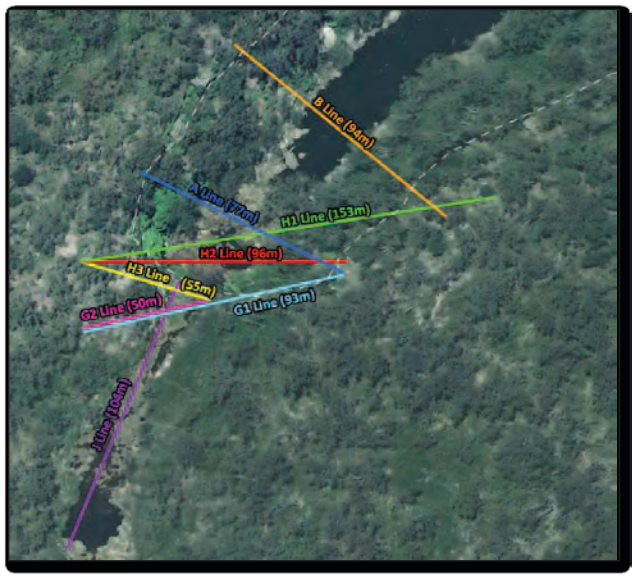



**Figure 4. Plan of location of high resolution survey lines.**

The stated precision of the new high resolution closure lines was ±1.0mm @ SD2 (~ 95% confidence interval). In practice, the observed survey data proved to be substantially more precise with results indicating long term precisions in the order of ±0.4mm @ SD2. These survey precisions were achieved by reverting to one dimensional (1D) closure lines (i.e. distance). The new survey network was established in such a way that the extremely high resolution total station instrument (Leica's TDA5005 industrial measurement total station), could be set up collinear with the measurement points being observed. This approach essentially eliminated angular inaccuracy as an error source.

A micro-seismic monitoring array was also set up in the area between the end of the longwall panels and Sandy Creek to measure mining induced micro-seismicity as mining approached.

This was used to detect both deep events associated with caving around the longwall face, and particularly looking for any shallower near-surface events which might indicate subsidence related fracturing or shearing ahead of the panel.

Following the completion of Longwall 6, the monitoring was further upgraded with additional stress change monitoring instruments; a repeat set of overcore stress measurements at Sites G and H; and the installation of several borehole inclinometers including a Shaped Accelerometer Array (SAA) at Site K that was able to record movements at 0.5m intervals over a 50m vertical section every minute. This instrument also provided a measure of the thermal gradient over the measuring section.

An additional control site, Site N, was established near Ryans Crossing downstream of the Cordeaux Dam to see if there was any evidence of natural changes remote from mining. This site included high resolution survey monitoring, an inclinometer, and a stress change monitoring instrument.

In 2012 at the completion of Longwall 7, additional instrumentation was installed including several more manual inclinometers, additional stress change monitoring, and an overcore stress measurement. The SAA inclinometer was moved to Site D2 and installed to measure two shear horizons that had been identified from earlier shear monitoring. The majority of additional monitoring was installed adjacent to Longwall 8, to measure the development of effects towards the Waterfall.

Pore pressures in the Hawkesbury Sandstone were monitored in two exploration boreholes drilled prior to any mining in the area using an array of vibrating wire piezometers. Rainfall was initially measured at several locations several kilometres from the waterfall, but an upgrade in early 2012 provided rainfall data at Sandy Creek.

A more detailed description of the monitoring investigations and analysis of results is provided by Walsh et al (2014a).

**Monitoring data analysis**

Extensive monitoring occurred across the entire array throughout the extraction of the three longwall panels. Analysis of the data was carried out using a combination of manual readings (survey lines and some inclinometers); data-logged monitoring of stress cells and some other instrumentation; and continuously logged and online downloading of other instrumentation. Walsh et al (2014a) provides a comprehensive review of the monitoring system data and an interpretation of the data with regard to a plausible hypothesis for the overall ground behaviour mechanisms – both due to mining, as well as clear evidence of a natural seasonal variation in near-surface behaviour responding to both rainfall and temperature effects, independent of any mining-induced effects.

Stress Cells - The stress cell data – both overcoring and stress change monitoring provided considerable insight into the direction of near-surface horizontal stresses existing in and around the waterfall rock structure, and the changes induced as mining from each successive longwall panel approached. This enabled the development of various plausible hypotheses regarding the state of stress in the rock mass forming the waterfall. Figure 5 is a good example of the quality of data achieved, indicating responses in the order of several megapascals, at the rear of the waterfall rock structure (Den15 cell, site G).

Micro-Seismics - The micro-seismic data was collected on-line and analysed weekly. A series of validation exercises were carried out during the investigation period to ensure the accuracy of the seismic event location – at least in plan. Small charges were let off on the surface and in boreholes, without forewarning the micro-seismic analysis team from CSIRO. In each case these events were detected and positioned on the surface plan within a reasonable (50 m) degree of accuracy, to provide confidence in the micro-seismic data. The system was effective in detecting shallow seismic events at less than 100m depth, associated with the development of subsidence. At the end of the analysis period, there were no shallow micro-seismic events detected close to the waterfall. However, unfortunately the system did not respond to the bedding plane shear that was detected by several inclinometers as mining approached the waterfall. The system was therefore deemed to be invaluable to investigate the overall rock fracturing systems ahead of a retreating longwall panel, but was not a reliable predictor of the low energy bedding plane shear deformation behaviour subsequently observed.

The two most effective monitoring systems for providing effective warning of mining-induced subsidence effects were the high resolution survey lines and the borehole inclinometers detecting shear deformation on bedding planes.

High Resolution Survey Lines - Figure 6 shows the results of the high resolution surveys. There was a gradual change evident during the approach of Longwall 6, especially on H Line - the longest of these lines. The change is less than the nominal resolution of the surveying and was therefore not considered grounds to cease mining but it is nevertheless consistent with stress increases measured by multiple stress cells. A significant increase in closure began on 25 January 2011 when Longwall 6 was at CH215m some 550m from Sandy Creek Waterfall. Similar increases in closure were observed for Longwall 7 on 12 December 2011 at CH220m and for Longwall 8 on 16 November 2012 at CH507m (equivalent to CH280m on the previous panels). In each case, these increased closures led to a decision to begin preparations to finish the longwall panels at the first available opportunity (normally the next available cut-through).

Some seasonal variation is evident in the high resolution surveying results, particularly during the finishing stages of Longwall 8. Practical issues around vegetation regrowth interfering with the line of sight and weather conditions appear to have influenced the accuracy of the measurements from time to time (which was resolved by pruning) but it is more difficult to explain the gradual increase in length of about 2mm on H Line over a period of eight months. A period of rainfall deficit occurred during this period. The opening of the valley observed may be related to this rainfall deficit either on a broad scale or at some local scale that affected the survey points.

The high resolution surveying provided the primary basis for decision-making because it clearly showed the onset of accelerated closure of the valley – when the longwall face was still over 500m distant from the waterfall in the case of Longwall 6 - resulting in final face positions approximately 350m, 400m and 500m distant from the waterfall for panels 6, 7 and 8 respectively. This onset of

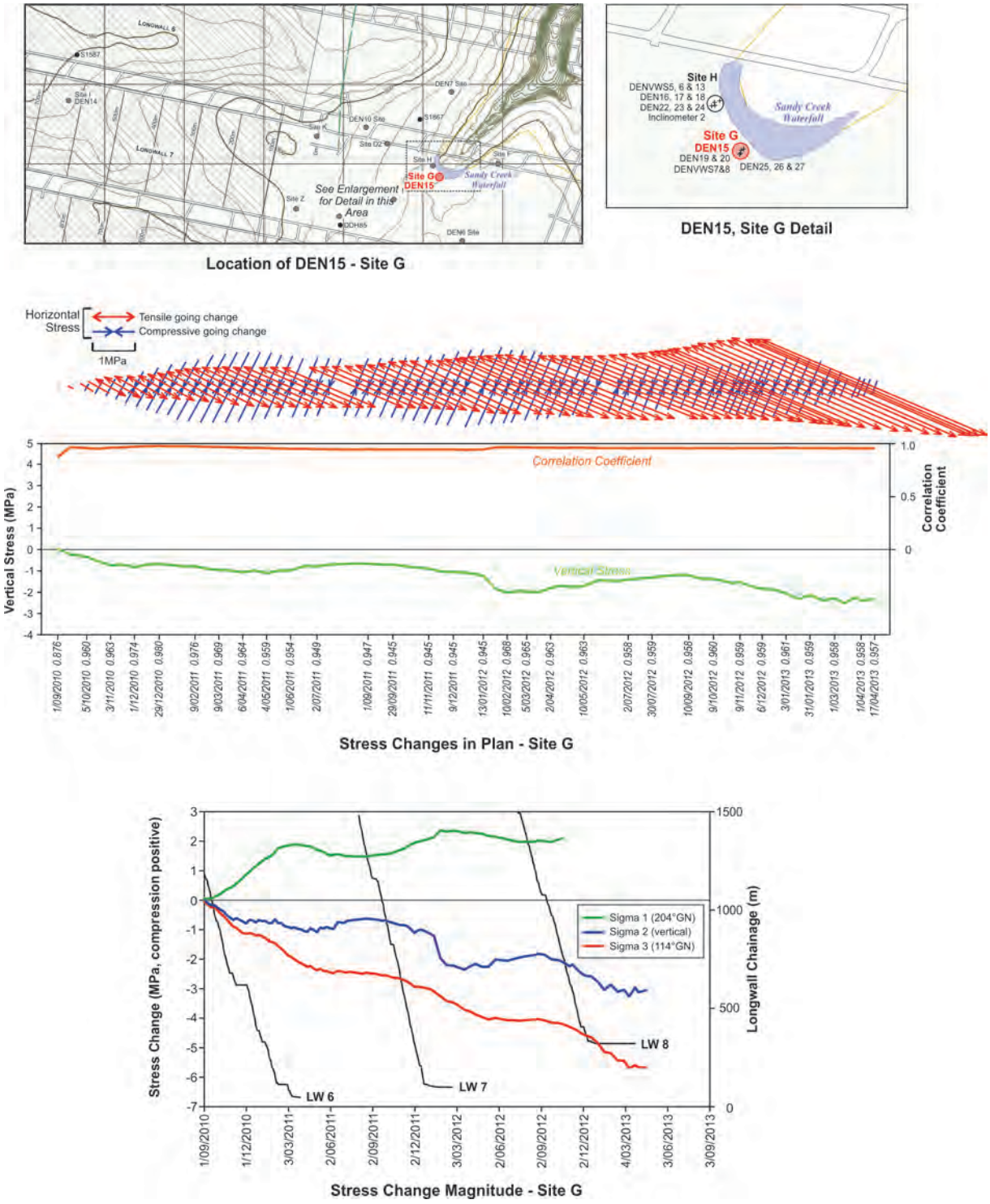



**Figure 5. Site G, DEN15 Stress Cell; Stress Change Data.**

closure is clearly well beyond a conventional angle of draw which would be less than 175m at these mining depths.

Inclinometer Data – The second very powerful tool for providing warning of increased mining-induced effects approaching the waterfall was the inclinometer data set. Inclinometers were installed in a number of boreholes in the region of the waterfall, and towards the end of panel face lines. These clearly and consistently detected bedding plane shear at several horizons. Figure 7 shows an example dataset from Inclinometer 7, taken during completion of Longwall 8, located at Site Z close to the end face positions for Longwalls 7 and 8 (see Figure 2). This siteclearly shows very distinct bedding plane shear at both 55m and 85m depth horizons.

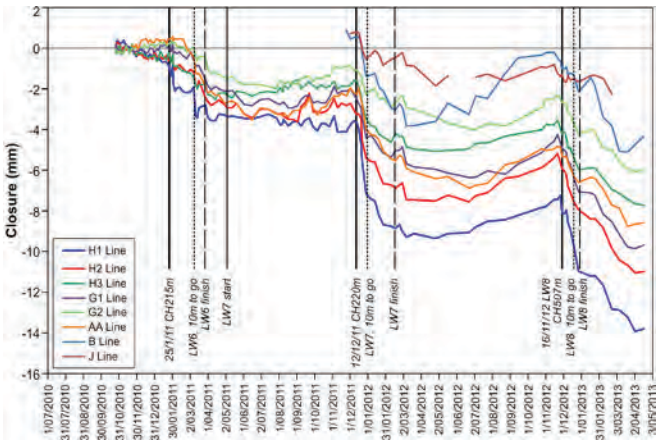



**Figure 6. High resolution closure line survey data.**

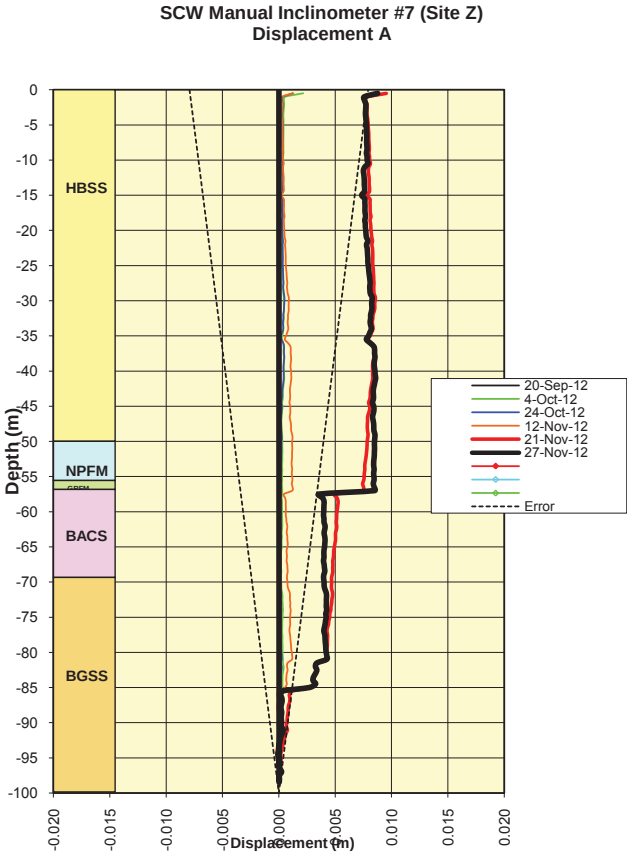



**Figure 7. Inclinometer No 7 Data; Site Z.**

Figure 8 shows two cross-sections through the region between the longwall ends and the waterfall, indicating the location of the shear horizons that were observed across multiple inclinometers. Two major shear horizons were detected. The first was located at an elevation ranging from RL311m at Site Z through to RL317m at Site K. This horizon correlates approximately with the elevation of the Newport/Garie formation at the base of the Hawkesbury Sandstone, approximately 6m below Sandy Creek upstream of the waterfall. The second is located some 20-30m deeper at an elevation between RL280m and RL290m in the upper part of the Bulgo Sandstone and seems to be split into two horizons at some of the inclinometer sites. This horizon correlates with a horizon estimated to be about 5-10m below the base of Sandy Creek downstream of the waterfall. The exact depth of the base of Sandy Creek downstream of the waterfall is difficult to determine precisely because of the boulder debris present in this area.

The two major shear horizons that have moved as a result of mining correspond to an elevation just below the floor of the adjacent valley. The direction of movement on all the inclinometers is in a downslope direction toward the valley. The approximately 30m high step in topography at Sandy

Creek Waterfall, allowing for the downstream boulder infill, correlates with the vertical separation between these two major shear horizons. This correlation is considered very significant in the context

of the mechanics of the processes that cause valley closure movements especially when the nature of the shear movements is also taken into account.

## MANAGEMENT SYSTEM

### Governance

The governance structure for the implementation and operation of the Sandy Creek Waterfall Management Plan consisted of a Steering Committee and a Technical Committee.

Steering Committee - The Steering Committee consisted of members of the Illawarra Coal Management Team including the Asset President, Dendrobium General Manager, Head of External Affairs and Head of Planning & Logistics. The Steering Committee was in a position to assess the implications of decisions on the business, regulators and customers. The Role of the Steering Committee was to:

a) Provide the resources to implement the Management Plan;
b) Endorse the Management Plan;
c) Review and assess information provided by the Technical Committee;
d) Assess the acceptability of the ongoing level of risk to the Waterfall;
e) Implement management actions to protect the Waterfall; and
f) Initiate Peer Reviews.

Critically, the Steering Committee could provide direction for the planning of the Dendrobium Mine to ensure longwall continuity and minimise the operational & reputational risk to the business.

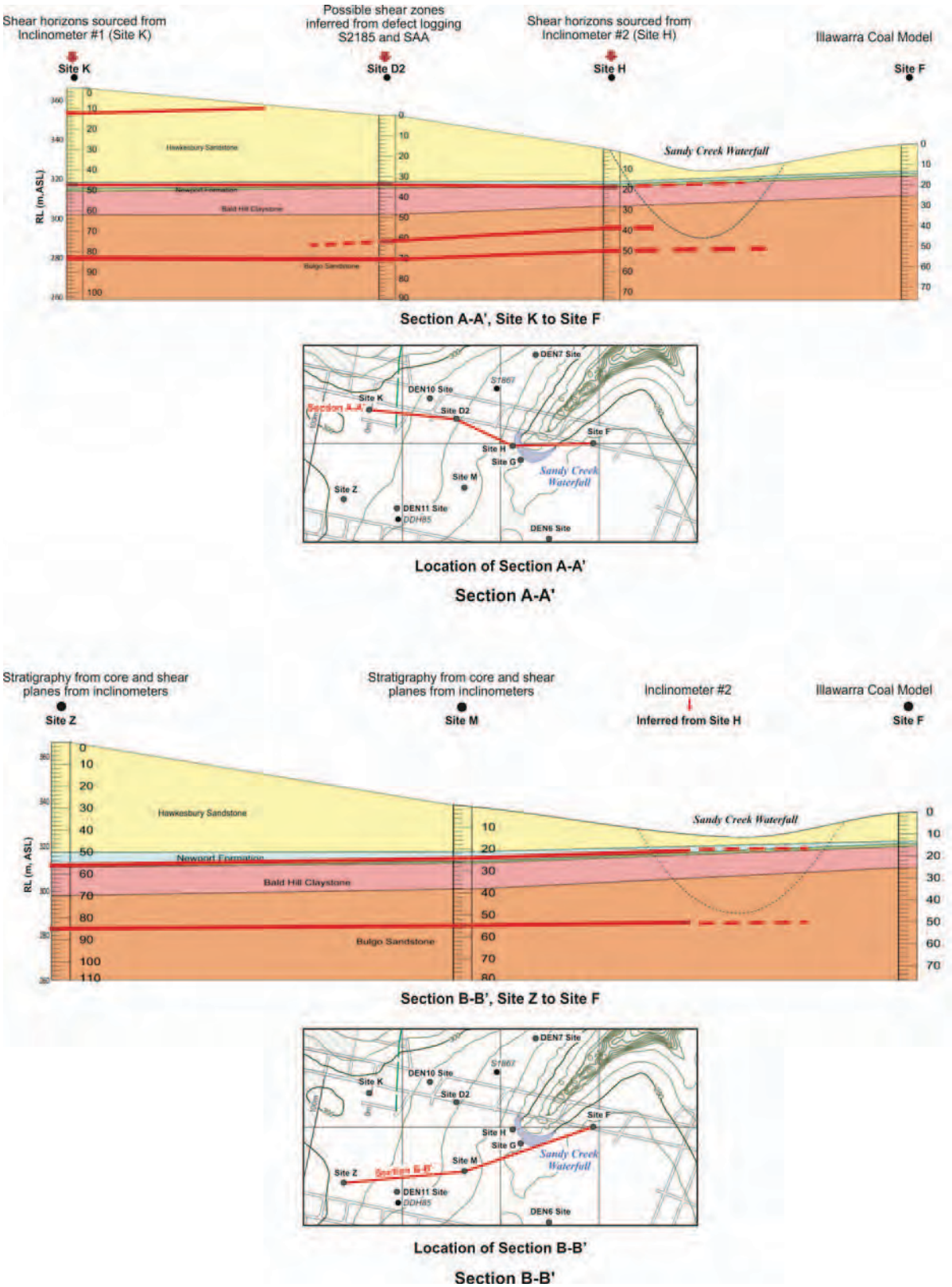



**Figure 8. Section showing multiple bedding plane shear towards the waterfall valley.**

Technical Committee - The Technical Committee formed by Illawarra Coal consisted of a group of consultants and employees with a strong geotechnical, subsidence and mining experience.

(i) Professor Bruce Hebblewhite – acting as an independent geotechnical/subsidence consultant (Head, School of Mining Engineering, University of NSW)
(ii) Dr Ken Mills – Principal Geotechnical Engineer, Strata Control Technology
(iii) James Barbato – Subsidence Engineer, Mine Subsidence Engineering Consultants
(iv) Richard Walsh – Manager Subsidence Engineering, Illawarra Coal
(v) Michael Nicholson – Manager Survey, Illawarra Coal
(vi) Peter Brannon – Planning Manager, Dendrobium Mine, (including his predecessors in this role - Sean Wood & David Thomason.)

Dr Gang Li, the Principal Subsidence Engineer from Department of Trade Investment, Regional Infrastructure & Services attended meetings as an "observer".

& Assoc.) and Illawarra Coal Resource & Exploration Department in aspects of micro-seismic monitoring, geology, drilling & installation of monitoring equipment, numerical modelling and communications systems.

**Management Plan**

Management Plans are a common tool for managing potential impacts from subsidence, for protection of built features including major infrastructure such as roads, railway lines, dams etc. The benefit of management plans for built features is the ability to define the "strength" (i.e. allowable capacity) of the structure and assess the likelihood of adverse impact due to subsidence movements. The ability to define the strength of the structure is fundamental to designing and implementing mitigation, monitoring and determining the acceptable levels of all subsidence effects. Understanding the "strength" and the appropriate factor of safety enables Triggered Action Response Plans (TARPs) to be developed which are a fundamental tool in built feature subsidence management plans.

| Monitoring Dimension | Measurement | Level 1<br>Condition after Longwall 7 | Level 2<br>Measurable change in observations beyond Level 1 condition (ie: above measurement tolerances) | Level 3<br>Definitive change in the rate of observations beyond Level 2 condition |
|---|---|---|---|---|
| Closure | Primary High Resolution Closure Lines G1, H2 & H3 | No measurable movement beyond end LW7 steady state | Repeatable Measurable Movement consistent with low level mining influence | Increasing rate of movement |
| Shear Movement | Inclinometers I1, I2, I4 , I5 & I6 | No measurable movement beyond end LW7 steady state | Repeatable Movement on Bedding Planes | Repeatable shear movements observed at I2, I4 & I5 [ ie within 150m of SCW ] |
| Ground Survey | Secondary High Resolution Closure Lines A, B, H1, G2 & Strain Line J | No measurable movement beyond end LW7 steady state | Repeatable Measurable Movement | Increased rate associated with mining or Abnormal Movements |
| Stress | ANZI cells<br>VW cells | No measurable change in indicated stress beyond end LW7 steady state (excluding thermal effects) | Change in indicated stress consistent with low level mining influence (excluding thermal effects) | Change in indicated stress consistent with significant mining influence (excluding thermal effects) |
| Shallow Micro-Seismic events | CSIRO Event Location [Accuracy +/- 50m] | No events within 150 metres of SCW | Isolated events within 150m of SCW | Three or more events within 150 metres of SCW [based on stated accuracy event is >50m from SCW] |
| Visual Observation | | No visible fracturing, ecological impact or water diversion in advance of Longwall face position | Visible fracturing, ecological impact or water diversion in advance of Longwall face position & beyond 150 metres of SCW | Visible fracturing, ecological impact or water diversion within 150 metres of SCW |
| Event Frequency | Scope | Level 1 | Level 2 | Level 3 |
| Measurement | Non real time information | Monthly till 1000m ex SCW then weekly | Twice weekly | Daily |
| Review | Technical Committee | Monthly | Weekly/Mid Pillar | Twice weekly |
| TC Reporting to SC | Technical Committee | Monthly | Weekly/Mid Pillar | Twice weekly<br>Notification of any Level 3 Status within 24 hours of review, including summary status report |

**Figure 9. Longwall 8 Decision Matrix.**

The Role of the Technical Committee was:

a) Recommend and implement the site investigations;
b) Recommend and implement the monitoring;
c) Develop the management plan including the Decision Matrix;
d) Review and interpret the results of the monitoring required in the Plan;
e) Assess the status of the waterfall monitoring as per the Decision Matrix;
f) Advise the Steering Committee of the interpretation of monitoring results with respect to the status of the waterfall.

The Technical Committee was formed in 2009 during the extraction of Longwall 5, the last longwall in Dendrobium Area 2 which was in excess of 900 m from the Waterfall. The Technical Committee received additional technical support as required, including Dr. Xun Luo (CSIRO), Dr. Peter Tune (SIGRA), John Doyle (Geosensing), Mike Coulthard (Coulthard

The conundrum for Sandy Creek Waterfall, as with many natural features, was that despite the abundance of geological and geotechnical data, the "strength" of the overhang that defines the Waterfall could not be defined. The existing stress on the Waterfall and the additional strain that the overhang could tolerate could not be defined. It was apparent from the lack of recent rock falls that the Waterfall was currently withstanding the normal cyclical environmental loading due to thermal variation and the volume of water flowing in the creek. However, as a result of this conundrum, it was cautiously assumed that no additional mining-induced subsidence effects could be accommodated.

The traditional TARP approach was determined to not be applicable, as there were no directly relevant or appropriate single parameters for which trigger levels could be set. The fundamental tool that was developed by the Technical Committee for the Waterfall Management Plan was a Decision Matrix which focussed on the identification of the onset and increase in rate of a range of

different mining-induced effects identified by each monitoring technique. Figure 9 is the Longwall 8 Decision Matrix developed by the Technical Committee.

The monitoring techniques were prioritised within the Decision Matrix. The most reliable and useful techniques used to recognise mining induced change were located at the top of the list. The preferred techniques invariably had a quick turn-around time between measurement and the availability of results. The frequency of Technical Committee meetings increased from monthly to bi-weekly teleconferences during the critical periods of extraction for each Longwall. Monitoring data needed to be updated and reproduced for review meetings. At critical times the preferred techniques were the only data sets available as the lower priority techniques took too long to process. The results of each Technical Committee meeting were reported to the Steering Committee

The Dendrobium Longwall 8 extracted an average of 50 m per week over the last kilometre of the panel. During the latter stages of each longwall the Technical & Steering Committee meetings were programmed prior to the Longwall passing each maingate cut-through. The meetings enabled the Technical Committee to determine if there was any mining-induced change at the Waterfall and hence advise on the current risk. If mining-induced change was not identified the longwall was authorised by the Steering Committee to extract beyond the cut-through. The rate of change of preferred monitoring techniques was a very useful guide for the Steering Committee as was the relationship with the trends from the previous longwalls (see Figure 6).

**Management Review**

The Technical Committee reviewed the monitoring and the Decision Matrix after the completion of each longwall. Illawarra Coal also sought additional advice from an independent geotechnical expert in a peer review role. Technical reviews were undertaken in November 2010 during Longwall 6 extraction and subsequently in May 2011, 2012 and 2013 after the completion of each longwall. The reviews focused on the Management Plan, its implementation and effectiveness, and the monitoring results. The reviews have informed the process for revising the Management Plan.

A more detailed description of the overall project management processes is provided by Walsh et al (2014b).

## CONCLUSIONS

Longwalls 6, 7 & 8 have been successfully mined in Area 3A. Longwall 8 was completed in December 2012 and fourteen months after the completion of Longwall 8 there has been no visible change to Sandy Creek Waterfall. The approved finish lines for Longwalls 6, 7 & 8 were considered to be a maximum footprint with the actual finish line determined by the Management Plan. Dendrobium adopted a conservative approach for business planning to ensure continuity between Longwalls 7 & 8, but also to Longwall 9 in the next mining domain.

With the successful implementation of the Management Plan, the Sandy Creek Waterfall was protected whilst maximising the coal resource recovered. The Management Plan was approved by the government regulator and progress reports were regularly provided to both regulators and stakeholders. The regulator approved a maximum footprint and Illawarra Coal managed the mining to meet the approved Statement of Commitments and the performance criteria. The required expertise was drawn together in the Technical Committee; and the process was controlled and managed by Illawarra Coal.

Throughout the mining of Longwalls 6 to 8, and extensive array of geotechnical and survey monitoring techniques were adopted, and a comprehensive array of high quality data was gathered. Analysis of this data provided valuable knowledge of the performance of regional ground conditions and subsidence behaviour ahead of mining, together with new insights into potential behavioural mechanisms for non-conventional subsidence in the vicinity of valleys. It also provided extensive new insights into the non mining-induced environmental behaviour of the land surface and sub-surface due to cyclical seasonal effects such as temperature and rainfall.

## REFERENCES

MSEC, (2014). Mine Subsidence Engineering Consultants (J Barbato) – Personal communication.

NSW Department of Planning. (2008). Impacts of Underground Coal Mining on Natural Features in the Southern Coalfield - Strategic Review. Chaired by B. K. Hebblewhite (July 2008).

Walsh, R. V., Mills K .W., Nicholson M. A., Barbato J., Hebblewhite B. K., Li G. and Brannon P. J. (2014a). Monitoring of ground movements at Sandy Creek Waterfall and implications for understanding the mechanics of valley closure movements. Mine Subsidence Technological Society – *9th Conference on Coal Mine Subsidence*, Pokolbin, NSW, Australia, 11-13 May, 2014.

Walsh R. V., Hebblewhite B. K., Li G., Mills K. W., Nicholson M. A., Barbato J., and Brannon P. J. (2014b). Successful management strategy for mining adjacent to a sensitive natural feature. Mine Subsidence Technological Society – *9th Conference on Coal Mine Subsidence*, Pokolbin, NSW, Australia, 11-13 May, 2014.

# Challenges of Room and Pillar Mining at 900 M Depths in the Czech Republic

**William J Schloemer**, Vice President - Project Director
OKD, A.S.
New World Resources
Karvina, Czech Republic

**Robert Vochta**, Head of Survey and Geology Dept
CSM Mine
OKD, A.S.
Karvina, Czech Republic

**Jiři Golasowski**, Head of Lt Planning & Mine Designing Dept
OKD, A.S.
Karvina, Czech Republic

**Milan Mikoláš** , Associate Professor
**Vlastimil Hudeček**, Professor
Všb –Tu Ostrava
Všb –Tu Ostrava
Ostrava, Czech Republic

## INTRODUCTION

The history of coal mining the Ostrava Region of the Czech Republic goes back nearly 250 years. Both coking coal for steelmaking and thermal coal for the production of energy are mined here; however, it was the coking capabilities that subsequently turned the region into a major steel-producing area in the early 1800's, something that continues to this day.

Ostrava lies in the northeast corner of the Czech Republic, near the southern border of Poland, and falls within the Upper Silesian Coal Basin. The region contains over 400 seams of coal of which about 150 have been mined over its history and continue to be mined. Eighty percent of the Upper Silesian coalfield lies in Poland and is presently mined by about 35 coal mines; the remaining 20% falls in the Czech Republic, which presently has four mines operated by OKD, a.s., a subsidiary of Amsterdam-based New World Resources. Traditionally, all the mines in this region have employed the longwall method of mining, of which subsidence is an unavoidable consequence. In fact, due to the long history of longwall mining here, there are areas where the overall subsidence has exceeded 37 meters (121 feet).

The region is fairly densely populated with residences and industry, and a considerable amount of coal lies under some of these areas where subsidence is not allowed or has to be minimized. It is this reason that has driven OKD to consider alternate methods of mining that will not create subsidence. The decision was made to consider the room and pillar method of mining in order to leave stable pillars of coal to support the surface. After considering several locations, OKD chose the shaft safety pillar at the ČSM mine as a test mining location. To say the least, this is a very challenging location in which to conduct a test. As with the entire region, there are many faults from tectonic activity, the seams are pitching at 12 to 20 degrees, the area is affected by high horizontal stress, *and* the depth of 750 to 900 meters is perhaps the deepest room and pillar coal mining ever attempted.

Roadways for the development of longwall mining areas are typically driven with either drill-and-blast technology or with roadheaders. Although conventional drum-type miners and bolting typically used in room and pillar mining have been tried in these areas, this is the first attempt at conventional room and pillar mining in this region with actual pillars and bolting as the sole means of support. No retreat mining will be considered, as it is the intent to minimize subsidence.

OKD considered various types of equipment and mining systems to employ for this project. The first concept considered was a bolter-miner with a continuous haulage system, this is more of a linear type of mining system where long parallel headings are driven without the use of cutting crosscuts. Although this system appeared to be viable, it was not considered to be as flexible to adapt to the local and changing conditions. A more conventional spread of equipment using a miner with shuttlecars was at first rejected because it was not believed that shuttle cars could effectively be utilized in the anticipated grades. After additional discussions with the equipment supplier, and taking a trip to a mine in Canada operating on 18-degree grades with shuttle cars, it was a concluded that it was possible to mine with shuttle cars on this grade.

In 1996, there was an attempt at mining with a bolter-miner in this safety pillar in the same seam. For various reasons, this mining was not considered a success; however, it did provide experience with a bolter-miner and bolting in this seam. From this experience it was concluded that mining should not advance more than two meters without roof support. For this reason, a bolter-miner had to be chosen; it would not be practical to use a miner without a bolting rig due to the numerous place changes that would be required with a 2 meter cut depth.

Once the basic type of equipment and methodology was selected, OKD chose to use a Joy 12CM30 bolter-miner along with Joy 10SC32 variable frequency drive shuttle cars. The 12CM30 does not have gathering arms or a gathering pan to collect the cut coal at the face. Rather, the cut coal is directed to the chain conveyor by the rotating scrolls of the cutting head. This method allows the onboard bolting units to be even closer to the face and the miner can bolt within almost 1 meter of the face, thus the 2 m requirement could be met. A contract was placed with Joy for the bolter-miner and two shuttle cars along with other complementary mining equipment, including a Joy feeder breaker, Alminco Scorpion single boom roof bolter, two GE Fairchild scoops and Hansen power center. The project turned into a truly global effort as the bolter-miner was built in the United Kingdom, the shuttle

cars in South Africa, the feeder in Poland and the bolter in Australia along with scoops from the United States, a CFT section fan from Germany and a power center and belt drives from the Czech Republic.

## MINE DESIGN

### Geological conditions

As mentioned earlier, the geological situation in the project area is quite complex and constituted one of the major challenges for the preparation of the mining plan and selection of the equipment. These depositional conditions and the shifting tectonic topography are in large part what makes longwall mining so difficult in this region, and likewise push the boundaries of the room and pillar mining method and the technical-operational capabilities of the selected individual machines and equipment. The approximate location of the room and pillar mining project is shown in Figure 1.

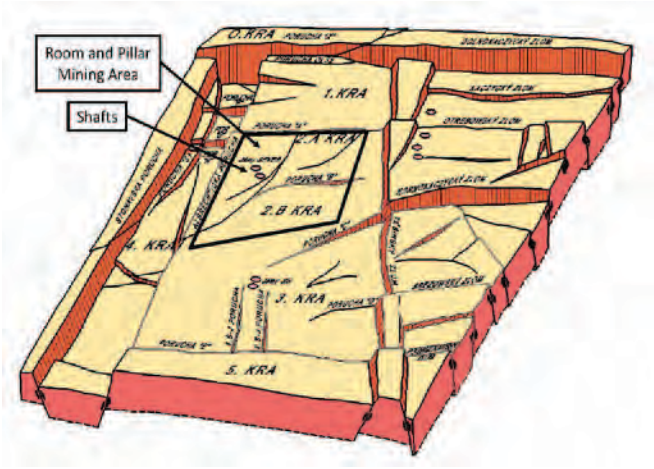



**Figure 1. Approximate location of room and pillar minings project.**

Seam 30, the target seam for the test, is at a depth of approximately 750 m to 900 m below the surface and dips from 10° to 15°, generally to the northeast. Like the entire region, this area chosen for the room and pillar plan is surrounded by tectonic features with significant faults, including throws ranging from 0.5 to 6 m to the north, south and east and a major fault with a throw of over 100 m to the west, around which all mining activities have to be planned. In the area immediately around a fault, the roof, floor, and coal seam can be severely broken, causing adverse ground control conditions. This was experienced upon initial development with a roadheader through a fault zone and could only be supported by conventional arches, as the roof and coal seam was too broken to support with bolts.

Within the shaft safety pillar, there are four seams proposed to be mined, as depicted in Figure 2. Mining in the lower seams will be determined by the success of mining in the upper seam, Seam 30. It is generally accepted that the best method of mining in multiple seams is to superimpose the mining; this concept was considered in the design, but the first step is to insure the success of mining in the first seam and make appropriate adjustments before finalizing a mine plan in the lower seams. Additionally, the first two seams are coking coal and the lower two seams are thermal, and the economics of mining the deeper (and thus higher cost) seams, coupled with a lower thermal coal price, is uncertain at this time.

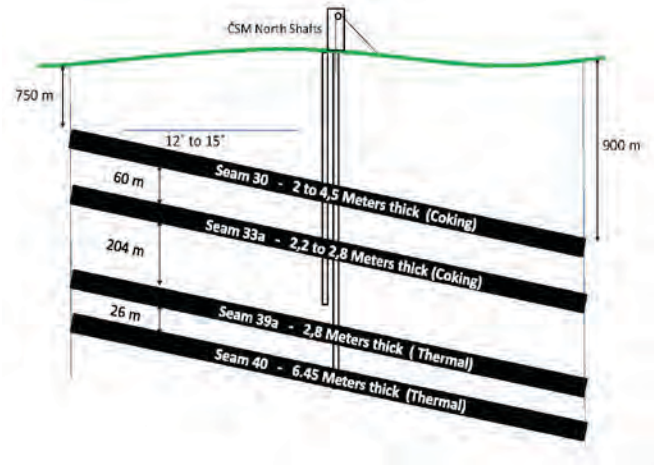



**Figure 2. Four seams proposed to be mined.**

### Horizontal stress

Horizontal stresses were measured by the Mining Institute of the Czech Academy of Sciences in Ostrava by the hydrofracking method over a period of time. It indicated a range from 9.5 Mpa to 29 Mpa with average of 16.11 Mpa for the principal horizontal stress, and 4.25 Mpa to 12.5 Mpa for the minor horizontal stress with an average of 7.46 Mpa. The average of the vertical stress measurements was 21 Mpa. It is noted that the vertical stress is greater than the horizontal stress. This is expected here due to the great depth of the seams. It is generally accepted that the optimum orientation of entries in regard to the principal horizontal stress is plus or minus 30° to its axis. This was taken into consideration in the mine plan and entries, and crosscuts generally were laid out in this fashion.

Another factor that was taken into consideration in the layout of the mine was the dip and grade. The general dip ranges from 10 to 15 degrees with local areas approaching 20 degrees. In an effort to lessen the grade, entries and crosscuts were designed at a cross-grade to the dip to maintain, as much as practical, a maximum grade of 10° for a more reasonable grade on which to operate equipment. Due to pre-existing mining and the general configuration of the mining area, it was not possible to orient every entry and crosscut in the optimal orientation in regard to horizontal stress or gradients, thus less-than-optimal compromises had to be taken to mine the given deposit. In such situations, it is understood that additional precautions may need to be undertaken to control roof cutter or floor heave if they occur in these areas. Mining on slopes of 10 to 15 degrees creates equipment and operational problems. As can be seen from a simplified cross-section in Figure 3, at these grades it is not always possible to cut within the coal seam, as the continuous miner must cut in a level horizon from side to side as much as possible. Oftentimes, a significant amount of rock will have to be cut on one side or the other of the entry cross-section. In this mining area, the roof rock is fairly strong (80 Mpa), making cutting the section even more difficult. In addition, the rib bolting requirements may be different on one side of the entry, as one side can be partially in rock and the other more in coal. The coal side can have more of a tendency to decouple or roll out, thus

a longer or a different type of bolt may be required. Additionally, cutting the crosscuts in slopes like this can be very difficult even for experienced operators.

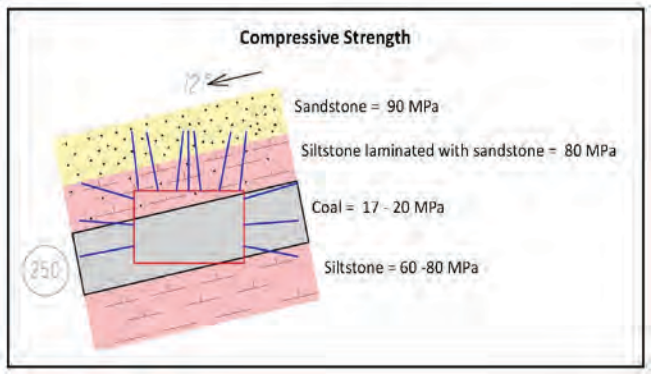



**Figure 3. Mining cross section.**

The mine plan shown in Figure 4 was developed with consideration for all of the aforementioned challenges: depth of mining, faulting, pitching seams, pre-existing mining and horizontal stress. Area I was the first area to be excavated, but was considered more of a construction area that provided access to the future mining areas. Even the access to Area I was quite challenging; new rock and coal corridors had to be cut to gain access. As the initial rock corridor was excavated with drill and blast techniques, a large equipment assembly room was excavated to allow room for mining equipment to be assembled. Each piece of equipment had to be lowered down the shaft in small components and reassembled – a huge undertaking in itself.

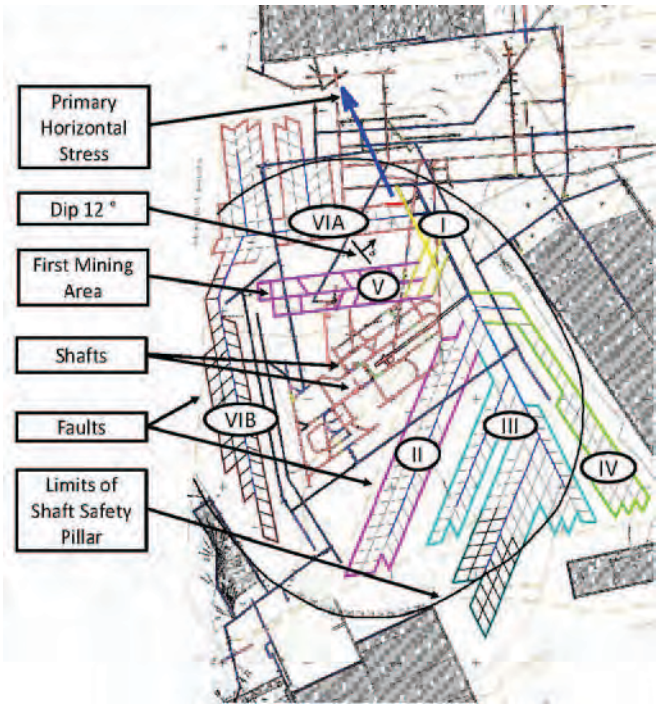



**Figure 4. Mine plan.**

The first mining area was to be Area II; however, it was later decided to first mine in Area V to gain access to a production area even sooner. Since the entire mining area is experimental, and Area V is the first test area, it is prudent to be very cautious with the initial section mining layout and pillar design.

**Pillar Design**

With the equipment chosen and the first mining area selected, efforts turned to roof and ground control. The type and size of the equipment has a direct impact on ground control and pillar design, and one of the key variables in pillar sizing is the width and height of the opening. The Joy 12CM30 bolter-miner is a full-face machine, meaning that it cuts the entire entry width at one pass. In this case, the cut width was 5.2 meters. Seam 30 has a thickness ranging from 2 m to 4.5 m and the 12CM30 can cut from 2.6 m to 3.8 m high. Additionally, a full-face miner allows development be advanced a greater distance before place changes, as opposed to a place-change miner. Table 1 provides the basic pillar design parameters.

There are several methods available to determine the size of pillars: most notably the Holland-Gaddy Formula, the Salamon Formula using the squat pillar design method, and the Mark-Bieniawski Formula used in the NIOSH ARMPS program, among others. These formulas use a stability factor or factor of safety that has been derived through experience and testing and/or a statistical analysis of collapsed pillars at varying depths. The safety factor recommended for the Salamon Formula is 1.6, but this is based on a statistical analysis of collapsed coal pillars in South Africa at depths not exceeding 220 m (721 ft) (Madden, 1991). Likewise, the ARMPS program is based on research of pillars in the U.S. with the maximum depth of about 2,000 ft (610 m) (Chase, 2003).

Herein is the problem for pillar design at OKD's ČSM mine. Since, to the author's knowledge, **this is perhaps the deepest that room and pillar coal mining has ever been attempted**, there is no history or statistics available on which to base an acceptable factor of safety. Salamon emphasized that the pillar strength formula was essentially empirical, and therefore should not be applied beyond the range of data used to derive it (Madden, 1998). Likewise, there are similar disclaimers with the ARMPS program when used beyond its range of statistics. Nevertheless, an acceptable method of pillar design had to be chosen. Due to the widely accepted Mark-Bieniawski Formula and the ease of use of the ARMPS program, the ARMPS program developed by NIOSH was selected as the main design tool. Other methods were also used and compared to the ARMPS program.

A point of considerable debate in the use of ARMPS at OKD was the proper pillar strength to use in the calculations. Mark (1997) determined that there was no correlation between unconfined compressive tests and in-situ pillar strength, and that pillar design was more reliable when uniform coal strength was used. It was found that the Unconfined Compressive Strength (UCS) was irrelevant to the in-situ strength largely due to the variability of the seam from partings, cleats, fractures, bedding planes, etc.; thus, the value 900 psi (6.21 Mpa) is recommended (Mark, 1997). Nevertheless, UCS testing on the coals of the four seams to be mined (Seams 30, 33a, 39a and 40) was conducted and indicated strengths of 30, 18, 18, and 16 MPa, respectively. The average is 20.5 Mpa. Additionally, testing was performed by Dr. Kot Unrug with an in situ penetrometer in Seam 30 with test results of 20.007 Mpa. This in-seam penetrometer corresponds to

**Table 1. Basic pillar design parameters.**

| Seam | Depth (m) | Height (cm) | Mining Height (cm) | Entry Width (m) | Immediate roof | Main roof |
|---|---|---|---|---|---|---|
| 30 | 700 - 900 | 190 – 450 | 350 | 5.2 | Siltstone and sandstone | Sandstone and Siltstone |
| 33a | 730 - 970 | 190 – 370 | 350 | 5.2 | Conglomerate | Siltstone |
| 39a | 960-1180 | 230 - 330 | 350 | 5.2 | Sandstone | Siltstone |
| 40 | 980 - 1220 | 440 - 780 | 350 | 5.2 | Siltstone | Siltstone |

the strength of laboratory testing and corresponded well with the average of the other testing, lending confidence in the test results. However, the UCS must be substituted in the Gaddy Equation to determine the strength of the critical cubical coal pillar (Peng, 2008) – the value to be used in the Mark-Bieniawski Formula in the ARMPS program. The method is as follows:

$$K = Sp\sqrt{3}$$

Where *K* is a coefficient for the coal to be tested and *Sp* is the UCS of a cubical coal specimen. The *K* value must then be substituted into the (Hustrulid, 1976) formula to obtain the proper value to use in the strength formula, the $S_{cube}$[5]:

$$Scube = k/\sqrt{36}$$

Thus:

$$K = 20.5\ MPa\sqrt{3} = 35.5\ then\ Scube = \frac{35.5}{\sqrt{36}} = 5.92\ MPa$$

5.92 Mpa is sufficiently close and corresponds well to the ARMPS default value of 6.21 Mpa, so the default value was used.

Another reason the ARMPS method was used was that it applies the Pressure Arch Theory. The ARMPS program is used for retreat mining, and although retreat mining will not be performed here, it was felt that it can provide a conservative design if the appropriate stability factors were utilized. Some slight convergence of the coal pillars is possible even if they are properly designed; if this occurs, load will be transferred to the barriers. This is the concept of the pressure arch.

In the 2010 version of ARMPS for cover greater than 650 ft (200m), an SF of 1.5 is recommended for pillars and 1.5 for the barriers. An alternate recommendation at greater than 1000 ft (305m) and with narrow panels less than 425 ft (130m) is for a pillar SF of 1.3 and a barrier of 2.0 (Agioutantis, 2010). Given this, and in an effort to provide a cautious, conservative design, the decision was made to isolate the mining panels with barriers and provide an even more conservative minimum SF of 1.6 for the pillars and 2.0 for the barriers.

Since this is an experimental mining program, and it is the first time room and pillar mining has been attempted in the region, this cautious design approach is warranted. The focus here is not come up with a design that works for all areas in this seam, nor is it necessarily to design the lower seams. The focus is to come up with a conservative design for the first mining area, then make appropriate adjustments if so required in the latter mining areas and seams. The design inputs and results for the ARMPS model in the first area, Area V, are presented in Table 2.

**Table 2. Design inputs and results for the ARMPS model.**

| **Inputs** | | **Results** | |
|---|---|---|---|
| Entry height | 3.5 meters | Pillar SF | **2.54** |
| Depth of cover | 850 meters | Barrier SF | **2.51** |
| Crosscut angle | 60° | | |
| Entry width | 5.2 meters | | |
| Number of entries | 3 | | |
| Crosscut spacing | 40 meters | | |
| In situ coal strength | 6.21 Mpa | | |
| Barrier width | 74 meters | | |

Even though the seam height can go up to 4.5 m and the miner can cut to 3.8m, the decision was made to limit mining height to 3.5m. Additionally, the ARMPS program showed that if the mining height did increase to 4.0 m the minimum factor of safety is still maintained. The stability factor values for the first mining area far exceeds even the higher minimum SF of 1.6 set by OKD for the project. Since there has been no room and pillar work at this depth, and thus no statistics available – and, thus, no certainty with the effectiveness of the ARMPS program with a SF = 1.5 -- OKD management deemed this to be a cautious decision in the first mining area.

OKD is proposing an extensive program to monitor the stress of the pillars, entry and rib convergence, roof bolting effectiveness, and surface subsidence. This monitoring program, coupled with observations during mining, will allow OKD to make changes as deemed appropriate on subsequent mining panels and areas. In summary, the conservative design approach is as follows:

- Use the default value of 6.21 Mpa for coal strength in the ARMPS program, even though previous thought suggested 10 Mpa or greater was acceptable.
- Utilize narrow panels with barriers to separate the panels, even though retreat mining will not be employed. The use of the barriers can be an effective means to minimize the effect of bounces should they occur.
- OKD's first design for Area V was for five entries; however, the number of entries was reduced to three, thus decreasing the panel width and increasing the stability factor (SF).

- Use a minimum design stability factor of 1.6 for the general mining area, but design the first mining area with an even higher stability factor to be more cautious. The appropriate minimum stability factor might have to be adjusted for future mining.
- A 30 m x 30 m entry center pillar with three entries met the minimum SF, but a 40 m x 40 m with an even larger SF was chosen.
- Limit the mining height to 3.5m, even though 4.0m still provides an acceptable SF.
- Closely monitor the pillars and subsidence.
- Make appropriate design changes on subsequent panels if deemed appropriate after monitoring.

## BOLTING

Ground support for entry development in this region typically employs the use of heavy steel arches in roadways cut by roadheaders or drill and blast. Bolting has been used here, but only a limited basis in areas where additional support beyond the arches is required. As previously mentioned, in 1996, an ABM 20 (Alpine Bolter-Miner) was used for some linear mining on a limited basis. The entries mined in 1996 are still accessible, and the roof bolting is still holding up quite well with little problems. Cutters have developed in entries that were oriented somewhat perpendicular to the line of maximum horizontal stress which would be anticipated. Some additional support was required in areas close to fault zones, but overall, the bolting appears to be sound, which is encouraging for the bolting proposed on this project.

The roof generally consists of a medium to strong siltstone or sandstone with UCS >40 MPa. The bolting system must consider not only the rock types, but also the type and capabilities of the selected mining equipment. The Joy 12CM30 (see Figure 5) has four bolting heads – two on each side. The bolter-miner cannot drill a bolt in the center of the entry; if conditions warrant the need for a center bolt, it will be drilled by the supplemental Alminco Scorpion single-boom bolter (see Figure 6). OKD has developed three basic bolting schemes for different mining conditions as follows (see Table 3).

Additional cable bolts will be installed in the intersections. Telltales to monitor convergence will be installed every 25m and must be installed within 5m from the active face.

The roof appears to be manageable; however, the ribs are of a greater concern, exemplified by the 1.3m of rib convergence during initial development of Area I with a road header. This convergence caused concern and was not anticipated, but it eventually reached a point of equilibrium and stabilized. It is not necessarily uncommon in these types of conditions at this depth. It is believed that the more uniform cutting of the ribs with the bolter-miner, and the closer and quicker installation of ribs bolts to the face with proper drilling equipment, will help to manage this.

**Table 3. Basic bolting schemes for different mining conditions.**

| Green Plan | Orange Plan | Red Plan |
|---|---|---|
| To be used for normal situations with no adverse conditions:<br>(4) 2.4-meter bolts to be installed by the bolter miner on cycle<br>Rows 1 meter apart<br>(2) additional 2.4-meter bolts to be installed by Alminco bolter in between the row of bolts installed by the bolter miner<br>(2) 1.9-m and 1 (3m) rib bolts<br>Roof and ribs fully meshed | To be used for more adverse conditions:<br>(4) 2.4-meter bolts to be installed by the bolter miner on cycle<br>(2) additional 2.4-meter bolts installed .5 meters behind first row installed by bolter miner<br>(2) additional 2.4-meter bolts to be installed by Alminco bolter<br>2.4-meter center bolt installed by Alminco bolter<br>Additional angled rib bolt into roof rock<br>Roof and ribs fully meshed | To be used for the most adverse conditions:<br>Same as the orange plan with the addition of:<br>(2) 6-meter cable bolts installed by the Alminco bolter in the intermediate row<br>Additional rib bolting as required.<br>Roof and ribs fully meshed |

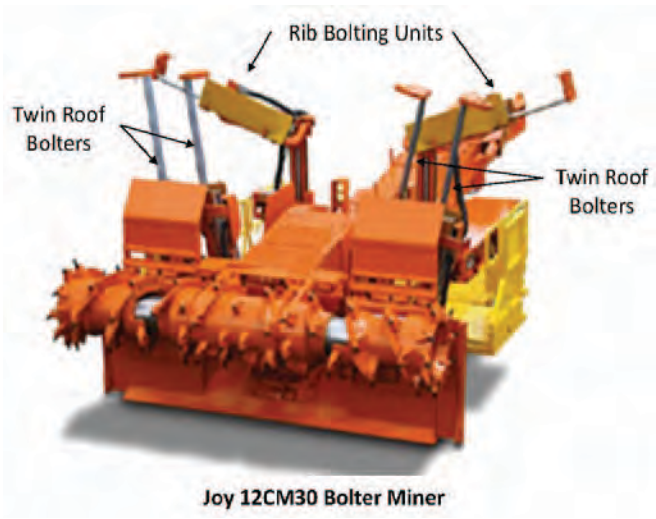



**Figure 5. Joy miner with four bolting heads.**

## SPONTANEOUS COMBUSTION MANAGEMENT

It has been determined that Seam 30 can be prone to spontaneous combustion, thus appropriate measures need to be adopted to manage this. Proper ground control plays an important role in this regard, as the crushed coal in the broken ribs that comes in contact with poor airflow can effectuate spontaneous combustion (Phillips, 2011). Because of this, it is important to have proper pillar sizing and rib control that can minimize this crushed




**Figure 6. Single boom bolter used to install center bolt.**

coal. In addition to the pillar and rib control, OKD is applying a CaCl chemical deterrent to be applied to all ribs immediately after mining. It is anticipated that proper ventilation, proper ground control measures, and the addition of the CaCl will allow OKD to manage spontaneous combustion.

## OTHER CONSIDERATIONS IN TERMS OF SAFETY AND OPERATION

OKD mines have several important aspects of safety risk that affect the implementation of its mining activities.

- All mines are classified as gassy in the strictest level of danger;
- All seams are classified as hazardous in regard to spontaneous combustion;
- Most of the coal seams are classified as bounce-prone; and
- All mines are quite deep, with the average depth of mining about 900m

All of the aforementioned risks must be treated with appropriate measures that address the applicable regulations prior to the new mining activities.

## LEGISLATIVE PROCEDURE

According to Czech legislation, any new mining method must go through a comprehensive review and reconciliation process prior to approval. The mining laws and regulations of the Czech Republic were established exclusively for the longwall method of mining. Since the room and pillar method encompasses an entirely different set of mining practices than that currently in use at OKD, it was apparent that many of these regulations did not apply. It was necessary, then, to cooperatively work with the mining authority to request exemptions from some and/or establish a number of new regulations or other means to address issues, particularly spontaneous combustion prevention, ventilation and precautions against bounces.

Very simply, several key steps can characterize the whole process. **First**, for a new mining method, a special project must be developed which describes the mining method along with possible deviations to applicable legislations – which must be assessed by an independent expert organization. **Second**, after the development of the project and its assessment, the organization can request the Czech Mining Authority to permit a trial run. **Third**, after a permit for trial operation is granted, where the Mining Authority sets all the conditions for implementation, the organization may apply for a permit to actually begin a test run in a particular place following the set conditions. **Fourth and finally**, during the trial operation, the organization shall be monitored and evaluated. The results must be submitted together with a proposal of conditions and actions to the District Mining Authority for approval of the new mining method for normal continuous operation. This shall include a draft of the measures necessary for the safe use of the new mining methods.

## MONITORING OF THE MINING METHOD

By decision, the Mining Authority imposes a duty of the organization within the course of the trial run to monitor the activities and evaluate the results after completion. In order to fulfill this obligation and be able to use this method in the future, special attention is needed to these areas:

### *Underground monitoring*

- Stability of the coal pillars
- Stability of the mining openings
- Effectiveness of the reinforcement (bolting) of the mining openings, including comparison of calculations with reality
- Bounce prevention prognosis and its effectiveness
- Geomechanical observations (occurrence of cracks and deformations in the mining area and adjacent mining areas)
- Prevention of spontaneous combustion of coal along with its repression and effectiveness
- General efficiency of mining

### *Equipment and machinery*

- Part of the monitoring process is to verify the effectiveness and reliability of the measures, which were established on the equipment during the certification process. This project employs several pieces of equipment that have never been used before in this region, and the unique and challenging mining conditions push the technological limits of this equipment. In addition, the equipment had to be adapted to comply with Czech and EU legislation. In the end, after a lengthy process, these technological and legislative issues were resolved.

### *Surface monitoring*

- As this method of mining was selected to minimize the subsidence impacts on the surface, a monitoring system will be set up to assess these impacts. It is obvious that the proposed new mining method will have lower reserve recovery and productivity than the longwall, but its advantage should be minimal effects on the surface, and therefore its ability to be used under areas in which subsidence must be limited or buildings must be protected. Due to

the fact that there is no history in this area of this type of mining and no basis or facts concerning the measurement of subsidence impacts, it was crucial that the test operation area be without the lingering effects of previous longwall mining so that stabilized points could be established on the surface. This establishes a true baseline for subsidence monitoring attributable to only this method of mining. In addition, it is important that OKD included the advice of experts well versed in the subsidence of the basin with sufficient practical experience and familiar with the contemplated mining method as well as its effects on the projected surface.

## IMPORTANT CONCLUSIONS OF THIS TRIAL PERIOD FROM A LEGISLATIVE STANDPOINT

If positive results are verified, it would be possible to amend legislation so that this method of mining is acknowledged as a method that can cause minimal impact on the surface and surface structures.

Almost the entire local coal basin is considered bounce-prone, and bolting is not allowed in bounce-prone areas per a resolution adopted in 1995-96. If the new experience, bolting methods, equipment and materials prove that bolting and other measures such as proper pillar and barrier design allowed for in this trial area are successful, then it may be possible to modify the "no bolting" resolution to allow bolting in this and other areas. This is a shift from the longwall caving mentality to one that relies on stable pillars and bolting for effective ground control.

## KEY CONCLUSION

Room and pillar mining has never been attempted before in this region, and an extensive amount of work has been undertaken to show this method can successfully be employed in these conditions. If the subsidence impacts can be eliminated or minimized, and the method proves to be safe and economically viable, a considerable amount of coal reserves can be mined under densely populated areas that cannot otherwise be mined by traditional longwall mining.

## REFERENCES

Madden, B., (1991). "A re-assessment of coal-pillar design." *Journal of South African Institute of Mining and Metallurgy*. January. 27-37.

Madden, B., Canubulat, I., York, G. (1998). "Current South African Coal Pillar Research." *The Journal of the South African Institute of Mining and Metallurgy.* January/February, 7-10.

Mark, C. and Barton, T.M., (1997), "Pillar Design and Coal Strength," Proceedings: New Technology for Ground Control in Retreat Mining, NIOSH Information Circular, No. 9446, 17-34.

Peng, S.S. (2008). *Coal Mine Ground Control, 3rd Edition*. West Virginia University. 239-241.

Agioutantis, Z., Mark, C.(2010). *Interpretation of ARMPS Stability Factors*. ARMPS 2010 (ARMPS version 6).

Chase, F., Mark, C., Heasley, K. (2003). "Deep Cover Pillar Extraction in the US Coalfields." *21st International Conference in Ground Control in Mining*. Morgantown, WV. 77-80.

Phillips, H., Uludag, S., Chabedi, K. (2011). *Prevention and Control of Spontaneous Combustion*. Coaltech Research Association 83.

Hustrulid, W.A. (1976). A Review of Coal Pillar Strength Formula, Rock Mechnics, vol. 8, 115-145

# Ground Response As a Longwall Advances Into a Backfilled Recovery Room under Low Cover

**David F. Gearhart**, Lead Research Engineer
**Tristan H. Jones**, Acting Team Leader
**Craig S. Compton**, Engineering Technician
**Todd A. Minoski**, Engineering Technician
Ground Control Branch
NIOSH, Office of Mine Safety and Health Research
Pittsburgh, PA

**Robert E. Ochsner**, Chief Mine Engineer
Bull Mountains No. 1 Mine
Signal Peak Energy
Roundup, MT

## ABSTRACT

A cooperative study was conducted between Signal Peak Energy and the National Institute for Occupational Safety and Health (NIOSH) to evaluate the behavior of a pre-driven recovery room under less than 200 ft of cover. The design of the support systems for a pre-driven recovery room must provide control of the roof and ribs during the changing stress environment experienced throughout the final advance of the longwall into the recovery room. It must also provide a stable area where mine personnel are not exposed to undue hazards during shield recovery operations.

This recovery room was constructed in two phases; each phase mined a 21-ft-wide room that was heavily supported, and subsequently fully backfilled with 800-psi, cellular concrete. Instrumentation to monitor the recovery room performance included borehole pressure cells (BPCs) placed in the headgate and tailgate pillars, at four locations across the longwall panel, in the fill material, and in the first row of outby pillars near the center of the panel. Four roof-to-floor convergence sensors were installed in the backfill material and a vertical, multipoint borehole extensometer (MPBX) measured the displacement of the strata above the recovery room. Surface surveys were conducted to measure MPBX collar movement.

The data show that the front abutment load was transferred onto the recovery room backfill and the outby pillars as the longwall panel was extracted. As the longwall approached the recovery area, the fender and shields yielded, but the backfill provided enough support to keep the room stable as the longwall advanced to its final position. The system worked as planned and the face was recovered in record time.

## INTRODUCTION

Pre-driven recovery rooms reduce hazards to miners by allowing the installation of roof and rib supports in a lower-stress environment than when the abutment stress from the longwall is present. Pre-driven, pre-supported recovery rooms also allow for the quickest advance of the longwall into the room, minimizing failures from overburden weighting or roof falls (Oyler, 1998). Furthermore, pre-driven recovery rooms can shorten the time required to remove equipment from the completed panel to the next setup room (Barczak, 2007).

The Bull Mountains Mine No. 1 is located 30 miles north of Billings, Montana. The mine has recently completed its third longwall panel in the ten-foot-thick Mammoth Seam. The panel was 22,500 ft long and 1,250 ft wide. The depth of cover at the recovery room was less than 200 ft. The Coal Mine Roof Rating (CMRR) in the recovery room was calculated to be 59.

Difficulty was encountered at the conclusion of the 1-Right and 2-Right longwall panels at the mine. The low overburden in the area, along with the difficult geology in the mine roof, combined to create very challenging conditions for recovery operations.

## LONGWALL RECOVERY CHALLENGES AT BULL MOUNTAINS NO. 1 MINE

While low overburden can improve mining conditions by reducing stresses, it has significantly complicated longwall recovery at Bull Mountains because of the presence of joints that are nearly parallel to the face and in some cases, extend all the way to the surface. A mine with higher overburden depth tends to benefit from some amount of pressure arching along the panel, or at the very least, has a greater thickness of rock in the roof with which to form a cantilever that can support the main roof. The joints and shallow depth at this mine reduce the possibility of this type of cantilever forming and result in heavy loading on the installed support and shields.

The typical roof geology at Bull Mountains is shown in the stratigraphic column in Figure 1. (Stankus, 2012) The Mammoth coal seam is overlain by two to three ft of shale, 25 to 26 ft of silty sandstone, and 1 to 2 ft of the Rehder coal rider seam. Above this, 110 to 150 ft of thick beds of shale, sandstone and siltstone make up the remainder of the overburden. The most troublesome aspect of this column with respect to recovery room stability is the 25-ft-thick sandstone above the Mammoth coal.

Repetitive joints about 20 ft apart, that are nearly aligned with the longwall face, can reach all the way to the surface. These joints give good caving characteristics during normal mining, but cancreate difficulties for recovery, especially when the joints shear and create a block that must be supported.

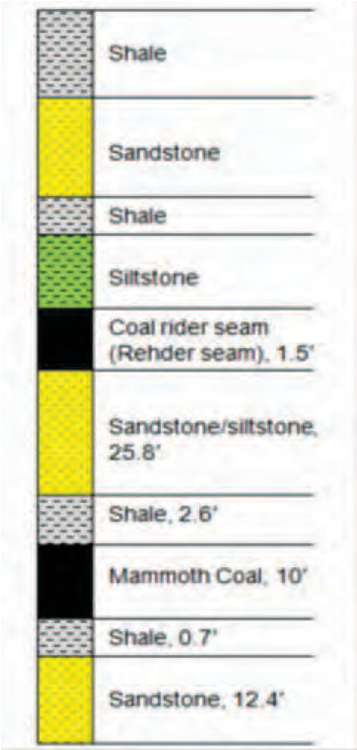



**Figure 1. Typical stratigraphic column (Stankus, 2012).**

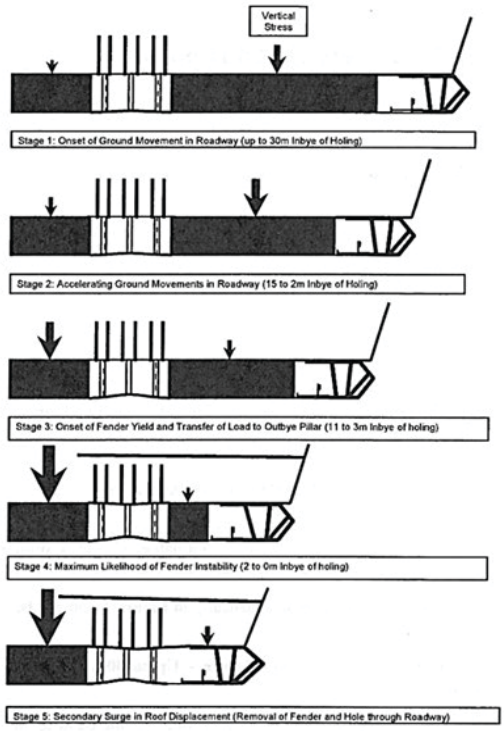



**Figure 2. Geomechanical model of longwall mining into a predriven recovery room (Thomas, 2008).**

## LONGWALL MINING INTO A PRE-DRIVEN RECOVERY ROOM

Thomas[4] (2008) describes a basic geomechanical model that includes five stages of changing stress that occur during the advance of a longwall into a pre-driven recovery room (Figure 2). This model, while idealized, is well validated by experiences at many other longwall mines in the United States and around the world. The general model is outlined as follows:

- Stage 1: Pressure increases on the remainder of the panel and significant ground movement begins in the recovery room as the face approaches. The model predicts that this behavior can occur up to 100 ft inby the recovery room.
- Stage 2: Pressure increases on the remaining fender pillar, as does the convergence in the recovery room.
- Stage 3: The fender pillar yields, transferring its load onto the outby pillars.
- Stage 4: This stage has the maximum likelihood of fender pillar instability. Because the fender has yielded, its shattered remains are susceptible to total failure.
- Stage 5: During this stage a secondary surge of roof convergence is experienced in the recovery room following fender removal.

Most longwalls that utilize pre-driven recovery rooms experience behavior that follows the general pattern of Thomas's model.

## NEW METHODS TO IMPROVE LONGWALL RECOVERY

Due to the difficulties encountered during the first two longwall recoveries at Bull Mountains, the decision was made to recover the third panel with a completely backfilled, pre-driven recovery room. The pre-driven recovery room used during the second panel was not successful, partly due to a low standing support density of only 46.3 psi (0.319 MPa).

The room installed for the 3-Right longwall move was 42 feet wide and completely pre-supported with roof bolts, cable bolts, straps, screens, and mesh, and then backfilled with cellular concrete. A full suite of instrumentation was installed to measure the changes in pressure on the longwall panel fender, cellular concrete fill, outby pillars, and gateroad pillars. Convergence in the recovery room and deformation above the recovery room were also measured.

To prepare for completion of the panel, the longwall face advance was halted about 175 ft from the end to allow all maintenance to be accomplished before the final, nonstop advance into the recovery room. Unfortunately, a mechanical delay was experienced on the second day of the final run (January 28th) that lasted from before 17:00 to after 21:00 hrs.

## PRIMARY AND SECONDARY SUPPORT IN THE RECOVERY ROOM

Primary support in both phases of the recovery room consisted of 5-ft-long by 0.804-in-diameter J-Bar, grade-75, non-tensioned, fully grouted roof bolts on 4-ft by 4-ft centers. The minimum yield load of these bolts is 42,081 lbf (Stankus, 2014). Wire mesh was

also installed for surface control of the roof. Cross-sectional views of the supplemental support are shown in Figure 3. Supplemental support varied between the protected ends and the mid-face zone. The protected ends of the recovery room are the portions of the recovery room within 100 ft of the gateroads. These end areas are protected by the adjacent chain pillars.

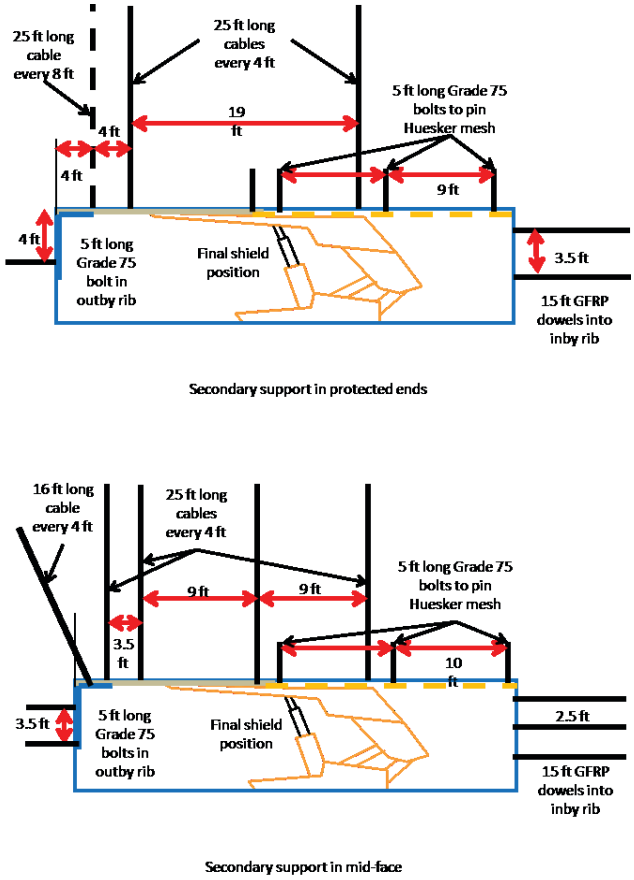



**Figure 3. Cross-sectional views of the supplemental supports in the protected ends and the mid-face area of the recovery room.**

In the protected ends two, 25-ft-long, 62-ton capacity Sumo cable bolts were installed vertically into the roof every four feet with a third Sumo bolt installed every eight feet. In the mid-face zone, there were four, 25-ft-long, 62-ton capacity Sumo cable bolts every 4 ft, installed vertically into the roof, and one 16-ft-long, 62-ton capacity Sumo cable bolt every 4 ft, installed at an angle over the outby rib.

The inby rib in the protected ends had two, 15-ft-long GFRP dowels every 4 ft and three dowels every 4 ft in the mid-face region. The outby rib had one, 5-ft-long, grade-75 roof bolt every 4 ft in the protected ends and two 5-ft-long, grade-75 bolts every 4 ft in the mid-face region.

The supplemental support for the inby 40 ft of the chutes was two, 25-ft-long, 62-ton-capacity Sumo cable bolts every 4 ft, and for the outby 32 ft there were two Sumo bolts every 8 ft. The rib support in the inby 40 ft of the chutes was two, 5-ft-long, grade-75 roof bolts every 4 ft, and in the outby 32 ft the support was one, 5-ft-long, grade-75 roof bolt every 4 ft.

Twenty-ft-wide rolls of Huesker mesh were installed beginning 3 ft outby the shield leg's final position. This mesh was secured to the mine roof by three rows of additional 5-ft-long bolts installed every 20 ft.

## REINFORCEMENT DENSITY INDEX (RDI) AND STANDING SUPPORT DENSITY INDEX (SSD)

The Reinforcement Density Index (RDI) and the Standing Support Density Index (SSD) are measures of the support installed in a given entry. The RDI is the capacity of each support element per unit area times the length of the element. The SSD is the load capacity per unit area for the standing support. It is recommended that the RDI exceed 30.84 tons/ft (0.9 MN/m) and the SSD exceed 174 psi (1.2 MPa) (Thomas, 2008).

The primary roof bolts and the secondary cable bolts and straps combine to give a Reinforcement Density Index (RDI) of 34.61 tons/ft (1.01 MN/m) in the protected ends and 57.92 tons/ft (1.69 MN/m) in the mid-face area. The Standing Support Density (SSD) was at least the minimum strength of the backfill or 800 psi (5.5 MPa).

## RECOVERY ROOM INSTRUMENTATION

The objective for the instrumentation installed in the pre-driven, pre-supported recovery room was to determine how the ground behaves as the longwall approaches the recovery room and how closely the behavior matches the model described previously.

The 42-ft-wide recovery room was developed in two phases. The first 21-ft-wide (Phase 1) room was driven across the panel, the roof and the fender were bolted, and the roof was screened and meshed. Before the Phase 1 room was backfilled with cellular concrete, twenty BPCs were installed at four locations across the longwall panel as shown in Figure 4. Sites 1 and 4 were located 75 ft from the gateroads, and Sites 2 and 3 were about 460 ft from the gateroads, across from their respective chutes. The depths of the five cells at each of the four locations were 30, 20, 12, 6, and 3 feet. The purpose of these cells was to measure the changing pressure on the longwall fender as the face advanced toward the recovery room. In addition, each of the four locations also included a BPC located 7 ft from the inby rib to measure the pressure on the fill material and a convergence sensor to measure the closure between the roof and floor.

After backfilling and curing of the fill in the Phase 1 room, the 21-ft-wide Phase 2 room was driven on the outby side, parallel to the Phase 1 room. The roof and outby rib of Phase 2 room were roof bolted, cable bolted, strapped, and screened; then three BPCs were installed in each of the gateroad pillars to detect the onset and measure the side abutment load development. Two BPCs were installed in each of the center outby pillars in chutes two and three, to detect the onset and measure the load transfer from the front abutment pressure, and BPCs were placed 12 ft from the outby rib at each of the four locations across the panel to measure the change in pressure on the Phase 2 fill material. The Phase 2 room was then backfilled with cellular concrete and allowed to cure.

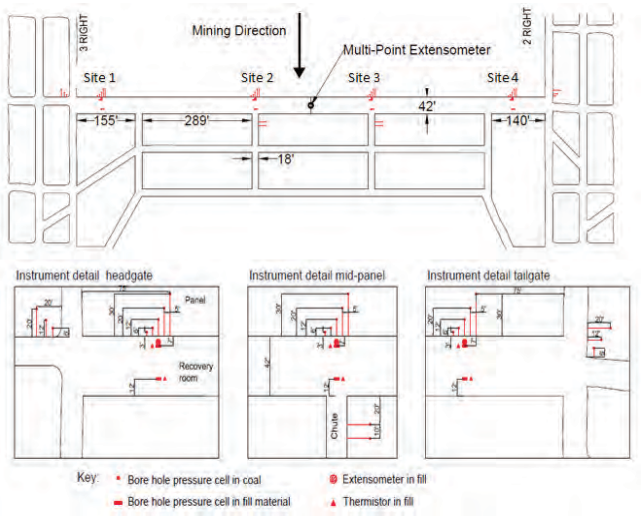



**Figure 4. Layout of the instruments in the 3-Right recovery room.**

A four-point MPBX was also installed on the surface above the center of the recovery room. Each sensor in the MPBX was 14 in long, so the resolution of the MIDAS (Jones, 2012) was approximately 0.0002 in per bit. The borehole for the MPBX was drilled to a depth of 138 ft, 5 ft above the top of the coal seam located at 143 ft below the surface. The anchors were set 10, 30, 60, and 110 ft above the coal seam, with the top anchor being 28 ft from the surface.

## INSTALLATION OF THE BOREHOLE PRESSURE CELLS AND CONVERGENCE SENSORS

The unpressurized BPCs were each installed in 2-in-diameter holes and were grouted in place with material that was similar to the cellular concrete used for the backfill. The intent was to have the boreholes filled with material that had nearly the same strength as the surrounding coal. Each of the BPCs had a capillary tube long enough to reach from its installed location out of the backfill and into a chute or gateroad. This prevented the heat of hydration during concrete curing from damaging the pressure transducers. After the backfill in the entry cured and cooled, the hydraulic pressure in the BPCs was increased to about 250 psi to prepare for overburden pressure monitoring during the advance into the recovery room. The 250-psi-prestress level was chosen to approximate the in situ vertical stress to which the cells would be exposed and to ensure that all of the pressure changes could be detected (Geokon, 2001).

The measurement range for each pressure transducer was 2,500 psi, so the resolution of the MIDAS (Jones, 2012) dataloggers was 0.038 psi per bit (2,500 psi / 65,536 bits) or better than 26 bits per psi. The convergence sensor at each location was 14-in long, so the resolution of the channel in the MIDAS datalogger was 0.0002 in per bit (14 in / 65,536 bits) or better than 4,681 bits per inch.

## CONVERGENCE AND PRESSURE CHANGES RECORDED DURING THE MINING INTO THE RECOVERY ROOM

The data for this study were zero subtracted at midnight on January 27, before mining was restarted for the final push to the recovery room, so the measurements are all relative to the pressure that existed in each cell at that time. The face was located 175 ft from the recovery room at this point.

The purpose of the BPCs in the panel, in the fill, and in the outby pillars was to detect the arrival of the front abutment load. The charts in Figure 5 show the pressure changes from each of the four sites across the longwall panel. Figure 6 shows the pressure changes in the backfill BPCs at each site and Figure 7 shows the pressure changes in the central outby pillar BPCs located at Sites 2 and 3. The gateroad pillar BPC pressure changes near Sites 1 and 4 are shown in Figure 8. Finally, the convergence readings at each site and the displacement measured by the MPBX located at the center of the panel between Sites 2 and 3 are shown in Figure 9.

### SITE 1

The Site 1 longwall panel BPC pressures displayed in Figure 5 show increases in all five cells as soon as mining was restarted at around noon on January 27th. The face was 175 ft from the recovery room at this time. Cell pressures slowly increased as the face approached the BPCs until about 15:00 hrs on January 28th, when the face was approximately 90 ft from the recovery room. For the next 5.5 hrs, load was shed either from caving behind the shields or by yielding of the panel. Yielding is considered unlikely because when mining resumed following the shearer repair, the pressure increased in the four cells that were closest to the face. There was no appreciable convergence measured at this time. When the shearer cut out the deepest (30-ft) panel cell, the pressure in the 20-ft cell continued to increase for several hours until the remaining four cells all showed signs of load-shedding. The MIDAS datalogger and the remaining three Site-1 panel cells were disconnected at about 04:30 on January 29th, to prevent loss of the equipment and data.

Figure 10 shows that the fender was yielding, since the BPC that was only 3 ft into the panel was shedding load and there was measurable convergence during the last four hrs before the BPC was cut out by the shearer at 07:35 hrs. This is when the convergence at the Site 1 location increased to over 1.3 inches in 20 minutes and then to over 1.7 inches in two hrs as the cell pressure in the Phase 1 fill increased to over 40 psi. The Phase 1 fill BPC and the convergence transducers that were located about seven ft from the inby rib of the recovery room were cut out by the shearer at approximately 10:11 hrs. Load continued to increase on the headgate pillar for about another 12 hours after the convergence sensor was cut out.

### SITE 2

In Figure 5, the Site 2 Panel BPC (across from Chute 2) pressures increased in four of the five BPCs after about 09:00 hrs on the second day, January 28th. Figure 6 shows that the pressures in the BPCs located in the fill slowly increased after 03:00 hrs on January 28th, and continued until the face entered the recovery room on January 29th. The pressure on the outby pillars began to increase (Figure 7) with the pressure on the fender and

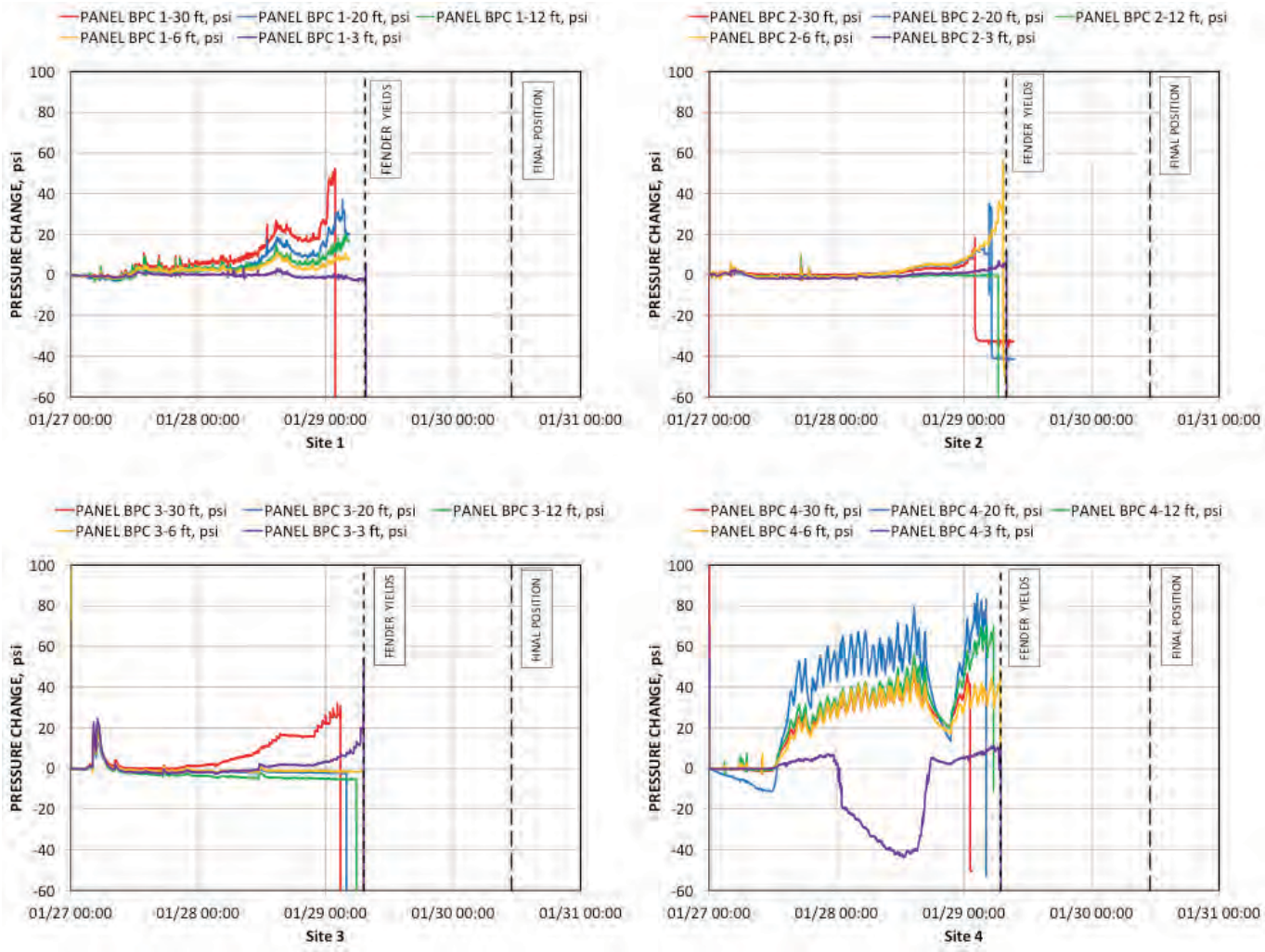



**Figure 5. Charts showing the panel BPC pressure changes at each site across the panel.**

before the panel BPCs were cut out by the shearer; therefore, the load had transferred onto the outby pillars before the fender was removed. Figure 11 shows that there was only approximately 0.5 in of convergence at Site 2 before the BPC installed three ft into the fender was cut out by the shearer, but then there was over two inches of fill convergence in the fifteen minutes following the removal of the three-ft BPC. Finally, there was an additional 1.85-in convergence, for a total of 4.25 in, before the fill convergence station was cut out by the shearer at 13:24 hrs on January 29th. The cell pressures in the outby pillar started to decrease about twelve hrs after the convergence sensor was cut out. It is suspected that the load was transferring back toward the gob as caving continued, causing this behavior.

## SITE 3

The Panel BPCs installed at the 30-ft and 3-ft depths were the only sensors that measured increasing cell pressure at Site 3, across from Chute 3. The 20-ft, 12-ft, and 6-ft BPCs recorded slightly decreasing pressures until they were cut out as shown in Figure 5. The 30-ft and 3-ft BPCs increased until 15:24 hrs on January 28th, when the pressure stopped changing. This was during the face stoppage for repair of the shearer. The cell pressures started increasing again at 22:00 hrs after mining was resumed. The 30-ft BPC was cut out at 02:45 hrs on January 29th, the 20-ft BPC at 03:56 hrs, and the 12-ft BPC at 05:32 hrs. The 6-ft and the 3-ft BPCs were cut out on the same pass at 07:11 hrs. The BPC in the Phase 1 fill showed dwindling pressure until the fender was cut out, then it increased by about 6 psi. The BPC in the Phase 2 fill showed slightly increasing pressure with only a 2 psi increase when the fender was cut and a 5.5 psi increase while the fill was being mined. The BPCs located in the outby pillar showed that they were taking load before the fender was cut out. The Inby BPC increased by 20 psi while the Outby BPC increased by 30 psi.

Figure 12 shows that the convergence increased 0.25 in before the fender was cut out, then another 1.2 inches in the next 11 minutes. The total convergence reached over 3 in at 10:43 hrs when the sensor was cut out by the shearer. After that point, the pressure in the BPC in the Phase 2 fill increased slightly and the pressure in the Inby BPC in Chute 3 decreased slightly. The pressure in the Outby BPC in Chute 3 showed little change.

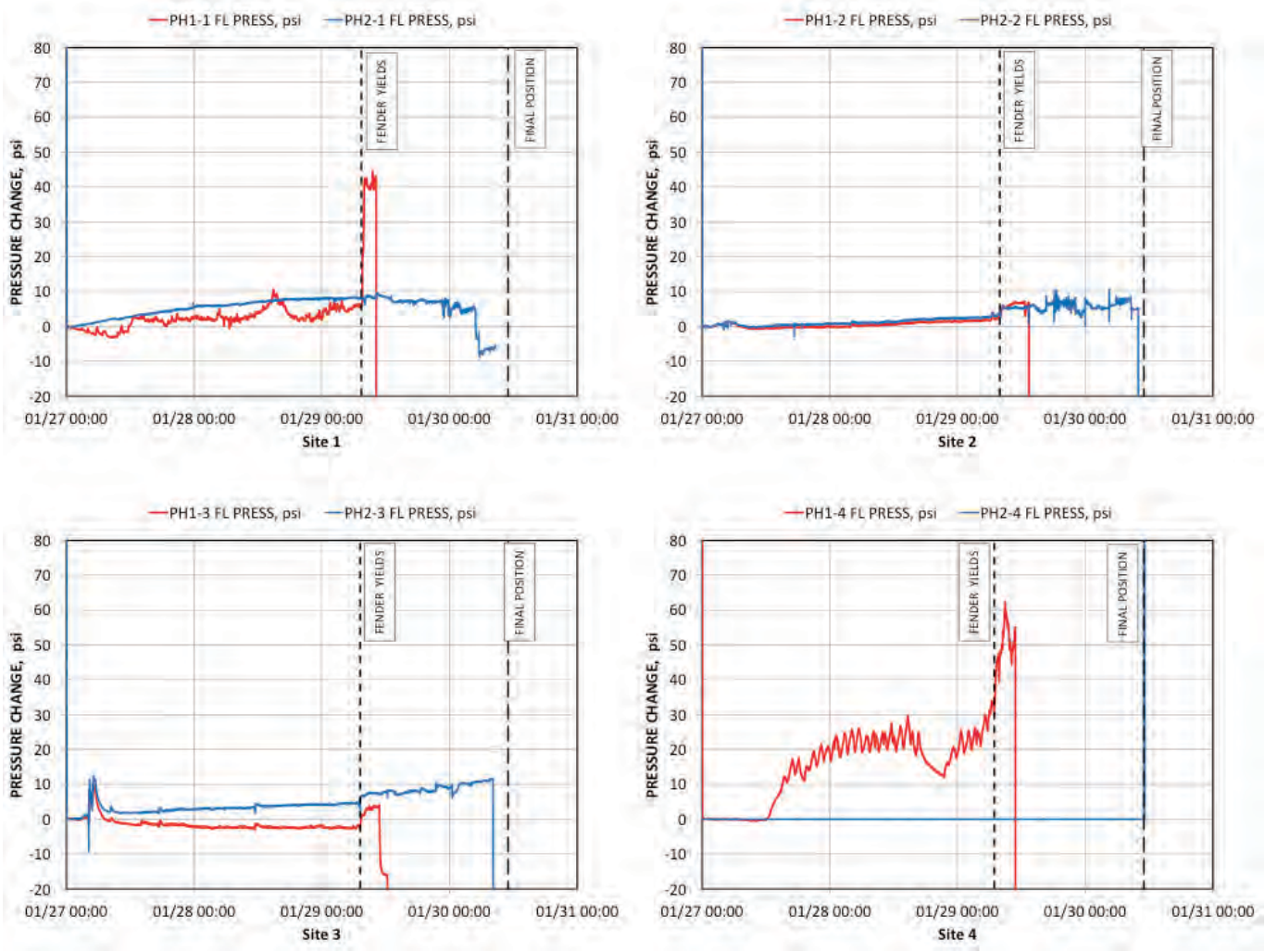



**Figure 6. Charts showing the backfill BPC pressure changes at each site across the panel.**

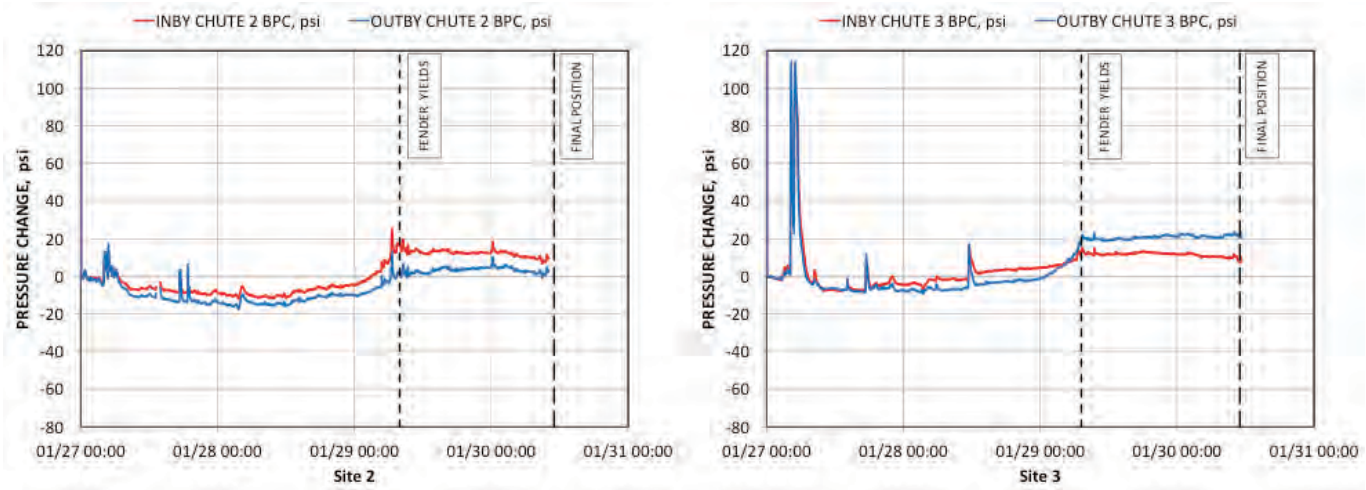



**Figure 7. Charts showing the outby pillar BPC pressure changes.**

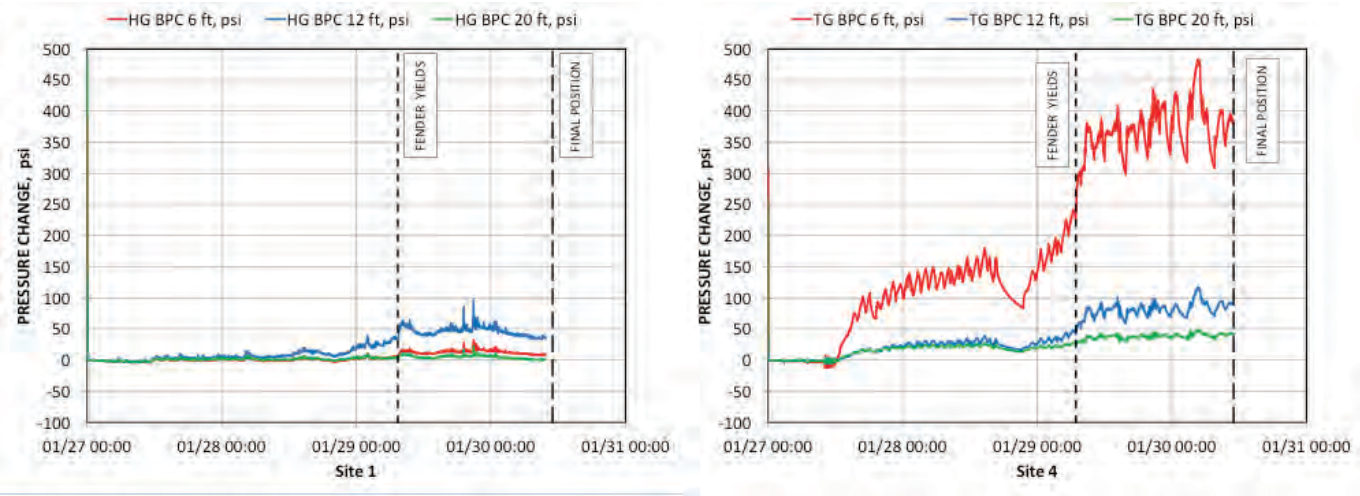



**Figure 8. Charts showing the gateroad pillar BPC changes.**

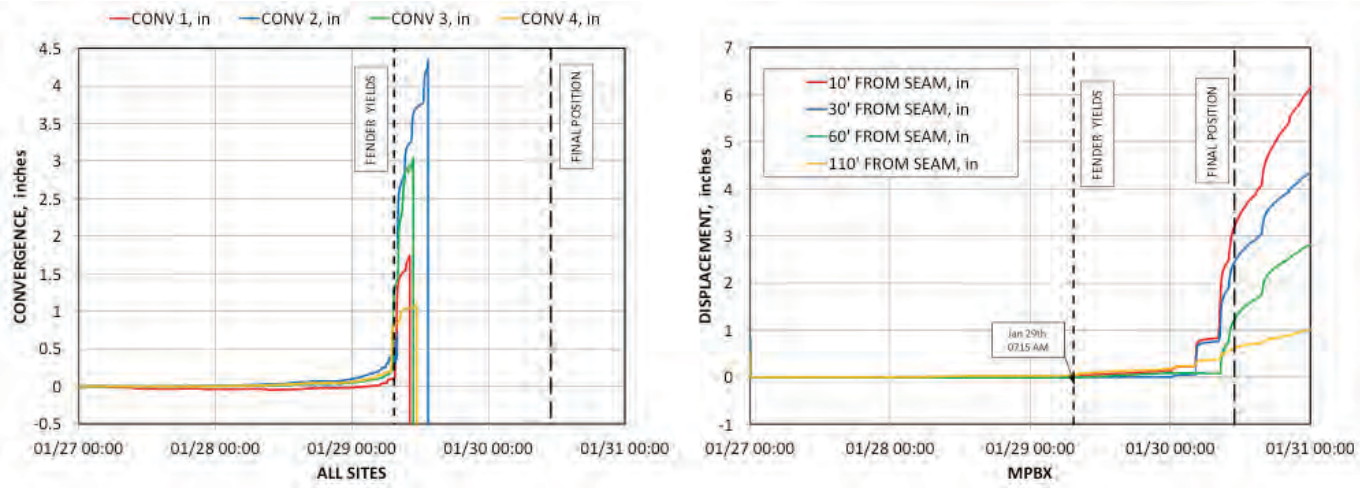



**Figure 9. Charts showing the convergence at each location across the panel and the displacement of the strata above the coal seam.**

## SITE 4

The BPCs at Site 4 were more responsive to the mining activity than at the other sites. The biggest difference was the 6-ft BPC in the tailgate pillar, which increased by nearly 500 psi. This increase was nearly an order of magnitude greater than any of the other BPCs, at any site.

The Site 4 curves in Figure 5 show that the pressures increased in all of the BPCs after mining started about noon on January 27th. The only cell that did not respond like the others was the 3-ft-panel BPC. At 16:41 hrs on January 28th, the pressures in all of the BPCs decreased during the mining delay. The pressures then began to increase around 21:30 hrs when mining resumed. When the 30-ft BPC was cut out, the pressure in all of the panel cells was increasing, but when the rest of the cells were cut, the pressures decreased, with corresponding increases in convergence, indicating that the fender was yielding. The convergence gradually increased to 0.2 in by 06:45 on January 29th, during which the first three cells were cut out by the shearer. It increased to 0.7 inches in the next 20 min when the 6-ft and 3-ft BPCs were cut out. The pressure in the Phase 1 BPC in the fill material and in the tailgate pillar increased as the fender was mined out. The BPC in the Phase 1 fill was mined out at 10:51 hrs and the convergence sensor was mined out at 11:24 hrs.

## MULTIPOINT BOREHOLE EXTENSOMETER

Figure 14 shows that no movement was detected before mining began on January 27th. Motions of 0.010 to 0.030 in were measured on January 28th. Then between 07:15 hrs and the end of the day on January 29th, the movement increased to nearly 0.2 in. At 11:00 hrs on January 30th, the shields reached their final position and the MPBX measurement 10 ft above the seam was 3.22 in. The measurement 30 ft above the seam was 2.45 in, 60 ft above the seam was 1.24 in, and 110 ft above the seam was 0.62 in. By the end of the day, the displacement measurement taken 10

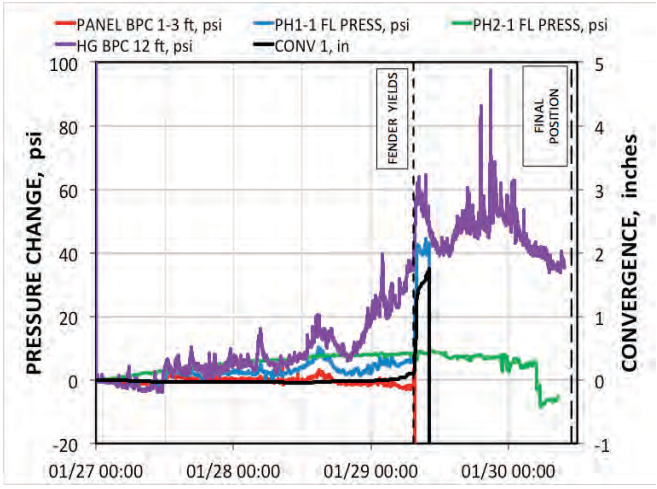



**Figure 10. Chart showing the reactions when the three-foot panel BPC was cut out by the shearer. For clarity, not all of the channels at Site 1 are shown on this chart. The cell pressure in the Phase 1 fill BPC increased to over 40 psi, the convergence at Site 1 moved to over 1.3 inches and then slowed to over 1.7 inches, and the cell pressure at the 12-ft-deep headgate BPC increased to over 60 psi.**

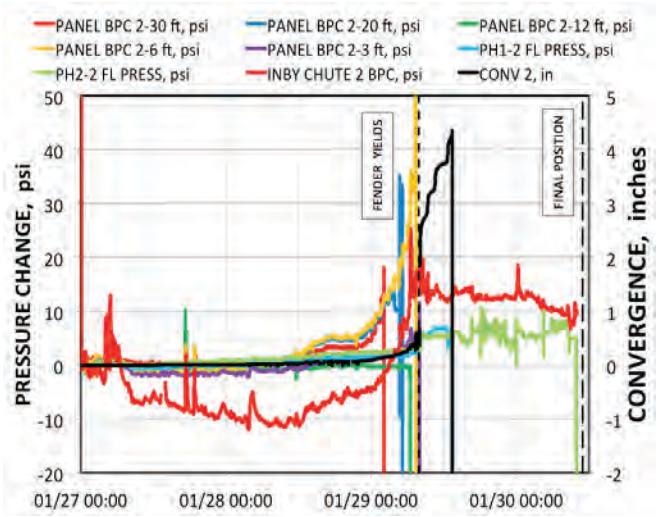



**Figure 11. Chart showing some of the instrumentation at Site 2 when Panel BPC 2-3 ft was cut out by the shearer. Load was transferred onto the outby pillars before the last BPC was cut out.**

ft above the seam increased to over 6.1 in. At the same time, the measurements taken 30 ft, 60 ft, and 110 ft above the seam were 4.3 in, 2.8 in, and 1.0 in, respectively.

## ANALYSIS AND DISCUSSION

The data recorded during the advance into the recovery room show that the ground behavior closely followed the geotechnical model described by Thomas[4] (2008). The first stage is confirmed by increasing pressure on the remainder of the panel and the onset of closure in the recovery room as the face approaches. The model predicts that this behavior can begin when the face is still up to 100 ft away from the recovery room. The increasing pressure was

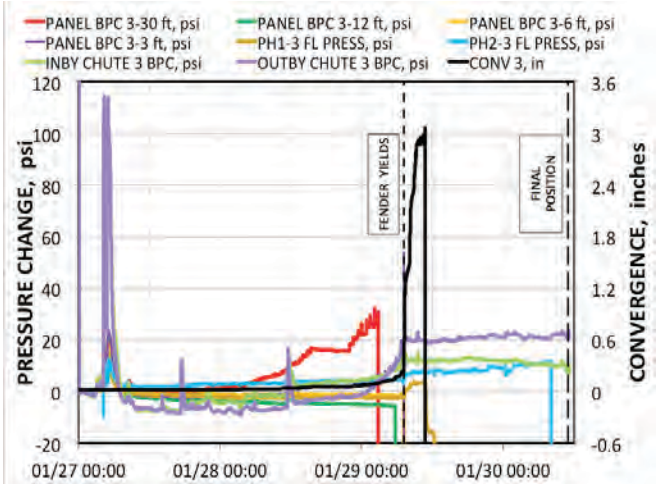



**Figure 12. Chart showing the reaction of the instrumentation at Site 3 when BPC 3-3 ft and Panel BPC 3-6 ft were cut out by the shearer. Load was transferred onto the fill and the outby pillars before the last BPCs were cut out.**

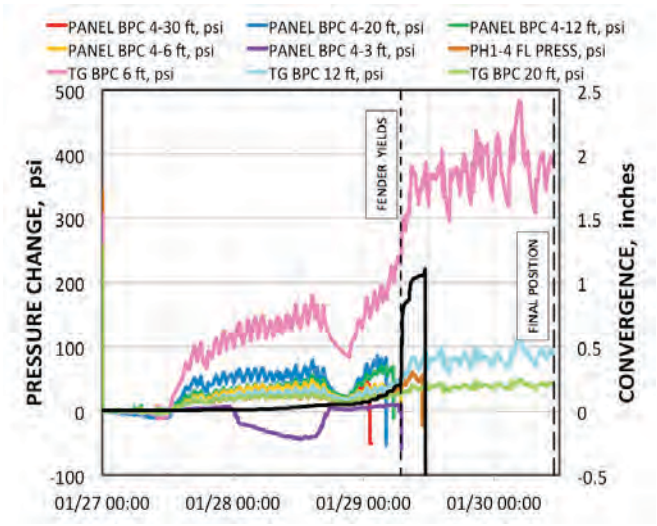



**Figure 13. Chart showing the reaction of the instrumentation at Site 4 when Panel BPC 4-3 ft and Panel BPC 4-6 ft were cut out by the shearer. Load was transferred onto the fill and the tailgate pillar before teh last BPCs were cut out.**

recorded by the BPCs in the panel fender at each site, and the onset of closure was measured by the convergence sensors that were located in the fill, 7 ft outby the final coal rib when the face was about 95 ft away.

Stage 2 is when the pressure on the remaining longwall panel fender increases more rapidly and the convergence in the recovery room accelerates. This behavior was detected at all four sites across the panel on January 28th at about 22:00 hrs, when mining was restarted following the shearer repairs.

The next phase, Stage 3, is the yielding of the longwall panel fender and transfer of load onto the outby recovery room pillars. The pressure increased on the remainder of the panel as the face advanced toward the recovery room until the longwall panel fender yielded when it was about 6 ft thick (January 29th at 08:00).

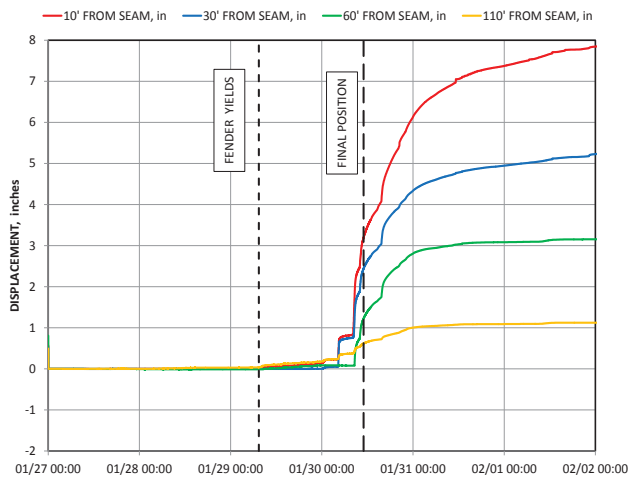



**Figure 14. Chart showing the output from the multipoint borehole extensometer. The largest displacement measured was about 0.20 inches until 00:00 on January 30th. Then about four hours later the displacements moved significantly.**

Simultaneously, increasing convergence was measured across the panel at all four sites and yielding of the shield legs across the face was observed. The convergence that occurred immediately following fender removal, shown in Figure 9, was 1.5 in or less in the protected ends and 2.0 in or more in the mid-face area of the panel. For Sites 2 and 3 near the middle of the face, the behavior of the ground is the same as the model predicts, while for Sites 1 and 4, the side abutment load is clearly transferred onto the gateroad pillars as the fender yields. There were no BPCs in the pillars outby Sites 1 and 4 to detect the front abutment loads.

The maximum probability of fender instability occurs during Stage 4, while Stage 5 includes a secondary surge of roof convergence following the longwall panel fender removal. The instability of the longwall panel fender was mitigated by the installation of cuttable, fiberglass rib bolts in the panel-side rib of the recovery room and by the extremely high SSD in the recovery room. The secondary convergence surge induced yielding of the shield legs as shown in the chart of the leg pressures in Figure 15 when the shields were in there final position (January 30th at 11:00) in the recovery room.

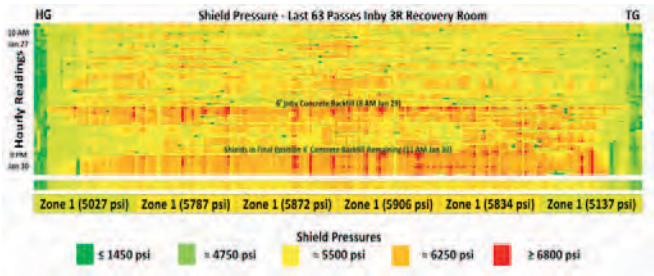



**Figure 15. Peak shield leg pressures during mining into the recovery room.**

The MPBX, located above the center of the recovery room, between Sites 2 and 3 began to show displacement at the same time, but it amounted to less than 0.1 in. It is hypothesized that the MPBX surface reference had begun to subside at this time as the load from the strata above the recovery room was transferred from the backfill onto the cable bolts, especially the bolt that was angled over the outby pillar. From surface surveys, the elevation of the MPBX measurement head dropped 4.56 in between the day before mining restarted (January 26th) to three days after the panel extraction was completed (February 2nd). The average subsidence above the fender position as measured by survey was 15 inches in the same period. The MPBX measurement reference head was located about 5 ft ahead of the shield legs and the fender was about 6.5 ft behind the gob shield when the shields were at their final position. This difference in the position of the measurements relative to the position of the shields can account for the difference between the subsidence measurements.

Another noticeable difference in the dataset was the cyclic behavior demonstrated at Site 4 and the tailgate pillar BPCs compared to the other sites. Not only did the BPCs exhibit variations (likely due to stress changes caused by each pass of the shearer), the average pressures recorded were much higher than at the other sites across the panel. The data at Site 4 were recorded on three different MIDAS dataloggers, all of which indicated this behavior in the readings. This eliminates datalogger and instrumentation error as a source of the variation. It is suspected that the roof in the vicinity of Site 4 and the tailgate was less restrained by the adjacent strata, and therefore was more responsive to the mining activity. The adjacent Panel 2 gob or local geologic variation could have played a role as well.

Finally, there was an occurrence recorded on the Chute 3 BPCs before mining started on January 27th, as seen in Figure 5. Notice that these events are also visible on the Chute 2 BPCs, the Site 3 Fill BPCs, and the Panel BPCs at Sites 2 and 3. The pressure in the Chute 3 pillar BPCs reached 115 psi, which was the second highest BPC pressure recorded. The BPC pressure recorded at the Site 3 Fill was about 12 psi and at the Site 3 Panel it was about 24 psi. At the Chute 2 outby pillar, the BPC pressure was about 17 psi and at the Site 2 Panel BPCs was only about 5 psi. The suspected cause for this event is that the roof above the Chute 3 outby pillar was 'working' and a crack formed that allowed the strata to move. The change in stress was then redistributed over the next few hours.

## CONCLUSIONS

The predriven recovery room for the third panel at the Bull Mountains No. 1 Mine was developed and supported using a Reinforcement Density Index (RDI) of 57.92 tons/ft (1.69 MN/m), and then was backfilled with cellular concrete for a Standing Support Density Index (SSD) of more than 800 psi (5.5 MPa). Borehole pressure cells (BPCs) were installed to monitor the front abutment load in the longwall panel, recovery room fill, and outby pillars. BPCs were also installed in the gateroad pillars to monitor the side abutment load. Four sensors were placed in the recovery room fill to measure the convergence of the roof and floor, and a multipoint borehole extensometer was installed above the recovery room to measure the movement of the overlying strata.

The data collected indicate that the ground around the recovery room behaved like the geotechnical model proposed by Thomas (2008) as the longwall panel was fully extracted. The cell pressures in the longwall panel adjacent to the recovery room increased as the longwall approached and the load was transferred onto the fill material and surrounding pillars. The fender began to yield when it was about 6 ft thick with the longwall shields yielding at the same time. The convergence measured in the recovery room fill ranged from 1 to 2 inches.

It is theorized that the cuttable fiberglass reinforcement installed in the panel rib was very important to the success of this predriven recovery room. The bolts allowed the fender to maintain its supporting capacity until it was only 6 ft thick, which means the shields were that much closer to the outby pillars and the distance spanned by the roof was that much shorter. The capacity and number of cable bolts angled over the outby pillars were also important to the success of this recovery room. Finally, the high density and capacity of reinforcement in the roof and the backfill in the recovery room allowed the longwall to advance to its final position and the face was recovered in record time.

## REFERENCES

Oyler, D., Frith, R., Dolinar, D., and Mark, C., (1998). International Experience with Longwall Mining into Pre-driven Recovery Rooms. Proceedings of the 17th International Conference on Ground Control in Mining, Morgantown, WV. Aug 4-6, pp 44-53.

Barczak, T. M., Tadolini, S. C., Zhang, P. Y. (2007). Evaluation of Support and Ground Response as Longwall Face Advances into and Widens Pre-Driven Recovery Room. Proceedings of 26th International Conference on Ground Control in Mining, Morgantown, WV, pp 160-172.

Stankus. J.C. and Hanson, B. (2012). Ground Control at Signal Peak Energy Bull Mountains No. 1 Mine. MINExpo INTERNATIONAL 2012, Las Vegas, NV. Sept 24-26.

Stankus, J. C., et al., (2014). A Case Study of Low Overburden Longwall Recovery with Pre-Developed Recovery Entries. Proceedings of 33rd International Conference on Ground Control in Mining, Morgantown, WV.

Thomas, R., (2008). Recent Developments in Pre-driven Recovery Road Design. Proceedings of 27th International Conference on Ground Control in Mining, Morgantown, WV, pp 197-205.

Jones, T. H., (2012). Knowledge is Power: Introducing the MIDAS, a New Permissible Datalogging System for Use in Mines. Proceedings 31st International Conference on Ground Control in Mining, Morgantown, WV, pp 1-6.

Geokon, (2001). Instruction Manual for Model 3200 Borehole Pressure Cell. 22 pages.

# Suspension Designs Required in the Logical Framework

**Ross W Seedsman**, Director
Seedsman Geotechnics Pty Ltd
Mittagong, Australia

## ABSTRACT

The logical framework recognises that a coal mine roof can be intrinsically stable or may collapse in one of four ways. Suspension of the immediate roof is one of fundamental ground control strategies available to a coal mine engineer and is recommended for three of the four collapse modes. Correctly implemented suspension offers the greatest improvement in roof stability and greatest reduction in longwall risk. For the control of maingates ahead of retreating longwall faces the ideal suspension support (if required) consists of angled, partially debonded, medium-length tendons installed as far behind the development face as practical. For situations where the roof may be subjected to tensile horizontal stress, immediate support by equally spaced short vertical tendons is required. The step away from fully-grouted tendons improves their survivability during the onset of compressive failure in the roof, minimises the risk of isolated loading, and allows a more robust TARP for roof movement. All suspension systems require a strap, sling or truss between the suspension elements.

## BACKGROUND

The logical framework (Seedsman, 2012) recognises that a coal mine roof can be intrinsically stable or may collapse in one of four ways (Figure 1). Associated with the framework are a set of relatively simple analytical methods and look-up charts that provide the geotechnical engineer the tools to conduct limit equilibrium type analyses. The logical framework sits between the empirical methods that are readily implemented by non-specialists and the complex numerical codes that need an appreciation of their complex mathematics and recognition of the limitations of the input data.

In most cases the immediate roof of a coal mine roadway consists of a regular assemblage of rectangular prisms of rock or coal defined by bedding and joints (Figure 1), with an important exception if the joints are not aligned normal to bedding (disordered roof) such as near faults. The framework starts by checking non-vertical joints, then checks for compressive failure using a new failure criterion (Seedsman, 2013). This compressive test can use the Uniaxial Compressive Strength (UCS) from core and also that derived from geophysical logs. Given the presence

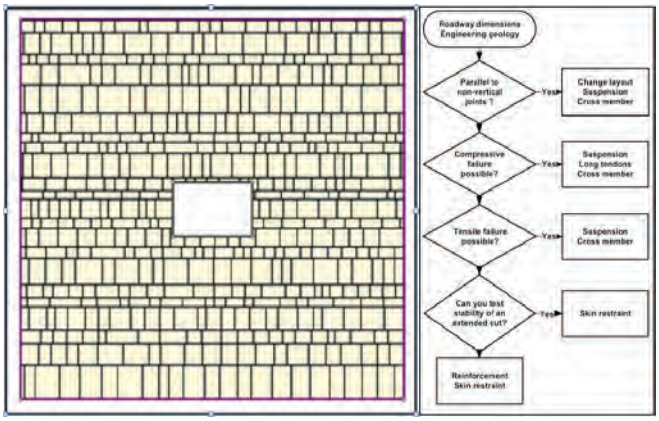



**Figure 1. Logical framework.**

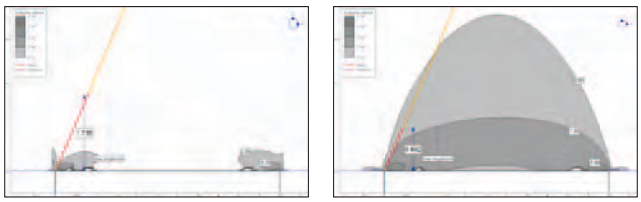
of joints, the roof horizon must be assumed to have zero tensile strength so the onset of any tensile stresses needs to be checked. There is then a need to check the bedding spacing and the possible need to build an adequately thick beam from thinly bedded roof rock. The ultimate test for bedded roof is the stability of an extended cut, but if the mining system does not allow this it must be assumed that the roof is thinly bedded. Implementing the framework does not necessarily require core.

The logical framework identifies suspension as the appropriate response to disordered roof, compressive failure and tensile failure. Recently, suspension design has been dismissed as fundamentally flawed (Frith and Colwell, 2011) on the basis that roof collapses have occurred even though calculations based on a suspension design give installed capacities in excess of the dead weight of the collapsed volume. In 2012 the framework was declared inadequate because it does not proscribe factors of safety (Colwell and Frith, 2012). This paper examines the details of a suspension design and highlights where engineering skills and judgement are required. The relatively simple case of suspension from a spanning unit is not addressed in this paper.

## NON VERTICAL JOINTS – DISORDERED ROOF

Non-vertical joints are those that dip at less than approximately $65^{o}$ - $70^{o}$ (complement of the joint friction angle). At these angles,

any roof stress condition can generate shear displacements along the joints which can then interact with bedding and lead to roof collapse. A simple elastic boundary-element program (Examine2D) indicates that the height of the joint shear failure increases as the horizontal to vertical stress ratio decreases (Figure 2) while the level of compressive brittle failure decreases.



(a) Horizontal/vertical stress = 1.0 (b) Horizontal/vertical stress = 1.5

**Figure 2. Shear along a joint dipping at 650 and onset of compressive brittle failure for horizontal to vertical stress ratios of 1.0 and 1.5 (Examine2D, 5.5m by 3.0m, depth=300 m, density=0.025 MN/m3, E1=E2=10000 MPa, G=667 MPa, UCS =10 MPa, friction angle=0 deg, Kn=400000 MPa/m, Ks=40000 MPa/m, joint cohesion=0 MPa, joint friction angle=30 deg.**

In flat-dipping coal measures non-vertical joints are mostly found within or in close proximity to fault zones: be they normal, reverse or thrust faults. It is noted that considerations regarding passive and active earth stresses imply that there should be comparatively lower horizontal to vertical stress ratios in the immediate vicinity of faults (as compared to the background stress field) and this means that roof control difficulties are in fact driven more by the angled joints and broken rock than by high stresses.

The mining implication of shear along angled joints is that the roof can readily collapse and the resulting overbreak can quickly result in delays in installing roof bolts. This is perhaps why the Australian underground coal industry uses bolter miners instead of extended cut development systems. Compared to say the Pittsburgh Seam, Australian coal seams are substantially more faulted. There are notable exceptions with some Australian operations achieving very high performance in seams with very steeply dipping normal faults and good advance knowledge of their location.

## COMPRESSIVE FAILURE

### Extent of compressive failure

Seedsman (2011) proposed a method to predict the height of compressive failure consistent with recent developments in the understanding of brittle rock strength and calibrated to mining experiences. In the method, the height of compressive failure is used as a proxy for the "height of softening" as determined by extensometry, with the conservative assumption that the height of softening represents the height to which the roof would collapse if it were to be unsupported. The rock strength criterion is further discussed in Seedsman (2013). The method allows the calculation of the maximum height of failure above any shaped opening as a function of the UCS, and the vertical and horizontal stresses. Figure 3 shows how the height of compressive failure can increase substantially between roadway development and subsequent longwall retreat. At the development face, normal bolting lengths (1.5 m - 1.8 m) may be adequate to suspend the failed rock but at the maingate longer tendons would be required. Close inspection of Figure 3 reveals lower strength factors towards the roof/ rib corners which can be interpreted to be a reflection of stress guttering reported in underground roadways

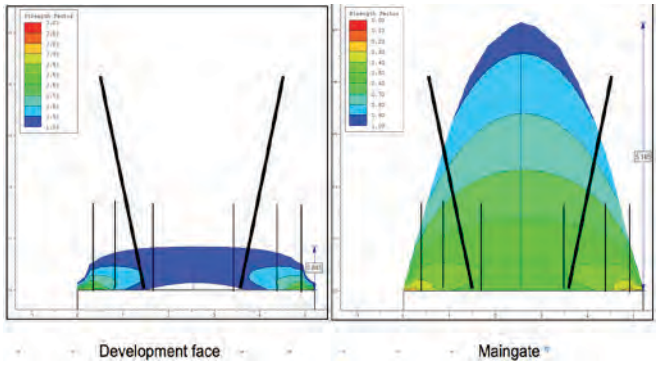



**Figure 3. Extent of compressive failure on development and at the maingate corner (depth = 300m, UCS = 45 MPa, frictional limit = 33 deg, K=1.5, reducing to 1.4 at maingate as the vertical stress doubles).**

The height of the zone in the roof with a strength factor less than unity depends on the ratio of the UCS to the pre-mining vertical stress (Roof Strength Index – RSI), the ratio of the horizontal to vertical stress (K) and the roadway span (Figure 4). Very high values of the RSI are required for the failure zone to disappear completely, and it is noteworthy that the zone needs to be in excess of 0.5 m in height before it extends fully across the roadway.

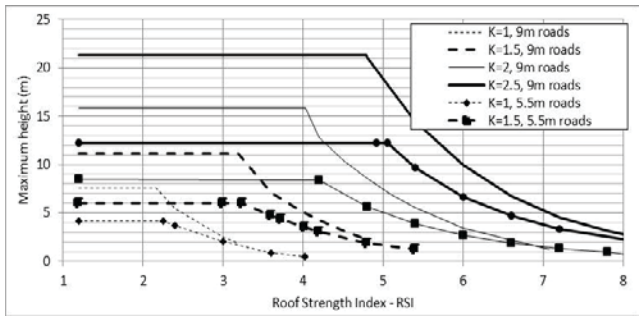



**Figure 4. Height of zone with a strength factor of less than 1.0 as a function of the roof strength index and the ratio of the horizontal to vertical stress.**

It is emphasised that these are elastic analyses such that the numerical model (Examine2D) does not redistribute the stresses after failure. Seedsman (2009) presented a conceptual model for stress redistributions in the immediate roof for conditions where the rock strength index would lead to the onset of large-scale compressive failure. In this model, horizontal stresses are not present within the immediate roof – these have been transferred to the stress arch as seen in the data reported by Mark et al (2007) and the earlier work of Gale and Mathews (1992) – refer to Figure 5. This redistribution of stresses is not recognised in AMCMRR (Analytical Method – Coal Mine Roof Rating, Colwell and Frith 2010) which relies on the presence of elevated stress in the immediate roof line to generate buckling.

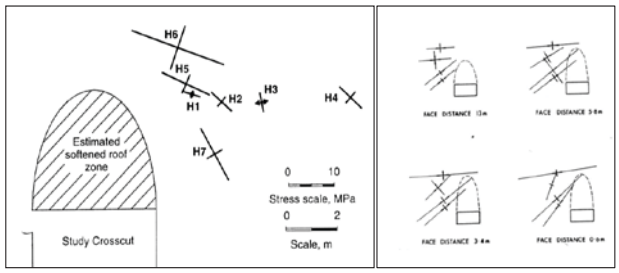



**Figure 5. Stress redistribution about softened zones (Mark et al. (2007), Gale and Mathews (1992)).**

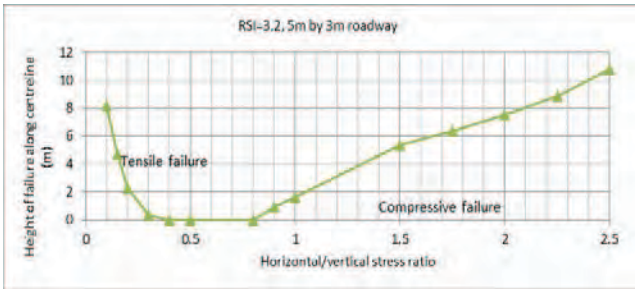



**Figure 6. Height of failure (strength factor = 1.0) varies with the ratio of the horizontal to vertical stress.**

There are several practical implications of the onset of brittle compressive failure as shown in Figure 3. Firstly, standard length roof bolts may be able to suspend the failed mass that is formed immediately outbye of the development face but demonstrably will not be adequate at the maingate corner. Secondly, shorter long tendons would be needed at the maingate if they can be angled. More importantly, the long tendons must be able to survive the deformations associated with the increased zone of failure and be intact when they are required to act in suspension. Finally, as highlighted in Figure 5, the specification of the long tendons does not have to consider applied horizontal stresses.

## TENSILE FAILURE

As a result of the presence of joints and bedding, the design process for any ground control strategy at the roadway scale must include the default assumption that the roof has zero tensile strength. This is totally consistent with the recommendations not to use the Generalised Hoek Brown criterion (Hoek and Brown, 1997) if there are only two discontinuity sets (joints and bedding). An important implication for numerical modellers is the need to use a tensile cut-off in a Mohr Coulomb criterion if continuum behaviour is assumed.

It is of interest to examine the height of failure (tensile or compressive) above the centreline of a typical development roadway for a rock mass with zero tensile strength and a Roof Strength Index (RSI) of 3.2 (Figure 6). Equally high zones may develop at very low horizontal to vertical stress ratios as at high stress ratios, for example 2m high for K values of either 0.2 or 1.05.

If zero tensile strength is assumed, the extent of any tensile failure is the same as the zone of tensile stress. The discontinuity set of interest for roof collapse are the joints that are normal to the bedding and hence effectively vertical. These joints will contribute to roof collapse if the horizontal stress is either zero or tensile. Whether shear failure along joints leads to roof collapse will depend on the kinematics of the joint-bounded blocks which is related to the amount of dilation of the joints. Small dilations may allow blocks to interact and result in the formation of a voussoir beam. Larger dilations may mean blocks simply fall. Figure 7 shows the distribution of tensile horizontal stress for isotropic and a simple implementation of transversely isotropic (E1=E2, E1/G=15) cases and three horizontal to vertical stress ratios. It is noted that the dimensions of the tension zones are independent of the magnitude of the applied stresses, and that the magnitudes of the tensile stress within the zones (and possibly the associated dilation) will increase as the tensile stress magnitudes increase. The height of the tensile zones at the centreline decreases with an increase in stress ratio (Figure 6). The "ears" in the K = 0.1 do not define kinematically acceptable blocks that could collapse.

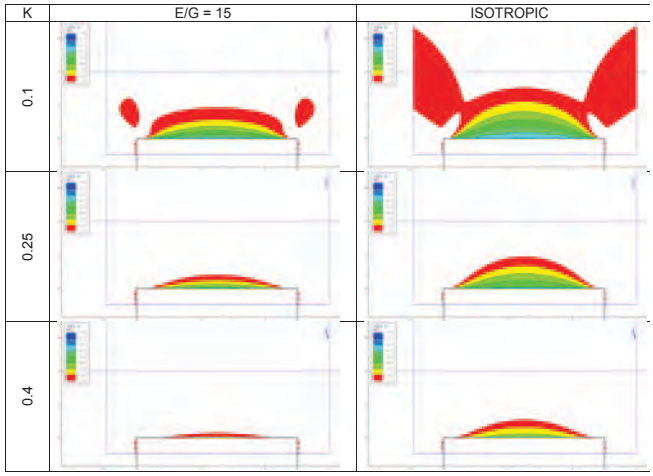



**Figure 7. Tensile horizontal stresses in the roof of a roadway.**

Elastic stress analyses, as well as closed-form solutions of stress around holes (Poulos and Davis, 1974, Brady and Brown, 1985) all indicate a reduction of roof stress as the vertical stress increases compared to the horizontal stress. This is opposite to that proposed by Frith (2000) who invoke the so called Poisson's Ratio effect, although the fundamental requirement for absolute zero lateral strain when invoking this effect cannot be satisfied at or near an excavation boundary given that the roadway itself deforms.

The key to anticipating the onset of tensile roof stress is to identify the situations where the vertical stress is higher than the horizontal stresses. The compilations of international stress data (Hoek and Brown, 1980) and Australian coal measures stress data (Nemcik et al, 2006) suggest that this is relatively rare. However in the coal mining sector, there are a number of specific environments where a low horizontal to vertical stress ratio should be anticipated as the "base-case":

- Thick coal seams where the immediate roof is coal (Seedsman, 2004). Very low horizontal to vertical stress ratios have been uniquely measured in coal and this is possibly related to shrinkage of the coal as it is dewatered by underground mining (gas may be of secondary importance). It is noted that lower stress ratios may result as the joint spacing in the coal reduces. A consequence is the need to be particularly vigilant when forming wide roadways with a coal roof.
- Undermining or overmining of pillars in multiple seam operations. Transverse isotropy induced by bedding appears to result in a columnisation of the vertical stress (Suchowerska et al 2013) and this is consistent with the author's observations and simple analyses (Figure 8). The spread of vertical stresses implied by the simple Boussinseq models may not be appropriate for coal mine pillars.

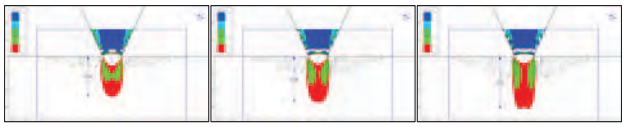



**Figure 8. Columnisation of vertical stress below a 30m-wide chain pillar with 250m-wide extraction panels.**

- Tailgates. The impact of yielding pillars and floor failure is discussed by Diederichs and Kaiser, 1999). Based on the author's observations and an interpretation of the ALTS method (Colwell, 1998), if the chain pillar is adequately designed the horizontal stress reduction associated with the adjacent longwall is not sufficient to lead to adverse stress ratios and the onset of tensile relaxation in the tailgate. Adequately sized in this context is one that is behaving elastically. If the pillar is designed to yield, then the additional vertical deflections in the pillar will lead to tangential relaxation in the roof line (Seedsman, 2001). This is considered to be the fundamental mechanism behind ALTS: the pillar strength equation is a yield criterion and roofs with low CMRR are those that are more closely bedded, more closely jointed and hence more susceptible to tensile failure. A bearing failure of weak layers in the floor of a pillar system may lead to sufficient vertical deformation to mobilise this mechanism as well.

## SPECIFYING THE SUSPENSION PATTERN

A suspension design is required in the circumstances outlined above and if there is a need to keep the roadway open for access or egress: the alternative would be standing support. The design model is simple and involves the dead weight of a volume of rock or coal with no imposed horizontal stresses. Some horizontal stress may be induced by subsequent block rotations within the fractured volume but these cannot be relied on in a robust support design. It is noted that these assumptions rule out the use of ground reaction curves – the model invokes gravity dead weight so there is no arching of loads or stresses.

The parameters to be considered are the height and weight of the suspended block, the length of the anchorage, the capacity of the tendon, the location of the tendons, the "sling" between tendons, the mode of installation, and a measure of the resultant improvement in the stability of the roof.

### Height and weight to be suspended

The density of the material to be suspended is usually well known (1.4 - 1.6 t/m$^3$ for coal, 2.5 t/m$^3$ for rock) so the design quickly focusses on the height and shape of the collapse volume. For compressive failure the height ($H_{max}$) can come from an analysis similar to Figure 4 and the shape can be assumed to be a parabola (cross sectional area = 2/3 base*height). For tensile failure, the height can come from analyses like Figure 7 with the shape assumed to be a rectangle.

### Tendon capacity

Assuming the anchorage is adequately designed (see below), the design capacity is either the tensile strength of the tendon or the collar assemblage if the tendon is simply point-anchored. There is an important question about whether the tendons will be equally loaded. This is likely to be the case for the spans being considered but it is good practice to have some ductility in the cables so that there is an increased ability to redistribute loads evenly between them.

### Anchorage length

The anchorage can be estimated using the methods of Littlejohn (1993), viz:

$$L_a = M*2*\cos\Phi*T/(\pi*d*UCS*(1-\sin\Phi))$$

where $L_a$ = required anchorage length, d = maximum diameter of the tendon or the borehole, T = tendon capacity, UCS of the rock or grout (MPa) and $\Phi$ = friction angle, and M is a confidence factor.

Analyses should be conducted for the cable/grout interface and at the grout/rock interface, with the former considering the maximum diameter of bulbed or nutcaged cables. Manipulation of the equation for typical tendon and hole diameters with resin with a shear strength of 30 MPa will show that failure at the grout/rock interface controls performance until the rock is in excess of about 80 MPa. Several implications come from this – large diameter holes are better so long as the resin is adequately mixed, and the load transfer properties of the steel/grout interface are only significant in high strength rocks and then the anchorage lengths are too short to be applicable in a practical sense.

### Active length and location

The vertical height of a parabolic shaped collapse zone as a function of location with respect to the roadway centreline is given by:

$$L_{vh}=H_{max} - 4x^2\, H_{max}/W^2$$

where $L_{vh}$ = vertical height, W = roadway width, and x is distance from the centreline. This equation can be used for vertical cables. The algebra for angled cables is more complex but it is easy to determine the length of such cables with a scale drawing.

For compressive failure, an optimum design is obtained by locating the cables angled away from centreline to reduce the exposure of the design to uncertainties in the height of failure that could lead to the anchorage being over-ridden (there may be little if any deformation warning of this) and also to reduce the required lengths. The collars should not be located within 1 m of the rib corner as the extent of damage may be too great to allow the transfer of loads from the tendon to the roof. In Australia pairs of cables are routinely used, spaced 1/3 and 2/3 across a development roadway and angled at no more than about 15° from the vertical. For tensile failures and suspension from a spanning unit, evenly spaced tendons are probably the best.

**Inclined tendons**

Hutchinson and Diederichs (1996) present a discussion on the capacity of angled tendons based on a series of laboratory tests of plain, nutcaged and bulbed cables (Figure 9). The results for the plain cable were anomalous and were the result of the cables slipping at the cable/grout interface which can be readily determined using the anchorage equation given above. For the other cable types, where the effective diameter of the cable was much greater, the experimental design was valid, and the results show no significant difference in the peak loads. The lack of impact has been attributed by many researchers to the yielding of the grout/rock ahead of the tendon (Holmberg and Stille, 1992). The decrease in capacity proposed by Frith and Colwell (2011) by referencing mechanical/structural engineering is not observed in rock.

The angled cables show greater deformation per unit load (less stiff) which is perhaps advantageous for a roadway suspension system in that it allows a greater opportunity to redistribute the loads between the cables and also provides a level of deformation that can be used in a deformation-based Triggered Action Response Plan (TARP).

**Stiffness - Post installation deformation**

The conventional view requires a stiff installation to limit the development of the height of softening. This view may have developed as a consequence of the way in which the empirical data has been presented (Figure 10). It is suggested that it is equally valid to plot the height of softening as the independent variable (abscissa) and the roof deflection as the dependent variable or ordinate. With this presentation an alternative interpretation is possible - that roof deflection is a response to failure in the roof, possibly in response to the dilation that occurs at failure. This interpretation leads to a conclusion that it is futile to seek to limit deflections given the very high stresses that drive rock failure. In rock masses, the ground stresses can arch above a roadway so the ground control approach can be to seek to control unacceptable deflections until the stresses are redirected into the arch (Figure 5).

This interaction between deflection and stress redistribution is the basis of the ground reaction concept which has been advocated in recent years for standing support and longwall chock design.. The classic presentation of this concept discussed the dangers of the early installation of stiff support. Referring back to Figure 3, installation of roof support at the development face or even in front of the longwall abutment front is "early" in the context of the stress changes that are about to impact the maingate corner. A stiff

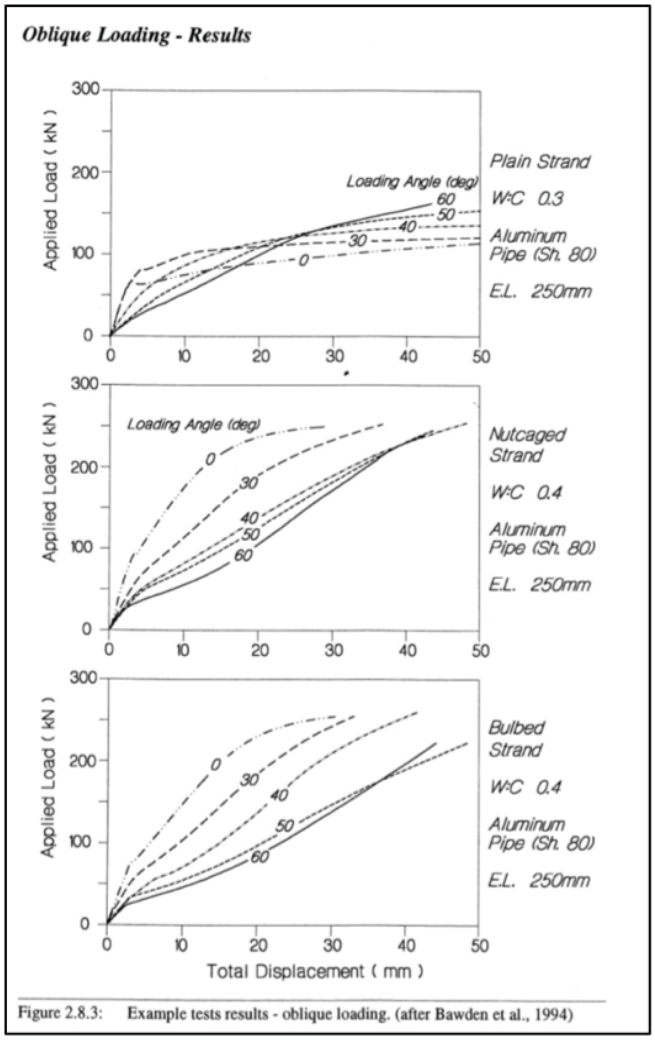



**Figure 9. Combined axial and tensile loading of tendons (reproduced from Hutchinson and Diederichs,1996).**

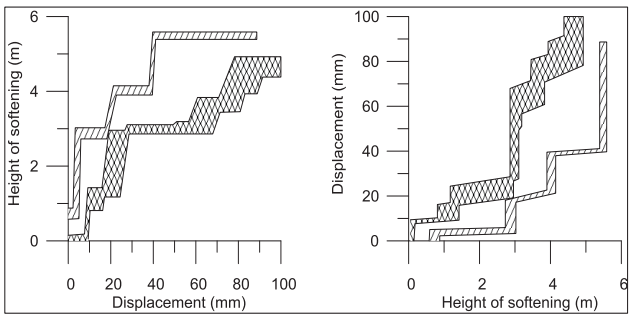



**Figure 10. Replotting of height of softening and roof deflection changes interpretation of empirical data (after Gale et al., 1992).**

installation will not be able to prevent the onset of failure in the roof and more importantly may not be able to sustain the associated deformations. Test data on double-embedment tension tests (Clifford *et al*, 2001) has a fully grouted cables failing at 7 mm to 8 mm of opening of a joint compared to in excess of 40 mm for a point anchored cable (Figure 11). Note that the vertical movement

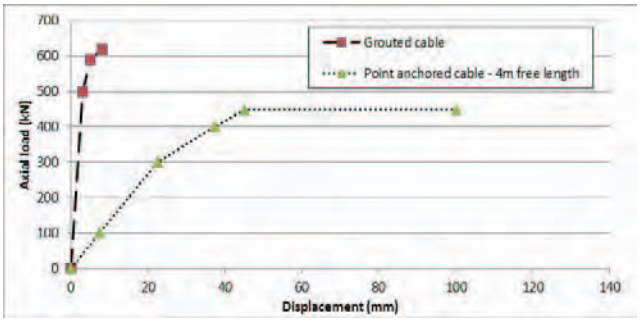



**Figure 11. Comparison of double embedment test on a grouted cable (after Clifford et al., 2001) and calculated deformation of a 4m free length of cable.**

of the roof line shown in Figure 10 has been measured to be 60 mm to 100 mm, suggesting the possibility that there could be enough strain localised at some horizon to fail the cable.

Under simple direct loading, a point-anchored cable has lower capacity than a fully grouted cable and this is the result of yielding and failure of the collar assembly. To address the stiffness concerns while still being able to mobilise the full tensile capacity of the cable it should be possible to fully grout the tendon but to decouple the middle section. As well as increasing the survivability of the tendon, the roof deflections before failure will be greater and this will allow a more robust deflection trigger for any TARP. The grout at the collar will tend to reduce if not stop deformation at the roof line.

**Mesh/sling**

If a broken de-stressed rock mass is assumed, there may be zones within the immediate roof that are not directly restrained by the tendons (Figure 12). If these zones were to collapse, the roof would unravel around the long tendons leading to total collapse. Depending on the load distribution angle beneath the collar and the spacing of the tendons, loads of up to 3 to 5 tonnes can be reasonably expected and these need to be retained by the roof mesh, W strap or a truss. Laboratory tests on standard mesh panels (Thompson, 2004) indicate a capacity of 2 to 3.5 tonnes depending on the bolt spacing. It is concluded that any suspension strategy must also include specific measures to ensure that collapse of the roof between the tendons does not lead to unravelling of the roof. Closer spaced, lower capacity tendons may be preferable despite the greater installation time.

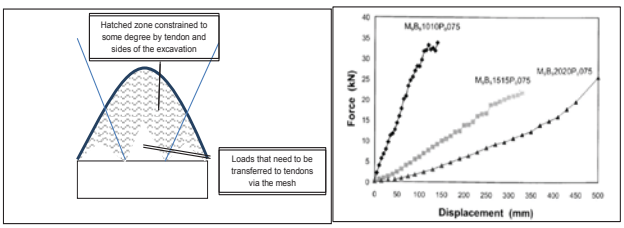



**Figure 12. Zones which need to be supported to transfer loads to the tendons and the capacity of typical mesh panels.**

**Design factors**

The term "Factor of Safety" is still commonly used although its misuse and incorrect application is now being recognised. At its simplest arithmetic level, a factor of safety is the ratio of the estimated strength to the estimated load. In the real world, there may be uncertainty in the estimates. A design is considered acceptable if the likelihood of the strength being exceeded by the load is acceptable given the consequences. In some industries, for example aerospace, the factors of safety can be relatively low compared to geotechnical designs because the uncertainties in the strength and load estimates are low even though the consequences of failure are high. In geotechnical designs, the factors are typically higher because of the difficulties in estimating the loads and particularly the strengths. From a design perspective, the level of confidence in these estimates determines the factor of safety that is acceptable.

With this use of the term in geotechnical engineering, factors of safety should not be pre-determined. It is unfortunate that mining regulation is tending to move that way. It is meaningless to apply factors of safety from other industries, for example lifting by cranes. If a factor of safety value is mandated onto a mine geotechnical engineer, it should be used to determine the required site investigation to reduce the uncertainties to the implied level.

When finalising the design, the mine geotechnical engineer should consider:

- Height factor – how reliable is the estimate of height? How reliable are the estimates of rock strength and the in-situ stresses, what have back analyses suggested, is there a precedent at your mine or close by? Lower bound strength values and any available stress data should be used when calculating the heights given by Figure 4. This parameter leads directly to the loads to be suspended, with little uncertainty regarding width or density.
- Loading factor – will the tendons be loaded equally? Given the general industry expectations regarding "Factors of Safety" it is may be appropriate to add about 20% to calculated loads.
- Survivability factor - could they fail due to deformation incompatibility? An arbitrary 50% reduction in the mobilised strength of fully grouted cables could be considered but it should be recognised that this is without technical justification – clearly more research is required.
- Anchorage length – The civil engineering literature suggests a doubling of the calculated length to address uncertainties about installation quality, values between 1.25 and 1.5 have been used by the author in the past.

## CONCLUSION

Correctly designed, suspension is a very robust roof support design approach. There are some important subtleties in the design which conflict with some of the concepts that have been published in the last decade. A suspension design accepts that it is not possible to prevent tensile or compressive failure of the roof and that what is needed is a support regime that can survive the onset of failure and then prevent the subsequent gravity-driven collapse. A corollary of this is that deformations are inevitable and can be utilised in a TARP process, recognising that the triggers

will be related to deformations of flexible systems. Suspension systems are installed proactively, in that they anticipate the onset of failure and are ready to prevent collapse. In better ground where compressive or tensile failure is not likely, it may be more efficient and economic to prevent the deterioration of a bedded roof by reinforcing against shear.

**REFERENCES**


Brady, B H G and Brown, E T, 1985. *Rock mechanics for underground mining*. London, UK: George Allen & Unwin.

Clifford, B, Kent, L, Altounyan, P and Bigby, D, 2001. Developments in the long tendon systems used in coal mining reinforcement. *In Proceedings, 20th International Conference on Ground Control in Mining.* Morgantown WV August 7-9, pp. 235-241.

Colwell, M G, 1998. *Chain Pillar Design – Calibration of ALPS*. Final Report – ACARP Project C6036, 67p.

Colwell, M G and Frith, R, 2010. AMCMRR – An analytical model for coal mine roof reinforcement. *10th Underground Coal Operators' Conference.* University of Wollongong and the Australasian Institute of Mining and Metallurgy, pp. 73-83. http://ro.uow.edu.au/coal/302/.

Colwell, M G and Frith, R, 2012. Analysis and design of faceroad roof support (ADFRS) – A roof support design methodology for longwall installation roadways. ACARP Project C19008.

Diederichs, M S and Kaiser, P K, 1999. Tensile strength and abutment relaxation as failure control mechanisms in underground excavations. *International Journal of Rock Mechanics and Mining Sciences*: 36, pp. 69-96.

Frith, R. 2000. The use of cribless tailgates in longwall extraction. *Proceedings 19th International Conference on Ground Control in Mining*. Morgantown, pp. 84-92.

Frith, R and Colwell, M G, 2011. Why Dead Load Suspension Design For Roadway Roof Support Is Fundamentally Flawed Within A Pro-Active Strata Management System. *Proceedings 30th International Conference on Ground Control in Mining. http://icgcm.conferenceacademy.com/papers /detail.aspx?subdomain=icgcm&iid=890.*

Gale, W J, Fabjanczyk, M W, Tarrant, G C and Guy, R J, 1992. Optimisaiton of reinforcement design of coal mine roadways. *11th International Conference Ground Control in Mining.* Wollongong, 7-10 July 1992. pp. 272-292. http://icgcm.conferenceacademy.com/papers/detail.aspx?subdomain =icgcm&iid=2001.

Gale, W J and Matthews, S M, 1992. *Stress control methods for optimised development and extraction operations.* Report to National Energy Research Development, and Demonstration (NERD&D) Program, Project 1301.

Hoek, E and Brown, E T, 1980. *Underground Excavations in Rock*. The Institution of Mining and Metallurgy, London.

Hoek, E and Brown, E T, 1997. Practical estimates of rock mass strength. *International Journal of Rock Mechanics and Mining Sciences*, 34 (8), pp. 1165-1186.

Holmberg, M and Stille, H, 1992. The mechanical behaviour of a single grouted rock bolt. *In Rock Support in Mining and Underground Excavation,* Edited by Kaiser and McCreath, Balkema. Rotterdam, pp473-481.

Hutchinson, D J and Diederichs, M S, 1996. *Cable bolting in underground mines.* Vancouver: Bitech, Richmond British Columbia.

Littlejohn, S, 1993. Overview of rock anchorages. *Comprehensive Rock Engineering,* 4:413-450. Oxford: Pergamon.

Mark, C, Gale, W, Oyler, D and Chen, J, 2007. Case history of the response of a longwall entry subjected to concentrated horizontal stress. *International Journal of Rock Mechanics and Mining Sciences,* 44, pp. 210-221.

Nemcik, J A, Gale, W J and Fabjanczyk, M W, 2006. Methods of interpreting ground stress based on underground stress measurements and numerical modelling. *Proceedings Coal 2006, 7th Underground Coal Operators Conference.* pp104-112. http://ro.uow.edu.au/coal/39/

Poulos, H G and Davis, E H, 1974. *Elastic solutions for soil and rock mechanics*. John Wiley and Sons Inc. New York.

Seedsman, R.W. 2001. The stress and failure paths followed by coal mien roofs during longwall extraction and implications to tailgate support. *n Proceedings, 20th International Conference on Ground Control in Mining.* Morgantown WV August 7-9, pp. 42-49.

Seedsman, R W, 2004. Failure modes and support of coal roof. Ground Support in Mining and Underground Construction, *Proceedings 5th International Symposium on Ground Support*. pp. 367-374.

Seedsman, R W, 2009. Stresses in the immediate roof of a coal mine roadway. *9th Australasian Coal Operators' Conference,* University of Wollongong and the Australasian Institute of Mining and Metallurgy, pp. 62-69. http://ro.uow.edu.au/coal/80/

Seedsman, R W, 2011. Application of the brittle failure criterion to the design of roof support in the soft rocks of coal mines. *Coal 2011 - 11th Australasian Coal Operators' Conference*, University of Wollongong and the Australasian Institute of Mining and Metallurgy, pp. 60-72. http://ro.uow.edu.au/coal/342/.

Seedsman, R W, 2012. The development and application of a logical framework for specifying roof and rib support/reinforcement in Australian underground coal mines. *7th International Symposium on Rock bolting and Rock Mechanics in Mining*. Aachen 30-31 May.

Seedsman, R W, 2013. A practical strength criterion for coal mine roof support design in laminated soft rocks. *Mining Technology, 122(4), pp 243-249*.

Suchowerska, A M, Merifield, R S and Carter, J P, 2013. Vertical stress changes in multi-seam mining under supercritical longwall panels. *International Journal of Rock Mechanics and Mining Sciences, 61, pp. 306-320.*

Thompson, A G, 2004. Rock support action of mesh quantified by testing and analysis. *Paper presented in Surface Support in Mining*. (Eds. Potvin, Y., Stacey, D., & Hadjigeorgiou, J.) Australian Centre for Geomechanics, pp. 391-398.

# Understanding and Optimizing the Performance of Passive Primary Support on Coal Mines

**Anthony Spearing**, Associate Professor
**Aditya Mishra**, Graduate Assistant
Todd Kostecki, Graduate Assistant
Southern Illinois University Carbondale
Carbondale, IL

**Richard Taushanoff,** Senior Development Chemist
Orica
Georgetown, KY

**Jeremy Sell**, R&D Engineer
Orica
Bowerston, OH

## ABSTRACT

There are approximately 68 million rockbolts installed annually in underground coal mines in the USA (Tadolini and Mazzoni, 2006). The most utilized is the passive fully grouted resin rebar bolt, which constitutes almost 90% of the primary support in US underground coal mines. Resin-grouted rockbolts are a very effective and safe support, but their performance still needs to be further optimized and improved. This paper investigates their performance and suggests operating conditions to optimize the performance of resin-grouted rockbolts. In addition, this paper discusses a small-scale test that can also be used to evaluate the performance of rockbolts that is quicker, easier, and less costly than short encapsulation tests.

## INTRODUCTION

While rock-related safety continues to improve, it still remains a serious concern, as shown in Figures 1 and 2 which depict the rockfall injury rate and fatalities on coal mines since the early 2000s.

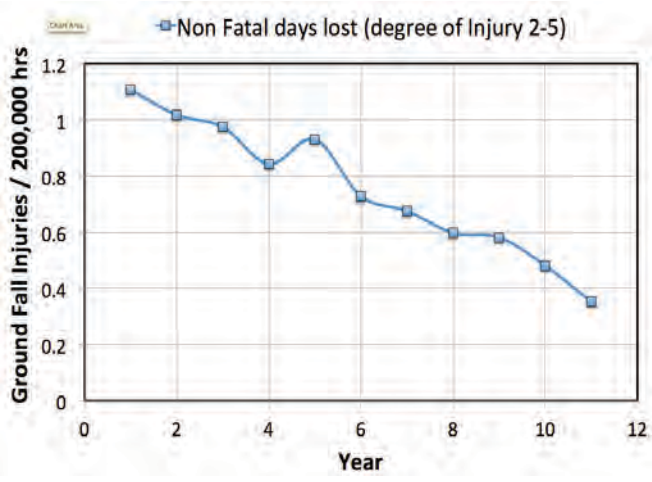



**Figure 1. Rockfall injury rate on coal mines.**

By definition, primary support is any support installed on-cycle and is the first line of defense against rockfall-related accidents.

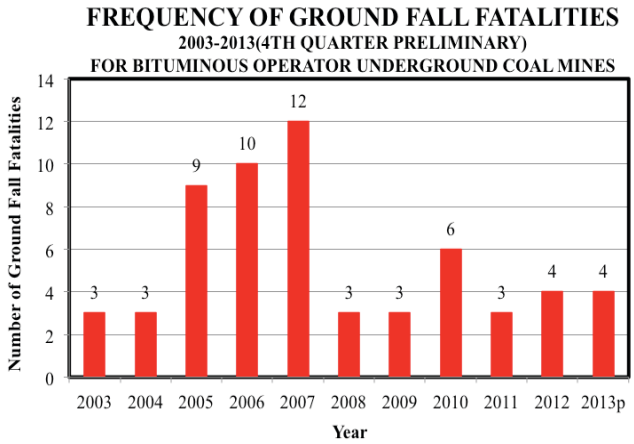



**Figure 2. Rockfall fatalities on coal mines.**

Primary rockbolts can be categorized as either active or passive bolts. An active rockbolt is tensioned during the installation process, while a passive rockbolt is not. However, the upward pressure exerted by the boom on a passive rockbolt after spinning can produce a tension of around 1 to 2 tons. Commonly used examples of primary support active resin-grouted rockbolts are the partially grouted resin assisted mechanical anchor bolt and the fully grouted tension rebar bolt.

In the most general sense, passive rockbolt systems are used because they are cheaper, provide adequate support in most roof strata, and are easier to install. Active rockbolts, especially those that are fully grouted, are used because they can limit rock movement, especially in shear and bending due to high, horizontal stress conditions because of the pre-tensioning on installation. The effects of active support on rock movement are still the subject of some debate, however. In regards to bolt usage, the trends seem to suggest a continuing increase in using resin-grouted rockbolts in coal mines, as shown in Table 1, which is, unfortunately, a little dated.

**Table 1. Trends in support usage over time in the USA (Dolinar & Bhatt, 2000).**

| Bolt Type | Percentage of Mines | | |
|---|---|---|---|
| | 1976 | 1988 | 1991 |
| Mechanical anchor | 80 | 35.3 | 34.1 |
| Fully grouted | 20 | 40 | 48.2 |
| Torque-tension | - | 3.5 | 4.6[1] |
| Resin-assisted mechanical anchor | - | 14.1 | 11.5 |
| Combination | - | 3.5 | - |
| Other[1] | - | 3.6 | 1.5 |
| Total[2] | 100 | 100 | 100 |
| [1] Includes both torque tension and combination bolts. | | | |
| [2] Data could not add to totals shown because of independent rounding. | | | |

## INSTALLATION PRACTICES AND RECOMMENDATIONS

The two most common support scenarios for coal mines are suspension and beam reinforcement. In the suspension support method, bolt anchorage into the overlying strong roof strata supports the weak and highly laminated immediate roof. Short encapsulation tests are particularly useful to design an effective suspension method. However, if these strong roof strata are water-bearing, this suspension method might not be suitable because water can be introduced into the already weak immediate roof, causing additional rock support issues. In the beam reinforcement method, laminated or bedded strata layers are held together to effectively create a reinforced single roof beam. Both methods are shown in Figures 3 and 4.

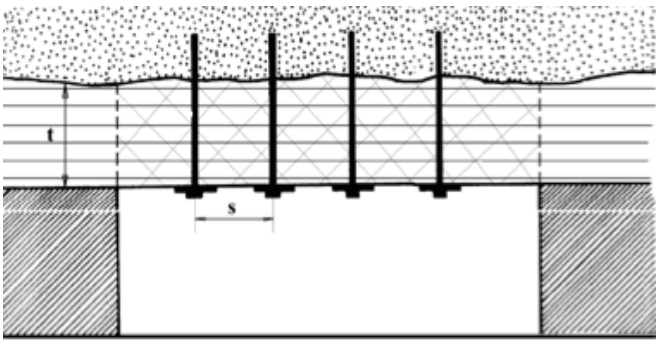



**Figure 3. The suspension support method.**

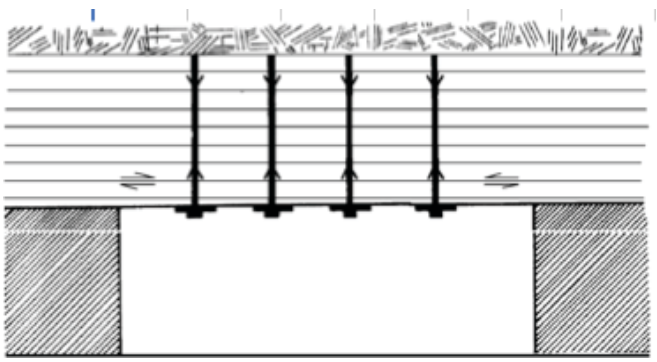


**Figure 4. The beam reinforcement method.**

The installation of a traditional, fully grouted, passive rebar rockbolt is relatively straightforward and simple. During installation, one or more resin cartridges are inserted into the drill hole. As the rockbolt is inserted into the drill hole, the resin cartridge bursts and is spun for an allotted number of seconds, as recommended by the manufacturer. The resin stays in the drill hole because of the thrust of the bolter unto the bolt, during which, the resin sets. The loading to the bolt is attributed to subsequent rock movement over time.

For two-speed, active torque tension rockbolts, two cartridges are inserted into the drill hole—a shorter, fast-setting resin cartridge followed by a longer, slow-setting resin cartridge. During the installation, the fast resin gels and sets first, and the bolt is tensioned using a threaded bolt and nut. The tension is kept on the bolt as the slower resin sets. A new development is a single cartridge containing two resin gel times (fast and slow); the fast resin is inserted into the drill hole first. This reduces the exposure of the bolter operators to the unsupported top because only one long resin cartridge is needed instead of two for a tensioned rebar bolt. The single cartridge system also improves bolting productivity significantly because it takes the bolter operators less time to insert the cartridges.

To use a partially grouted, resin-assisted mechanical anchor rockbolt, a mechanical shell is attached to the end of a bolt anchored in a grouted resin column section. This is generally a partial resin column due to the high-insertion, back pressures caused by the shell being forced through the resin column. There are some resin assisted mechanical anchor systems that can be fully encapsulated by using lower viscosity specialty resin. The bolt is spun which locks the mechanical shell in place at the back of the hole, then imparts a tension, and finally after the resin sets, it locks the tension in place.

Important operational parameters for the successful and cost-effective use of resin-grouted rockbolts are as follows:

- Standard practice is to drill the bolt hole an inch longer than needed.
- The annulus (annular gap) between the rockbolt and the hole is defined as half the diametric difference between the drill hole diameter and the rockbolt diameter. Keeping the annulus

low can facilitate the mixing of the resin components during installation. The optimum annulus is ⅛ inch. More than ¼ inch annulus should be avoided.

- Manufacturers typically recommend between 30–40 rotations during bolt rotation, which, with typical bolter speeds, equals 3–5 seconds for fast-setting cartridges. Fast cartridges are used so that installation time per unit is minimized. In room and pillar mining, installing support is the production bottleneck.

- After spinning the bolt, if it is passive, it is held for several seconds, then the bolter drill head is lowered. If the bolt is tensioned with the mechanical shell, it is tensioned (torqued) immediately. If the bolt is tensioned using two-speed resin, it is held for 3–5 seconds and then torqued by the rockbolter.

Table 2 shows the common rebar steel used for rockbolts. The most common are #5 Grade (Gr) 60 and #6 Gr 60.

- Both ends of the cartridge are clipped effectively, to stop liquid (particularly solvent) losses that otherwise could increase the viscosity of the cartridge over time.

- Rigidity to aid a rapid insertion into the drill hole.

- Viscosity and thixotropy so that the rockbolt can readily penetrate the resin cartridges and mix the two components during rotation.

- Low flammability and toxicity.

As mentioned previously, the use of resin-grouted rockbolts has increased dramatically because of their effectiveness when compared with other support systems. Current practice and understanding is mainly based on empirical knowledge, therefore the authors have tried to better understand the performance of resin-grouted rockbolts and improve upon current practice, by conducting mainly short encapsulation pull-out tests and durometer tests of resin-grouted rockbolts.

**Table 2. Commonly used steel for rock bolting and the hole diameters used.**

| Steel Material (size and grade) | Nominal Steel Diameter (inches) | Minimum Yield Stress (psi) | Recommended Hole Diameter (inches) | Annulus (inches) |
|---|---|---|---|---|
| #5 Gr 60 | ⅝ or 0.625 | 60,000 | 1.0 | 0.188 |
| #6 Gr 40 | $^{6}/_{8}$ (¾) or 0.750 | 40,000 | 1.0 | 0.125 |
| #6 Gr 60 | $^{6}/_{8}$ (¾) or 0.750 | 60,000 | 1.0 | 0.125 |
| #6 Gr 75 | $^{6}/_{8}$ (¾) or 0.750 | 75,000 | 1.0 | 0.125 |
| #7 Gr 40 | ⅞ or 0.875 | 40,000 | 1.125 or 1.375 | 0.125 or 0.250 |
| #7 Gr 60 | ⅞ or 0.875 | 60,000 | 1.125 or 1.375 | 0.125 or 0.250 |
| #7 Gr 75 | ⅞ or 0.875 | 75,000 | 1.125 or 1.375 | 0.125 or 0.250 |

## EFFECTIVE RESIN DESIGN

The concept of using a resin-grout cartridge started around 1972 (Blevins and Campoli, 2006). The downfalls of the earlier cartridges were slow gel times and impractical and costly designs. For example, in one early version, the catalyst was contained in a glass tube, which was both impractical and costly.

The two popular forms of grouting are either resin grouting or cement grouting. The main advantage of resin grouting over cement grouting is the setting time can be as quick as 5 seconds. Key design criteria for resin cartridges are as follows:

- Shelf life of at least 6 months, which could be more depending on the temperature and storage conditions.

- Two components—one that contains the resin (mastic) and the other that contains the catalyst. Both components must have similar viscosities and appropriate ratios.

- Containment material that is frangible during rotation and resistant to chemical losses (such as solvents) over time.

- Varying gel time speeds, depending on the specific applications.

- Varying cartridge diameters so that the required resin encapsulation length can be obtained.

## LARGE-SCALE LABORATORY TESTING

Short encapsulation tests can be done either in the laboratory or in situ, but underground they are difficult to interpret and arrange due to the following reasons:

- The immediate coal roof properties vary considerably over even short distances.

- The rockbolts cannot be reliably installed at right angles to the top. This induces other stresses in the support during pull-out tests that are not pure tension.

- The tests can adversely impact coal production on a mine.

- Ready access in and out from the site is difficult.

- Mine personnel must be present at all times.

For these reasons, it is more reliable, safer, quicker and easier to conduct full-scale tests in a laboratory environment, if one is readily accessible, if rockbolt performance is to be evaluated.

In a research collaboration between the University of Southern Illinois at Carbondale and Orica, full-scale laboratory testing was undertaken at the Orica North American Innovation and Technology Center in Bowerston, Ohio. The laboratory provided use of a drill test rig capable of drilling and inserting rockbolts into concrete blocks. The rockbolts were then pull-tested to obtain load versus displacement curves. The failure mechanism in the concrete is obviously not the same as what is in a bedded, immediate roof underground. However, the laboratory setting is safer than underground and is also useful because of the flexibility and control in the testing procedures, lower cost, and the laboratory testing procedures are the same as those conducted by one of the major rockbolt manufactures and suppliers. Additionally, the drill rig used for the testing is capable of modifying single insertion parameters to determine their effects. The test rig and rockbolter used for installation are shown in Figure 5.



**Figure 5. The test rig and rockbolter used.**

The Orica facility offers the advantage to install up to 4-ft-long rockbolts. In addition, the bolter is fully instrumented, and the following important parameters can be accurately set for each test:

- Resin insertion (spin) speed can be varied and set for each test in 5 rpm increments.
- Resin spin (insertion) direction can be set for clockwise, counterclockwise, or both, if needed (e.g., clockwise first, then counterclockwise to tension a rockbolt).
- Resin mix (spin) time can be set at any value in 1-second increments.
- Resin mix (spin) direction can be set for clockwise or counterclockwise.
- Resin hold time can be set at 1-second intervals.
- Torque can be set at 5-ft-lb increments, up to 500 ft-lb maximum.
- Torque spin direction can be set for clockwise or counterclockwise.

These effective test controls facilitate the bolt installation and, therefore, mitigate any operator-related variability that, otherwise, could be encountered in an underground scenario. Further, to ensure reliable results, at least three tests were performed for each set of the aforementioned parameters.

As previously mentioned, following the manufacturer recommendations is vital for effective and consistent rockbolt installations, and during testing, maintaining repeatability is also critical:

- The hole depth should always be about 1 inch longer than the bolt length that goes inside the drilled hole for short encapsulation tests. This space is ideally for the cartridge material and clips and to ensure the rockbolt is fully inserted into the hole and does not stick out.
- The drill hole and rockbolt diameters must be matched to produce a certain annulus (which is defined as half the diametric difference).
- Pull-out tests were always done one hour after installation, unless otherwise noted.

Two other parameters were measured during testing to ascertain their impact on the testing: ambient temperature and the temperatures of the steel and resin at time of insertion.

The parameters that were varied to observe their effect on the overall pull-out load were:

- Bolt size: #5 (⅝-inch nominal diameter), #6 (¾-inch nominal diameter, and #7 (⅞-inch nominal diameter) rebar
- Hole diameter: 1.0 inch, 1.125 inches, and 1.375 inches
- Resin cartridges: LIF20, LIF30, H20, and H35. The letters refer to the resin properties (e.g. LIF is “Low Insertion Force”), and the numbers are the nominal gel time in seconds depending on the temperature).
- Encapsulation length: 12 inches and 48 inches
- Resin mix (spin) speed: 300 rpm, 390 rpm, 540 rpm, and 675 rpm
- Resin mix (spin) time: 2 seconds, 3 seconds, 4 seconds, 7 seconds, and 9 seconds

Resin cartridge manufacturers typically recommend that resin cartridges be rotated between 30–60 revolutions for optimum mixing of the resin components. Coal mine rockbolt machines are generally set at a rotational speed of 540 rpm, but, for practical constraints, this is seldom checked. The difference in resin speeds used had no effect on the pull tests conducted an hour after installation. Overall, 130 individual tests have been performed to date, and some of the more relevant short encapsulation (i.e., 12-inch total encapsulation length) results are given in Figures 6 and 7 and explained below.

Figure 6 gives a summary of all the test results where the number of total mixing rotations stayed constant at 45, but the

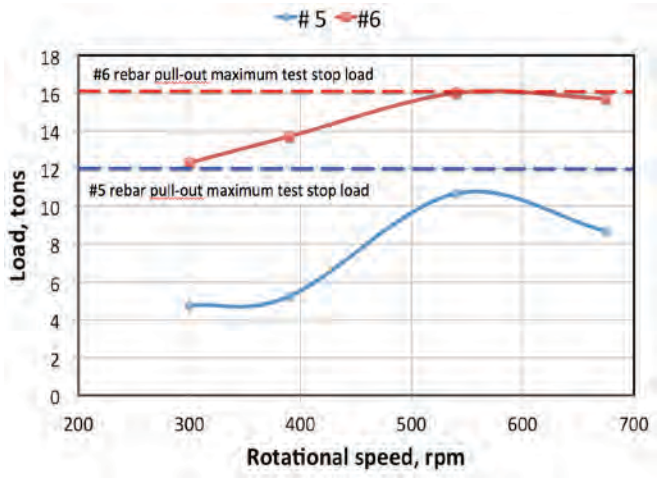



**Figure 6. Pull - out load as a function of rotational speed (no. of revolutions kept constant).**

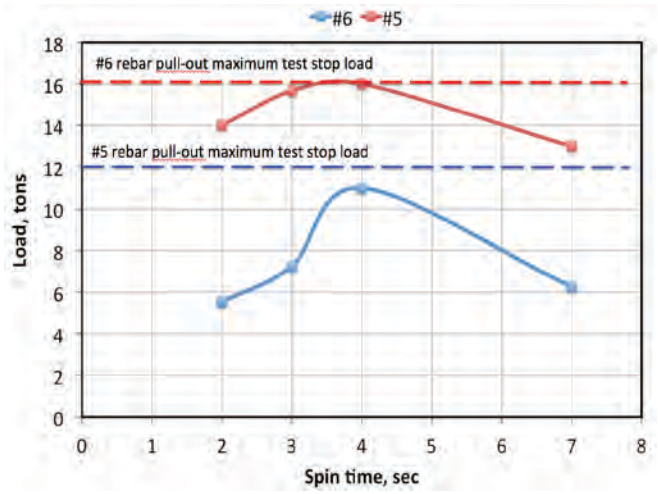



**Figure 7. Pull - out load as a function of spin tims (rotational speed kept constant).**

rotational speeds varied (i.e., 300 rpm for 9 seconds, 390 rpm for 7 seconds, 540 rpm for 5 seconds, and 675 rpm for 4 seconds). The resins used were H20, LIF20 and LIF35 and three tests were conducted at each rotational speed and the average used in the Figure. There were no differences in pull out loads between the resins, 1 hour after installation. The 45 rotations used during installation closely matches the manufacturers' recommendations and could be obtained using the various rotational speeds selected. It should be noted that, for safety considerations, the pull-out tests were stopped at 12 tons for #5 rebar (Grade 60) and 16 tons for #6 rebar (Grade 60). This is important because resin manufacturers generally specify a recommended number of rotations, depending mainly on the resin gel time, but they do not typically recommend a rotational speed. Rockbolter operators, however, spin the resin for a time that they estimate without using a stopwatch and assume a rotational speed.

The following conclusions can be drawn from the tests shown in Figure 6 (that all used a Grade 60 rebar material):

- For the resin that takes 10 to 20 seconds to gel, 450 rpm to 600 rpm appears to be the optimum range.
- For fast-setting resin (gel times of 20 seconds or less) a faster rotational speed is desirable because a slower one needs more spin time and starts interfering with the resin gel.
- In regards to pull-out load, the #6 rebar in a 1-inch hole significantly outperforms the #5 (Grade 60) rebar in the same size hole due to the smaller annulus.
- The pull-out performance of the #6 rebar is also significantly less affected by higher and lower rotational speeds during installation.
- For a #6 rebar installation, an acceptable rotational speed range was found at 450 rpm–700 rpm.
- For a #5 rebar installation, an acceptable rotational speed range was found at 500 rpm–575 rpm.

These conclusions will be further refined after more testing and the use of statistical analysis.

Further tests were performed that kept the rotational speed fixed and varied the spin time because this can happen underground during bolt installations. Figure 7 shows the results where the rotational speed was fixed at 540 rpm, and the rotational time was altered (from 2 to 7 seconds), so the number of rotations during installation (mixing) where changed. The rotational speed was fixed at 540 rpm because this is the typical rotation speed for coal mine rockbolters. H20 and LIF20 were used in these tests and 3 tests were used and averaged to produce each point on the Figure.

The following conclusions can be drawn (again using only Grade 60 material):

- The #6 rebar in a 1-inch hole significantly outperforms the #5 rebar in the same size hole due to the smaller annulus.
- For #6 rebar, the optimum mix-time range is between 2.5 seconds–5.0 seconds for the resin gel times typically used for primary rockbolt installations.
- For #5 rebar, the optimum mix-time range is between 3.5 seconds–4.5 seconds for the resin gel times typically used for primary rockbolt installations.

Again, appropriate statistical analysis will be carried out after more tests.

Although the #5 resin-grouted rebar is less costly than the #6, its cost per support ton is 32% more. This is based on material costs supplied by a manufacturer (S. Tadolini, personal communication, January 2014) and pull out performance. Considering Figure 6, the length of #6 rebar to be able to hold the 19.8 tons ultimate tensile load is about 15 inches (based on the +16 tons held on a 1-foot short encapsulation test and assuming a linear relationship). Using the same simple approach, the length of #5 rebar to be able to hold the ultimate tensile load of 13.8 tons is also about 15 inches. The effective load-bearing length of both bolts is, therefore, the same, but the #6 rebar system has a 143% higher load capacity.

## SMALL-SCALE LABORATORY TESTS

Large-scale laboratory tests might be easier, better controlled, and safer than in situ pull-out tests, but they are still time and resource consuming. For example, the four concrete block sets, which are used in the large-scale tests at Orica, must be poured and cured for about 28 days before use. Only 9 tests can be completed in each concrete block. Only 18 to 27 tests can be completed in a day, and a minimum of 3 people are needed. A small-scale laboratory test that can be done quickly, easily, and economically is, therefore, desirable to qualitatively represent short encapsulation tests.

At Southern Illinois University Carbondale (SIUC) a drill press was modified, in order to test its suitability as a test rig that would give results similar to those obtained with large-scale short encapsulation tests. The method would not be used as a replacement test but to initially establish trends that could be later quantified with limited full-scale laboratory short encapsulation tests. The equipment selected for these tests comprised of a used drill press that was modified (Figures 8 and 9) and a steel block that had a 1-inch hole at the center. This hole could be split into two halves axially along the diameter of the hole, as shown in Figure 10.

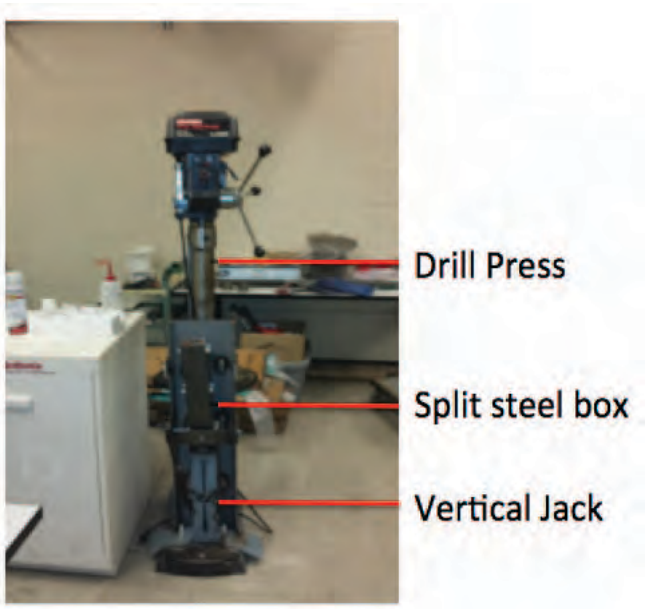



**Figure 8. Modified drill press.**

A mechanical jack was fitted at the base of the drill press where the split steel block could be mounted. The jack was useful because it increased the vertical travel by 12 inches, which helped in the insertion of rebar into the simulated drill hole in the steel block. The vertical travel of the stock drill press chuck was only around 5 inches. After resin mixing, the cured resin column was left to strengthen. It was then taken out of the steel block.

Earlier internal tests by Spearing (2010) indicated that resin hardness appeared related to short encapsulation pull-out loads. More appropriately stated, the higher the average resin hardness of the resin column, the higher the pull-out load. The resin

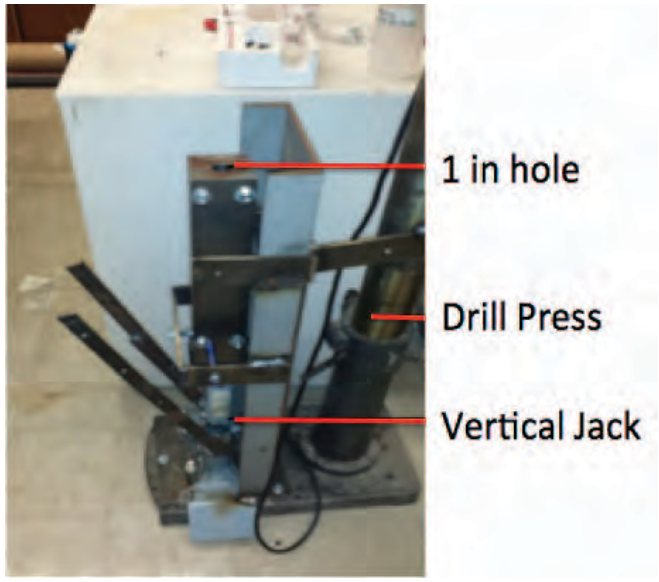



**Figure 9. Modified drill press (side view).**

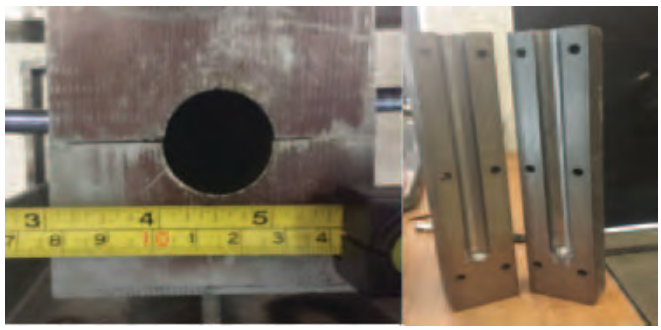


**Figure 10. The one inch diameter hole in a split steel block.**

hardness can be measured using a durometer, shown in Figure 11. A durometer is used to measure the hardness of mixed resins. The hardness is obtained by pushing a steel pin into the resin a fixed distance. Depending on the hardness of the resin, a smaller or greater force is needed, which is recorded on a graduated scale, as shown in Figure 11. Measurements are taken along the entire length of the resin column at regular intervals. All rebar tested to date using the modified drill rig, is Grade 60 to aid comparison with the full scale tests at the Orica Research Facility.

During initial tests with the drill rig and split steel block, not using a mold release proved ineffective because the resin adhered to the steel block. After several trials with different mold release systems, a small amount of grease was applied on the entire surface of both steel halves, which was then covered using a very thin plastic sheet. This completely eliminated the contact between the steel and cartridge resin, thus, the adhesion effect of steel with resin was drastically reduced and was kept consistent for all tests.

Another practical constraint was that the 3 horsepower motor on the drill press made a 1-foot encapsulation impossible because the rockbolt could not fully penetrate the resin cartridges and still be spun with any of the resin formulations. Therefore, a 6-inch encapsulation length had to be chosen. Three initial tests were



**Figure 11. The durometer to determine resin hardness.**

performed under the same conditions to check the reliability of the drill press method using H10 resin cartridges and these results are given in Table 3. The hardness is expressed as a value with no units.

**Table 3. The repeatability hardness tests.**

| Test | Spin Time (seconds) | Average Durometer Reading |
|---|---|---|
| Tests 1-5 | 2 | 54.82 |
| Tests 6-10 | 3 | 59.04 |
| Tests 11-15 | 4 | 63.34 |
| Tests 16-18 | 7 | 45.57 |

Based on these results, 18 more tests were conducted using a #6 grouted rebar and H10 (nominal 10-second gel time) resin. The rotation of the drill press was set to 580 rpm. Though this did not match the 540 rpms used for the large-scale laboratory tests, it was the closest revolutions allowed by the drill press without having to modify the factory installed belt driven motor. The viscosity of resin caused a drag, so the drill press took some time to reach the target speed and caused a few additional rotations after the power was turned off due to momentum. These errors are relatively small and were constant in all the tests.

The resin manufacturer recommended an ideal spin time of 3 seconds for this very fast resin. Four spin times were chosen: 2 seconds, 3 seconds, 4 seconds, and 7 seconds. These parameters were similar to those used in the tests conducted at the Orica Laboratory.

The test parameters are listed in Table 4.

Figure 12 shows an actual test with the rebar fixed into the drill chuck.



**Figure 12. Rebar being spun into split steel block.**

The average results from the summary of the tests are as follows in Table 5.

The hardness results from these small-scale tests were found to be qualitatively similar to the large-scale pull-out tests and are shown in Figure 13. It should be noted that, even with the grease and plastic wrap, the effective mixed resin column is only about 5 inches, and the top 1 inch is still intermixed with grease and was, therefore, not considered in the results.

From these tests to date, the small-scale laboratory encapsulation tests appear to qualitatively follow the same trends of the full-scale tests and could be used to preliminarily test new products or processes before conducting large-scale short encapsulation tests.

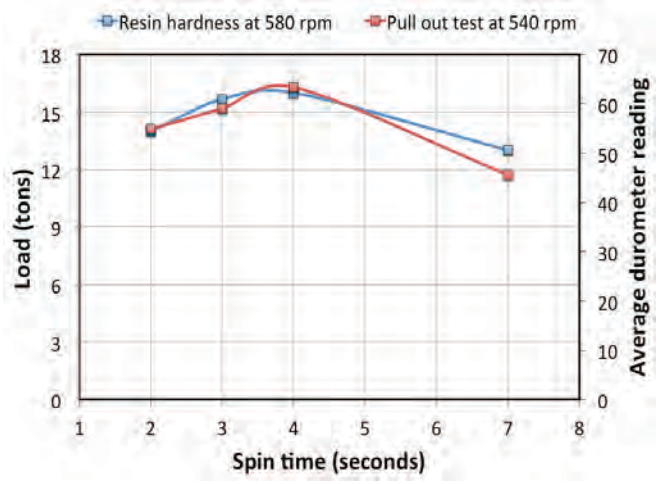



**Figure 13. Comparison betweem short encapsulation resin pull - out tests and resin hardness tests.**

**Table 4. Common parameters for all tests.**

| | |
|---|---|
| Bolt diameter | 0.75 inch (#6 rebar all Grade 60)) |
| Bolt length | 25.25 inches |
| Encapsulation length intended | 6 inches |
| Spin time (4 spin times taken) | 2 seconds, 3 seconds, 4 seconds, and 7 seconds |
| Rotational Speed | 580 rpm |
| Number of Rotations (including an estimate of the drill drag) | 19 rotations, 29 rotations, 38rotations, and 67 rotations, respectively +3-4 residual turns |
| Bolt tangential speed | 3.62 inches/second |
| Annulus | 0.125 inch |
| Note: The residual turns occur because after the power to the drill is turned off after the prescribed spin time, the drill and chuck assembly does not stop immediately (it has momentum). | |

**Table 5. Average results.**

| Test | Spin time (seconds) | Average durometer reading |
|---|---|---|
| Tests 1-5 | 2 | 54.82 |
| Tests 6-10 | 3 | 59.04 |
| Tests 11-15 | 4 | 63.34 |
| Tests 16-18 | 7 | 45.57 |

## CONCLUSIONS

Resin-grouted rockbolts remain the most effective primary support for coal mines. The performance can, however, be optimized and, based on the tests performed, the following should be considered:

- Although the material cost of #5 rebar (Grade 60) with resin is between 10–15% less (S. Tadolini, personal communication, January 2014) costly than #6 rebar (Grade 60) and resin, the #6 rockbolt outperforms the #5 rockbolt by over 30%.

- The #6 resin-grouted rockbolt is also significantly less sensitive to changes in spin time and to changes of rotational speed than the #5 rebar.

- Recording and adjusting the rockbolter rotational speed on a regular basis appears advantageous.

- Measuring resin hardness appears to be proportional to the resin pull-out load and is quicker and easier to perform. This test could, at least, be used initially as a screening test before full scale laboratory short encapsulation tests.

## REFERENCES

Blevins, C. and Campoli, A. (2006). "The origin and history of US mine resin." In: *Proceedings of the 25th International Conference on Ground Control in Mining.* Morgantown, WV: West Virginia University, pp. 409–411.

Dolinar, D. R. and Bhatt, S. K. (2000). "Trends in roof bolt application." In: *Proceedings of the New Technology for Coal Mine Roof Support*. Washington, DC: NIOSH, pp. 43–51.

Spearing, A. J. S. (2010). "Hardness and glove fingering using resin grouted rebar." *Internal Report.* Carbondale, IL: Southern Illinois University Carbondale.

Tadolini, S. and Mazzoni, R. (2006). "Twenty-four conferences; more than one-hundred and seventy papers; understanding roof bolt selection and design still remains priceless." " In: *Proceedings of the 25th International Conference on Ground Control in Mining.* Morgantown, WV: West Virginia University, pp. 382–389.

# Investigating the Contributing Factors to Rib Fatalities Through Historical Analysis

**Tristan H Jones**, Acting Team Leader
**Khaled M Mohamed**, Associate Service Fellow
**Ted M Klemetti**, Acting Deputy Branch Chief
Ground Control Branch
NIOSH, Office of Mine Safety and Health Research
Pittsburgh, PA

## ABSTRACT

Rib-related accidents in underground coal mines continue to cause injuries and take lives at a rate of 1.3 fatalities per year for the last 17 years. Prevention of these accidents cannot simply be a matter of installing more rib support, though the eventual final solution will undoubtedly include that component. Ultimately, rib safety will be brought about through an understanding of the causes and mechanisms that cause rib fatalities, and by fine-tuning mining methods and procedures that are currently in place.

This paper investigates the factors likely to be most influential in the occurrence of rib fatalities. A careful analysis has been conducted of the rib fatality reports documented by the Mine Safety and Health Administration between 1996 and 2013. The primary outcome is the determination of the relative impact of each type of rib fatality factor and a better understanding of the impact each factor has.

Among the rib fatality factors considered, the influence of rib profile is considered for the first time. Mining height, rib stratigraphy, mining cycle, and the standing position of a miner next to a pillar are also considered. Questions are also raised about the current interpretation of rib fatalities due to mining depth, with the indication being that mines operating at the greatest depths may actually have the most respectable rib fatality record among all mining depths. Additionally, a new method of considering rib exposure is developed. Based on the results, recommendations are made for future work. By gaining a better understanding of how particular factors contribute to rib fatalities as opposed to rib failure or stability, it is hoped that future efforts can be more precisely directed towards the desired outcome of fatality reduction.

## INTRODUCTION

Efforts to improve the performance of underground mine ribs have continued for decades. The first research into the stability of ribs was not completed with an eye towards improving rib safety, but rather to improve roof control through better pillar stability. Much of the earliest work was completed in the underground lead mines of the St. Joseph Lead Company in the Viburnum Trend of southeast Missouri and involved the wrapping of used hoist cables around the pillars as reinforcement (Wykoff, 1950). As mining technology advanced, rib reinforcement changed both in method and in purpose. Mines started utilizing pillar reinforcement less to improve pillar strength, and more to keep entries open. Adoption of first mechanical and then grouted bolts, straps, and bands helped to improve entry stability (Horino, Duvall, and Brady, 1971; Baumgarth, 1977; Weakly, 1976; O'Beirne and Shepherd, 1984; Gauna, 1983; O'Beirne et al., 1986). Work has continued by mining professionals around the world throughout the 1990s and 2000s as well, though much of this work has focused on rib support methodology and selection of proper support for a specific location (Dolinar and Tadolini, 1991; Smith, 1992; Colwell and Mark, 2004; Colwell, 2006; Gauna and Mark, 2010).

Given the ongoing rib-support-related research, it is unfortunate that there has been a continual occurrence of rib-related fatalities in the underground coal mines. While these efforts have contributed to the overall improvement in rib safety, the average fatality rate is still 1.3 fatalities per year over the last 17 years (Figure 1). Perhaps it is encouraging that there have been four years out of the past nine in which there were no rib-related fatalities (non-burst or yield pillar related). However, a three-year running average of fatalities over this time period, while showing a decline between 1998 and 2009, has again risen for no discernable reason and accurately forecasting future changes is difficult.

The research papers mentioned previously have detailed the proper types of rib support and methods of installation to use in many situations. In this paper we take a new approach to the problem. This paper considers the many variables that have been associated with the most hazardous situations specifically from the point of view of reducing rib fatalities as opposed to rib failures. This preliminary work will allow mines to begin focusing their attention directly on problem areas. It provides insight that should help mines to be proactive in their rib support, instead of reactive.

This work is based on the fatality reports from the 23 "pure" rib fatality cases – those not caused by bumps, bursts, or on yield pillars - that occurred from 1996 to 2013. These fatality reports are available from the Mine Safety and Health Administration (MSHA). Although 23 cases is a small dataset, these cases include every rib fatality that has occurred during the study period, representing over 1.43 billion total worker hours, allowing for

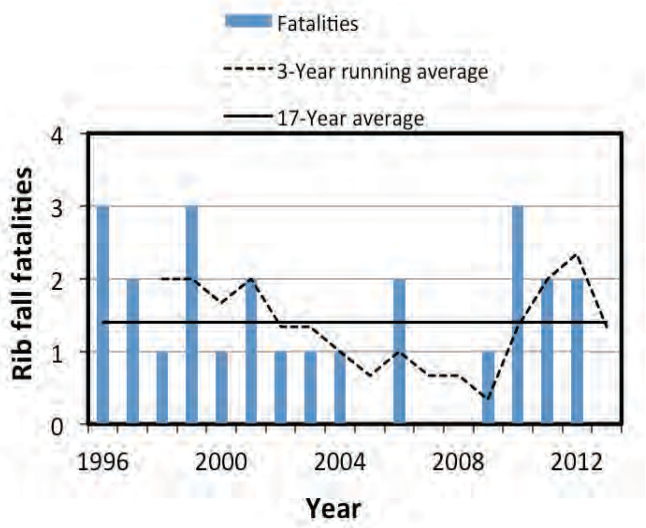



**Figure 1. Non-burst rib fall fatalities in US coal mines, with a 3-year running average shown.**

ample exposure time. An appendix is included that details the data used during this study.

## RIB FATALITY FACTORS

Rib failure mechanism, mining depth, mining height, rib stratigraphy, rib profile, mining stage, and the miners position with respect to the pillars, crosscuts, and panels in his or her environment have been included in this research as factors that have a strong influence on the occurrence of rib fatalities. Other stresses, such as horizontal or multiple seam, are discussed and considered as contributing to the mining stage variable and so are discussed in that respect.

One of the common steps when comparing datasets is the normalization of the data with respect to exposure. Usual methods of accomplishing this incorporate the number of man-hours worked or the amount of production under the influence of a particular factor. Reliable man-hours-worked data is available for mining height, and production-based estimates can be made for depth, but none of the other factors listed above can be normalized in the same way because the necessary data does not exist.

This dataset includes fatalities occurring over a huge number of man-hours-worked during the period studied. Given that extremely large amount of exposure, it is considered that the distribution of the number of fatalities occurring in each factor is related to the actual exposure within that factor. This justification is used in this paper in places where hourly or production-based exposure data is not available.

In the following sections each of the rib fatality factors are considered in greater detail. Discussion regarding their contributions to rib fatalities is included, along with an analysis of the rib fatality case histories available from MSHA. The results of the analysis show a much more detailed picture of the exact contribution of the different fatality factors. This analysis will be valuable for future research.

### Rib failure mechanism

The size and shape of a rib failure depend on interactions between three parameters: stresses (in-situ and mine-induced), the geometry of the mine workings (dimensions and orientation), and seam geology (strong and weak stratification, parting characteristics, and cleat, slickenside, and joint characteristics). The two major rib instability mechanisms found in underground coal mines are: (1) structurally driven rib failures, referred to as joints, wedges, or slickenside slips, and (2) stress-driven rib failures, such as rib buckling, sloughing, or rib brow formation. Different types of rib falls could be developed by these mechanisms, as described below.

*Granular rib falls*

Granular rib falls are characterized by small pieces of coal or rock with a maximum size of 0.3 m, and are characteristic of low-rank coal (Smith, 1992). They are highly dependent upon the variations in elastic properties found in the different coals within the same seam.

Williamson (1967) summarized the Stopes-Heerlen system that classifies the components of bituminous coals into four lithotypes: vitrain, durain, clarain, and fusain. Vitrain is the primary component of bright coal and tends to be brittle with lower strength. Clarain and fusain are other common constituents of bright coal, both tending towards weakness. Durain is usually dull, strong coal. Every coal seam is composed of several bands of anisotropic and non-homogeneous material. Coal seams always contain one or more layers of partings of different strength and thickness at different elevations (Peng, 2008).

Jeremic (1985) explained that the granular rib fall mechanism is a brittle coal failure in which deformation by the shear flow of individual layers within coal seam leads to cleat dilation and rib fracturing. Figure 2 shows a repetitious sequence of bright, weak, coal and dull, strong, coal found in most bituminous coal seams, and illustrates a typical failure progression. The differences between the elastic properties of strong and weak coals lead to the initiation of sloughing from the weak coal band. Progressive deterioration of the soft-coal layers causes unsupported fragments of adjacent hard-coal layers to loosen and fall with a tendency towards larger fragments. The size of the fragments depends on the degree of fracturing, cleat, and/or pre-existing fracture pattern (Smith, 1992). The system is not limited to strong-coal/weak-coal, as there are ample examples of moisture-sensitive or otherwise weak rocks preferentially deteriorating, as well as stronger rocks taking the place of hard coal, too.

Granular rib falls usually occur gradually over time, but can fail suddenly in some cases. Sudden failures are unlikely to be as hazardous to the miner as other failure types due to their granular nature and because they will tend to roll down the rib instead of falling outwards and onto the worker. Combined, these factors give granular ribs a lower fatality hazard to miners. Between 1996 and 2013, only two granular falls were directly linked to a rib fatality. Granular falls do, however, serve to advance the progression of other rib failure mechanisms and can be identified and used as a preliminary indication of future potential hazards.

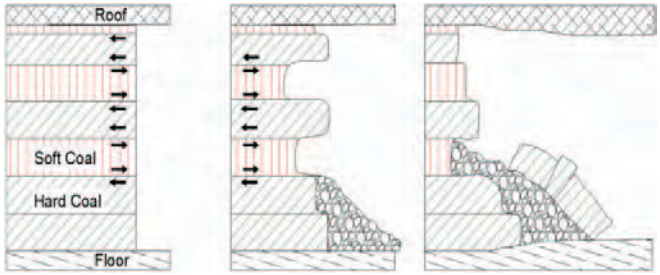



**Figure 2. The progression of granular failure leading to eventual brow formation and failure.**

*Blocky rib falls*

Blocky rib falls are characterized by large pieces of coal or rock with a minimum dimension greater than 0.3 m, and can be developed by different rib fall mechanisms. First, a block may be formed from a large overhang or brow that separates from the strata above after the supporting material beneath sloughs through granular failure (Figure 2, right side). This type of blocky fall is especially hazardous and it tends to increase the entry width and decrease pillar width, reducing overall pillar strength (Peng, 2008).

The second blocky failure mechanism is the "Mine-Induced Fracture" (MIF), introduced by O'Beirne et al. (1987). This describes the nearly vertical factures observed ahead of the face and at the sides of the entry. MIFs are caused by the stresses induced during mining and are independent of the natural coal cleating. In Australian coal mines, it was discovered that MIFs form ahead of and parallel to the development face, curling around at the face corners to run at a low angle to the riblines out into the pillar. If the MIFs intersect the cleat system at near right angles, blocky rib falls can be produced (Figure 3). Additionally, the presence of slippery or low friction layers at either the roof or floor interfaces or within the coal horizon can prevent or reduce any confining effect from the horizontal stresses in the roof and floor and allow rolling or/toppling of blocky rib falls (Figure 4).

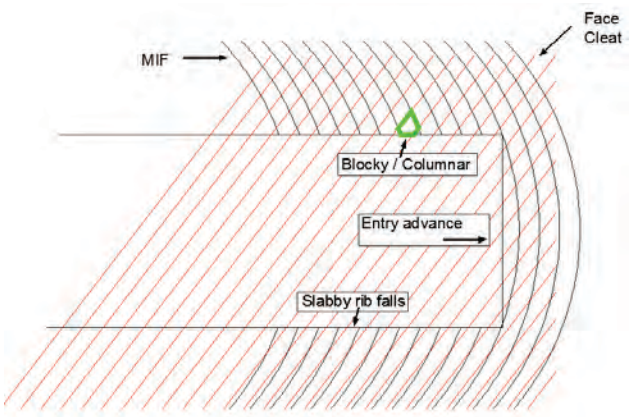



**Figure 3. Face cleat/MIF interaction in the formation of blocky rib failure, after Shepherd, J. et al. (1984).**

The MIF failure mechanism requires a third plane beyond the MIF and cleats in order to form blocks as opposed to slabs. The interfaces between different coal layers, at partings, clay streaks, or interbedded rock units all serve to create a third degree of freedom allowing block formation. This is the primary reason that blocky failures are more frequent in the United States compared with Austrailia, as much of Australian coal tends to have fewer interrupting layers.

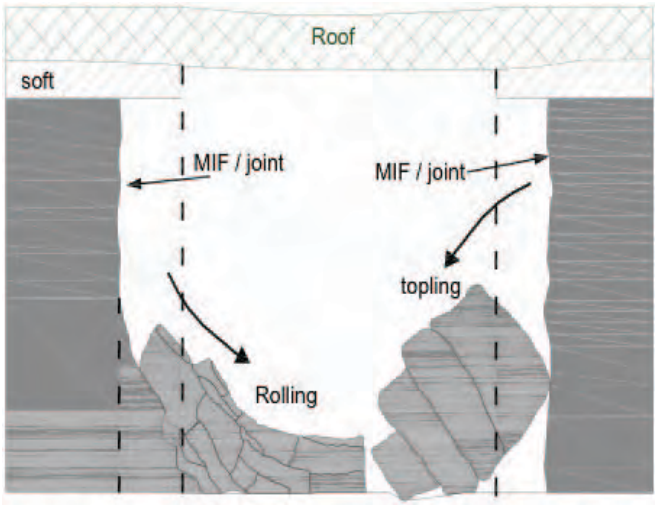



**Figure 4. The formation of slabby/columnar blocks through buckling, or blocky falls through cleat/joint sliding.**

Finally, loose blocks can be formed when an angled plane of weakness (slickensides or joints) exists on the bottom of a block and intersects the coal pillar above the floor line while a low-friction interface exists at the top. At the corner of a pillar, this scenario may be enough to cause the formation and movement of large, wedge-shaped blocks, similar to those encountered in surface rock slope failures (Figure 5). On the sides of a pillar, the same mechanism can interact with vertical MIF or cleat sets, adding degrees of freedom to a block and allowing it to slide. These "joint failures" are similar to wedge-type failures found in surface rock slopes.

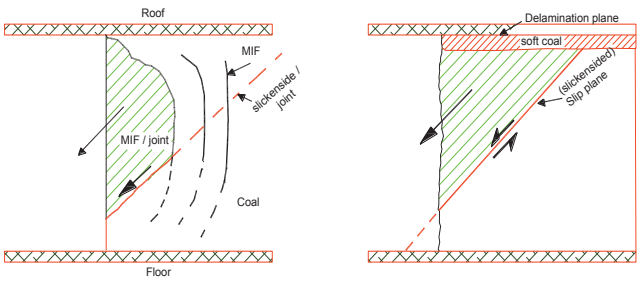



**Figure 5. Blocky wedge or sliding plane joint-type rib failures.**

When taken together, blocky rib failures are the most hazardous of all failure mechanisms. Between 1996 and 2013, a total of 18 rib fatalities can be attributed to this mechanism. Of these 18 fatalities, eight were caused by brow failures, three were blocky joint failures, and six were due to MIF or other potential blocky failures.

*Slabby rib falls*

Slabby rib falls are characterized by a continuous process of thin slabs or plates detaching from entry walls along open cleats or vertical/nearly vertical fractures. The slabby rib fall does not usually extend more than 0.1 m into the coal rib (Jeremic, 1985).

O'Beirne et al. (1987) found that slabs were formed when the roadway was driven sub-parallel to a well-developed cleat set. The slabby rib fall mechanism was explained as a buckling failure resulting from the vertical loading of the slabby ribs driven by roof and/or floor closure (Hebblewhite et al., 1998; Seedsman, 2006). Stone partings within a seam act as the end point of buckling slab (Colwell, 2006). "Rolling" of slabby rib falls occurs when the parting is close to the mine floor, while "toppling" of slabby rib falls occurs when the parting is close to the mine roof (Figure 6). During the study period, slabby rib falls were attributed to four fatalities.

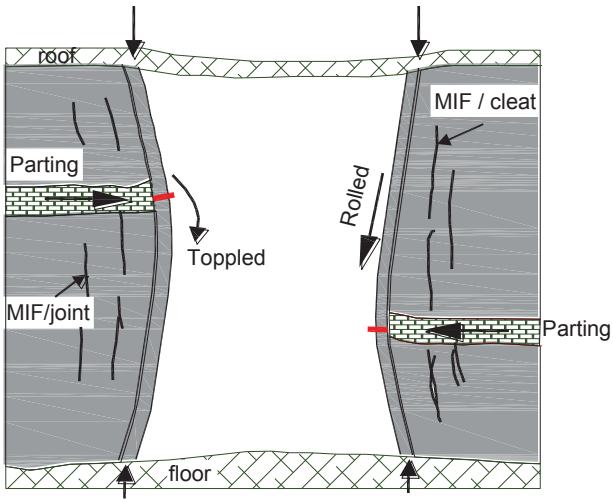



**Figure 6. Slab formation and the effect of partings in buckling failures.**

*Columnar rib falls*

Columnar rib falls are the least common of the mechanisms and were not attributed to any fatalities during the study period. This failure mechanism forms slender columns of coal and/or rock that detach from the entry walls. The columns result from interactions between MIF with existing joints (Figure 3) and tend to be an intermediate stage between blocky and slabby rib falls. The smallest dimension in the plane of the rib ranges between 0.1 m and 0.3 m (Hebblewhite et al., 1998). Similar to the slabby rib falls, the mechanism of columnar rib falls could be explained as a buckling failure of slender columns.

*Contribution of rib failure type in fatal accidents*

Many mines, pillars, or ribs have a tendency towards a particular type of failure that can usually be identified. This expected failure type can be one of the most significant components of the overall hazard of rib failure. The rib fatality database was used to determine the most likely failure type (or sub-type) for each fatality occurrence. Based on the results, the contribution of each failure mechanism to the total number of fatalities was calculated (Table 1).

**Table 1. Rib fatalities by failure mechanism, with associated fatality contribution.**

| Type | Fatalities | % Fatalities |
|---|---|---|
| Granular failure | 2 | 9 |
| Brow failure | 8 | 35 |
| Joint failure | 3 | 13 |
| Blocky failure | 6 | 26 |
| Slabby failure | 4 | 17 |
| Columnar failure | 0 | 0 |

**Mining depth**

Mining depth has always played a very important role in assessing rib stability and is one of the major topics concerning the design of rib support systems. In a 2010 publication by Gauna and Mark, they completed an analysis of rib fatalities that occurred between 1996 and 2010. One of their most prominent and influential findings was the identification of a relationship among fatalities, depth, and mining height (Figure 7). They found that for the 21 fatality cases included in their analysis (including two from yield pillars – not part of this study), over 75% occurred at depths 700 ft. or greater. A conclusion was to include rib support for cases deeper than 700 ft. This was also supported by the MSHA Program Information Bulletin (PIB) 11-29 (MSHA, 2011). Our research recreated their dataset to the greatest extent possible and then expanded it to include rib fatalities between 2010 and 2013 (Figure 7b). The 2013 dataset showed that 16 of 23 fatalities, or 70%, occur at depths 700 ft. or greater.

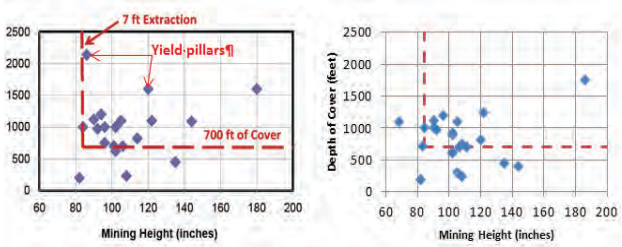



**Figure 7. Mining height/Depth of cover/Fatality relationship after Gauna and Mark, 2010 (left - 1996-2010) and the same relationship based on 1996-2013 data (right).**

Three of the four fatalities that occurred from 2010 to 2013 were at relatively shallow overburdens (300, 600, and 720 ft.) These three extra years of data have dropped the percentage of fatalities occurring at 700 ft. or deeper from 75% to 70%. At this point it is impossible to determine if the PIB release was causal to the recent reduction in high-overburden rib fatalities and the lower percentage of deep fatalities. A three-year running average of rib fatality depth shows that sudden decreases in average fatality depth have occurred a number of times in the past, even prior to PIB11-29 (Figure 8). This indicates that recent decreases in fatality depth are not necessarily due to the updated rib support guidelines, but may be part of typical fluctuation.

Figure 9 shows a graph of the cumulative number of fatalities as they increase in depth. The figure provides insight into the

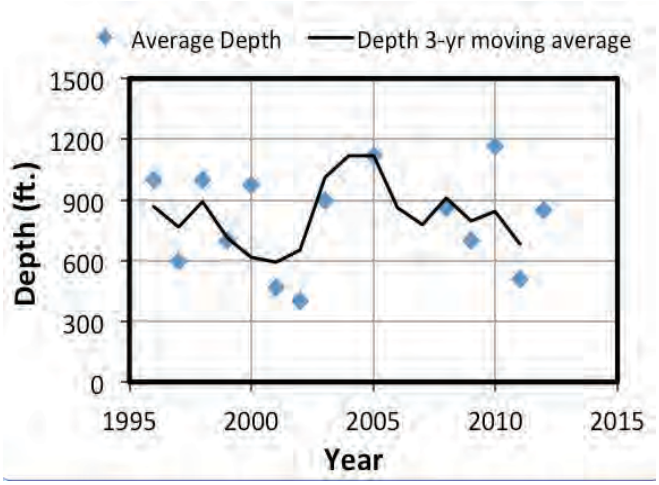



**Figure 8. A 3-year running average of rib fatality depth.**

effectiveness of rib support, pillar design, mining techniques, and hazard management during the studied time period as it relates to depth. The fatalities are divided into three zones: a low-depth zone, less than 700 ft.; a mid-depth zone, from 700-1250 ft.; and a high-depth zone above 1250 ft. Each of these zones is bounded by a breakpoint, shown by the vertical lines at 700 and 1250 ft. There is a noticeable shift in fatality rate between the three zones.

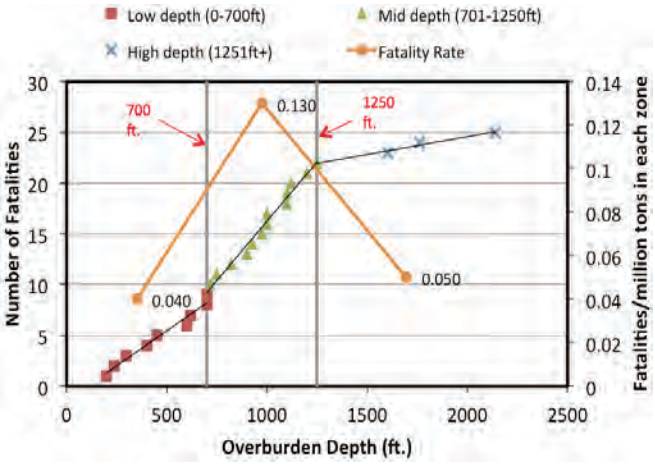



**Figure 9. Cumulative fatality graph showing the variations in fatality rate depending on their depth zone as compared to fatality rate normalized by production (fatals/1 million tons).**

Based on the data gleaned from the MSHA Accident Illness Injury and Employment database for the year 2010, production levels were estimated for both the 700 and 1250 ft. zone splits (Table 2). From these values fatality rates (fatalities/million tons) were computed for each zone (Table 3). These rates are also shown on Figure 9. The distributions of longwall and room-and-pillar coal production with respect to mining depth were categorized based on coal regions. While the distribution of coal production from longwall mines was available, room and pillar mine production depth distribution data was lacking. Therefore, the distribution of coal production from room and pillar mines with respect to mining depth was estimated based on the following assumptions:

- All the room-and-pillar mines in the Northern Appalachian region are operating at a mining depth less than 700 ft.
- The coal production from room-and-pillar mines in the Central and Southern Appalachian regions, and in the West has the same distribution with respect to mining depth as longwall mines operating in these regions.
- 85% of the coal production from room-and-pillar mines in the Illinois basin is competed with less than 700 ft. of overburden. The remaining 15% takes place between 700 and 1250 ft. deep.

The production distribution and fatality rates in each zone are estimated to be 50%/28%/22% and 0.04/0.13/0.05, respectively (Table 3).

The fact that there is an upwards transition point at 700 ft. provides support for the 700 ft. threshold found in the PIB. The lower fatality rate above 1250 ft. is likely due to the higher level of rib support that is common at these depths, while the low rate found when mining below 700ft is likely due to the shallow depth. These results bring into question the "low-production-therefore-low-fatality" sentiment that is commonly used to explain low fatality numbers at depth.

A comparison of fatality rates between zones shows that there is a 225% increase between the low and mid zones, which is attributable a production decrease of 46% and an increase in the number of fatalities of 44% between the two zones. Meanwhile, comparing the mid and deep zones reveals a decrease in production of 17% and a decrease in fatalities of 77%, which translate into a fatality rate reduction of 61%. To even further illustrate the differences in fatality rate between the mid and deep zones, of the fatalities depicted in Figure 9 occurring above 1250 ft., one "pure" rib fatality occurred in 1996. A second fatality occurred in 2010, but was actually caused by a standing roof support that was dislodged by a rib fall, subsequently hitting a miner on the head and killing him. The remaining two fatalities are yield pillar rib failures and are only included to help show how few "pure" rib fatalities have actually occurred at great depth. The common understanding is that ribs are more dangerous with increasing depth. Holding all other variables equal, that logic holds, but over the past 18 years ribs as built have been decisively *less* likely to cause fatalities at depth. These trends illustrate a poor correlation between depth and fatality rate. They also identify that the mid-depth zone is where the most effort should be focused for rib fatalities reduction. This trend also clearly shows the difference between rib fatality and rib hazard.

It seems likely that the combination of rib support, mining practices, pillar and entry design, management control, and the natural awareness and care that may be instilled in the miners when operating under greater depth, all combine to drastically reduce the occurrence of rib fatalities under high overburden. The conclusion is that even though we don't yet know if the recommendations in PIB 11-29 have caused the recent rib fatality reduction, it likely does not do enough to address the rib fatality problem. The most noteworthy rib fatality rates are found at the greatest depths, and it is unlikely this is due to lower mining exposure. This is a testament to the efforts of the mines operating in these conditions. Perhaps the mines in the mid-depth zone should strive to follow the example that the deep-cover mines are setting.

**Table 2. Estimated distribution of underground coal production with respect to depth. Values estimated based on 2010 production data. All values displayed in millions of tons.**

| Regions | Longwall | | | | Room & Pillar | | | |
|---|---|---|---|---|---|---|---|---|
| | Less than 701 ft | 701- 1250 ft | Greater than 1250 ft | TOTAL | Less than 701 ft | 701- 1250 ft | Greater than 1250 ft | TOTAL |
| **Northern Appalachian** | 24 | 50 | 5.9 | 80 | 22 | | | **22** |
| **Central Appalachian** | 4.6 | 3.9 | 4.7 | 13 | 29 | 25 | 30 | **84** |
| **Southern Appalachian** | 3.0 | 2.6 | 6.7 | 12 | 0.0 | 0.0 | 0.1 | **0.2** |
| **Illinois Basin** | 12 | | | 12 | 61 | | | **61** |
| **Western USA** | 13 | 10 | 27 | 50 | 0.6 | 0.5 | 1.3 | **2.4** |
| **TOTAL** | **57** | **66** | **44** | **167** | **113** | **25** | **31** | **170** |

**Table 3. Fatality contribution due to depth.**

| Depth (ft.) | Total UG production | Total % at depth | 2010 Dataset Fatalities/million tons | % Fatalities |
|---|---|---|---|---|
| Less than 700 | 170 | 50 | .04 | 32 |
| 701-1250 | 92 | 28 | .13 | 53 |
| Greater than 1251 | 76 | 22 | .05 | 15 |

For the purpose of this research, the fatality rates developed in Figure 9 are used to determine the boundaries for setting depth zones. The percentage of total fatalities occurring in each zone is then identified in Table 3.

**Mining height**

Entry height has substantial impact on the stability of ribs and the number of rib fatalities. Over 95% of fatalities occur at mining heights equal to or above 7 ft. (Gauna and Mark, 2010). New additions to the dataset since the analysis by Gauna and Mark and the elimination of yield pillars in this research have adjusted this value to 20 fatalities out of 23, or 87%, still a significant number. Otherwise, the analysis by Gauna and Mark remains valid, and will not be further discussed here. Table 4 shows the updated contribution to total fatalities as calculated for seam height.

**Table 4. Mining height contribution to Rib fatalities.**

| Entry Height (inches) | # Fatalities | % Fatalities |
|---|---|---|
| Less than 71 | 1 | 4 |
| 72-87 | 3 | 13 |
| 88-103 | 8 | 35 |
| 104-119 | 6 | 26 |
| 120+ | 5 | 22 |

**Rib stratigraphy**

One aspect of rib fatality hazard not frequently considered is the impact of seam stratigraphy on rib failure. The presence of multiple stratigraphic layers plays an important part in the destabilization of a rib, especially with respect to blocky failures. Geologic factors in general are complicated due to their inconsistent nature. Truly solving the geologic aspect of the rib hazard estimation would require massive funding, time, and effort beyond the scope of this research, though some headway has been made in other efforts.

A study completed by Colwell and Mark (2004) developed a design equation based on case studies and instrumentation sites. This concluded that 15% of the variation in recommended rib support could be accounted for by the Hardgrove Grindability Index (HGI). HGI itself is not geologic in nature, but rather a strength-of-materials index related to the friability of coal. That being said, HGI is a step forward in accounting for some of the variation due to the rib material itself. Additionally, due to differences between Australian and United States coal seams, HGI would not correlate as well in the United States.

The geologic component of the rib fatalities described here is based on the distribution of rib stratigraphy in the 23 rib fatality cases experienced since 1996. Each case history was examined and 21 of them provided clues about the stratigraphy of the rib at the fatality site. The number of independent stratigraphic units (coal, rock or clay bands) identified in each case history was counted, allowing for the formation of a rudimentary distribution. The distribution data is seen in Table 5 and Figure 10, respectively. As expected, a higher number of stratigraphic units provide more opportunities for differential degradation, leading to further rib sloughing.

**Table 5. Distribution of fatalities with respect to the number of stratigraphic units and the associated fatality contribution.**

| # Stratigraphic Units | # Fatalities | % Fatalities |
|---|---|---|
| 1 | 0 | 0 |
| 2 | 7 | 33 |
| 3 | 6 | 28 |
| 4+ | 8 | 38 |

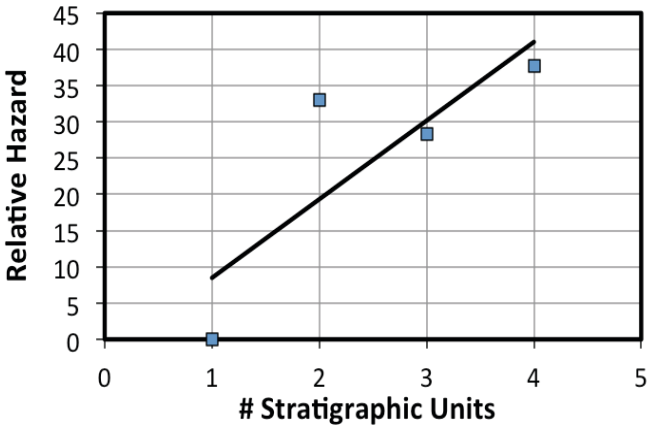



**Figure 10. Fatality contribution with respect to the number of stratigraphic units present.**

### Rib profile

While not generally distinguishable from the MSHA fatality case histories, it is recognized that the profile of a rib can have a major contribution to rib fatalities. It plays a role in the general instability of a rib and its likelihood to fail, and therefore cause a fatality. It plays a role in the ability for a miner to easily approach the rib closely enough such that a fatality is possible. It also plays a role in the cognitive state of the miner, the perceived danger of the rib, and therefore the likelihood that a person will choose to stay away from it. Figure 2 shows an example of a blocky rib failure profile through the first portions of its rib life-cycle.

The application of rib profile hazard for preventing rib fatalities cannot be applied as with the other hazards, calculating through percentages. Also, when making decisions regarding how to treat a particular type of rib profile those decisions will be applied depending on the circumstances. When used for planning purposes prior to mining, the rib profile should be treated as if it is standing upright, freshly mined. Planning use is intended to minimize the formation of hazardous conditions, so the goal should be to keep the rib in a freshly-mined-like state as long as possible. Rib support should be installed towards that end.

When used in response to observed conditions, the level of hazard for the different failure mechanisms should be included when considering the hazard posed by various rib profiles. If a rib is prone to failure, it will have a varying likelihood of causing a fatality throughout its stages of failure. Some examples of that varying likelihood are:

- A rib with a brow that has already formed will be more hazardous to a person standing next to it than a rib that will likely form a brow in the future.
- A rib with slabs that have already loosened, exhibiting clear joints or gaps, is more hazardous than a rib with slabs that might form in the future due to nearly parallel cleat and MIF systems.
- Any rib that has progressed through its failure cycle to near-complete failure (defined as a rib with a pile of spall from the roofline to the floor, lying at the angle of repose) will be less hazardous (from a rib fatality point of view) than a rib that is just beginning to fail.
- A rib that has already had its first major failure will be less hazardous than one that has not.
- Any other rib is more likely to cause a *rib* fatality than a rib that has completely failed.

More research is needed on this topic, but currently the best way to view this theory is through a simple graph for fatality contribution based on rib profile (Figure 11). A number of authors have produced rib rating guidelines that can be used to generalize rib failure stage along a 0 to 5 rating system (Karabin and Evanto, 1994; Heasley and Chekan, 1998; Lawson, Zahl and Whyatt, 2012) The general practice is that a freshly mined rib is ranked at 0, while a fully-failed rib with spall from floor to roof lying at the angle of repose is a 5. This type of concept is used here, but with an added attempt to include the mental aspect of perceived hazard through the miner's eyes, as well as the inability to get close enough to the rib for a fatality to occur, due to accumulated rib material. Refinement will be necessary on the final rating sequence for this purpose, but this is sufficient for introducing the concept. Since not all ribs eventually progress to total failure, this method offers flexibility in the way profile hazards are considered.




**Figure 11. The fatality contribution of the varying rib profiles experienced by a rib from initial mining through total failure.**

### Mining stage

Since, rib failure has been directly linked with loading condition of mining stage (Colewell, 2009), it is logical to assume that within a single mine the TG front abutment would be more hazardous than the HG side abutment, which is would be more hazardous than the TG previous-panel abutment. It needs to be recognized that having zero rib fatalities is distinctly different from having zero rib hazard. When considering rib fatalities with respect to mining stage (development and retreat), It is apparent that the number of

fatalities in each part of the mining cycle is highly similar to the expected distribution of exposure hours while operating in that part of the cycle (i.e. development hours are high, and development fatalities are high; tailgate hours are low, and tailgate fatalities are low).

Mining cycle exposure is determined by identifying the number of fatalities in the dataset that have occurred at each point of a mining cycle. This exposure actually includes two elements: exposure based on time spent in those areas of the mine, and exposure to the varying stress states of each part of the mining cycle. Workers in the development section of the mine have a very high time exposure, but a relatively low mining-stress exposure. Workers at the tailgate (TG) corner have a much higher mining-stress exposure, but a relatively low time exposure. The data was too sparse to allow for inclusion of exposure to multiple seam mining, but it should be noted that increased stresses due to this condition could potentially increase the stress component of mining cycle exposure.

Table 6 shows the categories that have been chosen for inclusion in mining cycle exposure. Development fatalities for room and pillar and longwall have been combined into one category. The "Other" category includes all occurrences of fatalities in travel or service areas of the mine, i.e. mains, belt transfer points, etc. These areas are usually lower stress and have only transitory or temporary time exposure. This is a complex category as these areas have longer lifespans than working areas and as such have the opportunity to experience more time-dependent degradation, increasing their relative hazard, but frequently have higher rib support densities to offset that.

**Table 6. Mining cycle exposure values calculated from adjusted fatalities.**

| Mining Cycle/Stress | # Fatalities | % Fatalities |
|---|---|---|
| Development | 19 | 83 |
| RP Retreat | 1 | 4 |
| HG Front Abutment | 1 | 4 |
| Other | 2 | 9 |

Of the three areas mentioned, there are a number of good reasons why fatalities may not have occurred. It is notable that in each of these areas miner exposure is generally decreased through management control, taking people out of harm's way. Also, the tailgate typically has a larger amount of roof and rib support, helping to control the entry. Finally, all of these areas are zones where significant rib damage occurs, which as stated previously, is likely to reduce the long-term fatality hazard.

**Miner position relative to pillars**

Rib failure and rib fatality hazards exist at varying levels in different positions relative to the pillars and panels of a mine. Pillar corners always experience greater degradation than mid-pillar locations, and pillar ribs usually experience greater degradation than panel ribs do. The number of fatalities that have occurred in these various locations fall well into line with expectations regarding position-based degradation and as such, can be used directly as data for examining position-based hazard and exposure. Only 20 of the 23 fatality cases contain enough data to determine fatality position.

The positions of workers relative to pillars have been divided into five groups. Four of the groups are identified in Figure 12, with the fifth group representing all other locations within the mine. Descriptions of each location can be found in Table 7. The number of fatalities experienced in various positions is clearly tied to their distance from the pillar corners, though in this dataset only the 0-10 ft. and 10-20 ft. distance from the rib stand out from the baseline value. With regard to the distance from the pillar, the fatalities typically occurred while the victim was less than 5 ft. from the rib.

Limiting exposure to a hazardous rib is one of the most basic ways to eliminate a rib fatality hazard—i.e., a rib is only fatally hazardous if there is a person for it to fall on. Reducing the access or exposure to dangerous ribs is a simple, inexpensive, and common method of mitigating hazard. It is regularly used in the tailgates of longwall mines, and is no different than prohibiting miners from working under unsupported roof, or teaching miners to walk in the center of an entry away from the rib.

## FUTURE EFFORTS

This research represents a starting point from which many improvements can be made towards the prevention of rib fatalities. In order to best achieve fewer fatalities, the research will continue and grow. Below are some of the topics that can best further this effort.

The frequency of occurrence for various rib failure types should be considered through field surveys to help better understand their contribution to fatalities. It should be determined whether rib brows cause more fatalities than other failure types because they form more frequently and therefore miners have higher exposure to them, or because they are a greater hazard and are more likely to fail if they form. This insight would provide clues regarding the best way to prevent future brow-related rib fatalities.

Further research is needed regarding perceived danger, and how that contributes to the hazards posed by rib profile. Gaining a better understanding of how miners of various age and experience levels react when presented with ribs at different levels of failure, or with different profiles is necessary. The outcome might also provide clues about why mines at great depth tend to have fewer rib fatalities than might be expected. How much of the fatality reduction is caused by increased levels of rib support, and can any be credited to behavior changes on the part of the miner? The insight gained from this research would help to better define management controls towards preventing rib fatalities.

Development is necessary on a method to determine rib profile in a repeatable, universal manner. Much research has been done on the development of rib rating systems, but that has been task or site specific. Ideally, this method should be usable in any mine and should give repeatable results between raters and over time. The method should be made as quantifiable as possible.

Some interesting interpretations can be drawn from Figure 9 regarding fatality rates in different depth zones. The most striking is a realization of just how well deep mines are performing regarding rib fatalities. In fact, it may be that mines operating at

**Table 7. Exposure value assigned according to fatalities experienced in a given location along the rib.**

| Position Group | Description | Fatalities | % Fatalities |
|---|---|---|---|
| 1 | 0-10 ft. from pillar corner, in pillar | 10 | 50 |
| 2 | 10-20 ft. from pillar corner, in pillar | 4 | 20 |
| 3 | 20-30 ft. from pillar corner, in pillar | 2 | 10 |
| 4 | 0-30 ft. from crosscut midline, in panel | 2 | 10 |
| 5 | All other positions | 2 | 10 |

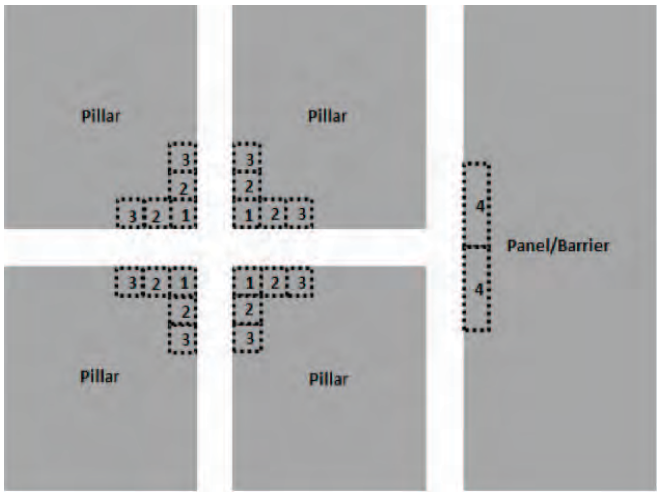



**Figure 12. Exposure positions relative to mining layout. Positions repeat at every pillar corner and panel T-intersection. While other mine layouts exist, the basic premise should hold true.**

great depths are best-positioned from a rib control/rib fatality point of view. Given this, more efforts should be directed towards reducing rib fatalities at other mines, specifically those in the mid-depth range. Economic and logistical issues may make this difficult, but step by step, this is a direction that should be investigated and pursued by mines at all depths. Additional research is necessary to better understand the factors influencing the occurrence of rib fatalities at different depths.

## CONCLUSIONS

This paper has developed the foundations for a future method of estimating rib fatality hazard by determining some of the initial contributions of many of its factors. The goal of the paper has been to discuss the components that most frequently contribute to rib fatalities in underground coal mines, and rudimentary steps have been made to begin quantifying each of those hazards. These steps were taken with a high focus on prior rib fatalities, and now the process begins to use those historical experiences to eliminate future rib fatalities.

The largest potential benefit of this research may be the simple act of approaching rib hazards from a new point of view. Work to improve mine safety often focuses on the elimination of accidents or fatalities, yet much of the effort that has been put into previous rib-related research has focused on failure or condition. Hopefully looking at this issue from a fatality-hazard point of view will lead to the next step in rib safety improvement, and better determining fatality contribution is a first step.

## DATA REFERENCE

Table 8 is a summary of the data used in this study. Blank cells indicate data that is missing or cannot be determined from the MSHA report. The asterisk in row 1 identifies a value that was estimated from historical data at the mine.

*Disclaimer*

The findings and conclusions in this report are those of the authors and do not necessarily represent the views of the National Institute for Occupational Safety and Health.

**Table 8. Data used in this study.**

| DATA APPENDIX | | | | | |
|---|---|---|---|---|---|
| **Date** | **Link to MSHA Report** | **Depth (ft)** | **Height (in)** | **# Units in Rib** | **Rib Failure Type** |
| 2/1996 | www.msha.gov/FATALS/1996/FTL96C04.HTM | 1100* | 122 | 3 | Brow |
| 9/1996 | www.msha.gov/FATALS/1996/FTL96C22.HTM | 1000 | 84 | 2 | Brow |
| 3/1997 | www.msha.gov/FATALS/1997/FTL97C06.HTM | 750 | 108 | | Granular |
| 7/1997 | www.msha.gov/FATALS/1997/FTL97C15.HTM | 450 | 135 | 4 | Blocky |
| 2/1998 | www.msha.gov/FATALS/1998/FTL98C06.HTM | 1000 | 90 | 2 | Brow |
| 7/1999 | www.msha.gov/FATALS/1999/FTL99C18.HTM | 1200 | 96 | 3 | Blocky |
| 12/1999 | www.msha.gov/FATALS/1999/FTL99C32.HTM | 200 | 82 | 2 | Brow |
| 1/2000 | www.msha.gov/FATALS/2000/FTL00C02.HTM | 974 | 92 | 2 | Blocky |
| 8/2001 | www.msha.gov/FATALS/2001/FTL01c15.HTM | 700 | 106 | 2 | Brow |
| 11/2001 | www.msha.gov/FATALS/2001/FTL01c41.HTM | 239 | 108 | 3 | Blocky |
| 8/2002 | www.msha.gov/FATALS/2002/FTL02c20.HTM | 400 | 144 | | Blocky |
| 2/2003 | www.msha.gov/FATALS/2003/FTL03c05.HTM | 900 | 102 | 2 | Blocky |
| 8/2004 | www.msha.gov/FATALS/2004/FTL04c16.HTM | 1120 | 90 | 2 | Slab |
| 2/2006 | www.msha.gov/FATALS/2006/FTL06c18.asp | 1100 | 105 | 9 | Slab |
| 10/2006 | www.msha.gov/FATALS/2006/FTL06c41.asp | 620 | 102 | 3 | Joint |
| 8/2009 | www.msha.gov/FATALS/2009/FTL09c10.asp | 700 | 111 | 3 | Brow |
| 1/2010 | www.msha.gov/FATALS/2010/FTL10c02.asp | 820 | 114 | 5 | Joint |
| 6/2010 | www.msha.gov/FATALS/2010/FTL10c38.asp | 1762 | 186 | 4 | Granular |
| 7/2010 | www.msha.gov/FATALS/2010/FTL10c42.asp | 925 | 102 | 4 | Joint |
| 6/2011 | www.msha.gov/FATALS/2012/FTL12c10.asp | 300 | 105 | 5 | Brow |
| 7/2011 | www.msha.gov/FATALS/2011/FTL11c09.asp | 720 | 83 | 5 | Slab |
| 3/2012 | www.msha.gov/FATALS/2012/FTL12c04.asp | 1100 | 68 | 3 | Slab |
| 6/2012 | www.msha.gov/FATALS/2012/FTL12c10.asp | 600 | 102 | 4 | Brow |

## REFERENCES


Baumgarth, T.P. (1977). "Rib stabilization using steel pillar banding." 1977 Coal Convention of the American Mining Congress. Pittsburgh, PA. 11p.

Colwell, M. (2006). A Study of the Mechanics of Coal Mine Rib Deformation and Rib Support as a basis for Engineering Design. Ph.D. Thesis. University of Queensland. Queensland, Australia.

Colwell, M. and Mark, C. (2004). "Analysis and design of rib support (ADRS) – A rib support design methodology for Australian collieries." Proceedings of the 24th International Conference on Ground Control in Mining. Vol. 24. Morgantown, WV: West Virginia University, pp. 12–22.

Dolinar, D.R. and Tadolini, S.C. (1991). "Entry stabilization using rib bolting procedures." U.S. Bureau of Mines Report of Investigation, RI-9366: 13p.

Gauna, M. (1983). "Angle bolts control rib side at No. 4 Mine, Brockwood, Alabama." Preprint number 83-310. SME-AIME Fall Meeting and Exhibit. Salt Lake City, UT: October 19-21.

Gauna, M. and Mark, C. (2010). "Protecting underground coal miners from rib falls." Proceedings of the 30th International Conference on Ground Control in Mining. Vol. 30. Morgantown, WV: West Virginia University, pp. 126–134.

Heasley, K.A. and Chekan, G. (1998). "Practical stress modeling for mine planning." Proceedings of the 17th International Conference on Ground Control in Mining. Vol. 17. Morgantown, WV: West Virginia University, pp. 129–137.

Hebblewhite, B.K., Ostle, S., Walker, R. and Lin, B. (1998). "Rib mechanics and support systems." ACARP research project C3059. University of New South Wales: 79p.

Horino, F.G., Duvall, W.I. and Brady, B.T. (1971). "The use of rock bolts or wire rope to increase the strength of fractured model pillars." U.S. Bureau of Mines Report of Investigation, RI-7568: 24p.

Jeremic, M. (1985). Strata Mechanics in Coal Mining. 1st ed. Rotterdam, Netherlands: A.A. Balkema, 580p.

Karabin, G.J. and Evanto M.A. (1994). "Experience with the boundary element method of numerical modeling as a tool to resolve complex ground control problems." Proceedings of the

13th International Conference on Ground Control in Mining. Vol. 13. Morgantown, WV: West Virginia University, pp. 201–213.

Lawson, H., Zahl, E. and Whyatt, J. (2012). "Ground condition mapping: A case study." Preprint number 12-122. SME Annual Meeting. Seattle, WA: February 19-22.

Mine Safety and Health Administration. (2011). "Protecting Miners from Hazards Related to Rib Falls." Program Information Bulletin PIB11-29. www.msha.gov/regs/complain/PIB/2011/pib11-29.asp.

National Institute of Occupational Safety and Health. (2010). "Research Report on the Coal Pillar Recovery Under Deep Cover." Report prepared in response to the 2008 Appropriation (Public Law 110-161), 79p.

O'Beirne, T.J. and Shepherd, J. (1984). "The failure of coal pillar ribs and possible methods of control." Proceedings of the 4th Australia-New Zealand Conference on Geomechanics. Vol. 4. Perth, Australia: Australia Geomechanics Society and New Zealand Geomechanics Society, pp 661–667.

O'Beirne, T.J., Shepherd, J., Rixon, L.K. and Napper, A. (1986). Coal rib stabili[s]ation – A new perspective. The Coal Journal. 14: 7–11.

O'Beirne, T.J., Shepherd, J. Rixon, L.K. and Napper A. (1987). "Instability and support of coal mine ribs." Australian Coal Industry Research Limited, Published Report 87-3: 130p.

Peng, S. (2008). Coal Mine Ground Control. 3rd ed. Morgantown, WV: West Virginia University, 750p.

Seedsman, R. (2006). "Joint structure and coal strength as controls on rib stability." Underground Coal Operators' Conference Paper 34. Wollongong, Australia: University of Wollongong, pp. 44–47.

Shepherd, J., Humphreys, D.R., Rixon, L.K., and Creasey, J.W. (1984). "Geotechnical investigations of roadway rib instabilities during mine development at Harrow Creek Trial Colliery, Queensland." Proceedings of the 5th Australian Tunneling Conference. Vol. 5. Sydney, NSW, Australia: Institution of Engineers, Australia, pp 186-191.

Smith, W.C. (1992). "Rib stability: Practical considerations to optimize rib design." U.S. Bureau of Mines Information Circular, IC-9323. 16p.

Weakly, L.A. (1976). "Room and pillar ground control utilizing the grouted reinforcing bar system." Proceedings of the 17th US Symposium on Rock Mechanics. Vol. 17. Snow Bird, UT, United States: American Rock Mechanics Association, pp 3A3-1–3A3-11.

Wykoff, B.T. (1950). "Wrapping pillars with old hoist rope." Transactions of the American Institute of Mining and Metallurgical Engineers. Vol. 187:898-902.

Williamson, I.A. (1967). Coal Mining Geology. London, United Kingdom: Oxford University Press, pp. 221-222.

# Update: Analysis and Case Study of Impact–Resistant Steel Sets for Underground Roof Fall Rehabilitation

**Dakota Faulkner**, R&D Mechanical Engineer
**Jinrong Kevin Ma**, Senior Ground Control Research Engineer
**John J Stankus**, President
Keystone Mining Services, LLC
Jennmar Corporation, Inc
Pittsburgh, PA

## ABSTRACT

Unexpected roof falls often occur in the entries or intersections of active mining sections in underground mines. For large roof falls (greater than 20 ft in height), it becomes dangerous and impractical to clean up the rock debris and re-bolt the newly exposed roof strata. To help mine operators rehabilitate the roof fall areas in a quick, safe, and economic manner, Jennmar Corporation and Keystone Mining Services, LLC (KMS) designed, tested, and developed various impact-resistant (IR) steel set designs, as initially detailed in the proceedings of the 30th International Conference on Ground Control in Mining (ICGCM). Since then, the IR steel sets have been successfully installed in more than 100 roof falls in 43 different coal mines. Significant data has been obtained from these installations, enabling further refinement to and improvement on the design.

This paper (1) updates drop test results of the IR lagging panel, (2) presents a case study of the performance of IR arch sets installed 56 months ago at a roof fall rehabilitation site, (3) demonstrates capacity evaluation of the IR steel set, and (4) outlines a preliminary applicability evaluation guideline of the IR steel set for a given roof fall condition. Field evaluation and structural numerical analysis indicate that impact capacity of the system is significantly higher than that of the IR lagging panel, as originally determined. It is concluded that, when evaluating the applicability of an IR steel set, ground control engineers should consider the IR lagging and steel set as an entire system and make a reasonable engineering decision based on actual roof fall geotechnical conditions.

## INTRODUCTION

Underground mines often experience roof falls in the entries, crosscuts, and intersections of active mining sections, main travel ways, and belt entries. Roof falls greater than 20 ft in height make re-bolting the newly exposed roof strata dangerous and impractical. Rehabilitating the roof fall area in a safe manner becomes a challenge to the ground control engineer and mine operator. To protect personnel, belts, moving vehicles, and other equipment, mine operators typically install steel structures, such as square or arch sets, in the roof fall areas and then backfill the voids between the steel set and roof. However, for large roof falls, which typically occur in intersections, complete void backfilling becomes impractical and prohibitively expensive.

As an alternate solution, Jennmar Corporation and Keystone Mining Services, LLC (KMS) designed, tested, and developed various IR steel set designs during the last few years. The IR steel set is a steel structure (square set or arch set) protected with IR lagging panels, which was initially detailed in the proceedings of the 30th ICGCM (Ma, Stankus, and Faulkner, 2011). Since then, various types of IR steel sets were fabricated and successfully installed in more than 100 roof fall rehabilitation projects in 43 different coal mines. However, various concerns and questions were raised by ground control engineers and the Mine Safety and Health Administration (MSHA), such as

- The previously reported impact capacity appears to be too conservative for practical use. Various field evaluations of IR steel sets, which were subjected to secondary roof falls, indicates that the IR steel set is capable of sustaining much higher impact load than the reported impact capacity.
- What is the most probable impact capacity of an IR steel set as a system?
- Given a specific roof fall condition, how does an engineer evaluate applicability of an IR steel set?

This paper first presents an update of laboratory drop test results of the IR lagging panel. To assess performance of the IR steel set, the paper details a field evaluation of IR arch sets installed 56 months ago at an actual roof fall rehabilitation site. With an IR square set as a case study, the paper demonstrates how to determine impact capacity of a steel set alone using an elasto-plastic analysis approach and presents a method to establish applicable roof fall scenarios using the Law of Conservation of Energy. To help engineers evaluate applicability of an IR steel set to a given roof fall condition, the paper outlines a preliminary applicability evaluation guideline.

## WHAT IS AN IR STEEL SET?

An IR steel set is a standing support system that, with the IR lagging panel as protection and its own energy absorbing capability, can sustain impact loads generated by falling rock pieces in roof fall areas, and can be used by the underground mine operators to

rehabilitate roof fall areas in a safe, quick, and economical manner. From an engineering design perspective, an IR steel set system needs to have the following:

- Sufficient support capacity to support the static load of rock debris piled on the canopy over time
- Capability to sustain dynamic loads by falling rock pieces without losing necessary serviceability
- Certain degree of installation mobility that will allow it to be dragged or pushed to the roof fall site
- A special lagging structure between the steel sets to provide full coverage and adequate flexural strength while effectively absorbing the impact energy generated by falling rock

An IR steel set canopy (typically 20ft long) usually consists of multiple courses of a single steel set (square or arch), spaced a few feet (typically 4 ft center to center), interconnected with each other with tie rods and spacer tubes, assembled with runner channels with sled tips at the front, and totally covered with IR lagging panels on the top and v-deck panels on the sides.

Once the IR steel set canopy is assembled in an adjacent safe area, a continuous miner can be driven underneath the canopy. By chaining the structure to the continuous miner, the IR steel canopy can be slightly lifted up and dragged/pushed forward. Doing so enables the operator to safely and gradually move IR steel canopies into the roof fall area while the rock debris is removed by the continuous miner. After the continuous miner cleans through the roof fall area, the IR steel set system is unchained and positioned at the designated roof fall area. By fixing the runner channel to the floor strata with rock bolts, the IR steel set system is installed and becomes a permanent standing support structure. With the specially designed IR lagging panel, it is technically feasible not to backfill the voids above the structure as long as accumulation of hazardous gas in the voids can be managed properly.

## UPDATED TEST RESULTS OF THE IR LAGGING PANEL

Since initially discussing the IR lagging panel design at the 30th ICGCM (Ma, Stankus, and Faulkner, 2011), industry professionals made various comments that the reported impact capacity of the IR lagging is conservative and that a more realistic capacity should be determined by allowing a higher deflection as testing criteria. Consequently, additional drop tests were conducted to determine the maximum impact capacity of the IR lagging panel.

### Testing Criteria

Previously, a 1 inch permanent mid-span deflection was used as testing criteria. However, from a serviceability perspective, it is considered that the IR lagging panel will serve its engineering purpose as long as the lagging assembly still remains on the steel set after being impacted by falling rock. To determine maximum allowable deflection, it is assumed that, upon a localized impact at mid-span, the IR lagging shall yield and deform to the extent that, at least 1 inch of the lagging will remain on the W-beam flange on either end. With this assumption, it is determined that the maximum mid-span deflection is 9.187 inches. However, to be conservative, a safety factor of 1.5 is applied, and an allowable mid-span deflection of 6 inches is considered as the testing criteria during the new laboratory drop tests. This assumption is considered reasonable, but conservative, given the acceptable 8 inches of deflection measured in the field.

### Test Results

Shown in Figure 1 is a typical sample after a drop test. Upon a free drop impact at mid-span by a 1541.5 lb weight falling from 63 inches high, the metal V-deck panel at the bottom experienced permanent deformation, and the special lagging block (SLB) fractured at the bottom but still maintained acceptable integrity.



**Figure 1. A typical IR lagging panel after drop test.**

The acceleration vs. time curve (Figure 2) recorded by the data acquisition system indicated that, due to the spring effect of the panel, the steel block bounced up and down several times in each test. As a result, the IR lagging was actually subjected to 4– 6 mini impacts. As shown in Figure 2, impact duration of the first and second mini impacts ranged from approximately 0.03–0.05 seconds, and the total duration of the impacts was approximately 0.7 second. The instantaneous impact load peaks at 77 kips. In this case, the V-deck panel deflected 1.75–3.375 inches at mid-span, and some deformation or fractures occurred to the SLB.

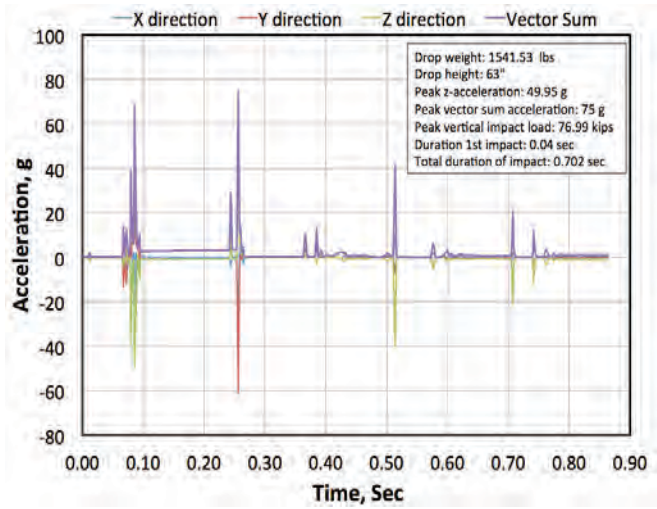



**Figure 2. Acceleration and load vs. time during impact test.**

By gradually increasing the steel block weight, a series of drop tests were conducted to determine the maximum impact capacity of the IR lagging. Listed in Table 1 are results of 16 samples tested using the impact tester. The lab tests verify that the IR lagging panel is capable of supporting an instantaneous impact load that was generated by a 1,541.5 lb metal block falling 63 inches with an acceptable mid-span deflection (less than 6 inches).

**Table 1. Drop test results, mid-span deflections.**

| Test # | Drop height | Drop weight (lb) | V-deck | | SLB | |
|---|---|---|---|---|---|---|
| | | | Side 1 | Side 2 | Piece 1 | Piece 2 |
| 1 | 63” | 1213.53 | 2.75” | 2.25” | 1.375” | 1.312” |
| 2 | 63” | 1129.03 | 2.375” | 1.875” | 1.625” | 1.5” |
| 3 | 63” | 1129.03 | 4.0” | 3.5” | 2.75” | 2.5” |
| 4 | 63” | 1129.03 | 2.75” | 3.25” | 1.625” | 2.125” |
| 5 | 63” | 1241.53 | 3.5” | 3.625” | 2.375” | 2.875” |
| 6 | 63” | 1241.53 | 1.25” | 1.5” | 0.375” | 0.375” |
| 7 | 63” | 1241.53 | 2.25” | 2.25” | 1.625” | 1.5” |
| 8 | 63” | 1241.53 | 0.625” | 0.375” | 0.375” | 0.125” |
| 9 | 63” | 1241.53 | 1.25” | 2.25” | 1.625” | 2.125” |
| 10 | 63” | 1241.53 | 0.375” | 2” | 0.125” | 1.875” |
| 11 | 63” | 1326.03 | 5” | 3.875” | 3.375” | 3” |
| 12 | 63” | 1410.53 | 1.625” | 3.375” | 0.875” | 2.25” |
| 13 | 63” | 1541.53 | 3.375 | 2.375 | 2.125 | 1.75 |
| 14 | 63” | 1541.53 | 5.375” | 4.5” | 3.5” | 3.125” |
| 15 | 63” | 1541.53 | 5.5” | 5.375” | 4.25” | 3.625” |
| 16 | 63” | 1541.53 | 1.75” | 2.75” | 1.25” | 1.5” |

**IR Capacity Interpretation**

To estimate the maximum size of falling rock that can be supported by the panel for different roof fall heights, the Law of Conservation of Energy (Tipler and Mosca, 2007; Cutnell and Johnson, 1997) is used. The law states that the total mechanical energy remains constant along the path of a falling object, provided that the net work done by external non-conservative forces is zero. For the impact test, non-conservative forces, such as air resistance and friction between the weight block and guide, are negligible. Assuming that the falling rock has the same potential energy (PE) as the steel block and will achieve the same amount of kinetic energy (KE) before impacting the SLB, the potential energy of the steel block and falling rock should be equal. Therefore, the following formula can be established:

$$W_s H_s = W_r H_r \qquad (1)$$

Where: $H_r$ = weight of the steel block, 1,541.5 lb

$W_r$ = weight of a falling rock, lb

$H_s$ = falling height of steel block, 63 inches or 5.25 ft

$H_r$ = falling height of a rock, ft

Table 2 lists various sizes of falling rock for different falling heights calculated based on Equation (1). The rock density is assumed to be 160 lb/ft$^3$. For example, the impact-resistant lagging panel can sustain an instantaneous dynamic impact load generated by a maximum of 578.1 lb of rock falling from a 14-ft height to the top of the impact-resistant lagging panel at mid-span.

**Table 2. Allowable falling rock size, IR lagging.**

| Fall Height, ft | Falling Weight, lb |
|---|---|
| 2 | 4,046.5 |
| 4 | 2,023.3 |
| 5.25 | 1,541.5 |
| 6 | 1,348.8 |
| 8 | 1,011.6 |
| 10 | 809.3 |
| 12 | 674.4 |
| 14 | 578.1 |
| 16 | 505.8 |
| 18 | 449.6 |
| 20 | 404.7 |
| 22 | 367.9 |
| 24 | 337.2 |
| 26 | 311.3 |
| 28 | 289.0 |
| 30 | 269.8 |

**CASE STUDY OF AN IR ARCH SET CANOPY**

A mining company in the Appalachian region experienced a large roof fall in the mains in early April 2009. MSHA shut down the mining section and requested that the operator rehabilitate the fall area before any coal production could be resumed. To quickly and safely rehabilitate the entry and to protect moving vehicles and personnel from falling rock, the mine decided to install IR steel canopies in the fall areas.

**Geotechnical Condition**

Coal is extracted from the Upper Freeport seam by the room-and-pillar mining method. The mining height is 55 inches, and the entry width is 20 ft. Overburden at the roof fall area is approximately 700 ft. Figure 3 shows the location of the roof fall area, which is approximately 120 ft long in the # 3 main entry and 60 ft across at the angled crosscut. Based on the underground examination and previous KMS analyses, it was found that the immediate roof consists of 4.5-ft-thick, thinly laminated, black shale that is interbedded with thin pyrite coal streaks at intervals ranging from 3–8 inches. Above the immediate roof is 5–6-ft-thick, layered, dark gray shale/sandy shale and massive competent sandstone. The mine was using 48 inch, #5, grade 60, fully grouted, non-tensioned rebar at 4 ft centers as primary support and 10–12 ft x 0.6 inch, grade 270, non-tensioned cable bolts as supplemental support. From the field examination, it appears that the roof fall is due to a localized problem caused by a change in geology and inadequate roof support.

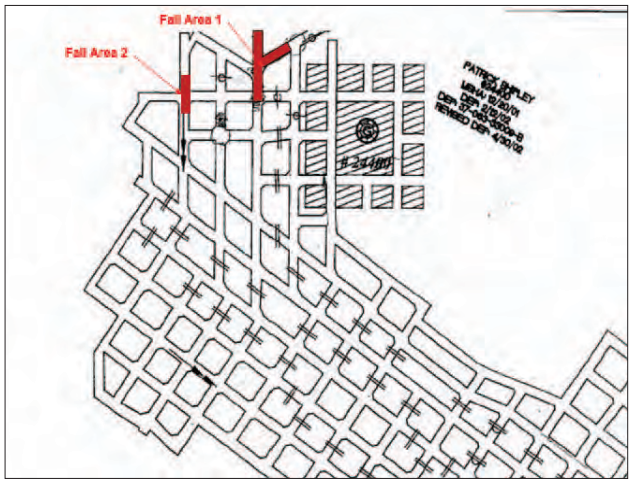



**Figure 3. Fall location.**

**Rehabilitation Plan**

Field evaluation indicated that the strata in the caved area had already reached a stable condition, and the exposed strata was mostly thinly laminated weak shale or dark gray shale, and falling rock pieces were fairly small (less than 2 $ft^3$). After the site visit and field evaluation, a rehabilitation plan was developed and proposed using W8 x 31 IR arch sets (Figure 4). Upon MSHA approval, the mine installed the IR arch set at the roof fall areas. To accommodate the continuous miner, the steel set had a minimum inside clearance of 16 ft x 5ft. In addition, the structure was designed to sustain possible impact loads generated by rock pieces falling from 16 ft high above the arch. During the rehabilitation process, the 20-ft-long IR arch canopy set was first assembled outby in an adjacent safe area. The set was then gradually moved to the roof fall areas using the continuous miner, which removed the rock debris.

The sets were successfully installed in the two roof fall areas in April 2009 without any accidents or injuries. According to a follow up visit with the mine, the impact-resistant steel sets performed very well, and no problems have been reported to date.

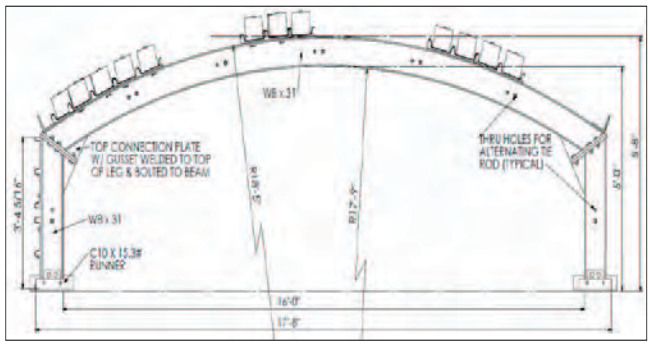



**Figure 4. W8 x 31 IR arch set (Upper left corner has an extra line or block).**

**Field Evaluation on 11/5/2010**

On November 5, 2010, KMS conducted a follow-up field evaluation 19 months after installation. In the #3 entry (belt) roof fall area, the overburden strata had stabilized. Only a few small rock pieces (less than 1 $ft^3$) fell on the canopy over the 19-month period, and the impact-resistant arch sets remained intact. At the #1 entry (air return) roof fall area, a small scale, secondary roof fall, composed of approximately 7–9 tons of rock fell off the 6-ft-high rib sometime in early 2010. This field investigation indicates that the impact-resistant arch sets performed very well, and there was no apparent structural deformation or lagging panel failure. Only one of the impact-resistant lagging panels was deflected, and that deflection was less than 3/4 inch at mid-span.

**Field Evaluation on 11/21/2013 - Area 1**

In the recent field evaluation on November 21, 2013, personnel from MSHA, KMS, and the coal company visited the #3 entry (belt) fall area to estimate the maximum falling height, to measure the secondary rock fall size, and to check the deformation of the impact lagging and steel set where the falling rock made impact. It appeared that various small scale secondary roof falls had occurred during the 56-month period. Shown in Figure 5 is the rock debris outby the cross cut.

With a laser distance meter, it was determined that the maximum roof fall height was approximately 14.5 ft from the top of the canopy. Rock pieces ranged from several cubic inches to 18.75 $ft^3$ in size, were mostly irregular slab-shaped, and were piled one on another. The relatively large piece landed across several lagging panels and individual steel sets. Since the fall area is not accessible, the rock size could not be exactly measured. By visual estimation, the piece as shown in Figure 5 is the largest and is estimated to be 3 ft x 7.5 ft x 10 inches (or 18.75 $ft^3$).

Underground examination of the steel set, lagging panels, and SLBs indicate that the installed W8 x 31 IR arch set performed very well during the last 56-month period. No lagging panels or SLBs were knocked off from the W-beam, and the steel sets did not exhibit any measurable deflection at the area where impacted by secondary roof falls. However, some V-deck lagging panels at several impacted locations did deform with a mid-span deflection ranging from 0.25–8 inches. The SLB fractured but the IR lagging is still providing support, although at a reduced capacity.



**Figure 5. Secondary roof fall.**

**Field Evaluation on 11/21/2013 - Area 2**

The roof fall Area 2 in #1 entry was also evaluated on November 21, 2013. A similar W8 x 31 long radius impact arch set was installed in this area in the same time frame. It looked like a secondary small scale roof fall occurred during the same 56-month period. The approximate measure of the maximum roof fall height was 11 ft to the top of the canopy. The rock pieces that fell on this canopy were generally smaller than those in Area 1. However, there were two large sandy shale blocks (3.5 ft wide x 7 ft long x 5ft thick) that fell off the roof/rib corner and onto the side corner of the steel set. Even so, under the impact areas, the steel sets were still intact and with no measureable deflection on the lagging panels.

**Summary of Field Evaluations**

Both KMS and MSHA personnel were impressed with the IR steel set performance. It was mutually agreed that the IR steel set has a higher capacity than previously reported, and the set should be applicable to any comparable roof fall areas in other coal mines.

## DEMONSTRATION OF AN IR SQUARE SET DESIGN

With a roof fall rehabilitation project as an example, the following demonstrates how to evaluate static and dynamic impact capacity of an IR square set system.

**Design Assumptions**

With the information provided by the mine, the following design assumptions are derived and adopted in the design and evaluation:

- Minimum inside clearance of the steel set is 14 ft x 3.5 ft.
- The steel set will be spaced on 4-ft centers, and five sets will be assembled together as a 20 ft long unit.
- Steel sets will be assembled outby at a safe area and then pushed into the fall area.
- Dynamic impact resistant lagging panels will be installed on the top of the structure, and regular V-deck panels will be installed on the sides.
- Overburden strata reaches an equilibrium state after the roof fall, and disturbance due to future mining activities is negligible.
- After the steel square set unit is positioned at the desired location, the runner channel will be bolted to the floor to provide adequate lateral constraint for the entire structure.
- The structure should support a maximum of 14 ft of piled, dead weight rock.
- The IR square steel set should sustain an impact load generated by a maximum of 24-inch-thick rock slab falling 14 ft to the canopy.
- Maximum allowable mid-span deflection of the square set or lagging panel is 8 inches.

**Recommended IR Square Set Design**

After a few design iterations, a W8 x 31 IR square set is considered appropriate. Shown in Figure 6 is a 2D drawing of the design.

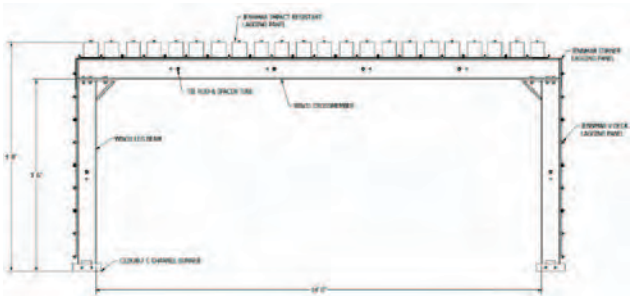


**Figure 6. W8 x 31 impact resistant square set (2D).**

**Structural Evaluation—Static Loading**

When overburden strata consists of thinly laminated weak rock, secondary roof falls can occur in a gradual manner, and the impact load of each single rock piece is insignificant. Eventually, the IR steel set may be buried underneath the fractured rock over time. In this case, it is reasonable to assume that the steel set may be subjected to static loading. Steel structure analysis, following the American Institute of Steel Construction (AISC) standard, indicates that the proposed square set is capable of sustaining a maximum of 52.42 tons of uniformly distributed static load or, equivalently, 14.89 ft of deadweight assuming 4-ft spacing and 120 lb/ft$^3$ average density of fractured rock.

**IR Capacity Evaluation of Steel Set**

In idealized elastic design, the deformation behavior of steel material is linear. This means that the force needed to deform the steel set is proportional to the beam deflection. The force increase is linear only up to the onset of yielding, which represents the limiting load in elastic design. However, in reality, most structural steel (A36, A992, A325, etc.) exhibit a strain-hardening characteristic. In practice, steel structure designs that are rugged enough to withstand large impact loads elastically without any material yield are costly and impracticably heavy. Plastic deformation of a steel set, due to the strain-hardening property of steel and structural non-linearity, are an excellent and an economical way to cushion against impact by allowing a certain amount of material yielding and structural deformation.

*Elasto-Plastic Design Concept*

To evaluate impact-resistant capacity, an elasto-plastic steel analysis was conducted for the W8 x 31 square set under an impact by a block with a weight (W) (mass x gravity) and a falling height (H) as shown in Figure 7.

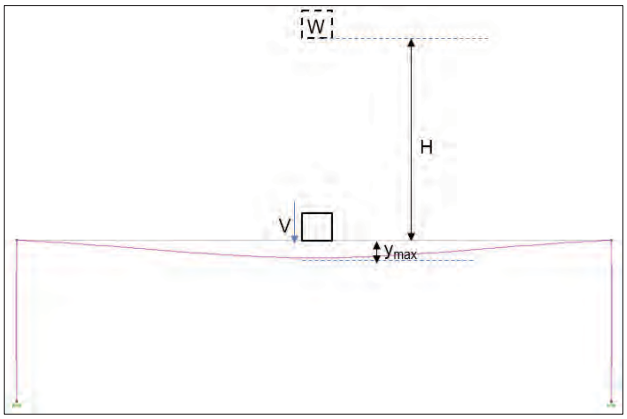



**Figure 7. Conceptual impact model.**

Prior to impacting, the block attains an initial impact speed of V given by Equation (2) and carries a kinetic energy of $E_k$ by Equation (3):

$$V = \sqrt{2gH} \tag{2}$$

$$E_k = WH = \frac{WV^2}{2g} \tag{3}$$

Where: g = Gravity constant, ft/sec$^2$

Shown in Figure 8 is an idealized elastic plastic load vs. deflection behavior of the steel set under impact load. The shaded area represents the energy absorbed by a steel set structure undergoing yielding upon impact load. The deflection increases linearly up to the yield load $F_u$, after which, the structure deforms nonlinearly with a slight increase of additional capacity with the increase of deflection. The energy absorbed $E_p$ is simply the area under the curve in Figure 8 and can be determined by Equation (4):

$$E_p = \int_0^y F\,dy = F_u y_{max} - \frac{F_u y_u}{2} + \frac{(y_{max} - y_u)(F_{max} - F_u)}{2} \tag{4}$$

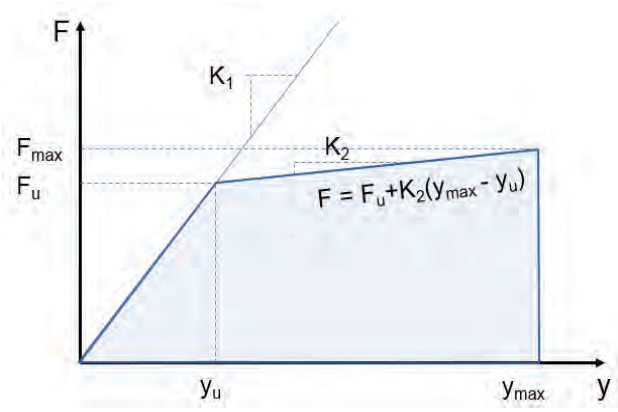



**Figure 8. Conceptual load vs. deflection curve.**

Based on the Law of Conservation of Energy, the energy to be absorbed, including the incoming kinetic energy and additional work done by the weight W, equates the work of elastic and plastic deflection, as described by Equation (5):

$$WH + Wy_{max} = F_u y_{max} - \frac{F_u y_u}{2} + \frac{(y_{max} - y_u)^2 K_2}{2} \tag{5}$$

Solving for weight W from Equation (5) gives Equation (6):

$$W = \frac{F_u y_{max} - \frac{F_u y_u}{2} + \frac{(y_{max} - y_u)^2 K_2}{2}}{12H + y_{max}} \times 1000 \tag{6}$$

Where: W = weight of falling rock, lb

H = falling height, ft

$F_u$ = yield load, kips

$y_u$ = deflection upon yield load, inches

$y_{max}$ = maximum allowable deflection, inches

$K_2$ = equivalent post-yield stiffness of steel set, kips/inch

From a design perspective, the weight of a falling block W, falling from a height H, with a maximum allowable mid-span deflection $y_{max}$ can be estimated using equation (6) if the yield load $F_u$, yield deflection $y_u$, and equivalent post-yield stiffness $K_2$ can be determined through either laboratory testing or numerical modeling.

*Elasto-Plastic FE Analysis*

In this evaluation, a 3D elasto-plastic finite element analysis was conducted to determine the parameters $F_u$, $y_u$, and $K_2$.The W8 x 31 square set was virtually tested and numerically analyzed to assess the yielding and deformation and to determine the relationship between deflection and a localized load at mid-span. Listed in Table 3 are the material properties of the steel members

used in the model.The stress-strain relationship for steel members was modeled using a multi-linear strain hardening constitutive model.

**Table 3. Material properties of steel members.**

| Steel Type | Young's Modulus, psi | Poisson's Ratio | Yield Strength, psi | Ultimate Strength, psi |
|---|---|---|---|---|
| A36 | 2.90E+07 | 0.3 | 36259 | 66717 |
| A992 | 2.90E+07 | 0.3 | 50000 | 75000 |
| A325 | 2.90E+07 | 0.3 | 92000 | 120000 |

An isotropic strain-hardening rule with Von Mises yield criteria was applied for simulating non-linear behavior of the steel member after yielding. Shown in Figure 9 is the equivalent stress (Von-Mises) distribution of the deflected W8 x 31 square set due to localized impact load at mid-span.

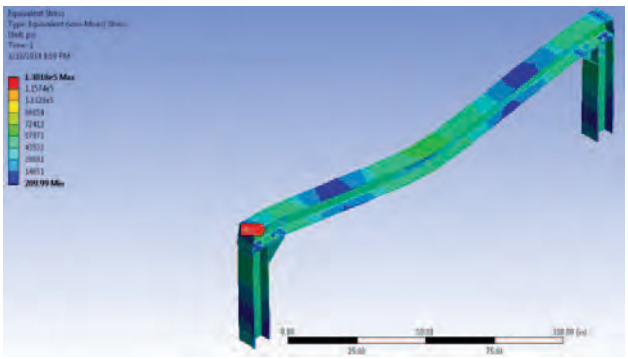


**Figure 9. Equivalent stress distribution.**

By increasing load F gradually, a load vs. mid-span deflection curve (Figure 10) was established based on the results derived from the elasto-plastic nonlinear FE model. From the curve, the equivalent stiffness of the square set prior to and after yielding were calculated as $K_1$ = 93.87 kips/inch and $K_2$ = 2.14 kips/inch. The square set starts to exhibit plastic yielding and deformation when the load exceeds $F_u$ = 87.82 kips and the mid-span deflection is greater than $y_u$ = 0.968 inch.

*Maximum Allowable Impact Weight*

With the aforementioned value of the variables $F_u$ , $y_u$, and $K_2$, and the 8 inches of maximum allowable mid-span deflection per the field data, the maximum allowable weight of the falling rock for a given falling height is determined using Equation (6).Listed in Table 4 are maximum weights of falling rock for various possible falling heights that the W8 x 31 square set can sustain with a maximum of 8-inches of deflection at mid-span.

**Validation - Dynamic Impact Simulation**

To validate the elasto-plastic analysis results of the design, a full-scale 3D nonlinear dynamic impact model was developed to evaluate the performance of the structure under a worst-case impact-loading condition. A weight block (1,937.3 lb) impacts the cross beam at mid-span with an initial speed of 43.93 ft/second, which is equivalent to a 30-ft falling height. Figure 11 shows the Von-Mises stress distribution of the steel set at t = 0.0099 second after initial impact. Figure 12 shows energy variation vs. time. Analysis indicates that the kinetic energy carried by the weight block was absorbed as internal energy through cross beam deflection and deformation of the structure. The mid-span deflection (Figure 13) of the cross member is approximately 8.25 inches after the weight block becomes stationary. The results match well with the elasto-plastic analysis results, and it is concluded that the W8 x 31 square set meets design requirements.

**IR Capacity of Entire System**

As an entire system, the IR steel set consists of two major components: steel set and IR lagging. The capacity of the system to sustain an impact load is contingent upon the location where the rock impacts. For a steel set, a localized impact loading at mid-span represents the worst-case loading condition. Considering the fact that the impact load will be distributed to the steel beam through the 18-inch-wide IR lagging panel, the rock slab thickness is evaluated on a unit basis (18 inches wide). Impact load by a rock slab that is greater than 18 inches wide is assumed to be shared by adjacent lagging panels.

Along the entry axial direction, there are two possible impact cases depending on the location of the falling rock with respect to the steel beam and lagging panel.

*Rock Fall Above the IR Lagging*

If the contact point and center of gravity of a falling rock slab are above and through the mid-span of the IR lagging panel, part of the rock fall kinetic energy will be absorbed by the IR lagging by means of SLB yielding, deformation of the cushion pad, and plastic deflection of the V-deck. Similarly, the maximum allowable thickness (listed in Table 5) of the falling rock slab that each IR lagging can sustain is estimated on a unit basis (12 inches long x 18 inches wide) using the maximum values in Table 2.

*Rock Fall Above the Steel Beam*

The majority of the impact load will be undertaken and absorbed by the steel set if the impact contact point and center of gravity of a falling rock slab are above and through the cross beam of the steel set. If the rock slab is long, it could span over multiple steel cross beams. It is reasonable to assume that impact load by a rock slab longer than the steel set spacing will be shared by adjacent steel cross beams. With this assumption, the maximum allowable thickness of the falling rock slab that each steel set can sustain is estimated on a unit basis (4 ft long or set spacing x 18 inches wide), using the maximum weight values in Table 4. Listed in Table 5 are maximum rock slab thicknesses that each W8 x 31 square set can sustain for different falling heights.

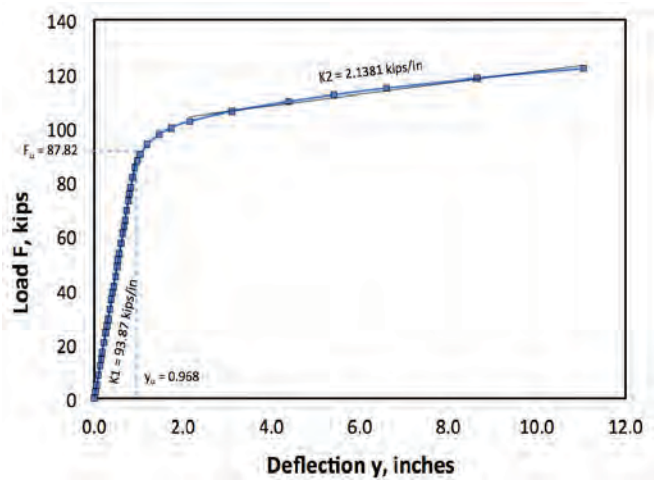



**Figure 10. Load vs. deflection of W8 x 31 square set.**

**Table 4. Allowable falling rock weight of the W8 x 31 square steel set.**

| Fall height, H, ft | Fall weight, lb |
|---|---|
| 2 | 22,278.9 |
| 4 | 12,730.8 |
| 5.25 | 10,041.2 |
| 6 | 8,911.5 |
| 8 | 6,855.0 |
| 10 | 5,569.7 |
| 12 | 4,690.3 |
| 14 | 4,050.7 |
| 16 | 3,564.6 |
| 18 | 3,182.7 |
| 20 | 2,874.7 |
| 22 | 2,621.0 |
| 24 | 2,408.5 |
| 26 | 2,227.9 |
| 28 | 2,072.5 |
| 30 | 1,937.3 |

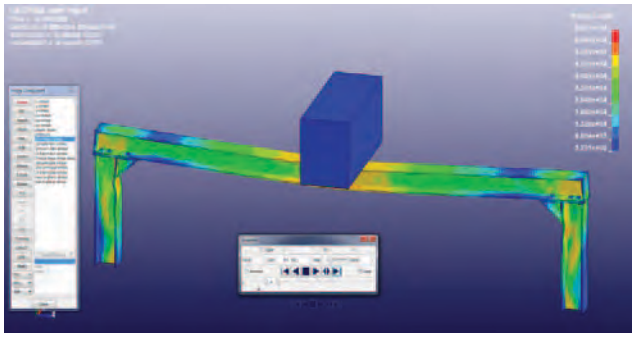


**Figure 11. Von-Mises stress distribution upon impact.**

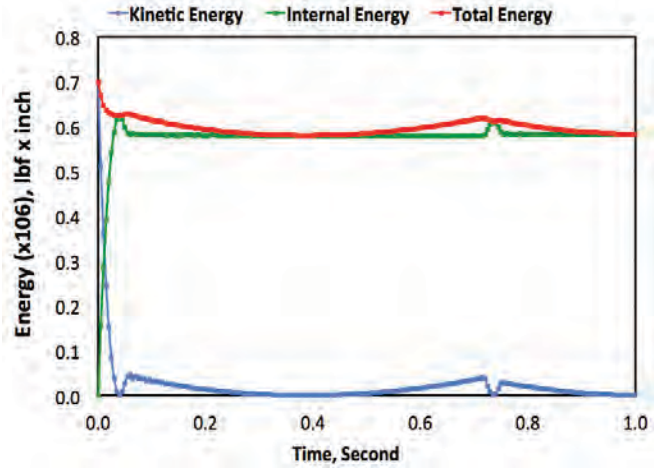



**Figure 12. Energy vs. time.**

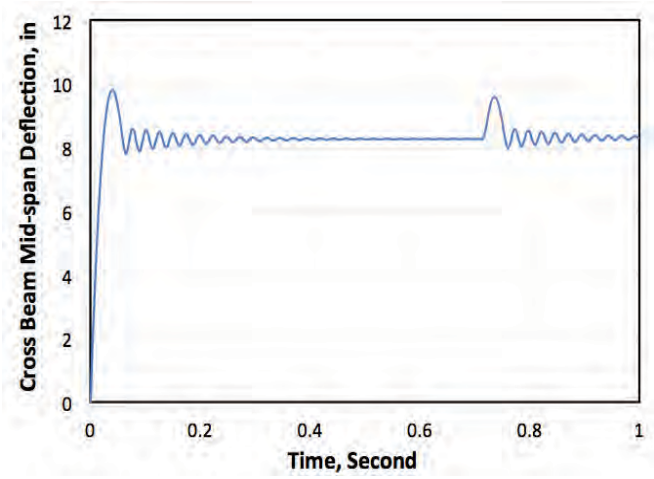



**Figure 13. Mid-span deflection vs. time.**

*Applicable Roof Fall Scenarios*

Listed in Table 5 are maximum allowable thicknesses of falling rock slab for different falling heights. Each combination represents a roof fall scenario where the IR steel set can sustain and absorb the impact kinetic energy by means of a possible 6-inch mid-span deflection on the IR lagging or an 8-inch mid-span deflection on the W8 x 31 square set cross member.

## PRELIMINARY APPLICABILITY EVALUATION GUIDELINE

Prior to the installation of the IR square set, mine engineers should carefully evaluate applicability of the design for a given roof fall condition. The following preliminary evaluation guidelines are offered for consideration:

- Evaluate the overburden stability of the affected mining zone by considering regional geological features, horizontal stress, orientation of affected entry, pillar size, adjacent mined out areas, possible nearby mining activities in the near future (longwall mining, pillar retreat mining, blasting), etc. If large-scale secondary roof falls triggered by nearby mining activities

**Table 5. Maximum allowable thickness of falling rock slab.**

| Fall Height, ft | Maximum allowable rock slab thickness, ft | |
|---|---|---|
| | If fall on IR lagging [1] | If fall on cross beam [2] |
| 2 | 16.9 | 23.2 |
| 4 | 8.4 | 13.3 |
| 5.25 | 6.4 | 10.5 |
| 6 | 5.6 | 9.3 |
| 8 | 4.2 | 7.1 |
| 10 | 3.4 | 5.8 |
| 12 | 2.8 | 4.9 |
| 14 | 2.4 | 4.2 |
| 16 | 2.1 | 3.7 |
| 18 | 1.9 | 3.3 |
| 20 | 1.7 | 3.0 |
| 22 | 1.5 | 2.7 |
| 24 | 1.4 | 2.5 |
| 26 | 1.3 | 2.3 |
| 28 | 1.2 | 2.2 |
| 30 | 1.1 | 2.0 |

Note:
Estimated on a unit basis (12 inches long x 18 inches wide) based on actual drop test results.
Determined on a unit basis (48 inches long x 18 inches wide) based on elasto-plastic structural analysis results of a W8 x 31 square set.

are of concern, applicability of the IR steel set will be limited. In this scenario it would be recommended that the voids above IR steel canopy should be backfilled with lightweight, foamed cementitious grout or similar material.

- Conduct field visits and collect relevant geotechnical information, including but not limited to the following: entry size, roof fall height, lithology of fallen rock, visual estimate of the size and thickness of fallen rock slab, shape of the roof fall opening, sign of any localized geological features (faults, folds, fractured zones, sandstone channel, slickensides, etc.), accessibility and entry dimension of adjacent safe area, type and overall dimension of available equipment that could be used to clean out the rock debris, and so on.

- Based on the field data, make a reasonable judgment regarding applicability of the IR steel set. For a given roof fall height, if the thickness of probable falling rock slab is less than the maximum allowable thickness (Table 5 or similar table if different IR steel set design), the IR steel set could be applicable. Otherwise, either an alternate IR steel set should be designed or a better cushioning effect should be created above the selected IR steel set design.

- Evaluate accessibility and entry size of adjacent safe area. Make sure that the selected area is stable, and there is sufficient space for the IR steel set to be assembled.

- Check overall dimensions of available mining equipment that could be used to rehabilitate the fall area. Make sure the IR steel canopy has sufficient room for the mining equipment to maneuver inside.

## SUMMARY

This paper updates the laboratory test results of the IR lagging panels. Applications of impact-resistant steel sets in various roof fall rehabilitation projects during the last few years have proven the design has higher IR capacity than initially determined. With the laboratory tests, field case study, elasto-plastic structural analysis, and dynamic impact numerical modeling, the following conclusions can be made:

- A steel set protected with IR lagging panels offers a viable solution for mine operators to rehabilitate the roof fall area in a safe, quick, and economical manner.
- Updated drop tests confirmed that the IR lagging panel is capable of supporting an instantaneous impact that was generated by a 1,541.5 lb metal block falling 63 inches with an acceptable mid-span deflection of less than 6 inches.
- Field investigation indicates that the installed impact-resistant arch sets have a higher impact capacity than previously reported and have met the intended engineering purpose.
- A case design project is used to demonstrate the IR steel set design methodology. Major steps are summarized as follows:
  - Static, uniform-load, support capacity of an IR steel set can be determined through AISC-based structural analysis.
  - An elasto-plastic analysis approach can be used to evaluate and determine the maximum impact support capacity of an IR square set for a given maximum allowable deflection at the cross beam mid-span.
  - A full-scale dynamic impact numerical model can be used to validate performance of the developed IR steel set under the worst-case impact-loading condition.
  - The Law of Conservation of Energy can be used to establish applicable roof fall scenarios.
  - A preliminary guideline is offered for engineers to evaluate if an IR steel set design is applicable to a given roof fall condition.

If the rehabilitated entry will be in service for the entire mine life, backfilling the voids between the steel canopies and caved roof with lightweight, foamed cementitious grouts or similar material should be considered. In cases where the IR lagging panel experiences more than 6-inch mid-span deflection due to unexpectedly high impact load by secondary roof fall, necessary measures (sand bags or some backfill) should be taken to prevent further deflection in the future. Similarly, if the cross beam experiences more than expected deflection, supplemental standing support, such as posts or props under the deflected beam, should be considered.

**REFERENCES**

Ma, K. J., Stankus, J., and Faulkner, D. (2011). "Development and application of impact-resistant lagging for steel sets installed at underground roof fall areas." In: *Proceedings of the 30th International Conference on Ground Control in Mining*. Morgantown, WV: West Virginia University, pp. 158–167.

Tipler, P. A. and Mosca, G. (2007). *Physics for Scientists and Engineers: 6th Edition*. New York: W.H. Freeman & Company, pp. 650.

Cutnell, J. D. and Johnson, K. W. (1997). *Physics: 4th Edition*. New York: John Wiley & Sons.

# Meeting the Challenges of Floor and Sidewall Strata Control in UK Deep Coal Mines

**Lorraine Kent**, Research Manager
**Jonathan Bowler**, Senior Rock Mechanic Engineer
Bretby Office
Golder Associates (UK) Ltd.
Burton on Trent, United Kingdom

**David Moore**, Group Geotechnical Engineer
UK Coal Production Ltd
Doncaster, United Kingdom

**Stuart Walker**, Geotechnical Risk Analyst
Thoresby Colliery Ltd
Mansfield, United Kingdom

## ABSTRACT

Excessive floor and side deformation are major problems in deep coal mine entries in Europe, and in particular in the UK where rockbolt support is used at depths of working of around 3000 ft. This has major economic and safety implications for the industry resulting in the potential for sidewall instability, disruption to mine infrastructure, (belt conveyors, floor mounted transport systems and powered supports), and the requirement to safely manage excavation of large quantities of floor material. European research aimed at improving deformation control is described. The outcomes include innovations in support systems, materials and installation practices, as well as better methods for predicting and monitoring deformation levels. As coal mines get deeper, some entry deformation is inevitable, and methods for mechanised removal of floor lift and repair of sidewalls have been developed to allow production to continue as mining clearances are re-established.

## INTRODUCTION

Most coal mines in Europe are operating at greater depths than those in the USA or Australia. The remaining UK mines for example have depths of working between 700 m and 900 m, (2300 -3000 ft). The in-situ vertical stress at this depth, (around 20 MPa), is usually further concentrated by interaction effects from previous workings above, and often below as well, (Lightfoot and Liu, 2010).

At this depth of working, longwall faces in Europe are invariably retreated between single entry rather than multi-entry roadway. Stable pillars are also left between panels in the UK, to help maintain entries in a safe and serviceable condition during panel retreat. Controlling side squeeze and floor heave in particular have become major considerations at UK Coal mines. In bolted entries a cumulative total of more than 4 metres of floor heave may be removed to allow mining (a process known as "dinting"), and sides can converge by more than one metre. Entry sides may then need to be cut back and re-supported to re-establish mining clearances, a process known as "cheeking off".

Bowler *et al.* (2009), describe how technical development and innovation brought significant benefits in controlling sidewall movement in both the short and long term at Daw Mill Colliery. Investigation of sidewall support problems was undertaken using a range of techniques including sidewall deformation measurements using a new robust extensometer system and laser surveying, sidewall inspection using a borehole camera and short encapsulation pull testing of a range of sidewall reinforcement consumables, both on site and in the laboratory. A shear dowel was also developed to give warning of possible tendon breakage. Testing of existing sidewall support systems confirmed that performance was limited by poor bond strength and for Glass Reinforced Plastic (GRP) systems, low end and bending strengths. The use of long GRP dowels for remedial sidewall reinforcement proved successful in stabilising high deformation sides. Textile webbing set in a diamond pattern was found to be an effective means of side surface support, used in addition to long dowels. Larger diameter (28 mm) steel and GRP bolts were specifically developed and used in longer lengths to provide improved long term stability in new gate entries developed with a coal roof horizon. These proved very effective. Using computer numerical modelling, a more effective support pattern was identified. This comprised 2.4 m long bolts and 4 m long flexibolts in the roof every 0.8 m, together with 3 m long side bolts. The innovations described by Bowler *et al.* (2009) were part of an ongoing improvement process which has been continued by the research work described in this paper.

This continuing challenge of excessive entry deformation has now been addressed by research funded by the European Commission and undertaken by a number of European partners including Golder Associates and UK Coal Production Ltd. This work focuses on both side and floor deformation control, and has resulted in support and mining practice innovations which are believed to represent the current state of the art in deformation control in deep mines.

The support and control measures described here may have increasing application in the USA and Australia in the future as deeper seams are mined and multi-seam working becomes more common.

## METHODS FOR IMPROVED UNDERSTANDING OF FLOOR AND SIDEWALL DEFORMATION IN DEEP COAL MINES

### Entry Deformation Mechanisms

In the UK the entry sides, as well as the roof are rockbolted. Normal practice is to use steel bolts on the pillar side of each entry with cuttable Glass Reinforced Plastic, GRP, bolts on the panel sides, Figure 1.



**Figure 1. Typical rockbolted UK mine exhibiting floor heave.**

The bedded nature of coal measured rocks means that the sides react to loading in a different way to the roof and floor. The immediate roof and floor of the seam are often laminated weak mudstones.

In the roof, dilation associated with bed shear is resisted by the bolts so restricting vertical displacement into the opening and limiting or preventing roof failure. In the floor the strata is free to lift and the failure mode will depend upon the strength of the strata.

Side deformation consists of lateral displacement into the opening with associated movements, fracturing and the opening up of sub- vertical breaks or partings such as coal cleat. If not supported or constrained there is a high risk of loss of operational clearances and slumping or toppling type sidewall failures.

The deeper the entry, the higher the stress levels, and the more likely that excessive deformation will develop. An understanding of how this deformation develops is vital in devising effective measures to resist it.

### Improved Understanding of Entry Deformation through Observation and Measurement

In the UK rockbolted roadways are designed by measurement (Altounyan, Arthur and Waite, 1998, Kent, Cartwright and Bigby, 1999). Initial rockbolt designs are verified with more sophisticated instrumentation to measure strata dilation and rockbolt loading, (sonic extensometers and strain gauged rockbolts). Once a rockbolt design is established safety monitoring using telltale type extensometers is used to confirm that the entry roof remains stable.

Sidewall laser surveying to measure closure and borehole camera surveys to determine fracture depths for sidewalls introduced at Daw Mill, Bowler *et.al.*(2009), proved invaluable in understanding deformation and have subsequently been deployed at the other UK Coal mines. At Thoresby Colliery borehole camera surveys have been used to determine sidewall fracturing in sections of roadway affected by increased vertical stress associated with pillar areas and roadways driven close to waste edges in underlying seams. At Kellingley Colliery breaks up to 5 m into the side were seen in the worst areas affected by faulting sub-parallel to the gate road. In all cases the quantity, nature and depth of fracturing were strongly related to the overall side movement and were used to aid decisions regarding suitable additional support.

Bowler *et.al.* (2009) described the development of a hollow "shear" dowel to identify potential side tendon breakage. This proved to be a good indicator of side wall shear movement, but did not verify if the tendon was actually fractured. As part of the research, various other methods of testing the integrity of installed steel and GRP bolts, by measuring the apparent bolt length, were assessed during the research. A successful method would be an important diagnostic tool, allowing identification of areas needing remedial support and of the length of additional support required. Methods assessed included a radio frequency technique which treats the bolt as an aerial antenna and an ultrasonic method sending signals applied to the bolt ends. These worked under some circumstances, (subject to ionic properties of the rock and rockbolt end condition) but not reliably in typical coal mine entry rock support conditions. An acoustic method based on measurement of the reverberations from a hammer blow to the end of the rockbolt was also investigated. Tests with prototype equipment demonstrated that the method also has potential but requires significantly more development work.

Bolts can be pre-instrumented to indicate if they become broken. One way of doing this for GRP bolts is to install twin copper wires in a longitudinal channel machined along the bolt to allow integrity to be measured. Time Domain Reflectometry, TDR, using an electronic pulse was also tried to measure the distance to any break in the wire. This was trialled at Daw Mill and appeared to indicate that some 3 m long GRP bolts were fractured, typically about 2 m into the side. On subsequent face retreat, some of these bolts were however seen to be bent at this point rather than broken, suggesting that a TDR reflection may have been generated by premature wire failure. Loading at the bolt end plate also caused connectivity problems in the sockets, indicating further design work was required.

In the UK mining legislation requires refuge holes ("manholes") to be excavated at pre-determined intervals along gate entries for personnel protection where free steered vehicles (FSV's) are in operation. At Daw Mill, poor ground control conditions and even ground failures had historically been associated with manhole positions. A study was undertaken to review side failure mechanisms in relation to manhole positions. This included a monitored trial manhole construction to identify the effect on the side condition and observe any subsequent time related deterioration in the surrounding side, Figure 2. The investigation concluded that ground control risks were increased by constructing

manholes in the sidewalls at Daw Mill. The work was reviewed by the UK Health and Safety Executive and it was agreed, based on balance of risk to persons working in or travelling the roadway, that manhole construction should be discontinued. Consequently none were used for subsequent entries, including those for 303's panel. Alternative personnel safety measures, were introduced where FSV's and other mobile plant were in use. These safety measures included elevated platforms marked by high visibility poles and a set of Managers Rules for mobile plant to park to allow pedestrians to pass safely. This represented a major step forward in terms of improving side control at Daw Mill Colliery.

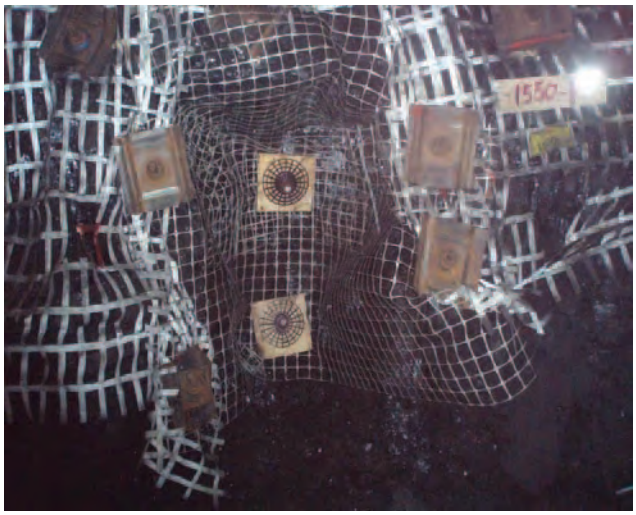


**Figure 2. Refuge excavated in the sidewall of entry at Daw Mill colliery.**

The floor failure mode in UK mine entries depends on the floor lithology. For very soft floors, such as Daw Mill, failed floor material moves continually into the entry from below so that horizontal layering eventually becomes vertical. Initially in the case of soft floor strata it can be seen to be bending up into the roadway, Figure 3 (a). At other sites, horizontal layers of stronger floor strata break at either side and uplift en masse into the entry. In some cases, vertical tensile cracks in the heaved material also develop along the entry axis, Figure 3 (b).

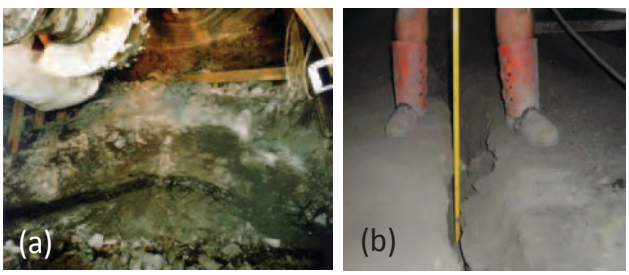



**Figure 3. (a) Soft floor strata bending, (b) Tensile fracture in competent floor strata.**

Monitoring of floor heave development at Thoresby Colliery was undertaken to more fully understand the floor behaviour in areas where vertical stress was increased by interaction from previous workings in a seam 30-40m below. Because future panels would be affected by similar interaction areas, floor heave was measured to determine rates and levels of lift to determine if they could be related to modelled vertical stress. This work resulted in improved understanding of the effect of previous underworking on entry deformation. Figure 4 shows the results from one of the gate entries subject to pillar interaction stresses. The information gained allows improved planning of dinting operations as described later.

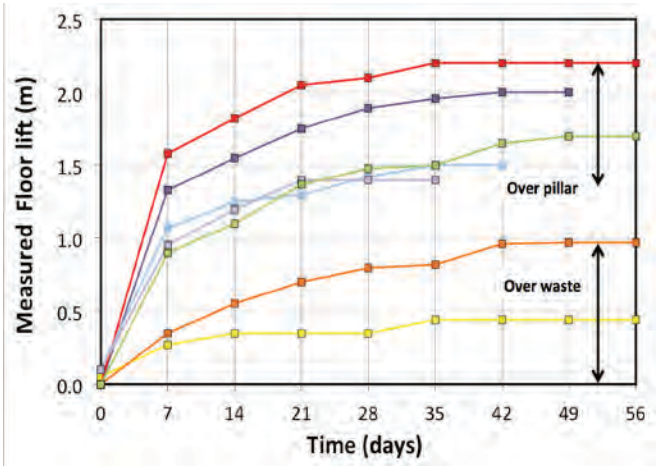



**Figure 4. Measured floor heave at Thoresby Colliery from a gate entry subject to variable vertical stresses.**

**Improved Understanding of Entry Deformation through Numerical Modelling**

Computer modelling was undertaken to investigate the deformation process and to assess possible new measures to reduce deformation magnitudes. Golder normally makes use of FLAC 3D (Itasca 2000), to model entry deformation as the finite difference technique on which it is based is well suited to modelling soft rock behaviour, allowing large strains and material failure. However it is a continuum method so cannot realistically model the situation beyond the point where open cracks form. In addition, both floor and side deformation typically show time dependency, where displacements continue to increase slowly as material creep takes place. This was not incorporated in the FLAC modelling.

Comparison of FLAC model predictions with actual outcomes from the mine sites confirmed that the modelling accurately predicted levels of roof deformation, but underestimated floor deformation, and, if large, side deformation was also usually underestimated, Figure 5. This has to be taken into account when making estimates of likely entry deformation levels.

Positioning of the entry roof and floor horizons in relation to weak layers and interfaces within and close to the seam can result in different deformation patterns, which may influence entry stability, as previously demonstrated at Daw Mill, Bowler *et.al*. (2009). Site observations also suggested that the layered nature of mine floors was a factor in the development of floor heave. To try to improve the model simulation of multi-layered strata in the floor, multiple bedding plane interfaces were incorporated in the modelled entry floor using the FLAC "interface" facility. This was found to significantly increase the predicted floor heave compared to no interfaces. Reducing the interface friction angle produced further increases in the model floor heave. This confirms

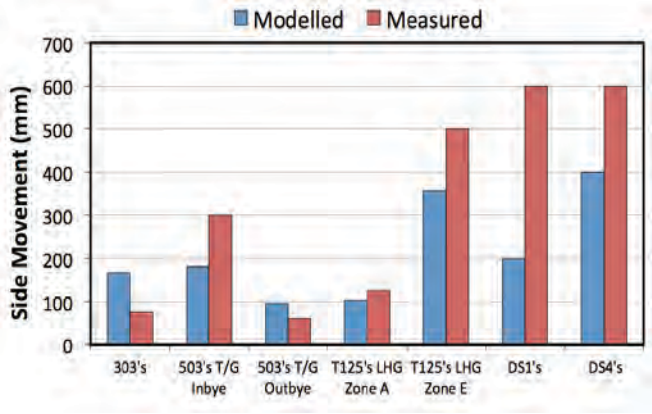



**Figure 5. Comparison of modelled and measured side movements on development.**

that low friction interfaces can be important in floor heave development. Making use of FLAC's interface facility however adds considerably to model coding complexity, and to date these have only been used routinely to represent the main bedding and weakness planes.

Numerical modelling has been applied in order to assess the scenario of broken side bolts and the effect of subsequent cheeking off and dinting to restore entry clearances for face retreat. This type of numerical modelling has aided decisions on the timing of cheek off and suitable additional reinforcement of sides prior to face retreat at Daw Mill and Kellingley Collieries. At Daw Mill, Figure 6, the effect of the simulation of broken bolts also aided the decision to support the sides with textile webbing (see later) on development to guard against the risk of sidewall failure as a result of broken bolts.

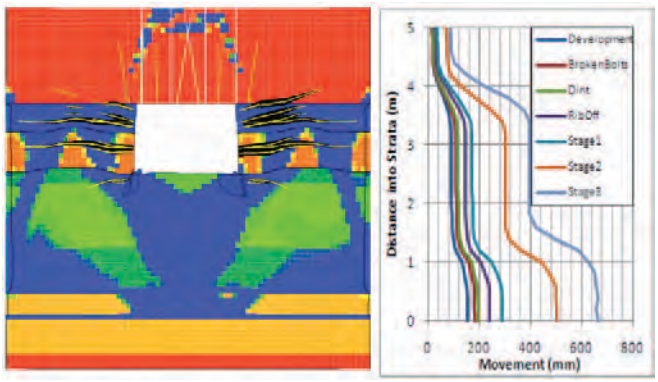



**Figure 6. Numerical model output from Daw Mill Colliery simulating broken bolts, floor dinting and sidewall cheek off (rib off). (Stages 1, 2 and 3 represent increasing front abutment stresses, Stage 3 = 2m in front of the face).**

Numerical modelling remains a key tool for stress evaluation, with MAP3D (Mine Modelling Pty) used by Golder to estimate stress redistributions around longwall panels subject to interaction from workings in other seams. Both prediction and subsequent experience have emphasized the importance of controlling vertical stress by positioning entries away from the highest stress areas. Stress control can be achieved at the planning stage by working panels in sequence and by ensuring the separating pillar between panels is wide enough, and that the tailgate entry rather than the maingate entry (used for coal transport) of the replacement panel is on the pillar side. Where multi -seam workings are present, as at two of the mine sites where research work was undertaken, highly stressed pillars in seams above or below can cause major entry deformation. Stress transmission is near vertical in these situations, and entry positioning should avoid these pillar interaction areas wherever possible. Conversely underlying or overlying waste areas can provide vertical stress relief which can be very beneficial.

## IMPROVED SIDE SUPPORT AND REINFORCEMENT METHODS

### Cuttable Sidebolting

GRP bolts are used on the face side of each entry because they can be later cut out by the longwall shearer. Entry sides supported by GRP bolts however exhibit more movement than those supported by steel bolts. Although this fact is sometimes masked by the effect of coal cleat direction or stress field differences, it has been firmly established from a number of recent studies.

GRP bar has a higher tensile strength than steel and tolerates a greater strain at the elastic limit, but it has virtually no post elastic range, fracture occurring at 2.5% strain. Rockbolt steel, in contrast, fractures at approximately 18% strain. It is this lack of elongation of GRP which makes it more susceptible to failure. It is also difficult to engineer high strength threads and end fittings using GRP. Failure of end fittings in tension is a constant feature of GRP bolted entries with significant side deformation and many bolts have to be replaced for this reason. Steel bolts are therefore preferred for side reinforcement whenever practicable.

During the research other cuttable materials were examined and tested as possible alternatives to GRP for side bolts. These included polyethylene and polypropylene. However the materials examined had shortcomings, particularly related to strength properties. An additional problem with many plastic materials is the low elastic modulus, which means that bolts will shrink in diameter as they stretch under load, weakening the frictional bond, and resulting in pullout at low loads. At present, for cuttable bolts, there does not seem to be a realistic alternative to GRP.

The most obvious way of improving GRP side bolt effectiveness is to increase the length and/or diameter of the bolts. This was done at Daw Mill, where 3 m long 28 mm diameter GRP bolts were introduced to replace 1.8 m long 24 mm diameter bolts (Bowler *et.al*. 2009). A corresponding change to 28 mm diameter steel bolts for both the roof and sides was made at the same time. Following the increases in bolt diameter and length, the rate of monitored side convergence reduced significantly.

Another cuttable side reinforcement consumable widely used as remedial reinforcement is the hollow GRP dowel. This is installed in longer lengths (typically 4 m) in conjunction with cementitious grout rather than polyester resin to reinforce entry sides following excessive deformation. The grout is pumped up the central hole and grout return down the annulus confirms full encapsulation. These proved effective at Daw Mill where they were used in conjunction with a grout sock to ensure full encapsulation by expanding to the hole profile. Pull testing and in service performance confirmed that

a high bond strength was achieved and the hollow dowels provided effective reinforcement.

**Sidewall Webbing**

The use of textile webbing as a safety measure to restrain the deformed side surface was also pioneered at Daw Mill, Bowler *et.al.* (2009). The webbing is placed over existing sidewall mesh and anchored between the roof and the floor using rockbolts, and tensioned to provide maximum protection in high risk areas. The webbing is available with tensile strengths of 10 or 20 tonnes. Each piece is secured individually in a diamond pattern so that failure of any one piece of webbing will not compromise the whole system. The tensioning buckles are designed to slip before the webbing fails.

For high deformation sidewalls webbing is now used systematically, in conjunction with long tendon reinforcement, especially prior to dinting and face retreat. At Daw Mill it was used in conjunction with long tendon reinforcement and polyurethane injection; the webbing being installed to floor level. The design at Kellingley is as shown in Figure 7. At this site the webbing is secured 1.0m above floor level. This practice helps avoid loss of webbing tension following floor heave at this site and also helps to reduce damage during dinting operations.

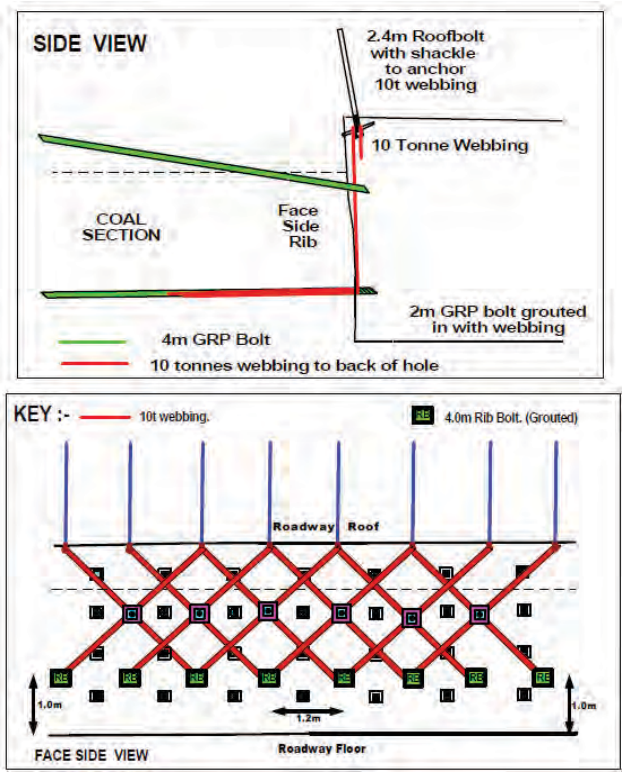



**Figure 7. Side webbing design at Kellingley Colliery.**

During the research project the attachment of the webbing to the bolts has been improved. Rather than attaching the webbing under the bolt plates, where it is vulnerable to being damaged by the edge of the plate, it is now fastened to attachment points on the bolt plates, Figure 8. An alternative method of securing the strap in position on the GRP side at the floor level was also developed at Daw Mill. The strap is pushed into a grout filled bolt hole using a GRP bolt which subsequently secures it in position as shown in the figure. This avoids problems when floor lift develops and dinting is carried out. Pull tests have confirmed the security of this type of anchorage.

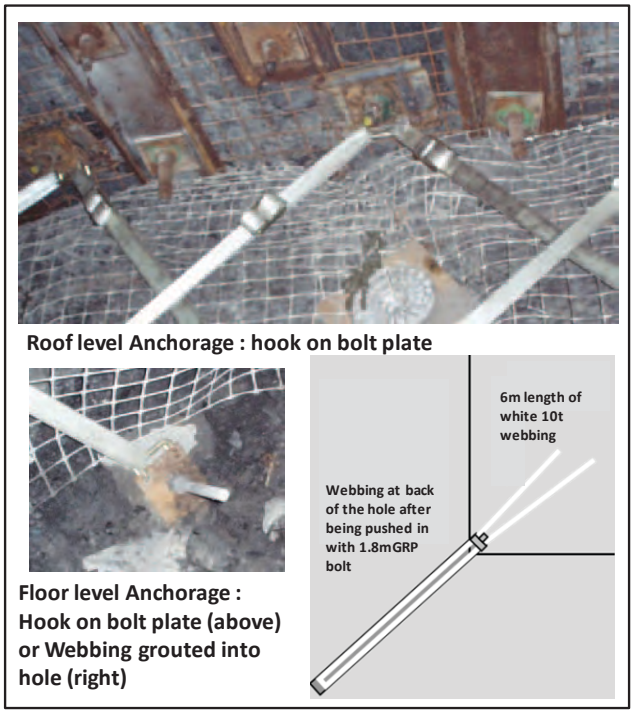



**Figure 8. Improved side webbing attachment.**

**Improved Plastic Mesh**

Plastic mesh is generally preferred to steel mesh for lining the entry sides because it is non corrosive, cuttable, and easier and safer to handle. The original plastic mesh adopted worked well for some time. However during the research it was noted that the mesh on occasions tended to fail at the welded intersections. The problem was solved by introducing an alternative product with woven intersections, which proved more resistant to failure.

**Polyurethane Resin Injection (PUR)**

Sidewall injection using polyurethane has successfully been undertaken at all the sites during the research. The main use was in strengthening sections of failed sidewalls in front of the face. The most commonly used polyurethane material is Bevedol WF Bevedan; a dual component polyurethane injection resin for permanent sealing and consolidation. It is available as either a WF16 or WF21 formulation. WF21 is slower setting than its WF16 counterpart and has a lower temperature reaction which makes it more suited to situations where spontaneous combustion is an issue. WF16 has a faster setting time but has the disadvantage that on contact with water it foams and therefore loses strength. However, in dry conditions, this faster setting time has the advantage that reduced volumes of PUR is required, proving more economical to use. Its other advantage is it can be used in situations close to the face where mining or cutting through is imminent.

The injection pressure and depth is varied depending on site conditions. In general higher injection pressures are used in the sides together with longer injection holes. On the coal face this also leads to the PUR permeating fractures and giving good consolidation further away from the face, so that it is not necessary to inject after each face cut. However, toward the surface, consolidation is less successful and the near surface is then susceptible to instability. At Daw Mill Colliery a trial was undertaken involving PUR injection via a drilled hole pattern comprising both long and short length holes. Long hole injection was undertaken as above and the short holes then injected initially using low pressure placement of the PUR. The injection pressure was then allowed to build up in some cases to 30Bar to achieve better penetration. This method successfully improved consolidation of the immediate face side and preventing slump failure of the face, although greater product usage was then required.

A similar 'targeted' placement of PUR has also been used to strengthen highly deformed sides prior to cheeking off. PUR injection is targeted at the deeper sidewall, beyond the distance to be cheeked off, facilitated by packers inserted into the holes at the appropriate depth. Because the PUR does not then strengthen the immediate sidewall, it is lot easier to cheek off as in a fractured state it falls off away from the bolts when excavated by the dint machine bucket.

Steel bolts also require removal from the pillar side during cheeking off; these are cut through using a hand held compressed air driven band saw.

### Geofoam Resin Injection

Geofoam is a low exothermic dual component urethane-silicate injection resin. The key advantage of this product is that it stays liquid for longer and consequently migrates further. The product can adhere and seal fractures, but also has the ability to foam for filling larger 'voids'. This product was trialled at Daw Mill Colliery on 32's Face as it retreated toward its face salvage position in ground affected by faulting. Geofoam was successfully placed to consolidate the face and roof above the powered supports. It proved successful, and on cutting the face, ribbons of the product could be seen in the face coal and in the roof mudstone confirming effective placement.

### Sprayed Liners

A phenolic foam sprayed liner was tried in order to help maintain sidewall integrity at Daw Mill Colliery. The product did improve side integrity, but the sealing and insulating properties resulted in heat build-up behind the liner. The Daw Mill coal is liable to spontaneous combustion, and leak points in the liner provided conduits for more oxygen rich air, and became nuclei for spontaneous combustion events. The liner consequently had to be removed from the sidewall. Use of similar sprayed liners should therefore be avoided where heating and potential spontaneous combustion are issues.

## IMPROVED FLOOR REINFORCEMENT AND CONTROL METHODS

### Floor Reinforcement: Rockbolting

Rockbolting the floor should, in principle, help to control floor failure and heave, although steel bolts in the floor would prevent mechanised dinting should this be required later. The use of GRP floor bolts, as used in the face side is however a possible option for reducing floor heave, and modelling was undertaken to predict how effective they could potentially be in current UK Coal mine conditions. Bolts modelled were 2.4 m long and installed vertically, Figure 9(a). The results suggested that floor bolts would be effective, with as few as 3 bolts significantly reducing the floor heave Figure 9(b). When a relatively low bond strength was assumed, to allow for weak floor material and difficult installation, this predicted improvement was still present.

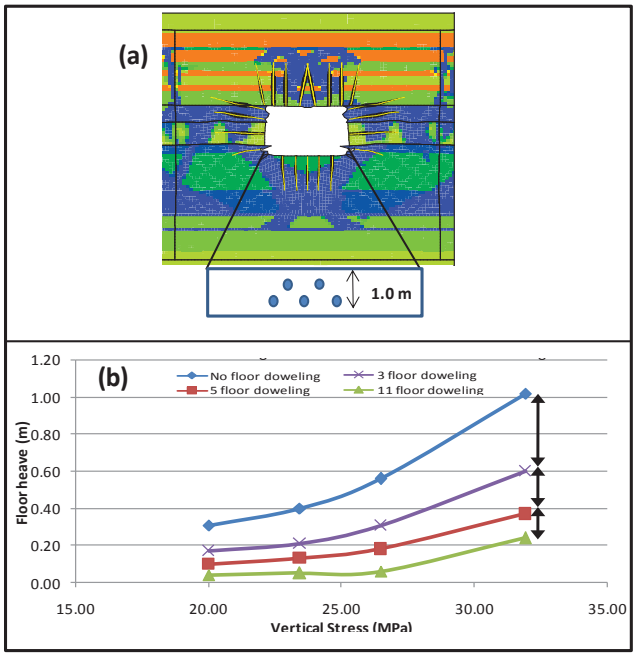



**Figure 9. (a) FLAC strain plot to show numerical model with floor bolts installed, (b) Resultant floor heave for the different pattern and stress regimes modelled.**

Historically floor bolting has been deployed in UK Coal mines but with mixed success. Currently there are still considerable practical difficulties in installing floor bolts, in terms of drilling and flushing down holes and inserting resin and bolts. For these reasons, and because of potential difficulty in subsequently removing reinforced floor material, if required, floor bolting is not currently practised in UK coal mines.

However a relatively recent exception was the use of 4m long hollow GRP dowels, installed and grout injected in a section of roadway floor under a belt conveyor at Daw Mill Colliery. This did prove successful in reducing floor heave, although this was in an area not subsequently subjected to face retreat front abutment stresses.

**Floor Reinforcement: Polyurethane Resin, PUR**

The other floor support improvement measure tried at the mines was PUR injection, which has been used to successfully strengthen the floor in specific circumstances. Trials were undertaken at Daw Mill on 32's panel where powered supports were sinking into the floor at the face ends. Injection was undertaken up to 2 m in depth. The trial proved successful, with the support penetration problem alleviated, and subsequent excavation showing good PUR penetration. Floor injection was subsequently applied on 303's panel at gate ends and along the faceline where this problem was again encountered.

PUR floor injection was not generally undertaken in gateroads for the same reasons as floorbolting; placement practicalities and removal difficulties should it not work. Historically it was tried at North Selby Mine in the 1990's. It consolidated the floor and reduced movement rates, but not sufficiently to maintain necessary clearances, and the consolidated floor was then difficult to excavate when dinting became necessary.

**Floor Control: Dinting**

As floor support is not currently feasible in UK Coal mines except for very site specific cases, dinting or removal of the heaved material is required. Currently a variety of machine types are deployed. The most common are the Hausherr dint and load bucket machines that are relatively small, Figure 10. EIMCO bucket machines are also still in use. One advantage of the use of a small bucket machine is that, when required, it can be turned round in the entry to work in the opposite direction. Where the smaller dinter loaders cannot operate, such as close to the stage loader in the coal gate entry, hand held jigger picks and manual shovelling on to a feeder conveyor are necessary.



**Figure 10. Dint and load bucket machine.**

Gerrard Jones Engineering supplies the DCL Dinter Cutter Loader machine which is a slightly larger machine with a range of bucket and cutter head attachment options to shovel weaker floor materials or cut harder floors or sidewalls.

In 2008, UK Coal purchased a Philips dinter cutter loader, Figure 11. This is a much larger machine, with a 6.0m wide cutting head similar to that of a continuous miner. It was used at Daw Mill Colliery, where it worked underneath the coal conveyor. This machine is equipped with a flexible "tail" enabling it to feed debris directly onto the conveyor.



**Figure 11. Phillips dinter loader.**

**MANAGEMENT OF FLOOR AND SIDE DEFORMATION**

Although the innovations described above have successfully contributed to reduced side deformation rates and improved safety, excessive deformation of the entry floor and sides remains an inevitable consequence of retreat mining in deep coal mines, and a significant challenge.

The main problem in managing floor and side movement is how to safely repair entries and restore clearances, without major interruption to production operations.

Management considerations include:

- Recognition that deformation is inevitable and resources must be allocated for on-going repair.
- Timing of dinting to restore operational clearances when required and avoid production delays.
- Planning of the number and size of dints undertaken. (Multiple smaller dints are more beneficial than a few deeper ones because dinting of heaved floor material removes restraint to further floor heave and side movement).
- Timing to minimise the consequences of subsequent re-activation of floor and side movement.
- Consideration of additional support measures needed to maintain stability post dinting.

Planning and the dedication of specific personnel from ground control teams to liaise with production and planning staff is key. The control of floor heave can be broken into:

- Reactive Measures: Removal of heaved floor material when it is at a level where transport/ventilation is restricted.
- Pro-active Measures : Application of monitoring and analysis and improved understanding in order to predict levels of floor heave and:
  - send in dinting machines early,

- improve side and roof support in order to help control floor lift (in the site specific cases where this is shown to be applicable).

Both the reactive and proactive approaches require consideration of operation and geotechnical constraints.

Operational constraints include:

- Number of dinters available
- Type of dinters available
- Manpower available
- Effect on mining operations in the entry, e.g. transport
- Scheduling of dint machines between sites, taking account of difficulty and delay in moving between sites

Geotechnical considerations include:

- Timing of dint: too early and it will have be done again, too late and it becomes reactive.
- Depth of dint:
  - Not deep enough and it will have to be done again
  - Too deep and could affect side and then roof behaviour
- Type of floor heave:
  - Soft floor 'squeezed' up (bucket dinter)
  - Strong floor -broken slabs (cutting head)

The management of dinting is about finding an optimum plan taking account of these operational and geotechnical factors.

**Management Examples: Thoresby Colliery**

Thoresby currently holds 10 dinting machines serving the operation of one longwall production face. Four of these are the loader type and 6 are cutter loader types. The current strategy is to deploy 2 machines in the coalgate entry. These machines will dint and cheek off in front of the retreating face. An initial 1m dint is taken 150m in front of the face followed by a further 0.5m dint 50m in front of the coal face. In areas of underlying pillars the outbye machine is also used to cheek off the side of the roadway whilst the inbye machine continues to dint.

In the entries of the next developing panel a cutter loader is deployed as the roadways reach any areas of pillar interaction or for the supply entry any areas affected by the adjacent retreating coal face. Therefore in supply entries 2 dinters are deployed, one dealing with the pillar interaction dinting and cheeking off to return the entry to original dimensions and one dealing with the rest of the entry dinting up to 0.5m. In coalgate entries 1 dinter deals with both the pillar areas and any dint required for clearance for face equipment installation. In order to optimize the timing of dinting in the supply entries at Thoresby Colliery, floor lift is being measured and related to modelled vertical interaction stresses from previously worked panels in the seam below. Figure 12 shows the data indicating a good relationship between measured floor heave and modelled vertical stress. This can be used to predict the floor heave magnitude. Vertical interaction stresses in future panels are predicted to reach 60-70MPa, suggesting the magnitude of floor heave to be anticipated could be around 3.0m.

A dinter is also deployed to each of the 2 lateral developments, following up the development system and removing around 0.5m

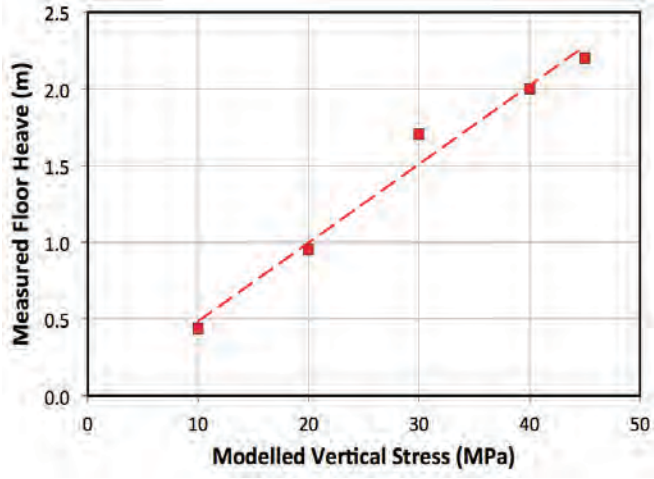



**Figure 12. Relationship between modelled vertical stress and measured floor heave for Thoresby Colliery.**

of dint around 200m behind the face of the development. The other dinters are deployed to outbye roadways especially areas affected by under workings or the abutment effects of the retreating panels. The Deep Soft Return roadway especially is affected by the front abutments as the faces reach their designated stop positions and requires a 1m dint and side cheek off in bolted zones after the face has reached its final position. In lengths of the return supported by steel arches, a dint only is undertaken. A dinter may also be required to maintain operational clearances for the longwall face undergoing salvage (recovery of the powered supports).

**Management Examples: Kellingley Colliery**

At Kellingley Colliery sections of 501's Maingate were affected by sub-parallel faulting causing large quantities of floor lift, 1.0-1.2m, on development, (floor lift is usually negligible for these Beeston Seam panels). At the time of face retreat the original roadway width had reduced from 6.2m to 4.7m and in excess of 3 m of floor lift occurred. Entry dimensions and equipment were planned to take into account the likely additional deformation for retreat. Following normal practice, the coal clearance conveyor, for example was suspended from the roof so that it was unaffected by minor floor heave. Lateral entry dimensions are also planned, where possible, to be large enough to accommodate subsequent side squeeze. This was the case for 501's Maingate. Two loader cutter machines were originally deployed, but severe roadway deformation meant that a third machine was brought in in order to maintain clearances. Operationally careful planning was then required in order to manage three machines and still undertake additional reinforcement, including cable bolting and trussing the roof, Figure 13.

At Kellingley the harder floor material requires the use of cutting heads for dinting more frequently than for either Thoresby or Daw Mill Collieries. Figure 14 shows Lateral Roadway repair work at Kellingley Colliery. At the time of writing the paper a major lateral dint was in progress in the main loco road. The Philips dinting machine had been removed from Daw Mill and was in use for this. This produced site specific challenges requiring the temporary support and suspension of the loco track to allow the Phillips machine to operate below it.

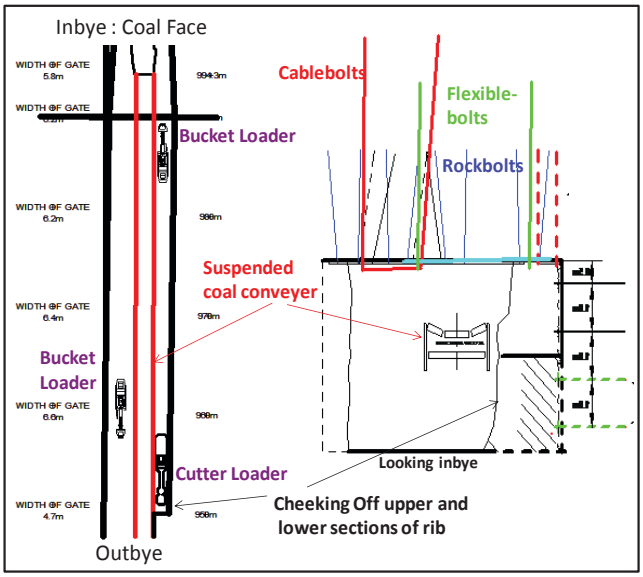



**Figure 13. Deployment of three dinter loaders in 501's maingate face end to maintain clearances.**



**Figure 14. Photograph of lateral roadway dinting at Kellingley Colliery.**

**Management Examples: Daw Mill Colliery**

The final retreat panel at Daw Mill Mine, 303's, made full use of the improvements made by Bowler et *al.* (2009) and further developments during the time of the research project. This was a particularly challenging retreat panel at depth, 750-810m, in weak geology. In addition, and for operational reasons, it was laid out so that the gate road entries were in the most unfavourable direction with respect to the horizontal stress. In anticipation of the higher stresses the sidewalls were webbed and long tendoned on development. This was also accompanied by the deployment of a member of the Colliery's Strata Control team dedicated to monitoring and reacting to ground movement as the panel retreated.

On retreat sidewall movement in the Coalgate entry increased in response to the front abutment stresses. Locally sidewalls moved inwards, particularly at the top of the side towards the roof, by up to 1 m and were observed to be overhanging. Additional sidewall support comprising "rib guards"was installed (Bowler *et.al* 2008). The face side sidewall was systematically dressed back and rebolted, long dowelled, meshed and webbed outbye of the stage loader.

A total of 5 dint machines were used in the main (coal) entry, removing a cumulative total of 4-5 m of floor lift. There was a spatial relationship between the amount of floor heave and the soft fireclay floor seam split, floor heave increasing where the seam split fireclay increased to 3.0 m of soft floor. Dinting was taken in a minimum of three stages to maintain clearances and move the equipment through the entry. Dinting below the original floor level triggered side and roof movement but lifting the dint to above original floor level was very beneficial. In the areas where dinting adversely affected rib condition, additional side bolts, meshing and extended webbing were installed.

Outbye of the dinting operations, the sidewalls were observed to be stable and in good condition with approximately 300 mm total movement which had taken place during development.

303's panel retreated at an acceptable rate in this difficult geotechnical environment. Despite the quantity of repair work required to the sidewalls and floor they were still the best conditions achieved at Daw Mill since working of the new deeper areas commenced some 10 years previously. Unfortunately Daw Mill closed in 2013, before 303's had finished retreating, following a major underground fire.

## CONCLUSIONS

The problem of excessive side and floor deformation in deep coal mine entries will continue but technical innovations in support systems, materials and installation practices and in the management of excessive deformation have resulted from recent work in part funded by a European Commission project.

Understanding deformation mechanisms is essential for making support management decisions for maintaining entry stability. Deformation monitoring using a range of techniques including sidewall closure, floor heave and borehole camera work to determine sidewall fracturing is also vital. Methods of bolt integrity determination in order to aid decisions on additional support were investigated, but need further development. Numerical modelling remains a vital tool for predicting deformation and has been used to model sidewall cheeking off and the effects of dinting in order to aid decisions on side and roof support. The modelling work emphasised the importance of controlling vertical stress by positioning entries away from the highest stress areas.

GRP bolts remain the most effective cuttable bolt for the face side. Textile webbing support of the sides, with optimised anchorage options, has also been introduced to improve safety. Other successful innovations included improved plastic mesh, and a greater understanding of optimisation of injection products.

Floor reinforcement in UK coal mines is still not feasible because of the practical difficulties in installing bolts. Polyurethane

resin injection has been successful for floor support but in very site specific cases (facelines and faceline junctions).

Floor control by removing the lifted material remains the most practical option for management. Optimised methods for mechanised removal of floor lift and repair of sidewalls have been developed to allow production to continue as mining clearances are re-established.

The innovations described are likely to have increasing application internationally as coal mining is undertaken at increasing depths and in areas subject to interaction from existing workings.

## ACKNOWLEDGEMENTS

The authors would like to thank UK Coal Production Ltd and S Hoult, Operations / Technical Director UK Coal Production Ltd for permission to publish this paper. Acknowledgement is also given of assistance provided by the Daw Mill, Thoresby and Kellingley Colliery Rockbolting Engineers.

The work has in part been funded by the European Commission through the Research Fund for Coal and Steel, Contract RFCR – CT-2010-00001.

The views expressed are those of the authors and not necessarily those of UK Coal Production Ltd or Golder Associates (UK) Ltd.

## REFERENCES

Altounyan P F R , Arthur J, Waite K. (1998). Guidance on the use of Rockbolts to Support Roadways in Coal Mines - A UK Code of Practice. Paper presented at Symposium of Rock Mechanics and Productivity and The Implementation of Codes of Practice, West Rand, South Africa, October 1998.

Bowler J, Altounyan P, and Robinson G. (2009). Rib Support Innovation at Daw Mill Colliery 28th Int Conf on Ground Control in Mining Morgantown WV USA

Itasca Consulting Group Inc., (2000). FLAC 3D Version 5.0, Thresher Square East, Minneapolis, Minnesota, USA.

Kent F L, Cartwright P B, & Bigby D N. (1999). Tunnel Deformation Monitoring “Action Levels” in Coal Mines for Support/Reinforcement Design. 18th International Conference on Ground Control in Mining, Morgantown, West Virginia, USA.

Lightfoot N and Na Liu (2010). The Prediction of Pillar Interaction Effects in Deep Multi Seam Working. 29th International Conference on Ground Control in Mining, Morgantown, West Virginia, USA.

MAP 3D, Mine Modelling Pty Ltd, Box 637, Mt. Eliza, Victoria, 3930 Australia.

# The Caterpillar HW300 Quickscan

**Pieter-Jan Kleiterp**, Application Engineer Highwall Miners
Caterpillar Global Mining
Caterpillar Highwall Mining Systems
Sliedrecht, Netherlands

## ABSTRACT

Caterpillar has been involved in highwall mining since the purchase of Bucyrus in 2011. The Cat® HW300 is a continuation of the Superior Highwall Miner that was first sold in the USA in 1994. Currently, there are more than 80 machines supplied worldwide, and Caterpillar envisions increasing the population steadily in the coming years.

The Cat highwall miner product group, based in Beckley, WV, has been involved in the sales of all miners to date. With the dealer model that Caterpillar is using, more people, dealers in particular, need to be trained on the application of highwall mining. A site investigation is a highwall specialist's work, and Caterpillar assists dealers and customers in determining the technical feasibility of highwall mining on mine sites. With the ever-increasing amount of requests, it proved to be important that people without highwall mining expertise, yet who are familiar with mining, could perform a very quick analysis of a potential highwall mining site to determine at an early stage if it is worthwhile to invest the time and money of all parties—customer, dealer, and Caterpillar—in further follow-up.

Therefore, Caterpillar would like to introduce the Cat HW300 QuickScan tool.

## EXISTING QUICK ASSESSMENT TOOLS FOR HIGHWALL MINING

In 1992, Seib proposed the Highwall Mining Index (HMI) for potential Australian highwall mining sites (Seib, 1992). This HMI was updated in 2001 using lessons learned from highwall mining experiences in the 9 years prior.

ACARP (Fama, Shen, and Maconochie, 2001) suggests looking at a number of conditions that would make highwall mining impossible. After all conditions are favorable, the HMI is used. These conditions are roof condition, mining reserve, seam methane content, seam dip, highwall/lowwall stability, seam thickness, pit width, and potential stone bands. Some conditions would result in negative advice for highwall mining in a particular site; whereas, with the HW300, it should have been positive based on our experience.

We concluded that the ACARP HMI is a useful approach, if adapted to some (but not all) equipment-specific parameters.

No other assessment tools are available to determine the feasibility of highwall mining. Mining consultants and the Cat highwall mining product group do most highwall mining evaluations. The main parameters that are studied are pillar stability, roof stability, and highwall stability. In some instances, the floor is also critical. Information that is available from potential highwall mining sites is usually limited to coal strength and roof strength. Additional data is generally taken from visual inspections from site visits that make it difficult to assess the feasibility of highwall mining without physically being there.

Caterpillar proposes the Cat HW300 QuickScan—a new software tool to be made available online— which allows dealers to discuss feasibility with potential mine sites. It can be used by anyone who is interested in determining the potential for highwall mining with the CAT HW300 such as mining engineers and mining consultants studying the feasibility of a potential highwall mining site. It starts with an initial scan with limited, possibly higher-level data. Depending on the output, additional data, such as the results of laboratory tests and bore hole logs, as well as data that is less reliable, such as estimates, can be entered to get more confidence. This step-by-step approach makes it possible to determine whether or not it makes sense to invest further in obtaining accurate data to get more certainty.

## THE CAT HW300 QUICKSCAN

The QuickScan tool is simple and quick to use. With most parameters available, the feasibility can be ascertained within 30 minutes or less. The QuickScan needs to be filled out by someone who is familiar with mining yet does not need to be a specialist in mining engineering or rock mechanics.

The user needs to fill out 12 parameters that are important to highwall mining in general and the feasibility of putting a Cat HW300 at the site. These 12 parameters are:

1) Strength of immediate overburden
2) Strength of coal

3) Seam dip (degrees)
4) Average highwall angle
5) Coal seam undulations
6) Weathering (Slake Durability)
7) Seam thickness
8) Overburden thickness
9) Methane content
10) Geology
11) Rock mass rating
12) Water inflow.

For every parameter, the user can choose from a selection of inputs that correspond to a rating. The user does not need to rate each parameter. This is a major difference between the QuickScan and the HMI. It makes it much easier to fill out the data. Some inputs trigger a no-go message saying that the site is unsuitable for highwall mining.

**Strength of immediate overburden**

In highwall mining, the roof span standup time is very important. To determine the stability of the roof, rock mechanical properties of the roof rock are required. In the last eight years, Caterpillar has been involved in many highwall mining evaluations. The experience shows that most mining companies that are looking at highwall mining do not have detailed rock mechanical properties available. Generally, the only available information is the unconfined compressive strength (UCS). The UCS is not the only parameter affecting the roof stability, but past evaluations showed that a UCS smaller than 2MPa does not result in a stable roof, regardless of depth below surface.

**Strength of coal**

Mining companies that are interested in highwall mining generally rely on coal strength estimates from experience or from other projects. Sometimes, the data is not available at all. In the USA, the in-situ strength of 6.2MPa (900psi) is used for pillar calculations (Mark and Chase, 1997), but, in other pillar formulae, such as the Sheorey formula (Sheorey, 1992), the UCS is required. Low coal strength results in wide pillars that can be uneconomical to mine with highwall mining. It is difficult to make a clear distinction between strong coal that is mineable and weak coal that is not. Caterpillar uses a limit of 2 MPa. Coal that is weaker than that is uneconomical for extraction with highwall mining. An example of this type of coal is lignite.

**Coal seam dip**

According to the Caterpillar brochure, The Cat HW300 can mine seams that dip between 5 degrees up dip and 12 degrees down dip without alterations to the equipment (Caterpillar, 2013). Caterpillar has experience with steep dip applications, when seams are between 12 degrees and 20 degrees down dip. Examples are mining operations in Russia and Alabama. Relationships between penetration depth, seam dip, and production rate have not yet been established.

**Highwall angle**

The highwall angle is an indication for the strength of the overburden. A mine operator looks at cutting the highwall as steeply as possible without jeopardizing the safety of the operation. Another consideration is that the vertical stresses on the pillar and the roof near the drive entry are very high. The lower the highwall angle, the higher the stresses near the drive entry. Caterpillar suggests disqualifying a project when the highwall angle is less than 30 degrees measured from the horizontal. These highwall angles have been recorded in lignite mines in Europe and in hard coal mines in Indonesia. Numerical models, as well as slope stability calculations, for a number of mines suggest that these slopes are unstable or have very low factors of safety when being undermined.

**Coal seam undulations**

The highwall miner can follow the floor of the coal seam even when the coal seam is undulating slightly. When the floor undulations are more than 2 degrees per pushbeam length (or 170m radius of curvature), this will lead to disproportional lower production and higher wear and tear.

**Slake Durability Index**

The Slake Durability Index (ASTM, 2014) is an indication of how easily rock weathers. This can give an indication of how safe it is to work near the highwall, but it also can give a good indication of the stability of the roof. It may be necessary to leave head coal to prevent the roof from weathering and caving.The Slake Durability Index is required for the immediate overburden.

**Seam thickness**

Initially, a seam thickness of less than 1.2m would be classified as a "poor" condition. The ACARP HMI has a cut-off of 1.5m. This means that, according to ACARP, highwall mining is not possible in seams thinner than 1.5m because it would be uneconomic to mine these seams. Caterpillar offers cutter heads that can mine seams as thin as 80cm. In Appalachia, most highwall miners are equipped with these low seam cutter heads. The maximum seam height that a Cat cutter head can extract in a single pass is 3.05m. Double pass operations are rare, but it is possible to mine seams that are thicker than 3.05m with 2 passes on top of each other. The seam thickness (pillar height) also has an effect on the strength of pillars. Thicker seams lead to lower extraction ratios.

**Overburden thickness**

The overburden thickness has a great effect on vertical stresses and on the pillar stresses. With thicker overburden, the extraction ratio decreases rapidly in order to maintain a suitable factor of safety. In some countries, there is a minimum overburden thickness, but there is never a maximum overburden thickness. Highwall miners generally operate in mines with overburden thicknesses of 40–160m. In Colombia, the HW300 is operating with more than 250m of overburden.

**Methane content**

Methane is a serious hazard in underground coal mining but also in highwall mining. A methane explosion should be prevented at all times. The intake air that is caused by natural ventilation can dilute low methane contents. When this is not sufficient, an air compressor system can be used to inject additional fresh air to

dilute the methane further. Caterpillar has also designed a system that will pump inert gas into the drive. Even though the methane content is high, the oxygen content will be low, which results in a mixture that is non-explosive. In 1992, methane was not recognized as a parameter that needed to be taken into account for highwall mining because highwall mining was still in its infancy (Seib, 1992). By 2001, however, it had become apparent that methane is a serious hazard.

**Geology**

The geology is a very important factor that will make a highwall mining project a success or a failure. It is important that the location of major faults, dykes, sills, stone bands, seam splits, and undulation changes are known. Already, in 1992, it had become clear that joints, cracks, and partings play a major role in highwall mining feasibility.

**Rock Mass Rating**

The Rock Mass Rating was first described by Bieniawski (1976). It gives an indication as to how strong a rock mass is. There are 5 rock classes: (1) very good rock, (2) good rock, (3) fair rock, (4) poor rock, and (5) very poor rock. The overburden in highwall mining needs to be competent (a rock class of fair or better). The Rock Mass Rating would be a combination of other factors that have been described before (geology, rock strength) but also of factors such as joints, water inflow, etc.

A geologist or a rock mechanics engineer generally determines the Rock Mass Rating. The person entering the data may not have the RMR available. The QuickScan tool offers the option to enter whether rock is competent or not when the RMR is not available.

**Water inflow**

Most highwall mining operations extract coal seams that are dipping at a shallow angle. When water flows in from the outside or ground water penetrates through the rocks into the drives, the electric motors of the cutter head could be at risk. Obviously, this risk will be higher with down-dipping drives. The HW300 can extract coal, including water, that enters the drive at a flow rate of up to 4 liters per second. When the water inflow is more in a down-dipping drive, the cutter head should be retracted.

## HOW IS THE TECHNICAL FEASIBILITY ESTABLISHED?

The parameters that are required for the QuickScan tool are subdivided into three categories. These categories are 1) critical parameters, 2) very important parameters, and 3) important parameters. The categories are each given a weight factor. Critical parameters are weighted with a factor of 3, very important parameters with a factor of 2, and important parameters with a factor of 1.

The critical parameters are parameters that must be favorable for highwall mining to succeed. Since highwall mining is a mining method that does not use any support other than coal pillars, the mechanical properties of the rock are considered critical. The coal strength must be high, as well as the roof strength. The Cat HW300 QuickScan is a tool that separates feasible projects from non-feasible projects. It does not distinguish between non-feasible and marginally feasible. As an example, when the roof conditions are very poor but the coal is strong, the project will still be dismissed. In the future, this may be changed.

Very important parameters are ones which influence machine performance. The HW300 can mine seams as thin as 80cm, but it is more productive when the seam is thicker. Other parameters that influence machine performance are seam dip, water presence, and seam undulations. The more ideal these parameters, the better the highwall miner performs.

The remaining parameters, named important parameters, are factors that influence site efficiency and resources. Parameters, such as weathering, roof conditions, and geology, could have an effect on the efficiency of the highwall mining operation and could have an effect on the total amount of coal resources. As an example, a fault in the highwall could make part of the coal not mineable. Very high overburden could result in very wide pillars or low extraction ratios. High methane content could require additional ventilation, resulting in lower production rate. However, none of the important parameters, individually, will result in a site not being suitable for highwall mining.

When using the QuickScan tool, each parameter needs to be rated. The data sets that need to be entered are easy to understand and can be entered by someone who is familiar with mining yet does not have to be an expert in (highwall) mining, geology, and rock mechanics. Eventually, however, mining companies will need to provide additional data from someone who has expertise in highwall mining.

The parameters and the values that can be entered are shown in Table 1 and Table 2. These tables also show the index assigned to each value entered and the weight of the parameter. The total HW300 index is the weighted average of the assigned indexes.

Another important part of the QuickScan is the confidence level of the data entered. In some instances, mining companies provide data, or the data is gathered on-site during site visits. In some cases, assumptions need to be made. In addition to the HW300 index, a confidence index is proposed. The ACARP HMI requires someone to enter a percentage of confidence. The Caterpillar tool requires the person entering the data to select how the data was obtained. This is then converted into a confidence index for each parameter. The total weighted average of the confidence indices is called the combined confidence index. Table 3 and Table 4 show how this is calculated.

The HW300 index and combined confidence index are plotted in a graph without numbers. This makes the graph easier to understand. There can be four different outcomes in the tool:

1. Good site for highwall mining. Contact Product Group.
2. Possibly a good site for highwall mining. Accurate information is required. Contact Product Group.
3. Site apparently unsuitable for highwall mining. Accurate information is required.
4. Site unsuitable for highwall mining.

This graph (Figure 1) and its results are similar to the graph proposed by ACARP in 2001. In the tool, an email address is provided for instances where “Contact Product Group” is

**Table 1. Parameters to determine HW300 index, part 1.**

| Parameter | Weight (W) | Input possibilities | Index (I) |
|---|---|---|---|
| 1) Strength of immediate overburden | 3 | 0-1MPa | 0 |
| | | 1-2MPa | 0 |
| | | 2-4MPa | 5 |
| | | 4-6MPa | 20 |
| | | 6-10MPa | 40 |
| | | 10-20MPa | 75 |
| | | >20MPa | 100 |
| 2) Strength of coal | 3 | 0-2MPa | 0 |
| | | 2-4MPa | 5 |
| | | 4-8MPa | 25 |
| | | 8-12MPa | 50 |
| | | 12-20MPa | 75 |
| | | >20MPa | 100 |
| 3) Thickness of coal seam | 2 | 0-0.8m | 0 |
| | | 0.8-1.0m | 50 |
| | | 1.0-3.2m | 100 |
| | | 3.2-6.4m | 80 |
| | | >6.4m | 60 |
| 4) Seam dip | 2 | <-15˚ | 0 |
| | | from -15˚ to -12˚ | 5 |
| | | from -12˚ to -5˚ | 75 |
| | | from -5˚ to 0˚ | 100 |
| | | from 0˚ to +5˚ | 80 |
| | | >5˚ | 0 |
| 5) Water (groundwater, rain, inflow) | 2 | Dry | 100 |
| | | Water inflow < 4 liters/sec | 80 |
| | | Water inflow >4liters/sec | dependent on seam dip |
| 6) Coal seam undulations | 2 | Flat seam - no undulations | 100 |
| | | undulations <2˚/pushbeam (radius of curvature <170m) | 70 |
| | | undulations >2˚/pushbeam (radius of curvature >170m) | 0 |

recommended. Figure 1 reflects the result of an evaluation of a Colombian coal mining operation. Table 5 shows the input data for this evaluation. One of the 12 input screens is shown in Figure 2.

## NO-GO VALUES

There are various “no-go” values built in the tool. When the coal is too weak or roof conditions are very poor, the QuickScan will automatically generate a HW300 index of 0. The QuickScan will also generate a HW300 index of 0 when the seam thickness is less than 80cm. Even though thinner seams are mined, thus extracting roof rock in the process, Caterpillar intends to use the QuickScan to distinguish between good and poor mining projects rather than determining how thin seams can be mined. The QuickScan is built in such a fashion that changes in the equipment can result in different no-go values. The QuickScan will be updated annually to reflect any changes to the Cat HW300 miner.

## AVAILABILITY

The QuickScan will be made available in July of 2014, and it can be accessed through https://mining.cat.com and http://www.cat.com.

## NEXT STEPS

The QuickScan can be completed within 30 minutes, and the results of the highwall assessment are known. Once it is established

**Table 2. Parameters to determine HW300 index, part 2.**

| Parameter | Weight (W) | Input possibilities | Index (I) |
|---|---|---|---|
| 7) Overburden thickness | 1 | 0-20m | 10 |
| | | 20-50m | 100 |
| | | 50-75m | 75 |
| | | 75-100 | 50 |
| | | 100-150m | 25 |
| | | >150m | 10 |
| 8) Methane content | 1 | No methane | 100 |
| | | Little methane (<0.1m³/tonne) | 75 |
| | | Low methane content (<1m³/tonne) | 50 |
| | | High methane content (1-5m³/tonne) | 50 |
| | | Very high methane content (>5m³/tonne) | 50 |
| 9) Average highwall angle | 1 | 0˚-30˚ | 0 |
| | | 30˚-50˚ | 25 |
| | | 50˚-70˚ | 75 |
| | | >70˚ | 90 |
| 10) Geology | 1 | no faults/dykes | 100 |
| | | fauls and dykes in highwall | 10 |
| | | faults in highwall | 20 |
| | | dykes in highwall | 20 |
| | | seam rolls | 20 |
| 11) Rock Mass Rating | 1 | unknown but roof is strong | 50 |
| | | unknown but roof is weak | 1 |
| | | 0-45 | 1 |
| | | 45-55 | 50 |
| | | >55 | 100 |
| 12) Weathering (Slake Durability) | 1 | unknown but weathers easily | 10 |
| | | unknown but does not weather easily | 50 |
| | | 0%-30% | 1 |
| | | 30%-60% | 25 |
| | | 60%-85% | 50 |
| | | 86%-95% | 80 |
| | | >95% | 100 |

that the site is good for highwall mining, the person at the site will know if more data is required for further assessment.

After the QuickScan determines that a project seems feasible with an adequate confidence level, the next step is to perform a detailed highwall mining evaluation that involves a detailed assessment of the coal seam, overburden conditions, highwall conditions, and total extractable resources. With empirical calculations, numerical models, production calculations, and more, the technical feasibility can be determined. This could also be the time to check on financial details, start the required environmental impact studies, start the process to get board approval for the investment, start land leases/land acquisitions, and to establish a time schedule. Initially using the QuickScan can provide more confidence that all these efforts will pay off.

## CONCLUSIONS AND RECOMMENDATIONS

The Cat HW300 QuickScan is a tool based on the ACARP Highwall Mining Index to determine very quickly the technical feasibility of a highwall mining site. Where the ACARP HMI requires data that is beyond the technical expertise of many people outside the mining industry, the HW300 QuickScan requires easy-to-understand data to be entered. The confidence levels of the data do not need to be determined by the person entering the data. The confidence levels are determined by the program based on the information entered.

The HW300 QuickScan can be used by Cat employees, dealers, and people outside of Caterpillar to determine the technical feasibility of highwall mining with the CAT HW300.

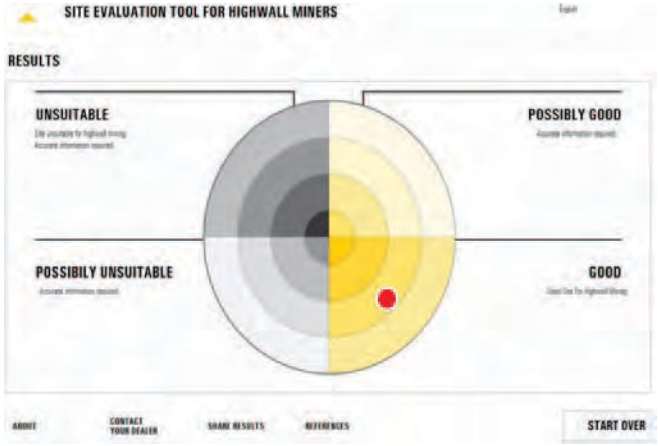



**Figure 1. Graph showing the output of the HW300 QuickScan.**

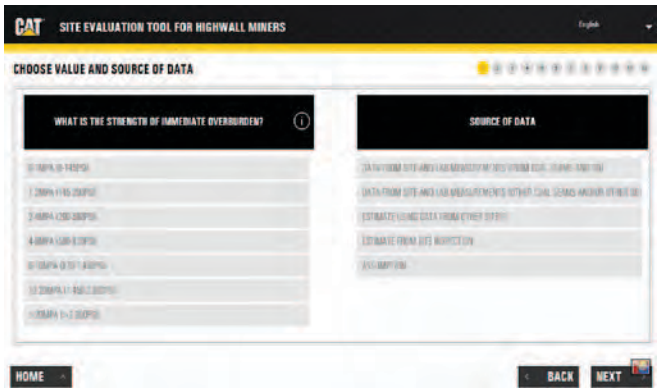



**Figure 2. Example of input screen.**


## ACKNOWLEDGEMENTS

I would like to thank my colleagues Robert Stein and Wrenn Miles for their valuable comments and remarks during the preparation of the QuickScan and this paper.


## REFERENCES


ASTM. (2014). *ASTM D4644-08: Standard Test Method of Slake Durability of Shales and Similar Weak Rocks*. http://www.astm.org/Standards/D4644.htm

Bieniawski, Z. T. (1976). "Rock mass classification in rock engineering". In: *Exploration for Rock Engineering: Proceedings of the Symposium on Exploration for Rock Engineering*. Leiden: Balkema, pp. 97–106.

Caterpillar. (2013). *HW300 Brochure*. http://xml.catmms.com/servlet/ImageServlet?imageId=C758613

Fama, M., Shen, B., and Maconochie, P. (2001). "Optimal design and monitoring for highwall mining." *ACARP Project C8033 Final Report*. http://www.acarp.com.au/abstracts.aspx?repId=C8033

Mark, C. and Chase F. E. (1997). "Analysis of retreat mining pillar stability (ARMPS)." In: *Proceedings of the New Technology or Ground Control in Retreat Mining*. Information Circular IC 9446. Washington DC: US Bureau of Mines, pp. 17–30.

Seib, W. T. (1992). "Advances in highwall mining." In: *Proceedings of the Third Large Open Pit Mining Conference*. Parkville: Australasian Institute of Mining and Metallurgy.

Sheorey, P. R. (1992). "Pillar strength considering in situ stresses." *Minetech 21* (3 and 4): 45–49.

# Ground Control in the Underground Coal Mines of Colombia

**Christopher Mark**, Mining Engineer; P.E.
Pittsburgh, PA

## ABSTRACT

Colombia is 11th largest coal producing nation in the world, and the world's fifth largest coal exporter. But while most of Colombia's coal is mined at large modern surface mines located near the Caribbean coast, there are also underground mines that produce high-grade metallurgical coal. These mines employ traditional hand-loading techniques in a variety of geologic environments, and they have some of the highest accident rates of any Colombian industry.

The National Institute for Occupational Safety and Health (NIOSH) has been collaborating with POSITIVA, the primary provider of worker's compensation insurance to the Colombian underground coal industry, to reduce the economic and social cost of rock falls in these mines. The specific goals of the collaboration are to 1) document practices and conditions in Colombian underground coal mines, 2) identify relevant international best practices, and 3) provide recommendations for developing a national campaign to reduce fatalities and injuries associated with roof falls.

NIOSH conducted a survey of seven underground coal mines in four separate coalfields. Five of the mines were characterized by steep dips and weak roof and floor rock. The coal was loaded by hand at all seven mines, though two employed partially mechanized longwall techniques. Wood posts were by far the most common ground support. Roof bolts were not observed in use at any of the mines, and they are unlikely to replace timbers any time soon.

While long-term entries generally appeared to be adequately supported, the survey found that less attention was paid to the temporary support that is installed right after the coal is removed. This temporary support is critical for protecting the workers from rock falls, however, because with hand-loading mining methods most of the activity takes place between the permanent supports and face.

The study concluded that improving the temporary support in the working faces would be the most effective way to reduce the number of rock fall injuries. The key principle should be that every worker is protected by *planned* roof support at all times. Ground Support Management Plans, consisting of specific rules about when, where, and what roof support is to be installed, should be the focus of the campaign. Each Plan should be tailored to a specific mine based on the geologic conditions and mining methods in use. The Plan provides miners with clear, simple rules that can be easily understood, while management can easily check to see if it is being followed. Ground Support Management Plans will also provide the campaign with a concrete focus for the necessary cultural change.

## BACKGROUND

Colombia produced 98.1 million short tons of coal in 2012, making it the 11th largest coal-producing nation in the world. Most of Colombia's coal is mined for the export thermal market at large, modern surface mines located near the Caribbean coast. With more than 90% of its coal going overseas, Colombia is the world's fifth largest coal exporter (EIA, 2014).

There is a second Colombian coal industry, however. Located along a 600 km belt in the Andean highlands are coalfields containing some of the highest-grade metallurgical coal in the world (figure 1). Small-scale underground mines have been operating here for decades, and they currently produce about 7 million tons per year. While the booming export trade in metallurgical coal has generated some interest from international investors (Mumford, 2011), currently only about 1 million tons of Colombian underground coal is exported annually. The rest is used domestically, either for steel production or for power generation.

The underground sector of the Colombian coal mining industry employs approximately 72,000 workers at some 2800 companies (POSITIVA, 2012). Most of the mines are very small, family-run operations. The traditional hand-loading mining methods that are employed even in larger mines are extremely labor intensive. The underground coal mines have one of the highest injury rates of any Colombian industry, with more than 100 fatal accidents each year. Statistics indicate that in Colombian underground coal mines, ground falls are responsible for more than one-quarter of the annual death toll and for thousands of injuries.

NIOSH has been collaborating with POSITIVA, the primary provider of worker's compensation insurance to the Colombian underground coal industry, to improve mineworker health and safety. The activities of this collaboration have focused in three




**Figure 1. Locations the main coal mining areas of Colombia.**

areas: capacity building (i.e. developing a body of mining safety and health professionals); diffusion of good safety and health practices (statutory, behavioral, and engineering); and the establishment of a surveillance system for detecting lung diseases in mineworkers and documenting in-mine exposures to mine dusts. These activities are aligned with the U.S. – Colombia High Level Partnership as commissioned by former Secretary of State Clinton (Clinton, 2011). This work is responsive to President Santos' request to President Obama for technical assistance to improve mine safety (White House Press Office, 2013).

Rock falls, and reducing their social and economic burden, is one focus of the collaboration. Three initial goals were defined:

1) Document practices and conditions in Colombian underground coal mines,

2) Identify relevant international best practices, and

3) Provide recommendations for developing a national campaign to reduce fatalities and injuries associated with roof falls.

To help achieve these goals, NIOSH and POSITIVA surveyed seven underground coal mines in four separate coalfields. This paper reports the geologic conditions and work practices that were observed during the survey. However, no representation is made as to whether these seven mines are "typical" of other Colombian coal mines.

## GEOLOGICAL CONDITIONS

The coalbeds in the Andean highlands are predominantly of Cretaceous age, and lie in distinct sub-basins that are oriented southwest-northeast in folds (synclines) formed during the Andean orogeny (Tewalt et al., 2006). The four coalfields that were visited during this trip were (figure 2):

- Cundinamarca (near Bogota)
- Boyaca (near Tunja)
- Norte de Santander (near Cucuta)
- Antioquia (near Medellin)




**Figure 2. Approximate locations of the four underground coalfields visited (red stars).**

Two mines were visited in each of the first three coalfields, and one was visited in Antioquia. Table 1 summarizes the characteristics of the seven mines. The following paragraphs discuss the most significant geologic factors that affect mining methods and ground control.

***Seam thickness and mining height***: By international standards, the coal seams observed in the seven mines were relatively thin, measuring between 0.8 and 1.2 m. The partial exceptions were the two mines in Norte de Santander and one in Boyaca that were extracting two seams simultaneously, together with a rock middleman. The total mining height at these mines was 1.8-2.5 m.

***Dip of the seam***: At most of the mines the coal seams were observed to be fairly steeply dipping, with dips between 20 and 60 degrees. The exceptions were the two mines in Norte de Santander, which were relatively flat lying. The dip is highly significant because mechanization is much more difficult where the dip exceeds 10 degrees or so. In the US, the steeply dipping anthracite coal beds of eastern Pennsylvania are still worked by traditional hand loading methods, even though the rest of the US coal industry was fully mechanized more than half a century ago.

***Coal seam characteristics***: The coal was generally very friable and soft. The seams were also tectonically disturbed, with many shears and angled joints. In most cases the coal is so soft that it can be mined by hand or with a pneumatic hammer. Only two mines, both in Norte de Santander, needed to use explosives. Even there, however, only the upper seam and the middleman were blasted while the lower seam was extracted by pneumatic hammer.

***Roof and floor rock competence***: The roof observed in most of the mines was weak in comparison with other coalfields around the world (Mark, 1998; Mark, 1999; Forgeron et al., 2001; Mark and Molinda, 2005). In Cundinamarca, the overburden observed in road cuts consisted of approximately 80% shale and only 20 % sandstone. Underground, the roof was thinly bedded, moisture sensitive shale, with an estimated strength of 10-20 MPa and a Coal Mine Roof Rating (CMRR; Mark and Molinda, 2005) of

**Table 1. Characteristics of the seven Colombian mines that were visited.**

| Coalfield | Mining Method | Seam Dip | Mining Height (m) | Roof Quality (CMRR) |
|---|---|---|---|---|
| **Cundinamarca** | Traditional | 55º | ~1.0 | Poor (30-35) |
| **Cundinamarca** | Traditional | 24º | 0.8-1.5 | Poor (30-35) |
| **Boyaca** | Partially Mechanized Longwall, Traditional | 35º | 1.2 | Very Poor (25-35) |
| **Boyaca** | Traditional | 55º | 1.8 | Very Poor (25-35) |
| **Norte de Santander** | Traditional | 8º | 2.3 | Good (65) |
| **Norte de Santander** | Traditional | 8º | 2.3 | Good (45-60) |
| **Antioquia** | Partially Mechanized Longwall | 20º | 1.5 | Poor (35-40) |

30-35. The floor consisted of 3 m of soft claystone. Roof cores observed in Boyaca consisted entirely of weak moisture sensitive shale, with RQDs ranging from 60 for typical roof down to 10 in tectonically affected roof (figure 3). The shale core also contained angled joints and slickensides, and even the intact sections could be broken by hand. In both cases, the CMRR was estimated to be 25-35. The roof at the mine in Antioquia was another weak shale, though some thinly laminated sandstone was also observed.



**Figure 3. Drill core from Boyaca, showing weak, moisture sensitive shale roof rock.**

The two mines in Cundinamarca were again the exceptions. Here the overburden contained thick, cliff-forming sandstone. The typical mine roof was also sandstone and siltstone, with estimated strengths of approximately 60 MPa. The roof did contain some joints and slips which required special control measures, and there were some localized area where the roof was weak shale. Overall, the CMRR for the typical roof was estimated to be 55-65.

***Mining Depth***: In six of the mines that were visited the seams outcropped at the surface, and the depths of working were less than 300 m. The seventh mine, in Antioquia, was accessed by a slope and depth of cover reached 450 m.

## MINING METHODS

Nearly all underground mines in Colombia employ traditional, non-mechanized methods. The traditional mining sequence includes:

- Coal cutting either by hand, with pneumatic hammers, or with explosives,
- Coal loading by hand,
- Haulage by cars on rails, powered by hand and/or rope hoist, and
- Roof support with timbers.

Traditional methods can be further subdivided depending on the dip of the seam.

***Steep pitch mining with traditional methods*** was observed in all four of the mines visited in Cundinamarca and Boyaca. At these operations, access to the coal was obtained with a horizontal drift that typically intersected several seams. Within the seams, slopes are driven down dip, and levels are driven off the slopes at 30-100 m intervals. Chutes are then driven 10-30 m apart to connect the levels and outline the stopes (figure 4). The stopes are extracted in a manner that takes advantage of the steep dip to move the coal by gravity to the haulage level, where it is loaded into cars.

***Flat pitch mining with traditional methods*** was observed in the two mines visited in Norte de Santander. Drift entries access the seam at the outcrop. Panels typically consist of 4 entries driven on 20-25 m centers, with crosscuts on similar centers (figure 5). The pillars are extracted on retreat, with thin barrier pillars left between panels. The coal is loaded at the face into wheelbarrows, and then moved to tracked haulage entries were it is loaded into cars.

A handful of Colombian mines are now ***partially mechanized***. The two such mines that were included in the survey (one in Boyaca and another in Antioquia) employed “longwalls” equipped with armored face conveyors (“panzers”) and conveyor belts

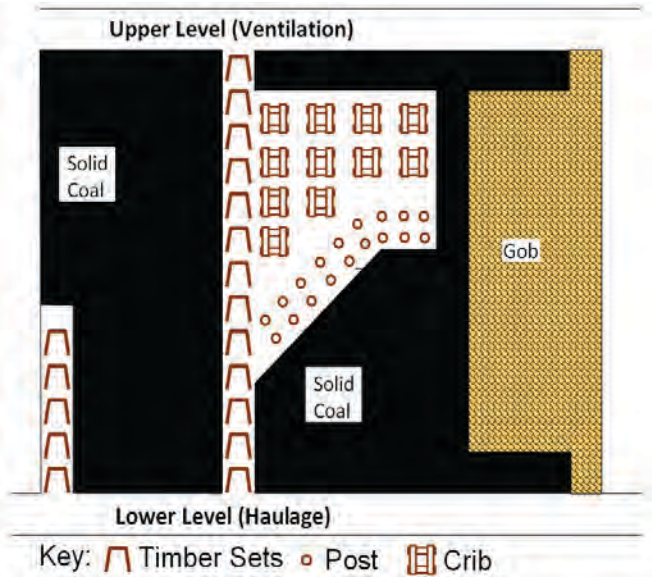



**Figure 4. Sketch showing method of steep pitch stope mining.**

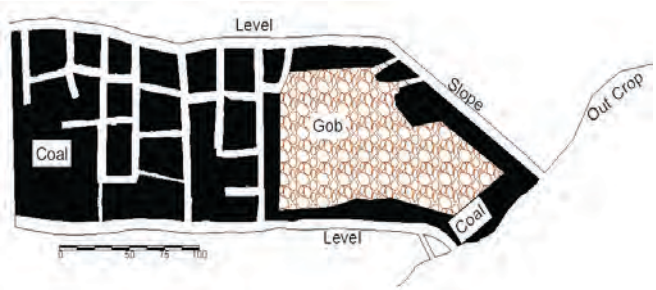



**Figure 5. Sketch showing method of flat pitch room and pillar mining.**

to move the coal out of the mine. Both mines used a kind of advancing longwall technique in relatively steeply pitching seams (12 degrees in one case, 35 degrees in the other). The longwall faces are 120-150 m wide, and are supported by steel prop supports that are advanced by hand (the supports will be discussed in more detail in the later "ground support" section). No shearer is used. Instead, the coal is won by a miner using a pneumatic pick, and then it is loaded by hand onto the panzer. No pillars are maintained between the extracted face and the headgate (lower level) and tailgate (upper level) entries (figure 6).

No mines in Colombia were yet using ***fully mechanized room and pillar mining*** techniques when the survey was conducted. However, a handful of operations were planning to install single room-and-pillar sections with continuous miners, shuttle cars, roof bolters, and conveyor belts (Mumford, 2011). At least two of these mines have been proposed for Norte de Santander, where the flat seams and competent roof are amenable to such methods. Norte de Santander also has relatively easy access to the coast, via Lake Maracaibo in Venezuela, making its metallurgical coal attractive for export.

## ROOF SUPPORT AND GROUND CONTROL ISSUES

The roof support observed in Colombian mines depended upon the excavation type, as follows:

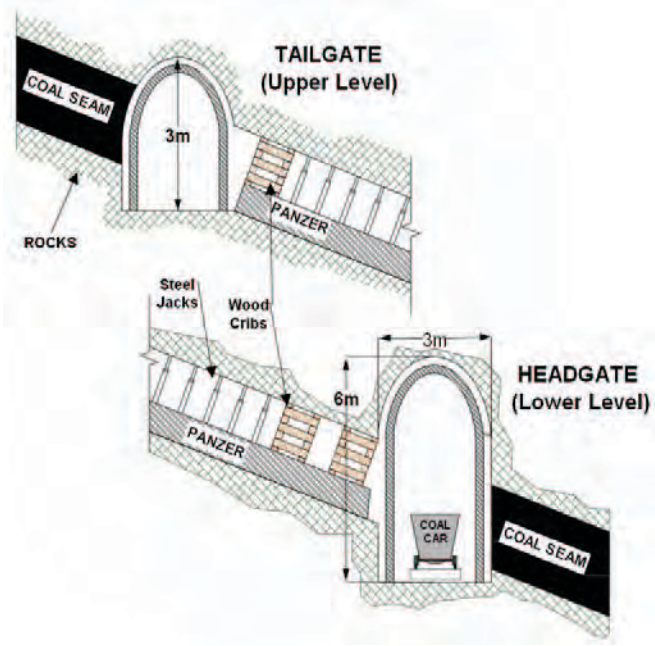



**Figure 6. Sketch showing method of steep pitch, semi-mechanized longwall mining.**

**Long-term entries*:*** Long-term entries include the main access drifts, slopes and levels. In mines that employ traditional mining methods, these entries are typically just 1.5-3 m wide at the top, 2.5-3.5 m wide at the bottom, and about 2.5 m high. These narrow spans are a great asset in weak ground, because they improve stability and limit the potential rock load that the supports must carry.

The most common support observed in long term entries is the "puerta allemana", which translates literally as "German door", a three-piece timber set. The ends of the timbers are cut where they meet to make a stronger joint (figure 7). In weak ground, lagging with wood boards provides full surface control. In stronger ground no lagging is used.

Steel arches were used in the partially mechanized mines and even in some mines that are considering mechanization. One reason for this is that slope entries with conveyor belts must maintain wider spans than the traditional track headings. Another is that some of the woods used for support, particularly the tropical species, degrade over time and must be replaced periodically.

In general, the long-term entries that were observed seemed to be adequately supported. Lagging was generally adequate, and it seemed that failing supports were generally replaced as necessary. Soft floor was a major problem for long term entries in many of the mines that were visited. The supports punched into the soft floor, and heaving reduced the working height. Several mines were in the process of rehabilitating large sections of their main headings due to floor failure.

**Stopes and pillar workings:** The long-term entries constitute a relatively small proportion of the overall mine workings. Most of the worker's time is spent mining in the production stopes and



**Figure 7. A long-term access entry in Cundinamarca, showing three-piece wood sets (puerta allemana) in the foreground, and yielding steel arches in the background.**

pillars. Therefore the greatest exposure to rock falls occurs there as well. Support in the stopes and pillar workings are of three types:

- ***"Permanent" support*** is installed in the short-term access and haulage entries that lead into the production workings. These supports are either wood posts with header boards, or three-piece wood sets. Lagging may be installed in poor ground. In mines that use explosives, the permanent supports are installed after the face has advanced far enough that the supports will not be affected by blasting (typically 3-5 m). No permanent supports are installed during retreat mining operations.
- ***"Temporary" support*** is installed right at the face, immediately after the coal is removed on either advance or retreat (see figure 4). Its function is to protect the workers while they load the coal and prepare the face for the next cut. Temporary support almost always consists of wood posts with caps (figure 8), with wood boards used for surface control in weaker ground.
- ***Gob support*** is set in the worked out stopes to prevent a sudden, massive roof collapse that might extend into the face area. Wooden cribs are the support of choice for this application (figure 9).

Of these three, the temporary support is the most critical for protecting the workers from rock falls, because with traditional mining methods most of the activity takes place between the permanent supports and face. Since the temporary supports are only needed for a short period of time, however, the workers have a strong temptation to skimp on them. In the mines with weak roof, it seemed that the temporary posts were mostly in place, but the lagging that protects workers from loose rock between the posts was not always installed. In the Norte de Santander mines with more competent roof, temporary posts were installed only where obvious slips were present in the roof.

**Support in longwall workings:** The roof support observed in the two longwall faces is very similar to that used in the earliest trials of mechanized longwall mining in the US, approximately 60 years ago. The face is supported by steel jacks, each with



**Figure 8. Temporary supports, consisting of wood posts with caps, installed in a development face in Norte de Santander.**



**Figure 9. Wood cribs installed in a retreat mine in Norte de Santander.**

approximately 40 tonne capacity. Each jack is capped with a length of steel beam approximately 1.0 m long. Four jacks are connected together to create a single support (figure 10), and these supports are spaced approximately 1.0 m apart along the face. As the face advances, the jacks are leapfrogged two at a time on each support. Because there are no steel canopies, wooden boards span the distance between the supports providing surface control. At the longwall in Antioquia, wood cribs are built between the supports and left to support the gob just as in pillar recovery. Additional steel jacks provide temporary support at the locations where the coal is being mined and loaded.

In the advancing longwall in Boyaca, yielding steel arches supported the headgate and tailgate. These entries typically converged 1 m or more behind the face. One or two rows of cribs were installed as a "packwall" to isolate the entries from the gob (figure 6). The tailgate seemed to be the Achilles heel at this mine. In some places the original mined height of 3 m had been reduced



**Figure 10. Longwall face supports installed on a face in Antioquia. Note the panzer in the center of the photo, and the cribs installed in the gob at left.**

to less than 1 m by roof convergence and floor heave, and laborious hand dinting of the floor was necessary. At the longwall mine in Antioquia, the tailgate corner was reportedly the location of two serious roof fall accidents.

It should be noted that the support density of the longwall face supports at the Colombian longwalls is approximately one-third of the support density in modern longwall faces. Fortunately, the weak roof rock caves very quickly behind the face, and is unlikely to generate the "periodic weightings" that were once common in US longwalls, particularly in coalfields with strong roof.

**Roof bolts** were not observed in use at any of the mines visited on this trip. Though bolts are an integral part of modern fully mechanized mining, they are unlikely to play much role in Colombia outside of Norte de Santander anytime soon. Steeply dipping seams, poor roof, and the small size of the potential market are all factors that will limit the application of roof bolting technology. Highly productive roof bolting machines cannot be used in steeply dipping seams, meaning that roof bolts would need to be installed by hand. Fully grouted resin bolts might work in the very weak roof, but resin has a finite shelf life and would likely be very expensive in small batches. Mechanical-shell point-anchor bolts would be much easier to use, but they are effective only in relatively strong roof that is not moisture sensitive.

Roof bolting might not be such a boon to Colombian underground miners in any case. When hand-held drills are used, temporary support is necessary to protect the operators. The use of roof bolts might also introduce significant health hazards because of the poor ventilation and the difficulty of capturing the dust generated by hand-held drills. In any case, timber supports are well suited to non-mechanized mining of steeply dipping thin seams, and are the main type of support used to this day in US anthracite mines.

## A UNIFIED PREVENTION STRATEGY FOR ROCK FALL INJURIES IN COLOMBIAN COAL MINES

In general, "inadequate" mining technology is not a fundamental cause of rock falls. Appropriate support systems and work practices can be developed for nearly any ground conditions or mining method. When roof fall injuries occur, they can generally be attributed to failures of mining engineering, mine planning, mining practice, and management/cultural factors.

Mine management, and mining regulations, is usually most concerned with the ***permanent support*** for long-term access tunnels. But most worker exposure occurs in the ***active face area***, between the permanent support and the coal face. In this area, the workers are protected by ***temporary support.*** Since it is only "temporary," it seldom receives the attention it deserves. Often, decisions about what temporary support to install, and where and when to install it, are left up to the face crew. When the eventual result is a fatality or a serious injury, the blame is generally placed on the workers themselves for their poor judgment, lack of training, or inadequate effort. But when a system fails over and over again, a more fundamental solution needs to be found.

Over time, modern ground control practice has come to rely on one key principle: *Every worker should be protected by planned roof support at all times*. In mining industries around the world, this is accomplished through the use of "Ground Support Management Plans." The concept of the Ground Support Management Plan (or "Roof Control Plan") was first formulated by mine safety specialists in the US in the 1920's (see Appendix), and it has been mandated for all US underground coal mines since 1969. Today the Plan is the basis of ground control practice in Australia, South Africa, the UK, and elsewhere. In essence, it is the application of modern risk management concepts to the problem of rock falls.

The Ground Support Management Plan consists of specific rules about ***when, where, and what*** roof support is to be installed at every ***stage of the mining process.*** It typically addresses:

- Spacings between supports,
- Allowable distances between the supports and the coal face,
- Types of support (posts, cribs, steel arches, etc; together with associated planks, caps, cross bars etc.)

The Ground Support Management Plan is tailored to each specific mine, based on the geologic conditions and mining methods in use. The rules should be flexible to account for changes in geologic conditions, and may even be specific to each working area within a mine. While the Plan defines the ***minimum*** support that must always be installed, additional support can always be added if necessary.

The Ground Support Management Plan provides a solid foundation for every aspect of roof control at the mine:

- It provides the ***miners*** with clear, simple rules that can be easily understood, and it can be posted in all working places.
- ***Management*** can easily check to see if it is being followed.
- ***Technical staff*** can focus their geologic evaluations and engineering design on optimizing the Plan.
- ***OS&H professionals*** can use it as a focus for worker training.

Implementing a Plan typically has little impact on costs or productivity, and in fact should save money by reducing the costs associated with rock fall injuries. It can also lead to technological improvements in the form of better use of support.

Ground Support Management Plans have been highly successful when law has mandated them. In the US, for example, nationwide roof fall fatality rates dropped by *two-thirds* in just six years after the 1969 Mining Health and Safety Act required Plans. Even where they are not mandated, however, progressive mining companies can reap substantial benefits by implementing them on their own.

To be successful the Plan needs buy-in from everyone involved. In particular, top management needs to clearly demonstrate its support. Like other risk management programs, a Ground Control Management Plan will be most successful if it is by a team that includes upper management, line supervision, technical staff, OS&H professionals, and workers. Such a team can best address the typical objections that include:

- The workers do not want to do unnecessary work where the roof is "stable." (Answer: Mine roof is treacherous, and a visual inspection cannot adequately determine which roof is stable and which is not).
- Managers can't be everywhere at once ensuring that support is installed. (Answer: Once support installation according the Plan becomes habitual, little management is required).
- Productivity will fall because too much time is spent on needless support. (Answer: The time required to properly install temporary supports is only slightly more than the time needed to do a partial and imperfect job).
- Costs will rise because more wood is wasted. (Answer: Most temporary supports can be re-used once permanent supports are set.)
- Rock falls are unpredictable no matter what support is installed. (This is not true. In fact, it is precisely *because* rock falls are unpredictable that systematic support is necessary!)

Auditing to ensure that the Plan is being followed should be done on a regular basis. If a rock fall accident occurs, an investigation is essential to ensure that the Plan is adequate. If an injury occurs where the investigation reveals that the Plan was being followed, then the Plan needs to be modified. On the other hand, if the Plan was not being followed, then the implementation was inadequate. Either way adjustments should be made.

In summary, a prevention strategy centered around Ground Support Management Plans has proven to be the most successful way to reduce rock fall injury rates. The strategy's two key principles are:

1. Every mine should have a Ground Support Management Plan that is appropriate for its geologic conditions and for the mining methods in use.
2. No one should ever work or travel in an area that is not supported according to the Plan.

These principles can be easily understood by everyone involved, and are applicable to any mining technology and support technique. The strategy also provides a concrete focus for the necessary cultural change.

## REFERENCE


Clinton, H. (2011). Clinton's remarks us-colombia high level partnership dialogue. Council on Foreign Relations press release. http://www.cfr.org/colombia/clintons-remarks-us-colombia-high-level-partnership-dialogue-may-2011/p25185

EIA (2014). Country Analysis: Colombia. http://www.eia.gov/countries/cab.cfm?fips=CO

Forgeron, S, Mark C, Forrester DJ [2001]. Standardization of geological and geomechanical assessment at underground coal mines in Canada. CIM Bulletin,vol 94, no. 1052, pp. 83-90.

Mark C [1998]. Comparison of Ground Conditions and Ground Control Practices in the United States and Australia. Paper in Proc. 17th International Conference on Ground Control, pp. 63-71.

Mark C [1999]. Ground Control in South African Coal Mines--A U.S. Perspective. Paper in the Proceedings of the 18th International Conference on Ground Control in Mining, Morgantown, WV, pp. 186-193.

Mark, C [2002]. The Introduction of Roof Bolting to US Underground Coal Mines (1948-1960): A Cautionary Tale. Proc. 21st Intl. Conf on Ground Control in Mining, Morgantown, WV, pp. 150-160.

Mark C, Molinda GM [2005]. The Coal Mine Roof Rating (CMRR)—A Decade of Experience. *Int. J. of Coal Geology,* Vol 64/1-2, pp. 85-103.

Mumford, Chris (2011). The Great Colombian Met Coal Rush. The Resource Investor. http://www.resourceinvestor.com/2011/09/26/the-great-colombian-met-coal-rush

POSITIVA (2012). Personal communication.

Tewalt, S. J.; Finkelman, R. B.; Torres, I. E.; and Simoni, F. (2006). "World Coal Quality Inventory: Colombia". In Alex W. Karlsen, Susan J. Tewalt, Linda J. Bragg, and Robert B. Finkelman (eds.). *World Coal Quality Inventory: South America*. U.S. Geological Survey Open File Report 2006. United States Geological Survey. pp. 132–157. http://pubs.usgs.gov/of/2006/1241/.

White House Press Office (2013). Fact Sheet: The United States and Colombia: A strategic partnership. http://www.whitehouse.gov/the-press-office/2013/12/03/fact-sheet-united-states-and-colombia-strategic-partners


## APPENDIX: THE HISTORY OF ROOF CONTROL PLANS IN US UNDERGROUND COAL MINES[1]

Throughout the 20th century, falls of roof were the greatest single safety hazard in US underground coal mines. In fact, roof falls were responsible for between one-third and one-half of mining fatalities in each decade.

1 The source for this Appendix is *Mark, C [2002]. The Introduction of Roof Bolting to US Underground Coal Mines (1948-1960): A Cautionary Tale. Proc. 21st Intl. Conf on Ground Control in Mining, Morgantown, WV, pp. 150-160.*

During the hand-loading era, which had largely ended by the 1950's, miners often had considerable discretion about the amount of support they installed. In weak shale roof, posts might be set 2.5 to 5 ft apart,[1] but where the roof rock was strong, no posts might be set at all. An important element in early roof support systems were "safety posts," which were set at the end of the track to protect miners while they loaded the coal or prepared the face for the next shot.[2] These temporary supports required extra time and effort, and their use was often at the discretion of the miner.

Under these circumstances, it is understandable that much of the blame for roof fall accidents was placed on the inexperience and carelessness of the miners themselves.[3] In 1912, the US Bureau of Mines (Bureau) asked: "How can you, the miner, escape harm from roof falls?" The answer was: "Be careful; do not take the risk of loading a car before putting up a prop set extra posts, even though they are in your way."[4]

Over time, however, safety professionals began to recognize that "a condition responsible for many fatalities from falls of roof is the absence of any policy on the part of management with respect to systematic methods of roof inspection and support."[5] Encouraging mine managers to prepare, promulgate, and enforce a *systematic timbering plan* became a key element in the Bureau's roof control efforts. Violations of the timbering plan would include:

- Timber too far from the face;
- Working under loose roof or loose roof not taken down;
- Props insecurely set;
- Spacing between posts too great, and;
- Safety post not set up.[6]

A 1951 study found that 74% of roof fall fatalities occurred within 25 ft of the working face, and that 3 out of 4 of these took place inby the last permanent support (between the last permanent support and the face).[7] The same study concluded that:

"These facts very definitely indicate management failure in providing sufficient roof support at working faces...Regardless of roof conditions, minimum standards of roof support suited to the conditions and mining system of each mine should be adopted and followed…The judgment of the person should never be substituted for the minimum support required in the systematic roof support plan." [8]

A major technological change took place after 1948, when roof bolts rapidly began to replace timber supports. Mine safety specialists expected a rapid decrease in the roof fall fatality rates, but it did not materialize. The explanation was that while the type of support had changed, the old methods of using them remained. Many mines still did not have systematic roof support plans or did not enforce compliance with the plans. At these mines, the use of safety posts was still optional, and miners were not always prevented from going inby supports.

Change finally arrived with the Federal Coal Mine Health and Safety Act of 1969. The Act required systematic roof support plans at every mine, with strict guidelines regarding support spacing, roof bolt length, entry width, and other ground control parameters. Working under unsupported roof without safety posts was banned. The results were quick and dramatic. By the mid 1970's, roof fall fatality rates had plummeted by two-thirds, and they maintained that level for the next decade (see figure 11).




**Figure 11. Roof fall fatality rates in US underground coal mines, 1900-2000.**

**Endnotes**

1 Paul JW, Calverly JG, and Sibray DL[1930]. Timbering Regulations in Certain Coal Mines of Pennsylvania, West Virginia, and Ohio. USBM Technical Paper 485, 40 pp.

2 Paul et al [1930]. Ibid, p. 3.

3 Dix K [1977]. Work Relations in Hand-Loading Era, 1880-1930. WVU Press, 126 pp.

4 Rice GS [1912]. Accidents from Falls of Roof and Coal. USBM Miner's Circular 9, 1912, 15 pp.

5 Paul JW[1927]. Stop, Look, and Listen! The Roof is Going to Fall. USBM IC 6032, 1927.

6 Paul JW[1930]. What the Mine Foreman Can Do to Prevent Injury from Falls of Roof in Coal Mines. USBM IC 6344, 1930, 7 pp.

7 Forbes JJ, Back TL, and Weaver HF [1951]. Falls of Roof: The No. 1 Killer in Bituminous Coal Mines. USBM IC 7605, pp. 1-3.

8 Ibid, p. 3 and p. 9.

# Strata Control Investigations During Fully Mechanized Coal Pillar Extraction in Indian Coalfields

**Rajendra Singh**, Scientist
**Sahendra Ram**, Technical Officer
**Amit Kr. Singh**, Technical Officer
**Rakesh Kumar**, Scientist
**Arun Kr. Singh**, Scientist
Thick Seam Mining and Strata Mechanics
CSIR-CIMFR, Dhanbad, India

## ABSTRACT

Considering the importance of a fully mechanized depillaring operation, the Indian coal mining industry has introduced a number of such depillaring operations at depths of cover ranging from 60 m to 377 m. The overlying strata of these depillaring faces vary widely from highly laminated, weak and easily caveable to massive, strong and difficult to cave. Most of these mechanized depillaring operations were carried out in difficult site conditions, however, performance monitoring in the field has showed good production, productivity and safety results. Field studies have shown that the use of roof bolts as breaker line support for this technology worked well for moderate strength overlying roof strata, but experienced difficulties for both extremely weak and strong/massive overlying roof strata. It is observed that the performance of a breaker line support along the goaf edge deteriorated with an increase in depth of cover of the depillaring face. Practice of a straight line of extraction (single row of pillars) during the mechanized depillaring below competent roof strata experienced a considerably large hanging area inside the goaf, which needs to be managed either by induced caving of the roof strata or through an increase in width of the excavation. Observations of good performance of a fully mechanized depillaring face under highly laminated and weak strata at a shallow cover is mainly due to a faster rate of extraction. However, the mechanized depillaring underneath laminated and weak roof strata for a deep-seated coal seam was forced to go for partial extraction mainly due to strata control problems. Discussing the implications of main technical and operational differences between the conventional (semi-mechanized) and fully mechanized depillaring, this paper presents results of different strata control studies conducted at different mechanized depillaring sites with varying geo-mining conditions.

## INTRODUCTION

India experienced a coal production shortfall of nearly 150 million tonnes (MT) in the final year of the 11th Five-Year Plan (2007-12). It is estimated by the Planning Commission of India that the country's coal demand is likely to go up to 1,000 MT by the end of the 12th Plan period (2012-2017) to meet the primary energy consumptions in the country. It is also estimated that our domestic output is unlikely to exceed 750 MT by the end of the 12th Plan period. Therefore, our coal deficit may widen by more than 200 MT by end of 12th Plan period. The Indian coal mining industry is attempting to reduce this deficit mainly through mechanization of the industry. Coal production by opencast mining is, more or less, successful in the mechanization, but the underground mining in the country is struggling to achieve the required level of mechanization mainly due to the existence of difficult geo-mining conditions.

The presence of large numbers of developed coal seams by the bord and pillar (room and pillar) method (Dixit & Mishra, 2010) attracts the attention of the coal mining industry. These coal seams of Indian coalfield are stranding on pillars due to different techno-economical reasons. Extraction of these pillars (depillaring) is a priority for coal production, as they are blocking mining activity in underlying coal seams. Most of the ongoing depillaring operations in these seams are semi-mechanized, where the mining industry has gained considerable experiences of operation and strata control issues. However, the industry finds this depillaring approach difficult for further improvement in production, productivity and safety. Semi-mechanized depillaring also experiences a slow rate of extraction, which becomes a source for adverse strata condition during the pillar extraction. A fully mechanized depillaring is providing faster rate of extraction, which may improve safety along with production and productivity of the depillaring faces. Therefore, the Indian coal mining industry has introduced a number of fully mechanized depillaring faces over the last 10 years. This approach of depillaring has many operational and technological differences with the conventional one. Therefore, in absence of experience of this approach, some of the mechanized depillaring operations in the country encountered strata control problems during their applications for pillar extraction underneath difficult roof strata. CSIR-CIMFR is associated with most of the mechanized depillaring operations in the country and has conducted different investigations in the field. On the basis of strata control investigations at different mechanized depillaring operations, this paper provides some results of the interaction of depillaring with local site conditions.

## MECHANIZED DEPILLARING SCENARIO

A fully mechanized depillaring operation in an Indian coalfield was first introduced in February 2003 (Leeming, 2003). Since then, at least six different coal mines have used this approach

for fast underground pillar extraction (Table 1). Depth of cover at these depillaring sites varies from 60 m to 377 m. The nature of the overlying strata of these panels varied from the easily caveable and laminated roof of the Pinoura Mine to the massive and strong overlying roof strata of the VK7 Mine. Out of these six fully mechanized depillaring practices, the three successful ones at the Anjan Hill, Jhanjra and Pinoura mines do not have deep cover (< 200 m). While depillaring at Tandsi was practiced at a depth of cover nearly 260 m, it achieved intermediate results. The deepest practiced mechanized depillaring panel in the county is at the CMP-1of VK7 Mine, at 377 m of cover. This depillaring encountered a fall of strong roof block of around 6 m in thickness before a main roof fall occurrence, which damaged the machine and adversely affected the pace of mechanization for pillar extraction. The actual cause of the problem is still being investigated, and finding a conclusion has proved to be difficult. However, as per core analysis results, a good understanding of the nature of the overlying strata might have guided the approach to a better pattern of pillar extraction, and the chance of failure might have been arrested. The sixth mechanized depillaring face is successfully being practiced at the GDK 11 Incline Mine at around 310 m of cover. Again here, the application of available knowledge of site conditions helped in the successful completion of mechanized depillaring operation in a number of panels.

an Indian coalfield generally keeps standing on pillars for years for different reasons. CMR provides relatively larger size coal pillars during development, and the shapes of these pillars are generally square or rectangular. Therefore, all applications, except Pinoura, adopted splitting of pillars mainly to adjust/optimize the operational capability of the continuous miner (CM) for larger size pillars.

Attempts are made to keep goaf velocity (pace of extraction) of a depillaring face, relatively, faster because the slow goaf velocity may initiate strata control problems at the goaf edge. Splitting of a larger size pillar and bolting of the roof strata over the splitted gallery consumes time, which causes some stagnancy of the face advance. Therefore, the splitting caused some retardation in goaf velocity but, more or less, the splitting provided an opportunity for the cutting machine (CM) to cover the width of a resulted fender (splitted part of the pillar) for slicing. The operational cycle of a CM, generally, keeps one pillar splitted ahead of the pillar under extraction. However, sometimes the one pillar ahead splitting practice is ignored when a large overhang of roof strata is noticed inside goaf during depillaring below strong and massive roof strata. Another frequently encountered problem arises due to existing pillars of square or rectangular shapes. Here, splitting and slicing by CM generally leaves a snook/rib of irregular shape (Figure 1). It becomes difficult to assess the efficacy of such a snook/rib because formulations for pillar strength are available for regular-shaped snooks/ribs only. Formation of a rhomboid shape of pillars would yield a regular-shaped snook/rib, resulting in better natural resistance for strata control.

**Table 1. Details of different mechanized depillaring faces in India.**

| Name of mine | Geo-mining parameters of different mechanized depillaring faces | | | | | | |
|---|---|---|---|---|---|---|---|
| | Depth cover | Pillar size (corner to corner) | Bord width | Working height | Overlying strata | Manner of extraction | Perform-ance |
| Pinoura | 60 | 18.5 x 19.5 | 6.5 | 3.0 | Easy to moderate | Single pass | Success |
| Anjan Hill | 85 | 28.2 x 28.2 | 6.6 | 4.5 | Moderate to difficult | Splitting & slicing | Success |
| Jhanjra | 125 | 26.0 x 26.0 | 6.0 | 4.2 | Moderate to difficult | Splitting & slicing | Delayed caving |
| VK7 | 377 | 40.0 x 40.0 | 5.0 | 4.6 | Extremely difficult | Splitting & slicing | Roof collapse |
| Tandsi | 260 | 40.0 x 40.0 | 5.0 | 3.0 | Unstable roof strata | Splitting & slicing | Partial extraction |
| GDK 11 | 325 | 48 .0 x 46.0 | 6.0 | 4.6 - 6.0 | Difficult | Splitting & slicing | Success |

## IMPORTANT PARAMETERS

On the basis of field experiences at different mechanized depillaring faces, site conditions of a coal mine are said to be difficult if it owns a coal seam, standing on pillars, at deep cover (Singh et al., 2011). Even at a shallow cover, if the overlying strata of a developed coal seam are either strong and massive or laminated and fragile, then the condition of the mine is said to be difficult. The behavior of overlying strata, depth of cover, manner of extraction and strata control observations are important factors for a mechanized depillaring operation.

### Pillar formation

Coal Mines Regulations (CMR) of India is known to provide stable pillars during and after development of a coal seam by the bord and pillar method (Table 2). A developed coal seam in

### Behavior of overlying strata

Most Indian coalfields encounter difficult overlying strata during underground mining. Here, both highly laminated/weak and massive/strong overlying strata are termed as difficult. The caveability index (I) is one of the established approaches for the assessment of the overlying strata (Sarkar, 1985), which is defined as:

$$I = \frac{\sigma l^{n} T^{0.5}}{5} \quad (1)$$

Where: s = Uniaxial compressive strength in kg/cm$^2$;

l = Average length of core in cm;

T = Thickness of the strong bed (in m), and the factor *n* has a value of 1.2 in the case of uniformly massive rocks with a weighted average of RQD of 80% and above. In all other cases, n = 1.

**Table 2. Pillar size variation, as per regulation 99 of Coal Mines Regulations (after CMR, 1957).**

| Depth cover, m | Pillar size (centre to centre) for different roadway widths (B), m | | | |
|---|---|---|---|---|
| | B=3.0 | B=3.6 | B=4.2 | B=4.8 |
| < 60 | 12 | 15 | 18 | 19.5 |
| 60 to 90 | 13.5 | 16.5 | 19.5 | 21 |
| 90 to 150 | 16.5 | 19.5 | 22.5 | 24.5 |
| 150 to 240 | 22.5 | 25.5 | 30.5 | 34.5 |
| 240 to 360 | 28.5 | 34.5 | 39.5 | 45 |
| > 360 | 39.5 | 42 | 45 | 48 |

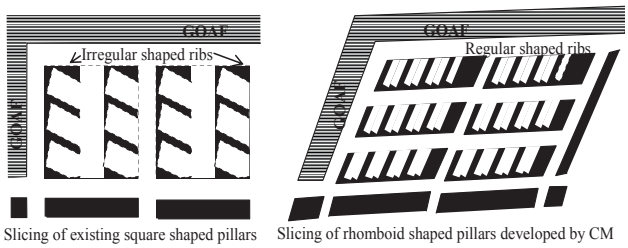



**Figure 1. Change in shape of ribs during depillaring of square/ rectangular and rhomboid pillars.**

An assessment of the caveability index is performed to understand the nature of overlying strata through examination and testing of core samples. The observed caveability index spectrum of all the mechanized depillaring sites of the country is shown in Figure 2.

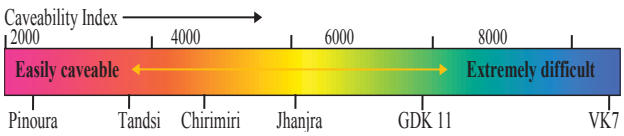



**Figure 2. Caveability Index of different mechanized depillaring faces in India.**

Depillaring at the Pinoura and Tandsi mines experienced excessive caving of the roof strata as the stand-up time of roof strata over the slices was found to be around only couple of hours. In fact, a relatively silent and fast rate of coal extraction (unlike the conventional drilling and blasting) by the CM proved to be an advantage for the mechanized system to be used at these sites. Presence of geological structures, like slips/joints in the roof strata, created some unexpected roof instability in the slices and even burial of the CM. It is worth noting here that burial of the CM during mining, below incompetent overlying roof strata, was found difficult to avoid. The CM worked mainly below freshly exposed areas where geological uncertainties always existed, and are difficult to be correctly anticipated in advance. A number of burials have been witnessed while working below incompetent roof strata, but generally the machines were recovered without any considerable damage. Different instruments, installed around the working to monitor stress change and strata movement, hardly picked up the initiation of such falls; however, here the blocks of fallen rock remained small in size. Therefore, most of the encountered damages to the CM, noticed after its recovery from the rock piles, were found to not be serious. One of the most severe burials from a fall of incompetent roof strata and recovery is mentioned below.

Working in the CM 1B panel at the Pinoura Mine, crews experienced a burial of the CM under the fallen roof material due to exposure of a hidden slip while extraction of a second push-out of pillar No. 49 was in progress (Figure 3). No significant strata movement observations were made through the Auto Warning Telltales (AWTTs), stress meters, telltales and instrumented bolts prior to this incident. The instruments installed near the incident area did not record any significant strata movement, even during recovery of the CM. Consecutive roof falls at close intervals were noticed over the trapped CM. These roof falls extended up to around 20 m height at the roof. The CM was recovered by making a tunnel under the fallen material with fore poling and an arch support system. It was interesting to note that the adjacent remnant of the second push-out is intact (Figure 3). This revealed that the fall was due to the hidden slip only, and there was no issue of any global instability. It was also observed that the severity of the hidden slip was more in the slice, where the machine encountered the roof fall. No significant induced stress was observed in the stook of pillar No. 57 during the total burial and recovery period.

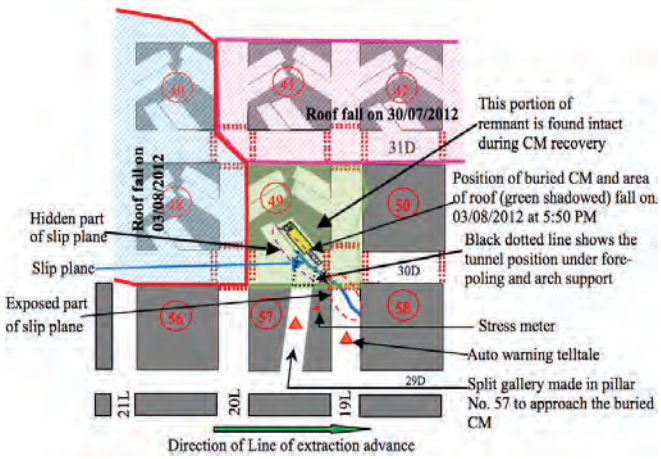



**Figure 3. Part plan showing the roof fall on a continuous miner at the Pinoura Mine.**

Contrary to the above mentioned observations, the CM received considerably severe damage due to a fall of a strong overlying stratum of around 5 to 6 m in thickness. Two such falls, each with about 6-m-thick strong sandstone roof stratum, took place over the

CM at the VK 7 Mine. Although both of these falls were local in nature, the first fall inflicted damage beyond repair for the CM. The second fall over the CM, of nearly the same thickness of strong sandstone roof stratum, also damaged the CM severely, but it was repaired after the replacement of many major components of the machine.

It was observed that the major fall of strong roof strata created dynamic loading over pillars/fenders facing the goaf line. Here, the menace of dynamic loading could successfully be encountered through the management of the natural support. Dilution of any pillar in and around the extraction line, other than the pillar under extraction, is avoided in presence of a goaf overhang. Here continuous monitoring (in time) of mining-induced stress with the help of a vibrating wire stress meter was found to be useful for both design and safety. Field investigations through underground instrumentation and monitoring showed distinct amounts of stress redistribution for depillaring underneath shallow and deep covers. At shallow depth of cover, an overhang of roof strata inside goaf induced stress over pillars. However, a sharp drop in the induced stress over pillars is observed with caving of the overhang inside the goaf. This keeps happening periodically and quite prominently with the face advance during depillaring at shallow depth of cover. Such observed prominence of a periodic loading during depillaring at shallow cover gets weakened during the depillaring of a deep-seated coal seam. In fact, generally after the first major fall, a depillaring of a deep-seated coal seam received almost continuous loading and spalling of pillars/stooks around the extraction line (Figure 4).

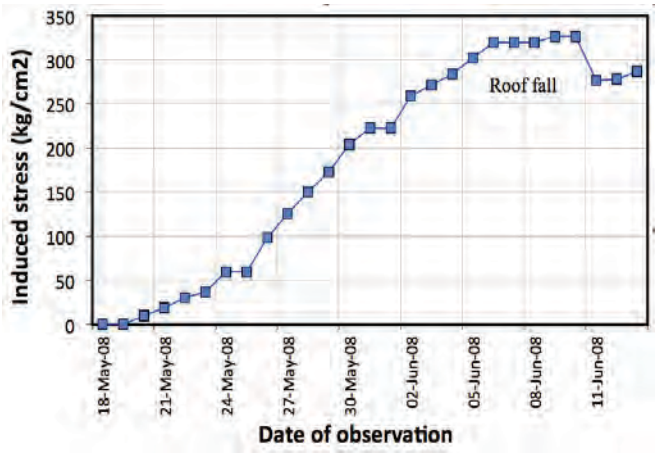



**Figure 4. Nature of mining-induced stress development after main fall at the VK 7 Mine.**

### Influence of Roof Strata on Supports

One of the most important achievements of using a CM-based mechanized depillaring method is the application of resin grouted, pre-tensioned, stiff and high capacity roof bolts as breaker-line supports, along with the systematic support of roof (SSR) for wider galleries (6.5 m) (Figure 5). In fact, the country's coal mining industry first experienced the application of roof bolts along goaf edges during CM-based mechanized depillaring only. Strata control studies by CSIR-CIMFR (Singh et al., 2004) demonstrated that the adopted SSR and breaker-line support could effectively arrest strata movement during different stages of depillaring. Instrumented bolts are used to optimize the design of breaker-line support through a study of load distribution along the bolts installed along the breaker-line. This study suggested that a breaker line of only two rows of bolts between the slices is sufficient for the conditions of the Anjan Hill Mine. Nearly 800 breaker lines were erected in a panel during work. Of this number, only a few (less than ten) breaker lines did not work effectively in a panel at the Anjan Hill Mine. They experienced two main types of failures: (a) due to presence of a slip plane along the row of the bolts, and (b) due to incorrect alignment with the neighboring stooks/ribs.

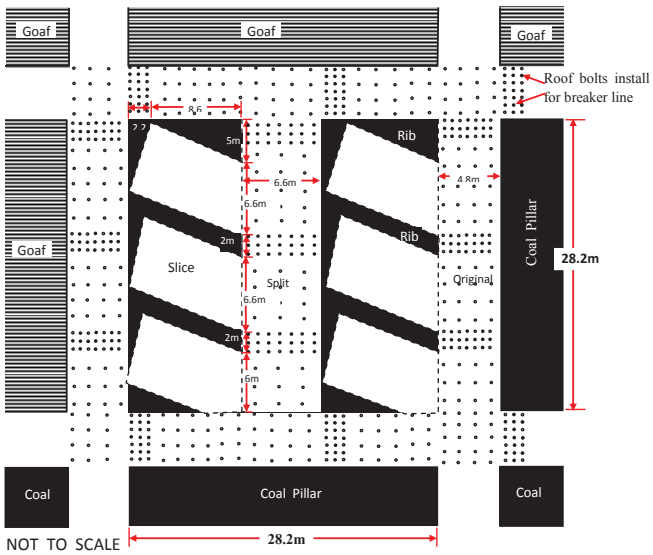



**Figure 5. Support details during depillaring by continuous miner (CM) at the Anjan Hill Mine.**

Field studies showed that the use of roof bolts as a breaker-line support for CM technology worked well for moderate overlying roof strata, but experienced difficulties for both extremely weak and strong/massive overlying strata. It was observed that the performance of a breaker-line support at the goaf edge deteriorated with an increase in depth of cover of the depillaring face. A study in a panel at GDK 11 Inline Mine (at 325 m of depth) showed nearly ten times more casualties of the breaker line (Figure 6) in comparison to those in a panel (at 85 m depth) at the Anjan Hill Mine. Spalling and partial crushing of pillars/stooks/ribs were observed to be the main cause for the high amounts of breaker-line casualty. Again, a field study at the Pinoura Mine did not show any significant load development along the roof bolts of the breaker-line support, and there was no case of goaf encroachment. Some local roof falls were observed ahead of the goaf line at the Pinoura Mine. These falls are mainly due to presence of the fractured roof strata due to geological disturbances, and not due to goaf influence. Observations of stress meters did not indicate any significant value of mining-induced stress over pillars/stooks/ribs at this mine.

## PARTIAL EXTRACTION UNDER DIFFICULT CONDITION

Mechanized depillaring at the Tandsi, GDK 11 and VK 7 mines are practiced at depth of cover of nearly 260, 325 and 377 m, respectively. Caving of the roof strata at GDK 11 was not very difficult, but the same was found to be challenging at the Tandsi and VK 7 mines. Tandsi experienced a roof, which is difficult to

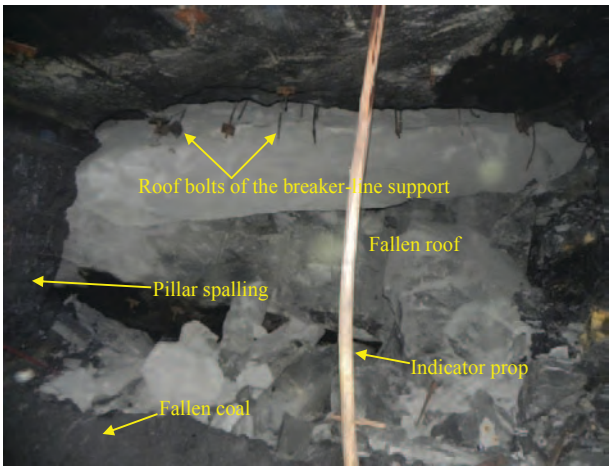



**Figure 6. Breaker line failure related goaf encroachment at the GDK 11 Mine.**

be controlled even over the galleries. However, adoption of smart-bolting practices effectively controlled the roof strata (Oldroyd et al., 2006).

To arrest strata control problems during depillaring, alternative large-sized stooks (Figure 7) were left inside the goaf. Creation of a nearly 20 m wide void resulted large amount of strata movement due to the presence of weak and incompetent roof atrata at high depth of cover. Therefore, a solid coal pillar of nearly 20 m width was left against each void of similar width to control the excessive strata movement. This resulted in partial extraction during the depillaring process at this site. Depillaring of the CMP-1 panel at VK 7 was attempted by a CM and shuttle car combination, but the depillaring experienced an unexpected collapse of immediate roof of around 6 m height. This caused the closure of the panel, and a partial extraction method (Figure 7) was followed in the two other panels of the mine.

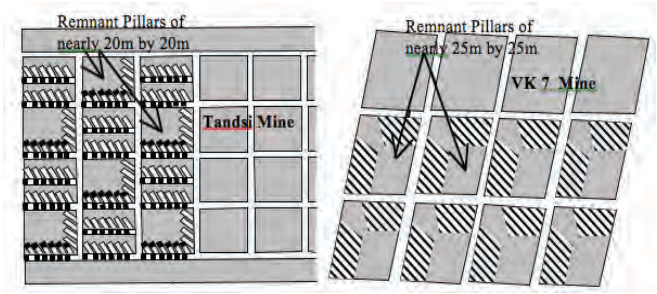



**Figure 7. Schematic layout of pillars extraction leaving remnant pillars at the Tandsi and VK 7 Mines.**

The adopted partial extraction at Tandsi did not cause problems after exhaustion of the panel. Probably, each individual void, created through the adopted partial extraction during the depillaring, got stabilized due to the highly caveable nature of roof strata at this mine. This stabilization seized the chance of catastrophic failure of pillars left inside the goaf. However, a similar partial extraction at VK 7 did not experience any roof caving during extraction. Each individual void, created due to the adopted partial extraction, remained empty cusing considerable amount of induced stress over the left out pillars inside the goaf. The stress built up over the left-out pillars inside the goaf started increasing with time because of nearly 50% extraction of the surrounding coal. While the second panel of the partial extraction (Figure 7) was in progress, heavy sound and seismic activities were noticed from a sealed neighboring panel of partial extraction, which resulted in the termination of the method. It was realized that the partial extraction during depillaring is difficult without caving of the roof strata for the site conditions similar to the VK 7 mine.

**Line of Extraction**

An important practical difference between fully mechanized and semi-mechanized depillaring faces is the orientation of the face line. A diagonal line of face advance of the semi-mechanized depillaring provides an opportunity to play with the length of the face to manage caving of the overlying strata. But it is difficult to follow this pattern of pillar extraction during the fully mechanized depillaring. Almost all the fully mechanized depillaring faces in the country adopted a straight line or single pillar extraction, which worked well for a moderate overlying stratum. The mechanized depillaring of the CMP-1 panel at the VK 7 mine saw an unexpected collapse of immediate roof of around 6 m height. This caused some casualties of men and machine. The compound effect of a number of geo-mining factors is thought to be responsible for this fall. The fall occurred during dilution of the final snook (against junction) of the fourth pillar (Figure 8). This fall covered a large area, but did not fill the goaf. Here, nearly 10,000 m$^2$ of goaf roof was exposed without any major fall before the roof collapse. Available experiences of conventional depillaring in this area show that a diagonal line of extraction was used to experience a main fall after encountering this much exposure of the goaf roof. An analysis of the freshly obtained core samples of the overlying strata (Figure 8) found that the beam of one pillar width over the goaf in the CMP-1 panel was competent enough to sustain. Here, the single row of pillar extraction provided a critical area of exposure from an air-blast point of view, but failed to provide enough width to break the beam for the first major roof fall. At least a width of two pillars is required for caving of the roof and, therefore, a straight line of extraction of two rows of pillars is realized for the site. This approach was later validated at the site during further depillaring of the developed pillars at the mine.

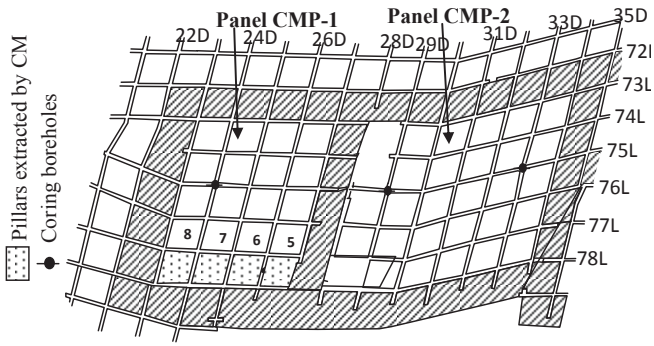



**Figure 8. Plan showing working by CM in the CMP-1 panel of the VK7 Incline mine.**

**Oversized Ribs**

As mentioned in Table 1, the site conditions of the Jhanjra Mine are not very difficult. Now the mechanized depillaring is successfully being adopted here to extract the R-VI seam. Depillaring in the first panel CM1 was attempted just after the collapse of immediate roof in the CMP-1 panel at the VK 7 Mine. Here, ribs of larger size were left inside the goaf (Figure 9) during depillaring, mainly due to apprehension of roof collapse at another mine. Oversized ribs left inside the goaf resulted in a delay of the caving of roof strata. This panel did not experience a roof fall even after a goaf area exposure of more than 10,000 $m^2$. Under these conditions, the working in the panel was stopped. Taking advantage of a shallow cover (125 m), the caving of overlying strata was managed through long-hole drilling and blasting from the surface (Mishra et al., 2013).

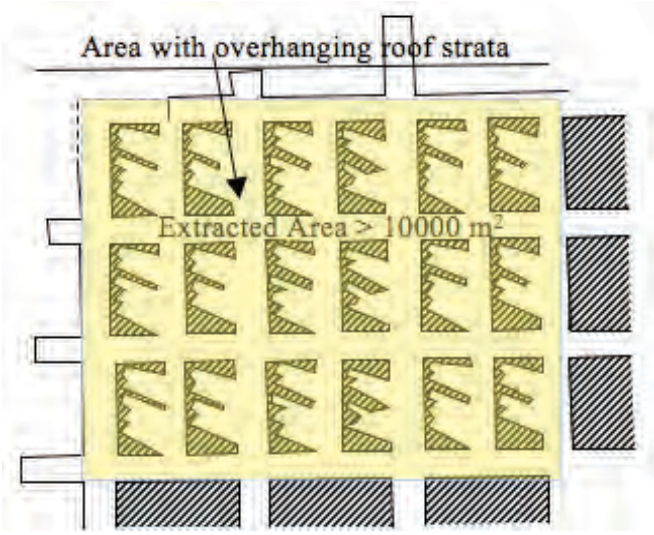



**Figure 9. Plan showing extracted area and left out ribs under overhanging roof strata (shaded portion) in CM1 panel.**

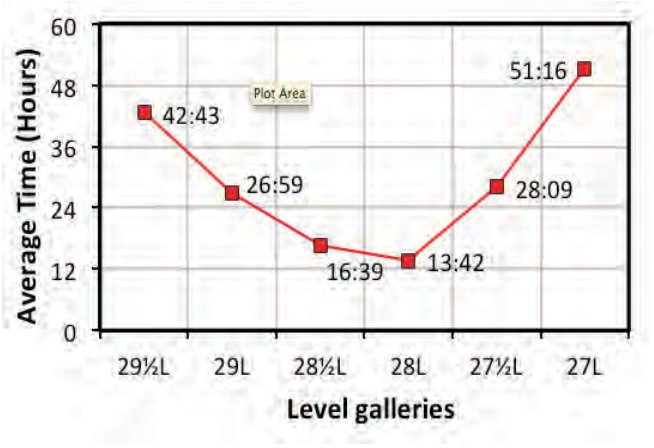



**Figure 10. Graph showing the overall average time interval between start of AWTT flashing and fall in different AWTTs installed at junctions of different levels with a dip-rise gallery.**

**STRATA CONTROL STUDIES**

It is challenging and technical to extract valuable information about strata control parameters during underground coal mining. Field experience, along with information about geo-mining conditions, is vital to judge the suitability of different types of instruments for visualization of rock mass response under the varying loading conditions of a mining face. The competency of overlying roof strata significantly affects the nature and amount of mining induced stress/deformation around an excavation, while the other parameters like the underground environment, depth of cover and dimensions of excavation are important for optimization of the techno-economical aspects of the measurement. Strata control studies have been conducted at most of the mechanized depillaring operations with the help of different geo-technical instruments, like Dual Height Telltale, Rotary Telltale, Auto Warning Telltale (AWTT), Extensometers, Instrumented Roof Bolts and Stress Meters. Lead wires of some of these instruments are extended to a safe observation station, where the data logger is used to connect it with computer for continuous (in time) monitoring.

However, strata monitoring experiences of the authors at different Indian depillaring panels shows nearly 30-40% of premature casualties of these instruments, mainly due to movement of machines along with roof and side falls over the connecting wires. AWTT is an independent device and does not require lead wire extension. It is set to trigger flashing after a certain value of cumulative displacement of strata, generally below a 15 m roof horizon. AWTTs are installed at every tri- and four-way junction of a panel. A good safety practice is achieved at an Indian mechanized depillaring on the basis of an experience about time interval between the start of AWTTs flashing and the occurrence of a roof fall around the respective instrument's position. However, this time interval was found to be influenced by roof blasting in the goaf, partial extraction of the adjacent pillar, the hanging area of roof inside the goaf, orientation of geological discontinuities, the barrier effect and the rate of goaf advance. An observed effect of barrier pillars over a time interval between the start of AWTTs flashing and occurrence of a roof fall is shown in Figure 10.

**CONCLUSIONS**

Coal mining is of strategic importance for the energy security of India. Existing conditions in the coal mining industry of the country requires the urgent use of mechanized extraction of coal pillars. However, the true potential of the technology is yet to be tapped, as we introduced only few mechanized depillaring workings in last 10 years. Mechanized pillar extraction is probably the best available approach for extraction of the developed coal seams, and foreign companies are providing good machines and technical inputs. However, the coal mining industry of the country inherits some geo-technical challenges. Here, the existing experience of our unique geo-mining conditions may provide valuable support for the success of modern mining technologies to minimize costly mistakes.

**REFERENCES**

Dixit, M. P., Mishra, K. (2010). "A unique experience of on shortwall mining in the Indian coal mining industry." *Proceedings of the 3rd Asian Mining Congress*, MGMI Kolkata, pp. 25-37.

Kaku, L. C. ed. (2000). *The Coal Mines Regulations* (1957), Lovely Prakashan, Dhanbad, 284 pages.

Leeming, J. (2003). "Joy introduces continuous miner: Technology into India." *Coal International/Mining and Quarry World,* Sep./Oct.: 203-206.

Mishra, A. K., Mishra, A. K. and Rout, M. (2013). "Blast induced caving from surface over continuous miner panel at a 110 m cover in an Indian Mine." *Arab. J Sci Eng*, 38(7):1861-1870.

Oldroyd, C., Bigby, D., Leeming, J., Meyer, L. (2006). "Successful Application of Rock Bolt Support and Mechanised Depillaring in Difficult Roof Conditions at Tandsi Mine, Western Coalfields, India." *Proceedings of the 25th International Conference on Ground Control in Mining*, Morgantown, WV, USA, 396-400.

Sarkar, S. K. (1985). *Longwall mining in India*. Scientific Mining Publishers, Dhanbad (India): 250 pages.

Singh, R., Mandal, P. K., Singh, A. K., Kumar, R. and Sinha, A. (2011). "Coal pillar extraction at deep cover: with special reference to Indian coalfields." *International Journal of Coal Geology*, Netherlands, 86(2-3): 276-288.

Singh, R., Mandal, P. K., Singh, Arun K., Singh, Amit K., Ram, Sahendra and Kumar, Nirmal (2004). "Mechanisation to meet the challenges of underground coal mining in India: a success story." *Proceedings of the International conference on Future of Indian Mineral Industry: Challenges and Opportunities*, 17-18 September. Organized by MGMI, India, 21-28.

# A Case Study for Multiple Seam Calibration of LaModel in Bump Prone Ground

**Kevin W Harris**, Graduate Research Assistant
**Michael J Raffaldi**, Graduate Research Assistant
**Kyle A Perry**, Assistant Professor
University of Kentucky
Lexington, KY

## ABSTRACT

Multiple-seam coal mining is a major issue in underground coal mining that adds additional complexity to the practice of ground control. As reserve exploitation is driven by economics, it is now difficult to mine coal without the existence of previous workings above and/or below the active seam; this is particularly true in the Appalachian coalfields. The frequency in which problematic multiple-seam interactions are now encountered has resulted in significant research regarding the underlying mechanisms of the problems and methods of mitigation. In the last few decades, a great deal has been learned about these interactions and the ability to minimize problems associated with these hazards has greatly advanced, resulting in better economics and improved safety.

Minimizing the adverse effects of stress interactions often requires a thorough understanding of site-specific geotechnical parameters and previous mining geometry. This is especially evident in bump-prone ground, where pillar behavior is highly dependent on local conditions. This paper presents a case study in a deep cover, Central Appalachian coal mine where three bump events occurred. Initially, empirical design software was used in an effort to analyze the situation and prevent further instability. The empirical study proved ineffective. A detailed investigation of the bump events using the boundary element software LaModel 3.0 was then performed. This study resulted in a site-specific calibration standard that will be applied in numerical pillar design for the remaining reserve.

## INTRODUCTION

As shallow reserves are depleted and induced stresses from multiple-seam mining introduce additional geotechnical challenges, bumps will remain a serious hazard for the coal mining industry. Due to the inherent nature of geologic materials, coal bump mechanics may never be completely understood and prevented. However, site conditions can be studied to develop and implement a probabilistic approach to bump prediction. These conditions most often include the following:

1. High-static stress concentration on critically loaded pillars (Peng, 2008)
2. Frictional constraint posed by roof/floor interface that elevates confining stress (Lu et al., 2008) and allows for the accumulation of strain energy
3. Dynamic stress that is a result of abrupt failure of nearby roof and/or floor material that can result in the loss of confining stress and release of stored strain energy (Maleki, 1995)
4. High extraction and/or productivity (e.g., retreat mining) which creates a dynamic loading environment, minimizing the time available for stable stress redistribution and yielding

While high overburden and multiple-seam conditions are largely responsible for high-static stress, the presence of strong near-seam strata (e.g., massive sandstone) is linked with conditions 2 and 3 (from the list above). Strong, massive strata on (or near) the coal seam are associated with strong roof/floor interfaces and can increase the seam strength (Perry et al., 2013). This allows significant strain energy to be stored and can result in sudden and violent failures of coal pillars. This is particularly likely during retreat mining where high abutment stresses are placed on the active mining zone (AMZ) and strong strata can lead to delayed or ineffective caving. Consequently, the determination of local geology is essential in recognizing the conditions that contribute to the occurrence of coal bump events. Modern coal operations in Central Appalachia must often contend with many or all of these conditions. The three coal bumps investigated in this case study occurred during the extraction of a B-seam reserve in Harlan County, Kentucky. This region has a significant history of deep cover room and pillar coal mining (Mark, 2009).

### *Background Information*

The three coal bumps (Figure 1) all occurred during development, in overburden exceeding 1,400 feet, while advancing directly over barrier structures in the underlying A-seam. The first two bumps occurred over barrier pillars located between first workings in the A-seam, as the surrounding panels were not retreat mined. However, the barrier pillars were highly stressed as if the A-seam panels had been retreat mined, indicating that the development pillars in these adjacent areas were yielding and not significantly supporting the overburden. The third bump occurred over a barrier pillar where the adjacent panel had been retreat mined. Coal bumps in the region have most often occurred during retreat mining. Newman (2007) concluded that development above

remnant structures and high cover were conditions present during the bumps. The events occurred nearly a decade ago, prior to the widespread use of the ARMPS/AMSS software. This software was initially chosen to assess the applicability of the empirical approach in the development of a pillar design methodology for the remainder of the B-seam reserve.

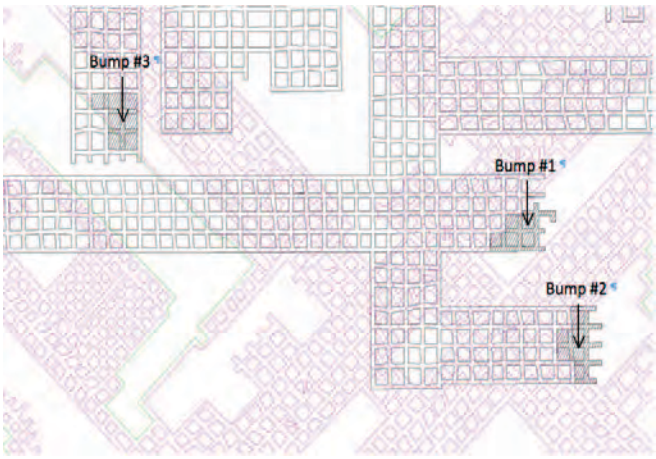



**Figure 1. Location of bump impact zones (Harris and Perry, 2014).**

***Empirical Results***

NIOSH recommends a stability factor of 1.30 when using ARMPS/AMSS to evaluate narrow panels located under deep cover with large barrier pillars, as was the case here. Table 1 shows that the calculated stability factors were well above 1.30; however, the stability factor for each of the three bump sites was remarkably consistent. It should be noted that the A-seam was treated as a gob-solid boundary during the analysis of the second bump, while the A-seam was considered as an isolated remnant pillar for the analyses of the first and third bumps. The AMSS database includes many case histories of pillar failure from Central Appalachia; however it does not include many bump cases. Based on the consistency of the stability factors, simply adjusting the coal strength downward in ARMPS/AMSS to normalize the stability factor may seem like a plausible option. However, assuming a lack of stability of all A-seam development pillars with full abutment loading on barrier structures may not be necessarily prudent. The stability of these development pillars and resultant load on barriers is uniquely a function of the site-specific loading environment, making it necessary to incorporate the use of numerical tools when further analyzing the multiple-seam effects on the B-seam workings.

The boundary element program, LaModel 3.0, was selected to study the three bump events in the B-seam reserve. LaModel uses the laminated overburden model. While this is a major simplification of the mechanical behavior of the rock mass, it has been shown to be effective in simulating pillar loading and multiple-seam stress-transfer and, consequently, has found use within the coal industry, particularly in these types of deep cover or multiple-seam applications. The initial LaModel analysis was performed using the technique developed by Heasley (2008) and Heasley et al. (2010). With this approach, the model is calibrated using the standard calibration wizards. The AMZ stress stability factors are then calculated and checked against a design value of 1.40, which comes from a statistical analysis of the ARMPS database of case histories (Heasley et al., 2010). However, this methodology proved to be ineffective in predicting instability for the three historical bump sites, necessitating a more rigorous investigation.

## MODELING RESULTS

The three bump events all occurred as development transitioned over barrier pillar edges in the underlying A-seam. Additionally, the first two bumps occurred over A-seam barrier pillars where the seam was not retreat mined. This indicates substantial yielding of main/panel development pillars, with most of the overburden supported by the large, intact barriers. This also suggests that the abutment distance was relatively small, with highly concentrated stress around the A-seam barrier pillar edges. Newman (2007) cited that section personnel found no indication of impending instability in the roof, floor, or pillars prior to the first bump event. Damage was mostly limited to the final row of pillars and outby portions of the belt heading. The second event was preceded by numerous small-face bumps within two days of the main burst, damaging a total of six pillars, and a clearly delineated edge of stress separating the bump areas was identified (Newman, 2007). Although failures resulted in excessive spans, the roof was largely intact, indicating the presence of strong and rigid strata (Newman, 2007). Consequently, this study aimed to achieve the following goals:

1. Model the A-seam in a single-seam environment to provide reasonable pillar stability but demonstrate yielding near the large, intact barriers associated with the B-seam bumps to model high-stress concentration on barrier pillar edges.
2. Determine an appropriate lamination thickness for each bump model that results in reasonable delineation of stability using the AMZ stability factor.
3. Modify the B-seam in-situ coal strength to normalize the AMZ stress stability factor.

**Table 1. AMSS results at three bump sites (Harris & Perry, 2014).**

| Bump | Interburden | Gob Width | Remnant Width | Cover | Height | Pillar Centers | AMSS |
|---|---|---|---|---|---|---|---|
| # | (ft) | (ft) | (ft) | (ft) | (ft) | (ft) x (ft) | SF |
| 1 | 165 | 345 | 190 | 1650 | 5.75 | 80 x 80 | 1.85 |
| 2 | 170 | 355 | - | 1700 | 6.00 | 80 x 80 | 1.87 |
| 3 | 145 | 405 | 130 | 1400 | 6.00 | 80 x 90 | 1.86 |

4. Correlate the lamination thickness for each bump site with site-specific geology, particularly interburden properties.
5. Evaluate the effectiveness of calibration methodology to additional mine workings.

***A-Seam Model***

The strain-softening material model was selected for the A-seam. This seam was initially modeled in a single-seam environment to perform a sensitivity analysis of lamination thickness and coal strength on pillar yielding. Initially, the standard 900 psi in-situ coal strength was used following Mark and Barton (1997), while the lamination thickness was adjusted within a range of reasonable values. This resulted in significant yielding for most of the A-seam workings. Because the actual workings were at least minimally successful, the pillar stability for most of the workings was unreasonably low. Therefore, the in-situ coal strength in the model was incrementally increased until the workings demonstrated reasonable stability, but the development pillars surrounding the large, intact barrier pillars were yielded (Figure 2). The selected in-situ coal strength for the A-seam was 1,250 psi.

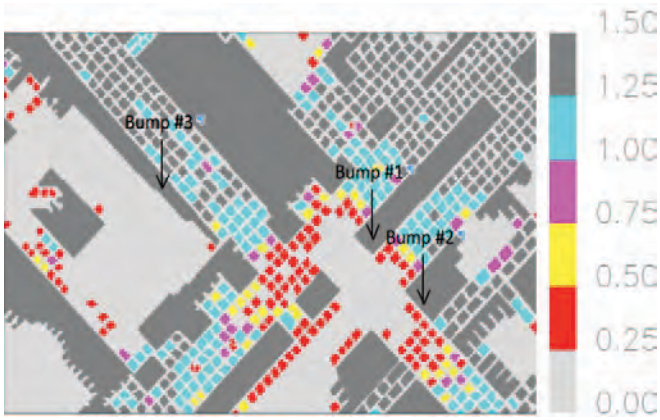



**Figure 2. Pillar stress stability factor for A - seam model (Harris and Perry, 2014).**

***Sensitivity Analysis***

While the authors do not have first-hand knowledge of the bumps, the documented extent of damage at each bump combined with the evidences provided by Newman (2007) help to delineate the abutment extent. A numerical sensitivity study was conducted for each of the three bump sites, and the abutment extent was examined as the lamination thickness was varied. The lamination thickness selected for each location was that which produced the best match to the expected abutment zone, demonstrating a clear delineation between the affected pillars and the outby crosscuts. This effort follows the advice of Heasley (2008) who recommends calibration to produce an abutment zone extent that is reasonable or follows field measurements. For each bump event, the selected lamination thickness, geologic information, and interburden thicknesses are presented in Table 2.

The selected lamination thickness was then compared with the site-specific geologic information. It was discovered that the chosen lamination thickness is proportional to the interburden thickness with the A-seam, along with the total massive sandstone present in the interburden for both the underlying A-seam and overlying C-seam. For example, the lamination thickness selected for the second bump is 5 feet thicker compared to the lamination thickness selected for the first bump. While the total massive sandstone is equivalent at both sites, the interburden between the B-seam and A-seam is 5 feet thicker at the second bump site. A similar comparison was also observed for the third bump site. Relative to the second bump location, the third bump area has 25 feet less interburden thickness and 5 feet less total massive sandstone. This total mirrored the difference (30 feet) in the initial selected lamination thickness. Using the second bump lamination thickness as a basis, a relationship (Equation 1) was developed based on these observations which is to be used to construct a lamination thickness isopach for use with future mine planning.

$$t = 90 + (C - 45) + (A - 170) + (SS - 120) \qquad (1)$$

Where:

t = Lamination Thickness (ft)

C = C-seam to B-seam interburden thickness (ft)

A = B-seam to A-seam interburden thickness (ft)

SS = Total massive sandstone thickness, C-seam to A-seam interval (ft)

As a final step, the in-situ coal strength of the B-seam was reduced from the standard 900 psi threshold (Mark and Barton, 1997) to 710 psi, which normalizes both individual pillar-stress stability and the AMZ-stress stability at a value of 1.00. This in-situ coal strength is very similar to the value (685 psi) used by Newman (2007). In other words, pillars with a stress stability factor of less than 1.00, within a system of pillars that have an AMZ stress stability factor of less than 1.00, are considered to have high bump potential because both the pillar and the system are critically loaded. This is demonstrated in the drop in AMZ stress stability factor (Figure 3) from the preceding crosscut of development to the final configuration (at which the bump occurred) for all three case histories (Table 3).

It is also interesting to note the modeled stress in the core of pillars that bumped. The peak total vertical stress met or exceeded an approximate level of 6,500 psi at all three bump sites in the final calibrated models. An area of eastern workings was then analyzed in an effort to provide validation. This region had both overlying C-seam works and underlying A-seam development. One particular panel encountered difficult ground upon development, and the model confirmed the presence of significant instability. However, the peak vertical stresses were much lower. This may help explain why the roof and rib difficulties occurred without bumping.

***Bump Risk Criteria***

The nature of geologic materials makes it impossible to predict bump events; however, this investigation sought to understand the conditions associated with previous bumps in the B-seam reserve and institute a program to assess bump potential as mining progresses. LaModel does not allow for the specific input of geological parameters, and determining this information can be

**Table 2. Interburden geology and selected lamination thickness for each bump event.**

| Bump | C-seam/B-seam Interval (ft) | | | B-seam/A-seam Interval (ft) | | | Total (ft) | | Lamination |
|---|---|---|---|---|---|---|---|---|---|
| # | Sandstone | Shale | Total | Sandstone | Shale | Total | Sandstone | Total | Thickness (ft) |
| 1 | 35 | 10 | 45 | 85 | 80 | 165 | 120 | 210 | 85 |
| 2 | 30 | 15 | 45 | 90 | 80 | 170 | 120 | 215 | 90 |
| 3 | 45 | 0 | 45 | 70 | 75 | 145 | 115 | 190 | 60 |

**Table 3. AMZ stress stability factor from prior crosscut to final state (Harris & Perry, 2014).**

| Bump | Step 1 | Step 2 (Bump) |
|---|---|---|
| # | Stability Factor | Stability Factor |
| 1 | 1.04 | 0.92 |
| 2 | 1.25 | 0.89 |
| 3 | 1.05 | 1.01 |

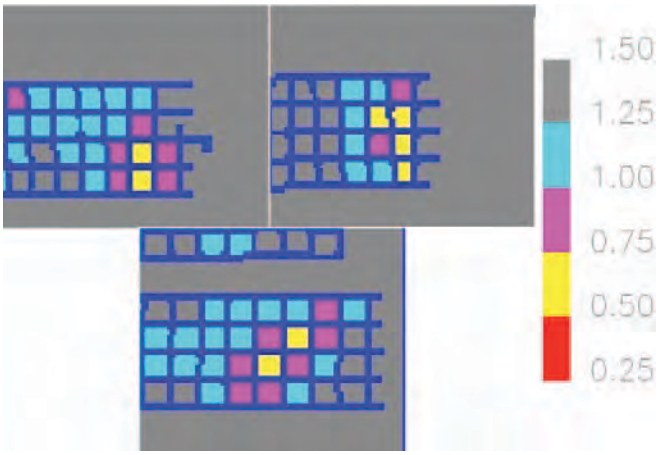



**Figure 3. Bump #1 (left), Bump #2 (right) and Bump #3 (bottom) pillar stress stability factor (Harris and Perry, 2014).**

problematic. As such, localized conditions including roof/floor composition, or the associated frictional properties of the pillar interfaces are not considered. However, the resulting calibration methodology is site-specific in that the lamination thickness is a function of interburden parameters associated with the near-seam geology. Consequently, abutment distance is minimal and provides a measurable level of conservatism when compared to empirically based approaches.

The B-seam in-situ coal strength was reduced to normalize the AMZ stress stability for the three bump sites to a value of 1.00. It is, however, prudent to provide a buffer above critical levels. Consequently, mine management has adopted the following approved criterion for all future development:

1. AMZ stress stability factor exceeding a value of 1.15
2. Individual pillar-stress stability factors exceeding a value of 1.00 for those located within the AMZ
3. For any single pillar in which the stress stability factor does not exceed a value of 1.00, then peak total vertical stress should not exceed a value of 6,500 psi.

Ultimately, it is better to more accurately classify failures than success. Recent workings in the mine completed under shallower overburden, including a series of right panels, were back-analyzed using this new approach. The area was initially designed and evaluated using LaModel with the standard empirical calibration. Mining in this district was mostly successful, and while a few locations demonstrated obvious multiple-seam influence, there were no bumps. Analysis using the new method indicated that all panels met the new criteria except the 2-Right Panel. Since the 2-Right Panel was successfully retreat-mined without bumps, the new criterion appears to be appropriately conservative. However, it is recognized that the lack of bumps in a single panel is not evidence of a lack of bump risk.

## CONCLUSION

The three bump events were associated with highly concentrated multiple-seam stresses. Empirical analysis using AMSS and a LaModel analysis, using the standard empirically based calibration, did not adequately reflect the bump risk in the B-seam. The bump risk appeared to be the result of significant yielding in the underlying A-seam workings, resulting in high-abutment stresses in barrier pillars. The bump events all occurred as development attempted to cross these underlying barrier pillars. Consequently, the A-seam was assumed to behave as strain-softening, in order to increase yielding. The lamination thickness was adjusted based on the interburden properties, including thickness and composition. The coal strength in the active seam was iteratively reduced until the active mining zone (AMZ) stress stability factor reached a critical threshold of 1.00.

The results were compared with other areas of the mine, and a consistent level for pillar core stress was determined for all three bump events. LaModel 3.0 was considered a viable modeling tool and was then used to devise a mine-specific risk evaluation methodology for the remaining B-seam reserve. The methodology was validated with recent successful case histories from the mine. Current development within the active mine is advancing in new areas of the reserve that were previously avoided due to concern of coal bumps. Mine planning follows the new protocol which, to date, has been successful.

## REFERENCES

Harris, K. W. and Perry, K. A. (2014). "Evaluating bump prone ground with LaModel through a site-specific calibration." Submitted for publication to SME *Transactions/ Mining Engineering*.

Heasley, K. (2008). "Some thoughts on calibrating LaModel." In: *Proceedings of the 27th International Conference on Ground Control in Mining*. Morgantown, WV: West Virginia University, pp. 7–13.

Heasley, K., Sears, M. M., Tulu, I. B., Calderon-Arteaga, C., and Jimison, L. (2010). "Calibrating the LaModel program for deep cover pillar retreat coal mining." In: *Proceedings of the ICGCM Pillar Design Workshop*. Morgantown, WV, West Virginia University, pp. 47–57.

Lu, J., Ray, A., Morsy, K., Peng, S. (2008). "Effects of rock/coal interface property on coal pillar strength." In: *Proceedings of the 27th International Conference on Ground Control in Mining*. Morgantown, WV: West Virginia University, pp. 262–267.

Maleki, H. N. (1995). "An analysis of violent failures in U. S. coal mines, case studies." In: *Proceedings of Mechanics and Mitigation of Violent Failure in Coal and Hard-rock Mines*. United States Bureau of Mines, Special Publication 0195, pp. 5–26.

Mark, C. (2009). "Deep cover pillar recovery in the US." In: *Proceedings of the 28th International Conference on Ground Control in Mining*. Morgantown, WV: West Virginia University, pp. 9.

Mark, C. and Barton, T. M. (1997). "Pillar design and coal strength." In: *Proceedings of the New Technology for Ground Control in Retreat Mining*. United States Bureau of Mines, Information Circular, IC 9446, pp. 49–59.

Newman, D. (2007). "Multiple seam mining in Appalachia: state-of-the-art, state-of-practice, state-of-the-future." In: *Proceedings of the SME Annual Meeting*. Englewood, CO: Society for Mining, Metallurgy & Exploration, pp. 8.

Peng, S. S. (2008). *Coal Mine Ground Control,* 3rd Edition, West Virginia University, pp. 434.

Perry, K. A., Unrug, K. F., Harris, K. W., and Raffaldi, M. J. (2013). "Influence of roof/floor interface on coal pillar performance." In: *Proceedings of the 32nd International Conference on Ground Control in Mining*. Morgantown, WV, West Virginia University, pp. 7.

# A Comparison Between ARMPS and the New ARMPS–LAM Programs

**Peng Zhang**
Carlson Software
Watertown, MA

**Keith A Heasley**, Professor
Department of Mining Engineering
West Virginia University
Morgantown, WV

**Zacharias G Agioutantis**, Professor
School of Mineral Resources Engineering
Technical University
Crete, Greece

## ABSTRACT

In previous research, the laminated overburden model from the LaModel program was effectively integrated with Analysis of Retreat Mining Pillar Stability (ARMPS) through ARMPS-like input to create a laboratory version of the new "ARMPS-LAM" program. This program takes the basic ARMPS geometric input for defining the mining plan and loading condition, and then automatically develops, grids, runs, and analyzes a full LaModel analysis of the mining geometry to output the section stability factor (SF), all without further user input. The initial ARMPS-LAM results were encouraging with a case history classification accuracy of 55% to 71%; however, a few of the input variables that were nominally included in the SF calculation showed independent significance in the classification accuracy.

Therefore, in order to further improve the accuracy of the ARMPS-LAM program, an investigation of the SFs calculated by the new ARMPS-LAM program and the ARMPS program is detailed in this paper. The initial results of a linear correlation between the ARMPS-LAM SF and the ARMPS SF showed a strong correlation ($R^2 = 0.88$), with the ARMPS-LAM SF averaging about 8% higher. The difference in SFs between the programs were further investigated, and, ultimately, the results indicated that the laminated overburden model as implemented in ARMPS-LAM distributes relatively more load on the section pillars for depths less than about 1,000 ft and less load for depths more than 1,000 ft. The results of this research highlight the potential for improving the ARMPS-LAM program in the future by implementing a more accurate loading calculation on the section pillars.

## INTRODUCTION

A computer code, ARMPS-LAM, has been developed to effectively integrate the laminated overburden model into the ARMPS program (Zhang and Heasley, 2013). ARMPS-LAM functions as an automated solution for a LaModel analysis of an ARMPS-type mine design. Basically, the ARMPS-LAM program takes the typical ARMPS geometric input and empirical parameters for defining the mining plan and loading condition and then automatically conducts a complete LaModel analysis to calculate the stability factor of the Active Mining Zone (AMZ) (and barrier pillars), all without further user input. The program contains the necessary modules for covering all aspects and procedures of a full LaModel analysis, from pre-processing to post-processing. From the user perspective, only the traditional ARMPS input is required. Additionally, similar to ARMPS, the output contains the AMZ SF, barrier pillars SF, and other loading and strength data; however, these output values are now calculated using the laminated overburden model (Zhang and Heasley, 2013).

The ARMPS-LAM program consists of three primary modules: pre-processing, numerical solution, and post-processing. The pre-processing module includes the necessary subroutines to import data, develop, and calibrate the laminated overburden model (Heasley, 2008). The numerical solution module solves the laminated overburden model, and the post-processing module contains the subroutines to automatically extract and calculate the SFs and pillar loadings and then output the important data. The initial ARMPS-LAM program has been successfully validated (Zhang and Heasley, 2013); however, to further improve its classification accuracy of successful and unsuccessful cases in the future, the differences in the SFs calculated from the ARMPS program and the new ARMPS-LAM program are investigated in this paper.

## STABILITY FACTOR INVESTIGATION

In previous research, the ARMPS 2010 and ARMPS-LAM programs were used to calculate the SFs for the 645 case histories in the original NIOSH ARMPS database (Zhang and Heasley, 2013). The results of the ARMPS analysis is based on the EXCEL version of ARMPS 2010, provided by the NIOSH for this research. It took only a couple of minutes of processing time to run the entire database with the EXCEL version of ARMPS. For the ARMPS-LAM analysis, the entire database took around 10 hours of processing time to run. The average running time for a single case history is 52 seconds, and the maximum running time of any case history in the database was 7 minutes. The ARMPS-LAM solution times depend on the complexity and size of the developed model. In this research, the SF criterion of 1.50 was used to separate the successful and unsuccessful case histories for both programs, and the calculated SFs between the two programs were compared to analyze their correlations and differences.

**Stability Factor Correlations**

To initially investigate the correlations between the two programs, the value of the calculated ARMPS-LAM SF was initially plotted versus the ARMPS SF, and a linear correlation was performed (see Figure 1). There was a fairly good correlation between their stability factors with an $R^2$ value of 0.8797 for the best-fit line (green dash line) and an $R^2$ value of 0.8794 for the best-fit line forced to go through the origin (blue solid line). This means that 88% of the variation of the ARMPS-LAM SF can be explained by the variation of the ARMPS SF for the given database. When the slope of the line is forced to go through the origin, the slope of the trend line (1.0811) indicates that the ARMPS-LAM SF averages about 8% higher than the ARMPS SF (blue line and equation, see Figure 1).

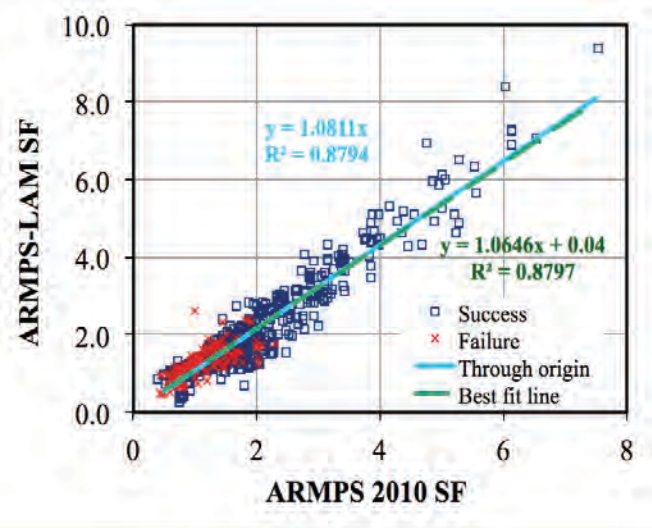



**Figure 1. Relationship between ARMPS-LAM SF and ARMPS SF.**

This strong correlation is not necessarily surprising. Both programs use the Mark-Bieniawski formula for determining the coal pillar strength. Also, both programs use the same abutment angle calculation for determining the magnitude of the abutment load. The big difference between the two programs is that ARMPS-LAM uses the laminated overburden model in a numerical determination of the relative stiffness of the support pillars (and gob) to ultimately determine the abutment (and overburden) load distribution, while ARMPS uses a number of empirically determined formulas for load distribution.

Although the ARMPS-LAM SF and the ARMPS SF show a strong correlation (trend line in Figure 1), some significant differences are also evident. Figure 1 indicates that some case histories have quite a different SF when comparing both programs. In order to further explore any significantly patterns in the differences between the ARMPS-LAM SF and the ARMPS SF, an SF ratio was created by dividing the ARMPS-LAM SF by the ARMPS SF for each case study (see Equation 1).

$$\text{SF Ratio} = \frac{\text{ARMPS - LAM SF}}{\text{ARMPS 2010 SF}} \quad (1)$$

Based on previous research and experience with the laminated overburden model (Esterhuizen, Dolinar, and Ellenberger, 2011; Heasley, 2012; Heasley et al., 2010; Sears and Heasley, 2013; Tulu, Heasley, and Mark, 2010), the SF ratio was analyzed against five potentially significant variables: depth, mining height, panel width, panel width-to-depth ratio, and pillar width-to-height ratio, looking for any significant trends. (For the pillar width-to height ratio (w/h), the average value of the section pillars is used. Because the strength of a rectangular pillar is different from that of a square pillar (Darling, 2011; Dolinar and Esterhuizen, 2007), the shape effect is considered by using a value four times the area (A) divided by perimeter (C) where w = 4A/C is a substitute for the pillar w/h ratio) (Wagner, 1980).

After reviewing the results from all of the potentially significant variables, there appeared to be a slight significant trend with the depth ($R^2$ = 0.21). In particular, it appears that the SF ratio decrease as the depth increases (see Figure 2). This means that the ARMPS-LAM SF is generally greater than the ARMPS SF when the depth is less than about 1,200 ft (as calculated from the regression equation). However, when the depth is greater than 1,200 ft, the ARMPS-LAM SF is generally smaller than the ARMPS SF.

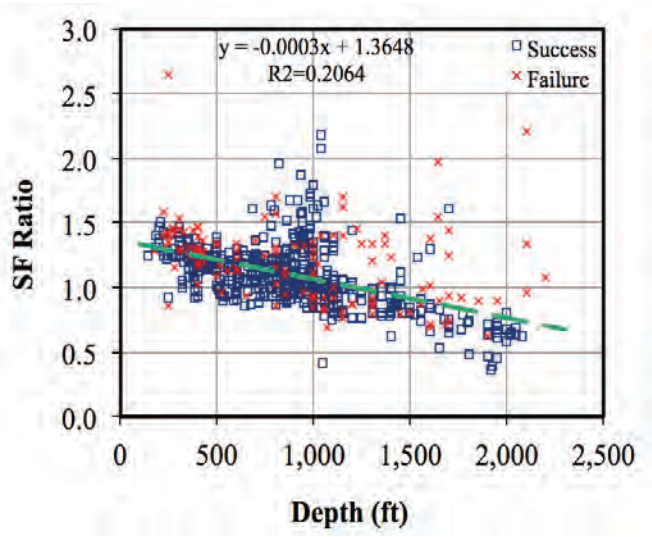



**Figure 2. Influence of the depth on the stability factor ratio.**

Any correlation between the SF ratio and the other potentially significant parameters, such as panel width, pillar width-to-height ratio, panel width-to-depth ratio, and mining height, was also investigated, and the results are presented in Figure 3, 4, 5 and 6, respectively. Figure 3 shows that the SF ratio is scattering around 1.08 at different panel widths with very little correlation ($R^2$ = 0.008). Figure 4 indicates that the SF ratio slightly decreases with increasing pillar width-to-height ratio, but the results are still very scattered, and the correlation is poor ($R^2$ = 0.060). In Figure 5, the SF ratio is seen to increase with the increase of panel width-to-depth ratio, but, again, the results are very scattered, and the correlation is poor ($R^2$ = 0.050). Finally, Figure 6 shows that the SF ratio is varying around 1.08 with different mining height and a poor correlation of $R^2$ = 0.049. Therefore, in comparing the ratio of the SFs between ARMPS-LAM and ARMPS, the only significant variable is the depth.

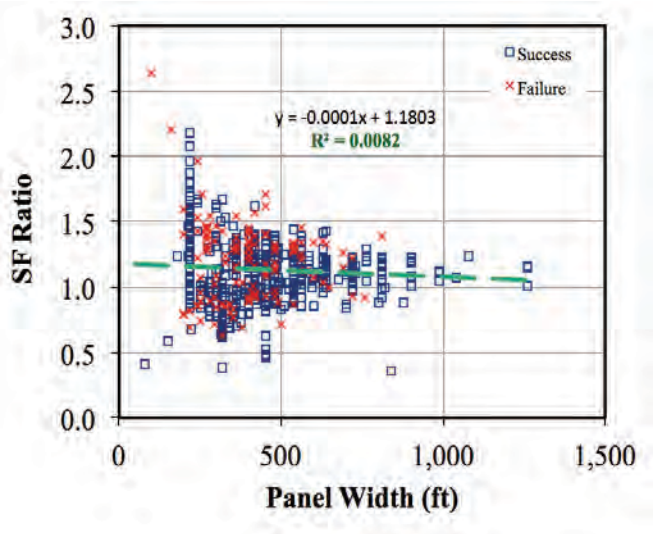



**Figure 3. Influence of the panel width on the stability factor ratio.**

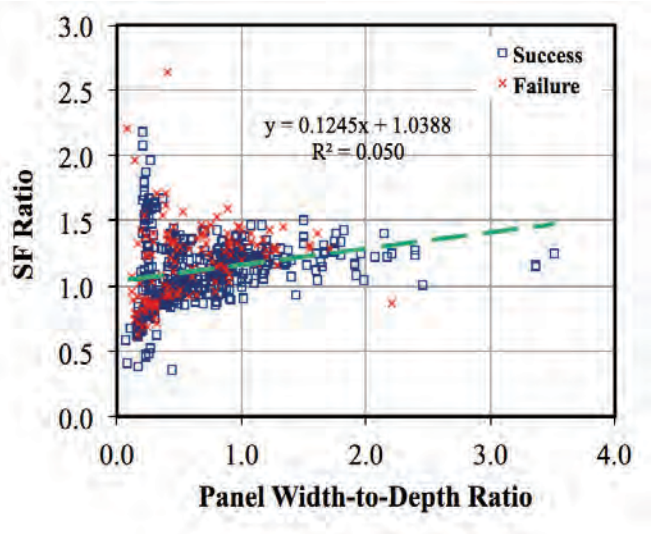



**Figure 5. Influence of the panel width-to-depth ratio on the stability factor ratio.**

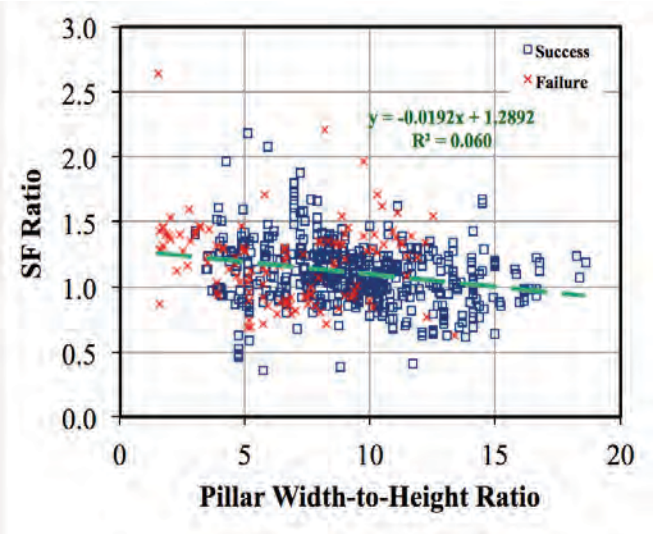



**Figure 4. Influence of the pillar width-to-height ratio on the stability factor ratio.**

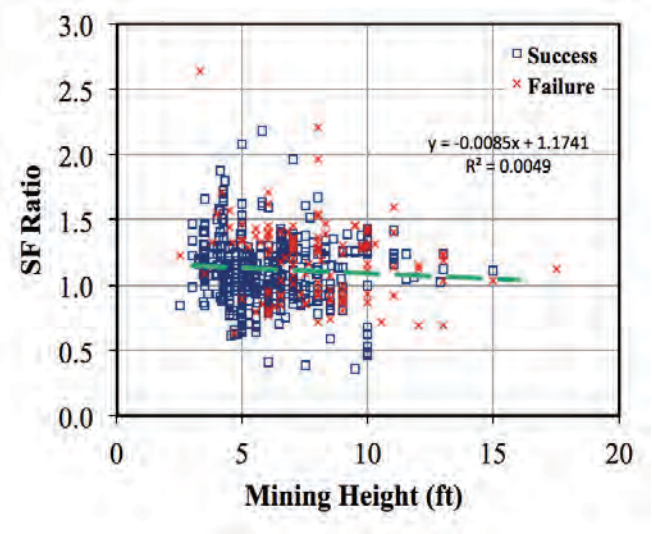



**Figure 6. Influence of the mining height on the stability factor ratio.**

**Stability Factor Differences**

To further analyze the differences between the SFs calculated by ARMPS-LAM and ARMPS, the differences in classification accuracy were examined. For both programs, the SF value of 1.50 was used to separate successful from unsuccessful case histories. In the classification accuracy analysis, it was found that both programs correctly classified 349 of the case histories (270 successes and 79 failures), and both programs incorrectly classified 187 of the case histories (172 successes and 15 failures). For the remaining 109 case histories, the two different programs gave opposite classifications. This means that, in these 109 case histories, when ARMPS-LAM classified the case history as a success, ARMPS classified it as a failure, or vice-versa. Thus, in these 109 cases, only one of the programs gives the correct classification. This small subset of the database was used to further explore the differences between the two programs with the intent of identifying potential improvements to the ARMPS-LAM program.

Table 1 further expands the analysis of the small subset of 109 case histories that were oppositely classified by ARMPS-LAM and ARMPS. In this subset, ARMPS-LAM correctly classified 47 of them (43%) compared with ARMPS which correctly classified the remaining 62 case histories (57%). Specifically, there are 78 successful case histories (72% of total) where ARMPS-LAM correctly predicted 38 (49%) of them (ARMPS fails), and ARMPS correctly predicted the remaining 40 (51%) successes (ARMPS-LAM fails). In addition, there are 31 failed case histories (28% of total) where ARMPS-LAM correctly predicts 9 (29%) of them (ARMPS fails), and ARMPS correctly predicts the remaining 22 (71%) failures (ARMPS-LAM fails).

To further explore the case histories in Table 1, the ARMPS-LAM SF was plotted versus the depth with the case histories divided into successes and failures and then further split into two sub-categories: ARMPS-LAM is correct, or ARMPS is correct

**Table 1. Case histories where the two programs disagree on classification.**

| Program | Prediction Result | Case Histories with Opposite Results from Programs | | |
|---|---|---|---|---|
| | | Total Opposite | Case Success | Case Failure |
| | | 109 | 78 | 31 |
| **ARMPS-LAM** | Correct | 47 | 38 (<1,000 ft) | 9 (>1,000 ft) |
| **ARMPS 2010** | Correct | 62 | 40 (>1,000 ft) | 22 (<1,000 ft) |

(see Figure 7). This figure shows that the difference in prediction accuracy between the programs is strongly correlated to the depth (H). This figure indicates that, when the depth is less than around 1,000 ft, the ARMPS-LAM SF is greater than 1.50 for both successes and failures, and the ARMPS-LAM program predicts more successfully than ARMPS. However, when the depth is greater than 1,000 ft, the ARMPS-LAM SF is less than 1.50 for both successes and failures and is often incorrect. This trend (see Figure 7) partially explains why ARMPS-LAM correctly classified 49% of the successes from the subset of the database (because their depth is less than 1,000 ft, and ARMPS-LAM gets SFs larger than 1.50) and why ARMPS-LAM can only correctly classify 29% of the failures (because their depth is greater than 1,000 ft, and ARMPS-LAM gets SFs smaller than 1.50).

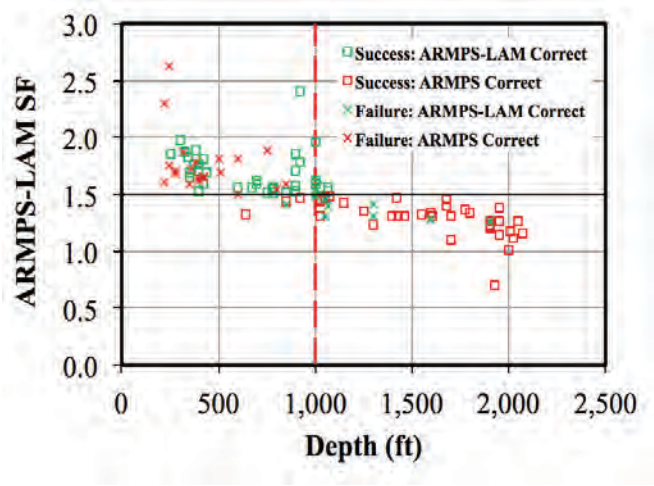



**Figure 7. ARMPS-LAM SF vs. depth using the classification disagreement database.**

Based on the analysis above, it can be seen that, when compared with ARMPS, ARMPS-LAM gets a higher SF for shallower cover (depths less than 1,000 ft) and gets a lower SF for deeper cover (depths greater than 1,000 ft). To further explore this trend, the results from ARMPS-LAM for the entire database were analyzed. Figure 8 is the plot of the ARMPS-LAM SF versus the depth with the case histories divided into the categories of successes and failures. These main categories are further split into two sub-categories: ARMPS-LAM is correct, or ARMPS-LAM is wrong. In this graph, it can be seen that most of the incorrectly classified successes occur with low ARMPS-LAM SF at deep cover and that most of the incorrectly classified failures occur with high ARMPS-LAM SF at shallow cover.

The details of the classification accuracy related to depth, as shown in Figure 8, are tabulated in Table 2. The trends observed in Figure 8 are duplicated in the table where ARMPS-LAM is seen

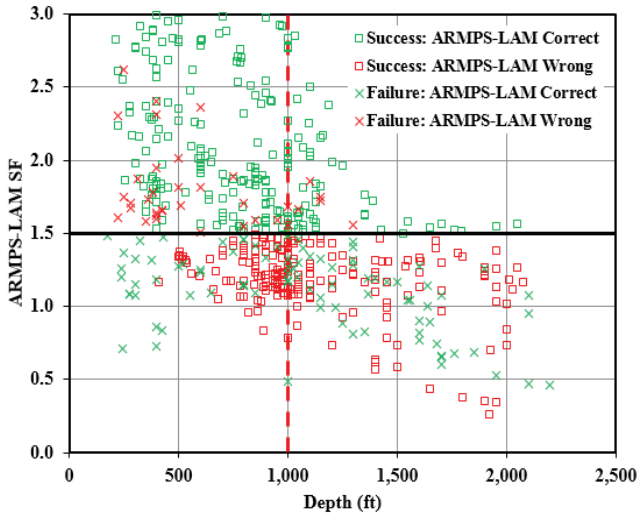



**Figure 8. ARMPS-LAM SF vs. depth using ARMPS database.**

to be good at classifying the shallow (less than 1,000 ft) successes (258 out of 372, 69%) and the deep (greater than 1,000 ft) failures (47 out of 52, 90%). Of course, the corollary is also true (see Table 2). ARMPS-LAM incorrectly classifies: 44% of shallow failures (32 out of 73) and 66% of deep successes (98 out of 148). It should be noted that it is not absolute that ARMPS-LAM has a greater SF for shallow mines and smaller SF for deeper mines, but there is a definite trend.

The highlighted trend in classification accuracy with ARMPS-LAM with depth is more than likely caused by the loading mechanics of the laminated overburden model, which, apparently, distributes less load on the AMZ for shallower cover (depths less than 1,000 ft), resulting in a higher stability factor, and more load on the AMZ for deeper cover (depth greater than 1,000 ft), resulting in a lower stability factor. This observation suggests that one of the potential future improvements to ARMPS-LAM (and LaModel) is to distribute more load on the AMZ for shallower cover and less load for deeper cover. This change would help ARMPS-LAM more accurately identify the failures with shallow cover and the successes with deep cover (see Figure 7). (However, it should be noted that this change could cause LaModel to fail to predict some successes with shallow cover and some failures with deep cover.)

## SUMMARY AND CONCLUSIONS

Pillar stability is critical to safe and economic operations of room-and-pillar retreat mines. In previous research, a computer code, ARMPS-LAM, was developed to effectively implement the laminated overburden model (from LaModel) into the ARMPS program. This ARMPS-LAM program automatically develops,

**Table 2. Classification accuracy of ARMPS-LAM using the SF guideline of 1.5.**

| Case History Category | ARMPS-LAM SF | ARMPS-LAM Prediction | Total | | H <= 1,000 | | H > 1,000 | |
|---|---|---|---|---|---|---|---|---|
| | | | Val. | Per. | Val. | Per. | Val. | Per. |
| Successes | > 1.5 | Correct | 308 | 59% | 258 | 69% | 50 | 34% |
| | <= 1.5 | Wrong | 212 | 41% | 114 | 31% | 98 | 66% |
| | Total | | 520 | 100% | 372 | 100% | 148 | 100% |
| Failures | <= 1.5 | Correct | 88 | 70% | 41 | 56% | 47 | 90% |
| | > 1.5 | Wrong | 37 | 30% | 32 | 44% | 5 | 10% |
| | Total | | 125 | 100% | 73 | 100% | 52 | 100% |

runs, and analyzes a full LaModel analysis of an ARMPS-type mine design. An analysis of the SFs calculated by the new ARMPS-LAM and the ARMPS programs was performed and discussed in this paper. Based on the results of the analysis, it was seen that there is a strong correlation between the two stability factors ($R^2$ = 0.88) and that the ARMPS-LAM SF averages about 8% higher than the ARMP SF. In a more detailed analysis of the two SFs, depth was found to be a significant variable, with the ARMPS-LAM SF generally decreasing with depth in relation to the ARMPS SF.

In an analysis of the classification accuracy of ARMPS-LAM, it was seen that ARMPS-LAM generally calculated a higher SF and was more successful at shallow cover (depths less than 1,000 ft), while it generally calculated a lower SF and was less successful at deeper cover (depths greater than 1,000 ft). This analysis indicates that the laminated overburden model (as implemented in LaModel/ARMPS-LAM) distributes less load for shallow cover and more load for deep cover than may be accurate. This observation indicates that a potential improvement for the laminated overburden model might be to enhance the accuracy of its load distribution mechanisms by increasing the AMZ load at shallow cover and decreasing the AMZ load at deeper cover. For instance, the new abutment loading algorithm proposed by Tulu and Heasley, (2012) could achieve this result. Also, in the future, more accurate coal pillar strength models (for instance strain-softening) could potentially improve the accuracy of ARMPS-LAM.

## REFERENCES


Darling, P. (2011). *SME Mining Engineering Handbook: 3rd Edition.* Englewood, CO: Society for Mining, Metallurgy, and Exploration, pp. 1840.

Dolinar, D. R. and Esterhuizen, G. S. (2007). "Evaluation of the effect of length on the strength of slender pillars in limestone mines using numerical modeling." In: *Proceedings of the 26th International Conference on Ground Control in Mining*. Morgantown, WV: West Virginia University, pp. 304–313.

Esterhuizen, G. S., Dolinar, D. R., and Ellenberger, J. (2011). "Pillar strength in underground stone mines in the United States." *International Journal of Rock Mechanics and Mining Sciences 48* (1): 42–50.

Heasley, K.A. (2008). "Some thoughts on calibrating LaModel." In: *Proceedings of the 27th International Conference on Ground Control in Mining*, pp. 29–31.

Heasley, K. A. (2012). "Calibrating the LaModel program for site specific conditions." In: *Proceedings of the 31st International Conference on Ground Control in Mining*. Morgantown, WV: West Virginia University, pp. 1–8.

Heasley, K. A., Sears, M. M., Tulu, I. B., Calderon-Arteaga, C. H., and Jimison II, L. W. (2010). "Calibrating the LaModel program for deep cover pillar retreat coal mining." In: *Proceedings of the ICGCM Pillar Design Workshop*. Morgantown, WV: West Virginia University, pp. 47–57.

Sears, M. M. and Heasley, K. A. (2013). "Calibrating the LaModel program for shallow cover multiple-seam mines." In: *Proceedings of the 32nd International Conference on Ground Control in Mining*. Morgantown, WV: West Virginia University, pp. 99–106.

Tulu, I. B. and Heasley, K. A. (2012). "Investigating abutment load." In: *Proceedings of the 31th International Conference on Ground Control in Mining*. Morgantown, WV" West Virginia University, pp. 1–10.

Tulu, I. B., Heasley, K. A., Mark, C. (2010). "A comparison of the overburden loading in ARMPS and LaModel." In: *Proceedings of the 29th International Conference on Ground Control in Mining*. Morgantown, WV: West Virginia Universiy, pp. 28–37.

Wagner, H. (1980). "Pillar design in coal mines." *Journal of the South African Institute of Mining and Metallurgy Jan. 1980*: 37–45.

Zhang, P. and Heasley, K. A. (2013). "Initial results from implementing a laminated overburden model into ARMPS." In: *Proceedings of the 32st International Conference on Ground Control in Mining*. Morgantown, WV: West Virginia University, pp. 239–247.

# FlexKnot: An Innovation in Roof and Rib Surface Control

**Anand Bhagwat**, Technology Steel Lead
Ground Support
Orica
Bowerston, OH

**Dale King**, Customer Technical Relations Manager
Bekaert Corporation
Van Buren, AR

## ABSTRACT

Surface control can prevent the falls of ground between primary roof support systems and rib support. Using existing industrial products, and adopting them for mining applications, has historically attained surface control in underground mining. However, the latest innovative solution, a revolutionary wire mesh product, is designed specifically for underground mining applications jointly by Bekaert and Orica. This knotted wire mesh, FlexKnot™ 2500 and FlexKnot™ 3500, uses smaller gauge, higher tensile strength wires, than a chain link fence or welded wire mesh. The higher tensile wire enables the mesh to achieve greater ultimate load-bearing capacity, with significantly lower overall weight. Test results, obtained at the National Institute for Occupational Safety & Health (NIOSH) Mine Roof Simulator facility, illustrate the comparisons of the new FlexKnot with traditional 8- and 10-gauge welded steel mesh. The FlexKnot is superior in deflection, load-bearing capacity, and stiffness–categories that are critical in achieving safer surface control. It also offers enhanced corrosion resistance because of the galvanized coating applied on the individual wires prior to the knotting process. Case studies from underground coal mine installations confirm that FlexKnot has the ability to significantly reduce installation cycle time and to minimize use and repetitive manual handling of individual mesh panels. An added advantage is the ability to supply FlexKnot in rolls for quick and easy handling for either rib or roof support application. When using rolls, the bolter can install the entire roll with one continuous forward motion, unlike the wasteful back and forth travel for mesh panel.

## INTRODUCTION

Roof and rib falls continue to be one of the greatest hazards in underground coalmines. The Mine Safety and Health Administration (MSHA) recognized this hazard and codified mine responsibility. In the Code of Federal Regulations (United States Department of Labor, 2013), it states, “The roof, face, and ribs of areas where persons work or travel shall be supported or otherwise controlled to protect persons from the hazards related to falls of the roof, face, or ribs and coal or rock bursts.” Support systems, consisting of bolts and mesh, have been used to control the immediate roof and coal rib in U. S. mines for many years (Smith, 1992; Dolinar and Tadolini; 1991).

The ground fall statistics support the MSHA hazard recognition. Ground falls traditionally cause between 500 to 600 injuries, and 10% to 15% of mine fatalities (Center for Disease Control and Prevention, 2014). The roof material involved varies in size, from small pieces of rock falling between roof bolts to larger materials that can result in injury or fatality. A recent tragic example occurred in 2013 when a 16-inch-thick slab of bolted roof, 7 feet wide by 8 feet long, fell and fatally injured the miner operator. Installing roof screens during the production cycle can significantly reduce these types of ground fall injuries (Robertson and Hinshaw, 2001).

Rib wall statistics are concerning. Fall of face/ribs attributed to 10 fatalities in underground U. S. coal mines from 2010 to 2013 (Mine Safety and Health Administration, 2014). Between 2006 and 2010, there were 525 injuries caused by rib falls, representing about 25% of the injuries from ground fall accidents. Seventy-five percent of the reportable rib fall injuries are lost time accidents with an average of over 100 days lost per incident (Mine Safety and Health Administration, 2014).

A closer review of the injury and fatality statistics highlight seam height and mine depth as some of the main factors that cause a coal rib hazard to form. The injury rate clearly increases with seam height due to the increased possibility of toppling failures. All but one of the fatalities during the 2010 to 2013 time period occurred at mine rib heights above 7 feet. Interestingly, most of the rib fall fatalities occurred at mine depths greater than 700 feet. This makes sense, considering the stresses imposed on mine ribs at these depths are significant. Additionally, higher rib walls combined with these depths increases the potential for high-energy intensive rib failures. Figure 1 is an example of how this condition allowed dangerous rib slabs to form and topple almost across the entire entry.

The basic purpose of any design for mine roof control is to provide safe containment of small pieces of roof or rib material that may fall between roof bolts. Containment provides miners with critical time to respond to a ground control situation, such as evacuation or installation of additional reinforcement. Therefore, the reinforcement must maintain a controlled containment response across its entire load capacity. The structural integrity of the reinforcement should not change unexpectedly.



**Figure 1. High ribs and roof supported withroof bolts and wire mesh.**

The current roof and rib support methods for U. S. mines fall into two main categories: welded wire mesh applied with intrinsic bolting systems and geo-grid materials that can be applied during or after the primary bolting cycle.

Intrinsic-based or rib-bolt-based support systems are the most widely used type of rib control. This system requires a roof bolt machine that can install a bolt fixture into the rib. The appropriate level of support needed to control the ribs with an intrinsic-based support system, as well as the design parameters for those support systems, vary by mine conditions.

The rib-bolt-based support system has been under evaluation in Australian coalmines for the over 25 years. In the 1980s, the Australians developed basic concepts on the rib failure mechanisms and possible support strategies. These studies determined that rib failure was, to a large extent, the result of the interaction between the coal seam structure and mining-induced fractures. Buckling was a key component of the failure process (O'Bierne and Shepherd, 1984; O'Beirne, Shepherd, Rixon, and Napper (1986). This was further confirmed in studies done in the 1990s (Fabjanczyk, Tarrant, and Guy, 1992; Frith and Ditton, 1993; and Ostle, Rataj, and Hebblewhite, 1998). These studies also looked at the performance and effectiveness of various rib support systems. It was found that rib support systems could be developed that would be able to keep damaged or failed coal in place without limiting the total rib displacement. Concrete reinforcement welded wire mesh became the primary solution because it was readily available in large quantities.

Now there is a new, innovative solution—a revolutionary wire mesh product that is designed specifically for underground mining applications. This knotted wire mesh, FlexKnot, is unique in its ability to respond to changing surface loading conditions while maintaining structural integrity. This is in contrast to welded mesh, originally designed for (the completely unrelated application of) concrete tension reinforcement. While concrete can withstand very high compressive loads on its surface, it does not perform well in tension as it begins to load. Therefore, the steel welded mesh, bonded in the concrete, provides tensile strength in the x-y plane and allows concrete to resist compressive bending.

However, the primary characteristics needed in mine roof control are both compressive bending force resistance due to surface loading and tension resistance due to bolt loading. Welded mesh was never designed to perform in this manner and, therefore, is limited in the key performance characteristic needed in mine surface control. Welded mesh, when used as roof/rib control, has two limiting factors: welded joint and tensile strength of wire. The weakest link is the welded joints, while loading capability is limited by the relatively low breaking strength of the individual wire. In fact, the minimum required weld shear strength is less than 50% of the strength of wire. Shear strength of wires, as a general rule of thumb, is approximately 50% of the tensile strength.

In mine roof application, severe bending of the mesh greatly increases the shear stresses in the welded joints. These stresses can cause the welds to fail before the wire reaches the tension point at which it will break (Figure 2). When the welds break, the roof surface load distributes across an increasingly smaller number of wires and reduces the structural integrity of the steel mesh. This can potentially lead to a chain reaction of weld failures (sometimes called "unzipping"). The unpredictable loss of structural integrity, thereby, diminishes the ability for the mesh to contain falling rock. This is illustrated later in a load vs. displacement relationship. Although weld mesh provides a resistance to load in the early stage of the surface loading, it rapidly diminishes once weld failures start to occur. Breakage of the welds results in the loss of structural integrity and in inconsistent or diminished load-bearing capacity throughout the remaining loading cycle.

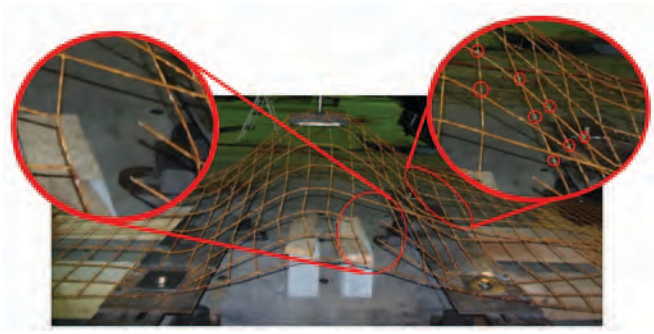


**Figure 2. Welded mesh illustrating wire breakage at the welds.**

In contrast, the FlexKnot design does not use welds to join wires together. Instead, the high-tensile strength wires are joined by a unique steel wire knot (Figure 3). Therefore, FlexKnot can use the full tensile strength of the high carbon steel wires in the x-y plane, following the predictable stress-strain response of the steel. With the unique knot design, the wires can bend in the z-plane without concern for brittle weld fracture. The tensile strength of the

FlexKnot wires is over 3 times higher than 8-gauge welded mesh wire produced per ASTM A1064-12 (ASTM, 2013). FlexKnot wires are also galvanized to offer superior corrosion resistance.

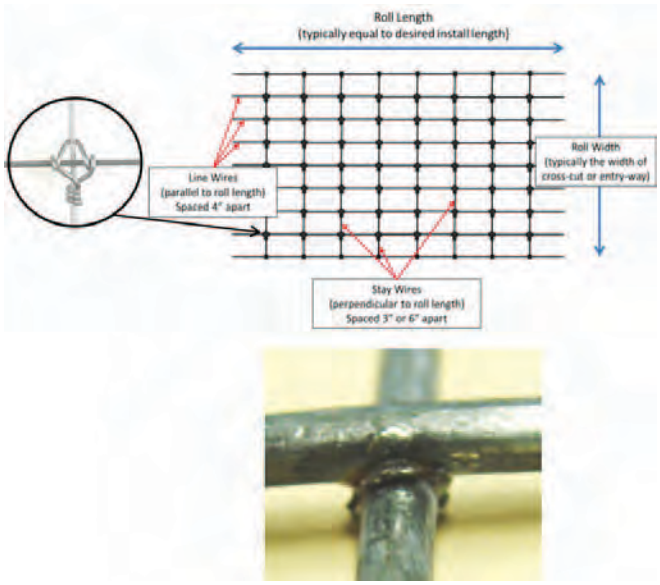



**Figure 3. Flexible knot in the new wire mesh (top) in comparison to welded mesh (bottom).**

The unique knot used in FlexKnot also provides the mesh with far greater flexibility than comparable welded wire mesh. The knot design allows the mesh to keep loads distributed over all wires rather than accumulating in a few wires. When loading increases too much in one location, the knot can slide slightly and distribute the load over more mesh surface area. By keeping the wires intact in both directions, FlexKnot continues to behave as a system almost across its entire loading capability. This process repeats itself until maximum loading is reached. The FlexKnot wire mesh also offers ergonomic benefits by significantly lowering weight per square foot compared to welded mesh panels (Table 1).

| Mesh Type. | Aperture, (inch x inch). | Weight, (lbs). |
|---|---|---|
| Welded Wire Mesh - 4 gauge | 4 x 4 | 81.5 |
| Welded Wire Mesh - 6 gauge | 4 x 4 | 59.1 |
| Welded Wire Mesh - 8 gauge | 4 x 4 | 42.1 |
| Welded Wire Mesh - 10 gauge | 4 x 4 | 29.2 |
| FlexKnot™ 2500 | 4x 6 | 13.9 |
| FlexKnot™ 3500 | 4 x 3 | 21.5 |

FlexKnot mesh can be applied easily in secondary support situations, where the roof areas that have only been supported with primary roof bolts are now progressively failing. This usually occurs after exposure to the cyclical effects of humidity and additional loading. Traditionally, to remedy these areas, a roof bolter is returned to the area, and additional bolts are installed with welded mesh panels. For areas supported with Tension Rebar (TR) bolting systems, an alternative system is available using FlexKnot rolls and Orica patented Gripper Plates that eliminates need for additional bolting. FlexKnot combined with Gripper Plates can provide savings in labor and costs.

FlexKnot rolls can be customized in size to approximate entry spacings at the required width and length. The roll is brought into the entry requiring support and unrolled onto the floor. The FlexKnot is pushed over the existing TR bolts and secured in place using the Gripper Plates (Figure 4). A gripper plate is installed on every bolt, overlapping about a foot at the seams of the next roll. The gripper plates were designed, developed, and tested to maximize the capacity of the FlexKnot mesh. The Gripper Plates have also been used successfully to affix mesh onto the last row of bolts during primary screening support programs, eliminating the need for additional bolting.

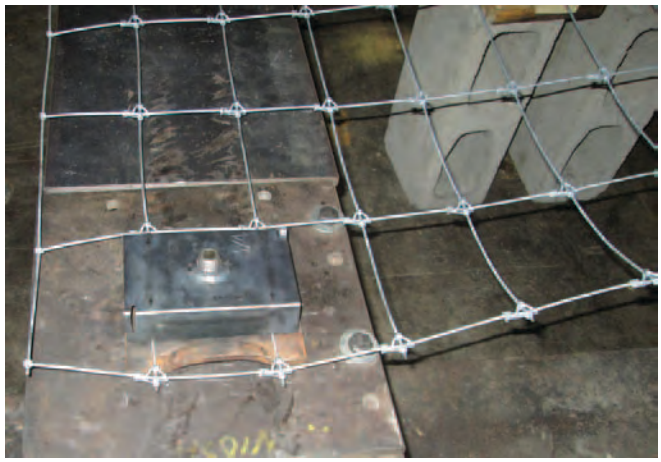


**Figure 4. Testing at NIOSH of the FlexKnot material on TR bolts fastened with Orica Gripper Plates.**

## LABORATORY SET UP AND TEST PROCEDURE

The NIOSH testing protocol and application hardware were used to evaluate the FlexKnot designs (Dolinar, 2006). To complete the NIOSH testing protocol, a test frame was installed in the Mine Roof Simulator (MRS). The NIOSH-designed frame allows for varying the bolt spacing from 4 feet to 5 feet. The test material was attached to the frame with four bolts (Figure 5). A one-foot-square load plate with rounded corners was used to apply the load to the center of the screen to simulate roof or rib material loading.

The tests were conducted in displacement control mode, with a displacement rate of 2 inches per minute. The FlexKnot mesh was displaced up to 20 inches during testing. The load was measured using a 20,000-lb external load cell with an accuracy of ± 20 lb. The screen displacement was monitored by using the Linear Variable Differential Transformer (LVDT) for the MRS control system with an accuracy of ± 0.01 inches. A computer recorded the load and displacement.



**Figure 5. Test frame set-up to test mesh materials using the NIOSH testing protocol (after Dolinar, 2006).**

To hold the screen on the test frame, 3/4-inch-diameter bolts, torqued to 150 ft-lb, were used with bearing plates. The bearing plates were flat, grade 4, and either 6 inches by 6 inches or 8 inches by 8 inches in size, with a thickness of 3/8 inch. The FlexKnot mesh was placed in a square configuration with respect to the test frame and bolts (Figure 5), similar to the typical installation in an underground mine. The mesh was sized to allow for a 6-inch extension beyond the bolts on all sides.

## RESULTS AND DISCUSSION

The FlexKnot wire tensile strength, with 2.48 mm diameter, is over 3 times higher than the 8-gauge welded mesh. This is illustrated in Figure 6.

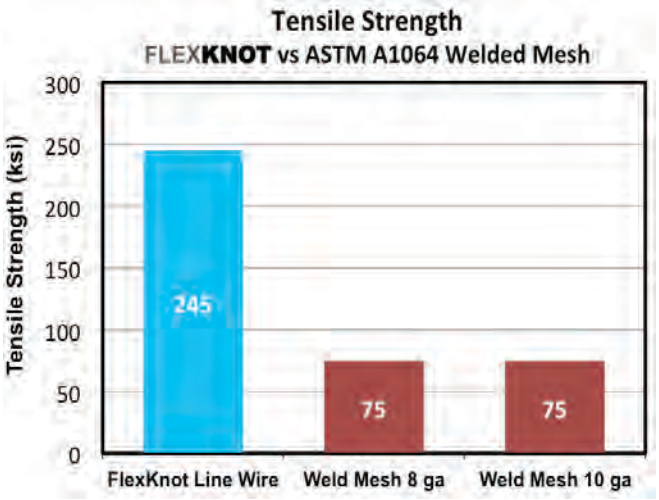



**Figure 6. Comparison of tensile strength of FlexKnot, 8 gauge and 10 gauge welded mesh.**

In laboratory testing at NIOSH, FlexKnot showed superior performance in deflection, load-bearing capacity, and stiffness compared to 8-gauge and 10-gauge welded mesh, as shown in Figures 7, 8, and 9.

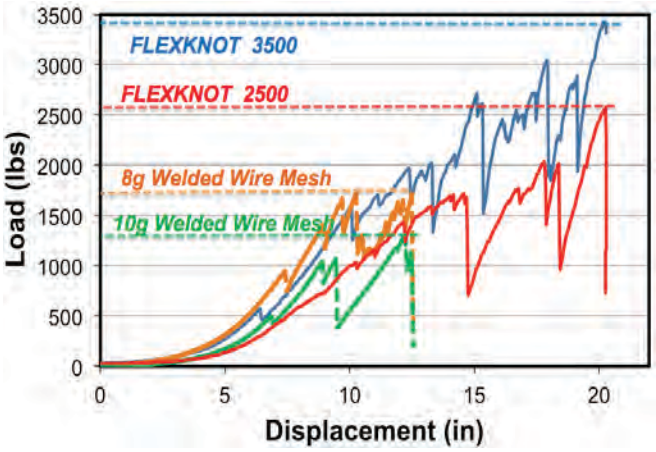



**Figure 7. Load/Displacement performance of FlexKnot and welded mesh.**

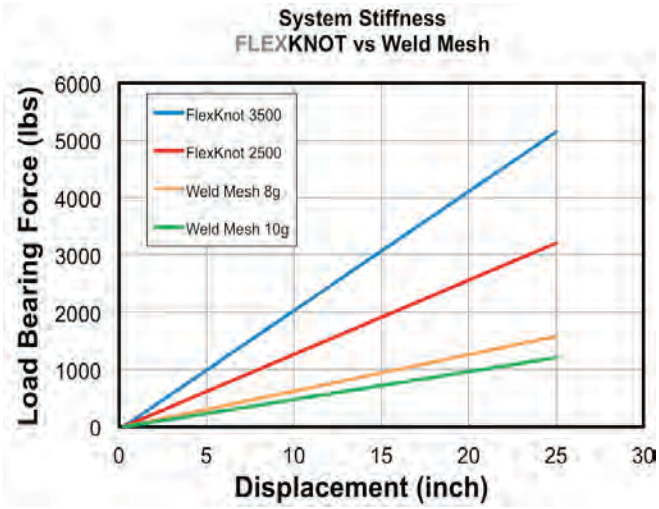



**Figure 8. Normalized load/displacement performance of FlexKnot.**

Because the FlexKnot design is based on a unique steel wire knot, and not welded joints, it uses the full tensile strength of all the high carbon steel wires. The end result is higher designed loading when compared to welded mesh, as shown in Figure 7. The sharp drop in Load for FlexKnot results from sliding and position adjustment of stay wire over line wire along the knots, whereas, it is due to weld and wire break in case of welded wire mesh.

The unique knot design of the FlexKnot mesh, combined with the use of high carbon steel wires, results in higher and consistent loading response, known as load-bearing capacity (loading force per displacement inch), throughout the loading cycle. This is illustrated in Figure 8, where a normalized load-bearing capacity of 8- and 10-gauge welded mesh is compared to FlexKnot 2500 and 3500. The Load/Displacement curve for each type of mesh was normalized by filtering the individual drops during the loading cycle, and by considering slope of the curve from start to finish of the loading cycle. It shows that the load-bearing capacity of FlexKnot 2500 is 2.6 times greater than 10-gauge welded mesh, and the FlexKnot 3500 is over 4 times greater than the 10-gauge welded mesh. This is due to the ability of FlexKnot to adjust and

distribute loading over more of its surface, maintaining structural integrity throughout the loading cycle. This comparison confirms that FlexKnot will carry more load than welded mesh. Holding more ground fall material in place provides miners additional protection and more time to respond to roof and rib fall events, directly improving safety.

When a roof/rib screen begins to load, it shows a characteristic known as "bagging" (Figure 9). As long as the screen maintains structural integrity throughout the loading cycle, bagging is a progressive visual warning of surface movement. However, if, during the loading cycle, the structural integrity of the screen fails (e.g., broken welds or wires), the bagging could lead to immediate, catastrophic failure. The "bagging" chart (Figure 10) shows that FlexKnot 2500 can "bag" more than welded mesh when the load is above 1000 lbs, because the FlexKnot maintains structural integrity. The higher "bagging" gives the desired progressive warning regarding rock fall, instead of the catastrophic failure or potential "unzipping" that is possible with welded wire mesh products.



**Figure 9. A wire mesh in roof support illustrating bagging.**

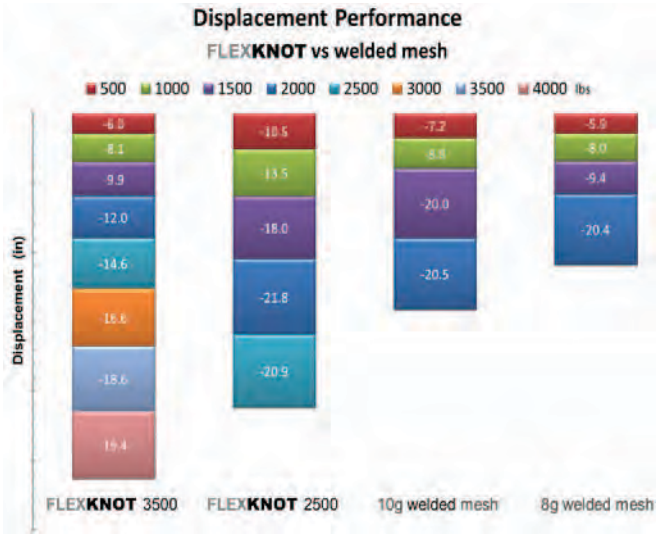



**Figure 10. Bagging performance of FlexKnot.**

## CASE STUDIES

### FlexKnot Used on Primary Bolting Cycle

FlexKnot 2500 was successfully tested underground at a coalmine in Western Kentucky. The trial was conducted with a fabricated payoff device, mounted to an existing bolting machine (Figures 11 and 12). This allowed the mining operation to use rolls of FlexKnot instead of panels. The FlexKnot rolls were customized so that the length matched the typical cut depth of the mine. The rolls were loaded on the bolter at the start of each bolting pass. The customized length allowed the entire roll to be installed without having to stop and cut any excess length.

The trials confirmed up to 50 percent reduction in cycle time, which was attributed to avoiding individual handling of mesh panels, minimizing the need to reload mesh panel stack between shifts, and eliminating the need to reverse the bolter at each mesh



**Figure 11. Fabricated pay-off device, attached to an existing bolter.**

panel loading to avoid exposure under unsupported roof. During the trial, the bolter started at the cut depth entrance and continued in a forward motion to the end of the cut length. The cycle time was reduced by almost 50 percent, yielding a lower operational cost of the bolter, as well as total labor cost of handling. These reductions translate to a potential increase in productivity by reducing the overall bolting cycle. The results of the testing were positive and showed tremendous promise for this newly developed roof support system by adding value through safety, productivity, and cost savings. Additional full-scale test areas are being negotiated with several different mining operators.

### FlexKnot Used on Remedial Support

An entry that was supported with FlexKnot is shown in Figure 13. The project prevented a bolting machine from moving back into the section. Using Gripper Plates eliminated the additional costs of rebolting and greatly reduced material and labor costs. The plates hold the mesh tight against the roof, developing the capacity of the mesh.



**Figure 12. Mesh being installed from a roll using an ATRS-mounted roll handler system. During the bolting cycle, the roll handler is designed to unroll FlexKnot up and over the front of the ATRS, as needed, automatically each time the bolter advances.**



**Figure 13. An entry was screened using combinations of FlexKnot and Gripper Plates.**

### FlexKnot for Rib Support

FlexKnot also minimizes hazardous rib sloughage and toppling failures. The material comes in rolls at the height pre-determined for the application. Once standing, the material can be bolted and formed into cavities and around corners using combinations of roof bolts and bearing plates. Figure 14 shows an application in a longwall operation where the ribs are subjected to heavy loading as the panel is extracted. The material provides protection for the workers and equipment during the complete mining cycle—development and panel recovery.

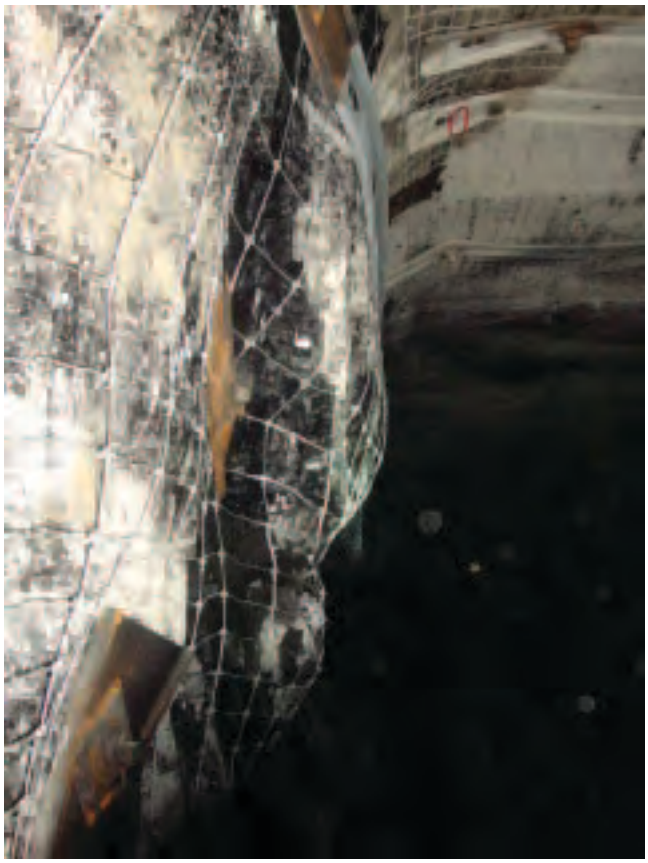


**Figure 14. FlexKnot conforms easily to irregular surfaces and wraps tightly around pillar corners.**

## CONCLUSIONS

The latest innovative solution, a revolutionary wire mesh product, is designed specifically for underground mining applications. Test results showed that FlexKnot is superior in deflection, load-bearing capacity, and stiffness, which are critical in achieving enhanced surface control.

The knotted wire mesh of FlexKnot 2500 and FlexKnot 3500 uses smaller gauge, higher tensile strength wires than those of a chain link fence or welded wire mesh. This results in 2.6 times more load-bearing capacity in FlexKnot 2500 and 4.2 times more in FlexKnot 3500, as compared to a 10-gauge and 8-gauge welded wire mesh, while lowering the overall weight. This weight reduction is especially important for ergonomic exposure of miners and lower transportation costs.

Through NIOSH tests, FlexKnot mesh also exhibits higher "bagging," which gives a progressive warning regarding roof falls instead of a catastrophic failure or "unzipping," as found in traditional welded wire mesh products. FlexKnot also offers enhanced corrosion resistance because of the galvanized coating applied on the individual wires prior to the knotting process.

Case studies from underground coalmine installations confirm that FlexKnot has the ability to significantly reduce installation cycle time, reduce handling of individual mesh panels, and

minimize reloading the stack of panels between shifts. In this case study, with the placement of the FlexKnot the need to reverse the roof bolter to avoid exposure to unsupported roof, which can occur when placing welded mesh panels was eliminated. Use of the rolled mesh provides the miners with a safer, more ergonomic product by eliminating the excessive bending, twisting, and lifting motions associated with working with mesh panels. The reduced product weight is more ergonomic, as well. Overall, this improves safety, reduces costs, and gets the miner back into coal quicker, which improves mining efficiency and increases total productivity.

FlexKnot has been used successfully to rehabilitate entries that were previously mined without mesh by attaching the material to the roof using Gripper Plates. Additionally, FlexKnot is a perfect application for rib support because continuous rolls of material can be easily bolted to support the ribs.

## ACKNOWLEDGEMENTS

The authors would like to acknowledge the invaluable testing assistance provided by the Ground Control Branch at the Office of Mining Safety and Health Research, Pittsburgh: Dennis Dolinar, Dave Gearhart, Tim Batchler, Tim Mathews, and Don Sellers.

## REFERENCES

ASTM. (2013). *ASTM A1064/A1064M: Standard Specification for Carbon-Steel Wire and Welded Wire Reinforcement, Plain and Deformed, for Concrete*. http://www.astm.org/Standards/A1064.htm

Center for Disease Control and Prevention—National Institute for Occupational Safety and Health. (2014). *Statistical Data on Occupational Incidents in Underground Mining*. www.cdc.gov/NIOSH/

Dolinar, D. R. and Tadolini, S. T. (1991). *Entry Stabilization Utilizing Rib Bolting Procedures*. US Bureau of Mines RI-9366, pp. 13.

Dolinar, D. R. (2006). "Load capacity and stiffness characteristics of screen materials used for surface control in underground coal mines." In: *Proceedings of the 25th International Conference on Ground Control in Mining*. Morgantown, WV: West Virginia University, pp. 152–158.

Fabjanczyk, M. W., Tarrant, G. C., and Guy, R. J. (1992). "Summary report no. 2: factors affecting design of rib reinforcement." *Final Report for AMIRA Project No. P207S-Optimization of Coal Mine Roof/Rib Reinforcement and Design Methods*.

Frith, R. C. and Ditton, S. (1993). "Stage 1 and 2 monitoring report for geomechanics of rib failure and development of appropriate support technology." *ACIRL Report EGE 3087/1*.

Mine Safety and Health Administration. (2014). *Accident, Illness and Injury and Employment Self-Extracting Files (Part 50 Data)*. http://www.msha.gov/STATS/PART50/p50y2k/p50y2k.HTM

O'Beirne, T., Shepherd, J., Rixon L. K., and Napper, A. (1986). "Coal rib stabilization - a new perspective." *The Coal Journal 14*: 7–11.

O'Beirne, T. and Shepherd, J. (1984). "The failure of coal pillar ribs and possible control methods." In: *Proceedings of the 4th Australia-New Zealand Conference on Geomechanics*. Perth, Australia: Preprint, pp. 661–667.

Ostle, S., Rataj, M., Hebblewhite, B., and Galvin, J. (1998). "Rib mechanics and support systems." *Final Report: ACARP Research Project C3059*. http://www.acarp.com.au/abstracts.aspx?repId=C3059

Robertson, S.B., and G. Hinshaw. (2001). "Roof Screening: Best Practices and Roof Bolting Machines," *Proceedings of the 21st International Conference on Ground Control in Mining*, Morgantown, WV, pp. 189-194.

Smith, W. (1992). "Rib Stability: Practical Considerations to Optimize Rib Designs." Bureau of Mines, IC 9323, pp. 16.

United States Department of Labor. (2013). *Title 30 Code of Federal Regulations: Part 75*. http://www.msha.gov/30cfr/75.0.htm

# Development of Road Header Roof Bolting Module

**Sean C Farrell**, Project Engineer
J.H. Fletcher & Co.
Huntington, WV

## ABSTRACT

In underground mining and tunneling, machine design is predominantly dictated by mine conditions and individual customer desires. In partnership with Australian companies WDS Limited and Cram Fluid Power, the engineering department of J.H. Fletcher & Company was tasked to design and manufacture roof bolting modules to be mounted off both sides of a roadheader, providing in-cycle bolting.

The objective was to produce a boom and bolt module that would allow an operator to bolt from a remote location, eliminating the need for miner to work in unsupported ground. The bolt module needed to operate in front of the cutting boom, but retract to a parked position out of the way during the cutting cycle. Due to Australian electrical approval requirements, it was desirable to design the module with minimal use of electrical controls. The need for multiple, complex, drill steel and bolt handling steps led to the need for a custom hydraulics package to automate several of the movements.

The result of the design is dual drill and bolt modules mounted to a multistage boom with over 24 feet (7.31 m) of extension. Each unit rotates and tilts to meet the bolt pattern requirements in conjunction with the stow and load requirements. The bolt module builds on previous designs incorporating a modular assembly with each sub-component designed to be replaceable and adjustable independently from other machine components. Each major component is painted a different color to help the operator make the connection visually from the module to the operator's control valves. Hydraulic package valves were designed to automatically control several of the sub-components during the drill cycle, reducing the number of steps a drill operator would, otherwise, have to do manually.

This design removes the operator from working in unsupported roof and away from other inherent hazards, putting them at a safe distance on the operator's platform. The cutting and bolting equipment has been combined into one machine, which is advantageous in single entry drifts because there is no need to place change equipment. The hydraulic package valves eliminate the need for any electronics, thus avoiding any electrical regulations with respect to the controls. The addition of these modules to the roadheading machine increases miner safety and streamlines production while meeting the ground control support requirements.

## BACKGROUND

Eagle Downs Coal is a mine that is currently in development, located in Central Queensland, Australia. The contract to develop the twin 1.24 mile (2 kilometer) drifts has been awarded to WDS Limited, an Australian-based mining development and engineering firm (Latimer, 2013). In the spring of 2013, J.H. Fletcher and WDS were finalizing the specifications for a set of booms and roof bolting modules to be mounted off the side of their Mitsui Roadheaders.

The critical requirements for the project were that the module must be able to work inby the roadheader cutterhead, be able to retract to a parked position that would not interfere with the roadheader during its cutting cycle, and be able to install two different customer-specified bolts within 15-3/4 inches (400 mm) of the face. WDS did not wish to use a pass-by bolter, a separate piece of mobile equipment named for its narrow stance that allows it to pass by the side of cutting equipment and bolt the roof. This was driven by the desire to not expose equipment operators to the ground inby the last row of supported roof.

Design requirements for underground mining equipment in Australia are shaped by the New South Wales *Mining Design Guidelines* (MDG) (New South Wales Trade & Investment, 2014). The project schedule was very tight; therefore, we did not want to introduce new electrical components because it would take time to design them to the MDG requirements. This shifted the focus for drilling controls from a controller area network (CAN) bus-based software to using a combination of sequences and cam valves.

The initial proposal revolved around a traditional bolt module from the Fletcher AR-D roof bolter, used primarily in US metal/non-metal mines. This module consists of two drill feeds on a rotating shaft. One feed is dedicated to drilling the hole, while the second feed picks up a bolt from a magazine that is capable of storing multiple resin bolts and install them at the proper torque. Additionally, the module is fitted with a resin arm that swings to the hole centerline. The reliability of this design has been proven over the past three decades but, ultimately, was deemed to be

unacceptable because the bolts could only be installed to within 39.37 inches (1 m) of the mine face.

## THE DESIGN

Fletcher has operated with a singular focus for many years: to work with a vigilant focus on finding ways to improve mining processes and reducing risk for the people who work there. From this focus has come the development of a series of semi-autonomous bolt modules designed to allow an operator to install roof bolts from a remote location. A recent iteration of this module, deployed in South Africa, met the bolt installation requirements for the Eagle Downs project.

This module allows WDS to install bolts to within 15-3/4 inches (400 mm) of the face as required. It also was lighter and packaged tighter than the AR-D bolter, qualities that were desirable given the massive length of boom that would be required to reach inby the cutterhead. However, the module was not without drawbacks. The unit did not have the long history like the AR-D, nor had Fletcher developed one without the use of electrical components. Additionally, the South African unit was designed around 67-inch (1.7 m) long bolts and would need to be lengthened to work with a 106-inch (2.7 m) bolt.

The top centralizer uses three arms that close in an innovative camera shutter concept. The arms are able to fully retract to allow a roof plate to pass through, but they provide complete support to the drill steel or bolt when deployed. With a change out of the manipulator hand and top centralizer clamps, as well as the bolt carousel plates, the customer is able to use a variety of bolt types and sizes. The resin arm also has a replaceable nozzle to accommodate shooting resin cartridges for one bolt type or pumping grout for the post grouting operation that takes place with the mechanical bolts.

It was determined that the boom structure holding the module would need approximately 24 feet (7.3 m) of reach. This would require a new boom design incorporating one of the largest extensions that Fletcher has ever built. A parallel linkage design (See Figure 1) was part of the early proposals. This design allowed for some of the extension to be accounted for off the side of the machine. The links reduced the amount of boom section that would be cantilevered out of the cradle, but they had drawbacks. The links traveled in an arc, creating the need for complete clearance above the boom to avoid crashing components together. Below the boom, where the links were located, also needed to remain clear to allow operation. After several months of development, WDS ultimately decided that the space the links occupied was needed for mounting other components, and the design moved in a different direction.

What resulted was an improved design that was built: a two stage box section boom, with 146 inches (3.7 m) of extension for each section (See Figure 2 and Figure 3). Through experience with Fletcher metal/non-metal bolters, Fletcher identified that the area the boom rollers contacted on the box sections could potentially be a weak spot. In lieu of a single boom roller, large dual diameter rollers were mounted onto a central pivot, keeping the surface stresses to acceptable levels. The dual rollers were used on the front and back of the cradle, on the bottom of the outer boom and the top of the inner boom.

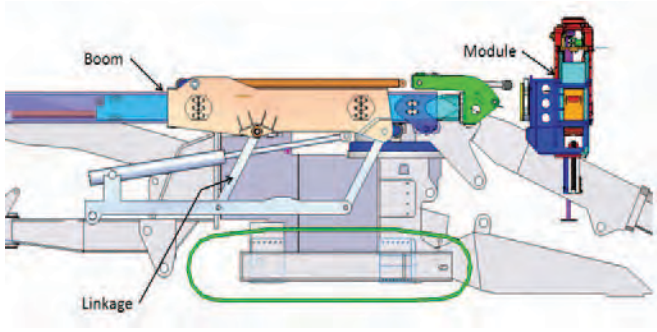



**Figure 1. Side view of early proposal with linkage style boom extension.**

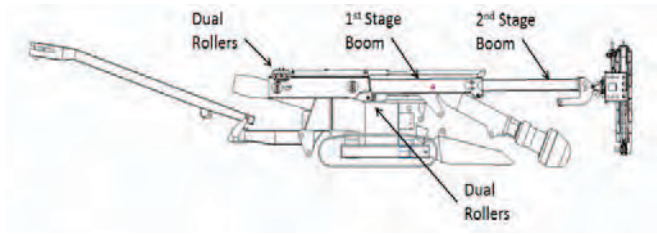



**Figure 2. Side view of final design showing module extended in its drilling position.**

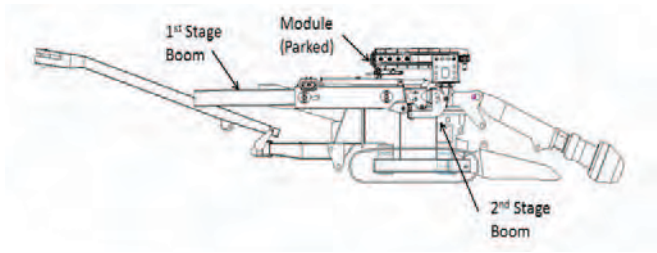



**Figure 3. Side view of final design showing module in parked position.**

The project not only presented the engineering staff with new and unique challenges, but also challenged Fletcher welders to develop new techniques to fabricate these large booms. The size of the boom sections was such that manufactured shapes, such as square or rectangular tubing, were not practical. Therefore, we opted to fabricate box sections out of high-strength steel. The outer booms reached over 28 feet (8.5 m) in length and required even and complete pre-heating to weld properly. Custom heat tables were constructed to assist in the fabricating and pre-heating the booms. The welding for each component was completed in one continuous session in an effort to not waste the energy of pre-heating, as well as to prevent the long boom from bowing due to repeated heating and cooling cycles.

The final challenge in the design phase was being able to complete the functions required to drill and install bolts with the module (See Figure 4) from a remote location nearly 40 feet (12.2 m) away. The following list details the steps required to drill the hole:

1. Use Manipulator hands to retrieve drill steel from storage rack.
2. Position drill steel over drillhead and couple into drill chuck.
3. Slightly open Manipulator hands to act as drill guide.

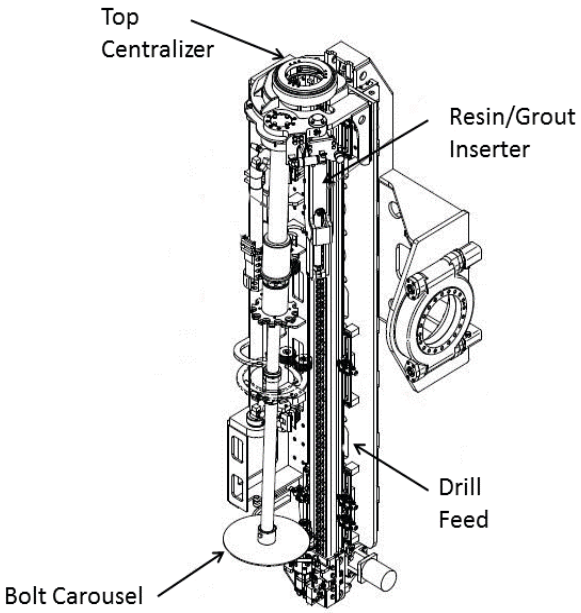



**Figure 4. ISO view of bolt module.**

4. Actuate feed and rotation to begin drilling hole.
5. Move midpoint centralizer to drill centerline.
6. Close midpoint lock to guide drill steel.
7. When drill depth allows, open manipulator hands.
8. Retract manipulator hands to stored position.
9. Open midpoint centralizer lock.
10. Retract midpoint centralizer to stored position.
11. Open top centralizer.
12. After hole has reached full depth, reverse feed direction to bring drill steel out of hole.
13. Move manipulator hands to drill centerline.
14. Close manipulator hands to guide retracting drill steel.
15. Stop the drillhead at the correct height for uncoupling.
16. Uncouple drill steel and clamp with manipulator hands.
17. Lower drillhead and store drill steel.

This list does not include boom positioning, applying resin/grouting, or installing and torqueing the bolt. The tasks required can be overwhelming for a drill operator without the assistance of a computer system to help automate the process. Through a series of custom package and cam valves, Fletcher was able to automate steps 5 through 15, significantly aiding the drill operator in their duties without adding any electric components that would need to meet the Australian MDG regulations.

## BUILDING/TESTING

In early January 2014, with the assembly of the booms and modules nearing completion, test drilling began. It was quickly determined that the new style top centralizer was fouling with drill cuttings. The pieces were modified with reliefs in the housings to allow for the cuttings to clear when the centralizer arms retract.

The test drilling also identified areas for improvement available in the hydraulic system. The midpoint centralizer did not have a manual override to retract it to its parked position. Deployed by actuating a cam valve during the forward drilling cycle, there was no way to return the midpoint to its home position without actuating an upper cam valve. In an aborted drillings cycle, this may not be possible. The updated package allowed the manual return of the midpoint centralizer. This also allowed Fletcher the opportunity to upgrade the size of all the sequence and shuttle valves internal to the block, reducing the pressure losses in the system.

## CONCLUSIONS

As of Spring of 2014, the booms and modules are currently in Australia and being fitted to the roadheader machines by WDS. The first of two roadheaders is due to leave their facility and travel to the mine site at the beginning of April 2014.

Because the machines have not yet been deployed to the mine, a review of the project objectives is in order to determine the success of the project:

- The bolt modules and booms successfully meet all the roof control requirements.
- A change out of parts allows conversion between multiple bolt types.
- The need for an operator to work in unsupported ground is virtually eliminated.
- No electrical allowed for quick adherence to MDG rules.
- Complex steps are aided by semi-autonomous hydraulic drilling operations.

The machines are due to be the center point of a multiple-year project at Eagle Downs Mine. We have, at this point, met all the engineering and manufacturing challenges. As this design goes to work in its intended environment, J.H. Fletcher & Company looks forward to providing more innovative solutions to improve operator safety and mine production.

## REFERENCES

Latimer, C. (2013). "WDS wins massive Eagle Downs coal contract." *Australian Mining*. http://www.miningaustralia.com.au/news/wds-wins-massive-eagle-downs-coal-contract

New South Wales Trade & Investment. (2014). *Mining Design Guidelines*. http://www.resourcesandenergy.nsw.gov.au/miners-and-explorers/safety-and-health/publications/mdg

# Development of Mechanized Ground Support Installation Equipment for Improved Safety in Narrow Vein Mine Conditions

**William Kendall**, Manager of Research and Development Engineering
J.H. Fletcher & Co.
Huntington, WV

**Mark Ferster**, Ground Control Engineer
Stillwater Mining Co.
Nye, MT

## INTRODUCTION

Stillwater Mining Company, with its two underground, hard rock mines in South Central Montana, is the largest primary producer of palladium and platinum in the Western Hemisphere. Platinum Group Metals (PGMs) are mined from a specific zone within the Stillwater Complex, a layered mafic/ultramafic igneous intrusion, named as the J-M Reef. Over much of the J-M Reef, the economically minable, mineralized horizon is contained at typical horizontal widths of 6.5 ft to 8 ft wide. This feature of narrow mining widths has made it challenging to safely and effectively mine these areas of the J-M Reef using mechanized cut and fill and sublevel sill development mining methods. Mechanization of most or all of the steps of the mining process is important to Stillwater in the continuous pursuit of high standards in safety and health. Mechanized bolting within the J-M Reef ore production headings is an important piece of reaching these objectives.

In general, metal/non-metal mining requires varied mining techniques, as compared to more traditional bedded mineral/resource deposits. Narrow vein mining is a selective mining technique that generates a minimal amount of waste material while obtaining the more valuable ore deposits. Drilling and bolting in narrow vein mining has traditionally been performed with air-powered, hand-held "jackleg" equipment because mechanized equipment is, typically, too large for the selective narrow vein techniques. In addition, traditional hand-held pneumatic equipment provides significant flexibility for small-opening, narrow-vein developments, reducing waste rock handling and improving ore recovery management. The hand-held equipment is also relatively inexpensive to purchase. Due to its simplicity, it is also relatively easy to train operators to use hand-held equipment.

Hand-held equipment has been routinely used to safely install ground support and to develop production faces in hard rock mines for many years. Although it is effective, the hand-held equipment requires operator exposure to certain inherent hazardous conditions in the active face/development mine areas. These include falling rock, tripping hazards, bending/twisting/lifting hazards, high noise levels, and chemical fumes from the hammer exhaust. Based on health and safety statistics from the Stillwater mines, operation of the rotary-percussive hand-held equipment adversely affects the long-term health of the operator—continual jackleg operation frequently results in long term damage to hearing, shoulders, arm and wrist joints, and back injuries. This reduces the quality of life for the operator and also results in higher personnel turnover rates for the mining company.

Mechanized equipment has the possibility to improve workplace safety, reduce operator exposure (compared to hand-held equipment), and provide improvements to the health of the underground hard rock miners (Figure 1 – Jackleg Operation).



**Figure 1. Picture of jackleg drilling.**

With the goal to improve the safety and health of the mining workforce, the Stillwater Mining Company, in conjunction with J.H. Fletcher & Company, initiated the development of a machine for narrow opening ground support installation in February 2012. J.H. Fletcher has a long, proven history for the development of mechanized drilling and ground support installation machines to improve safe extraction of mineral resources.

The machine had to be acceptable to the miners and be cost effective. It needed to not only provide a safer environment for ground support installation, but also match the flexibility of the hand-held equipment, perform the ground support installation in a productive manner, and compare favorably to the current support installation process. This meant the machine had to be able to install a variety of roof support types and mesh for surface control. It also had to provide a reliable tram system, capable of negotiating uneven floor, make 90-degree turns in narrow openings, and travel ramps of up to 19% grade (Figure 2 – Stope Cross Section).

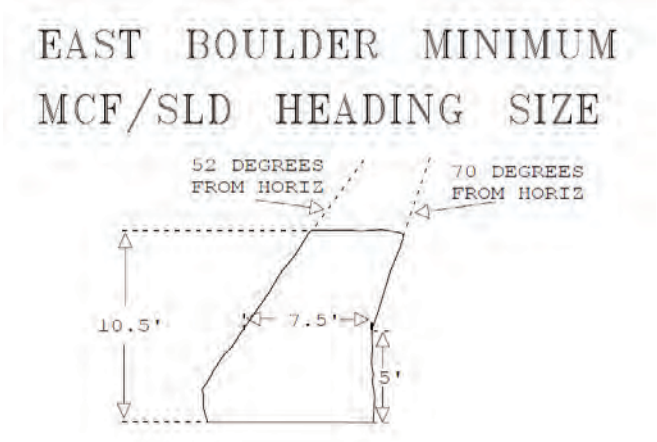



**Figure 2. East Boulder heading size drawing.**

J.H. Fletcher design engineers worked with Stillwater engineers, operators, managers, and maintenance personnel at both mine sites to identify specific characteristics and requirements (mine opening irregular dimensions, available power systems, operational production sequencing, etc.). Throughout the process, Stillwater personnel were actively involved in the design of the machines. In 2013, Stillwater ordered two machines, one for each mine, to allow evaluation of the concept and the machines (Figure 3 – Bolter on Surface).



**Figure 3. Picture of bolter on the surface at East Boulder Mine.**

The machines (one for the East Boulder Mine and one for the Nye Mine) were delivered at the end of 2013. They are 4.5 ft wide, rubber tired, articulated chassis, diesel tram, electric bolt, HDR-D/E bolters. They use a lifting and swinging boom to keep the operator close to the work area. The operator can tram from the chassis or the bolting platform where they are under an MSHA approved canopy. The machine uses a low profile rotary percussive drill head and can install virtually any type or length of bolt.

During the first six weeks of 2014, they were trammed up and down numerous ramps and operated by a variety of operators in different areas of both mines to gain experience. Modifications were made as needed. In mid-February of 2014, the machines were turned over to the mines as production machines.

The machines were evaluated against the following design requirements:

- Improve safety (versus a jackleg)
- Tram effectively, negotiate ramps and intersections, and be stable
- Tram, drill, and bolt in 6.5-ft-wide stopes
- Reach to a maximum bolting height of 14.5 ft
- Install bolts as perpendicular to all rock faces as practical
- Install 5-ft friction bolts
- Install 8-ft and 12-ft torque tension rebar bolts with no changes to the machine
- Aid in the handling of 4 ft x 8 ft wire mesh panels
- Be efficient enough to support (drill, bolt, and mesh) two 9-ft-deep to 11-ft-deep places and tram up to 1.5 miles in one shift

The following are comments on the evaluation points.

**Improve safety versus a jackleg**

- Operator is under a protective canopy for protection from rock falling while bolting and installing mesh.
- Operator only handles drilling tools and bolts versus handling the jackleg with hoses and handling mesh.
- Wire mesh can be installed remotely using the machine—no temporary supporting of mesh on scaling bars or using "mickies" (short split set bolts which fit inside existing split set bolts)
- The noise level is reduced versus a jackleg. Maximum noise level at the operator's ear was measured at 113.6 dba. (For reference, a jackleg drill operates at 117 dba to 125 dba.)
- The lifting and swinging boom keeps the operator close to the drilling area, even at a maximum working height of 14.5 ft.

**Tram effectively, negotiate ramps and intersections, and be stable**

(see Figure 4 – Machine Articulated and Figure 5 – Basket Offset to Chassis)

- The machine efficiently trams up and down the ramps (up to 19% grades) and negotiates turns and 90-degree intersections.
- Engine torque during tramming is between 33% on flat ground to a maximum of 47% on 19% grade. No overheating is experienced.
- Machine is very stable while tramming and bolting.
- Operator visibility and lighting is adequate while tramming and bolting.




**Figure 4. Picture of machine articulated.**




**Figure 5. Overhead picture with basket parallel to chassis.**




**Figure 6. Picture of SV-32 Hammer.**

**Tram, drill, and bolt in 6.5-ft-wide stopes**

(see Figure 6 – Low Profile Hammer, Figure 7 - Bolting, Figure 8- Bolting, and Figure 9- Canopy Contour)

- Machines have successfully bolted in stopes 6.5 - 8 foot wide. Figure 6 – Low Profile Hammer, Figure 7 - Bolting
- They fit and bolt in 6.5-foot-wide stopes. Figure 8- Bolting, and Figure 9- Canopy Contour
- Machines are averaging approximately 3 hours to bolt a cut. They have bolted cuts in approximately 2.5 hours. This time isexpected to improve with planned modifications and improved operator skill level.



**Figure 7. Picture of bolter in the stope.**



**Figure 8. Picture bolting at maximum height.**




**Figure 9. Picture of canopy and roof.**

- Drill and bolt time for a 5-ft friction bolt is approximately 2 minutes.
- As expected, correct tooling, two-piece 8-ft bolts, feed length, and safe mesh handling are all critical to safe, efficient operation.
- Even bolting at full back height, there is adequate room for the operator, positioning of feed, and handling of steels and bolts.

**Install bolts as perpendicular to all faces as practical**

(See Figure 10 – Bolts Perpendicular)

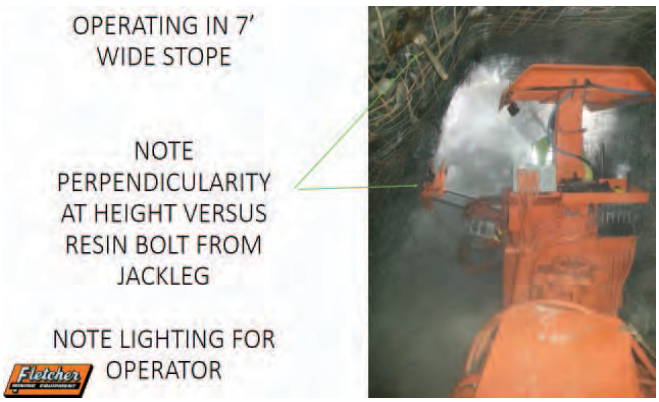



**Figure 10. Picture of bolting the hanging wall.**

- Lifting boom allows bolts to be installed perpendicular to faces even at height. (Figure 10 – Bolts Perpendicular)
- The machine possibly allows for changes to the blast pattern for better ore recovery since the high reach bolts can be installed at a better angle than was possible with jacklegs.

**Handling mesh with feed**

- Operators can wire together up to three pieces of mesh and lift them into position using the feed.
- The operator can bolt the mesh into place without leaving the machine, installing "mickies," or setting scaling bars.

## MAJOR ACCOMPLISHMENTS

- The machine fits in the 6.5-ft-wide stopes with angled hanging and foot walls
- The machine is very stable.
- There is adequate room for the operator, positioning of the feed, and handling of steels and bolts, even when the canopy is up to the back.
- The machine drills very well. It drills at 3/4 in/sec (3.75 fpm).
- The machine inserts 5-ft friction bolts in 9–10 seconds.
- Noise level at the operator has been lowered by over 3 Decibel.
- Zero injuries have been experienced during the trial period.

## MACHINE ACCEPTANCE BY THE OPERATORS

Although the machines have met all technical specifications, the operators have not fully accepted them. Part of the reason for non-acceptance is cultural. It is a significant change, due to complexity of the machine versus a jackleg. The new machine also requires the operators to learn a new piece of equipment and change their operating techniques. In addition, further modifications to the machines are required to reduce the reach of the operator when changing drill steels and handling bolts, improve controls, and improve feed positioning ability.

## SIGNIFICANT PROBLEMS – INEFFICIENCIES

Although the new machine is an improvement, there are still some inefficiencies to address. The operators must become familiar with the controls and gain experience in using a mechanized piece of equipment. This can be a difficult change for many operators. Ergonomics must also be improved. Currently, the valve placement obstructs the operator movements. The movement direction and number of control valves has proved to be a challenge. Efficiency in positioning of the machine is limited by lack of a basket extend and auto basket level. During planned upgrades all control valves will be replaced with electro-hydraulic joysticks and a 3 operating mode selector system to reduce the number of controls, space required, and to provide logical movement direction of the handles. Written labels will be replaced with pictograms back lit with distinctive light colors based on mode of operation. Auto basket level and basket extend will be added. Changes will be made to the feed positioning system to provide a more open material handling area.

## WHERE WE GO FROM HERE

Stillwater is very committed to continuing development of new generation drilling and roof bolting machine to replace jacklegs. To date they have shown that they are safe to operate with reduced operator exposure and no injuries to date, reduced noise level, flexible in the type and length of bolts which can be installed, and comparable to a jackleg from a productivity standpoint (planned upgrades should significantly improve efficiency). The current machines will run until the upgrades are available in mid-2014. After the upgrades are complete, Stillwater will re-evaluate both machines.

# Introduction of a New Superior Coating on Ground Support Products

**Renn Oler**, Engineering Director
DSI Underground Systems Inc
West Jordan, UT

**Jinsheng Chen**, Director of Rock Mechanics/Technical Support
DSI Underground Systems Inc
Martinsburg, WV

## ABSTRACT

Corrosion can often cause significant strength reduction and failure of steel rockbolts, thus demanding continuous rehabilitation and posing challenges to underground mines in maintaining long term ground support. The mining industry has traditionally applied galvanized and epoxy coatings for protection of ground support and reinforcement in corrosive environments due to cost considerations. However, under a harsh and corrosive groundwater condition with extreme pH levels, failure of the existing coated rockbolts often results in failure and falls of the mine roof, especially in long-term mine drifts or entries. To prevent the roof falls induced by corrosive bolt failure, DSI developed a new polymer coating, called "Obduro AP coating," to combat harsh and corrosive ground conditions. The new polymer coating was tested in extreme conditions to identify weaknesses and was found to be capable of handling highly corrosive mine water solutions.

This paper highlights the challenges faced by underground mines with corrosive bolt failure and shows that the DSI Omega Bolt™ can withstand the most corrosive ground conditions when it is coated in the new, economic Obduro AP coating.

## INTRODUCTION

Traditionally, a variety of finishes have been used to reduce the corrosion of steel rockbolts and other components of a rockbolting system, such as steel plates and washers. However, these have proven ineffective in extreme acidic and alkaline substrates. Using a zinc galvanized finish is very common in the hard rock mining industry. The chemical bond provides excellent abrasion resistance and corrosion creep properties. In general, the thicker the zinc coating, the longer the life of the product. Zinc is an excellent shielding agent in alkaline conditions, but performs poorly in an acidic environment. The overall cost of manufacturing and applying a coating add to the challenge of providing an economically sound product. It is also difficult to apply a zinc coating to some products that requires a great deal of flexibility, such as the Omega Bolt. Epoxies are also challenged in a corrosive environment, especially where flexibility is a requirement. Although some are resistant to acid corrosion, their inflexibility and high costs are a limiting factor in their use.

Under extreme, corrosive, underground conditions, a rockbolt using traditional coatings can deteriorate rapidly, and its ultimate strength can also drop significantly due to pitting or stress corrosion cracking (Aziz et al., 2013). Therefore, the reduced ultimate strength of rockbolts due to corrosion will further weaken the integrity of the bolted mine roof. In this scenario, rehabilitation is often required and must be performed on a regular basis to eliminate safety hazards caused by roof failure and falls. This regular rehab requirement renders the traditional epoxy and zinc galvanized rockbolts obsolete in terms of miners' safety and ground control cost.

Figure 1 shows the failed rockbolts due to corrosion at Mine A, where both the rebar bolt (A) and the zinc galvanized, inflatable (ERB) bolt failed 30 days after the installation. It should be noted that the inflatable bolt was pulled out by hand. A similar corrosive ground condition was also found at Mine B, where roof/rib meshes were destroyed within 6 days after the installation, as illustrated in Figure 2. Both mines are located nearby Elko, Nevada, USA. These two mines required regular rehabilitation every 30 to 45 days before the new DSI coated bolts were used.

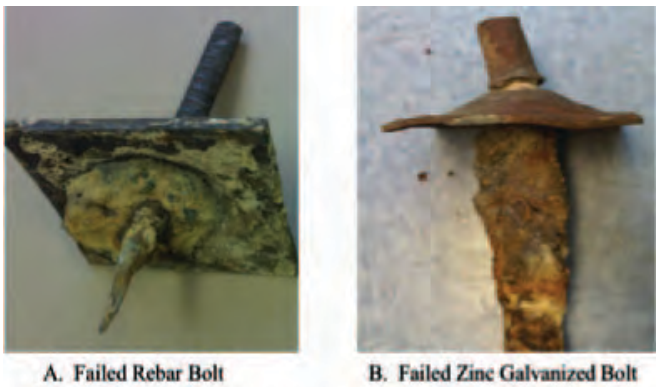



**Figure 1. Failed rockbolts after sixty days at Mine A.**

After reviewing the market requirements, some key criteria were identified in selecting the rockbolt coating. Molecular bonding of the traditional coatings is a clear weakness, along with other key characteristics, such as strength, durability, and flexibility. Certain polymers have the characteristics to overcome these challenges.

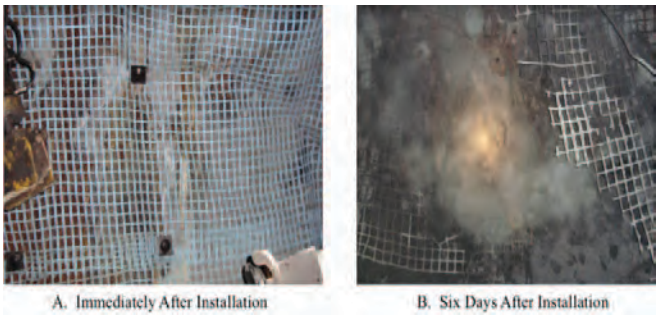



**Figure 2. Mesh damaged in six day at Mine B.**

## LABORATORY TESTING AND RESULTS

DSI developed a new polymer coating and tested it in highly acidic and electromagnetic underground solutions from two underground gold mines in Nevada, USA. The new coating was also tested in extreme pH conditions, using chemicals, such as sulfuric acid, hydrochloric acid, and sodium hydroxide. Table 1 lists the more volatile solutions tested. Also included in testing were hydrogen peroxide, hypochlorous acid, and sodium hypochlorite.

**Table 1. Acid-base types.**

| | |
|---|---|
| $H_2SO_4$ | Sulfuric Acid |
| HCl | Hydrochloric Acid |
| NaOH | Sodium Hydroxide |
| Mine 1 | High acidic mine solution |
| Mine 2 | High acidic mine solution |

The coated product samples used for testing were as follows: cut Omega Bolt sections, a washer, and the polymer coating itself. The thicknesses varied and have been proprietarily optimized per environment and product feature requirements. These samples were tested in the various solutions at different concentration levels. Tests were performed in glass jars, test tubes, or glass/plastic Petri dishes. Figures 3 and 4 illustrate the test containers and the new coating samples used. For purposes of comparison, the traditional zinc galvanized bolt was also tested in the various solutions at different concentration levels.

Table 2 outlines the details of the testing results for the DSI new coating samples. The DSI new coating Omega Bolt did not corrode in either of the two high acidic mine solutions after 72 days, as shown in Figure 5. The same thing is true for the DSI new coating washers too, shown in Figure 6. It can be seen, from Figure 7, that no corrosion occurred after the washers were left in both solutions for 72 days. There was one interesting event during testing of the Omega Bolt and the washer in the hydrochloric acid; immediate oxidation of the hydrochloric acid occurred, but there was no reaction with the coating after 72 days, as illustrated in Figures 8 and 9.

At lower concentrations of 14 percent and 32 percent, the new coating does not show any signs of corrosion in a 72-day period. The Mine 2 solution was highly corrosive to the traditional zinc galvanized bolt, which reacted violently with Mine 2 solution after only 30 minutes of exposure.



**Figure 3. Containers used for testing: petri dishes, glass jar and test tubes.**




**Figure 4. The tested DSI new coating sample.**

## FIELD TESTING RESULTS

DSI conducted a series of underground tests of the new polymer-coated Omega Bolts in both Mines 1 and 2, where highly acidic mine solutions have been present since January 2012. These two mines had to be rehabilitated every 30 to 45 days after bolt installation when the traditional zinc galvanized bolts were used. Figure 10 illustrates the result of the pull test conducted on an Omega Bolt 90 days after it was installed at Mine 2. The bolt was successfully pulled the expected 12 tons without damaging the bolt. DSI also cored out the area around one of the bolts. The bolt was completely coated in acid solution buildup, however, after rubbing off the buildup, the bolt had no surface damage, and the point anchoring locations did not cut through to the bolt. At the same location, the traditional zinc galvanized bolts, which were installed at the same time, were pulled out by hand, as illustrated in Figure 11.

Using DSI Omega Bolts with the new coating (identified as DSI's Obduro AP coating) has reduced the rehabilitation requirements at both mines since early 2012. DSI is currently reviewing the coated Omega Bolts bi-annually.

## SUMMARY AND CONCLUSIONS

The new DSI polymer coating, Obduro AP, is capable of handling both highly acidic and corrosive mine water solutions, as well as sodium hydroxide 50 percent or less, hydrochloric acid 36 percent or less, and sulfuric acid 32 percent or less. DSI tested the Obduro AP coating in extreme conditions to identify weaknesses. None of the acids or bases tested are seen in nature above 30 percent concentration and, even that, is a rarity.

There are three key reasons this new coating shows greater promise than what is currently on the market:

**Table 2. Results of the tested DSI new coating samples.**

| Sample | Coating | Acid Type | pH | Concentricity | Entry Date | Results |
|---|---|---|---|---|---|---|
| A | Omega Bolt | Mine 1 | very low | 10% - 20% | 2-Jun-11 | None (no corrosion) |
| E | Washer | Mine 1 | very low | 10% - 20% | 2-Jun-11 | None, clear acid |
| F | Washer | $H_2SO_4$ | 0.3 | 14% | 2-Aug-11 | None, clear acid |
| I | Omega Bolt | $H_2SO_4$ | 0.3 | 93% | 26-Jul-11 | None, clear acid |
| J | Omega Bolt | HCl | 0.8 | 36% | 26-Jul-11 | Slight yellow oxidation, no corrosion |
| K | Washer | $H_2SO_4$ | 0.3 | 93% | 26-Jul-11 | None, clear acid |
| L | Washer | HCl | 0.8 | 36% | 26-Jul-11 | Slight yellow oxidation, no corrosion |
| M | Washer | NaOH | 14 | 50% | 2-Aug-11 | None, clear acid |
| T | Polymer | $H_2SO_4$ | 0.3 | 32% | 2-Aug-11 | None, clear acid |
| P | Washer | NaOH | 13 | 25% | 2-Aug-11 | None, clear acid |
| Q | Washer | $H_2SO_4$ | 0.3 | 32% | 2-Aug-11 | None, clear acid |
| S | Washer | Mine 2 | very low | 10% - 20% | 1-Aug-11 | None |

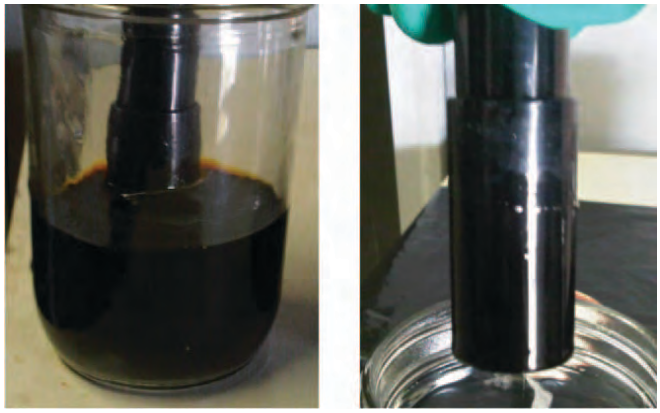


**Figure 5. Sample A - Cut Omega Bolt (no corrosion in Mine 1 solution after 72 days).**

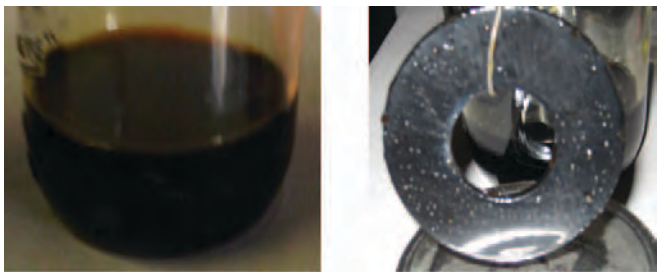


**Figure 6. Sample E - washer (no corrosion in Mine 1 solution after 72 days).**



**Figure 7. Sample J - Omega Bolt (immediate oxidation of the hydrochloric acid, no reation with the coating).**

- Molecular or covalent bonding occurs between the polymer and the steel Omega Bolt. This ensures that the coating does not peel or scrape easily. It also prevents the polymer from acting as a containing cell for the acid if the acid should break through due to the lack of adhesion or bonding. The acid will corrode along the inside of the coating.
- The polymer is highly flexible; it not only allows the Omega Bolt to expand but also allows for a smooth surface finish, as well. A smooth finish is additionally beneficial because it reduces the friction between the bolt and the surrounding rock during installation. This, coupled with the high scratch strength of the polymer, makes it very advantageous in hard rock conditions, ensuring the integrity of the product.
- Most importantly, the polymer coating is resistant to the most extreme pH levels, higher than what is typically found in underground mines. This makes the Obduro AP polymer idealfor sites with corrosive conditions because it eliminates the need for constant rehabilitation. In situations where the mine rehabilitates frequently, such as every 30 days, the additional cost of the Obduro AP coating is mere pennies to the dollar comparatively.

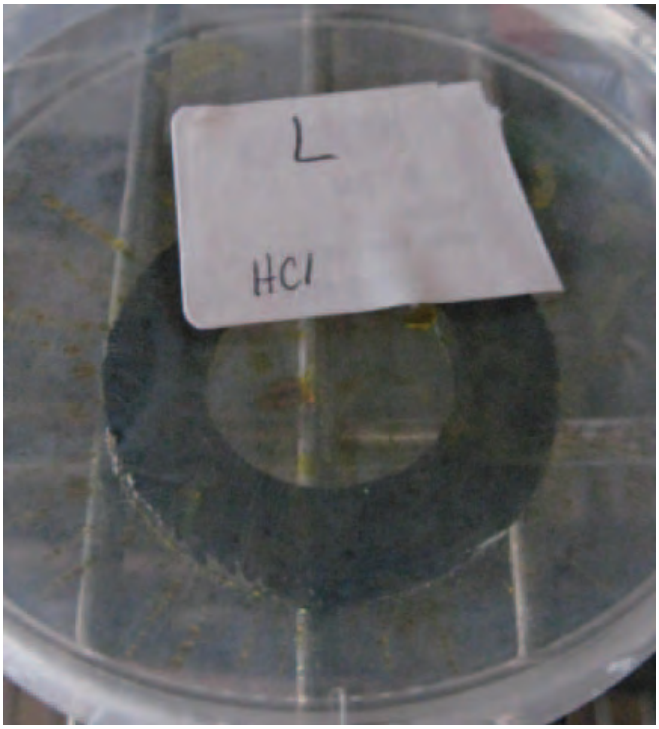



**Figure 8. Sample L - washer (no reaction with the hydrochloric acid, simple oxidation occurred with the oxygen in the air).**



**Figure 9. Zinc galvanized bolt (react violently with Mine 2 solution after only 30 minutes of exposure).**

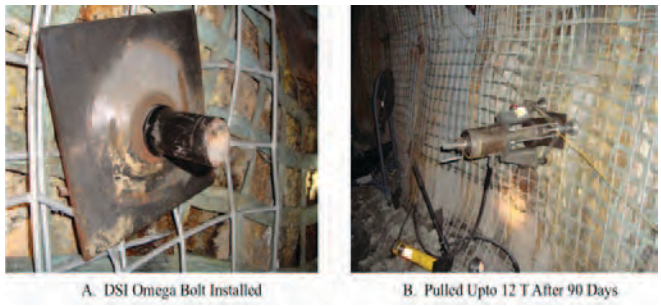



**Figure 10. Performance of the DSI Omega Bolts at Mine B.**



**Figure 11. Performance of the traditional zinc galvanized bolts (pulled out by hands).**

## REFERENCES

Aziz, N., Craig, P., Nemcik, J., and Hai, F. (2013). "Rock bolt corrosion - an experimental study." In: *Proceedings of the Coal Operators' Conference*. Wollongong, Australia: University of Wollongong, , pp. 144–151.

# Fiber Reinforced Polymer Rockbolts for Ground Control in a Strong Jointed Rock Mass

**Samrat Mohanty**, Senior Engineer
**Tom Vandergrift**, Principal
**Timothy Ross**, Vice President and Principal
Agapito Associates, Inc.
Golden, CO

**Gan Chin Hwi**, Project Manager
**Mee Nee Lee**, Project Manager
Parsons Brinckerhoff Pte, Ltd.
Singapore

## ABSTRACT

The construction of underground hydrocarbon storage caverns in Jurong Island, Singapore, is nearing completion. The facility, located beneath the seabed of Banyan Basin, is comprised of five storage caverns with a storage capacity of approximately 1.5 million cubic meters. The galleries of each cavern are 20 m wide by 27 m high and approximately 340 m long. In addition to the storage caverns, various access and operations tunnels are required to support the facility. Among these are water curtain galleries to ensure that hydrostatic pressures in excess of hydrocarbon storage pressure are maintained in the rock mass surrounding the storage caverns.

Early in the design process, conventional steel rock bolts with resin polymer grout were considered for ground control. However, the construction contractor proposed using fiber-reinforced polymer (FRP) bolts with cement grout due to the corrosive hydrologic environment, weight and handling considerations, local construction preferences, and the requirement to have a cavern design life of 50 years. FRP bolts with cement grout were ultimately chosen for the project. The FRP bolting system has proven to be very successful, with no ground failures experienced where systematic FRP bolting has been applied. This paper discusses the properties of FRP bolt/cement grout bolting systems, their characteristics in relation to steel bolt/resin bolting systems, and numerical modeling results assessing their performance.

## INTRODUCTION AND BACKGROUND

Construction is nearing completion at the Jurong Rock Caverns (JRC) project in Jurong Island, Singapore. Fiber-reinforced polymer (FRP) bolts are being used as primary support on the project, which is being constructed by Hyundai Engineering and Construction (HDEC) of Seoul, Republic of Korea. HDEC is supported on the geotechnical design by Parsons Brinckerhoff Pte. Ltd. (PBPL), Singapore, PB Energy Storage Services (PBESS), Houston, Texas, and Agapito Associates, Inc. (AAI), Golden, Colorado. JRC is the first underground facility in Southeast Asia to be constructed for storage of liquid hydrocarbons, such as crude oil, condensate, naphtha, and gasoil. In total, five hydrocarbon storage caverns will be excavated during Phase 1 of the project, consisting of nine individual galleries, some of which are interconnected. JRC is located below the water of Jurong Island's Banyan Basin, with the top of the storage caverns approximately 119 m below sea level. The total designed storage capacity of the caverns is approximately 1.5 million cubic meters . Storage pressures are above atmospheric, with the maximum storage pressure anticipated to be 0.36 megapascals (MPa) (gage). The caverns are designed to be in commission for at least 50 years.

Jurong Island was created for industrial utilization through a combination of marine land reclamation and an amalgamation of seven pre-existing islands. The decision to locate the underground caverns in Jurong Island was governed by the scarcity of land within the city-state of Singapore. Placing the storage facilities below ground is estimated to free up about 60 hectares (ha) (approximately 150 acres) of usable land above ground. The storage spaces were developed to provide infrastructural support to the major petrochemical operators in the region.

The finished cavern dimensions are 20 m wide by 27 m high (Figure 1), and as tall as a 9-story building. Individual cavern galleries are approximately 340 m long. Given their significantly large dimensions, the cavern storage galleries are excavated by drill and blast methods using three 9-m-high cuts (a top heading and two benches).

In addition to the storage caverns, several other accessory underground openings are required, including access tunnels, operations tunnels, and water curtain galleries (Figure 2). These accessory openings add approximately 700,000 $m^3$ of excavation to the project, bringing the total excavation for Phase 1 of the project to 2.2 million $m^3$ and the total linear drivage to about 12 km (Kim, et al., 2012). A planned Phase 2 of the project will double the storage capacity at JRC.

The host rock mass consists of sandstone, siltstone, and alternating sandstone/siltstone. Regional metamorphism and contact metamorphism with igneous dykes has greatly hardened the rock mass. Weathering of these rock types has occurred beneath the seabed and decreases with depth. Representative intact rock properties are given in Table 1.

Ground support for the caverns and associated underground openings is based on the Norwegian Geotechnical Institute Q



**Figure 1. Storage gallery of the Jurong Rock Caverns project. Each of the nine galleries in the project measures 27 m high by 20 m wide by approximately 340 m long.**

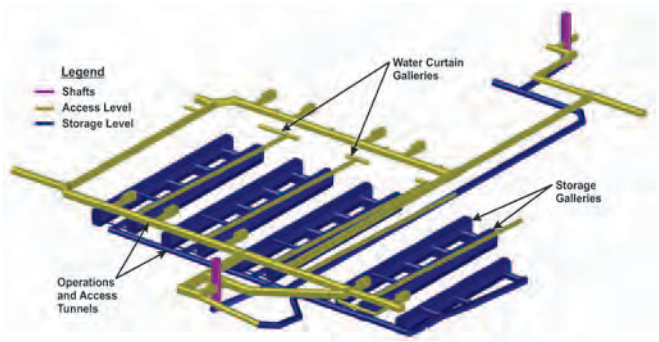



**Figure 2. Excavation is on two levels, an upper level for access and piping infrastructure, and a lower storage level.**

**Table 1. Representative intact rock properties.**

| Rock Type | Proportion of Rock Mass (%) | Rock Quality Designation (RQD) | Uniaxial Compressive Strength (MPa) | Young's Modulus (GPa) |
|---|---|---|---|---|
| Weathered rock | 23 | 36 | 130 | 46.3 |
| Sandstone | 51 | 98 | 117 | 65.6 |
| Siltstone | 10 | 100 | 174 | 40.3 |
| Alternating sandstone/siltstone | 16 | 100 | 162 | 71.4 |

System (Barton, et al., 1974) and on associated design charts (Grimstad and Barton, 1993). The range of ground support includes spot bolting, systematic bolting, and systematic bolting in combination with shotcrete. Either plain shotcrete or steel fiber-reinforced shotcrete is used, depending on ground conditions. The headings are mapped on a round by round basis, and Q values and resulting support plans are assigned.

The Q system design charts address bolt density (pattern) and length, but not bolt type or capacity. In the initial stages of the design process, a bolt system consisting of steel bolts 22 mm in diameter, Grade 60 (420 MPa), fully encapsulated in resin grout was specified, with a design capacity of 160 kN in tension, and 80 kN in shear. However, due to concerns related to steel bolt durability in the presence of corrosive water and because of weight and handling considerations, HDEC proposed using FRP (fibreglass reinforced polyester) rockbolts. The cavern design team agreed that, as long as the FRP bolts met or exceeded the design specifications of steel bolts, they could be used with the same pattern and length. The selected bolts are 25 mm in diameter and have a capacity of 346 kN in tension and 160 kN in shear. Table 2 compares characteristics of FRP bolt/cement grout system with the originally proposed steel bolt/resin grout system.

**Table 2. Steel rock bolt and resin grout characteristics.**

| Parameter | FRP Bolt/ Cement Grout | Steel Bolt/ Resin Grout |
|---|---|---|
| Bolt diameter (mm) | 25 | 22 |
| Bolt density (kg/m$^3$) | 2,200 | 7,800 |
| Bolt Young's modulus (GPa) | 50 | 200 |
| Bolt yield load (kN) | 346 | 160 |
| Bolt ultimate load (kN) | 346 | 240 |
| Bolt shear load (kN) | 160 | 80 |
| Grout bond shear stiffness (N/m/m) | $1.0 \times 10^8$ | $1.12\times 10^7$ |
| Grout shear strength (N/m) | $1.88 \times 10^5$ | $1.75 \times 10^5$ |

As shown in Table 2, the FRP bolt is significantly lighter and stronger compared to the steel bolt and is less stiff. The yield strength and the ultimate strength of the FRP bolt are the same, and both are significantly greater than those of the steel bolt.

## CHARACTERISTICS OF FRP BOLTS

FRP bolts are manufactured as composite materials with two major constituents, continuous glass fibers embedded in a polyester resin matrix. The bolts are produced with a continuous external thread that accepts a nut and plate, and they can be cut easily to any length. In the context of the JRC project, FRP bolts have a number of inherent advantages over steel bolts.

The most significant attribute of FRP rockbolts relative to steel bolts at the JRC project is their corrosion resistance and longevity. Steel rockbolts are susceptible to corrosion in alkaline environments or in the presence of high concentrations of

chlorides, both of which are encountered at JRC. Though steel bolts would be encapsulated in resin grout, and corrosion-resistant coatings could be used, imperfect encapsulation and coating defects could lead to corrosion and possible bolt failure over the 50-year design life of the project. The FRP rockbolts are made with unsaturated resin, which transforms into cross-linked molecules during manufacturing, making the resin saturated. Since the resin transition is irreversible, the FRP bolts are highly inert to chemical attacks. Thus, the alkaline, chloride-rich marine water is unlikely to have a weakening effect on the FRP rockbolts in the long term, allowing them to maintain their design support capacity. Even the stored hydrocarbons are unlikely to react with the FRP bolts because their own long-chain molecules are unlikely to penetrate the saturated FRP bar resin. Laboratory tests were performed to substantiate the claims of the manufacturer regarding the resistance of the FRP bolts to alkaline water and hydrocarbons, including simulations of long-term exposure.

Material costs for FRP bolts are approximately 50% higher than for comparable uncoated steel bolts. However, costs for FRP bolts compare favorably with steel bolts with corrosion-resistant coatings.

The relative density of FRP bolts, just 28% that of steel bolts, lends to ease of handling in underground situations, resulting in greater productivity and less chance of material-handling injuries. This is particularly advantageous for the JRC project due to the large crown and sidewall spans, which result in bolt lengths in excess of 5 m.

As mentioned previously, the yield strength of a 25-mm FRP bolt at the JRC project is 346 kN, much higher than the 160-kN specification. At the same time, the stiffness of the 25-mm FRP bolt is about one-third of the 22-mm steel bolt that was used for comparison. Therefore, for a given load below the elastic limit of the steel bolt, the FRP bolt will allow three times the deformation of a steel bolt, or, to put it another way, for a given deformation, a steel bolt will carry three times the load of a FRP bolt (Figure 3) (FiReP International, 2009). These relationships are represented in the plot in Figure 3. The tradeoff between strength and stiffness was one of the factors taken into consideration before the decision to use FRP bolts was made.

It should be noted that the "weak link" of the FRP system is the thread strength, which is rated at 180 kN. High loads at the bolt collar would be expected in softer rock environments due to dilation. This has not been experienced at the JRC project, however, not surprisingly, given the competence of the rock matrix and the generally tight nature of the joints.

## LABORATORY AND FIELD TEST RESULTS

Several laboratory tensile yield load tests were performed to evaluate the performance of the selected FRP rock bolt. The tested specimens were 1 m long. The ends of the specimens were embedded in platens, and 0.2 m were exposed in the middle during testing. A summary of the results is presented in Table 3, and a representative plot for one of the tested bolt specimens is presented in Figure 4. The test results were consistent with strength properties provided by the rock bolt vendor.

In addition to the laboratory testing, short encapsulation pull tests (SEPT) were performed underground. The tests were performed on FRP bolts with cement grout and an encapsulation

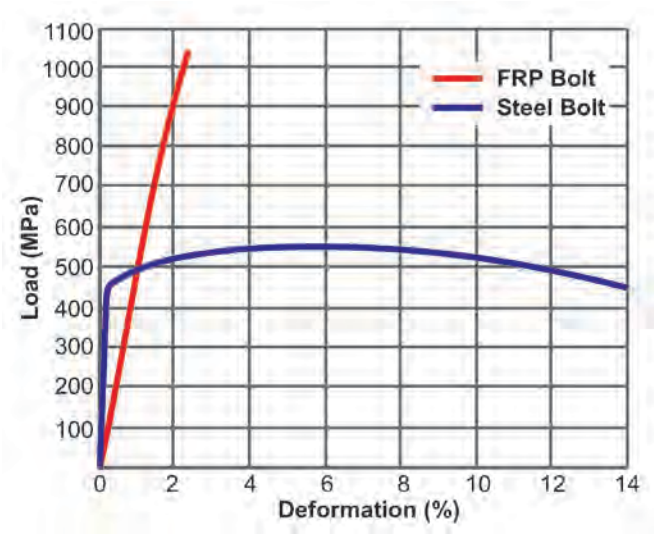



**Figure 3. Load-deformation characteristics of FRP and steel bolts (after FiReP International).**

length of 0.5 m. To measure the effects of grout cure time, the pull tests were performed 6, 12, and 24 hours after the installation. The tests were carried out in both dry and wet holes to gauge the sensitivity of the bolt support capacity to the presence of water in the rock mass. A summary of the SEPT results is presented in Table 4. The tests showed that the full capacity of the system was reached within 12 hours of bolt installation, and that, in three of the tests, the thread strength significantly exceeded its 180-kN rating.

Ground monitoring is routinely performed at JRC using surveying techniques and extensometers. No significant closure has been observed, and it appears that FRP-bolted ground is maintaining equilibrium.

## NUMERICAL MODELING RESULTS

Numerical modeling was performed to evaluate the performance of both the steel and FRP bolting systems. Representative models of the designed storage gallery and the systematic support pattern, including rockbolts and shotcrete lining, were simulated using the two-dimensional distinct element modeling code UDEC (Itasca, 1996). Model inputs were based on measurements and observations from the site, including joint patterns, and in situ stresses. Rock mass and joint properties were based on the intact rock values given in Table 1 using the Hoek-Brown failure criterion (Hoek, et al., 2002), and engineering judgment. Three scenarios were simulated: unsupported cavern, cavern with steel bolts and shotcrete lining support, and, lastly, cavern with FRP bolts and shotcrete lining support. The bolt and grout properties presented in Table 2 were used in the analysis. Results are discussed briefly below.

The yield condition plot for the unsupported cavern is presented in Figure 5, which shows potential zones of tensile failure and zones that have yielded in the past. Zones with yielding in the past show signs of slippage of rock blocks, with respect to each other, prior to the ultimate equilibrium of the rock mass surrounding the

**Table 3. Summary of FRP rock bolt laboratory test results (averaged).**

| Parameter | Value |
|---|---|
| Breaking load (kN) | 358 |
| Tensile strength (MPa) | 1,035 |
| Young's modulus (GPa) | 44.13 |
| Maximum strain (%) | 2.35 |

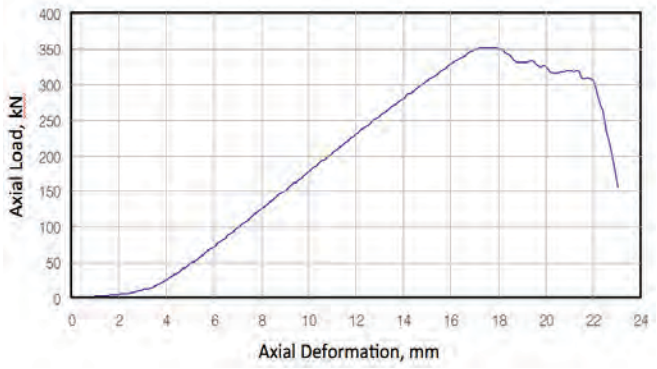



**Figure 4. Representative load-deformation test of FRP bolt used on the project.**

**Table 4. Summary of SEPT test results for FRP rock bolts.**

| Hole Condition | Grout Cure Time (hours) | Failure Load (kN) | Failure Mode |
|---|---|---|---|
| Dry | 6 | 110 | Grout |
| | 12 | 185 | Thread |
| | 24 | 225 | Thread |
| Wet | 6 | 50 | Grout |
| | 12 | 270 | Thread |
| | 24 | 250 | Thread |

excavation. Zones of tensile failure show blocks that are likely to detach. The model indicates that loosening and failure of sidewall and crown wedges created by the intersection of joint sets is likely in the absence of ground support.

The yield condition plots for the supported cavern are presented in Figures 6 and 7, for the steel-bolted and FRP-bolted openings, respectively. The yield plots indicate the stabilizing effects of reinforcement provided by the rock bolts. The modeling results indicate that FRP bolts (with cement grout) are as effective as steel bolts in stabilizing the wedge/block separation in the crown and sidewalls.

In order to contrast the performance of FRP bolts with steel bolts, the peak axial loads carried by each of the 31 rockbolts in the cavern model are presented in Table 5. Steel bolts No. 17, 18, and 20 (in the right hand portion of the crown) have reached their yield point, whereas the FRP bolts are well within their design strength of 346 kN.

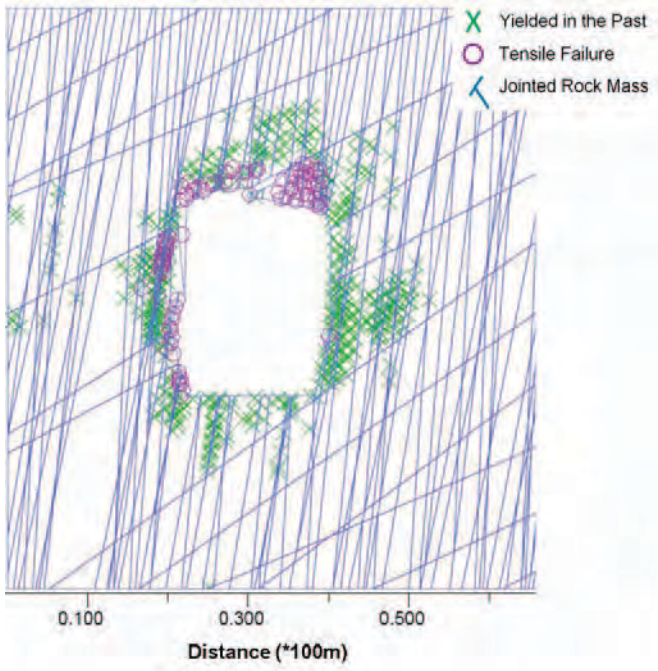



**Figure 5. UDEC model results showing the yield conditon of an unsupported cavern gallery.**

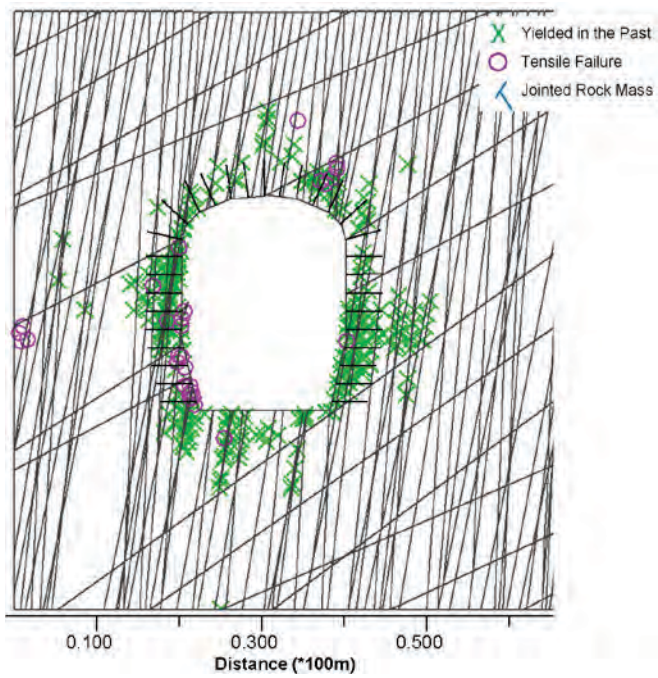



**Figure 6. UDEC model results showing the yield condition of a cavern gallery supported with steel bolts and resin grout.**

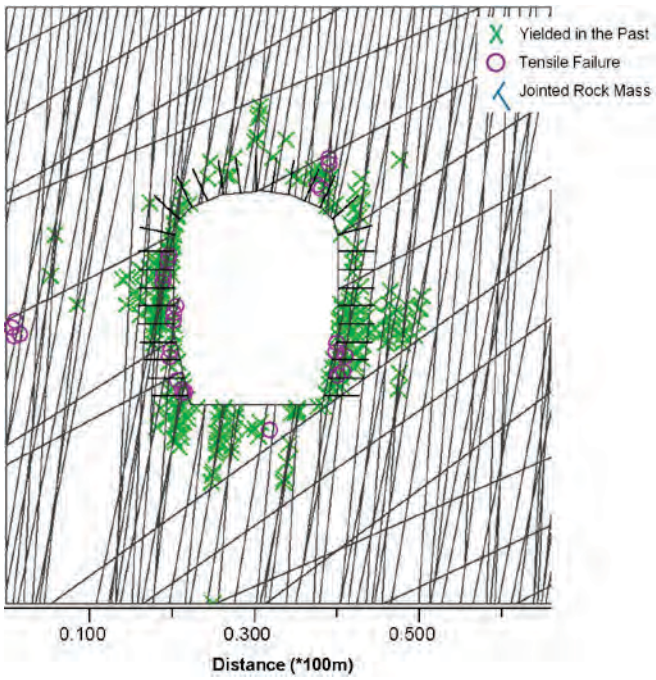



**Figure 7. UDEC model results showing the yield conditon of a cavery gallery supported with FRP bolts and cement grout.**

## CONCLUSIONS

Cement-grouted FRP rock bolts have been used successfully at the Jurong Rock Caverns project. In the nearly 5-year construction period to date, no significant ground failures have been experienced in areas systematically supported with FRP bolts. For the geotechnical setting of the JRC project, FRP bolts have inherent advantages over conventional steel bolts in corrosion resistance, weight, ease of handling, and ultimate strength. FRP bolts have been successfully applied on other civil construction and mining projects, and there appears to be good potential for their increased use as additional successful case studies are compiled.

**Table 5. Predicted maximum axial bolt loads.**

| Bolt No. | Axial Load (kN) | |
|---|---|---|
| | Steel Bolt/Resin Grout | FRP Bolt/Cement Grout |
| Bolt 1 | 10 | 27 |
| Bolt 2 | 12 | 16 |
| Bolt 3 | 30 | 34 |
| Bolt 4 | 59 | 69 |
| Bolt 5 | 81 | 113 |
| Bolt 6 | 70 | 80 |
| Bolt 7 | 97 | 142 |
| Bolt 8 | 89 | 176 |
| Bolt 9 | 94 | 89 |
| Bolt 10 | 34 | 35 |
| Bolt 11 | 47 | 41 |
| Bolt 12 | 55 | 64 |
| Bolt 13 | 42 | 45 |
| Bolt 14 | 20 | 24 |
| Bolt 15 | 4 | 2 |
| Bolt 16 | 2 | 1 |
| Bolt 17 | 165* | 188 |
| Bolt 18 | 165* | 277 |
| Bolt 19 | 74 | 94 |
| Bolt 20 | 165* | 253 |
| Bolt 21 | 14 | 55 |
| Bolt 22 | 36 | 51 |
| Bolt 23 | 33 | 43 |
| Bolt 24 | 50 | 53 |
| Bolt 25 | 30 | 32 |
| Bolt 26 | 22 | 39 |
| Bolt 27 | 14 | 22 |
| Bolt 28 | 15 | 22 |
| Bolt 29 | 21 | 41 |
| Bolt 30 | 14 | 24 |
| Bolt 31 | 15 | 35 |
| *At yield load. | | |

## REFERENCES

Barton, N. R., Lien, R., and Lunde, J. (1974). "Engineering classification or rock masses for the design of tunnel support." *Rock Mechanics 6* (4): 189–239.

FiReP International. (2009). "FiReP rebar technology: durability for the future." Product Brochure. FiReP International AG, Switzerland.

Grimstad, E. and Barton, N. (1993). "Updating the Q system for NMT." In: *Proceedings of the International Symposium on Sprayed Concrete*. Fagernes, Norway: Norwegian Society of Chartered Technical and Scientific Professionals (Tekna), 46–66.

Hoek, E., Carranza-Torres, C. T., and Corkum, B. (2002). "Hoek-Brown failure criterion - 2002 edition." In: *Proceedings of the North American Rock Mechanics Society Meeting*. Toronto, Canada: American Rock Mechanics Association, 267–273.

Itasca. (1996). *UDEC User Manual*. Minneapolis, Minnesota: Itasca Consulting Group, Inc.

Kim, Y., Teo, T. Y., and Ng, M. (2012). "Construction of tunnels and caverns for phase 1 Jurong Rock Caverns." In: *Proceedings of the 13th World Conference of Associated Research Centers for Urban Underground Space*. Singapore: Associated Research Centers for Urban Underground Space.

# A Novel and Effective Method to Develop Tension in a Roof Bolt

**Phillip E Gramlich**, Business Development Manager
**James R Clingan**, Director of Operations - Resins
DSI - North America
DSI Underground Systems
Martinsburg, WV

## ABSTRACT

Through extensive practical experience and multiple studies, tensioned roof control systems have proven beneficial in difficult mining conditions. Due to increased mining of less desirable seams, tensioned roof control systems have claimed a progressively larger share of the total number of roof bolts installed in the US coal industry. Each tensioned roof control system has its benefits, but also has problems concerning cost, cycle time, stress concentration, load retention, and protrusion into the mine opening.

For example, resin-assisted mechanically anchored bolts (also known as resin point anchor bolts) have a fast cycle time and the potential for high tension loading, but the stress from the mechanical shell is concentrated in a small area and can create concerns with certain roof structures (Zhang and Peng, 2001). Resin point anchor bolts can be difficult to fully grout. The cost of resin point anchor bolts can be an issue; a two-piece resin point anchor bolt has a large number of parts (10) and manufacturing steps (9), adding to its higher cost.

Tension rebar bolts can achieve high loads and are easier to fully grout but have longer cycle times. In addition, a high percentage of the installed load can "bleed off" if the resin mixing time or the "hold time" before tensioning is short-circuited. Tension rebar bolts can be notorious for protruding into the mine opening, creating an obstruction for man and machine (Figure 1), in particular, with reduced mining heights.

A new tensioned roof control system has been developed that doesn't have moving parts, is cost effective, provides fast cycle times, has a low profile, and is simple to install.

## INTRODUCTION

DSI Underground Systems is currently developing a new, patented tensioned bolting system called TensionLoc HTB. "HTB" stands for "Headed and Tensioned Bolt." Unlike tension rebar, this bolt has a forged head creating a flat installed profile (Figure 1 and 2). Similar to resin point anchor systems, the tensioning device is contained entirely in the borehole. The bolt is produced from Grade 75, 0.677-inch or 0.810-inch round stock or, alternatively, from Grade 75, 0.677-inch or 0.810-inch Hot Notch Bar (HNB) that has been partially peeled. A thread is cold-rolled onto 24 or 30 inches of the distal (penetrating) end of the bolt, and a special friction-reducing coating is applied over the thread. The proximal end receives a standard hot forged head. This system uses a specially developed polyester resin as the "nut." To achieve load, the bolt threads into the hardened resin nut.

Installations of TensionLoc HTB proceed almost exactly like tension rebar:

1. Drill a one-inch hole to the correct depth.
2. Install the fast resin, or alternatively a fast and slow resin.
3. Fully seat the bolt and plate to the roof.
4. Spin counterclockwise to mix the resin.
5. Hold in place to allow the fast resin to cure.
6. Spin clockwise to tension the bolt.

## DEVELOPMENT OF THE PRODUCT

Prior to DSI acquiring the patent rights to this concept, several attempts were made to develop a suitable product, and these attempts were met with varying degrees of success. DSI found that the key was identifying and quantifying the mechanisms that create friction. Friction absorbs the rotational energy imparted on the bolt, which limits the load that can potentially be induced. The largest friction-creating component came from the interface of the bolt and the resin. DSI found that a polished steel threaded bolt embedded in cured resin had an astonishingly high static coefficient of friction. Repeated testing showed that the static coefficient of friction was 27–35 ft-lb per inch of embedment. For a 24-inch resin anchor, the static coefficient of friction was a staggering 648–840 ft-lb. For comparison a typical roof bolting machine in the coal mining industry might generate 400 ft-lb of torque. Early versions of a friction reduction coating included Teflon or silicone based paints. This proved to reduce the static coefficient of friction only marginally. Amazingly, metal cladding of the bolt increased the static coefficient of friction. Some of the tested friction reduction coatings and the results are listed in Table 1. An exhaustive process led to the development of a DSI Underground Systems patent-protected proprietary coating that has a static coefficient of friction less than 5 ft-lbs per inch.

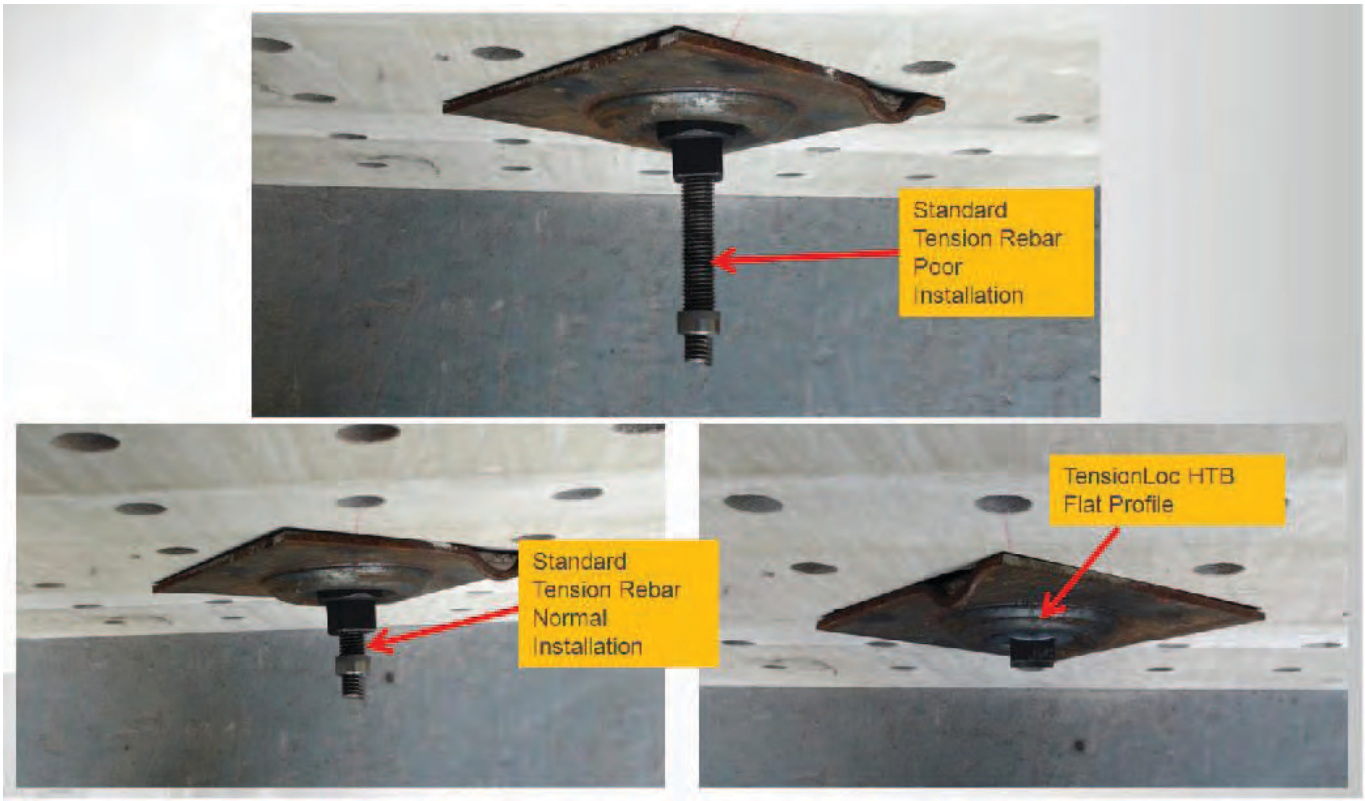



**Figure 1. Bolt profiles.**

**Table 1. Friction reduction coating type and results.**

| | |
|---|---|
| DSI Proprietary Coating | 4.0 ft-lbs per inch |
| Silicone Paint | 22.2 ft-lbs per inch |
| PTFE Paint | 22.9 ft-lbs per inch |
| Baked on Teflon Coating | 24.0 ft-lbs per inch |
| No Coating - Polished Bolt | 30.0 ft-lbs per inch |
| Chrome Plating | 72.8 ft-lbs per inch |

Other novel and established processes were put in place to reduce the remaining source of friction which is located between the bearing plate and bolt head. The solution for this friction source included:

- A specialized friction reduction washer.
- A modified washer seat for the bolt head.
- Special attention to minimize the flashing on the underside of the bolt head.
- Minimizing the thrust on the bolt head during the torque cycle, which reduces friction.

Pitch of the cold-rolled thread was shown to be another concern. Thread pitch is defined as the distance from thread-peak to- thread-peak, but pitch is also used interchangeably in the English system of measurement with the term "threads per inch" (TPI). A high TPI thread could generate additional mechanical advantage to aid in bolt loading, but this proved detrimental to forming the resin nut. A low TPI thread would have a lower mechanical advantage and result in unsatisfactory installed load. The testing process revealed that a 3.5-pitch, ACME-style thread pattern provided good mechanical advantage, good bolt loading and resulted in a well-defined resin nut (Figure 3 and 4).

A third concern was the resin. The resin for this concept bolt had to generate a fast cycle time and be able to sustain a high grip factor with the TensionLoc HTB coating. Extensive research, development and testing resulted in a proprietary resin product that provides a cycle time exceeding tension rebar and rivals the cycle time of a resin point anchor bolt (shown in Table 2). Pull tests of coated and uncoated bolts show a minimal difference in deflection and no difference in pull strength (Figure 5).

## INSTALLATION AND FIELD TESTING

At the time of this writing, the TensionLoc HTB bolt has passed the testing required by MSHA Pittsburgh Safety and Health Technology Center, Roof Control Division, having met the minimum criteria for the ten-degree wedge test, limestone block pull test, loading test and elongation tests. Field trials are now under way to obtain district approvals for the TensionLoc HTB.

To achieve optimum loads for the TensionLoc HTB, the following machine settings are recommended:

- 550–650 RPM
- 300 ft-lb torque
- To insert bolt—Up to 5,000 lb. of thrust (normal machine setting with torque/thrust valve disengaged)
- To torque bolt—Engage torque/thrust valve, which lowers thrust to 1,500-2,000 lb., Torque is maintained at 300 ft-lbs. Rotate the bolt until the machine stalls.

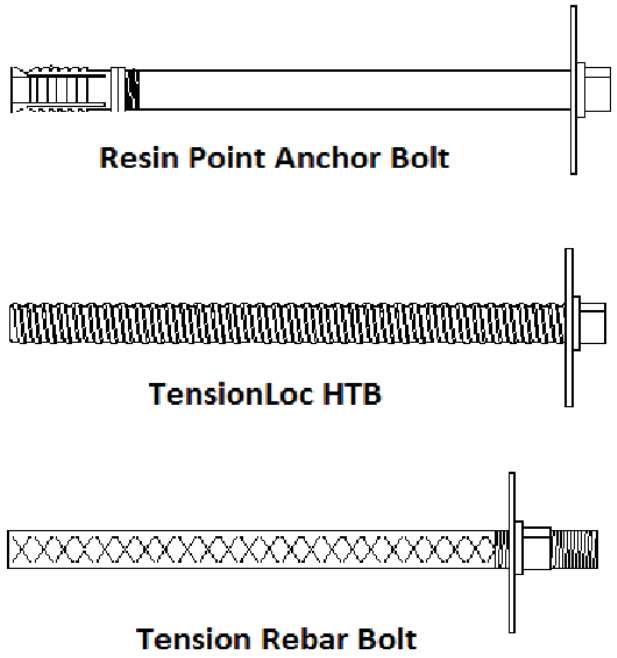



**Figure 2. Comparison of profile, tension rebar, and TensionLoc HTB bolt.**

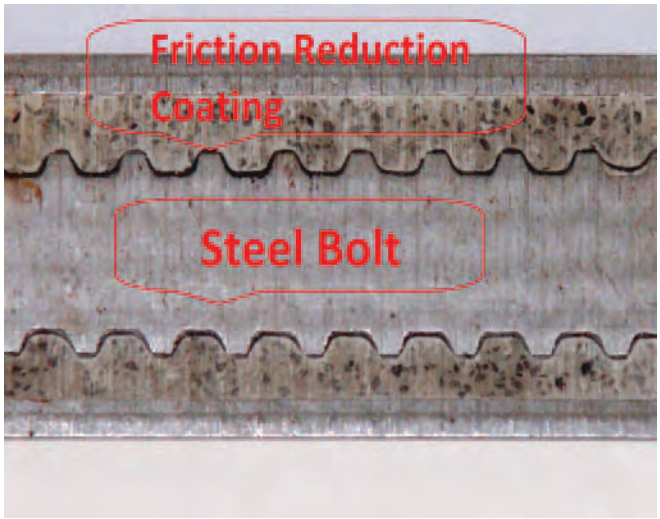



**Figure 3. Embedded TensionLoc HTB.**

**Table 2. Cycle times of tensioned bolting systems.**

| System | Spin | Hold | Torque | Total |
|---|---|---|---|---|
| Point Anchor Resin Bolt | 4 | 0 | 0 | 4 |
| TensionLoc HTB | 2-3 | 4-6 | 1-2 | 7-11 |
| Tension Rebar | 4-5 | 6-8 | 3-4 | 13-17 |

Proven TensionLoc HTB tension loads at these settings are 12,000 to 18,000 lb. Torque-to-tension ratio averages 50:1 (50 lb of tension load per ft-lb of torque). Future proprietary work could improve this torque-to-tension ratio. It should be noted that post-installed torque cannot be measured with a torque wrench due to cohesion or adhesion of the bolt, coating, and resin. The torque-

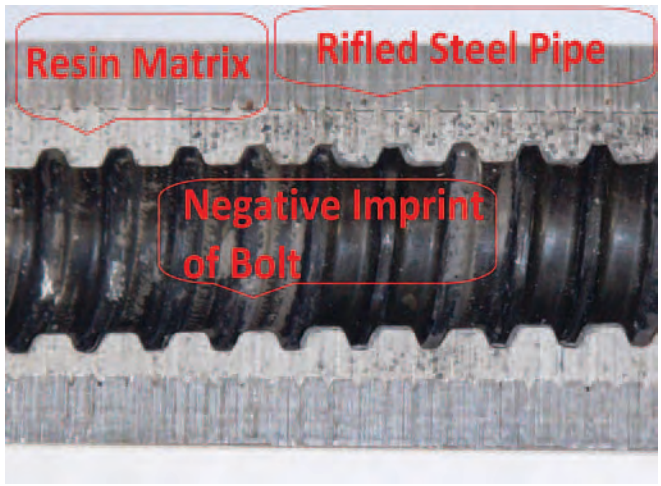



**Figure 4. Negative thread profile of TensionLoc HTB.**

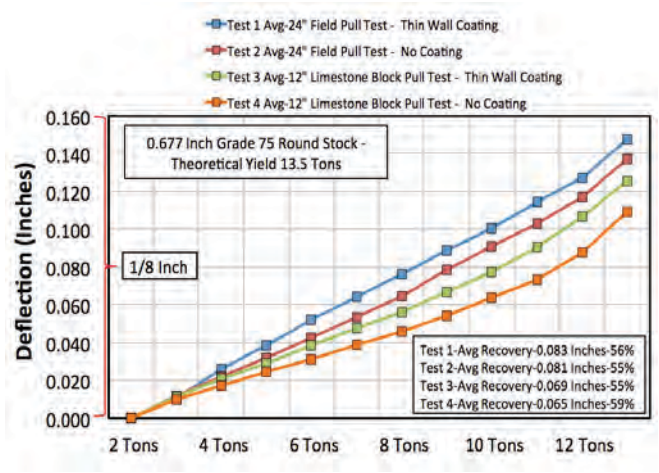



**Figure 5. Pull test results of TensionLoc HTB.**

to-tension ratio was calculated by comparing the measured machine torque prior and after the installation and the measured installed load on the bolt via an electronic load cell (Figure 6).



**Figure 6. Electronic load cell.**

Load retention for TensionLoc HTB is excellent. Full-scale lab tests indicate 98% load retention. Lab tests indicate that the resin anchor does not creep. The load retention data is shown in Table 3. It should be noted that the laboratory tests don't include the bearing

**Table 3. Installed load, load loss, torque to tension ratio.**

| Test Number | Machine Torque (ft-lbs) | Installed Load (lbs) | Retained Load (lbs) | Bleed Off % | Torque to Tension Ratio |
|---|---|---|---|---|---|
| Test 8 | 300 | 12,580 | 12,300 | 2.2% | 41.9 |
| Test 15 | 300 | 17,800 | 17,650 | 0.8% | 59.3 |
| Test 17 | 300 | 15,630 | 15,350 | 1.8% | 52.1 |
| Test 29 | 300 | 14,750 | 14,500 | 1.7% | 49.2 |
| Test 32 | 300 | 16,530 | 16,450 | 0.5% | 55.1 |
| Test 36 | 300 | 13,880 | 13,650 | 1.7% | 46.3 |
| Test 43 | 300 | 14,600 | 14,100 | 3.4% | 48.7 |
| Test 69 | 300 | 16,250 | 15,990 | 1.6% | 54.2 |
| Test 76 | 300 | 12,900 | 12,740 | 1.2% | 43.0 |
| Test 81 | 300 | 16,250 | 15,770 | 3.0% | 54.2 |
| Test 100 | 300 | 15,600 | 15,320 | 1.8% | 52.0 |
| Test 101 | 300 | 13,860 | 13,600 | 1.9% | 46.2 |
| Test 113 | 300 | 11,090 | 10,880 | 1.9% | 37.0 |
| Test 117 | 300 | 15,100 | 14,850 | 1.7% | 50.3 |
| Average | | 14,773 | 14,511 | 1.8% | 49.2 |

plate to rock interface, typical of field-installed bolts, which is known to relax under load and provide an additional mechanism for loss of installed load.

When performed on the TensionLoc HTB, a standard torque test has proven unreliable. To counter this, DSI will employ a visual load indication washer rated at 10,000 lbs (Figure 7). Various types of load indication washers have been described in publications (Leonhardt, 2000) and employed in the industry. Also, collaborative efforts are being explored to further refine and develop a field unit that can safely, quickly and accurately determine the load on an installed bolt via sonic or ultrasonic means. One such device under consideration is the GRANIT system (Starkey, Ivanovic, Nielson and Rodger, 2000). For monitoring and better control of the installed load DSI recommends refitting the bolting machine with pressure gauges on the torque and thrust circuits so that line pressure, and by default, thrust and torque, can be readily monitored by the bolt installer (Cybulski and Gray, 1990). This procedure is currently used to monitor resin point anchor installations at several major mining companies. The testing configuration to determine quality of installed bolts is still being evaluated. One potential configuration is to;

- Verify the machine settings on a daily basis.
- Monitoring of the thrust and torque line pressures.
- Determine the actual installed load on a series of bolts on a daily or weekly basis.
- Maintain load indication washers on a percentage of bolts.



**Figure 7. Load indication washer.**

## SUMMARY

Tensioned bolting systems are proven to assist in difficult mining conditions. The percentage of tensioned bolts verses non-tensioned bolts consumed by the US coal mining industry is increasing every year. The system is currently going through regulatory approval.

TensionLoc HTB has no moving parts, is simple to install, and solves some of the problems associated with tension rebar and resin point anchor bolts.

**REFERENCES**

Cybulski, J. A. and Gray, W. J. (1990). "An alternative to a manual torque check on roof bolts." In: *Proceedings of the 10th International Conference on Ground Control in Mining*. Morgantown, West Virginia: West Virginia University, pp. 85–89.

Leonhardt, J. C. (2000). "Visual recognition of the load of roof-bolts by an indicator." In: *Proceedings of the 20th International Conference on Ground Control in Mining*. Morgantown, West Virginia: West Virginia University, pp. 362–366.

Zhang, Y. and Peng, S. (2001). "Design considerations for tensioned bolts." In: *Proceedings of the 21st International Conference on Ground Control in Mining.* Morgantown, West Virginia: West Virginia University, pp. 131–140.

Starkey, A., Ivanovic, A., Neilson, R., and Rodger, A., (2000) "A New Approach to the Integrity Testing of Ground Anchorages" In: *Proceedings of the 20th International Conference on Ground Control in Mining*. Morgantown, West Virginia: West Virginia University, pp. 374–377.

# Development and Application of the TT Anti–Friction Washer for Use with Tensioned Roof Bolt Systems

**Thomas A Cook**, Mining Engineer
**Travis M Sub**, Research and Development Mechanical Engineer
**John C Stankus**, President
Keystone Mining Services, LLC
Jennmar Corporation, Inc
Pittsburgh, PA

## ABSTRACT

The effectiveness of tensioned roof bolt systems has been well researched and documented over the years (Stankus, 1990, 1991, 1997; Guo, 1997; Denton, 2000; Su, 2007). Higher and more consistent installed tension has been shown to improve the beaming effect and associated roof stability especially in highly-stressed, weak, laminated roof strata. To accomplish higher and more consistent bolt-installed tensions, various types of anti-friction washers have been developed and applied to many types of tensioned roof bolt systems. In addition to increasing bolt-installed tension, these washers also provide a lubricating effect that minimizes sparking during the bolt torqueing cycle.

The most popular and widely used anti-friction washer configuration consists of a plastic washer that is used in conjunction with a standard hardened steel washer. This washer configuration has performed well in the field in terms of increasing the bolt-installed tension (or plate load) and the related tension/torque ratio (the amount of tension achieved per one ft-lb of applied torque). However, the installed tension does not always maintain consistency. One reason for this inconsistency is that the plastic anti-friction washer sometimes dislodges and shreds or tears before the bolt torqueing cycle is complete. This condition prevents the plastic washer from acting as an anti-friction medium for the entire torqueing cycle.

Jennmar Corporation and Keystone Mining Services, LLC, developed the "TT" washer in early 2012. The "TT" anti-friction washer is comprised of two zinc-coated (galvanized) hardened steel washers that are joined together with an exclusive polymer. The "TT" washer has been extensively tested and applied in the Sewickley, Pittsburgh, and Indiana #5 coal seams. The test results indicate an average increase in installed load and tension/torque ratio of 20%. More importantly, the installed load consistency improved, with a significant reduction in the standard deviation of values. This paper will detail the development and testing of the "TT" anti-friction washer with case studies of actual mine applications.

## INTRODUCTION

A common roof bolt system used by the mining industry is a point-anchored, resin-assisted, fully tensioned bolt system. This system is typically comprised of headed rebar with a threaded expansion shell and plug assembly that is specifically designed to be used with resin. The bolt is installed with a bearing plate to support the roof strata. The bolt is tensioned by applying torque to the head of the bolt and tightening the shell and plug assembly. As the tension in the bolts increases, the laminated roof strata compresses across the entry, creating a beaming effect.

During tensioning, friction generates between the head of the bolt and the bearing plate. This friction reduces the amount of torque actually applied to the bolt, consequently reducing the amount of tension applied to the bolt. Anti-friction washers (AFW) are used between the bolt head and the plate to reduce the friction, allowing higher installed loads. Jennmar currently uses a high-density polyethylene (HDPE) plastic washer sandwiched between two hardened steel washers as the AFW configuration. The heat generated from rotational friction during installation softens the plastic washer creating a lubricating effect.

## DEVELOPMENT OF THE "TT" WASHER

The plastic washer has been a good anti-friction medium, but it has demonstrated inconsistency in the field of both installed load and tension/torque ratio. One common installation problem with the traditional plastic washer is that, while tensioning the bolt, the plastic washer will often shred instead of softening. Another installation problem with the plastic washer is its tendency to tear and dislodge from the hardened steel washers. Without the lubricating surface, the steel washers act upon each other, creating more friction. In both instances, the installed load and higher torque advantage of the AFW is adversely affected.

To eliminate the inconsistency and installation problems, Jennmar Corporation and Keystone Mining Services, LLC, developed the "TT" washer. It consists of two zinc-coated (galvanized) hardened steel washers joined together with an exclusive polymer. The "TT" washer works in the same manner as the plastic washer: heat generated by friction during installation melts the lubricant providing an anti-friction agent. The "TT"

washer increases the tension/torque ratio of the bolt and is more consistent compared to the plastic washer. The galvanized coating of the "TT" washer also reduces friction. The thickness and material properties of the zinc, which make up the galvanized coating, are key parameters in maximizing the friction-reducing capability of the washer.

## TEST SAMPLES

Numerous underground tests have been conducted at coal mines in different areas of the United States. The primary bolt used for the "TT" testing consisted of the INSTál system, either in a one- or two-piece configuration (Figure 1). The INSTál II (two-piece bolt) consists of a grade 75, 0.804" (20 mm) J-Bar top section with J-8, 4-prong expansion shell (split base), roll pin coupler and 3/8" (10 mm) round support nut. The bottom section consists of a smooth-headed bar. The INSTáL III consists of the same shell configuration as the INSTál II but is a one-piece bolt system comprised entirely of 0.804" (20 mm) J-Bar.

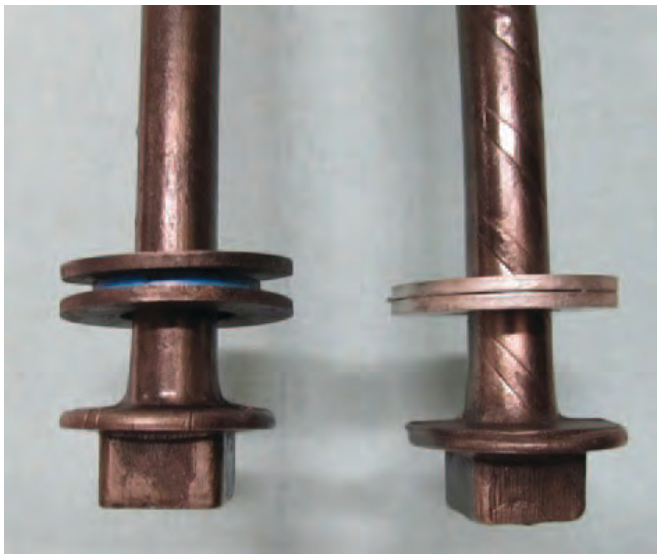


**Figure 1. Plastic washer on INSTaL II system and TT washer on INSTaL III system.**

## UNDERGROUND TESTING PROCEDURE

Normal INSTál II and INSTál III installation procedures (excluding resin) were conducted, except for placing a calibrated Glotzel load cell between two, 6" x 6" (15 x 15 cm) flat plates. The installation procedure of the bolt consists of drilling a 1-3/8" (35 mm) diameter hole the length of the test bolt completely assembled. Insert the assembled INSTál II or INSTál III bolt into the drill hole. For INSTál II systems, ensure the top and bottom section are completely threaded into the coupler snug against the roll pin. Then, with the bolt assembly in the bolt wrench, rise until snug against the roof and begin the torqueing process until the bolting machine stalls.

After installation, the installed load (tension) is recorded from the load cell. A calibrated torque wrench is used to measure the installed torque. The readings are used to determine the installed load and tension/torque ratio for each test. The tension/torque ratio is the amount of bolt tension (lb) obtained for each ft-lb of applied torque. After the readings are taken, the bolt is rotated counter-clockwise, and bolt, plates, and load cell are removed from the roof.

## CASE STUDY 1

Case Study 1 was in the Sewickley Seam in southwest Pennsylvania. The mine is a room and pillar operation with roof consisting of highly fractured and laminated dark shale strata. A video-scope examination confirmed that the roof strata are 5 feet and 7 inches (1.7 m). The mine roof is subjected to regional and localized horizontal stress, and mining-induced stress from previous under-mining.

The INSTál II bolts installed with the plastic and "TT" washer followed the normal underground testing procedure. The plastic washer produced an average install load of 24,375 lb (108 kN) and average tension/torque ratio of 71:1 (Table 1). The "TT" washer produced an average install load of 24,431 lb (109 kN) and average tension/torque ratio of 85:1 (Table 2).

**Table 1. Installed load test data - plastic anti-friction washer - Sewickley Seam.**

| Test Number | Install Load (lb) | Torque (ft-lb) | Tension/ Torque Ratio |
|---|---|---|---|
| 1 | 20,250 | 384 | 53 |
| 2 | 30,375 | 328 | 93 |
| 3 | 22,500 | 325 | 69 |
| **Average** | 24,375 | 345 | 71 |
| **Standard Deviation, ±** | 4,341 | 27.00 | 16.30 |

In summary, the average tension /torque ratio of the "TT" anti-friction washer was 85:1 compared to 71:1 with the plastic washer. The new "TT" washer increased the tension/torque ratio by 20%.

In addition, the consistency of the installed two-piece bolt with the "TT" washer was much better. The Sewickley Seam "TT" tests produced a tension/torque ratio with a standard deviation of ±7.7. The plastic washer configuration produced a standard deviation of ±16.3. The more consistent installed load and tension/torque ratio will significantly improve the beaming effect and roof stability in the highly stressed and laminated roof in the Sewickley Seam.

## CASE STUDY 2

Case Study 2 was in the Pittsburgh #8 Seam in southwest Pennsylvania. The mine is a longwall mine operation with an immediate roof comprised of weak, laminated shale, sandy/shale, and coal bands. The roof strata is influenced by high regional horizontal stress. A video-scope analysis confirmed the anchoring roof strata at 6 feet consisted of finely laminated sandy/shale. The one-piece INSTál III bolts were installed in the development section of the longwall panel.

The four tests conducted with the INSTál III bolts with the plastic washer produced an average installed load of 18,113 lb

**Table 2. Installed load test data—"TT" anti-friction washer - Sewickley Seam.**

| Test Number | Install Load (lb) | Torque (ft-lb) | Tension/ Torque Ratio |
|---|---|---|---|
| 1 | 22,500 | 320 | 70 |
| 2 | 23,625 | 295 | 80 |
| 3 | 23,625 | 310 | 76 |
| 4 | 23,175 | 250 | 93 |
| 5 | 25,875 | 310 | 83 |
| 6 | 28,125 | 300 | 94 |
| 7 | 25,875 | 300 | 86 |
| 8 | 20,250 | 220 | 92 |
| 9 | 24,750 | 250 | 99 |
| 10 | 25,875 | 300 | 86 |
| 11 | 24,750 | 300 | 83 |
| 12 | 24,750 | 300 | 83 |
| **Average** | 24,431 | 288 | 85 |
| **Standard Deviation, ±** | 1,921 | 29.26 | 7.72 |

(81 kN) and average tension/torque ratio of 57:1 (Table 3). The five installed load tests with the same INSTál III with the "TT" washer generated an average installed load of 19,890 lb (88 kN) and average tension/torque ratio of 72:1 (Table 4).

**Table 3. Installed load test data - plastic anti-friction washer - Pittsburgh Seam.**

| Test Number | Install Load (lbs) | Torque (ft-lbs) | Tension/Torque Ratio |
|---|---|---|---|
| 1 | 16,875 | 290 | 58 |
| 2 | 18,450 | 350 | 53 |
| 3 | 20,250 | 325 | 62 |
| 4 | 16,875 | 310 | 54 |
| **Averages** | 18,113 | 319 | 57 |
| **Standard Deviation, ±** | 1,392 | 22 | 3.69 |

Compared to the plastic washer configuration, this equates to a 10% increase in installed load and 27% increase in the tension/ torque ratio. In summary, the average tension/torque ratio of the "TT" washer was 72:1 compared to 57:1 with the current system. The higher values would improve the beaming effect and roof stability, especially in the high-stress, weak, laminated roof found in the Pittsburgh Seam.

## CASE STUDY 3

The "TT" washer was implemented in the Indiana #5 coal seam with INSTáL III bolts. The mine is a room and pillar operation that was experiencing abnormal roof conditions, such as roof sag and cutter. The mine roof strata is influenced by a high regional horizontal stress. The mine requested a new type of anti-friction

**Table 4. Installed load test data - "TT" anti-friction washer - Pittsburgh Seam.**

| Test Number | Install Load (lbs) | Torque (ft/ lbs) | Tension/Torque Ratio |
|---|---|---|---|
| 1 | 18,000 | 250 | 72 |
| 2 | 16,200 | 250 | 65 |
| 3 | 23,625 | 280 | 84 |
| 4 | 19,575 | 290 | 68 |
| 5 | 22,050 | 300 | 74 |
| **Averages** | 19,890 | 274 | 72 |
| **Standard Deviation, ±** | 2,680 | 21 | 6.73 |

washer to maximize the installed load and beaming effect of the primary bolts. Both plastic and "TT" washers were installed and tested in Section #1, the mains.

The seven tests conducted with the plastic washer produced an average installed load of 17,196 lb (76 kN) and average tension/ torque ratio of 61:1 (Table 5). The seven installed load tests with "TT" washer generated an average installed load of 23,143 lb (103 kN) and average tension/torque ratio of 82:1 (Table 6).

**Table 5. Installed load test data - plastic anti-friction washer - Indiana #5 Seam.**

| Test Number | Install Load (lb) | Torque (ft/lb) | Tension/Torque Ratio |
|---|---|---|---|
| 1 | 15,750 | 285 | 55 |
| 2 | 18,000 | 290 | 62 |
| 3 | 15,750 | 240 | 66 |
| 4 | 18,000 | 265 | 68 |
| 5 | 19,125 | 305 | 63 |
| 6 | 20,250 | 300 | 68 |
| 7 | 13,500 | 300 | 45 |
| **Average** | 17,196 | 284 | 61 |
| **Standard Deviation, ±** | 2,289 | 22 | 7.60 |

Compared to the plastic washer configuration, this equates to a 10% increase in installed load and 35% increase in the tension/ torque ratio. In summary, the average tension/torque ratio of the "TT" washer was 82:1 compared to 61:1 with the current system. The higher values would improve the beaming effect and maximize the installed load for the bolt system.

## CONLUSION AND SUMMARY

The "TT" washer produced a significantly higher and more consistent installed load and torque/tension ratio in all case studies. The current testing and underground observations indicate that the plastic washer configuration is providing some friction reducing effect. However, the bolt does not achieve its maximum installed load and consistency. This is because the plastic washer typically

**Table 6. Installed load test data - "TT" anti-friction washer - Indiana #5 Seam.**

| Test Number | Install Load (lb) | Torque (ft/lb) | Tension/Torque Ratio |
|---|---|---|---|
| 1 | 22,500 | 285 | 79 |
| 2 | 30,375 | 285 | 107 |
| 3 | 20,250 | 275 | 74 |
| 4 | 22,500 | 325 | 69 |
| 5 | 19,125 | 250 | 77 |
| 6 | 24,750 | 250 | 99 |
| 7 | 22,500 | 325 | 69 |
| **Average** | 23,143 | 285 | 82 |
| **Standard Deviation, ±** | 3,394 | 29 | 13.78 |

comes apart between the two hardened washers and ejects from the washers before the installation is complete (Figure 2). This prevents the plastic washer from acting as an anti-friction medium for the complete bolt torqueing process. This condition also creates steel-on-steel rotation that generates friction and sparks.



**Figure 2. Plastic washer from underground installation.**

The "TT" washer design eliminates this condition because the polymer converts into a lubricant and remains between the washers during the entire installation. The combination of the galvanized coating and the polymer lubricant produces a much better friction-reducing medium.

Based on these case study results, the "TT" washer can maximize the effectiveness of tensioned primary bolts due to the following:

- The higher and more consistent installed load and tension/torque ratio will significantly improve the beaming effect and roof stability in weak, high-stressed, and laminated roof.
- The higher installed load will increase the frictional resistance along laminated and weak bedding planes, making the strata less susceptible to horizontal-stress-induced lateral movement and the resultant roof weakening effect.
- The coating will minimize washer corrosion during shipping, handling, and storage of roof bolts (Figure 3).
- The coating will eliminate potential sparking during the bolt rotation and torqueing process.
- The "TT" washer provides a very cost effective way to maximize the performance of tensioned bolt systems.



**Figure 3. Underground installation of TT washer.**

**REFERENCES**

Denton, T. and Stankus, J. (2000). "Application of bolt design criteria at Galatia Mine." In: *Proceedings of the 19th International Conference on Ground Control in Mining.* Morgantown, WV: West Virginia University, pp. 219–224.

Guo, S. and Stankus, J. (1997). "Control mechanism of a tensioned bolt system in laminated roof with large horizontal stress." In: *Proceedings of the 16th International Conference on Ground Control in Mining.* Morgantown, WV: West Virginia University, pp. 167–172.

Stankus, J. C. (1990). "Jennmar compression roof control system." In: *Proceedings of the 9th International Conference on Ground Control in Mining.* Morgantown, WV: West Virginia University, pp. 22–29.

Stankus, J. C. (1991). "Tension point anchor resin system versus non-tensioned fully grouted rebar - two case studies." In: *Proceedings of the 10th International Conference on Ground Control in Mining.* pp. Morgantown, WV: West Virginia University, pp. 65–75.

Stankus, J. C. and Guo, S. (1997). "New design criteria for roof bolt systems." In: *Proceedings of the 16th International Conference on Ground Control in Mining.* Morgantown, WV: West Virginia University, pp. 158–169.

Su, D. and Poland, R. (2007). "Fully-grouted, high-strength, mechanical shell tensioned bolt improves Pittsburgh Seam primary roof support." In: *Proceedings of the 26th International Conference on Ground Control in Mining.* Morgantown, WV: West Virginia University, pp. 235-241.

# Time Dependent Mining Induced Subsidence Measured by Differential Interferometric Synthetic Aperture Radar

**Jessica M Wempen**, Ph.D. Student
**Michael K McCarter**, Professor
Department of Mining Engineering
University of Utah
Salt Lake City, UT

## ABSTRACT

Differential Interferometric Synthetic Aperture Radar (DInSAR), a satellite-based remote sensing technique, has been demonstrated as a potentially practical method for measuring mining induced surface subsidence. Unlike traditional methods of subsidence monitoring, DInSAR has the capacity to generate subsidence data on a regional mining scale with a relatively high data density. Using DInSAR to evaluate subsidence over large regions with relatively long time scales has the potential to help quantify the impact of subsidence in the mining region, and provide a means for validating whole-mine geotechnical models.

In this study, nine pairs of interferometric data from the Japanese Advance Land Observing Satellite (ALOS) were processed using DInSAR to generate displacement maps for a group of trona mines in southwest Wyoming. The data cover a time span from December 2007 to March 2011. The maximum subsidence for one of the mines totaled 1.3 meters for this period. Cumulative DInSAR displacement maps show the development of subsidence over time. In this mining region, surface subsidence is generated primarily by extraction of trona using retreating longwalls. Additionally, trona is extracted by solution mining, which also generates measurable surface subsidence.

## INTRODUCTION

The United States has significant resources of trona, an evaporite mineral used for the production of soda ash. The trona deposits near Green River, Wyoming, account for about 80% of the known global resource of natural soda ash (Gandhi, 2013). Mining began in this region in 1947, and has historically been carried out using traditional underground coal mining techniques including room and pillar, shortwall, and longwall; mining depths typically range from 245 to 460 meters (Brown, 1995; Mannion, 1975). Currently there are five mining leases in this region, shown by the blue boundaries in Figure 1, and the majority of trona is produced using longwall and solution mining, and to a lesser extent by development entries.

With the trona mines in Wyoming progressing toward higher extraction ratios and more longwall development, there is a greater potential for surface subsidence. Subsidence caused by mineral extraction impacts relatively large regions of land, and has the potential to affect future land use and local hydrology. Subsidence also has the potential to damage surface and underground structures (National Coal Board, 1975). Both the Green River and Interstate 80 overlay this mining region leading to areas where surface subsidence may not be tolerable. Additionally, potential damage to oil and gas pipelines is a notable concern (James, 2012).

Because subsidence is an important consideration during mine development, mines generally monitor subsidence on a regular interval, at least yearly. Subsidence monitoring has traditionally been carried out using conventional surveying with levels and total stations, Global Positioning Systems (GPS), aerial laser scanning and photogrammetry (Ge et al, 2008; Donovan and Ismaya, 2010). Conventional surveying and GPS are capable of millimeter-level precision, but these methods require site accessibility, and typically only specific control points are monitored. Aerial surveys generally provide more data over a larger spatial extent than conventional and GPS surveys. However, aerial surveys still require control points with known locations on the ground, and the accuracy of aerial surveys tends to be lower than conventional surveys and GPS.

Differential Interferometric Synthetic Aperture Radar (DInSAR), a satellite-based remote sensing process, could be an effective method of enhancing traditional subsidence monitoring. DInSAR can be used to detect centimeter-level changes in the position of the earth's surface and has the capacity to generate subsidence data on a regional mining scale with a relatively high data density. Two previous studies have used DInSAR to measure subsidence: Ge et al. (2008) measured subsidence over two underground coal mines in New South Wales, Australia, and Ismaya and Donovan (2012) measured surface subsidence over underground coal mines in Utah, United States. Both of these studies show high data density and reasonable agreement between displacements measured using DInSAR and displacement measured using traditional surveys.

In this study, the application of DInSAR to measure surface subsidence in the Wyoming trona mining region is evaluated. The DInSAR data are used to observe the development of mine subsidence over time. DInSAR data source, processing and comparison with limited conventional measurements are included. A new procedure for reducing noise and refining the extent of subsidence is presented.

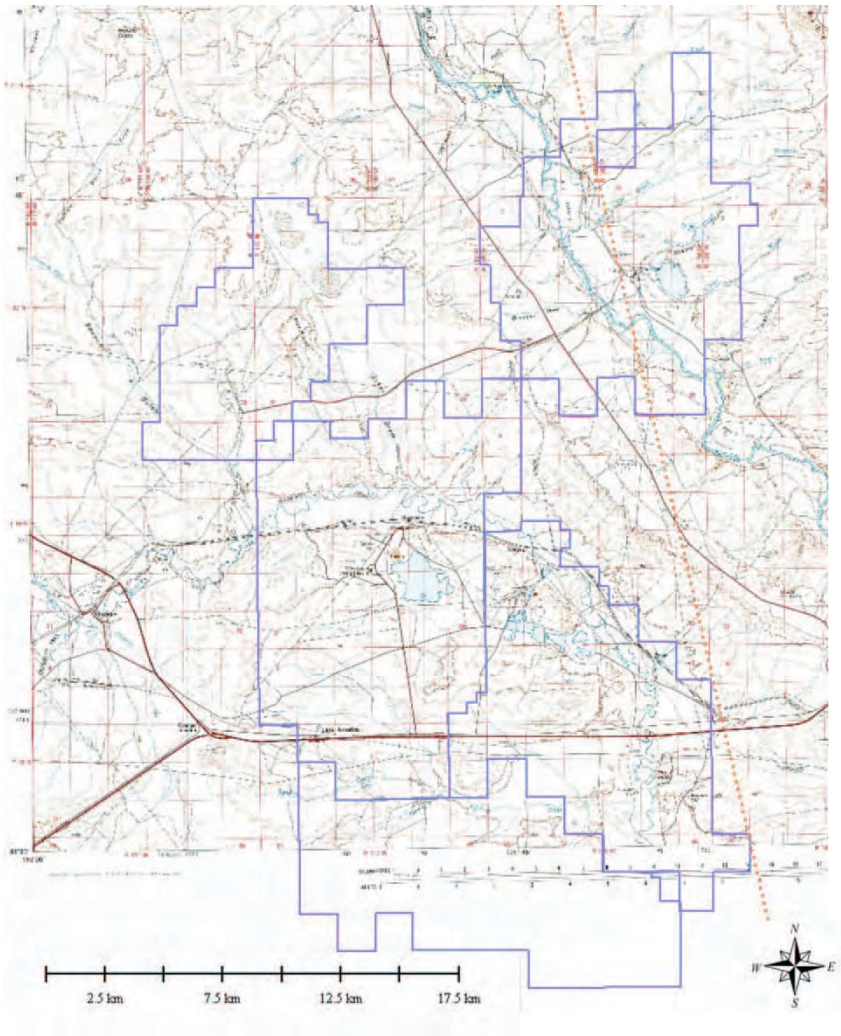



**Figure 1. Southwest region of Wyoming with blue boundaries showing the approximate locations of the trona mine leases, and the orange dashed line showing a portion of the east edge of the SAR data scene (Wyoming Public Records, 2013; U.S. Geological Survey, 1981).**

## DATA

The Synthetic Aperture Radar (SAR) data used in this study were acquired by the Japanese Advance Land Observing Satellite (ALOS) using its Phased Array type L-band Synthetic Aperture Radar (PALSAR). L-band radar has a wavelength of 24 centimeters, and this relatively long wavelength has been found to provide better penetration of ground cover compared to shorter wavelengths: both Ge et al. (2008) and Ismaya and Donovan (2012) produced consistent subsidence data by processing data from ALOS PALSAR. In this study, nine scenes, acquired over the period from December 2007 to March 2011, are processed. A portion of the east edge of the scene is shown in Figure 1 by the dashed orange line, and the acquisition dates are included in Table 1. The data were chosen from a collection of SAR data maintained by the Alaska Satellite Facility.

## PROCESSING

DInSAR works by measuring the phase shift of a radar signal between two SAR scenes acquired over the same area at different times (Rosen et al, 2000; Forrester, 2012). The shift in the radar phase between the two scenes is related to changes in the path length of the signal. When two SAR scenes are paired, an interferogram that contains the phase shift data is generated. In the interferograms, the phase shift includes contributions from the topography, changes in the satellite position, ground movement, atmospheric affects and noise (Sarmap, 2009).

Interferograms that include only changes in the signal path length caused by ground movement are created by reducing the phase shift caused by the topography, changes in the satellite position, atmospheric effects and noise. The phase shifts caused by changes in the topography are minimized using a Digital Elevation Map (DEM).When the baselines, the distances between the satellite's positions during each pass over a scene, are known, the phase shifts caused by the changes in the satellite's position can be

**Table 1. SAR data pairs.**

| Acquisition dates | | | Critical | Mean |
|---|---|---|---|---|
| 12/4/2007 - 7/21/2008 | 230 | 1,736 | 6,552 | 0.49 |
| 7/21/2008 - 10/24/2009 | 460 | 493 | 6,545 | 0.47 |
| 10/24/2009 - 6/11/2010 | 230 | 1,395 | 6,555 | 0.49 |
| 6/11/2010 - 7/27/2010 | 46 | 377 | 6,554 | 0.59 |
| 7/27/2010 - 9/11/2010 | 46 | 161 | 6,554 | 0.64 |
| 9/11/2010 - 10/27/2010 | 46 | 423 | 6,555 | 0.57 |
| 10/27/2010 - 1/27/2011 | 92 | 743 | 6,552 | 0.32 |
| 1/27/2011 - 3/14/2011 | 46 | 756 | 13,105 | 0.31 |
| 12/4/2007 - 3/14/2011 | 1,196 | 2,603 | 6,552 | 0.20 |

removed. To appropriately generate an interferogram, the baseline of a SAR scene must be less than the critical baseline, which depends on the range resolution of the satellite, the incidence angle of the signal with the ground surface, and the signal wavelength. In remotely sensed data, atmospheric effects are difficult to quantify (Jensen, 2005); however, in data generated using radar signals with long wavelengths and good atmospheric penetration, atmospheric effects are often assumed to be negligible. Finally, filtering reduces the effects of noise.

In this study, the commercially available software SARscape 4.1 running in ENVI 4.6 was used to process the SAR data. Initially, each SAR scene was focused. Focusing gathers the phase and amplitude of the radar pulse reflected from the ground surface into pixels. The focused data were then paired to generate interferograms with approximately 13.5 x 18.5 m pixels. A SRTM-3 DEM was used to remove the topographic phase from the interferograms (CGIAR-CSI, 2008). With the topographic phase removed, the interferograms were filtered and the coherence, a measure of the image quality, was calculated for each interferogram. Coherence is related to the change of the signal intensity between the paired data and can range from zero to one, where one represents excellent quality data with no change in the signal intensity between the scenes. Next, the interferograms were unwrapped. Until phase unwrapping, the interferometric phase data are stored as modulo $2\pi$, which makes the data ambiguous. Phase unwrapping resolves the ambiguity. Finally, the unwrapped phase data were converted to displacements and the resulting displacement maps were properly geo-located.

## RESULTS

In this study, a total of ten displacement maps were generated: eight sequential maps and two cumulative maps. The eight sequential maps all span relatively short time frames during the period from December 4, 2007, to March 14, 2011. An additional displacement map spanning the entire time sequence was generated by pairing the SAR data from December 4, 2007, and March 14, 2011. For comparison with this map, the displacement data in each of the eight sequential maps were added together to generate a cumulative displacement map spanning the same period from December 4, 2007 to March 14, 2011. The satellite acquisition dates of the SAR data are summarized in Table 1 along with the baselines, the critical baselines, and the mean coherence of the interferograms used to generate the displacement maps.

Displacement maps for the eight sequential data pairs are shown in Figures 2 and 3, with the region of maximum subsidence in each map identified by a black box. The maximum subsidence values are summarized in Table 2. All of the regions of maximum subsidence occurred above longwall panels. The subsidence generated by solution mining was significantly less than the subsidence generated by longwall mining: over the entire period from December 4, 2007, to March 14, 2011, solution mining generated a maximum subsidence of 0.52 m.

**Table 2. Summary of the subsidence data for eight sequential SAR data pairs.**

| Acquisition dates | Elapsed time (days) | Maximum Subsidence (m) |
|---|---|---|
| 12/4/2007 - 7/21/2008 | 230 | 0.53 |
| 7/21/2008 - 10/24/2009 | 460 | 0.78 |
| 10/24/2009 - 6/11/2010 | 230 | 0.68 |
| 6/11/2010 - 7/27/2010 | 46 | 0.52 |
| 7/27/2010 - 9/11/2010 | 46 | 0.58 |
| 9/11/2010 - 10/27/2010 | 46 | 0.47 |
| 10/27/2010 - 1/27/2011 | 92 | 0.48 |
| 1/27/2011 - 3/14/2011 | 46 | 0.43 |

The displacement map generated by pairing the SAR data from December 4, 2007, and March 14, 2011, and the cumulative displacement map generated by adding the displacement data from the eight sequential data pairs are given in Figure 4. Both maps show displacement for the entire 1,196-day period. In the map generated from the single SAR data pair, shown on the left in Figure 4, the maximum subsidence is 0.79 m. In the cumulative displacement map generated by adding the displacement data from the eight sequential data pairs, shown on the right in Figure 4, the maximum subsidence is 1.3 m. It is difficult to quantify the

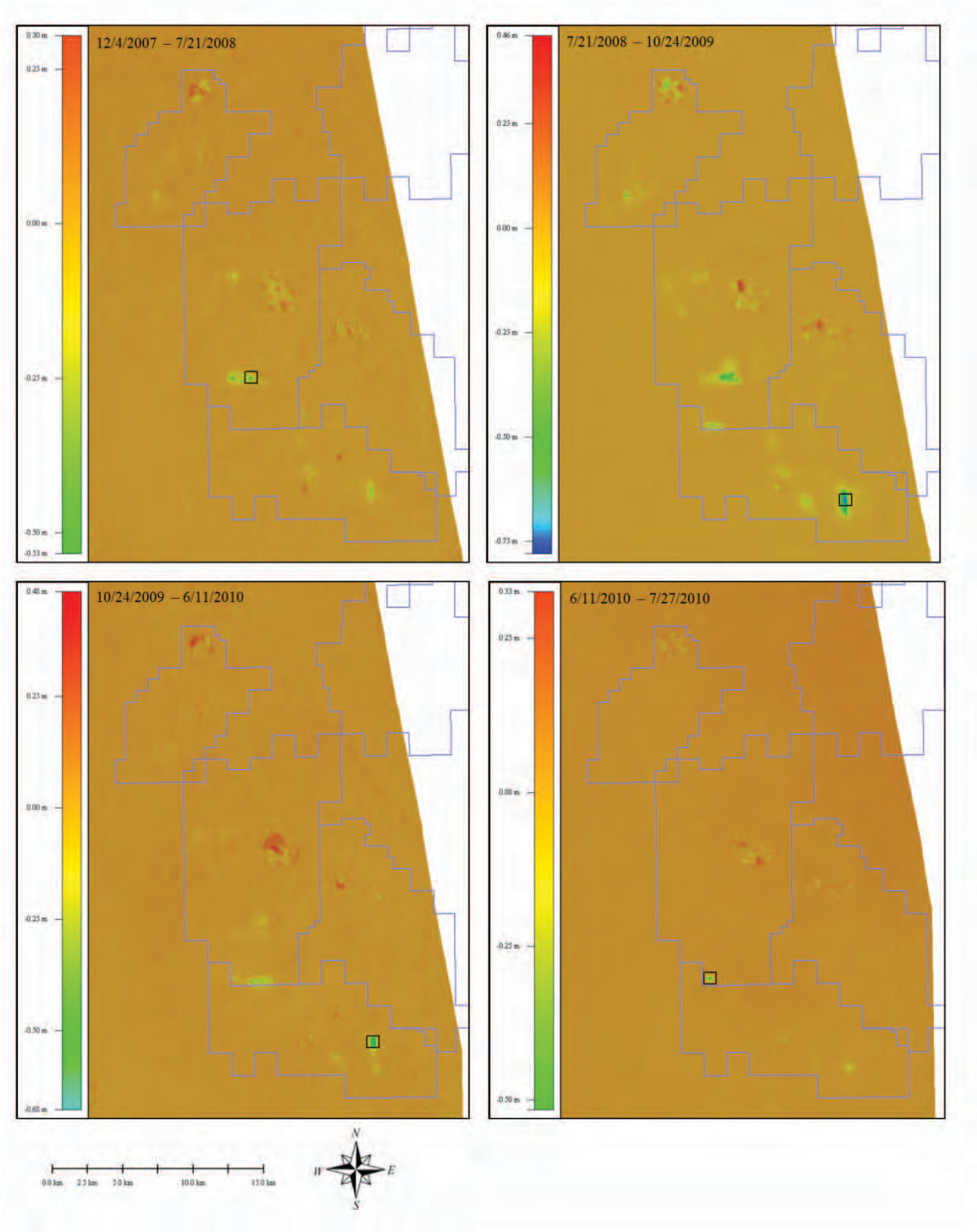



**Figure 2. Displacement maps derived from the following DInSAR data pairs: 12/4/2007 - 7/21/2008, 7/21/2008 - 10/24/2009, 10/24/2009 - 6/11/2010, 6/11/2010 - 7/27/2010. To show the maps with the most definition, the displacement color scale varies in each image. Blue outlines indicate mine leases, and black boxes indicated the region of maximum subsidence for each time period.**

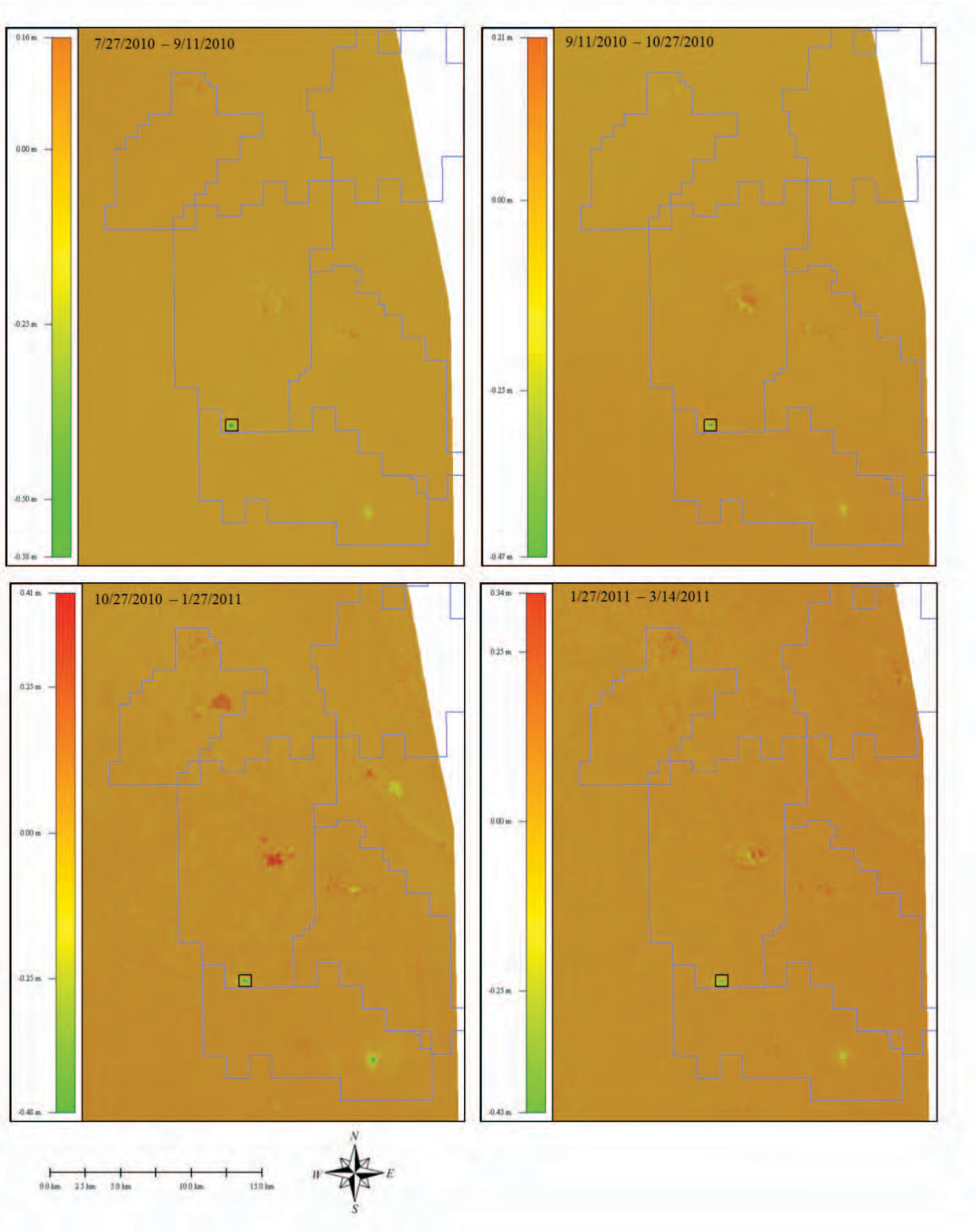



**Figure 3. Displacement maps derived from the following DInSAR data pairs: 7/27/2010 - 9/11/2010, 9/11/2010 - 10/27/2010, 10/27/2010 - 1/27/2011, 1/27/2011 - 3/14/2011. The color scale varies in each image, and black boxes indicated the region of maximum subsidence for each period.**

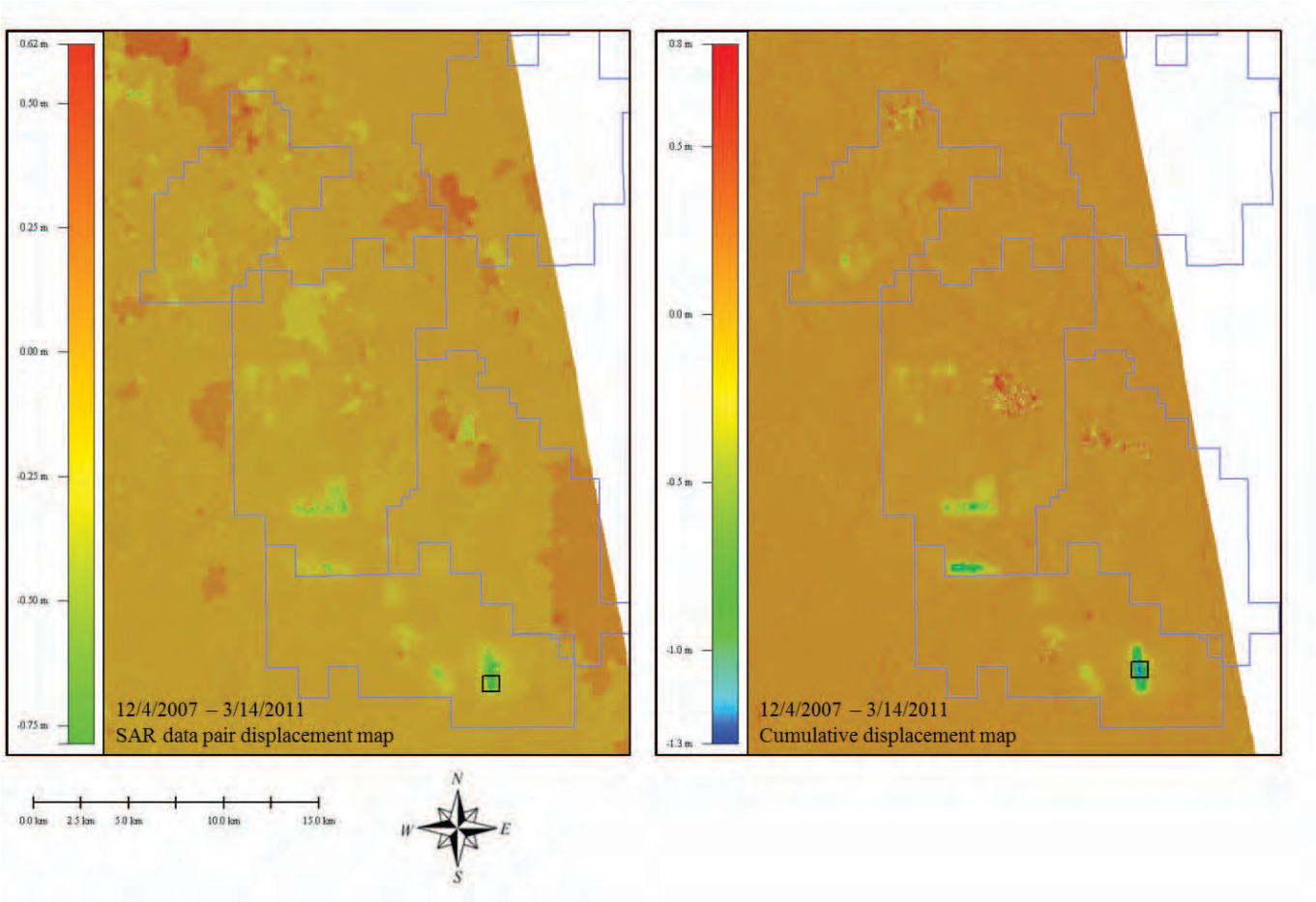



**Figure 4. Displacement maps from 12/4/2007 to 3/14/2011. The map on the left was generated using a single SAR data pair. The map on the right was generated by summing the displacement in the eight sequential SAR data pairs present in Figures 2 and 3. The color scale, representing the displacement varies. The location of maximum subsidence is indicated by the black box in each image.**

error in each of these displacement maps; however, in regions where there was no ground movement, the cumulative map shows displacements closer to zero than the map generated from the single SAR data pair. This indicates that as the sequential data are combined the errors tend to cancel.

The accuracy of the displacement data was evaluated by comparing the only available subsidence from 2010 to 2011 at one mine, which exhibited less than the maximum subsidence. Accuracy of the SAR data is difficult to evaluate because the timeline of ground survey in this comparison does not correspond exactly with the timeline of the SAR data acquisition. The best available timeline was used. For the mine evaluated, the maximum subsidence from 2010 to 2011 reported to the State of Wyoming was 0.12 m. A cumulative displacement map data covering the period from June 11, 2010 to March 14, 2011 was developed from the SAR data. From this map, the maximum displacement for the mine was 0.2 m. Better information for comparing the subsidence data was not available.

## DISCUSSION

This study demonstrates that, for the trona mining region in southwest Wyoming, subsidence data generated using DInSAR can supplement data from traditional subsidence monitoring methods. The displacement maps in Figures 2 and 3 show that in this mining region subsidence occurs due to both solution mining and longwall mining. It is notable that, during each period, longwall mining produced the most significant subsidence. The maximum subsidence measured by DInSAR totaled 1.3 m for the period from December 2007 to March 2011, and this subsidence occurred over a longwall panel.

Though DInSAR data can be useful for quantifying the effect of subsidence in a mining region, this study shows that the elapsed time between SAR pairs can significantly affect the accuracy of the measured displacements. Over time, SAR data are affected by spatial and temporal decorrelation. Long elapsed times lead to large differences in the path of the satellite and a high change gradient on the surface. These decorrelations, which are more significant over longer elapsed times, cause significant errors in unwrapping the phases, which lead to errors in the displacements. The errors caused by incorrect phase unwrapping are demonstrated in Figure 4, in the displacement map generated by pairing the data from December 4, 2007 and March 14, 2011. In this map, significant phase unwrapping errors are identified by abrupt transitions from areas with significant uplift to areas with significant subsidence. However, even in the higher quality displacement maps in Figures

2 and 3, there are regions of poor data quality with uplift and subsidence in relatively concentrated areas. These regions are likely tailings ponds that poorly reflect the radar signal and consequently have very low coherence. During data processing, errors similar to the phase unwrapping errors caused by decorrelation are generated in these regions of low coherence.

Although pairing SAR data over long timeframes can lead to poor quality displacement maps, long-term displacement maps can be generated by pairing the SAR data over shorter periods and summing the displacements. In this study, summing the displacement from the eight sequential maps produces a relatively high-quality cumulative displacement map with few phase unwrapping errors. Notably, the maximum subsidence in this map is more than 1.5 times the maximum subsidence in the cumulative map generated from the single SAR data pair.

In addition, this study shows some discrepancy between the maximum subsidence from the DInSAR data and the maximum reported subsidence, for the same mine over similar time periods. The magnitude of the subsidence from the DInSAR data is 0.2 m and the magnitude of the reported subsidence is 0.12 m. Although the subsidence values are different, the magnitude of the subsidence from the DInSAR data is not unreasonable. Additionally, the average subsidence is on the order of a centimeter per year. This is a small displacement over a fairly long time scale, and accurate detection of such displacement rates is likely beyond the sensitivity of DInSAR. The discrepancy indicates that DInSAR may not be appropriate for monitoring centimeter-level displacements that occur over time scales longer than a single orbit of the satellite, typically 46 days. Over longer time scales the correlation of SAR data pairs tends to decrease, making it difficult to measure small changes in displacement. If the DInSAR displacement and reported subsidence had been compared at a mine with more significant subsidence, the magnitude of the subsidence would likely have been in better agreement. Subsidence was not calculated for a mine with more significant subsidence, because reported subsidence data were not readily accessible.

Finally, though there are some problems using DInSAR to measure subsidence, including limited accuracy, the data presented in this study indicate that DInSAR can be useful for evaluating subsidence over large regions with relatively long time scales. The displacement maps derived from DInSAR can quantify the development of subsidence over time, the impact of subsidence in a mining region, and also identify when subsidence is complete. DInSAR data may also provide a useful input for validating geotechnical models used in mine planning.

## ACKNOWLEDGEMENTS

Funding for this research was provided by the National Institute for Occupational Health and Safety (NIOSH). The support of NIOSH is thankfully acknowledged; however, the conclusions expressed in this paper are those of the authors and do not represent the opinions or policies of NIOSH.

Additionally, the authors would like to thank the Alaska Satellite Facility for the access to a significant resource of SAR data, Amy Boyle with the Wyoming Department of Environmental Quality for help accessing mine data, and Fitra Ismaya for patiently answering DInSAR related questions.

## REFERENCES

Brown, N.A. (1995). “Union Pacific instrumental in developing Wyoming trona.” *Mining Engineering* 47(2): 135-141.

CGIAR-CSI. (2008). “SRTM 90m digital elevation data.” [http://srtm.csi.cgiar.org/].

Donovan, J., and Ismaya, F. (2010.) “Case study: measuring subsidence above coal mines using differential interferometric synthetic aperture radar.” In: *The 44th US Rock Mechanics Symposium* and *5th U.S.-Canada Rock Mechanics Symposium*. Alexandria, Virginia: ARMA.

Gandhi, S. (2013). “Industrial minerals review: soda ash.” *Mining Engineering* 65(7): 103-104.

Ge, L., et al. (2008). “Spaceborne radar interferometry for mine subsidence monitoring in Australia.” In: *Proceedings of the First International Future Mining Conference and Exhibition 2008*. Carlton South, Victoria, Australia: AusIMM, 119-124.

Ismaya, F., and Donovan, J. (2012). “Applications of DInSAR for measuring mine-induced subsidence and constraining ground deformation model.” In: *Proceedings of the GeoCongress 2012: State of the Art Practice in Geotechnical Engineering*. Reston, Virginia: ASCE, 3001-3010.

James, R. (2012). “FMC playing it safe with trona mining project.” In: *Billings Gazette*. [http://billingsgazette.com/news/state-and-regional/wyoming/fmc-playing-it-safe-with-trona-mining-project/article_01ad16ae-b52f-5cf6-beae-cf2c73811f03.html].

Jensen, J. R. (2005). *Introductory Digital Image Processing*. 3rd ed. Upper Saddle River, New Jersey: Pearson Prentice Hall.

Mannion, L.E. (1975). “Wyoming trona.” In: *Proceedings of the SME Fall Meeting.* Salt Lake City, Utah: SME.

National Coal Board. (1975). *Subsidence Engineers’ Handbook*. Mining Department of the

National Coal Board, United Kingdom.

Rosen, P., et al. (2000). “Synthetic aperture radar interferometry.” *Proceedings of the IEEE*. 88(3): 333-382.

Sarmap. (2009). “SAR guidebook: synthetic aperture radar and SARscape.” [http://www.sarmap.ch/pdf/SAR-Guidebook.pdf].

U.S. Geological Survey. (1981). 1:100 000-scale metric topographic map of Rock Springs Wyoming. [http://store.usgs.gov/b2c_usgs/catalog/setCurrentItem/(isQuery=yes&layout=6_1_61_58&uiarea=2&ctype=catalogQuery&next=seeItem&carea=0000000009&citem=00000019110000000040)/.do].

Wyoming Public Records. (2013). Wyoming Department of Environmental Quality.

# Tracking and Tracing in Terms of Transportation Logistics of Hard Coal Mines

**Marcel Mondring**, Senior Engineer
RAG Mining Solutions
Herne, Germany

**Lothar Berger**, President
ECOM Instruments Inc.
Katy, TX

## ABSTRACT

Transportation and the logistic requirements are set very high for the German coal mining industry. Short transportation resources, crowded quarters, and long transportation distances to destinations are some basic conditions that logistic employees of the mines have to deal with. Therefore, in the context of these processes, human effort and technology are faced with great challenges.

There can be a total of 300 transport units, depending on the size of the mine. Every day, they are moved through a nearby 150-km-long transportation network of floor and monorail tracks. Of these transport units, 150 are new, and the other 150 units are split into cross traffic units that are moved only in the underground and return travel units.

Beside track-bounded transports, all material transports take place in the shaft. As a result, many involuntary transports and changes in the means of transportation make the daily work more difficult. Typical transports in the shaft include the supply of new materials from above to below, as well as returnable goods from below to above. Cross traffics throughout several levels, which are rather rare, would have to be handled above the shaft. Due to limited shaft capacity, these cross traffics should be avoided when possible.

Based on the gas resources in coalmine slopes, track-bounded transports using monorails (powered by diesel or rechargeable means) are preferred. This depends on the road degree, the depth, and track cross section of the shaft/slope. The variety of the material spectrum includes more than 100,000 different types of material.

The following image (Figure 1) gives an overview of the difficulties during loading and transportation:

## OBJECTIVE OF THE PAPER

To fulfil the requirements of logistics, especially in terms of transportation, it is necessary and indispensable to have transparency throughout the whole transportation chain. The use of an IT-based solution is particularly useful to offer support for the processes and transparency.

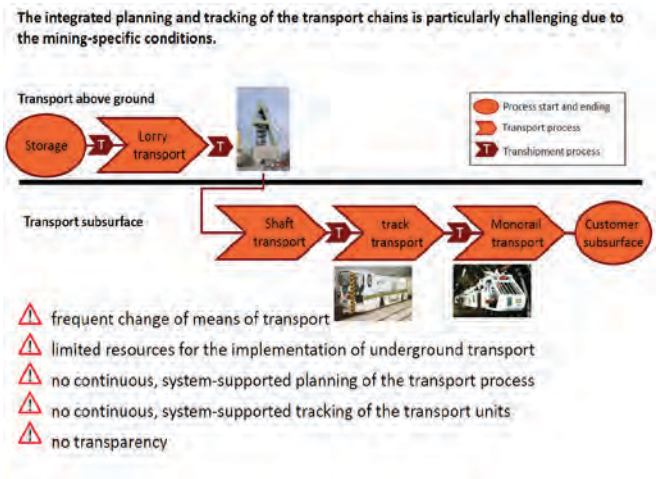



**Figure 1. Overview Transport chain.**

Personal digital assistants (PDAs), which are explosion-protected and suitable for underground use, make it possible for employees to collect and transmit required information (see Figure 2). For tracking purposes, all transport units, regardless of whether they are new, cross traffic, or return travel, get a unique identification number and barcode label. Employees identify which transport unit they are tracking by using the PDA. This allows all employees of logistics to track the exact position of the materials on the surface and underground. The information is then transmitted via WI-FI access points; this can take place at the surface or subsurface. This makes it possible to create an overall timetable for transportation logistics and to allocate moving orders for several drivers (for example, locomotive and monorail drivers). In turn, this timetable ensures smooth transportation.

In addition to the use of PDAs and access points, fibre optic cables for data transfer are necessary from a technical point of view because they function as an interface between the data collection below ground and the data processing above ground. On the part of the IT, several essential systems flank/mark the processes, which will be explained further in the next 3 chapters:




**Figure 2. PDAs ecom instruments.**

## PRONET AND PROTRANSNET

With the aid of the application ProNet, the surveying data of the mine (distances, incline of the gates, and depths) can be assimilated and visualized by a 3D-model (i.e., the whole gate system of a mine can be displayed). Furthermore, ProNet offers the opportunity to display information from multiple parts of a mine. For example, this can be the product extraction with the help of the application ProBand (conveyors, coal bunker, armoured face conveyor, and crusher), the supply with ProEnergie (cold water, fresh water, cooler, and air supply) and the transport infrastructure with ProTransNet (floor and monorail network, stations, switch points, and shaft-landings). In addition, all telephones and access points of the mine can be visualized. By using the ProTransNet example, this will be explained in more detail (see Figure 3 and Figure 4).

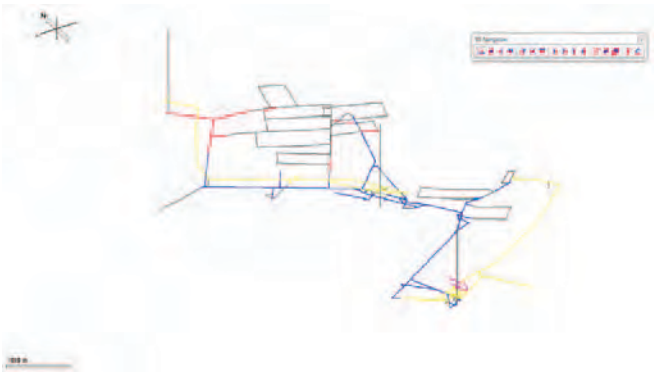


**Figure 3. ProNet illustration mine PH.**

Every color of the lines of these figures stands for another level in the mine respectively the depth of the tracks. All horizontal tracks at each level will normally be used for track-bounded means of transport.

## TRANSPORT STEERING SOFTWARE (TS/4)

For the coordination of transports, RAG Mining Solutions developed a transport steering software called TS/4. With the aid of this system, the transportable goods are grouped into

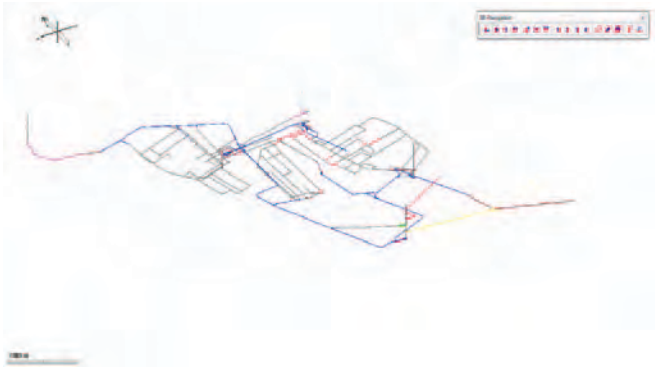


**Figure 4. ProNet illustration mine PH.**

"commissions." These commissions are then used to create a general schedule (including the order of transports before the shaft, shaft transport, rail transport, and monorail transport). In addition, TS/4 defines transportation routes to the destination working points. Details of road degree, distances, and the estimated run-time for each destination are arranged here. Rather than be dependent on the local road conditions of a mine, TS/4 can show that the existence of an alternative transportation route is possible (for example, a working point can be reached by several monorail stations). This route can be considered and added in the transport steering system.

## MATERIAL TRACKING AND TRACING SYSTEM (T&T)

The material tracking and tracing system at RAG is a web-based application, which is using the RAG intranet and is available to all employees. There is a wide variety of searching criteria available to locate the position of a transport unit.

Important search criteria are as follows:

- Selection of the mentioned mine (preselection)
- Receiver of the goods (destination working point)
- District
- Material number
- Commission number
- Kind of transport (new, return, cross)
- Position

The layout of this mask is shown in Figure 5.




**Figure 5. Search mask material T and T system.**

The material tracking and tracing system can be regarded as an interface to TS/4 of each mine because all provided data are requested of TS/4.

## SCHEDULING PROCESS

Day-to-day, a 24-hour valid schedule is created that considers all orders of new material and all declarations of cross traffic and return material from the subsurface. The system relies on a defined number range of 7 positions, which clearly classifies the commissions in the type of material. New material begins with a 4 in the number range of RAG – Deutsche Steinkohle, cross traffic begins with a 6, and return material with a 7. As a colour design feature, all commission papers have clearly defined colours: for new material white, for cross traffic red, return material blue, and emergency deliveries pink (see Figure 6, Figure 7, Figure 8, and Figure 9) (Standard RAG-mine Prosper-Haniel, Bottrop). Like the scheduling process, the commission numbers and the associated commission papers for new material and emergency deliveries are automatically generated from the available number range of the system. In comparison, the commission papers of cross travel and return material are assigned as blank papers with preprinted commission numbers. However, a responsible employee of the issuing working point has to register the material at the transportation control center to enable the commission number in the system.

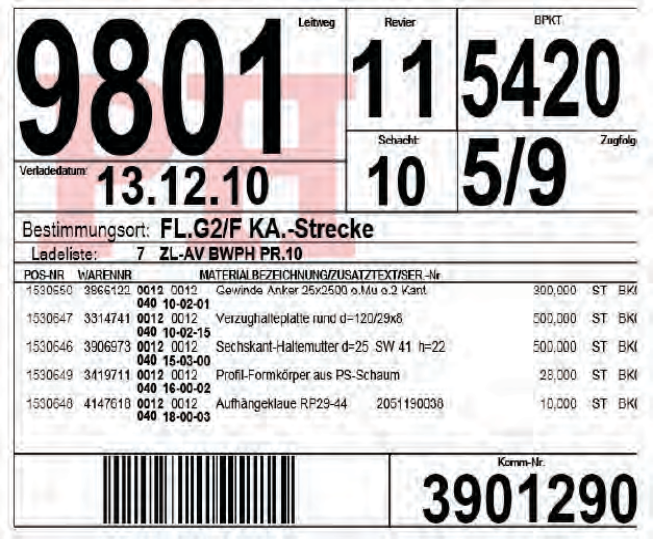



**Figure 6. Commission paper new material mine PH.**




**Figure 7. Comparison paper cross travel PH.**




**Figure 8. Commission paper return material PH.**




**Figure 9. Commissions papers AV.**

To secure a flawless collection of commission papers, barcode technology is used for the collection processes. Manual data input naturally includes many entry errors, which would have a negative impact on the overall process. Most of the new materials at RAG are general material (i.e., these materials are ordered automatically by the daily meter advance reportings of the heading and longwall departments). The system works based on gross bills of material, which are clearly defined by the material demand for each meter of longwall and heading roadways. Other new materials are ordered on demand and after permission are integrated in the actual valid schedule, as well. To avoid loss of production, downtime, and risks, emergency deliveries can also be integrated into the ongoing schedule. Despite these interventions in the daily schedule, more than 95% of all new deliveries come within 24 hours to the customer.

The scheduling process also takes into account the empty boxes and undercarriage contingents, as well as several configurations of the monorail lifting bars of the mine to carry out all actually planned transports (see Figure 10).

## DAILY TRANSPORT PROCESS FROM THE POSITIONING TRACK TO THE CUSTOMER

The basis for the daily transport workflow is the established timetable with a validation of 24 hours, created a day before. The start of the timetable depends on the mine layout (especially in terms of the material shaft and time frame for the conveying) and is set at 2 pm (Auguste Victoria Mine) or at 6 pm (Prosper-Haniel Mine). Besides the consideration of new materials, cross traffics, and returns, a succession for new materials in the positioning track is created on the surface and sorted by the destination working point. That means this schedule defines the exact positioning of the material, as well as the exact starting time, for the transport through the material shaft. In case of two or more monorail stations

underground, the process is much more important. In this special case, the transport units are already sorted by monorail stations and by final destinations on the surface loading area (see Figure 11).




**Figure 10. Transport process and T and T system.**



**Figure 11. Loading technology mobile crane.**

With the positioning of the transport units at the surface, the material tracking and tracing system is activated. The first logging with the PDA occurs near the landing stage by the banksman. Before loading the materials in the conveyor cage, the barcodes are scanned (see Figure 12). Up to three units are transported at the same time, according to the size of the transport units and the layout of the conveyor cage. Notwithstanding the three units is the transport of pipes. Related to the length, in this special case, an empty (under) carriage is needed. Even big transport units, like shields and conveyor parts, are marked with commission numbers to make them traceable. It does not matter whether these materials are transported as new or return materials or as cross traffic transports underground.

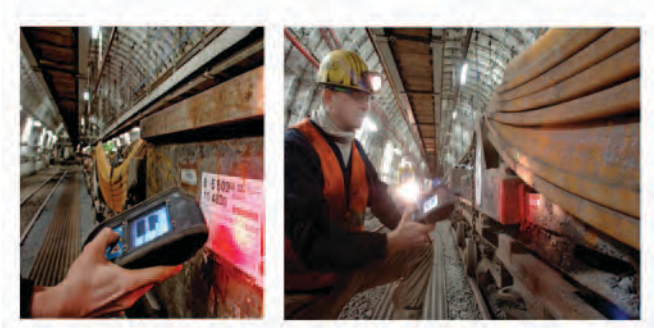


**Figure 12. Barcode scan PDA.**

The next step in the registration chain is the reception of the transport units at the shaft-landing by the locomotive driver. At this point, the barcode labels of the commission papers are scanned again, and a departure signal via PDA is transmitted using the WI-FI. Afterwards, the units are transported to the central monorail distribution station of the mine, with regard to the peripheral monorail distribution station. That depends on the underground circumstances and the transportation infrastructure of the mine. It is important that all barcodes be scanned. When all units are registered, shipments are guaranteed to reach their destinations (see Figure 13).



**Figure 13. Barcode scan PDA.**

The following position report occurs at the monorail station (central/peripheral) by the locomotive driver (see Figure 14 and Figure 15). All commissions that were transported from the shaft-landing to the monorail station are scanned again. The transport from the monorail station to the final working point via monorail is the last step in the transportation chain. The monorail operators are scanning all units for their special working points, which they will receive within their shifts. Before the departure, they transmit the commissions of their lifting bars and starting time via PDA and WI-FI to the particular destinations. Each customer (material recipient) is able to track the units from the beginning to the end. The system is comparable to well-known tracking and tracing systems like DHL. With the knowledge of the commission number, it is possible to have a look into the tracking and tracing system at any time, in order to find information on the units that a customer is waiting for. As an alternative, the system can search for the destination working points and all materials for these working points can be illustrated (Compare chapter material tracking and tracing system (T&T System)).

After the completed transport to the working point or customer, the monorail driver scans the units one last time and sends a delivery message to the system. This process (scanning, departure message, and delivery message) is consistent from the loading at the surface to the actual customer in the mine.

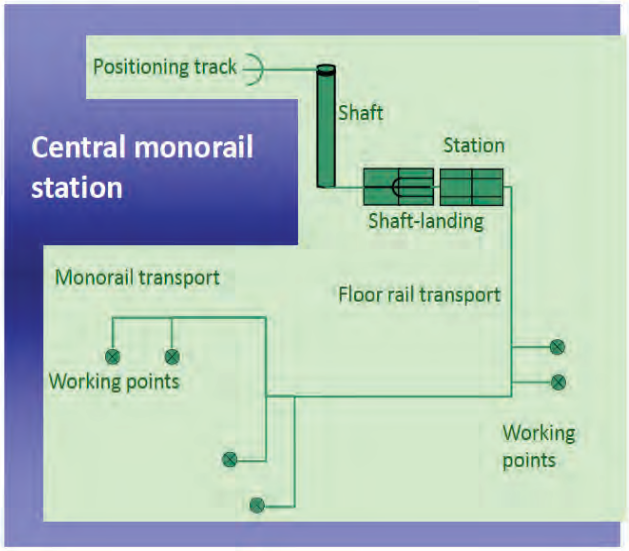



**Figure 14. Plan central monorail station.**

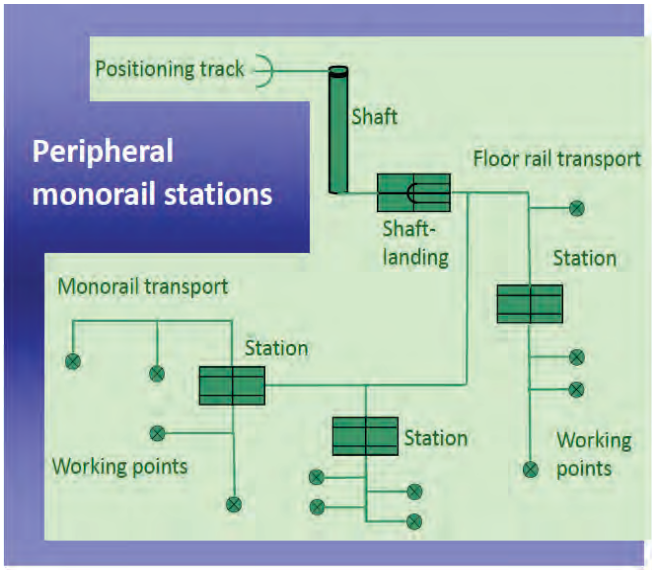



**Figure 15. Plan perifial monorail stations.**

## KEY FINDINGS

Within the first year of implementing the tracking and tracing systems and establishing the overall schedule, there has been a fundamental increase in the transport service level. As stated before, 95% of all planned transports are reaching their working points within 24 hours. The system immediately leads to a significant transparency and improvement of the transport steering in a working day. In addition, it offers the possibility to react easily during unplanned events, like the breakdown of a monorail, shaft troubles, emergency deliveries, etc.

The use of PDAs, which provides a total tracing of the material units to the final customer, shows that the tested technologies above ground are also usable underground. The total advantages are available the same way.

Because of transparency of the processes and the traceability of the material units, double orders can be avoided. The material availability can be increased. At the same time, the allocation of the limited transport resources above and below are optimized. These resources optimally use the vertical shaft capacity, the corresponding means of transportation (like monorails, floor rails, and wheel excavators) at the surface, as well as the complete portfolio of the auxiliary means of transportation (undercarriage, long containers, lining pallets, fuel containers for liquids, etc.).

## KEY CONCLUSIONS

With the implementation of the tracking and tracing system, the following advantages are realized:

- Savings in terms of money and manpower
- Reduction of the total transport appearance
- Better allocation of the existing transport resources (machines and employees)
- Transparency of the whole transportation process, beginning with loading above to the customer on site
- Enables an efficient transport equipment management

The weaknesses, described in the beginning problem statement, are nearly solved.

Investing in a tracking and tracing system produces financial benefits within a short period of time.

# Photogrammetric Monitoring of Rock Mass Behavior in Deep Vein Mining

**Donovan J Benton**
**Stephen Iverson**, Mining Engineer
**Jeffrey C Johnson**, Mining Engineer
**Lewis A Martin**, Research Mechanical Engineer
NIOSH, Office of Mine Safety and Health Research
Spokane, WA

## ABSTRACT

Photogrammetric methods are advancing rapidly and show considerable promise as a ground control research tool. The ability to quickly capture three-dimensional geometry, especially changes in geometry, in underground and laboratory settings is a significant advance from point distance measurements. Photogrammetry is being applied in both of these settings as part of the NIOSH ground control research. This paper describes these applications and the equipment and software being employed. It also describes tests conducted to quantify the accuracy of these systems. Accuracy varied with system specifics and procedures. A factory-calibrated camera produced results within 1/32 of an inch, plus 0.04%. A user-calibrated camera was found to be less accurate, at 1/20 of an inch, plus 0.24%. These calibrations demonstrate that photogrammetry can produce research quality measurements in laboratory and mine settings.

## INTRODUCTION

### NIOSH Mine Safety Research

The National Institute for Occupational Safety and Health (NIOSH) is currently performing ground control research to improve mine safety. Accurate and efficient measurement of geometry, displacement, and volume changes is important to these efforts. This paper discusses implementation of two photogrammetric systems and assessment of their measurement accuracies.

Photogrammetry is currently being applied in two ways. One is to monitor the in situ evolution of excavations and their associated support integrity. Quarterly mine visits are made to take photographs used to assess excavation closure, rock mass integrity, and fault crossings. Changes are detected by comparing these to photographs from previous visits. A second application is to track deformation of shotcrete panels tested in the laboratory. In both cases, the ability to track changes in surface geometry and estimate changes in volume is essential to project success.

### State of photogrammetry

Recent developments in full-field measurement techniques and equipment have made total system measurements feasible (Viggiani and Hall, 2008). To demonstrate, full-field reconstructions of underground openings using photogrammetry can easily produce 200,000 points from which cross sections, closure measurements, etc., can be made.

There are two primary full-field technologies that have been applied to ground monitoring: LiDAR and photogrammetry. Photogrammetry has two significant advantages over LiDAR in mining environments (Paar and Kontrus, 2006):

- Photos can be taken easily with relatively inexpensive devices, require minimal operator training, and minimal interference with operations. A site visit might take only five minutes.
- Digital images are produced to correspond to site geometry and environment. These images contain additional information such as paint markings, corrosion, water, and damage to support installations. Some LiDAR devices also produce digital images, but these are additional to the survey itself. Photogrammetry produces point clouds directly from the images.

## FIELD APPLICATIONS

### Field photogrammetry system

One Nikon® D80 digital SLR camera with a Sigma 10mm to 20mm zoom lens was used for the field photogrammetric system. The camera provides user-friendly focus, lighting, and shutter speed options. The camera and lens specifications are in Table 1. Generally the highest cost portions of a photogrammetry system are the software, camera calibration, and auxiliary lighting. ShapeMetrix$^{3D}$ photogrammetry software from 3GSM (3GSM, 2011) was used to complete the 3D field site reconstructions. The software was developed specifically for mining and construction applications and includes a camera, lens, tripod, a survey range pole, and a camera/lens calibration. ShapeMetrix$^{3D}$ does not allow users to calibrate their own cameras.

**Table 1. Overview of field photogrammetry equipment.**

| | |
|---|---|
| Camera type | Nikon D80 digital SLR |
| Lens | Sigma 10mm to 20mm zoom |
| Horizontal field of view (10mm zoom) | 99 degrees |
| Vertical field of view (100mm zoom) | 76 degrees |
| Effective image pixels | 10.2 million |
| Pixel resolution at 5 m | 0.3 cm by 0.3 cm |

Auxiliary lighting for site visits was provided by three Pelican® 9430 Remote Area Lighting Systems (RALS). The RALS generated sufficient lighting to capture true color and fine detail of the rock surfaces and support systems. The RALS remained stationary during each photogrammetric session and had sufficient battery power to facilitate day-length surveys. Camera settings were selected to provide the best image quality, including low ISO (generally 100) and medium f-stop (typically 8). The camera shutter speeds at these settings required a tripod to prevent camera movement during image capture.

**Excavation monitoring**

Preliminary field applications of this technology have focused on monitoring excavation closure, rock mass integrity, and fault zones. Field visits at one underground mine included eight sites where faults cross a ramp system. Mine engineers installed crack meters at these sites, allowing for eventual cross-referencing of the fault movement data. Site visits were scheduled on days during which mine traffic was at a minimum. This is not always necessary for photogrammetric surveys, but the extensive procedures used for research purposes required minimal interference.

At each site, the RALS units were deployed against one rib facing the opposite rib. Tools, hoses, bags, and other unnecessary items were removed from the target rib to reduce interference and increase reconstruction quality. Reconstructions are created by combining the visual and point cloud data from digital image pairs into a 3D "reconstructed" scene. Removal of extraneous objects from the scene prior to image capture simplifies point cloud data, making visual data overlay more accurate. Three permanent survey targets were spray-painted and located non-collinearly on the rib. These points were later surveyed by mine surveyors to serve as control and scaling for 3D reconstruction measurements. A range pole was also set on the periphery of the image field as a back-up to the surveyed control points. Lastly, the camera tripod was placed between two RALS units to capture the images of the opposing rib. Figure 1 shows the typical field setup.

A total of 24 photographs were taken at each site, 12 of each rib. At each camera position, photo pairs were taken at three different angles: directly at the face, approximately 45° upwards, and approximately 45° downwards. To take a photo pair, the tripod is moved a distance to the left or right roughly equal to one-sixth of the rib-to-rib distance (i.e., two feet for a twelve-foot-wide opening). The three photo pairs taken at the first camera location were centered between the near and center RALS units. Experience showed that it was best to take a left and right pair




**Figure 1. Typical field setup of the photogrammetry system for underground surveys.**

sequentially for each camera direction. This process was repeated at a second camera location between the center and far RALS units. The photogrammetric survey was completed by moving the RALS units across the excavation and repeating the entire process, photographing the opposite rib. In this manner the entire fault crossing was reconstructed. Figure 2 shows a reconstruction completed using this method.

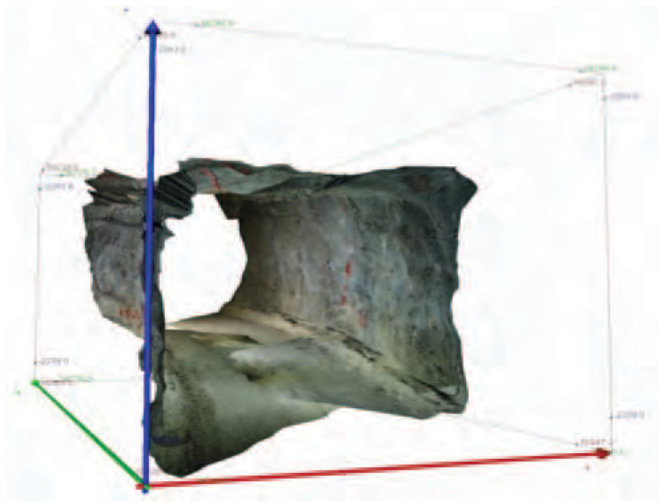


**Figure 2. Photogrammetric reconstruction of underground mine workings.**

It should be noted that there have been no significant fault activations or rock movements at the study site since the photogrammetric surveys began. Figure 3, however, shows the potential for analysis should movement occur. A cross section of an opening can be represented via points and coordinates. If these cross-sectional profiles are compared over time, rock bulging and other forms of deterioration can not only be visualized, but measured using the point cloud data. The cross sections may be developed at any location and at any orientation to allow for total site analysis.

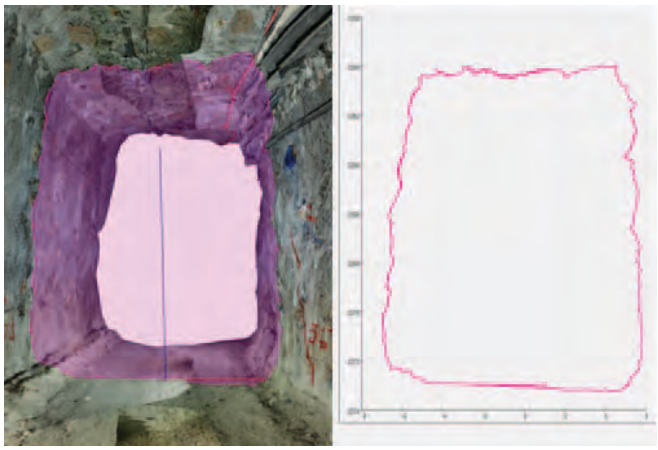


**Figure 3. Cross-sectional profiles obtained through photogrammetric reconstruction.**

## LABORATORY APPLICATIONS

### Laboratory photogrammetry system

The laboratory photogrammetric system consists of two Nikon® D800 digital SLR cameras. The camera and lens specifications are in Table 2. It is fully intended for the D800 cameras to be employed in the field once laboratory testing has been completed. 3DM Analyst photogrammetry software from AdamTech (Birch, 2008) was used to complete the 3D reconstructions of laboratory testing. This software has a built-in volume calculation function that is designed primarily to calculate inventory stockpiles in mining applications. 3DM Analyst also has the benefit of allowing users to calibrate their own cameras.

**Table 2. Overview of the lab photogrammetry equipment.**

| | |
|---|---|
| Camera type | Nikon D800 digital SLR |
| Lens | Sigma 20mm |
| Horizontal field of view | 84 degrees |
| Vertical field of view | 61 degrees |
| Effective image pixels | 36.3 million |
| Pixel resolution at 5 m | 0.1 cm by 0.1 cm |

### Laboratory test monitoring

The laboratory photogrammetry system has been used to monitor commissioning tests of a high energy high displacement (HEHD) testing system. The HEHD system was designed and constructed at the Spokane NIOSH lab to test shotcrete panels representative of deep vein mine support systems. The panel testing system, shown in Figure 4, is based on similar testing conducted by Kirsten (1992, 1993) and Tannant and Kaiser (1997). The planned tests differ by focusing on the use of mesh reinforcement as opposed to fibers. Furthermore, the system uses a ram and mushroom head because little difference was found in the behavior of the testing materials between uniform and point loading conditions (Kirsten 1993).

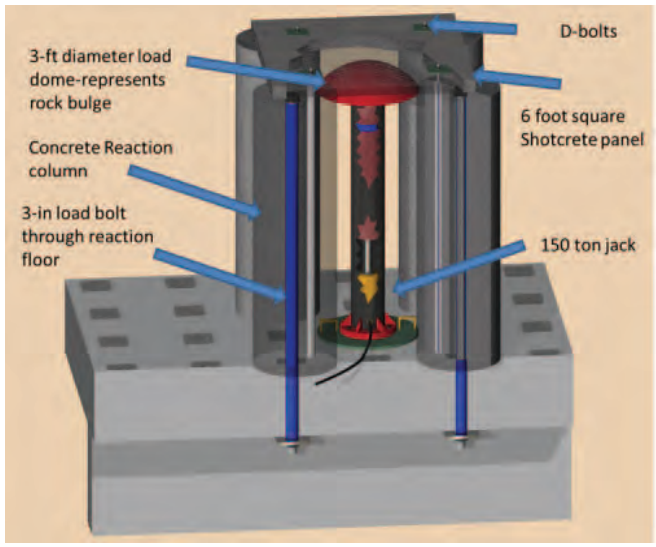



**Figure 4. High energy high displacement (HEHD) panel testing system used to characterize in situ support systems.**

The goal of panel testing is to determine if the system can withstand the anticipated loading on the mine opening supports. One measurement is peak flexural load capacity, which represents the maximum load the support panel can withstand prior to cracking. A second measurement, residual load capacity, is reported in terms of resistive load at subsequent increasing deflections. Important for energy calculations, toughness is derived from the aggregate area under the load capacity versus displacement curve and is indicative of the energy required to displace the specimen through a given distance. Flexural load capacity and toughness testing can supply specific material properties for the shotcrete/mesh panels that are then comparable to known specifications. The pressure and the displacement of the ram are recorded by the data acquisition system during each test. These data are used to calculate the work, or equivalently the energy, applied to the panel.

Prior to each test, the Nikon D800 cameras are mounted on the observation deck above the HEHD system. Each camera's internal clock is synchronized with the computer system used to record data from the HEHD system's instrumentation. A Nikon Sync cable is used to ensure that each camera captures simultaneous image pairs at 1-second intervals throughout the test. The photos are used to correlate the amount of visual damage and volume change to the load that has been applied to the panel. Figure 5 shows a textured (top) and triangulated mesh (bottom) reconstruction of subsequent reconstructions, overlain. The difference in volume between the blue (latter) and red (former) reconstructions equals the volume of deformation experienced by the panel.

To correlate volume change with energy input, data recorded by the HEHD's instrumentation is reduced. Energy is calculated by the force and the displacement of the ram on the panel. The force applied to the panel is computed from the pressure of the pump multiplied by the area of the jack piston (30.78 $in^2$/198.58 $cm^2$). The displacement of the ram is measured using a rotary potentiometer. The energy applied to the panel at different test times is then compared to their corresponding photogrammetric reconstructions. A correlation is made between

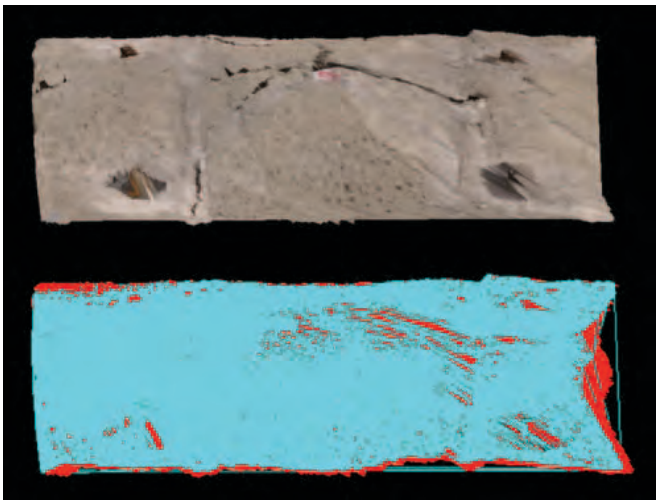


**Figure 5. Textured (top) and triangulated mesh (bottom) reconstructions used to monitor volume change.**

the amount of energy applied to the panel and its volume of deformation. By using the method described here, subsequent photogrammetric pairs of photographs over a given time period can be used to calculate volume change and estimate the amount of energy absorbed.

## CALIBRATION

### Calibration procedure

Photogrammetry has very high planimetric accuracy (perpendicular to line-of-sight), but a topographic depth accuracy (parallel to line-of-sight) that varies depending on bed-to-depth (B:D) ratios (Lato, Kemeny, Harrap, and Bevan, 2013). ShapeMetrix$^{3D}$ documentation suggests a B:D ratio between 5.0 and 8.0. An average ratio of 6.5 was chosen for the laboratory verification. This corresponds to a camera spacing ("B" or "bed") of 11 inches with a distance to target ("D" or "depth") of roughly 72 inches. In Figure 6, a cross-sectional diagram of the test setup is shown. The "line-of-sight" corresponds to the 72-inch distance to target (D).

As depicted in Figure 6, a 45° line-of-sight was chosen because it allowed the vertically rising stack of boxes to be observed equally in both planimetric and topographic fields. This line-of-sight orientation was constant throughout the testing process. A camera bracket was purpose-built in-house to facilitate camera spacing and orientation. The bracket allowed for three axes of freedom in camera placement: 1) angle from horizontal, 2) rotation about anchor point, and 3) camera spacing. Its composition included a 1/4-inch steel plate with a 1/8-inch slot lathed along the center. This allowed for adjustments in camera spacing and orientation. Welded to both ends of the bracket were 1/2-inch steel plates. The plates were bolted to the yellow uprights (shown in Figure 6), and allowed 360° movement about the horizontal plane.

### Field system accuracy verification

Tests were conducted to verify the accuracy of the ShapeMetrix$^{3D}$ software and D80 camera with respect to their linear measurements. The calibration testing consisted of

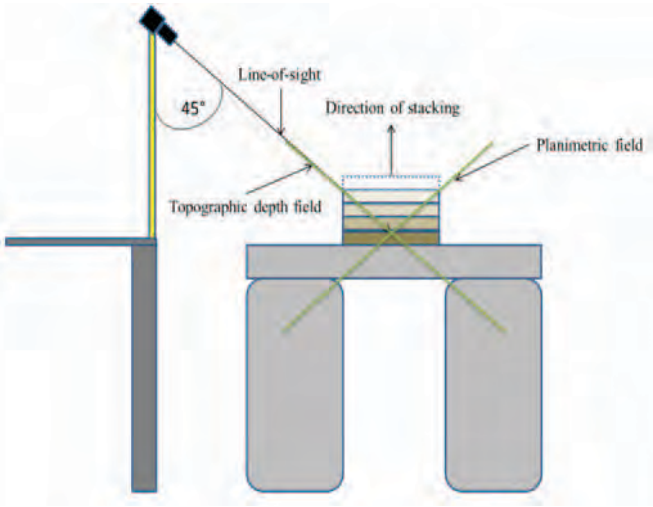



**Figure 6. Side-view of linear photogrammetric calibration.**

photographing twelve sequentially stacked wooden boxes. The boxes were constructed of 1/4-inch plywood and boards to achieve the desired dimensions of 2x2x12 inches. The boxes were numbered 1 through 12, and measuring points were placed centrally on three of the four edges. The height of each point above the base level was measured using a metal tape with measure divisions of 1/16-inch. The tape measurements were interpreted to 1/32-inch, resulting in an expected error +/- 0.03 inches for each measurement. Due to the minimal distances measured, temperature and sag corrections were not applied.

As each box was placed a photo pair was taken. The stereo photo pairs were imported into the ShapeMetrix$^{3D}$ software, and three-dimensional images were reconstructed. The red lines in Figure 7 show the linear distance between measuring points on two different boxes. The length of these lines is equal to the change in vertical-axis position of the measurement points. The tape-measured heights of the measurement points and the absolute value of the photogrammetric measurement differences are compared in Table 3.

Graphical interpretation of the differences between the photogrammetric and tape measurements is shown in Figure 8. The average photogrammetric error was +/- 0.03 inches, with a proportional increase in error of 0.04% per unit increase in known height. The maximum recorded error was 0.08 inches, while the minimum was 0.00 inches. Recalling the accuracy of the tape measure (+/- 0.03 inches), it can be concluded that at minimum the field photogrammetric system has equivalent accuracy.

### Laboratory system linear verification

Tests to verify the accuracy of the linear and volumetric measurements made with the 3DM Analyst software and D800 cameras were conducted. The tests used four particle board cutouts with known dimensions, each cut into truncated four-sided pyramids with 45° chamfers. The chamfers were used to prevent shadowing. "Shadowing" occurs in photogrammetric reconstructions when portions of the scene are obscured or hidden from the camera's perspective. Without photographic information the photogrammetric reconstruction extends adjacent color and

**Table 3. Field system verification measurements for ShapeMetrix3D photogrammetry software and D80 camera.**

| Left Marker | | Right Marker | | Front Marker | |
|---|---|---|---|---|---|
| Tape (in) | Shape-Metrix$^{3D}$ (abs error) | Tape (in) | Shape-Metrix$^{3D}$ (abs error) | Tape (in) | Shape-Metrix$^{3D}$ (abs error) |
| 2.00 | 0.06 | 1.94 | 0.02 | 1.97 | 0.00 |
| 3.94 | 0.04 | 3.91 | 0.05 | 3.94 | 0.01 |
| 5.90 | 0.05 | 5.84 | 0.04 | 5.88 | 0.00 |
| 7.90 | 0.00 | 7.84 | 0.05 | 7.88 | 0.03 |
| 9.75 | 0.07 | 9.78 | 0.03 | 9.82 | 0.03 |
| 11.81 | 0.01 | 11.75 | 0.02 | 11.82 | 0.02 |
| 13.81 | 0.04 | 13.75 | 0.04 | 13.85 | 0.03 |
| 15.75 | 0.02 | 15.66 | 0.07 | 15.82 | 0.02 |
| 17.69 | 0.05 | 17.56 | 0.01 | 17.75 | 0.04 |
| 19.62 | 0.01 | 19.53 | 0.05 | 19.75 | 0.08 |

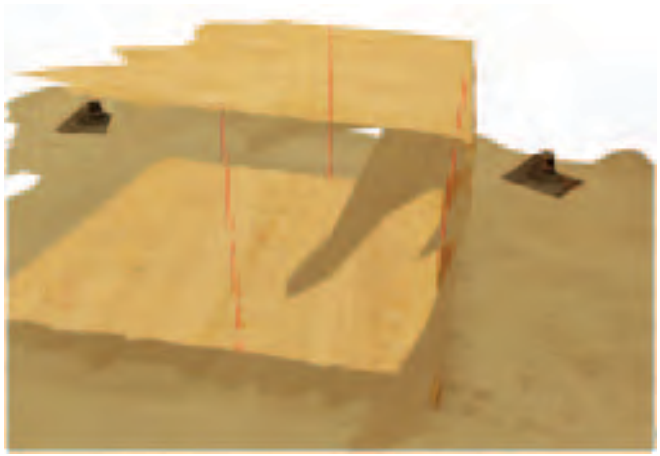


**Figure 7. The lines mark the vertical distance between measuring points in subsequent reconstructions.**

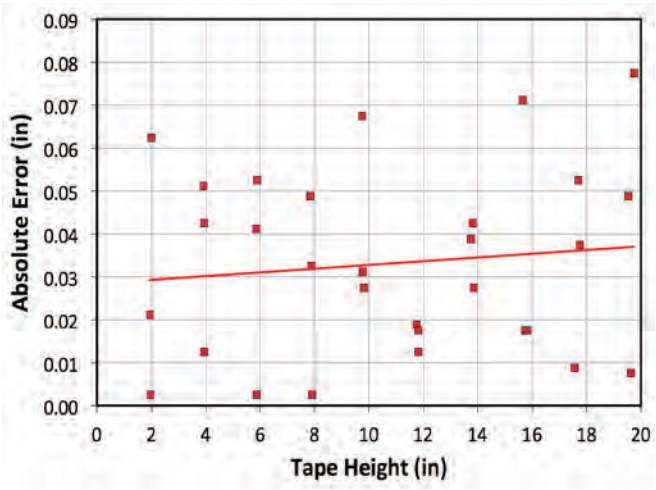



**Figure 8. Comparison of ShapeMetrix3D photogrammetric error to tape-measured height reveals and average error of +/- 0.03 inches and 0.04% per unit increase in measured distance.**

texture to the hidden areas. The resulting textures are smeared or shadowy, making measurements that incorporate these areas inaccurate. The line-of-sight of the cameras was changed to 50° from horizontal to enable capture of the rear edges of the boards. The increased potential for topographic field error caused by the change in line-of-sight angle was considered largely insignificant. Camera spacing was adjusted to 12 inches to maintain a 6.5 B:D ratio.

The linear component of the laboratory system verification was conducted similarly to the field system verification test. The same steel tape measure was used to determine the dimensions of each board, and temperature/sag correction factors were unnecessary due to the short distances involved. Measurements were made for the following dimensions: board thickness, lengths of the top and bottom sides, and diagonal distance across the top side. Sequential photo pairs were taken as each board was stacked. The photo pairs were reconstructed in 3DM Analyst and then measured using software functions. Complementary measurements were made in perpendicular directions for the length and diagonal dimensions, and opposite sides of each board for thickness, to assess software consistency and increase data collection. The tape-measured dimensions of each board and the absolute error of the photogrammetric measurements are compared in Table 4.

Graphical interpretation of the absolute error of the photogrammetric measurements, shown in Figure 9, yielded an average photogrammetric error of +/- 0.05 inches, exceeding the +/- 0.03-inch errors of the steel tape and ShapeMetrix$^{3D}$ software. At 0.24% the proportional increase in error per unit increase in each measured dimension was also higher than that generated by the ShapeMetrix$^{3D}$ software. The maximum recorded error was 0.33 inches, while the minimum was 0.02 inches. The decreased accuracy of the 3DM Analyst software is likely due to camera calibration. Whereas 3GSM will calibrate one camera specifically for use in ShapeMetrix$^{3D}$, users conduct their own camera calibrations for 3DM Analyst. Ultimately this is a superior capability of 3DM Analyst, but it may take several calibration attempts to obtain optimal lens and camera correction factors.

**Table 4. Laboratory system verification measurements for 3DM Analyst photogrammetry software and D800 cameras.**

| | Tape (in) | 3DM Analyst 1 (abs error) | 3DM Analyst 2 (abs error) |
|---|---|---|---|
| Thickness | 0.74 | 0.13 | 0.10 |
| | 1.48 | 0.12 | 0.09 |
| | 2.22 | 0.13 | 0.08 |
| | 2.97 | 0.05 | 0.13 |
| Length of Top | 5.24 | 0.04 | 0.07 |
| | 14.08 | 0.01 | 0.03 |
| | 17.84 | 0.08 | 0.05 |
| | 30.16 | 0.02 | 0.07 |
| Length of Bottom | 6.67 | 0.03 | 0.02 |
| | 15.53 | 0.11 | 0.19 |
| | 19.31 | 0.01 | 0.07 |
| | 31.59 | 0.09 | 0.32 |
| Diagonals | 7.40 | 0.01 | 0.07 |
| | 19.91 | 0.07 | 0.03 |
| | 25.23 | 0.08 | 0.09 |
| | 42.65 | 0.15 | 0.33 |

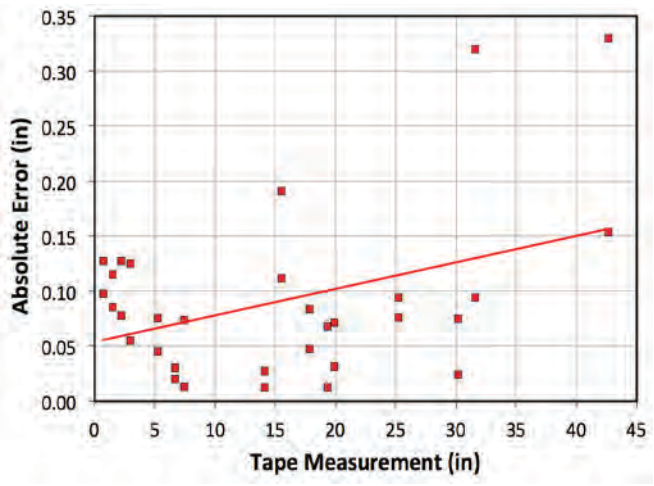



**Figure 9. Comparison of 3DM Analyst photogrammetric error to tape-measured height reveals an average error of +/- 0.05 inches and 0.24% per unit increase in measured distance.**

**Laboratory system volumetric verification**

The volumetric measurement verification of the 3DM Analyst and D800 cameras was conducted using the same boards as in the linear verification. The volume of each board was calculated from the tape-measured dimensions used in the linear verification. The same reconstructed photo pairs were then compared volumetrically to test for accuracy. Figure 10 depicts a side view of a reconstruction made with all four boards stacked showing both textured (top) and triangulated mesh (bottom) representations. The volume calculation process is illustrated by the mesh representation, in which the difference in volume between the blue and red meshes equates to volumetric change between reconstructions. The photogrammetrically measured volume difference was compared to the known volume difference, as shown in Table 5.

**Table 5. Volumetric verification measurements for 3DM Analyst photogrammetry software and D800 cameras.**

| Board | Known Volume ($in^3$) | 3DM Analyst Volume ($in^3$) |
|---|---|---|
| Base | 688.34 | |
| Total | 1126.60 | |
| Difference | 438.27 | 430.55 |

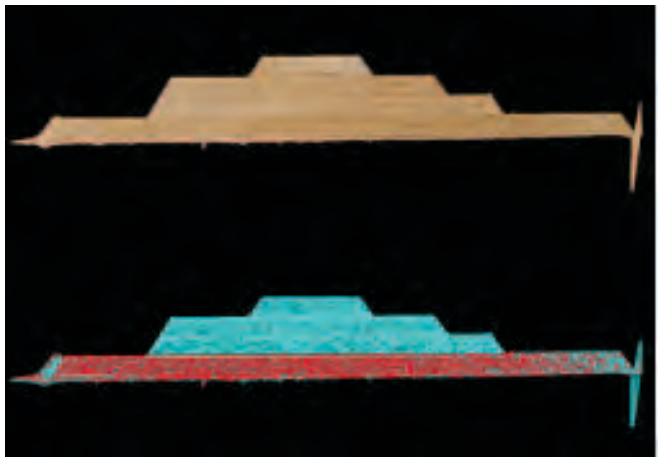


**Figure 10. Textured (top) and triangulated mesh (bottom) reconstructions used in photogrammetry calibration.**

The minimum resulting error was 1.79% (roughly 1 part in 55). The relative corresponding size of this error equals the volume of a cube with a side dimension of 2 inches. To establish a benchmark for accuracy in the volumetric application, steel tape measurements of the calibration board dimensions were conducted in two independent sessions. These measurements indicated a certain amount of error to be accounted for in the standards set for photogrammetric measurements. The maximum difference in tape measurements yielded a linear error of +/- 0.44%. The volume error was interpreted using a cube relationship of dimensions X (+/- 0.44%), Y (+/- 0.44%), and Z (+/- 0.44%). The volume of such a cube yields a maximum potential error of +/- 1.34%. The minimum error achieved through verification testing was 1.76%, or only 0.42% greater than the expected error in tape measurements. This was not unexpected, as the increased value corresponds with the increased absolute error value obtained through linear measurement testing of the same system. Additional camera calibration should help to reduce error.

## CONCLUSIONS

Verification testing of the field and laboratory photogrammetry systems has yielded promising results. The field system (ShapeMetrix$^{3D}$ and D80 cameras) has an average error of only +/- 0.03 inches. This value is comparable with steel tape measurements. The laboratory system (3DM Analyst and two D800 cameras) has an average linear error of +/- 0.05 inches, and

a volumetric error of +/- 1.76%. Both are well within acceptable bounds for these applications. Reconstructions and measurements can be made more quickly using 3DM Analyst, but there is a slight improvement in accuracy when using ShapeMetrix$^{3D}$.

This photogrammetric measurement method fills a void created by the inadequacy of point-based instrumentation techniques in monitoring systems that require quantitative measurements. Overall accuracy of photogrammetric systems may be improved in a number of ways (Gaich, Pötsch, and Schubert, 2006). Reducing the distance between the camera and target can improve image definition, in turn improving precision when selecting measuring points. In addition, having multiple photo sets with overlapping fields of view reduces shadowing in reconstructions, thus improving object definition. Software with sub-pixel targeting capability may improve accuracy by allowing for more precise point identification during reconstruction merging. This would help preserve alignment across multiple reconstructions. Lastly, monitoring and experimentation with various camera settings will help to identify optimal combinations of ISO, f-stop, lighting settings, and focal lengths for each unique application of photogrammetry.

## ACKNOWLEDGEMENTS

The authors gratefully acknowledge 3GSM and AdamTech for their guidance and cooperation in this research. Cooperating industry entities who allowed access and assistance in field research are also gratefully acknowledged. The work described in this paper would not have been possible without their time and expertise. The authors also acknowledge those who participated in the development of the HEHD testing system and construction of the shotcrete panels. Special thanks to the following NIOSH personnel: Curtis Clark and Michael Stepan for their laboratory assistance, Heather Lawson for her help in the field, and Jeffrey Whyatt and Michael Jenkins for their assistance in editing and reviewing a preliminary version of this manuscript.

## REFERENCES

3GSM (2011). *ShapeMetrix® 3D White Paper* available at http://www.3gsm.at/downloads/ SMX_Info_en_v3.5.1.pdf

Birch, J. (2008). Using 3DM analyst mine mapping suite for underground mapping. *Laser and Photogrammetric Methods for Rock Tunnel Characterization.* American Rock Mechanics Association.

Gaich, A., Pötsch, M., and Schubert, W. (2006). "Basics and application of 3D imaging systems with conventional and high-resolution cameras." *Laser and Photogrammetric Methods for Rock Face Characterization*. Tonon, F. and Kottenstette, J. (eds.). American Rock Mechanics Association, pp. 33-48.

Kirsten, H (1993). Equivalence of mesh and fibre reinforced shotcrete at large deflections. Can. Geotech. J., Vol.30, pp. 418-40. Ottowa, Canada National Research Council.

Kirsten, H (1992). Comparative efficiency and ultimate strength of mesh and fibre-reinforced shotcrete as determined from full scale bending tests. J.S. Afr. Inst. Min. Metall., Vol.92, No.11/12, Nov/Dec, pp. 303-23.

Lato, M., Kemeny, J., Harrap, R. M., & Bevan, G. (2013). Rock bench: Establishing a common repository and standards for assessing rockmass characteristics using LiDAR and photogrammetry. *Computers & Geosciences*, *50*, pp. 106-14.

Tannant, D and Kaiser, PK (1997). Evaluation of shotcrete and mesh behaviour under large imposed deformations. International symposium on rock support – Applied solutions for underground structures. Lillehammer Norway. Broch, E Myrvang, A stjern, G (ed). June 22-25, pp. 782-92.

Paar, G., & Kontrus, H. (2006). "Three-dimensional tunnel reconstruction using photogrammetry and laser scanning." Proceedings of the 3rd Nordost, 9. Anwendungsbezogener Workshop zur Erfassung, Modellierung, Verarbeitung und Auswertung von 3D-Daten.

Viggiani, G., & Hall, S. A. (2008). "Full-field measurements, a new tool for laboratory experimental geomechanics." Proceedings of the 4th International Symposium on Deformation Characteristics of Geomaterials, pp. 3-26.

# Introduction of a Measurement Based Ground Control Management System to a Deep Level Potash Mine

**Alexandra Garcia**, Rock Mechanics Engineer
**Jonathan Bowler**, Rock Mechanics Engineer
**Andrew Preddy**, Rock Mechanics Engineer
Golder RMT (Golder Associates (UK) Ltd.
Burton-on-Trent, United Kingdom

**Haydn Duffty**, Rock Engineer
Cleveland Potash Ltd, Boulby Mine
Redcar and Cleveland, United Kingdom

## ABSTRACT

A measurement-based ground control management system, commonly employed in coal mines, has been successfully implemented in a UK potash mine operating at a depth of over 800 m. This system includes the routine deployment of telltales in roadways throughout the mine to mitigate against the risk of large-scale roof falls and the deployment of detailed "design monitoring" instrumentation for ongoing design verification. The routine monitoring systems used in coal mines have not been, to date, commonly applied in potash mines, despite the similar, variable weak geology and associated ground control hazards. Monitoring information from the site indicates that telltales can be deployed to monitor roof conditions, with action levels based on differential rates of strain, as opposed to absolute movement.

## INTRODUCTION

In addition to traditional experience-based routine observation to confirm mine roadway reinforcement design and to maintain safe working conditions, using in situ strata monitoring is well established for rockbolting in weak ground conditions. To that end, it is a legal requirement for all underground mines in the UK to have a scheme in place to "assess the adequacy of the ground control measures." These measures are (though not limited to) the reinforcement system. Since the introduction of rockbolt reinforcement in UK coal mines, in situ monitoring instrumentation has been routinely deployed to actively monitor strata deformation. The use of telltales, for example, has meant that large-scale roof falls are extremely rare because the need to perform remedial work in response to indicated movement beyond action levels is an integral part of every mine scheme.

For coal mines, there is specific UK industry guidance (Deep Coal Mines Industry Advisory Committee, 1996), which was developed over many years of rockbolting and monitoring experience. The guidance outlines the minimum requirements of such a scheme and following it generally means compliance with ground control regulations, in addition to what would be regarded as "best practice." However, there is little guidance material available for non-coal mine operators, which leaves them to develop unique schemes, which may fall short of the UK current regulations.

In non-coal mines with broadly similar ground conditions to deep coal mines with weak geology, it may be preferable to adapt and make use of the existing coal mine guidance procedures, which now have a long and successful track record. Deep potash mines are one such example. This paper describes the way in which Boulby Mine, a deep level potash mine operating in the UK, has implemented, with the assistance of Golder Associates, an instrumented ground control monitoring system based directly on "best practice" coal mining in the UK.

### Geotechnical Setting

Boulby operates at depths ranging from 800 m to1300 m, producing up to 2 million tonnes of potash ore annually (Highley, 2011; Talbot, 1982). The potash horizon is on average 7 m thick, though the underground workings which are predominately advancing multi-entry panel systems, extract a mining height of approximately 4 m, with roadways 8 m wide. The roadways are systematically supported on development by a polyester resin encapsulated steel rockbolt system.

The potash deposit, which gives way immediately above to carnallitic marl, is underlain by several metres of halite and anhydrite. The material itself varies in "evaporite" mineral composition, from pure clean sylvite to a dirty clay rich ore (Woods, 1979). Consequently, the geotechnical parameters and fabric vary. The material can be regarded as weak with an unconfined compressive strength (UCS) of 30 MPa (Salamon and Quinteiro, 1991), which is a strength comparable to most carboniferous coal-bearing rocks in the UK. Roadways are developed with periodic assessment of the roof geology, and the roof horizon is varied to ensure that the reinforced height is contained within the potash horizon.

## IMPLEMENTATION OF SAFETY MONITORING SYSTEM

### Ground Control Risks

Coal and potash strata can be classified as "soft rock" mining environments. However, the material properties and failure mechanisms of coal and potash are dissimilar. Coal mine roof strata in deep mines, subject to high ground stress conditions, typically deform through brittle shear failure. This may also be

true of potash in certain situations, though commonly the material demonstrates ductile deformation, also known as creep. In the mining environment, the roof reinforcement systems aim to control both forms of deformation. However, in both cases, should the ground control measures fail in their purpose, the risk of the following increases:

- A large-scale roof fall (full width of roadway)
- A small-scale roof fall (localised, between rockbolts)

**Defining Safety Monitoring Needs**

The systematic deployment of telltales provides a visible indication of roof movement at regular intervals. Their presence largely aids mitigation of the risk of large-scale roof falls, and their use as safety devices is now well proven because they are routinely used by coal mines in a number of countries in various ground conditions. However, the adoption of telltale systems in potash mines would appear, based on published information, to be almost non-existent, despite the apparent suitability of the ground conditions for their application.

The most common instrument design in use is that of the dual-height telltale (Bigby, 1995). This was developed by British Coal in the early 1990s to monitor the weak mine roof conditions encountered in UK coal mines. The dual-height telltale is relatively inexpensive and is simple to install and interpret. Typically, the design is such that real-time roof movement is shown on tri-colour banded (green-yellow-red) vertical indicators. The banding corresponds to "action levels," and all parties working underground are trained to respond to the level of displacement indicated. Mines generally have a remediation action plan in place, detailing the additional support required, as appropriate for their mining environment, to prevent ongoing roof deformation. These plans remove the "human factor" in deciding what additional support is required and when.

Fundamental to using the telltale as a safety device is setting the appropriate action levels, and this relies on an understanding of the strata failure mechanisms. In coal mines, the failure mechanisms associated with weak ground conditions are well understood and, consequently, enshrined in the UK guidance documentation; the default range of movement of the colour bands on standard dual-height telltales are green (0 to 25 mm), yellow (25 to 50 mm), and red (50 to 75 mm). However, for potash, there is little monitoring experience on which to define a suitable action scale. Therefore, as was the case during the early days of introducing telltales in British Coal, detailed (instrumented) design monitoring and observation are required in the first instance, coupled with widespread telltale deployment on a trial basis.

**Deploying Instrumentation**

In order to gain a better understanding in the way that potash deforms around the mine roadways, a series of design monitoring stations were installed throughout the mine in all new developments. These stations comprised strain-gauged bolt (SGB) arrays and sonic roof extensometers. Strain-gauged bolts measure the distribution of loads along their full length to identify the positions of any excessive loading and potential bending (due to shear). Extensometers measure rock movement at multiple locations in the immediate roof and can be used to identify the rate of displacement and the precise horizons where movement occurs. Combining these two measurements aids derivation of appropriate action levels.

In addition, given the impracticality of installing sonic extensometers and SGB everywhere, telltales (which are essentially a basic extensometer) equipped with shear detection springs were installed at intervals not exceeding 20 m in all roadways on development to obtain as much roof monitoring data as possible. The routine installation of telltales provided optimal monitoring coverage required to fine tune action levels. Provisional action levels were specified at 25 mm increments for roof movement within the bolted height. However, based on observation of a number of localised roof falls in abandoned areas, which were known to occur suddenly, a more conservative initial action level of 10 mm was selected for movement above the bolted height.

## MONITORING RESULTS

The roof extensometers installed demonstrate the creep characteristic of potash, with the deformation typically uniform throughout the entire monitored height (Figure 1), despite the installation reinforcement. The rate of strain varies with time, though tending towards stability in the long term in most cases. The rate of strain also appears depth-related, with increased rates, and, ultimately, greater roof displacement, noted in the deeper mine workings (Figure 2). Given that the roof deformation usually extends right to the top extensometer anchor, it is reasonable to assume the strata are also mobile above the monitored height. This trend is not common in reinforced coal mine strata, which typically demonstrate varied rates of strain throughout the monitored height and are typically confined to discrete horizons within the roof.

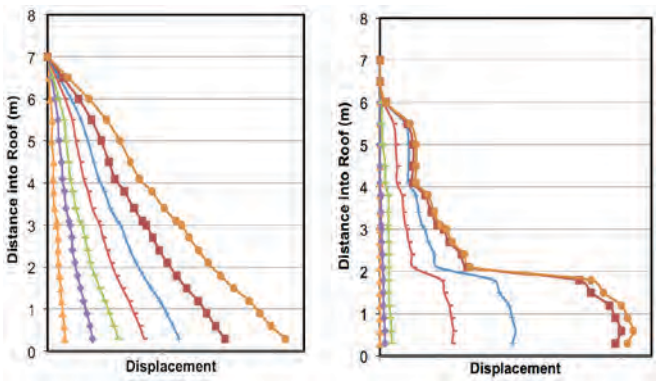



**Figure 1. Typical extensometer trace (displacement with time) from a potash roof (left) and coal mine strata (right).**

Results from strain-gauged bolts demonstrate the classic uniform load distribution expected of fully encapsulated rockbolts with the maximum load generated within the centre of the bolt. These rockbolt data do not show roof shear as a predominant mode of roof failure, given the absence of any bending moment (Figure 3). In addition, in contrast to coal mines, there is not a strong preference for asymmetric bolt loading across the roadway width.

Currently, several potash panels, worked at various depths and geology, have been developed and equipped with telltales. Given the wide coverage and number of dual height telltales installed,sufficient data has now been obtained to begin to assess

trends and themes (Figure 4). As with extensometer data, the rates of strain on telltales in the deeper parts of the mine are greater. However, there are no clear trends that movement above or below the reinforcement height are more or less significant.

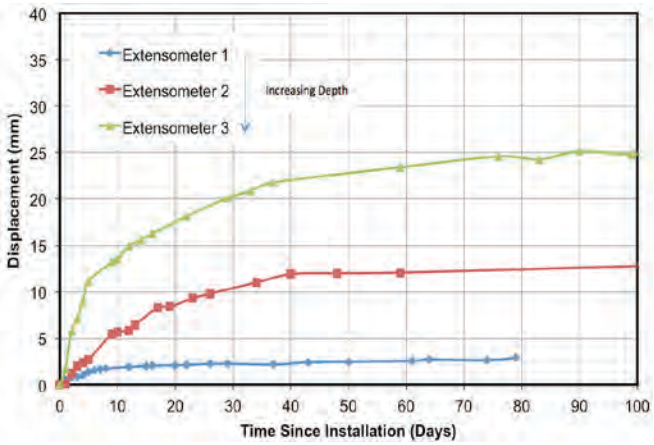



**Figure 2. Plot of potash roof deformation at various depths.**

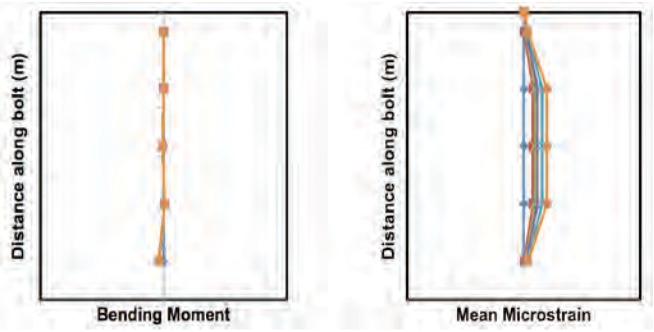



**Figure 3.Typical strain gauged bolts profiles: (Left) showing bending moment and (right) showing mean microstrain.**

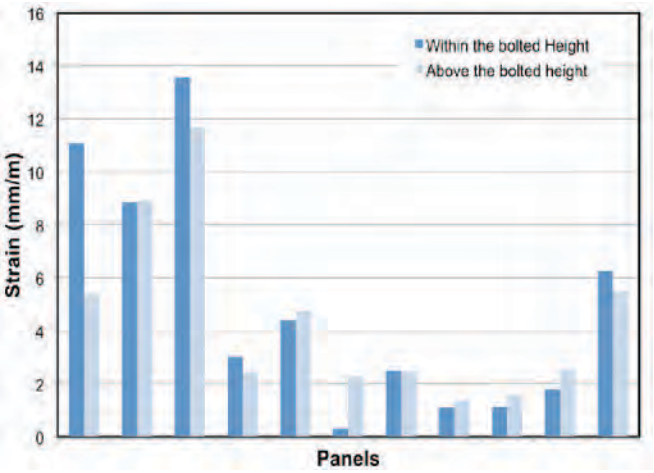



**Figure 4. Average rate of strain from dual height telltale data from various depths.**

## DISCUSSION

At the time of writing this paper, the process of introducing a measurement-based ground control management system to the mine is into its second year. Therefore, sufficient data is available on which to draw some conclusions.

For weak coal mine roofs, there is the general expectation that an appropriately designed roof bolt reinforcement system will suitably control the strata so that the "height of softening" does not progress further up into the roof with time. Therefore, telltale action levels are set with the assumption that there is a level of movement that is acceptable. However, the uniform creep characteristics demonstrated by the extensometers for potash suggest that setting absolute action levels might not be appropriate. The amount of roof movement deemed acceptable needs to take into account the height of monitoring. For example, twice the amount of movement would occur in a 2 m monitored height, than in a 1 m height, given uniform creep throughout the strata. The design of telltale and anchor positions must accommodate this. In the case of a dual height telltale, for example, the monitored height for both A and B indicators should be the same, or the action levels would need to be different for each indicator (i.e., between 0 – 2 m and 2 – 4 m (Figure 5)). In addition, as creep rate is related to a number of factors, depth being one, there may be a need for variable action levels across the mine. This has the potential to lead to an excessively complex and confusing monitoring system.

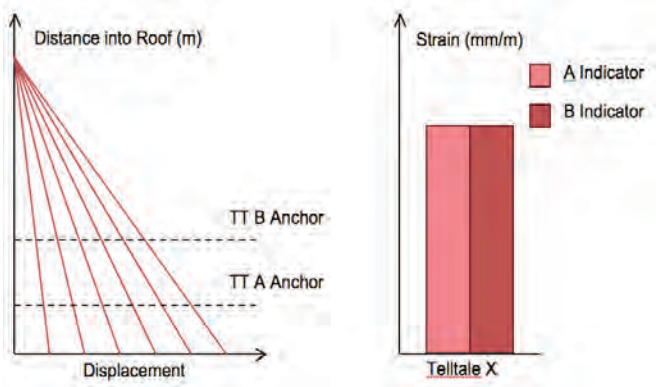



**Figure 5. Expected extensometer/telltale trend given uniform strain.**

A possible solution, however, may be to base potash action levels on strain rather than absolute movement. The following are the deformation characteristics of the rock mass that may be of concern:

- creep that is not controlled with time
- differential (non-uniform) strain in the roof

It would be reasonable to assume that, given uniform creep in an ideal setting, the indicators on a dual height telltale should read the same level of displacement where the monitored height of each anchor was equal. Non-uniform behaviour, which may indicate control failure, would be indicated by an anomalously high reading on one of the two indicators.

There are two basic scenarios:

- High strain above the bolted height relative to the bolted height suggests rock above the bolted height is not being adequately controlled (Figure 6).
- High strain in the bolted height relative to above the bolted height suggests that the lower roof is not being adequately controlled (Figure 7).

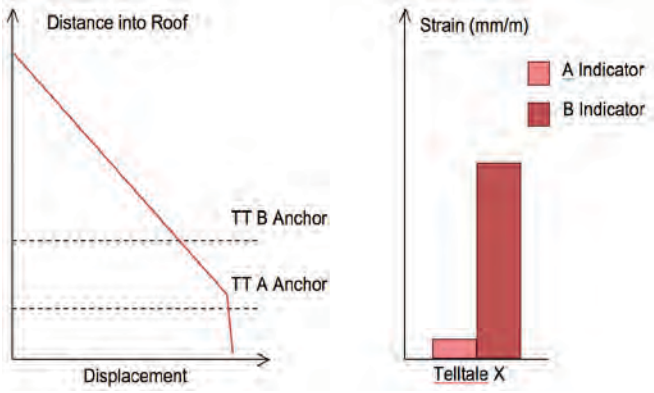



**Figure 6. Postulated extensometer/telltale trend given uniform strain where upper roof is uncontrollable.**

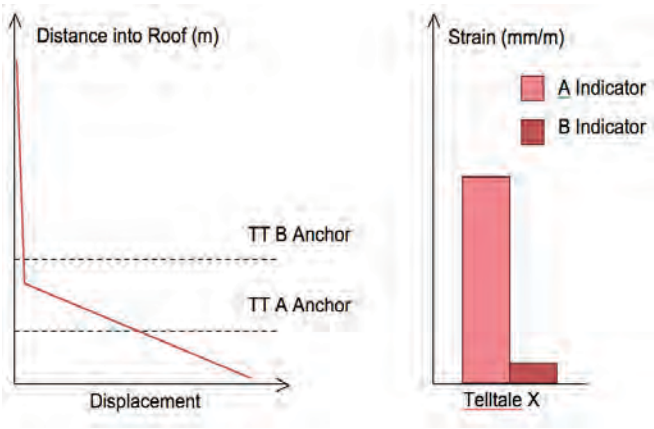



**Figure 7. Postulated extensometer/telltale trend given uniform strain where lower roof is uncontrollable.**

Generating sufficient data to prove these assumptions is likely to take some time. If found to be valid, the development of a "differential rate telltale" represents a novel solution in the monitoring of potash ground conditions, which will improve safety and potentially optimise roadway support design.

## CONCLUSIONS

For almost 25 years, measurement-based ground control management systems for coal mines have been a major contributor to ground control safety in the UK and elsewhere. With adaptation, this established coal mine "best practice" can be applied to other mining environments. Monitoring information from Boulby, a deep UK potash mine, indicates that telltales can also be deployed at this site to monitor roof conditions, though action levels based on differential rates of strain, as opposed to absolute movement, may be more appropriate.

## REFERENCES

Bigby, D. (1995). "Rock mechanics design for rockbolted roadways in British coal mines." In: *Proceedings of the International Mining Tech '95 Symposium*. Beijing, China: Central Coal Mining Research Institute, pp. 258–268.

Deep Coal Mines Industry Advisory Committee. (1996). *Guidance on the Use of Rock Bolts to Support Roadways in Coal Mines*. http://www.hse.gov.uk/pubns/mines01.pdf

Highley. D. (2011). *Mineral Planning Factsheet: Potash*. British Geological Survey. http://www.bgs.ac.uk/mineralsuk/planning/mineralPlanningFactsheets.html

Salamon, M. D. G. and Quinteiro, C. R. (1991). "A summary report to Cleveland potash limited on stress analysis project." Report T-4122. Golden, CO: Department of Mining Engineering.

Talbot, C. J., Tully, C. P., and Woods, P. J. E. (1982). "The structural geology of Boulby (potash) mine." *Tectonophysics 85* (3–4): 167–204.

Woods, P. (1979). "The geology of Boulby Mine." *Economic Geology* 74 (2): 409–418.

# A Liquid Settlement System for Measuring Roof Sag During Development Mining - A Comparison Between Place Change Mining and a Miner–Bolter

**Andy L Shaffer**, Project Engineer
Agapito Associates Inc.
Grand Junction, CO

**James D Pile**, Senior Mining Engineer
BHP Billiton
Waterflow, NM

## ABSTRACT

A novel liquid settlement system (LSS) was installed in advance of mining at a western United States (U.S.) longwall mine to measure total roof sag from the time of cutting to days after mining during gateroad development. The system was used to compare differences in roof sag between conventional place-change mining using a Joy continuous miner and a Fletcher roof bolter and mining using a miner-bolter. The LSS was installed with an intrinsically safe, miniature data acquisition system (MIDAS) to record roof response at four locations in the same gateroad. The system utilized pressure transducers to measure roof sag by the principle of falling head (fluid pressure) in fluid-filled tubes installed in the immediate roof. Details of the LSS design, installation, data collection, post-processing, and future applications are discussed.

## INTRODUCTION

Until recently, real time roof sag measurements at the time of mining were not possible in coal mines due to equipment permissibility restrictions. Intrinsically safe miniature data acquisition systems (MIDAS) data loggers with the capability to store the large density of data generated are a new development.

The combination of MIDAS dataloggers with overflow settlement measurement practices adapted from dam and embankment monitoring by RST Instruments Ltd. (RST) (known as "liquid settlement system" [LSS]) were used indirectly to measure roof sag by measuring fluid pressure in water-filled tubes at four horizons in the immediate roof. Changes in pressure are recorded by the transducers and, during post-processing, the measured pressures are converted to changes in height or roof sag.

The LSS was devised to be installed in the roof ahead of mining and measure roof sag ahead of and at the face in real-time while mining. The system was installed at a western United States (U.S.) longwall mine as part of a geotechnical study comparing differences in roof response between standard place change mining and mining with a miner-bolter. The LSS was intended to measure any ground control advantage that a miner-bolter might offer with earlier installation of roof bolts. The LSS coupled with the MIDAS dataloggers were installed by Agapito Associates, Inc (AAI) in early October 2013 at crosscut (XC) 6 in entries 1 and 2 and approximately one month later at XC 7 in entries 1 and 2 in a development gateroad (Figure 1).

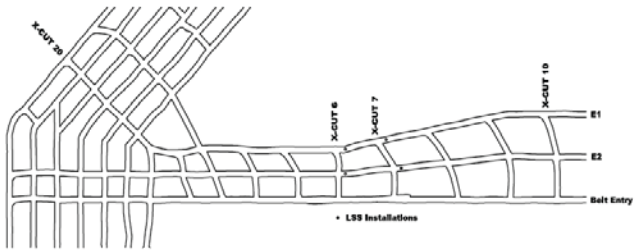



**Figure 1. Location map.**

LSS SYSTEM COMPONENTS

The LSS system is comprised of three main components (see Figure 2):

- A 2.9-inch outside diameter overflow tube assembly that is approximately 31.6 ft long that houses four smaller ⅜-inch tubes that vary in length from 16 to 31 ft for measurements at differing horizons as well as a large aluminum 'head' assembly for securing to roof.
- Honeywell Model TJE 0–5 pounds per square inch (psi) pressure transducers.
- MIDAS M4GP16A dataloggers with M4IAGPA instrument amplifiers. Dataloggers were read wirelessly using the accompanying M4UIA User Interface.

## INSTALLATION

The installation of the LSS required drilling 3 equally spaced NQ (2.985-inch) gauge holes in the roofs of Entries 1 and 2 (at XC 6 and 7) at an angle of approximately 4 degrees (°) up from the local coal seam dip (Figure 3). The LSS tube assembly was inserted into the boreholes immediately after drilling. The four ⅜-inch tubes were then carefully routed and secured to the roof mesh (Figure 4) and connected to the Honeywell TJE 0–5 pounds

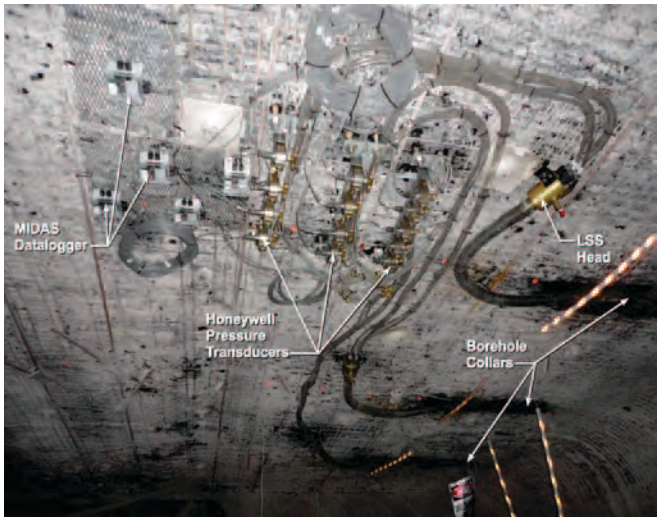



**Figure 2. Entry 2, XC 6 transducer and MIDAS LSS installation in roof.**

per square inch (psi) pressure transducers on the outby end. The opposite (inby) end of the ⅜-inch tubing was connected to a centering spacer via a hose barb fitting and open to the atmosphere in the overflow tube at four varying heights in the overflow tube. Each tube was filled with water via a quick disconnect fitting from the transducer until return was observed coming back from the end of the tube at the LSS head. Care was taken to not over-pressurize the transducers while filling took place.

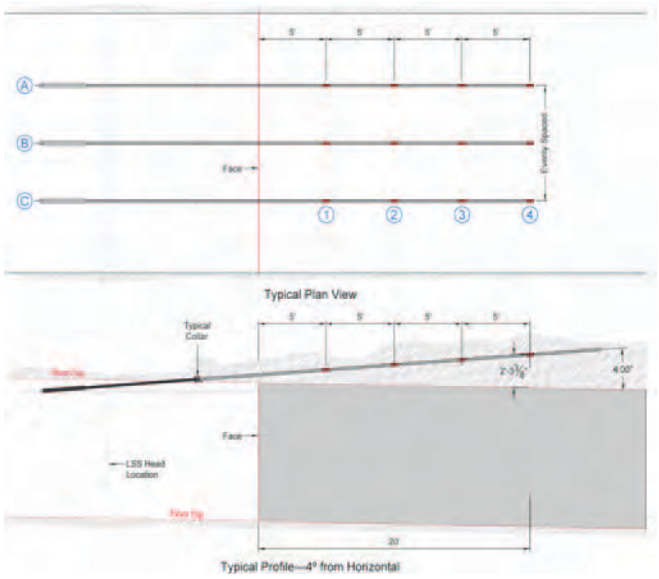



**Figure 3. LSS installation layout.**

Pressure transducers for the LSS system were anchored near each LSS head with 18-inch epoxied threaded bar and the LSS "heads" were mounted with 12-inch epoxied threaded bar. MIDAS dataloggers were mounted to expanded metal and attached to the roof mesh near each corresponding transducer.

For the comparison of roof sag in each entry, all conventional place-change mining operations took place in Entry 1 and the miner-bolter operated out of Entry 2 in XC 6 and XC 7. Local



**Figure 4. Securing LSS Tubing to Roof Mesh at XC 6 Entry 1.**

geology around the XC 6 and XC 7 installation locations had a sandstone roof, which differs from the typical mudstone roof at the mine. The sandstone roof is likely stiffer than the typical mudstone roof, resulting in smaller magnitudes of roof sag.

## DATA PROCESSING

By design, each instrumented entry was equipped with a stationary "reference" transducer open to the mine atmosphere. The reference transducer was intended to capture the localized pressure changes in each entry and, later, correct LSS gage data by either adding or subtracting the collected reference data.

Raw data during each respective cut in entries 1 and 2 at XC 6 and XC 7 were collected every 10 seconds for approximately the first day, after which the frequency was reduced to once every hour. Figure 5 shows the raw data for the middle (B) LSS XC 6 Entry 2 (top). The data show the change in height (inches) experienced by each cell starting at the beginning of the mining cycle (November 1, 2013 to November 26, 2013). The reference transducer data (in cyan) and change in temperature (in heavy black) are also plotted.

Atmospheric temperature and barometric pressure fluctuations have a strong observable effect on the gage responses. These phenomena can be seen in Figure 5 where large changes in temperature (in heavy black) influence the data at similar time points. Pressure effects seem to play a smaller role in most entries where the local atmosphere is generally stable, except for the data in XC 7 Entry 1 which shows large pressure regimes thought to be a byproduct of section ventilation fans (not shown). Therefore, the correction applied to the raw LSS data is twofold, a temperature-based correction and a pressure-based correction.

The current derived empirical temperature correction is based upon control data from an LSS system test experiment conducted at AAI's Grand Junction, Colorado laboratory. The correction is based on a factor of –0.03 inches/degrees Celsius (°C) using the linear best fit of three LSS cell height and temperature data. This factor is applied to the delta temperature at each data point of the current LSS data as either an added or subtracted correction from the change in height measured. Following the temperature correction, the reference transducer (pressure) corrections are applied. This is justified because the reference data appears to be isolated from the temperature effects observed in the raw LSS data. The temperature and reference corrected data for middle (B)

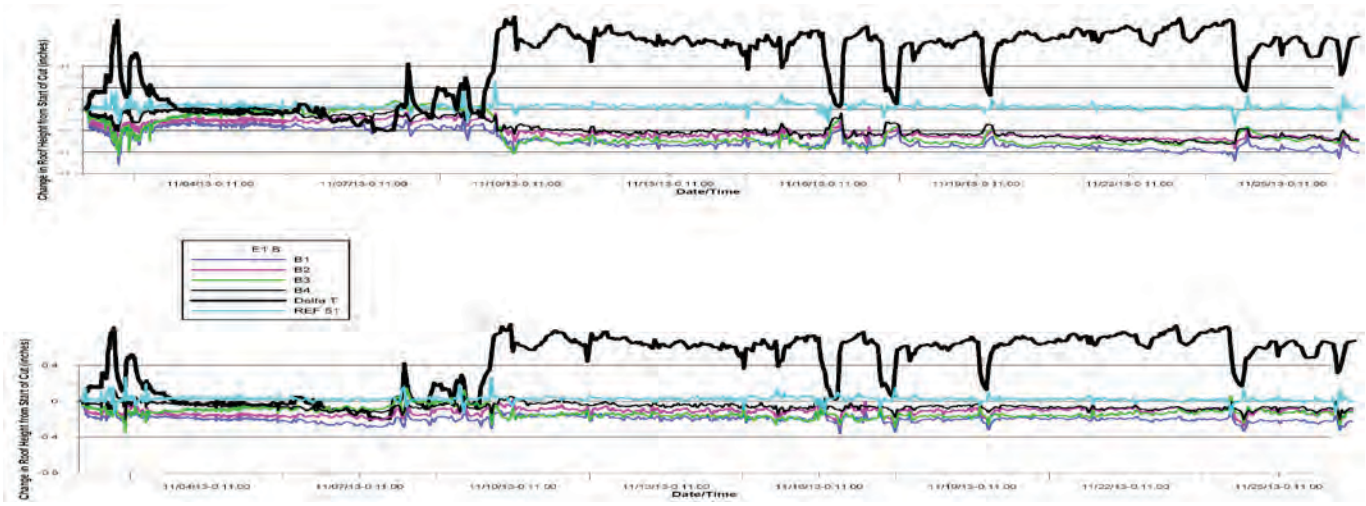



**Figure 5. XC Entry 2 Middle LSS (B) raw and processed data.**

LSS XC6 Entry 2 are shown in Figure 5 (bottom). No smoothing algorithms have been applied to these data.

## INTERPRETATION OF DATA

The corrections made to the data to date have been in response to the pressure and temperature trends discussed above since the instrumented cuts were taken. While these two corrections do seem to account for the majority of the pressure and temperature fluctuations, there may be other influences that have a bearing on the overall LSS system. Since this assemblage of instruments and dataloggers is new to the application of roof sag monitoring, relevant case studies for comparison are not available.

Figures 6 and 7 are plots showing temperature- and pressure-corrected data from the first 24 hours following the start of each cut with notes showing approximate mining cycle times. The initial response measured in the first 24 hours during the mining and bolting cycle(s) show the type of behavior that is expected of the roof. Exceptions to this are at XC 7 Entry 1 (as discussed) and Entry 2 (where the "A" borehole was exposed in several locations during mining and at the "B" borehole where the miner-bolter hit the outer LSS overflow tube).

Measurements from the first 24 hours are considered the most meaningful data. Later measurements show increased influence from atmospheric changes leading to instrument drift that, thus far, cannot be reliably corrected.

No strong distinction is clearly evident between the overall amount of roof sag in the place change entry (E1) versus the miner-bolter entry (E2). This is largely because of uncorrectable "noise" in the LSS system which obscures the pure roof sag response. Neither AAI nor the instrument manufacturer (RST) has been able to correct for atmospheric variables to a degree sufficient to isolate the pure roof sag response. While the LSS system appears to be functioning properly, preliminary indications are that the magnitude of roof sag with the immediate sandstone roof in either entry is so small as to be near the limit of precision possible with the LSS system as compared to a less stiff mudstone roof. This alone might

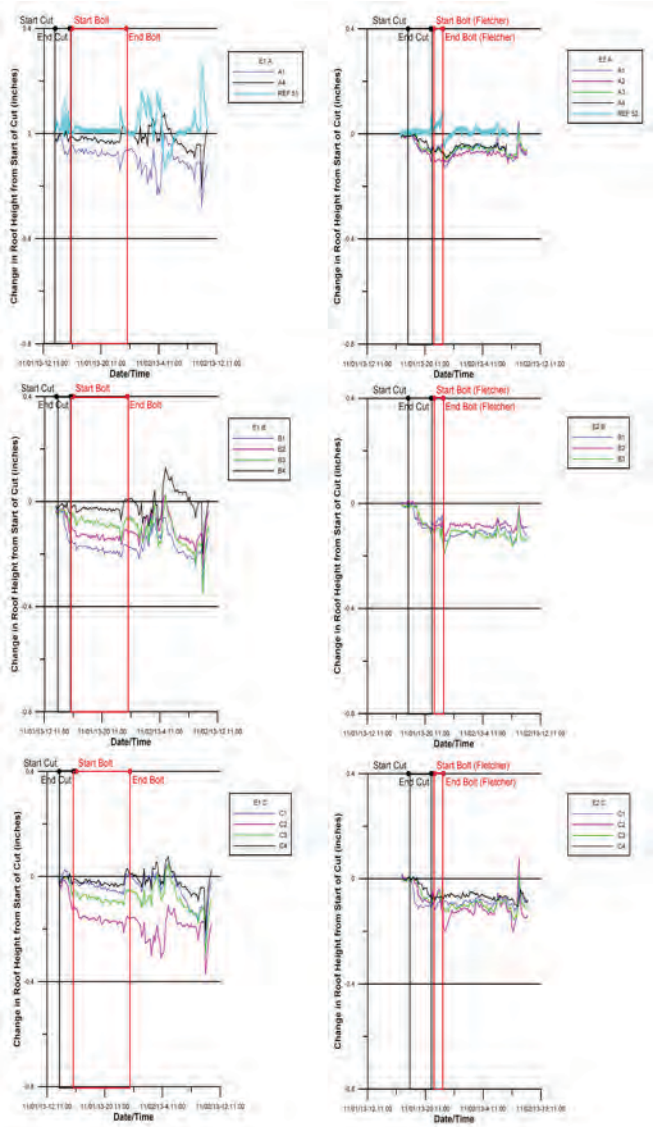



**Figure 6. XC 6 Entries 1 and 2, first 24 hours of processed LSS data.**

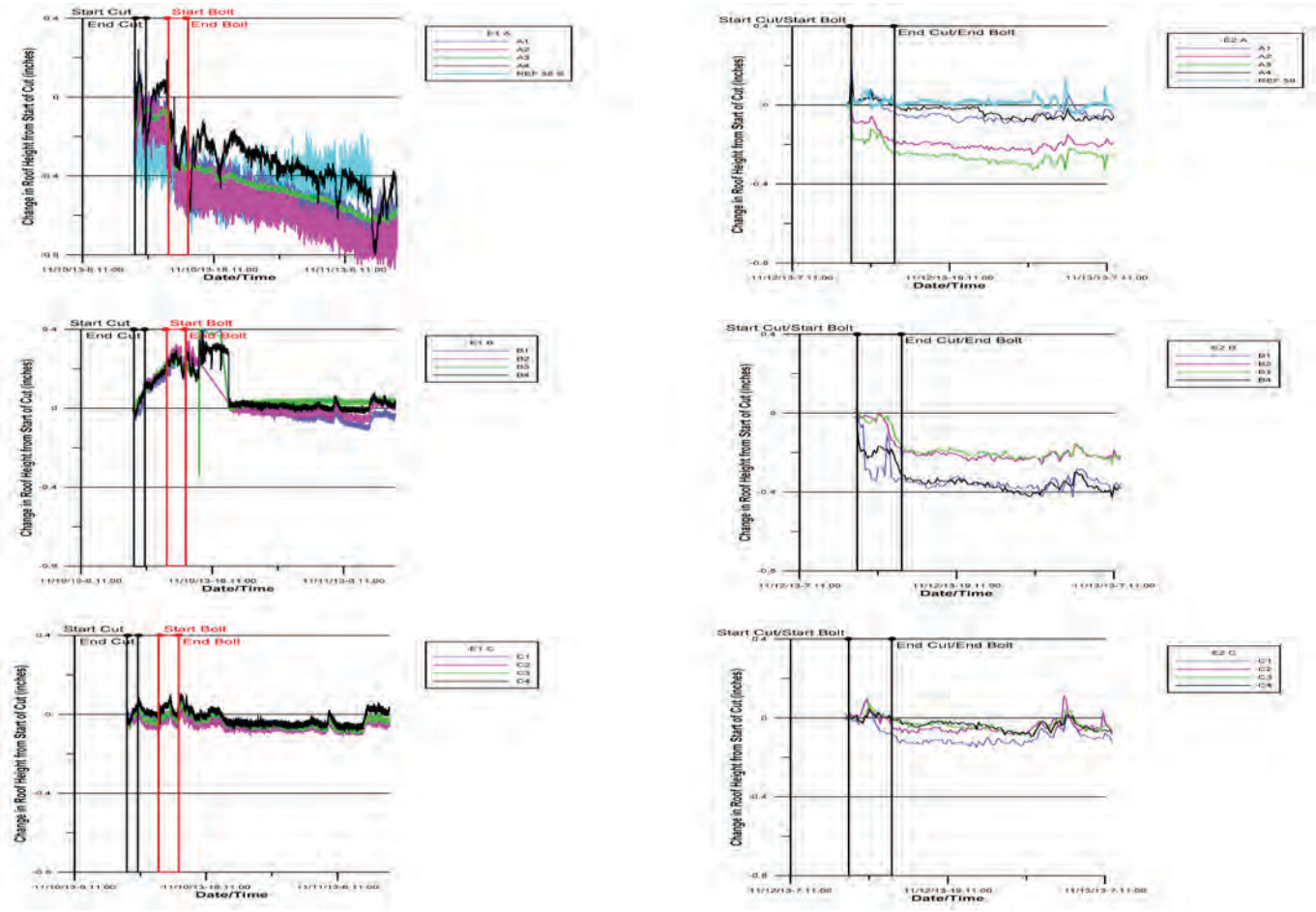



**Figure 7. XC 7 Entries 1 and 2, first 24 hours of processed LLC data.**

suggest that the roof sees little difference between the two types of mining equipment tested considering the actual level of precision relationships between temperature, pressure, and gage response, and provide a more certain basis for atmospheric correction.

## CONCLUSIONS

Roof sag data were collected every 10 seconds during the cut-and-bolt sequences in each of four instrumented entries during the first 24 hours of mining. The LSS provided relatively stable roof sag measurements with relatively little drift and the MIDAS datalogger reliably collected a high density of data. Results indicate that while the system is capable of providing sag measurements to within fractions of an inch, improved precision will be necessary for effectively distinguishing roof behavior between place-change and on-board miner-bolter cut sequencing in environments with very small amounts of roof sag. Moreover, the MIDAS datalogger combined with the LSS is innovative permissible technology that shows promise for stable, real time measurements of roof sag and other ground responses in coal mines using commercially available, relatively low cost hardware.

Areas for future investigation include:

- Use of transducers with a smaller pressure range (e.g., 0–2.5 psi) to allow for greater overall resolution in measurement, depending on the expected amount of total sag to be measured.
- Further refinement of established temperature and pressure corrections, and identification of other environmental corrections to further isolate actual roof sag data from LSS data.
- Use of a medium other than water in the LSS tubes to increase longevity (by reducing or eliminating evaporation) and sensitivity (by using a heavier liquid). Additionally, a smaller diameter tube could also be used to minimize the effects of evaporation.

Other exciting potential applications of LSS and MIDAS datalogger system include:

- Installation above and inside coal mine yield pillars to measure convergence inside the pillar during yielding. Armored tubes likely would be required in the pillar.
- Installation during backfill emplacement to measure backfill settlement and convergence.

# Rock Slope Stability Comparison Between Deterministic and Probabilistic Block Theory Analyses for An Open Pit Mine

**Pinnaduwa H.S.W. Kulatilake**, Director
**Jun Zheng**, Visiting Ph.D. Student
**Biao Shu**, Graduate Research Assistant
**Taghi Sherizadeh**, Graduate Research Assistant
Rock Mass Modeling and Computational Rock Mechanics Laboratories
University of Arizona
Tucson, AZ

**Jianhui Deng**, Professor
College of Water Resources & Hydropower
Sichuan University
Chengdu, China

## ABSTRACT

A new formulation is given to conduct a probabilistic block theory analysis. A new computer code (BTAC) has been developed to perform both deterministic and probabilistic block theory analyses. The variability of the discontinuity orientation and shear strength is incorporated in the probabilistic block theory analysis. Discontinuity orientation is treated as a bivariate random variable including the correlation that exists between the dip angle and dip direction. BTAC code was applied to perform both deterministic and probabilistic block theory analyses for a part of an open pit mine in the U.S. Needed geological and geotechnical data for the analyses were obtained from field and laboratory investigations. The variability of the discontinuity orientations resulted in important differences between the probabilistic and deterministic block theory analyses results. The results confirmed that the design value selected for the Maximum Safe Slope Angle (MSSA) for a particular region in the open pit mine based on the deterministic block theory analysis can be on the unsafe side. In summary, the results showed clearly the superiority of probabilistic block theory analysis over the deterministic block theory analysis in obtaining additional important information with respect to designing rock slopes.

**Key words:** block theory; probabilistic analysis; instability probability; rock slope; open-pit mine

## INTRODUCTION

The open pit mine slope stability is one of the geotechnical subjects dominated by variability and uncertainty because the slopes are composed of natural heterogeneous materials containing a large number of discontinuities. In discontinuous hard rock masses, the variability and uncertainty of rock slope stability analyses mainly arise from discontinuity geometry and discontinuity strength. Application of probabilistic analysis has provided an objective tool to quantify and model variability and uncertainty (Ang and Tang, 1984). The first two types of probabilistic analyses to rock slope stability have been applied using either kinematic or limit equilibrium analysis (Kulatilake, 1987 and 1988).

The block theory, introduced by Shi (1982) and Goodman and Shi (1985), is a very useful technique to investigate possible failure modes of rock blocks and to determine the maximum safe slope angles (MSSA) for rock slopes (Kulatilake et al., 2011; Um et al., 2001). The block theory considers block formation by discontinuity planes along with a cut slope, without assuming presence of lateral release planes as in kinematic analysis. Therefore, the results coming from the block theory analysis can be considered to be closer to reality than that coming from the kinematic analysis (Kulatilake et al., 2011; Um et al., 2001). However, the block theory is usually used to perform deterministic analysis using single fixed values (typically mean values) to represent orientation of discontinuity sets and strength parameters (Kulatilake et al., 2011; Um et al., 2001). The deterministic block theory analysis is usually conducted using the stereographic projection method. In performing analysis for a field rock slope stability problem, it is tedious and very time consuming to use the stereographic projection method to perform a probabilistic block theory analysis because a probabilistic analysis requires changing the discontinuity orientation combinations as well as changing the discontinuity strength. The vector based method is more suitable to perform probabilistic block theory analysis.

A few studies have been conducted to estimate key block formation probabilities and likelihood of key block failure (Hatzor, 1993; Chen, 2012). In this paper, an entirely different type of probabilistic block theory analysis compared to the ones discussed above, is presented for a part of the rock mass [see Figure 1] that exists in an open pit mine in the US. In the analysis, the joint orientation has been considered as a bivariate random variable including the correlation that exists between the joint dip angle and dip direction angle. Also, the variability of the discontinuity shear strength is incorporated in the analysis. To accomplish the task, first the data available on geology and discontinuity orientations measured through manual mapping were obtained from the mining company. Remote fracture mapping were conducted in the field by the research group from the University of Arizona to obtain the discontinuity geometry that exists in these formations. Also, laboratory direct shear tests were conducted on the discontinuities at the University of Arizona geo-mechanics laboratory to estimate the friction angle of the discontinuities and its possible variability.




**Figure 1. Aerial view of the open pit mine and the location of the studied slope (from Google Earth).**

## GEOLOGY

Based on the geological information received from the mining company, the considered section of the slope can be divided into two major lithological formations: (a) Devonian Rodeo Creek (DRC) unit, and (b) Devonian Popovich (DP) unit. The DRC formation rocks consist of argillite, sandstone and interbedded siltstone, and argillite-mudstone. The DP formation rocks consist of laminated limy to dolomitic mudstone and micritic limestone. The dip direction of the considered section of the slope face varies approximately from 140° to 240° (see Figure 1). Therefore, to study the effect of this changing pit slope face dip direction on stability, eight values (140, 155, 170, 185, 200, 215, 230, and 245 degrees) were used, starting at 140° with an increment of 15°, as possible cut slope dip direction (CSDD) angles to perform computations given in the paper.

## ORIENTATIONS OF DISCONTINUITY SETS

For the conducted study, 804 discontinuities were mapped in the DRC formation and 481 discontinuities were mapped in the DP formation. In each domain, the discontinuities can be divided into three sets, as shown in Figure 2.

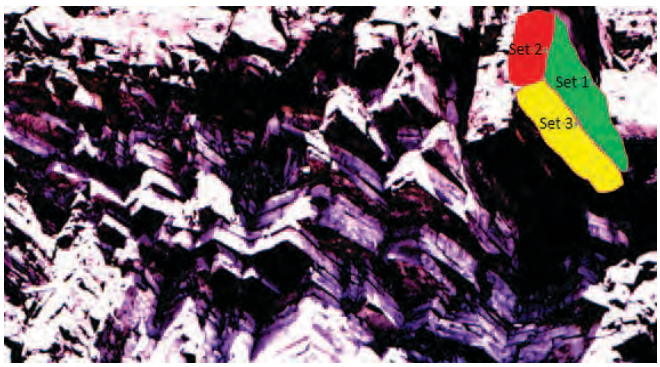



**Figure 2. The considered rock slope at the open pit mine and the three discontinuity sets that exist in DRC formation.**

An instrument known as the VX spatial station was used to perform remote fracture mapping. This instrument has the capability to function as a total station, a camera and a laser scanner. Figure 2 shows the typical discontinuity system of both rock masses. The data obtained through the VX spatial station is perfect to calculate orientation values for discontinuity sets 1 and 2. It was difficult to capture some of the flat lying discontinuities belonging to set 3 (bedding planes) through remote fracture mapping, when the dip angle was close to zero. Therefore, the set 3 discontinuity values were obtained from manual mapping conducted by the mining company. Discontinuity normal vectors plotted on upper hemispherical equal angle polar nets and mean discontinuity orientations for both the DRC and DP formations are given in Figure 3.

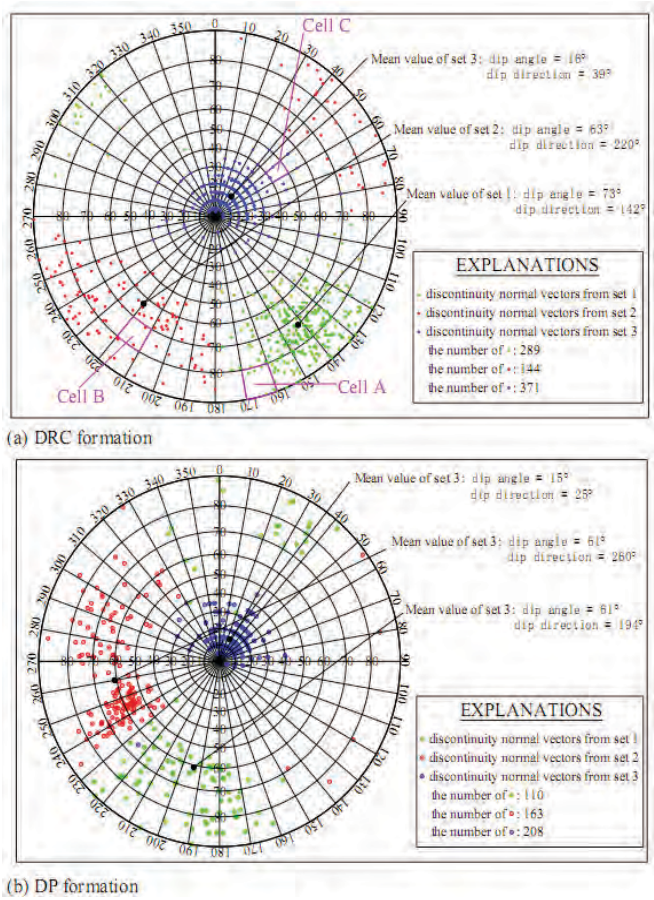



**Figure 3. Orientation distributions of discontinuity normal vectors of DRC and DP rocks on upper.**

The block theory analysis should consider formation of polyhedral blocks resulting from different combinations of discontinuities from different sets intersecting with the excavation surface. In the considered slope, three sets of discontinuities exist in both the DRC and DP formations. Therefore, the tetrahedral blocks under no repetition joint set case and prismatic blocks under repeated joint set case were considered in the analyses. The three discontinuity sets in the DRC formation have 289, 144, and 371 discontinuities, respectively, as given in Figure 3. Hence, there are 289 × 144 × 371 = 15439536 possible discontinuity intersection combinations for DRC formation, which is a huge number. Figure 3(a) shows that many discontinuity normal vectors are located

close by. Therefore, it was decided to sort the discontinuity normals using 10° × 10° cells as shown in Figure 3 to reduce the number of discontinuity intersection combinations to perform block theory calculations as follows:

(1) For each discontinuity set, all the discontinuity normal vectors that exist in a cell of size 10° × 10° are assigned the same orientation, which is the mean orientation of the cell plus a random number $\delta$ between -1 and 1. If a discontinuity normal vector is located on the boundary of a cell, it is allocated to the right or upper cell which has the said boundary. For example, in Figure 3(a), all the discontinuities appearing in Cell A are allocated 85° + $\delta_A$ and 165° + $\delta_A$ as their dip angle and dip direction, respectively; all the discontinuities in Cell B are allocated 75° + $\delta_B$ and 215° + $\delta_B$ as their dip angle and dip direction, respectively; and all the discontinuities in Cell C are allocated 45° + $\delta_C$ and 55° + $\delta_C$ as their dip angle and dip direction, respectively. Note that in a few cells normal vectors from different sets appear. Calculation problems can arise with respect to block formation if the same mean orientation is assigned for these normal vectors coming from different sets. Therefore, the aforementioned random value $\delta$ is added to the mean orientation for each cell as stated above to provide a slightly different value for the normal vectors coming from each set.

(2) As the second step, the number is counted of discontinuity normal vectors appearing in each cell. For example, six discontinuity normal vectors exist in Cell A, belonging to discontinuity set 1; hence, the repeat number (RN) is 6 for dip angle 85° + $\delta_A$ and dip direction 165° + $\delta_A$. Two discontinuity normal vectors exist in Cell B belonging to discontinuity set 2; hence, the RN is 2 for dip angle 75° + $\delta_B$ and dip direction 215° + $\delta_B$. Similarly, because four discontinuity normal vectors belonging to discontinuity set 3 exist in Cell C, the RN is 4 for dip angle 45° + $\delta_C$ and dip direction 55° + $\delta_C$.

(3) Then the total repeat number for each discontinuity cell combination i ($TRN_i$) is counted as: $TRN_i = RN_{i1} \times RN_{i2} \times RN_{i3}$, where $RN_{i1}$, $RN_{i2}$, and $RN_{i3}$, are the RN of the discontinuities from set 1, set 2 and set 3 of combination i, respectively. For example, the TRN of the combination of cell A, cell B, and cell C is equal to $RN_A \times RN_B \times RN_C = 6 \times 2 \times 4 = 48$. Obviously, the sum of all TRNs is equal to the original total number of combinations, 15439536.

According to the aforementioned simplification, for the DRC formation the number of cells for the discontinuities from the three sets are 44 (set 1), 48 (set 2), and 84 (set 3), respectively; hence, the number of discontinuity cell combinations for the DRC formation is 44 × 48 × 84 = 177408. Therefore, only 177,408 discontinuity combinations need to be used to perform block theory analysis for the DRC formation. However, note that the final number of discontinuity combinations used for calculating the probability is still the original number, 15,439,536, because the TRN for each discontinuity combination is included in the final calculation as given in Section 6. Similarly, the same technique was applied for the DP formation to reduce the number of block theory analyses. After the said reduction, for the DP formation the number of cells for the discontinuities from the three sets are 39 (set 1), 44 (set 2), and 52 (set 3).

## DISCONTINUITY STRENGTH PROPERTIES

Based on the direct shear tests conducted in the laboratory, the discontinuity friction angle (ϕ) for all the three discontinuity sets belonging to DRC rocks varies between 19° and 34° from 16 test results. For DP rocks ϕ varies between 20° and 32° from 9 test results. Because the discontinuities are open with no filling material the cohesion value is zero for the discontinuities. The number of ϕ data available for each domain is not sufficient to establish realistic probability distributions for the friction angle. For both the DRC and DP rock discontinuities, the data do not indicate any firm asymmetry around the mean value; the data show no significant dominance of relative frequencies around the mean value. The data basically show up and down variations with increasing ϕ values. All these observations indicate that the data are insufficient to establish reliable probability distributions. On the other hand, a truncated normal distribution, a beta distribution or a symmetric distribution around the mean value, is expected as the most probable distribution to represent the variability of the friction angle. Therefore, to perform probabilistic block theory analysis, the symmetric distributions shown in Figure 4 were used to represent the variability of ϕ for the DRC and DP rock discontinuities.

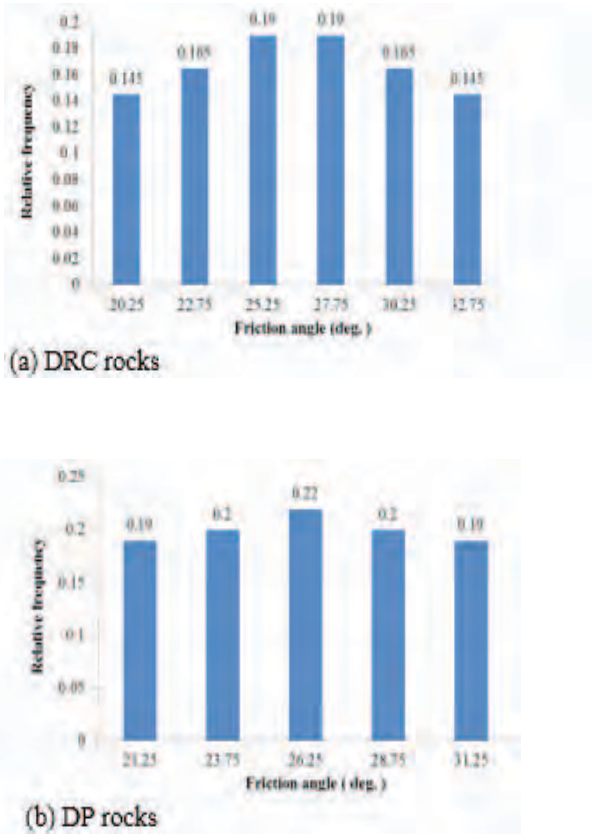



**Figure 4. Probability distributions used for the friction angle.**

## DETERMINISTIC BLOCK THEORY ANALYSIS

### Introduction

The main idea behind block theory analysis (Shi, 1982; Goodman and Shi, 1985) is that it allows many different blocks

formed by combinations of discontinuities to be passed over and to directly identify and consider critical blocks known as "key blocks." Figure 5 shows five types of blocks in a surface excavation formed by discontinuities. Although the actual blocks are in three dimensions, to simplify the illustration a two-dimensional figure is used (Goodman and Shi, 1985). For details on the block theory, the reader is referred to Shi (1982) and Goodman and Shi (1985).

Except for key blocks, all other blocks are considered to be stable under the gravitational loading. Therefore, the MSSA for them is equal to 90°. For each key block, the MSSA is equal to the minimum cut slope angle corresponding it to be a finite block in the stereo plot (Shi, 1982; Goodman and Shi, 1985). The failure modes of key blocks dealt with in this paper include single plane sliding and double plane (wedge) sliding. The free fall mode is not applicable because the case dealt with is a non-overhanging slope. Therefore, six failure modes exist for DRC rocks as well as DP rocks: S1, S2, and S3 (sliding along the discontinuity plane from set 1, set 2 and set 3, respectively); and S12, S13, and S23 (sliding along the line of intersection of two discontinuities from set 1 and set 2, set 1 and set 3, and set 2 and set 3, respectively).

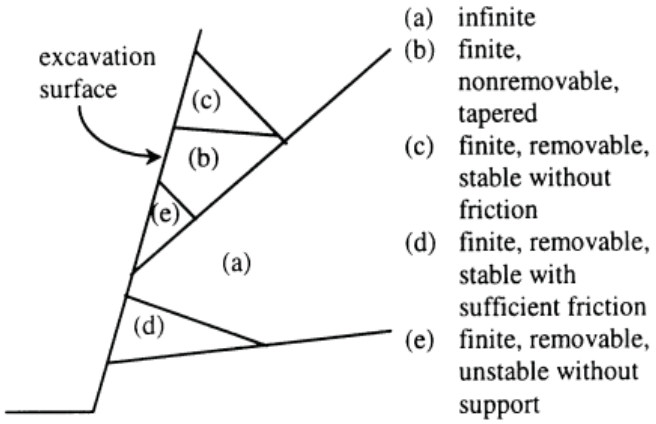



**Figure 5. Blocks in a surface cut: (a) infinite; (b) tapered; (c) stable; (d) potential key block; (e) key block (after Kulatilake et al., 2011).**

Note: For all the block theory analysis conducted in the paper, only the gravitational loading is considered.

Because the case study dealt with in the paper required a computer code to perform calculations for a large number of discontinuity combinations efficiently, a block theory analysis code (BTAC) based on the vector method was developed by the first two authors of this paper to calculate MSSA of blocks, to determine their failure modes and to calculate the corresponding net sliding forces and factor of safety values.

**Results**

To perform deterministic block theory analysis, the mean values were used for the orientations and friction angles of discontinuity sets. Therefore, only one discontinuity orientation combination exists for DRC rocks as well as DP rocks. As stated previously, CSDD has eight values. Block theory analysis was conducted using BTAC to obtain MSSA and their corresponding failure modes for DRC rocks and DP rocks under each of the CSDD value.

The obtained results (Figure 6) show the following: (a) the MSSA range between 62° and 74° for DRC rocks, and between 56° and 88° for DP rocks for the CSDD values in the range 140°-245°; (b) the CSDD has a significant impact on MSSA and failure modes (shown in Figure 6) for both the DRC and DP rocks; (c) when the CSDD is between 185° and 200°, the MSSA reaches the minimum value of 62° for DRC rocks; when the CSDD is 230°, the MSSA reaches the minimum value of 56° for DP rocks; (d) hence, 185°-200° and 230° seem to provide the worst CSDD for possible instability of slopes in the DRC formation and DP formation, respectively; (e) the most favorable CSDD for both the DRC and DP formations is 140° within the CSDD range of 140° to 245°; (f) within the CSDD range of 140° to 245° the slope seem to be stable for both the DRC and DP formations for cut slope dip angles less than 56°. To check the accuracy of the BTAC code the MSSA and the corresponding failure modes were obtained through the stereographic projection method for the worse case CSDD scenarios of the DRC and DP rocks. The accuracy was found to be perfect.

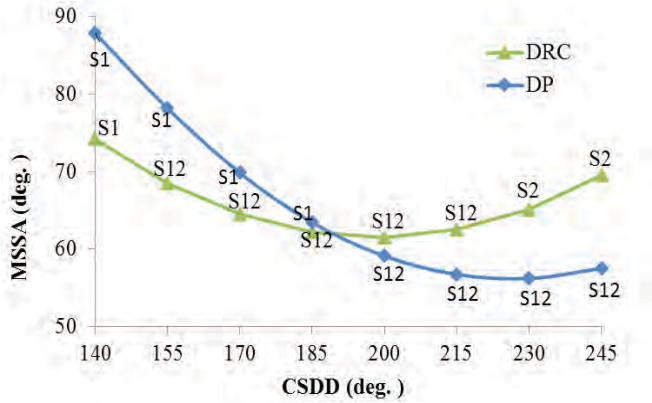



**Figure 6. Relation between maximum safe slope angle (MSSA) and possible cut slope dip direction (CSDD) for DRC and DP rock formations.**

## PROBABILISTIC BLOCK THEORY ANALYSIS

**Development of the probabilistic formulation**

As stated in Section 3, each discontinuity combination is formed by taking one mean orientation value applicable for a particular cell from each set. As stated in Section 2, eight values are selected for CSDD to perform probabilistic block theory analysis. As stated in Section 4, 6 and 5 values are selected for $\phi$ to perform probabilistic block theory analysis. This means for the DRC rocks 48 different combinations exist based on the different CSDD and $\phi$ values. Similarly, for the DP rocks 40 different combinations exist based on the different CSDD and $\phi$ values. The computer program BTAC was used to perform block theory analysis for each of the aforementioned CSDD and $\phi$ combinations using each of the DRC and DP rock discontinuity combinations at a time. Block theory analysis results were used to count the number of MSSA between 0 and $m$ (cut slope dip angle) of key blocks for each of the different combinations of $\phi$, and CSDD separately for each of the failure modes stated in Section 5. Note that $m$ is excluded in performing this counting. The calculations were performed for each

of the following *m* values: 10°, 20°, 30°, 40°, 50°, 60°, 70°, 80° and 90°. The aforesaid calculations led to filling out the form shown in Figure 7 for each combination of CSDD and FA for each of the two rock types (DRC and DP). Hence, 48 different sheets of Figure 7 and 40 different sheets of Figure 7 were completed for the DRC and DP rocks, respectively.

| Formation: | | | | | | CSDD = | | φ = | |
|---|---|---|---|---|---|---|---|---|---|
| Failure | Number of MSSA between 0 and m of key blocks | | | | | | | | |
| modes s | m=10° | m=20° | m=30° | m=40° | m=50° | m=60° | m=70° | m=80° | m=90° |
| S1 | | | | | | | | | |
| S2 | | | | | | | | | |
| S3 | | | | | | | | | |
| S12 | | | | | | | | | |
| S13 | | | | | | | | | |
| S23 | | | | | | | | | |
| S | | | | | | | | | |

Note: S is the sum of numbers of all failure modes.

**Figure 7. A sample form to summarize the results of MSSA of key blocks for each combination of ϕ and CSDD and each of the different failure modes.**

If CSDD = $\alpha$ and friction angle = $\varphi_k$, for a particular rock type the total number of MSSA between 0 and *m* of all key blocks of discontinuity combination i with respect to failure mode *s*, $n_{ims}$, can be obtained by:

$$n_{ims} = \sum_{j=1}^{J_i} n_{ijms} \tag{1}$$

where $J_i$ is the total number of key blocks for cell combination *i*; $n_{ijms}$ is the number of MSSA between 0 and m of key block *j* of cell combination *i* with respect to failure mode *s*. The total number of MSSA between 0 and *m* of all key blocks for all discontinuity combinations considering the TRN with respect to failure mode *s*, $n_{ms}$, can be expressed as:

$$n_{ms} = \sum_{i=1}^{I} n_{ims} \cdot TRN_i \tag{2}$$

where *I* is the total number of cell combinations and $TRN_i$ is the TRN of cell combination *i*. The total number of all blocks formed by all discontinuity combinations considering the TRN, *n*, is determined by:

$$\sum_{i=1}^{I} 2^3 \cdot TRN_i$$
$$n = 2^3 \cdot I \cdot TRN_i \tag{3}$$
$$n = \sum_{i=1}^{I} 2^3 \cdot TRN_i$$

where $2^3$ is the total number of blocks formed by an arbitrary combination of three discontinuities and a slope plane for a considered cut slope dip direction. Hence, the instability cumulative probability $P_{ms}(\alpha, \varphi_k)$ of the slope with CSDD = $\alpha$ and friction angle = $\varphi_k$ with respect to failure mode *s* can be obtained as:

$$P_{ms}(\alpha, \varphi_k) = \frac{n_{ms}}{n} \tag{4}$$

The instability cumulative probability $P_{ms}(\alpha)$ of the slope with CSDD = $\alpha$ with respect to failure mode *s* including the distribution of ϕ can be expressed as:

$$P_{ms(\alpha)} = \sum_{k=1}^{K} P_{ms}(\alpha, \varphi_k) \cdot f(\varphi_k) \tag{5}$$

where *K* is the number of possible ϕ values and $f(\varphi_k)$ is the relative frequency of $\varphi_k$ obtained by Figure 5. From Eqs. (1-5), the final formula for $P_{ms}(\alpha)$ can be expressed as:

$$P_{ms(\alpha)} = \sum_{k=1}^{K} \frac{\sum_{i=1}^{I} \left[\sum_{j=1}^{J_i} n_{ijms}\right] \cdot TRN_i}{\sum_{i=1}^{I} 2^3 \cdot TRN_i} \cdot f(\varphi_k) \tag{6}$$

**Results**

Figure 8 shows the instability cumulative probability of the slope obtained with cut slope dip angle for each failure mode for the selected CSDD values for the DRC formation. Note that these results were obtained using equation (6) given above. These figures also provide the cumulative probabilities obtained by summing up the values obtained for different failure modes. Also, each of the figures show the MSSA obtained for each CSDD under the deterministic block theory analysis along with the corresponding failure mode. Figure 8 shows that the most probable failure mode changes from $S_1$ to $S_{12}$ to $S_2$ as CSDD increases from 140° to 245° as in the case of the deterministic analysis results. Hence, there is very good agreement between the probabilistic analysis and the deterministic analysis results on the most probable failure mode. The probabilistic block theory analysis shows that, to bring the instability cumulative probability to zero and covering all the CSDD values, it is necessary to reduce the cut slope dip angle (or MSSA) to slightly less than 50°. On the other hand, the deterministic block theory analysis resulted in MSSA values in the range 62° to 74° for the same CSDD range of 140° to 245°. Figure 9 shows the total instability cumulative probability of the slope resulting from all modes of failure for different cut slope dip angles for the selected CSDD values for the DRC formation. This figure can be used to estimate the maximum cut slope dip angle corresponding to any selected CSDD and instability cumulative probability level. The same figure shows that the worst case CSDD obtained under probabilistic analysis (highest instability cumulative probability) for DRC rocks is around 185°. This result agrees quite well with the worst case result obtained with the deterministic analysis results. Note that for the worst case scenario (CSDD = 185° to 200°), there is an approximately 12° difference in MSSA value between the deterministic analysis result and the probabilistic analysis result corresponding to zero instability cumulative probability. This difference has resulted from the variability of the discontinuity orientations. This indicates that the design value selected for MSSA for a particular region in the open pit mine based on the deterministic block theory analysis can be on the unsafe side. The aforementioned discussion clearly shows the superiority of probabilistic block theory analysis over

the deterministic block theory analysis in obtaining additional important information with respect to designing rock slopes.

Figure 10 provides plots similar to Figure 8 for DP rocks. These results were also obtained using equation (6) given above. Figure 10 shows that the most probable failure mode changes from $S_1$ to $S_{12}$ as CSDD increases from 140° to 245°, as in the case of the deterministic analysis results. There is perfect agreement between the probabilistic and the deterministic analyses results on the most probable failure mode corresponding to each CSDD value. Figure 10 shows that, to bring the instability cumulative probability to zero for DP rocks, it is necessary to reduce the cut slope dip angle (or MSSA) to a value between 40° and 60°, depending on the CSDD angle. On the other hand, the deterministic block theory analysis resulted in MSSA values in the range 56° to 88° for the same CSDD range of 140° to 245°.

probability. Figure 11 shows the total instability cumulative probability of the slope resulting from all modes of failure for different cut slope dip angles for the selected CSDD values for the DP formation. This figure shows that the worst case CSDD obtained under probabilistic analysis (highest instability cumulative probability) for DP rocks is around 230°. The same figure also indicates the best CSDD is 140° for DP rocks. These results agree perfectly with the results obtained through the deterministic analysis. Note that for the worst case scenario (CSDD = 230°), there is an approximately 16° difference in MSSA value between the deterministic analysis result and the probabilistic analysis result corresponding to zero instability cumulative probability. This difference has resulted from the variability of the discontinuity orientations. This confirms that the design value selected for MSSA for a particular region in the open pit mine based on the deterministic block theory analysis can be on the unsafe side. The

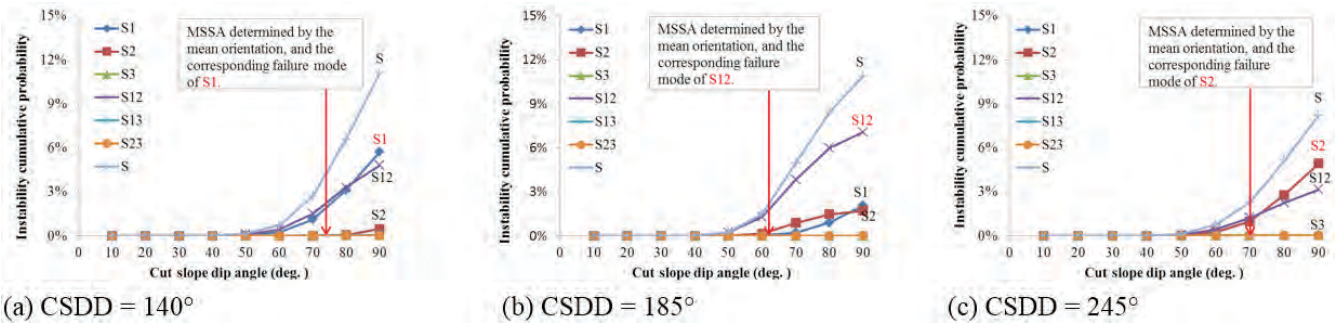



**Figure 8. Instability cumulative probability of the slope obtained with cut slope dip angle for each failure mode for the selected CSDD values for the DRC formation.**

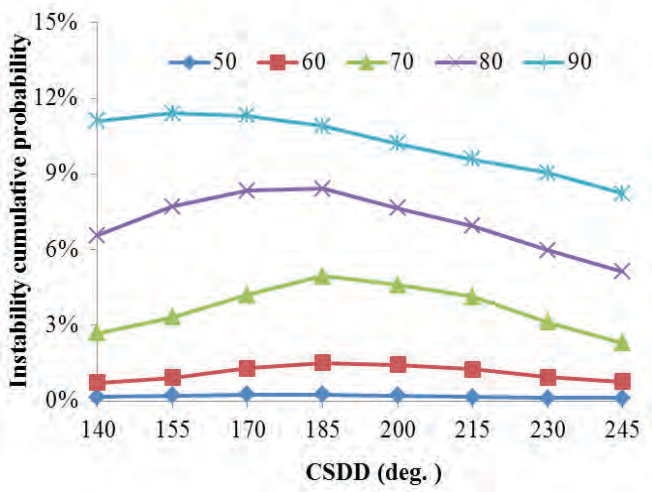



**Figure 9. Total instability cumulative probability of the slope resulting from all modes of failure for different cut slope dip angles (50° to 90°) for the selected CSDD values for the DRC domain.**

For this particular case of DP rocks, the MSSA angle mostly decreases with increasing CSDD angle with respect to the results of both the probabilistic and deterministic analyses. For each CSDD angle, the MSSA obtained through the deterministic analysis is about 10° to 28° higher than the MSSA obtained under the probabilistic analysis corresponding to zero instability cumulative

aforementioned discussion clearly again shows the superiority of probabilistic block theory analysis over the deterministic block theory analysis in obtaining additional important information with respect to designing rock slopes.

## CONCLUSIONS

A new formulation is given to conduct a probabilistic block theory analysis. A new computer code (BTAC) was developed to perform both deterministic and probabilistic block theory analysis. The deterministic analysis provided the following results: (a) the MSSA ranges between 62° and 74° for the DRC rocks, and between 56° and 88° for the DP rocks for the CSDD values in the range 140°-245°; (b) when the CSDD is between 185° and 200°, the MSSA reached the minimum value of 62° for the DRC rocks; when the CSDD is 230°, the MSSA reached the minimum value of 56°for the DP rocks; (c) hence, 185°-200° and 230° seem to provide the worst CSDD for possible instability of slopes in the DRC domain and DP domain, respectively; (d) within the CSDD range of 140° to 245° the slope seem to be stable for both the DRC and DP domains for cut slope dip angles less than 56°.

Very good agreement was found between the deterministic and probabilistic block theory analyses results on the failure modes and the worst and best case CSDD values for both the DRC and DP rocks. The probabilistic block theory analysis showed that to bring the instability cumulative probability to zero, covering all the CSDD values in the range of 140° to 245°, it is necessary to reduce the cut slope dip angle (or MSSA) to slightly less than 50° for the DRC rocks. On the other hand, the deterministic block theory

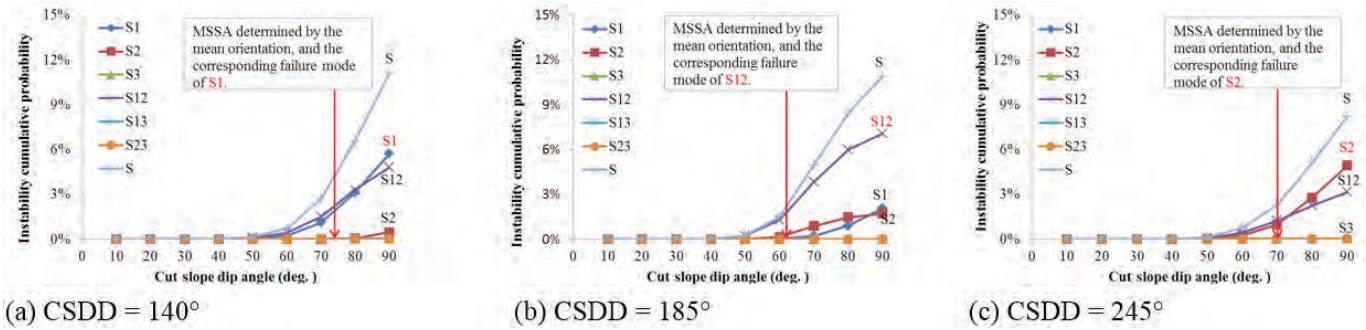



**Figure 10. Instability cumulative probability of the slope obtained with cut slope dip angle for each failure mode for the selected CSDD values for the DP formation.**

analysis resulted in MSSA values in the range 62° to 74° for the same CSDD range for the DRC rocks. This difference resulted from the variability of the discontinuity orientations. For the worst case scenario (CSDD = 185° to 200°) of the DRC rocks, there is an approximately 12° difference in MSSA value between the deterministic analysis result and the probabilistic analysis result corresponding to zero instability cumulative probability. To bring the instability cumulative probability to zero for the DP rocks, it is necessary to reduce the cut slope dip angle (or MSSA) to a value between 40° and 60°, depending on the CSDD angle. On the other hand, the deterministic block theory analysis resulted in MSSA values in the range 56° to 88° for the same CSDD range of 140° to 245° for the DP rocks. For each CSDD angle, the MSSA obtained through the deterministic analysis is about 10° to 28° higher than the MSSA obtained under the probabilistic analysis corresponding to zero instability cumulative probability. For the worst case

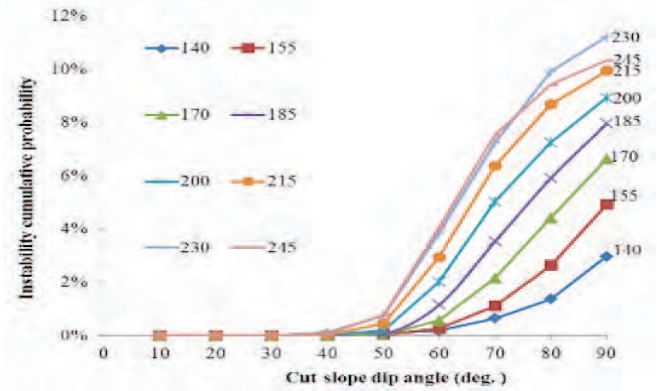



**Figure 11. Total instability cumulative probability of the slope resulting from all modes of failure for different cut slope dip angles for the selected CSDD values (140° to 245°) for the DRC formation.**

scenario (CSDD = 230°) of DP rocks, there is an approximately 16° difference in MSSA value between the deterministic analysis result and the probabilistic analysis result corresponding to zero instability cumulative probability. The results confirmed that the design value selected for MSSA for a particular region in the open pit mine based on the deterministic block theory analysis can be on the unsafe side. In summary, the results showed clearly the superiority of probabilistic block theory analysis over the deterministic block theory analysis in obtaining additional important information with respect to designing rock slopes.

## REFERENCES

Ang, A.H.S., Tang W.H. (1984). *Probability concepts in engineering planning and design*, Vols. I and II. New York: John Wiley & Sons.

Kulatilake, P.H.S.W., Fuenkajorn, K. (1987) "Factor of safety of tetrahedral wedges: a probabilistic study." *Int J of Surface Mining*. 1987.

Kulatilake, P.H.S.W. (1988). "Minimum rock bolt force and minimum static acceleration in tetrahedral wedge stability: a probabilistic study." *Int J of Surface Mining*. 2(1):19-26.

Shi, G. (1982). "A geometric method of stability analysis of discontinuous rocks." *Scientia Sinica* 25(1):125–143.

Goodman, R.E., Shi, G. (1985). *Block theory and its application to rock engineering*. Englewood Cliffs: Prentice-Hall.

Kulatilake, P.H.S.W., Wang, L., Tang, H., Liang, Y. (2011). "Evaluation of rock slope stability for Yujian River dam site by kinematic and block theory analyses." *Computers and Geotech.* 38:846–860.

Um, J., Kulatilake, P.H.S.W. (2001). "Kinematic and block theory analyses for shiplock slopes of the Three Gorges Dam Site in China." *Geotechnical and Geological Eng.* 19:21- 42.

Hatzor, Y. (1993). "The block failure likelihood: a contribution to rock engineering in blocky rock masses." *Int J Rock Mech Min Sci & Geomech Abstr*. 30(7):1591-1597.

Chen, G. (2012). "Probabilistic key block analysis of a mine ventilation shaft stability –a case study." *Geomechanics and Geoengineering*. 2012; 7(4):255-262.

# Combined Effects of Rock Bedding Orientation and Topography on Stresses Around Mine Openings

**Amirhossein Molavi Tabrizi**, Ph.D. Student
Department of Civil Engineering
University of Akron
Akron, OH

**W. Ashley Griffith**, Assistant Profesosor
Department of Earth and Environmental Science
University of Texas at Arlington
Arlington, TX

**Ernian Pan**, Professor
**Yanfei Zhao**, Ph.D. Student
Department of Civil Engineering
University of Akron
Akron, OH

## ABSTRACT

In this paper we introduce a realistic model for mine openings that explicitly considers the effects of local irregular topography. Also, we consider the effect of entry orientation and rock anisotropy on the induced stress fields around mine openings under the given in-situ stress field. A triangular mesh formulation is derived for representing complicated irregular surface topography and underground openings. Each element contains three internal collocation nodes. Parts of the surface which are far from the mine openings are discretized by infinite elements. The rectangular infinite elements with three internal nodes are introduced specifically for this problem so they are compatible with the triangular elements. With the corresponding boundary element method (BEM) formulation, we then investigate the combined effect of the topography and entry orientation on the stress fields induced by openings in anisotropic rocks under *in-situ* stresses. A single rectangular opening in the anisotropic ground with topography and *in-situ* stresses is simulated using data from the Carroll Hollow mine in Ohio. The results of these simulations show that topography, rock anisotropy, orientation of the regional stress field and mine opening geometry all have appreciable effects on the stress fields around underground openings, yet these factors can all be accounted for in an efficient code with no need to discretize the model domain. Future applications using this new BEM formulation will provide useful guidance on selecting the optimal opening orientation in the mine in order to minimize undesirable stress concentrations around underground mine workings.

## INTRODUCTION

Design of mine openings requires prior knowledge on the strength of the nearby Earth's ground materials as well as the quantification of stress states at the walls and around the opening. While in-situ experimental analyses are vital for all mine opening excavations, analytical methods can be utilized to guide mine design and analysis. The boundary element method (BEM) is a powerful computational tool for analyzing stresses in infinite and semi-infinite regions (Liu et al., 2011; Tonon, Pan and Amadei, 2001). The use of Green's functions for half-space or half-plane problems has found many applications in the field of rock mechanics with several important applications including hydraulic fracturing (Pan et al., 2013), earthquake measurements (Irikura, 1963), and mine exploration (Tonon and Amadei, 2002). For a semi-infinite space (or semi-infinite plane for two-dimensional problems) in particular, half-space or half-plane Green's functions are commonly implemented into the BEM formulation to remove the need for discretization along the surface of the half-space (Pan, Amadei and Kim, 1998). However, there are situations for which it is better to solve a half-space problem using full-space Green's functions. To do so, one needs to define an infinite element to discretize the infinite part of the boundary surface (i.e., the portion of the boundary surface which extends beyond the local region of interest). Liang and Liew (2001) used Kelvin's solution for modeling three-dimensional (3D) half-space problems. The advantage of their method was avoiding the strongly singular line integral, and it also led to a more accurate result with less computation time. Liew and Liang (2003) also used this method to set up the BEM formulation for a transversely isotropic piezoelectric half-space. They used both half-space and full-space Green's functions to overcome the computational difficulties.

For underground mine openings with irregular surface topography, the topography needs to be discretized; therefore, it is necessary to use the full-space Green's function and discretize the irregular surface of the half-space with suitable elements. Furthermore, when representing underground openings and excavations near the surface, the geometry of mine openings with respect to the local topography and entry is of particular importance. A poor choice for orientation of the excavation could result in dangerous perturbations in the *in-situ* stress field, introducing unsafe mining conditions.

The objective of this research was two-fold. First, we introduced a realistic model for underground mine openings considering the perturbing effect of local irregular topography. Second, we also considered the effect of entry orientation and rock anisotropy on the induced stress fields around mine openings under the given in-situ stress field. In this study, a triangular mesh formulation was derived for representing complicated irregular surface topography and underground openings.

Each element contains three internal collocation points. Parts of the surface which are far from the mine openings are discretized using infinite elements. Because we used triangular elements with three internal nodes, we developed a new infinite element with

three internal points and suitable shape functions which decay to zero at infinity. Using the corresponding BEM formulation, we then investigated the combined effect of the topography and entry orientation on the stress fields induced by openings under *in-situ* stresses. One rectangular opening in the ground with topography and *in-situ* stresses was simulated using data from the Carroll Hollow Mine in Ohio. Future applications using this new BEM formulation will provide useful guidance on selecting the optimal opening orientation in order to minimize undesirable stress concentrations around underground mine workings.

This paper has four remaining sections. First, we will present the problem and solution methodology and the BEM formulation for solving the problem. Next, we introduce the numerical scheme used to solve the problem. Two different types of elements and their corresponding shape functions are introduced in this section. Then we will provide example solutions for selected problems. In this section, all the stress components on the top side (roof) of the opening are derived and compared with each other. The stress components are calculated for different orientations of the opening with/without considering the effect of topographic surface of half-space. The effect of anisotropy of rock is also investigated in this portion of our work. Finally, we will summarize the works and present our key conclusions.

## BEM FORMULATION

In a linearly elastic medium, the total displacements, stresses, and tractions can be expressed as follows:

$$u_i^t = u_i^h + u_i^p; \qquad \sigma_{ij}^t = \sigma_{ij}^h + \sigma_{ij}^p; \qquad T_i^t = T_i^h + T_i^p$$

where superscripts *t, p,* and *h* denote the total solution, a particular solution corresponding to the body forces and the far field stresses, and the homogenous solution, respectively.

Pan and Amadei (1996) have shown that the total internal displacement solution at one point $\boldsymbol{x}_p$ can be expressed as equation 2 below:

$$\begin{aligned} u_i^t(\boldsymbol{x}_p) = &-\int_{S_o \cup S_t \cup S_i} T_{ij}^*(\boldsymbol{x}_p, \boldsymbol{x}_s) u_j^t(\boldsymbol{x}_s) dS(\boldsymbol{x}_s) \\ &+\int_{S_o \cup S_t \cup S_i} U_{ij}^*(\boldsymbol{x}_p, \boldsymbol{x}_s) T_j^t(\boldsymbol{x}_s) dS(\boldsymbol{x}_s) \\ &+\int_{S_o \cup S_t \cup S_i} T_{ij}^*(\boldsymbol{x}_p, \boldsymbol{x}_s) \left[u_j^p(\boldsymbol{x}_s) - u_i^p(\boldsymbol{x}_p)\right] dS(\boldsymbol{x}_s) \\ &-\int_{S_o \cup S_t \cup S_i} U_{ij}^*(\boldsymbol{x}_p, \boldsymbol{x}_s) T_j^p(\boldsymbol{x}_s) dS(\boldsymbol{x}_s) \end{aligned}$$

where $U^*_{ij}$ and $T^*_{ij}$ are the displacement and traction Green's functions respectively and are given exactly for a transversely isotropic solid with arbitrarily oriented isotropic plane as can be found in Pan and Yuan (2000). $S_o$, $S_t$, and $S_i$ are different parts of the surface which are shown in Figure 1, and the subscripts *s* and *p* indicate points on the surface and within the underground, respectively. $S_o$ is the surface of the opening in the ground, $S_t$ is the topographic surface which is finite and above the opening, and $S_i$ is that part of the topographic surface which is far enough from the opening and is extended from the edges of $S_t$ to infinity and is assumed to be horizontal.

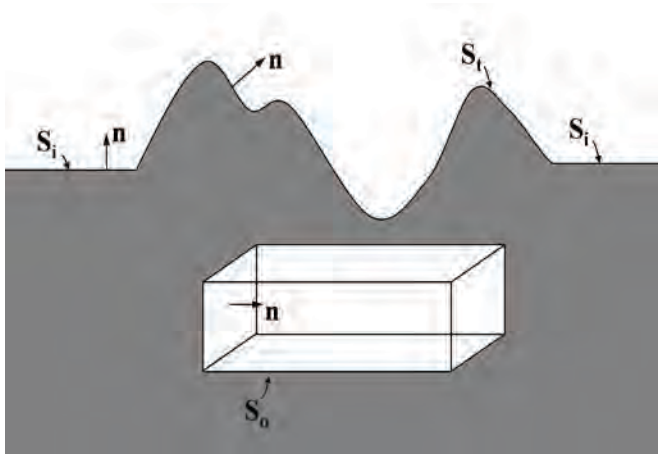



**Figure 1. Geometry of the problem. So is surface of the opening, St is the finite part of topographic surface above the opening and Si is the part of topographic surface which extends from the edges of St to infinity.**

The following boundary integral equation for displacements can be derived from Equation 2 when the internal point $\boldsymbol{x}_p$ approaches point $\boldsymbol{y}_s$ on one of the surfaces $S_o$, $S_t$, or $S_i$:

$$\begin{aligned} &b_{ij} u_j^t(\boldsymbol{y}_s) + \int_{S_o \cup S_t \cup S_i} T_{ij}^*(\boldsymbol{y}_s, \boldsymbol{x}_s) u_j^t(\boldsymbol{x}_s) dS(\boldsymbol{x}_s) = \\ &\int_{S_o \cup S_t \cup S_i} U_{ij}^*(\boldsymbol{y}_s, \boldsymbol{x}_s) T_j^t(\boldsymbol{x}_s) dS(\boldsymbol{x}_s) \\ &+\int_{S_o \cup S_t \cup S_i} T_{ij}^*(\boldsymbol{y}_s, \boldsymbol{x}_s) \left[u_j^p(\boldsymbol{x}_s) - u_i^p(\boldsymbol{y}_s)\right] dS(\boldsymbol{x}_s) \\ &-\int_{S_o \cup S_t \cup S_i} U_{ij}^*(\boldsymbol{y}_s, \boldsymbol{x}_s) T_j^p(\boldsymbol{x}_s) dS(\boldsymbol{x}_s) \end{aligned}$$

In Equation 3 above, $b_{ij}$ are coefficients that depend only on the local geometry of the boundary at point $\boldsymbol{y}_s$. All terms on the right-hand side of the above equation have weak singularities and are integrable. The second term on the left-hand side of Equation 3 has a strong singularity which can be treated by the rigid-body motion method avoiding further calculation of $b_{ij}$.

## NUMERICAL SCHEME

Two different types of elements have been used to discretize all surfaces. Triangular elements with three internal nodes are used to discretize $S_o$ and $S_t$ and rectangular infinite elements with three internal nodes are used to discretize $S_i$ (Figure 2). For each element, the displacement and traction can be approximated by their nodal values.

$$u_i = \sum_{k=1}^{3} \phi_k u_i^k; \qquad T_i = \sum_{k=1}^{3} \phi_k T_i^k; \qquad i = 1, 2, 3$$

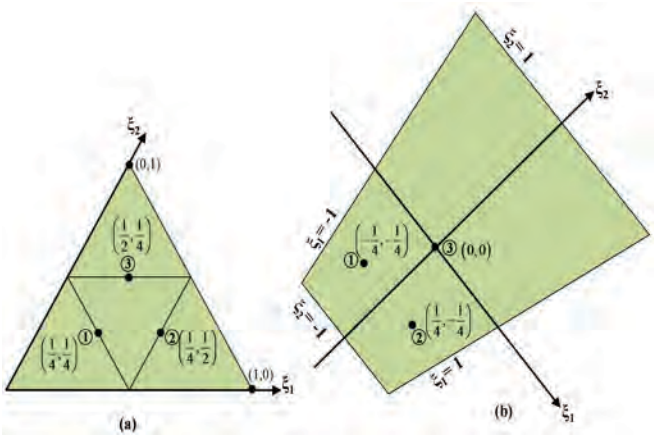



**Figure 2. The shape of the elements and internal nodes and local coordinates xi;1 and xi;2. (a) Triangular element with three internal nodes which is used to discretize So and St. (b) Rectangular infinite element with three internal nodes which is used to discretize Si.**

where $\phi_k$ are the shape functions as defined in Equations 5 and 6 below. $u_i^k$ and $T_i^k$ are the nodal displacements and tractions at node $k$, respectively. Shape functions for the triangular element are:

$$\phi_1^1 = -4\xi_1 - 4\xi_2 + 3; \qquad \phi_2^1 = 4\xi_1 - 1; \qquad \phi_3^1 = 4\xi_2 - 1$$

The intrinsic coordinates $\xi_1$ and $\xi_2$ are defined in Figure 2. For the rectangular infinite element, which is used to discretize the boundary $S_i$, the shape functions can be defined in equation 6 as follows:

$$N_1 = -2\xi_1 - 2\xi_2; \quad M_1 = \left(-\frac{9(\xi_2 - 1)}{5(2 - \xi_2)}\right)^2; \quad \phi_1^2 = N_1 \times M_1;$$

$$N_2 = 2\xi_1 - 2\xi_2; \quad M_2 = \left(-\frac{9(\xi_2 - 1)}{5(2 - \xi_2)}\right)^2; \quad \phi_2^2 = N_2 \times M_2;$$

$$N_3 = 4\xi_2 + 1 \quad M_3 = \left(-\frac{2(\xi_2 - 1)}{(2 - \xi_2)}\right)^2 \quad \phi_1^2 = N_3 \times M_3$$

$N_1$, $N_2$, and $N_3$ are regular-shape functions which satisfy the condition that equals to one at their corresponding node and zero at the other two nodes, and $M_1$, $M_2$ and $M_3$ are decaying functions which are unit at their corresponding node and approach zero when $\xi_2$ approaches one. The final shape functions are multiplications of the corresponding $N$ and $M$ functions. The shapes of the elements and the internal nodes are shown in Figure 2.

## NUMERICAL RESULTS AND DISCUSSION

To investigate the effects of the topographic surface and the orientation of the opening, the following example was designed. One opening with the length of 10m, width of 2m and height of 2m was assumed in a half-space. The half-space was assumed to be transversely isotropic with $E$=10GPa, $E'$=30GPa, $v$=$v'$=0.25 and $G'$=4GPa. These material properties can be considered to be approximately representative of a highly anisotropic package of sedimentary rocks, such as alternating layers of shale, coal, sandstone, and limestone present in the Allegheny Group, the rocks found at the site of the Carroll Hollow Mine.

To consider the effect of topography, two different situations were assumed. First, the surface of half-space was flat at $z$ = 0 (Figure 3) and, second, we used data from the Carroll Hollow Mine in Ohio to introduce the topographic surface (Figure 4). According to the dimension of opening the surface of half-space was divided into two parts ($S_t$ and $S_i$). The top surface of the opening is 2m×10m, consequently a 6m×30m rectangle on the half-space surface immediately above the opening was discretized with triangular elements and the rest of the half-space surface was discretized with rectangular infinite elements. Since these two cases are subjected to comparison, the depth of opening was set in such a way that the distance of opening to $S_t$ on the surface of half-space was the same for both cases. For the topographic surface, the mean elevation of points on $S_t$ was used to set the depth of the opening.

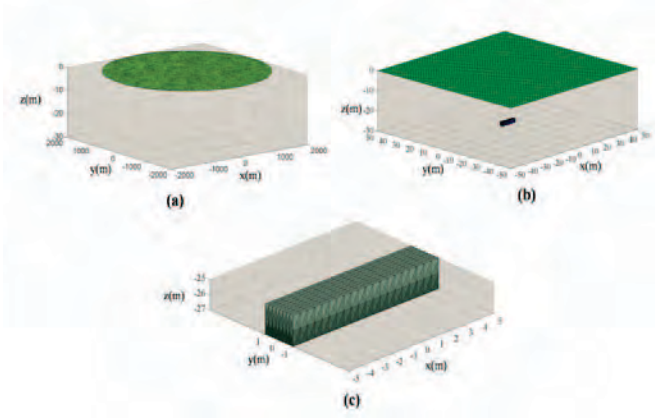



**Figure 3. Case 1: Opening in half-space with flat surface. a) The surface of the half-space, b) The surface of half-space above the opening, c) the discretized opening.**

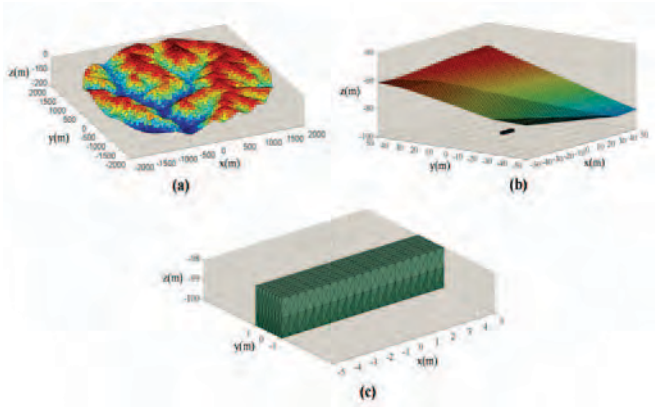



**Figure 4. Case 2: Opening in half-space with topographic surface. a) The surface of the half-space, b) The surface of half-space above the opening, c) the discretized opening.**

To investigate the effect of orientation of the opening, three cases for the far-field stresses were considered. The three cases avoid the need to rotate the opening within the model. All the combined situations are presented in Table 1. In this table, two cases (1d and 2d), which are used to investigate the effect of rock anisotropy, will be discussed at the final part of this section.

The results for stress components on the roof of the opening for different cases are shown in Figures 5, 6 and 7. Figure 5 shows stress components on the roof of the opening for Case 1a and 2a, where there is a far-field stress in $x$-direction only. This

figure shows that the topographic surface has a small effect on the magnitude of stress components. Also, it does not change the distribution of $\sigma_{xx}$, but it affects the shape of contours for $\sigma_{yy}$ and $\sigma_{xy}$. The extent of effects is expected to vary, depending on the placement of the opening with respect to undulations in the overlying topography.

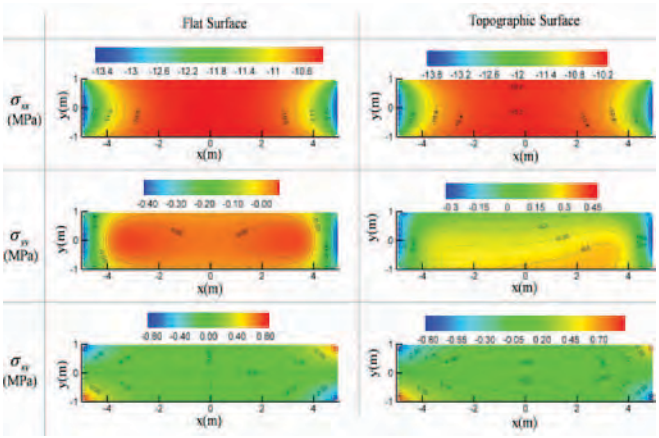



**Figure 5. Stress components on the roof of the opening for Case 1a on the left column and Case 2a on the right column.**

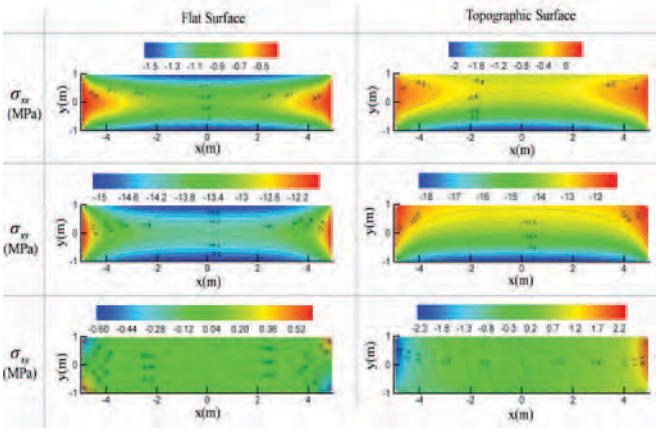



**Figure 6. Stress components on the roof of the opening for Case 1b on the left column and Case 2b on the right column.**

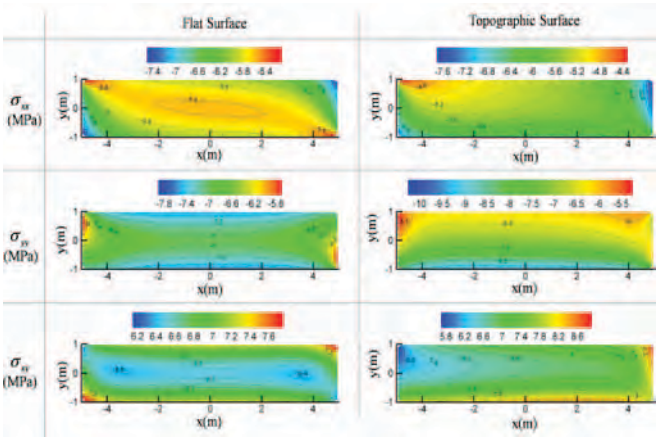



**Figure 7. Stress components on the roof of the opening for Case 1c on the left column and Case 2c on the right column.**

In Figure 6, the stress components on the roof of the opening are shown for Cases 1b and 2b. In these cases, the non-zero far-field stress is along the $y$ axis. It is observed from this figure that the topographic surface has a noticeable effect on both the shape of the contours and their magnitude. We can also see the same effects for Figure 7, which is for Cases 1c and 2c, where the far-field stress is rotated by 45°.

Comparing the three figures with each other, one can investigate the combined effect of topography and entry orientation. These figures indicate that the topographic surface and orientation of the opening can have a drastic effect on the distribution and magnitude of stress components and should be considered wisely.

The results of the stresses on the roof of the opening that are shown in Figures 5-7 are for a transversely isotropic rock with a horizontal plane of isotropy. Since we show the results on the top roof of the opening, which is a horizontal surface, the contours shapes are expected to be the same as in the corresponding isotropic half-space. To investigate the effect of rock anisotropy, two new cases were defined (Cases 1d and 2d). One opening with the same geometry as above examples is considered: a half-space with flat surface and a half-space with a topographic surface; however, the plane of isotropy was rotated by the angle of 45° about the $y$ axis ($\psi$=45°, $\beta$=0°). The non-zero far-field stress is assumed to be compression and along the $x$ axis. Similar to the work by Wang et al. (2012), the transform matrix is introduced in Equation 7 below:

$$\begin{bmatrix} x \\ y \\ z \end{bmatrix} = \begin{bmatrix} -\cos\psi\sin\beta & -\cos\psi\cos\beta & \sin\psi \\ \cos\beta & -\sin\beta & 0 \\ \sin\psi\sin\beta & -\sin\psi\cos\beta & \cos\psi \end{bmatrix} \begin{bmatrix} x_1 \\ y_1 \\ z_1 \end{bmatrix}$$

where the angles $\psi$ and $\beta$ and the global axes $x$, $y$, and $z$ as well as the local material axes $x_1$, $y_1$, $z_1$ (with $z_1$ being the symmetry axis of the material) are defined in Figure 8. The stress components on the roof of the opening for these two cases are shown in Figure 9.

Comparing Figure 9 and Figure 5 shows that the rock anisotropy could drastically affect the magnitude and distribution of $\sigma_{yy}$, however other stress components does not change noticeably. It demonstrates that these results could depend closely on the size and orientation of the opening, and also the shape of the topographic surface. Therefore, this work demonstrates the fact that both topography and elastic anisotropic properties can exert significant influence on the 3D distribution of the stress in the roof of underground openings. This work further shows the importance of selecting the entry orientation because some orientations may lead to safer designs for mine tunnels. The new code based on the proposed BEM formulation allows us to consider the effects of topography and rock anisotropy on the stress field around underground openings efficiently, with no need to discretize the model domain. Future development of this code will allow for simulation of stresses around realistic mine geometries.

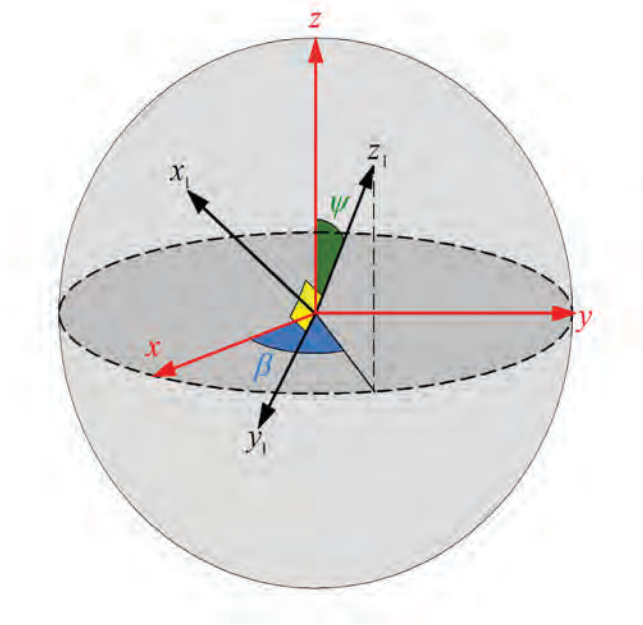



**Figure 8. Relation between the global (x, y, z) and local material (x1, y1, z1) coordinates.**

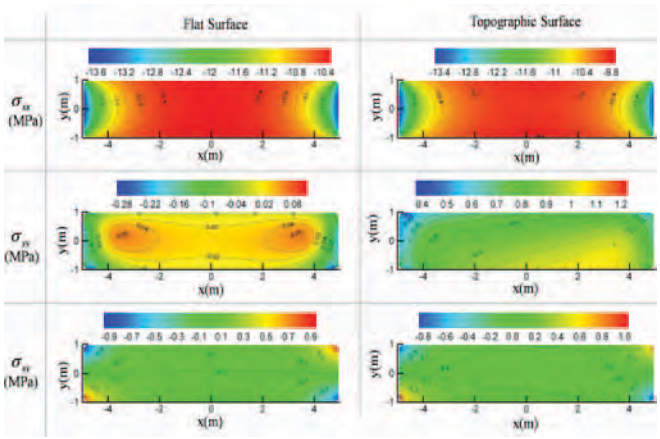



**Figure 9. Stress components on the roof of the opening for Case 1d on the left column and Case 2d on the right column.**

## CONCLUSIONS

In this paper, we investigated the combined effect of entry orientation and topography on stress components on the roof of a mine opening in the anisotropic rock. We used the BEM formulation to find the stresses in the domain. The boundary of the problem was discretized using two types of elements: triangular and rectangular, both with three internal nodes. The triangular element was used to mesh the boundary of the opening and the finite part of the half-space surface above the opening. The rectangular element was used to discretize the infinite part of the half-space surface, which was suitably far from the opening.

The results indicate that if the mine opening is close enough to the earth's surface, the surface topography can have a drastic effect on the magnitude and distribution of stress components. Also, the orientation of mine tunnels could change the shape and magnitude of stress components completely. Furthermore, we investigated the effect of rock anisotropy by rotating the plane of isotropy, and the results indicate that its effect can be significant. As a result, to have a realistic estimation of the local stress fields around underground mines, the topographic effect of the surface as well as the rock anisotropy should be considered. Safe design for mining tunnels requires the orientation of tunnels with respect to the regional stress field, with respect to the rock anisotropy, and the overlying topography to be selected wisely.

## REFERENCES

Irikura, K. (1986). Prediction of strong acceleration motion using empirical Green's function. *In Proc. 7th Japan Earthquake Engineering Symposium.* 151-156.

Liang, J., and Liew, K. M. (2001). Boundary elements for half-space problems via fundamental solutions: A three-dimensional analysis. *International Journal for Numerical Methods in Engineering*. 52(11), 1189-1202.

Liew, K. M., and Liang, J. (2003). "Three-dimensional piezoelectric boundary element analysis of transversely isotropic half-space." *Computational Mechanics*. 32(1-2), 29-39.

Liu, Y. J., Mukherjee, S., Nishimura, N., Schanz, M., Ye, W., Sutradhar, A., Pan, E., Dumont, N. A., Frangi, A. and Saez, A. (2011). "Recent advances and emerging applications of the boundary element method." *Applied Mechanics Reviews*. 64(3), 030802.

Pan, E., and Amadei, B. (1996). "Fracture mechanics analysis of cracked 2-D anisotropic media with a new formulation of the boundary element method." *International Journal of Fracture*. 77(2), 161-174.

Pan, E., Amadei, B., and Kim, Y. I. (1998). "2-D BEM analysis of anisotropic half-plane problems - application to rock mechanics." *International Journal of Rock Mechanics and Mining Sciences*. 35(1), 69-74.

Pan, E., Tabrizi, A. M., Sangghaleh, A., and Xia, K. (2013). "Stress perturbation around a fault by hydraulic fracturing." *International Journal of Geomechanics*.

Pan, E., and Yuan, F. G. (2000). "Boundary element analysis of three-dimensional cracks in anisotropic solids." *International Journal for Numerical Methods in Engineering*. 48(2), 211-237.

Tonon, F., and Amadei, B. (2002). "Effect of elastic anisotropy on tunnel wall displacements behind a tunnel face." *Rock Mechanics and Rock Engineering*. 35(3), 141-160.

Tonon, F., Pan, E., and Amadei, B. (2001). "Green's functions and boundary element method formulation for 3D anisotropic media." *Computers & Structures*. 79(5), 469-482.

Wang, H. M., Pan, E., Sangghaleh, A., Wang, R., and Han, X. (2012). "Circular loadings on the surface of an anisotropic and magnetoelectroelastic half-space." *Smart Materials and Structures*. 21(7), 075003.

# Stability of a Gateroad Used Simultaneously for Two Retreating Longwall Faces

**Stanisław Prusek**, Professor, Head Department
**Andrzej Walentek**, Ph.D., Assistant Professor
Department of Extraction Technologies and Mining Support
Central Mining Institute
Katowice, Poland

**Leszek Kloc**, Director
Kompania Weglowa S.A.
Katowice, Poland

**Leonard Klabis**, Acting Deputy Branch Chief
**Andrzej Malesza**, Director
Colliery Bobrek-Centrum
Kompania Weglowa S.A.
Bytom, Poland

## ABSTRACT

In this paper, results of underground measurements conducted in gateroad 3, seam 615, at the Bobrek-Centrum Colliery are presented. The Bobrek-Centrum Colliery is owned by Kompania Węglowa, the largest hard coal producer in the European Union. Yearly production at the colliery, including the longwall system, is about 2 million tonnes. Gateroad 3 was used simultaneously for two retreating longwall faces, No. 1 and No. 2. This working was also employed for the conveyor belt for longwall No. 1 and served as a transport road for longwall No. 2. Approximately 100 meters of gateroad 3 was maintained behind the face of longwall No.1 and then, with the progress of longwall No. 2, it was liquidated.

In this paper, we present the results of underground measurements of vertical and horizontal convergence in gateroad 3. We also present the results of numerical modeling for deformation of the working. Finally, we analyse the accuracy of the numerical calculations by comparing them to the actual deformation of gateroad 3.

## INTRODUCTION

In mining practice, cases of significant deformation of roadways are frequent. The intensity of the deformations depends on numerous factors, often referred to as geological and mining. There are several methods of selecting a type of support for roadways, each of which takes the geological and mining conditions into consideration and enables calculations of the load of the rock mass to facilitate the correct selection of a support. Our experiences show that the biggest rock mass movements and deformations of support occur most often in roadways affected by the active mining works in their vicinity. Both in undermined workings and those overmined by an active mining front, we can observe significant deformations. Rock mass movements occur also in gateroads, yet their intensity varies. It may be strongly concluded that convergence ought to be considered while designing workings. Both horizontal and vertical convergence of a given working should be considered to estimate its cross-section, and then analysed to determine whether the deformations will allow safe and effective mining. The case study we present in the following paper helps us expand our knowledge of the scope for predicting the sequence of gateroad deformations. The underground tests and their reference to prediction methods employing numerical modelling have allowed us to evaluate the accuracy of predicted deformations in the gateroads with the method.

## DESCRIPTION OF GEOLOGICAL AND MINING CONDITIONS IN THE AREA OF THE UNDERGROUND TESTS

Gateroad 3, where we made the underground measurements, was a working between longwall No. 1 and longwall No. 2 in the Bobrek-Centrum colliery. Longwalls 1 and 2 were extracted in seam 615, in the northeastern part of the Bytom-Centrum mining area in Bytom Trough, in its northern wing. Seam 615 in the area is located at a depth between 720 m and 890 m, and sinks to the southeast at an angle of 9-12°. The thickness of the seam varies between approximately 1.4 m and 3.3 m (together with interlayers of clay shale). Seam 615 shows a dual structure; the upper part of the seam, at a thickness between 1.32 m and 2.1 m, is homogeneous and the lower part, between 0.15 m and 1.1 m in thickness, is interbedded by clay shale at a total thickness of between 0 and 0.4 m. The upper and the lower parts of seam 615 are separated with a layer of clay shale measuring between 0.15 and 1.1 m in thickness.

In the roof of seam 615, there are layers of clay shale (2.0 m) and sandy shale (3.3 m). The immediate floor stratum is a layer of clay shale measuring 7.4 m thick. The detailed profile of the roof rocks and the floor rocks is presented in Figure 1.

Due to natural hazards, seam 615 in the described area was marked as a seam of:

- degree III for seismic activity/rock burst hazard;
- category IV for methane hazard;
- class B for dust hazard;
- degree I for water hazard; and
- group IV for spontaneous ignition susceptibility.

Above (up to 160 m) seam 615 within the influence of longwalls 1 and 2, there had been no earlier mining, but below (up to 60 m) the seam 620 had been extracted with a longwall system with a caving goaf.

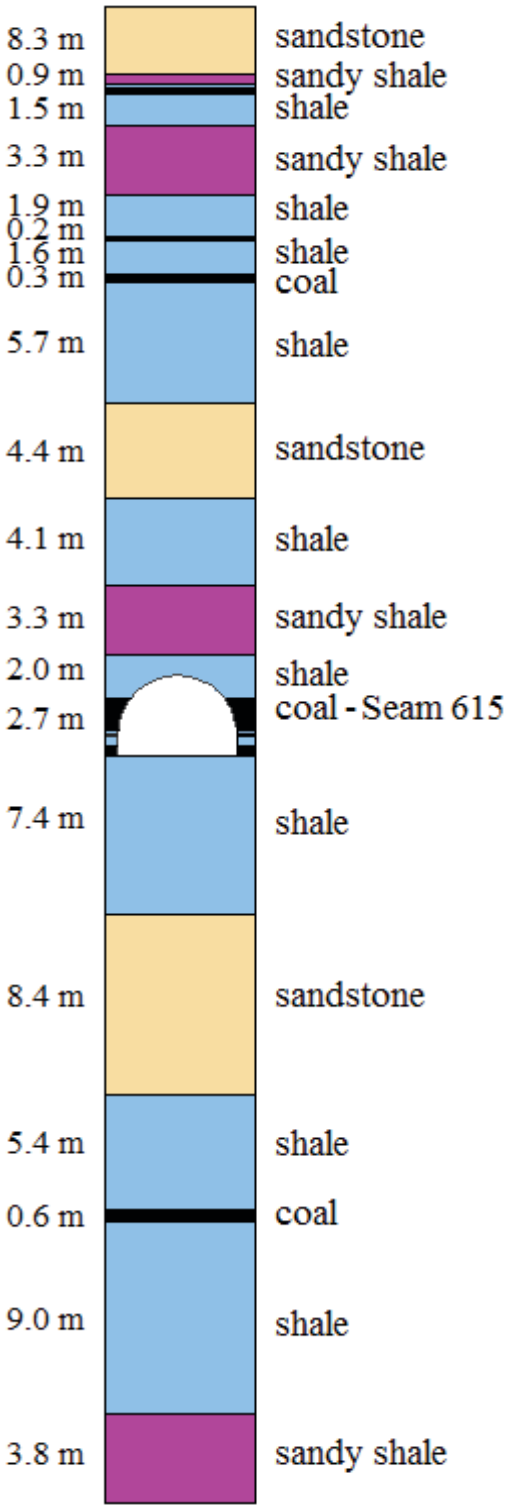



**Figure 1. Profile of roof rocks and floor rocks of seam 615.**

Gateroad 3 was a working located between longwalls 1 and No. 2, as seen in Figure 2. Approximately 100 m of the gateroad was maintained behind the face of longwall 1, then it was closed in conjunction with the advance of longwall 2. Gateroad 3 played the role of conveyor road for longwall 1 and an access transport working for longwall 2.

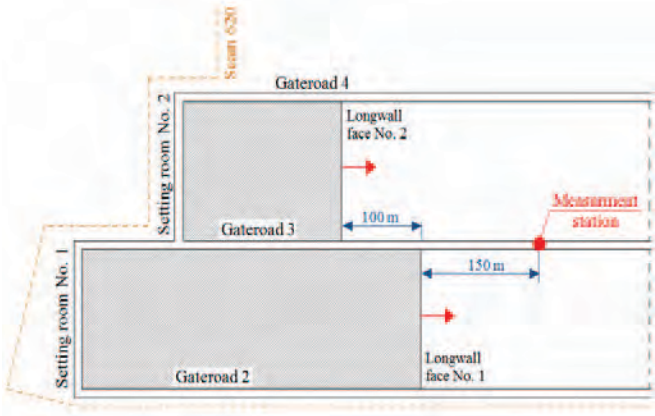



**Figure 2. Exploitation fields of longwalls 1 and 2 in seam 615.**

Longwall 1, at a width of 180 m, was extracted to a height of 1.9 m while surrounded on both sides by coal, using the *diagonal longwall* method with roof caving, advancing from west to east. The length of the longwall is approximately 1,360 m. Longwall 2, measuring 180 m in width, was extracted to a height of 1.8 m also with the *diagonal longwall* method with roof caving advancing from west to east, adjacent to the goaf of extracted longwall 1.

Gateroad 3 was supported by yielding steel arches LP10 (with a width of 5.5 m and a height of 3.8 m). The distance between the arches was 0.8 m. Steel arches were made from steel V-shaped cross-sectional profiles with an elementary mass of 29 kg/m (Prusek et al., 2011).

In the area of longwall 1, the roadway junction, support sets were reinforced with:

- three stabilising steel horseheads, assembled on the roof arches at least 10 m ahead of the face of the longwall;
- a wooden horsehead with SV29-type friction prop; and
- a wooden horsehead stabilised with a wooden expansion bar.

Schematics of reinforcement for the support ahead of the face of longwall 1 is shown in Figure 3.

Behind the face of longwall 1, to maintain its functionality for longwall 2, gateroad 3 was additionally reinforced with two wooden horseheads with SV29-type friction props and wooden cribs built along the goaf of longwall 1 (crib parameters: height 2.6 m, width 1.8 m, length 2.2 m, diameter of wood ø16 mm). Schematics of reinforcement for the support of gateroad 3 behind the face of longwall 1 are shown in Figure 4.

## UNDERGROUND MEASUREMENTS OF CONVERGENCE OF GATEROAD 3

Before measuring convergence in gateroad 3 using a borehole penetrometer, we made *in situ* tests aimed at evaluating the strength parameters of the rocks surrounding the working. Figure 5 presents a borehole penetrometer typically used in Polish underground mining.

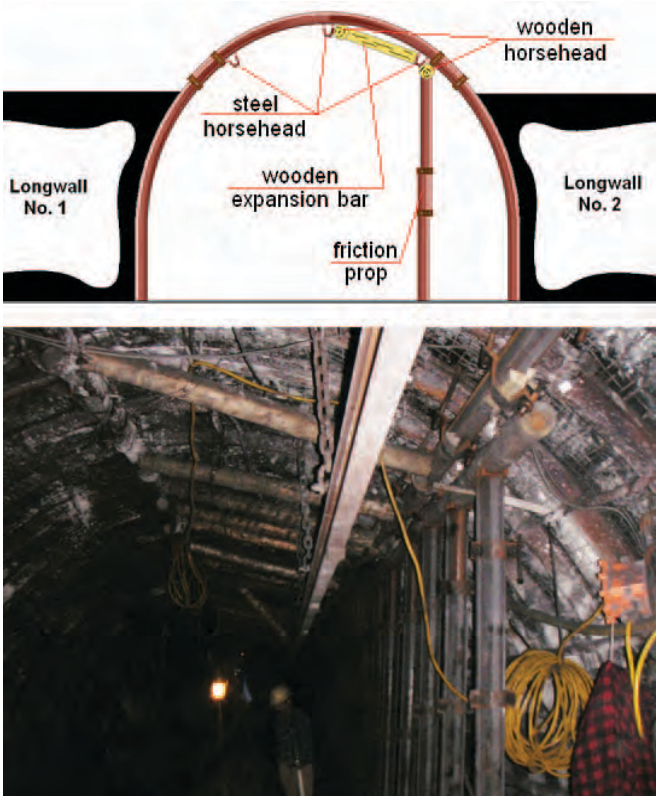



**Figure 3. Reinforcement of LP support of gateroad 3 outby longwall face 1.**

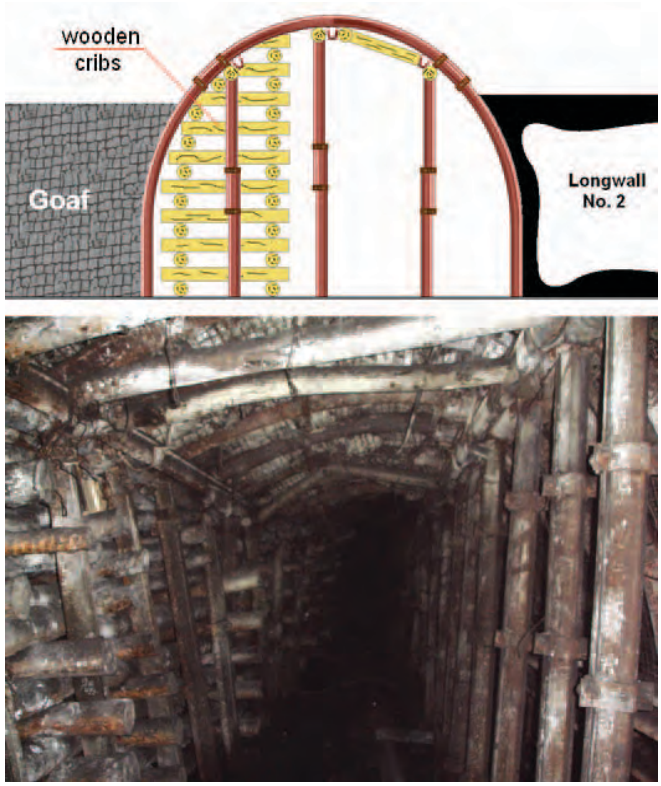



**Figure 4. Reinforcement of LP support of gateroad 3 inby longwall face 1.**

Penetrometric tests were made approximately 150 m ahead of the face of longwall 1 in the place where convergence in gateroad 3 was measured. To conduct the tests, two Ø 95 mm boreholes were drilled in the roof and the floor, 10 m and 5 m long, respectively. Figure 6 shows an example of the results from the penetrometric tests for the roof rocks in gateroad 3.

The results of the penetrometric tests show that the roof rocks surrounding gateroad 3 (up to a height of 10 m from the level of the working) were of medium compressive strength of approximately 28 MPa. In the case of the floor rocks, we concluded that the compression strength of the clay shales in the immediate floor was 33 MPa.

To evaluate the scale of deformation in gateroad 3 due to the influence of longwall faces 1 and 2, we made *in situ* measurements of vertical convergence (V), horizontal convergence (H) and floor rock heave (F). The measurements were conducted following Central Mining Institute methodology (Prusek, 1998, 2008) at a place located in gateroad 3, starting approximately 150 m ahead of the face of longwall 1. The schematic of the convergence measuring arrangement in gateroad 3 is presented in Figure 7.

The results of measurements of deformation in gateroad 3, in relation to the distance from longwall face 1, are presented in Figure 8. This Figure illustrates that, in the area of longwall face 1, the value of vertical convergence in gateroad 3 was approximately 280 mm, of which 160 mm was roof subsidence and 120 mm



**Figure 5. Borehole penetrometer used during in situ tests evaluating rock strength.**

was floor heave. As far as horizontal convergence in the area of longwall face 1 was concerned, it was around 400 mm.

A significant increase in the value of convergence occurred behind the face of longwall 1. Approximately 100 m behind the face of longwall 1, where there was also the face of longwall 2, the value of vertical convergence in gateroad 3 was 1,025 mm, of which 411 mm was roof subsidence and 614 mm was floor heave. Horizontal convergence of gateroad 3 in the area was 1,420 mm. It is necessary to note that the maximum values of vertical convergence and horizontal convergence shown in Figure 8 were influence by both longwalls 1 and 2.

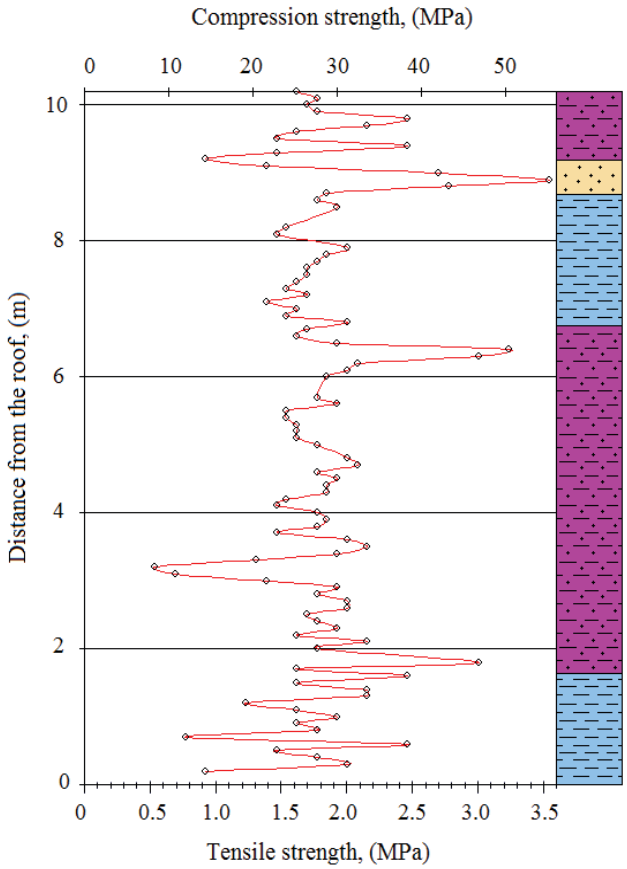



**Figure 6. Strength profile of roof rocks in gateroad 3.**

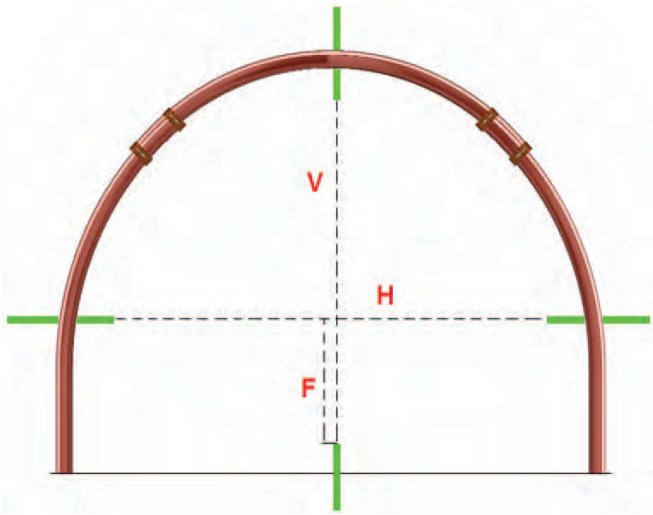



**Figure 7. Schematics of measurements: V - vertical convergence, H - horizontal convergence, F - floor heave.**

Analysing the results of the measured deformation in gateroad 3, in the context of the results of previous research studies which have been conducted in GIG in recent years (Prusek, 2008), we can conclude that the value of deformation in the given longwall entry behind the face of longwall 1 remained at an average level. As experiences of the Bobrek-Centrum colliery show, the functionality

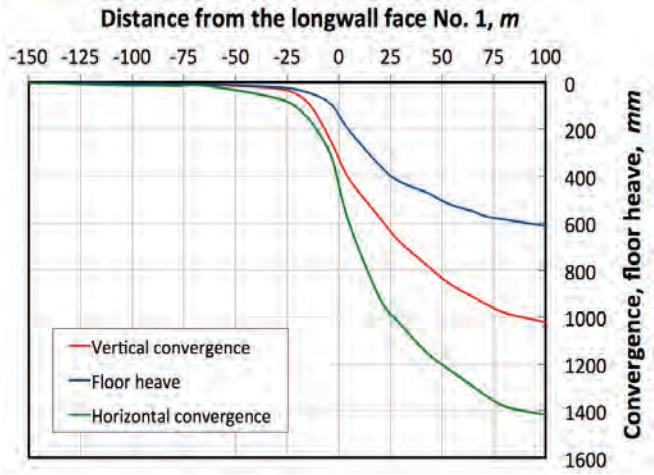



**Figure 8. Values of measurements of vertical convergence, horizontal convergence and floor heave in gateroad 3, depending on distance from the face of longwall 1.**

of gateroad 3, through proper reinforcment, was satisfactory and allowed safe extraction of both longwalls 1 and 2.

## PREDICTION OF DEFORMATION IN GATEROAD 3 WITH NUMERICAL MODELLING

The research conducted in GIG on the use of numerical modelling to predict deformation in gateroads allowed us to devise a method to determine the value of convergence depending on the distance from the face of a longwall (Prusek, 2008), as well as to predict propagation of the fracture zone around a gateroad (Walentek, 2010). The influence of the extraction face causes an increase in stresses in the surrounding rock mass and affects its strength-deformation parameters in the vicinity of the gateroads. That is why we assumed that, in the models of rock mass surrounding the working; we will lower the parameters of rocks to obtain the value of deformation observed in underground conditions (Prusek, 2008, Walentek, 2009).

To do so, we used Phase2 v 7.0 software based on the finite element method (Hoek, 2007). The deformation condition is calculated according to the Hoek-Brown failure criterion and for the fractured rock mass it is defined as (Hoek, Carranza-Torres, Corkum, 2002; Hoek, 1999, 2007):

$$\sigma'_1 = \sigma'_3 + \sigma_{ci}\left(m_b \frac{\sigma'_3}{\sigma_{ci}} + s\right)^a \quad \text{, MPa}$$

where:

$\sigma'_1$ and $\sigma'_3$ = effective maximum and minimum stress at failure (MPa)

$m_b$ = value of the Hoek-Brown parameter for the rock mass

$s$ and $a$ = parameters, determined on the basis of rock mass properties

$\sigma_{ci}$ = uniaxial compressive strength of rock sample (MPa)

The method developed in GIG to predict convergence in gateroads assumes modifying selected parameters in the Hoek-Brown failure criterion (Prusek, 2008). Values of parameters $m_{bz}$ and $s_{z,}$ depend on the distance from the face of a longwall when calculated with the Central Mining Institute method, and are as follows:

- for coal:

$$m_{bz} = 0{,}6278 \cdot e^{-0{,}0024 \cdot d}$$

$$s_z = 0{,}000494 \cdot e^{-0{,}00393 \cdot d}$$

- for clay shale:

$$m_{bz} = 0{,}3197 \cdot e^{-0{,}0148 \cdot d}$$

$$s_z = 0{,}00041 \cdot e^{-0{,}01592 \cdot d}$$

- for sandy shale:

$$m_{bz} = 0{,}5093 \cdot e^{-0{,}0127 \cdot d}$$

$$s_z = 0{,}000762 \cdot e^{-0{,}01881 \cdot d}$$

- for sandstone:

$$m_{bz} = 0{,}7568 \cdot e^{-0{,}0127 \cdot d}$$

$$s_z = 0{,}001647 \cdot e^{-0{,}01697 \cdot d}$$

where:

*d* – distance from the face of a longwall (assumes negative values ahead of a longwall, and positive ones behind a longwall).

The presented formulas allow us to calculate post-failure parameters of the coal seam and surrounding rocks occurring in Upper Silesia Coal Basin (GZW) conditions. That, in turn, allows us to calculate, with the use of numerical modelling, displacements of the rock mass which can occur in gateroads in a certain distance from the face of a longwall.

For the purposes of calculating deformation in gateroad 3, two 70x70 m models of the rock mass were made (Figure 9). The composition and rock types surrounding the working was assumed based on the profile of roof rocks and floor rocks of seam 615, as presented in Figure 1. Model I (Figure 9a) reflects the situation outby longwall face 1, whereas model II (Figure 9b) reflects the situation inby longwall face 1.

Basic values of the parameters of the rock layers, including the ones describing the Hoek-Brown failure criterion, were assumed based on results of rock mass strength tests made with a hydraulic

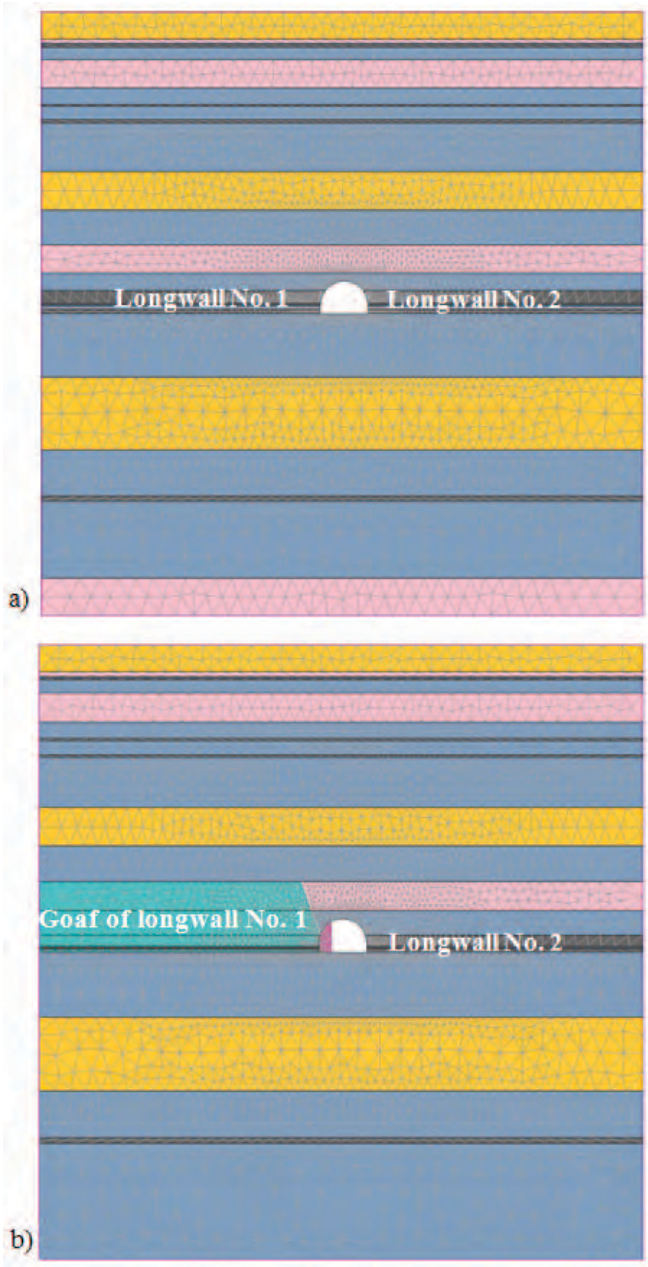



**Figure 9. Rock mass model around gateroad 3: a) outby the face of longwall 1, b) inby face of longwall 1.**

borehole penetrometer in the research area and analytical basis determined with RocLab software. The basic values of rock layer parameters adopted for calculations are presented in Table 1; among them are those describing the Hoek-Brown failure criterion (Hoek, Carranza-Torres, Corkum, 2002; Hoek, 2007).

Moreover, in the analysed models we made the following assumptions: no displacements on the vertical and horizontal edges of the model; the modelled rock mass is a plastic medium and the layers it consists of have isotropic properties; primary stresses result from the depth and location of the working of 800 m, and average specific gravity of the overburden ($\gamma$=0.025 MN/m$^3$).

**Table 1. Basic parameters of rock layers adopted for numerical calculations.**

| Types of rock | Young`s modulus E (MPa) | Poisson`s ratio υ | Compression strength $R_c$ (MPa) | Parameter $m_b$ | Parameter s |
|---|---|---|---|---|---|
| Coal | 1700 | 0.30 | 14.0 | 0.783 | 0.0003 |
| Shale (roof) | 2800 | 0.24 | 28.0 | 1.100 | 0.0006 |
| Shale (floor) | 3600 | 0.24 | 33.0 | 1.600 | 0.0009 |
| Sandy shale | 3985 | 0.23 | 35.0 | 1.800 | 0.0010 |
| Sandstone | 6890 | 0.22 | 50.0 | 2.022 | 0.0070 |
| Goaf | 600 | 0.40 | 5.0 | 0.275 | 0.0002 |

In the developed models, we also considered basic elements of the support used in gateroad 3, like support sets of a steel arch support (LP), steel props and wooden cribs. To model the steel arch support, we used a "liner" type support in the form of beam elements. The elements were attributed parameters of a V-type profile of which the support was made. The reinforcements of the arch support in the form of steel props and wooden cribs were also modelled with "liner" type beam elements, which were attributed material parameters of steel and wood, respectively (Walentek, 2010).

Examples of numerical calculations of the deformations in gateroad 3 affected by longwall faces 1 and 2 are presented in rock mass displacement maps in Figures 10 and 11. The maps illustrate the situation in the area of longwall face 1 (Figure 10) and 100 m inby the face of longwall 1 (Figure 11). Moreover, in Figure 12, to compare results of *in situ* measurements with the results of numerical calculations, there are curves of convergence and floor heave in the modelled length of gateroad 3.

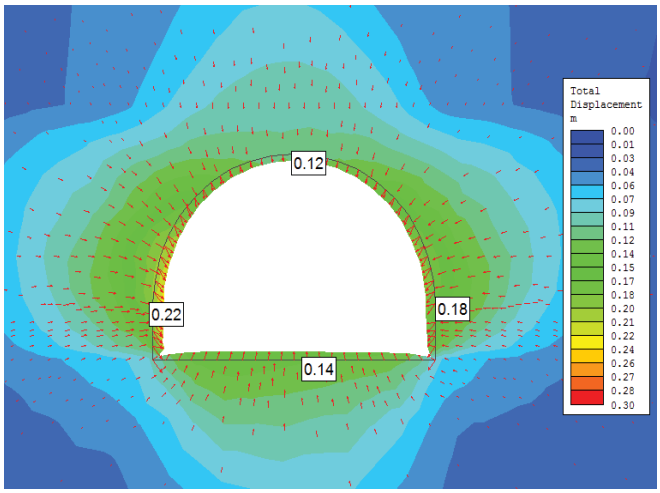



**Figure 10. Map of rock mass displacement around gateroad 3, area around the face of longwall 1.**

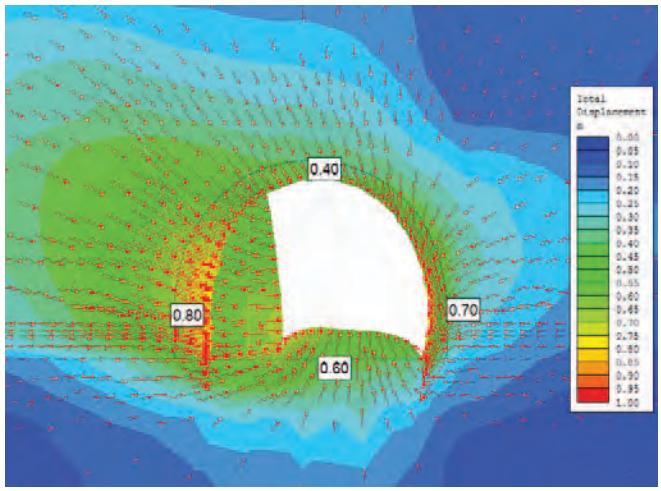



**Figure 11. Map of rock mass displacement around gateroad 3, 100 m inby the face of longwall 1.**

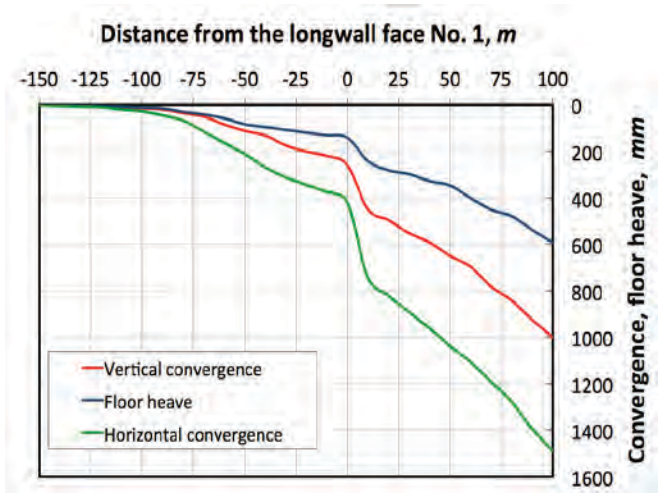



**Figure 12. Results of numerical calculations of vertical convergence, horizontal convergence and floor heave in gateroad 3, depending on the distance from the face of longwall 1.**

Figures 11 and 12 show that the maximum value of prediction vertical convergence in gateroad 3, at the distance of 100 m inby the face of longwall 1, is 1,000 mm, of which 400 mm is roof subsidence and 600 mm is floor heave. As far as horizontal convergence is concerned, its maximum prediction value is 1,500 mm. Comparing results of underground measurements of convergence in gateroad 3 (Figure 8) and results of numerical modelling (Figure 12), it may be concluded that the method of predicting deformation in gateroads using Phase2 software devised by GIG (Prusek, 2008) worked perfectly in the mining conditions in the Bobrek-Centrum colliery.

## SUMMARY

This paper presents the results of underground measurements of rock mass movements. The measurements were made in gateroad 3, a working between longwalls 1 and 2 extracted in seam 615 of the Bobrek-Centrum colliery. Based on the results of underground measurements, we can conclude that movements of rock mass occurring in gateroad 3 in the form of roof subsidence, floor heave and displacements of the sidewalls were on the average level. Factors influencing such a level of deformations were, first of all, good geological and mining conditions in the area of mining activities, in addition to well prepared and well selected reinforcement of the support in gateroad 3. Applying reinforcement to the support in the form of friction props and wooden cribs, from the point of view of the colliery, brought good results which enabled safe extraction of longwalls 1 and 2 with one common gateroad.

Comparing the results of numerical modelling with Phase2 software to the underground measurements showed good agreement between the modelled values and the ones actually measured *in situ*. That supports the conclusion that the method of predicting convergence in gateroads developed by GIG can be successfully used in the conditions at the Bobrek-Centrum colliery.

In spite of such satisfying results from the method developed for convergence prediction, the actual convergence in gateroads will be still be verified and the prediction method further perfected using further underground tests conducted in various geologic and mining conditions.

## REFERENCES

Hoek , E. (1999). Rock engineering - course notes. Evert Hook Consulting Engineer Inc., Toronto.

Hoek E., Carranza-Torres C., Corkum B. (2002). Hoek-Brown failure criterion – 2002 edition. Toronto, Proceedings NARMS-TAC Conference, s. 267-273.

Hoek E., (2007). Practical Rock Engineering. In; Rocscience Inc, . [http://www.rocscience.com/education/hoeks_corner]

Prusek S. (1998). Measurements of convergence, delamination of roof rocks and load on roadside pack in gateroads. Materiały XXII Zimowej Szkoły Mechaniki Górotworu. Kraków.

Prusek S. (2008). Modification of parameters in the Hoek-Brown failure criterion for gate road deformation rediction by means of numerical modeling. Glückauf No. 9.

Prusek S. (2008). Methods of predicting deformation of gateroads in the areas exploited with roof caving. Prace Naukowe GIG nr 874. Katowice.

Prusek, S., Lubosik, Z., Dvorsky, P., Horak, P. (2011). "Gateroad support in the Czech and Polish coal mining industry – present state and future developments." In: *Proceedings of the 30th International Conference on Ground Control in Mining*.

Walentek A. (2009). Numerical model of destruction zone around gateroad. Kwartalnik GIG 1/2009. s.67-80.

Walentek A. (2010). Metoda obliczania obciążenia chodnika przyścianowego narażonego na wpływy ciśnień eksploatacyjnych z wykorzystaniem modelowania numerycznego, uwzględniającego strefy spękań górotworu. (Method of calculating load in a longwall entry exposed to the influence of exploitation pressure with the use of numerical modelling method considering rock mass fracture zones) Praca statutowa GIG.

# Three Dimensional Analysis of Strain and Ground Surface Displacement Caused By Underground Mining in the Vicinity of Geotechnical Barriers

**Rafał Misa**, Ph.D. Student
**Krzysztof Tajduś**, Ph.D., Eng. Geomechanics
Strata Mechanic Research Institute Polish Academy of Science, AGH University of Science and Technology
Crakow, Poland

**Anton Sroka**, Univ. Prof. Dr.-Ing. Habil. Geomechanics
Technische Universität Bergakademie Freiberg, Strata Mechanic Research Institute Polish Academy of Science
Freiberg, Germany

## ABSTRACT

In order to prevent the formation of mining damage or to reduce its reach, it is advisable to look for technical solutions which would enable effective protection of construction sites from the impacts of underground mining. So far, other authors have mainly focused on developing methods of securing construction sites in order to minimize the damage resulting from underground mining; the issue of geotechnical methods for protecting buildings against mining damage has not been thoroughly covered in those articles. It should be noted that there are relatively few publications directly related to this issue, nor are there practical examples of geotechnical protection. In this paper, a geotechnical solution available for securing building structures is discussed. Trenches presented in this research reduce the size and range of mining deformation. The results of numerical modelling for sample protective solutions, aimed at reducing the impact of mining activity on the terrain surface under various conditions, are presented. The calculations were performed with the aid of the Abaqus 6.10-2 software, based on the Finite Element Method.

**Keywords:**

numerical methods, FEM (Finite Element Method), geotechnical methods of building protection, decompression trench, ground surface displacement, horizontal displacement

## FOREWORD

Movements of rock and soil, both within the rock mass and on the terrain surface, resulting from underground mining extraction are likely to cause mining damage to building structures. It is a serious issue in urbanised Europe, where the repair of mining damage and payments of potential compensation account for a high percentage of the overall production cost for a ton of coal. In Germany, for example, the expenses to cover the cost of mining damage in 2009 were €12 per ton of mined coal, with the cost of mining damage to buildings accounting for €6.80/ton (Sroka et al., 2012). In order to prevent mining damage or reduce its range, and consequently cut down the overall cost of coal production, measures have been taken to find technical solutions to enable effective protection of buildings from the effects of underground mining exploitation. Analysing the existing solutions, it can be concluded that other authors have focused mainly on developing methods for structural protection of buildings to minimise the damage (Kwiatek, 1997). Geotechnical methods aimed at protecting buildings from mining damage have been given hardly any attention compared to structural or mining protection. In spite of that, there are examples of practical applications of geotechnical methods for protection of buildings in the world, including Germany (Sroka, 1994), the USA (Luo, Peng, 1991) and the UK ("Subsidence Engineers' Handbook", 1975). Some of them have already been successfully applied in Poland, and the effects of reducing surface strain and mining damage are more than satisfactory (Misa, Tajduś, 2010; Misa, 2013).

## NUMERICAL MODELLING OF GEOTECHNICAL PROTECTION MEASURES IN THE FORM OF DECOMPRESSION TRENCHES

A numerical model was created to enable proper analysis and a qualitative approach to determine the principles and effectiveness of geotechnical protection measures to reduce terrain surface strain from underground mining exploitation. The Abaqus software pack, based on the Finite Element Method (FEM), was used for the numerical modelling (Simulia, 2013). The model was comprised of a building structure and a part of a surface subjected to a strain processes invoked by underground mining extraction.

Around the building, in order to reduce the influence of mining strain, a trench filled with compressible material was modelled, thus forming the area in which the strain would concentrate. This way, the trench served as a "damper", protecting the immediate subsoil of the building from excessive strain. The authors, by means of numerical calculations, tested the influence of decompression trenches on the reduction of adverse effects of underground mining exploitation on the building structure. To this end, numerical calculations were performed for several dozen scenarios, differing as to the geometrical and mechanical properties of the rock medium assumed. Note that the calculations were of a qualitative nature, and the parameters adopted were based on the literature available and data received from Polish hard coal mines (Tajduś, 2009).

Since the resulting outcomes are quite voluminous and complex, this article presents only the selected results which

are most interesting, and those which most clearly provide evidence of the influence of geotechnical structures on the minimisation of displacement and strain of the soil medium and the reduction of stress in building foundations in the vicinity of the decompression trench.

## NUMERICAL MODEL STRUCTURE – MODEL GEOMETRY AND BOUNDARY CONDITIONS APPLIED

The model geometry included a section of subsurface rock mass layers together with a building constructed on them. The building dimensions in horizontal projection were 10 m x 10 m and the foundation depth was 2 m. Within 5 m from the building, a trench was modelled and filled with compressible material, with a width of 30 cm and a depth below the building foundation level. This paper presents the results of numerical simulations for two depths of the trench: 3 m and 5 m (Figure 1). To downsize the workload, system symmetry in relation to a vertical plane *1-3* was adopted. The model was dimensioned so as to eliminate the effect of disturbance caused by the boundary conditions on the stress and strain in the vicinity of the building and the protective trench.

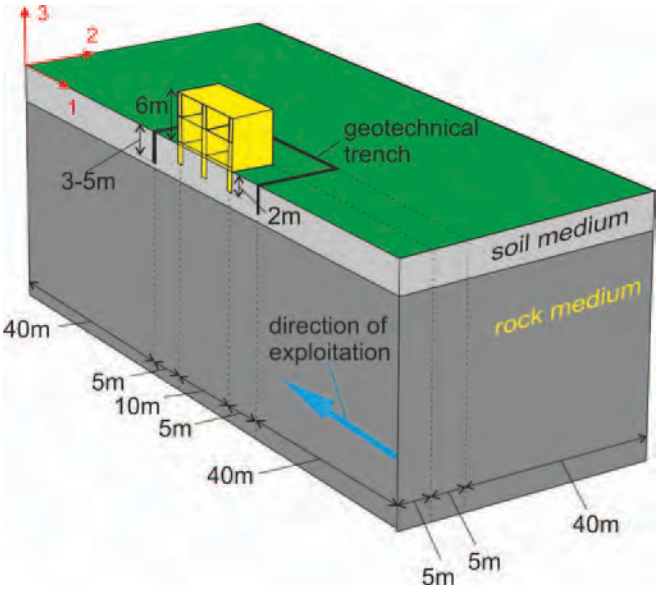



**Figure 1. General arrangement of the calculation model.**

It was assumed that the building was influenced by longwall extraction at a depth of about 455 m, at a rate 2.3 m/day. Extraction of the wall begins at a distance 450 m from the building centreline and continues along the direction *1* of the coordinate system, as shown in Figure 2. The assumed thickness of the exploited bed thickness was 2 m. Displacement vectors were assigned to the boundaries in the model. These displacement values were calculated with a prepared sub-program based on Knothe's geometric-integral theory (Knothe, 1951) for the above mining scenario. The maximum deformation indices calculated for the mining scenario involved are:

- maximum terrain subsidence: $w_{max}$ = 1.2 m;
- radius of main influence range: $r$= 227.5 m;
- maximum horizontal displacement: $u_{1max}$ = 0.48 m; and
- extreme linear horizontal strain: $\varepsilon_{max/min}$ = ±3.2 mm/m.

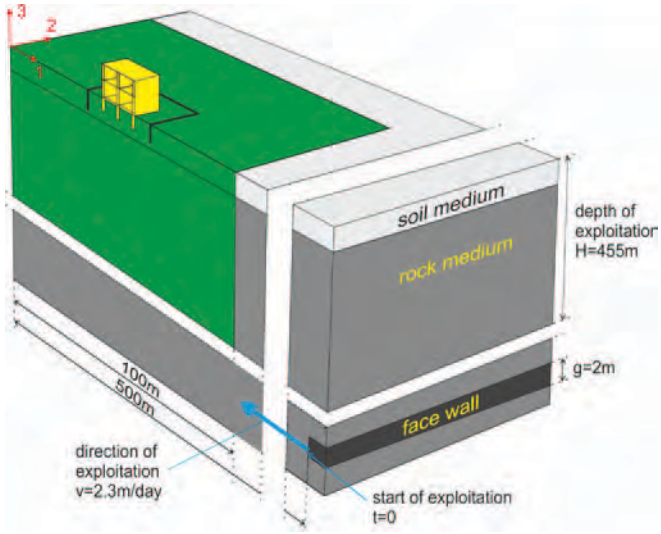



**Figure 2. Scheme of the exploitation efforts.**

In the calculations, it was assumed that the adopted material models, describing both subsoil and building behaviour, were isotropic, ideally elastic Hook material. According to Figure 1, two geotechnical layers were identified in the subsoil:

- an upper layer representing behaviour of the soil medium (3m thickness); and
- a lower layer representing behaviour of the rock medium (27m thickness).

Two additional material models were also defined at the building area:

- a model representing the wall medium; and
- a model representing properties of the reinforced concrete floor.

Parameters assumed for the individual materials are listed in Table 1.

## NUMERICAL MODEL COMPARISON TO KNOTHE'S MODEL

By means of spatial and time discretization processes, a discrete model was created which constitutes a system of equations with a finite number of degrees of freedom. Cubic, eight-node, linear finite elements with reduced integration points were applied to both the building and the rock mass. The lattice of elements is shown in Figure 3. The numerical model analysed contained almost 480,000 finite elements.

In order to verify the accuracy of the FEM numerical modelling assumptions, calibration of the numerical model was performed for each calculation scenario. Calculations were made while changing the parameters of the rock mass (soil and rock medium) being modelled, and then the subsidence results obtained from the numerical calculations were compared to the results calculated with Knothe's theory (Knothe, 1951), according to the *back analysis* method. The calculations were continued until the subsidence trough, obtained from numerical calculations (the term *FEM trough* was adopted), was matched to the subsidence trough obtained from

**Table 1. Parameters assumed for numerical calculations.**

| Substitute material | Young's modulus E [GPa] | Poisson's factors $\nu$[-] | Volume density r [kg/m$^3$] |
|---|---|---|---|
| Upper geotechnical layer (soil medium) | 0.14 | 0.32 | 2000 |
| Lower geotechnical layer (rock medium) | 16.4 | 0.14 | 2500 |
| Wall | 9.0 | 0.26 | 1700 |
| Reinforced concrete structural floor | 18.0 | 0.28 | 2400 |
| Trench filling material | 2.0E-06 | 0.33 | 1000 |

Source: Own study

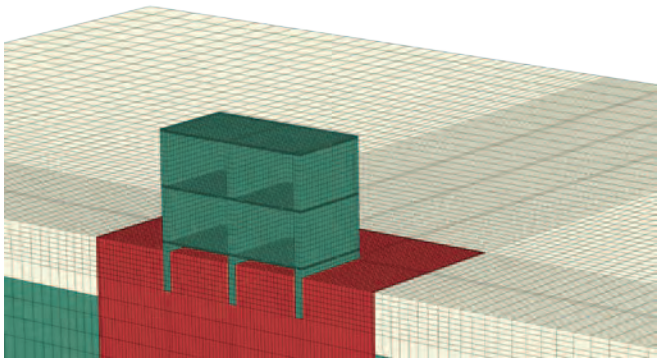


**Figure 3. Latttice of the finite elements assumed.**

calculations based on Knothe's theory (*B-K trough*). That method was successfully applied to analyse 11 regions of Polish hard coal mines (Tajduś, 2010).

Figure 4 shows comparison of vertical displacement $u_3$ at a point *P*(50, 0, 0) in the building centreline for one calibrated model.

## ANALYSIS OF NUMERICAL MODELLING RESULTS OBTAINED

A series of calculations was performed to describe the influence of the protective solution considered on the reduction of mining damage in the building structure and in the immediate vicinity of the protected building. Numerical simulations covering the entire process of the formation of the mining trough were performed:

- for an unprotected building;
- for a building protected with a trench with a depth 1 m below the foundation level (a 3-metre-deep trench); and
- for a building protected with a trench with a depth 3 m below the foundation level (a 5-metre-deep trench).

The results of the numerical calculations confirm the soil behaviour observed in real conditions near soil dilatations (e.g., natural fault). The results obtained for various scenarios (with different parameters assumed for numerical calculations) are of a similar nature.

Figure 5 shows the distributions of horizontal displacement $u_1$ in selected time moments corresponding to days 0, 215, 251 and 287 from the start of the extraction. Displacement plots are shown for the unprotected building scenario, and for a building surrounded with a protective trench in twodepth variants (3- and 5-metre-deep trenches).

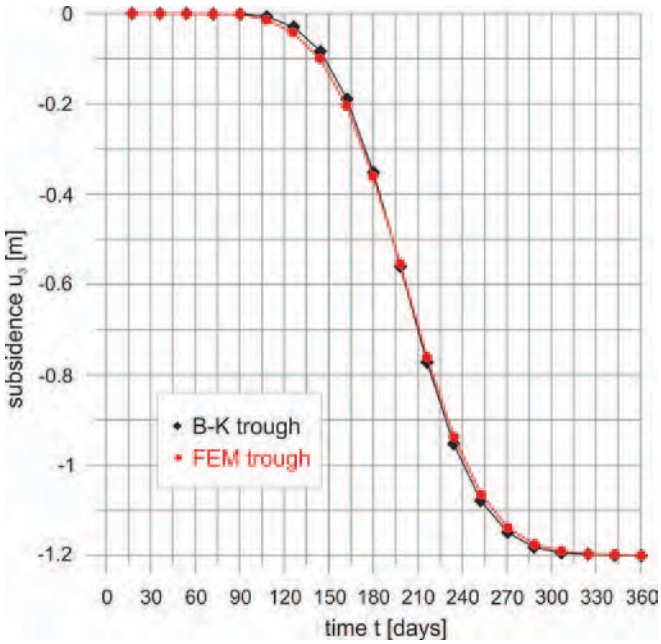



**Figure 4. Comparison of u3 subsidence at point P(50, 0, 0) in time, according to Budryk-Knothe theory (black line - B-K trough) and that obtained from numerical calculations (red line - FEM trough).**

The time moments of 215, 251 and 287 days correspond to building being located in the area of compressive impacts in relation to the subsidence field. Compressive effects are much more adverse for the building.

A comparison of displacement distributions at the same point in time for the unprotected building and the building protected with a trench with different depths enables a determination of the fixed area set around the building created by a gap in the soil. That area is most visible in the case of a deeper trench. The displacement plots provided show that the subsoil around the gap is displaced towards the dilatation and causes compression of the trench. Around the trench, an area with considerable strain is formed, thus reducing the occurrence of large compressive strains in the soil surrounding the foundation.

In Figure 5, the area of increased displacement around the trench is clearly visible (in particular, for the 5-metre-deep trench) for the time moments of 215, 251 and 287 days.

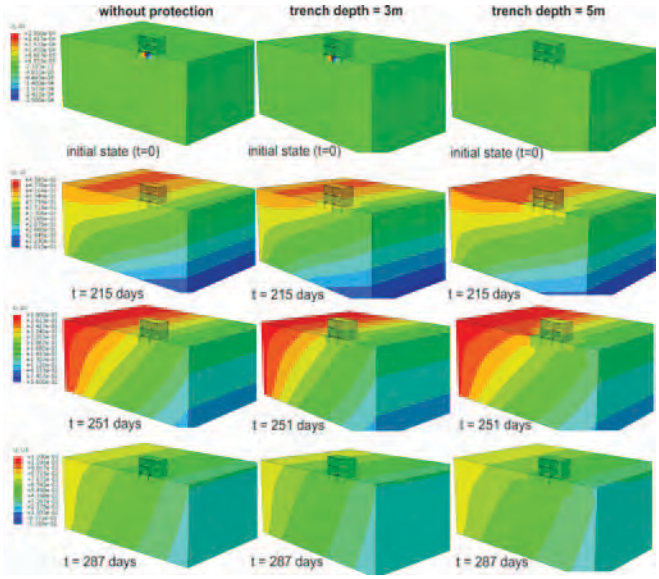



**Figure 5. Distributions of horizontal displacements u1 in selected mine moments of the deformation process for a subsoil model with a building without protection and for a model protected with a 3- and 5-metre-deep trench.**

The effect of strain reduction is clearly visible in Figure 6, which shows distributions of strain $\varepsilon_{II}$ over the time period of maximum compressive strain. Compression of the trench causes a local concentration of strain inside (Figure 6a). This area acts as a strain damper and dictates that strains are considerably reduced in the area surrounded by the trench. It is noticeable in Figure 6b, which shows strain distributions excluding the trench area, which makes it relatively easy to see the considerable difference in the subsoil strain values around the building.

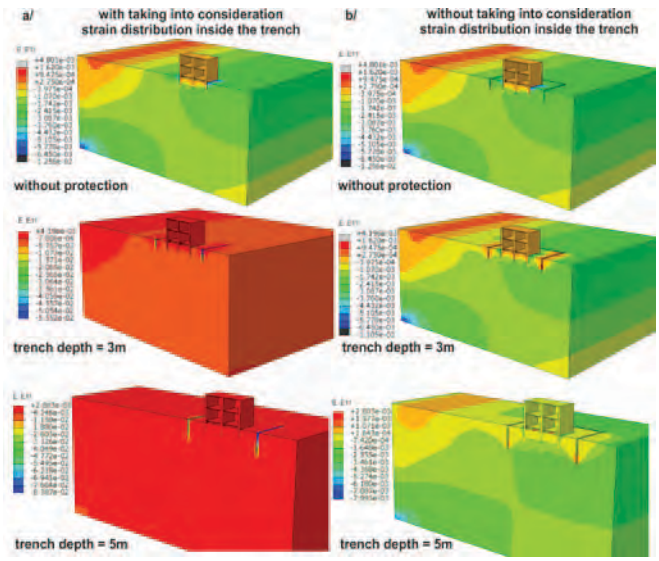



**Figure 6. Distribution of linear horizontal strains E11 for t=215 days (extreme compression) for a scenario with and without taking into consideration the strain inside the trench.**

The reduction of compressive strains, achieved by making the dilatation trenches, decreases the stress caused within the building structure by the mining extraction. The analysis performed for two protection variants (3- and 5-metre-deep trenches) proved that the reduction of subsoil strain acting on the foundation was more effective using a deeper trench. In calculations using a trench reaching 1 m below the building foundation depth, the value of strain $\varepsilon_{II}$ acting on the foundation was reduced by 40%, whereas, for a trench reaching 3 m below the foundation depth, the reduction was more than 70% of the strain value, as compared to the unprotected building scenario.

Figures 7 and 8 show distributions of the maximum and minimum stress in the building for several stages of the deformation process.

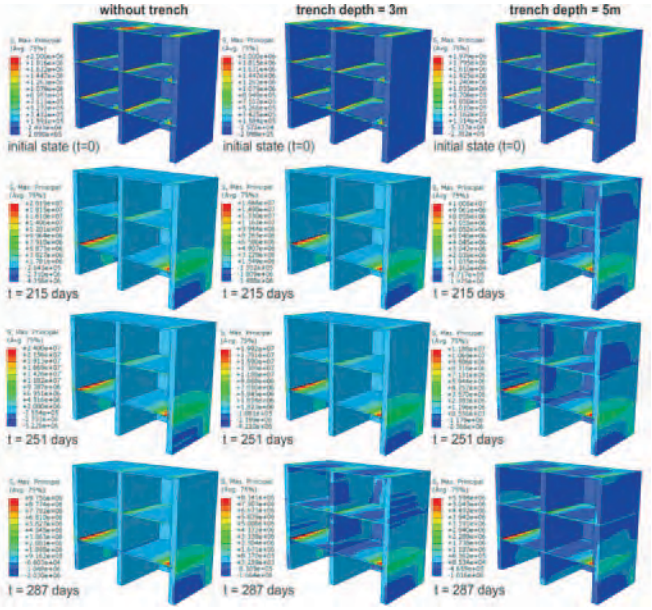



**Figure 7. Distribution of maximum principal stress Smax (Pa) in a building without protection and protected with 3- and 5-metre-deep trench.**

Figure 7 shows that, for the time moment t = 215 days, the value of the maximum principal stress at the contact point of the external walls and the ground floor is almost two times lower in a building protected with a 5-metre-deep trench than in an unprotected building. Also, the buildings protected with a 5-metre-deep trench show a greater decrease in stress in relation to buildings protected with a 3-metre trench. Similar stress reductions can be seen for time moments t = 251 and 287 days.

Analysing distributions of the minimum principal stress, a similar qualitative nature of changes in the building can be seen as in the case of the maximum stress. Along with the increase of the trench depth, the influence of the trench grows on the decrease of stress in the building structure. Figure 9 shows distribution of the normal stress $\sigma_{II}$, $\sigma_{33}$ and shear stress $\sigma_{23}$ in a chosen detail for the foundation walls perpendicular to the exploitation direction. Comparing the distributions of stress caused by compressive strain, the presence of a decompression trench is found beneficial to the reduction of such stress.

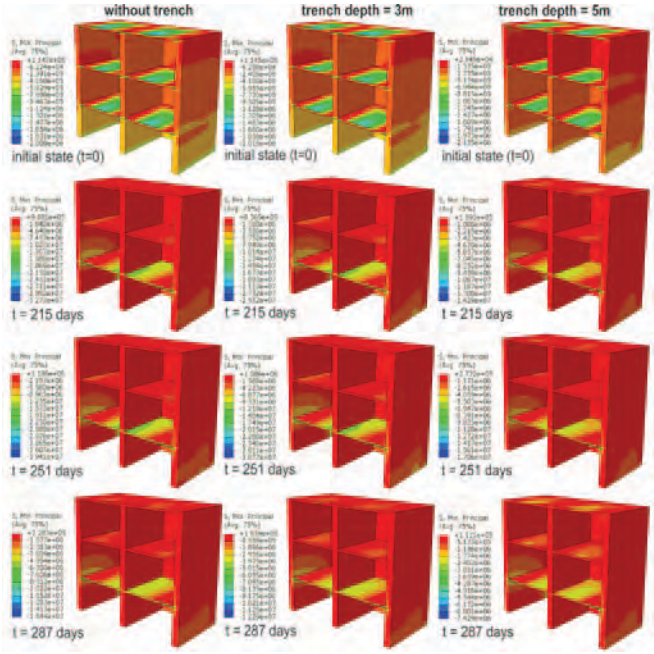



**Figure 8. Distribution of minimum principal stress Smin (Pa) in a building without protectionand protected with 3- and 5-metre deep trench.**

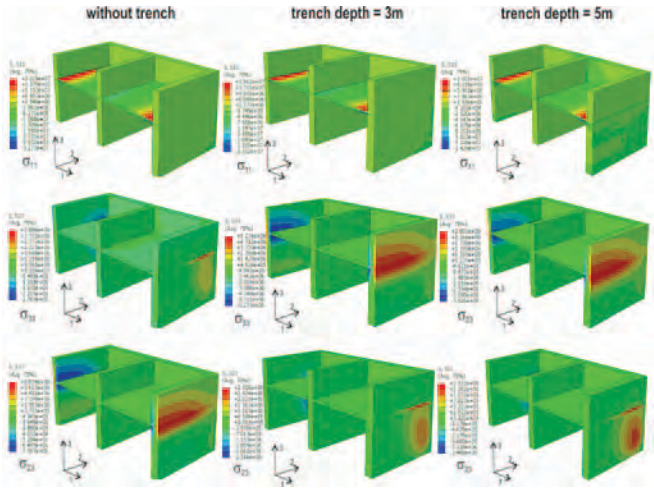



**Figure 9. Stress distributions (Pa) in foundation walls of an unprotected building and a building protected with a 3- and 5-metre trench, subjected to compressive strain (t=215 days).**

## FINAL REMARKS

According to the analyses presented, making a geotechnical trench (dilatation gap) in soil considerably improves the reduction of deformation and stress inside a building. In the protected area, i.e. between the trench (gap) and building, there is a zone with reduced displacement value in relation to a scenario without such trenching. The differences range up to several tens of percent. Outside the protected area, however, the recorded terrain deformations increase. It is important that in the "compression" area, a greater importance of such structures is noticeable because approximately 80-85% of the cost of mining damage incurred in this respect relates to buildings located in a zone of compressive deformation, and only 15 to 20% refers to buildings located in a zone of tensile deformation zone.

The calculations performed in this paper proved both the reduction of compressive strain in the subsoil and the resultant reduction of levels of stress generated in the building structures due to surface strain caused by mining extraction. For such analyses, it should be noted that the effect of underground mining extraction on the surface is a very complex phenomenon, depending on many factors from both a mining and geological nature. The numerical models applied so far are only an approximation of the real conditions and do not take into consideration all factors. Moreover, the values of stress and strain determined depend on the material models and values of the specific model parameters. It is obvious that the values of the results will change according to the actual geological and structural conditions of a real system and by conforming to in-situ observations. However, the potential reduction of the influence of mining effects is unquestionable. The analysis performed in this paper constitutes a qualitative evaluation of a sample geotechnical protection used to protect buildings in mining areas.

The project was financed with the funds of the National Science Centre granted based on the decision No. DEC – 2011/01/D/ST8/07280. This research was partially supported by PL-Grid Infrastructure.

**REFERENCES**

Knothe, S. (1951). ”Wpływ podziemnej eksploatacji na powierzchnię z punktu widzenia zabezpieczenia położonych na niej obiektów.” (in Polish), Dissertation, 1951, AGH Krakow.

Kwiatek, J. (1997). ”Ochrona obiektów budowlanych na terenach górniczych.” (in Polish), (Collective work), Katowice, Wydawnictwo Głównego Instytutu Górnictwa.

Luo, Y., Peng, S. S. (1991). ”Protecting a Subsidence Affected House: a Case Study.”, Kentucky (USA), *International Society for Mine Surveying 1991*.

Misa, R. (2013). ”Numeryczna analiza rozwiązania geotechnicznego minimalizującego wpływy przemieszczeń powierzchni terenu wywołanych podziemną eksploatacją górniczą.” (in Polish), Przegląd Górniczy, (11):25-31.

Misa, R., Tajduś, K. (2010). ”Przegląd geotechnicznych metod ochrony obiektów budowlanych przed wpływem podziemnej eksploatacji górniczej.” (in Polish), Prace Naukowe GIG Górnictwo i Środowisko 2010, 4(1):266-281.

Simulia. (2013). ”Abaqus/CAE User’s Manual.”

Sroka, A. (1994). ”Rowy ochronne – wyniki pomiarów in situ w Zagłębiu Ruhry.”, unpublished material, 1994.

Sroka, A., Tajduś, K., Misa, R., Knothe, S., Hejmanowski, R., Florkowska, L. (2012). ”Wykorzystanie metod geotechnicznych w celu ograniczenia wpływów eksploatacji podziemnej na obiekty budowlane.” (in Polish), unpublished material.

”Subsidence Engineers’ Handbook.” London, National Coal Board 1975.

Tajduś, K. (2009). ”New method for determining the elastic parameters of rock mass layers in the region of underground mining influence.” *International Journal of Rock Mechanics & Mining Science*. 46(8):1296-1305.

Tajduś, K. (2010). ”Determination of Approximate Value of a GSI Index for the Disturbed Rock Mass Layers in the Area of Polish Coal Mines.” *Archives of Mining Sciences*. 55(4):879-890.

# Multi–stage Testing Procedures, Verification, and Results for Strong, Brittle Sandstone

**Michael Murphy**, Mining Engineer
**Gabriel S. Esterhuizen**, Senior Scientist
**Gerald S. Morrow**, Electronics Technician
Ground Control Branch
NIOSH, Office of Mine Safety and Health Research
Pittsburgh, PA

## ABSTRACT

A multi-stage triaxial procedure has been developed for the enhanced servo controls and feedback systems at the National Institute for Occupational Safety and Health (NIOSH) rock mechanics laboratory. Due to the difficulty of preparing multiple rock specimens for single-stage triaxial tests at different confinements, multi-stage testing provides a huge advantage if only a few samples of coal measure rocks can be prepared from the drill core. A multi-stage test can provide mechanical properties, post-failure properties, and a complete failure envelope for a single specimen. For the multi-stage test procedure, a parameter used to define the slope of the stress-radial strain curve was developed and monitored in real time in order to successfully predict peak strengths at different confining stages. For this paper, multi-stage tests have been conducted on sandstones of varying strengths, including Berea sandstone which has well-documented properties, and fine-grained and coarse sandstone from a western US coal mine. For the tests conducted on the fine-grained sandstone, it was found that the ramp rate was an important factor in the success of obtaining peak strengths during the multi-stage tests. For each rock type, a table including Young's modulus, Poisson's ratio, unconfined compressive strength, friction angle, cohesion, residual friction angle, and residual cohesion are reported. The values from these tables have been used as input parameters for projects at NIOSH requiring numerical model input parameters.

## INTRODUCTION

Presently at the National Institute for Occupational Safety and Health (NIOSH), numerical models are being developed to realistically simulate the failure mechanics and stability of the rock surrounding coal mine entries. In coal mines where the ground stress exceeds the geologic strengths of the materials, the rock mass near an excavation can be in a post peak condition in relation to the stress-strain curve. Due to the condition of the rock mass, the numerical models must include accurate post peak strengths and properties to best represent the mechanical properties in the field. Accurate input parameters to represent the rock mass are extremely important to help calibrate simulated results to field site results. Laboratory testing of rocks is a way to provide the essential input parameters for advanced numerical model development and verification. In the past, NIOSH has been involved in compiling representative databases of rock properties from various sources, and NIOSH has access to much of the available data within the mining industry (Rusnak, 2000; Zipf, 2007). NIOSH has used its own rock mechanics laboratory in order to conduct conventional uniaxial and triaxial single stage tests with a Hoek cell (Dolinar, 1982). However, there is a lack of data on the post-peak behavior of coal measure rocks and particularly of the shear properties of bedding planes in coal mine strata.

The post-peak behavior of coal measure rocks could be found by conducting single-stage triaxial tests on multiple samples at varying confinements to record the peak and residual strengths. If angled core is drilled, the same triaxial testing methods could be used to measure bedding plane properties. However, these conventional single-stage triaxial tests require a large number of core samples to define the strength envelope (Crawford, 1987). Since most coal measure rocks are laminated, this presents a problem when preparing multiple samples from weak drill core rock. A solution is to conduct a multi-stage test on a single sample, which involves using multiple confinements to collect peak and residual strengths. If four confinements are used to develop the strength envelope, four single-stage triaxial tests are needed for every one multi-stage test. Multi-stage testing provides a huge advantage if only a few samples of coal measure rocks can be prepared from the drill core. However, the validity of the results may be questioned, since each loading stage potentially introduces additional failure in the sample which can impact the strength results. The quality of the results depends on the ability to detect the onset of failure at an early stage, so that the sample is not excessively damaged during the early stages of the test.

Multi-stage testing of rock samples has been conducted in the past by using a Hoek (or triaxial) cell (Kim, 1979). A Hoek cell uses a self-sealing rubber sleeve that protects the sample from contamination and can provide confinements of up to 69 MPa (10,000 psi) (Hoek, 1968). When using a Hoek cell, the axial strain of the rock sample is either measured from the platen movement, which can be inaccurate, or from a thin strain strip placed on the rock sample, which requires a large amount of time for efficient installation. NIOSH has recently updated its rock mechanics laboratory in order to carry out more sophisticated procedures on rock specimens than in the past. With the recent upgrades, a Hoek cell is no longer required. Enhanced servo controls and

feedback systems have been installed to allow multi-stage tests to be conducted that are able to produce a series of triaxial peak and residual strength results from a single specimen, allowing greater insight into the post-failure behavior of a variety of rock types.

The aim of this paper is to describe the procedure NIOSH is using to conduct multi-stage tests on rock samples. Conventional single-stage triaxial and multi-stage tests were conducted on Berea sandstone samples to verify the methods used in this paper. The unconfined compressive strength, Young's modulus, Poisson's ratio, friction angle, and cohesion are reported and compared with literature for verification. Once the procedure was established, multi-stage tests were conducted on sandstone samples collected at a western US coal mine.

## METHODS AND PROCEDURES

The most important factor in the multi-stage procedure is the criterion for determining the point at which the sample exhibits the onset of failure and the next loading stage is initiated. The "next stage" is defined by the point where the confining pressure is raised to the next level. Historically, the next stage would be initiated based on the judgment of the multi-stage test operator, who observes when the axial load no longer increases with the axial strain (Kim, 1979; Kovari et al., 1983; Law et al., 2003; Youn, 2010). A problem with using this criterion is the introduction of excessive mechanical failure in the rock sample, causing the successive stages to give unreliable results. Crawford and Wylie proposed observing the volumetric strain for determining the point to initiate the next stage (Crawford, 1987). However, they had difficulty with the procedure on harder rocks as they encountered sudden failure during loading. Youn and Tonon were able to confirm using volumetric strain for observation when conducting multi-stage tests on harder rocks (Youn, 2010). Their research found that when the sample is loaded using radial strain control (as opposed to axial strain control in previous research), the axial strain plot becomes very dense (more data per unit time) near the peak strength and the specimen approaches failure very slowly. The multi-stage test operator is then able to detect the failure with more accuracy and initiate the next stage before volumetric strain exceeds the Poisson effect. The research showed that if the stress-radial strain curve is plotted during the test, the curve flattens near the failure point, giving the multi-stage test operator a visual indication to initiate the next stage. This point has been described by Bieniawski as the transition from stable crack propagation to unstable crack propagation, and increasing load beyond this point can cause partial or total failure of the sample (Bieniawski, 1967).

Using Youn and Tonon's research as a starting point, researchers at NIOSH have developed a multi-stage test procedure to use with the newly acquired equipment. The procedure involves using radial strain control to load the sample during the increasing confinements, then switching to displacement control when the final stage of the procedure is initiated. After the sample has ultimately failed, a series of residual strengths are found by decreasing the confinement. The first confinement of the multi-stage procedure was set at 1.72 MPa (250 psi) and then the successive confinements were doubled until 13.8 MPa (2,000 psi) was reached, giving four total stages. On the post-peak side of the stress-axial strain curve, residual strengths were measured by decreasing the confinement by 1.72 MPa (250 psi) until 0 MPa was reached, giving eight total stages. A summary of the confinements used in this paper can be seen in Table 1.

**Table 1. Summary of confinements used during the multi-stage tests for finding the peak and residual strengths.**

| Peak Strengths | | | Residual Strengths | |
|---|---|---|---|---|
| $\sigma_3$ (psi) | $\sigma_3$ (MPa) | | $\sigma_3$ (psi) | $\sigma_3$ (MPa) |
| 250 | 1.7 | | 2000 | 13.8 |
| 500 | 3.4 | | 1750 | 12.1 |
| 1000 | 6.9 | | 1500 | 10.3 |
| 2000 | 13.8 | | 1250 | 8.6 |
| | | | 1000 | 6.9 |
| | | | 750 | 5.2 |
| | | | 500 | 3.4 |
| | | | 250 | 1.7 |

A typical stress-axial strain curve for a multi-stage test conducted on a rock sample is shown in Figure 1. The stages described in Table 1 are highlighted on each side of the multi-stage stress-axial strain curve. After each peak strength has been measured, the curve shows that the load does not decrease. Previous literature has shown different stress paths, such as the load returning to zero or slight shedding of the load while the confinement is increased to the next stage. Based on the stress and strain data during the test, a number of mechanical properties can be calculated using standard rock mechanics equations. For cohesion and friction angle results, a straight line Mohr-Coulomb relationship is assumed.

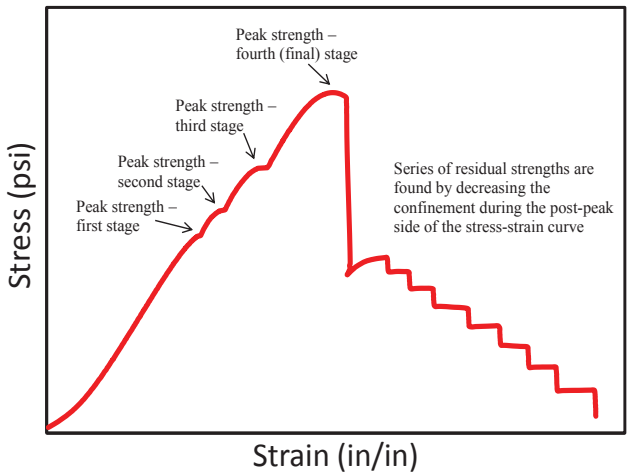



**Figure 1. Representative multi-stage stress-axial strain curved found during the study. Four peak strengths and eight residual strengths are measured. These peak and residual strengths are used to develop Mohr-Coulomb failure properties.**

To detect when the next stage should be initiated, the slope of the stress-radial strain curve was monitored. A parameter used to define the slope of the stress-radial strain curve, called $\Delta_{load}$, was

developed from measurements obtained from a circumferential displacement gage. A full explanation of the equipment, sample preparation and multi-stage procedure is given in the Appendix.

## RESULTS AND DISCUSSION

For this paper, two different sets of results are presented. First, a set of procedure verification tests were conducted in order to show the validity of the multi-stage procedure described in Section 2. A series of single-stage triaxial and multi-stage tests were conducted on Berea sandstone and the results were compared. Berea sandstone was chosen because of its well-documented properties and consistency. Second, multi-stage tests were conducted from sandstone obtained from a western US coal mine. Two different sets of results are presented from sandstone drilled high above the mine roof and below the mine floor.

### Procedure verification tests

Table 2 shows the number of Berea sandstone specimens for the single-stage and multi-stage verification tests. The table also shows the elastic properties of Young's modulus and Poisson's ratio measured during the verification tests. For the multi-stage tests, the values were calculated for only the 1.72 MPa (250 psi) confinement stage. These elastic value properties are in the same range that has been measured in other experiments (Lama, 1978). It can also be seen that as confinement is increased, the Young's modulus is increased and the Poisson's ratio is decreased. This is because the natural pores or cracks in the Berea sandstone are closed at higher confining pressures, causing the elastic properties to change (King, 1970).

into the rock), causing slightly lower estimates of peak strength. The peak strengths found for the 13.8 MPa (2,000 psi) confinement for both the multi-stage and single-stage triaxial tests are almost identical. This is an important result because it illustrates that for the multi-stage test very little damage is being initiated during the previous confinement stages.

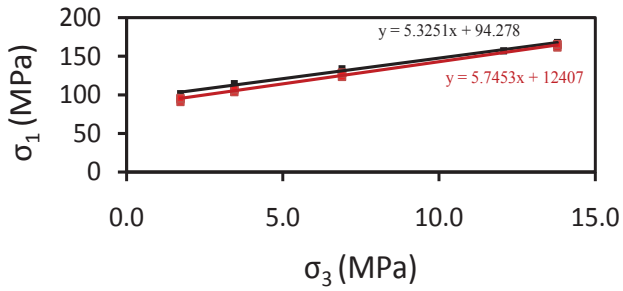



**Figure 2. Peak strength vs. confinement values for the Berea sandstone verification tests. The black dots represent the single-stage triaxial tests and the red x's represent the multi-stage tests.**

Table 3 reports the friction angle and cohesion values calculated from the series of single-stage triaxial tests and each of the multi-stage tests. For the friction angles and cohesion calculated from the peak strengths, the multi-stage tests show very similar results to one another and are only slightly different from the single-stage triaxial series. These friction angle and cohesion values also

**Table 2. Elastic properties of Berea sandstone for single stage (SS) and multi-stage (MS) verification tests.**

| Sample Name | Confinement (psi) | Confinement (MPa) | Young's Modulus (GPa) | Poisson's Ratio |
|---|---|---|---|---|
| SS-1 | 250 | 1.7 | 23.2 | 0.46 |
| SS-2 | 500 | 3.4 | 23.8 | 0.43 |
| SS-3 | 500 | 3.4 | 23.4 | 0.41 |
| SS-4 | 500 | 3.4 | 23.9 | 0.42 |
| SS-5 | 1000 | 6.9 | 24.0 | 0.40 |
| SS-6 | 1750 | 12.1 | 25.0 | 0.30 |
| SS-7 | 2000 | 13.8 | 26.1 | 0.23 |
| MS-1 | 250, 500, 1000,2000 | 1.7, 3.4, 6.9, 13.8 | 23.1 | 0.47 |
| MS-2 | 250, 500, 1000,2000 | 1.7, 3.4, 6.9, 13.8 | 23.1 | 0.46 |
| MS-3 | 250, 500, 1000,2000 | 1.7, 3.4, 6.9, 13.8 | 22.9 | 0.46 |

Figure 2 plots the peak strength ($\sigma_1$) versus the confinement pressure ($\sigma_3$) for the verification tests listed in Table 2. The single-stage triaxial tests are plotted with black dots and the multi-stage tests are plotted with red x's. The figure shows that the multi-stage tests give very similar results to the single-stage triaxial tests. For the 1.72 MPa, 3.45 MPa, and 6.89 MPa (250 psi, 500 psi, and 1,000 psi) confinement stages, the multi-stage tests show slightly lower peak strengths. This is because during the multi-stage test, the next stage is initiated prior to the sample starting to fail (theoretically the point at which the stress-axial strain curve goes from elastic to yield so that mechanical failure is not introduced

are in the same range as other results found for Berea sandstone in literature (Pagoulatos, 2004; Dehler, 2007). For the residual strength results, there is more scatter in the values. However, they were still within the same approximate range of one another. No results could be found in literature for these post-peak properties of Berea sandstone. Due to the anisotropic nature of rock and the closeness of all the measured properties during the verification tests, the multi-stage procedure was found to be sufficient to determine rock properties for general rock characterization used in numerical modeling.

**Table 3. Summary of post-peak properties for Berea sandstone found during the verification tests.**

| | Peak Strength | | | Residual Strength | | |
|---|---|---|---|---|---|---|
| Test | Friction Angle (degress) | Cohesion (psi) | Cohesion (MPa) | Friction Angle (degress) | Cohesion (psi) | Cohesion (MPa) |
| Single-stage series | 43.1 | 2963 | 20.4 | 42.2 | 448 | 3.1 |
| MS-1 | 44.8 | 2500 | 17.2 | 45.0 | 152 | 1.0 |
| MS-2 | 44.8 | 2607 | 18.0 | 43.3 | 347 | 2.4 |
| MS-3 | 44.6 | 2658 | 18.3 | 43.2 | 437 | 3.0 |

**Multi-stage tests for sandstone from a western US coal mine**

Sandstone core from an operating coal mine was tested using the multi-stage procedure described earlier. The core was drilled in the middle of a crosscut at the mine in both the roof and floor. The sandstone core from the roof was described as fine-grained gray sandstone with interbedded shale streaks and was located approximately 3.7–6.7 m (12–22 ft) into the roof. The sandstone core from the floor was described as coarse sandstone and was located approximately 8.2–9.1 m (27–30 ft) into the floor.

*Results for multi-stage tests on fine-grained sandstone*

A summary of the multi-stage tests conducted for the roof sandstone is shown in Table 4. It can be seen in the table that there is a large scatter in strengths and elastic properties. The unconfined compressive strength ranges from approximately 82.7 to 241 MPa (12,000 to 35,000 psi) for this sandstone. The reason for the scatter is because of the shale streaks present in some samples, photographed in Figure 3. The sandstone sample in the top photographs was RoofSS-4, which had an unconfined compressive strength of 238 MPa (34,500 psi). The sandstone sample in the bottom photographs was RoofSS-7, which had an unconfined compressive strength of 100 MPa (14,500 psi). A large shale streak present in sample RoofSS-7 caused the mechanical properties of the rock to be much different.

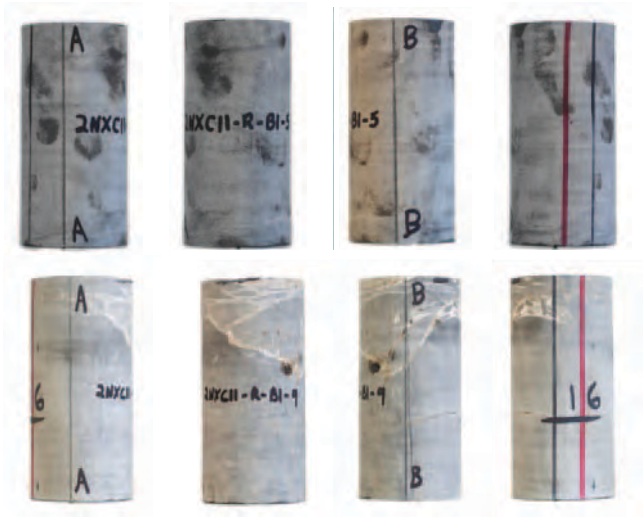


**Figure 3. The shale streaks contained in some of the sandstone samples (bottom) resulted in a much lower unconfined compressive strength when compared to the very fine-grained sandstone samples (top).**

Previous literature described earlier has documented problems and solutions with multi-stage testing of very hard rock. The multi-stage stress-axial strain curve for RoofSS-4, which was the most brittle rock tested for this experiment, is shown in Figure 4. The axial strain is an average between the gages on each side of the sample. The circumferential displacement was converted to radial strain. It can be seen that despite this being the strongest rock tested, the peak strengths for each stage were able to be successfully predicted with no observable failure occurring in the rock. On the radial strain plot, the slope starts to change in the vicinity of the peak strengths indicated, which was much easier to monitor real-time during the test using $\Delta_{load}$. The post-peak characteristics shown in the stress-axial strain curve give indication to the degree of difficulty of testing this sample using the multi-stage procedure. Once the sample violently failed, a series of residual strengths were unable to be obtained because the sample was completely destroyed due to the high stress levels reached during testing. It appears that any loading into the yield zone can cause sudden failure. During the multi-stage confinement process, it is believed that if RoofSS-4 had continued to be loaded slightly past the predicted peak strengths, sudden failure would occur.

**Table 4. Elastic and failure strength properties found for a fine-grained sandstone with interbedded shale streaks from a western US coal mine.**

| Core Name | Height (cm) | Diameter (cm) | W:H | Density (kg/m$^3$) | $E_a$ (GPa) | $E_b$ (GPa) | $\nu_a$ | $\nu_b$ |
|---|---|---|---|---|---|---|---|---|
| RoofSS-1 | 8.94 | 4.47 | 2.00 | 2665 | 39.71 | 41.73 | 0.24 | 0.26 |
| RoofSS-2 | 8.89 | 4.47 | 1.99 | 2683 | 51.46 | 42.89 | 0.20 | 0.17 |
| RoofSS-3 | 8.79 | 4.47 | 1.97 | 2709 | 46.38 | 50.26 | 0.22 | 0.24 |
| RoofSS-4 | 8.81 | 4.47 | 1.97 | 2715 | 61.41 | 62.70 | 0.22 | 0.22 |
| RoofSS-5 | 8.89 | 4.47 | 1.99 | 2669 | 43.01 | 45.42 | 0.25 | 0.26 |
| RoofSS-6 | 8.71 | 4.47 | 1.95 | 2624 | 33.64 | 32.76 | 0.20 | 0.20 |
| RoofSS-7 | 8.86 | 4.47 | 1.98 | 2656 | 51.36 | 50.05 | 0.20 | 0.20 |
| RoofSS-8 | 9.07 | 4.47 | 2.03 | 2611 | 39.80 | 42.13 | 0.22 | 0.23 |
| RoofSS-9 | 8.79 | 4.47 | 1.97 | 2603 | 35.70 | 37.36 | 0.18 | 0.19 |
| RoofSS-10 | 8.94 | 4.47 | 2.00 | 2715 | 28.79 | 29.57 | 0.23 | 0.23 |
| RoofSS-11 | 8.94 | 4.47 | 2.00 | 2633 | 21.62 | 21.78 | 0.23 | 0.24 |
| RoofSS-12 | 8.79 | 4.47 | 1.97 | 2659 | 38.41 | 47.80 | 0.16 | 0.20 |
| RoofSS-13 | 8.92 | 4.47 | 1.99 | 2698 | 34.93 | 36.38 | 0.19 | 0.20 |

| Core Name | UCS (MPa) | Φ peak (degrees) | C peak (MPa) | Φ residual (degrees) | C residual (MPa) | | | |
|---|---|---|---|---|---|---|---|---|
| RoofSS-1 | - | - | - | - | - | | | |
| RoofSS-2 | - | - | - | - | - | | | |
| RoofSS-3 | 197 | 47.1 | 39 | 49.9 | 3.61 | | | |
| RoofSS-4 | 238 | 42.4 | 53 | - | - | | | |
| RoofSS-5 | 194 | 44.8 | 40 | 50.2 | 3.25 | | | |
| RoofSS-6 | 155 | 32.5 | 42 | 51.8 | 1.34 | | | |
| RoofSS-7 | 223 | 45.4 | 46 | 52.7 | 2.69 | | | |
| RoofSS-8 | 101 | 39.9 | 23 | 47.5 | 4.50 | | | |
| RoofSS-9 | 125 | 46.8 | 25 | 46.9 | 3.09 | | | |
| RoofSS-10 | 139 | 43.5 | 30 | 46.9 | 4.65 | | | |
| RoofSS-11 | 126 | 31.7 | 35 | 38.5 | 2.65 | | | |
| RoofSS-12 | 83.4 | 52.8 | 14 | 47.6 | 2.98 | | | |
| RoofSS-13 | 145 | 45.4 | 30 | 47.8 | 1.47 | | | |

| | E (GPa) | ν | UCS (MPa) | Φ peak (degrees) | C peak (MPa) | Φ residual (degrees) | C residual (MPa) | |
|---|---|---|---|---|---|---|---|---|
| Average | 41.0 | 0.21 | 157 | 42.9 | 34.3 | 48.0 | 3.02 | |
| Standard Deviation | 10.3 | 0.03 | 50.0 | 6.25 | 11.2 | 3.92 | 1.09 | |

For the multi-stage procedure, there was an observable fine line for monitoring the $\Delta_{load}$ parameter. As stated in the Appendix, theoretically the next stage would be initiated when $\Delta_{load}$ becomes zero. For RoofSS-1 and RoofSS-2, which were very fine-grained sandstones with no shale streaks, $\Delta_{load}$ began as a large positive number and fell steadily to around 0.15–0.20. At this point, $\Delta_{load}$ started to quickly drop to zero. When $\Delta_{load}$ began the sudden drop to zero, there was about a three-second window to catch it and initiate the next stage.

At the beginning of this experiment a circumferential ramp rate of 0.047 mm/min (0.00185 in/min) was used, which worked very nicely for Berea sandstone. For samples RoofSS-1 and RoofSS-2, the subsequent stages could not be initiated because $\Delta_{load}$ went negative during the first stage and the sample failed. This is why these samples do not have reportable data in Table 4. Using this knowledge, it was known that once $\Delta_{load}$ had a value of approximately 0.15 it was very close to failure and the next stage should be initiated. Starting with RoofSS-3, the circumferential displacement ramp rate was changed to 0.0156 mm/min (0.0006125 in/min), which is approximately three times slower than the previous ramp rate, in an attempt to control $\Delta_{load}$'s sudden drop to zero once it reached 0.15. After making the ramp rate three times slower, the drop towards zero was not as drastic and the next stage could be initiated with better control. This is why there was a successful multi-stage test for the very fine-grained samples

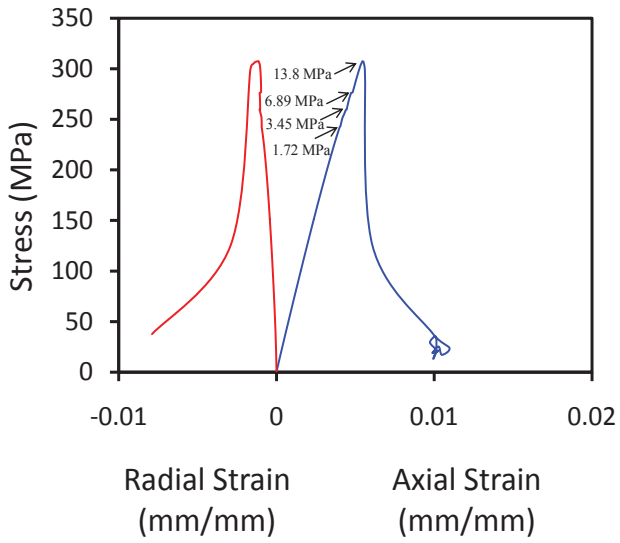



**Figure 4. Multi-stage stress-strain curve showing the comparison between the radial strain and axial strain for RoofSS-4. The peak strength at each confinement is highlighted on the axial strain curve.**

RoofSS-3 and RoofSS-4, but not with RoofSS-1 and RoofSS-2. For all testing afterwards, the circumferential displacement ramp rate was kept at 0.0156 mm/min (0.0006125 in/min) to secure the ability to test fine-grained samples.

*Results for multi-stage tests on coarse-grained sandstone*

A summary of the multi-stage tests conducted for the floor sandstone is shown in Table 5. The low density, coarse floor sandstone was much more consistent because it did not contain any shale streaks. Photographs of FloorSS-7 pre- and post-test are shown in Figure 5, which was a typical result for all the coarse sandstone samples. The unconfined compressive strength ranges from 56.5 to 71.0 MPa (from 8,200 to 10,300 psi), which is much weaker than the sandstone tested from the roof. A multi-stage stress-axial strain curve for FloorSS-4 is plotted in Figure 6. It can be seen on the radial strain curve that the slope change is much easier to observe compared to the finer-grained sandstone example seen in Figure 4. Due to the coarse grains contained in these samples, monitoring $\Delta_{load}$ was much easier. There was a gradual decline of $\Delta_{load}$ from a large value to zero which helped the multi-stage test operator initiate the next stage prior to unstable crack propagation in the specimen. Unlike the fine-grained sandstone, $\Delta_{load}$ could be brought to a value in the range of 0.01 without fear of sample failure. It is believed that this behavior will be similar when testing coal measure rocks, and that as long as the samples can be protected from contamination, multi-stage testing will be successful.

## CONCLUSIONS

A multi-stage procedure has been developed for the enhanced servo controls and feedback systems at the NIOSH rock mechanics laboratory. Literature review of multi-stage testing revealed that a successful method to test brittle rocks is to load the sample in radial strain control and monitor the flattening of the stress-radial strain curve. For the multi-stage tests conducted for this paper, a parameter used to define the slope of the stress-radial strain curve, called $\Delta_{load}$, was developed from measurements obtained from a circumferential displacement gage. This parameter gave the multi-stage test operator a value to monitor real-time, which allows for more consistent prediction of peak strengths.

Multi-stage tests have been conducted on sandstones of varying strengths. For procedure verification tests, single-stage triaxial tests at different confinements and multi-stage tests were conducted on Berea sandstone samples. Similar strength properties defining the Mohr-Coulomb failure envelope were found for both the triaxial and multi-stage tests and the procedure was verified to work properly. In addition to the Mohr-Coulomb failure envelope, residual strength friction angle and cohesion were also reported for Berea sandstone.

After the procedure verification tests, multi-stage tests were then conducted on fine-grained and coarse sandstone from a western US coal mine. For the tests conducted on the fine-grained sandstone, it was found that the ramp rate was an important factor in the success of obtaining peak strengths during the multi-stage tests. If the ramp rate is too fast, $\Delta_{load}$ is an unreliable monitor because there will be no clear indication that the sample is close to failure, resulting in poor identification of peak strength. However, if the ramp rate is slowed down, using $\Delta_{load}$ to predict the peak strength becomes much more reliable. For the coarse sandstone tests, the rock specimens were found to be much weaker. This sandstone also had a very low density and $\Delta_{load}$ was very reliable in predicting the peak strengths. In the future, it is believed that the testing procedure for this coarse sandstone can be applied to coal measure rocks, because the grains in both rock types are not as highly compacted as fine-grained sandstone. A table of Young's modulus, Poisson's ratio, unconfined compressive strength, peak strength friction angle and cohesion, and residual strength friction angle and cohesion are reported for the fine-grained and coarse sandstones. The values from these tables have been used as inputs for projects at NIOSH requiring numerical model input parameters and have been added to the database of rock properties. In the future, it is expected to continue obtaining mechanical and post-peak properties of different rock types using the multi-stage method to develop a database of inputs required for reliable numerical models.

## APPENDIX

### Equipment

*Triaxial testing machine*

A photograph of the upgraded equipment in the NIOSH rock mechanics laboratory is shown in Figure 7. On the left, the triaxial cell can be seen. The specimen sits inside of the triaxial cell during testing. Next to the triaxial cell frame is the confining pressure cabinet. Oil is pumped into the triaxial cell from the confining pressure cabinet. With the new servo controls added to the system, the confining pressure can be more effectively controlled during the test than in the past. The multi-stage test operator can program the procedure to increase confining pressure to a precise value over a specified time period. This is very important when conducting a multi-stage test because no time is wasted when stepping up to a new confinement. A pore pressure cabinet was also purchased by NIOSH; however it is not used in this experiment.

**Table 5. Elastic and failure strength properties found for a coarse sandstone from a western US coal mine.**

| Core Name | Height (cm) | Diameter (cm) | W:H | Density (kg/m$^3$) | $E_a$ (GPa) | $E_b$ (GPa) | $\nu_a$ | $\nu_b$ |
|---|---|---|---|---|---|---|---|---|
| FloorSS-1 | 8.59 | 4.47 | 1.92 | 2310 | 14.97 | 14.89 | 0.24 | 0.24 |
| FloorSS-2 | 8.84 | 4.47 | 1.98 | 2291 | 14.75 | 14.81 | 0.29 | 0.29 |
| FloorSS-3 | 8.81 | 4.47 | 1.97 | 2255 | 15.11 | 15.08 | 0.28 | 0.28 |
| FloorSS-4 | 8.86 | 4.47 | 1.98 | 2292 | 14.52 | 14.59 | 0.26 | 0.26 |
| FloorSS-5 | 8.84 | 4.47 | 1.98 | 2257 | 14.21 | 14.27 | 0.31 | 0.31 |
| FloorSS-6 | 9.02 | 4.47 | 2.02 | 2275 | 14.39 | 14.97 | 0.32 | 0.33 |
| FloorSS-7 | 8.89 | 4.47 | 1.99 | 2300 | 14.92 | 14.91 | 0.43 | 0.43 |
| FloorSS-8 | 8.84 | 4.47 | 1.98 | 2291 | 15.04 | 15.12 | 0.35 | 0.35 |
| FloorSS-9 | 8.86 | 4.47 | 1.98 | 2287 | 15.36 | 15.68 | 0.28 | 0.28 |
| FloorSS-10 | 8.86 | 4.47 | 1.98 | 2283 | 15.63 | 15.89 | 0.29 | 0.30 |
| FloorSS-11 | 8.97 | 4.47 | 2.01 | 2294 | 14.81 | 14.99 | 0.29 | 0.29 |

| Core Name | UCS (MPa) | Φ peak (degrees) | C peak (MPa) | Φ residual (degrees) | C residual (MPa) | | | |
|---|---|---|---|---|---|---|---|---|
| FloorSS-1 | 68.6 | 38.0 | 16.7 | 34.0 | 3.39 | | | |
| FloorSS-2 | 68.8 | 37.4 | 17.0 | 35.3 | 2.65 | | | |
| FloorSS-3 | 65.5 | 37.1 | 16.3 | 41.0 | 0.13 | | | |
| FloorSS-4 | 70.8 | 36.6 | 17.8 | 33.9 | 1.77 | | | |
| FloorSS-5 | 62.1 | 36.0 | 15.8 | 33.5 | 4.52 | | | |
| FloorSS-6 | 63.5 | 35.4 | 16.4 | 31.6 | 2.92 | | | |
| FloorSS-7 | 56.7 | 35.2 | 14.7 | 32.2 | 2.56 | | | |
| FloorSS-8 | 56.5 | 34.4 | 14.9 | 36.3 | 1.89 | | | |
| FloorSS-9 | 61.7 | 36.8 | 15.5 | 33.1 | 2.55 | | | |
| FloorSS-10 | 62.1 | 37.5 | 15.3 | 33.7 | 3.19 | | | |
| FloorSS-11 | 61.1 | 37.6 | 15.0 | 37.8 | 3.50 | | | |

| | E (GPa) | ν | UCS (MPa) | Φ peak (degrees) | C peak (MPa) | Φ residual (degrees) | C residual (MPa) | |
|---|---|---|---|---|---|---|---|---|
| Average | 15.0 | 0.30 | 63.4 | 36.5 | 15.9 | 34.8 | 2.64 | |
| Standard Deviation | 0.43 | 0.05 | 4.45 | 1.10 | 0.94 | 2.60 | 1.08 | |

*Measurement instruments*

A dual axial strain gage, MTS Model no. 632.11 B-20, and a circumferential displacement gage, MTS Model no. 632.12B-20, were used for the multi-stage test experiments. The dual axial strain and circumferential displacement gages can measure strains with a resolution of +50 micro-strain. The dual axial strain gage allowed for two measurement locations on the rock specimen and a circumferential displacement gage was used to monitor the radial strain of the sample. A photograph of the measurement instruments on a rock sample is shown in Figure 8. The circumferential displacement gage was always placed around the middle of the sample and the two axial strain gages were on opposite sides. Throughout the paper, the strain gages are referred to as axial strain gage A and axial strain gage B. A standard protocol for the multi-stage tests was to draw two lines on the rock sample, 180 degrees apart, to mark the placement of axial strain gages A and B. This was used as a forensic post-test tool, because inaccurate strain gage readings in the yield zone of the stress-axial strain curve could be linked to cracks in the instrument location. For standard calculations based on axial strain measurements such as Young's modulus and Poisson's ratio, the average values between the two axial strain gages were used.

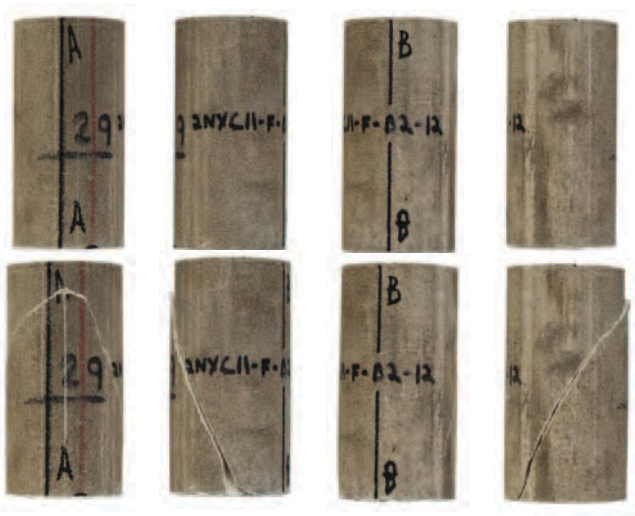


**Figure 5. Pre-test photographs (top) and post-test photographs (bottom) for FloorSS-7.**

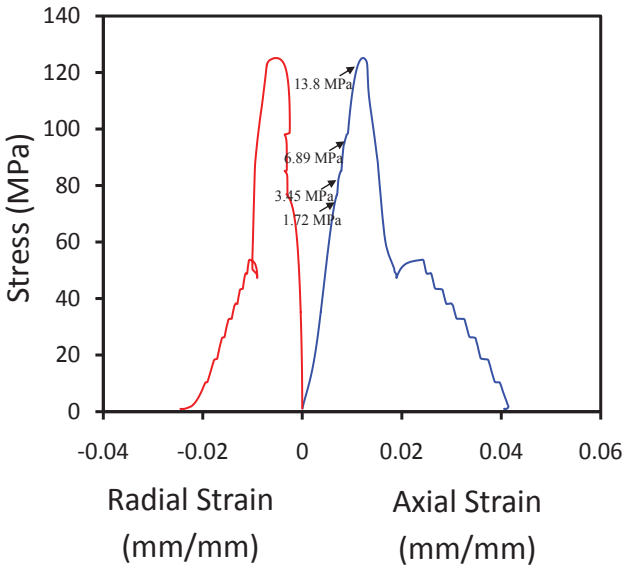



**Figure 6. Multi-stage stress-strain curve showing the comparison between the radial strain and axial strain for FloorSS-4. The peak strength at each confinement is highlighted on the axial strain curve.**

In Figure 8, the triaxial cell is seen to be raised and the sample is seated on a platen. When the triaxial cell is closed during the test, the rock specimen, cables, instruments, and wires are all surrounded by the oil used to provide confining pressure. Because of this, the sample must be protected from the confining oil so it is not contaminated during the test.

**Procedure**

As mentioned earlier, the radial strain is a reliable visual indicator to initiate the next stage prior to sample failure. Since radial strain

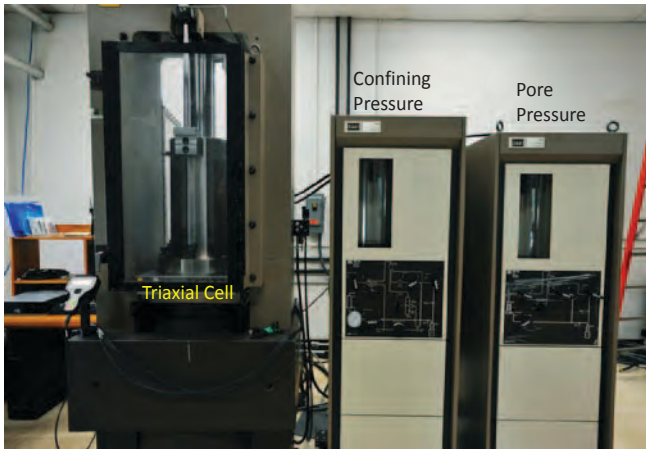



**Figure 7. Multi-stage testing equipment in the NIOSH rock mechanics laboratory.**

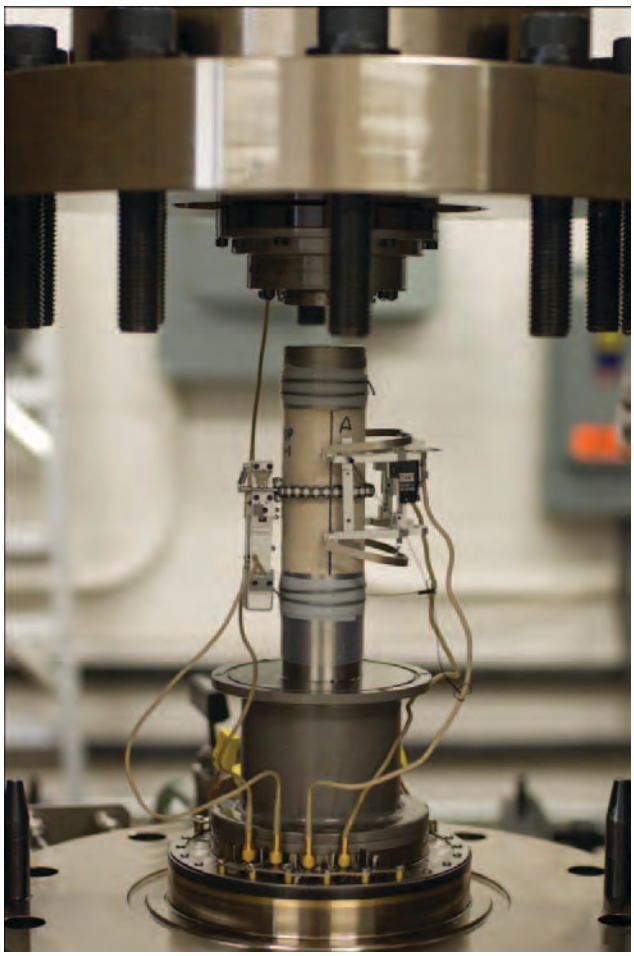


**Figure 8. Photograph of the circumferential displacement gage and two axial strain gages placed on a rock specimen.**

can be calculated using a circumferential displacement gage, the circumferential displacement was monitored and displayed in real time during the procedure so that the multi-stage test operator knew when to initiate the next stage. The circumferential displacement ramp rate was initially set to 0.047 mm/min (0.00185 in/min), which was found to load a Berea sandstone sample to failure in the first stage of a multi-stage test in approximately seven minutes, typical of ASTM standards. For this procedure, once each peak strength has been measured, the experiment is temporarily switched to load control so that the load can be held constant while the confinement pressure is increased. The time required to increase the confinement pressure for the next stage is approximately five seconds. This was found to be an appropriate amount of time because an "instantaneous" increase could potentially cause unwanted sample failure.

To demonstrate the visual indication of failure by plotting the circumferential displacement during a test, a triaxial single-stage test with a confinement of 1.72 MPa (250 psi) was conducted on Berea sandstone. The sample failed but the experiment was continued into the post-peak side of the stress-axial strain curve in order to find a series of residual strengths. A comparison of stress versus circumferential displacement and axial displacement can be seen in Figure 9. The circumferential displacement was plotted on the negative side of the x-axis so that it can be visually compared to the axial strain by the operator during the test. For this example, it can be seen that by strictly using the axial strain as an indicator for peak strength, very little warning is given and the sample failure is sudden. However, by monitoring the circumferential displacement, the slope of the curve begins to change as failure is approaching and is at a value of approximately zero when failure ultimately occurs.

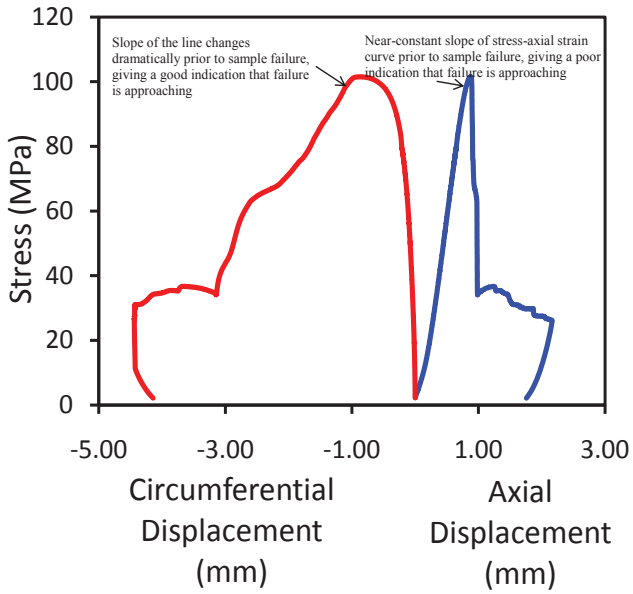



**Figure 9. Comparison of stress versus circumferential displacement and axial displacement. Prior to sample failure, the circumferential displacement gives a visual indication.**

To help define the slope of the circumferential displacement curve, a parameter named $\Delta_{load}$ was created so that the multi-stage test operator could monitor a numerical value in real time in order to initiate the next stage. This approach was expected to obtain more consistent results for predicting peak strengths, instead of the operator using judgment by watching the circumferential displacement curve flatten. The parameter $\Delta_{load}$ is simply the average force on the sample over a period of 1 second subtracted from the average force on the sample over a period of 0.1 seconds. By subtracting an average force of a long interval from a short interval, small inconsistencies in the curve can be ignored; however, gradual flattening of the curve can be easily observed. Before the sample has failed, $\Delta_{load}$ will be a positive value; right at failure $\Delta_{load}$ will be zero; and after failure $\Delta_{load}$ will be a negative value.

**Sample preparation**

For the verification tests, 2-inch-diameter samples were cored from a block of Berea sandstone and prepared in accordance with ASTM guidelines (ASTM D7012). For the sandstone samples collected from a western US coal mine, the rock was cored at the mine using NX-conventional coring equipment which resulted in a sample diameter of 1.76 inches. For preparing these samples for multi-stage testing, a length-to-diameter ratio of 2:1 was maintained and the two ends were ground in accordance with ASTM guidelines.

During all tests described in this paper, the sample was placed inside of the triaxial chamber which is filled with the oil that is pressurized to provide confinement. Steps must be taken in order to ensure that the sample is not contaminated by the oil. Prior to the multi-stage testing of the sandstone samples reported in this paper, some trial and error tests on a variety of rock types were conducted to determine an appropriate procedure for sealing the sample from oil contamination. The samples were prepared and tested at varying confinements to test the integrity of the seal.

A reliable method to seal the sample from contamination is shown in Figure 10, similar to a method found in literature (Pagoulatos, 2004). The rock specimen is located between two platens that have a slightly larger diameter than the sample. For each platen, on the edge closest to the sample, 3M Scotch® 70 Self-Fusing Silicone Rubber Electrical Tape[1] is wrapped around the circumference of the platen twice. Shrink tubing with a supplied 2.1-inch inner diameter and shrink ratio of 2:1 is placed over the rock/platen assembly. It is important to have appropriately sized shrink tubing so when heat is applied there is a tight fit around the specimen. Once the shrink tubing is heated to fit the sample, two pieces of aircraft wire are used to tighten the seal around the top and bottom platens where the tape was applied. The tape that was placed around the top and bottom platens helps give the aircraft wire twist a tighter seal. For both platens, the locations of the twists in the two pieces of aircraft wire are 180 degrees apart. During the trial and error testing of sample preparation, observations of sample contamination were made at high confinement pressures when the specimen was not appropriately sealed. It is common for the oil to enter into the edges of the shrink tubing on the top and bottom platens; however, if applied correctly, the tape and aircraft wire seal prevents the oil from traveling further to the sample.

During the sample protection trials, another issue was observed while preparing weaker rocks. The presence of chips around the edge of the sample, which commonly occur during the grinding

1 Mention of specific products and manufacturers does not imply endorsement by the National Institute for Occupational Safety and Health.

process, provides an entry point for oil at high confinement pressures. An example is shown in Figure 11. In the figure, a very small chip can be seen at the bottom of the coal sample. If nothing is done to protect this small void, at high confinements the oil can pierce through the shrink tubing at this location and cause contamination. This has been observed by inspecting the jacket of contaminated samples and lining up the point of entry of the oil to voids in the rock. To prevent this, a brass shim is wrapped on the inside of the shrink tubing around the area of the void.

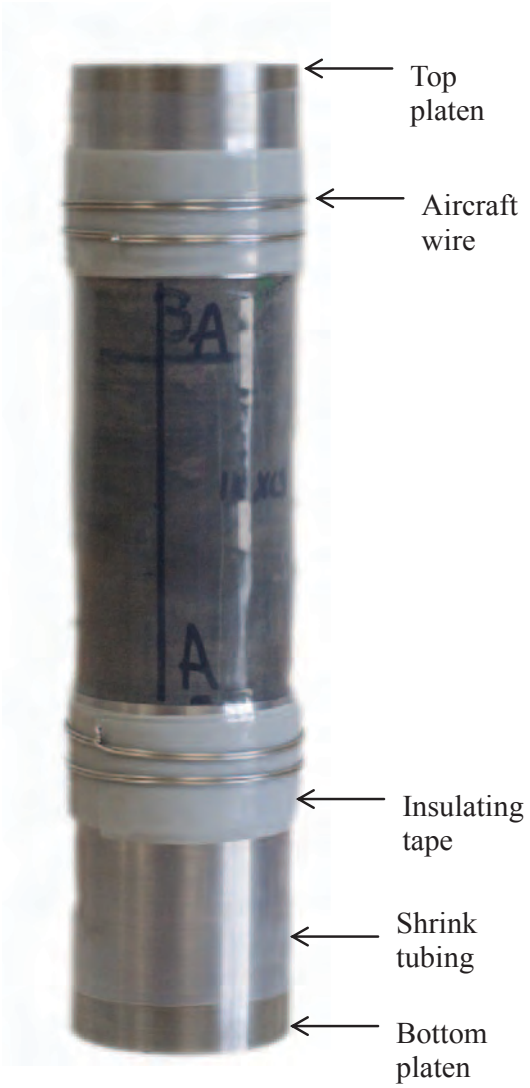



**Figure 10. Photograph showing the materials used to seal the rock specimen for multi-stage testing.**

In addition to using weak rocks to learn more about sample protection, concrete cores of varying strength were prepared. A major problem found with using concrete cores is that tiny air pockets can exist underneath the surface of the specimen. Unlike the coal sample which contained a point of entry along the bottom edge of the sample, the concrete core contained points of entry all along the sample which could not be protected with a brass shim. An example of a fully contaminated concrete core is shown in Figure 12. Although a pre-testing photograph is not available, the surface of the concrete sample before testing did not exhibit a porous characteristic as it did after confinement was introduced.




**Figure 11. Photograph showing the method used if a chip is present on the edge of a weak rock specimen.**

After confinement was introduced, the photograph shows many holes in the sample, all of which were created when the oil was able to pierce through the shrink tubing and cause contamination. The sample was sawed in half to verify that it was fully contaminated and not just on the surface. It is possible that future testing of coal or other porous rocks might show similar means of contamination. A possible solution is using a thicker-walled shrink tubing.

## DISCLAIMER

The findings and conclusions in this report are those of the authors and do not necessarily represent the views of the National Institute for Occupational Safety and Health.



**Figure 12. Photograph showing a fully contaminated concrete specimen.**

## REFERENCES


American Society of Testing Materials. Standard Method of Test for Compressive Strength and Elastic.

Moduli of Intact Rock Core Specimens under Varying States of Stress and Temperatures. ASTM.

Designation: D-7012-10, ASTM Standards.

Bieniawski, Z.T. (1967). "Mechanism of brittle failure of rock." National mech. Engineering research institute. Pretoria, South Africa.

Crawford, A.M., Wylie, D.A. (1987). "A modified multiple failure state triaxial testing method." 28th US Symposium on Rock Mechanics. Tucson; 29 June-1 July 1987. pp. 133-140.

Dehler, W., Labuz, J.F. (2007). "Stress path testing of an anisotropic sandstone." Journal of Geotechnical and Geoenvironmental Engineering. Vol 133, No 1. pp. 116-119.

Dolinar, D.R., Horino F.G., Hooker V.E. (1982). Mechanical Properties of Oil Shale and Overlying Strata, Naval Oil Shale Reserve, Anvil Points, Colorado. US Bureau of Mines Report of Investigations 8608. United States Department of the Interior.

Hoek, E., Franklin, J.A. (1968). "A simple triaxial cell for field and laboratory testing of rock." Trans. Instn Min. Metall. 77, A22-26.

Kim, M.M., Ko, H.Y. (1979). "Multistage triaxial testing of rocks." Geotechnical Testing Journal. Vol 2, No 2, June 1979, pp. 98-105.

King, M.S. (1970). "Static and dynamic elastic moduli of rocks under Pressure." In: Rock Mechanics – Theory and Practice. Eleventh Symposium on Rock Mechanics. pp 329-351.

Kovari, K., Tisa, A., Einstein, H.H., Franklin, J.A. (1983). "Suggested methods for determining the strength of rock materials in triaxial compression: revised version." International Journal of Rock Mechanics and Mining Sciences. 1983, vol. 20, no. 6, pp. 283-290.

Lama, R.D., Vutukuri, V.S. (1978). Handbook on Mechanical Properties of Rocks – Testing Techniques and Results Volume II. Trans Tech Publications.

Law, S., Eberhardt, E., Loew, S., Descoeudres, F. (2003). "Geomechanical properties shear zones in the Eastern Aar Massif, Switzerland and their implication on tunneling." Rock Mechanics Rock Engineering. 2003; 364. pp. 271-303.

Pagoulatos, A. (2004). Evaluation of Multistage Triaxial Testing on Berea Sandstone. Thesis. The University of Oklahoma Graduate College. Mewbourne School of Petroleum and Geological Engineering.

Rusnak, J., Mark, C. (2000). "Using the point load test to determine the uniaxial compressive strength of coal measure rock." In: Proceedings of the 19th International Conference on Ground Control in Mining, Morgantown, WV: West Virginia University, Peng SS, Mark C, Khair AW, Heasley KA, eds., pp. 362-371.

Youn, H., Tonon, F. (2010). "Multi-stage testing on brittle rock." International Journal of Rock Mechanics and Mining Sciences. 2010, vol 47. pp. 678-684.

Zipf, R.K. (2007). "Numerical modeling procedures for practical coal mine design." In: Proceedings of the International. Workshop on Rock Mass Classification in Underground Mine Design. National Institute for Occupational Safety and Health, Information Circular 9498, pp. 153-162.

# Use of a Plate Loading Device to Quantitatively Evaluate Weak Rock Mass Classifications in the Underground Gold Mines of Nevada, USA

**Raj R Kallu**, Assistant Professor
**Evan Keffeler**, Graduate Research Assistant
**Sean Warren**, Graduate Research Assistant
**Robert J Watters**, Professor
University of Nevada, Reno
Reno, NV

## ABSTRACT

Underground gold mines in Nevada are typically hosted in geologic zones with a wide range of geotechnical properties ranging from blocky competent rock to faulted and highly altered soil-like material. Geotechnical engineering design in weak rock utilizes rock mass classification systems as inputs to both empirical and numerical methods. The most common rock mass classification system utilized in the gold mines of Nevada is the easy-to-use Rock Mass Rating (RMR) system; however, in practice it is difficult to apply in weak to very weak rock masses. This paper attempts to improve the sensitivity of RMR in weak rock masses by utilizing W-RMR—a modified procedure for calculating RMR—and evaluates its performance against other methods of determining RMR for predicting in situ moduli. In-situ rock mass moduli were determined using a portable plate loading device (PPLD), and these data were used to quantify the improved sensitivity of the modified RMR versus existing classification systems. The PPLD was designed for performing rapid and economical in-situ deformability tests in a mining environment. Tests were performed at eight sites yielding thirteen rock mass moduli measurements. Statistical analyses indicate Detailed-Discontinuity RMR-89 and W-RMR provide the best correlations to the in-situ moduli compared to other methods of calculating RMR.

## INTRODUCTION

Underground gold mines in the state of Nevada have increasingly exploited relatively deep ore bodies that are hosted in weak to very weak rock masses. The ground in the production zones is typically intensely fractured and highly altered with Rock Mass Ratings (RMR) less than 45 (Sandbak and Rai, 2013; Sun and Chen, 2013). These weak ground conditions pose challenges in designing and implementing effective ground control systems for mining methods limited to cut-and-fill and long-hole stoping methods. The initial ground-support systems are typically derived from rock mass classification data collected on core and existing design charts originally developed for the tunneling industry. These support designs are then refined based on site-specific experience.

This paper aims to quantify which easy-to-use systems provide the best performance for predicting rock mass modulus, which requires cataloging the common rock mass classification techniques currently employed by the underground mining industry in Nevada. One of the classifications systems evaluated for this study is W-RMR, which is the formalization of a concept proposed by Bieniawski (2011) for calculating RMR in weak rock masses. Rock mass deformability tests were performed using a portable plate loading device (PPLD), and the measured rock mass moduli were statistically compared to the classification schemes to evaluate their effectiveness at predicting rock mass mechanical properties.

## ENGINEERING ROCK MASS CLASSIFICATION IN NEVADA'S UNDERGROUND MINES

Commonly used underground rock mass classification systems in Nevada are the Geological Strength Index (GSI), RMR, and the Tunneling Quality Index (Q). GSI is a description of rock mass fabric and structure but does not use information on groundwater, intact material strength, or block size (Marinos, Marinos, and Hoek, 2005). As such it is not considered a comprehensive classification system. Because GSI is determined by comparing the rock fabric and joint conditions to a graph, the GSI can be rapidly determined in the field making it useful for rapid assessments of rock quality and for comparison purposes. GSI can also be used as an input for estimating rock mass modulus (Hoek and Deiderichs, 2006) and strength (Hoek, Carranza-Torres, and Corkum, 2002). However, GSI cannot be determined from core, limiting its applicability to existing excavations or natural outcrops.

Q is a comprehensive rock mass classification system originally developed for estimating ground support for civil engineering underground excavations and assesses rock mass quality on a logarithmic scale based on the number of joint sets, joint roughness, joint alteration, groundwater conditions, Rock Quality Designation (RQD), and stress conditions (Barton, Lien, and Lunde, 1974). As the system was developed for civil engineering projects, it focuses on the joint set(s) most likely to cause instabilities. Q has relatively good sensitivity in weak ground compared to other classification systems, and its main applications are preliminary estimation of ground support in man entry excavations (Palmstrom and Broch, 2006) and for determining maximum stable stope dimensions (Nickson, 1992).

However, Q has extensive classification charts, each with several exceptions and special notes; for example, there are 16 descriptions for the stress reduction factor plus several special notes that an engineer or geologist must navigate through when face mapping or logging core. Consequently, Q can be intimidating to the novice, is time consuming to log, and has limited applicability. In spite of these challenges, Q has become popular in tunneling in part because those projects typically only have a few working faces and accurately determining ground conditions is a contractual obligation. However, in mining where geotechnical resources are limited, it is common to calculate Q from RMR using standard correlations.

The majority of the geotechnical data collected for underground mines in Nevada is RMR, which is based on the uniaxial strength of the intact rock, joint spacing, RQD, joint conditions, and groundwater. The most commonly used versions are RMR-76 (Bieniawski, 1976) and RMR-89 (Bieniawski, 1989), with the maximum ratings of each shown in Table 1. RMR-76 has one table for determining the parameter ratings, and engineering judgment is required when interpolating between the binned values. Experience has shown that determining a representative joint condition rating based on the brief descriptions in the table can be difficult. RMR-89 has a general ratings description table, plots for determining intact rock strength, RQD, and fracturing frequency ratings, and a sub-table to calculate the joint condition rating based on persistence, aperture, roughness, infilling, and weathering. This in principal allows for more sensitivity and less ambiguity when assigning parameter ratings.

**Table 1. Maximum ratings for RMR-76 and RMR-89.**

| | Intact Rock Strength | Joint Spacing | RQD | Joint Conditions | Ground Water |
|---|---|---|---|---|---|
| RMR-76 | 15 | 30 | 20 | 25 | 10 |
| RMR-89 | 15 | 20 | 20 | 30 | 15 |

The mining industry in Nevada primarily uses three methods for calculating RMR, which for the purposes of this paper are termed "Binned," "Interpolated," and "Detailed-Discontinuity."

1) The Binned approach is most common and discretizes parameter ratings to the median bin values. The discontinuity condition rating is determined from the brief description given in the RMR classification table.

2) The Interpolation method involves estimating the most reasonable parameter rating using the median bin values for guidance or by reading the fracture frequency, intact rock strength, and RQD ratings directly from plots. The discontinuity condition rating is typically determined from the brief description given in the RMR classification table.

3) The Detailed-Discontinuity approach utilizes the parameter rating plots for fracture frequency, RQD, and intact rock strength and the discontinuity condition rating sub-table to calculate RMR.

Experience has shown the Binned method is the simplest but unfortunately yields the least sensitivity, while the Detailed-Discontinuity approach has the most sensitivity but also requires the most geotechnical data in use. Although RMR has long been known to be insensitive in weak rock masses (Hoek and Brown, 1980), it is widely used in the mining industry because of its applications, which include rock mass strength, stand-up time, foundation design, rock mass deformability, and ease of excavation among others (Bieniawski, 1989).

## W-RMR

In production zones of Nevada's underground gold mines, geomechanical behaviors of rock masses border between weak rock and highly-consolidated soil, and it is universally recognized that the RMR system is difficult to apply to very weak rock masses (Hoek *et al*, 1995; Hoek and Marinos, 2007; Mathis and Page, 1995). The main problem with using the Binned RMR-89 method (as presented in Bieniawski, 1989) for weak rock classification is that ratings are not sensitive to changes in RQD when RQD < 25% and fracture spacing is < 60mm. As a result, the RQD and fracture frequency ratings for sound rock with 24% RQD and fracture spacing of 2 inches would receive the same ratings as clay, 3 and 5 respectively. The other limitation of RMR-89 is that it cannot be zero because of the minimum ratings of 3 and 5 for RQD and fracture frequency, respectively (Bieniawski, 1989); in fact an RMR of zero would be associated with soil.

Geotechnical mapping was conducted at 132 sites at two underground gold mines in Nevada. Figure 1 illustrates the problem with using the traditional or "Binned" RMR classification table in the weak rock range (below around 36). The lowest RMR value is 13 and there are essentially only 4 RMR-89 ratings, 19, 29, 30 and 35. These spikes represent the major divisions of ratings for RQD and fracture frequency such as the rating of 3 for RQD < 25% and 8 for 25%<RQD<50%.

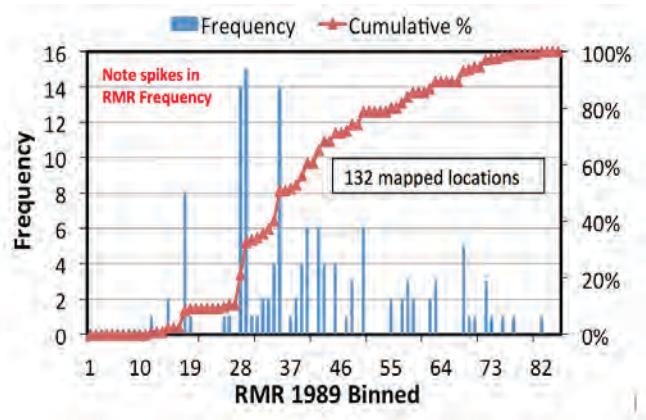



**Figure 1. RMR-89 frequency plots of geotechnical mapping locations in Nevada.**

To increase the sensitivity of RMR in weak rock we propose a modified method of assigning ratings to weak rock masses based on equations derived from the RMR-89 table. These modifications are referred to as W-RMR or "Weak Rock Mass Rating." Bieniawski

(2011) stated that the ratings on the RMR tables are the average ratings for the range of geotechnical conditions they represent. Hence, a rating of 3 for 0%<RQD <25% would plot on the graph as RQD 12.5%, Rating 3. This principle was applied to all ratings on the RMR-89 chart and plotted on a graph with a best fit line forced to the rating to zero. These graphs are presented in Figure 2.

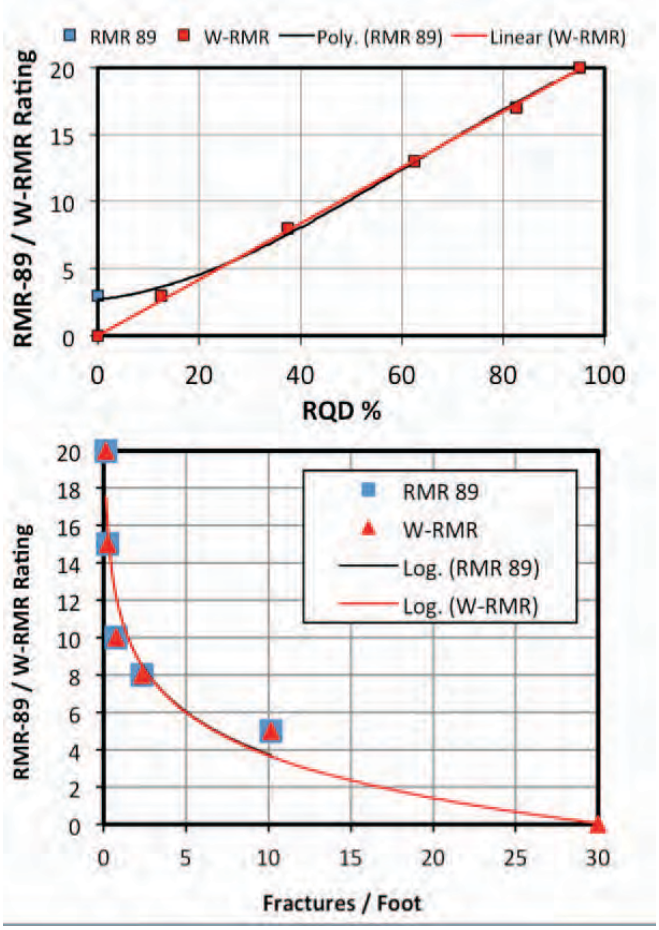



**Figure 2. Binned RMR-89 and W-RMR classification systems.**

Based on Figure 2 the following equations were determined for assigning W-RMR ratings for RQD and fracture frequency

- RQD Rating= 0.209 x RQD%
- Fracture Frequency Rating = -3.303 ln (fracture frequency f/ft) + 11.301

For fracture frequency ≤ 30 fractures /foot

For increased sensitivity in weak rock we recommend that the ratings for intact rock strength (ISRM-R strength) and joint condition rating (JCR) be interpolated between major categories and if time allows the "guidelines for classification of discontinuity conditions" table should be used.

Figure 3 compares the results of applying the W-RMR and RMR-89 table ratings to geotechnical data collected for this project. This graph illustrates two important points

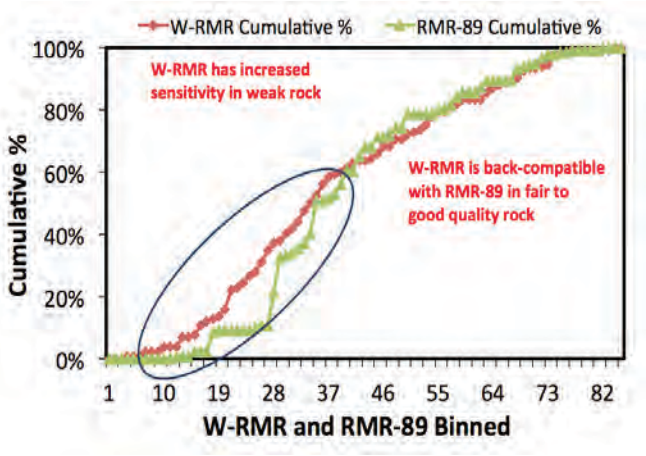



**Figure 3. Cumulative frequency of W-RMR equations and binned RMR-89 ratings.**

1. In the weak rock range (RMR<36) W-RMR is more sensitive to changes in rock quality and W-RMR can be zero. This provides a more useful numerical comparison of weak rock mass ratings
2. Above RMR ~36, RMR-89 and W-RMR are approximately in agreement making W-RMR back compatible with the RMR-89 table ratings in fair to good quality rock

## IN-SITU DEFORMATION MODULUS MEASUREMENTS

To quantitatively rate the sensitivity of the various schemes for calculating RMR, the ratings should be compared to a measurable rock mass property, and the resulting scatter evaluated. To this aim, plate loading tests were performed at two of Nevada's underground gold mines to measure the in-situ rock mass deformation modulus, and each test included sufficiently-detailed rock mass characterizations for the various RMR values to be calculated. The measurements were performed using a PPLD (Figure 4) that was specifically designed for testing the deformability of weak rock masses and has a total axial force of 100 tons and six inches of stroke. The device was fitted with 10- and 12-inch diameter rigid bearing plates that are at least 10-times larger than the average joint spacings of the rock masses. Tests were performed horizontally in drifts with widths varying between 10 and 19-feet wide. The device has 31-inches of vertical adjustability, so for each test site a reasonable compromise could be made between maintaining distance from the sill and ground-support elements. The PPLD allows for rapid and economical in-situ tests in working mines, and each test takes approximately 10-20 working hours while yielding two moduli values because each plate's deformation is monitored independently.

The PPLD is essentially simple with limited instrumentation; therefore it was critical to develop a test method to negate or minimize potential sources of error. The first step in performing a plate loading test was to thoroughly scale the test site to remove any loose material that may pose a safety hazard or bias the test results. The machine was then assembled, and the load train adjusted so the bearing plates were within 1 to 2 inches of the ribs. A high-strength, fast-curing gypsum-cement grout was cast directly between the bearing plates and excavation surfaces to create smooth bearing pads. By casting the grout directly against



**Figure 4. Portable plate loading device used for measuring in-situ rock mass deformability.**

the bearing plates, soft interfaces were eliminated. After the grout had sufficiently cured, load was applied stopping periodically to record force and displacements. An initial loading path was applied to close joints within the rock mass, and then two or three unload reload cycles were applied to measure the in-situ deformability. After each test was completed, the rock mass exposed on the excavation surface in each plate's zone of influence was geotechnically characterized.

The rock mass deformation moduli calculated from best fit slopes are specific to portions of the force-displacement plots (Figure 5) using the following equation adapted from ASTM (2012):

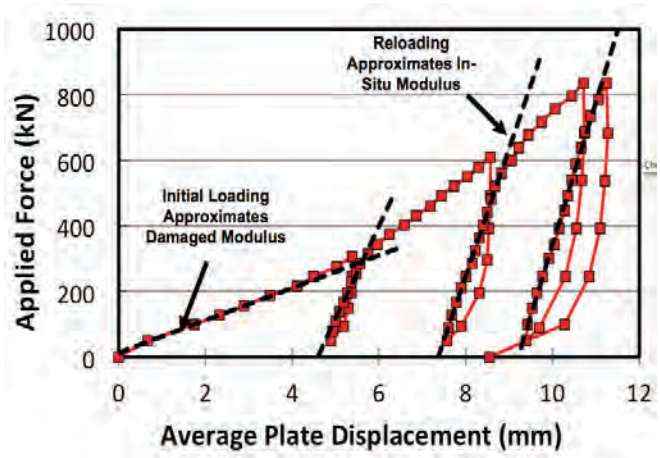



**Figure 5. Force-displacement plot from plate loading test.**

$$E = \frac{\left(1-\mu^2\right)}{2R} m \qquad (1)$$

*Where:*

$E$ = rock mass elastic modulus

$\mu$ = Poisson's ratio, assumed value of 0.25

$R$ = plate radius

$m$ = slope of $P$ versus $W_a$

$W_a$ = average displacement of the plate

$P$ = force applied.

Equation (1) was derived from elasticity theory assuming a semi-infinite elastic half-space. Although underground excavation surfaces are far from this assumption, the associated error can be minimized if the excavation surface span or height is at least 1.5 times the plate diameter and tests are not conducted within 1.5 spans of the entry or face (Unal, 1997). Damaged moduli can be calculated from the initial loading portion of the force-displacement plot, and moduli calculated from the reloads approximate the in-situ values (Figure 5). Given that plate loading tests where only surface displacements are measured are prone to underestimating moduli, the maximum reload moduli for each test was taken as the best approximation of the in-situ value. Modulus values from 13 plate loading tests in weak rock are summarized in Table 2, and for each test RMR was calculated by the various methods employed in the mining industry as summarized above.

## DATA ANALYSES

The fundamental question this paper seeks to answer is what method of determining RMR yields the least scatter when plotted against rock mass moduli. The data have been plotted against the variously calculated RMR as shown in Figure 6. Linear, logarithmic, power, and exponential models were fit to the data sets, and coefficients of determination (R-squared values) were calculated as summarized in Table 3. In all cases, the power fit had the highest coefficient of determination. This result is consistent with previous studies that have found the modulus is highly non-linear when correlated with RMR (Gokceoglu, Sonmez, and Kayabasi, 2003; Nicholson and Bieniawski, 1990; Serafim and Pereira, 1983). To quantify the spread of the scatter, the root mean square error (RMSE) was calculated between the moduli and best-fit model as summarized in Table 4. The RMSE measures both bias and lack of precision with a low value indicating a good fit and low error between the model and the data (Helsel and Hirsch, 2002). Detailed-Discontinuity RMR-89 produces the least scatter, and W-RMR also has relatively low scatter, while Binned RMR-76 has the most scatter.

## CONCLUSIONS

Classifying ore rocks at Nevada's underground gold mines for effective ground control design has proven difficult when employing the easy-to-use RMR system. By comparing the various methods of calculating RMR against rock mass modulus as measured by plate loading tests, we have quantitatively shown that the two best methods of calculating RMR in these rock masses are the Detailed-Discontinuity RMR-89 and W-RMR. While Detailed Discontinuity RMR-89 has the best performance at predicting rock mass mechanical properties in these cases, it requires the most geotechnical data, which can typically only be collected by face mapping.

**Table 2. Rock mass moduli as determined by plate loading tests and corresponding RMR values.**

| Test | Interpolated RMR-76 | Binned RMR-76 | Binned RMR-89 | Detailed-Discontinuity RMR-89 | W-RMR | In-Situ Modulus (GPa) |
|---|---|---|---|---|---|---|
| 1 | 15 | 15 | 15 | 18 | 10 | 0.25 |
| 2 | 16 | 13 | 16 | 21 | 13 | 0.37 |
| 3 | 16 | 12 | 15 | 21 | 13 | 0.031 |
| 4 | 37 | 31 | 44 | 47 | 43 | 2.48 |
| 5 | 35 | 34 | 42 | 45 | 41 | 1.7 |
| 6 | 34 | 28 | 41 | 44 | 36 | 1.3 |
| 7 | 40 | 37 | 47 | 44 | 44 | 1.1 |
| 8 | 41 | 39 | 44 | 49 | 43 | 1.4 |
| 9 | 40 | 42 | 47 | 51 | 48 | 1.4 |
| 10 | 47 | 42 | 47 | 51 | 46 | 0.71 |
| 11 | 20 | 18 | 23 | 28 | 20 | 0.90 |
| 12 | 45 | 34 | 47 | 54 | 45 | 4.2 |
| 13 | 32 | 39 | 34 | 45 | 37 | 2.3 |

**Table 3. Coefficients of determination (R2 values) for best-fit models to RMR-modulus data.**

| | Coefficient of Determination | | | |
|---|---|---|---|---|
| Data Set | Linear Model | Logarithmic Model | Power Model | Exponential Model |
| Binned RMR-89 | 0.36 | 0.39 | 0.63 | 0.57 |
| Detailed-Discontinuity RMR-89 | 0.48 | 0.46 | 0.64 | 0.62 |
| Interpolated RMR-76 | 0.37 | 0.39 | 0.57 | 0.50 |
| Binned RMR-76 | 0.25 | 0.32 | 0.60 | 0.50 |
| W-RMR | 0.38 | 0.40 | 0.61 | 0.57 |

**Table 4. RMSE between data sets and best-fit power models.**

| Data Set | RMSE (GPa) |
|---|---|
| Binned RMR-89 | 0.91 |
| Detailed-Discontinuity RMR-89 | 0.79 |
| Interpolated RMR-76 | 0.93 |
| Binned RMR-76 | 1.0 |
| W-RMR | 0.88 |

W-RMR, on the other hand, provides a good balance between ease-of-use and sensitivity in the weak rock masses common in the underground gold mines of Nevada. W-RMR can be determined from both core logging and face mapping and is back-compatible with RMR-89 in fair to very good rock masses. Additionally, the sensitivity of W-RMR can be further improved by utilizing the detailed discontinuity rating table from RMR-89 instead of just using general descriptions. Based on the preceding discussion, W-RMR is one of the more versatile methods for classifying weak rock masses when Q is too difficult to implement but GSI does not provide sufficient detail.

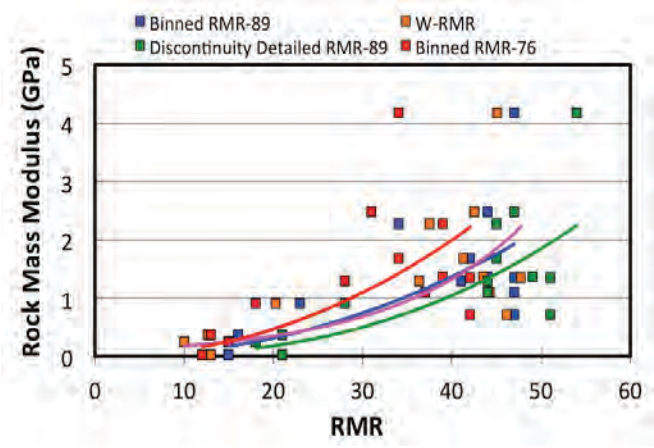



**Figure 6. Rock mass module plotted against RMR calculated by various means showing best-fit power models for each data set.**

**ACKNOWLEDGMENTS**

Funding for this research was provided by NIOSH Research Contract 200-2011-39965, Principal Investigator R. Kallu. The authors wish to thank the mine managers who allowed access to the mines for underground data collection and all of the mines' engineers and operators who helped coordinate the field work.

**REFERENCES**

Barton, N., Lien, R., Lunde, J. (1974). "Engineering classification of rock masses for the design of tunnel support." Rock Mechanics. 6:189-236.

Bieniawski, Z.T. (1976). "Rock mass classifications in rock engineering." In: Bieniawski, Z.T., ed. Exploration for Rock Engineering. vol. 1. Cape Town, South Africa: A.A. Balkema, pp. 97-106.

Bieniawski, Z.T. (1989). Engineering Rock Mass Classifications. New York: John Wiley & Sons.

Bieniawski, Z.T. (2011). Misconceptions in the applications of rock mass classifications and their corrections. www.geocontrol.es, link to: Bieniawski's window

Gokceoglu, C., Sonmez, H., Kayabasi, A. (2003). "Predicting the deformation moduli of rock masses." International Journal of Rock Mechanics and Mining Sciences. 40:701-710.

Helsel, D.R., Hirsch, R.M. (2002). Hydrologic Analysis and Interpretation, Chapter A3: Statistical methods in water resources. Reston, VA: USGS.

Hoek, E., Brown, E.T. (1980). Underground Excavations in Rock. London: The Institution of Mining and Metallurgy.

Hoek, E., Kaiser, P.K. and Bawden. W.F. (1995). Support of Underground Excavations in Hard Rock. Rotterdam: Balkema.

Hoek, E., Diederichs, M.S. (2006). "Empirical estimation of rock mass modulus." International Journal of Rock Mechanics & Mining Sciences. 43:203-215.

Hoek, E., Carranza-Torres, C., Corkum, B. (2002). "Hoek-Brown failure criterion: 2002 edition." In: Bawden, R.W., Curran, J., Telesnicki, M., ed. Proceedings of NARMS-TAC 2002, Toronto, Canada, pp. 267-273.

Hoek, E., Marinos, P., (2007). "A brief history of the development of the Hoek-Brown failure criterion." Soil and Rocks, No. 2

Marinos, V., Marinos, P., Hoek, E. (2005). "The geological strength index: applications and limitations." Bulletin of Engineering Geology and the Environment. 64: 55-65.

Mathis, J.I., Page, C.H. (1995). "Drifting in very poor rock – experience and analysis." Presented at the 101st annual Northwest Mining Association Convention, Spokane, Washington, Dec 6-8.

Nicholson, G.A., Bieniawski, Z.T. (1990). "A nonlinear deformation modulus based on rock mass classification." International Journal of Mining and Geological Engineering. 8:181-202.

Nickson, S.D. (1992). "Cable support guidelines for underground hard rock mine operations." MASc. thesis, University of British Columbia.

Palmstrom, A., Broch, E. (2006). "Use and misuse of rock mass classification systems with particular reference to the Q-System." Tunnels and Underground Space Technology. 21:575-593.

Sandbak, L.A., Rai, R.A. (2013). "Ground support strategies at the Turquoise Ridge Joint Venture, Nevada." Rock Mechanics and Rock Engineering. 46:437-454.

Serafim, J.L., Pereira, J.P. (1983). "Considerations of the geomechanical classification of Bieniawski." In: International Symposium on Engineering Geology and Underground Construction. Lisbon, Spain: Portuguese Geotechnical Society, pp. 33-44.

Sun, C., Chen, J. (2013). "Ground control practice at Leeville underground mine." In: 32nd International Conference on Ground Control in Mining. Morgantown, WV: 8 p.

Unal, E. (1997). "Determination of in-situ deformation modulus: New approaches for plate-loading tests." International Journal of Rock Mechanics and Mining Sciences. 34:897-915.

# Roof Geotechnical Properties for Roof Control Purposes in Illinois Coal Field

**Abdolreza (Reza) Osouli**, Assistant Professor
Civil and Mining Engineering
Southern Illinois University Edwardsville
Edwradsville, IL

**Iman Shafii**, MSc Student
**Behrooz Moradi Bajestani**, MSc Student
Southern Illinois University Edwardsville
Edwardsville, IL

## ABSTRACT

Determining the roof stability condition of underground coal mines in the Illinois Basin is sometimes very challenging. The roof stability of Illinois mines are mostly affected by two types of shales: Anna Shale and Energy Shale. These layers are sometimes weak in parallel bedding when subjected to horizontal stresses. The roof rocks in the Illinois Basin are are typically more moisture sensitive than the other coal fields. In this study the geotechnical properties of some of the shale units as well as limestone layers will be presented. The geotechnical properties of roof rocks consist of moisture content, unconfined compressive strength, slake durability, indirect tensile strength, and point load tests (Axial and Diametral). The correlation of indirect tensile strength versus diametral point load strength as well as unconfined compressive strength versus axial point load test are explored and discussed. These correlations will help in identifying the roof mass index and planning appropriate roof control measures. This study also evaluates the application of CMRR rock mass index for an Illinois coal mine.

## INTRODUCTION

Despite the advancement of mining methods and roof support systems, the roof falls continue to be the greatest hazard in underground mines. One of the reasons is that the roof units are not built of man-made material and the engineering properties of rock can vary from mine to mine and even within individual mines. Therefore, engineers rely heavily on previous mining experience and employ empirical methods to characterize roof mine conditions and design support systems.

Rock mass characterization is the first, but the most important, step in order to evaluate the roof conditions and design roof support system. A mischaracterized roof will lead to erroneous roof control and mining methods, and therefore will result in prohibitively high cost. The most universally used roof rock mass classification system is Coal Mine Roof Rating (CMRR), which was developed using a limited number of coal mine case studies, mainly from Appalachian coal fields. The CMRR was developed based on roof fall analyses in over 37 coal mines (Gadde, Rusnak, Mark, 2007, Mark, Molinda, Barton, 2002). It takes into account uniaxial compressive strength (UCS), intensity and shear strength of bedding and other discontinuities, moisture sensitivity, and presence of strong bed in the bolted interval (Mark, Molinda, Barton, 2002). CMRR weighs the geotechnical factors that contribute to roof competence, and combines them on a single rating scale of zero to 100. The CMRR is calculated by: 1) determining unit rating for each rock strata in the bolted interval, 2) averaging all the unit ratings within the bolted interval and applying appropriate adjustments.

The CMRR has been commonly used by coal industry in Australia, Canada, South Africa, and the U.S. It helps engineering practice by: 1) reducing varied rock properties to a single, meaningful, and repeatable parameter, 2) allowing to present meaningful CMRR contours on a single plan rather than a number of contours of UCS, shear strength, lithology, Rock Quality Designation (RQD), 3) facilitating the communication of geotechnical and geological engineers and the general workforce in roof evaluation, 4) providing a useful measure to compare the ground control experience among the sites and develop empirical design guidelines, 5) indicating the potential for extended cuts, 6) indicating the required intensity of primary support requirements and the need for supplemental support, 7) allowing to develop ground control and trigger response action plans, 8) being flexible for various adjustments.

Colwell (2003) adapted the CMRR calculation procedure for applications in Australia by introducing different weighting factors for the input parameters. In addition, a number of mining planning design tools such as Analysis of Longwall Pillar Stability (ALPS), Analysis of Longwall Tailgate Serviceability (ALTS), Analysis of Roof Bolt Systems (ARBS), Analysis of Multiple-Seam Stability (AMSS), and Support Technology Optimization Program (STOP) have also been developed by NIOSH which are related to CMRR.

In this study an extensive laboratory and field investigation was conducted on roof units of a coal mine in the Illinois Basin. Geomechanical properties of shale and limestone roof units were determined using laboratory tests including point load test, unconfined compressive strength, indirect tensile strength, and slake durability. The CMRR roof rock mass indices were determined using laboratory parameters. Furthermore, during site visits, underground CMRR was also determined and compared to drill core CMRR indices.

## ILLINOIS BASIN

The Illinois Basin and Illinois have 132.8 (i.e. 27% of the U.S. reserve) and 104.2 billion short tons of coal, respectively (Department of Energy, 2010). According to this data, it is estimated that 84% of the total Illinois coal reserve is available via underground mining. Roof falls in underground mines are problematic; therefore, controlled by roof support. The roof control cost is about 7 to 20% of total production costs depending upon site-specific geological and geotechnical conditions (Chugh et al., 2009). This cost is in the higher ranges in Illinois due to the weakest roof conditions and significantly higher rate of roof falls among the U.S. coal reserves occurring there (Molinda et al. 2008). It was demonstrated that a strong biaxial horizontal stress field as well as weak, highly moisture-sensitive roof rock are the primary causes of significant roof falls in the Illinois Basin (Nelson and Bauer, 1987; Molinda et al., 2008; Rusnak and Mark, 2000).

Interbedded sandstone and shale roof layers (i.e. stackrock), which are weak in parallel bedding and unstable when subjected to horizontal stresses, are common in the Illinois Basin. Stackrock can result in development of cutters at the intersection of roof and rib as well as progressive roof spalling (i.e. fall of rock between bolts). Furthermore, the roof rocks in the Illinois Basin are in average more moisture sensitive than the other coal fields (Molinda et al., 2008; Molinda and Mark, 2010). Therefore, supplemental supports are systematically installed at intersections. However, the quantity, installation pattern, and type of supplemental support are determined based on trial and error (Gadde, 2006). The failure mechanism, effective supplemental support, and interaction between primary and secondary supports depend primarily on mass strength of roof units. Consequently, the mass strength of roof units must be well-understood to improve the mine safety and optimize the mining operation cost.

## CASE STUDY

The coal mine of this study is located in the Illinois Basin. The compiled laboratory test results and geologic information for the studied mine show 28 boreholes throughout the mine map. The boring logs, rock mechanics test data and rock units within the 3 to 5 m (10 to 15 ft) of the roof units were studied and summarized to develop roof rock geotechnical properties for each layer (i.e. shale, limestone, shale and limestone interbeds, etc.). The moisture content tests were conducted using ASTM D2216. The UCS and Indirect Tensile Strength (ITS) tests were performed based on ASTM D7012-10 and ASTM D3967-08, respectively. The point load index tests were conducted following ASTM D5731 procedure. The point load tests have been conducted on specimens with diameters ranging from 70 to 80 millimeters (2.76 to 3.15 inches). The slake durability test was conducted based on ASTM D4644.

Nine layers were identified in the immediate roof of the mine. Table 1 shows the geomechanical properties of all shale layers. It is worth mentioning that the research team paid specific attention to classify the layers and use engineering judgment to come up with representative layers for rock mass characterization.

The average unconfined compressive strength of shale units are 29.2 MPa (4229 psi) with a standard deviation of 28.8 MPa (4178 psi). This indicates the variability of shale units in the coal field. The average slake durability index for shale units is 58% showing severely sensitive units in the roof. The severely sensitive roof may reduce CMRR rating up to 15 points. As a result, the underground mine, which have stable roof conditions during development, may experience roof instability sometime after mining when the sensitive roofs are affected by moisture.

## POINT LOAD TEST CORRELATIONS

In the axial test, the load is applied parallel to the longitudinal axis of the core, whereas in the diametral test the load is applied perpendicular to the longitudinal axis of the core. The number of samples tested for each rock type and the statistical data regarding the UCS, ITS, Point Load-Axial (PLA) and Point Load Diametral (PLD) values are presented in Tables 2 and 3.

According to Table 2, the average UCS values vary from 11 to 27 MPa (1,595 to 3,916 psi) for shale and claystone rock types and from 90 to 111 MPa (13,053 to 16,099 psi) for limestone and shale limestone rock types. Therefore, according to Bieniawski and Bernede (1979), the shale and claystone rocks of this site are categorized as low strength rocks, while limestone and shale limestone rock types are higher strength rocks.

The ITS-PLD and PLA-UCS sets of data are categorized in six different groups of shale, black shale, sandy shale, claystone, limestone, and shale-limestone. The PLA-UCS and PLD-ITS scatter chart is shown in Figure 1 and Figure 2. In contrast to the PLA-UCS sets of data, for which linear regression analysis seems reasonable, the linear regression method is not appropriate for the PLD-ITS data set.

A linear correlation is observed between PLA and UCS data. The average conversion factor of 21 is calculated for converting PLA to UCS for layers investigated in this study except for sandy shale and claystone layers. As it is apparent from the Figure 1, the limestone and shale limestone data points have higher UCS and PLA values. The best appropriate regression method for the correlation between ITS and PLD data sets was found to be a power regression relationship (Equation 1).

$$ITS = a\,(PLD)^{b} \quad (1)$$

The PLD and ITS values are in MPa. The appropriate regression lines for five rocks (i.e. shale, sandy shale, black shale, claystone and limestone) are plotted in Figure 3. The statistical analyses concluded that the a and b parameters for shales are 4.2 and 0.34 and for limestone are 5.1 and 0.56, respectively.

## ROCK MASS CHARACTERIZATION

The rock within the bolted interval above the roof is divided into rock units. Bolt lengths of 1.8 m (6 ft.) were assumed as part of roof control plan in the analyses. Figure 4 shows the wet CMRR within the mining area using drill core information for 1.8 m (6 ft.) bolted interval. This figure shows out of 28 bore holes, 3 boreholes (in the north and two in the south of property) have a CMRR less than 35. In other coal fields, a CMRR of less than 35 is considered a weak unit and the mining is recommended using miner bolter and narrower room widths. It is anticipated that the contour lines are a very rough estimate of CMRR values between boreholes becausethere are scarce number of bore holes in the northern half of the site and the geology of the site is very variable.

**Table 1. Geomechanical properties of shale units of the immediate roof.**

| Test type | Number of data | Minimum | Maximum | Average | Standard Deviation |
|---|---|---|---|---|---|
| Moisture Content (%) | 368 | 0.4 | 17.6 | 5.7 | 3.4 |
| Unit Weight (kg/m$^3$) | 353 | 1318.3 | 2769.6 | 2468.4 | 166.6 |
| Unconfined Compressive Strength (kPa) | 352 | 241.3 | 173865.1 | 29162.8 | 28808.4 |
| Indirect Tensile Strength Index (kPa) | 424 | 27.6 | 16313.0 | 2779.3 | 2367.4 |
| Axial Point Load Index (kPa) | 301 | 27.6 | 10011.2 | 1553.4 | 1589.2 |
| Diametral Point Load Index (kPa) | 82 | 13.8 | 3888.6 | 738.4 | 1029.4 |
| Slake Durability Index (%) | 181 | 0 | 99.6 | 58.3 | 32.9 |

**Table 2. Statistical data for UCS and PLA tests conducted on roof rock cores.**

| | No of pairs of data | Min. UCS (kPa) | Max. UCS (kPa) | Mean UCS (kPa) | STD. UCS (kPa) | Min. PLA (kPa) | Max. PLA (kPa) | Mean PLA (kPa) | STD. PLA (kPa) |
|---|---|---|---|---|---|---|---|---|---|
| Shale | 28 | 1.365 | 176.623 | 24.185 | 35.872 | 172 | 3.868 | 1.270 | 1.089 |
| Black Shale | 7 | 5.281 | 20.815 | 11.218 | 6.349 | 262 | 1.407 | 779 | 402 |
| Sandy Shale | 31 | 1.338 | 167.605 | 27.159 | 35.600 | 145 | 4.661 | 1.655 | 1.320 |
| Shale Limestone | 6 | 58.150 | 156.270 | 111.106 | 41.358 | 2.723 | 5.619 | 4.408 | 1.069 |
| Limestone | 38 | 490 | 265.124 | 89.518 | 56.516 | 97 | 9.239 | 4.044 | 1.703 |
| Claystone | 19 | 2.337 | 64.700 | 19.726 | 19.570 | 117 | 5.102 | 1.503 | 1.665 |

**Table 3. Statistical data for ITS and PLD conducted on roof rock cores.**

| | No of samples | Min. ITS (kPa) | Max. ITS (kPa) | Mean ITS (kPa) | STD. ITS (kPa) | Min. PLD (kPa) | Max. PLD (kPa) | Mean PLD (kPa) | STD. PLD (kPa) |
|---|---|---|---|---|---|---|---|---|---|
| Shale | 28 | 379 | 9.177 | 3.345 | 2.608 | 14 | 3.585 | 417 | 735 |
| Black Shale | 22 | 441 | 4.990 | 2.433 | 1.264 | 23 | 487 | 187 | 141 |
| Sandy Shale | 37 | 703 | 12.762 | 3595 | 3.024 | 21 | 3.787 | 769 | 1.004 |
| Shale Limestone | 5 | 2.068 | 10.466 | 7.054 | 3.145 | 1.744 | 5.900 | 3.622 | 1.508 |
| Limestone | 29 | 62 | 19.250 | 9.129 | 4.386 | 14 | 1.0418 | 3224 | 2.558 |
| Claystone | 9 | 186 | 12.224 | 3.401 | 4.126 | 34 | 2.979 | 681 | 1.079 |

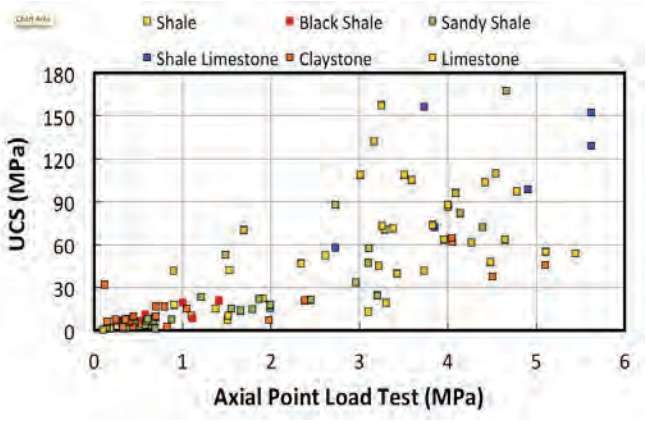



**Figure 1. UCS and PLA values for limestone, claystone and different shale rock samples.**

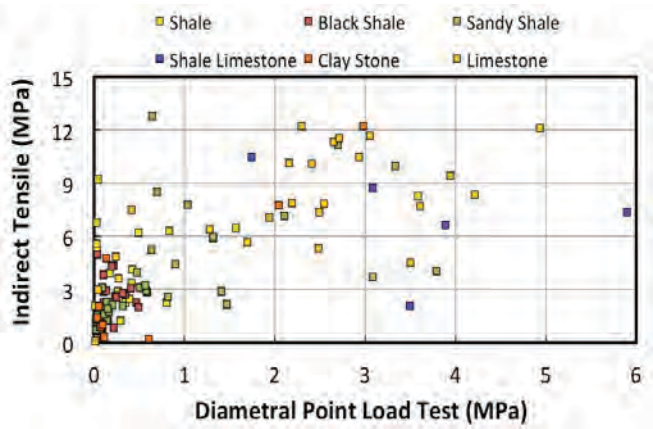



**Figure 2. Scatter chart regarding ITS and PLD values of the tested samples for limestone, claystone and different shale rock samples.**

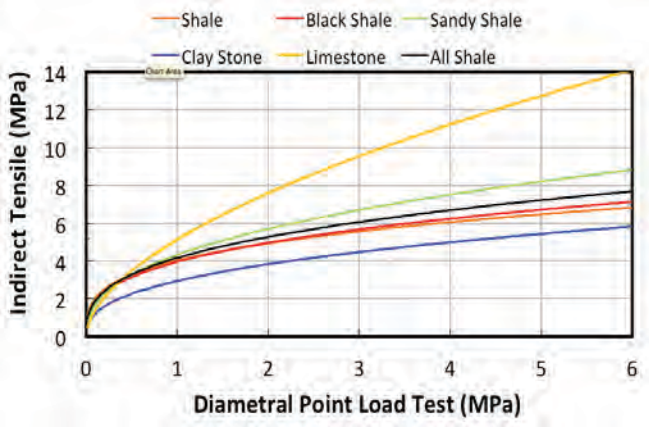



**Figure 3. Relationship between ITS and PLD for limestone, claystone and different shale rock samples.**

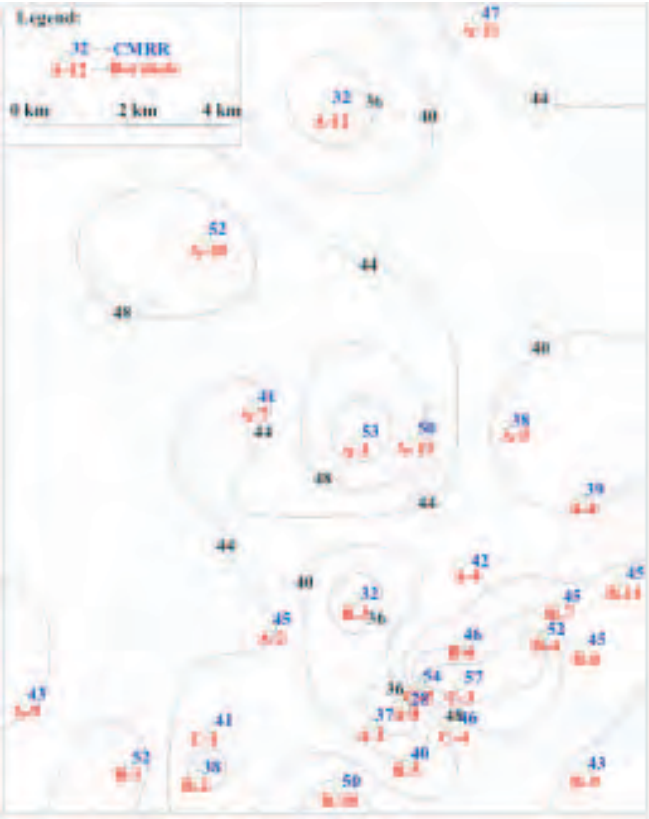



**Figure 4. Wet CMRR contours using 1.8 m (6 ft.) bolt length and exploratory drill core information.**

In addition, in order to compare the CMRR values from drill core information and underground information, a site visit was made and underground information was collected for six locations within the mined out areas. Figure 5 shows the zoomed out section of Figure 4 to compare wet CMRR using exploratory drill core and underground information. This figure shows four predetermined testing locations (i.e., U-1, U-2, U-3, and U-4) which are in the vicinity of boreholes (C-2, B-3, D-1, and D-2 respectively). The underground CMRR indices derived from these four testing locations are in agreement with the drill core CMRR contours. For U-2 and U-3 locations, this compatibility is more noticeable. Locations labeled as UR-1 and UR-2, had previous massive roof falls. Roof falls had 7.6 m (25 ft.) to 9.1 m (30 ft.) length and 5.5 m (18 ft.) width. The observed roof fall depth is also reported as 3 m (10 ft.) to 3.7 m (12 ft.). During the mine visit, it was noticed that at these roof fall locations yellow dark gray shale with very weak strength and severely moisture sensitivity was in the immediate 0.9 m (3 ft.) of the roof. It is worth noting that the wet CMRR values for these locations are less than 35. Mining in these low ranges of CMRR requires more caution and supplemental support. Although both of these locations had roof screen protection and were supported with eight 3 m (10 ft.) to 3.65 m (12 ft.) length cable bolts and 1.8 m (6 ft.) roof bolts, roof falls still occurred. Since the UR-1 and UR-2 locations are about 645 m (2,110 ft.) from the closest bore hole and the geology variability was significant, it is not unreasonable to observe difference between CMRR contours and CMRR indices obtained from underground information.

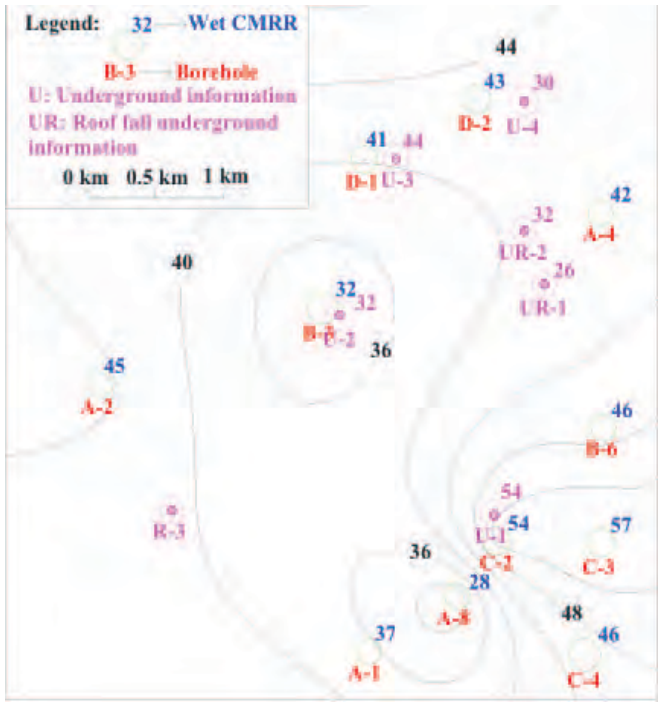



**Figure 5. Comparison of wet CMRR values using drill core and underground information.**

## ROOF SUPPORT

Observations have indicated that more than half of the roof falls in coal mines occur in intersections, with roof falls being more probable in wider spans (Molinda et al 1998). Bolt length, capacity, and standing pattern of the bolts are also critical parameters, which can determine roof support. Consequently, ARBS variable is developed by Molinda et al., (2001) as a representative roof support intensity index. Using Equation 2, ARBS values are obtained for different mining locations.

$$ARBS = \frac{(L_b)(N_b)(C)}{14.5(S_b)(W_c)} \quad (2)$$

Where,

$L_b$ = Length of bolt (m),

$N_b$ = Number of bolts per row,

C = Bolt capacity (kN),

$S_b$ = Spacing between rows of bolts (m).

$W_c$ = Entry width (m).

Figure 6 shows the correlations between wet CMRR and ARBS indices. It is demonstrated that mine zones with larger CMRR values need less support. Mark et al. (2001) suggested that areas which have ARBS values more than suggested $ARBS_g$ (see Equation 3) have less frequency of roof falls.

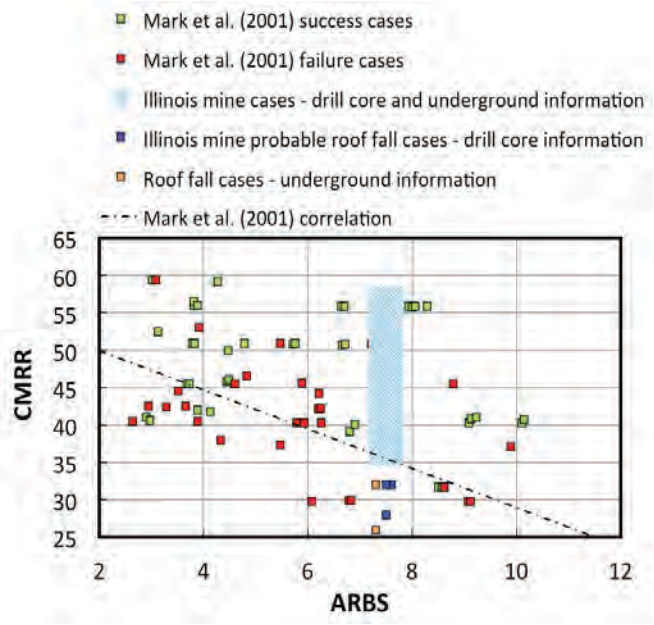



**Figure 6. Wet CMRR vs. ARBS values when 1.8 m (6 ft.) bolt length is used.**

$$ARBS_g = (5.7 \log H) - 0.35CMRR + 9.4 \quad (3)$$

where, H (m) is depth of cover. Therefore, Equation 3 was used to define the suggested discriminant dashed line for the Illinois Basin case study. For this mine, 5 typical 1.8 m (6 ft.) tension rebar SRD grade 75 bolts per row with 1.2 m (4 ft.) spacing was planned in the mines. In addition, five typical 1.8 m (6 ft.) headed rebar fully grouted Grade 60 bolts per row were utilized in the panels. Entry width of the studied mine was designed to be 5.5 m (18 ft.) to 5.8 m (19 ft.).

Figure 6 shows all the boreholes including boreholes A-8, A-12, and B-3, which are below the trend line. There are also two observed roof fall spots (UR-1 and UR-2) below the suggested line which show the compatibility of suggested trend line and observed fall locations. It is anticipated A-8, A-12, and B-3 locations, which are not mined out yet, are also prone to roof falls and will need supplemental supports. It is worth mentioning that these areas have a wet CMRR index of less than 35.

## CONCLUSION

Geomechnical properties of the roof system in an Illinois coal mine is presented in this study. The laboratory tests show a high variability and moisture sensitivity for shale units in the immediate roof of the mine. The axial point load and unconfined compressive strengths tests show this to be a linear correlation between these parameters. However, the diametral point load test and indirect tensile strength are correlated nonlinearly. The comparison of drillcore with underground CMRR shows a reasonable compatibility between two methods for this site. The roof bolt intensity of the mine indicated that significant support is needed to avoid roof failures for the range of CMRR indices observed in the mine shadow area.

## ACKNOWLEDGEMENT

The authors would like to acknowledge the support of the Prairie State Generating Co. LLC and Dr. Joseph Hirschi of Illinois Clean Coal Institute. This research was made possible with support, in part, by the Office of Coal Development of the Illinois Department of Commerce and Economic Oppurtunity through the Illinois Clean Coal Institute. The authors also wish to thank Mr. Brent M. Vaughn, laboratory specialist and lecturer in Civil Engineering department at Southern Illinois University Edwardsville, for providing laboratory support in this study.

## REFERENCES

ASTM D2216-10. (2010). "Standard Test Methods for Laboratory Determination of Water (Moisture) Content of Soil and Rock by Mass.", Annual book of ASTM standards, 4.08, Philadelphia, Pennsylvania.

ASTM D4644-08. (2008). "Standard Test Method for Slake Durability of Shales and Similar Weak Rocks.", Annual book of ASTM standards, 4.08, Philadelphia, Pennsylvania.

ASTM D7012-10. (2010). "Standard Test Method for Compressive Strength and Elastic Moduli of Intact Rock Core Specimens under Varying States of Stress and Temperatures.", Annual book of ASTM standards, 4.08, Philadelphia, Pennsylvania.

ASTM D3967-08. (2008). "Standard Test Method for Splitting Tensile Strength of Intact Rock Core Specimens.", Annual book of ASTM standards, 4.08, Philadelphia, Pennsylvania.

ASTM D5731-08. (2008)."Standard Test Method for Determination of the Point Load Strength Index of Rock and Application to Rock Strength Classifications." Annual book of ASTM standards, 4.08, Philadelphia, Pennsylvania.

Bieniawski, Z.T. and Bernede, M.J. (1979). "Suggested methods for determining the uniaxial compressive strength and deformability of rock materials: Part 1. Suggested method for determining deformability of rock materials in uniaxial compression." International Journal of Rock Mechanics and Mining Sciences & Geomechanics.16:138-140.

Colwell, M. (2003).“A manual for assessing the Coal Mine Roof Rating (CMRR).”, Colwell Geotechnical Services.

Chugh, Y. P., Li, S., Gurley, H., Kollipara, V., Williams J., Pulliam J., Bell, W. (2009), “Development of Improved roof support systems for Illinois underground mines.” Technical report, ICCI 03-1/1.1E-1, 30 pages.

Department of Energy, U.S. Energy Information Administration. (2010). Annual Energy Review, DOE/EIA-0384(2010), 384 pp.

Gadde, M. (2006). “Behavior of welded wire mesh used for skin control in underground coal mines.” 25th International Conference on Ground Control in Mining, Morgantown, WV.

Gadde, M.M., Rusnak, J. A., Mark, C. (2007). “An integrated approach to support design in underground coal mines.” Proceedings of the international workshop on rock mass classification in underground mining, DHHS (NIOSH) Publication No. 2007-128, Pittsburg, PA, pp. 49-56.

Mark, C., Molinda, G.M., Dolinar, D.R. (2001). “Analysis of roof bolt systems.” In:Peng S.S. et al., ed. Proceedings of the 20th International Conference on Ground Control in Mining, Morgantown, WV: West Virginia University, pp. 218-225.

Mark, C., Molinda, G. M., Barton, T.M. (2002). “New developments with the coal mine roof rating.” 21st International Conference on Ground Control in Mining, Morgantown, WV, pp. 294-301.

Molinda, G. M., Mark, C. (2010). “Ground failures in coal mines with weak roof.” Electronic Journal of Geotechnical Engineering, Jan 15(F), 547-588.

Molinda, G.M., Mark, C., Debasis, D. (2001). “Using the Coal Mine Roof Rating (CMRR) to assess roof stability in U.S. coal mines.” Journal of Mines, Metals and Fuels. 49:314-321.

Molinda, G.M., Mark, C., Bauer, E.R., Babich, D.R., and Pappas, D.M. (1998). “Factors Influencing Intersection Stability in U.S. Coal Mines”. In: Peng S.S. et al., ed. Proceedings of 17th International Conference on Ground Control in Mining., Morgantown, WV: University of West Virginia, pp. 267-275.

Molinda, G.M., Mark, C., Pappas, D. M., and Klemetti, T. M. (2008). “Overview of coal mine ground control issues in the Illinois Basin.” Trans. Soc. Min. Metall. Explor., Dec, 324, pp. 41-48.

Nelson, J.W. and Bauer, R.A. (1987). “Thrust faults in southern Illinois – result of contemporary stress?” Geol. Soc. Am. Bull., Vol. 98, March, pp. 302-307.

Rusnak, J., and Mark, C. (2000). “Using the point load test to determine the uniaxial compressive strength of coal measure rock.” 19th International Conference on Ground Control in Mining, Morgantown, WV., pp. 362-371.

# Application of Various Probing Methods for Rock Characterization in Boreholes Drilled for Roof Bolting

**Ali Naeimipour**, Graduate Research Assistant
**Jamal Rostami**, Associate Professor Mining
Penn State University
State College, PA

## ABSTRACT

Availability of accurate geological information about the rock mass surrounding a tunnel or mine working is the key to enhance and optimize the required ground support measures. Various approaches have been used to obtain data on ground conditions, including the possibility of characterizing the ground while drilling for roof bolts, by the Measurement While Drilling (MWD) system, via optical, sonic and acoustic televiewers, and using various types of gamma probes. While there are many different systems for characterizing the ground in longer, larger-diameter holes drilled downward, the options for using probes and logging systems in short, small-diameter holes drilled in horizontal or an upward direction are very limited. This paper will present the results of recent field tests using optical televiewer (OPTV) to analyze the joints and voids in boreholes drilled in different directions. The studies show that OPTV is a promising tool; however, getting a good quality image from the upward drill holes still need to be studied. Meanwhile, estimated in-situ strength of the intact rock is needed to complement the jointing pattern for rock mass classification. For this purpose, preliminary steps for the development of a borehole scratcher to estimate rock strength will be discussed in this paper.

## INTRODUCTION

Understanding the ground condition is the first step in the development of an efficient and optimized ground control and ground support system for any underground opening in mining and civil applications. This requires accurate characterization of the rock in the roof and ribs in terms of the rock type, strength, jointing frequency and joint conditions. Often this type of information is unavailable during the excavation of a heading in the mine or a tunnel that is under construction, and the design of the ground support is based on information from geotechnical borings that are far apart. Obtaining localized information about the rock strata surrounding the opening inevitably entails diamond drilling of the roof and ribs as well as rock mechanics testing of the core. This is not feasible in many applications, since it is very costly and disruptive to operations. However, since many of these operations use rock bolts for ground support, the possibility of probing these boreholes for ground characterization will offer a quick, less disruptive, and cost-effective means to obtain sufficient information about ground conditions during the excavation cycle.

Various borehole logging and probing systems have been proposed and used in recent years to offer an estimate of rock strength and rock mass structural features, such as joint frequency and joint conditions. These probes have been fairly successful in larger down-holes drilled for various applications, but have limited or no use in shorter, smaller size boreholes often used in underground applications. Thus, there is a dire need to look into probing and logging systems that can be used in underground mining and construction for rock characterization. In an ideal world, if Measurement While Drilling (MWD) systems could generate reliable data about surrounding rock mass in a tunnel or mine working, it would be the best option since it is the least disruptive, most efficient and most reliable source of information that can offer a view of the formations beyond the tunnel walls. They could also offer real-time evaluation of the ground conditions and, by virtue of having many holes in the ground for roof bolting, offer a tight grid of hole locations to allow for a more detailed analysis of ground conditions.

The application of MWD for roof characterizations has recently been gaining some traction, where roof bolt drilling systems collect additional information such as torque, thrust, rotational velocity and penetration rate that can be used for estimating the rock strength and evaluating rock mass conditions. This information can be utilized for mapping of the roof, producing a hazard map, and creating a 3-D visualization of the geological information. Moreover, the geological data can potentially be utilized to evaluate the effectiveness of ground support for a given section. A series of studies has demonstrated the potential for analyzing drilling parameters from roof bolters to estimate rock properties and to identify discontinuities (Itakura et al., 2001; 2008). In a more recent study, it has been shown that vibration and acoustic measurements, along with signal processing tools, can also be used to improve the accuracy of the void detection and rock characterization algorithms on roof bolting devices (Bahrampour et al., 2013). However, the current MWD systems are not very reliable in the detection of joints and voids, and cannot offer an accurate estimation of rock strength. Ongoing studies on this topic are underway with the support of the National Institute for Occupational Safety and Health (NIOSH) (Bahrampour et al., 2013).

Borehole logging is an effective alternative to address this issue while more accurate MWD systems are being developed. Borehole logging, or well logging, is the practice of recording continuous information on some physical properties of rocks in the borehole. Well logging is commonly used in boreholes drilled for oil and gas, groundwater, mineral, geothermal, environmental and mining applications. There are many different logging methods, namely electric, radiation, sonic, acoustic and optical. Well or borehole logging systems consist of various sub-groups to measure a target physical parameter in a particular situation. While well logging in the oil industry utilizes probes with a relatively large size and in long vertical holes filled with water, in civil and tunneling operations slimmer and shorter devices should be used to log small, short and dry holes often drilled upward.

The current study focuses on slimmer, lighter probes that are needed to be used in roof bolt holes. These holes are typically about 25-50 millimeters (1-2 inches) in diameter, about 2-6 m (6-20 ft) long, and should be accessed from smaller spaces where they can be set up and deployed. Some attempts have been made in the past to employ borehole logging methods to verify the validity of the results from the instrumented roof bolter in field tests. Gu (2003) and Tang (2006) mentioned the application of a simple borehole camera system in addition to coring to verify the sequence of formations encountered by the roof bolter during the underground tests. In addition, various geophysical methods have been examined to estimate different properties of the rock mass, especially the rock strength (Zhou et al., 2005; Oyler et al., 2010). Also, borehole televiewers and cameras are often used to take a picture of the borehole wall to detect discontinuities (Ellenberger, 2009; Bae et al., 2011).

Unlike most studies where the logging runs were done in downhole boreholes, except for borehole scopings, the logging of roof bolt holes involves probing upward/dry slim holes. Hence, probing upward/slim/short/dry boreholes, which is the focus of this study, is a logistical issue that should be addressed to pave the way for further investigation of the application of borehole logging for rock characterization within the boreholes drilled for roof bolting.

It can be deduced that Uniaxial Compressive Strength (UCS) of intact rock and condition of the discontinuities are two of the most important parameters for Coal Mine Roof Rating classification (Mark et al. 2002). While the condition of the discontinuities can be examined by borehole televiewers, like optical TVs, estimation of UCS remains a challenge in the development of rock mass classification. UCS of the rock is commonly correlated to the results from the sonic logging method, but sonic methods are not optimized for application in upward holes and do require water in the hole for transmission of sonic waves. This paper will present the field application of optical TV and the related analyses on images for characterizing the joints and discontinuities in the rock mass. Also, the preliminary steps to estimate the strength of rock through the development of a borehole scratcher will be briefly discussed.

## FIELD TESTS WITH OPTICAL TV

An optical TV, commonly used in down-hole applications, and a Slim Borehole Scanner (SBS) were investigated during this study. These probes are both powerful tools for capturing high resolution images from borehole walls. Though they are designed for slim boreholes, they target different markets and applications.

ALT-Mount Sopris, QL40OBI optical televiewer, is 42 mm in diameter and about 1.3 m in length. It can be used in boreholes with a diameter range of 50-533 mm, depending on the water and borehole conditions. The camera is a DSP-based digital CCD with 24-bit RGB color resolution. The horizontal resolution of the camera is 90-720 pixels per turn (360º). The higher resolution is used in larger diameter boreholes. The vertical resolution depends on different parameters, specifically the smoothness of the wall and speed of the logging operation. This parameter can be adjusted by changing sampling rates, which can be set based on the time or depth sampling mode. A vertical resolution of as low as 2 mm is achievable with this tool (Lahti, 2004). Logging speed is commonly between 1-3 m/min; however, for high vertical resolution, speeds in the range of 0.1-0.3 m/min might be needed.

During the logging operation, the tool can record and display various information, namely image, temperature (°C), deviation sensor temperature, azimuth from the magnetic North (Azimuth, deg), inclination from verticality (Tilt, deg), tool relative bearing calculated from both accelerometer (Roll, deg) and magnetometer (MRoll, deg), magnetic field surrounding the borehole (MagnField, μT) and absolute value of the Earth gravity (Gravity, g). The three-axis magnetometer/3 accelerometers APS 544 sensor enables the device to record the orientation of the borehole assuming that the axis of the tool and borehole are always parallel. The accuracies for azimuth and inclination measurements are ±0.5 and ±1.2 degree, respectively.

The data is transferred from the probe by a coaxial 4- or 7-conductor wire cable to the data logger attached to the winch system. Data transmission speed can be as high as 500 Kbits per second, depending on the wireline. The wire cable also has the function of winch wire to facilitate moving the probe inside the borehole. This cable passes through a depth encoder, which digitally records the position of the probe relative to the borehole collar, and the obtained image will be adjusted with position data. For accuracy of depth measurement, the wire should be kept stretched during the logging. The weight of the probe will help in achieving this goal. Also for this reason, the depth measurement is more accurate when the logging is done from the bottom to the collar. Depth information can further be calibrated using cores and by knowing the exact depth of some more distinctive geological features.

The optical televiewer used in this study, QL40OBI, was tested in three different surface and underground mines to check the suitability and capabilities of the device for probing horizontal and upward holes. Since this device is designed for down-hole applications, some extra equipment were developed and used during some of the logging operations. During the field testing, down/upward and sub-horizontal boreholes were logged, as discussed in the following section.

### Logging in downward boreholes

The first set of operations was carried out in King Coal Crown and Welker coal mines, which are two surface coal mines near Philipsburg, Pennsylvania. Boreholes in these mines were downward and about 203 mm in diameter. All the loggings were

performed with about 1 m/min speed and a 360 azimuth resolution (point/turn). The image property setting used in these tests was lightness 60% (recommended by manufacturer for normal dry boreholes); chroma of 50%; normal (Default) image; gamma correction "on" (as default); and sampling rate of 0.004 m.

Figure 1a and Figure1b show pictures of the settings used in field operations. Figure 2a and Figure 2b show the resulting images taken from the borehole in downward (collar-to-bottom) and upward movement on the left and right, respectively. These images are almost identical for both directions of logging. The first borehole image set in Figure 2a is an exception in which the probe head passed the groundwater level, which starts at the point the image become unclear, and the deposited fines at the bottom of the hole blurred the image. This incident left some dirt on the window of the probe, as can be seen on the image on the right. Considering the accuracy of the depth measurement, upward logging proved to be a better approach in this case since the winch wire was always stretched. These operations were a help to understand the operation of the device without considering the challenges in the upward-borehole logging practices. As Figure 1a shows, two non-metal centralizers were installed on the probe to help keep the probe centralized and improve the quality of images. Figure 1b shows the tripod, winch, depth encoder and data logger manufactured by Mt Sopris Inc. Unlike Figure 2a, some dark interbeds, probably coals, can be observed in Figure 2b.

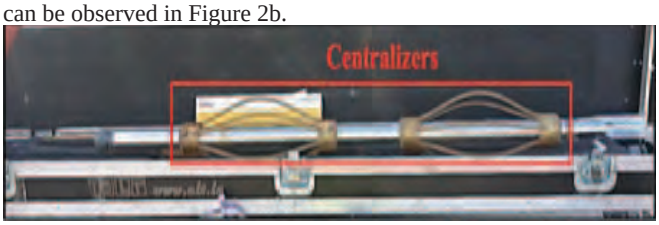



**Figure 1a. Pictures of the setting for borehole logging operations at the King Coal Crown mine with the QL40OBI probe.**

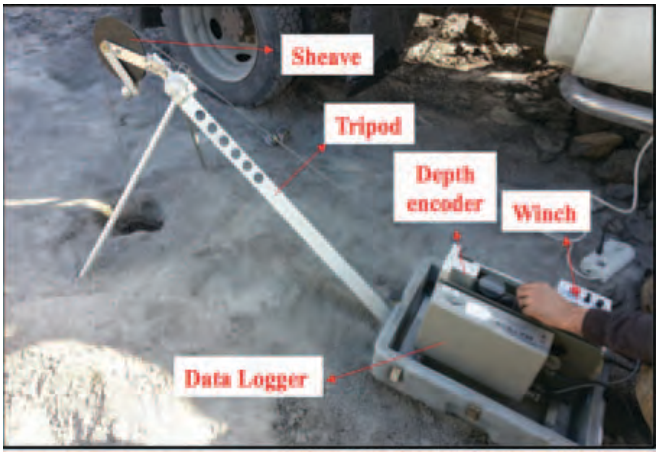



**Figure 1b. Pictures of the setting for borehole logging operations at the King Coal Crown mine with the QL40OBI probe.**

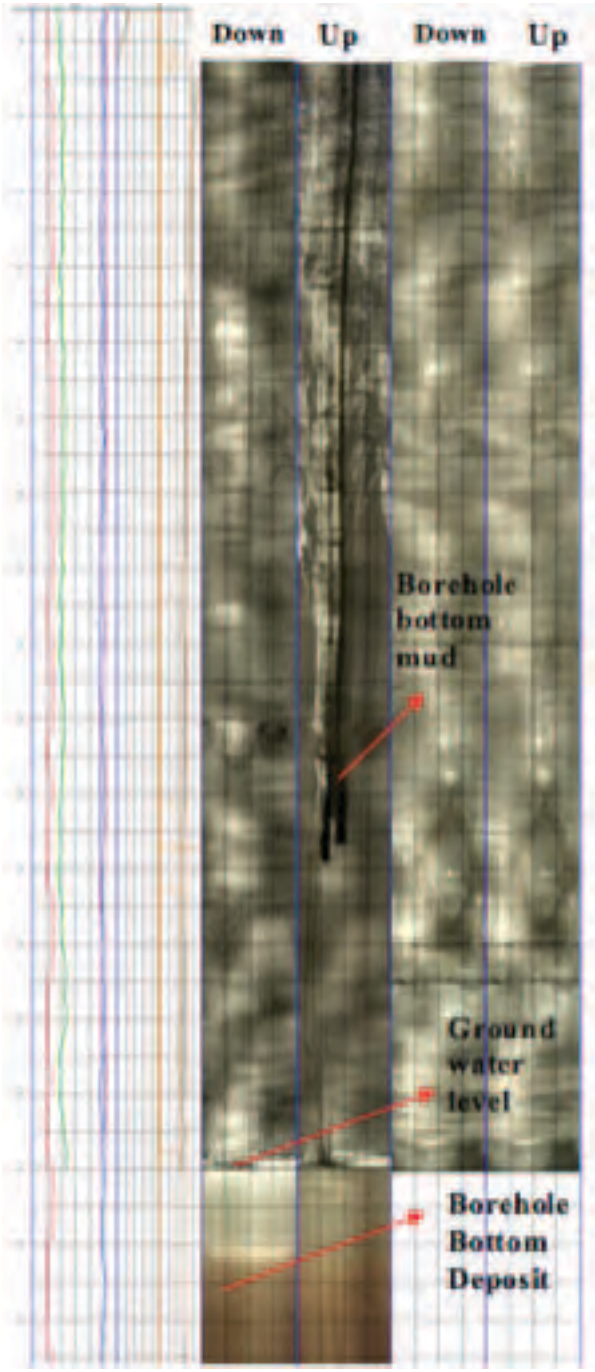



**Figure 2a. The images resulted from logging operations at the King Coal Crown mine.**

**Logging in upward boreholes**

Some upward boreholes of about 50 mm in diameter were also tested for probing with the optical televiewer. These probing operations were done at the Graymont underground limestone mine near Pleasant Gap, Pennsylvania. For this set of experiments, a special centralizer, a drum and couple of push rods were designed and made at Penn State University. The concept of upward logging and the designed equipment are shown in Figure 3. All these loggings were performed with 360-azimuth resolution

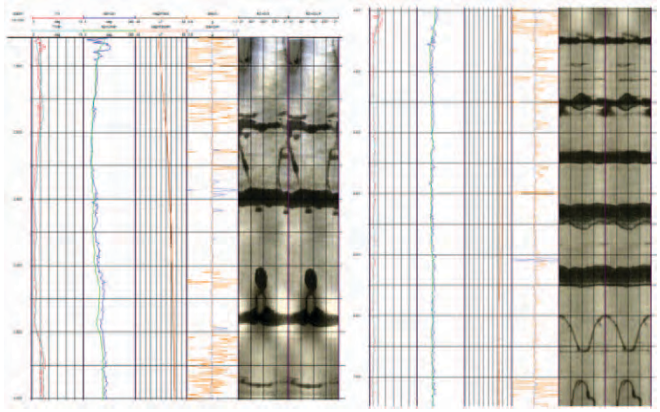


**Figure 2b. The images resulted from logging operations at the Welker coal mine with the QL40OBI probe.**

(point/turn). It was not possible to maintain the speed of logging constant mainly because the probe got stuck in the borehole. The imaging parameters were set as lightness 60% (recommended by manufacturer for normal dry boreholes); chroma: 50%; normal (Default); gamma correction "on" (as default); and sampling rate of 0.004 m.

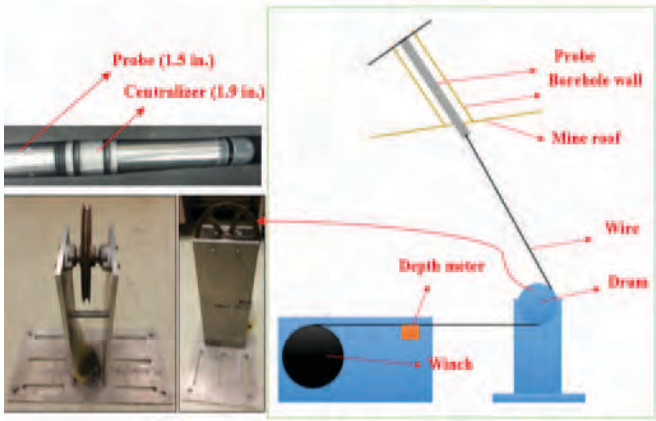



**Figure 3. The concept of upward logging operations and the devices, centralizer and drum, designed and made for this setting.**

The additional pieces, to some extent, helped improve the results and facilitate the upward logging. However, since the device is relatively heavy, approximately 7 kg (15 lbs) with a diameter close to the diameter of the hole, there were many difficulties during the operation including keeping the wire in a constant tension to have a smooth probing with constant speed. Also, the probe was stuck a few times in the borehole, which needed significant force and displacement to release it. A constant wire speed is essential for accurate measurement of the depth, and variable speed logging will lead to unclear and grainy images. Figure 4a and Figure 4b show the setting for this operation and the image from one of the boreholes. In Figure 4a, abrupt changes in azimuth and magnetic field records can be noticed due to the retrieving of the probe after it was stuck. This set of logging needed at least three people to control all the components involved during the operation, as shown in Figure 4b. This made the probing operation inefficient, labor intensive and hard to manage.

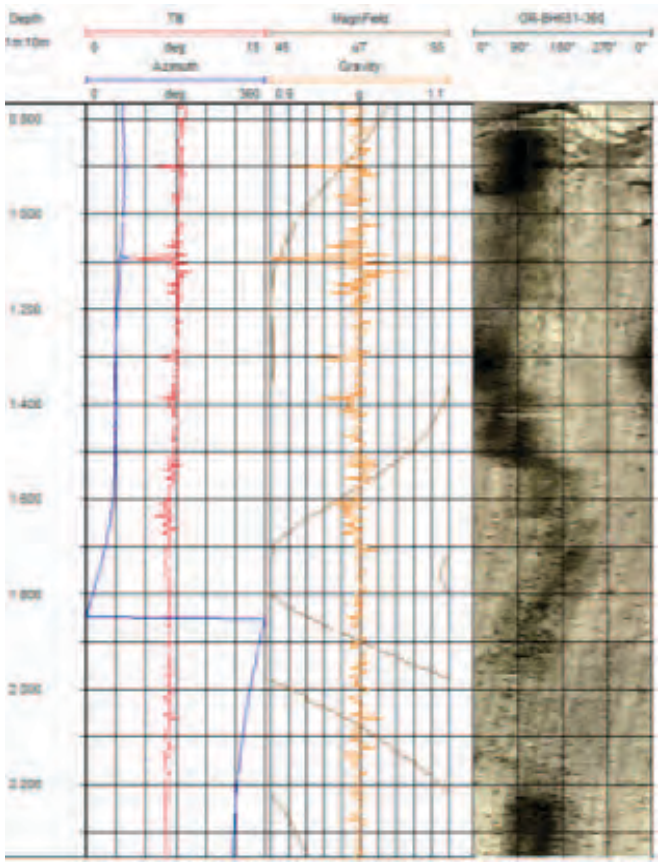


**Figure 4a. Upward borehole logging with QL40OBI probe at Graymont mine and a typical resulted image.**

**Logging in sub-horizontal boreholes**

Some sub-horizontal boreholes were also drilled and logged at the Graymont mine. Figure 5a and Figure 5b show the operational setting and the image from a borehole. Six boreholes were logged in this study. The images resulting from the first five adjacent boreholes are shown in 5a, according to the relative position the boreholes have from each other. The main goal in this series of operations was to check the effect of azimuth resolution and logging speed on the quality of the images. Azimuth or peripheral resolution of 180, 360 and 720 (point/turn) and logging speeds of 0.1, 0.2 and 0.3 m/min were investigated. The other image setting parameters were kept constant, including lightness 60% (recommended by manufacturer for normal dry boreholes); chroma 50%; normal (Default); gamma correction "on" (as default); and a sampling rate of 0.004 m.

The logging process was generally the same as down-hole probing. However, in this set the extension rods were employed to push the probe into the borehole. The image of the borehole was not recorded at the entry cycle, but when retrieving the probe by the winch. The operation went smoothly enough that logging speeds as low as 0.1 m/min could mostly be maintained. It was concluded that the minimum peripheral resolution (180) would be sufficient for the small boreholes tested (50 mm). Also, using lower speeds was not found to have much effect on the image quality for the 4 mm sampling rate condition.



**Figure 4b. Upward borehole logging with the QL40OBI probe at the Graymont mine and a typical resulted image.**

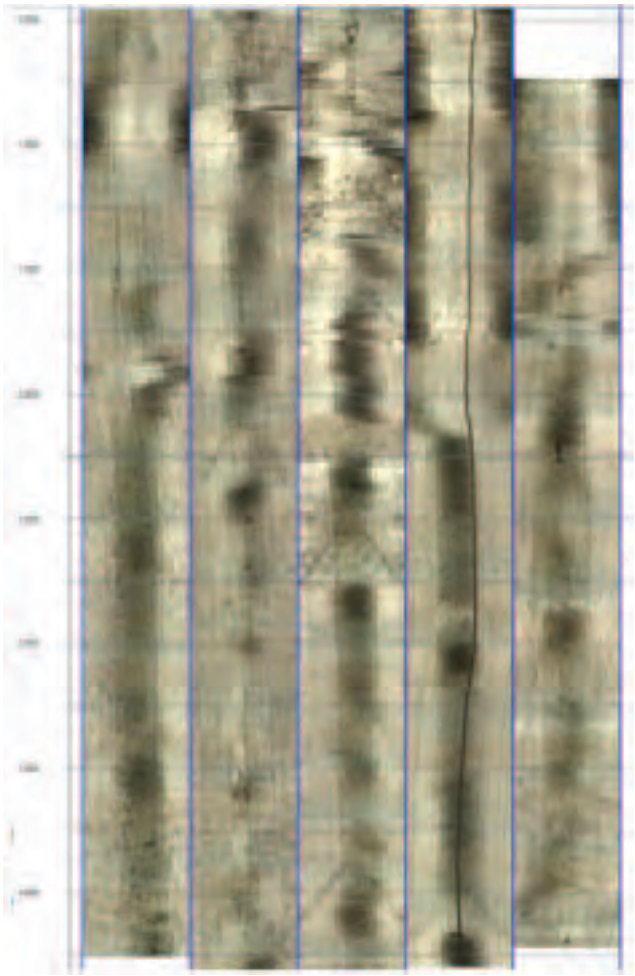


**Figure 5a. Sub-horizontal borehole logging with the QL40OBI probe at the Graymont mine and a typical resulted image.**

## ANALYSIS OF THE IMAGES

For further analyses of the images at this stage, it was decided to just evaluate the images obtained from the last series of the logging operation in the sub-horizontal boreholes. In the five adjacent boreholes logged, three fractures were detected, one in the right middle (RM) borehole and the remainder in the center borehole (Figure 6a). Also, two sub-parallel cracks were found in right middle (RM) and left side (LS) boreholes (Figure 6b). The three detected fractures and discontinuities were analyzed by WellCAD software developed by ALT Mount Sopris Company. Prior to analyzing the structural features, the images were processed. In this procedure, the no data or null traces were compensated for and the brightness and contrast of the images were corrected.

Before getting the structural data from the images, they should be corrected relative to the common global coordinate system (horizontal datum being the surface) (Figure 7a). This means that the recorded images are all captured considering the local (probe) coordinate system, which is parallel to the axis of the borehole (Figure 7b). Although these images are shown in the local system, the true and non-apparent values for apertures, dips and azimuth are stored in the files.

As shown in Figure 8, the semi-automatically selected fractures in the images are corrected to the global coordinate system. This change of system is more complicated than just adding the tilt of the borehole axis to the apparent dip angle. In these calculations, both dip and azimuth values will change. The azimuth of the image was also corrected from the tool recorded magnetic north to true north. The difference between these was determined to be 10.91 degrees at the Graymont mine. Table 1 summarizes the obtained results for the joints detected in this exercise.

The corrected data can be used further for defining the structural features of the ground as needed for rock mass classifications or other applications. In this particular field test, not many voids/fractures/joints were detected and, as a result, the obtained information from structural analyses is limited. Figure 9a and Figure 9b show stereonet or Wolff (angle-equal/lower hemisphere) and Rosette plots for the fractures in the center borehole in the depth range of 2.14-4.29 m. As can be seen, the fractures have a (more or less) similar dip/dip direction, and the mean values are not very different. The dip and azimuth of all the detected fractures are more or less the same. However, since they were just found in two out of five nearby boreholes, it is hard to assume that these fractures belong to a joint system.

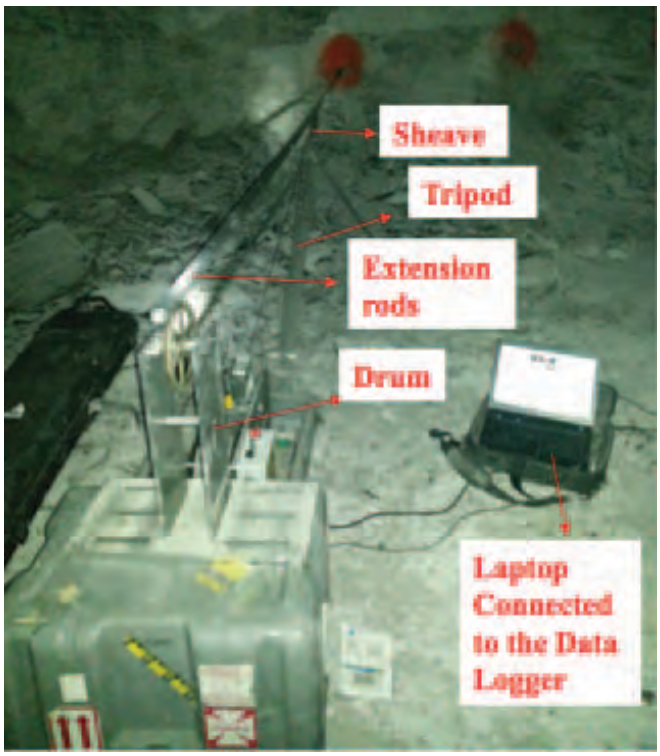



**Figure 5b. Sub-horizontal borehole logging with the QL40OBI probe at the Graymont mine and a typical resulted image.**

The field testing and subsequent analysis showed that it is very difficult to use the optical televiewers that are designed for surface down-hole applications in an underground environment for logging upward smaller diameter holes. Thus, there is a need for further evaluation of alternative methods for obtaining structural information from the boreholes in underground environments. One strong alternative is the Slim Borehole Scanner (SBS) probe, which is an explosion-proof borehole imaging tool specifically designed for application in a coal mine. The device is designed to operate without a cable, so there is no need for a tripod and winch, and it is light enough to be used by one operator. The SBS is 23 mm in diameter and around 300 mm in length, which makes it very suitable for use in normal 25-50 mm roof bolt boreholes. This product has the good features of a borescope, ease of operation and suitable geometry along with the advantages of regular OPTVs for getting an unwrapped 360-degree picture of the borehole wall and orientation of the borehole including the depth of log from the collar. However, the real-time picture of the borehole wall cannot be seen during logging operations. This system is not fully waterproof and has limitations related to battery life and memory space. Additional testing on a SBS system manufactured by the DMT Company in Germany is underway to evaluate its potential for offering the required information on joints for rock mass classification.

## SCRATCH TEST

To complement the studies performed for the selection of a suitable borehole imaging device, estimation of the rock strength (intact rock) by means of borehole probes was investigated. The findings show that the most suitable approaches for estimation of the intact rock strength inside the upward/short/small boreholes

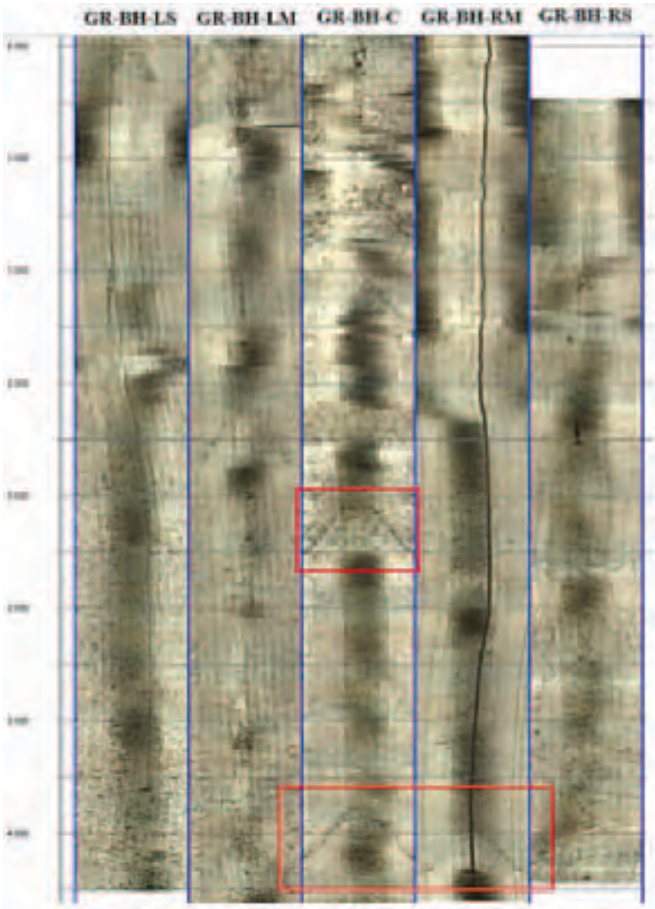



**Figure 6a. Detected fractures inside the sub-horizontal boreholes.**

are mechanical methods (Rostami et al, 2014). This is based on the study of various probing systems that can be used for this purpose, and the relative success of a system that would evaluate rock strength based on scratching the rock using a drag-type tool – or as it is called, "the stamp test" or scratch tests.

Stamp tests and borehole penetrometeter tests are among the methods that were considered to estimate the strength of the rock mass (Wagner and Schümann, 1971; Wijk, 1989; von Unrug, 1999) with some degree of success. However, these methods give non-continuous information about some points along the borehole. On the other hand, the scratch test was shown to be a relatively accurate and reliable approach (Roberto and Fabrice, 2002; Schei and Detournay, 2000). This method can be employed to provide continuous information about the strength of the rock mass surrounding the borehole by making a scratch on its surface. Yet, the existing scratch test devices are only capable of measuring the rock strength by scratching the side of a core sample of on a flat/sawn rock surface. These systems have not been used in boreholes for rock strength measurement.

To develop a suitable borehole scratch test device, the research team decided to initiate a series of testing on various drag-type tools to assess the magnitude of forces on various bits to be used for inscribing a scratch inside the borehole. For this purpose, a milling machine was recently acquired with which to conduct scratch tests (Figure 10a). In this series of experiments, different

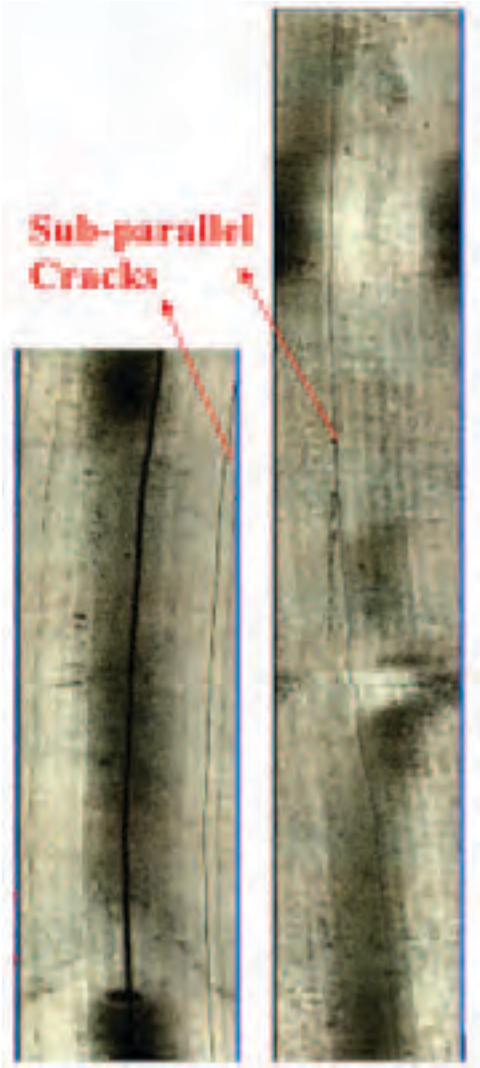



**Figure 6b. Detected sub-parallel cracks inside the sub-horizontal boreholes.**

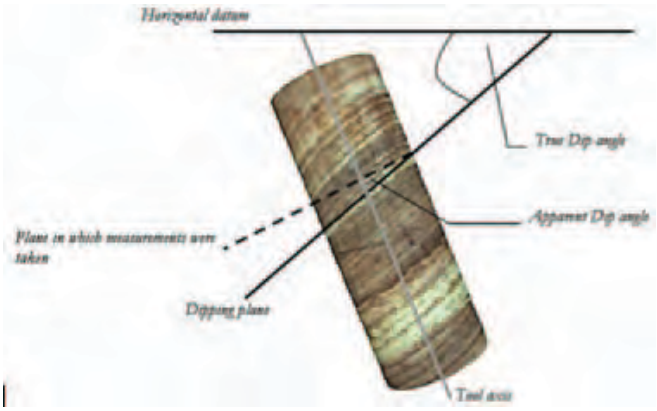



**Figure 7a. Local (probe) coordinate systems (WellCAD manual).**

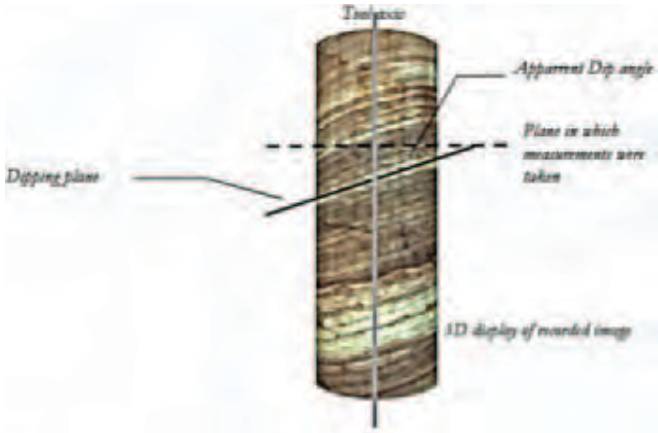



**Figure 7b. Global coordinate systems (WellCAD manual).**

rock types will be tested using various testing conditions including different bit geometry, cutting parameters such as depth of penetration, and rock surface curvature. The rock samples will be cored in order to measure their strength and other properties via standard geomechanics lab tests such as the Uniaxial Compressive Strength (UCS) test.

The cored blocks can then be used and cut for running scratch tests inside the hole with designated curvature and the sample flat surface as schematically shown in Figure 10b. The process for preparation of rock samples and schematic geometry of bits are presented in Figure 10b and Figure 10c, respectively. The milling machine will feature sensitive load cells and a 3-D positioning system to measure the normal and drag forces while performing the scratches. These tests will help us to estimate the cutting forces needed to inscribe a groove on the rock by the scratchers inside the borehole, as well as selecting the suitable geometry of the bit to be used. The information will be used for final design of the borehole scratcher probe.

## CONCLUSION

The field experiments showed that the images generated by the standard optical televiewers for downward and sub-horizontal boreholes can be used to evaluate the joint conditions in a borehole; they are fairly convenient to operate under these conditions. However, these devices are not suitable for performance in upward logging due to the basic design of the system and the procedures used for tracking borehole depth. Weight and size of the typical down-hole probes makes it very difficult to have a smooth operation in underground applications. Therefore, the Slim Borehole Scanner (SBS) is considered as an alternative and will be evaluated for probing smaller diameter upward holes drilled for roof bolting. Further studies are also underway to develop a borehole scratch testing device for use in the underground environment to estimate rock strength. The combination of rock strength and joint conditions will allow for the development of rock mass classifications that could be used for 3-D imaging of the ground conditions around an underground opening as well as hazard maps for the roof.

**Table 1. Depth, azimuth and dip of the detected structures in local, true coordinate system and true north.**

| Apparent Azimuth and Dip | | | | | True Azimuth and Dip | | | True North | |
|---|---|---|---|---|---|---|---|---|---|
| # | BH Name | Depth (m) | Azimuth | Dip | Depth (m) | Azimuth | Dip | Azimuth | Dip |
| 1 | GR-BH-C-720 | 2.65 | 357.90 | 65.70 | 2.65 | 158.70 | 23.90 | 147.80 | 23.90 |
| 2 | | 4.00 | 358.90 | 65.40 | 4.00 | 158.80 | 25.00 | 147.90 | 25.00 |
| 3 | GR-BH-RM-720 | 4.08 | 358.60 | 61.60 | 4.08 | 158.80 | 27.00 | 147.90 | 27.00 |

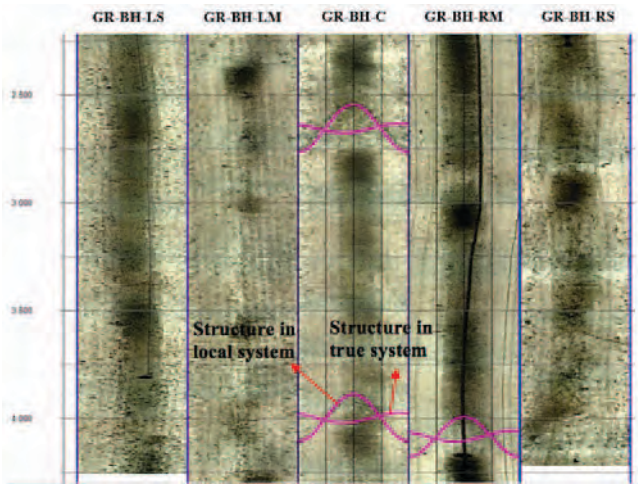



**Figure 8. Structures detected and the changes of the structure shapes after coordinate system correction.**

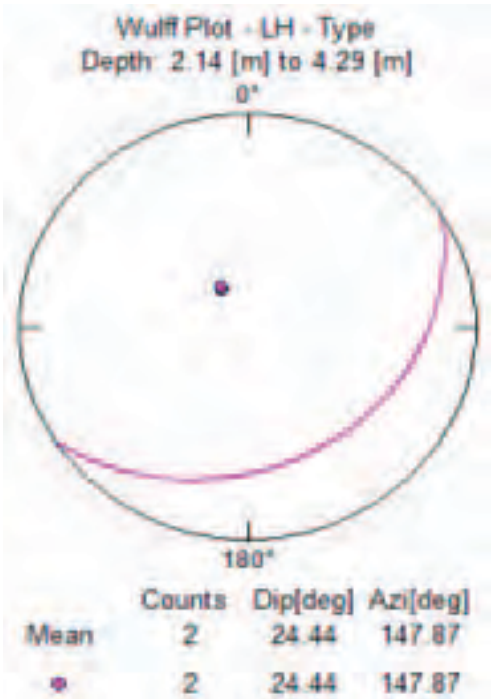



**Figure 9a. Wolff (angle-equal/lower hemisphere) plots for the center borehole.**

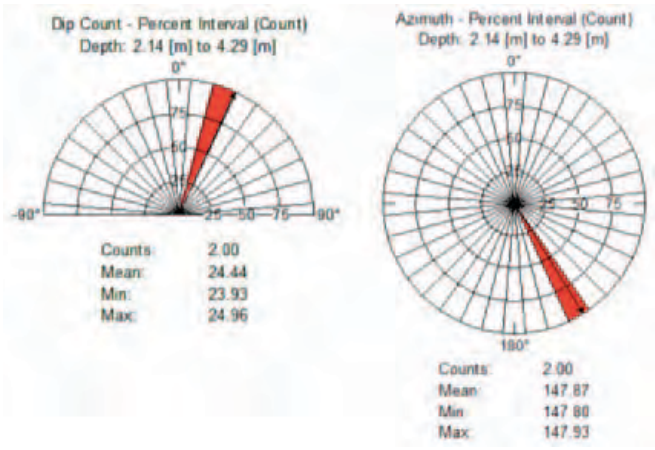



**Figure 9b. Rosette plots for the center borehole.**



**Figure 10a. Milling machine for conduction of scratch tests.**




**Figure 10b. Schematic process for sample preparation.**



**Figure 10c. Varied geometry of bits including disc shape and bits with sharp, round and rectangular tips.**

**AKNOWLEDGEMENT**

The National Institute for Occupational Safety and Health (NIOSH) ground control group under the contract No. 211-2011-41138 has funded this project. The authors would like to express their gratitude for this funding and acknowledge the active support of NIOSH project manager Mr. John Ellenberger in this study. Also, we want to acknowledge the support and help of Dr. Kamini Singha, associate professor at the Colorado School of Mines (CSM), as well as Casey Rhodes, John Miller and Jim Winfield at Graymont, Jay Elkin at Wampum Hardware Co. and James Murphy, graduate student at Penn State University.

**REFERENCES**

Bae, D., Kim, K., Koh, Y., Kim, J. (2011). "Characterization of Joint Roughness in Granite by Applying the Scan Circle Technique to Images from a Borehole Televiewer." *Rock Mechanics and Rock Engineering* 44 (4): 497–504.

Bahrampour, S., Rostami, J., Naeimipour, A., Collins, C., Kahraman, S. (2013). "Instrumentation of a Roof Bolter Machine for Void Detection and Rock Characterization." *In: Proceedings of the 32th International Conference on Ground Control in Mining.* Morgantown, WV.

DMT (2013). "DMT SlimBoreholeScanner." In: DMT SlimBoreholeScanner. [http://www.dmt.de/fileadmin/PDF/Broschueren/Produkte/DMT_SlimBoreholeScanner_1109.pdf].

Ellenberger, J. (2009). "A Roof Quality Index for Stone Mines Using Borescope Logging." *In: 28th International Conference on Ground Control in Mining* (Class I): Morgantown, WV, 143–148.

Gu, Q. (2003). "Geological Mapping of Entry Roof in Mines." *Dissertation* (PhD in Mining Engineering), West Virginia University, 190.

Itakura, K., Sato, K., Deguchi, G., Ichihara, Y., Matsumoto H. (2001). "Visualization of geostructure by mechanical data logging of rockbolt drilling and its accuracy." *In: Proceedings of the 20th International Conference on Ground Control in Mining.* Morgantown, WV: West Virginia University, 184–190.

Itakura, K., Goto, T., Yoshida, Y., Tomita, S., Iguchi, S., Ichihara, Y., Mastalir, P. (2008). "Portable intelligent drilling machine for visualizing roof-rock geostructure." *In: Proceedings of the Rock Bolting in Mining & Injection Technology and Roadway Support Systems Conference*. Aachen, Germany, 597–609.

Lahti, M. (2004). "Digital borehole imaging of the boreholes KR6, KR8 continuation, KR19, KR19b KR20, KR20b, KR21, KR22, KR22b, KR23, KR23b and KR24 at Olkiluoto during autumn 2003." Posiva Oy, Working report 2004-27

Oyler, D.C., Mark, C., Molinda, G.M. (2010). "In situ estimation of roof rock strength using sonic logging." *International Journal of Coal Geology* 83: 484–490.

Mark, Ch., Molinda, G. M., Barton, T. M. (2002). "NEW DEVELOPMENTS WITH THE COAL MINE ROOF RATING." *In: Proceedings of the 21st International Conference on Ground Control in Mining*. Morgantown, WV.

Mount Sopris (2013). "Q40 OBI-1000." In: Q40 OBI-1000 Optical Televiewer. [http://mountsopris.com/products/downhole-probes/item/q40obi-1000?category_id=12]

Roberto, S. R., Jørn, S. T., Fabrice, D. (2002). "Continuous scratch testing on core allows effective calibration of log-derived mechanical properties for use in sanding prediction evaluation." *In: SPE/ISRM Rock Mechanics Conference*.

Rostami, J., Naeimipour, A., Bahrampour, S., Dogruoz, C. (2014). "Logging of Roof Bolt Holes for Ground Characterization in Underground Construction." In: *World Tunnel Congress (WTC),* Brazil.

Schei, G., Fjær, E., Detournay E. (2000). "The Scratch Test: An Attractive Technique for Determining Strength and Elastic Properties of Sedimentary Rocks." In: *SPE Annual Technical.*

Tang, X. (2006). "Development of Real-Time Roof Geology Detection System Using Drilling Parameters During Roof Bolting Operation." *Dissertation* (PhD in Dept. of Mining Engineering), West Virginia University, 357.

Unrug, K. F. (1999). "Characterization of rock strength and jointing 'in situ'." In: *The 37th U.S. Symposium on Rock Mechanics (USRMS)*, Vail, CO.

WellCAD Manual, Book 3- Image and Structure, V.2011.10.18

Zhou, B., Fraser, S., Borsaru, M., Aizawa, T., Sliwa, R., Hashimoto, T. (2005). "New Approaches for Rock Strength Estimation from Geophysical Logs." In: *Proceedings of Bowen Basin Symposium- The future for coal - Fuel for thought*. Yeppoon, Queensland, Australia: GSA Coal Geology Group, 151-164.

# Rock Characterization Using Time - Series Classification Algorithms

**Soheil Bahrampour**, Ph.D. Student
**Jamal Rostami**, Associate Professor
**Ali Naeimipour**, Ph.D. Student
Pennsylvania State University
State College, PA

**Craig Collins**, Senior Engineer
J.H. Fletcher
huntington, WV

## ABSTRACT

Development of measurement while drilling (MWD) systems for ground control applications in mining applications has recently been an active research topic. The main goal is to utilize the drilling information for characterizing the ground condition. Such characterization is the key to the accurate and efficient mapping of hazards and proper planning of ground support. However, most of the existing drilling units and measurement while drilling systems are mainly developed for joints and voids detection, and much less research is done to estimate rock strength. This paper focuses on rock classification based on estimated strength from the drilling data. For this purpose, data from J.H. Fletcher roof bolters instrumented with the vibration and acoustic sensors as well as torque, thrust, penetration rate, RPM and position signals is used. All the available data was utilized for rock classification using pattern recognition algorithms. The algorithms were developed based on data from drilling, and into three different rock types. The classification is performed using a simple feature extraction algorithm with a well-known pattern recognition algorithm. The results demonstrate the suitability of the proposed algorithms in identifying the rock types based on their strength properties, which can be adopted in measurement while drilling systems.

## INTRODUCTION

The applications of rock bolts have become a standard part of ground support in mining and tunneling operations due to their effectiveness in reinforcing the ground and ease of installation. Effective design and application of rock bolts depends on the correct mapping of geological conditions, including identification of discontinuities and rock strength, as they tend to vary, even within a short distance (Gu, 2003). Many drilling parameters including thrust, torque, penetration rate and drill revolutions are being collected for utilization to estimate the location of joints and discontinuities as well as rock strength for evaluation of ground conditions (Peng, 2003). A series of studies have demonstrated the potential for analyzing drilling parameters from roof bolters to estimate rock properties and to identify discontinuities (Itakura et al., 2001; Itakura et al., 2008).

Among early attempts for analyzing the drilling parameters to characterize the rock, also known as measurement while drilling (MWD) systems, Signer and King (1992) and King et al. (1993) proposed an unsupervised learning technique as an expert system which could interface with the instrumented roof bolter to determine geological features. The system could identify the significant roof features in relation to the support parameters and suggest improvements to the support design. The system could measure the drilling parameters and calculate the specific energy of drilling as an indicator of the type of rock being drilled. This system was successfully tested in an underground coal mine (Frizzell et al., 1992). Hoffman (1994) proposed an integration of the roof mapping with the control units and added vibration analysis to increase the safety of roof bolting in underground coal mines. An attempt for application of pattern recognition algorithms, such as neural networks for classification of mine roof strata in terms of relative strength, was proposed by Utt et al. (2002). LaBelle et al. (2000) and LaBelle (2001) also studied neural networks for rock strata classification of five layers of concrete using a portable hydraulic-powered coal mine roof bolter. Preliminary field experiments were also performed with the hand-labeled data, and their algorithm was unable to correctly classify coal and shale mainly due to limited training samples.

Luo et al. (2002) proposed a systematic approach for estimating rock strengths using the acquired drilling parameters in roof bolting operations. The mathematical model developed based on this approach took into consideration several factors including bit geometry and bit wear that rarely were previously considered. The sensitivity analysis was performed, however, only with simulations. Both the bit geometry and the drilling operating parameters were important factors in the determination of the thrust and torque required in the drilling process. Bit geometry was used for quantitative evaluation of the effects of bit wear on the drilling performance. More recently, Li and Itakura (2011a, 2011b) proposed a model to relate rock properties to bit shapes and drilling parameters. In this approach, the drilling process is divided into successive cycles, where each cycle includes two motions of feed and cutting. According to the model, drilling torque consists of four components generated from cutting, friction, feed and idle running. It was shown that the first three components are all proportional

to the uniaxial compressive strength (UCS) when the penetration rate is kept constant. Their field experiments suggested that UCS is correlated with the torque and penetration rate. The proposed model and equations indicate the possibility of eliminating useless components of cutting forces when investigating the relation between mechanical data and physical properties of rocks. More recent studies also confirm that UCS of rocks can be estimated using specific energy generated by the model extracted from regression analysis (Li and Itakura, 2012).

It was shown in Mirable (2003) and Mirable et al. (2004) that torque-thrust ratio and shear stress - normal stress ratio are indicative features in distinguishing hard rocks from soft rocks. In a similar studies using J.H. Fletcher & Co.'s HDDR dual-head roof bolter, extensive experiments demonstrated that the magnitude of feed pressure is also another descriptive variable among the drilling parameters to estimate the strength of the rock because of its high correlation with the penetration rate and the RPM (Collins et al., 2004; Peng et al., 2005a; Peng et al., 2005b; Tang, 2006). Their algorithm estimates the location of the interface between different rock layers based on the observed trend in data sets from different rock strength groups.

In this paper, a time-series classification algorithm is used to address the problem of rock classification using drilling information. The data are collected using a drilling unit at the J.H. Fletcher facility (Bahrampour et al., 2013). The drilling unit is equipped with vibration and acoustic sensors. For rock strength classification, the time-series data such as feed pressure, rotation pressure and penetration rate, as well as the vibration and acoustic signals, are utilized. Also, specific energy and torque thrust ratio are estimated from the measurements and are considered in this study. A set of statistical parameters and features are extracted from these time-series, which are then fed into a pattern recognition algorithm. The use of a support vector machine (SVM) is proposed to efficiently classify the time-series data. The proposed algorithm is evaluated on drilling data collected by drilling into three different rocks embedded within concrete blocks.

## OVERVIEW OF FLETCHER ROOF MAPPING SYSTEM AND DATA COLLECTION

J. H. Fletcher & Co. has developed the Fletcher Information Display System, which uses a programmable logic controller (PLC) to monitor drilling operations. This system features a drill control unit (DCU) to automate the cycle of drilling and bolting for safety and productivity reasons (Anderson and Prosser, 2007). The DCU processes the drilling parameters including torque, thrust, rotation rate and position, along with vacuum or water pressure used for flushing, bit breakage or bending of the drill by controlling the drilling parameters without deteriorating the optimum drilling operation. Several modifications have been made to improve the accuracy of measuring bit position and torque (Gu, 2003). The software was modified to communicate with the DCU to display the information from four separate drill holes side-by-side so that trends could be easily observed in real time. These graphs can show the material hardness and can display the location of voids or other discontinuities in the mine roof structure. Also, rotation events like stalls and water events, which may indicate that the drill steel is being plugged with soft material, are marked with colored lines and letters (Anderson and Prosser, 2007). Figure 1 shows the recent J. H. Fletcher & Co. instrumented roof bolter along with the new vibration and acoustic sensors installed on the rig. Bahrampour et al (2013) have discussed how vibration and acoustic signals can be used for void detection. Data from these sensors are also monitored to provide additional information for rock strength classifications.



**Figure 1. J.H. Fletcher drill unit with the newly added vibration and acoustic sensors.**

Rock characterization is performed on three types of rocks collected from different mines in Pennsylvania. Rock types include shale, sandy shale and limestone. The rock samples were embedded within a concrete block, as shown in Figure 2. This forms a "sandwich" of rocks, which facilitates comparison of drilling parameters when different types of the rocks are drilled in one hole. Overall, three blocks were drilled with different combinations of rocks. To correlate the drilling parameters with the rock types, each drilled hole is bore-scoped and the positions of the different layers are marked (Figure 3).

## TIME-SERIES CLASSIFICATION FOR ROCK CHARACTERIZATION

In this section a time-series classification algorithm proposed for real-time rock characterization is discussed. Feed pressure, rotation pressure, penetration rate, acoustic and vibration signals are utilized in conjunction with the time series classification algorithm to identify various rock types. Samples of time-series data for drilling a hole in a composite sample, consisting of two shale and one limestone rock embedded in a concrete block, is shown in Figure 4. An estimated strength of the different layers of the block is also shown in the figure, which is obtained from rock mechanics tests on core samples from each rock type. The figure shows a clear correlation between the rock strength and the drilling signals. For example, it is seen that higher feed pressure is required to drill the limestone compared to the shale if the RPM and feed rate is fixed. Feed pressure data is less variable during drilling of the shale




**Figure 2. Rock samples are casted in concrete block, which form a "sandwich" of rocks.**

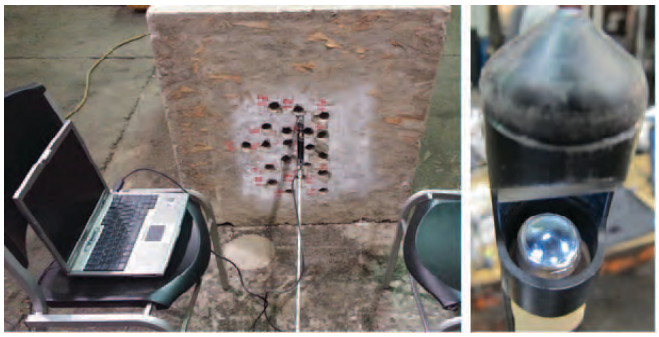


**Figure 3. Bore-scoping of the drilled holes to identify the positions of different rock layers.**

samples compared to relatively higher variability while drilling (non-homogeneous) concrete. In this paper, the time-series is classified into three different classes of shale, limestone and concrete. The shale samples have the lowest strength in these experiments and are labeled as class 1. Concrete has the relatively higher strength compared to shale and is labeled as class 2. Finally, limestone is the strongest type of the rocks in our experiments, and is labeled as class 3.

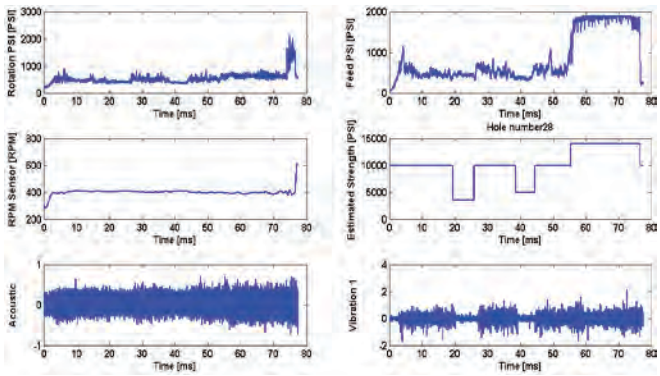



**Figure 4. Samples time-series data obtained by drilling into a sandwich of rocks consists of three layers of rocks embedded in a concrete block.**

The time-series are analyzed in a series of windows of one second in length, where the consecutive windows have 50% overlap. For each window, a set of simple statistical features are obtained, which are then fed into the classification algorithm. The feed pressure and rotation pressure signals are low-pass filtered before the feature extraction. The specific energy of the drilling (Teale, 1965) and scaled torque-thrust ratio have also been calculated. These parameters have been shown to be strongly correlated to the strength of the rock. The torque and thrust values have been estimated from the rotation pressure and feed pressure signals, respectively. In other words, the ratio between the rotation pressure and feed pressure is used as an estimation of torque thrust ratio; therefore, the rock strength classification is performed using the filtered feed pressure and rotation pressure, and their ratios in addition to the specific energy, acoustic and vibration signals. For each signal, in each window of one-second data, mean, variance and kurtosis are calculated as features. Therefore, in the feature extraction step, a total of 18 features are extracted for each window. Some of the calculated features are demonstrated in Figure 5. These features correspond to the data shown in Figure 4. The ground-truth label for each window is also shown in this figure. Note that each window is labeled based on the bore-scoped measurement of the middle sample.

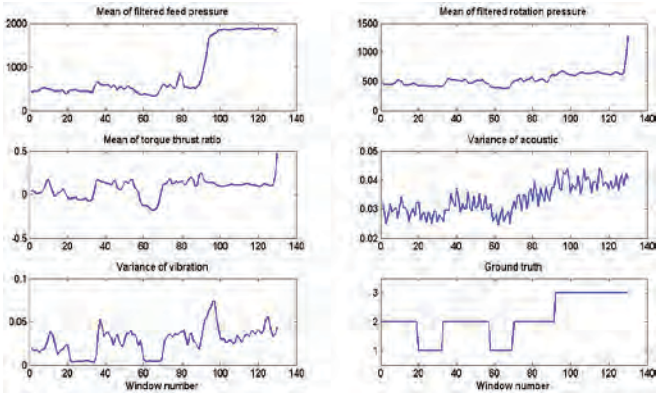



**Figure 5. Some of the features that are used for rock-strength classification. The ground-truth label for each window is also shown.**

For classifying each window, different pattern recognition algorithms can be utilized. In this paper, support vector machine (SVM), which is a state-of-the-art pattern recognition algorithm, is utilized. SVM is a binary classification algorithm which finds an optimal separating hyper-plane, represented by $w \varepsilon R^n$ where n is the dimension of the feature vector to classify the training samples from two different classes, as depicted in Figure 6. The new test sample, represented by a feature vector x, can then be classified into one of the two classes by finding the sign of $w^T x$. To use SVM for our multi-class classification problem, a one-versus-all setting is utilized in which a separate SVM classifier is trained for each class and learns a hyper-plan that separates each class of the data from the rest of training data. The test sample is then evaluated by all the classifiers and the probabilities of it belonging to different classes are calculated. The label of the test sample is assigned as the class with the highest probability. For a detailed description of the SVM algorithm, please refer to work by Bishop (2006). It should be noted that all the calculated features are standardized using the training data to have similar range of values before being fed into the classifier.

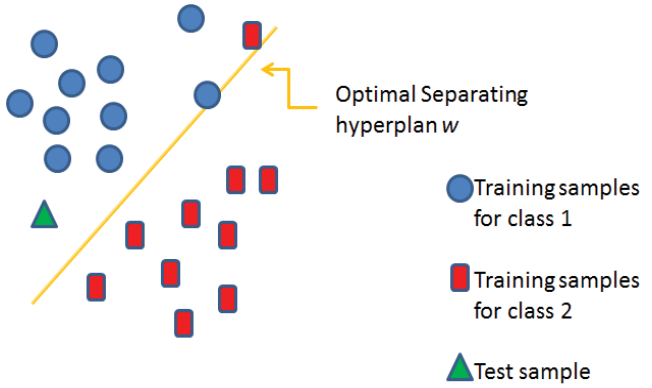



**Figure 6. Schematic figure for the SVM classifier.**

## CLASSIFICATION RESULTS AND DISCUSSIONS

This section discusses the results of rock strength classification obtained using the drilling data collected from 65 tests. Each test consists of drilling into different layers of rock and concrete, as discussed before. The data is randomly split into training and test sets, where the training portion consists of 45 drilling tests and the rest of the data is used as test data. The support vector machines (SVM) are trained using only the training data and the performance of the classification is reported on test data.

Figure 7 shows sample probabilities generated by the SVM classifiers in a drilling test. The drilling starts with a concrete layer and, as drilling progress, it consecutively reaches shale, concrete, shale, concrete, and limestone layers. These layers are correctly identified by the proposed classification algorithm. Each window is classified as the class with the highest probability. Figure 8 compares the predicted labels with the ground truth and, as shown, the algorithm successfully identified the different layers. There are some oscillations in the predicted label, which mostly appeared at the interface between the different layers.

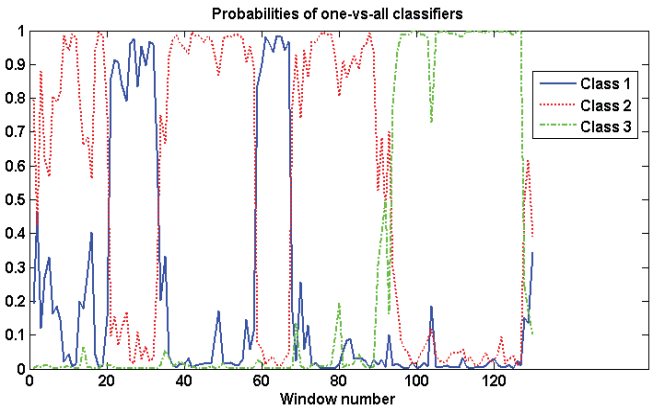



**Figure 7. Probabilities of a given window of the data belonging to the different classes, as calculated by the SVM classifiers.**

It should be noted that SVMs classify each window of time-series independent of other windows. To reduce the oscillations, and also utilize the information carried by the consecutive windows, a simple post-processing step is utilized. In this step, the assigned label for each window is compared with its adjacent windows and a majority voting procedure is used to predict the class. While a more advanced tool, such as Kalman filtering, can also be used for this post-processing step, it is observed that this simple post-processing is still efficient in reducing the oscillations of the predicted class (as shown in Figure 8). Table 1 summarizes the correct classification rates obtained on the test data. The algorithms result in high correct classification rate, even without using the acoustic and vibration sensors. This demonstrates that the proposed algorithm can be readily utilized within the framework of the existing roof-mapping systems (without adding instruments) for a relatively accurate rock characterization. It should be noted that, for the vibration and acoustic signals, the feature extraction is applied on the raw data. It is envisioned that using signal processing tools to pre-process these signals can further improve the classification performance, which is a topic for future research.

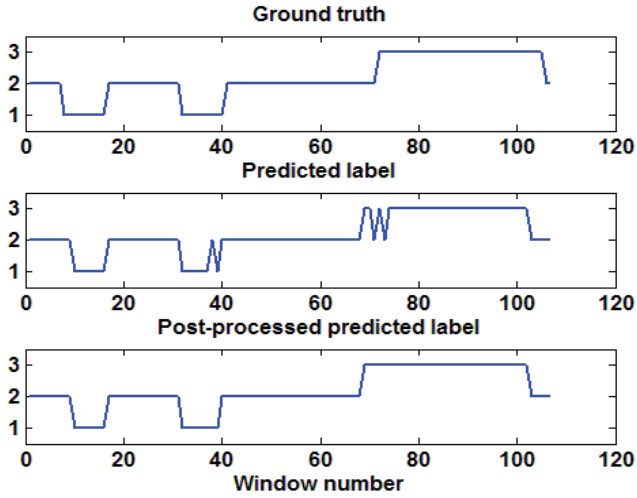



**Figure 8. Ground truth and the predicted labels generated on a drilling test into a sandwich of rocks.**

**Table 1. Correct classification rates obtained on the test data.**

| Correct classification rates | Without post-processing step | With post-processing step |
|---|---|---|
| Without acoustic and vibration | 85.56% | 85.69% |
| All sensors | 86.35% | **87.46%** |

## CONCLUSIONS AND FUTURE WORKS

The issue of estimating rock strength using drilling information was the focus of this study. To solve this problem, a time-series classification is proposed by using a pattern recognition algorithm. This algorithm uses simple, and yet efficient, statistical features extracted from the time-series data. The proposed algorithm was tested using data collected at the J. H. Fletcher facility by drilling into soft and hard rocks which are embedded in concrete blocks. The results suggest that the proposed algorithms can be efficiently used for real-time rock strength classification within the framework of the MWD system. Testing the algorithm on filed data from different mines as well as finding more discriminative features are among the topics for future research. Also, while the current study has focused on classification of rock strength in a known series of strata, additional emphasis will be placed on the estimation of rock strength in future steps. This allows the rock strength estimated from drilling parameters to be used in rock mass classification system and evaluation of ground support measures.

**REFRENCES**


Anderson, R. and Prosser, L.J. (2007). "Improving the Capability for Real Time Assessment of Roof Conditions Through Intelligent Roof Bolt Drilling Operations." *Proc. 26th Int. Conf. Ground Control in Mining*, July 31 - August 2.

Bahrampour S., Rostami J., Naeimipour A., Collins C.M. (2013). "Field Testing of a Real-Time Roof Mapping Drilling Display System in a Limestone Mine." *Proc. 32nd Int. Conf. on Ground Control in Mining*, West Virginia University, August 2013.

Bishop, Christopher M. *Pattern recognition and machine learning*. Vol. 1. New York: Springer, 2006.

Collins C.M., Wilson G., Tang D. and Peng S. (2004). "Field Testing of a Real Time Roof Mapping Drilling Display System in a Limestone Mine." *Proc. 23rd Int. Conf. on Ground Control in Mining, West Virginia University, Dept. of Mining Engineering*, August 3-5, 2004.

Frizzell, E.M., Howie, W.L. and Smelser, T.W. (1992). "Automated Geophysical Sensing and Data Processing Roof Drill." *Proc. 23rd International Symposium on the Application of Computers and Operations Research in the Minerals Industries (APCOM)*, Arizona, USA, 297-305.

Gu, Q., (2003). "Geological Mapping of Entry Roof in Mines." PhD Dissertation, Dept. of Mining Engineering, West Virginia University.

Hoffman, M.P. (1994). "Computer-Based Monitoring and Control of a Mast-Type Roof Drill." *SME Annual Meeting, Albuquerque, New Mexico*, February 14-17.

Itakura, K., Sato, K., Deguchi, G., Ichihara, Y. and Matsumoto, H. (2001). "Visualization of Geostructure by Mechanical Data Logging of Rockbolt Drilling and Its Accuracy." *Proceedings, 20th International Conference on Ground Control in Mining*: August 7-9, Morgantown, WV, USA. 184-190.

Itakura, K., Goto, T., Yoshida, Y., Tomita, S., Iguchi, S., Ichihara, Y. and Mastalir, P. (2008). "Portable Intelligent Drilling Machine for Visualizing Roof-rock Geostructure." *Proc. Aachen Int. Mining Symposium*, 14-15 May, Aachen, 597-609.

King, R.L., Hicks, M.A. and Signer, S.P. (1993). "Using Unsupervised Learning for Feature Detection in a Coal Mine Roof." *Engineering Applications of Artificial Intelligence*. (6): 6, 565-573.

LaBelle, D., Bares J. and Nourbakhsh I. (2000). "Material classification by drilling." *Presented at the 17th International Symposium on Automation and Robotics Construction*, September, in Taipei, Taiwan.

LaBelle, D. (2001). "Lithological Classification by Drilling." Thesis Proposal, Robotics Institute, Carnegie Mellon University, Pittsburgh, USA.

Li, Z. and Itakura, K. (2011a). "Fundamental Research on Drilling Processes Using Drag Bits." *Advanced Materials Research* 243-249: 3612-3617.

Li, Z. and Itakura, K. (2011b). "Prediction of Rock Strength from Mechanical Data of Drilling." *22nd World Mining Congress & Expo*, Eskikaya, S. (Ed.), 11-16 September, 407-412.

Li, Z. and Itakura, K. (2012). "An analytical drilling model of drag bits for evaluation of rock strength." *Soils and Foundations* 52(2): 216–227.

Luo, Y., Peng, S.S., Mirabile, B., Finfinger, G. and Wilson, G. (2002). "Estimating Rock Strengths Using Drilling Parameters During Roof Bolting Operations - Progress Report." *21st International Conference on Ground Control in Mining: Proceedings*, August 6-8, Morgantown, WV, USA, 288-293.

Mirabile, B., (2003). "Geologic Features Prediction Using Roof Bolter Drilling Parameters." Master's Thesis, Department of Mining Engineering, West Virginia University.

Mirabile, B., Peng, S. S., Luo, Y., Tang, D. X. (2004). "Roof Bolter Drilling Parameters as a Tool for Strata Prediction." *2004 SME Annual Meeting*, Denver, Colorado.

Peng, S.S., Tang, D.X., Mirabile, B., Luo, Y., Wilson, G., (2003). "Mine Roof Geology Information System (MRGIS)." *Proceedings, 22nd International Conference on Ground Control in Mining*, August 5-7, Morgantown, WV, edited by Syd S. Peng et al., 127-135.

Peng, S.S., Tang, D., Sasaoka, T., Luo, Y., Finfinger, G. and Wilson, G. (2005a). "A Method for Quantitative Void / Fracture Detection and Estimation of Rock Strength for Underground Mine Roof." *24th International Conference on Ground Control in Mining: Proceedings*, August 2-4, WV, USA. 187-195.

Peng, S.S., Sasaoka, T., Tang, D., Luo, Y., and Wilson, G. (2005b). "Mine Roof Geology Information System - A method for Quantitative Void/Fracture Detection and Estimation of Rock Strength for Underground Mine." *Coal Age*, May, 44-49.

Signer, S.P. and King, R. (1992). "Evaluation of Coal Mine Roof Supports Using Artificial Intelligence." *23rd International Symposium 1992 - Application of Computers and Operations Research*, 889-985.

Tang, X. (2006). "Development of Real Time Roof Geology Detection System Using Drilling Parameters During Roof Bolting Operation. PhD Dissertation, Dept. of Mining Engineering, West Virginia University.

Teale, R. "The concept of specific energy in rock drilling." *International Journal of Rock Mechanics and Mining Sciences & Geomechanics Abstracts*. (2):1. Pergamon, 1965.

Utt, W.K., Miller G.G., Howie, W.L. and Woodward, C.C. (2002). "Drill Monitor with Strata Strength Classification in Near-Real Time." *The National Institute for Occupational Safety and Health (NIOSH), USA, Report of Investigations 9658*. 14.

# Estimating Coal Strength Based on Historical Laboratory Tests and Geomechanics Classification

**Andre Zingano**, Senior Lecturer
Dept. of Mining Engineering
University Federal of Rio Grande Do Sul
Porto Alegre, Brazil

**Roger Cabral**, Mine Engineer
Inspection Division
Departamento Nacional Da Produção Mineral
Brasilia, Brazil

**Selmar Oliveira**, Acting Deputy Branch Chief
Inspection Division
Departamento Nacional Da Produção Mineral
Florianopolis, Brazil

**Sarah Guazelli**, Ph.D. Student & Mining Engineer
Mining Engineering Department
Univ Fed Rio Grande Do Sul
Porto Alegre, Brazil

**Jair Koppe**, Professor
Mining Engineering Department
Univ Fed Rio Grande Do Sul
Porto Alegre, Brazil

## ABSTRACT

The coal seam strength and the failure criteria that represent the behavior of the coal seam are very important for mine section and pillar design. Additionally, mine section and pillar design take into account roof and floor layers, which form the roof-pillar-floor system. Therefore, underground ground control design begins, most importantly, with rock mass characterization. Another issue is the distribution or behavior of the coal seam strength for the whole mine area. Sometimes, the coal seam strength is assumed to be the same for an entire area, but this is not true because the coal seam is heterogenic and anisotropic, and also the coal strength is affected by faults and spacing between fractures. The objective of this paper is to demonstrate the use of the methodology for geomechanics characterization to determine the strength for the Bonito coal seam, and discuss the coal seam strength distribution around the entire mine area. The intact coal strength was determined by laboratory tests that were completed during the last 17 years, including triaxial and uniaxial strength tests. It was noted that there is a strong correlation between all laboratory strength tests with 90% confidence interval. The explanation for this coal seam strength variation is the presence of the discontinuities and their variation in quantity and quality at each location in the mine area, because the coal seam rock classification and its behavior will be affected by the quantity and quality of fractures.

Key words: coal strength, rock mass classification, failure criteria.

## INTRODUCTION

The coal mining companies in Santa Catarina State use the room-and-pillar mining method due to some features of the coal seam, such as the shallow depth of the coal seam, but the primary reason is that subsidence has not been allowed since the 1980s. There are two mineable coal seams: (i) Barro Branco and (ii) Bonito seam. Both seams are almost flat and cut by faults. The faults cause relative movement between blocks, which changes the depth of the coal seam in each block. These tectonic forces also cause changes in the coal seam strength due to fractures and joints.

The coal seam strength and the failure criteria that represents the behavior of the coal seam are very important for mine section and pillar design. Additionally, mine section and pillar design take into account roof and floor layers, which will form the roof-pillar-floor system. Therefore, underground ground control design begins, most importantly, with rock mass characterization. The coal seam geomechanics characterization takes into account the description of the core from drilling in terms of RQD, quantity and quality of the discontinuity, and laboratory tests, mainly uniaxial and triaxial compressive strength for intact rock. Based on the geomechanics description, the rock mass classification can be applied using GSI, RMR and CMRR rock mass classification approaches for the coal seam, and roof and floor layers. After that, the failure criteria using the Hoek and Brown approach was considered to determine the rock mass mechanics properties (friction, cohesion, and strength) for the coal seam. Another issue is the distribution or behavior of the coal seam strength for the whole mine area. Sometimes, the same coal seam strength is assumed for an entire area, but this is not true because the coal seam is heterogenic and anisotropic, and also the coal strength is affected by faults and spacing between fractures.

Despite the fact that coal mining in Brazil has existed since the beginning of the last century, some geomechanics characteristics still need some study, such as the influence of the discontinuities on the coal seam strength. The objective of this paper is to demonstrate the use of the methodology for geomechanics characterization to determine the strength for the Bonito coal seam, and discuss the coal seam strength distribution around the entire mine area.

Over approximately the last 20 years, a lot of geomechanics characterization for different purposes has been done on the Barro Branco and Bonito coal seams. However, the primary purpose was to determine the coal strength and pillar design for both coal seams. In-situ tests and laboratory tests were used to estimate the seam strength (Gonzatti *et al*., 1993; Zingano, 2002; Zingano *et al.,* 2013).

At the end of the 1990s, the Bonito coal seam began to be mined at the Treviso and Lauro Muller counties area, and included five underground room-and-pillar mines. Many borehole samples from these mines were tested and geomechanics descriptions were done during these last years. Uniaxial and triaxial tests were performed to complete the geomechanics description of the borehole samples,

including quantity and quality of the discontinuities (spacing, RQD, and roughness). The coal seam strength was estimated (or calculated) using the Hoek-Brown failure criteria (Hoek and Brown, 1997). Those laboratory tests were made in different laboratories and in different test machines (both servo-controlled and non-servo-controlled devices) which can cause problems due to lack of consistency.

## GEOMECHANICS CHARACTERIZATION

The geomechanics characterization is the approach to estimate the rock mass strength, which considers the rock sample strength (uniaxial and triaxial strength), the description of the discontinuities in terms of quantity (spacing and RQD) and quality (mainly roughness). The geomechanics classification (RMR, CMRR, and GSI) and the Hoek-Brown failure criteria (Hoek and Brown, 1997) were used to determine the coal seam strength. To obtain the parameters necessary to determine the RMR it is necessary to get the structural geology, water content and the strength of the rock. Laboratory tests (uniaxial and triaxial tests) estimate the strength of the rock, but the point load test could also be used.

### Geomechanics Description

The geomechanics descriptions are conducted using fresh borehole core samples. The geomechanics analysis assumes the range of 10-15m above (roof) and below (floor) of the coal seam, and the coal seam itself. The description takes into account four parameters: (i) geology rock type, (ii) discontinuity spacing, RQD, and quality of the fracture. The discontinuity spacing and RQD are determined for each geologic unit. The fracture spacing is the separation between fractures and is reported as he average spacing for the same rock layer. The quality of the fractures is mainly represented by the roughness, but the filling material and aperture (sometimes) can also influence the shear strength of the discontinuity.

### Laboratory Tests

After the geomechanics description, some samples were separated to prepare for uniaxial and triaxial compressive strength testing. The UCS is one of the parameters of the RMR and CMRR. The uniaxial and triaxial compressive tests follow the standard procedure from ASTM D 4543-85 and ASTM D 2664-95, respectively. Sample lengths are 2-2.5 times the diameter (5 cm, 2 in). The faces of the samples must be parallel and the loading rate during the test must be 1 MPa/sec. In addition, before the compressive tests, the sonic velocity can be determined (compressive and shear wave) to determine the dynamic elastic constants, considering the density of the rock.

The UCS defines the compressive strength of the rock, and the Young's modulus and Poisson's ratio. The depth of the coal seam dictates the confinement pressure of the triaxial test. The maximum depth of the Bonito coal seam is from 60 to 350m, and then the confinement pressure (s3) considered 2.5, 5.0 and 7.5MPa. The axial pressure (s1) is proportional to the confining pressure (s1 = *f*(s3)). The Mohr envelope estimates the values of cohesion (c) and friction angle (ϕ) for intact rock (Equations 1, 2, and 3).

$$\tau = c + \sigma_n tan\emptyset \tag{1}$$

$$\tau = \frac{1}{2}(\sigma_1 - \sigma_3)sin2\beta \tag{2}$$

$$\sigma_n = \frac{1}{2}(\sigma_1 + \sigma_3) + \frac{1}{2}(\sigma_1 - \sigma_3)cos2\beta \tag{3}$$

### Rock Classification

Most of the rock mass classifications consider the following parameters: (i) quantity of the discontinuities, by RQD and fracture spacing; (ii) quality of the discontinuities, mainly by roughness; (iii) rock strength; (iv) presence of water or sensitivity to water; and (v) stress and relation between fracture orientation and orientation of the excavation. All of this information is collected from the geomechanics description of the borehole or field survey.

The main purpose of the rock classification is to determine the influence of the fractures on the rock mass strength and the scale reduction of the strength from intact rock to the rock mass. It means that the scale reduction of the rock strength considered is the Hoek-Brown failure criteria (Hoek and Brown, 1997) to estimate the coal seam strength. The rock mass classification most used for coal seam characterization is the RMR – Rock Mass Ratio (Bieniawski, 1973), followed by CMRR – Coal Mine Roof Rating (Molinda and Mark, 1994). The GSI – Geological Strength Index (Hoek and Brown, 1997) considers the rock structure features and the quality of the discontinuities (Figure 1), but could be estimated by RMR minus five (RMR-5).

### Failure Criteria

The geomechanics behavior of the rock mass compared with the intact rock is different. In the intact rock there are not fractures or defects that could interfere with the strength. The laboratory tests are performed with intact rock. The rock mass presented many different defects, such as joints and bedding planes, which will cause the reduction of its strength (Bieniawski, 1976). The Hoek-Brown failure criteria for rock mass takes into account the rock mass classification to estimate the coal seam strength. Three main parameters are considered for the Hoek-Brown failure criteria: (i) intact rock strength ($s_{ci}$); (ii) the rock constant $m_b$; and (iii) the rock classification GSI – Geological Strength Index (Hoek, 1994; Hoek *et al.,* 1995). The Hoek-Brown failure criteria is the following equation (4), where *s* and *a* are constants related to the GSI.

$$\sigma_1^{'} = \sigma_3^{'} + \sigma_{ci}\left(m_b * \frac{\sigma_3{}'}{\sigma_{ci}} + s\right)^a \tag{4}$$

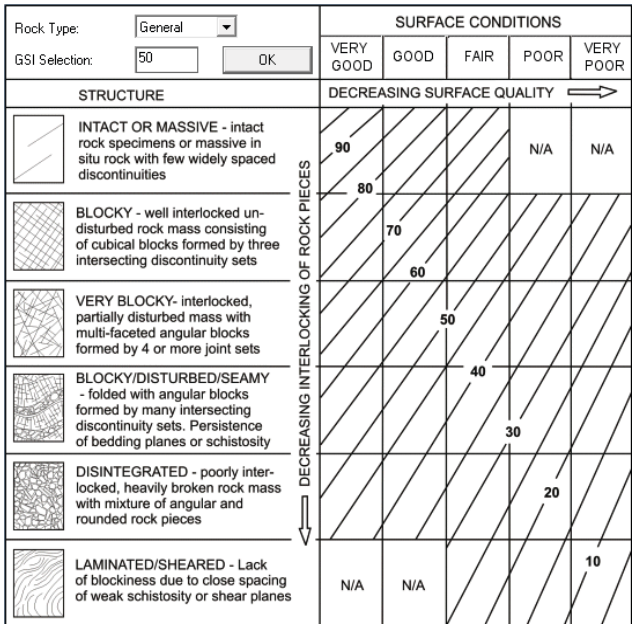



**Figure 1. Table to determine GSI; Geological Strength Index (Hoek and Brown, 1997).**

For GSI < 25:

$$s = 0 \tag{5}$$

$$a = 0.65 - \frac{GSI}{200} \tag{6}$$

For GSI > 25:

$$s = \exp\left(\frac{GSI - 100}{9}\right) \tag{7}$$

$$a = 0.5 \tag{8}$$

The constant $m_b$ can be determined using the equation (9)

$$m_b = m_i * \exp\left(\frac{GSI - 100}{28}\right) \tag{9}$$

The Hoek-Brown failure criteria for intact rock is (Equation 10), where $m_i$ is the constant for intact rock, which could be determined based on the triaxial test, and *s = 1* and *a = 0.5*

$$\sigma_1' = \sigma_3' + \sigma_{ci}\left(m_i * \frac{\sigma_3'}{\sigma_{ci}} + s\right)^a \tag{10}$$

Therefore, the rock mass strength ($s_{cm}'$) can be determined using equation (11) (Hoek and Brown, 2002), considering the constants a, s, and $m_b$ based on the GSI classification (see equations above).

$$\sigma_{cm}' = \sigma_{ci} * \frac{[m_b + 4s - a\,(m_b - 8s)\,]\left({}^{m_b}/_{4+s}\right)^{a-1}}{2\,(1+a)\,(2+a)} \tag{11}$$

**Estimating the Coal Seam Strength for the Bonito Coal Seam**

The methodology proposed above has been used for geomechanics characterization since 1997. The geomechanics description and classification determined for many boreholes from five different mines located in the region that includes the Treviso and Lauro Muller Counties (Figure 2). Table 1 shows the mines where the boreholes came from.

**Table 1. List of the boreholes considered on this study.**

| Mine | Num of drillholes from the Mine | Num of Species Tested |
|---|---|---|
| A | 1 | 10 |
| B | 3 | 13 |
| C | 2 | 6 |
| D | 6 | 26 |
| E | 3 | 17 |
| Total | 15 | 72 |

*Triaxial compressive test*

This study selected 72 triaxial compressive tests, which considered different confinement pressure (σ3) and different compressive frame equipment. The objective was to join together all these triaxial tests in the same database to study the behavior of the coal and estimate the uniaxial compressive strength.

The Figure 3 shows the chart that correlates the confined pressure (σ3) with axial pressure (σ1). The lines represent the linear correlation of the data set, and confidence of interval of 70%. It can be observed that there is a good correlation considering the very large range of time of the borehole drilling and different locations where the laboratory tests were done.




**Figure 2. Location of the underground coal mines at the region of Treviso and lauro muller counties.**

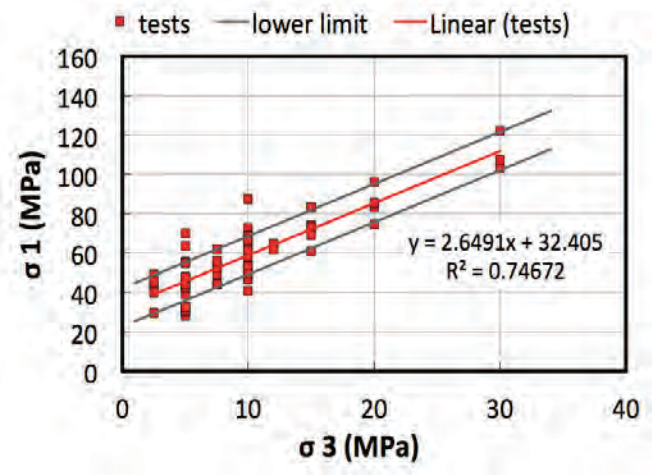



**Figure 3. Correlation chart for s3 and s1, including the interval of confidence of 70%.**

Figure 3 shows the confidence of interval of 70%, and the coefficient of correlation is 0.7, this is because the dispersion of the results for each confinement pressure. The variation of the axial pressure (σ1) is due to the heterogeneity and anisotropy of the coal seam in the area of study. Therefore, there is a strong correlation with compressive strength. The average uniaxial compressive strength for the coal of the Bonito seam is 32.4MPa, considering only the triaxial tests.

The dispersion of the results for each confinement pressure is also observed for uniaxial compressive test. Figure 4 shows the histogram for 15 uniaxial compressive tests for the Bonito coal seam. The uniaxial compressive strength represents the average UCS for each borehole. The total average compressive strength based on the uniaxial compressive tests is 30.9MPa, which is fairly close to the strength estimated from the triaxial test. The standard deviation is 8.41MPa, and the maximum and minimum values are 20 and 40Mpa, respectively.

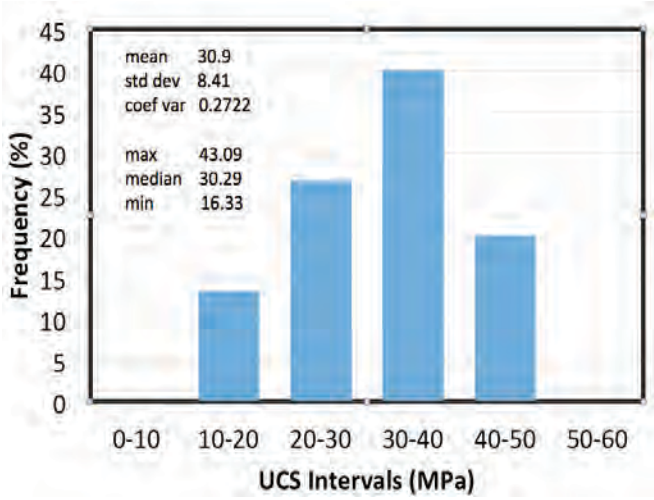



**Figure 4. Histogram of frequency of the uniaxial compressive strength test for the Bonito coal seam.**

*Rock classification and coal strength*

The results of compressive strength tests (triaxial and uniaxial tests) show a good correlation for the whole area of study. The question is that the coal seam strength could not have the same behavior because the presence of the discontinuities. Therefore, the GSI classification was correlated with the uniaxial strength for each borehole to try to understand and check if there is some relation between the UCS and coal seam strength with the GSI classification.

The RMR and GSI classification methods take into account the quality and quantity of the discontinuities at the cores of the boreholes. Table 2 shows the GSI classification for the 15 samples that were considered for uniaxial compressive tests.

Table 2 shows the GSI for intact rock, and GSI for the rock mass for each borehole. The coal seam strength for each borehole related to the GSI classification is shown at Table 2. The GSI for intact rock assumed a value of 100 because in the intact rock there is no discontinuity. Therefore, the average strength for intact rock was calculated and the Hoek-Brown failure criteria calculated the strength for intact coal. Once the GSI rate for rock mass was applied, the coal seam strength reduced due to the presence of the discontinuities and bedding planes. In this case, the GSI was calculated based on the RMR classification (RMR-5) for each borehole, and then the coal seam strength was calculated.

Figure 5 shows the strength of the coal rock and for the Bonito coal seam related to the GSI. It can be observed that there is a strong correlation between the strength for coal and seam and the

**Table 2. GSI classification of the coal seam compared with the uniaxial strength and coal seam strength.**

| Mine | Borehole | UCS | Intact Rock | | Rock Mass | |
|---|---|---|---|---|---|---|
| | | (MPa) | GSI | Strength (MPa) | GSI | Strength (MPa) |
| A | 1 | 40.74 | 100 | 37.79 | 33 | 3.72 |
| B | 2 | 30.29 | 100 | 28.09 | 49 | 4.07 |
| | 3 | 23.43 | 100 | 21.73 | 35 | 2.25 |
| | 4 | 38.85 | 100 | 36.04 | 43 | 4.53 |
| C | 5 | 43.09 | 100 | 39.97 | 55 | 6.68 |
| | 6 | 36.80 | 100 | 34.14 | 55 | 5.71 |
| D | 7 | 16.33 | 100 | 15.14 | 38 | 1.69 |
| | 8 | 23.14 | 100 | 21.46 | 47 | 2.70 |
| | 9 | 42.21 | 100 | 39.15 | 55 | 6.54 |
| | 10 | 25.84 | 100 | 23.97 | 48 | 3.39 |
| | 11 | 30.50 | 100 | 28.29 | 49 | 4.10 |
| | 12 | 19.95 | 100 | 18.51 | 35 | 1.92 |
| E | 13 | 30.29 | 100 | 27.09 | 57 | 4.76 |
| | 14 | 23.43 | 100 | 24.01 | 59 | 4.44 |
| | 15 | 38.60 | 100 | 35.81 | 57 | 6.29 |
| Average | | 30.90 | | 28.75 | | 4.19 |

GSI. This is because the influence of the quantity and quality of the discontinuities considered the rock mechanics classification RMR and GSI. The Bonito coal seam is very fractured, thus the coal seam strength drops significantly from 30.9MPa to less than 7MPa.

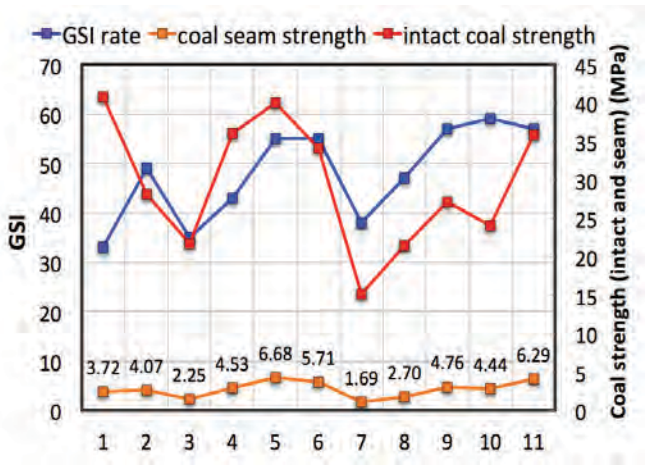



**Figure 5. Intact coal and coal seam strength related to GSI.**

The data of this study demonstrated the behavior very close or similar to the studies that determined the range of the Bonito coal seam strength. The average Bonito coal seam strength, considering the borehole analysis of this study is 4.19MPa, and the maximum and minimum values are 6.68 and 1.69MPa, respectively.

Zingano (2002) made a very extensive structure survey to determine the influence of the discontinuities on the coal seam strength, and concluded that the least coal seam strength is 4.06MPa. Gonzatti (2007) estimated the coal seam strength between 4.08 and 5.7MPa. Both considered the Hoek-Brown failure criteria.

The map on Figure 6 shows the coal seam strength distribution in a mine area. This distribution could be explained by the proximity of faults and other regional structures. Therefore, it is important to calculate or estimate the coal seam strength, but it is necessary to correlate with the structural map of the mining area to check the influence of faults on the coal seam strength.

## CONCLUSIONS

The strength of the intact coal has uniform behavior for the whole region considered in this study. However, the coal seam strength has more anisotropy due to variation of quantity and quality of the discontinuities, mainly when the borehole is close to faults.

Therefore, the study demonstrated the importance of the coal seam geomechanics characterization. Only the coal intact strength determination is not enough to estimate the seam strength. It is necessary to determine the quantity and quality of the fractures.

Another step of understanding is found for the Bonito coal seam behavior, and this behavior can be incorporated into the pillar design process.

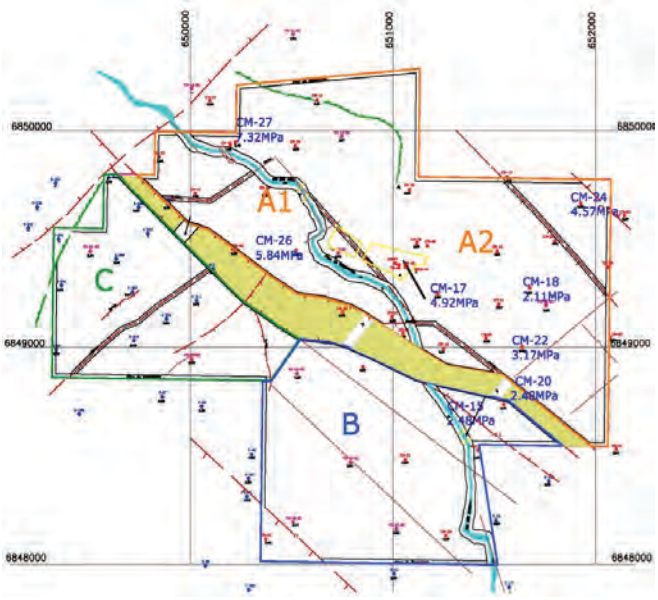



**Figure 6. Map the mining area that shows the location of the boreholes with the respectively coal seam strength, and the position of faults.**

## REFERENCES


Bieniawski, Z. T., (1973). Engineering classification of jointed rock masses. *Trans S. Afr. Inst. Civ. Engrs*, **15**(12): 335–44.

Bieniawski, Z. T.,(1974). Estimating the strength of rock materials. J. S. Afr. Inst. Min. Metall., 74(8): 312–20.

Bieniawski, Z. T., (1976). Rock mass classifications in rock engineering. Exploration for Rock Engineering (ed. Z. T. Bieniawski), 1: 97–106. A. A. Balkema: Cape Town.

Brady, B.H.G.; Brown E. T., (1985). Rock Mechanics for Underground Mining, George Allen and Unwin Editora, Londres.

Hoek, E. (1994). Strength of rock and rock masses. ISRM New Journal 2(2), 4-16, 1994.

Hoek, E.; Kaiser, P. K.; Bawden W. F. (1995). Support of underground excavation in hard rock. 1995, Balkema, Rotterdam. p. 215.

Hoek, E.; Brown, E.T., (1997). Practical Estimates of Rock Mass Straight, Int. J . Rock Mech. and Min. Sci.

Hoek, E., Kaiser, P.K. E Bawden, W.F. (1998). Support of Underground Excavation in Hard Rock., Balkema Pub., 215 pp.

Hoek, E.; Brown, E. T. Failure criterion. 2002. Consulting Engineer, Vancouver, Canada. Carlos Carranza-Torres, Itasca Consulting Group Inc., Minneapolis, USA and Brent Corkum, Rocscience Inc., Toronto, Canada.

ASTM D4543-85 Standard Practices for Preparing Rock Core as Cylindrical Test Specimens and Verifying Conformance to Dimensional and Shape Tolerances.

ASTM D3148-02 Standard Test Method for Elastic Moduli of Intact Rock Core Specimens in Uniaxial Compression.

ASTM D2664-04 Standard Test Method for Triaxial Compressive Strength of Undrained Rock Core Specimens Without Pore Pressure Measurements.

Zingano, A.Z., (2002). Modelamento Geomecânico para o dimensionamento de pilares de carvão, Tese de doutorado, PPGEM-UFRGS.

Gonzatti, C., (2007). Proposta para a estimativa da resistência à compressão uniaxial in-situ de camadas de carvão com utilização de geofísica, Tese de doutorado, USP-São Carlos.

Zingano, A, Stein, M, Karas, R., (2010). Estimativa do comportamento mecânico das camadas que formam o sistema piso-camada-teto em minas de carvão, VI Congresso brasileiro de Mina Subterrânea e VI Congresso Brasileiro de Mina Céu-aberto – IBRAM, Belo Horizonte, setembro de 2010

# Mechanics of Horizontal Movements Associated with Coal Mine Subsidence in Sloping Terrain Deduced From Field Measurements

**Ken W Mills**, Principal Geotechnical Engineer
SCT Operations Pty Ltd
Wollongong, Australia

## ABSTRACT

The ground movements associated with underground coal mining and, in particular, longwall mining, are recognised to include horizontal subsidence movements, but the mechanics of the processes that cause these horizontal movements are not well understood. Over the last two decades, three-dimensional subsidence monitoring has become routine in Australia and has provided a wealth of measurements of horizontal movements caused by mining subsidence. These measurements and other sub-surface observations allow the processes that cause mining-induced horizontal movements to be inferred and, subsequently, verified. In this paper, the mechanics of the processes that cause horizontal movements, particularly those in sloping topography, are described and discussed on the basis of field observations.

There are several processes recognised to generate horizontal subsidence movements. In flat terrain, systematic horizontal movements cause the surface to move initially toward the newly created goaf and, subsequently, in the direction of mining. Tectonic energy stored as horizontal stress is released by mining, and, when the horizontal stresses are high, the magnitude of this horizontal stress relief movement is large enough to be perceptible for some kilometres from the panel. In sloping terrain, there is an additional component of horizontal movement that occurs in a downslope direction. This movement, sometimes referred to as valley closure movement, has a magnitude that is typically much greater than systematic or stress relief movements.

## INTRODUCTION

Vertical subsidence movements above coal mining operations have been observed and quantified for almost two centuries (Whittaker and Reddish, 1989). This is primarily because vertical movements can be readily measured using levelling techniques that were well-developed throughout this period. The mechanics of the two main processes that cause vertical subsidence, sag subsidence over individual longwall panels and elastic strata compression subsidence above the chain pillars, have also been recognised for some time (Mills, 1998).

By comparison, the measurement of horizontal subsidence movements has been hampered by challenges associated with measuring exact horizontal position in an environment where large tracts of ground are moving differentially with low magnitudes. Gaining more of an understanding of the mechanical processes that cause these horizontal movements has been delayed by the challenges of obtaining reliable three-dimensional subsidence data.

For most of the last century, measuring horizontal movements has been limited to peg-to-peg distance along subsidence lines and converting changes in this distance to strain (change in length over length) without any measurement in the direction perpendicular to the line or even recognition that horizontal movements were occurring in this direction. In New South Wales (NSW) Australia, the ready availability of three-dimensional, total station, surveying instruments and their adoption in routine subsidence monitoring, from the late 1980s through the 1990s, has allowed a significant improvement in measurement capability allowing subsidence movements to be measured in three dimensions.

Since about 2000, the availability and routine access to satellite global positioning systems with sufficient accuracy for subsidence monitoring (±20mm) has meant that distance-independent, three-dimensional survey control is now possible with careful design of the survey network, such as Anderson, Patterson, and Nicholson (2007) and Mills, Morphew, and Crooks (2011) describe. The more accurate measurement of three-dimensional ground movements over large areas has allowed better understanding of the mechanical processes that cause these horizontal movements.

This paper describes the mechanics of horizontal movements inferred from subsidence monitoring and other measurements. The three main components of horizontal movement are described in general terms. The mechanics of the horizontal movements in sloping terrain are discussed in detail.

## COMPONENTS OF HORIZONTAL MOVEMENT

Three main components of horizontal movement are readily identifiable from the results of three-dimensional subsidence monitoring above longwall panels in NSW:

- Systematic horizontal movements associated with sag subsidence above individual panels or trough subsidence above multiple panels, involving a change of direction soon

after the longwall face has passed and, typically, with a magnitude of less than about 200–300mm.

- Horizontal movements associated with release of horizontal tectonic stresses within the overburden strata, typically, with a magnitude of less than 200mm at the goaf edge but extending up to several kilometres from the active panel.

Horizontal movements that occur in a downslope direction in sloping terrain (also referred to as valley closure movements). These movements have a magnitude that ranges up to about the magnitude of vertical subsidence in steep terrain but is usually less than about 0.3–0.5 times the magnitude of vertical subsidence.

**Systematic Horizontal Subsidence Movements**

Systematic horizontal subsidence movements are most readily observed in flat terrain and low horizontal stress conditions when the other two processes that cause horizontal movements are not present.

Figure 1 illustrates the horizontal movements typically observed above a single retreating longwall panel in flat terrain. Initial movements are in a direction toward the active mining area from all sides. Typically, the magnitude of this initial movement is of the order of 10% of the eventual vertical subsidence, so 100–150mm of initial movement is typical for subsidence of 1–1.5m.

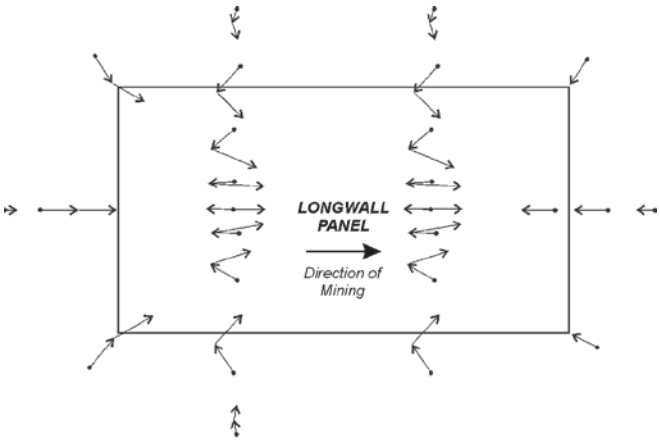



**Figure 1. Sketch illustrating the direction of systematic horizontal movements observed in flat terrain.**

When the vertical subsidence has reached about half of its maximum, typically, some 0.3 times the depth after the longwall face has passed, there is a change in direction so that subsequent horizontal movements occur in a direction toward the retreating longwall face.

Above the central part of the longwall panel, this change causes a complete reversal in direction. The magnitude of the subsequent movement is typically larger than the initial movement, so there is a permanent offset in the direction of mining. In other places around the panel, the change in direction is more subdued. At the start of the panel, both the initial movement and the subsequent movement are in the same direction, so the two are additive. Systematic horizontal movements are, therefore, typically greatest at the start of the panel. At the finishing end of the panel, only the initial movement occurs. The subsequent movement does not occur because the longwall does not continue past the finishing line. As a result, systematic horizontal movements over the finishing rib of the panel tend to have lower magnitude than elsewhere around the panel edge.

**Horizontal Stress Relief Movements**

Horizontal tectonic stresses within the overburden strata store considerable energy as evidenced by the damage caused when these stresses are released suddenly during earthquake events. In coal mining areas, the release of energy occurs when the rock strata overlying the longwall panel fails in horizontal compression. This allows elastic stress relief to occur within the surrounding strata extending, when the circumstances are right, for several kilometres from the goaf edge of active mining.

Reid (1998, 2001) reports on first order surveys in the Southern Coalfield of NSW showing perceptible horizontal movements occur at distances of up to about 1.5km from active mining. The direction of movements observed is predominantly in a northeast, southwest orientation consistent with the regional horizontal stress direction.

Hebblewhite, Waddington, and Wood (2000) report on horizontal ground movements around the Cataract and Nepean Gorges at Tower Colliery. These movements are not aligned with the direction of the major horizontal stress but, instead, with the direction toward the free surface of the Nepean Gorge. The magnitude of horizontal closure across the gorge approached 300mm when the gorge was directly mined under.

Usually, stress relief horizontal movements occur incrementally with longwall retreat, but there is evidence from far-field monitoring observations at Ulan Coal Mine and elsewhere that initial movements could occur as several discrete events rather than incrementally (Mills, Morphew, and Crooks, 2011). The characteristics of the movements observed at Ulan are consistent with elastic stress relief of in situ horizontal stresses causing the ground to move laterally up to 200mm.

Pells (2011) presents the results of far-field horizontal subsidence monitoring from Appin West Colliery in NSW. A simple elastic model is shown to be capable of explaining the far-field movements. These movements have a magnitude at the goaf edge of about 200mm and are detectable using a well-controlled survey network for several kilometres outside the mining area.

The mechanics of the process of horizontal stress relief movements are consistent with the failure of rock strata directly above individual longwall panels. The interpretation of the sag subsidence above individual longwall panels combined with extensometer and other monitoring data indicate that a zone of rock failure extends upward to a height above the mining horizon equal to about 1.4—1.7 times the longwall panel width (Mills, 2012 and Mills and O'Grady, 1998). This failure process allows tectonic energy stored as horizontal stresses within the rock mass beyond the panel edges to be released and, thereby, allows the ground to move toward the failed rock strata above each longwall panel or in very steep topography toward the gorge.

**Horizontal Movement in a Downslope Direction**

The effects of topography are widely recognised to modify subsidence behaviour, although the mechanics of the processes have only become apparent relatively recently. Kapp (1973, 1980) reported high compressive strains at topographic low points in NSW consistent with valley closure. Holla and Barclay (2000) note similar experience in the USA as what is reported by Gentry and Abel (1978) and Ewy and Hood (1984). Holla and Barclay observe that, given the varying geological settings, the occurrence of large ground strains and reduced vertical subsidence in topographic low points appears to be due to forces generated by topography rather than being a unique characteristic of the geological setting.

Holla (1997) describes the results of horizontal movements in steep terrain in NSW based on levelling and peg-to-peg strain measurements. Holla recognised the effect of horizontal movements but, with only having strain measurements in one direction, found it difficult to interpret the mechanics involved.

Kay (1991) presents the results of a program of three-dimensional surveying at Baal Bone

Colliery that measured horizontal movements in steep terrain. These and other measurements conducted subsequently at the colliery (Mills, 2001) show that horizontal movements in steep terrain include a component of movement in addition to the systematic horizontal movements in a direction toward the valley (i.e., in a downslope direction).

Seedsman and Watson (2001) illustrate this effect by removing systematic horizontal movements calculated for flat terrain from the measured subsidence vectors in an area where a topographic ridge had been mined under. The resulting vectors showed that the residual movement not associated with systematic subsidence occurred as movements in a downslope direction off both sides of the ridge in response tothe surface topography.

Waddington and Kay (2004) present a handbook reviewing the experience of mining under cliffs and river channels. They recognise the effect of valley closure and present an empirical method for predicting an upper bound magnitude. This method remains the primary method for estimating valley closure in NSW.

Waddington and Kay also postulate on the mechanics of the processes that cause valley closure, but they focus on horizontal stress concentrations in the base of the valley as the primary cause of the phenomenon. While this mechanism could contribute to the observed valley closure in the Southern Coalfield (where the Waddington and Kay study is primarily focused), the phenomenon of horizontal movement in a downslope direction is also observed in areas where the in situ horizontal stresses have been measured, and the magnitude is small and insufficient to give rise to the magnitude of movements observed (Mills, 2001). The characteristics of a horizontal stress-driven mechanism for valley closure are also not consistent with the behaviour observed at multiple sites or with the low horizontal stresses measured in valley floors (ACARP, 2009).

Figure 2 shows the horizontal movements measured in section at natural scale and in plan above Longwall 7 at Baal Bone Colliery. The subsidence line was surveyed in three dimensions before and after mining. The displacement vectors shown are exaggerated in magnitude but are drawn at natural scale so that both the vertical and horizontal components are at the same scale. The overburden depth ranges from 100m in the valley to 175m on the ridge tops. The longwall panels create a mined area that is 211m wide. The seam section mined is approximately 2.5m thick.

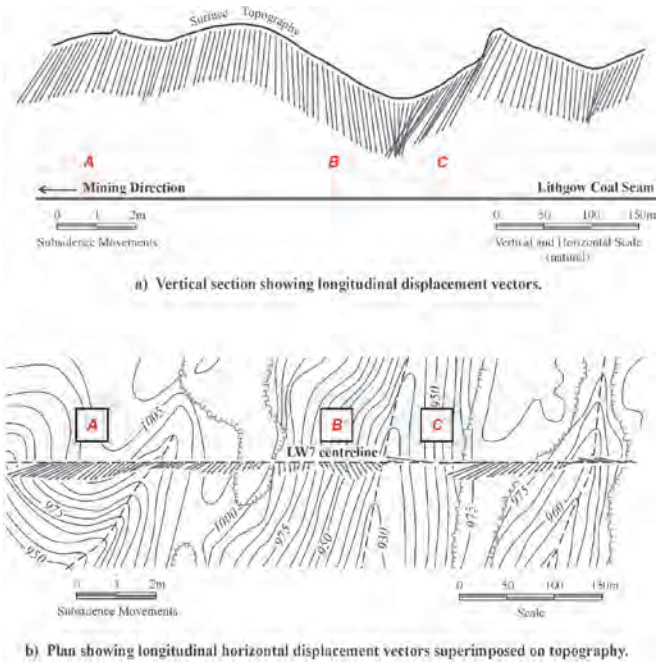



**Figure 2. Three dimensional subsidence movements observed above Longwall 7 at Baal Bone Colliery (after Mills 2001).**

These measurements show that there is a general tendency for horizontal movement in the direction of mining, as in flat terrain. In addition to this general tendency is a downslope directional component that responds to surface topography. In the area where the direction of mining and the slope coincide (C), the horizontal movements occur directly downslope. In areas where there is a cross-slope (A), there is a component of horizontal movement in the direction of this cross-slope. In areas where the slope is opposite to the direction of mining (B), there is still downslope movement, but the absolute magnitude is lower because of the offsetting effects of the systematic movement in the opposite direction and other effects discussed in the next section.

## MECHANICS OF HORIZONTAL SUBSIDENCE MOVEMENTS IN A DOWNSLOPE DIRECTION

Observations from multiple sites of horizontal subsidence movements at the surface and shear movements within the overburden strata are consistent with the following hypothesis as a potential explanation of the mechanics that cause downslope directional horizontal movements.

Longwall mining has the effect of removing the vertical stress supporting the overburden strata. The resulting downward movement releases potential energy that is available to do work. The downward movements associated with mining-induced

subsidence movements in a vertical direction cause the overburden rock strata to dilate or grow in volume as it fails and fractures are formed.

This process is recognised as a property of granular geomaterials, such as sand and rock, and is known in the soil and rock mechanics literature as dilatancy. The term dilatancy typically refers to the volume increase that is observed in the elastic range prior to rock failure, but dilatancy is used in this context to also include the volume increase associated with macro-scale rotations of adjacent blocks of rock strata and normal displacements on irregular fracture surfaces. Post failure dilation is also referred to as bulking in the context of caving and overburden fracturing but the term bulking does not adequately convey the lateral forces that are generated during displacement.

The effect of dilatancy is that the rock strata occupies more volume after it has failed and fractured than it does in its pre-failure state. Lateral horizontal movement associated with strata dilation is largely suppressed in flat terrain where systematic horizontal movements and horizontal stress relief movements tend to dominate. In effect, the horizontal dilation is largely constrained by the intact, undisturbed material on either side of the panel moving inward toward the extracted panel.

In sloping terrain, however, there is an imbalance in the constraint on the downslope side that is set up by the terrain. As the overburden strata subsides over the goaf below a hillside, the free surface of the valley cannot offer any resistance to the dilating strata within the slope. There is also no horizontal stress to oppose the tendency for dilation. The law of conservation of energy governs the direction of movement. Horizontal dilation occurs in all directions, but the path of least resistance is directly toward the valley in the direction of maximum gradient (i.e., in a downslope direction). As a result, horizontal movement occurs in this downslope direction.

As shown in Figure 2, the magnitude of horizontal movement in a downslope direction can be as high as 1.5m in steep terrain but is usually in the range 0.3–0.7m for more moderate terrain.

Dilatancy is recognised to be sensitive to confining pressure with greater dilatancy observed when the confinement is less. This phenomenon contributes to the different horizontal movement observed in Figure 2 on either side of the valley.

In the stretching phase of the systematic subsidence cycle that occurs ahead of and immediately behind the longwall face, confinement is reduced. Therefore, the potential for dilatancy is greater than during the compression phase of the systematic cycle that occurs subsequently over the subsiding panel. As mining approaches the valley from under the hill, the slope is being stretched at the same time as the hillside is subsiding and dilating laterally, so horizontal movements are large and, in the case shown in Figure 2, approach the magnitude of the vertical subsidence because of the steepness of the terrain.

As mining proceeds from the valley toward the hill, there is no dilatant lateral push to cause downslope movement until mining is well under the hill. By the time this push starts, the slope is in the compressive phase of the systematic subsidence cycle, and dilatancy is suppressed by the increased confinement associated with this compression, so horizontal movements are decreased.

The result of these effects is much larger horizontal movements when mining from high ground toward a valley compared to mining from a valley toward high ground.

**Basal Shear Horizon**

Figure 3 shows how the propensity for horizontal movement in a downslope direction that can cause horizontal movements above the level of the valley floor is constrained below the valley floor by the presence of rock strata on the opposite side of the valley. The difference in horizontal movement above and below the valley floor needs to be accommodated within the rock strata. Visual observations, borehole observations, and inclinometer monitoring indicate that the difference in horizontal movements is accommodated as horizontal shearing along a bedding plane or similar horizon at the level of the valley floor or just above, but more typically, just below the valley floor, as illustrated in Figure 3.

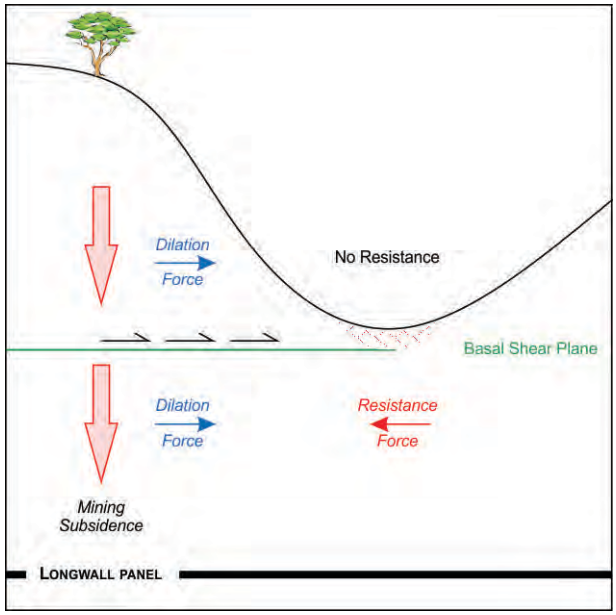



**Figure 3. Sketch illustrating the mechanics of the process that causes horizontal movement in a downslope direction.**

Although valley closure movements are common, it is less common to be able to directly observe the presence of shear horizons because they usually occur just below the floor of the valley where they cannot easily be seen. Lizard Creek Waterfall in the Southern Coalfield of NSW is located in an area adjacent to longwall mining. The waterfall spills from an incised valley half way up a vertical cliff into an amphitheatre of near vertical cliffs. The presence of the vertical cliffs provides a window into the sub-surface where a horizontal shear horizon can be observed directly. A mining-induced shear horizon is evident along the face of this cliff at the level of the base of the incised channel. Iron-stained water flows from this shear horizon, which is consistent with being freshly formed by mining, hydraulically conductive, and laterally extensive.

A borehole caliper logging program in approximately 100 shallow boreholes was conducted in the base of the Waratah Rivulet in the Southern Coalfield of NSW to characterise the nature of mining-induced fractures. These measurements are reported by Mills (2007) and in an Australian Coal Association Research Program report (ACARP, 2009). They indicate that a horizontal shear horizon located at approximately 4–6m below the surface of the river channel has accommodated valley closure of up to about 600mm. The shear horizon was observed in boreholes to extend at least 60m from the river channel as a fracture zone with elevated hydraulic conductivity. Surface subsidence monitoring indicated that the shear horizon most likely extended below the entire hillside to the centre of the ridge, but no confirmation of this inference was possible until recently.

Recent monitoring at Sandy Creek Waterfall (Walsh et al, 2014) provides definitive confirmation of the presence of horizontal shear horizons and mining-induced subsidence movement localised onto these planes. The bed of Sandy Creek drops about 30m in elevation at a waterfall. When horizontal closure movements were first detected on inclinometers distributed across the site up to 350m from the creek, they were localised onto two horizons that corresponded in elevation with approximately 6m below the base of Sandy Creek, upstream of the waterfall and about 10–15m below Sandy Creek downstream of the waterfall. The presence of large boulders in the bed of the creek downstream of the waterfall makes it difficult to determine the effective elevation of the creek bed, but it is likely that the deeper shear horizon also corresponded with an elevation at or just below the solid base of the creek downstream of the waterfall.

The effects of nearby longwall mining were closely monitored using a range of instruments, including several manual inclinometers and a shaped accelerometer array (SAA). First evidence of closure movements were observed across the array of inclinometers on two main shear horizons when the longwall panels approached the waterfall. The initial movements were of low magnitude and did not have potential to significantly affect the integrity of the waterfall rock structure. Mining continued for several hundred metres more before the movements were considered large enough to be a potential threat to the integrity of the waterfall, and the longwall was stopped (Walsh et al, 2014).

The SAA inclinometer recorded the inclination at 0.5m intervals over a 50m vertical section at 1 minute intervals allowing the nature of the initial shear movements to be determined. Figure 4 shows the initial movements that were observed and the changes that have been observed since. The initial step change occurred at 9:56pm on 16 November 2012. Movements since then have continued incrementally with additional longwall retreat, and then more gradually, once the longwall finished. Since the completion of mining, there have been several high-intensity rainfall events. These events have been accompanied by small step changes in shear, but the shear movements have gradually stabilised since adjacent mining finished.

At the Sandy Creek Waterfall site, the amount of available monitoring data was sufficient to allow an analysis of the body forces acting on a two-dimensional slice through the site, as shown in Figure 5. The horizontal stresses were measured at several locations, including high up on the slope and in the valley floor. Piezometers measured the groundwater level and a 4m rise in

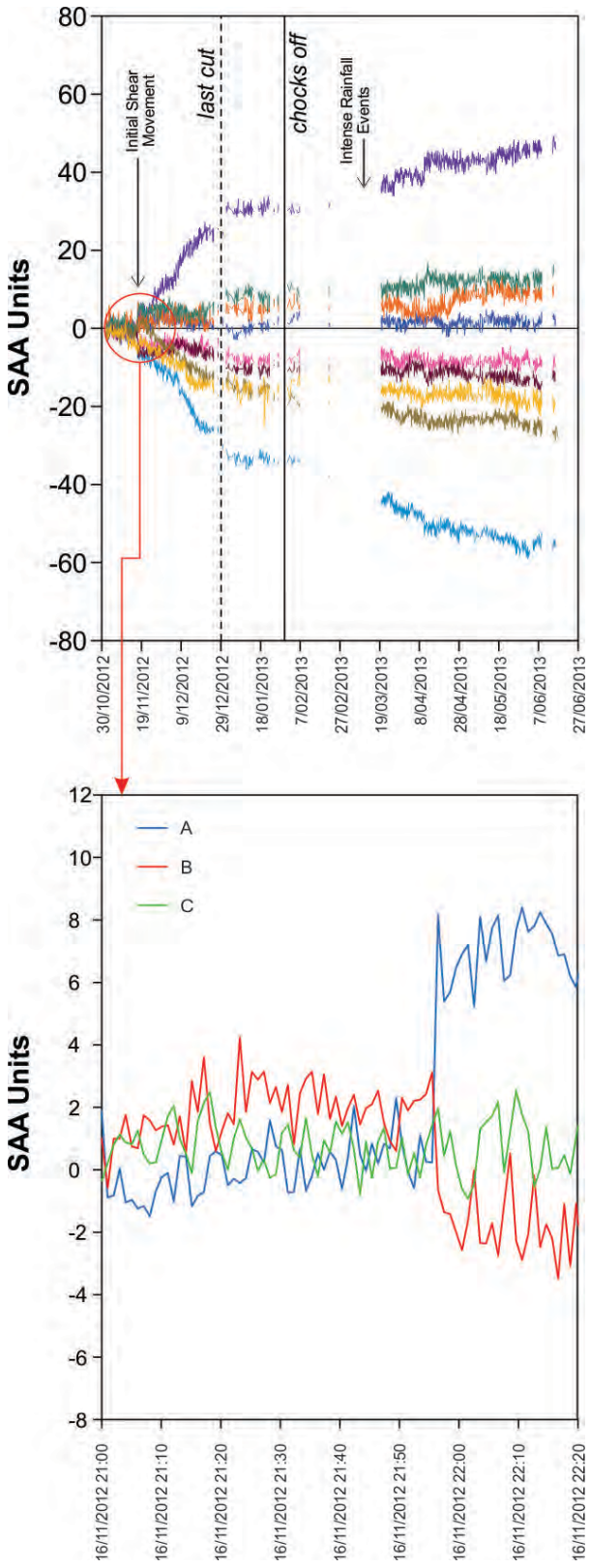



**Figure 4. Results of shear monitoring observed on a Shaped Accelerometer Array (SAA) Inclinometer illustrating the deformation characteristics of the basal shear plane.**

water level due to two high-intensity rainfall events that occurred after mining was complete. These two events were sufficient to cause remobilisation of downslope movement and shear on the basal shear plane. By considering the balance of horizontal forces at limiting equilibrium in the two cases of no movement prior to the rainfall events and the movement following a 4m rise in pore pressure, the friction angle on the basal shear plane can be estimated with a high degree of confidence. This analysis indicates that the friction angle on the basal shear plane is in the range of 9°–14°, depending on assumed pore pressure conditions within the rock mass. This friction analysis is consistent with the range that would be expected for bedding planes in Hawkesbury Sandstone based on laboratory shear tests.

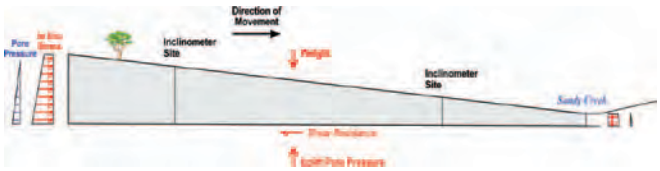



**Figure 5. Free body diagram showing loads on the valley side above Sandy Creek sliding horizontally along basal shear plane.**

The key observations of interest from the Sandy Creek Waterfall monitoring in terms of characterising the shear horizons are as follows:

- The nature of the shear movements observed is consistent with movement on near-horizontal shear surfaces at an elevation just below the base of the valley.
- A step in the elevation of the valley floor leads to the development of two shear horizons, each just below the floor of the valley.

The timing and magnitude of the shear movements are consistent with the valley closure movements observed.

- The movement observed is consistent with shear on a residual shear surface without the large energy release that would be associated with fracturing fresh rock.
- The remobilisation of shear movement following rainfall events and the gradual reduction in shear over time indicate that the shear surface is in a state of limiting equilibrium where even very small changes in horizontal load are capable of causing additional horizontal movement.
- The basal shear horizon extends outward from the valley as far as required to accommodate the horizontal movements observed on the surface.

**Special Case: Horizontal Movements in Dipping Strata**

A special case of dilatant strata behaviour and associated horizontal movement has been observed at a site where the strata dips at a rate faster than the surface topography.

Ashton Coal underground coal mine is located in the Hunter Valley of NSW. The longwall panels are located in strata that dips to the west more steeply than the surface topography. The horizontal movements observed directly above each longwall panel consistently show movement of about 200–250mm in an upslope direction (SCT, 2009). This movement is atypical of subsidence movements at other sites but is consistent with dilation of the strata toward a free surface. Figure 6 illustrates the effect of rotating the strata so that the up-dip movement in dipping strata is essentially the same as the downslope movement in horizontally bedded strata. The observation of upslope movement suggests that the strata dilation process is capable of generating large forces within the overburden strata.

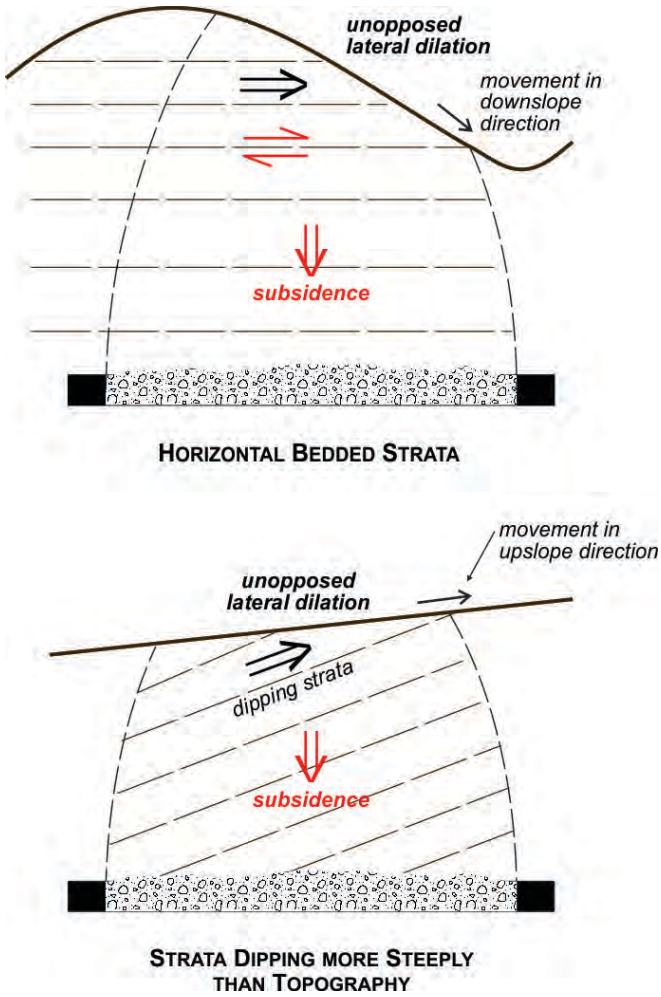



**Figure 6. Illustration of the rock dilation processes inferred to be causing the horizontal movements in an up dip direction observed at Ashton Coal Mine.**

## CONCLUSIONS

An understanding of the mechanics of horizontal subsidence movements is developing as well-controlled, three-dimensional survey data becomes available from more and more sites.

Three separate components of horizontal movement are recognised:

1. Systematic horizontal movements with a magnitude of typically less than 200mm that occur in two stages toward the void created by mining—initially toward the approaching longwall face and, subsequently, in the direction of mining.

2. Horizontal movements caused by stress relief with a magnitude of typically less than 200mm can occur up to several kilometres from mining in a direction toward the void created by mining but usually biased in the direction of maximum horizontal stress.

3. Horizontal movements in a downslope direction associated with topographic variation and dilation of subsiding strata below topographic high ground. The magnitude of this movement varies with the steepness of the topography but is usually much greater than other components and can reach the magnitude of vertical subsidence in steep terrain.

Observations and field measurements indicate that horizontal movements in a downslope direction occur along near-horizontal shear surfaces at an elevation just below the base of the valley. The basal shear horizon extends outward from the valley as far as required to accommodate the horizontal movements observed on the surface. The shear movement observed is consistent with shear on a residual shear surface without the large energy release that would be associated with fracturing fresh rock.

The remobilisation of shear movement following rainfall events and the gradual reduction in shear over time indicate that the shear surface is in a state of limiting equilibrium in its natural conditions where even very small changes in horizontal load are capable of causing additional horizontal movement.

In strata dipping relative to the surface topography, the same mechanism that causes horizontal movement in a downslope direction has been observed to cause horizontal movement in an up-dip direction. This observation suggests that the strata dilation process is capable of generating large forces within the overburden strata.

## REFERENCES


ACARP. (2009). "Damage criteria and practical solutions for protecting river channels." *Australian Coal Association Research Project Report C12016*. http://www.acarp.com.au/abstracts.aspx?repId=C12016

Anderson, L., Patterson, D., and Nicholson, M. (2007). "Measuring mine subsidence – BHP Billiton Illawarra Coal's diversified approach." In: *Proceedings of the Seventh Triennial Conference of the Mine Subsidence*. Sydney, New South Wales, Australia: Mine Subsidence Technological Society pp. 53–68.

Ewy, R. T. and Hood, M. (1984). "Surface strain over longwall coal mines: its relation to the subsidence trough curvature and to surface topography." In: *International Journal of Rock Mechanics, Mining Sciences, & Geomechanics Abstracts 21*(3): 155–160.

Gentry, D. W. and Abel, J. F. (1978). "Surface response to longwall coal mining in mountainous terrain." *Association of Engineering Geologists Bulletin 15*(2): 191–220.

Hebblewhite, B., Waddington, A., and Wood, J. (2000). "Regional horizontal surface displacements due to mining beneath sever surface topography." In: *Proceedings of the 19th International Conference on Ground Control in Mining*. Morgantown, WV: West Virginia University, pp. 149–157.

Holla, L. (1997). "Ground movement due to longwall mining in high relief areas in New South Wales, Australia." *International Journal of Rock Mechanics, Mining Sciences, & Geomechanics Abstracts 34*(5): 775–787.

Holla L. and Barclay, E. (2000). *Mine Subsidence in the Southern Coalfield of NSW, Australia*. New South Wales: Department of Mineral Resources, pp. 118.

Kapp, W. A. (1973). "Subsidence at Kemira Colliery." In: *Proceedings of the Symposium on Subsidence in Mines*. Carlton, Victoria, Australia: Australasian Institute of Mining and Metallurgy, pp. 7.1–7.9.

Kapp, W. A. (1980). "A study of mine subsidence at two collieries in the Southern Coalfield, New South Wales." In: *Proceedings of Australasian Institute of Mining and Metallurgy*. Carlton, Victoria, Australia: Australasian Institute of Mining and Metallurgy, pp. 1–11.

Kay, D. (1991). *Effects of Subsidence on Steep Topography and Cliff Lines*. Canberra: Energy Research and Development Corporation, pp. 126.

Mills, K. W. (1998). "Subsidence mechanisms about longwall panels." In: *Proceedings of International Conference on Geomechanics/Ground Control in Mining and Underground Construction*. New South Wales, Australia, University of Wollongong, pp. 745–756.

Mills, K. W. (2001). "Observations of horizontal subsidence movement at Baal Bone Colliery." In: *Proceedings of 5th Triennial Conference of the Mine Subsidence Technological Society*. New South Wales, Australia: Mine Subsidence Technological Society, pp. 99–111.

Mills, K. W. (2007). "Subsidence impacts on river channels and opportunities for control." In: *Proceedings of the Seventh Triennial Conference of the Mine Subsidence*. Sydney, New South Wales, Australia: Mine Subsidence Technological Society, pp. 207–217.

Mills, K. W. (2012). "Observations of ground movements within the overburden strata above longwall panels and implications for groundwater impacts." In: *Proceedings of the 38th Symposium on the Advances in the Study of the Sydney Basin*. pp. 1–14.

Mills, K. W. and O'Grady, P. (1998). "Impact of longwall width on overburden behaviour." In: *Proceedings of the Coal 1998: Coal Operators' Conference*. Carlton, Victoria, Australia: Australasian Institute of Mining and Metallurgy, pp. 147–155.

Mills, K. W., Morphew, R. H., and Crooks, R. J. (2011). "Experience of monitoring subsidence at Ulan Coal Mine." In: *Proceedings of the 8th Triennial Conference of the Mine Subsidence Technological Society*. Pokolbin, New South Wales, Australia: Mine Subsidence Technological Society, pp. 89–100.

Pells, P. J. N. (2011). "A simple method of estimating far field movements associated with longwall mining." *Australian Geomechanics 46*(3): 1–8.

Reid, P. (1998). "Horizontal movements around Cataract Dam, Southern Coalfield." In: Proceedings of the Fourth Triennial Conference on Buildings and Structures Subject to Ground Movement., Newcastle, New S.W: Mine Subsidence Technological Society, pp. 157–170.

Reid, P. (2001). "Further analysis of horizontal movements around Cataract Dam, 1980 to 1997." In: *Proceedings of 5th Triennial Conference of the Mine Subsidence Technological Society*. New South Wales, Australia: Mine Subsidence Technological Society, pp. 211–218.

SCT. (2009). "Longwall 4 – End of panel subsidence report." *Strata Control Technology Report to Ashton Underground Mine*. http://www.ashtoncoal.com.au/Resources/Reports--Publications/Mining/End-of-Panel-Reports/Appendix-1A---EoP-LW4-Report-Subsidence-ash3602_Final-2.pdf

Seedsman, R. W. and Watson, G. (2001). "Sensitive infrastructure and horizontal ground movements at Newstan Colliery." In: *Proceedings of 5th Triennial Conference of the Mine Subsidence Technological Society*. New South Wales, Australia: Mine Subsidence Technological Society, pp. 171–180.

Waddington, A. A. and Kay, D. (2004). "Management information handbook on undermining cliffs, gorges, and river systems." *ACARP Research Projects C8005 and C9607*.

Walsh, R. V., Hebblewhite, B. K., Li, G., Mills, K. W., Nicholson, M. A., Barbato, J., and Brannon, P. J. (2014). "Sandy Creek Waterfall – Case study of successful management of the impacts of longwall mining a sensitive natural surface feature" In: *Proceedings of the 33rd International Conference on Ground Control in Mining*. Morgantown, WV: West Virginia University.

Whittaker, B. N. and Reddish, D. J. (1989). *Subsidence: Occurrence, Prediction and Control (Developments in Geotechnical Engineering)*. Waltham, MA: Elsevier Science, pp. 528.

# Development of An Enhanced Methodology for Ground Movement Predictions Due to Longwall Mining in the Illinois Basin

**Zach G Agioutantis**, Professor
School of Mineral Resources Eng. Technical Univ.
Crete, Greece
VCCER, Virginia Tech
Blacksburg, VA

**Michael Karmis**, Professor
Department of Mining and Minerals Engineering
Virginia Tech
Blacksburg, VA

**Daniel Barkley**, Mining Engineer, P.E.
Land Reclamation Division
Illinois Dept of Natural Resources Office of Mines and Minerals
Springfield, IL

**Scott D. Elrick**, Acting Head - Coal and Petroleum Geology Section
Illinois State Geological Survey
University of Illinois
Champaign, IL

## ABSTRACT

The Illinois Basin has an extensive history with the use of mechanized longwall mining dating back to the early 1970's. In recent times, technological advances have resulted in increased panel widths from 800 feet to over 1400 feet and daily panel advance rates have also increased significantly. The prediction and control of subsidence and surface deformation due to underground mining are important considerations in the permitting, planning, and monitoring of these coal mining operations. The prediction of mining-induced ground movements using the influence function method is a mature technology, well utilized in the Illinois basin, and widely used by researchers and planning engineers around the world. This paper utilizes subsidence data, recently measured in longwall operations in Illinois, to develop an updated ground movement prediction capability implemented by the Surface Deformation Prediction System (SDPS) software package.

## INTRODUCTION

In recent years, overall Illinois production has increased primarily due to an increase in longwall mines and longwall productivity. Illinois has seen a rise in annual tonnage over the past five (5) years. The 2013 coal production approached 52 million tons, the highest annual production since 1994.

Historically, over 285 longwall panels have extracted coal and subsided more than 45,000 acres of land. Subsidence has impacted structures and infrastructure of all kinds and vast acreage of prime farmland. Predicting subsidence accurately in flat topography is an important part of evaluating potential impacts and a key element of mine permitting. Drainage restoration is a vital part of reclamation of subsidence.

As subsidence modeling tools and software became available, it became apparent that models developed primarily on Appalachia longwall subsidence data did not translate well to the Illinois basin. Illinois subsidence deformation parameters such as angle of draw were not being accurately predicted by the available models. Limited regional parameters for the Illinois basin were recently developed (Karmis et al, 2008) and are now frequently used by the industry to address permitting requirements. Still, further work is necessary to fully realize the potential and capabilities of tools such as SDPS.

In addition, since the development of the subsidence parameters for the Central US Coalfields, technological advances have resulted in increased panel widths from 800 feet to over 1400 feet. Daily panel advance rates have also increased significantly. It is believed that these technological advances have changed the resultant surface deformation parameters triggering the need to evaluate newer available surface subsidence data and adjust the modeling accordingly to better reflect the resultant surface subsidence trough and improve induced strain prediction.

## COAL GEOLOGY AND RESERVES

Illinois Coal is part of the Eastern Region of the Interior Province, which also encompasses Indiana and Western Kentucky (Figure 1). This region is also referred to as the Illinois Basin, and coal seams were deposited during the Pennsylvanian (late Carboniferous), approximately 300 million year ago. During the Pennsylvanian, Illinois was located at, or near, the equator. Regular, repeating, glacial cycles, driven by earth orbit fluctuations, caused ice to wax and wane at the poles, sea level to rise and fall, and equatorial climates to oscillate between dominantly wet, and seasonally dry. Broad, low relief lowlands typified the landscape of Illinois and the continental interior.

During glacial episodes, ice formed at the poles, dropping sea level, and exposed the Illinois landscape. As polar ice masses increased in size, equatorial climate changed from seasonally dry to wet. Soils with seasonally dry characteristics initially formed on the exposed landscape. As climate became wetter the Illinois landscape became waterlogged and transitioned to forming peat swamps. As glacial intervals ended and polar ice melted back, equatorial climates become less wet, and sea level rose, drowning the peat swamps, resulting in black shales and limestone followed by thick gray shales and sandstones (which may downcut into underlying strata and coal seams) (Cecil, 2003). Over time these glacial oscillations repeated, the Illinois Basin slowly subsided, and a repeating sequence of coal bearing strata called cyclothems were deposited (Figure 2). These depositional conditions resulted in at least 50 named coal seams in Illinois, and well over 200 billion tons of coal in the ground. Approximately 36,800 square miles in Illinois are underlain by coal.




**Figure 1. Extent of the Pennsylvanian System in the Illinois Basin (Korose, 2002).**

The immediate floor of most Illinois coal mines is composed of clay-rich former soil (underclay, fire clay) that varies from 0 to several feet thick and is typically weak. Overlying strata usually consists of a few feet of fissile black shale, overlain by 0 to several feet of hard marine limestone, and in turn by tens of feet of silty shale to sandstone of varying consistency. In coal seams where large contemporaneous rivers flowed through the ancient peat swamps (Walshville River and Galatia River of the Herrin and Springfield coals respectively), the roof lithology is often different and variable. Coal seams near these ancient rivers are often missing the overlying fissile black shale and marine limestone completely and are instead covered by tidally laminated siltstone and sandstone 'stack rock', and sandstone. The 'stack rock' lithology has in the past proved to be problematic for mining, being difficult to bolt into and support, and prone to moisture sensitivity. At the same time, coal under 'stack rock' roof is tempting to extract due to it generally being thick and low in sulfur. The 'stack rock' facies changes in character away from the courses of these ancient rivers, transitioning to finer grain sizes, thinner beds, and erosional pod-like geometries towards the distal edges.

The complex depositional history of the region create unique and challenging mining conditions. Pillar punching and floor heave can be highly variable and unpredictable based on changes in immediate underclay thickness over short distances. Floors that become wetted or inundated can weaken resulting in localized pillar punching reducing void height in short periods of time. Weak roof rock can be difficult to control and is often intentionally cut and removed or unintentionally falls and is removed creating more unpredictable void heights, a key parameter in subsidence modeling.

## COAL PRODUCTION IN ILLINOIS

Approximately 20 coal seams have been mined since the first recorded coal mining in 1810, however, the majority of historic production (90%) has been from the Herrin and Springfield coal. Current and future production will be predominantly from these two coals as well. All five (5) active longwall mines in Illinois extract from the Herrin Coal Seam.

The earliest coal mining was performed by underground mining methods. As surface mining methods and machinery improved, surface extracted coal reached approximately 50 percent of the total

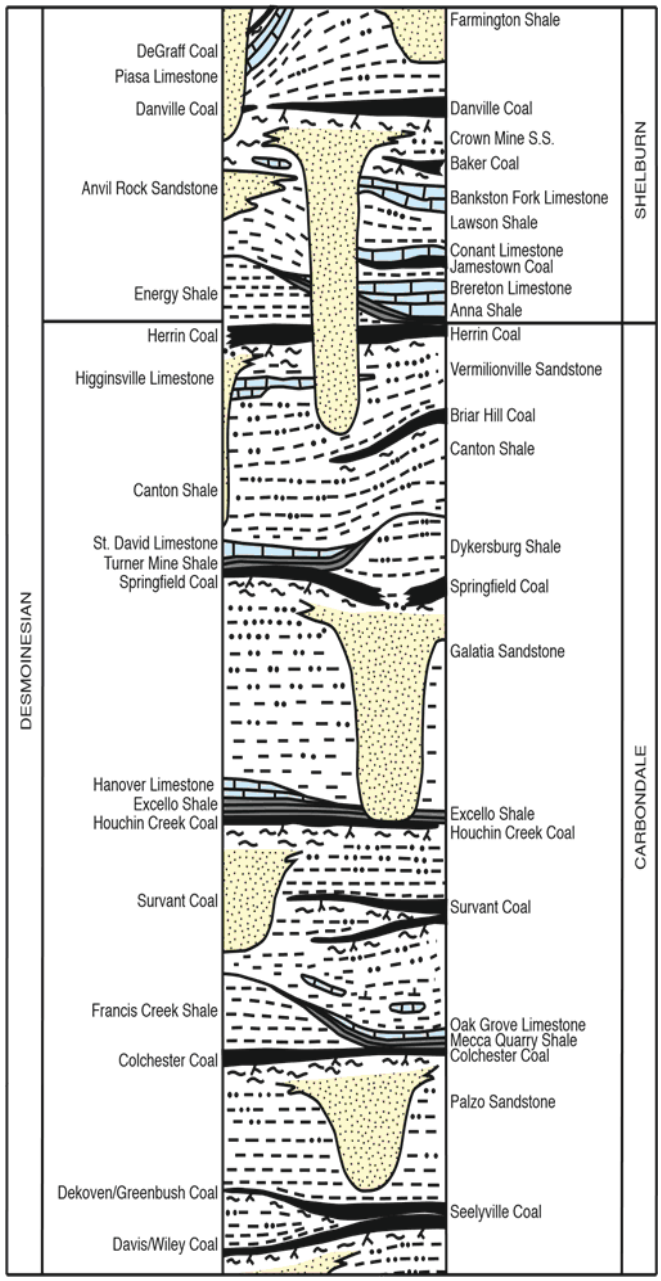



**Figure 2. Generalized stratigraphic column of Pennsylvania coals in Illinois (modified from Nelson et al., 2011).**

production in the 1960's. As surface minable coal along the basin rim were depleted, underground mining production again dominated. Today, approximately 89 percent of coal is produced by underground methods (Figure 3).

Annual production peaked in 1944 at approximately 74 million tons. Production dipped to record lows of 31 to 33 million tons from 2000 through 2007 as the impact of the Clean Air Act greatly reduced the demand for Illinois Basin high sulfur coal. Illinois has seen a recent surge in production (Figure 3) driven by market economics. Two main reasons contributed to this: a) new investments in longwall equipment and b) the fact that about half of the production is exported internationally. There has been a 51.2 percent increase in total annual tonnage over the past 5 years, primarily due to a surge in the use of longwall mining (Figure 4).

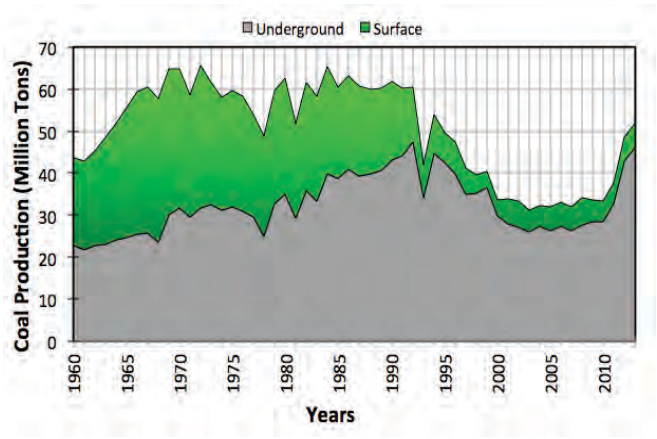



**Figure 3. Total Illinois coal production since 1960 (IDNR 2013).**

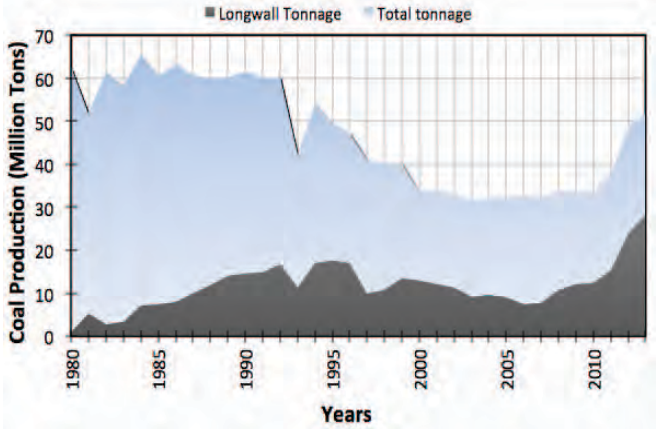



**Figure 4. Illinois Longwall vs. total tonnage since 1980 (IDNR 2013).**

## IMPACTS OF LONGWALL SUBSIDENCE

Longwall mining and the resultant planned subsidence has affected numerous surface structures and facilities in the past 40 years. Homes, buildings, utilities, major pipelines, railroads and state highways have been impacted. The approach to dealing with subsidence damage minimization and mitigation of structures and infrastructure is handled similarly throughout the longwall areas of the country. Planning for subsidence of sensitive structures requires an understanding of the ground movements that will occur and the resultant induced strains.

What is unique to Illinois and longwall mining are the impacts to relatively flat surface lands and the resultant impediment of surface drainage. Farming is a major industry in Illinois with approximately 60 percent of the surface area of Illinois planted in either corn or soybean. The result of lowering the land surface though a series of adjacent longwall panels interrupted by the presence of chain pillars can leave a pronounced washer board effect on the surface. This can result in large areas of drainage impaired land. Water ponding areas can take a toll on farmland production by drowning crops and preventing farm machinery access until properly mitigated.

Illinois longwall mines are therefore required to provide existing contours and projected post subsidence contours typically at two (2) foot intervals. Areas of anticipated inundation are delineated and potential course of drainage restoration defined to demonstrate mitigation can be achieved. Mitigation is accomplished by deepening existing waterways and installation of new drainage courses. Subsurface drainage tiles that are impacted must be replaced, and in some instances supplemented with additional tiling, to achieve pre-subsidence drainage conditions.

Intermittent or perennial stream channels may require dredging downstream of the subsided area to reestablish pre-mining flow paths and prevent backup of water. This may also involve permitting through the Corps of Engineers in order to allow mitigation to occur within the banks of Corps jurisdictional streams. Accurate prediction of the resultant contours over a series of longwall panels provides the tools necessary to meet permitting requirements and assist in developing mitigation plans.

## THE SDPS PACKAGE FOR GROUND DEFORMATION PREDICTION

The development of rigorous and well-accepted ground deformation prediction methodologies for assessing mining impacts on surface structures and facilities is an important issue for subsidence control. A number of subsidence prediction techniques have been developed and subsequently validated using measured deformations (e.g. vertical and horizontal movements, ground strains, etc), over mined panels. This task can be extremely complex because of the number and nature of the parameters affecting ground deformation induced by underground mining. Subsidence parameters, surface morphology, mine plan, coal structure characteristics, rate of mining, overburden lithology, and the type of surface facility to be protected must all be considered in the analysis.

The Surface Deformation Prediction System (SDPS) is a software package widely used by the US mining industry and state and federal agencies for subsidence planning, prediction, and control. It primarily utilizes the influence function method for subsidence prediction which is a well-established and accepted technique. The influence function methodology implemented in SDPS to calculate final surface deformations relies on a few subsidence engineering parameters, i.e., the angle of influence, the supercritical subsidence factor and the edge effect offset distance. Empirical relations are available that allow the estimation of the edge effect offset as a function of the width to depth ratio and the calculation of the supercritical subsidence factor as a function of the percent hardrock in the overburden. The edge effect is the offset of the location of the inflection point of the subsidence profile from the rib of the excavation.

Although this package was initially developed over 25 years ago as a result of an integrated research effort at VPI&SU (1987), it has been constantly updated with the incorporation of new analysis features (e.g. dynamic deformations, calibration routines, long-term stability calculations, etc) since then (Karmis et al. 1990a, 1990b & 1992, 2008; Jarosz et al. 1990). SDPS has evolved into a versatile prediction tool that can handle complex tasks, including multiple calibration routines, dynamic subsidence evaluation as well as an estimation of long-term subsidence effects under different scenarios (Karmis et al, 2008,). More recently (2013), the effect of sloping

terrain in the prediction of horizontal displacements has been incorporated allowing for accurate three dimensional predictions of deformation vectors over undermined areas in hilly or mountainous terrain. Furthermore, The SDPS software has been tested extensively in numerous case studies (VPI&SU, 1987; Karmis et al., 1989; Newman et al., 2001, Agioutantis and Karmis, 2002; Karmis and Agioutantis, 2004).

As subsidence modeling tools and software became available, it became apparent that models developed based primarily on Appalachia longwall subsidence data did not translate well to the Illinois basin. Illinois subsidence deformation parameters such as the angle of influence or the maximum subsidence factor were not accurately predicted by the available models. As a result, in 2008 a module was created within the Subsidence Deformation Prediction System (SDPS) (VPI&SU 1987, Agioutantis and Karmis 2013), to adapt the model to different conditions, i.e. central and western US coalfields. The case studies utilized in that research effort, however, were based on historical data which do not reflect current longwall practices in these areas.

## INFLUENCE OF SOFT FLOOR CONDITIONS

In this paper, data from current longwall operations in the Illinois basin have been analyzed in an effort to more accurately estimate the subsidence engineering parameters needed for accurate predictions. An additional complication when analyzing data from Illinois basin operations is the influence of the weak floor as discussed previously. When the gate road pillars are loaded by the abutment loads created by the extraction in the two adjacent panels, the stresses transferred from the pillars to the floor may overcome the bearing capacity of the underclay (fire clay) immediate floor and, thus, pillars may sink or punch into the floor without failing. This mine level deformation will be promoted and accelerated under wet conditions.

Figure 5 presents the subsidence troughs generated due to mining of adjacent panels with and without gate road pillar punching. Pillar punching of the gate road pillars, when isolated (middle drawing Figure 5), effectively generates a smaller trough, but with potentially different subsidence characteristics than the troughs of the mined out panels, i.e. the corresponding influence angle and edge effect values may be different.

The technique of modelling a "pseudopanel" superimposed over the gateroad pillars in order to allow for pillar shrinkage due to pillar loading has been previously applied through the SDPS package (Hasenfus, 2013). This approach can successfully be utilized for direct subsidence calculations; however this technique can not be applied when using the SDPS calibration routines for multiple panels, where subsidence parameters are varied at mine level rather than at panel level.

To overcome this issue, the calibration routines in the SDPS package have been updated to handle different parameter requirements per panel. Thus, the mechanism of subsidence generation when pillars punch into the floor strata can be accommodated by assuming an "*equivalent extraction thickness*".

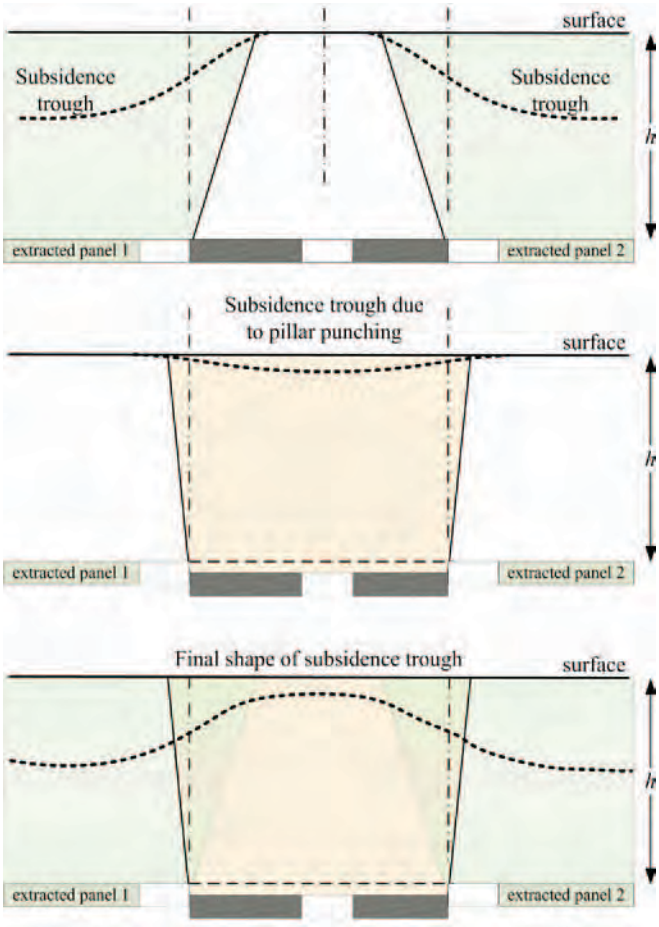



**Figure 5. Equivalent subsidence trough due to gate road pillar punching (panel 1 and panel 2 are fully extracted).**

This feature is optional and should be used only if the operator expects pillar punching or pillar shrinkage (reduced pillar size due to rib spall or rib rashing) in an area, or when investigating different ground movement scenarios.

## ANALYSIS OF RECENT ILLINOIS BASIN CASE STUDIES

This investigation included the analysis of a number of monitoring lines (pin lines) spanning three separate coal mines. Typically, long wall operations collect survey data over the first two panels mined. The purpose of the monitoring is to define movements at the rib, at the panel corner and on the panel long axis. Furthermore a number of pin lines where located over the gate road pillars between two panels, thus movements could be monitored both when the first panel passed by and when both panels had been mined. Figure 6 shows a typical layout of monitoring lines over Mine A.

### Mine A

One of the critical issues when collecting and processing data for subsidence engineering is to determine the actual extraction thickness. Boreholes provide the geological thickness of the deposit. In the case of high capacity longwall mines, it is very common to set the shearer to mine some roof and/or floor material for a number of reasons, such as enhanced productivity, adequate

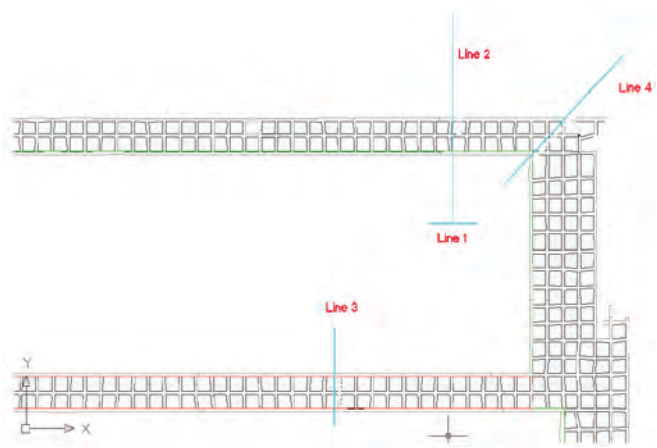



**Figure 6. Typical layout of monitoring lines for Mine A.**

roof stability at the face, etc. In addition, weak shale roof rock that typically falls onto the pan line chain conveyer and conveyed out also contributes to the actual extraction thickness and must be considered in the calculations. When predicting surface deformation due to underground mining, it is important to consider the actual extraction thickness and not the geologic thickness of the extracted seam, especially if the geologic thickness is variable.

The coal seam at the first mine operation (Mine A) lies about 550 feet deep. The seam thickness below the general location of the pin lines is about 6 feet. According to mine personnel, the extraction thickness for this mine varies between 7 and 7.5 feet. Panel widths are about 1300 feet including the width of the entries adjacent to the panels. The edge effect values predicted (Agioutantis and Karmis, 2013) for this width to depth ratio varies between 110 feet (conservative estimate) and 138 feet (average estimate). Figure 7 shows a typical range of influence angle values in the parametric analysis for site calibration for pin line 4. The procedure generates a set of prediction curves based on the parameter range specified by the user. The program then calculates the best fit between the calculated and the measured profile. The parameters used to generate this fitted profile are considered representative of the specific mine or regional location, i.e. the subsidence model is calibrated to the measured data for a particular location. It should be noted that fitted profiles representing the entire curve often do not necessarily fit data at or beyond the panel edge, because the best fit is calibrated for the entire range of data. Figure 8 shows a typical match between fitted and measured data for pin line 2.

Table 1 presents a summary of the analysis conducted using two different extraction thickness values. Note that pin line 1 is located along the longitudinal axis at the center of the panel and, therefore, is not affected by the edge effect offset. As expected, the variation in the assigned extraction thickness affects only the value of the calculated maximum subsidence factor. The best fit values for the edge effect and the tangent of the influence angle do not change. In all cases, the calculated edge effect value is between the minimum and maximum value of the edge effect as predicted by the methodology described in Agioutantis and Karmis (2013).

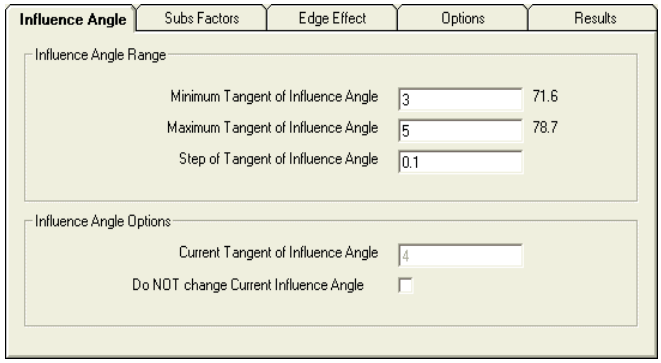



**Figure 7. Specified range for the influence angle during calibration (screenshot from SDPS package).**

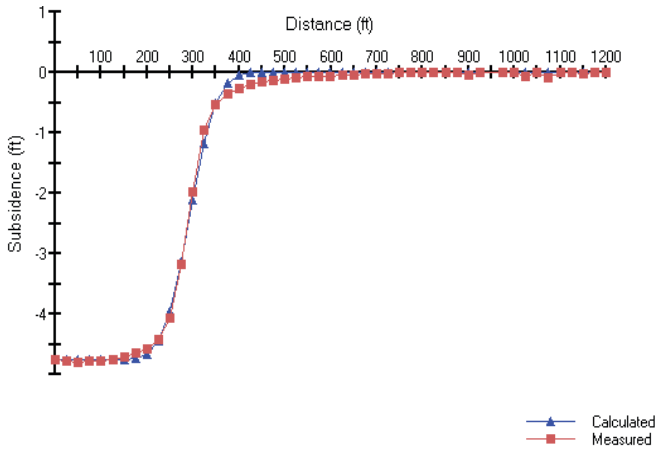



**Figure 8. Measured and calculated data for best fit parameters (Mine A, Pin Line 2).**

### Mine B

The coal seam at the second mine operation (Mine B) is at a depth of about 530 feet. The extraction thickness at the general location of the pin lines is about 10 feet. Panel widths are over 1400 feet including the width of the adjacent entries. The edge effect values predicted for this width to depth ratio varies between 106 feet (conservative estimate) and 133 feet (average estimate).

Table 2 presents a summary of the analysis conducted for Mine B. Note that pin line 1 is located along the longitudinal axis at the center of the panel and, therefore, is not affected by the edge effect offset. Also, pin line 3 spans two panels and the same extraction thickness was assumed for both panels, although results indicate that this may not be the case as shown in Figure 10. In addition, results shown in Figure 10a do not include the effect of the pillars punching into the floor. By applying the procedure described previously (Figure 5), i.e. after defining an equivalent extraction area (pseudopanel) to allow for pillar punching and specifying different edge effect and influence angle values for this area. Figure 10b was generated as the best fit line between measured and calculated subsidence values.

**Table 1. Site specific calibration results for Mine A.**

| | | | | | Values for best fit curve | | | |
|---|---|---|---|---|---|---|---|---|
| Operation | Pin Line | Extraction Thickness, m (feet) | Number of Contributing Panels | Predicted Edge Effect (feet) (*) | Tangent of Influence Angle | Smax/m percent (@) | Edge Effect (feet) | Percent Error (**) |
| Mine A | 2 | 7 | 1 | 110 - 138 | 4.9 | 68 | 120 | 4.4 |
| Mine A | 4 | 7 | 1 | 110 - 138 | 5.2 | 78 | 130 | 22.4 |
| Mine A | 1 | 7.5 | 1 | N/A | 4.8 | 63 | N/A (***) | 0.88 |
| Mine A | 2 | 7.5 | 1 | 110 – 138 | 4.9 | 64 | 120 | 4.7 |
| Mine A | 4 | 7.5 | 1 | 110 – 138 | 5.2 | 74 | 130 | 22.2 |
| (*) edge effect predicted by SDPS – conservative and average values<br>(@) supercritical subsidence factor<br>(**) percent of sum of differences between measured and calculated with respect to the sum of measured subsidence values<br>(***) Pin line is at supercritical conditions and is not affected by edge effect offset | | | | | | | | |

**Table 2. Site specific calibration results for Mine B.**

| | | | | | Values for best fit curve | | | |
|---|---|---|---|---|---|---|---|---|
| Operation | Pin Line | Extraction Thickness, m (feet) | Number of contributing Panels | Predicted Edge Effect (feet) | Tangent of Influence Angle | Smax/m (percent) | Edge Effect (feet) | Percent Error |
| Mine B | 1 | 9 | 1 | N/A | 3 | 74 | N/A | 3.1 |
| Mine B | 2A | 9 | 1 | 106 – 133 | 3 | 68 | 60 | 3.1 |
| Mine B | 4 | 9 | 1 | 106 – 133 | 2.9 | 80 | 70 | 3.9 |
| Mine B | 3 | 9, 9.5, (2.5) (*) | 2 | 106 – 133 | 3.2 | 66 | 60 | 5.5 |
| (*) pillar punching was simulated using an equivalent extraction thickness of 2.5 feet, a steep influence angle and no edge effect | | | | | | | | |

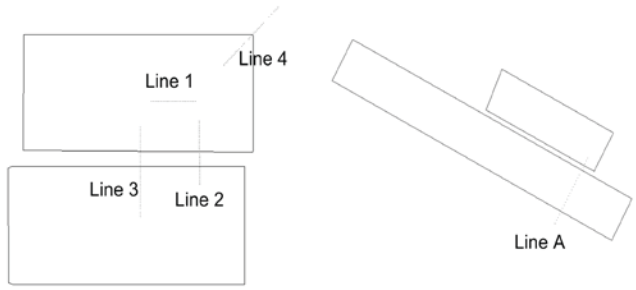



**Figure 9. (a) Monitoring lines for Mine B (b) Monitoring line for Mine C.**

**Mine C**

The coal seam at the third mine operation (Mine C) is at a depth of about 580 feet. The extraction thickness at the general location of the pin lines is about 6.3 feet. Panel widths are about 1350 feet including the width of the adjacent entries. The edge effect values predicted for this width to depth ratio varies between 116 feet (conservative estimate) and 145 feet (average estimate). The percent hardrock for this mine ranged from 15 to 19% between different boreholes. The predicted Smax/m based on this percent hardrock ranges between 69 and 72%.

Table 3 presents a summary of the analysis conducted for Mine C. The analysis includes points on one monitoring line spanning three adjacent panels. The analysis was performed by utilizing all the monitoring points or points over specific parts of the panels. The angle of influence remains pretty consistent, the edge effect value averages 70 feet which is below the values predicted for the particular panel geometry.

## DISCUSSION OF RESULTS

Table 4 presents a summary of the average values for the subsidence engineering parameters estimated at each of the three sites. The average influence angle for Mine A is over 78 degrees, while the influence angle for the other mines is in the order of 72 degrees. The average value for Appalachia is about 67 degrees. The edge effect offset value for Mine A is between the average value (0.25 * depth) and the conservative value (0.20 * depth) as shown in Agioutantis and Karmis (2013). However, the edge effect values estimated for the other mines are about half of the recommended value. It should be noted that it would be important for accurate ground deformation calculations to determine whether the edge effect offset is affected by pillar punching or not.

**Table 3. Site specific calibration results for Mine C.**

| | | | | | | Values for best fit curve | | | |
|---|---|---|---|---|---|---|---|---|---|
| Operation | Pin Line | Extraction Thickness, m (feet) | Number of Panels | Predicted Smax/m (percent) | Predicted Edge Effect (feet) | Tangent of Influence Angle | Smax/m (percent) | Edge Effect (feet) | Percent Error |
| Mine C | 1 | 6.33 | 2 | 69-72 | 116 – 145 | 3 | 70 | 70 | 9.5 |
| Mine C | 1A | 6.33 | 2 | 69-72 | 116 – 145 | 3 | 70 | 75 | 6.8 |
| Mine C | 1B | 6.33 | 1 | 69-72 | 116 – 145 | 3 | 70 | 65 | 1.6 |

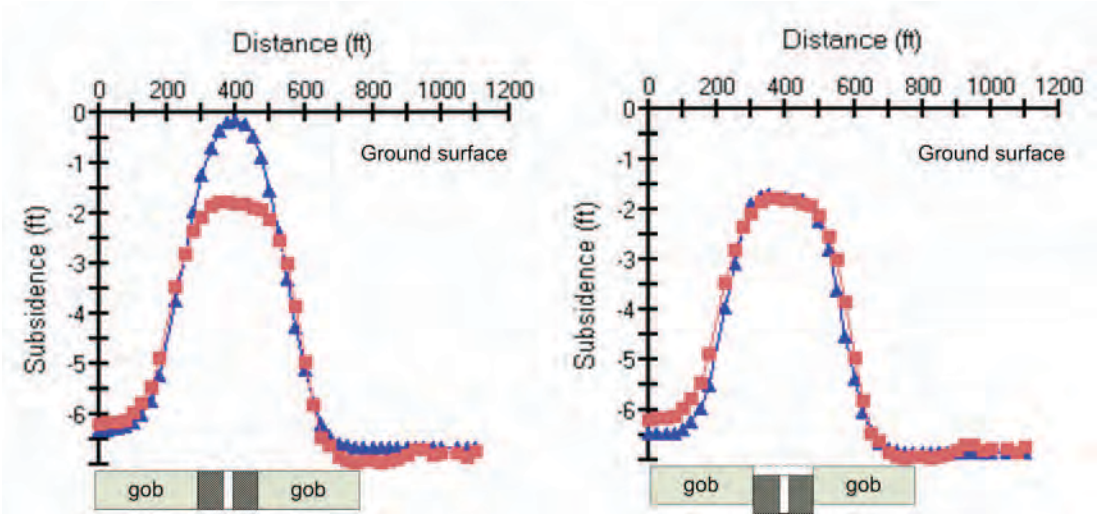



**Figure 10. (a) Best fit between measured and calculated profiles assuming gate road pillars between panels are stable (b). Best fit line assuming an equivalent extraction area in the location of the gate road pillars (the blue lines show calculated values and the red lines show measured values).**

**Table 4. Summary of calibration results for all mines.**

| Site | Width (feet) | Depth (feet) | Extraction Thickness, m (feet) | Width/Depth Ratio | Smax/m (%) | Tangent of Influence Angle | Edge Effect (feet) |
|---|---|---|---|---|---|---|---|
| Mine A | 1300 | 550 | 7 – 7.5 | Supercritical | 69 | 5 | 125 |
| Mine B | 1400 | 540 | 9 – 9.5 | Supercritical | 72 | 3 | 63 |
| Mine C | 1350 | 580 | 6.33 | Supercritical | 70 | 3 | 70 |

The roof of Mine A varies both vertically and laterally, in some cases by substantial amounts. Pod shaped lenses and wedges of gray shale that range from 2 to 20 feet thick and 10s to 100 feet in diameter are distributed throughout the mine. These gray shale pods are the erosional remains of a previously more extensive, and thicker deposit that emanated from peat-contemporaneous river channels that flowed through the peat swamp, and was subsequently removed during marine transgression over the peat swamp. Where the gray shale is eroded, marine black shale and limestone fill in the gaps between the pods. Both the marine black shale and limestone often thickens into these eroded gaps, increasing by as much as several feet. Because of this depositional history, roof lithology can potentially be quite variable over relatively short distances, changing in both thickness and height above the coal, and in cases of very large gray shale pods, both black shale and limestone can be completely absent. In short, this roof is best summarized as heterogeneous.

In contrast, the roof of Mine B is relatively uniform, consisting mainly of a few feet or less of marine black shale and approximately 3 feet of limestone. Minor local variation from these conditions can occur, but there is little deviation across the mine. Mine C follows suit with a uniform roof lithology consisting of black shale and limestone. In both cases the roof of Mine B and C is best summarized as homogeneous.

The floor in all three mines is similar, consisting of a clay rich, gray colored paleosol developed a few feet into silty parent material, with local variation in overall thickness.

It is possible that the greater percent errors and higher tangent of influence angle in Mine A versus Mine B and C are a result of the heterogeneous nature of the lithology of the roof in Mine A. The immediate roof lithology can affect caving characteristics, subsequent gob compaction and ultimately affect surface subsidence parameters. Therefore, variable roof conditions of limestone appearing and disappearing, and large gray shale pods shrinking and swelling, all within tens to a few hundred feet, might reasonably be expected to create variable model results. On the other hand, similar roof lithology thickness, and overall homogeneous roof in Mine B and C may explain the similar model results of Mine B and C.

## CONCLUSIONS

In recent years, there has been an increase in longwall mines and longwall productivity in the Illinois coal basin. Since longwall mining will continue to impact large surface areas, the ability to accurately project subsidence profiles and induced strains is integral to the continued use of the longwall mining method. Coal companies and regulatory agencies require valid and accurate modeling tools to assist in predicting the potential impacts of planned subsidence. Accurately defining the limits and characteristics of planned subsidence will benefit both permitting and the efficient management of subsidence impacts.

In this work, subsidence data from current longwall mining in Illinois was analyzed in an effort to refine regional subsidence engineering parameters developed primarily for other coalfields. Special attention was paid to geologic influences such as weak floor in gate roads and the importance of using the best estimate of the actual extraction void as opposed to seam thickness.

The overall result is an improvement in the SDPS modeled profile fit with an option to consider pillar punching in the gate roads for more accurate subsidence simulation over a series of panels. Further work will be focused on the analysis of dynamic parameters and the analysis of ground strains for the same area.

## REFERENCES


Agioutantis, Z., Karmis, M., (2013). Surface Deformation Prediction System for Windows version 6.1m, Quick Reference Guide and Working Examples, Virginia Polytechnic Institute and State University, August, 330p.

Agioutantis, Z., Karmis, M., (2002). SDPS for Windows: An Application for Subsidence Prediction, Optimum Mine Design and Environmental Control, 7th Symposium on Environmental Issues and Waste Management in Energy and Mineral Production, October 7-10, Cagliari, Italy, 6p.

Cecil, C.B., Dulong, F.T., West, R.W., Stamm, R., Wardlaw, B., (2003). Climate controls on the stratigraphy of a Middle Pennsylvanian cyclothem. In: Cecil, C.B., Edgar, N.T. (Eds.), Climate Controls on Stratigraphy, SEPM (Society for Sedimentary Geology) Special Publication, 77, pp. 151–180.

Hasenfus, G. (2013). Personal communication.

IDNR, (2013). Annual Statistical Report on Coal, Illinois Department of Natural Resources (IDNR), State of Illinois.

Jarosz, A., Karmis, M., Sroka, A., (1990). Subsidence Development with Time – Experiences from Longwall Operations in the Appalachian Coalfield, International Journal of Mining and Geological Engineering, Vol. 8, pp. 261-273.

Karmis, M., Agioutantis, Z., (2004). A Risk Analysis Subsidence Approach for the Design of Coal Refuse Impoundments Overlying Mine Workings, Proceedings, 8th International Symposium on Environmental Issues and Waste Management, in Energy and Mineral Production (SWEMP), May 17-20, 2004, Antalya, Turkey, pp. 205-210.

Karmis, M., Agioutantis, Z., Andrews, K., (2008). Enhancing Mine Subsidence Prediction and Control Methodologies, Proceedings, 27th International Conference on Ground Control in Mining, July 29-31, Morgantown, WV, pp. 131-136.

Karmis, M., Agioutantis, Z., Jarosz, A., (1990a). Subsidence Prediction Techniques in the United States: A State-of-the-Art Review, Mineral Resources Engineering, Vol. 3, No. 3, pp. 197-210.

Karmis, M., Agioutantis, Z., Jarosz, A., (1990b). Recent Developments in the Application of the Influence Function Method for Ground Movement Predictions in the U.S., Mining Science and Geotechnology, Vol. 10, pp. 233-245.

Karmis, M., Haycocks, C., Agioutantis, Z., (1992). The Prediction of Ground Movements caused by Mining, Proceedings, 3rd Workshop on Surface Subsidence due to Underground Mining, Morgantown, WV, pp. 1-9.

Karmis, M., Jarosz, A., Agioutantis, Z., (1989). Predicting Subsidence with a Computer, Coal, Vol. 26, No. 12, pp. 54-61.

Korose, C.P., Treworgy, C.G. Jacobson, R.J., Elrick, S.D., (2002). Availability of the Danville, Jamestown, Dekoven, Davis, and Seelyville Coals for Mining in Selected Areas of Illinois, Illinois State Geological Survey, Illinois Minerals 124, 44 p.

Nelson, W.J., Askari Khorasgani, Z. Elrick, S.D., (2011). Revised Upper Pennsylvanian Stratigraphy of Illinois Basin with Regional Correlations: Geological Society of America Abstracts with Programs, v. 43, no. 5, poster no. 249-18.

Newman, D., Agioutantis, Z., Karmis, M., (2001). SDPS for Windows: An Integrated Approach to Ground Deformation Prediction, Proceedings of the 20th International Conference on Ground Control in Mining, Morgantown, WV, pp. 157-162.

VPI&SU, Department of Mining and Minerals Engineering, (1987). Prediction of Ground Movements due to Underground Mining in the Eastern United States Coalfields, Final report, Contract No. J5140137, Office of Surface Mining, Reclamation and Enforcement, U.S. Department of Interior, Vols I, 205p, and II, 112p.

# Mine Water Vs. Drinking Water—Technical Execution and Legal Relationship in Germany

**Tobias U Papst**, Ph.D. Student & Mining Engineer
**Axel Preusse**, Director, Univ. Prof. Dr.-Ing.
Institute For Mine Surveying, Mining Subsidence Engineering and Geophysics In Mining
RWTH Aachen University
Aachen, Germany

## ABSTRACT

The German Ruhrgebiet is slowly transitioning into a post-mining state. It has been subjected to industrial-grade hard coal mining operations for more than 150 years. Due to a political decision, German hard coal mining will come to an end in 2018. By then the surface will have subsided up to 20 meters.

After all mining activities in the area have ended, there will be no need to maintain the current mine water level. Accordingly, the company operating the last remaining coal mines has decided to let the water level rise to an as yet undetermined level. Alongside other issues that may be caused by rising groundwater levels, the protection of the area's drinking water supply is of utmost importance. This notion is also represented by European and German law. The primary intent of the applicable laws is to protect the health of the citizenship. This means protecting ground water that may be used by humans from being contaminated by the mine water.

This paper outlines the consequences of European and German legislature on mining aftercare using the example of one of Europe's largest agglomerations.

## INTRODUCTION

Every mining operation agrees with the need to regulate the water in the rock mass. Usually water is being pumped away from the mining operation towards the surface. Another consequence of underground mining operations is the inevitable subsidence of the surface and the need to lower the drinking water horizons close to the surface.

The German Ruhrgebiet (Ruhr-District) has been subjected to industrial-grade hard coal mining operations for more than 150 years. Due to a political decision, German hard coal mining will come to an end in 2018. By then the surface, and the adjacent drinking water horizons, will have subsided up to 65 ft and the groundwater level will have been lowered to approximately 4900 ft.

The end of industrial mining will render the continuation of lowering the water to such a depth pointless. Accordingly, the company operating the last remaining coal mines decided to let the water level rise to an as yet undetermined level. Alongside the issues of potential damage to the surface that may be caused by rising groundwater levels, the protection of the area's drinking water horizons is of the utmost importance.

The Ruhrgebiet is Europe's largest metropolitan area and has a population of more than 5 million people. Therefore, the task of protecting the drinking water is driven by three factors: the social responsibility to guarantee clean drinking water to the population, the legal regulations regarding the interaction of mining and drinking water set by the European Union and the German legislation, the technical and geotechnical processes regarding the production of drinking water, and the possible interferences of drinking water and mine water.

This paper will outline the legal and technical issues of the potential interaction between mining water and drinking water in the Ruhrgebiet and present the resulting scenario of post-mining water management.

## REGIONAL STRUCTURE

The Ruhrgebiet is located in the western part of Germany in the federal state of North Rhine-Westphalia (Figure 1). It has the size of 1713 mi² and is the home to more than 5 million people. The area is not considered a political or geographical entity; it is to be seen as a socioeconomic entity that derived from mining activity in the region. The area consists of 53 autonomous cities and counties and has an average population density of 3,100 people per square mile (Regionalverband Ruhr, 2013).

Although the population density surpasses the German average by almost 500% (compared to 600 people per square mile), 72% of the land has been designated to be used as open landscape. About 4% of these areas are covered by water (Regionalverband Ruhr, 2013).

## GEOLOGY AND HYDROGEOLOGY OF THE RUHR DISTRICT

The Ruhrgebiet is part of the European Hard Coal Belt that stretches from England, via France, to Germany, but, as mentioned before, it is not a geological entity. It belongs to four




**Figure 1. Location of the Ruhr District in Germany.**

different geological areas including Münsterländer Becken (Münsterländer basin), Niederrheinisches Tiefland (Niederrhein lowland), Rheinisches Schiefergebirge (Middle Rhine Highlands) and Teutoburger Wald (Teutoburg Forest) (Hahne, Schmidt, & Müller, 1982).

The common ground of those areas is the Carboniferous layer. It contains all hard coal seams being mined in the Ruhrgebiet. The Carboniferous layer strikes to the surface in the south of the region, along the river Ruhr – hence the name Ruhrgebiet. The layer dips to the north and reaches a depth of more than 3000 feet at the northern border of the Ruhrgebiet. The Carboniferous Layer is covered by an overburden consisting of different layers from the Paleozoic, Mesozoic and Cenozoic (Drozdzewski, Kunz, Wrede, & Bornemann, 1980).

The general stratigraphic structure of the region is influenced locally by the four different geological areas. The result is a multitude of local basins, anticlines and minor and major faults that influence both the shape of mining activities and the hydrogeological conditions of the region (Figure 2). Hence, the region is differentiated into two different areas regarding groundwater and three different areas regarding mine water.



**Figure 2. Map of Carbonifersous layer including basins, anticlines and fault lines.**

## GROUND WATER

Regarding groundwater conditions, the region is differentiated into two areas: the northern Westphalia area and the southern Niederrhein area. These areas differ in terms of hydrogeological structure and composition of the groundwater.

In the Westphalia area there are two groundwater horizons. Both of them are located in the overburden and are separated by the Emscher-Mergel, a layer of marl acting as an aquifuge with a thickness between 1000 ft and 1600 ft. While the upper layer plays a major role in the region's water supply, the lower layer is not used for this purpose. Therefore, there will be no detailed description of the lower groundwater layer. The upper groundwater layer consists of fissure water aquifers and pore aquifers. The main part of this layer is the pore aquifer Halterner Sands. The water in the upper layer changes from fresh water to salt water in a depth between 150 ft and 600 ft below the surface. The fresh water contains minor traces of hydrogen carbonate and sulfate. With greater depth, the water contains increasing traces of sodium chloride (Wedewardt, 1995).

The hydrogeological structure of the Niederrhein area is more complex. There is a multitude of different groundwater aquifers that are primarily of only local relevance. The aquifers are fissure water aquifers in different rock types, as well as, fissure water aquifers and pore aquifers in various bunter layers. The upper groundwater layers contain minor traces of different chemical bonds and most may be used as a water supply. The lower layers usually contain large amounts of sodium chloride, are classified as salt water and, therefore, are not used as a water supply (Wedewardt, 1995).

## MINE WATER

The Ruhrgebiet is divided into three mine water zones (Figure 3): a southern zone, a central zone and a northern zone. The zones are separated by major fault lines that act as hydrological barriers. The northern zone and smaller parts of the central zone coincide with the Westphalia area (groundwater). The southern zone and major parts of the central zone coincide with the Niederrhein area (Hahne, Schmidt, & Müller, 1982).

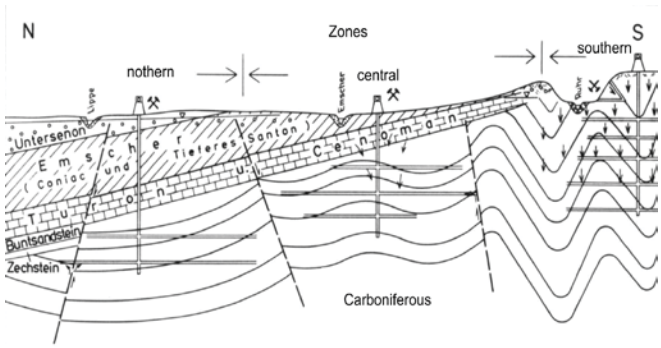



**Figure 3. Mine water zones of the Ruhrgebiet.**

The southern zone has little overburden; therefore, the amount of newly generated mine water is proportional to the amount of precipitation. The mine water in the southern zone has pH values below 7 and contains larger concentrations of metals as well as hydrogen carbonate and sulfates.

The central zone has an overburden of less than 1200 ft. The amount of newly generated mine water is connected to amount of precipitation and the amount of mine water flowing into the zone from other areas. The mine water of the central zone contains large amounts of different metals.

The northern zone has an overburden of more than 1200 ft. The amount of newly generated mine water depends mostly on the amount of mine water flowing into the zone from other areas. The mine water in the northern zone has a high concentration of sodium chloride and a temperature of up to 140° Fahrenheit.

## DRINKING WATER PRODUCTION IN THE RUHRGEBIET

The Ruhrgebiet is supplied with drinking water from two sources. The northern part of the region is supplied with drinking water from the Halterner Sands, and the central and southern part is supplied with drinking water produced by bank filtration at the river Ruhr (Grabert, 1998).

The Halterner Sands is a large pore aquifer embedded in a geological basin of sealing layers. The region has a high amount of annual precipitation (756 mm/a). The geological seal, the precipitation and the consistency of the Halterner Sands (99% quartz) make them a reservoir of good quality and high volume. The drinking water is produced by artificial wells that have been drilled into the fresh water layers of the Halterner Sands (Grabert, 1998).

The amount of drinking water that can be produced from the areas' groundwater is not sufficient to satisfy the regions' demand for drinking water. Therefore, the drinking water in the southern part of the Ruhrgebiet is produced by bank filtration alongside the river Ruhr. As the natural amount of water in the river would also not be sufficient, additional water is piped into the bank filtration facilities from large hydro dams located in the Sauerland – a region of mid-range mountains south of the Ruhrgebiet. The bank filtration is a five-step process: sedimentation of insoluble minerals via sedimentation tanks, 1st oxygen enrichment via open air cascades, gross filtration via gravel tanks, 2nd oxygen enrichment via open air cascades, and fine filtration via sand filters. (Grabert, 1998).

## LEGAL REQUIREMENTS REGARDING WATER

The German legal system is integrated into the legal system of the European Union. Based on the Treaty of Lisbon, the European nations hand a part of their national sovereignty to the European Union in order to facilitate a common European legislature. As a result, the European Union is able to enact different types of laws. The most important kinds are regulations and directives. Regulations have the highest legal force and are directly applicable in Member States. National legislation must be consistent with European regulations; in the case of nonconformity, national laws are trumped by European regulations. National legislation may be applicable if national legislation is stricter than European law and does not contradict the spirit and purpose of the European regulation. European directives commit the nations to enact national laws that aim to achieve the goals set by the directive. The nations have the freedom of choice regarding means, methods and forms to achieve those goals (Bundesamt für politische Bildung, 2014).

The European directive 98/83/EG addresses the quality of water for human usage. It states limits for the minimal purity of water to be deemed suitable for human usage. The directive is implemented into German law by the Law on the Prevention and Control of Infectious Diseases (IfSG). In terms of water, the law states in §37.1 that water for human usage must not cause any damage to humans if consumed or used (Union, 98/83/EG, 1998) (Germany, Gesetz zur Verhütung und Bekämpfung von Infektionskrankheiten (IfSG), 2000).

The European directive 2000/60/EG addresses the quality of water bodies. It states that there must not be any impairment on any above-ground waters. National law enables the directive in the Law on the Organization of the Water Balance (WHG). It states that the groundwater may only be influenced if the quality of the water is not impaired in any way – this includes the ecological and chemical quality of the water, as well as, the water temperature. Furthermore, if groundwater is influenced, this must happen in a way to preserve or attain a good chemical and ecological state (Germany, Gesetz zur Ordnung des Wasserhaushalts (WHG), 2009) (Union, 2000/60/EG, 2000).

Considering the composition of the groundwater and the mine water in the Ruhrgebiet, the application of the IfSG and the WHG means that the groundwater of the Ruhrgebiet must not mix with the mine water, as its ecological and chemical quality is considered inferior to the groundwater's or may influence the temperature of the groundwater. Mine water may be discharged in above-surface water bodies if the quality of the water body is not impaired in a way such that the water body could be harmful to human health in any way.

## ORGANIZATION OF MINE WATER AND ABOVE-SURFACE WATER MANAGEMENT

Due to the long history of mining in the Ruhrgebiet, the surface of the region was subjected to extensive and large-area subsidence; in some places, the surface is subsided more than 60 ft. As a consequence, the drainage capability of the region was influenced. Without the management of mine water, groundwater and above-surface waters, parts of the region would be subjected to inundation and the natural waterways could not stay in their given paths. The management of those consequences is split between the mining company *RAG Aktiengesellschaft* (RAG) and the *Emschergenossenschaft Lippeverband* (EGLV), a water association acting in the public interest to uphold the surfaces drainage capabilities and prevent inundation (Fischer & Wildhagen, 2006).

RAG is responsible (cf. legal requirements) for the mine water handling. In this regard, RAG is pumping about 3,200 million ft³ of mine water to the surface annually. In compliance with German and European law, the mine water is pumped into the rivers Ruhr (40%), Emscher (26%), Lippe (21%) and Rhine (13%). The river Ruhr is used to produce drinking water for the central and southern parts of the Ruhrgebiet (cf. drinking water production). Impairment of the river's water quality can be ruled out: the mine water pumped into the Ruhr originates from the southern mine water zone and therefore is minimally mineralized. Additionally the mine water dilutes to a harmless concentration by mixing with the river's water (Kirchner, Welz, & Weissbeck, 2006) (Fischer & Wildhagen, 2006).

The EGLV is also handling the aftermath of the region's mining activities. Some of the association's tasks are to regulate water flows, flood protection and wastewater treatment. In order to counteract the effects of subsidence – impairment of the surface's drainage capability and of rivers' flow paths – dams and sluices had to be installed. Flood prevention required the embankment of rivers (Figure 4) (elgv.de, 2014).




**Figure 4. Exemplary flood protection measures.**

## CONCLUSION

The Ruhrgebiet is slowly transitioning into a post-mining state. By the time all mining activities in the area will have tapered off, there will be no need to maintain the current mine water levels. Potential scenarios for the final mine water level are restricted by European and German law. The intent of these laws is to protect the health of the citizenship. With respect to the mine water, this means preventing it from mixing with groundwater altogether and only allowing it to mix with above-surface water bodies if human health is protected. The latter may be considered complied with as long as the water body's consistency remains within the limits specified by national law.

The present practice of pumping mine water into the Ruhrgebiet's rivers to keep the mine water at an artificial level will be required for the foreseeable future. Under current legislation, any mining activity in Germany that lowers (or will lower) the mine water level after the shutdown of active mining activities has to consider the repercussions to groundwater quality in the future.

## REFERENCES

Bundesamt für politische Bildung. (2014). Retrieved 03 12, 2014, from http://www.bpb.de/internationales/europa/europaeische-union/42965/grafik-gesetzgebung

Drozdzewski, G., Kunz, E., Wrede, V., & Bornemann, O. (1980). Beiträge zur Tiefentektonik des Ruhrkarbons. Krefeld: Joh. van Acken.

elgv.de. (2014). Retrieved 03 12, 2014, from http://www.eglv.de/en/waterportal.html

Fischer, P., & Wildhagen, E. (2006). Wasserhaltung Ruhr im Rahmen der Anpassung der Förderkapazität unter technischen und Kostenaspekten. In 8. Aachener Altlasten- und Bergschadenkundliches Kolloquium. Clausthal-Zellerfeld: GDMB.

Germany, F. R. (2009). Gesetz zur Ordnung des Wasserhaushalts (WHG). Berlin: Federal Republic of Germany.

Germany, F. R. (2000). Gesetz zur Verhütung und Bekämpfung von Infektionskrankheiten (IfSG). Berlin: Federal Republic of Germany.

Grabert, H. (1998). Abriss der Geologie von Nordrhein-Westfalen. Stuttgart: Schweizerbart.

Hahne, C., Schmidt, R., & Müller, W. (1982). Die Geologie des Niederrheinischen Steinkohlengebietes. Essen: Glückauf.

Kirchner, Welz, & Weissbeck. (2006). Vorlage 34/04/06: HInterlassenschaften des Bergbaus. Arnsberg: Bezirksregierung Arnserg .

Regionalverband Ruhr. (2013). Retrieved 12 05, 2013, from http://www.metropoleruhr.de/land-leute/daten-fakten/lage-und-geografie.html

Ulrich, D. (2014). Wikipedia.com. Retrieved 01 14, 2014, from http://commons.wikimedia.org/wiki/File:Ruhr_area-map.png

Union, E. (2000). 2000/60/EG. Richtlinie zur Schaffung eines Ordnungsrahmens für Maßnahmen der Gemeinschaft im Bereich der Wasserpolitik .

Union, E. (1998). 98/83/EG. Richtlinie übder die Qualität von wasser für den Menschlichen Gebrauch .

Wedewardt, M. (1995). Hydrochemie und Genese der Tiefenwässer im Ruhr-Revier. Essen: DMT.

# Risk Analysis and Risk Ranking in Tunneling: A Case Study

**Behdeen Oraee**, Ph.D. Student
Centre For Environmental Policy
Imperial College London
London, United Kingdom

**Navid Hosseini**, Assistant Professor
**Hamid R Eskandar**, MSc Student
Mining Engineering Department
Azad University of Iran
Tehran, Iran

**Kazem Oraee**, Professor
Department of Management
University of Stirling
Stirling, United Kingdom

## ABSTRACT

Constructing tunnels underground is generally described as a high-risk activity because conditions in the surrounding area tend to be unpredictable. This would and can create unique dangers in every situation.

It is important to gain a deep understanding of the risks associated with tunneling in order to reduce the likelihood of their occurrence and severity of their consequences should they occur. For this to be achieved, different risks should first be evaluated and ranked according to their relative importance and criticality.

The Amir Kabir tunnel is considered one of the most dangerous tunnels in Tehran, Iran, in terms of the risks involved in its excavation and their potential consequences. In particular, part T4 of the tunnel passes through a zone of different strata and also a compound of various soils.

This paper studies part T4 of the Amir Kabir tunnel from a risk analysis and risk management point of view. In doing so, factors increasing total cost, causing delay in the project completion time, decreasing the operation rate and downgrading project quality were identified and ranked according to their importance using the aggregate primary index risk method. For this purpose, a comprehensive questionnaire was designed and completed by tunneling experts. By responding to the questionnaires, the experts determined the relative likelihood of occurrence of the studied factors and their potential consequences. As a result, the experts suggested several alternatives to reduce the risks involved in this particular study. Moreover, the experts completed new questionnaires whilst taking into account different alternatives. In the next step, the risks before and after applying the alternatives were compared. As a result of performing the said analyses, it was concluded first that the aggregate primary index risk is an effective tool in identifying the risks involved in such projects. Second, it was concluded that, by taking into account different alternatives when analyzing and ranking the risks, severity of the said risks can potentially be reduced. Also, by considering such matters when analyzing tunneling risks, the projects' efficiency can greatly increase as a result of reducing risks that threaten financial and human resources. The approach introduced in this paper, together with the methodology described, can be adopted by the mining design engineer in all similar situations. They will be of particular advantage in such methods as room and pillar mining, where the number of similar tunnels required is high.

## INTRODUCTION

The speed at which tunneling projects are being carried out has increased dramatically in recent years in Iran.

Constructing tunnels underground is generally described as a high-risk activity because conditions in the surrounding area tend to be unpredictable. This would and can create unique dangers in every situation.

The word "risk" has varying meanings, depending on different contexts used. To the common man, risk simply is the concept of probability and severity of an outcome (Oraee-Mirzamani, 2014). Many studies on this have been carried out by scholars due to its importance in every project. For example, Sharifzadeh et al., in their research, chose the most convenient Tunnel Boring Method (TBM) to excavate the Nosoud tunnel using risk analysis (2008). Baccarini analyzed the effect of time, cost and quality on ranking project risks using risk management techniques (Baccarini, 2001). Furthermore, Beard analyzed tunneling safety management and the decrease in risk using different indices (2010), and Isaksson explained the cost, design time and building the underground tunneling projects in a function of probability (Isaksson and Stille, 2005).

Although many tunneling projects have been carried out in safe conditions, unexpected events have also happened in some projects, resulting in delays, an increase in project costs, injuries and death (Sousa, 2012). Therefore, risk analysis and risk management is a crucial part of any tunneling project. Risk evaluation is a part of risk management that can help decision makers to consider better reactions and perceptions by ranking the existing dangers (Fouladgar et al., 2012).

The aim of this paper is to rank the risks associated within the part T4 of the Amir Kabir tunnel project using the aggregate primary index risk in terms of their criticality and importance.

## THE AMIR KABIR TUNNEL

The project of constructing the Amir Kabir tunnel is one the most important projects in Tehran; it commenced in 2009 and is located in the east of Tehran's Bazaar. The tunnel is 2350 m long and divided into six main parts.

The first part is an underpass, which has been constructed using the cut-and-cover technique. The second part holds a two-sided tunnel that passes under a street beneath a construction site with a three-story underground parking structure and four-story building with its basement connected to the tunnel. The fourth part consist of a two-sided tunnel that passes under a street which then divides into two one-sided tunnels at a major square. The fifth and sixth parts begin from the square as two one-sided tunnels and continue until it reaches a major highway. The studied zone is this extension from the square to the highway. Figure 1 shows a plan view of the location of the tunnel and the section which has been studied in this paper.




**Figure 1. The plan view of the Amir Kabir tunnel.**

The Austrian method, or New Austrian Tunneling Method NATM, was applied to excavate the Amir Kabir tunnel. In this method, an appropriate design is implemented based on the adjacent land from the tunnel and controlled by exact devices. The subsidence is experimentally controlled by regulating excavation speed, completing the casing and facing the excavating surface in NATM excavation. Such specifications have led to the NATM method serving as a suitable option for tunneling engineers.

It should be noted that the NATM is not a specific excavation and support technique. It involves a combination of many established ways of excavation and tunneling, but the difference is the continual monitoring of the risk movement and the revision of support to obtain the most stable and economical lining (Aşçioğlu, 2007).

In this method, it is best to completely excavate the working face leading to a perfect stress distribution. Excavating segment by segment (Figure 2) is necessary in projects carried out on loose land, such as the Amir Kabir tunnel project.

Fore-polling was applied to the tunnel of this study, supported by lattice and dry shotcrete. Moreover, rock bolts were not used in this tunnel. Fore-poling is applied in order to limit the pressure around the top of the tunnel by acting as a pre-supported system, making excavation safe and secure.

Underground water can increase different risk factors in tunneling projects, such as time and cost. In this part of the

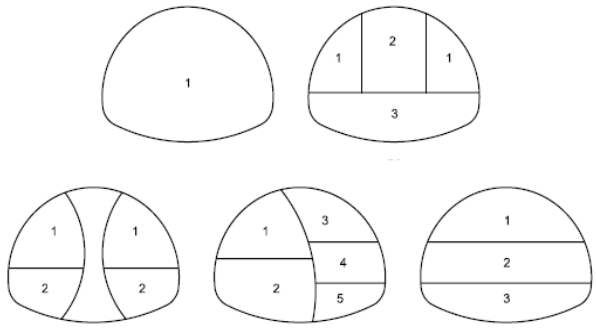



**Figure 2. The plan view of the Amir Kabir tunnel.**

tunnel, the underground water level is less than that of the tunnel; therefore, the possibility of any water seeping into the tunnel only arises when it is raining or when the water supply is destroyed. As shown in Figure 3, insulation can be used in these cases to mitigate risk and reduce the chance of water seepage into the tunnel (Kolymbas, 2005).

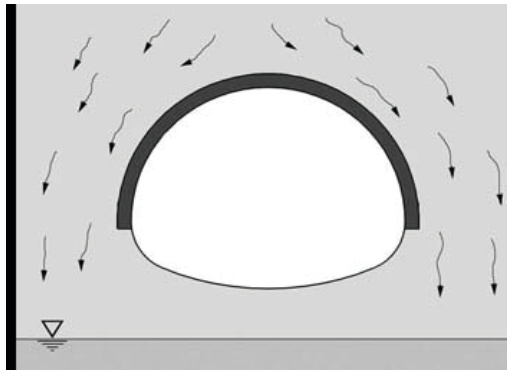


**Figure 3. Umbrella waterproofing.**

Subsidence is considered as one of the significant negative effects in civil engineering tunneling projects; furthermore, it is essential to control the subsidence that results to structures above tunnels.

Moreover, subsidence depends on various factors, including geological, hydrogeological and geotechnical conditions, tunneling geometry and depth excavation methods as well as the quality of workmanship and management. It is, however, clear that a shallow tunnel will tend to have greater effect on surface structures in comparison to a deep one (Eric, 2006).

In the case of this study, a certain tunnel length is considered for risk analysis purposes. The tunnel diameter is approximately 11 m and the overburden height is almost 9 m. Due to the overburden height, the weight of structures above should be considered in when analyzing subsidence risk. In the considered section of the tunnel, the thickness of the dry shotcrete is 30 centimeters and the final lining thickness is 40 cm.

According to the classification of sands by USGS (Memarian, 2009) (Table 1 and Table 2), a major section of the studied zoned

**Table 1. Classification of sands.**

| Major Divisions | | | Group Symbols | Typical names |
|---|---|---|---|---|
| Coarse grained soils (more than 50% of material is larger than No.200 sieve size) | Gravels More than half of coarse fraction is larger than No. 4 sieve size. | Gravels with fines (appreciable amount of fines) | GM | Silty gravels, gravel-sand-silt mixtures |
| | | | GC | Clayey gravels, gravel-sand-clay mixtures |
| | | Clean gravels (little or no fines) | GW | Well-graded gravels, gravel-sand mixtures, little or no fines |
| | | | GP | Poorly-graded gravels, gravel-sand mixtures, little or no fines |
| | Sands More than half of coarse fraction is smaller than No. 4 sieve size. | Clean sands (little or no fines) | SP | Poorly graded sands, gravelly sands, little or no fines |
| | | Sands with fines (appreciable amount of fines) | SC | Silty sands, sand-silt mixtures |
| | | | SM | Silty sands, sand-clay mixtures |
| Fine grained soils (50% or more of material is smaller than No.200 sieve size) | Silts and clays Liquid limit less than 50 | | ML | Inorganic silts and very fine sands, rock flour, silty of clayey fine sands or clayey silts with slight plasticity |

**Table 2. Material properties.**

| Core No. | TP13 | TP12 | TP11 | TP10 | **TP9** |
|---|---|---|---|---|---|
| Angle of internal (degree) | 32 | 31.9 | 33.4 | 32.1 | **33.3** |
| Cohesion (kg/ sq cm) | 0.13 | 0.11 | 0.14 | 0.13 | **0.1** |

includes very tiny particles of sand, layer sand, a combination of sand, gravel and much smaller particles, clean gravels and sands with appropriate grain size distribution and mixtures of sand and gravel.

## RISK

Risk management generally entails an iterative process encompassing risk detection, risk assessment, planning against risk, risk stability and controlling and reviewing the risk (Figure 4). The risk level in any given scenario is defined by the result of the multiplication of the likelihood of occurrence of the risk by its consequence, should it occur (Equation 1).

$$\text{Risk level} = \text{Likelihood} \times \text{Consequence} \quad (1)$$

This paper determines the risks in accordance with time, cost, project quality and operation. Equation 1 can be expanded in different ways, depending on one's needs, in order to identify the risk level and its rating in accordance with its importance and criticality. In order to analyze the risks, weights have to be assigned to the factors being studied: time, cost, project quality and operation in order to increase the risk rating accuracy. The Primary Index Risk formula (Equation 2) and the Aggregate Primary Risk Index (Equation 3) can be applied to rate the risks (Foroughia, 2013).

$$PIR = \sum \left(W_i (P.I_i)\right) \quad (2)$$

Where

$P$ = Probability

$I$ = Level of Influence

$W$ = Weight of the consequence of time, cost, quality and operation factors

$$\sum_{i=1}^{4} W_i = 1$$

(The sum of the presented factors will be)

Such indexes are aggregated using the weighted total average method. In this process, the aggregate primary index risk is calculated for each risk using Equation 3.

$$APIR = \frac{\sum_{j=1}^{m} \left(\left(n_j \times PIR_j\right)\right)}{N} \quad (3)$$

Where

$M$ = Expert members

$N_j$ = Number of people in group $j$

$PIR_j$ = The primary index risk for each one of the risks in group $j$

$N$ = Total number of experts

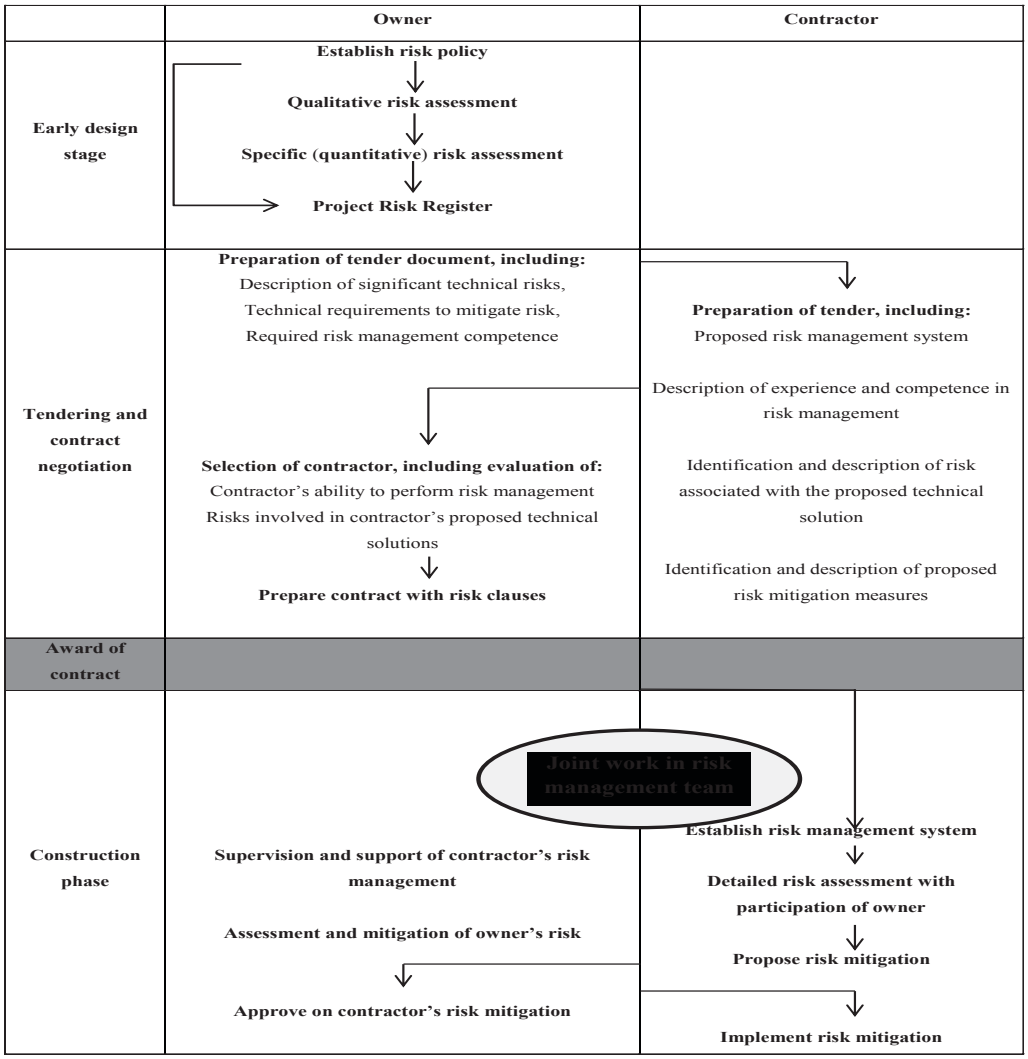



**Figure 4. Risk management activity flow for the owner and contractor.**

For this purpose, a comprehensive questionnaire was designed and completed by tunnelling experts, who were asked to complete the questionnaires using PMBOK and LIKERT standards (shown in Table 3 and Table 4) to determine the relative likelihood of occurrence of the studied factors and their potential consequences. The experts were then asked to suggest new alternatives in order to reduce the likelihood and occurrence of the risks and complete the tables accordingly. It was observed that by suggesting simple alternatives, it was possible to dramatically decrease the completion time and cost of the project as well as increase project quality.

In this research, experts' opinions were collected using surveys and then studied using the Delphi technique, the conference method and brainstorming with a group of seven experts, a group of six experts, two groups with five experts each and another two groups with four experts. Some of the said experts were project managers working on this very tunneling project. As a result of the expert consultation, weights of 0.35, 0.4, 0.15 and 0.1 were assigned to cost, time, operation and project quality, respectively. Table 5 displays the studied risks within this study, the aggregate primary index risk and the alternatives.

Furthermore, some of the alternatives suggested by the experts to reduce the risks associated with this tunneling project included:

- Monitoring and controlling tunnel facing work
- Suitable drainage
- Accurate and exact planning
- Choosing an experienced contractor
- Using experienced personnel and holding training courses for those less experienced
- Wearing helmets and safety gloves
- Using standard machinery
- Precise mapping
- Employing instrumentation and controlling subsidence
- Providing sufficient light in the workshops

Figure 5 illustrates the difference between the aggregate primary index before and after the new alternatives were suggested. Furthermore, Figure 6 shows the dispersion of the aggregate primary index before and after using the new alternatives.

**Table 3. Questionnaire to determine relative likelihood of occurrence of factors investigated in study.**

| | Likelihood | | | | |
|---|---|---|---|---|---|
| **PMBOK** | <5% | 6% - 25% | 26% - 50% | 50% - 71% | 71%< |
| **LIKERT** | Very low | Low | Moderate | High | Very high |
| | 0.1 | 0.3 | 0.5 | 0.7 | 0.9 |

**Table 4. Questionnaire to determine relative consequence of the factors investigated in study.**

| Consequence | | | | | |
|---|---|---|---|---|---|
| **Project Objective** | Very low 0.5 | Low 0.10 | Moderate 0.20 | High 0.4 | Very high 0.80 |
| **Cost** | Insignificant cost increase | <10% cost increase | 10-20% cost increase | 20-40% cost increase | >40% cost increase |
| **Time** | Insignificant time increase | <5% time increase | 5-10% time increase | 10-20% time increase | >20% time increase |
| **Performance** | Quality degradation barely noticeable | Only very demanding applications are affected | Quality reduction requires sponsor approval | Quality reduction unacceptable to sponsor | Project end item is effectively useless |
| **Quality** | | | | | |

A graph is depicted and risk changes can be pondered only by considering the co-efficiency of *P* and *I* (before and after presenting the alternatives) in Figure 7.

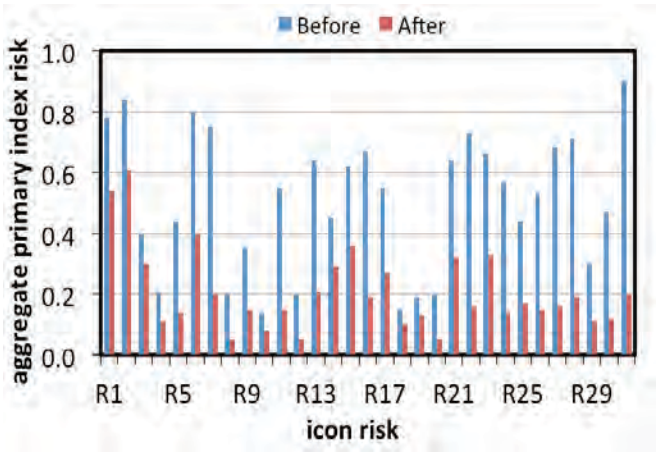



**Figure 5. Graph of the primary risk index before and after practicing the risk reduction alternatives.**

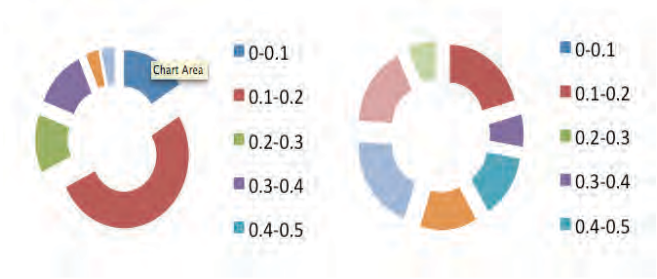



**Figure 6. The primary index risk dispersion before and after a reduction in the risk.**

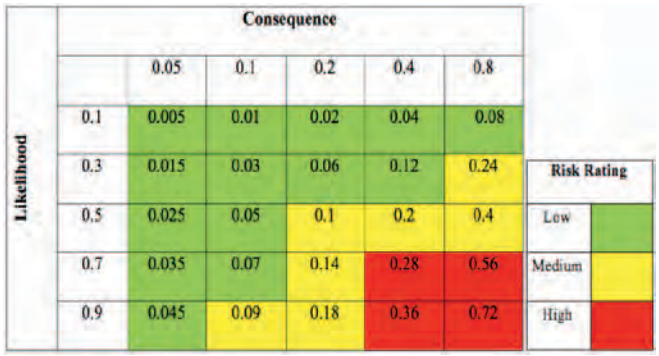



**Figure 7. Consideration of the coefficiecy of P and I before and after presenting the alternatives. .**

**Table 5. Studied risks for the before and after alternative designs.**

| | Risk | Aggregate primary index | |
|---|---|---|---|
| | | Before | After |
| R1 | Subsidence | 0.78 | 0.54 |
| R2 | Walls falling down and facing work | 0.84 | 0.61 |
| R3 | Not having enough information on mapping | 0.4 | 0.3 |
| R4 | Not being well-informed from the zone's geotechnical information | 0.21 | 0.11 |
| R5 | Water entering into the tunnel whilst excavating | 0.44 | 0.14 |
| R6 | Lack of cooperation between employer and contractor | 0.80 | 0.4 |
| R7 | The risk of tunnel's water proofing layer being damaged and torn | 0.85 | 0.2 |
| R8 | Injury to personnel whilst installing water proofing layer | 0.2 | 0.05 |
| R9 | Incorrect installation of armature | 0.35 | 0.15 |
| R10 | Injury to personnel whilst installing the armature | 0.14 | 0.08 |
| R11 | Damage to excavating machinery | 0.55 | 0.15 |
| R12 | Injury to personnel whilst excavating | 0.2 | 0.05 |
| R13 | Damage to machinery carrying the materials | 0.64 | 0.21 |
| R14 | Personnel injuries while carrying the materials | 0.45 | 0.39 |
| R15 | Inappropriate excavating while installing the fore-poling | 0.62 | 0.36 |
| R16 | Incorrect installation of pipes in fore-poling | 0.67 | 0.19 |
| R17 | Incorrect injection in fore-poling | 0.55 | 0.27 |
| R18 | Personnel getting injured while installing the fore-poling | 0.15 | 0.1 |
| R19 | Incorrect installation of lattice | 0.19 | 0.13 |
| R20 | Injuries while installing the lattice | 0.2 | 0.05 |
| R21 | Not having access to practical equipment | 0.64 | 0.32 |
| R22 | Wasting the concrete whilst applying shotcrete | 0.73 | 0.16 |
| R23 | Unskilled operator in regulating the amount of water in shotcrete | 0.66 | 0.33 |
| R24 | Dust | 0.57 | 0.14 |
| R25 | Injury whilst applying shotcrete | 0.44 | 0.17 |
| R26 | Not supplying materials on time | 0.53 | 0.15 |
| R27 | Materials' low quality | 0.68 | 0.16 |
| R28 | Delay in concrete production | 0.71 | 0.19 |
| R29 | Pumps' failure at the final concrete mold | 0.30 | 0.11 |
| R30 | Damage to final mold's jacks | 0.47 | 0.12 |
| R31 | Injury to personnel whilst working with final mold | 0.9 | 0.20 |

## CONCLUSIONS

This paper detected and evaluated 31 risks within the Amir Kabir tunnel project in order to gain a better understanding of the risks involved, and, therefore, take necessary actions to minimize their occurrence and consequences. Furthermore, performing different risk analyses and risk management techniques has led to a better understanding of the risks involved in the operation phase, hence minimizing the threat to human, environmental and financial resources. The expert surveys were completed by industry experts, including those who were involved in the design and implementation stages of this tunneling project as well as experts from academia. Therefore, one can assume that the results of this study are as close as reliable as possible given the circumstances.

From Figure 5 and Figure 6, it can be concluded that the likelihood of occurrence and subsequent consequences of risks can potentially be significantly reduced as a result of taking simple actions, reducing completion time and project cost while also increasing the project's operation and quality. Moreover, before implementing the actions that resulted in a reduction of the said risks, 60% of the risks were placed in the high-risk category —and reduced to 10% thereafter. Furthermore, according to Figure 6, the highest primary index risk dispersion was in the range of 0.6 to 0.7, which was equivalent to 21%, but was reduced to 3% after using the alternatives to reduce risks. As a result, the highest primary risk dispersion was changed to be in the range of 0.1 to 0.2, which was equivalent to 51%.

The results of this study show that "walls falling down and facing work," "subsidence" and "water entering into the tunnel whilst excavating" have the highest risk ratings after risk reduction techniques have been employed. Therefore, it is essential that tunneling project designers, project managers and contractors pay special attention to these risks.

## REFERENCES


Aşçioğlu, Gökhan (2007). "Analysis of Support Design Practice at Elmalik Portals of Bolu Tunnel." Thesis submitted to Graduate

Baccarini D., Archer R. (2001). "The Risk Ranking of Projects: a Methodology." *International Journal of Project Management*, (19) 139-145.

Beard, A.N. (2010). "Tunnel Safety, Risk Assessment and Decision Making." *Tunneling and Underground Space Technology*, (25) 91-94.

Eric, W.G., Leca, B. (2007). "ITA/AITES Report 2006 on Settlements Induced by Tunneling in Soft Ground." *Tunneling and Underground Space Technology*, (22) 119-149.

Eskesen, S., Tengborg, P., Kampmann, J., Veicherts, T.R. (2004). "Guidelines for Tunneling Risk Management: International Tunneling Association, Working Group No. 2." *Tunneling and Underground Space Technology*. (19) 217-237.

Foroughia, A., Esfahanib, M.J. (2012). "An empirical study for ranking risk factors using linear assignment: A case study of road construction." *Management Science Letters*, (2) 615-622.

Fouladgar, M.M., Yazdani-Chamzini A., Zavadskas E.K. (2012). "Risk evaluation of tunneling projects." *Civil and Mechanical Engineering*, (12) 1-12.

Isaksson T., Stille H. (2005). "Model for Estimation of Time and Cost for Tunnel Projects Based on Risk Evaluation." Rock Mechanic. *Rock Engineering*, (38): 5, 373–398.

Kolymbas, D. (2005). Tunneling and tunnel mechanics A Rational Approach to Tunneling.

Memarian, H. (2009). *Engineering Geology and Geotechnics*. University of Tehran Press, 5th ed.

Oraee-Mirzamani, B. (2014). Environmental Risk Analysis Associated with Carbon Capture and Storage. Ph.D. Thesis.

Sharifzadeh M., Shahriar K., Khademi Hamidi J. (2008_. "Geotechnical risk assessment based approach for rock TBM selection in difficult ground conditions." *Tunneling and Underground Space Technology*, (23) 318–325.

Sousa, Rita L. and Einstein, Herbert H. (2012). "Risk analysis during tunnel construction using Bayesian Networks: Porto Metro case study." *Tunneling and Underground Space Technology*, (27) 86–100.

School of Natural and Applied Sciences of Middle East Technical University. http://www.risk-assessments.org/risk-assessment-matrix-5x5.html

# Strata Movement Around Large Mining Height Face Area with Fully Mechanized Method in Steeply Dipping Thick Seam

**Yongping Wu**, Professor
**Panshi Xie**, Mine Engineer
**Hongwei Wang**, Ph.D. Student
**Juan Dou**, Mine Engineer
**Xicai Gao**, Ph.D. Student & Mining Engineer
**Youfu Zeng**, Ph.D. Student & Mining Engineer
Xi'an University of Science and Technology
**Dongfeng Yun**, Professor
Xi'an University of Science and Technology
Xi'an, China

## ABSTRACT

The steeply dipping coal seams in this paper refer to those with the angle of inclination ranging from 35° to 55°. The reserves of the steep coal seams account for approximately 15%~20% of the total coal reserves in China. In the past 12 years, the top-coal caving mining method had been used to mine the steeply dipping thick (11.5-16.4 ft or 3.5-5.0m) coal seams. However, the mining process of top coal caving is complex with low recovery rate and nearly 30% of coal was wasted. Those problems can be solved by using the single pass large mining height (11.5-16.4 ft or 3.5-5.0m) method. But the movement of the overlying strata around the mining face area of large mining height is complex and it is hard to control the stability of "rock-shield support" system. Therefore, field measurement, numerical simulation and physical (similarity material) simulation methods were used simultaneously to analyze the strata movement, roof structure and rock-shield support interaction characteristics. The results indicate that strata movement, which is the same as mining the steeply dipping seams with conventional mining heights, is asymmetrical about the dipping direction of the face; deformation, failures, and movement of the surrounding rocks are more intense; the roof weighting interval decreases; the weighting intensity increases significantly; and face sloughage occurs frequently. In the gob, the space for sliding and rolling of the roof increases; the broken main roof tends to form an anti-dip pile structure; the backfilling and compactness of broken roof increase at the lower portion of the face, thereby inducing significant unbalance in stress distribution between the upper and lower portions of the face. The overlying strata above the face form a multi-level step structure. The characteristics of contact and loading of roof-shield support system are more complex. The range of shield load variation is larger, and interaction between shield supports occurs frequently. Anti-toppling and anti-sliding devices at the face become more difficult to implement. The research results provide a theoretical basis for the mining practices in the steeply dipping thick seams with a large mining height. The practice in panel 25221 of 2130 coal mine indicates that the accident rates have been greatly reduced and good technical and economic benefits have been realized.

## INTRODUCTION

The steeply dipping coal seams refer to those with dipping angle in the range of 35°~55°. In China, the reserves of this type of coal seams account for approximately 15%~20% of the total coal reserves. More than 50% of the steeply dipping seams are high quality coking coal and anthracite that are special and rare in China. Normally, the maximum mining height of most steeply dipping coal seams is lower than 9.8 ft (3m) in China. For example, the maximum mining height of the Xinjiang 2130 coal mine is 8.2 ft (2.5m) (Huang et al., 2013), and the mining height of the Dongxia coal seam is 7.5 ft (2.3m) (Wu et al., 2006). The single pass large height mining (11.5-16.4 ft or 3.5-5.0m), having a simple mining process and a high recovery rate, is a better approach to mine this type of coal seams. However, an extensive literature search had found that there have been few studies on the ground control issues of mining the steeply dipping seams with large mining height. Previous research and practices of mechanized longwall mining in the steeply dipping seams (Xie, 2011, Xie, Wu et al., 2012) had found that there are significant differences in the characteristics of the surround rocks and shield support between the single pass large mining height mining method and the top-coal caving mining method, in particular, in the following three aspects: (1) During the large mining height mining process, the increase of mining height increases the offset of the center of gravity of the shield support, making it more liable to topple; (2) The roof deformation, failure and movement become more intense, especially at the top section of the face; and (3) The gob space that allows the caving roof to slide, rotate, and backfill is enlarged, leading to more complex moving and filling characteristics of the collapsed rock blocks. By using multiple well-proven research methods including the physical and numerical simulations and field monitoring and practice at a large mining height longwall face, this paper researched the formation and development mechanics of the stress field in the surrounding rocks around the mining face. It also researched the dynamic stability control issues among the "support-surround rock" system under the caving roof with different mining heights. The goal is to provide a theoretical foundation for handling the stability issues of the roof-shield support and the control of failure of surrounding rocks and large area strata movement.

## BACKGROUND OF PROJECT

The 2130 Coal Mine is owned by Xinjiang Tar Coal Group in Xinjiang Province, China. The #5 coal seam is uniform and simple in structure with an average thickness of 5m and an average dipping angle of 45°. The coal is weak and loose with f = 0.3-0.5. The main roof is sandstone with an UCS (uniaxial compressive strength) of 79.9-100.2MPa.The floor is mud stone with an UCS of 9.14-12.76MPa.The width of panel 25221 along the dip direction is 344 ft (105m) and the length along the strike direction is about 5,792 ft (1,766m). The average mining height using the fully-mechanized longwall mining method is about 13.8 ft (4.2m). Figure 1 shows the panel layout.

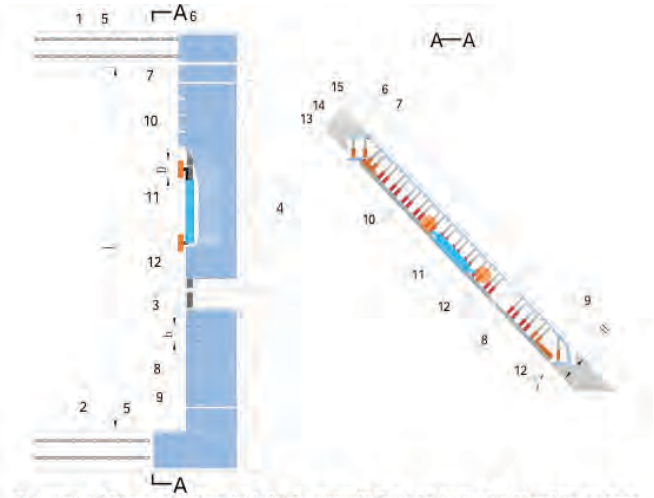


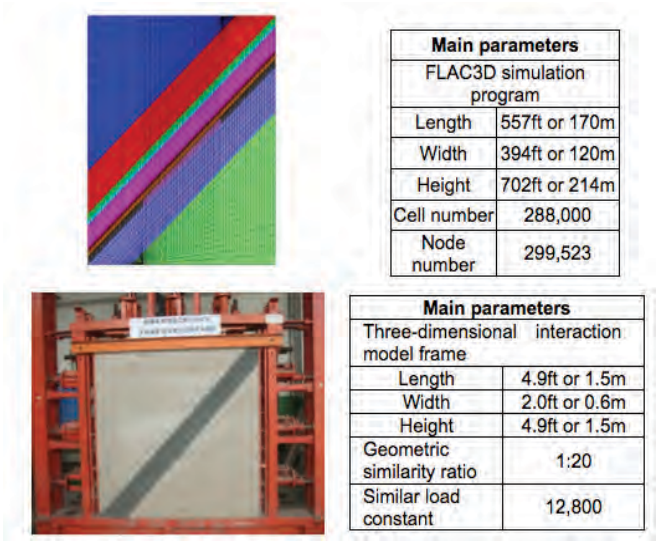

**Figure 1. Layout of large mining height longwall face in steeply dipping seam.**

## DEFORMATION AND MOVEMENT OF THE SURROUNDING ROCKS

Based on the mining and geological conditions stated previously, the numerical and physical simulation models were established as shown in Figure 2.

### Deformation and Movement of Strata Surrounding the Longwall Face

*Stress distribution in the surrounding rocks:* When mining a steeply dipping thick seam, the stresses are relieved in the middle of the immediate roof and floor and concentrated at the two ends of the face. The stress distribution in the immediate roof and floor along the dipping direction is asymmetric, and the area of stress relief in the middle and upper parts of the face is larger than the lower part; the maximum stress concentration at the upper part is smaller than the lower part area.



| Main parameters | |
|---|---|
| FLAC3D simulation program | |
| Length | 557ft or 170m |
| Width | 394ft or 120m |
| Height | 702ft or 214m |
| Cell number | 288,000 |
| Node number | 299,523 |

| Main parameters | |
|---|---|
| Three-dimensional interaction model frame | |
| Length | 4.9ft or 1.5m |
| Width | 2.0ft or 0.6m |
| Height | 4.9ft or 1.5m |
| Geometric similarity ratio | 1:20 |
| Similar load constant | 12,800 |

**Figure 2. Models of numerical and physical simulations.**

The stress distribution around the face is almost the same for different mining heights. However, the stress decreases with increasing mining height in the area of stress relief in the immediate roof and floor, as well as the stress concentration area at the lower end of the face. Whereas, the stress increases with increasing mining height in the stress concentration area at the upper end of the face. This phenomenon is mainly induced by the different filling condition (different mining height) at the lower end of the face. Figure 3 shows the stress distributions.

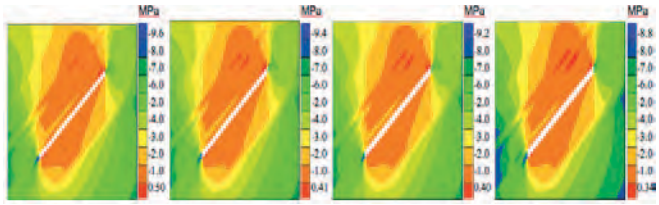


**Figure 3. Vertical stress distributions around the inclined faces under different mining heights (a) 3.5 m, (b) 4.0 m, (c) 4.5 m, and (d) 5.0 m.**

Along the strike (panel length) direction, the stress relief area in the roof is larger than that in the floor. The stress distribution around the face is almost the same for the different mining heights. However, the stress in the stress relief area increases with increasing mining height (see Figure 5). Furthermore, in the face with large mining height, the stress distribution is same as the conventional mining heights (<11.5 ft or 3.5m), except that the area of stress relief increases significantly under the large mining height.

*Distribution characteristic of plastic zone:* The plastic failure areas formed in the roof and floor are larger and are of tensile failures. At the upper and lower ends of the face, the plastic failure areas are smaller and are of compression and shear failures. The failure area of the upper end of the face is larger than that of the lower end. Under different mining height conditions, the distribution of plastic failures is the same around the mining area, but the areas of compression and shear failures at the lower part increase with increasing mining height. The plastic failure distribution is shown in Figure 4.

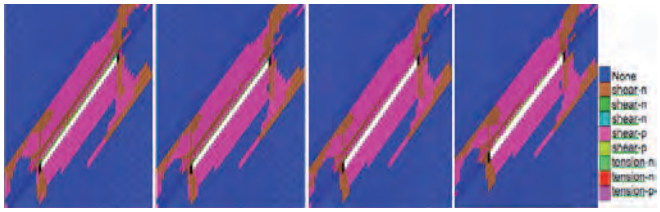


**Figure 4. Plastic zones around the inclined face under different mining heights (a) 3.5 m, (b) 4.0 m, (c) 4.5 m, and (d) 5.0 m.**

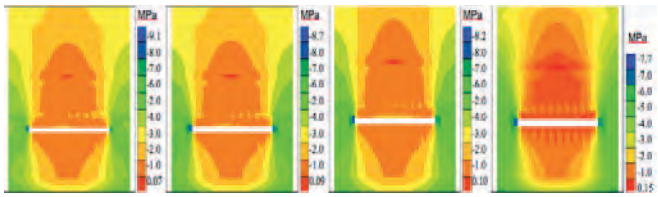


**Figure 5. Vertical stress distribution along the panel length direction under different mining heights (a) 3.5 m, (b) 4.0 m, (c) 4.5 m, and (d) 5.0 m.**

*Distribution characteristic of abutment stress:* Along the strike (panel length) direction, the area and magnitude of stress concentration in the coal face increase with increasing mining height. When the mining height is 16.4 ft (5m), the maximum stress is 7.66 MPa and the stress concentration ratio is 2.04 (see Figure 5). At the first weighting when mining height is 14.8 ft (4.5m), the maximum abutment stress located at 8.2ft (2.5m) deep into the coal face is 5.28 MPa and the stress concentration ratio is 1.54. During the periodic weighting, the maximum abutment stress is 7.71 MPa and the stress concentration ratio is 2.25.

**Deformation and movement of the face**

*Movement of surrounding rocks:* During the process of large height mining in steeply dipping seams, the displacement of the roof area is larger than that of the two ends of the face, with the smallest deformation occurring at the floor. Along the face direction, the maximum displacement of the immediate roof occurs in the middle section, while the minimum displacement occurs at the lower end of the face. Under different mining heights, the movement characteristics of the surrounding rocks are almost the same, except that the displacement of surrounding rocks increases gradually with increasing mining height.

When the mining height is 9.8 ft (3.0m), the first caving interval of the main roof is 172.2 ft (52.5m) while the periodic weighting interval is 44.3 ft (13.5m). The collapsed roof of the lower strata is relatively intact. When the mining height is 13.1ft (4.0m), the first caving interval of the main roof is 157ft (48m) while the periodic weighting interval is 37.7ft (11.5m). The collapsed roof of the lower strata becomes smaller. When mining height is 16.4 ft (5.0m), the first caving interval of the main roof is 131 ft (40m) while the periodic weighting interval is 32.8 ft (10.0m). The collapsed roof of the lower strata becomes more fragmented, while the size of collapsed roof of the higher strata is large, that may has an impact on the shield support as shown in Figure 6.

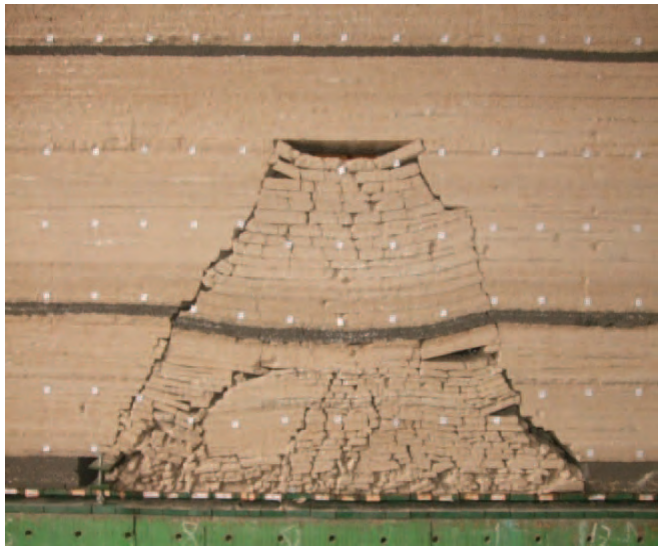


**Figure 6. Characteristics of weighting when the face advances.**

In the large mining height operation, the increased movement space in the gob for caving roof results in the increased caving height of the overlying rock mass. The collapsed rock blocks slip downward and fill the lower area of the face. Consequently the collapsed roof assumed a pattern clearly resembling a ladder. In other words, a multi-step structure is formed over the face of a large mining height. The periodical instability of the ladder structure has a significant effect on the stability of the shield support and coal face. For convenience this structure is called the "key ladder stratum structure". It is formed only in the face of steeply dipping seams with large mining height. Figure 7 shows the structure.

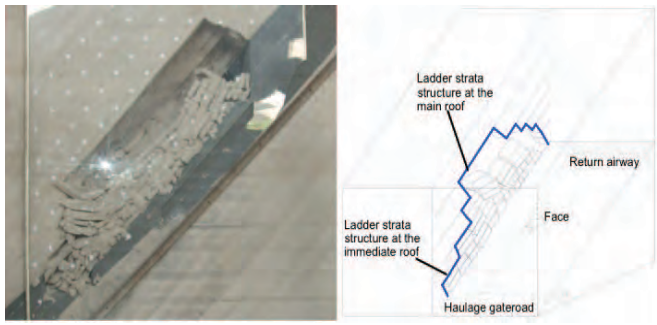



**Figure 7. Ladder strata structure above the face.**

Based on different lithology, roof thickness, and mining height, the key ladder stratum structure can be divided into second level, third level, and so on. The ladder distribution characteristics are different under different levels. The first level ladder stratum structure is located at the lower area of the face and its height is smaller. The affected area of the first level structure is about 40%~ 50% of the panel width (or face length). The second or the third level ladder stratum structure is located in the middle and upper sections of the face and its height is larger. The affected area of the second or the third level structure is about 50%~ 60% of the panel width.

Furthermore, the weighting cycle, interval, and intensity are different with different ladder structures. Normally, the second

or third level ladder structure results in a short weighting cycle, smaller interval, higher intensity, and stronger impact. However, the first level ladder structure normally has a long weighting cycle, larger interval, and lower intensity. Furthermore, the failure of the first level ladder structure may cause the second and third level ladder structures to de-stabilize, eventually affecting the stability of the rock-shield support system.

*Interaction of rock-shield support system:* During mining of the steeply dipping thick seams, the load imposed on the shield supports has an obvious zoning characteristic. The support load in the middle and lower sections of the face is greater than that of the upper section where the support load varies considerably and vanishes at some shields. According to field monitoring and experimental results, the working resistance of the shield support is about 6,000-6,500kN. The maximum lateral load between the support bases is 460kN with an average of 114kN. The maximum lateral load between the caving shields is 615kN with an average of 97kN.The maximum lateral load between the canopies is 348kNwith an average of 79kN. Furthermore, the lateral load varies greatly in the upper section, where as it is relatively stable in the middle and lower sections of the face. Comparing to the conventional mining of steeply inclined seams, its lateral load increases significantly, as shown in Figure 8.

The shield load from the main roof is also different. At the lower part of the face, the shield load is imposed through the immediate roof; at the middle and upper parts of the face, the load is imposed on the shield support directly. In this area, the anti-dip sliding pile structure (Wu et al., 2010) may form behind the shield support due to the large gob space and easily affects the stability of shield supports.

At the face of a steeply dipping seam, the sliding and filling of the gob space by the broken roof is the key factor for the variability the state of load on the shield support and in the surrounding rocks. As the mining height increases, the degree of rock filling at the lower part of the face is considerably higher than that of the face with the conventional mining height, and the unbalance of the support loads at the lower and upper sections of the face is more obvious. The support load decreases at the lower part due to the filling of the collapsed and slipped rocks, while at the upper part of the face, the ground control issues became more severe because of the huge caving space and the more variable support loads

## BEHAVIOR OF GROUND PRESSURE

Underground ground control monitoring had been performed at the large mining height face in the steeply dipping seam in Xinjiang Province, China. The general distribution patterns of the shield support resistance and face sloughage were obtained and shown in Figures 10 and 11.The first caving interval of the main roof was 131 ft or (40m) and the periodic weighting interval was 42.7 ft or (13.0m) and lasted for 2-3 days as shown in Figure 10. Comparing with those obtained from the conventional mining height (<11.5 ft or 3.5m) operations, the first weighting and periodical weighting intervals decrease considerably, while the weighting intensity is stronger. During the weighting period, the frequency and area of face sloughage increase (Figure 11). Furthermore, the load on the front legs of the shield support was

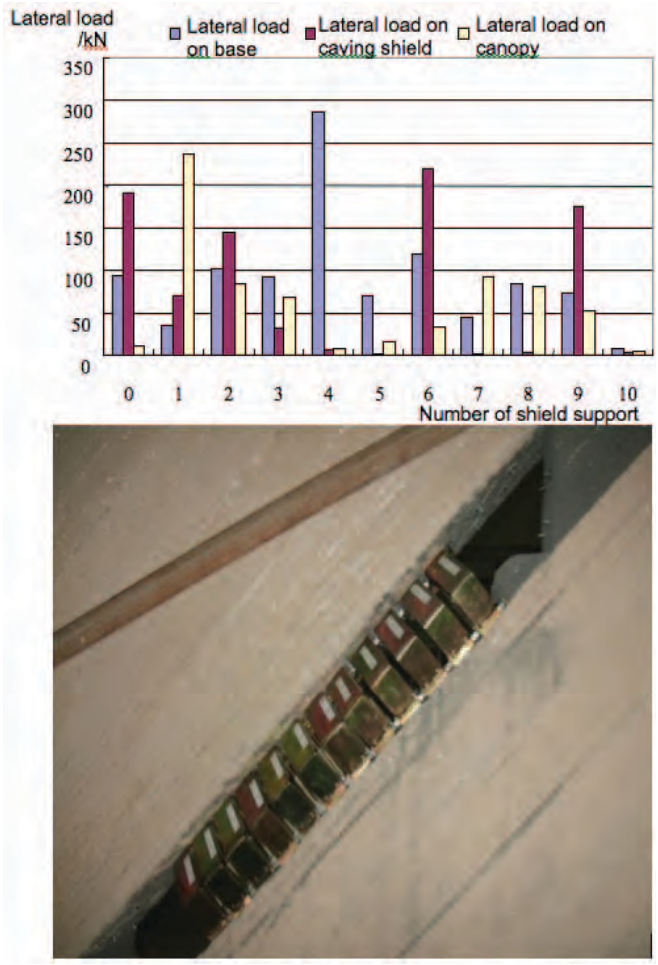



**Figure 8. Lateral load on shield supports.**

70% larger than the rear ones. Some shield supports were yielded and squeezing between two adjacent shield supports was severe. Consequently the tendency of instability of the shield support-rock system is much higher than that experienced with the conventional mining height in the steeply dipping seams.



**Figure 9. Characteristics of roof slipping and filling in the gob.**

## KEY TECHNIQUE AND EQUIPMENT

Based on the combined results of theoretical analysis, field monitoring and laboratory experiments, the characteristics of strata movement, roof structure, and rock-shield support interaction were analyzed. The results indicate that strata movement is similar to

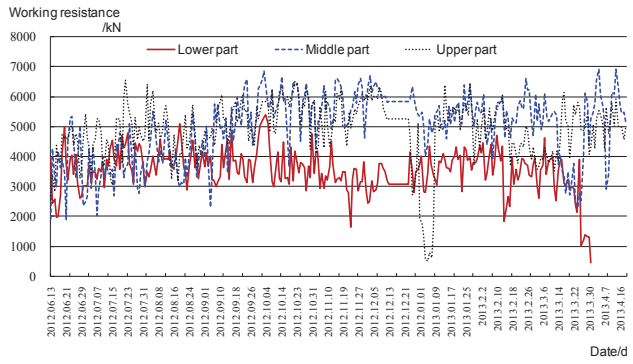



**Figure 10. Characteristic of shield support resistance in different areas of the face.**

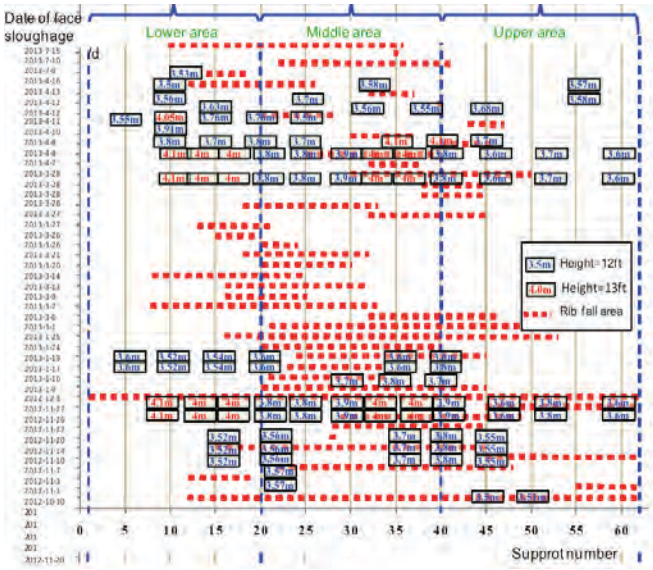



**Figure 11. Relationship between face sloughage and mining height.**

that of conventional mining height in the steeply dipping seams, except that the deformation, failure and movement of the surrounding rocks are more intense; the roof weighting interval decreases; and the weighting intensity increases significantly with severe face sloughage. The multi-level ladder strata structure is formed in the overlying strata above the face. The key techniques and equipment required are developed as follows:

The concept of the "key ladder stratum structure" and some basic measures such as layout the face in wedge cross section and dividing roof control into different sections are proposed.

The following prevention and control methods of face sloughage are proposed: strict control of shield support resistance, hard roof weakening, advanced reinforcement of face, and decrease of the false inclined angle of the face. Those techniques combined can handle the face sloughage issue effectively for the large mining height faces in the steeply dipping coal seams. The proposed techniques are shown in Figures 12 and 13.

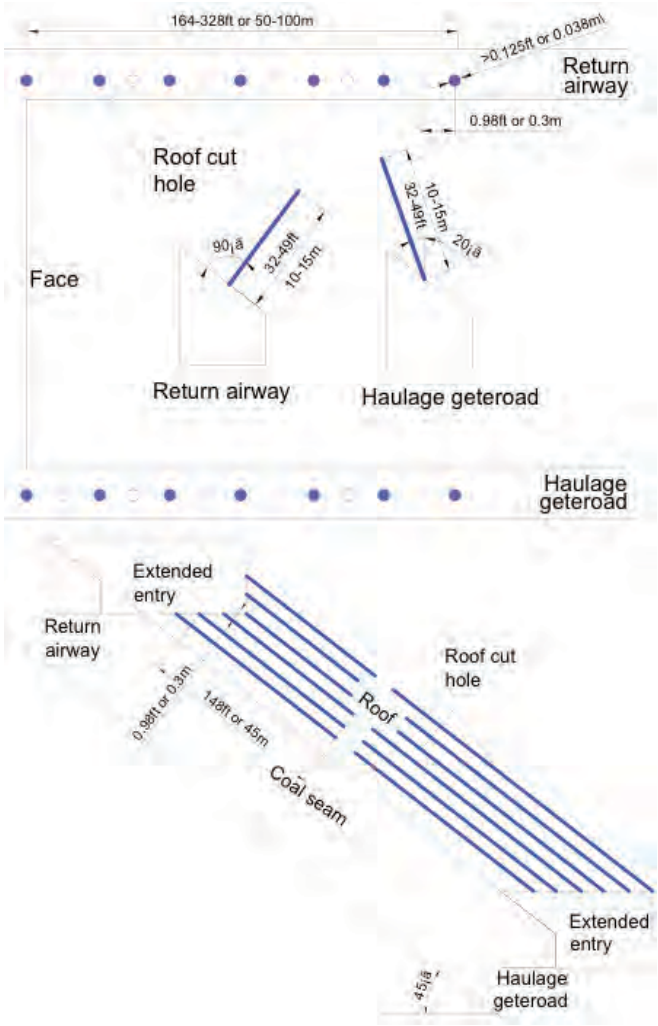



**Figure 12. Layout of roof cut holes.**

Three major machines for large mining height mining in the steeply dipping seams had been developed. These machines are the shield support, AFC (armored face conveyor), and the shearer. In particular, the shield support is capable of adjusting its width from 5.08 to 5.74 ft (1.55 to 1.75m) and generating a greater resistance (the maximum resistance is 6,500 kN). The anti-sliding and anti-toppling problems have been solved effectively. The three major machines are shown in Figures14.

## PRACTICAL APPLICATIONS

Comparing with the top coal caving mining in the same geological conditions, the top coal caving process is eliminated and the mining processes are greatly simplified by using the single-pass large mining height method. Furthermore, the labor is greatly reduced and the working environment is improved. Based on the statistical data, the annual production reached 0.66 Mt, increasing by about 0.18 Mt more than by using the top coal caving method (0.48 Mt). The recovery rate at the face reached 94.86%, increasing by 14.1% more than by using the top coal caving method. Accident rates have been greatly reduced. Consequently, good technical and economic benefits are realized in the 2130 coal mine.

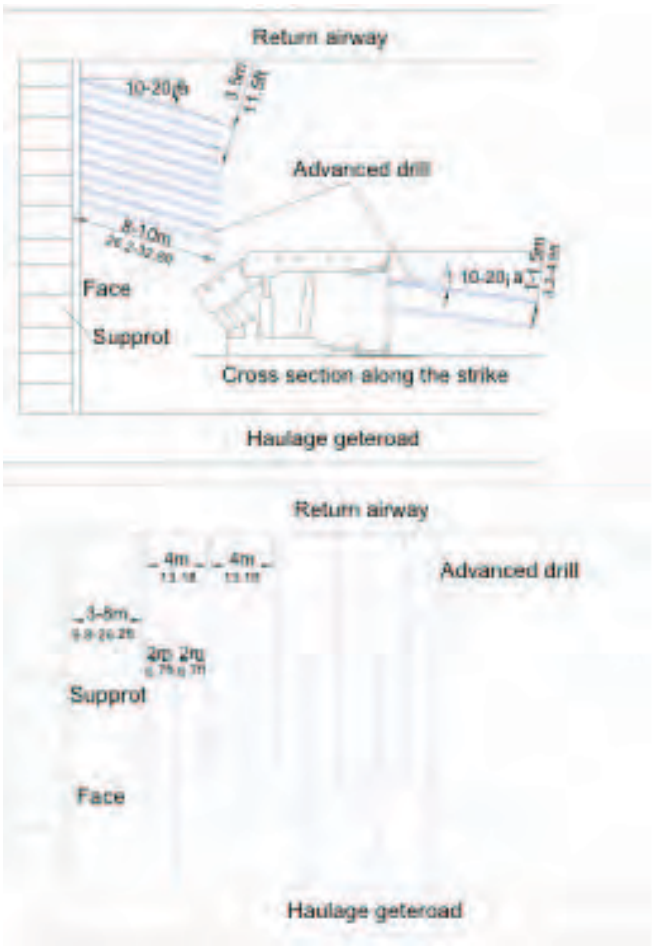



**Figure 13. Layout of advanced face reinforcement holes.**



**Figure 14. The three major machines for large mining height extraction in the steeply dipping seams.**

## CONCLUSIONS

Researches on the large mining height mining in the steeply dipping seams in China in the past two years have reached the following key conclusions: (1) the deformation, failure and movement of the surrounding rocks are more intense; the roof weighting interval decreases; but the weighting intensity increases significantly; (2) A multilevel ladder strata structure is formed in the overlying strata over the face. The gob space for the caved roof to slip, roll and fill the gob increases and the anti-dip pile structure is formed easily after main roof failure; (3) The characteristics of contact and loading of the roof-shield support system is more complex, load variation is larger and interaction between shield supports occurs frequently, anti-toppling and anti-sliding devices at the face are more difficult to implement.

As a result of applying the theories and technologies developed in this research, safety in mining has improved and the production and recovery ratio have increased in the 2130 coal mine. The technology provides a more scientific and feasible method (comparing with top coal caving method) for safe and efficient exploitation of steeply dipping thick (11.5-16.4 ft or 3.5-5.0m) seams in China.

## ACKNOWLEDGMENTS

The author would like to gratefully acknowledge the support for this project from the National Natural Science Foundation of PRC (51074120, 51204132) and *Science* and Technology Innovation Team Program of Shaanxi Province (2013KCT-16).

## REFERENCES

Wu Y. (2013). "Technology research around large mining height fully-mechanized face area in steeply dipping seam" (in Chinese). Wulumuqi: Xinjiang Tar Coal Group Co. Ltd, Xi'an: Xi'an University of Science and Technology (November).

Liu B., Wu Y. (2003). "Technology of longwall top coal caving along the strike in steeply dipping thick and inflammable coal seams" (in Chinese). Lanzhou: Huating Coal Group, Xi'an: Xi'an University of Science and Technology (December).

Wu Y., Yun D., Zhou B. (2000). "Study on the elementary problems of full-mechanized coal mining in greater pitching seam." *Journal of China Coal Society*25 (5):465-468.

Shi P. (1999). "The complexity of movement in broken overlying strata of steep coal seam mining." *Journal of Ground Pressure and Roof Control* 3:26-28.

Wu Y., Xie P., Wang H. et al. (2010). "Incline masonry structure around the coal face of steeply dipping seam mining." *Journal of China CoalSociety*35 (8):1252-1256.

Yin G., Xian X., Dai G. et al. (2001)."Basic behaviors of strata movement in seam with deep dip angle." *Chinese Journal of Geotechnical Engineering*23 (4):450-453.

Wu Y., Xie P., Ren S. et al. (2007). "Numerical simulation and complexity analysis of strata movement in exploiting steep coal seams group." *Journal of Mining & Safety Engineering* 24 (4):392-395.

Huang J. (2002). "Structural analysis for roof movement for steep coal seams." *Journal of China University of Mining &Technology* 31 (5):411-414.

Wu Y., Xie P., Yun D. et al. (2013). "Theory and practice of fully mechanized longwall mining in steeply dipping coal seams." *Mining Engineering* 65(1):35-41.

Zhao Y., Zhang X., Tu M. (2007). Roof caving characteristic and strata behavior in exploiting steep coal seams." *Journal of Mining & Safety Engineering* 24(2):231-234.

Cheng W., Wang J., Yun D. et al. (2003)."Technology of longwall top coal caving along the Strike in steeply dipping thick coal seam" (in Chinese). Lanzhou: Jingyuan Coal Group, Xi'an: Xi'an University of Science and Technology (December).

Xie P. (2011). "Response of overburden structure and its stability around the longwall mining face area in steeply dipping seam" (in Chinese). Xi'an: Xi'an University of Science and Technology (July).

Xie P., Wu Y., Wang H.et al. (2012). "Stability analysis of incline masonry structure and support around longwall mining face area in steeply dipping seam." *Journal of China Coal Society* 37(8):1275-1280.

# Study on the Modified Model of Probability Integral Method

**Zhang Hongzhen**
**Deng Kazhong**, Professor
**Fan Hongdong**, Associate Professor
China University of Mining and Technology
Xuzhou, China

## ABSTRACT

The fast convergence of boundary is a major problem of probability integral method, especially for the prediction of mining under thick alluvium, abandoned mine goaf, etc. To solve this problem and improve the accuracy of probability integral method, a modified model is constructed for surface movement and deformation based on theoretical analysis. In which, three weighted values i.e. 1, $-1/t_1$, $1/t_2$ are set for the mining movement and deformation of three different major influence radius i.e. $r_1$, $R_1$, $R_2$, respectively, then the parameters are selected as following: (1) Parameters are inversed based on the observation data, in which the subsidence factor q, deviation of inflection point s, displacement factor b are considered as generic parameters, the tangent of major influence angle tanβis modified as $\tan\beta_2$, that is the major influence radius r is modified as $r_2$. (2) Inversion parameters of tangent of major influence angle tanβ or major influence radius r, based on the observation station edge data which beyond major influence radius distance from work-face mining boundary. The inversed tanβ and r will be used as tangent of major influence angle $\tan\beta_1$ and major influence radius $r_1$, respectively. (3) Other relevant parameters i.e. $t_1$, $t_2$, $R_1$, $R_2$, are calculated with the algorithm of this paper. A comparison experiment between the traditional and modified models has been conducted using the observation data from a observation station, the results show that in its central area, 58.6 percent of observation points accuracy is improved and 36.6 percent is decreased, while in its edge area, 61.5 percent is improved and 15.4 percent is decreased, totally, 68.6 percent is improved and 30 percent is decreased. Therefore, we can draw the conclusion that our modified model can improve the prediction predication accuracy, in particular, the boundary region.

## INTRODUCTION

The probability integral method is based on stochastic medium method(SMM), which was first introduced into the research on strata movement by Poland scholars J. Litwiniszyn in the 1950s, and developed into probability integral method by China scholars Liu Baochen, Liao Guohua etc.. For the advantages of the theoretical foundation, easy to program, easy parameter selection, good versatility etc., it has been developed into one of the most widely prediction method in china.

The prediction error of probability integral method is divided into model error, parameter error(Zha et al. 2008), and many scholars have studied and improved them, such as: prediction modified model of different mining influence: utmost non-full extraction, small mining face, etc., and geologic structure: anticline, mountain, etc., parameter inversion by using neural networks, support vector machines, pattern recognition etc., and these researches have greatly enriched and promoted the mining subsidence theory.

In the condition of prediction of thick alluvium mining, deep mining, abandoned mine goaf, etc., The fast convergence of boundary i.e. problem of difference between prediction and measured data near the boundary, is a major problem of probability integral method. the mining influence boundary is crucial to the determination of mining influence, working face stopping line design, building(structure) protection etc.. To solve this problem, the modified model of probability integral method is theoretically constructed, and easy to calculate and program, simple and practical.

## MODIFIED MODEL OF PROBABILITY INTEGRAL METHOD

According to the basic principles of the probability integral method, the unit subsidence is:

$$W_e(x) = \frac{1}{r} e^{-\pi \frac{x^2}{r^2}}$$

$$r = \frac{H}{\tan\beta}$$

Where: $W_e(x)$ is the unit subsidence; r is the major influence radius; H is mining depth; $tan\beta$ is tangent of major influence angle.

The relationship between unit subsidence and tangent of major influence angle is shown in Figure 1, which shows the relationship with convergence of boundary, maximum subsidence and tangent of major influence angle. As can be seen from

Figure 1: The smaller is tangent of major influence angle, the slower is convergence of boundary, the smaller is the maximum subsidence; Conversely, The bigger is tangent of major influence angle, the faster is convergence of boundary, the greater is the maximum subsidence.

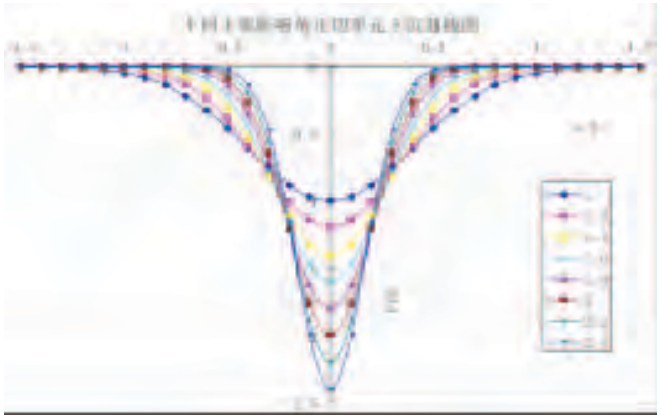


**Figure 1. Relationship between unit subsidence curve and tangent of minor influence angle.**

According to this property (in Figure 1), in order to be modified for the fast convergence of boundary, at the same time be sure for other regional prediction accuracy in this paper, different weighted values are set for the mining movement and deformation of different tangent of major influence angle, respectively, while both of them can't be realized by traditional probability integral method with one tangent of major influence angle. The modified model is as follows:

Assume that there are two different tangent of major influence angle i.e. tanβ1, tanβ2, respectively, and tanβ1<tanβ2, subsidence of distance from working face boundary to x is:

$$W_e(x) = W_e(x)_1\left(1 - e^{-\omega\frac{x^2}{H^2}}\right) + W_e(x)_2 e^{-\omega\frac{x^2}{H^2}}$$

Where: $W_e(x)_1$, $W_e(x)_2$ are different Subsidence with different tangent of major influence angle i.e. $tan\beta_1$, $tan\beta_2$, respectively; ω is Proportional coefficient, determined according to the actual situation, generally can be equal to 1.

According to the previous analysis, in two-dimensional case, the unit subsidence is developed into as follows:

$$W_e(x) = \frac{1}{r_1}e^{-\pi\frac{(x-s)^2}{r_1^2}} - \frac{1}{t_1}*\frac{1}{R_1}e^{-\pi\frac{(x-s)^2}{R_1^2}} + \frac{1}{t_2}*\frac{1}{R_2}e^{-\pi\frac{(x-s)^2}{R_2^2}}$$

Where:

$$R_1 = H\sqrt{\frac{\pi}{\pi\tan^2\beta_1 + \omega}} \qquad t_1 = \sqrt{1 + \frac{\omega}{\pi\tan^2\beta_1}}$$

$$R_2 = H\sqrt{\frac{\pi}{\pi\tan^2\beta_2 + \omega}} \qquad t_2 = \sqrt{1 + \frac{\omega}{\pi\tan^2\beta_2}}$$

In three-dimensional case, the movement and deformation of any point, coordinates(x,y),calculation schematics is shown in Figure 2, which shows the relationship among coordinate systems, predicted point, predicted direction, size of working face, etc.

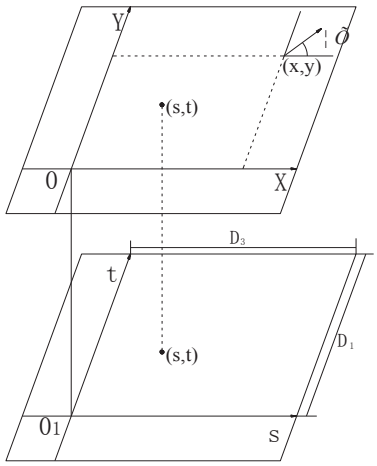



**Figure 2. Movement and deformation of any point calculation schematics.**

In three-dimensional case, any point subsidence, coordinates(x,y), is developed into as follows:

$$W_e(x,y) = \frac{1}{r_1^2}e^{-\pi\frac{(x-s)^2+(y-t)^2}{r_1^2}} - \frac{1}{t_1}*\frac{1}{R_1^2}e^{-\pi\frac{(x-s)^2+(y-t)^2}{R_1^2}} + \frac{1}{t_2}*\frac{1}{R_2^2}e^{-\pi\frac{(x-s)^2+(y-t)^2}{R_2^2}}$$

$$= W_{e-r1}(x,y) - \frac{1}{t_1}W_{e-R1}(x,y) + \frac{1}{t_2}W_{e-R2}(x,y)$$

Where: $W_{e-r1}(x,y)$, $W_{e-R1}(x,y)$, $W_{e-R2}(x,y)$ are different unit Subsidence with different major influence radius i.e. $r_1$, $R_1$, $R_2$, respectively.

As the thickness of coal seam is m, the sizes of working face are $D_3$, $D_1$(in Figure 2), any point subsidence is as follows:

$$
\begin{aligned}
(x,y) &= W_0 \int_0^{D_3}\int_0^{D_1} W_e(x-s,y-t)\,dtds \\
&= \frac{1}{W_0}\left[W_{r1}(x)-W_{r1}(x-D_3)\right]\left[W_{r1}(y)-W_{r1}(y-D_1)\right] \\
&\quad -\frac{1}{W_0 t_1}\left[W_{R1}(x)-W_{R1}(x-D_3)\right]\left[W_{R1}(y)-W_{R1}(y-D_1)\right] \\
&\quad +\frac{1}{W_0 t_2}\left[W_{R2}(x)-W_{R2}(x-D_3)\right]\left[W_{R2}(y)-W_{R2}(y-D_1)\right] \\
&= W_{r1}(x,y)-\frac{1}{t_1}W_{R1}(x,y)+\frac{1}{t_2}W_{R2}(x,y)
\end{aligned}
$$

where: $W_{r1}(x,y)$, $W_{R1}(x,y)$, $W_{R2}(x,y)$ are different Subsidence with different major influence radius i.e. $r_1$, $R_1$, $R_2$, respectively, in the condition the thickness of coal seam is m, the sizes of working face are $D_3$, $D_1$.

According to the basic principles of the probability integral method, the other movement and deformation can be deduced as follows:

$$i(x,y,\varphi)=i_{r1}(x,y,\varphi)-\frac{1}{t_1}i_{R1}(x,y,\varphi)+\frac{1}{t_2}i_{R2}(x,y,\varphi)$$

$$K(x,y,\varphi)=K_{r1}(x,y,\varphi)-\frac{1}{t_1}K_{R1}(x,y,\varphi)+\frac{1}{t_2}K_{R2}(x,y,\varphi)$$

$$U(x,y,\varphi)=U_{r1}(x,y,\varphi)-\frac{1}{t_1}U_{R1}(x,y,\varphi)+\frac{1}{t_2}U_{R2}(x,y,\varphi)$$

$$\varepsilon(x,y,\varphi)=\varepsilon_{r1}(x,y,\varphi)-\frac{1}{t_1}\varepsilon_{R1}(x,y,\varphi)+\frac{1}{t_2}\varepsilon_{R2}(x,y,\varphi)$$

$$S(x,y,\varphi)=S_{r1}(x,y,\varphi)-\frac{1}{t_1}S_{R1}(x,y,\varphi)+\frac{1}{t_2}S_{R2}(x,y,\varphi)$$

$$\gamma(x,y,\varphi)=\gamma_{r1}(x,y,\varphi)-\frac{1}{t_1}\gamma_{R1}(x,y,\varphi)+\frac{1}{t_2}\gamma_{R2}(x,y,\varphi)$$

Where: $i_{r1}(x,y,\varphi)$, $i_{R1}(x,y,\varphi)$, $i_{R2}(x,y,\varphi)$ are different tilt deformation, $K_{r1}(x,y,\varphi)$, $K_{R1}(x,y,\varphi)$, $K_{R2}(x,y,\varphi)$ are different curvature deformation, $U_{r1}(x,y,\varphi)$, $U_{R1}(x,y,\varphi)$, $U_{R2}(x,y,\varphi)$ are different horizontal movement, $\varepsilon_{r1}(x,y,\varphi)$, $\varepsilon_{R1}(x,y,\varphi)$, $\varepsilon_{R2}(x,y,\varphi)$ are different horizontal deformation, $S_{r1}(x,y,\varphi)$, $S_{R1}(x,y,\varphi)$, $S_{R2}(x,y,\varphi)$ are different distortion deformation, $\gamma_{r1}(x,y,\varphi)$, $\gamma_{R1}(x,y,\varphi)$, $\gamma_{R2}(x,y,\varphi)$ are different angle deformation, with different major influence radius i.e. $r_1$, $R_1$, $R_2$, respectively, in the condition the thickness of coal seam is m, the sizes of working face are $D_3$, $D_1$.

Therefore, in this paper, we constructed the modified model of probability integral method for surface movement and deformation based on theoretical analysis, in which, three weighted values i.e. 1, $-1/t_1$, $1/t_2$ are set for the mining movement and deformation of three different major influence radius i.e. $r_1$, $R_1$, $R_2$, respectively.

## PARAMETERS SELECTION PRINCIPLE

In this paper, the modified model parameters i.e. subsidence factor q, tangent of major influence angle tanβ, or major influence radius r, deviation of inflection point s, displacement factor b, are equal physical meaning to the parameters of probability integral method.

According to the above theory analyses and deduction of modified model, the tangent of major influence angle $\tan\beta_1$, $\tan\beta_2$, or the major influence radius $r_1$, $r_2$, are the key in the modified model of probability integral method. The parameters are selected as follows:

(a) Parameters are inversed based on the observation data, in which the subsidence factor q, deviation of inflection point s, displacement factor b are considered as generic parameters in the modified model, that is these parameters are equal to different major influence radius, while the tangent of major influence angle tanβ is modified as $\tan\beta_2$, that is the major influence radius r is modified as $r_2$.

(b) Inversion parameters of tangent of major influence angle tanβ or major influence radius r, based on the observation station edge data which beyond major influence radius distance from work-face mining boundary. The inversed tanβ and r will be used as tangent of major influence angle $\tan\beta_1$ and major influence radius $r_1$, respectively.

(c) Other relevant parameters i.e. $t_1$, $t_2$, $R_1$, $R_2$, are calculated with the algorithm of this paper, when ω is equal to 1, they are as follows:

$$R_1 = H\sqrt{\frac{\pi}{\pi\tan^2\beta_1+1}} \qquad t_1=\sqrt{1+\frac{1}{\pi\tan^2\beta_1}}$$

$$R_2 = H\sqrt{\frac{\pi}{\pi\tan^2\beta_2+1}} \qquad t_2=\sqrt{1+\frac{1}{\pi\tan^2\beta_2}}$$

## EXAMPLE ANALYSIS

### Observation Station

Mining time of working face is from 2006 Sept. to 2007 Sept., the south side is the other laneway, the other sides i.e. east, west, north, are not excavated. Mining method is longwall large mining height fully-mechanized face, working face is 1400 meters in length and 200 meters in width. Mining seam is 3# coal seam of Shanxi formation, and thickness is between 4.3m and 4.7m, the average is 4.6m. The declining angle is between 0° and 6°, the average is 3°. Mining depth is between 485m and 565m, the average is 525m. The alluvium average thickness is 21.03m.

According to the actual situation, observation station with a half strike line and a whole dip line was laid, one observation data was as the final data, only subsidence data was analyzed, the measured data is shown in Table 1 and Table 2.

### Parameter Inversion

In this paper, "Mining Subsidence Prediction System" software package, developed by Mining Damage and Protection Research Institute, China University of Mining and Technology, was used to parameters inversion.

*Based on all subsidence data (80 observation points*

The inversion parameters are as follows: the subsidence factor q is equal to 0.63, the tangent of major influence angle tanβ is equal to 2.94, the propagation angle of extraction θ is equal to 84.5°, the right deviation of inflection point s is equal to 57.41 meters, the up deviation of inflection point s is equal to 18.45 meters, the down deviation of inflection point s is equal to 24.6 meters.

*Based on subsidence data (39 observation points) nearby edge*

The total selected data is 39, which number are No.1~5, 30~43, 61~80, the inversion parameters are as follows: the subsidence factor q is equal to 0.2, the tangent of major influence angle tanβ is equal to 1.67, the propagation angle of extraction θ is equal to 84.5°, the right deviation of inflection point s is equal to 57.41 meters, the up deviation of inflection point s is equal to 26.21 meters, the down deviation of inflection point s is equal to 12.7 meters.

### Experiment Analysis

*Parameters selection*

(a) Traditional probability integral method: The subsidence factor q is equal to 0.63, the tangent of major influence angle tanβ is equal to 2.94, the propagation angle of extraction θ is equal to 84.5°, the right deviation of inflection point s is equal to 57.41 meters, the up deviation of inflection point s is equal to 18.45 meters, the down deviation of inflection point s is equal to 24.6 meters.

(b) Modified model of probability integral method: The subsidence factor q is equal to 0.63, the tangent of major influence angle $\tan\beta_1$ is equal to 1.67, the tangent of major influence angle $\tan\beta_2$ is equal to 2.94, the propagation angle of extraction θ is equal to 84.5°, the right deviation of inflection point s is equal to 57.41 meters, the up deviation of inflection point s is equal to 18.45 meters, the down deviation of inflection point s is equal to 24.6 meters, the proportional coefficient ω is equal to 1.

*Comparative analysis*

The comparative subsidence with the prediction of traditional probability integral method, the prediction of modified model of probability integral method, and the measured data are shown in Table 1 and Table 2. As can be seen from these tables:

(a) In the center part of goaf, including observation point from No.6 to No. 29, and from No.44 to No.60, a total of 41 points, in the different subsidence between modified model of probability integral method and traditional probability integral method, 65.9 percent of observation points is in less than 10 millimeter, 19.5 percent is in between 11 millimeter and 20 millimeter, 14.6 percent is in between 21 millimeter and 42 millimeter. The comparison experiment between the traditional and modified models shows that 58.6 percent of observation points accuracy is improved and 36.6 percent is decreased with the modified models.

(b) In the edge part of goaf, including observation point from No.1 to No. 5, from No. 30 to No.43, and from No.61 to No.80, a total of 39 points, in the different subsidence between the modified model and the traditional, 53.8 percent of observation points is in less than 10 millimeter, 20.5 percent is in between 11 millimeter and 20 millimeter, 25.7 percent is in between 21 millimeter and 44 millimeter. The comparison experiment between the traditional and modified models shows that, by the modified models, 61.5 percent of observation points accuracy is improved, 15.4 percent is decreased, and the prediction is more conformed to the measured data.

(c) On the whole, the comparison experiment between the traditional and modified models shows that, by the modified models, 68.6 percent of observation points accuracy is improved, 30 percent is decreased, especially in the boundary region, the prediction accuracy has been significantly improved. That is, the improved prediction accuracy of the edge area has a very practical significance to the determination of mining influence and working face stopping line design etc.

## CONCLUSIONS

The modified model is constructed for surface movement and deformation based on theoretical analysis. In which, three weighted values i.e. 1, $-1/t_1$, $1/t_2$ are set for the mining movement and deformation of three different major influence radius i.e. $r_1$, $R_1$, $R_2$, respectively, and the method is built.

The parameters selection principle is constructed, they are as follows: (1) Parameters are inversed based on the observation data, in which the subsidence factor q, deviation of inflection point s, displacement factor b are considered as generic parameters, the tangent of major influence angle tanβis modified as $\tan\beta_2$, that is the major influence radius r is modified as $r_2$. (2) Inversion parameters of tangent of major influence angle tanβ or major influence radius r, based on the observation station edge data which beyond major

**Table 1. Comparison of Subsidence.**

| Strike points | Subsidence, mm | | | Difference of subsidence, mm | | | Dip points | Subsidence, mm | | | Difference of subsidence, mm | | |
|---|---|---|---|---|---|---|---|---|---|---|---|---|---|
| | Measured | Modified | Traditional | Modified measured | Traditional measured | Modified traditional | | Measured | Modified | Traditional | Modified measured | Traditional measured | Modified traditional |
| 1 | 0 | 20 | 7 | 20 | 7 | 13 | 30 | 7 | 0 | 0 | 7 | 7 | 0 |
| 2 | 13 | 35 | 19 | 22 | 6 | 16 | 31 | 15 | 1 | 0 | 14 | 15 | 1 |
| 3 | 26 | 63 | 45 | 37 | 19 | 18 | 32 | 14 | 2 | 0 | 12 | 14 | 2 |
| 4 | 61 | 118 | 102 | 57 | 41 | 16 | 33 | 16 | 2 | 0 | 14 | 16 | 2 |
| 5 | 133 | 208 | 196 | 75 | 63 | 12 | 34 | 18 | 3 | 0 | 15 | 18 | 3 |
| 6 | 268 | 349 | 342 | 81 | 74 | 7 | 35 | 23 | 6 | 0 | 17 | 23 | 6 |
| 7 | 471 | 549 | 544 | 78 | 73 | 5 | 36 | 28 | 10 | 0 | 18 | 28 | 10 |
| 8 | 733 | 800 | 797 | 67 | 64 | 3 | 37 | 36 | 16 | 0 | 20 | 36 | 15 |
| 9 | 1000 | 1071 | 1071 | 71 | 71 | 0 | 38 | 43 | 19 | 1 | 24 | 42 | 18 |
| 10 | 1233 | 1316 | 1318 | 83 | 85 | 2 | 39 | 52 | 26 | 3 | 26 | 49 | 23 |
| 11 | 1447 | 1546 | 1554 | 99 | 107 | 7 | 40 | 57 | 39 | 8 | 18 | 49 | 32 |
| 12 | 1611 | 1725 | 1735 | 114 | 124 | 9 | 41 | 76 | 61 | 22 | 15 | 54 | 39 |
| 13 | 1777 | 1849 | 1861 | 72 | 84 | 12 | 42 | 101 | 94 | 50 | 7 | 51 | 44 |
| 14 | 1799 | 1924 | 1937 | 125 | 138 | 14 | 43 | 158 | 149 | 106 | 9 | 52 | 43 |
| 15 | 1817 | 1964 | 1977 | 147 | 160 | 12 | 44 | 238 | 255 | 213 | 17 | 25 | 42 |
| 16 | 1836 | 1979 | 1993 | 143 | 157 | 15 | 45 | 373 | 421 | 379 | 48 | 6 | 42 |
| 17 | 1771 | 1980 | 1993 | 209 | 222 | 12 | 46 | 561 | 652 | 616 | 91 | 55 | 36 |
| 18 | 1822 | 2005 | 2014 | 183 | 192 | 9 | 47 | 899 | 972 | 947 | 73 | 48 | 26 |
| 19 | 1900 | 2010 | 2015 | 110 | 115 | 6 | 48 | 1238 | 1301 | 1284 | 63 | 46 | 16 |
| 20 | 1936 | 2012 | 2015 | 76 | 79 | 3 | 49 | 1599 | 1648 | 1640 | 49 | 41 | 8 |
| 21 | 2031 | 2018 | 2020 | 13 | 11 | 2 | 50 | 2017 | 1959 | 1955 | 58 | 62 | 5 |
| 22 | 2056 | 2020 | 2021 | 36 | 35 | 1 | 51 | 2306 | 2180 | 2178 | 126 | 128 | 2 |
| 23 | 2189 | 2025 | 2025 | 164 | 164 | 0 | 52 | 2324 | 2275 | 2277 | 49 | 47 | 2 |
| 24 | 2251 | 2020 | 2019 | 231 | 232 | 1 | 53 | 2374 | 2218 | 2225 | 156 | 149 | 6 |
| 25 | 2248 | 2019 | 2018 | 229 | 230 | 1 | 54 | 2210 | 2018 | 2017 | 192 | 193 | 1 |
| 26 | 2210 | 2018 | 2017 | 192 | 193 | 1 | 55 | 1826 | 1718 | 1710 | 108 | 116 | 8 |
| 27 | 2104 | 2003 | 2002 | 101 | 102 | 1 | 56 | 1396 | 1330 | 1317 | 66 | 79 | 13 |
| 28 | 2113 | 2030 | 2029 | 83 | 84 | 1 | 57 | 907 | 952 | 936 | 45 | 29 | 17 |
| 29 | 2040 | 2036 | 2035 | 4 | 5 | 1 | 58 | 487 | 589 | 562 | 102 | 75 | 28 |

influence radius distance from work-face mining boundary. The inversed tanβ and r will be used as tangent of major influence angle $\tan\beta_1$ and major influence radius $r_1$, respectively. (3) Other relevant parameters i.e. $t_1$, $t_2$, $R_1$, $R_2$, are calculated with the algorithm of this paper.

A comparison experiment between the traditional and the modified models has been conducted using the observation data from a observation station, the results show that, the modified model of probability integral method can effectively solve the problem of the fast convergence of boundary to the traditional.

**ACKNOWLEDGEMENTS**

This research was sponsored by the National Natural Science Foundation of China through Contract No. 41272389 and the Basic Research Project of Jiangsu Province (Natural Science Foundation) through Contract No. BK20130174. Also, the authors would like to express their sincere appreciation and gratitude to Dr. Syd Peng for his review of this paper.

**Table 2. Continued Comparison of Subsidence.**

| Dip points | Subsidence, mm | | | Difference of subsidence, mm | | |
|---|---|---|---|---|---|---|
| | Measured | Modified | Traditional | Modified measured | Traditional measured | Modified traditional |
| 59 | 358 | 383 | 347 | 25 | 11 | 36 |
| 60 | 229 | 220 | 179 | 9 | 50 | 41 |
| 61 | 100 | 110 | 70 | 10 | 30 | 39 |
| 62 | 74 | 68 | 33 | 6 | 41 | 35 |
| 63 | 52 | 42 | 13 | 10 | 39 | 30 |
| 64 | 35 | 29 | 4 | 6 | 31 | 26 |
| 65 | 31 | 23 | 1 | 8 | 30 | 22 |
| 66 | 42 | 15 | 0 | 27 | 42 | 15 |
| 67 | 27 | 9 | 0 | 18 | 27 | 9 |
| 68 | 24 | 6 | 0 | 18 | 24 | 6 |
| 69 | 20 | 3 | 0 | 17 | 20 | 3 |
| 70 | 19 | 2 | 0 | 17 | 19 | 2 |
| 71 | 15 | 1 | 0 | 14 | 15 | 1 |
| 72 | -15 | 1 | 0 | 16 | 15 | 1 |
| 73 | -34 | 0 | 0 | 34 | 34 | 0 |
| 74 | 16 | 0 | 0 | 16 | 16 | 0 |
| 75 | 13 | 0 | 0 | 13 | 13 | 0 |
| 76 | 11 | 0 | 0 | 11 | 11 | 0 |
| 77 | 11 | 0 | 0 | 11 | 11 | 0 |
| 78 | 9 | 0 | 0 | 9 | 9 | 0 |
| 79 | 6 | 0 | 0 | 6 | 6 | 0 |

## REFERENCES


Zha J.F., Guo G.L., Zhao H.T., Jia X.G. (2008). "Present situation and prospect of correction system for probability integral method." (1): 15-18 (in Chinese).

Yang F., Ma F.H.(2004). "Neural network method used in adopting parameters for prediction of surface displacement." The Chinese Journal of Geological Hazard and Control 15(1): 102-106 (in Chinese).

Guo W.B., Deng K.Z., Zou Y.F. (2004). "Artificial neural network model for predicting parameters of probability-integral method." Journal of China University of Mining & Technology 33(3): 322-326 (in Chinese).

Dai H.Y., Wang J.Z.(2003). "Prediction model for surface movement and deformation induced by sub-critical extraction." Journal of China Coal Society 28(6): 583-587 (in Chinese).

Zou Y.F. (2001). "The determining method of predication parameters on mining subsidence." Journal of Jiaozuo Institute of Technology (Natural Science) 20(4): 253-257 (in Chinese).

Chai H.B., Zou Y.F., Guo W.B. (2005). "Determination of mining subsidence predicting parameters using fuzzy pattern recognition." Journal of China Coal Society 30(6): 701-704 (in Chinese).

Dai Z.Q., Guo G.L., Wang J.L. (2001). "Discussion on Predicted Parameter of Minimal Working Face." Jiang Su Coal (3): 15-18 (in Chinese).

Guo G.L., Wang Y.J. (2000). "Study of determining parameters model for probability-integral method and its application." Acta Geodaetica et Cartographica Sinica 29(2): 162-165 (in Chinese).

Wu K., Ge J.X., Zhou M., Yu F.D. (1998). "Some modifications of using probability integral method to predicate model." Journal of China Coal Society 23(1):33-36 (in Chinese).

Li P.X., Tan Z.X., Yan L.L., Deng K.Z. (2011). "Time series prediction of mining subsidence based on SVM." Mining Science and Technology (China) (21):557-562 (in Chinese).

Li P.X., Tan Z.X., Yan L.L., Deng K.Z. (2011). "A method to calculate displacement factors using SVM." Mining Science and Technology (China) (21): 307-311 (in Chinese).

Song S.J. (2013). "Study on the stratification transfer prediction method of the mining subsidence based on the key geological and mining factors." Xi'an: Xi'an University of Science and Technology (in Chinese).

# Overburden Strata Movement for the Longwall Mining of Shallow Seam under the Gobs of Room and Pillar Mining

**Fangtian Wang**
**Shihao Tu**, Professor
**Anxiu Liu**, Ph.D. Student
School of Mines
China University of Mining and Technology
Xuzhou, China

**Zhenglin Zhang**, Mine Engineer
**Xiyou Ma**, Engineering Manager
Production Technology Department
Ordos Wulan Coal Group Corporation Limited
Ordos, China

## ABSTRACT

The fully mechanized longwall mining was employed in a shallow coal seam that was under the gobs of room and pillar mining and overlain by thin bedrock and thick loose sands. Operational practices have demonstrated that severe accidents would occur including roof structure instability, roof steps, damages of shield supports, and face bumps triggered by the large area roof weighting, resulting in serious threats to the safety of underground miners and equipment. This paper uses Shigetai Mine, located in the Ordos area, Inner Mongolia, as the study site. It fully considers the geological conditions of 3-1-2 coal seam and employs theoretical analysis, 3DEC numerical simulation, and field measurements to analyze the overlying strata movement for the shallow seams under an abandoned room and pillar mine without pillar extraction. The research results serve as an excellent guide to mining in similar geological and mining conditions.

## KEY WORDS

Shallow seam; abandoned room and pillar mining; closely-separated coal seams; longwall mining; overlying strata movement

## INTRODUCTION

The typical shallow coal seams in Ordos coalfield have three major characteristics: shallow (less than 492 ft (150 m) deep), overlain by thin bedrock (no more than 164 ft (50m) thick), and thick loose sands. Longwall mining under those conditions may cause the whole overburden to collapse or large roof steps on the surface (Huang, 2002; Ma et al., 2008a). The coal seams located in the Shendong Coalfield have many advantages including shallow depth and simple geological conditions. Prior to the large-scale fully mechanized longwall mining, room and pillar mining was commonly employed that left coal pillars to support the roof and control surface subsidence (Li et al., 2013; Liu et al., 2013), for instance Shigetai Mine, Dadijing Mine, and many mines in the Yushen Mine Area. In Ordos alone, the area of abandoned room and pillar mines exceeds 116 $mi^2$ (300 $km^2$), and the sterilized coal reserves are more than 1.98 billion tons (1.8 billion metric tons).

Researchers in China have performed numerous studies on ground pressure for mining under shallow coal seams, and obtained the key stratum dynamic load distribution and their load transfer for shallow coal seams with thick sand layer using physical simulation models (Huang, 2005; Huang and Zhang, 2004; Ma et al., 2008b). Hou (2000) applied the key stratum theory to the shallow coal seams with thick unconsolidated materials, and analyzed the roof "Rotation-Slide"(R-S) stability. He pointed out that the key to roof control is to control the stability of the combined key strata. Modern longwall mining of shallow seams with small interburden under the abandoned room and pillar mines exhibits many unique features in overlying strata movement and ground pressure, resulting in many accidents such as roof structure instability, large roof steps, damages of shield supports, and face bumps triggered by large area roof weighting. Those problems pose serious threat to the safety of underground miners and equipment (Wang et al., 2013; Tu et al., 2011; Xie, 2012). Yet, few studies have been made to investigate the overlying strata movement under the mining conditions mentioned above (Dehghan et al., 2013; Li et al., 2011).

This paper, using the case of the geological conditions of shallow seam at Shigetai Mine, Ordos City, investigates the overlying strata movement for the fully mechanized mining of shallow seams under an abandoned room and pillar mine without pillar extraction. It employs the combined methods of theoretical analysis, numerical calculation, and field observation. The research results serve as an excellent guide to mining in similar geological and mining conditions.

## GEOLOGICAL CONDITIONS

The 3-1-2 seam at Shigetai Mine is a typical shallow seam with depth about 80.8 m (265.1 ft), thin bedrock (164 ft (50 m) or less), and thick unconsolidated sand. Its average thickness is 9.8 ft (3.0 m), and its roof is mainly interbedded sandy mudstone and fine sandstone, with localized sandstone roof. The floor is mainly sandy mudstone, followed by siltstone and fine sandstone. The average thickness of the 3-1-1 seam is 7.5 ft (2.3 m) without rock partings. Its roof is mainly sandstone and sandy mudstone. The three boreholes in panel 131201 showed that the spacing between the 3-1-1 and 3-1-2 seams is 0.66-44.00 ft (0.20-13.41 m) with an average of 19.7 ft (6.0 m).

Prior to 2008, Shigetai Mine employed the room and pillar mining method to extract the 3-1-1 coal seam without pillar

extraction. The room and pillar mining method has the following disadvantages: low recovery rate (less than 30%), high labor intensity, and plenty of potential risks (Liu et al., 2008). In order to increase the recovery rate and economic and social benefits, the fully mechanized longwall mining method was implemented to exploit the 3-1-2 coal seam. Figure 1 shows the Longwall mining model of shallow seam lying at a close distance to the overlying abandoned room and pillar mine.

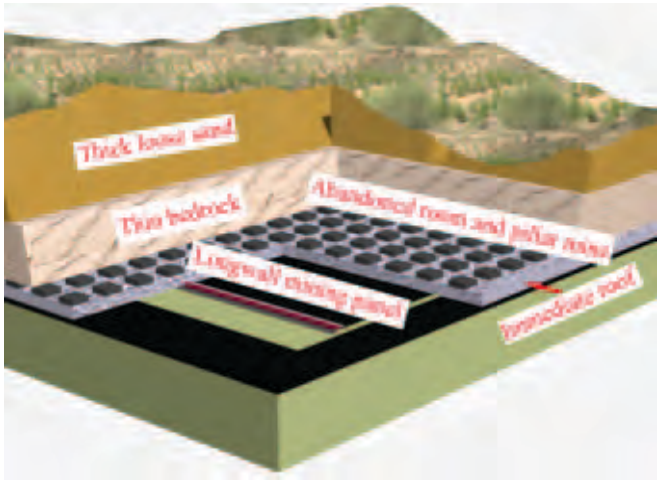



**Figure 1. Longwall mining model of shallow seam lying in close distance to the overlying abandoned room and pillar mine without pillar extraction.**

## THE STRUCTURAL MECHANICS OF OVERLYING STRATA

Since determining the shield support capacity is the key to roof control, it is necessary to study the interaction of "support-rock" system to determine the support capacity in the most severe case. Due to the remnant pillars left in the overlying abandoned room and pillar mine, the pressure induced by the collapse of main roof is transferred to the immediate roof and the shield supports through the remnant pillars. In the worst case, accidents such as the immediate roof shearing and caving along the faceline and shield supports being crushed are likely to occur. Therefore, research on the characteristics of overlying strata structure movement of shallow seams under the abandoned room and pillar mines should concentrate on the study of the pressure evolution of main and immediate roof structures, thereby determining the mechanisms of the immediate roof shearing and caving along the faceline and shield support being crushed. Figure 2 shows the overlying strata movement model.

The load from the upper rock layers is first loaded on the key block and then through the remnant pillar and immediate roof, it is finally supported by the shield support. Thus this system of loading mechanics can be simplified as shown in Figure 3.

In Figure 3, $q$ is the load of main roof and overlying strata, $q_z$ is support resistance to the immediate roof, $w_1$ is the main roof deflection, $w_2$ is the immediate roof deflection, $Lc$ is distance from the faceline to the main roof fracture, $T$, $T_f$, $T_d$, and $T_F$ are the horizontal and frictional forces of the key block tail-end and front-end acted by the adjacent blocks, respectively, $T$ *and* $T_f$ are the

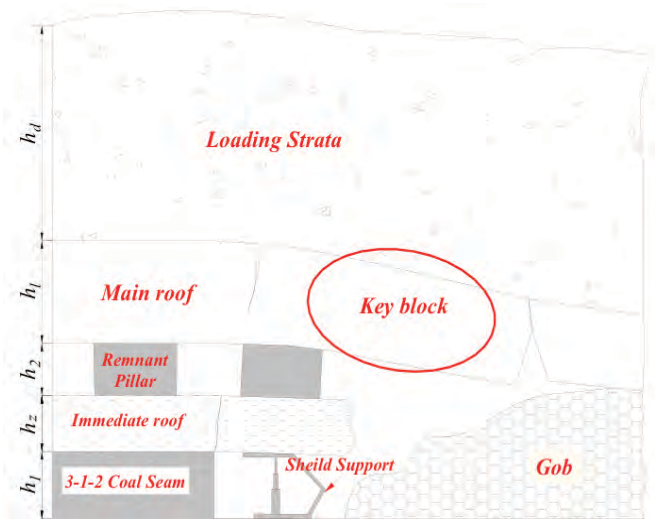



**Figure 2. The overlying strate movement model.**

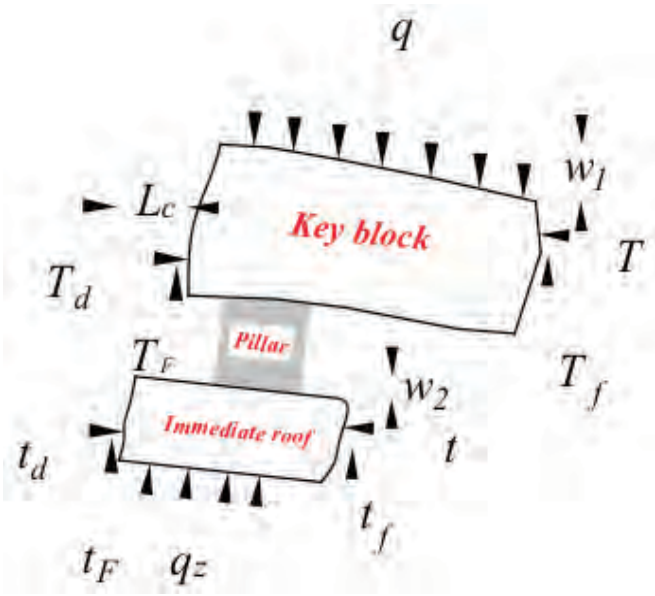



**Figure 3. Overlying strata movement model.**

horizontal and vertical components of the immediate roof tail-end force acted by the gob waste rock, respectively, $T_d$ and $T_F$ are the horizontal and frictional forces of the immediate roof tail-end and front-end acted by the adjacent blocks, respectively.

In order to investigate the interaction of "support-rock" system, the "Loading strata-Main roof-remnant pillars-Immediate roof-shield support" system can be divided into two interconnected systems: "Loading strata-Main roof-remnant pillars" system and "Remnant pillars -Immediate roof-shield support" system. The two systems are connected through the transferred load from the breakage process of main roof block movement to the remnant coal pillars.

**Loading strata-Main roof-Remnant pillars system**

Figure 4 is the key block mechanics model.

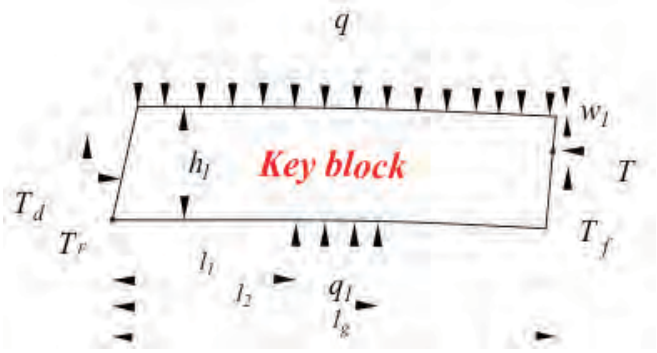



**Figure 4. The key block mechanics model.**

where $q_1$ is the load from the remnant pillars to the key block, $l_1$ and $l_2$ are the distance between the right and left sides of the pillar and the key block front-end, and *lg* is the key block length.

Based on the underground pressure and strata control theories, combining the equilibrium conditions for the horizontal and vertical forces on the front-end of the key block,

$$T = \frac{q{l_g}^2 - q_1({l_2}^2 - {l_1}^2) - 2T_f l_g}{h_l - l_g \sin\theta_1} = \frac{q_{gd}{l_g}^2}{h_l - l_g \sin\theta_1} \tag{1}$$

where $\theta 1$ is key block rotation angle, and $q_{gd}$ is key block equivalent load, which in this case is:

$$q_{gd} = \frac{q{l_g}^2 - q_1({l_2}^2 - {l_1}^2) - 2T_f l_g}{{l_g}^2} \tag{2}$$

The tail-end deflection of the key block is:

$$w_1 = h_l\left(1 - \sqrt{\frac{1}{3i_g K_g K_{g'}}}\right) \tag{3}$$

where *Kg* is the coefficient of key block loading condition, $k_{g'}$ is ratio of squeezing ($\sigma_p$) to compressive strengths ($\sigma_{gc}$) of the key strata, which may be 0.4 according to physical experiments, $i_g$ is a ratio of compressive to tensile strengths, which is 10 according to the laboratory test results. When $h_l$= 47.6 ft (14.5 m), the expansion ratio of the immediate roof ($K_z$) is 1.35. When mining height ($h_l$) is 9.8 ft (3.0 m), the immediate roof thickness ($h_z$) is 19.7 ft (6.0 m), the pillar height ($h_2$) is 7.5 ft (2.3 m). When both the gob and remnant pillar are 19.7 ft (6.0 m) wide, there remains a gap of 7.9 ft (2.4 m) in the gob. Obviously the maximum deflection of the tail-end of the key block is no more than 7.8 ft (2.4 m). The tail-end deflection of the key block is

$$w_1 \le h_1 + h_2 - (K_z - 1)h_z - \frac{w^2 K_z}{(a+w)^2}h_2$$

Due to different mining space, the loading conditions of the key block vary. Combining with Equation (3), key block loading coefficient becomes:

$$K_g = \frac{(a+w)^2{h_l}^2}{3i_g K_{g'}((h_1 + h_z + h_2 - h_l - K_z h_z)(a+w)^2 - K_z h_2 w_2)^2} \tag{4}$$

According to the key block movement model, the horizontal force of the key block becomes:

$$T = \frac{h_l - l_g \sin\theta_1}{2}\sigma_p = \frac{h_l - l_g \sin\theta_1}{2}K_{g'}\sigma_{gc} \tag{5}$$

Consequently based on the equilibrium conditions of the "Loading strata-Main roof-Remnant pillars" system, i.e., the support resistance from the remnant pillar to the key block can be determined by:

$$q_1 = \frac{2{l_g}^2 q + K_{g'}\sigma_{gc}({h_l}^2 + {l_g}^2\sin^2\theta_1 - 2h_l l_g \tan\varphi - 2h_l l_g \sin\theta_1 + 2{l_g}^2 \sin\theta_1 \tan\varphi}{2(2l_g - l_1 - l_2)(l_2 - l_1)} \tag{6}$$

**Remnant pillars-Immediate roof-shield support system and support capacity determination**

Considering the worst case scenario for the immediate roof in the "Remnant pillars-Immediate roof-shield support" system, i.e., the loading conditions of the immediate roof at the threshold of instability such as that shown in Figure 5, where $q_1$' is the sum of pillar self-weight and the load from the main roof.

From Figure 5, the shield support capacity is equal to the coal pillar load acting on the immediate roof and immediate roof rock weight, i.e.,

$$S_{t0} = q_z(l_h - l_q)b = [(L_2 - L_1)(q_1 + h_2\gamma_2)\eta_m + h_z l_z \gamma_z]b \tag{7}$$

where $S_{t0}$ is shield support capacity (tons), *b* is shield support width (ft), $\eta_m$ is remnant coal pillar load impact factor. According to Equation (7), the shield support capacity is calculated as 708 tons/unit (6,300 kN/unit) in the most severe situation. To be more conservative, the two-leg shield with a yield load of 764 tons (6,800 kN) was chose to control roof at Shigetai Mine. Note that the adaptable mining height for the selected shield ranges from 5.6 to 11.4 ft (1.7 to 3.5 m).

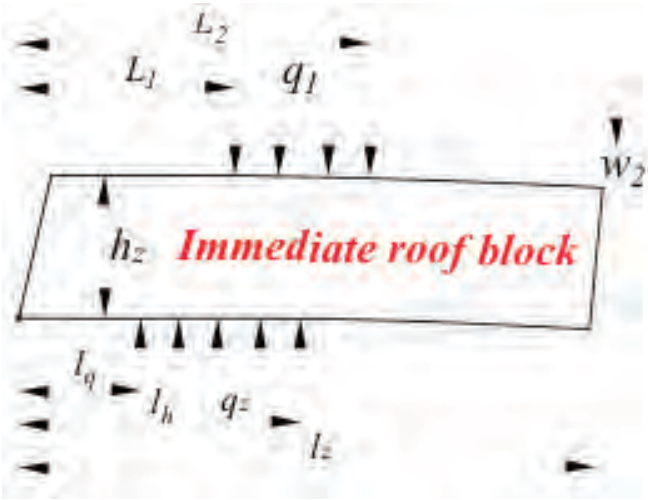



**Figure 5. Loading model of the immediate roof at threshold of instability.**

Equation (7) shows that shield support capacity is mainly related to the immediate roof thickness, strata strength, relative position to remnant coal pillars, and the load from the main roof when it collapses, which in turn is related to the remnant pillar size, main roof thickness and load transferred to the main roof.

**Mechanisms of immediate roof shearing and caving along coalface**

Based on the field investigation, the model of the immediate roof shearing and caving along the coalface was established, as shown in Figure 6.

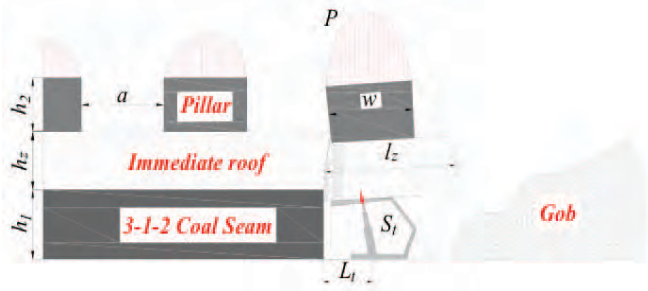



**Figure 6. Model of the immediate roof shearing and caving along coalface.**

With the load transferred from the remnant pillars to the immediate roof in the "Remnant pillars-Immediate roof-shield support" system, the immediate roof can be considered as a cantilever beam. Assuming the required shield yield load is known (in this case it was 764 tons/unit (6,800 kN/unit)), the required shield load to resist shearing along the faceline can be found by the equilibrium conditions of the cantilever beams:

$$\left(L_2{}^2 - L_1{}^2\right)(q_1 + h_2\gamma_2) + h_z l_z{}^2\gamma_z - \frac{(l_q + l_h)S_{t0}}{1000b} \geq \frac{h_z{}^2\sigma_{zt}}{3} \quad (8)$$

where $\sigma_{zt}$ is the immediate roof ultimate tensile strength.

## NUMERICAL SIMULATION

3DEC (Three Dimension Distinct Element Code) was adopted to analyze the overlying strata movement for the fully mechanized mining of shallow seam under an abandoned room and pillar mine without pillar extraction (Liu, 2005; Ma et al., 2008c). Note that the model used in this study has been validated by Wang (2012). After room and pillar mining, stress concentration in the remnant pillars in the 3-1-1 seam is very obvious, exhibiting the state of "Elastic inside-Plastic outside". Their vertical stresses reach up to 942.75~1305.34 psi (6.5-9.0 MPa) with a stress concentration factor about 4-5, as shown in Figure 7.

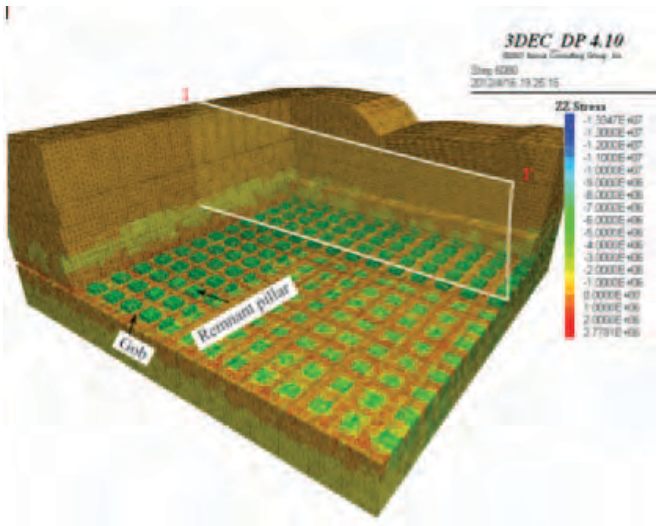



**Figure 7. Stress fields of room and pillar mining as modeled by 3DEC.**

Longwall mining was carried out for the 3-1-2 seam under an abandoned room and pillar mine without pillar extraction . The vertical stress distributions in the overlying strata (along cross-section I-I' in Figure 7) are shown in Figure 8.

(a) when the face has advanced 164.04 ft (50 m) from the set-up room

(b) when the face has advanced 360.89 ft (110 m) from the set-up room

(c) when the face has advanced 459.32 ft (140 m) from the set-up room

Figure 8 shows that when the face has advanced 164.04 ft (50 m) from the set-up room, caving and fracturing in the overlying strata have caused obvious collapse pits on the surface, and the pillars in front of the face have high stress concentrations (about 2552.67 psi (17.6 MPa)). When the face advances from 164.04

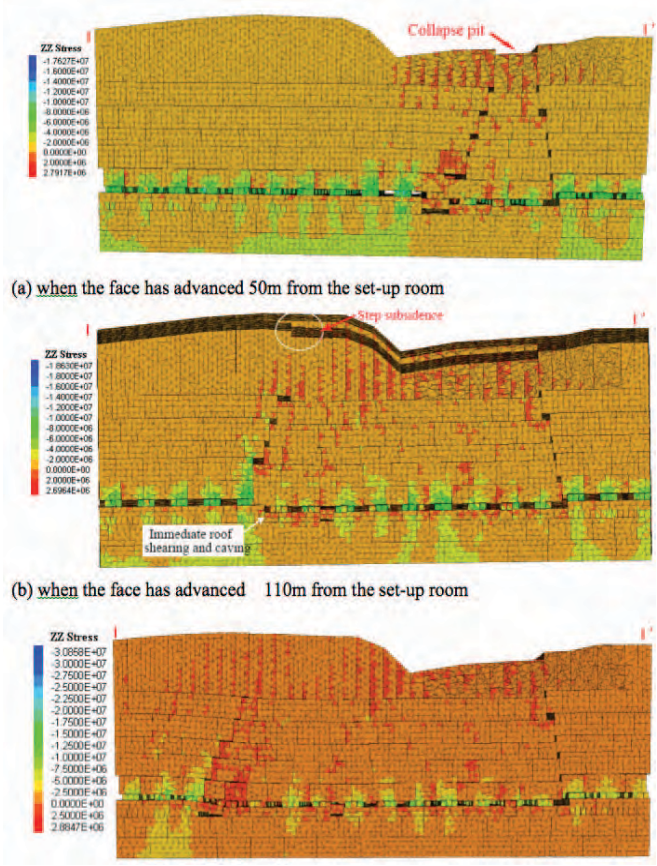



**Figure 8. Vertical stress distribution in the overlying strata induced by longwall mining.**

ft (50 m) to 459.32 ft (140 m), periodic caving and weighting in the main roof continue with an interval of about 49.21 ft (15 m). Due to the effect of concentrated stresses in the coal pillar during the roof weighting period, the immediate roof above the face shears and caves along the coalface, resulting in a maximum step subsidence of more than 3.28 ft (1.0 m) and possibly crushing the shield supports (e.g., when the face advances to 360.89 ft (110 m)). The overburden is in a stable state in the mined out area, when for example the face has advanced to 459.32 ft (140 m).

The mining induced vertical displacement distributions in the overlying strata (along cross-section I-I' in Figure 7) are shown in Figure 9.

(a) when the face has advanced 164.04 ft (50 m) from the set-up room

(b) when the face has advanced 229.66 ft (70 m) from the set-up room

(c) when the face has advanced 426.51 ft (130 m) from the set-up room

Figure 9 shows that when the face has advanced 164.04 ft (50 m) the caving angles are 79° and 70° in the set-up room and face sides, respectively. The mining induced strata displacement increases gradually from the face side to the gob side with distinct horizontal partitioning features. After the face has advanced 229.66

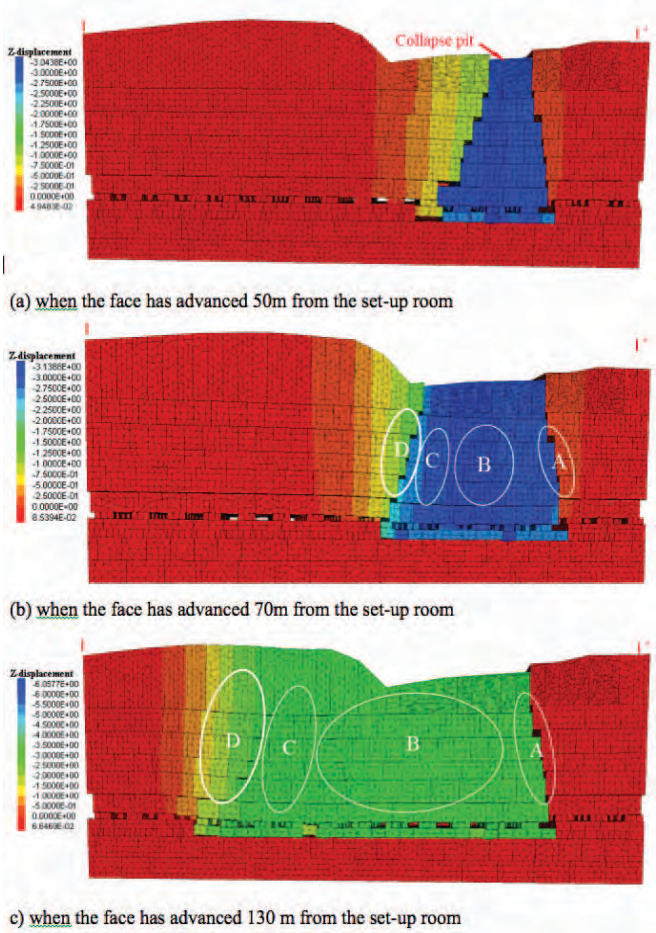



**Figure 9. Minining induced vertical displacement distributions in overlying strata.**

ft (70 m), the overlying strata movement along the mining direction can be divided into four zones based on the compaction state of the gob (see Figure 9b): (A) set-up room side "permanently fractured zone"; (B) "re-compaction zone" in the gob central area; (C) "fracture closure zone"; and (D) "dynamic fractured zone" around the face side. As the fractures in (A) and (D) zones cannot close up within a short period of time, they serve as conduits for water and alluvium in-rush and flow. Air will flow from these fractures to the gobs causing spontaneous ignition. It requires timely measures such as sand backfilling to prevent it from occurrence.

## FIELD OBSERVATION

Real-time monitoring on the shield support resistance and surface cracks during mining of the panel 131201 was conducted. The results were used to forecast the large area roof shearing and caving along, and bump at, the face. It determined that the first and periodic roof weighting intervals were 122.05 ft (37.2 m) and 41.99 ft (12.8 m), respectively. The dynamic weighting factor was 1.71. 50% of the measured shield leg working resistances was less than 382 tons(3,400 kN), which indicated that the selected two-leg shield support has a sufficient spare capacity, and satisfies the roof support demand beneath the shallow room and pillar gobs.

The mining induced overlying strata movement eventually developed to the ground surface, inducing horizontal and vertical displacements on the surface. The development sequence of surface crack is shown in Figure 10.

(a) Surface crack generation and expansion

(b) Surface step subsidence

(c) Surface crack closure

The development of surface cracks generally goes through the following four stages: (1) surface crack generation stage: firstly, a series of tensile open cracks of different width but parallel to the face appeared 65.62-98.43 ft (20-30 m) in front of the face, as shown in Figure 10(a); (2) crack expansion stage: the horizontal and vertical displacements of the cracks continue to expand due to the continuing strata movement; and (3) surface step subsidence stage: an obvious surface step subsidence appeared when the face advanced right after a periodic weighting interval. The amount of subsidence ranged from a few centimeters to 3.28 ft (1 m), as shown in Figure 10(b); (4) surface crack closure stage: with the face continued to advance, the offset of surface step subsidence gradually decreased, surface cracks closed up automatically and finally manifested as a whole-body surface subsidence, as shown in Figure 10(c). The surface step subsidence can be detected by the numerical modeling (see Figure 10b), while Figure 10b shows the field observation of the surface step subsidence, which indicates that the numerical modeling is reliable. The whole process of the surface crack development occurs in a short period, indicating that the duration of roof weighting for longwall mining under the gobs of room and pillar mining is short with strata movement directly reaching the surface.

## CONCLUSIONS

Based on the geological conditions of two adjacent shallow seams in which longwall mining with small interburden under an abandoned room and pillar mine without pillar extraction was implemented, an overburden strata structural mechanics model was established to analyze the causes of the immediate roof shearing and caving along the coal face and crushing of shield supports. From the analysis the proper shield support yield load capacity was determined. The shield support yield load capacity is mainly related to the immediate roof thickness, the size of remnant pillars and gob, the main roof thickness, the key block length, and the loads from the loading strata that are transferred to the main roof.

In shallow seam mining, cracks develop continuously following the advancing face until it reaches the surface. Along the face advancing direction, the overlying strata movement forms four zones: “permanently fractured zone” in the set-up room side, “re-compaction zone” in the gob central region, “dynamic fractured zone” around the face, and “fracture closure zone”. The development of surface cracks generally goes through four stages: surface crack generation, crack expansion, surface step subsidence, and surface crack closure. The whole process of the surface crack development lasts only for a short period of time.




**Figure 10. The sequence of development of surface cracks.**

**ACKNOWLEDGMENTS**

Financial support for this research was provided by the National Natural Science Foundation of China (NO.51304202), the Chinese National 863 High Technology Plan (NO.2012AA062101), the Natural Science Foundation of Jiangsu Province of China (NO. BK20130190), the Fundamental Research Funds for the Central Universities (NO.2013QNA28), and the Priority Academic Program Development of Jiangsu Higher Education Institutions (NO. SZBF2011-6-B35). The authors gratefully acknowledge financial support of the above-mentioned agencies. The authors are grateful to Ordos Wulan Coal Group Corporation Limited for their financial support and the field tests, and the authors express their special gratitude to Prof. Syd S. Peng and Dr. W. Li for their constructive comments.

**REFERENCES**

Dehghan, S., Shahriar, K., Maarefvand, P., Maarefvand, P., and Goshtasbi, K. (2013). "3-D modeling of rock burst in pillar No.19 of Fetr6 chromite mine." International Journal of Mining Science and Technology 23(2): 231-236.

Hou, Z.J. (2000). "Analysis of combinatorial key strata stability in shallow coal seam with thick loose bed." Journal of China Coal Society 25(2): 127-131.

Huang, Q.X. (2002). "Ground pressure behavior and definition of shallow seams." China Journal of Rock Mechanics and Engineering 21(8): 1174-1177.

Huang, Q.X., and Zhang, P. (2004). "Study on dynamic load distribution on key roof blocks of under thick sandy soil stratum." Chinese Journal of Rock Mechanics and Engineering 23(24): 4179-4182.

Huang, Q.X. (2005). "Studies on load-transmitting factor of thick sandy soil layer on key roof stratum in shallow seam mining." Chinese Journal of Geotechnical Engineering 27(6): 672-676.

Li, C., Xu, J.H., Wang, Z.L., and Qin, S. (2013). "Domino instability effect of surrounding rock-coal pillars in a room-and-pillar gob." International Journal of Mining Science and Technology 23(6): 913-918.

Li, Q., Xu, H., Bu, W.K., and Zhao, G.Z. (2011). "An analytic solution describing the visco-elastic deformation of coal pillars in room and pillar mine." Mining Science and Technology (China) 21(6): 885-890.

Liu, C.L., Tan, Z.X., Deng, K.Z., and Li, P.X. (2013). "Synergistic instability of coal pillar and roof system and filling method based on plate model." International Journal of Mining Science and Technology 23(1): 145-149.

Liu, C.X. (2005). "Numerical simulation of moving features of hard roof with three-dimensional discrete element method and nonlinear dynamic analysis." Rock and Soil Mechanics 26(5): 759-762.

Liu, Y.D., Zhang, D.S., Ma, L.Q., Zhao, Y.F., and Wang, H.S. (2008). "Classification of conditions for short-wall continuous mechanical mining in shallowly buried coal seam with thin bedrock." Journal of China University of Mining and Technology 18(3): 389-394.

Ma, L.Q., Zhang, D.S., Qiao, J.L., Wang, S.Y., and Wang, Y. (2008a). "Physical simulation of water crack distribution characteristics in overlying strata under coal mining conditions." Journal of Liaoning Technical University (Natural Science) 27(5): 649-652.

Ma, L.Q., Zhang, D.S., Liu, Y.D., Wang, A., Zhao, Y.F., and Zheng, T.B. (2008b)."Aquifer-protective mining technology in shallow coal seam with thin bedrock." Journal of Hunan University of Science & Technology (Natural Science Edition) 23(1): 1-5.

Ma, L.Q., Zhang, D.S., Jing, S.G., Zhang, W., and Fan, G.W. (2008c). "Numerical simulation analysis by solid-liquid coupling with 3DEC of dynamic water crannies in overlying strata." Journal of China University of Mining & Technology 18(3): 347-352.

Tu, S.H., Dou, F.J., Wan, Z.J., Wang, F.T., and Yuan, Y. (2011). "Strata control technology of the fully mechanized face in shallow coal seam close to the above room-and-pillar gob." Journal of China Coal Society 36(3): 366-370.

Wang, F.T. (2012). "Overlying strata movement laws and ground control of the longwall face mining in a shallow depth seam in proximity beneath a room mining goaf." PhD. Thesis, China University of Mining and Technology, Xuzhou, China.

Wang, F.T., Tu, S.H., Yuan, Y., Feng, Y.F., Chen, F., and Tu, H.S. (2013). "Deep-hole pre-split blasting mechanism and its application for controlled roof caving in shallow depth seams." International Journal of Rock Mechanics & Mining Sciences 64: 112-121.

Xie, X.Z. (2012). "Study on the characteristics of strata behavior in shallow seam longwall mining under the room-and-pillar mining goaf." Journal of China Coal Society 37(6): 898-902.

# Development of the 3D Numerical Modeling of Roof Bolts for Studying the Bolt/Rock Interaction

**Wenfeng Li**, Ph.D. Student
**Jianbiao Bai**, Professor
China University of Mining and Technology
Xuzhou, Jiangsu, China

**Vietdoan Dao**
Hanoi University of Mining and Geology
Tu Liem,China

## ABSTRACT

A 3D roof bolt model with the consideration of rebar, resin, bearing plate, and resin/rock interface was developed for studying the bolt/rock interactions of the tensioned and fully-grouted resin bolts. For the tensioned bolts, 2 ft compressive zone above the roofline is generated by the 10 tons pretension. Since the free portion of the tensioned bolts displays a higher vertical stress, the increase of the bearing capacity of the rocks in such range is much larger. For the fully grouted resin bolts, despite no pretension is generated during installation, the roof sag can indirectly generate a compressive zone near the roof line. In addition, the analysis on the differences in bolt/rock interactions when employing the tensioned or fully-grouted resin bolts indicates that the fully-grouted resin bolts are preferred as the primary support when weak and thinly-bedded immediate-roof is present. Meanwhile, it is found that both the tensioned and fully-grouted resin bolts may have very limited effect in preventing and/or control the cutter roof.

## INTRODUCTION

The U.S. coal industry consumes hundreds of thousands of roof bolts every year for the past four decades (Peng 2008). Several researches have been done on the roof bolt design using various approaches such as analytical method, field measurement, statistical method, and numerical modeling (Yassien et al., 2002; Zhang and Peng, 2002; Mark et al., 2000; Stankus and Peng, 1994; Maleki, 1992). These researches have all contributed toward the development of the roof bolt design criteria. However, there is no widely-accepted criteria for roof bolt design up to now (Tadolini and Mazzoni, 2006) since the bolt/rock interaction has not been understood completely. The bolt/rock interaction involves how much the strength of the roof strata can be increased by the roof bolts.

Existing analytical tools are not sufficient to analyze the complex bolt/rock interaction; therefore, numerical models are very essential to investigating its behavior. Many previous roof bolt models employed mathematical models to represent bolts and simulate roof bolt behavior (Itasca, 2007a and 2007b). None of them considered the effects of the bolt installation procedure and in case of tensioned roof bolting, the effect of pretension and bolt accessories, for instance the bearing plate.

By using the finite element program ABAQUS, realistic numerical simulation models for the tensioned and fully-grouted resin bolts have been developed by Yassien et al., (2002) and Zhang and Peng (2002). The detailed bolt/rock interactions for both types of bolts were studied. However, they did not quantitatively discuss how much the strength of the roof strata in the bolting range was increased during or after the mining activities. Additionally, since the Itasca programs, such as FLAC$^{3D}$ and 3DEC, have gained widely acceptance in the field of coal mine ground control, it is necessary to develop a 3D numerical model of roof bolts employing FLAC$^{3D}$ for studying the bolt/rock interaction. Meanwhile, the stress and strength change of the host rocks during underground mining operations will be quantitatively discussed in the present study.

## NUMERICAL MODELING

### Global model

A typical longwall panel layout in southern Appalachia (see Figure 1) with overburden depth of 1,300 ft was used to model the effect of roof bolting. The panels were 1,200 ft wide, and the chain pillars in the gateroads and bleeder system were all 90 ft wide by 90 ft long. All the entries were 20 ft wide. A global model representing the cross-section R-R' in Figure 1 was generated, as shown in Figure 2. The size of the global model was 1,440×245.2×4 ft with half of each panel and the gateroad system between them. All the boundaries were roller-constrained except for the top of the global model. The upper boundary was subjected to a vertical stress of 1,312 psi. The horizontal stress was assumed as 1.2 times of the vertical stress.

The calibrated inputs for the coal and rock layers in the global model are shown in Table 1.The Mohr-Coulomb failure criterion was used to simulate the coal and rock strata except for the gob, which was assumed to behave as a strain-hardening material following the Salamon's theoretical gob-model (Salamon, 1990;Pappas and Mark, 1993). Table 2and Table 3 show the mechanical properties and ‹cap pressure› of the numerical gob material, respectively. The double-yield model was used to simulate the gob material in FLAC$^{3D}$. The approaches forcalibrating the inputs for coal, rock, and gob materials can be found in Li et al., (2013).

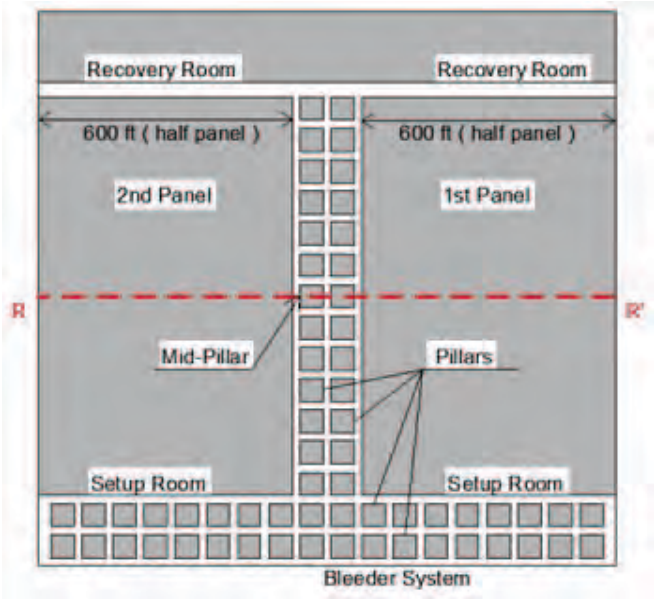



**Figure 1. A typical longwall panel layout in southern Appalachia.**

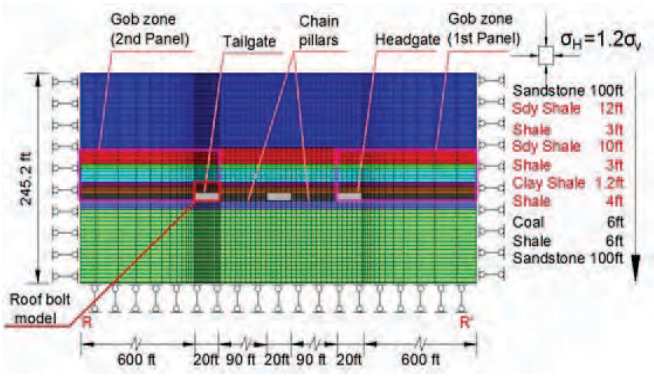



**Figure 2. Global model along cross-section R-R'.**

The global model was solved in three steps following the operations of underground mining activities. The global model was generated and the geostatic stress condition was applied in the first step. In the second step, all the entries were developed and the roof bolts were installed in the tailgate. Thereafter, the first panel was retreated in the third step by assigning the gob model into the caving zone (i.e. the gob zone of the first panel in Figure 2). It should be pointed out that in this case, the caving zone was assumed as 33.2 ft high above the coal seam of interest and consisted of shale, clay shale, shale, sandy shale, shale, and sandy shale in the ascending order (see the rock layers in red color in Figure 2). The cutting height was 6 ft.

There are two types of roof bolts that are mainly used for roof control in modern underground mines: tensioned and fully-grouted resin bolts. Both of them will be discussed in this paper.

**Tensioned bolt model**

The tensioned bolts are modeled by a three-dimensional beam with 1.5 ft long resin anchor on the upper end and a 6×6×1/4-in bearing plate on the lower end (see Figure 3a). The bolts are 8-ft long and 3/4-in in diameter, while the borehole for bolt installation is 1-in in diameter. The bearing plate is subjected to a uniformly distributed stress (556 psi) to represent the 10 tons pretension. The contact surfaces between the resin anchor and the host rocks and between the bearing plate and the roof surface are modeled as a contact interface, i.e. slippage occurs once its shear strength is exceeded.

Giraldo et al., (2005) conducted plenty of pull out tests on the tensioned and fully-grouted resin bolts and concluded that the average «Grip Factor» for the tensioned bolts is 0.66 ton/in. The «Grip Factor» is defined as the bolt›s resistance to pull out per inch of resin annulus length. Based on their conclusions, a pull out model (see Figure 4) was developed to calibrate the inputs for the bolt rebar and the interface between the resin anchor and the host rocks. In the pull out test model, a single tensioned-bolt was installed in a rock block, the left, right, and bottom boundaries of the model were roller-constrained. The resin anchor was 1.5 ft long. A constant-velocity displacement ($1\times10^{-5}$) was applied to the end of the bolt, and the load and displacement of the bolt were recorded (see the curve in Figure 4). The predicted maximum load of the tensioned bolt is 11.88 tons that equals to the theoretical result of the bolt load. The corresponding or the validated inputs for the bolt rebar and the resin/rock interface are shown in Table 1 and Table 4, respectively.

**Table 1. Rock and coal properties used in the global model.**

| Rock Strata | Density, lb/in$^3$ | Shear Modulus, $10^6$psi | Bulk Modulus, $10^6$psi | Friction Angle, degree | Cohesion, psi | Tensile Strength, psi |
|---|---|---|---|---|---|---|
| Sandstone | 0.0939 | 1.495 | 1.745 | 44 | 1319 | 236 |
| Sdy shale | 0.0939 | 1.35 | 1.6 | 41 | 1029 | 207 |
| Shale | 0.0906 | 1.19 | 1.49 | 39 | 920 | 181 |
| Clay shale | 0.0901 | 1.17 | 1.47 | 38 | 900 | 179 |
| Coal | 0.0505 | 0.249 | 0.448 | 34 | 436 | 116 |
| Rebar/Resin | 3.28 | 1.38 | 1.31 | 70 | 222,605 | 60,002 |

**Fully-grouted resin bolt model**

As describing for the tensioned bolts, the fully-grouted resin bolts are also modeled by a three-dimensional beam with a 6×6×1/2-in bearing plate on the lower end (see Figure 3b). The parameters for the bolt length and diameter and the borehole diameter are the same as those of the tensioned bolts. There is no pretension for the fully-grouted resin bolt model since no pretension is applied

**Table 2. Mechanical properties for the gob material.**

| Property | Density, lb/in$^3$ | Bulk modulus, $10^6$psi | Shear modulus, $10^6$psi | Friction angle, degree | Dilation angle, degree |
|---|---|---|---|---|---|
| Value | 0.036 | 1.26 | 0.92 | 20 | 5 |

**Table 3. "Cap pressure" for the gob material.**

| Strain, in/in | 0.0 | 0.01 | 0.02 | 0.03 | 0.04 | 0.05 | 0.06 | 0.07 | 0.08 |
|---|---|---|---|---|---|---|---|---|---|
| Stress, psi | 0 | 35 | 73 | 117 | 167 | 224 | 289 | 365 | 455 |
| Strain, in/in | 0.09 | 0.1 | 0.11 | 0.12 | 0.13 | 0.14 | 0.15 | 0.16 | |
| Stress, psi | 564 | 696 | 856 | 1073 | 1357 | 1755 | 2350 | 3341 | |

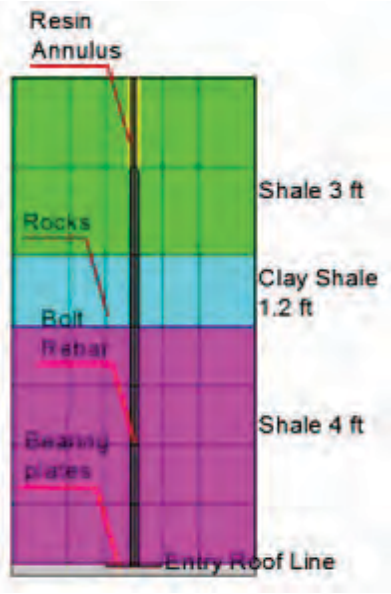



**Figure 3a. Tensioned bolt.**

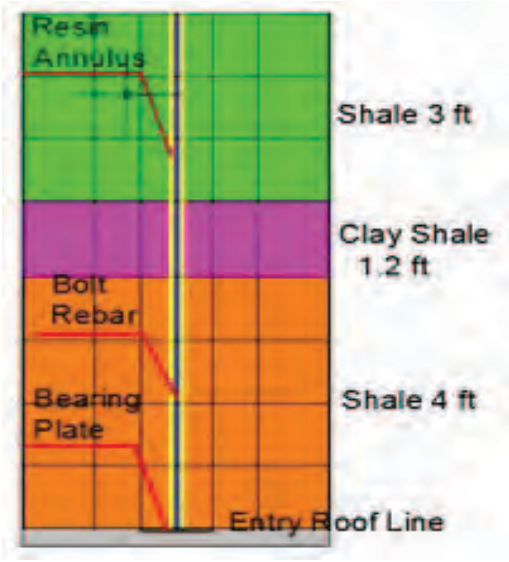



**Figure 3b. Fully grouted resin bolt.**

**Table 4. Input properties for the resin/rock interface.**

| Property | Normal stiffness, | Shear stiffness, | Cohesion, psi | Friction angle, degree |
|---|---|---|---|---|
| Value | 1.225×$^1$08 | 1.146×$10^8$ | 3748 | 34 |

during the installation of fully-grouted resin bolts in practice. The inputs for the interfaces between the resin anchor and the host rocks and between the bearing plate and the roof surface are the same as those used for the tensioned bolts (see Table 4).

**When to install roof bolts**

Another important question that needs to be addressed for roof bolt simulation is that when to install or activate the roof bolt model? Zhang and Peng (2002) believed that more than 80% of the roof deformation has already developed when the bolts are installed in practice. However, Esterhuizen et al., (2013) installed the support units in their model after 30% of the roof deformation had taken place. Several published in-mine instrumentation data (Stankus et al., 2001; Li et al., 2013) indicates that the roof sag after bolt installation may have reached up to 4in, depending on the geological and stress conditions. In this respect, it seems more reasonable to activate the roof bolt model when 30% of the roof deformation has occurred. In fact, the less time dependent deformation involves after the bolt installation, the less amount of load is induced in the bolts. Figure 5 shows the roof deformation after entry development in the present numerical model. Each colored line represents the deformation curve of the relative colored point or points in the roofline. Note that the bolt was installed after 30% of the elastic roof deformation has occurred.

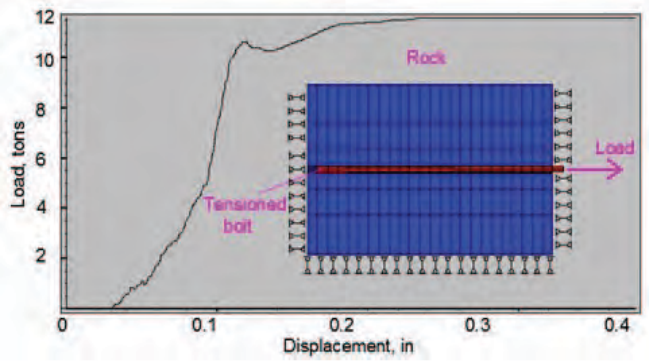



**Figure 4. Pull out test for determining the strength of the resin/ rock interface.**

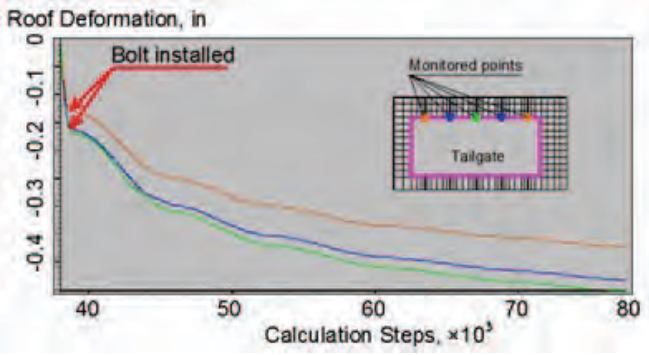



**Figure 5. Simulated roof deformation after entry development.**

### Spacing of the roof bolts

The bolts were installed in the tailgate (see Figure 2). As discussed previously, the entry was 20 ft wide. Hence, the simulated spacing of the tensioned and fully-grouted resin bolts were 4 ft×4 ft, as shown in Figure 6.

## BOLT/ROCK INTERACTION OF TENSIONED BOLTS

The vertical stress distributions of the tensioned bolts after tailgate development is shown in Figure 7, while Figure 8 presents that after retreating of the first panel. In each figure, the upper part of the tensioned bolts is grouted by the resin and called the resin-grouted portion, while the lower part is highlighted as the free portion.

The maximum vertical stress in the tensioned bolts after entry development is located in the free portion, reaching to 7,130-7,160 psi (see Figure 7). It is slightly increased to 7,980-8,820 psi (see Figure 8) after the retreating operation of the first panel. It is noted that the vertical stresses in the free portion of the tensioned bolts are not uniformly distributed (see Figure 7 and Figure 8). The bearing plates will be inclined in certain degree due to the roof sag after entry development, resulting in the different vertical displacements occurring in the opposite sides of the bolt end (see Figure 9). Hence, the sectioned vertical stress distribution in the free portion can be found.

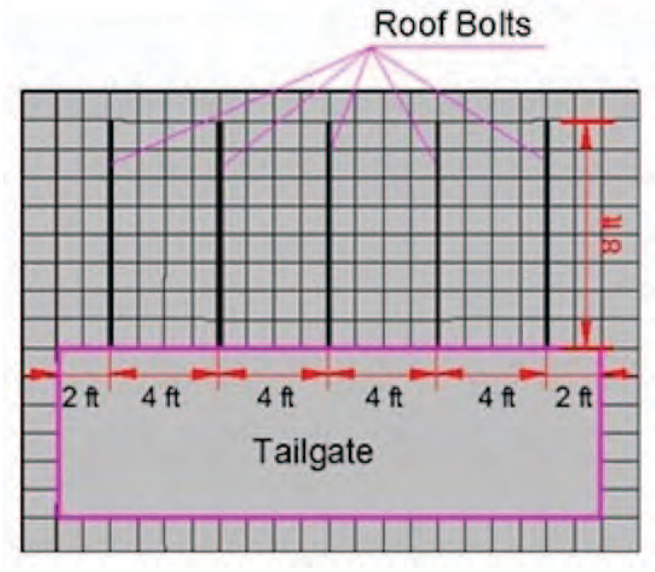



**Figure 6. Spacing of the tensioned (or the fully-grouted) bolts in the model.**

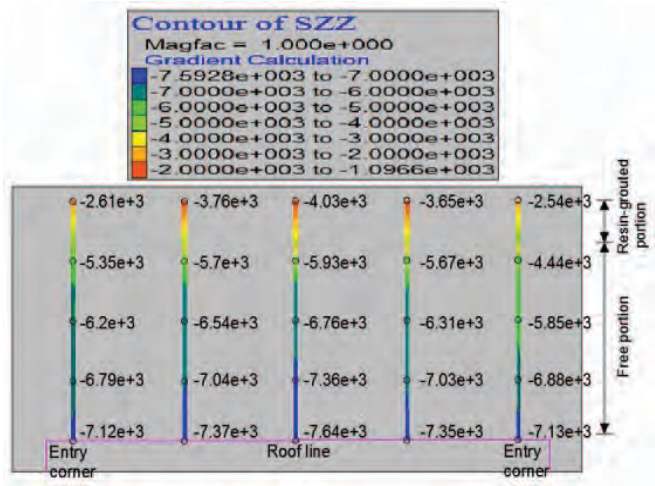



**Figure 7. Vertical stress in the tensioned bolts after tailgate development, psi.**

The vertical, horizontal, and shear stresses in the roof rocks after panel retreating are shown in Figs. 11a, 11b, and 11c, respectively. The yielding state of the roof rocks in the bolting range is shown in Figure 10. Note that points A and B in Figure 11a are located in the yield zone, while points C and D are located in the elastic zone.

For the three tensioned bolts installed near the middle of the roof span, 2 ft compressive zone above the roofline are generated by the pretension of 10 short tons. However there is no compressive zone for the two side bolts (see Figure 11a). Since the pretension of the roof bolt is much smaller than the vertical stresses concentrated in the entry corners, thus the compressive zone of the side bolt is invisible. In addition, it can be found in Figure 11a that the vertical stress at point B (in the middle between the adjacent bolts) is almost 0, while that at point A (close to the tensioned bolt) is much larger, reaching to 200 psi. On the other hand, The vertical stress in the rocks at point D is 440 psi (by prorata estimation), while that

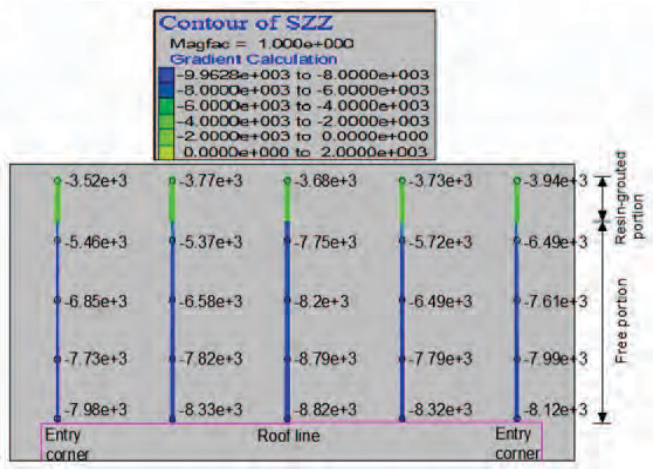



**Figure 8. Vertical stress in the tensioned bolts after retreat of the first panel, psi.**

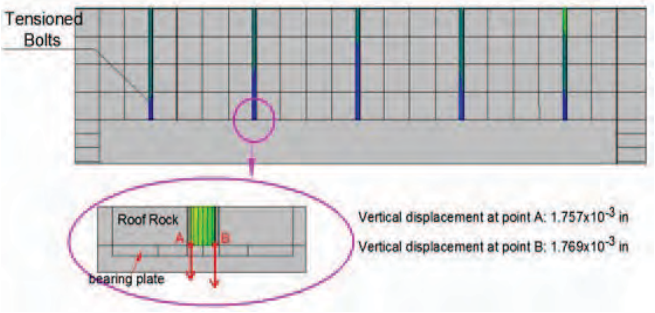



**Figure 9. The effect of the inclined bearing plates on the sectioned vertical stress distribution in the tensioned bolts after tailgate development.**

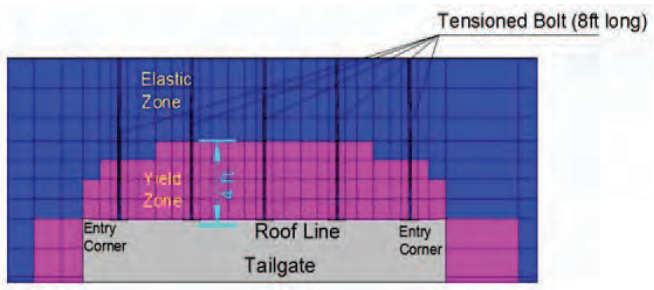



**Figure 10. Yield zone around tailgate after retreat of the first panel (tensioned bolts).**

at point C (close to the tensioned bolt) is slightly larger, reaching to 500 psi. If no roof bolt is installed, the vertical stress in points A and B (or C and D) should be close to one another since they are in the same elevation. However, the installed tensioned-bolts can significantly increase the bearing capacity of the rocks in the yield zone.

Figure 11b shows the horizontal stress of the roof rocks after the retreat of the first panel when employing the tensioned bolts. The gob (the first panel) is located at the right side of the entry, thus the horizontal stress at the right side is larger than that at the left side. It can be noted that the tensioned bolts can cut down the horizontal

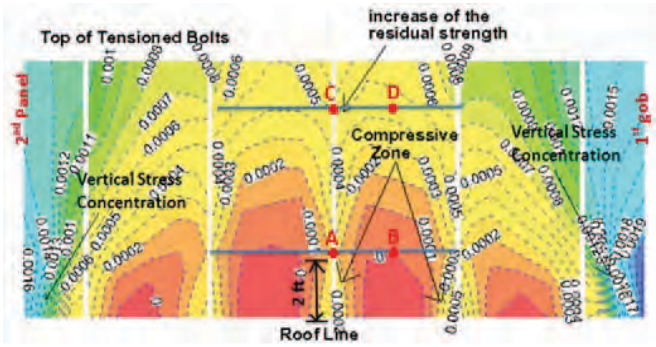



**Figure 11a. Vertical stress, E+6 psi.**

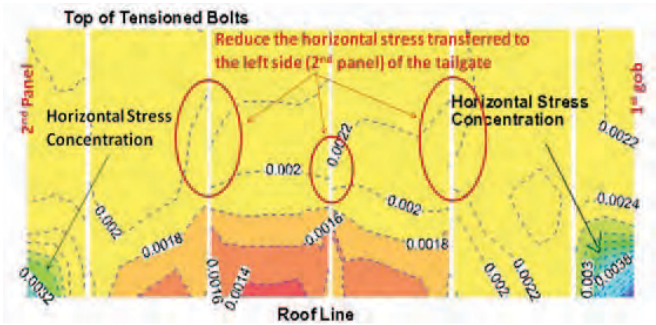



**Figure 11b. Horizontal stress, E+6 psi.**

stress transferred to the left side of the entry (see the highlighted circles in Figure 11b).

It is generally believed that the shear stress at the entry corners is a main contributor to the cutter roof development. Figure 11c shows the shear stress ($\sigma_{xz}$) of the roof rocks after the retreat of the first panel when employing the tensioned bolts. The gob (the first panel) is located at the right side of the entry, thus the shear stress at the right side is greatly larger than that at the left side. Meanwhile, it is noted that the shear stress distribution at entry corners was not affected effectively by the tensioned bolts (see the highlighted circles in Figure 11c). Hence the tensioned bolts may have limited effect on the cutter roof development.

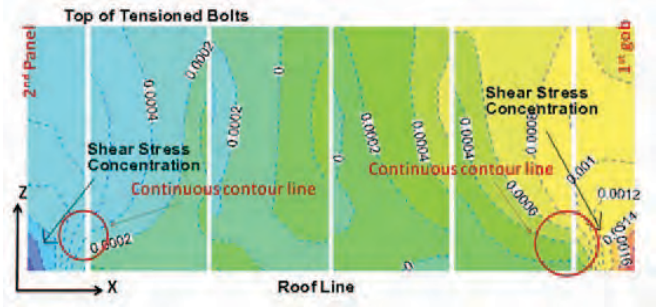



**Figure 11c. Shear stress, E+6 psi.**

## BOLT/ROCK INTERACTION OF FULLY-GROUTED RESIN BOLTS

As analyzed in the last section, the stresses in the bolts and roof rocks will be discussed in detail to determine the bolt/rock interaction of the full-grouted resin bolts.

The maximum vertical stress of the full-grouted resin bolts after entry development ranges from 7,580-17,800 psi (see Figure 12a). It is greatly increased to 29,000-54,700 psi (see Figure 13a) after the retreating operation of the first panel. On the other hand, the maximum shear stress of the resin bolts after entry development is only 1,380-4,570 psi (see Figure 12b). However, it is increased to 2,620- 8,180 psi after panel retreat (see Figure 13b). Note that some of the resin bolts display the maximum vertical stress at the upper part, while others show the maximum vertical stress at the lower part. The maximum shear stress of the resin bolts always occurs near the roof line.

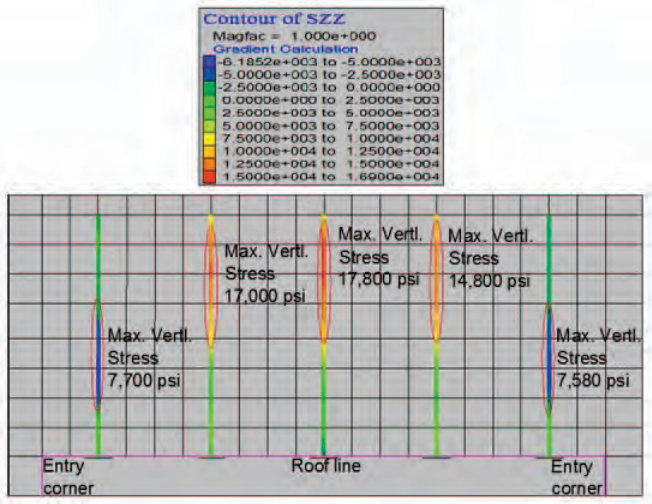



**Figure 12a. Vertical stress.**

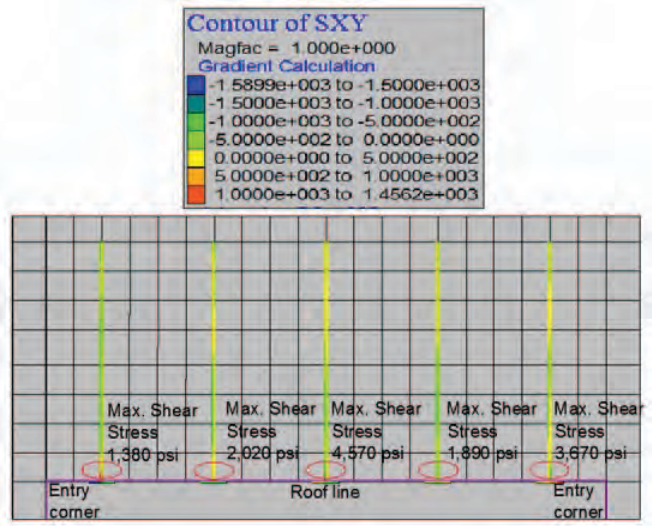



**Figure 12b. Shear stress.**

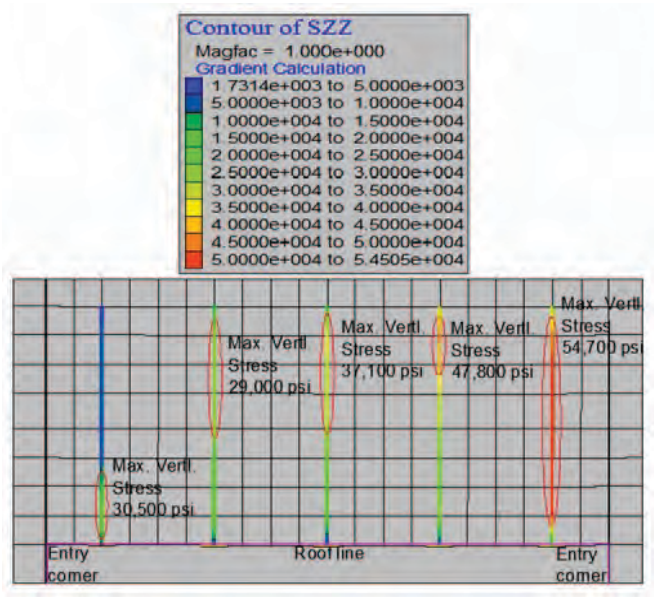



**Figure 13a. Vertical stress.**

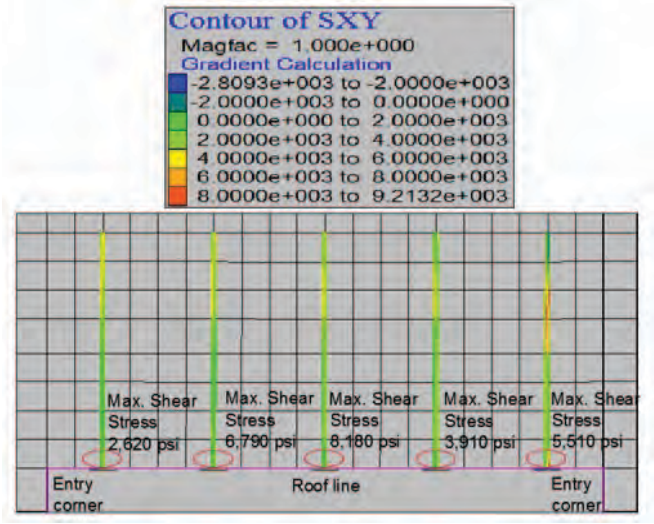



**Figure 13b. Shear stress.**

The yielding state of the roof rocks in the bolting range is shown in Figure 14. The vertical, horizontal, and shear stresses of the roof rocks after panel retreating are shown in Figs. 15a, 15b, and 15c, respectively. Note that points A, B, C, and D in Figure 15a are located in the yield zone.

Despite no pretension is generated during the resin bolt installation, a 2 ft compressive zone is developed near the roof line for the three bolts installed near the middle of the roof span (see Figure 15a). It is believed that the retreating-induced abutment load will cause the roof sag thus create the compressive zone. In addition, it can be found in Figure 15a that the vertical stress at point B (in the middle between the adjacent bolts) is almost 60 psi (by prorate estimation), while that at point A (close to resin bolt) is much larger, reaching to 400 psi. On the other hand, the vertical stress of the rocks at point D (in the middle between the adjacent bolts) is 340 psi, while that at point C (close to resin bolt) is only

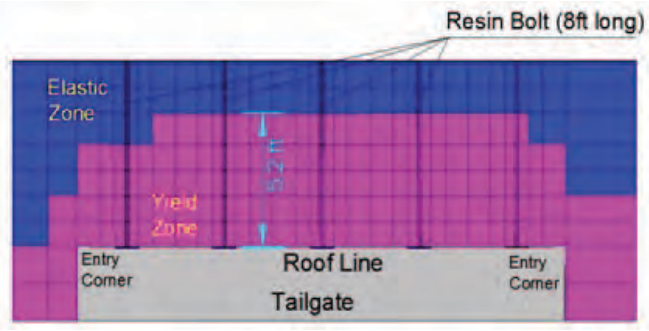



**Figure 14. Yield zone around tailgate after retreat of the first panel (resin bolts).**

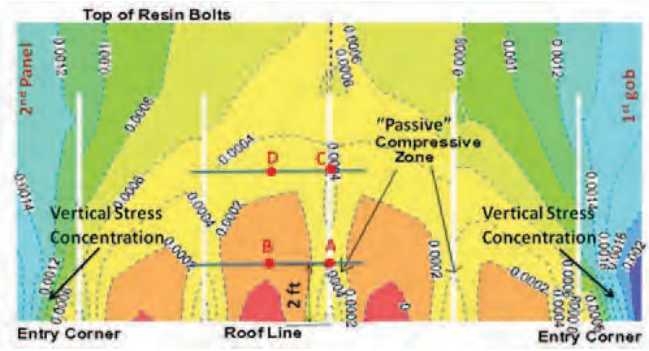



**Figure 15a. Vertical stress, E+6 psi.**

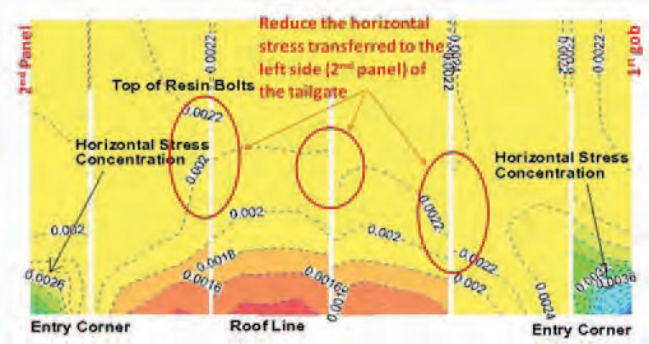



**Figure 15b. Horizontal stress, E+6 psi.**

slightly larger, reaching to 400 psi. Hence, the resin bolts can significantly increase the bearing capacity of the rocks in the lower part of roof yield zone, while they have limited effect on the rocks in the upper part of the roof yield zone.

Figure 15b shows the horizontal stress in the roof rocks after the retreat of the first panel when employing the resin bolts. The horizontal stress at the right corner is larger than that at the left corner since the right side is closer to the previous mine-out panel or gob. It has been noted that the resin bolts can cut down the horizontal stress transferred to the left side of the entry (see the highlighted circles in Figure 15b).

Figure 15c shows the shear stress ( $\sigma_{xz}$) in roof rocks after the retreat of the first panel when employing the resin bolts. The resin bolts may have limited effect on the cutter roof development since the propagation of the shear stress contour line at entry corners is not significantly affected by the resin bolts (see the highlighted circles in Figure 15c).

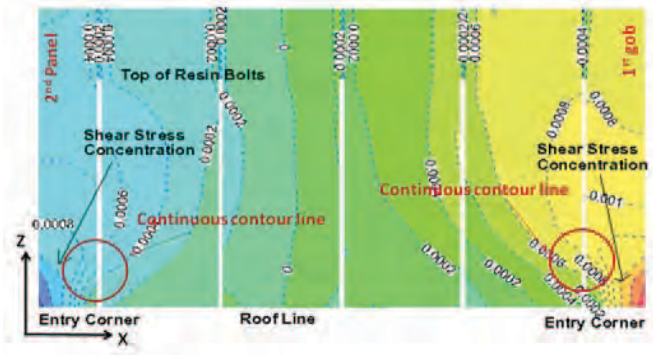



**Figure 15c. Shear stress sxz, E+6 psi.**

## DISCUSSION

For the specified case with a weak and thinly-bedded immediate-roof in this study, the vertical stresses in the tensioned bolts are significantly smaller than that in the resin bolts after retreat of the adjacent panel. Hence, the fully-grouted resin bolts provide more loads for the supporting of the entry roof in this case. In addition, the bearing capacity of the rocks in the lower yield zone of the entry roof is increased more when the fully-grouted resin bolts are installed. The aim of the roof bolting is to increase the strength of the roof rocks thus reduce the potential roof instability. In this respect, the fully-grouted resin bolts are preferred as the primary supports when the weak and thinly-bedded immediate-roof presents. It agrees with the conclusions found by Unrug et al., (2004).

## CONCLUSIONS

3D roof bolt models considering the rebar, resin, bearing plates, and resin/rock interface were developed for studying the complicated bolt/rock interaction during underground mining activities.

For the tensioned bolts, the vertical stresses in the bolts installed in the tailgate roof will be increased slightly after the retreat of the first panel. Meanwhile, a 2 ft compressive zone above the roof line is generated by the pretension of 10 short tons. Since the free portion of the tensioned bolts displays a higher vertical stress, the increase of the bearing capacity of the rocks in such range is much larger. In addition, it is found that the tensioned bolts may not be used to prevent the potential of cutter roof since they have very limited effect on the propagation of the shear stress at entry corners.

The similar conclusions can be obtained when employing the fully-grouted resin bolts in the specified tailgate. It should be emphasized that despite no pretension is generated during the installation of fully-grouted resin bolts, the roof sag can passively generate a compressive zone near the roof line. Comparing to the increase of the bearing capacity of the rocks in the lower yield zone of the roof when the tensioned bolts are used, bearing capacity of the rocks in lower roof is increased more when the fully-grouted resin bolts are installed. Hence, the fully-grouted resin bolts should be preferred as the primary supports when a weak and thinly-bedded immediate-roof exists.

**REFERENCES**

Esterhuizen G.S., Bajpayee T., Murphy M.M., and Ellenberger J. (2013). Validation of entry stability factors determined by the strength reduction method against empirical approaches. Proceedings of the 32nd International Conference on Ground Control in Mining. West Virginia University, Morgantown, WV, August 2013.

Giraldo L., Cotton S., Farrand J., and Pile J. (2005). Improved Pull-Out Strength of Fully-Grouted Roof Bolts through Hole Geometry Modification. Proceedings of the 24th International Conference on Ground Control in Mining, S.S. Peng et al., editors. West Virginia University, Morgantown, WV, August 2005, 279-284.

Itasca Consulting Group (2007). FLAC3D Instruction manual, Minnesota 2007.

Itasca Consulting Group (2007). 3DEC Instruction manual, Minnesota 2007.

Li W., Bai J., Peng S.S., Wang X., Xu Y. (2013). Numerical Modeling for Yield Pillar Design: A Case Study. Rock Mech Rock Eng 2013, DOI 10.1007/s00603-013-0539-8.

Maleki H.N. (1992). In-Situ Pillar Strength and Failure Mechanisms for U.S. Coal Seams. Proceedings of the Workshop on Coal Pillar Mechanics and Design. A.T. Iannacchione, et al., editors. U.S. Bureau of Mines, IC 9315, 1992, 73-77.

Mark C., Dolinar D.R., and Mucho T.P. (2000). Summary of Field Measurements of Roof Bolt Performance. Proceedings of New Technology for Coal Mine Roof Support. NIOSH, IC 9453, 2000, 81-86.

Pappas, D.M. and Mark C. (1993). Behavior of Simulated Longwall Gob Material. Bureau of Mines, 1993, RI 9458.

Peng S.S. (2008). Coal mine ground control, third edition. Peng SS publisher, Morgantown, WV, 2008. pp. 186.

Salamon M.D.G., Munro A.H. (1967). A study of the strength of coal pillars. Journal of South African Institute of Mining and Metallurgy, 1967, 68: 55-67.

Stankus J.C. and Peng S.S. (1994). Floor Bolting for Control of Mine Floor Heave. Mining Engineering, 46(9), September 1994, 1099-1102.

Stankus J.C., Suder T., and Williams D. (2001). Tensioned Cable Bolts as Primary Support: Update. Proceedings of the 20th International Conference on Ground Control in Mining, S.S. Peng et al., editors. West Virginia University, Morgantown, WV, August 2001, 252-258.

Tadolini S.C. and Mazzoni R.A. (2006). Twenty-Four Conferences: More Than One Hundred and Seventy Papers; Understanding Roof Bolt Selection and Design Still Remains Priceless. Proceedings of the 25th International Conference on Ground Control in Mining, S.S. Peng, et al., editors. West Virginia University, Morgantown, WV, August 2006, 382-389.

Unrug K., Padgett P., and Campoli A. (2004). Coal Mine Primary Support Selection: Tensioned Versus Non Tensioned Roof Bolt System. Proceedings of the 23th International Conference on Ground Control in Mining, S.S. Peng et al., editors. West Virginia University, Morgantown, WV, August 2004, 258-260.

Yassien A.M., Zhang Y., Han J., and Peng S.S. (2002). Comparison of Some Aspects of Bolting Mechanisms between Fully-Grouted Resin and Tensioned Bolts in Underground Mine Entries. Proceedings of the 21st International Conference on Ground Control in Mining, S.S. Peng et al., editors. West Virginia University, Morgantown, WV, August 2002, 114-125.

Zhang Y. and Peng S.S. (2002). Design Considerations for Tensioned Bolts. Proceedings of the 21st International Conference on Ground Control in Mining, S.S. Peng et al., editors. West Virginia University, Morgantown, WV, August 2002, 131-140.

# The Impact Factors of Overburden Movement in Longwall Mining of Shallow Coal Seams

**Yang Li**
**Jiachen Wang**, Professor, Head Department
Dept. of Mining Engineering
China University of Mining and Technology Beijing
Beijing, China

**Syd S Peng**, Charles E. Lawall Chair Emeritus
West Virginia University
Morgantown, WV

## ABSTRACT

For the study of overburden movement in longwall mining of shallow coal seams, most scholars merely consider the thickness of bedrock and top soils. In this paper, the overburden movement in longwall mining of shallow coal seams with thin top soils and key strata group was studied. By using numerical simulation, the development of fractures in the overburden was analyzed for different ratios of panel width to depth (W/D) and depth to mining height. The results show that the overburden movement changed with the variation of mining height, panel width and depth under the specific geological conditions. It also explain how different overburden disturbance structures, such as "three zones" (caved, fractured, and continuous deformation zones), "two zones"(caved and fractured zones) or "steps-like collapse"are formed under different mining conditions.The resultsbroaden the vision for research on overburden movement in longwall mining of shallow coal seams.

## INTRODUCTION

When a longwall panel of sufficient width and length is excavated, the overburden roof strata are disturbed in order of severity from the immediate roof toward the surface (Peng, 2006), or even the aquifers, which can lead to serious mine-flooding accidents and increased damages of the ecological environments (Peng, 2008). Thus it is absolutely essential to determine the overburden strata movement for the prevention of water in rush and protection for groundwater resources.

The movement characteristics of overburden strata in shallow coal seams are not just confined to the total collapse of the whole overburden and step subsidence (Li, 2011). In fact, different geological conditions such as different overburden strata and bedrock thickness produce different subsidence characteristics (Li, 2012).

## MODEL ESTABLISHMENT

The longwall panel studied in this paper is located in the Appalachia Coalfield, United States, where most coal seams are shallow. With a depth of 575ft (175m), the overburden strata are mostly bedrock, and the panel widthcan reach up to 1,430ft (435m), which is common in the United States, but rarely seen in China. Thus in this case, the practical experience and the theories developed provide the basis for further research on wider panels of shallow coal seam mining in western China (Wang, 2009).

In the numerical model selected for this research, under the thick alluvium in the overburden, there is an aquiclude group composed of gray shale, sandy shale, and limy shale. Underneath the overburden, there aresandstone key strata groups. The overburden stratigraphic sequence is shown in Figure 1.

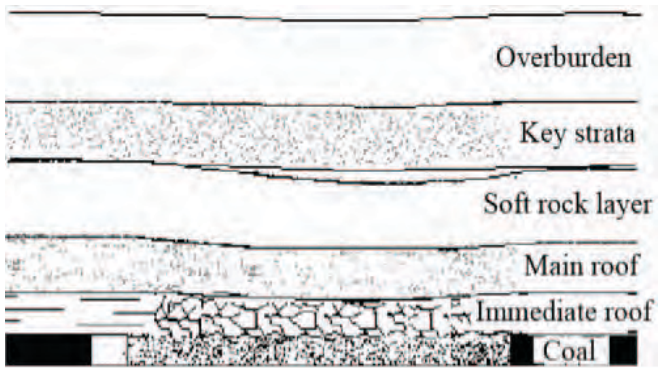



**Figure 1. Stratigraphic sequence used in the model.**

**Simulation purposes**

(1) Obtain, through numerical analysis of shallow longwall mining, the relationship between the characteristics of overburden movement and panel width; analyze the stress distributions in the surrounding rocks under different panel widths, but similar geological conditions.

(2) Obtain, through numerical analysis of shallow longwall mining, the relationship between the characteristics of overburden movement and mining height; analyze the stress distributions in the surrounding rocks under different mining height, but similar mining depth.

(3) Analyze, through numerical analysis of shallow longwall mining of different mining heights, surface subsidence and

ground movement under different ratios of panel width to mining depth (W/D).

(4) Analyze the impact of mining on groundwater under different ratios of panel width to mining depth (W/D) by comparing the overburden strata movement and the range of fracture development in different mining height.

**Establishment of the Three-dimensional Model**

(1) Numerical simulation model of longwall Panel

On the basis of the modeling principle of FLAC3D, the panel model was established with the geological conditions of a longwall panel in the Pittsburgh coal seam. The model length, width, and height are 1,930ft (588m), 40ft (12m), and 682ft (208m), respectively. To simulate more closer to the actual situation, the model was established by using the geologic column located in the panel of interest, with a total of 27 layers, from the floor up to the surface. According to the drillhole information, the Pittsburgh seam in the panel is 575ft (175m) deep, and the thickness of unconsolidated layer on the surface is only 20ft (6m).

The model is divided into 75,626 grid cells, and the number of grid nodes is 103,212. The density of grid cells is adjusted in order to ensure the speed and accuracy of the calculation.

(2) Numerical simulation models with different W/D

According to the results of borehole extensometer measurements and numerical simulation ofoverburden movement, when mining height is 7ft (2m) high and seam depth is 575ft (175m), three zones are formed in the overburden strata, instead of a "steps-like" collapse or whole piece overburden collapse. Thus more factors such as overburden structure, ratio of thickness of surface soil layer to rockbed, panel width, and mining height should be considered in the research onoverburden strata movement in shallow coal seams. In order to describe the overburden stratamovement in shallow coal seams with different panel widths, the model is simulated with different W/D of 2.5, 1.7, 1.2 and 0.87.

(3) Numerical simulation models with different mining height

In order to determine the impact of different mining height on the overburden strata movement and ground pressure, four different mining heights, i.e., 7ft (2m), 10ft (3m), 13ft (4m), and 16ft (5m) are simulated to observe the overburden strata movement, surface subsidence and stress change.

(4) Numerical simulation models of overburden fracture development with different W/D, and different mining height

The development of fractures on the surface and in the overburden during mining process is one of the key factors affecting groundwater system.The simulation of fracture development with different W/D anddifferent mining heights can help observe the range of fractured zonedevelopmentand fracture trend of main aquifuge.

Figure 2 shows the three-dimensional numerical simulation model.

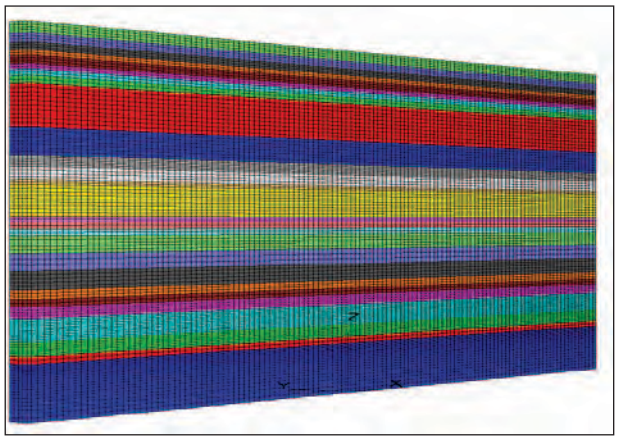


**Figure 2. Three-dimensional numerical model.**

**Physical and Mechanical Parameters ofOverburden Stratain the Model**

Rock property (see Table 1) is one of the important parameters affecting the overburden strata movement. Therefore it is also an essential parameter in computer modeling of groundwater flow. In this study, rock samples were collected from the boreholes thatwere located near the gateroads of the panel of interest.

**ANALYSIS OF THE SIMULATION RESULTS**

**Simulation Results with Different W/D**

(1) Overburden strata movement under different W/D

As coal mining proceeds, the overburden strata above the gob will subside, separate and fracture. The vertical displacement in the simulation reflects well the subsidence of overburden strata in the mining process. Figure 3, Figure 4, Figure 5, and Figure 6 show the overburden strata vertical movement with different W/D and mining height. Figure 7 and Figure 8 show the surface subsidence subjected to different W/D's and mining heights.

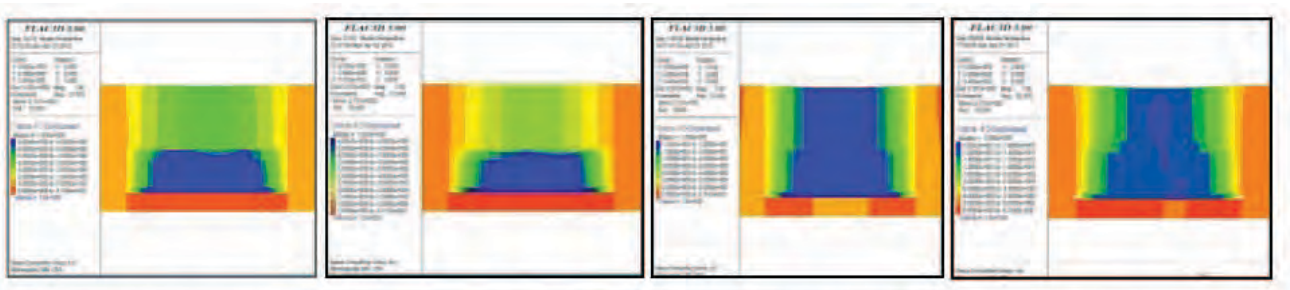
When W/D = 2.5 and mining height is less than 10ft (3m), the overburden strata form a stable structure of "three zones". The subsidence factor is around 0.5.When mining height is larger than 10ft (3m), the overburden strata forma stable structure by itself and collapse in a whole unit or in step subsidence. The subsidence factor is around 1, which means the whole overburden drops down as a unit.

When W/D = 1.7 or 1.2, the overburden collapse is similar to that of when W/D = 2.5. The overburden strata forma stable structure of "three zones" just as the case when mining height is less than 10ft(3m). When mining height is larger than 13ft (4m), the overburden strata form a stable structure by itself and collapse in a whole unit or in step subsidence. The subsidence factor is around 1.

When W/D = 0.87, the overburden strata form a stable support structure itself as well. Surface subsidence is reduced significantly, with the subsidence factorless than 0.15. When mining height is larger than 10ft (3m), failure of overburden continues until it

**Table 1. Rock properties of overburden strata used in the model.**

| Lithology | Tensile strength (Pa) | Density ($Kg/m^3$) | Friction angle ($^0$) | Elastic modulus (Pa) | Poisson ratio | Cohesion (Pa) | Bulk modulus (Pa) | Shear modulus (Pa) |
|---|---|---|---|---|---|---|---|---|
| 27 topsoil | 1.38×[1]06 | 2274.84 | 25 | $1.16\times10^9$ | 0.35 | $1.45\times10^6$ | $1.85\times10^{11}$ | $0.62\times10^{11}$ |
| 26 sandstone shale | $7.76\times10^6$ | 2691.36 | 35 | $4.74\times10^9$ | 0.22 | $5.39\times10^6$ | $4.06\times10^{11}$ | $2.80\times10^{11}$ |
| 25 gray shale | $5.29\times10^6$ | 2691.36 | 34 | $4.62\times10^9$ | 0.27 | $3.85\times10^6$ | $4.82\times10^{11}$ | $2.62\times10^{11}$ |
| 24 limestone shale | $1.44\times10^6$ | 2691.36 | 32 | $11.5\times10^9$ | 0.27 | $3.85\times10^6$ | $12.0\times10^{11}$ | $6.54\times10^{11}$ |
| 23 sandstone shale | $7.76\times10^6$ | 2691.36 | 34 | $4.74\times10^9$ | 0.22 | $5.39\times10^6$ | $4.06\times10^{11}$ | $2.80\times10^{11}$ |
| 22 gray shale | $5.29\times10^6$ | 2691.36 | 34 | $4.62\times10^9$ | 0.27 | $2.76\times10^6$ | $4.82\times10^{11}$ | $2.62\times10^{11}$ |
| 21 sandstone shale | $7.76\times10^6$ | 2691.36 | 34 | $4.74\times10^9$ | 0.22 | $5.39\times10^6$ | $4.06\times10^{11}$ | $2.80\times10^{11}$ |
| 20 sandstone | $6.01\times10^6$ | 2531.16 | 43 | $1.26\times10^9$ | 0.22 | $4.64\times10^6$ | $10.8\times10^{11}$ | $7.42\times10^{11}$ |
| 19 limestone shale | $5.40\times10^6$ | 2675.34 | 34 | $4.62\times10^9$ | 0.27 | $4.38\times10^6$ | $4.82\times10^{11}$ | $2.62\times10^{11}$ |
| 18 WB sandstone group | $6.28\times10^6$ | 2643.3 | 43 | $12.6\times10^9$ | 0.22 | $6.89\times10^6$ | $10.8\times10^{11}$ | $7.42\times10^{11}$ |
| 17 gray shale | $3.34\times10^6$ | 2675.34 | 34 | $4.62\times10^9$ | 0.27 | $4.38\times10^6$ | $4.82\times10^{11}$ | $2.62\times10^{11}$ |
| 15 sandstone | $6.66\times10^6$ | 2563.2 | 44 | $12.6\times10^9$ | 0.22 | $9.16\times10^6$ | $10.8\times10^{11}$ | $7.42\times10^{11}$ |
| 15 gray shale | $6.63\times10^6$ | 2723.4 | 34 | $4.62\times10^9$ | 0.27 | $4.38\times10^6$ | $4.82\times10^{11}$ | $2.62\times10^{11}$ |
| 14 UN sandstone group | $6.28\times10^6$ | 2515.14 | 43 | $12.6\times10^9$ | 0.22 | $9.16\times10^6$ | $10.8\times10^{11}$ | $7.42\times10^{11}$ |
| 13 gray shale | $6.63\times10^6$ | 2723.4 | 33 | $4.69\times10^9$ | 0.27 | $4.38\times10^6$ | $4.89\times10^{11}$ | $2.66\times10^{11}$ |
| 12 limestone | $5.03\times10^6$ | 2739.42 | 45 | $18.0\times10^9$ | 0.3 | $12.5\times10^6$ | $21.6\times10^{11}$ | $9.99\times10^{11}$ |
| 11 gray shale | $6.63\times10^6$ | 2723.4 | 34 | $4.69\times10^9$ | 0.27 | $4.38\times10^6$ | $4.89\times10^{11}$ | $2.66\times10^{11}$ |
| 10 limestone | $5.03\times10^{-6}$ | 2643.3 | 45 | $18.0\times10^9$ | 0.3 | $12.5\times10^6$ | $21.6\times10^{11}$ | $9.99\times10^{11}$ |
| 9 gray shale | $6.07\times10^{-6}$ | 2739.42 | 34 | $4.69\times10^9$ | 0.27 | $3.42\times10^6$ | $4.89\times10^{11}$ | $2.66\times10^{11}$ |
| 8 limestone | $5.03\times10^{-6}$ | 2643.3 | 45 | $12.0\times10^9$ | 0.3 | $12.5\times10^6$ | $14.4\times10^{11}$ | $6.67\times10^{11}$ |
| 7 gray shale | $6.07\times10^{-6}$ | 2739.42 | 34 | $4.62\times10^9$ | 0.27 | $3.42\times10^6$ | $4.82\times10^{11}$ | $2.62\times10^{11}$ |
| 6 sand shale | $7.76\times10^{-6}$ | 2691.36 | 35 | $4.74\times10^9$ | 0.22 | $5.39\times10^6$ | $4.06\times10^{11}$ | $2.80\times10^{11}$ |
| 5 gray shale | $6.29\times10^{-6}$ | 2739.42 | 34 | $4.62\times10^9$ | 0.27 | $3.42\times10^6$ | $4.82\times10^{11}$ | $2.62\times10^{11}$ |
| 4 limestone | $5.03\times10^{-6}$ | 2723.4 | 45 | $12.0\times10^9$ | 0.3 | $12.5\times10^6$ | $14.4\times10^{11}$ | $6.67\times10^{11}$ |
| 3 gray shale | $6.63\times10^{-6}$ | 2739.42 | 30 | $4.62\times10^9$ | 0.27 | $3.42\times10^6$ | $4.82\times10^{11}$ | $2.62\times10^{11}$ |
| 2 coal | $0.69\times10^{-6}$ | 1409.76 | 28 | $2.48\times10^9$ | 0.34 | $0.71\times10^6$ | $3.72\times10^{11}$ | $1.33\times10^{11}$ |
| 1 gray shale | $6.07\times10^{-6}$ | 2739.42 | 39 | $4.62\times10^9$ | 0.27 | $3.42\times10^6$ | $4.82\times10^{11}$ | $2.62\times10^{11}$ |



(a) mining height 7ft(2m) (b) mining height 10ft(3m) (c) mining height 13ft(4m) (d) mining height 16ft (5m)

**Figure 3. Overburden strata movement under different mining height when W/D = 2.5.**

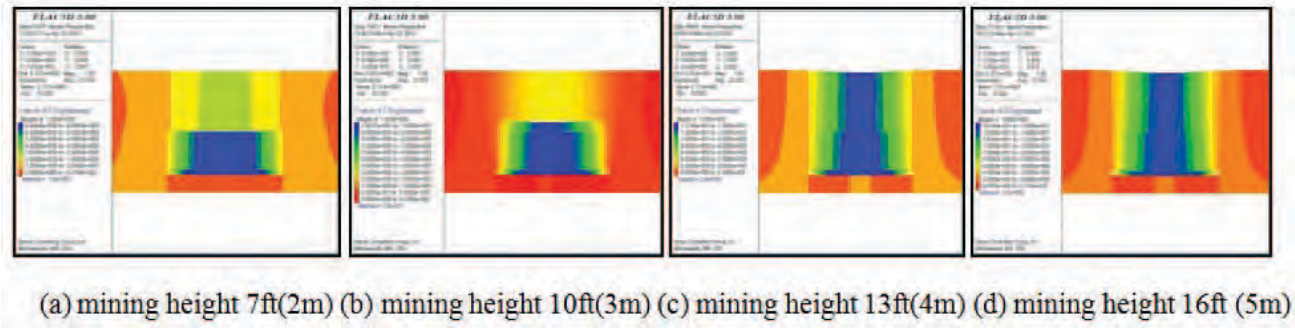



**Figure 4. Overburden strata movement under different mining height when W/D = 1.7.**

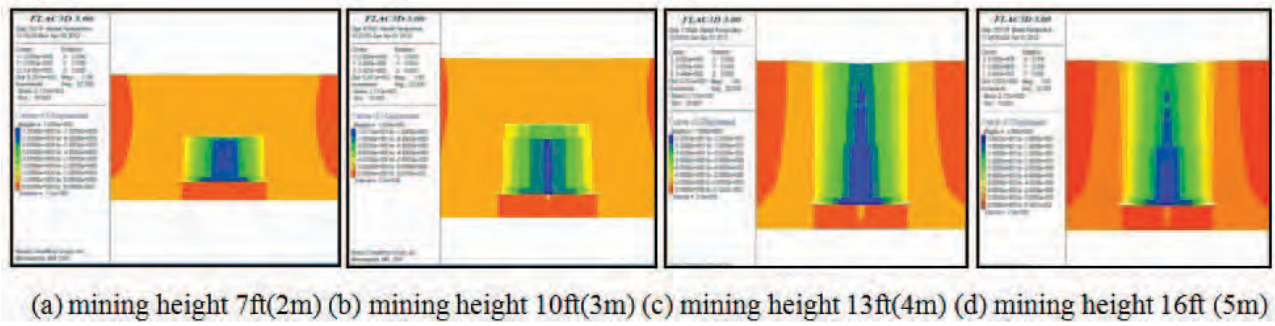



**Figure 5. Overburden strata movement under different mining height when W/D = 1.2.**

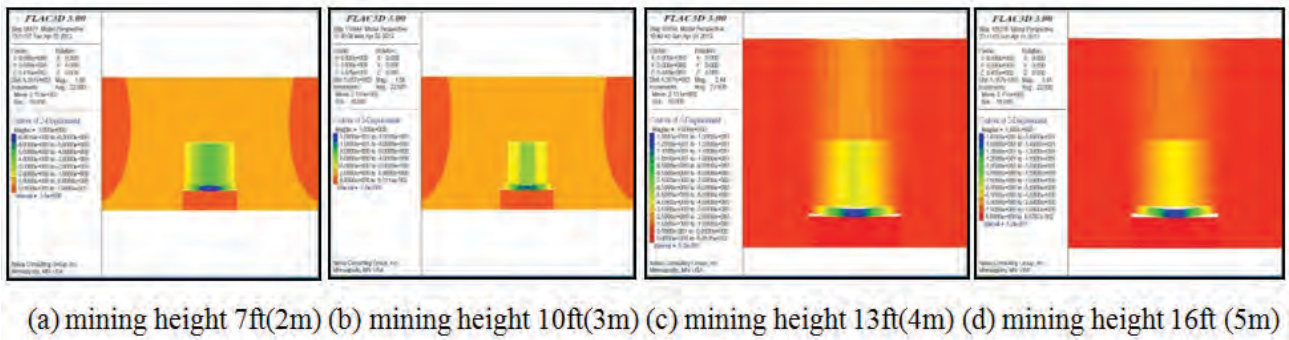



**Figure 6. Overburden strata movement under different mining height when W/D = 0.87.**

reaches the surface in "two zones", i.e., the fractured and caving zones. When mining height is less than 10ft (3m), the overburden strata form a stable structure of "three zones".

(2) Stress Change in Overburden Strata underDifferent W/D

The area of vertical stress concentration is mainly located in the roof around the coal pillar and above the key stratum. Figure 9, Figure 10, Figure 11, and Figure 12 show the vertical stress distribution with different W/D and mining height. The maximal stress is generally located along the faceline, while the stress onthe floor is transferred to the interior of the coal pillar. Dark red in the stress diagram indicates vertical stress, and the magnitude in the stress concentration zone indicates the capacity of the overburden to carry the load.

As is shown in these figures, one of the overburden strata is the area of stress concentration indicating that when W/D is larger than 1 and the mining height is less than 10ft (3m), it can carry the load and form a stable structure. When mining height is higher than 10ft (3m), the area of stress concentration decreases or even disappears as the mining height increases further.

When W/D is less than 1, the area of stress concentration would appear in the overburden strata. When mining height is larger than 10ft (3m), the numbers of stress concentration zone is more than 1. In other words, the higher the mining height is, the larger the area of fracture is. But the strata would not collapse because there are certain hard rock strata that support the overburden all the way up to the surface.

(3) Calculation Steps

Figure 13 shows once the model reaches equilibrium how the calculation steps vary with W/D under different depths of overburden. It can be seen that with the exception of mining height = 7ft (2m), when W/D is less than 1, the required calculation step is the minimum before the model reaches the equilibrium condition. As W/D increases, the required calculation steps decreases, indicating that when panel width increases, or mining depth decreases, to some extent, the roof will subside quickly to achieve a stable structure, and the damage would be more severe after mining.

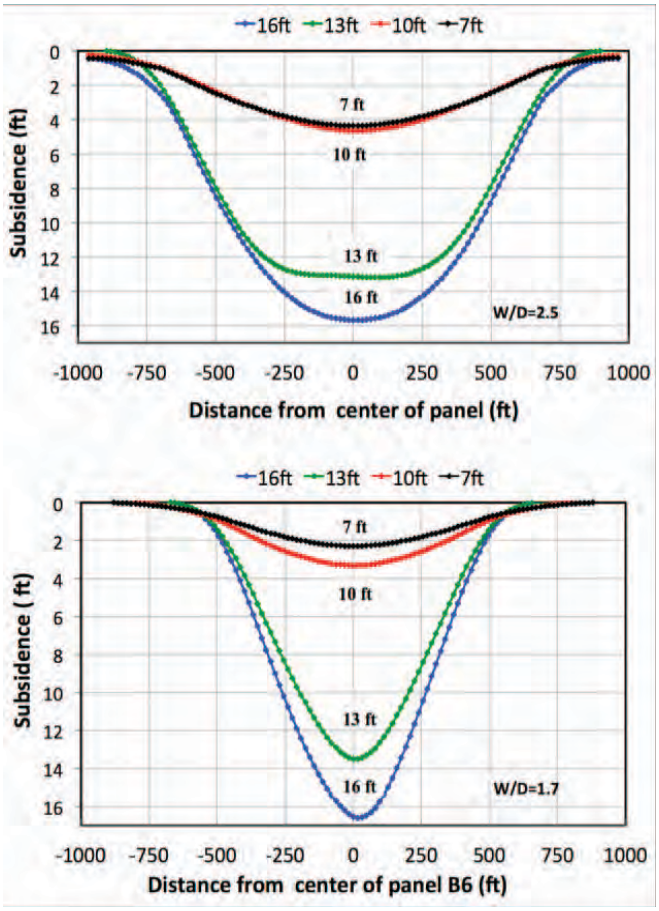



**Figure 7. Surface subsidence under different mining height when W/D = 2.5 and 1.7.**

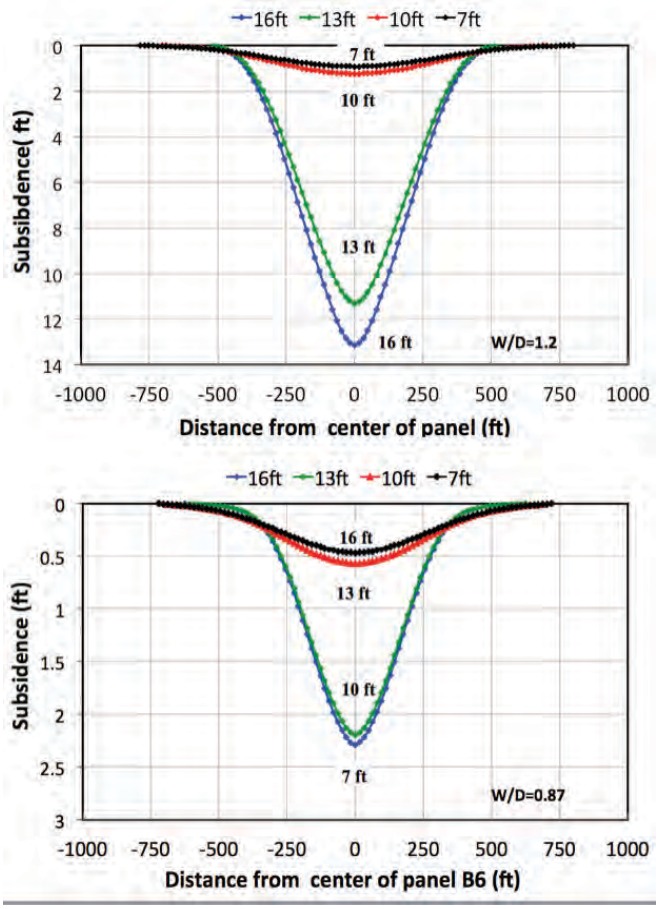



**Figure 8. Surface subsidence under different mining height when W/D = 1.2 and 0.87.**

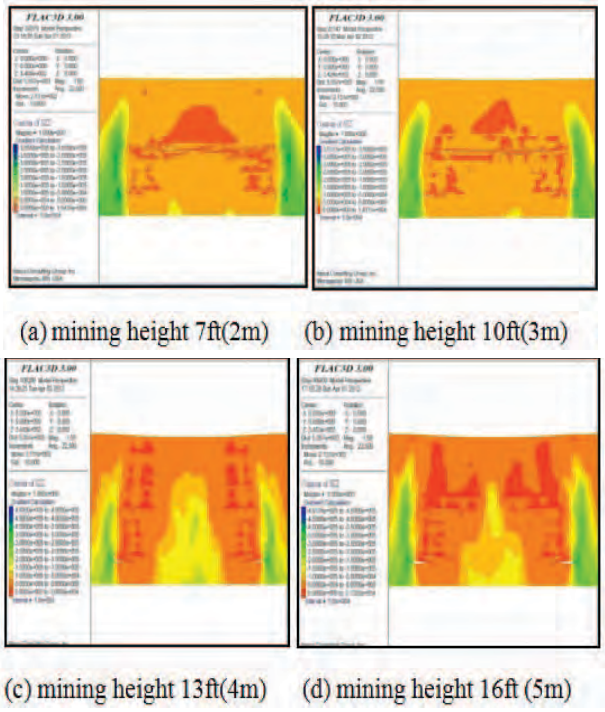



**Figure 9. Vertical stress distribution under different mining height when W/D = 2.5.**

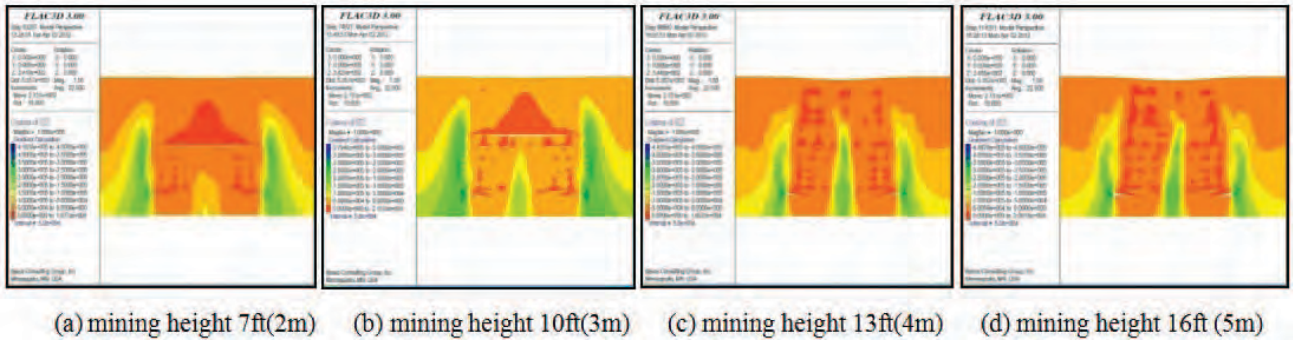



**Figure 10. Vertical stress distribution under different mining height when W/D = 1.7.**

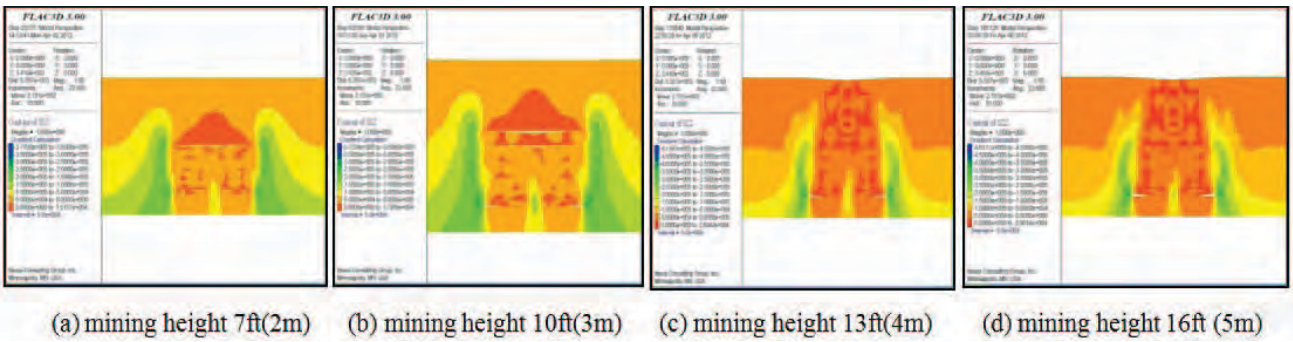



**Figure 11. Vertical stress distribution under different mining height when W/D = 1.2.**

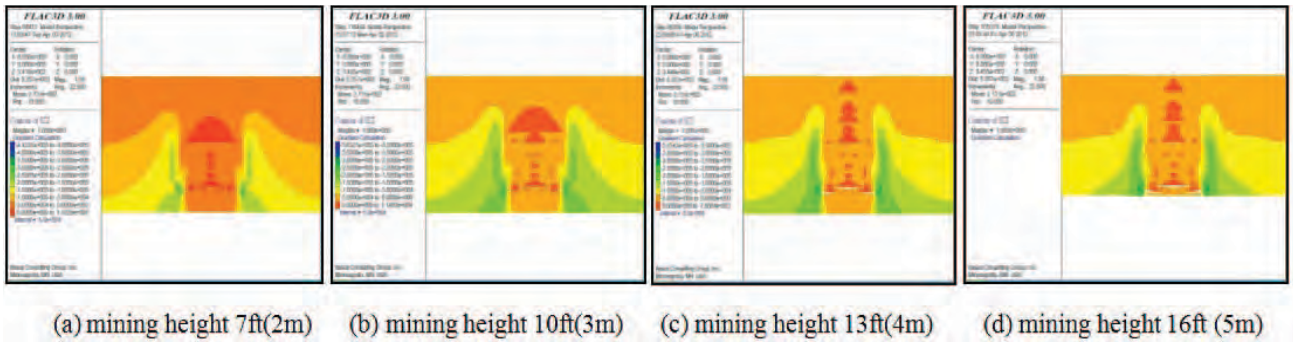



**Figure 12. Vertical stress distribution under different mining height when W/D = 0.87.**

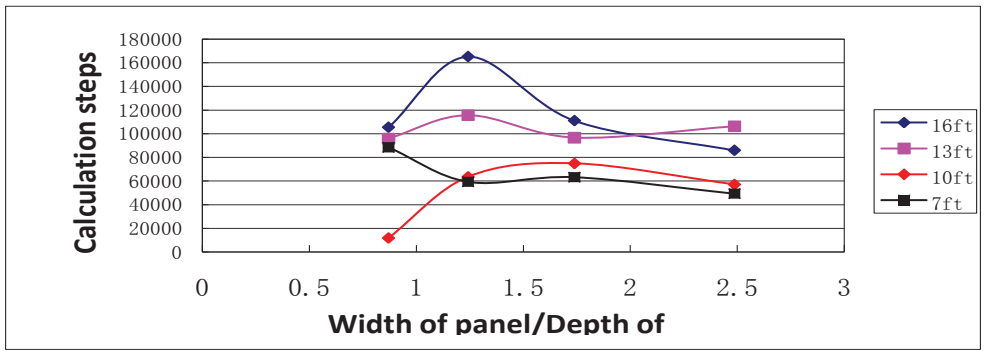



**Figure 13. Calculation steps vs W/D.**

## CONCLUSIONS

(1) When W/D > 1 and the mining height is less than 10ft (3m), the overburden strata forma stablestructure of "three zones". When the mining height is larger than 10ft (3m), the overburden strata do not form a stable structure themselves. As a result the overburden strata would collapse in a whole unit or in step subsidence. The subsidence factor is around 1.

(2) When W/D < 1, the overburden strata form a stable structure themselves, and surface subsidence is reduced significantly. The subsidence factor is less than 0.15.

(3) The areas of stress concentration: the area of stress concentration in the hard stratum that supports the overlying strata is larger and appears in a" horse saddle" pattern. The stress concentration zone is mainly foundin the "three zones" structure, especially above the key stratum.

## ACKNOWLEDGEMENT

Supported by the Fundamental Research Funds for the Central Universities (2013QZ03). National Natural Science Foundation of China (NO.U1361209).

## REFERENCES

Peng S.S. (2006). Longwall Mining. 2nd ed. Morgantown, WV: Peng S.S. publisher, pp. 46-55.

Peng, S. S. (2008). Coal Mine Ground Control. 3rd ed. Morgantown, WV: Peng S.S. publisher, pp. 319-330.

Li Y. (2011). "Overburden movement in solid waste rock cemented backfill mining methods." MeitanXuebao/Journal of the China Coal Society. 36( S1): 370–374.

Li Y, Qiu B. (2012). "Investigation into key strata movement impact to overburden movement in cemented backfill mining method Source." Proceedings of International Conference on Advances in Computational Modeling and Simulation. V. 31. Amsterdam, Netherlands: Elsevier Ltd, pp. 727-733.

Wang J.C. (2009). The Theory and Technique on the Thick Coal Seam Mining. Beijing, China: Metallurgical Industry Press, pp. 147-155.

# Underground Mining Technology in Chinese Coal Mines

**Jiachen Wang**, Professor, Head Department
**Lei Wang**
**Yang Li**
**Baogui Yang**, Associate Professor
China University of Mining and Technology (Beijing)
Beijing, China

## ABSTRACT

China is the largest coal producing country in the world. Coal is widely distributed in China and thus the mining conditions are complex and diverse. This paper summarizes the important achievements in the last 20 years in various mining methods including the extra thick seam with large mining height top coal caving, the thick seam with large mining height and top coal caving mining, the steep seam with top coal caving and fully-mechanized mining, the thin seam automated mining, and the backfill mining. At the same time, the rapid advance in the development of mining machinery and manufacturing has also contributed to the advancement of coal mining technology and the great improvement of coal mine safety. The future direction of China's coal mining is to further improve mine safety as to improve the coal recovery rate, promote the pillarless mining technology, develop high-efficiency backfilling technology, develop steep seam high-efficiency mining technology for seams less than 10m thick, and high recovery mining techniques for extra thick seams, improve the reliability of mining equipment, and strengthen the protection and restoration of surface environments and water resources.

## CHARACTERISTICS OF CHINESE COAL RESOURCES

### Characteristics of China's energy resources

According to the report of "Statistical Review of World Energy" (BP), China became the world's largest energy consumer in 2010. The primary energy consumption was 2,432.2Mtoe, accounting for 20.30% of the world's energy consumption. However, the per capita consumption was about 28.8% of the U.S.

China is not an energy-rich country. It is short of oil and gas resources, but coal energy is relatively abundant. Therefore, in terms of types of energy consumption in China, coal resources are the main energy, accounting for about 70% of the total energy consumption. This type of energy consumption is difficult to change in the short term.

Chinese coal production ranked No. 1 in the world in 2012, with 3.65 billion metric tons (mt) and accounted for 47.5% of the global coal production. Coal production in China was 3.7 billion mt in 2013, a slight increase comparing to 2012; Mine safety has improved that the fatality rate was 0.288 person per million mt of coal, a greatly decrease from 0.374 of 2012. However, the number of fatalities is still very large, so much more work remains to be done in the future.

### Basic Characteristics of Chinese coal resources

Coal is widely distributed in China. All provinces, autonomous regions and municipalities have coal resources for mining except Hong Kong and Shang Hai. In terms of coal seam thickness, dip, methane gas, geological conditions, and hydrogeological conditions, China's coal resources can be divided into three types: less difficult mining, difficult mining, and extremely difficult mining. In general, coal reserves in the western and northern regions are less difficult mining; reserves in the southwest and northeast regions are extremely difficult mining; and those in the central region are difficult mining. However, different coal reserves face different challenges. For example, extra thick seam and steeply dipping seam mining problems in the western region. High gas outburst seam and inclined thin seam mining problems in the southwest and northeast regions. Deep mining and gassy coal seam mining problems in the central region. In 2012 the eastern region of China including, Beijing, Hebei, Liaoning, Jilin, Heilongjiang, Jiangsu, Fujian, and Shandong provinces produced 473 million mt of coals, about 13% of the national production. The central region including Shanxi, Anhui, Jiangxi, Henan, Hubei, and Hunan provinces produced 1.22 billion mt of coals, about 33.4% of the national production. The western region including Inner Mongolia, Guangxi, Chongqing, Sichuan, Guizhou, Yunnan, Shaanxi, Gansu, Qinghai, Ningxia and Xinjiang provinces produced 1.957 billion mt of coals, about 53.6% of the national production. So Western China is the main producing area, and it is also the focus of the future coal mining development area.

In consideration of the prevailing conditions of coal reserves, China's coals are mainly mined by underground methods. Underground coal mining produced about 90% of total production. Even if in the future open-pit coal mining has fully developed, the percentage of underground coal mining production will not be less than 85% of the total. Underground coal mining is basically all longwall mining. Due to the large amount of coal production in China from various complex mining conditions, mining methods

vary considerably. Consequently there are different mining methods with different special features for different coal reserves.

## UNDERGROUND COAL MINING METHODS IN CHINA

### The extremely thick seam coal mining methods: coal seam height ≥ 39.4 ft (12 m)

In China thick seams refer to those seams more than 3.5m (11.5 ft) thick.. In recent years with mining developed into very thick seams, such as 10m, 20m, 30m (32.8ft, 65.6ft, 98.4ft), and even thicker large-scale mining, people always try to use the most simple, more efficient ways to mine these extra thick seams. Mining technology used for seam height less than 12m (39.3ft) is relatively matured. Mining technology for gently-inclined extra thick seams, more than 12m thick, has made considerable advancement. Tashan mine of Datong Coal Group is the typical representative one. They have developed the extra large mining height top coal caving technology, capable of mining up to 20m(65.6ft) thick in one pass. So far they have completed fives panels. Panel width is 210m (689ft). The shearer's cutting height is 4 ~ 5m (13ft-16ft). Average monthly production is more than 900,000 mt and annual production reaches 10.849 million mt. Col recovery is 88.9%.

The extra thick seam in Tashan mine of Datong Coal Group is the carboniferous Taiyuan group #3 ~ #5 coal seams. They are 300 ~ 500m (984ft-1640ft) deep. Seam thickness varies considerably with an average of 19.4m (63.6ft). The seam dip is 0~4°. They are multiple seams with igneous intrusions. Both the coal seams and roof are damaged to various degrees. So it is difficult to mine. The immediate roof is carbonaceous mudstone 2m thick, and the main roof is coarse-grained sandstone 20m (65.6ft) thick.

In China, Tashan coal mine is the first one to use the single pass mining method to extract the near horizontal extra thick seam more than 19m(62.3ft) thick. There is no precedent in the world. In order to mine this type of coals, they developed a dedicated shield support for top coal caving mining. The shield's operating height was increased; the canopy's capability to resist impact load was strengthened; the coal-drawing window was enlarged; and coal-caving efficiency was enhanced. They also developed the heavy-duty rear armored face chain conveyor suitable for the uneven and impact encountered in top coal caving with extra thick seams. The three face equipment are shown in Figure 1 and their major specifications are shown in Table 1.

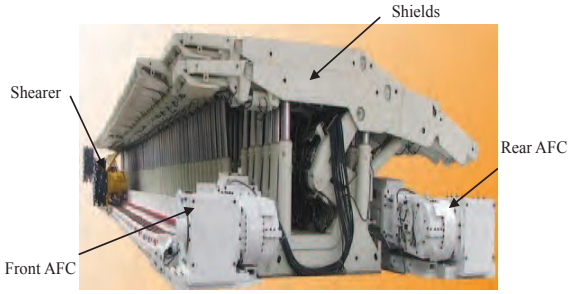



**Figure 1. Model ZF15000/28/52 shield and the equipment for large-cutting-height longwall mining.**

**Table 1. Major types of the panel equipments.**

| | Equipment | Model | Power | capacity |
|---|---|---|---|---|
| 1 | Shield supports | ZF15000/28/52 | | 15000KN |
| 2 | Shearer | MG750/1915-GWD | 1915 | 2000t/h |
| 3 | Front AFC | SGZ1000/1710 | 2×855 | 2500t/h |
| 4 | Rear AFC | SGZ1200/2000 | 2×1000 | 3000t/h |

In order to develop a large-cutting-height top-coal mining technique, the "cantilever beam-hinged rock beam" structural mechanics model for the overlying strata was developed based on the theoretical analysis, numerical simulation, similar material simulation and field micro-seismic monitoring technique. The model has been used to explain the movement characteristics of the overlying strata and guidelines for shield selection. It also points out that the immediate roof caves irregularly. In addition, the model describes that the lower main roof behaves like a cantilever beam and breaks periodically, and that the upper main roof forms a hinged rock beam structure. The periodic caving in the lower main roof and the height and caving position of the upper main roof are determined through micro-seismic and roof movement monitoring. The periodic caving interval of the lower main roof is about 1/2 of that for the upper main roof. The periodic weighting in the lower main roof produces the small periodic weightings. Whereas, when the hinged beam structure of the upper main roof collapses, it creates a large periodic weighting. This is the basic features of roof weighting occurred in large mining height top coal caving .

The relationships between the stability of coal face and factors such as roof pressure, coal face strength, support capacity, cutting height, and horizontal capacity of shield support are established based on the slip line field and the limit equilibrium theory. From those relationships, the vertical and horizontal capacities of shield required the stability of the coal face capacity are defined; the binary rules of support resistance is determined based on roof pressure and maintenance of coal face stability are proposed; and the design of shield capacity and the 2nd stage cover plate of the face sprag were implemented, thereby solving the difficult problems of roof and face stability in extra thick large mining height top coal caving mining.

During the top coal caving mining operation of extremely thick coal seam, the waste rocks between two adjacent shields tend to move preferentially into the caved coal drawing window and resulting in highly diluted coal product. For this reason, a three-dimensional top coal caving theory was developed. It describes the three-dimensional caving morphology, three-dimensional interface between the top-coal and the waste rock, and the actual height of drawn material. It has been used to guides the extra thick top coal caving mining technique and determine the values of various required parameters. The recovery rate of top-coal has

reached 86.67% by using the following techniques: one web cutting followed by one drawing of caved coal, alternate multiple window drawing of caved coal, installation of enhanced shaking mechanism on the shield, top coal collection device, and weakening of top coal in the initial mining period.

**The thick seam coal mining methods: coal seam height 3.5 m~12 m**

There are two major mining methods for thick coal seam in the range of 3.5~12m (11.5ft-39ft). The 3.5m-5m (11.5ft-39ft) thick seams employs single pass full seam fully-mechanized longwall mining method. It is commonly called the large mining height mining. For the 5m-7m thick seams, both the single pass full seam and thick seam top coal caving mining methods have been used depending on coal hardness and fracture conditions. For those more than 7m thick the top coal caving mining method is exclusively used.

(1) Large-cutting-height mining method

Large-cutting-height mining method refers to cutting height larger than 3.5m (11.5ft). During the past 20 years, large-cutting-height mining method has been developed rapidly in China. Especially the advancement in equipment manufacturing for shield and the shearer promotes the development of large-cutting-height mining method technology. At present, the annual production capacity reaches 15Mt per panel with large-cutting-height mining.

From the global perspective, research and application of the large-cutting-height mining method began in the late 1970's. Many countries including Germany, Poland, the United States, France, South Africa, and Australia had performed research and its application about the large-cutting-height mining technology. China's large-cutting-height mining began in 1978 by importing from Germany the G320-20/37 and G320-23/45 shields and its ccmpatible mining and transportation equipment. They were used to mine the 3.3~4.3m (10.8ft-14.1ft) thick coal seams successfully with an average monthly production of 70,819 mt. In 1980, Chinese-made model BYA329-23/45 two-leg shields and compatible equipment were employed successfully in the 4.3~4.8m (14.1ft-15.7ft) thick coal seam at Dongpang mine, Xingtai. In the past 10 years, China's large mining height technology has developed rapidly. The single pass mining height advances from 3.5m to 7m (11.5ft-23ft), Chinese-made face equipment including shield, the shearer, AFC (armored face chain conveyor) has gradually matured, reaching near the levels of the foreign manufacturers' standards in capacity and reliability. Among them, China made the largest capacity shields in the world for large cutting height mining. Shield capacity is common in the range of 1,000-2,000 mt (10,000-20,000KN), shield width is 1.75~2.05m, and maximum shield height is 7.2m.

In the beginning, the shearers for the large-cutting-height mining rely mainly on imports, including Germany Eickhoff's shearers of model SL500,and SL1000 series and U.S. JOY's shearers of model 7LS6 and 7LS7 series. But in recent years, Chinese made shearers gradually replaces the imported ones, for example, Xi'an Coal Factory developed the shearers of models MG750/1910-WD and MG900/2210-GWD series. In particular, the performance of model MG900/2210-GWD shearer is similar to JOY's 7LS6 shearer; the maximum cutting height is 6.5m (21.3ft), cutting power is 2×900KW, installed power is 2210KW, drum cutting depth (web) is 800mm(31.5in), maximum haulage speed is 31.5m/min (103ft/min), the whole machine weight is 151 mt, and the production capacity is 4500t / h. Other Chinese made shearers have roughly the same performance standard. Total power of the shearer is from 2,000KW to 2,500KW.

Similar advancement has made with shearer remote control and monitoring systems. For example, the model MG900/2210-GWD shearer is equipped with central control at the headgate T-junction. The operational data of the shearer are instantaneously transmitted via Ethernet to the surface control room. At surface control room, attendants can set the shearer operating parameters, shearer memory cutting function and remote correction of memory cutting, and shearer's virtual 3D monitoring function.

The panel width for the large-cutting-height mining method is generally 250~300m (820ft-984ft), depending on the coal seam conditions. The face height is from 3.5m to 7m (11.5ft-23ft). Panel production capacity is up to 15 million mt/year.

(2) Top-coal caving mining method

The top-coal caving mining method began with Europe in the 1950s. At that time, it was mainly used for the residual coal blocks and recovery of coal pillars. The Chinese top-coal caving mining was borrowed from the European countries such as France, Hungary, and Poland. In 1984, the first top-coal caving panel was employed on trial basis with Chinese made shields in Puhe coal mine of Shenyang Coal Bureau, China. The technique evolved slowing and gained popularity gradually in China. Nowadays, the top-coal caving longwall mining is the major mining method for for seams larger than 7m thick. The top-coal caving longwall mining has attained outstanding results in various types of coal seams, including near-horizontal thick seams, gently-inclined thick seams, steeply-inclined thick seams, and extremely thick seams. Top-coal caving mining is a better choice for coal seams with the following characteristics: less gassy or gas that can be effectively controlled, low seam hardness or fractures well-developed, seams from 6 to 12m (19.7 to 39.6 ft) thick, and seam dipped less than 30°. As for coal seams that dip more than 60° and more than 10m (32 ft) thick, the sublevel top-coal caving mining method is a better method.

In China, the top-coal caving mining method is employed in all suitable coal seams all over the country. The 4-leg shield support was used in the early stage. In recent years, the two-leg shield is gradually adopted, but in coal seams with hard roof, the 4-leg shields are still the main type of support for top coal caving mining.

The Yanzhou coal mining area is the first one to use the two-leg shield for top-coal caving mining. It then expanded to Baode mine and Liuta mine of Shenhua Coal Group, Anjialing #1 mine in Pingshuo coal company, Xiandewang mine in Jizhong Energy Group in Hebei province, and finally Austar coal mine in Australia. The advantages for the 2-leg shields are simple in structure, easily adaptable to shields automation, and fully utilized the shield's capability.

Excellent results with the top-coal caving mining method have been achieved in Pingshuo, Luan, Yanzhou, Datong and Huaibei coal areas, China. The annual production ranges from 3 to 10

million mt with a single top-coal caving panel, depending on the seam thickness, seam inclination, gas content, and coal hardness. In the past 30 years, the top-coal caving mining method has accomplished the following major achievements in China:

- The overburden movement for the top-coal caving mining method has been generalized as follows: the fractured top-coal will absorb some dynamic loading from the main roof thereby reducing the effect of its impact; the pressures in the front legs of the 4-leg shield supports are larger than the rear legs. The peak front abutment pressure is smaller but distributes in larger area.
- The theory and technique of the top-coal caving and drawing has been proposed. In terms of the fracture property of the top coal, the concept that the fracture distribution and development of the top coal are much more important than the strength of broken coal was proposed. The model of predicting the size of broken top-coal has been established. In full consideration of the shields advance, top-coal caving, and the influence of extending the rear canopy, Wang (2009) developed and refined the loose medium flow field theory for the top-coal caving. It points out the difference and connection with the ellipsoid drawing theory found in hard rock mining. Considering all other types of geological conditions, a new set of top coal caving mining technique and parameters have been established (Wang, 2009).
- A series of shield supports for the top-coal caving mining has been developed for different coal seams, including the top-coal caving shields for soft coal seams, shields for large dip angle coal seams, shields for the hard coal seams, shields for the extremely thick coal seams and shields for the high production high efficiency coal seams.

**The large dip angle coal mining method (The dip angle of the coal seam 30°-50°)**

The large dip angle coal seam refers to dip angle from 30°~50°. For this type of coal seam, it is difficult to mine. The main problems are support toppling, sliding downdip of shields and AFC, uneven roof caving, difficult to implement normal production cycle, and low production. In order to solve those problems, there are five methods: (1) proper face layout and reduce the dip angle; (2) develop dedicated anti-sliding and anti-toppling devices; (3) Shield and AFC are anchored together to maintain stability; (4) determination of proper mining technology and parameters; and (5) Guarantee the stability of equipment at the headgate T-junction. One typical examples of large dip angle mining are described as follows.

The designed annual production capacity for Wang Jia Shan coal mine of Jing Yuan company, Gansu province is 1.8 million mt. Panel 44407 employs the large dip angle top coal caving mining method. The panel width is 95m along the dip direction and 605m long along the strike direction. Its mining depth is about 300m. The seam and thus the panel faceline dip 43.5°. Coal seam is 15.5m (51ft) thick. The hardness coefficient of the coal is 1.

The panel face advances along the seam strike direction employing the full seam cutting height in one pass. In order to reduce the dip angle of the faceline and maintain stability of shields and other floor toward the head end, the headgate is located near the seam roof, while the tailgate is developed along the seam floor.

The model MG200/500-QWD double-ended ranging drum shearer was employed. The drum cutting height is 2.6m (8.5ft) and the top coal caving height is 12.9m (42.3ft). The model ZFQ3600/16/2 shields with lower position top coal support are used. Shields are 1.5m (4.9ft) wide center-to-center. The monthly production is 706,81 mt with an average recovery rate of 82.27%.

**The thin seam coal mining methods: coal seam height ≤1.3 m, 4.3ft**

The thin seams are defined as those less than 1.3m(4.3ft) thick. It accounts for 20% of the coal reserves in China. But its production is only 6 to 7% of the total production. Generally, 85% of the coal mines in China have to deal with problems related to thin coal seams. These problems are mainly caused by the low mining height and poor working environment. As a result, the size and power of the mining equipment is restricted. Remote control is, therefore, the main solution to the problems. In recent years, Jizhong Energy Fengfeng Group developed the equipment and technology, thus making a significant breakthrough in thin coal seam mining (0.6m–1.3m) (2ft–4.3ft). The technology has been widely used in China (Figure 2).



**Figure 2. Control center at the headgate in thin coal seam mining.**

A set of shearer-operated automated thin seam longwall mining system has been developed. It includes a large-capacity, thin body height shearer, a large carrying capacity thin pan AFC, shields with large extension ratio, and manless full automation at the face. An intelligent video monitoring system, a safety pre-warning system, and an intelligent surface control center were developed, making it possible that all operations are controlled remotely far from the headgate without miners staying at the face. With this mining system Xuecun coal mine of Fengfeng Coal Group produced 118,000 mt per month with a peak annual production of 1 million mt.

## THE BACKFILLING GROUND CONTROL MINING METHODS

In China the sterilized coals under the water body, railway or buildings in some old mining areas are becoming a serious issue in recent years because of the large demand for coal. Therefore, technically-advanced, environment-friendly and economically-rational mining techniques are badly needed in order to make sure that the Chinese coal industry will keep pace with sustainable

development. Since the backfill mining can positively control surface subsidence, it is an effective solution to this problem.

Over the past few years, the conventional backfilling mining methods using solid wastes as the backfill materil were popular in China. Nowadays, however, the modern backfilling methods such as rock waste-backfilling, high-water material backfilling, paste material backfilling, paste-like material backfilling and high concentration cemented material backfilling are widely used in China.

**Rock waste-backfilling mining method**

Waste rocks from coal mining are the main filling material in this mining method. First of all, the waste rocks are first processed on the surface and then dropped down underground. Thereafter, the specially-designed conveyor belt, AFC and stowing shield support are used to deliver the material to the face and into the gob. This method is simple in process and high in mechanization. However, the backfilled material cannot effectively form a dense material to fill up the gob space resulting in poor control of overburden movement and surface subsidence. Figure 3 is the rock waste stowing shield support (Liu, et al., 2011).

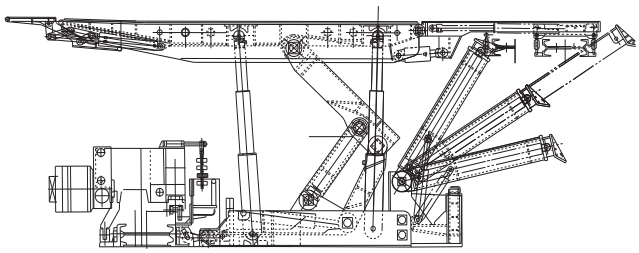


**Figure 3. Waste rock backfilling shield support.**

**High-water material backfilling mining method**

The high-water rapid-curing material is used in this backfilling mining method. Generally, the material consists of two components, material A and material B. Material A is composed of monohydrallite, gypsum and composite slow-curing dispersant and Material B is made up of gypsum, lime and composite accelerator. A and B are mixed in the ratio of 1 to 1 and water is added as required. The compressive strength of the mixed material can be adjusted according to the weight of A, B and water. The curing time is also adjustable from 8 to 90 minutes. After 28 days, the compressive strength is expected to reach 0.66 ~1.50MPa (95.7psi-217.6psi).

**Paste material backfilling mining method**

The mass concentration of this material is 81%~88%. The maximum shrinkage is around 100mm~150mm (3.9in-5.9in). Generally, the backfilling material move as a whole with the whole cross-section moves at the same speed, just like a moving piston. Besides, this material does not settle, separate, or exude when flowing. What's more, the compression ratio always keeps at 1%. Therefore it can effectively prevent surface subsidence causing damage to buildings. However, this backfilling material is not cost-effective. It is difficult to deliver because of the resistance.

**Paste-like material backfilling mining method**

Literally, the paste-like material is similar to the paste material. The aggregate is made of the industrial solid wastes from mines and power plants, or sands from the river. The aggregate is mixed with other small-sized ingredients and binding material. The concentration of the mixture should be kept at 72% ~78%. Once finished, this backfilling material appears like a paste.

The strength of the paste and paste-like material shows no difference. As for fluidity, the paste-like material is far superior. At present, the paste-like material needs to be dehydrated underground. The produced wastewater ponds are at the face, which has a negative influence on production.

**High concentration cemented material backfilling mining method**

The backfilling materials consist of coal waste rocks, coal ash, cement, additives and water. After mixing to become a high-density mixture it is pumped through pipelines to underground and then move to fill the gob. This material contains lots of fine materials. As one kind of dispersant, the specific surface area of the thixotropic material increases. When stirred, the fluidity is also enhanced, causing the cemented particles evenly distributed.

The mass concentration of this backfilling material ranges from 74%~82%. The shrinkage is around 200 mm (200mm~240mm to be exact) (7.9in-9.4in). This backfilling method can effectively ensure a uniform distribution of particles and cement and makes it easy to be pumped down. Apart from that, this material is highly valued for its strength, integrity and stability. It does not need to be dehydrated.

## THE FUTURE DEVELOPMENT IN COAL MINING METHODS IN CHINA

Chinese coal mining technology has developed rapidly in the past 20 years, and has made important progress. But with the changes in mining conditions, there are many issues that need to be further researched and practiced. These main issues are steep seam mining technique, high recovery mining techniques, pillarless mining technique, efficient backfilling mining technique, thick seam mining technique, and efficient high inclined seam mining technique.

(1) Develop high efficient mining technique for inclined seams. Recently with the development of coal resources in western China, there are many coal seams more than 10m thick and seam inclination more than 45°. This type of coal reserve is a technical problem for high efficient mining technique because an appropriate mining method has not been developed. If the seam inclination is small, the fully mechanized longwall mining method is used But as the seam inclination becomes larger, the difficulty of applying the fully mechanized longwall mining method get more severe, and coal production is poor. It is also difficult to find coal seams sufficiently thick to employ the horizontal sublevel caving mining method. Therefore, the development of such efficient mining methods is a priority.

(2) High recovery rate mining technique. High recovery rate mining technique is the eternal theme. Areas for improving the

recovery rate include face layout, section pillar design, enhance management of mining during initial and end of panel mining, and determine the proper mining technique and parameters. Currently the main reasons for loss of coal are section coal pillars and the residual thickness of coal left in thick seam mining.

The width of section coal pillars has been gradually reduced. For example, Shendong mine has reduced it to 10m wide from the 20m (65.6ft) used previously. The problems associated with reducing pillar width are increase in roadway pressure and in difficulty in roadway maintenance. In order to increase coal recovery, the pillarless mining technique has gained acceptance for use in recent years. The technique requires no coal pillar between adjacent panels, rather a roadside packwall is used. The roadside packwall is filled with materials such as gravel, sand, fly ash, and cement based self-compacting concrete. The mixed material is pumped into the forms installed in the gateroad. After 2-4 hours, it cures to form a solid wall that is used to isolate the gob and protect roadway. The width of the backfilled solid wall depends on the site specific conditions. It is normally 2~3m (6.6ft-9.8ft) wide. Its uniaxial compressive strength is larger than 25MPa (3626psi). After the gobside solid wall has been installed, the "Y" style face ventilation pattern of the working face is used instead of the conventional "U" or "U+L" style. The methane gas drainage of the worked out sections can be easily done behind the face. Recently the pillarless coal mining method described above has been widely used for coal seams less than 4m thick. More research is needed to determine its suitability for thicker seams and the top caving mining.

The situation that not all the coals can be mined when mining the thick seam coal is called thickness loss, such as 8m (26.2ft) coal seams with large-cutting-height mining method, only 7m (23ft) thickness of coal can be taken out, which means that 1m thickness of coal seam would be loss. When using top coal caving, if the coal cutting height is 3m (9.8ft), coal height is 5m (16.4ft), the top-coal recovery is 75%, and the actual production of coal thickness is 6.75m (22ft) with a loss of 1.25m (4.1ft) thickness coal. In order to reduce the loss of seam thickness, the selection of mining technology, determination of mining parameters, equipment selection, and production organization etc. must be focus on.

(3) Low-cost high-efficiency backfilling mining. Backfilling mining technology is a matured technique. It has been used in many coal mines in China. Recently the main problems of this technology are low production and high costs, especially during recent period of depressed coal market, it will not be accepted for large-scale application soon. The backfilling mining technique must improve its ability to increase production in the future to reach 1 million mt per year, and reduce the cost. At the same time, develop new low cost backfilled materials to replace coal mine waste rocks and fly ash. In order to for the backfilling mining technique to continue to develop in the future, it must provide a cheap but abundant backfill material.

## CONCLUSION

China is the largest coal producing country in the world. Coal is widely distributed in China. However, the mining conditions are complex and diverse. In the last 20 years with the rapid development of Chinese economy, the demand for coal energy is so huge that it promotes the rapid development of coal mining technology, resulting in many highly productive mines. There are many significant developments in the extra thick seam with large mining height top coal caving, the thick seam with large mining height and top coal caving mining, the steep seam with top coal caving and fully-mechanized mining, the thin seam automated mining, and the backfill mining. All the developments are derived from a high demand for coal. At the same time, the rapid advance in the development of mining machinery and manufacturing has also contributed to the advancement of coal mining technology and the great improvement of coal mine safety. Coal mine safety has greatly improved from 2005 to 2013, but there are still ample room to improve. The future direction of China's coal mining is to further improve mine safety as to improve the coal recovery rate, promote the pillarless mining technology, develop high-efficiency backfilling technology, develop steep seam high-efficiency mining technology for seams less than 10m thick, and high recovery mining techniques for extra thick seams, improve the reliability of mining equipment, and strengthen the protection and restoration of surface environments and water resources.

## ACKNOWLEDGEMENTS

The research was supported by the National Nature Science Foundation of China(NO.U1361209) and "973 Program(2013CB227903)".

## REFERENCES

Wu haiyan, (2010). Development and application of high-power large mining height electric haulage coal mining machine [J]. Heavy-duty machinery. No.6, pp. 9-12.

Wang Jiachen, Zhong Shuhuan. (2013). Introduction to energy engineering [M]. China Mining University Press, pp.15-20.

Wang Jiachen, (2009). Theory and technology in mining thick coal seams [M]. Beijing, Metallurgical Industry Press, pp. 23-36.

Liu Changyou, Yang Peiju, (2012). Two column type bearing characteristics of the fully mechanized support cover and top beam stability study. Coal Industry Press, pp. 17-23.

Zhang Zhongwen, (2011). Study on Suitability of Hydraulic Powered Two Lag Shield Caving Support in Pingshuo Mining Area Coal [J]. Science and Technology, 39[11], pp. 31-35.

Liu Jiangong, Zhao Qingbiao, (2011). Theory and technology of coal mining with filling method [J]., Coal Industry Press, Beijing. Pp. 19-25.

# Overburden Failure Characteristics of Extra–Thick Seam Using Top Coal Caving Mining Method at Tongxin Coal Mine

**Zhijie Zhu**, Ph.D. Student
**Hongwei Zhang**, Professor, Head Department
**Ying Chen**, Ph.D., Research Associate
College of Mining Engineering
Liaoning Technical University
Fuxin, China

**Bin Yu**, Senior Manager
Datong Coal Mine Group Company
Datong, China

**Lijie Huo**, Managing Director
Datong Coal Guodian Tongxin Coal Mine Co. Ltd.
Datong, China

## ABSTRACT

In order to determine the overburden failure characteristics of extra-thick seam mining, EH4 electromagnetic image system and borehole televiewer survey were applied to panel 8100, Tongxin coal mine. EH4 electromagnetic imaging system was used to map the overburden strata before and after mining. Analysis of the distribution of the electrical conductivity showed that the fractured zone height was 492-558 ft (150-170m); Observation through the borehole televiewer showed that the fractured zone height of water conductivity (or water flowing fractured zone height) was 110m-142m. The results of the two methods showed that the fractured zone height of water conductivity was 492-558 ft (150-170m) or 10-11.3 times the mining height.

## INTRODUCTION

The fractures formed in the overburden due to underground longwall mining are the channels for mine water inrush. Thus the development process of fractures in the overburden is the basis for determining the occurrence, and predicting and formulating control measures for mine water inrush (Dou et al., 2012). At the same time, in order to properly layout the mine and to efficiently drain the methane gas, it is also very important to accurately determine the fracture characteristics of the overburden (Liu et al., 2012). Many researchers in China had performed numerous researches on the fractured zone height of water conductivity. For example, Chen et al., (2006) used RFPA software to simulate the whole process of overburden deformation and caving during mining and determined the fractured zone height of water conductivity. Wang (2006) applied microseismic monitoring method to determine the fractured zone height of water conductivity. Xu et al., (2012) presented a prediction method using the location of the key strata to determine the fractured zone height of water conductivity. Zhang et al., (2012) built an improved FOA-SVM model to predict the fracture zone height of water conductivity based on statistics analysis.

In this paper, EH4 electromagnetic image system and borehole televiewer were applied to panel 8100, Tongxin coal mine to study the fracture characteristics of the overburden in top coal caving mining.

## GEOLOGY AND MINING CONDITIONS

The coal seam mined in panel 8100, Tongxin coal mine was the No. 3-5 seam. Its average thickness was 50.2 ft (15.3 m) and dipped 2 ° to 3 °. The panel width along the dip direction was 633 ft (193m), and the panel length along the strike direction was 4613 ft (1406m). The top coal caving method was used to extract the full seam thickness with mining height 12.8ft (3.9m) at the bottom of the seam and the remaining 37.4 ft (11.4m) on the top by natural caving. The main roof 7.2 - 27.2 ft (2.2 - 8.3m) thick was pebbly coarse sandstone consisting of silica and feldspar. Its pores were filled with water. The immediate roof was sandy mudstone and carbonaceous mudstone with well-developed laminations. The gob of the No. 14 seam located 574-636 ft (175-194m) above the No. 3-5 seam covered about half of the panel length.

## SURVEY OF WATER CONDUCTING FRACTURED ZONE HEIGHT BY ELECTROMAGNETIC IMAGE SYSTEM

### Survey schemes

EH4 electromagnetic imaging system (Cai et al., 2012) was used in panel 8100 to classify the fractured and caved zones of the overburden by utilizing the different electrical conductivity characteristics of various strata. The survey was performed in three stages: (1) Pre-mining of intact overburden in May 2011; (2) Post-mining of mined-out gob in August 2011; and (3) Post-mining after movement of overburden had stabilized in May 2012. Two survey lines were laid out in panel 8100 (see Figure 1). Survey line #1 was located in area of panel 8100 where no mining would be performed, while survey line #2 was located above the gob of panel 8100. The length of survey line #1 was 160 m, containing nine measuring points. Survey line #2 was oriented at N21°W. It was 1115 ft (340 m) long and contained 18 measuring points. In the second and third stages of surveys, survey was repeated along survey lines #1 and # 2. When the second stage of survey was performed the panel had been mined out for one month. When the third stage of survey was performed the panel had been mined out for 10 months.

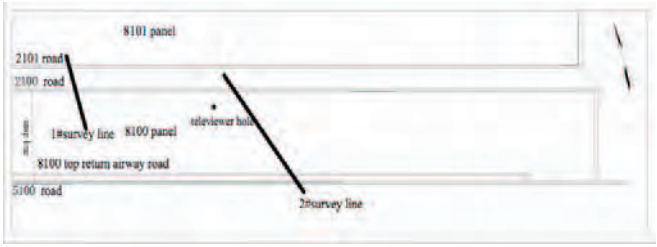



**Figure 1. Panel layout.**

**Analysis of Survey Data**

The two-dimensional earth resistivity inversion of survey line #1 at each stage (double black dashed line is the seam position) is displayed. It can be seen from Figure 2a that the resistivity contours are smooth and continuous; there is little abnormal change of electrical conductivity density and no dislocation. The distribution of resistivity contours is layered except some fluctuations in shallow layers. The results confirmed that this area was not affected by coal mining, and the overburden was undisturbed. Similarly, it can be seen from Figure 2b that there were closed contour lines of abnormal electrical resistivity in an area bounded in the horizontal direction between 262 ft (80 m) and 591 ft (180 m) and in the vertical direction between +2625 ft (+800 m) and +2887 ft (+880 m) (the red dotted line). This abnormal area coincides with the dimensions of panel 8100 shown in Figure 1. Therefore, it can be inferred that this high resistance anomaly area was the caved zone about 262 ft (80 m) high. The blue dashed line was the boundary of the fractured zone. It was about 492 ft (150m) high. The continuous deformation zone covered the area from the boundary line of the fractured zone to ground surface. Again it can be seen from Figure 2c that high resistivity was distributed within a certain distance above the coal seam (double black dashed line is the seam position). Within this area the resistivity contours were smooth, continuous and layered, indicating that overburden movement had reached a steady state after one year of mining. Loose rocks and fractures are the cause of high electrical resistance. Resistivity contours are restored to the smooth layered distribution found in pre-mining condition after overburden strata movement ceased and became compacted.

The two-dimensional earth resistivity inversion of survey line #2 at each stage (double black dashed line is the seam position) is displayed. It can be seen from Figure 3a that there was a closed contour line bounded in the horizontal direction between 262 ft (80 m) and 984 ft (300 m) and in the vertical direction between +2625 ft (+800 m) and +2953 ft (+900 m) (the red dotted line). The abnormal area matched with the dimensions of panel 8100 shown in Figure 1. Therefore, it can be inferred that this high resistance anomaly area was the caved zone about 100m high. The blue dashed line was the boundary of the fractured zone. It was about 170m high. The continuous deformation zone covered the area from the boundary line of the fractured zone to the ground surface. The abnormal region in Figure 3b is consistent with the region in Figure 3a. There was a closed contour line in the horizontal direction between 262 ft (80 m) and 984 ft (300 m) and in the vertical direction between +2625 ft (+800 m) and +2953 ft (+900 m). So it can be inferred that the caved zone is about 100m high and the fractured zone is about 170m high. It can be seen from Figure 3c that resistivity contours was smooth, continuous, and layered, indicating that overburden movement had reached a steady

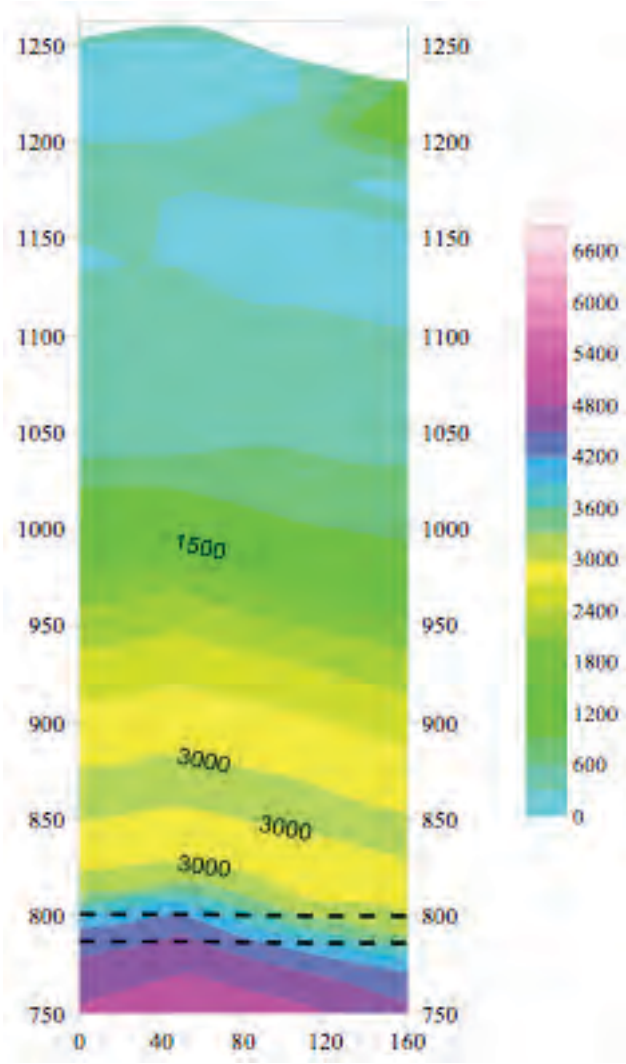



**Figure 2a. EH-4 two-dimensional inversion profiles of survey line No 1, the first stage (May 2011).**

state after one year of mining. Loose rocks and fractures are the cause of high electrical resistance. Resistivity contours are restored to the smooth layered distribution found in pre-mining condition after overburden strata movement ceased and became compacted.

Table 1 is the summary of the EH4 geophysical survey results. The caved and fractured zones height at Tongxin mine was 492-558 ft (150-170m) after mining of panel 8100 or 10 to 12 times of mining height (mining height = 49 ft (15 m)).

**Table 1. EH4 survey results showing the height of the two zones in the gob.**

| Survey line | Caved zone height | Fractured zone height |
|---|---|---|
| 1 | 262 ft (80 m) | 230 ft (70 m) |
| 2 | 328 ft (100 m) | 230 ft (70 m) |

## DETERMINATION OF FRACTURED ZONE HEIGHT OF WATER CONDUCTIVITY BY BOREHOLE TELEVIEWER

### Borehole layout

The fractured zone height of water conductivity of panel 8100 was determined by using the JL-IDOI (A) Drilling TV Smart Imager (Figure 4) in July 2011. The surface borehole was located in the gob of panel 81000 about 1496 ft (456m) from the panel stop line. The distance between the borehole and 2100 transport

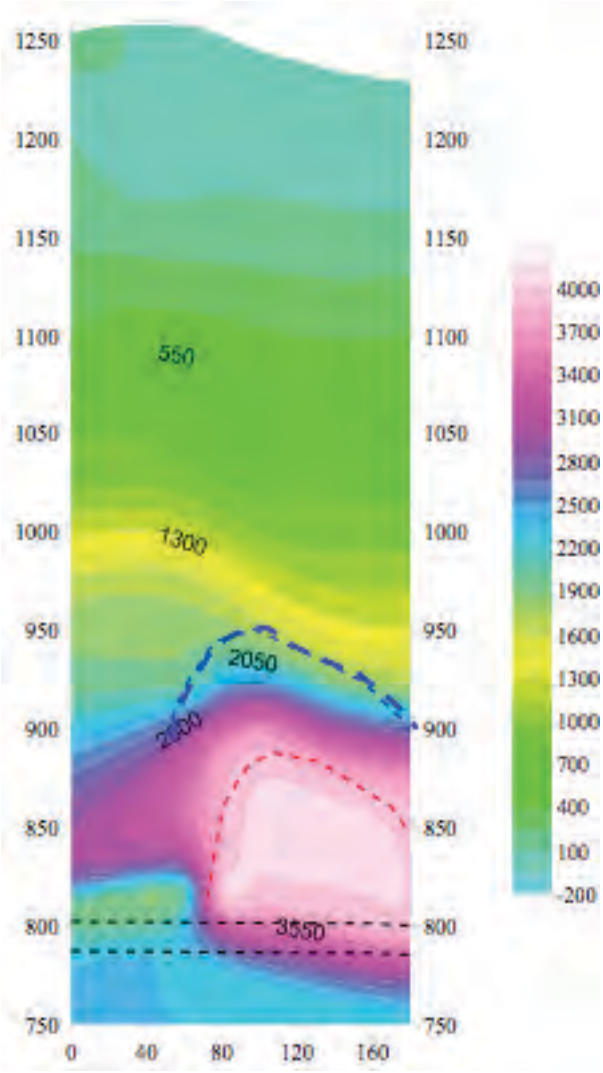



**Figure 2b. EH-4 two-dimensional inversion profiles of survey line No 1, the second stage (August 2011).**

road was 105ft (32 m) (Figure 1). The vertical distance between borehole mouth and coal seam floor was 1435.4 ft (437.5m), and the bottom end of the borehole was 60m above the coal seam roof. The data collected by the borehole televiewer were used to analyze the fractures in various strata and finally the caved and fractured zones were determined.

### Results of the borehole televiewer

Analysis of the images as viewed from the borehole televiewer indicated that the observation segments can be divided into four parts (Figure 5). The first part was the tiny fissure zone. It was 361-328 ft (110-100m) from the coal seam roof or 1007-1040 ft (307-317m) from the ground surface. In this region the fine sandstone is more or less intact with localized microcracks. This region was located within the fractured zone. The second part was the visible fractured zone, being located 1040-1079 ft (317-329m) from the ground surface. There were visible criss-cross cracks with bed separations. The third part was bed separation fractured zone, being located 1079 -1132 ft (329-345m) from the ground surface. In this

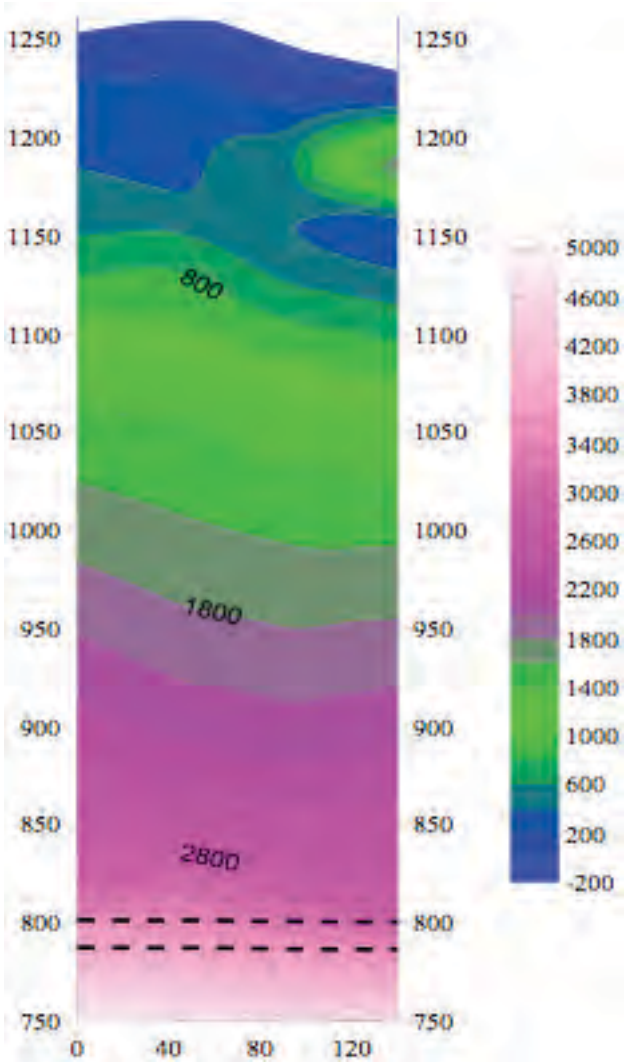



**Figure 2(c). EH-4 two-dimensional inversion profiles of survey line No 1, the third stage (May 2012).**

region, broken rock, bed separation and intact rocks alternated. This part bordered the caved zone. The fourth part was the badly broken zone, being located 1132-1148ft (345-350m) from the ground surface. The drill bit was lost in this part. Being in the caved zone, rocks were visibly broken. Due to the fact that all image data began from the ground surface at 1007 ft (307m), the

boundary of the fractured zone could not be determined. Based on the above analysis, the caved zone height was about 236 ft (72 m), that of the fractured zone was 125-230 ft (38-70m), and the height of overburden failures was 361-467 ft (110-142 m) (Figure 6).

## SUMMARY

Since there were no clayey rock strata between No. 3-5 coal seam of Tongxin coal mine and the overlying No.14 coal seam, the interburden is unable to form an impermeable key stratum. During mining of the No. 14 seam, the floor was broken by the abutment pressures. The broken rocks were compressed and fractures were closed when the overburden roof in the gob caved down and piled up. Those fractures reopened once subjected to the influence of mining in the underlying No.3-5 coal seam, reducing the thickness of the stable strata in the interburden and thereby increasing the potential of connection between the fractures created by mining of these two seams at different times.

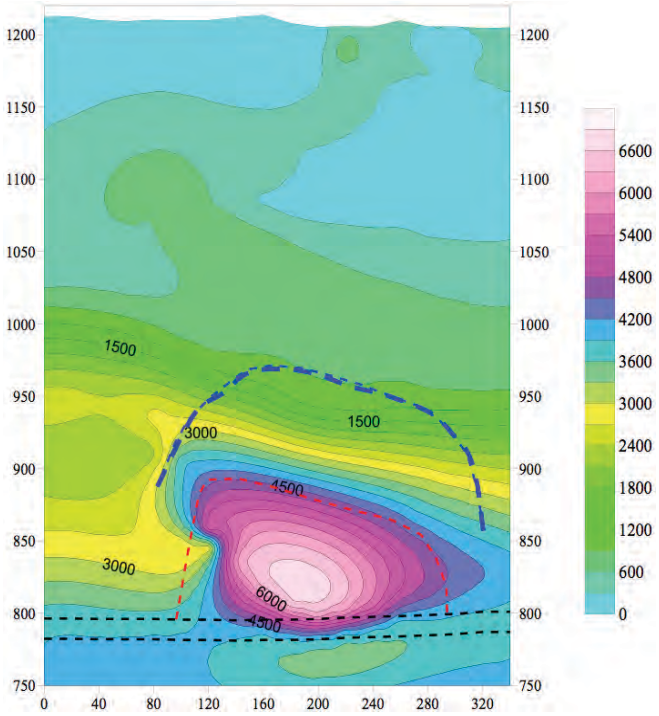



**Figure 3(a). EH-4 two-dimensional inversion profiles of survey line No 2, the first stage (May 2011).**

The overburden failure height of panel 8100 was determined by using two different methods. The results of EH4 geophysical survey and surface borehole televiewer observation were mutually agreeable. The height of overburden failure was finally determined to be 492-558 ft (150-170m), or 10 to 12 times of the mining height (mining height was 49 ft (15 m)). The distance between panel 8100 in the No. 3-5 seam and the overlying No 14 seam was 574-636 ft (175-194m), more than the height of overburden failure zone. Therefore cracks in the No. 3-5 seam did not connect to those in the No. 14 seam. The distance between 8106 in the No. 3-5 seam and the overlying No 14 seam was 410-459 ft (125-140m), less than the height of overburden failure zone, cracks created by the two seam mining were connected in the gob, further validating the survey results. In areas where the interburden is thinner, the total mining height should be reduced to prevent the connectivity of the cracks created by mining of the two seams.

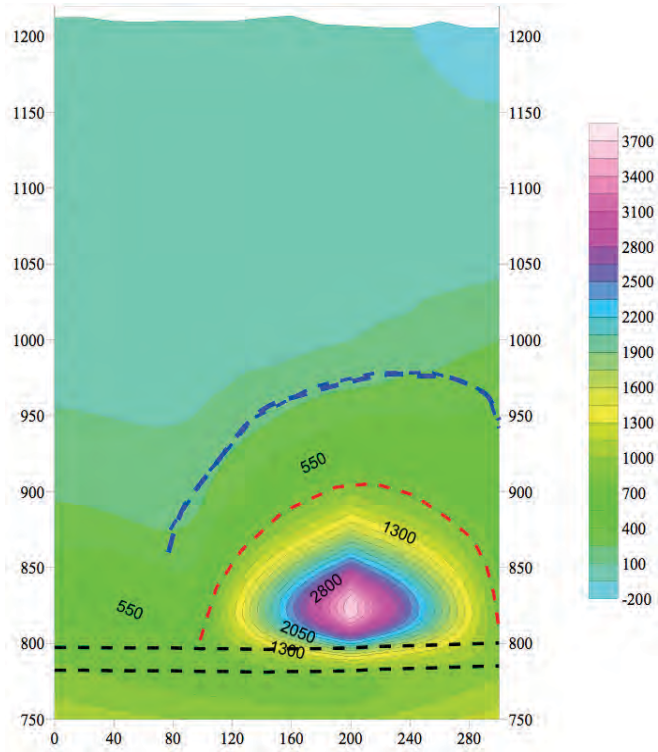



**Figure 3(b). EH-4 two-dimensional inversion profiles of survey line No 2, the second stage (August 2011).**

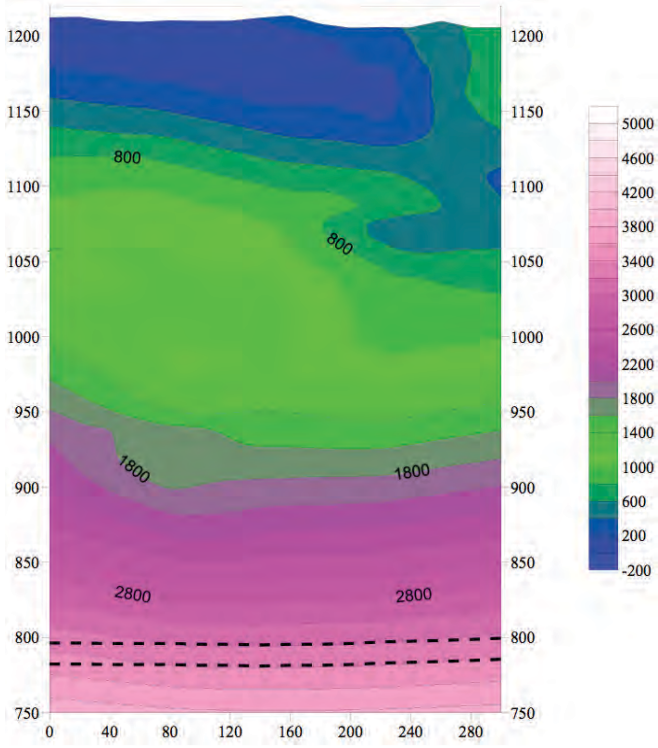



**Figure 3(c). EH-4 two-dimensional inversion profiles of survey line No 2, the third stage (May 2012).**

## CONCLUSION

(1) Through EH4 geophysical survey, the height of caved zone was determined to be about 100m, while that of the fractured zone was about 558 ft (170m). The overburden failure height was determined to be 492-558 ft (150-170m), or 10 to 12 times of mining height.

(2) Based on the result of borehole televiewer survey, the caved zone covers up to 236 ft (72m) and the fractured zone covers the area 236-361 ft (72-110m) above the seam top. The overburden failure height was 361-467 ft (110-142 m). As the borehole located near panel border, the height would be lower.



**Figure 4. Smart drilling TV camera.**

(3) The combined results of EH4 geophysical survey and borehole televiewer observation determined that the fractured zone height of water conductivity was 492-558 ft (150-170m), or 10 to 12 times of mining height. In areas where distance between No.3-5 seam and No.14 seam is smaller, the cracks created separately by mining of No.3-5 and No.14 seam will be connected.

(4) The overburden failure height in the conventional single seam mining is about 20 to 30 times of mining height in China. In this research the overburden failure height of extra-thick mining is 10 to 11.3 times of mining height in Tongxin coal mine. It indicates that the overburden failure characteristics in Tongxin coal mine is unusal and requires further study.

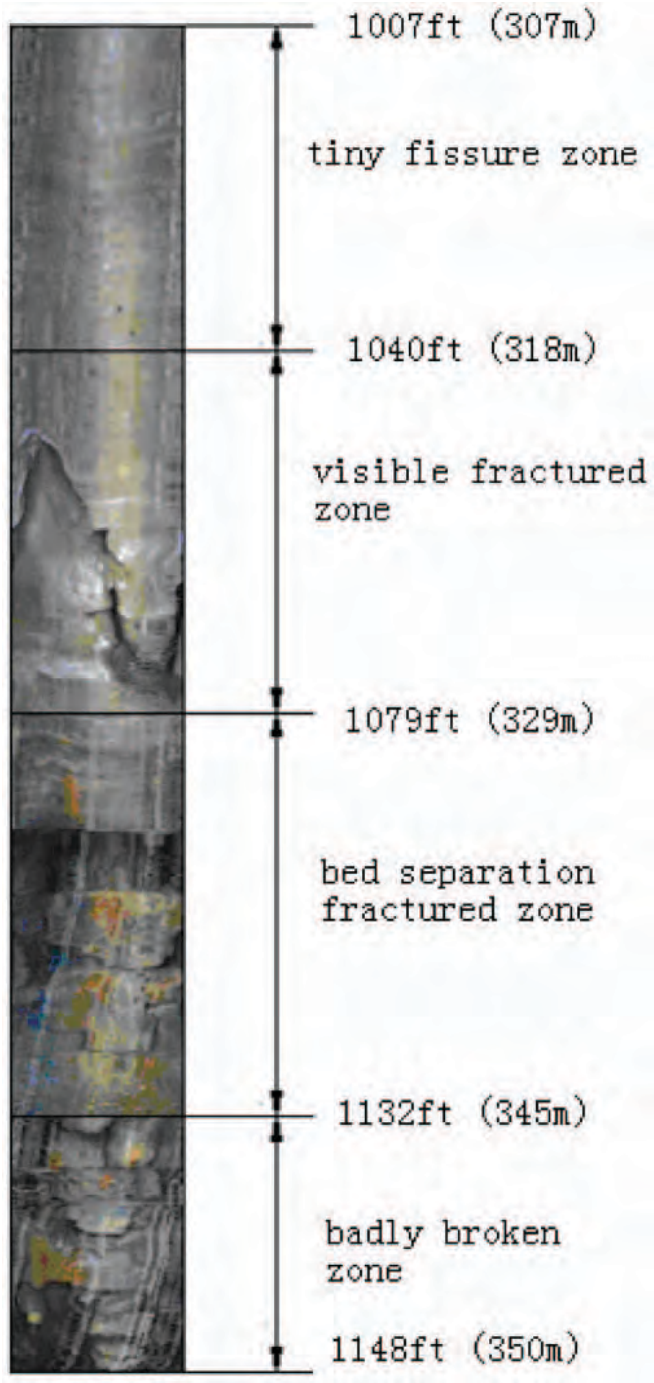



**Figure 5. Damage characteristics of the hole wall.**

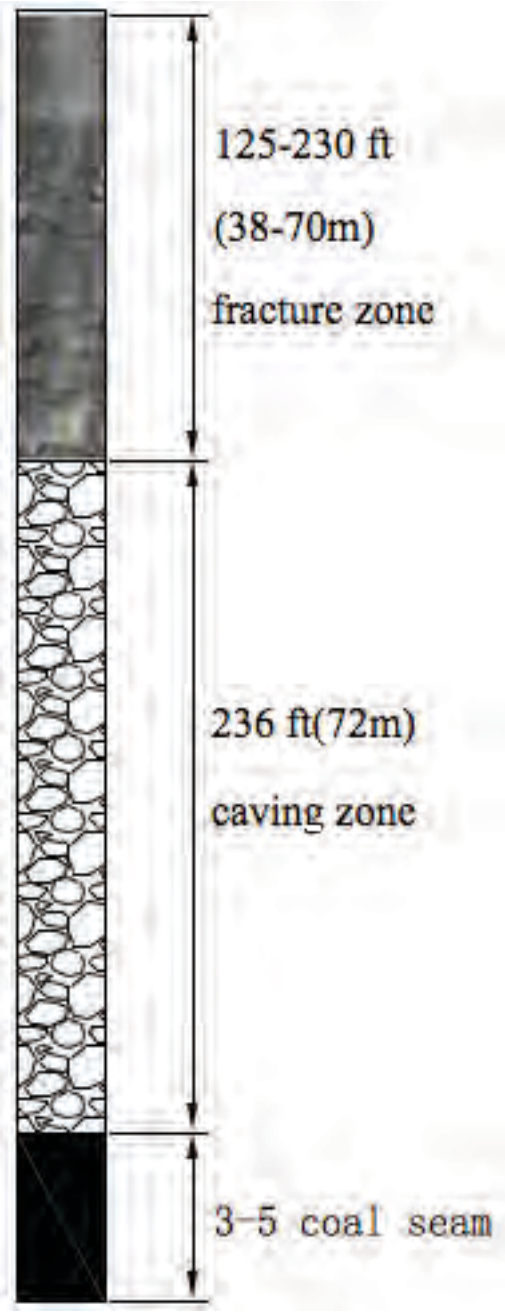



**Figure 6. Caved and fractured zone heights.**

## REFERENCES

Dou L.M., He J., Gong S.Y., et al. (2012). A case study of micro-seismic monitoring goaf water-inrush dynamic hazards. Journal of China University of Mining & Technology, 41(1), PP.20-25(in Chinese).

Liu H.Y., Cheng Y.P., Chen H.D., et al. (2012). Characteristics of mining gas channel and gas flow properties of overlying stratum in high intensity mining. Journal of China Coal Society, (9), pp. 1437-1443 (in Chinese).

Chen R.H., Bai H.B., Feng M.M. (2006). Determination of the height of water flowing fractured zone in overburden strata above fully mechanized top coal caving face. Journal of Mining & Safety Engineering, 23(2), pp. 220-223 (in Chinese).

Wang H.J. (2006). Research on microseism monitor in height of water flowing fractured zone of cover rock. Express Information of Mining Industry, 03, pp. 27-29 (in Chinese).

Xu J.L., Zhu W.B., Wang X.C. (2012). New method to predict the height of fractured water-conducting zone by location of key strata. Journal of China Coal Society, 37(5), pp. 762-769(in Chinese).

Zhang H.W., Zhu Z.J., HUO B.J., et al. (2013). Water flowing fractured zone height prediction based on improved FOA-SVM. China Safety Science Journal, 23(10), pp. 9-14 (in Chinese).

Cai S., Liu J.X., Hu Z.J., et al. (2011). Application of EH4 electric conductivity imaging system to coal goaf. Chinese Journal of Engineering Geophysics, 8(6), pp. 687-691 (in Chinese).

# Validation of Overburden Failure Zone in Complex Extra Thick Coal Seam by EH–4 Magnetotelluric Method

**Hai Rong**, Ph.D. Student
**Hongwei Zhang**, Professor and Director
**Jun Han**, Associate Professor
College of Mining
Liaoning Technical University
Fuxin, China

**Guohong Li**, Mine Manager
**Fawu Yang**, Mining Engineer
Laohutai Coal Mine
Fushun Mining Group Co. Ltd.
Fushun, China

## ABSTRACT

EH-4 Electrical conductivity imaging system has been playing an important role in prospecting, looking for water resource, and determining coal mine gob boundary by virtue of its significant advantages such as collection of large volume of data, light weight, fast analysis, high-precision, and low cost. However, it has little application in determining the overburden failure zone and development of water flowing fractured zone and bed separation space in complex extra thick coal seam conditions. In order to confirm the overburden failure range and evolution of water flowing fractured zone and bed separations in complex extra thick coal seam conditions the panel 63005 of Laohutai coal mine in China was selected for study in this paper,. EH-4 magnetotelluric method was used to determine the overburden failure zones and bed separations in the overburden. Theoretical analysis and numerical simulation were employed to verify the EH4 survey results. The results show that the failure height in the overburden of the three coal splits was 120m to 170m before panel mining, and increased to 150m to 220m after panel mining. The overburden failure height was on average 7.4 times the equivalent mining height in complex extra thick coal seam condition of Laohutai coal mine when the sand backfilling and fully mechanized top coal caving methods were employed. After mining of panel 63005 started, bed separations were found on the hanging wall and footwall of the $F_{18}$ fault where water bodies existed. The results obtained in this research not only provide a theoretical guidance for safe mining at Laohutai coal mine but also serve as a reference for predicting and preventing water inrush accidents for coal mines under similar condition in China.

## PRINCIPLE OF EH-4 MAGNETOTELLURIC METHOD

Mining activities inevitably lead to the deformation, failures and movement of the rock strata surrounding the mining operations. If a water body with bursting potential exists and channels for water flow are available in the surrounding rocks, serious mine water disasters are likely to happen (Wang et al., 2012; Chen et al., 2006). Studies have shown that the open space of bed separations in the overlying strata is the primary condition for water inrush(Jing et al., 2006; Zhu et al., 2009). The water flowing fractured zone that denotes the combined area of the caving zone and fractured zone is a primary indicator for damage range and water conductivity of overburden strata. The development of water flowing fractured zone provides the theoretical basis for prediction, prevention and control of water inrush (Xu et al., 2012; Xu et al., 2009). Therefore, it's very important to confirm the position of water flowing fractured zone and bed separation space for safe coal mine production. At present, the major methods for determining the overburden failure area are drilling flushing fluid observation method, transient electromagnetic method, high-pressure water injection method, and borehole video imaging method (Liu et al., 2013). However, these methods are often subjected to many limitations during the actual measurement process, such as very difficult to implement, high cost, susceptibility to interference, and limited applicability. EH-4 Electrical conductivity imaging system has been playing an important role in prospecting, looking for water resource, and determination of coal gob boundary by virtue of its significant advantages such as collection of large volume of data, light weight, high-precision, high efficiency, and low cost. It has become an important device for locating the orebody and engineering exploration (Zhang et al., 2011; Liu et al., 2012; Cai et al., 2011). Shen et al., (2008) used EH-4 electrical conductivity imaging system to orient the location of 25 kinds of metallic ores. Xu et al., (2006), Yu et al., (2008), Dai et al., (2013) and other scholars used EH-4 to confirm the boundaries of molybdenum mines. Wang et al., (2012) used EH-4 to predict land subsidence caused by shallow bauxite gob successfully, the results of which have been verified by Biot consolidation theory. Li et al., (2012) used EH-4 to look for hot-water underground in the western region of China. Liang et al., (2012), Wang et al., (2009), and Tan et al., (2011) used EH-4 to look for mineral resources. However, EH-4 has little application in determining the overburden failure range and development of water flowing fractured zone and bed separation space under complex extra thick coal seam conditions.

In this paper, the authors used EH-4 magnetotelluric method to survey the failure structure in the overburden of the 3rd coal split before and after mining of panel 63005, Laohutai coal mine, China. The survey results were validated by theoretical analysis and numerical simulation. Simulation results confirmed specific changes in the overburden failure range before and after mining of panel 63005; determined the location of bed separation space; and establish a relationship between the failure height of overlying strata and mining height. These findings will provide a theoretical guidance for safe mining of Laohutai coal mine and a reference

for prediction and prevention of water inrush for coal mines under similar conditions in China.

## ENGINEERING CASE STUDY AND SURVEY SCHEME

### Engineering case study

Panel 63005 was located in the east wing of Laohutai coal mine with return airway of panel 63003 in the east, 4th level gob of panel 705 in the west, tuff floor in the south, and in the north, the eastern gob of panel 68002 and roof oil shale. The Upper and lower parts of panel 63005 were backfilled during the early era of drill and blast mining. The upper part was backfilled to the height between 45m and 50m. Above the backfills it was the oil shale of about 210 m thick. Above the oil shale it was green shale, about 370 m thick. The $F_{18}$ fault layer was located in the green shale to the north of panel 63005. Figure 1 shows the geological cross-section of panel 63005.

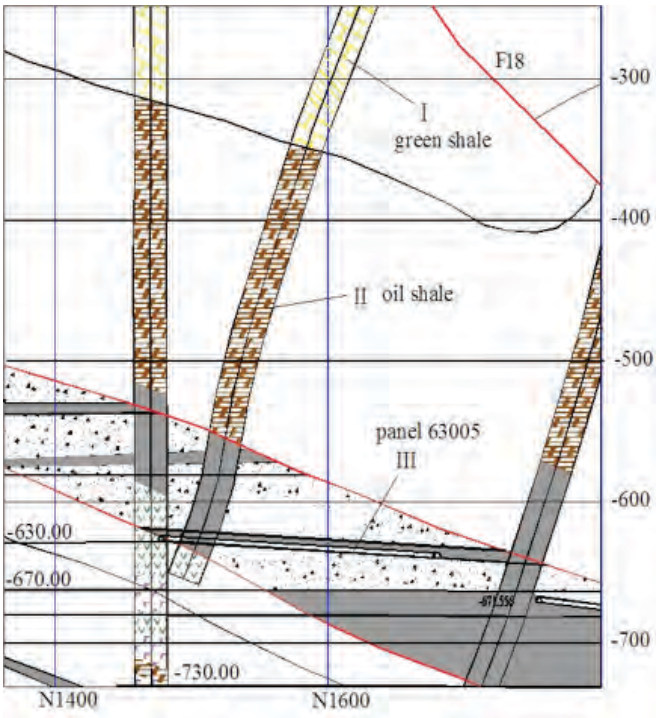



**Figure 1. Stratigraphic section of panel 63005.**

Panel 63005 was 485 m long along the strike direction, and 184m to 204m wide along the dip direction. It was 641.5m to 625.5m deep. Coal seam averaged 6m thick and dipped 6°. The fully mechanized top coal caving mining method with face advancing on the strike direction was used. Its coal recovery was 90%.

Prior to the top coal caving mining, the inclined slicing blasting caving method was used to mine the stage pillars left by panels 705 and 704 sand backfilling mining at the 630m level. The remnant stage pillars dipped steeply. They were very thick composite coal seam containing partings. The partings divided them into Nos. 3, 4, and 5 splits. The three splits were 28.64m, 14m and 22m thick, respectively. All three splits were 150m long along the strike direction and about 125m wide along the dip direction. The average inclination was 25°. The two partings among the three splits were 12m and 10m thick and served as the roof for the 4th and 5th splits, respectively. The roof of the 3rd split was oil shale as shown in Figure 2. After completion of mining the 3rd, 4th and 5th splits, their gobs were hydraulically backfilled. According to field investigation, the gob of each split was about 70% filled up. In this paper, the failure range in the overburden strata of the 3rd was confirmed before and after mining of panel 63005.

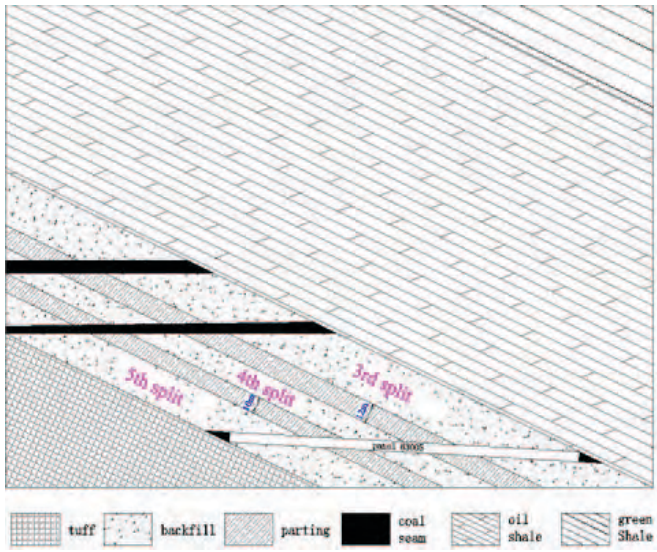



**Figure 2. Relative position of each split during sand backfilling mining stage.**

### Survey scheme

The EH-4 magnetotelluric method is based on the principle of electromagnetic induction, which takes natural electromagnetic field as magnetic field source. The method is often used to explore electric and magnetic fields on the earth. The water flowing fractured zone is formed after panel mining. Comparing to intact strata, the strata in the water flowing fractured zone are loose and rock density is lower. Since the cracks are filled with the air, electrical conductivity of rock is lower. Therefore, the apparent resistivity of rock in the water flowing fractured zone is higher and displays as a high resistivity anomalies in EH4 survey data. Bed separation space exhibits the same high electrical resistivity anomaly. If the water flowing fractured zone is filled with water, the rock conductivity of this area will increase rapidly, the apparent resistivity of rock in the water flowing fractured zone will be lower, and the EH-4 display will have low resistivity anomalies. In summary, differences in conductivity provide geophysics foundation for EH-4 magnetotelluric method.

In order to confirm the failure range of the roof of the 3rd split before and after mining of panel 63005 and to establish a relationship between the failure height of the overlying strata and mining height, a 2-step EH-4 survey scheme was developed. First, prior to mining of panel 63005, the first EH4 survey was performed to determine the relationship between the failure height of the overlying strata and equivalent mining height when hydraulic backfilling mining method was used. Second, after mining of panel 63005 had proceeded for 3 months, the second EH4 survey was performed to determine the relationship between the failure height of the overlying strata and equivalent mining height in top coal

caving mining method. The survey line was 240m long from north to south and oriented at N8°E. There were 13 measuring points spaced at 20m interval (Figure 3).

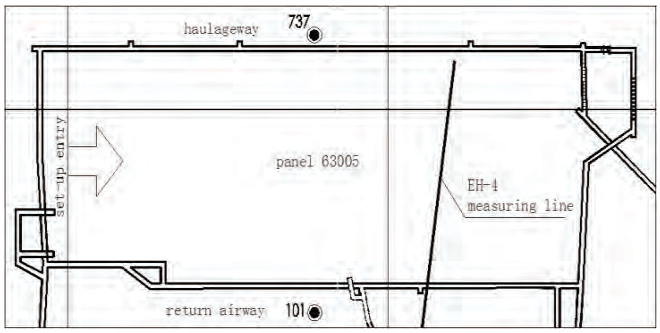



**Figure 3. Location of EH-4 measuring line in panel 63005.**

## ANALYSIS OF THE EH4 SURVEY RESULTS

### Prior to mining of panel 63005

Prior to mining of panel 63005, EH-4 survey depth was from 140m to 1,700m. The resistivity varied from 20 Ω•m to 780 Ω•m. Emphasis was placed on the analysis of survey data above the 700m level because panel 63005 was located at the 630m level. A comparison is made between EH-4 resistivity profile and borehole stratigraphic column before and after mining of panel 63005. By comparing Figure 4a and Figure 4b, it can be seen that the overlying strata resistivity ranged from 20 Ω•m to 340 Ω•m before mining of panel 63005. The resistivity was relatively low and increased gradually from shallow to deep areas.

Resistivity contours of the region above the 320m level were nearly horizontal, and the resistance values were under 280 Ω•m. Resistivity of the region between the 320m and 390m level maximized around 280 Ω•m to 300 Ω•m. Resistance values decreased from 300 Ω•m to 280 Ω•m between the 390m and 410m levels. Resistivity ranged from 270 Ω•m to 280 Ω•m at the region between the 410m and 600m levels. Resistance values increased from 280 Ω•m to 340 Ω•m at the region between the 600m and 700m levels. From the resistivity distribution in the overburden of panel 63005, the measured resistivity can be divided into four grades: First, the resistivity incremental zone in the region above the 320m level. In this region, the maximum resistivity value was 280 Ω•m. Second, the resistivity zone of stable high value in the region between the 320m and 390m levels. In this region, the resistivity value was between 280 Ω•m and 300 Ω•m. Third, the resistivity zone of relative high value in the region between the 390m and 600m levels. In this region, the resistivity value was between 270 Ω•m and 280 Ω•m. And fourth, the resistivity incremental zone in the region between the 600m and 700m levels. In this region the maximum resistivity value was between 280 Ω•m and 300 Ω•m.

It can be seen from Figs. 2 and 4 that borehole 101 was located to the south of the return airway of panel 63005, and borehole 737 was located to the north of the haulageway of panel 63005. The elevation of hole mouth of borehole 101 was 81m above the sea level. The stratigraphic column in borehole 101 was in descending order: top soils from 81m to 64m above sea level, 17 m in average

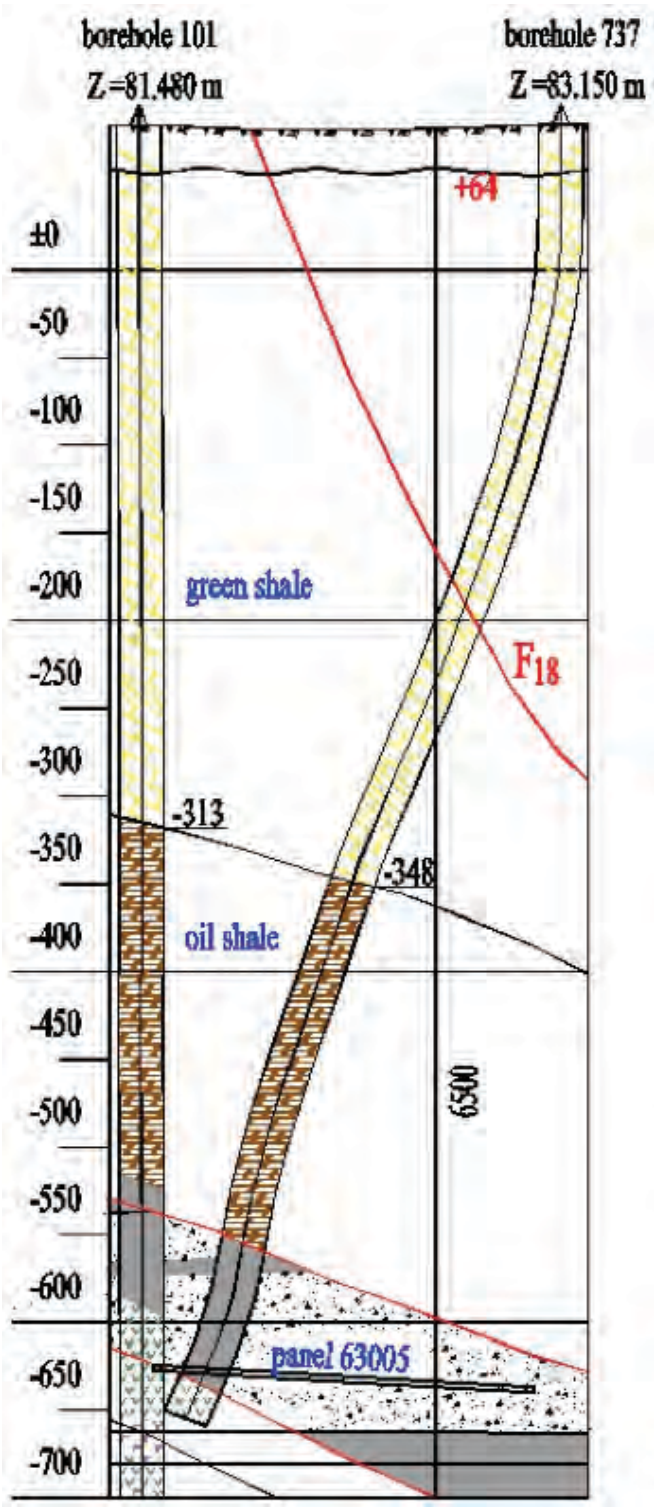



**Figure 4(a). Comparison between EH-4 resistivity profiles and stratigraphic column before and after panel 63005 mining stratigraphic column of panel 63005, stratigraphic column of panel 63005.**

thickness. Green shale from 64m above the sea level to 313m below the sea level, 377m in average thickness. Oil shale from 313m to 519m below the sea level, 206m in average thickness. Coal seam from 519m to 630m below the sea level, 81m in average thickness. Sedimentary tuff beds below 630m. The elevation of

hole mouth of borehole 737 was 83m above the sea level. The stratigraphic column in borehole 737 was in descending order: top soils from 83m to 64m above the sea level, 19m in average thickness. Green shale from 64m above the sea level to 348m below the sea level, 412m in average thickness. Oil shale from 348m to 554m below the sea level, 206m in average thickness. Coal seam from 554m to 645m below the sea level, 91m in average thickness. Sedimentary tuff beds below 645m. By comparing EH-4 resistivity profile with borehole stratigraphic column, the strata morphology revealed by EH-4 surveys basically matches with that shown in the stratigraphic column. Resistivity incremental zone confirmed by EH-4 matches green shale shown in drillhole column, in which resistivity ranges from 20 Ω•m to 280 Ω•m. Resistivity zone of stable high value and relative high value measured by EH4 were confirmed by drillhole column as oil shale, and resistivity incremental zone in the fourth part confirmed by EH-4 matches coal seam and sedimentary tuff. Resistivity zone of stable high value and relative high value in the second and third parts matches oil shale, but the appearance of high value in the second part indicates that bed separation space occurs in the middle of green shale and oil shale. After hydraulic backfilling mining, the caving and fractured zones in the overlying strata of panel 63005 appeared in the lower part of oil shale. The upper part of oil shale and green shale were in the continuous deformation zone. Bed separation space occurred due to the differences in mechanical property between green shale and oil shale, and this leads to the difference in subsidence and deformation. EH-4 was not used for shallow surface survey, so there was no data above the 60m elevation. From the results of EH-4, the area with abnormal high resistivity value was not large. The change in resistivity value between the upper and lower strata was small. Consequently, the area where bed separation occurred was relatively small.

Through the analysis of EH-4 survey results, it can be concluded that the resistivity within 170m of the 3rd split roof rock increased before mining of panel 63005. This implies that rock structure in this area had changed from the primary structure, thus forming the deformed overlying strata induced by mining. The results show that hydraulic backfilling mining caused the change of the overlying strata structure within 120m to 170m above the coal seam. Equivalent mining thickness of the 3rd, 4th and 5th splits is shown in Table 1, and the sum of the equivalent mining thickness is 19.4m. Thus the overburden failure height of the 3rd split roof rock was 6.2 to 8.7 times the equivalent mining height with an average of 7.45 times before mining of panel 63005.

**After mining of panel 63005**

After mining of panel 63005, EH-4 survey depth was from 140m to 1,500m below the sea level, and resistivity changes from 20 Ω•m to 600 Ω•m. By comparing Figure 4a and Figure 4c, it can be seen that the overlying strata resistivity ranged from 20 Ω•m to 340 Ω•m after mining of panel 63005. Block characteristics of resistivity distribution appeared, unlike the resistivity distribution before mining. Resistivity zone of high value appeared between 100m and 220m below the sea level in vertical belt distribution with resistance values ranging from 260 Ω•m to 400 Ω•m. Resistivity zone of high value also appeared between 300m and 600m below the sea level with resistance values ranging from 200 Ω•m to 400Ω•m. Resistivity zones of high value were mainly distributed in the middle and right side of the profile in the transverse direction. All other parts were resistivity zones of low value.

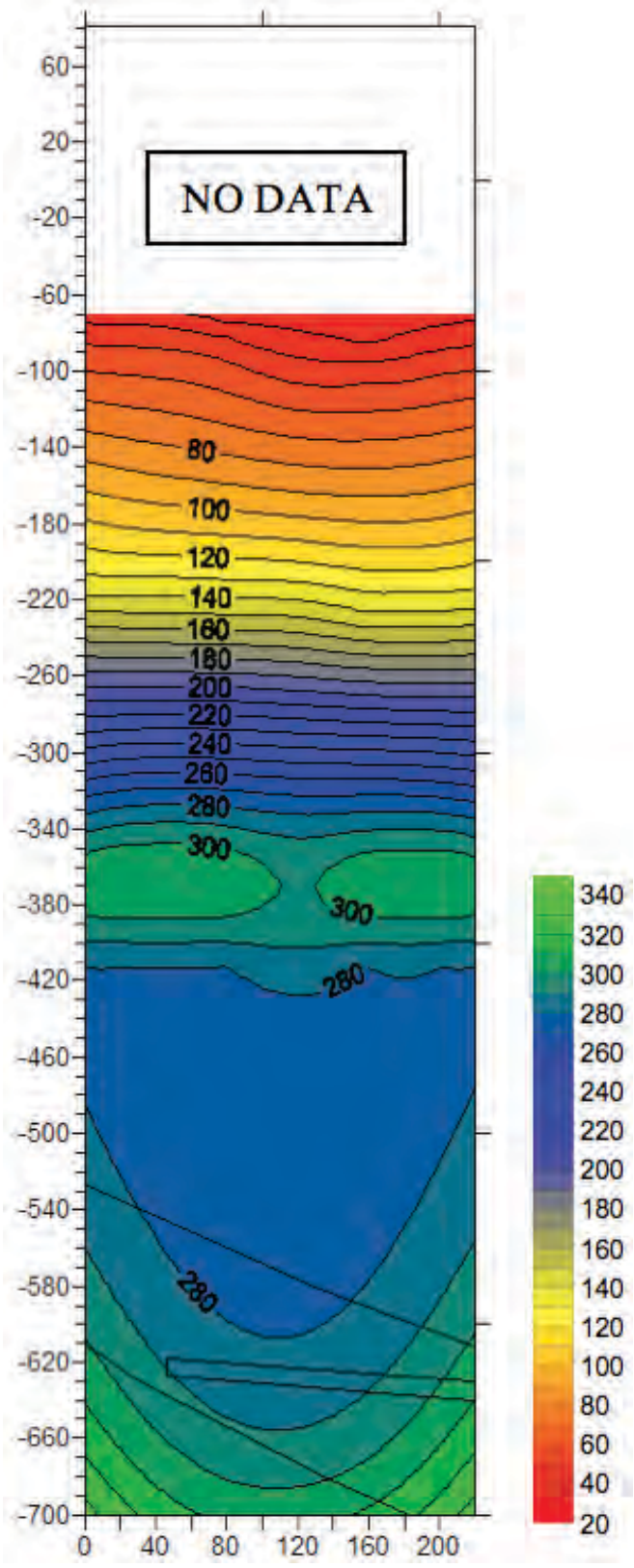



**Figure 4(b). Comparison between EH-4 resistivity profiles and stratigraphic column before and after panel 63005 mining, resistivity profile prior to mining of panel 63005.**

**Table 1. Caving and fractured zone heights formed after mining of 3rd, 4th, and 5th splits.**

| | 3rd split | 4th split | 5th split |
|---|---|---|---|
| Actual mining height, m | 28.64 | 14 | 22 |
| Backfilled rate | 70% | 70% | 70% |
| Equivalent mining height, m | 8.6 | 4.2 | 6.6 |

By comparing EH-4 resistivity profiles and borehole stratigraphic column, it can be seen that after mining of panel 63005, the resistance values increased within the range of 150m to 220m in the roof of the 3rd split. Furthermore, its failure zone reached up to 220m in height with the resistivity significantly different from that in the non-failure regions. Therefore the height of overburden failure was 6-8.8 times of the equivalent mining height with an average of 7.4 times after mining of panel 63005. In the area south of panel 63005, the resistance values were low. Therefore the failure zone in the roof of the 3rd split expanded further due to the influence of mining panel 63005. The resistance value in the region beyond the influence of mining changed very little. The resistivity zones of high value in the transverse direction were corresponding to the $F_{18}$ fault. It indicated that after mining of panel 63005, bed separation appeared at the hanging wall and footwall of the $F_{18}$ fault.

Comparing the results of EH-4 surveys before and after mining of panel 63005, it can be seen that the failure zone and degree of damage of the overlying strata expanded and increased substantially after mining of panel 63005. The height of overburden failure reached 220m in the roof of the 3rd split, and failures appeared especially along the fault plane of the $F_{18}$ fault. Thus the height of overburden failure was on average 7.4 times of the equivalent mining height in complex extra thick coal seam in Laohutai coal mine, either in the sand backfilling mining or the fully mechanized top coal caving periods. Green shale was resistive to water. The bed separation space in the hanging wall and footwall of the $F_{18}$ fault became the major sources of water inrush in Laohutai coal mine. Failures will be created in the strata surrounding the mining operation. The failure zones may provide channels for water flow. These two conditions pose potential threat to Laohutai coal mine.

## THEORETICAL ANALYSIS OF OVERBURDEN FAILURE HEIGHT

"Buildings, water, railway, coal pillar and coal mining regulations" of China (hereinafter referred to as the "regulations") has been widely used in the prediction of the height of water flowing fractured zone. However in some specific cases, the predicted results deviated greatly from the actual measurements. Its application is limited often by multiple slicing mining thickness, accumulated mining thickness, and seam dip angle. Xu et al., (2009, 2012) proposed and validated that the height of water flowing fractured zone is 7 to 10 times of the equivalent mining height. The backfilled space of the gob was assumed to be 70% in this paper and therefore the equivalent mining height of each

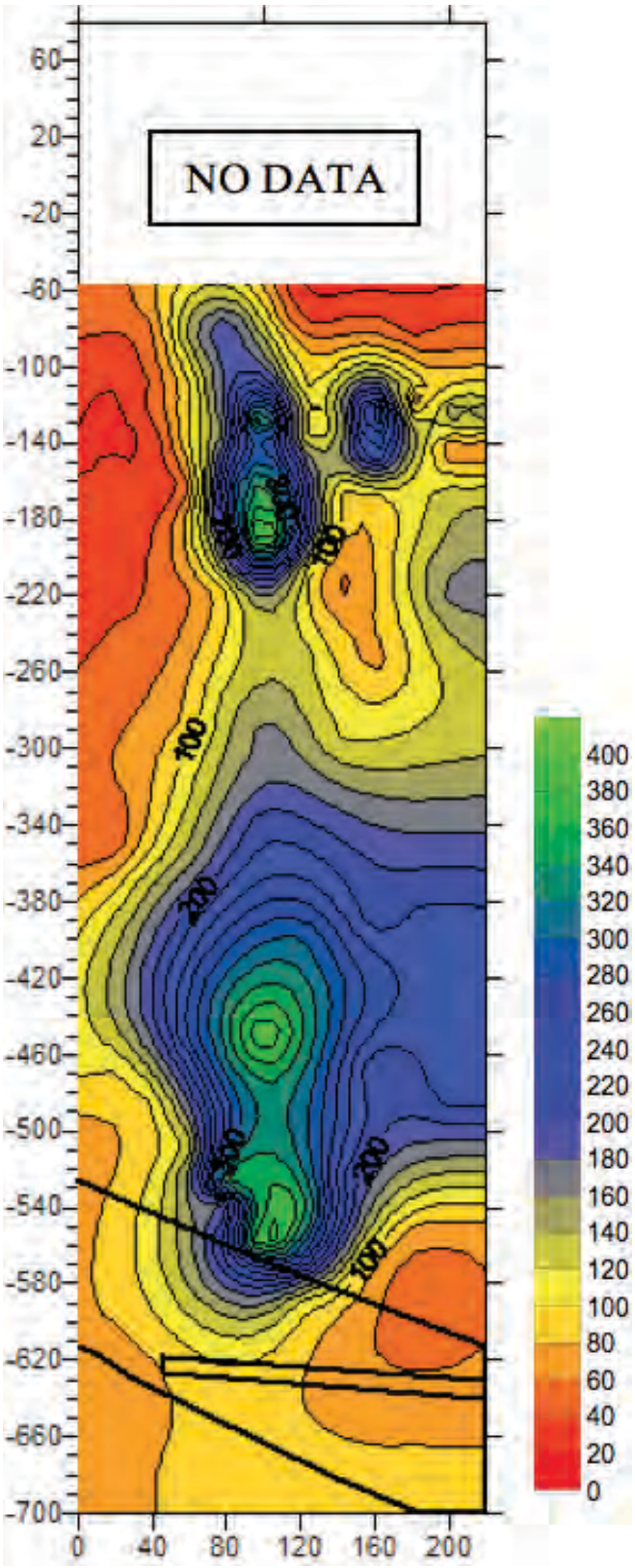



**Figure 4(c). Comparison between EH-4 resistivity profiles and stratigraphic column before and after panel 63005 mining, resistivity profile after mining of panel 63005.**

of the 3rd, 4th and 5th splits was 30% of actual mining height, as shown in Table 1. Overall, mining of each split of coal caused damage to the top and bottom of the coal seam. At the same time the water flowing fractured zone also caused damage to the strata near the coal split. Therefore after mining of the 3rd, 4th and 5th splits, the caving and fractured zones created by mining of each split overlapped in portions along both the strike and dip directions. The overlapped parts would expand the failure range further under the influence of repeated mining. Consequently, the sum of equivalent mining heights was used to establish the relationship between the height of overburden failure and the sum of equivalent mining height.

The sum of the equivalent mining height of the 3rd, 4th and 5th splits was 19.4m. According to the proposed method by Xu et al., (2009, 2012), the height of overburden failure was 135.8m-194m prior to mining of panel 63005. Since coal seam in panel 63005 was 6m thick with 90% recovery rate, the equivalent mining height would be 5.4m. The sum of the equivalent mining height became 24.8m after mining of panel 63005 and the height of overburden failure was 173.6m-248m. So the result matched that of EH-4 surveys.

## ANALYSIS OF NUMERICAL SIMULATION

In order to fully and systematically reflect the relationship between the height of overburden failure and the sum of equivalent mining height after mining of the 3rd, 4th, and 5th splits and panel 63005, FLAC$^{3D}$ which employs the finite difference method was used for numerical simulation. The model had 156,920 units and 166,971 nodes as shown in Figure 5. The dimensions of the model were 1005m × 200m × 880m (length ×width ×height). The model was subjected to stresses of 30.8 MPa and 17.6 MPa in the x and y directions, respectively. An equivalent load of 22 MPa was applied to the bottom of the model. The Z axis direction was subject to gravity load.

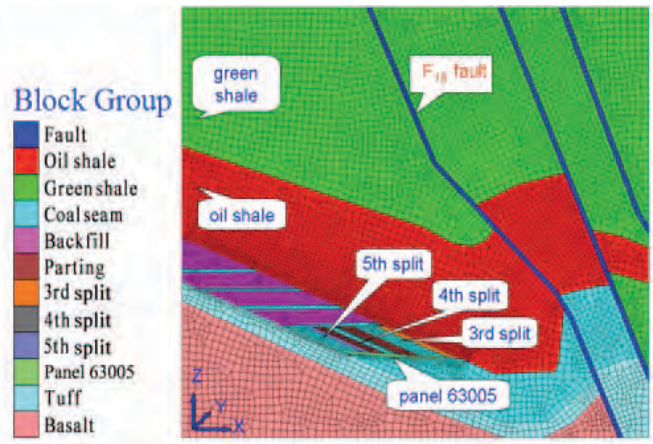



**Figure 5. FLAC3D model for panel 63005 simulation.**

Figure 6 shows the plastic zones after mining in panel 63005 had reached the fully development stage. Combined with the practical experience, the water flowing fractured zone is believed to be composed of zones of tensile fractures, tension shear failures and shear failures (Hu et al., 2013). The overlying strata failure zone includes zones of tensile fractures, shear failures, and tensile shear failures. In other words, "tension", "shear" and "Shear and tension failures coexist". Broken rocks in the caving zone reflect mainly the tension effect, while those in the fractured zone reflects mainly the shear effect. Partition of overburden failures created by each stage of mining of the three splits and panel 63005 was not feasible due to the effect of interaction among them. Therefore, the height of overburden failures in this area should be confirmed by the maximum height within the tensile fracture, shear failure and tensile shear failure zones. From Figure 6, the maximum height of overburden failures reached 190m after mining of panel 63005. Its shape was different from the commonly found "Saddle" type. The shear failures occurred in the footwall of $F_{18}$ fault due to the influence of mining; this area can be regarded as the "bed separation space". Therefore, it can be confirmed by numerical simulation method that the maximum height of overburden failures was 190m, which was 7.7 times of equivalent mining height. The bed separation space occurred in the footwall of the $F_{18}$ fault, matching the results obtained by EH-4 surveys.

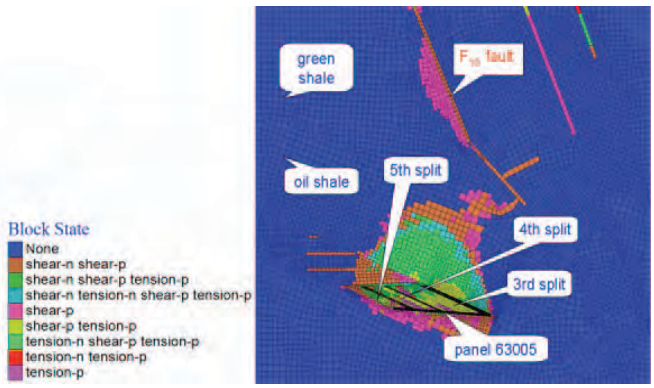



**Figure 6. Distribution of plastic zone after mining of panel 63005.**

## CONCLUSION

(1) EH-4 magnetotelluric method was successfully applied to confirm the overburden failure range and evolution of water flowing fractured zone and bed separation space in complex extra thick coal seam conditions in different mining phases in Laohutai coal mine, China. Prior to mining of panel 63005, the overburden failure height of all the three coal splits was 120m-170m, 6.2-8.7 times of the equivalent mining height with an average of 7.45 times. After mining of panel 63005, the overburden failure height in the same area was 150m-220m, 6-8.8 times of the equivalent mining height with an average of 7.4 times. In addition, bed separation space was found in both the hanging wall and footwall of the $F_{18}$ fault after mining of panel 63005.

(2) Theoretical analysis determined that the overburden failure height of the three coal splits was 135.8m-194m prior to mining of panel 63005; and that it increased to 173.6m-248m after mining of panel 63005. It was therefore compatible to that by EH-4 surveys.

(3) FLAC$^{3D}$ numerical simulation also determined that the maximum height of overburden failure of the three coal splits was 190m after mining of panel 63005, 7.7 times of the equivalent mining height; and that bed separation space occurred in the footwall of the $F_{18}$ fault, matching the results obtained by EH-4 surveys.

(4) Based on the results of field surveys and theoretical analyses, the height of overburden failure in Laohutai coal mine was 7.4 times of the equivalent mining height during both sand backfilling mining stage or the fully-mechanized top coal caving mining stage. After mining of panel 63005, bed separation structure occurred in the hanging wall and footwall of the $F_{18}$ fault.

## REFERENCES


Wang X.Z., Xu J.L., Zhu W.B. (2012). Influence of primary key stratum structure stability on evolution of water flowing fracture. Journal of China Coal Society, 37(4), pp. 606-612 (in Chinese).

Chen R.H., Bai H.B., Feng M.M. (2006). Determination of the Height of Water Flowing Fractured Zone in Overburden Strata Above Fully-Mechanized Top-Coal Caving Face. Journal of Mining & Safety Engineering, 23(2), pp. 220-223 (in Chinese).

Jing J.D., Shi Q.L., Li Z.L., et al. (2006). Mechanism of Water-Inrush from Roof in Huafeng Mine. Journal of China University of Mining & Technology, 35(5), pp. 642-647 (in Chinese).

Zhu W.B., Wang X.Z., Kong X., et al. (2009). Study of Mechanism of Stope Water Inrush Caused by Water Accumulation in Overburden Separation Areas. Chinese Journal of Rock Mechanics and Engineering, 28(2), pp. 306-311 (in Chinese).

Xu J.L., Zhu W.B., Wang X.Z. (2012). New method to predict the height of fractured water-conducting zone by location of key strata. Journal of China Coal Society, 37(5), pp. 762-769 (in Chinese).

Xu J.L., Wang X.Z., Liu W.T. et al. (2009). Effects of Primary Key Stratum Location on Height of Water Flowing Fracture Zone. Chinese Journal of Rock Mechanics and Engineering, 28(2), pp. 380-385 (in Chinese).

Liu G., Zhang H.X., Liu Z.G., et al. (2013). Observation and simulation research on development features of overlying strata failure in conditions of fully-mechanized top-coal caving mining under river. Journal of China Coal Society, 38(6), pp. 987-993 (in Chinese).

Zone. Coal Technology, 30(8), PP.1-2(in Chinese).

Liu J.X., Luo X., Tong X.Z., et al. (2012). Joint analysis of EH4 data in time-frequency domain and application in gob areas of coal mine. Progress in Geophysics, 27(5), pp. 2160-2167 (in Chinese).

Cai S., Liu J.X., Hu Z.J., et al. (2011). Application of EH4 Electric Conductivity Imaging System to Coal Goaf. Chinese Journal of Engineering Geophysics, 8(6), pp. 687-691 (in Chinese).

Ye Y.X., Deng J.Z., Fang G.X. (2011). The Test Research of High Frequency Magnetotelluric Sounding to Reservoir Structure Survey: Taking the Fuzhou Geothermal Area in Jiangxi Province as an Example. Geology and Exploration, 47(4), PP.649-653 (in Chinese).

Xu B.S., Wang E.D., Chen Q.K., et al. (2006). Determination of Coal Mine Gob Edges by EH-4 System. Journal of Northeastern University (Natural Science), 27(7), pp. 810-813 (in Chinese).

Yu C.T., Liu H.F., Gao J.P. (2008). The Experimental study on the Dual frequency induced polarization method detecting coal mine gob. Progress in Geophysics, 23(5), pp.1603-1609 (in Chinese).

Dai Q.W., Hou Z.C., Chai X.C. (2013). Application of transient electromagnetic method and EH-4 to investigation of mined-out areas of molybdenum deposits. Progress in Geophysics, 28(3), pp. 1541-1546 (in Chinese).

Wang F., Guo X.J., Yang Z.H. (2012). Detection of shallow bauxite mined area and induced ground subsidence prediction. Progress in Geophysics, 27(4), pp. 1769-1774 (in Chinese).

Li J.S., Qi W., Xu W.D. (2012). Effective method for exploring hot water-For example EH4 conductivity imaging system finding hot water in Nima county of Tibet. Progress in Geophysics, 27(3), pp. 1243-1253 (in Chinese).

Liang T., Yuan W., Lu R. (2012). EH4 Magnetotelluric section from Guxian Reservior to Quanbaoshan Mountain, southwest Luoning County, western Henan Province, and its implications for deep ore prospecting. Progress in Geophysics, 27(5), pp. 2177-2182(in Chinese).

Wang C., Dong P., Sun B., et al. (2009). Application of EH4 Electromagnetic Eounding in the Deep and Peripheral of Chengmenshan M ining Area, Jiangxi. Geology and Exploration, 45(6), pp. 741-747 (in Chinese).

Tan H.Y., Lv J.C., Liu G.X., et al. (2011). Application of the Audio-Frequency Magnetotelluric Method to Search for Concealed Ore bodies in Southeastern Hubei Province. Geology and Exploration, 47(6), 1133-1141 (in Chinese).

Hu W., Xu Z.M., Liu G.X., et al. (2013). Research on development of water flowing fractures in soft overlying strata for coal mining under sea. Journal of China Coal Society, 38(8), pp. 1339-1344 (in Chinese).

# AUTHOR'S INDEX


**A**

Agioutantis, Z. 170, 312

**B**

Bahrampour, S. 293
Bai, J. 352
Barbato, J. 71
Barkley, D. 312
Benton, D. 221
Berger, L. 216
Bhagwat, A. 175
Bowler, J. 134, 228
Brannon, P. 71
Bucks, P. 47

**C**

Cabral, R. 298
Campbell, R. 27
Chen, J. 189
Chen, Y. 373
Clingan, J. 199
Collins, C. 293
Compton, C. 87
Cook, T. 204

**D**

Dao, V. 352
Deng, J. 236
Dou, J. 331
Duffty, H. 228

**E**

Elrick, S. 312
Eskandar, H. 324
Esterhuizen, E. 1
Esterhuizen, G. 261

**F**

Farrell, S. 182
Faulkner, D. 63, 124
Ferster, M. 185

**G**

Gao, X. 331
Garcia, A. 228
Gearhart, D. 87
Golasowski, J. 80
Gramlich, P. 199
Griffith, W. 243
Guazelli, S. 298
Gu, R. 22

**H**

Han, J. 379
Hanson, B. 63
Harris, K. 165
Hasenfus, G. 35, 54
Heasley, K. 170
Hebblewhite, B. 71
He, M. 13
He, P. 13
Hongdong, F. 338
Hongzhen, Z. 338
Hosseini, N. 324
Hudeček, V. 80
Huo, L. 373

**I**

Iverson, S. 221

**J**

Johnson, J. 221
Jones, T. 87, 113

**K**

Kallu, R. 272
Karmis, M. 312
Kazhong, D. 338
Keffeler, E. 272
Kendall, W. 185
Kent, L. 134
King, D. 175
Klabis, L. 248
Kleiterp, P. 144
Klemetti, T. 1, 113
Kloc, L. 248
Koppe, J. 298
Kostecki, T. 105
Kulatilake, P. 13, 236
Kumar, R. 158

**L**

Lee, M. 193
Li, G. 71, 379
Liu, A. 344
Liu, D. 13
Li, W. 352
Li, X. 63
Li, Y. 360, 367
Lu, J. 35

**M**

Ma, J. 124
Ma, L. 63
Malesza, A. 248
Mark, C. 150
Martin, L. 221
Ma, X. 344
McCarter, M. 209
Mikoláš , M. 80
Mills, K. 71, 304
Minoski, T. 87
Misa, R. 255
Mishra, A. 105
Mohamed, K. 113
Mohanty, S. 193
Mondring, M. 216
Moore, D. 134
Morrow, G. 261
Murphy, M. 261

**N**

Naeimipour, A. 284, 293
Newman, D. 41
Nicholson, M. 71

**O**

Ochsner, R. 63, 87
Oler, R. 189
Oliveira, S. 298
Oraee, B. 324
Oraee, K. 324
Osouli, A. 278
Ozbay, U. 22

**P**

Pan, E. 243
Papst, T. 320
Peng, S. 8, 360
Perry, K. 165
Peterson, S. 47
Pile, J. 232
Preddy, A. 228
Preusse, A. 320
Prusek, S. 248
Pugh, J. 47

**R**

Raffaldi, M. 165
Ramani, S. 158
Rashed, G. 8
Rong, H. 379
Ross, T. 193
Rostami, J. 284, 293

**S**

Schloemer, W. 80
Seedsman, R. 97
Sell, J. 105
Shaffer, A. 232
Shafii, I. 278
Sherizadeh, T. 236
Shu, B. 236
Singh, A. 158
Singh, R. 158
Spearing, A. 105
Sroka, A. 255
Stankus, J. 63, 124, 204
Stull, L. 35, 54
Sub, T. 204
Su, D. 35, 54
Sumner, J. 1

**T**

Tajduś, K. 255
Taushanoff, R. 105
Tulu, I. 1
Tu, S. 344

**V**

Vandergrift, T. 193
Vass, C. 47
Vochta, R. 80

**W**

Walentek, A. 248
Walker, S. 134
Walsh, R. 71
Wang, F. 344
Wang, H. 331
Wang, j. 367
Wang, J. 360
Wang, L. 367
Warren, S. 272
Watters, R. 272
Wempen, J. 209
Wu, Y. 331

**X**

Xie, P. 331

**Y**

Yang, B. 367
Yang, F. 379
Yu, B. 373
Yun, D. 331

**Z**

Zeng, Y. 331
Zhang, H. 373, 379
Zhang, P. 47, 170
Zhang, Z. 344
Zhao, Y. 243
Zheng, J. 236
ZHU, Z. 373
Zingano, A. 298